

11th CIRP Conference on Photonic Technologies [LANE 2020]

Edited by M. Schmidt, F. Vollertsen, E. Govekar

Volume 94,

Pages 1-966 (2020)

© 2020 Elsevier B.V. All rights reserved.

This journal and the individual contributions contained in it are protected under copyright by Elsevier B.V. and the following terms and conditions apply to their use:

Photocopying

Single photocopies of single articles may be made for personal use as allowed by national copyright laws. Permission of the Publisher and payment of a fee is required for all other photocopying, including multiple or systematic copying, copying for advertising or promotional purposes, resale, and all forms of document delivery. Special rates are available for educational institutions that wish to make photocopies for non-profit educational classroom use.

For information on how to seek permission visit www.elsevier.com/permissions or call: (+44) 1865 843830 (UK) / (+1) 215 239 3804 (USA).

Derivative Works

Subscribers may reproduce tables of contents or prepare lists of articles including abstracts for internal circulation within their institutions. Permission of the Publisher is required for resale or distribution outside the institution. Permission of the Publisher is required for all other derivative works, including compilations and translations (please consult www.elsevier.com/permissions).

Electronic Storage or Usage

Permission of the Publisher is required to store or use electronically any material contained in this journal, including any article or part of an article (please consult www.elsevier.com/permissions).

Except as outlined above, no part of this publication may be reproduced, stored in a retrieval system or transmitted in any form or by any means, electronic, mechanical, photocopying, recording or otherwise, without prior written permission of the Publisher.

Notice

No responsibility is assumed by the Publisher for any injury and/or damage to persons or property as a matter of products liability, negligence or otherwise, or from any use or operation of any methods, products, instructions or ideas contained in the material herein. Because of rapid advances in the medical sciences, in particular, independent verification of diagnoses and drug dosages should be made.

Although all advertising material is expected to conform to ethical (medical) standards, inclusion in this publication does not constitute a guarantee or endorsement of the quality or value of such product or of the claims made of it by its manufacturer.

Preface

Welcome to our 11th LANE, the first virtual LANE conference.

In recent years LANE has developed into the event it is today thanks to your excellent contributions. Intensifying the exchange between photonic research and its application is our ongoing task. We do this via organizing a platform for a fruitful exchange of relevant content and via encouraging you building contacts in the community.

This year the situation around Covid-19 challenged us to create a virtual conference that still is a LANE conference, means transferring its main assets into the virtual world. Thus, LANE 2020 is more than just attending a video call and viewing a live stream. You can expect high-class keynote speakers, plenary discussions on hot topics, a socializing event, a virtual bar, discussion and breakout rooms, attendees' profiles, a sponsors' platform and some more.

We encourage you to see LANE 2020 as a chance to meet, to talk, to discuss, and to create new ideas to bring Photonic Technologies forward also in these challenging times.


Our proceedings shall again provide important information and be inspiration for future topics.

Now let us look forward to interesting scientific and industrial presentations on developments in the traditional topics of laser material processing, but also on upcoming technologies such as E-Mobility or Additive Manufacturing – not forgetting the social aspects that make our community strong.

Erlangen, September 2020
The Editors



M. Schmidt



F. Vollertsen



E. Govekar

International Review Committee

- H. Amler**, Photon Energy GmbH, Germany
M. Apel, Access e.V., Germany
C. B. Arnold, Princeton University, USA
P. Aubry, CEA/Université Paris-Saclay, France
S. Barcikowski, University of Duisburg-Essen, Germany
P. Bartolo, The University of Manchester, United Kingdom
J. P. Bergmann, Technische Universität Ilmenau, Germany
D. Bourell, The University of Texas at Austin, USA
M. Brandt, RMIT University, Australia
B. Chichkov, Laser Zentrum Hannover e.V., Germany
S. Christiansen, Fraunhofer IKTS, Germany
A. Clare, The University of Nottingham, United Kingdom
B. Colosimo, Polytechnic University of Milan, Italy
G. Dearden, University of Liverpool, United Kingdom
P. Delaporte, Aix-Marseille Université, France
I. Drstvenšek, University of Maribor, Slovenia
D. Drummer, Friedrich-Alexander-Universität Erlangen-Nürnberg, Germany
J. Duflou, KU Leuven, Belgium
C. Emmelmann, Hamburg University of Technology, Germany
R. Fabbro, Arts et Métiers ParisTech, France
E. Ferraris, KU Leuven, Belgium
A. Fougères, Institut National d'Optique (INO), Canada
T. Frick, Technische Hochschule Nürnberg Georg Simon Ohm, Germany
P. Galarneau, Institut National d'Optique (INO), Canada
E. Govekar, University of Ljubljana, Slovenia
T. Graf, University of Stuttgart, Germany
C. Grigoropoulos, University of California at Berkeley, USA
D. P. Hand, Heriot-Watt University, United Kingdom
T. Hausotte, Friedrich-Alexander-Universität Erlangen-Nürnberg, Germany
G. Hennig, Daetwyler Graphics AG, Switzerland
P. Hoffmann, ERLAS Erlanger Lasertechnik GmbH, Germany
R. Holtz, University of Applied Sciences and Arts Northwestern Switzerland, Switzerland
H. Huber, Munich University of Applied Sciences, Germany
Y. Ito, Nagaoka University of Technology, Japan
A. Jesacher, Medical University of Innsbruck, Austria
W. Jüptner, Universität Bremen, Germany
S. Kaierle, Laser Zentrum Hannover e.V., Germany
A. Kaplan, Luleå University of Technology, Sweden
M. Kogel-Hollacher, Precitec GmbH & Co. KG, Germany
D. Kracht, Laser Zentrum Hannover e.V., Germany
P. Krakhmalev, Karlstad University, Sweden
J.-P. Kruth, KU Leuven, Belgium
V. Kujanpää, Lappeenranta University of Technology LUT, Finland
M. Lang, FSKZ e.V., Germany
M. Lanzetta, University of Pisa, Italy
J. K. Larsson, Autokropolis Engineering, Sweden
B. Lauwers, KU Leuven, Belgium
G. Levy, TTA Technology Turn Around, Switzerland
C. Leyens, Technische Universität Dresden, Germany
L. Li, The University of Manchester, United Kingdom
K. Löffler, TRUMPF Lasertechnik GmbH, Germany

J. Meijer, University of Twente, The Netherlands
J. Mergheim, Friedrich-Alexander-Universität Erlangen-Nürnberg, Germany
C. Merklein, Schaeffler Technologies AG & Co. KG, Germany
M. Merklein, Friedrich-Alexander-Universität Erlangen-Nürnberg, Germany
I. Miyamoto, Osaka University, Japan
C. L. Molpeceres Alvarez, Technical University of Madrid, Spain
S.-J. Na, Xi'an Jiaotong University, China
B. Neuenschwander, Bern University of Applied Sciences, Switzerland
S. Nolte, Friedrich Schiller University Jena, Germany
F. Oefele, BMW AG, Germany
Y. Okamoto, Okayama University, Japan
S. Olschok, RWTH Aachen University, Germany
L. Orazi, University of Modena & Reggio Emilia, Italy
A. Ostendorf, Ruhr-Universität Bochum, Germany
A. Otto, Vienna University of Technology, Austria
L. Overmeyer, Laser Zentrum Hannover e.V., Germany
F. Palm, Airbus Defence and Space GmbH, Germany
M. Pereira, Universidade Federal de Santa Catarina, Brazil
D. Petring, Fraunhofer ILT, Germany
F. E. Pfefferkorn, University of Wisconsin-Madison, USA
A. Piqué, U.S. Naval Research Laboratory, USA
P. Plapper, University of Luxembourg, Luxembourg
J. M. Pou, University of Vigo, Spain
R. Ramsayer, Robert Bosch GmbH, Germany
U. Reisgen, RWTH Aachen University, Germany
M. Rethmeier, Bundesanstalt für Materialforschung und -prüfung, Germany
G.-W. Römer, University of Twente, The Netherlands
A. Salminen, Lappeenranta University of Technology LUT, Finland
P. Salter, University of Oxford, United Kingdom
M. Schaper, Paderborn University, Germany
D. Schmid, AUDI AG, Germany
M. Schmidt, Friedrich-Alexander-Universität Erlangen-Nürnberg, Germany
R. Schmitt, Fraunhofer IPT, Germany
W. Schulz, Fraunhofer ILT, Germany
V. Schulze, Karlsruhe Institute of Technology, Germany
J. Sehart, Ruhr-Universität Bochum, Germany
I. Smurov, École Nationale d'Ingénieurs de Saint-Etienne, France
K. Sugioka, RIKEN Center for Advanced Photonics, Japan
H.-K. Tönshoff, Leibniz Universität Hannover, Germany
E. Toyserkani, University of Waterloo, Canada
J. Tremel, Robert Bosch GmbH, Germany
G. Turichin, Peter the Great St.Petersburg Polytechnic University, Russia
F. Vollertsen, BIAS GmbH, Germany
K. Wegener, ETH Zurich, Switzerland
P. Weidinger, Brose Fahrzeugteile GmbH & Co. KG, Germany
G. Witt, University of Duisburg-Essen, Germany
K. Wudy, Technische Universität München, Germany
M. F. Zäh, Technische Universität München, Germany
Z. Zalevsky, Bar-Ilan University, Israel
M. Zhong, Tsinghua University, China
D. Zibar, Technical University of Denmark, Denmark

Conference Organization

M. Schmidt, Friedrich-Alexander-Universität Erlangen-Nürnberg, Germany

S. Roth, Bayerisches Laserzentrum GmbH, Germany

H.-J. Krauß, Bayerisches Laserzentrum GmbH, Germany

M. Döring, Friedrich-Alexander-Universität Erlangen-Nürnberg, Germany

S. Wiedenmann, Bayerisches Laserzentrum GmbH, Germany

K. Meyerhöfer, Bayerisches Laserzentrum GmbH, Germany

M. Kestler, Bayerisches Laserzentrum GmbH, Germany

The 11th CIRP Conference on Photonic Technologies [LANE 2020] is organized by

Bayerisches Laserzentrum GmbH (blz)



in cooperation with

Institute of Photonic Technologies (LPT)
Friedrich-Alexander-Universität Erlangen-Nürnberg



LANE 2020 is funded by the Deutsche Forschungsgemeinschaft (DFG, German Research Foundation) – project number 448435784, and is supported by



International Union of Pure and Applied Physics

To secure IUPAP sponsorship, the organizers have provided assurance that the 11th CIRP Conference on Photonic Technologies [LANE 2020] will be conducted in accordance with IUPAP principles as stated in the IUPAP resolution passed by the General Assembly in 2008 and 2011. In particular, no bona fide scientist will be excluded from participation on the grounds of national origin, nationality, or political considerations unrelated to science.



Erlangen Graduate School in Advanced Optical Technologies



German Academic Association for Production Technology



German Scientific Laser Society

11th CIRP Conference on Photonic Technologies [LANE 2020] on September 7-10, 2020

On the relationship between the bulge effect and the hot cracking formation during deep penetration laser beam welding

Antoni Artinov^{a,*}, Marcel Bachmann^a, Xiangmeng Meng^a, Victor Karkhin^b, Michael Rethmeier^{c,a,b}

^a *Bundesanstalt für Materialforschung und -prüfung (BAM), Unter den Eichen 87, 12205 Berlin, Germany*

^b *Peter the Great St. Petersburg Polytechnic University, Department of Welding and Laser Technologies, 195251 St. Petersburg, Russia*

^c *Technische Universität Berlin, Departments of Machine Tools and Factory Management, 10623 Berlin, Germany*

- Keynote Paper -

* Corresponding author. Tel.: +49 3081043101; E-mail address: Antoni.Artinov@bam.de

Abstract

Recent studies have confirmed the widening of the weld pool interface, known as a bulge effect, during deep penetration high power laser beam welding. The link between such geometric particularities of the weld pool shape and the hot cracking phenomena is significant. The present work seeks to extend the level of understanding by investigating their relationship. A coupled multiphysics, multiscale numerical framework is developed, comprising a series of subsequent analyses. The study examines the influences of the bulge on the three most dominant effects causing hot cracking, namely the thermal cycles, the mechanical loading, and the local microstructure. The bulge in the weld pool shape forms approximately in the middle of the plate, thus correlating with the location of hot cracking. It increases the hot cracking susceptibility by enhancing the three dominant effects. The numerical results are backed up by experimental data.

© 2020 The Authors. Published by Elsevier B.V.

This is an open access article under the CC BY-NC-ND license (<http://creativecommons.org/licenses/by-nc-nd/4.0/>)

Peer-review under responsibility of the Bayerisches Laserzentrum GmbH

Keywords: Hot cracking; Bulge effect; Numerical modelling; Laser beam welding; Deep penetration

1. Introduction

Nowadays, the laser beam welding process is an established high-performance joining technology. It brings several technical advantages compared to conventional arc welding methods, such as locally highly concentrated and precise heat input, allowing welding with minimal distortion of large-area components [1]. Thus, laser beam welding is a reliable state of the art joining process, especially for the production of long joints on relatively thin sheets, e.g., rail vehicles, containers, and cars.

With the rapidly increasing availability of higher laser power of up to 100 kW [2], applications in the sheet thickness range

of more than 20 mm are reachable [3, 4]. However, as earlier and latest research results show, with increasing welding speed and sheet thickness, defects occur that are untypical for unalloyed and low-alloy steels under conventional welding conditions. These include, above all, hot cracking in the inner part of the weld metal, especially in the area where the crystallization fronts collide [5-8]. The nature of such solidification cracks is highly complex, and only a few material phenomena from the welding field were so thoroughly investigated in the last five decades [9, 10]. The cracks initiate in the fusion zone, at temperatures above the solidus temperature. Solidification shrinkage and thermal contraction lead to a localized stress/strain across the grain boundary liquid

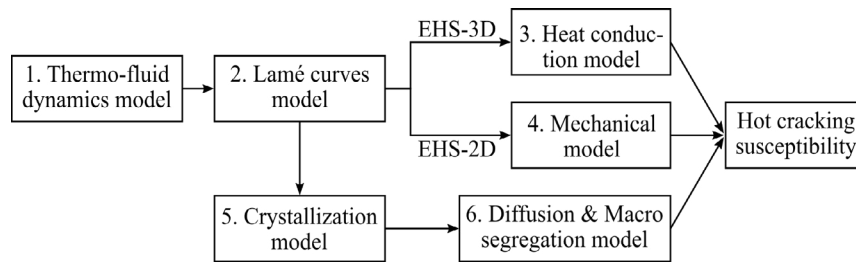


Fig. 1. Scheme of the numerical framework using the concept of an equivalent heat source (EHS) to couple the models

film, which in turn causes their formation [11, 12]. The presence of elements constituting low melting eutectics, such as sulfur and phosphorus and their segregation, can further increase the hot cracking susceptibility by extending the solidification temperature range [13, 14].

A detailed literature review shows that the complex interactions between the thermal, mechanical, and metallurgical factors determine the cracking behavior of the welded part [15].

All these factors are strongly coupled and depend on the weld pool shape and vice versa. The underlying physical phenomena in the weld pool are long known to be crucial for the formation of defects during the solidification stage of the process, e.g., hot cracking [16]. Studies on deep penetration electron beam welding from the early 1980s demonstrate the importance of the weld pool shape on the formation of solidification cracking. The authors examined a widening of the weld pool interface, nowadays referred to as a bulge region, with a delay in the solidification behavior, which in turn led to the formation of cracks within this region [17]. The results show a link between the bulge and the defect occurrence [18, 19]. The influence of the bulge on the thermal cycles and thus on the stress/strain distribution in the cracking region was investigated in [20, 21]. The strong correlation between the bulge region in the weld pool and the formation of hot cracking was confirmed in [22, 23].

The observation and investigation of the bulge effect during the welding process is a highly challenging task due to the optical inaccessibility. Despite this fact, a bulge region can be found in several numerical works, even though not being the object of analysis [24-30]. The latest research experimentally proves the existence of a bulge during laser beam welding of thick sheets by using a specially designed set-up with a transparent quartz glass [31, 32]. To the best of the authors' knowledge, there are only a few research results published on the occurrence of bulging during welding with high power lasers. The correlation between the cracks and the bulge seems to be significant and yet poorly understood. Most attempts to connect the bulging phenomena to hot cracking concentrate on one or two of the dominant factors for crack formation, e.g., the solidification range, the critical stress/strain, and do not examine their complex interactions. Considering the current state of knowledge, the need arises to expand the understanding of these phenomena and their interactions.

The present work seeks to deepen the level of understanding by investigating their relationship. A coupled multiphysics, multiscale numerical framework is developed, comprising a series of subsequent analyses. The study examines the

influences of the bulge on the three most dominant effects causing hot cracking, namely the thermal cycles, the mechanical loading, and the local microstructure.

2. Numerical framework

Altogether, six numerical models are linked by one-dimensional coupling in the proposed numerical framework, see Fig. 1.

In step (1), the bulge effect is reproduced in a steady-state thermo-fluid dynamics problem considering the coupling between the melt flow and the heat transfer on a local level. The steady-state weld pool shape is a result of step (1), which according to [33, 34] can be used as an equivalent heat source (EHS) to obtain the global temperature cycles. Step (2) presents a novel approach allowing a 3D reconstruction of the weld pool interface to an EHS. The 3D and 2D temperature fields calculated with the EHS are subsequently used in steps (3) and (4), respectively. The former is used to analyze the steady-state solidification behavior of the melt and the latter as a thermal load for the 2D mechanical model described in step (4). In (5), a technique for calculating the main crystallization parameters, e.g., the geometry of the crystal axis, the growth rate of the crystal, and its cross-sectional area, based on the outcomes from (1) and (2) is derived. The results from (5) are finally utilized in a combined diffusion and macro segregation model in step (6). The model estimates the extended solidification temperature range due to a solute enrichment in the liquid, ahead of the solid-liquid interface. Further details on the single steps of the numerical framework are described in the following subsections.

2.1. Thermo-fluid dynamics model

The thermo-fluid dynamics problem aims to obtain a steady-state solution for a weld pool interface including a bulge region, as experimentally observed in [32]. It includes the coupled solution of the mass and energy conservation equations, the Navier-Stokes equations, and the transport equations for the turbulent kinetic energy and the turbulent dissipation rate. The model is based on several previous works with some further improvements and modifications [35-37].

Here some of the main assumptions will be discussed, whereby further details can be obtained from [38]. In the proposed set-up, the workpiece moves relative to the origin of the Cartesian coordinate system which coincides with the origin of the laser source. A fixed keyhole geometry is utilized in the

model based on the assumption that the recoil pressure in the keyhole is perfectly balanced by the surface tension force. The surface temperature of the keyhole is replaced by the evaporation temperature of the material. This assumes that the temperature inside the keyhole should be at least equal or higher than the evaporation temperature of the material. The approach does not allow to directly consider the effects of the focal position and multiple reflections on the energy absorption. Thus, it is advisable to increase the horizontal cross-sectional area of the conical keyhole in the middle of the plate. This enhances the formation of a bulge in the weld pool shape, especially in the narrow regions around the keyhole. The model considers the most relevant physical effects, such as Marangoni and natural convection, latent heat of fusion, and temperature-dependent material properties up to evaporation temperature.

2.2. Reconstruction of the weld pool interface by Lamé curves

The reconstruction of the numerically obtained weld pool geometry is realized with Lamé curves (superellipses). For this the solid-liquid interface from 2.1 is discretized by a set of data points. The procedure starts by dividing the data into a certain number of levels along the thickness direction of the weld pool. The vertical distance between the planes is variable along the thickness direction improving the approximation of the interface even in the more complex-shaped areas influenced by the thermo-capillary driven flow. The data points in each level are approximated by two Lamé curves, one for the front and one for the rear part of the weld pool.

Every 2D contour in each plane is sufficiently defined by eight parameters. To obtain these at least eight data points are required. However, the accuracy of the approximation is improved by taking more data points. The fitting procedure of the curves makes use of the least square method to optimally reproduce the 2D contour for each level. The algorithm provides the parameters for a single plane and is repeated for each plane. The data in the gaps between two planes are obtained by interpolation between the known values or polynomial fitting. Further details can be found in [39].

2.3. Heat conduction model with an equivalent heat source

The calculated shape parameters of the weld pool interface define the equivalent heat source. This is subsequently applied in a global heat conduction simulation to compute the temperature fields. The algorithm detects the nodes within the EHS and replaces their temperature values by the solidus temperature, thus, assuring an equivalent energy input. The EHS moves with the processing speed in the welding direction. In the 2D case the EHS is moved perpendicular through the two-dimensional plane of interest. This technique allows the coupling of the local thermo-fluid dynamics simulation and the global temperature field. Hence, the influence of the bulge in the weld pool on the thermal history of the part can be investigated.

In addition, it offers high accuracy and efficiency by solving the heat transfer problem during welding compared to common volumetric heat sources, such as the cylindrical heat source model or the conical Gaussian heat source model [21]. More

information on the concept of an equivalent heat source can be found in [38-40].

2.4. Mechanical model

A 2D plane strain model is used to examine the mechanical loading on the part. The 2D temperature field from 2.3 is applied as a thermal loading. Hence, the effect of the weld pool shape, and particularly of the bulge region, on the temporal and spatial distribution of the stress/strain can be studied in-depth. The model considers solid-solid phase transformations from ferrite (base material) to austenite during heating and austenite to martensite during cooling. The boundary conditions were obtained experimentally by using the concept of restraint intensity [41]. Therefore, the model considers the influence of the stiffness of the solid material around the weld pool on the stress/strain development during solidification. A full description of the model can be found in [21].

2.5. Crystallization model

The crystallization model in the presented numerical framework is based on previous research from [42]. It considers the movement of the solidification front (tail part of the weld pool), reconstructed numerically by Lamé curves, see 2.2, using the set of data points computed in 2.1. The movement and the shape of the solidification front determine the rate and direction of crystallization, which are crucial factors for the final microstructure of the weld and the solute enrichment ahead of the solid-liquid interface. The model is extended numerically to three dimensions based on the following assumptions:

- The crystallization process reaches a steady state, where the solidification front does not change with time.
- The solidification front is defined by the liquidus isotherm.
- The local decrease of the liquidus temperature due to the rising impurity concentration is neglected.
- The direction of crystallization coincides with the direction of the temperature gradient.

2.6. Diffusion & Macro segregation model

Generally, the concentration of impurities, such as sulfur, rises ahead of the solidification front. Thus, the liquidus temperature of the material decreases locally having a great influence on the hot cracking resistance. To determine the local microstructure the mass transfer problem for the sulfur element needs to be solved. The challenge of obtaining a solution to this problem is the concentration discontinuity at the solid-liquid interface, defined by the distribution coefficient. This challenge is overcome by making use of the concept of mass transfer potential and solubility of the impurity element [43]. The mathematical formulation presented in [43] is further extended to consider temperature-dependent solubility and diffusion coefficients of the sulfur element in both solid and liquid state. The basic assumptions remain hereby unchanged. The model uses the outcomes from 2.1-2.3 and 2.5, the reconstructed shape of the solidification front, the crystal axis and cross-

sectional profile, the solidification rate, the space and time-dependent temperature distribution along the crystal axis, etc. as input data.

3. Experimental procedures

The numerically obtained results were validated by experimental data from several experiments. These included temperature measurements with thermocouples, thermal imaging cameras, and a high-speed camera. The geometrical dimensions of the computed weld pool were compared to metallographic cross-sections along the weld and numerically estimated weld end crater shape [44]. The restraint intensity was obtained by a Controlled Tensile Weldability test (CTW). Additional horizontal sections on the top surface were used to validate the crystallization model. Further details about the single experiments is given in the references cited in 2.1-2.6.

4. Results & Discussion

Three factors, namely the thermal cycles, the mechanical loading, and the local microstructure are identified as decisive for the determination of the cracking behavior of the welded part. The results in the following subsections are structured in such a way that the influence of the bulge effect on every single factor is estimated and analyzed. Furthermore, their correlation to the decrease in hot cracking resistivity is studied.

4.1. Influence of the bulge on the thermal factor

The bulge effect was numerically obtained in the thermo-fluid dynamics model presented in 2.1. It is part of the three-dimensional weld pool interface computed by the model, see Fig. 2a. The results show a bulge effect in both the cross and longitudinal sections, see Fig. 2b and 2c. The shape and size of the bulge are mainly defined by the thermo-capillary effect in the upper and lower part of the weld pool, highlighted in Fig. 2b. These flows ensure mass conservation by bringing part of the cooled material back to the vicinity of the keyhole, causing two necking areas. The combination of these flows, also known as Marangoni flows, and the relative movement of the laser source to the workpiece results in the formation of this geometrical particularity.

For the analysis of the bulge on the thermal factor the results from both the local temperature field calculated in 2.1 and the global temperature field calculated in 2.3 can be used. Here the results from 2.1 are preferred since they provide additional data

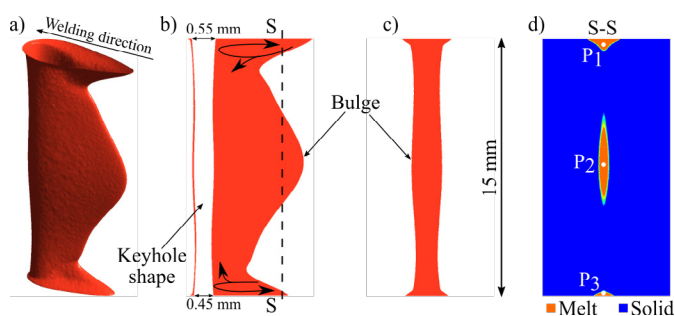


Fig. 2. Results from the thermo-fluid dynamics model: a) three-dimensional weld pool interface, b) longitudinal section of the weld pool in the symmetry plane, c) cross-section of the weld pool and d) liquid metal in the cross-section S-S according to [21, 32]

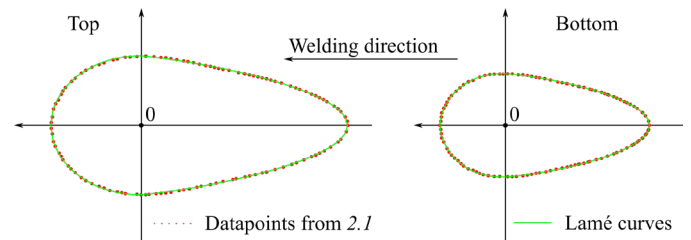


Fig. 3. Reconstructed weld pool shape on the top and bottom surfaces by Lamé curves according to [39]

from inside the weld pool. Therefore, an exemplary reconstruction of the top and bottom surfaces of the weld pool interface by Lamé curves, described in 2.2 and subsequently applied in 2.3 as an EHS, is shown in Fig. 3.

The steady-state temperature field provides information about the regions of the weld pool which solidify at last. Such regions are of main interest since the formation of hot cracking requires the presence of a liquid film between the grain boundaries. Thus, any geometrical characteristic of the weld pool interface can play a crucial role in the hot cracking formation.

A detailed analysis of the steady-state temperature field and the liquid-fraction shows how critical the bulge region can be. A longitudinal view of the weld pool geometry is shown in Fig. 2b. The solidification behavior of the liquid metal is studied in the cross-section S-S, see Fig. 2d. Three regions, highlighted by the points P₁, P₂, and P₃ show a delay in solidification. The delay in the middle of the cross-section is due to the bulge observed in the longitudinal section.

The presence of a liquid film between the grain boundaries leads to a decrease in the cracking resistivity in these regions. Thus, the bulge region can be identified as particularly susceptible to hot cracking, as it will be shown in the following subsections.

4.2. Influence of the bulge on the mechanical factor

The study of the influence of the bulge on the mechanical factor is based on the localized stress/strain across the grain boundary liquid film, which in turn causes the formation of cracks. In general, both localized stress and strain can be used to estimate the hot cracking susceptibility. Nevertheless, considering the high sheet thickness of the sample, the stress is used to evaluate the influence of the bulge on the hot cracking susceptibility in the presented model.

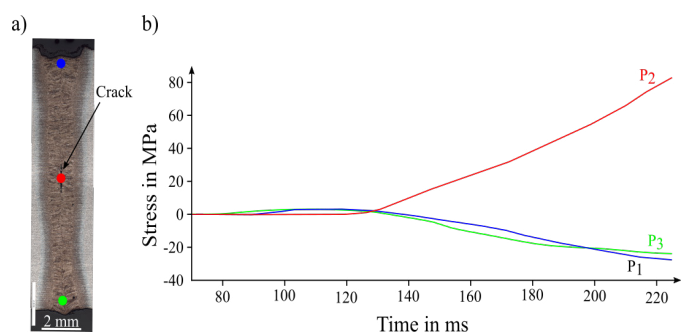


Fig. 4. a) An exemplary metallographic cross-section for 12 mm thick weld with a longitudinal crack and b) temporal distribution of the transversal horizontal stress at the locations P₁, P₂, and P₃ according to [21]

In 4.1 three regions are identified as critical since the melt solidifies there at last. Thus, the temporal transversal horizontal and vertical stress evolution during the cooling stage of the process in the three points P_1 , P_2 , and P_3 is studied. These points are marked on a metallographic cross-section with a longitudinal hot crack appearing in the bulge region, see Fig. 4a. The results of the temporal transversal horizontal stress evolution are presented in Fig. 4b. Note, that the stress-time curve at each of the three locations is highlighted by the same color as the corresponding point in Fig. 4a.

As can be seen from Fig. 4b the mechanical behavior at the locations P_1 and P_3 is almost identical. As the material starts solidifying a small increase of a tensile stress appears, which after a short period becomes compressive with a maximum value of approx. -30 MPa. In contrast to that, the transversal horizontal stress in the bulge region remains tensile during the solidification process. It shows a nearly linear increase of up to approx. 80 MPa at the corresponding Fe-S eutectic temperature of around 988 °C. Since the growth direction of the dendrites is opposite to the calculated transversal stresses, a rupture of the liquid film between the grain boundaries in the bulge region is very likely to occur.

4.3. Influence of the bulge on the metallurgical factor

The third dominant effect on hot cracking formation is the metallurgical factor. In general, the accumulation of sulfur ahead of the solid-liquid interface due to segregation and diffusion defines the local microstructure. In regions with locally increased sulfur content the hot cracking resistivity of the material decreases due to the extended solidification temperature range or with other words due to the extended dwell time of the liquid film between the grain boundaries.

In fact, two factors contribute to the local microstructure and material properties. The first factor is the concentration of impurities ahead of the solidification front and the second the direction of crystallization. Crystals converging to a small area contribute to the total local accumulation of sulfur, and thus further decrease the cracking resistivity.

The bulge on the weld pool interface influences both factors. It leads to more complex crystal geometries, irregular solidification rates and crystal cross-sectional profiles. Thus, the state of heterogeneity of the material can exceed the theoretical limit determined by the distribution factor and the initial concentration of the impurity. As an example, the case of sulfur with initial concentration C_0 and distribution factor 0.05 is considered. Assuming a constant solidification rate and cross-sectional profile the theoretical limit of the relative concentration is twenty times C_0 . If the bulge effect on the solidification rate and the cross-sectional profile is included the limit can exceed this factor up to several times.

The impact of the bulge on the second factor is schematically explained in Fig. 5a and 5b. Based on the assumptions made in 2.6 the direction of crystallization coincides with the direction of the temperature gradient. Due to the bulge on the solid-liquid interface the crystals C_1 , and C_3 (from above and below the bulge plane, respectively) will converge in the bulge plane. Thus, the accumulated sulfur ahead of the solid-liquid interface is pushed to the same area, leading to a further rise of the local sulfur concentration. This solidification behaviour is observed in the longitudinal section, see Fig. 5a, as well as in the cross-section, see Fig. 5b.

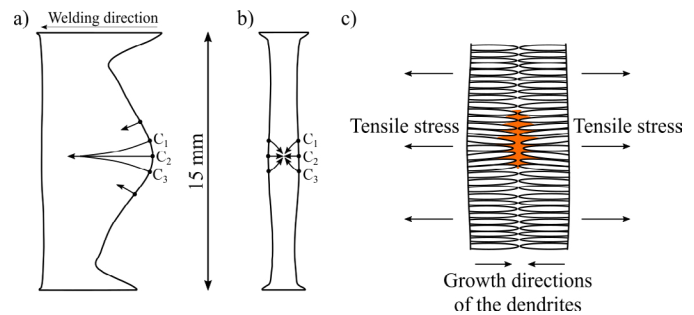


Fig. 5. Schematic projection of the crystal axis on a) the longitudinal section in the symmetry plane, b) the cross-section and c) increased hot cracking susceptibility due to the bulge effect according to [21]

The more sulfur accumulates the longer the dwell time of the liquid film between the grain boundaries will be. The extended dwell time increases the probability for the liquid film to be ruptured by the rising with time tensile stress in the bulge region, calculated in 4.2, see Fig. 5c.

The bulge in the cross-section, see Fig. 5b, has an additional impact on the hot cracking formation. The larger distance between the seam flanks hinders the coalescence of the dendrite tips. The combination of this effect with the local tensile stress is a further indicator of increased hot cracking susceptibility in the bulge region, as shown schematically in Fig. 5c.

Considering all three effects of the bulge region on the local microstructure, its impact is identified to be critical for the cracking susceptibility of the material.

5. Conclusions

A coupled multiphysics, multiscale numerical framework is developed, comprising a series of subsequent analyses. The study examines the influences of the bulge on the three most dominant effects causing hot cracking, namely the thermal cycles, the mechanical loading, and the local microstructure.

The following conclusions are drawn from the obtained numerical and experimental results:

- Fluid flow effects lead to a bulge formation in the weld pool shape approximately in the middle of the plate.
- The bulge on the solid-liquid interface leads to a delay in the solidification behavior in the cracking region (steady-state solidification).
- The temperature loading due to the equivalent heat source results in maximum tensile stress around the melt in the bulge region. This can lead to a possible rupture of the liquid film between the grain boundaries.
- The solidification conditions become even more critical due to the accumulation of sulfur in the bulge region, caused by segregation, diffusion, and predominant crystals growth into the hot-cracking region.
- The bulge in the weld pool shape increases the hot cracking susceptibility by enhancing the three dominant effects.

Acknowledgements

Financial funding by the Deutsche Forschungsgemeinschaft (DFG, German Research Foundation) - project Nr. 411393804 (BA 5555/5-1) is gratefully acknowledged.

References

- [1] J.F. Ready, D.F. Farson (Eds.). LIA Handbook of Laser Materials Processing. Laser Institute of America. Orlando; 2001.
- [2] M. Bachmann, A. Gumenyuk, M. Rethmeier. Welding with high-power lasers: Trends and developments. *Phys. Procedia* 83; 2016. p. 15–25.
- [3] X. Zhang, E. Ashida, S. Tarasawa, Y. Anma, M. Okada, S. Katayama, M. Mizutani. Welding of thick stainless steel plates up to 50mm with high brightness lasers. *J. Laser Appl.* 23; 2011; 022002.
- [4] A. Fritzsche, V. Avilov, A. Gumenyuk, K. Hilgenberg, M. Rethmeier, M. High power laser beam welding of thick-walled ferromagnetic steels with electromagnetic weld pool support. *Physics Procedia*; 2016; 83; p. 362–372.
- [5] J. Schuster, S. Keitel, E. Schulze, H. Maly. Fachbeiträge-Entstehung erstarrungsbedingter Risse in Laserstrahlschweißverbindungen an unlegierten und niedriglegierten Baustählen. *Schweißen und Schneiden*; 1999; 51; p. 252–257.
- [6] J. Schuster. Heißrisse in Schweißverbindungen: Entstehung, Nachweis und Vermeidung. DVS-Verlag; 2004.
- [7] M.O. Gebhardt, A. Gumenyuk, M. Rethmeier. Numerical analysis of hot cracking in laser hybrid welded tubes. *Advances in Materials Science and Engineering*; 2013; 520786.
- [8] A. Artinov, N. Bakir, M. Bachmann, A. Gumenyuk M. Rethmeier. Weld pool shape observation in high power laser beam welding. *Physics Procedia*; 2018.
- [9] M. Rappaz, J. Dantzig. *Solidification*, first, EFPL Press; 2009.
- [10] J. Lippold. *Welding Metallurgy and Weldability*, first, John Wiley & Sons; 2014.
- [11] G. Agarwal, A. Kumar, I.M. Richardson, M.J.M. Hermans. Evaluation of solidification cracking susceptibility during laser welding in advanced high strength automotive steels. *Materials & Design*; 2019; 183: 108104.
- [12] J. Draxler, J. Edberg, J. Andersson, L.E. Lindgren. Modeling and simulation of weld solidification cracking part I. *Welding in the World*; 2019; 63(5); p. 1489–1502.
- [13] S. Kou. *Welding Metallurgy*, second, John Wiley & Sons, Inc.; 2003.
- [14] M.E. Glicksman. *Principles of Solidification: An Introduction to Modern Casting and Crystal Growth Concepts*. Springer New York; 2011.
- [15] C. Cross. On the origin of weld solidification cracking. In *Hot cracking phenomena in welds*. Springer; 2005; p. 3–18.
- [16] T. Shida, H. Okumura, Y. Kawada. Effects of welding parameters and prevention of defects in deep penetration electron beam welding of heavy section steel plates. *Weld. World*; 1979; 17; p. 196–207.
- [17] S. Tsukamoto, H. Irie, M. Inagaki. *Welding Defects and Molten Metal Behaviour in Electron Beam Welding*. The fourth international Symposium of the Japan Welding Society; 1982; p. 115–120.
- [18] S. Tsukamoto, H. Irie. Welding defects and molten metal behaviour in low speed electron beam welding. *Welding in the World*; 1985; 23; p. 130–140.
- [19] S. Tsukamoto, H. Irie. Mechanism of locally delayed solidification in electron beam welding. *Welding international*; 1991; 5; p. 177–183.
- [20] M.O. Gebhardt. Einfluss von Konstruktion und Schweißparametern auf die Erstarrungsrissentstehung beim Laser-MSG-Hybridschweißen dickwandiger Bauteile: experimentelle und numerische Analyse. Technische Universität Berlin; 2013.
- [21] N. Bakir, A. Artinov, A. Gumenyuk, M. Bachmann, M. Rethmeier. Numerical simulation on the origin of solidification cracking in laser welded thick-walled structures. *Metals*; 2018; 8(6): 406.
- [22] L.D. Barbetta. Solidification flaw and porosity formation in hybrid laser: GMA welding of thick API 5L X70 steel plates; 2014. (Master's thesis).
- [23] L.D. Barbetta, W.L. Weingaertner, O. Seffer, R. Lahdo, S. Kaierle, S. Influence of molten pool geometry and process parameters on solidification cracks formation in hybrid laser-GMA welding of thick 5L X70 steel plates; In ABCM International Congress of Manufacturing Engineering (COBEM), 8th Brazilian Congress of Manufacturing Engineering; Brazil; 2015.
- [24] W.-I. Cho, S.-J. Na, C. Thomy, F. Vollertsen. Numerical simulation of molten pool dynamics in high power disk laser welding. *Journal of Materials Processing Technology*; 2012; 212; p. 262–275.
- [25] M. Bachmann, V. Avilov, A. Gumenyuk, M. Rethmeier. Experimental and numerical investigation of an electromagnetic weld pool support system for high power laser beam welding of austenitic stainless steel. *Journal of Materials Processing Technology*; 2014; 214(3); p. 578–591.
- [26] M. Bachmann, V. Avilov, A. Gumenyuk, M. Rethmeier. Experimental and numerical investigation of an electromagnetic weld pool control for laser beam welding. *Physics Procedia*; 2014; 56; p.515–524.
- [27] M. Bachmann, R. Kunze, V. Avilov, M. Rethmeier. Finite element modeling of an alternating current electromagnetic weld pool support in full penetration laser beam welding of thick duplex stainless steel plates. *Journal of Laser Applications*; 2016; 28(2), p. 022404.
- [28] F. Lu, X. Li, Z. Li, X. Tang, H. Cui. Formation and influence mechanism of keyhole-induced porosity in deep-penetration laser welding based on 3D transient modeling. *International Journal of Heat and Mass Transfer*; 2015; 90; p. 1143–1152.
- [29] M. Sohail, S.-W. Han, S.-J. Na, A. Gumenyuk, M. Rethmeier. Numerical investigation of energy input characteristics for high-power fiber laser welding at different positions. *International Journal of Advanced Manufacturing Technology*; 2015; 80; p. 931–946.
- [30] Z. Gao, P. Jiang, G. Mi, L. Cao, W. Liu. Investigation on the weld bead profile transformation with the keyhole and molten pool dynamic behavior simulation in high power laser welding. *International Journal of Heat and Mass Transfer*; 2018; 116; p. 1304–1313.
- [31] A. Artinov, N. Bakir, M. Bachmann, A. Gumenyuk, M. Rethmeier. Weld pool shape observation in high power laser beam welding. *Procedia CIRP*; 2018; 74; p. 683–686.
- [32] A. Artinov, N. Bakir, M. Bachmann, A. Gumenyuk, S.J. Na, M. Rethmeier. On the search for the origin of the bulge effect in high power laser beam welding. *Journal of Laser Applications*; 2019; 31(2); 022413.
- [33] V. Pavelic. Experimental and computed temperature histories in gas tungsten arc welding of thin plates. *Welding Journal Research Supplement*; 1969; 48; p. 296–305.
- [34] D. Radaj, H. Häuser, S. Braun. Numerische Simulation von Eigenspannungen und Verzug bei Schweißverbindungen aus AlMgSi-Legierungen. *Konstruktion*; 1998; 50(7-8); p. 31–37.
- [35] M. Beck. *Modellierung des Lasertiefschweißens*. Teubner; 1996.
- [36] R. Rai, S.M. Kelly, R.P. Martukanitz, T. DebRoy, T. A convective heat-transfer model for partial and full penetration keyhole mode laser welding of a structural steel. *Metallurgical and Materials Transactions A*; 2008; 39(1); p. 98–112.
- [37] M. Bachmann, V. Avilov, A. Gumenyuk, M. Rethmeier. Numerical simulation of full-penetration laser beam welding of thick aluminium plates with inductive support. *J. Phys. D Appl. Phys*; 2011; 035201.
- [38] A. Artinov, M. Bachmann, M. Rethmeier, Equivalent heat source approach in a 3D transient heat transfer simulation of full-penetration high power laser beam welding of thick metal plates, *Int. J. Heat Mass Transf.* 2018; 122; p. 1003–1013.
- [39] A. Artinov, V. Karkhin, N. Bakir, X. Meng, M. Bachmann, A. Gumenyuk, M. Rethmeier. Lamé curves approximation for the assessment of the 3-D temperature distribution in keyhole mode welding processes. *Journal of Laser Applications*; 2020; 32; 022024.
- [40] A. Artinov, V. Karkhin, P. Khomich, M. Bachmann, M. Rethmeier. Assessment of thermal cycles by combining thermo-fluid dynamics and heat conduction in keyhole mode welding processes. *International Journal of Thermal Sciences*; 2019; 145; 105981.
- [41] K. Satoh, Y. Ueda, H. Kiharak. Recent trend of researches on restraint stresses and strains for weld cracking. *Trans. JWRI*; 1972; 42; p. 53–68.
- [42] V. A. Karkhin V. A. Thermal processes in welding. Springer; 2019.
- [43] V.A. Karkhin, P.N. Khomich, P. Rayamaki. Analysis of chemical macroheterogeneity in the vicinity of the fusion boundary in fusion welding. *Welding International*; 2010; 24:2; p. 125–130.
- [44] A. Artinov, V.A. Karkhin, M. Bachmann, M. Rethmeier. Mathematical modeling of the geometrical differences between the weld end crater and the steady-state weld pool. *Journal of Laser Applications*; 2020; 32; 022024.

11th CIRP Conference on Photonic Technologies [LANE 2020] on September 7-10, 2020

Use of (nano-)additives in Laser Powder Bed Fusion of Al powder feedstocks: research directions within the last decade

Ihsan Murat Kusoglu^a, Bilal Gökçe^a, Stephan Barcikowski^{a,*}

^aTechnical Chemistry I, Center for Nanointegration Duisburg-Essen (CENIDE), University of Duisburg-Essen, Universitätsstr. 7, D-45141, Germany

* Corresponding author. Tel.: +49-201-183-3150; fax: +49-201-183-3049. E-mail address: stephan.barcikowski@uni-due.de

Abstract

An exponential increase for the number of Scientific Citation Index (SCI) expanded articles in the field of Laser Powder Bed Fusion (L-PBF) of metal powder feedstocks are generated within the last decade. Al powder feedstocks have become one of the most cited metal alloys in this field. By in-depth analyzing the experimental research data provided within SCI-expanded articles, it is obvious that material properties and laser process properties have a high impact to produce as-built parts with crack free microstructure, high density, high mechanical properties and high repetition rates of as-built parts. As a future research trend of using additive powders in Al powder feedstocks are found to be promising candidates to develop L-PBF of as-built Al parts. This study quantitatively evaluates the effect of compositions and mass fractions on several Al alloy powder feedstocks by extracting research data given in the SCI-expanded articles. The latest research directions showed that several additives are useful to refine microstructure and to enhance the mechanical properties of as-built Al parts. The effect of additives on processability, as-built density, tensile properties, and flexural properties of several Al alloy parts are discussed.

© 2020 The Authors. Published by Elsevier B.V.

This is an open access article under the CC BY-NC-ND license (<http://creativecommons.org/licenses/by-nc-nd/4.0/>)

Peer-review under responsibility of the Bayerisches Laserzentrum GmbH

Keywords: laser powder bed fusion; L-PBF; selective laser melting; SLM; AlSi10Mg; nanoparticles; additives; Zr; TiB₂

1. Introduction

A decision on research trends in L-PBF of metals can be done by using commercial reports provided by individuals or commercial organizations [1, 2]. On the contrary, bibliometric studies as SCI-expanded articles are peer-reviewed by journals and provides academia or industry high-quality researches on new material formulations, processes, and technologies. The scientific literature pool on L-PBF has been growing rapidly and approximately 5000 research articles related to this topic were recorded by Web of Science (WoS) as of November 2019 within the last decade. L-PBF of metal powder feedstock uses a digital model to build 3D parts by scanning metal powders with a laser beam. It is a high-potential process able to manufacture complex parts for the metal industry where other conventional processes cannot be used [3, 4, 47]. High solidification rates during processing cause some metallurgical defects, such as anisotropic grain growth with a columnar grain

structure [5, 9, 35, 36, 38], phase segregations in the build volume [8, 39, 50], and the formation of cracks [11, 13, 35] that adversely affect the properties of the as-built parts. The literature on L-PBF of metal parts has been increasing rapidly during the last decade to overcome material-based and process-based failures in L-PBF of metals [48, 49]. Additives in Al powder feedstocks are useful to overcome those failures in L-PBF and improve the as-built part properties. This study is focused on additives in L-PBF of Al powders, their effects on processability, and as-built part properties.

2. Bibliometric overview and extraction of material properties referred to in the literature

The WoS search engine was used for several metals produced by L-PBF to determine the impact of SCI-expanded articles within the last decade. Keywords as “powder bed fusion” and “selective laser melting” are combined with

aluminum (Al), titanium (Ti), stainless steel and steel, copper (Cu), magnesium (Mg), nickel (Ni), and Cobalt-Chromium (Co-Cr) respectively and searched in the WoS engine. As shown in Fig. 1, the sum of publications/year for named metals have been rapidly increasing during the last decade. The annual growth rate has positive values except the year 2010 but a decrease in the growth rate is obtained in the last two years for the named metals with in the last decade. Al is the third most published metal for L-PBF and has a total publication number of 534 with an average growth rate of 40% in the last decade.

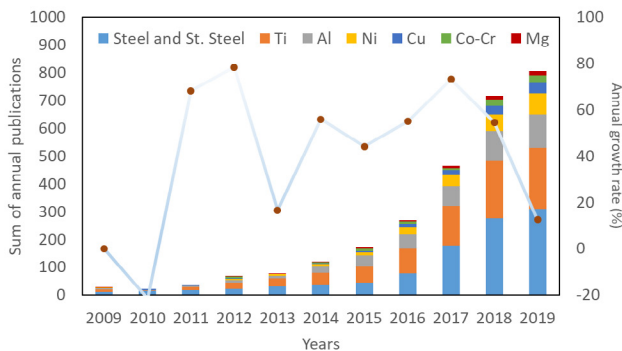


Fig. 1. Sum of annual publications and annual growth rates for L-PBF of several metals between 2009-2019.

Typical material properties [5-35] that were specifically given in the studied publications are plotted in Fig. 2. Metal powder feedstock chemistry is an important property that affects melting-resolidification kinetics and phase transformation during solidification for both heat-treatable and non-heat-treatable metal parts. After the chemistry of the powder, the size ranges of the powder and the D50 values of the particle size distribution are the most referred properties of the powder. Narrow size distribution is beneficial for flowability and to avoid segregations during processing while a wide size distribution develops a higher powder bed density after deposition onto the next powder layer [40]. Surprisingly, no accurate analytical information was provided concerning the flowability of the metal powders. Flowability can be affected by powder size distribution, powder chemistry, powder shape, and satellites in gas atomized metal powders. Hall and carney apparatus are common techniques to measure the flowability of metal powders but the latest investigations show that more process-relevant details on the flowability of metal powders can be determined by using an avalanche angle test [41]. The flowability will influence the density of powder after deposition onto the building platform, the pore formations during processing, and the density of as-built parts [42]. Determining the properties of the material is important for reproducibility and the standardization of L-PBF by using the seed data given in the SCI-expanded publications.

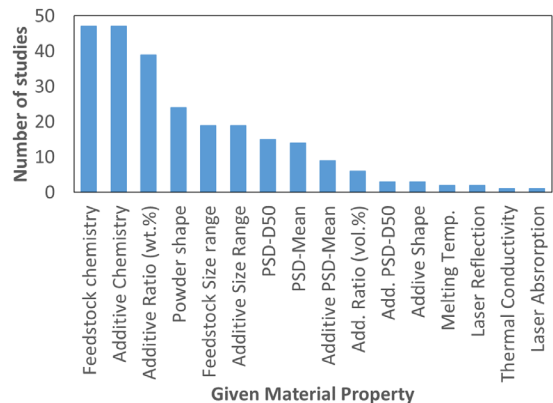


Fig. 2. Histogram showing the material properties for L-PBF of additivated Al powder feedstocks given in the studies between 2009-2019.

Several Al powder feedstock compositions have been reported in the literature [5-35]. A subset total of 51 compositions with several additives are evaluated in this paper. As seen in Fig. 3, the most-studied Al alloys are Al-Si-Mg, Al-Si, and Al-Cu-Mg with a share of 44%, 22%, and 13% respectively [5-35]. AlSi10Mg is found to be the most studied Al alloy powder material which is a eutectic Al-Si alloy. Eutectic alloys are desirable to avoid crack formations [45]. AlSi10Mg is also a heat-treatable alloy where the microstructure of as-built parts can be re-arranged for desirable mechanical properties [46]. AlSi10Mg is a good candidate for future trends in L-PBF of Al matrix composites to understand the effect of additives on structural properties. The most used powder size distribution values are mean and D50. The averages of both values are found to be around 30 μm . The average powder layer thickness is found to be 33% higher of mean or D50 value (see Fig. 6b) [5-35]. Intended build layer thickness is a limiting factor for max powder size fraction in powders to obtain higher powder layer density. Correlation between powder layer thickness and powder size distribution as mean and D50 might be helpful for the standardization of L-PBF of metal powder feedstocks.

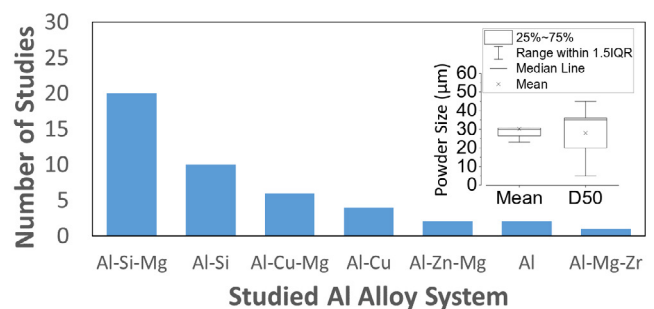


Fig. 3. The distribution of Al and its alloys within the studies. The inset shows the most given powder size distribution property as Mean and D50 of the powders studied.

The additives used in the analyzed literature are plotted in Fig. 4. Metal additives (Zr, Mg, Cu, Si, Sc, and Ni) are mostly used in the studies. Given metallic additives are highly soluble in the Al melt phase and form intermetallic precipitates during solidification of the melt pool. Those precipitates also act as

nucleation sites and refine the microstructure of Al parts [5, 11, 53]. The grain refinement in Al alloys highly depends on the solute content and the number density of nucleant particles [54]. Zr, which is the most used metallic additive, is found to avoid crack formation for higher process scan speeds, develop heterogeneous nucleation for finer microstructure and have better mechanical properties in as-built Al-Cu-Mg alloy [11, 12] and Al-Zn-Mg alloy [5]. The second most used additives are non-oxides as TiC, SiC, TiB₂, and AlN. Those non-oxide additives have high melting points, stay in solid form in the melt pool, and do not react with Al melt. Their high hardness is useful to enhance the mechanical properties of Al parts. The specific material properties of those additives also can be transferred to Al alloy parts [51]. Carbide additives are found to increase the hardness of the as-built parts as well as the wear resistance of Al parts [22, 29, 30, 31]. It is found that TiB₂ additives in eutectic Al alloys end with a similar yield and ultimate tensile strength of Al-Cu-Mg alloys which is over 400 MPa [23] (see Fig. 7a-b). Carbon-based additives as CNT, synthetic diamond, and graphene are used in the studies. Carbon-based additives have a low friction coefficient that develops wear properties in Al parts. Those additives are good electrical and thermal conductors with their high laser absorption properties [15, 19, 21]. Oxides as Fe₂O₃ and MgAl₂O₄ are also, hard materials and have higher melting points compared to Al [10, 28]. As seen in the inset of Fig. 4, the mass fraction of employed additives varies between 0.3 wt. % and 35 wt.%. There is no correlation obtained between the additive type and additive ratio (loading) for the optimization of the process. But often, higher yield strength and ultimate tensile strength are gained with the additives having a mass fraction below 2 wt. % [5-35].

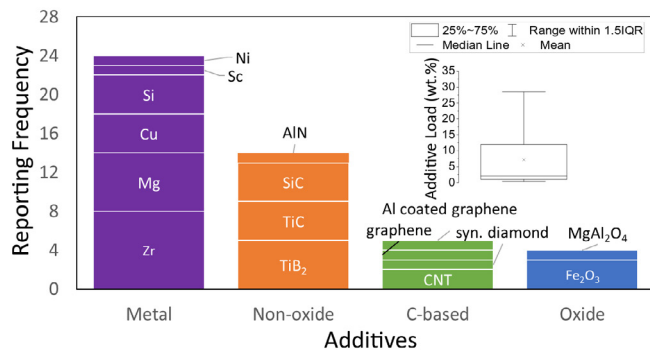


Fig. 4. Classification and distribution of additive materials according to their material properties. The inset shows the distribution for mass fraction (wt.%) of additives in Al powder feedstocks.

3. Extraction of laser process parameters and as-built Al part properties referred to in the literature

The laser process properties specifically mentioned in the studied literature [5-35] are plotted in Fig. 5. The most often mentioned laser process parameters are (obviously) laser power, hatch spacing, and scanning speed. Those process parameters (Fig. 5) were used to optimize the L-PBF process by gaining the highest relative densities and to obtain the best mechanical properties with the desired microstructures of the as-built parts. L-PBF of Al powder feedstocks depends strongly

on the volumetric energy densities applied during processing. The volumetric energy density (VED) is calculated by Eq. (1):

$$VED = P/(v \cdot h \cdot t) \quad (1)$$

where P is the laser power applied (W), v is the scanning speed (mm/s), h is the hatch spacing (mm), and t is the thickness of the powder layer (mm). The calculated VED (J/mm³) values are plotted in Fig. 6c.

$$AED = P/(v \cdot h) \quad (2)$$

The areal energy density (AED) (J/mm²), which is independent of the powder layer thickness [Eq. (2)], also were calculated, and the distribution of the values is given in Fig. 6d.

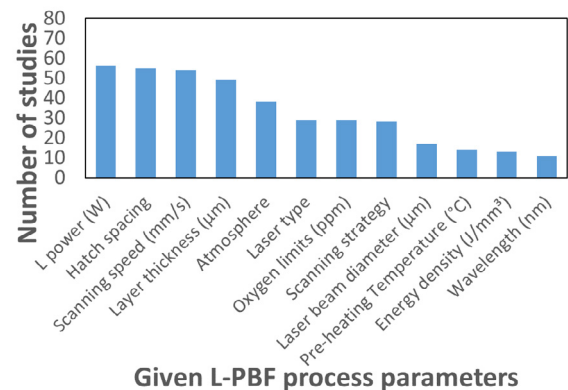


Fig. 5. Histogram showing the laser process properties given in studies on L-PBF of additivated Al powder feedstocks between 2009-2019.

The values of the laser power and the powder layer thickness given in the mentioned studies are plotted in Fig. 6a-b. The used laser power in the studied literature has an average value of 240 W while the highest power of 400 W was used for an Al-Zn-Mg alloy with 1 vol. % of Zr additives [5] and for an AlSi10Mg alloy with 1 wt. % of CNT additives [15]. The average powder layer thickness in all these studies has an average value of 38 μm which is 33% higher than the average mean or D50 value of powders (see Fig. 3). The highest thickness of 80 μm was given in the work on Al-Cu-Mg alloys with 1 vol. % of Zr additives [5]. Wide distribution is obtained both for VED and AED values given in the literature. The average VED was 245 J/mm³ with the highest value of 669 J/mm³ for L-PBF of Al-Cu-Mg alloy with 0.6 wt. % Zr [12] and with the lowest value of 25 J/mm³ for L-PBF of Al with 30 wt. % Al₆₅Cu₂₀Fe₁₀Cr₅ [32].

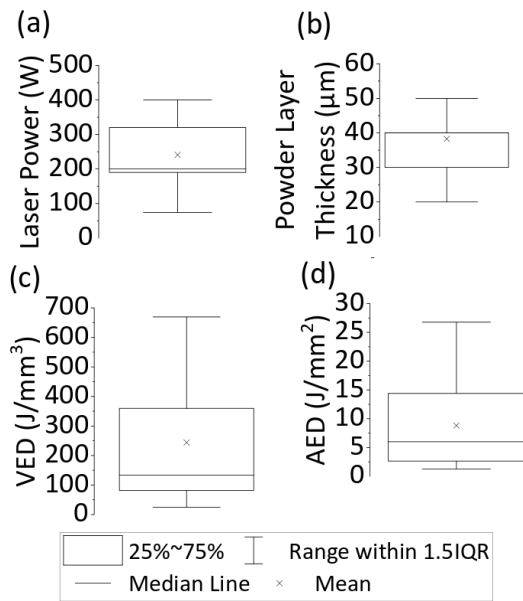


Fig. 6. The distribution of (a) laser power, (b) powder layer thickness, (c) volumetric energy density, and (d) areal energy density for L-PBF of additivated Al powder feedstocks. Outlier points are not shown.

Higher volumetric energy densities are studied for L-PBF of Al-Cu-Mg alloys [11, 12]. The average AED was $9 \text{ J}/\text{mm}^2$ with the highest value of $27 \text{ J}/\text{mm}^2$ for L-PBF of an Al-Cu-Mg alloy with 0.6 wt. % of Zr addition [12] and the lowest value of $1 \text{ J}/\text{mm}^2$ was calculated for L-PBF of AlSi10Mg powder with an addition of 0.5 wt. % MgAl_2O_4 [28] and for L-PBF of AlSi10Mg powder with 5 wt. % Ni [33]. Fixing VED and AED in scientific studies are found to be helpful to understand the effect of several additive mass fractions and additive particle sizes on the processability and as-built part properties [16, 22]. Increasing the amount of Zr additive up to 2 wt. % in Al-Cu-Mg alloy powder resulted in a faster process by decreasing VED and AED [12].

Regarding as-built part properties, the statistics on the relative density of built parts show an average value of 96%, with the highest relative density of 99.8% obtained for an Al-Cu-Mg alloy with 2 wt.% of Zr additive, while the lowest relative density of 72% was reported for Al with 15 wt. % of Fe_2O_3 additive [10] (Fig. 7a). The yield strength of as-built Al parts has an average value of 290 MPa, with the highest yield strength of 490 MPa for Al-Cu-Mg alloy with 0.6 wt. % Zr [12] and the lowest yield strength of 155 MPa for Al-4Si with 0.3 wt. % Mg [16] (Fig. 7b). Ultimate tensile strength of as-built Al parts has an average value of 407 MPa, with the highest UTS of 530 MPa for AlSi10Mg with 12 wt. % TiB_2 [23] and the lowest was 290 MPa for Al with 30 wt. % $\text{Al}_{65}\text{Cu}_{20}\text{Fe}_{10}\text{Cr}_5$ [32] (Fig. 7c). Elongation of as-built Al parts has an average value of 9%, with the highest elongation of 20% for Al-4Si with 0.3 wt. % and 0.6 wt. % Mg [16] and the lowest elongation of 2.7% for Al-Cu-Mg alloy with 2 wt. % Zr additives [11] (Fig. 7d).

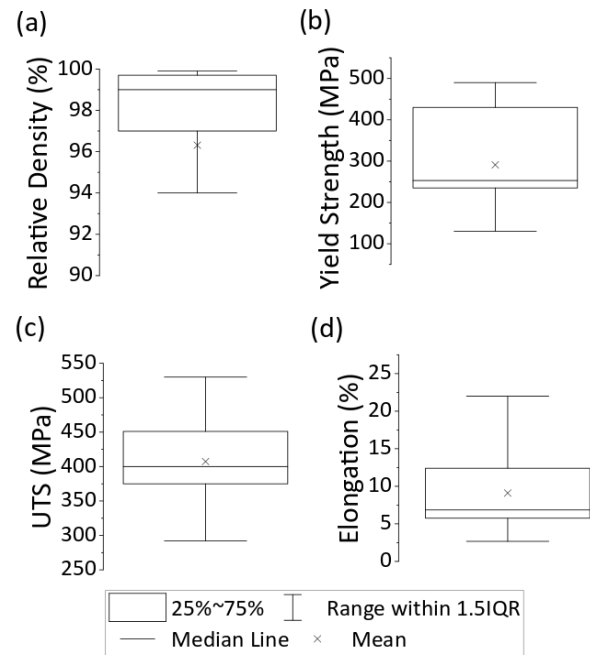


Fig. 7. The distribution of (a) relative density, (b) yield strength, (c) ultimate tensile strength, and (d) elongation for L-PBF of additivated Al powder feedstocks. Outlier points are not shown.

Even though additives at high mass loadings enhance the mechanical properties, they also adversely affect the as-built part density. A negligible decrease in as-built density is obtained for lower (2 wt. %) additive amounts, especially, for the metallic ones [11, 16, 35]. The chemical interaction of Al and additive at high temperatures in the melt pool play an important role in the final part properties. A good wettability and strong bonding between Al and additive, increase both the as-built density and mechanical properties of as-built parts [7, 23]. A poor wettability as of carbon-based or carbide additives can also improve the mechanical properties of as-built parts but will decrease the as-built part density [15, 19, 20]. The particle size of additives affects the final part properties [52]. Decreasing the D50 of SiC powders from $50 \mu\text{m}$ to $5 \mu\text{m}$ with the same mass fractions in AlSi10Mg powder resulted in higher as-built densities and almost double the hardness of as-built parts [22]. Overall, by optimization of the additive size and the mass fractions in Al powder, improved properties can be obtained in as-built Al parts and those properties can be rearranged in heat-treatable Al alloys.

Please note that statistically determined average values of the material, process, and as-built part properties are not necessarily optimal or recommended values to process an (additivated) Al alloy powder feedstock. There are some limitations to obtain the optimal value of a property. Properties of the commercially available powders, non-standardized powder characterization techniques, limitations of commercial L-PBF machines for a specific process property, and non-standardized mechanical testing conditions can change the extracted property values. However, extraction of these reported properties as performed in our study might guide the way for future studies that explore a link between the material,

process, and as-built part properties by using a Principal Component Analysis (PCA). Such a PCA could find a correlation between two properties given in multiple datasets and estimate the trends between highly correlated two variables.

4. Conclusion

Useful data is extracted from bibliometric studies for the effect of additives in L-PBF of Al powders. We found that Al-Si-Mg and AlSi10Mg alloys are the most studied Al alloy powders in the context of L-PBF. Eutectic compositions of Al-Si alloys are helpful to avoid crack formations during processing so it is found to be a good candidate for Al matrix composites. Not only the chemistry of the powder but also powder size distribution has to be optimized for higher powder bed densities and higher final part densities. Mean and D50 values have statistically the narrowest scattering in experimental publications and have nearly the same average value of 33 μm where the average of powder layer thickness during processing is 33% higher. Metallic additives are mostly used in the L-PBF of Al alloy powders. Zr is found to be the most studied additive material to avoid crack formations during processing Al-(Cu,Zn)-Mg alloy powders. The maximum laser power of 400 W can be used to process several Al alloy powders. It is found that higher VED and AED are necessary for processing Al-Cu-Mg alloy powder feedstocks and additives as Zr can decrease the VED and AED with faster scanning speeds. TiB_2 , as an additive, is found to have beneficial effects on the properties of Al-Si-Mg and Al-Cu-Mg. Higher densities are obtained for the built parts in case of the mass fraction of the employed additives is low, i.e. < 2 wt.% indicating that the degree of dispersion is important rather than the amount of additives. Carbon based additives can be used in low weight loads (<1 wt. %) to enhance mechanical properties. Higher mechanical properties are obtained for Al-Cu-Mg alloys. Optimization of the powder size distribution and the mass (volume) fraction of (nano-) additives in the Al powder are evidently emerging research trends in L-PBF. Also, further investigations will be required to increase the density of the powder bed in the build volume of L-PBF by optimization of powder size distribution. Additives in L-PBF of metal powder feedstocks are found to be a future research trend for designing as-built part properties. The effect of additives on laser interaction of powder feedstock, flowability, spreadability and processability will be future research trends.

Acknowledgment

This study is supported by Deutsche Forschungsgemeinschaft (DFG) under the Priority Program of "Materials for Additive Manufacturing" (SPP 2122).

References

- [1] Wohlers T, Wohlers Report. 3D printing and additive manufacturing state of the industry. Wohlers Associates, Fort Collins; 2019
- [2] additive-manufacturing-report.com, 2019, Ampower GmbH & Co, K.G. Accessed 14 February 2020
- [3] Zhang J, Song B, Wei Q, Bourell D, Shi Y. A Review of Selective Laser Melting of Aluminum Alloys: Processing, Microstructure, Property and Developing Trends. *J Mater Sci Technol* 2019;35(2):270-284.
- [4] DebRoy T, Wei HL, Zuback JS, Mukherjee T, Elmer JW, Milewski JO, Beese AM, Wilson-Heid A, De A, Zhang W. Additive manufacturing of metallic components – Process, structure, and properties. *Progress in Materials Science* 2018; 92:112–224.
- [5] Martin JH, Yahata BD, Hundley JM, Mayer JA, Schaedler TA, Pollock TM. 3D printing of high-strength aluminium alloys. *Nature* 2017;5:365-369.
- [6] Wang P, Gammer C, Brenne F, Niendorf T, Eckert J, Scudino S. A heat treatable $\text{TiB}_2/\text{Al}-3.5\text{Cu}-1.5\text{Mg}-1\text{Si}$ composite fabricated by selective laser melting: Microstructure, heat treatment, and mechanical properties. *Composites Part B* 2018;147:162-168.
- [7] Xi LX, Zhang H, Wang P, Li HC, Prashanth KG, Lin KJ, Kaban I, Gu D. Comparative investigation of microstructure, mechanical properties and strengthening mechanisms of Al-12Si/TiB₂ fabricated by selective laser melting and hot pressing. *Ceramics International* 2018;44:17635-17642.
- [8] Montero-Sistiga ML, R. Mertens, B. Vrancken, X. Wang, B. V. Hooreweder, J.-P. Kruth, J. V. Humbeeck. Changing the alloy composition of Al7075 for better processability by selective laser melting. *Journal of Materials Processing Technology* 2016;238:437-445.
- [9] Yang KV, Shi Y, Palm F, Wu X, Rometsch P. Columnar to equiaxed transition in Al-Mg(-Sc)-Zr alloys produced by selective laser melting. *Scripta Materialia* 2018;145:113-117.
- [10] Dadbakhsh S, Hao L. Effect of Al alloys on selective laser melting behavior and microstructure of in situ formed particle reinforced composites. *Journal of Alloys and Compounds* 2012;541:328-334.
- [11] Zhang H, Zhu H, Nie X, Yin J, Hu Z, Zeng X. Effect of Zirconium addition on crack, microstructure and mechanical behavior of selective laser melted Al-Cu-Mg alloy. *Scripta Materialia* 2017;134:6-10.
- [12] Nie X, Zhang H, Zhu H, Hu Z, Ke L, Zeng X. Effect of Zr content on formability, microstructure and mechanical properties of selective laser melted Zr modified Al-4.24Cu-1.97Mg-0.56Mn alloys. *Journal of Alloys and Compounds* 2018;764:977-986.
- [13] Zhou L, Pan H, Hyer H, Park S, Bai Y, McWilliams B, Cho K, Sohn Y. Microstructure and tensile property of a novel AlZnMgScZr alloy additively manufactured by gas atomization and laser powder bed fusion. *Scripta Materialia* 2019;158:24–28.
- [14] Dai D, Gu D, Xia M, Ma C, Chen H, Zhao T, Hong C, Gasser A, Poprawe R. Melt spreading behavior, microstructure evolution and wear resistance of selective laser melting additive manufactured AlN/AlSi10Mg nanocomposite. *Surface & Coatings Technology* 2018;349:279-288.
- [15] Wang L-Z, Chen T, Wang S. Microstructural characteristics and mechanical properties of carbon nanotube reinforced AlSi10Mg composites fabricated by selective laser melting. *Optik* 2017;143:173-179.
- [16] Kimura T, Nakamoto T, Ozaki T, Sugita K, Mizuno M, Araki H. Microstructural formation and characterization mechanisms of selective laser melted Al-Si-Mg alloys with increasing magnesium content. *Materials Science & Engineering A* 2019;754:786-798.
- [17] Wang P, Deng L, Prashanth KG, Pauly S, Eckert J, Scudino S. Microstructure and mechanical properties of Al-Cu alloys fabricated by selective laser melting of powder mixtures. *Journal of Alloys and Compounds* 2018;735:2263-2266.
- [18] Zhao X, Gu D, Ma C, Xi L, Zhang H. Microstructure characteristics and its formation mechanism of selective laser melting SiC reinforced Al-based composites. *Vacuum* 2019;160:189-196.
- [19] Ma Y, Ji G, Li XP, Chen CY, Tan ZQ, Addad A, Li ZQ, Sercombe TB, Kruth JP. On the study of tailorable interface structure in a diamond/Al12Si composite processed by selective laser melting. *Materialia* 2019;5:100242.
- [20] Yuan P, Gu D, Dai D. Particulate migration behavior and its mechanism during selective laser melting of TiC reinforced Al matrix nanocomposites. *Materials and Design* 2015;82:46-55.
- [21] Jiang LY, Liu TT, Zhang CD, Zhang K, Li MC, Ma T, Liao WH. Preparation and mechanical properties of CNTs-AlSi10Mg composite fabricated via selective laser melting. *Materials Science & Engineering A* 2018;734:171-177.
- [22] Chang F, Gu D, Dai D, Yuan P. Selective laser melting of in-situ Al₄SiC₄ + SiC hybrid reinforced Al matrix composites: Influence of starting SiC particle size. *Surface & Coatings Technology* 2015;272:15-24.
- [23] Li XP, Ji G, Chen Z, Addad A, Wu Y, Wang HW, Vleugels J, Van Humbeeck J, Kruth JP. Selective laser melting of nano-TiB₂ decorated

- AlSi10Mg alloy with high fracture strength and ductility. *Acta Materialia* 2017;129:183-193.
- [24] Gao C, Xiao Z, Liu Z, Zhu Q, Zhang W. Selective laser melting of nano-TiN modified AlSi10Mg composite powder with low laser reflectivity. *Materials Letters* 2019;236:362-365.
- [25] Zhao Z, Bai P, Misra RDK, Dong M, Guan R, Li Y, Zhang J, Tan L, Gao J, Ding T, Du W, Guo Z. AlSi10Mg alloy nanocomposites reinforced with aluminum-coated graphene: Selective laser melting, interfacial microstructure, and property analysis. *Journal of Alloys and Compounds* 2019;792:203-214.
- [26] Xi LX, Zhang H, Wang P, Li HC, Prashanth KG, Lin KJ, Kaban I, Gu D. Comparative investigation of microstructure, mechanical properties and strengthening mechanisms of Al-12Si/TiB₂ fabricated by selective laser melting and hot pressing. *Ceramics International* 2018;44:17635-17642.
- [27] Gu D, Wang H, Dai D, Yuan P, Meiners W, Poprawe R. Rapid fabrication of Al-based bulk-form nanocomposites with novel reinforcement and enhanced performance by selective laser melting *Scripta Materialia* 2015;96:25-28.
- [28] Marchese G, Aversa A, Lorusso M, Manfredi D, Calignano F, Lombardi M, Biamino S, Pavese M. Development and Characterisation of Aluminium Matrix Nanocomposites AlSi10Mg/MgAl₂O₄ by Laser Powder Bed Fusion. *Metals* 2018;8:175.
- [29] Gu D, Wang H, Chang F, Dai D, Yuan P, Hagedorn Y-C, Meiners W. Selective Laser Melting Additive Manufacturing of TiC/AlSi10Mg Bulk-form Nanocomposites with Tailored Microstructures and Properties. *Physics Procedia* 2014;56:108-116.
- [30] Zhou Y, Duan L, Wen S, Wei Q, Shi Y. Enhanced micro-hardness and wear resistance of Al-15Si/TiC fabricated by selective laser melting. *Composites Communications* 2018;10:64-67.
- [31] Dai D, Gu D. Tailoring surface quality through mass and momentum transfer modeling using a volume of fluid method in selective laser melting of TiC/AlSi10Mg powder. *International Journal of Machine Tools & Manufacture* 2015;88:95-107.
- [32] Kang N, Mansori ME, Lin X, Guittonneau F, Liao HL, Huang WD, Coddet C. In-situ synthesis of aluminum/nano-quasicrystalline Al-Fe-Cr composite by using selective laser melting. *Composites Part B* 2018;155:382-390.
- [33] Aversa A, Lorusso M, Cattano G, Manfredi D, Calignano F, Ambrosio EP, Biamino S, Fino P, Lombardi M, Pavese M. A study of the microstructure and the mechanical properties of an AlSiNi alloy produced via selective laser melting. *Journal of Alloys and Compounds* 2017;695:1470-1478.
- [34] Doñate-Buendía C, Frömel F, Wilms MB, Streubel R, Tenkamp J, Hupfeld T, Nachev M, Gökce E, Weisheit A, Barcikowski S, Walther F, Schleifenbaum JH, Gökce B. Oxide dispersion-strengthened alloys generated by laser metal deposition of laser-generated nanoparticle-metal powder composites. *Materials & Design* 2018;154:360-369
- [35] Li R, M, Yuan T, Song B, Chen C, Zhou K, Cao P. Selective laser melting of a novel Sc and Zr modified Al-6.2 Mg alloy: Processing, microstructure, and properties. *Powder Technology* 2017;319:117-128.
- [36] Streubel R, Wilms MB, Doñate-Buendía C, Weisheit A, Barcikowski S, Schleifenbaum JH, Gökce B. Depositing laser-generated nanoparticles on powders for additive manufacturing of oxide dispersed strengthened alloy parts via laser metal deposition. *Japanese Journal of Applied Physics* 2018;54:4
- [37] Kaufmann N, Imran M, Wischeropp TM, Emmelmann C, Walther F. Influence of Process Parameters on the Quality of Aluminium Alloy EN AW 7075 Using Selective Laser Melting (SLM). *Physics Procedia* 2016;83:918-926.
- [38] Boussinot G, Apel M, Zielinski J, Hecht U, Schleifenbaum JH. Strongly out-of-equilibrium columnar solidification during laser powder-bed fusion in additive manufacturing. *Physical Review Applied* 2019;11:014025,1-9
- [39] Rowolt C, Milkereit B, Gabuer M, Seidel C, Müller B, Kessler O. In-Situ Phase Transition Analysis of Conventional and Laser Beam Melted AlSi10Mg and X5CrNiCuNb16-4 Alloys. *Journal of Heat Treatment and Materials* 2018;73:6,317-334.
- [40] Vock S, Klöden B, Kirchner A, Weißgärber T, Kieback B. Powders for powder bed fusion: A review. *Progress in Additive Manufacturing* 2019;4:383-397.
- [41] Brown CU, Jacob G, Stoudt M, Moylan S, Slotwinski J, Donmez A. *Journal of Materials Engineering and Performance* 2016;25:8,3390-3397.
- [42] Ahuja B, Schaub A, Junker D, Karg M, Tenner F, Plettke R, Merklein M, Schmidt M, *South African Journal of Industrial Engineering* 2016;27:2,30-42.
- [43] Hoeges S, Zwiren A, Schade C. Additive manufacturing using water atomized steel powders. *Metal Powder Report* 2017;72:2,111-117.
- [44] Sutton AT, Kriewall CS, Leu MC, Newkirk JW. Powder characterization techniques and effects of powder characteristics on part properties in powder bed fusion processes, *Virtual and Physical Prototyping*, 2017;12:1, 3-29
- [45] Olakanmi EO, Cochrane RF, Dalgarno KW. A review on selective laser sintering/melting (SLS/SLM) of aluminium alloy powders: Processing, microstructure, and properties. *Progress in Materials Science* 2015;74:401-477.
- [46] Zhuo L, Wang Z, Zhang H, Yin E, Wang Y, Xu T, Li C. Effect of post-process heat treatment on microstructure and properties of selective laser melted AlSi10Mg alloy. *Materials Letters*. 2019;234:196-200.
- [47] Röttger, A, Geenen, K, Windmann, M, Binner, F, Theisen, W. Comparison of microstructure and mechanical properties of 316L austenitic steel processed by selective laser melting with hot-isostatic pressed and cast material. *Materials Science & Engineering A* 2016;678:365-376.
- [48] Ullsperger T, Matthäus G, Kaden L, Engelhardt H, Rettenmayr M, Risse S, Tünnermann A, Nolte S. Selective laser melting of hypereutectic Al-Si40-powder using ultra-short laser pulses, *Appl. Phys. A*, 2017;123:798.
- [49] Gieseke M, Nölke C, Kaieler S, Maier HJ, Haferkamp H, Selective Laser Melting of Magnesium Alloys for Manufacturing Individual Implants. In: A. Demmer (Ed.), *Proceedings/DDMC 2014, Fraunhofer Direct Digital Manufacturing Conference*, 2014, pp. 12.-13.
- [50] Witzendorff P, Kaieler S, Suttman O, Overmeyer L, In Situ Observation of Solidification Conditions in Pulsed Laser Welding of AL6082 Aluminum Alloys to Evaluate Their Impact on Hot Cracking Susceptibility, *Metallurgical and Materials Transactions A* 2015;46:4: 1678-1688
- [51] Sehr JT, Kleszczynski S, Notthoff C, Lau M, Gökce B, Barcikowski S, Laser powder bed fusion of nano-WC-modified and nano-TiO₂-modified metal powders, *Proceedings of 6th International Conference on Additive Technologies - iCAT 2016, Nürnberg, Germany, 29th-30th November 2016*; 26-38
- [52] Barth N, Schilde C, Kwade A, Influence of Particle Size Distribution on Micromechanical Properties of thin Nanoparticulate Coatings, *Physics Procedia*, 2013;40:9-18
- [53] Wulf, E., Alpei, L. D., Westphal, D., Seitz, J.-M., Schaper, M., Becker, J. A., Feldhoff, A., Bach, F.-W.: Grain refining of aluminium alloys and silicon by means of boron nitride particles, *International Journal of Materials Research* 2013;104(03):266-274
- [54] Easton M, StJohn D. An Analysis of the Relationship between Grain Size, Solute Content, and the Potency and Number Density of Nucleant Particles, *Metallurgical and Materials Transactions A*, 2005;36A:1911-1920

11th CIRP Conference on Photonic Technologies [LANE 2020] on September 7-10, 2020

Surface inoculation of aluminium powders for additive manufacturing of Al-7075 alloys

P. Vieth^{a*}, M. Voigt^a, C. Ebbert^a, B. Milkereit^b, E. Zhuravlev^b, B. Yang^b, O. Keßler^b, G. Grundmeier^a

^aPaderborn University, Technical and Macromolecular Chemistry, Paderborn

^bUniversity of Rostock, Materials Technology and Competence Center ^cCalor, Rostock

* Corresponding author. Tel.: +495251602596; E-mail address: pfsvieth@mail.uni-paderborn.de

Abstract

For laser powder bed fusion (LPBF), particularly during solidification after the laser melting process the generation of high-strength aluminium materials (such as Al-7075) possesses a particular challenge, since the high energy input often causes defects like pores and cracks in the material. To overcome this issue, nanoparticles were adsorbed on the surface of the powder used for the L-PBF process. This addition aims at the grain refinement and thereby at the reduction of hot crack formation during the manufacturing process. This contribution presents the process of surface inoculation of aluminium particles with TiC nanoparticles, as well as the measurement of the melting and solidification temperature by means of differential fast scanning calorimetry (DFSC). With the help of DFSC, a modified solidification process could be observed. Accordingly, the nanoparticles act as nuclei with improved nucleation barrier during the rapid solidification of the aluminium powder.

© 2020 The Authors. Published by Elsevier B.V.

This is an open access article under the CC BY-NC-ND license (<http://creativecommons.org/licenses/by-nc-nd/4.0/>)

Peer-review under responsibility of the Bayerisches Laserzentrum GmbH

Keywords: AA7075, Surface inoculation, L-PBF, DFSC, Nanoparticles

1. Introduction

Additive manufacturing (AM) is gaining increasing attention due to its high potential to completely redesign complex components.^[1] Due to the potentially high geometric complexity this technique finds application in aerospace or automotive parts, mainly using established aluminum cast alloys. The laser powder bed fusion (L-PBF) process is difficult for some basically attractive high strength aluminum wrought alloys, because those materials tend to hot cracking.^[2] The vast majority of aluminum wrought alloys cannot be additively manufactured due to the melting and solidification dynamics during the manufacturing process.^[3,4] The addition of nanoparticles is one option to produce uniform, fine and equiaxed microstructure of additively manufactured aluminum components due to a grain refinement introduced by a change

in the nucleation mechanism during solidification. The effect of grain refinement was shown for TiB₂ nanoparticles.^[5] In addition, nanoparticles concentrate at the solid/liquid interface during solidification process and as a result decrease heat transport.^{[6][7]} The nucleation of Al on TiC nanoparticles is crystallographic favorable because of similar crystal structure of the cubic NaCl structure and the fcc structure of the α -Al.^[8] The aim of this report, therefore, is to investigate the effects of the surface inoculation of Al 7075 with TiC nanoparticles to produce a grain-refined microstructure. Herein, a suitable wet inoculation process was established, and the characteristic melting/ solidification temperatures were studied utilizing differential fast scanning calorimetry (DFSC).^[9]

2. Materials and Method

Commercial TiC powder (Iolitec Nanomaterials) was used in this study. The average particle size was 40 nm and the specific surface area was determined with $>50 \text{ m}^2/\text{g}$. Polyethyleneimine with an average molecular weight of 25000 (PEI) (Sigma-Aldrich) was used as a dispersant. The Al 7075 spherical particles were purchased from ENGINEERING FOR YOU GmbH (Villingen, Germany) with a particle size from 10 to 45 μm . The chemical composition, which was analyzed with XRF, is given in the following table 1.

Table 1. Chemical Composition of Al 7075 powder

Element	Al	Zn	Mg	Cu	Cr	Fe	Mn
Wt %	Basis	5,5	1,85	2,0	0,25	0,5	0,39

2.2. The procedure of surface inoculation

The inoculation was done by a wet deposition process. TiC nanoparticles were dispersed in water mixed with an inoculation agent. Subsequently the 7075-aluminum alloy powder were wetted by this dispersion.

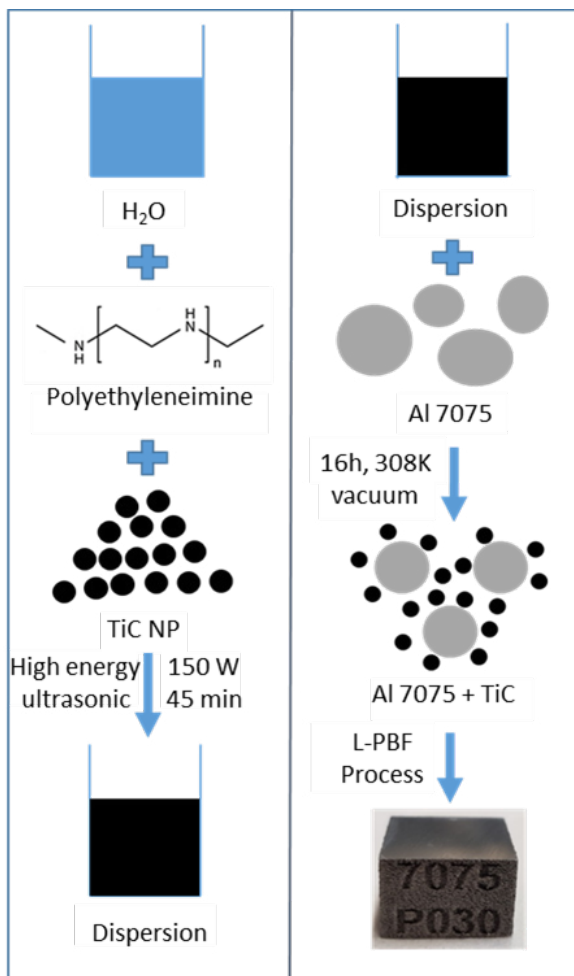


Fig. 1. Schematic illustration of surface inoculation procedure with H_2O , PEI and Titaniumcarbide nanoparticles via high energy ultrasonic and vacuum drying

Finally, the wet parts were dried again leaving 7075 powder with TiC surface inoculation. Ultrapure Milli-Q water was employed to perform all experiments. Within the process of preparing the inoculation dispersion the nanoparticles tend to agglomerate due to their increased surface area and surface energy.^[10] The main method for dispersing nanoparticles is, therefore, adding a dispersant (inoculation agent) to prevent the nanoparticles from agglomeration. Stable aqueous nanoparticle dispersions were prepared with polyethyleneimine (PEI).^[11] PEI is known as polyelectrolyte dispersant in neutral or acidic electrolytes.^[12] The dispersion consisted of 500 ml deionized water as a solvent, 1,5 g PEI as a stabilizer and 10 g TiC nanoparticles. The dispersion was processed via high-energy ultra-sonication for 45 min at a power of 155 W. The solution was cooled with ice during the sonication process. The formed dispersion was sprayed on aluminum 7075 powder and the resulting slurry was subsequently dried under vacuum at 308 K for 16 hours. The inoculated aluminum powder was then processed by L-PBF. The schematic illustration of the surface inoculation process is given in Figure 1.

2.3. Surface Characterization

Scanning electron microscopy (SEM) and energy dispersive X-Ray spectroscopy (EDS) were performed using a ZEISS Neon 40 with an accelerating voltage between 0,1-30 kV. EDS mappings were measured using an ultra-dry detector from Thermo-Fisher Scientific.

X-ray photoelectron spectroscopy (XPS) analysis was performed using an Omicron ESCA+ system at a pressure of $5 \cdot 10^{-10}$ mbar. The energy of the monochromatic Al $K\alpha$ X-ray was 1486.7 eV, the spot diameter was 600 μm and the take-off angle was 30°. The C 1s peak was located at 285 eV to calibrate the spectra. The deconvolution of the spectra was done using CASA XPS software, using a Shirley background and a deconvolution with Gauss (30%) and Lorentzian (70%) functions.

2.4. Differential fast scanning calorimetry (DFSC)

The measurement of the solidification temperature of the nanoparticle-modified powder was performed using a self-designed DFSC device. The temperature scanning rates range from 10 K/s to 10^6 K/s. The heaters and thermopiles of the used Mettler Toledo UFH 1 high temperature sensors XI469, made by Xensor Integration B.V., are made of doped polysilicon deposited on the 500 nm thin silicon-nitride membrane.

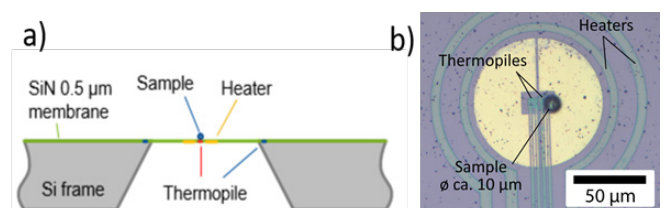


Fig. 2. a) schematic cross-section of differential fast scanning calorimeter measuring cell b) Sensor with spherical particle

schematic cross-section (a) and an image of the sensor (b) are given in Figure 2.

3. Results

3.1. Surface characterization

The SE-SEM image of the surface inoculated aluminum 7075 particles is depicted in Figure 3. The inoculated TiC nanoparticles on the surface of the aluminum alloy powder particle can be clearly observed. The nanoparticles are not homogeneously distributed due to the vacuum drying process and the surface roughness of the aluminum particle. The surface inoculation was further analyzed using EDS (see Figure 3).

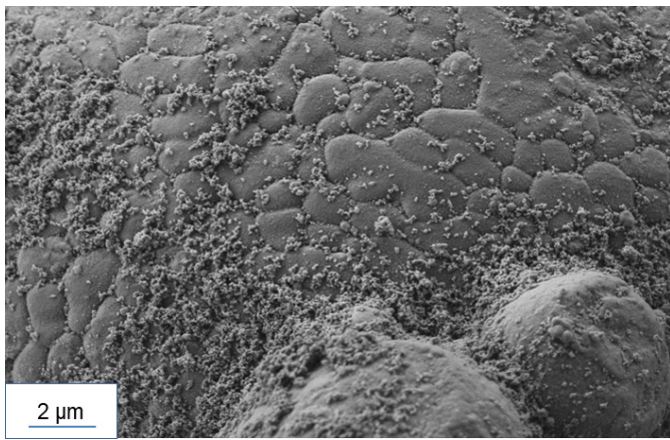


Fig. 3. SE-SEM image of 7075 alloy powder after surface inoculation procedure with inhomogeneous distribution of nanoparticles

The elemental maps of Ti and C and Ti+C are shown in Figure 4 a), b) and c) respectively. TiC nanoparticles could successfully inoculated on the aluminium particle surface. However, the distribution of Ti and C was not uniform in agreement with results shown by Martin *et al.*^[3]

The modified surface was further characterised by means of XPS. The resulting XPS data in Figure 6 approved the successful inoculation and a modified surface chemistry. Prior to the inoculation process, aluminium and adventitious carbon could be detected.^[13]

After the wet-chemical surface inoculation process, the native oxide layer of aluminum was found to be thickened. The metallic peak of the Al 2p and the Mg 2p peak were completely

diminished and the peak intensity for aluminum oxide was increased. The presence of the Ti 2p/2 core level peak confirmed the adsorption of TiC nanoparticles. The peak intensities of the XPS element spectra are shown in Table 2. :

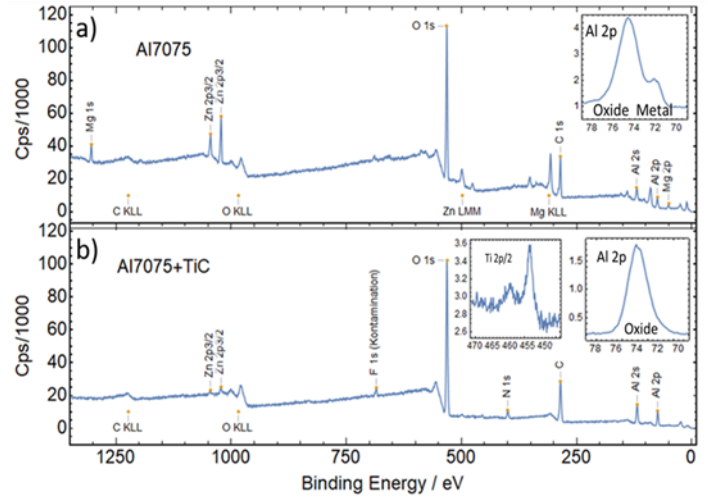


Fig. 5. XPS of Al7075 a) before and b) after surface inoculation procedure, proofed inoculation of titanium carbide and thickening of oxide layer

Table 2. XPS peak positions and atomic concentrations derived from element spectra

	O 1s at-%	C 1s at-%	Al ^{III} 2p at-%	Al ⁰ 2p at-%	Ti 2p at-%	Mg 2p at-%
Al 7075	41.9	29.0	13.5	2.0	-	9.7
Al 7075+TiC	43	35.2	21.4	-	0.4	-

As it is indicated by Figure 3 due to the alkaline pH of the dispersion the process of particle adsorption leads to etching of the Al particle. The formed Al hydroxides are then redeposited as oxyhydroxide films with adhering TiC nanoparticles during the drying process.^[3]

However, concerning the L-PBF process thicker oxide layers might cause a radial inward flow of the melt pool during L-PBF process from lower temperature to increasing temperature. This would lead to a higher critical temperature of the Marangoni coefficient.^[14] Therefore, such an increase in the oxide thickness is critical for a subsequent L-PBF process.

3.2 DFSC results

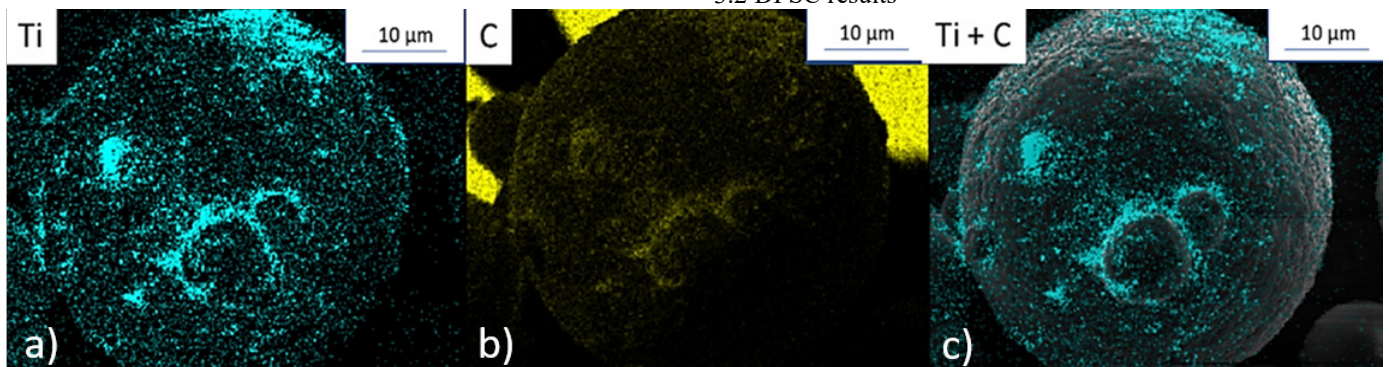


Fig. 4. EDS-mapping of 7075 alloy powder after surface inoculation procedure for a) Ti, b) C and c) Ti+C

DFSC was applied to study the solidification behavior of the surface inoculated aluminum powder. Figure 6 shows the DFSC heat flow curves of a heating and cooling scan at a rate of 500 K/s as function of the temperature. The raw heat flow signals of three samples are given: the Al 7075 powder reference, of a Al 7075 sample that was treated solely with the basic inoculation agent liquid H₂O + PEI (without TiC nanoparticles) as well as a sample that was surface inoculated with TiC nanoparticles.

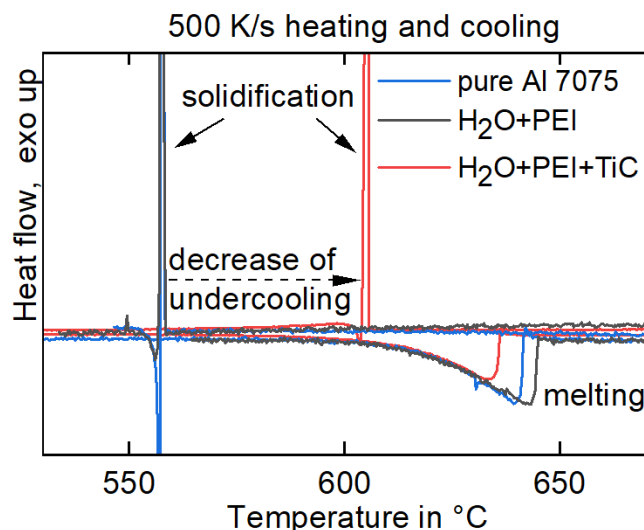


Fig. 5. DFSC curves, modified solidification due to inoculation of AL 7075 alloy powder with Titanium carbide

The curves show a modified solidification behavior of the inoculated sample, in particular the TiC nanoparticles reduce the undercooling prior solidification nucleation of Al7075 significantly. As a result, TiC nanoparticles can be considered to act as very effective nuclei during rapid solidification of Al 7075. For substantially slower cooling rates Sokoluk et al. showed an opposite effect of increased undercooling for nanoparticle modified Al7075 solidification behavior.^[15]

4. Conclusion

In this paper, a wet-chemical surface inoculation process of Al 7075 powder was studied. The SEM-EDS and XPS results confirmed the successful surface inoculation of Al7075 with TiC nanoparticles from PEI containing aqueous solutions. However, the oxide surface film thickness increased during this process due to an etching and redeposition process. The solidification behavior of inoculated aluminum alloy powder was studied by means of DFSC.

These studies showed that TiC nanoparticles on the surface of 7075 powder particles could substantially reduce the undercooling prior solidification of Al 7075.

5. Acknowledgement

The authors acknowledge the German Research Foundation for funding the work under the SPP2122 (Surface Inoculation of Aluminum Powders for Additive Manufacturing Guided by Differential Fast Scanning Calorimetry).

6. References

- [1] a) D. Gu, H. Wang, D. Dai, P. Yuan, W. Meiners, R. Poprawe, *Scripta Materialia* **2015**, 96, 25; b) W. E. Frazier, *J. of Materi Eng and Perform* **2014**, 23, 1917.
- [2] a) O. Gharbi, S. Kumar Kairy, P. R. de Lima, D. Jiang, J. Nicklaus, N. Biribilis, *npj Mater Degrad* **2019**, 3, 151; b) A. Benedetti, M. Cabeza, G. Castro, I. Feijoo, R. Mosquera, P. Merino, *Surf. Interface Anal.* **2012**, 44, 977; c) D. Herzog, V. Seyda, E. Wycisk, C. Emmelmann, *Acta Materialia* **2016**, 117, 371.
- [3] J. H. Martin, B. D. Yahata, J. M. Hundley, J. A. Mayer, T. A. Schaedler, T. M. Pollock, *Nature* **2017**, 549, 365.
- [4] N. Kaufmann, M. Imran, T. M. Wischeropp, C. Emmelmann, S. Siddique, F. Walther, *Physics Procedia* **2016**, 83, 918.
- [5] L. Xi, P. Wang, K. G. Prashanth, H. Li, H. V. Prykhodko, S. Scudino, I. Kaban, *Journal of Alloys and Compounds* **2019**, 786, 551.
- [6] T. M. Yue, C. F. Dong, L. J. Yan, H. C. Man, *Materials Letters* **2004**, 58, 630.
- [7] A. L. Greer, *The Journal of chemical physics* **2016**, 145, 211704.
- [8] Y. Birol, *Journal of Alloys and Compounds* **2006**, 422, 128.
- [9] a) E. Zhuravlev, C. Schick, *Thermochimica Acta* **2010**, 505, 1; b) C. Schick, V. Mathot (Eds.) *Fast Scanning Calorimetry*, Springer International Publishing; Imprint; Springer, Cham, **2016**.
- [10] a) H. Yang, T. Gao, G. Liu, X. Zhao, H. Chen, H. Wang, J. Nie, X. Liu, *Materialia* **2019**, 6, 100333; b) V. A. Popov, M. Burghammer, M. Rosenthal, A. Kotov, *Composites Part B: Engineering* **2018**, 145, 57.
- [11] A. Vilinska, S. Ponnurangam, I. Chernyshova, P. Somasundaran, D. Eroglu, J. Martinez, A. C. West, *Journal of colloid and interface science* **2014**, 423, 48.
- [12] L. Wen, Q. Wang, T. Zheng, J. Chen, *Front. Chem. Eng. China* **2007**, 1, 277.
- [13] U. Tiringner, A. Durán, Y. Castro, I. Milošev, *J. Electrochem. Soc.* **2018**, 165, C213-C225.
- [14] E. O. Olakanmi, *Journal of Materials Processing Technology* **2013**, 213, 1387.
- [15] M. Sokoluk, C. Cao, S. Pan, X. Li, *Nature communications* **2019**, 10, 98.

11th CIRP Conference on Photonic Technologies [LANE 2020] on September 7-10, 2020

Laser powder bed fusion of WE43 in hydrogen-argon-gas atmosphere

Arvid Abel^{a,*}, Yvonne Wessarges^a, Stefan Julmi^b, Christian Hoff^a, Jörg Hermsdorf^a, Christian Klose^b, Hans Jürgen Maier^b, Stefan Kaierle^a, Ludger Overmeyer^a

^aLaser Zentrum Hannover e.V., Hollerithallee 8, 30419 Hannover, Germany

^bInstitut für Werkstoffkunde, Leibniz Universität Hannover, An der Universität 2, 30823 Garbsen, Germany

* Corresponding author. Tel.: +49-511-2788-482; fax: +49-511-2788-100. E-mail address: a.abel@lzh.de

Abstract

Growing demand for individual and especially complex parts with emphasis on biomedical or lightweight applications enhances the importance of laser powder bed fusion. Magnesium alloys offer both biocompatibility and low density, but feature a very high melting point of oxide layers while the evaporation temperature of pure magnesium is much lower. This impedes adequate part quality and process reproducibility. To weaken this oxide layer and enhance processability, a 2 %-hydrogen-argon-gas atmosphere was investigated. A machine system was modified to the use of the novel inert gas to determine the influence of gas atmosphere on hollow cuboids and solid cubes. While processing a 20.3 % decrease in structure width and 20.6 % reduction in standard deviation of the cuboids was determined. There was no significant influence on relative density of solid cubes although eight of the ten highest density specimen were fabricated with the hydrogen addition.

© 2020 The Authors. Published by Elsevier B.V.

This is an open access article under the CC BY-NC-ND license (<http://creativecommons.org/licenses/by-nc-nd/4.0/>)

Peer-review under responsibility of the Bayerisches Laserzentrum GmbH

Keywords: additive manufacturing; laser powder bed fusion, magnesium, magnesium alloys, hydrogen

1. Introduction

The increasing demand for efficient transportation drives the research for lightweight materials especially in additive manufacturing. Furthermore, due to high human life expectancy, innovative solutions for individual and complex biomedical implants are under special focus of research. Magnesium as a material for laser powder bed fusion (also known as Powder Bed Fusion by Laser Beam, PBF-LB/M) suits both applications having a low density while being highly biocompatible [1]. First studies to fabricate single tracks out of magnesium were carried out by Ng et al. in 2009 [2]. They proved that the fabrication of sintered tracks is possible, despite the tendency of balling and spattering. Since then developments in magnesium alloy composition and processing parameters improved the processability [3,4]. The first dense specimen were created in 2012 using magnesium alloy AZ91 with a density of 99.5 %. However, the use of aluminum for

alloying impairs the biocompatibility [4,5,6,7]. A promising magnesium alloy was created in 2016. With an yttrium (Y) content of 4 % and rare earth elements (RE) of 3 % this material (WE43) can be used as a biodegradable material. In PBF-LB a laser melts a multitude of particles in a powder bed, in which these particles are combined into geometric shapes. Due to the fabrication and handling of the magnesium powder, oxygen superficially oxidizes the particle's surface [8]. The obstacle in PBF-LB of magnesium is this formation of oxide layers. The challenge is the high melting point (2852 °C) of the enveloping oxide layer with respect to the pure magnesium's low vaporizing temperature (1110 °C). Due to this gap in processable temperature, the melt pools tend to overheat during the laser exposure. This leads to partial evaporations of the magnesium, which causes porosity [5]. This paper describes the use of a novel inert gas mixture and the effects on the processability of the magnesium alloy WE43 based on a series of investigations on hollow cuboids and solid cubes.

2. Materials and methods

2.1. Machine set up and materials

The machine setup is a SLM125HL PBF-LB system by SLM Solutions GmbH (Luebeck, Germany) with a 100 W continuous wave ytterbium fiber laser. The laser has a focus diameter of 70 μm and a wavelength of 1070 nm. Carpenter Additive (Cheshire, Great Britain) supplied the WE43 alloy.

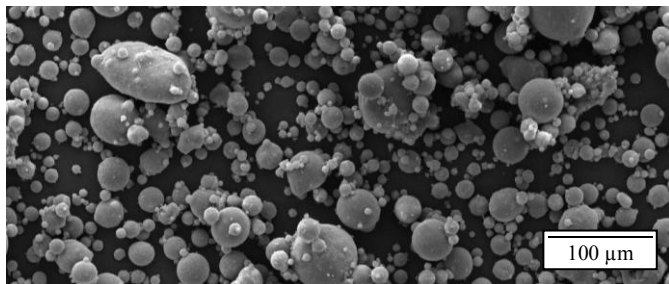


Fig. 1. WE43 powder

After the building process, the specimen are embedded in a two-component epoxy resin. Cross sections of the specimen will be made with a Tegamin-30 by Stuers (Ballerup, Denmark). The evaluation is based on microscopic images of these sections made with a Stemi 2000-C by Zeiss (Oberkochen, Germany) and a VK-X1000 by Keyence (Neu-Isenburg, Germany). The determination of width and density of these images is done with python scripts. To prevent negative consequences of hydrogen use, silica bags are applied in the process chamber, to absorb the resulting moisture of the reaction of hydrogen and the remaining oxygen, which impairs the flowability of the powder and thus the powder application.

2.2. Experimental set up and methods

In this paper, the influence of an admixture of hydrogen in the existing argon inert gas is investigated. This addition is set at 2 % to reduce the risk of oxyhydrogen detonating reactions, but to allow the remaining oxygen to be reduced to moisture, thus reducing oxidation of the molten magnesium. At first, investigations are carried out to determine the influence of the atmosphere on the structure width of single tracks in hollow cuboids. In a second step, the influence on solid cubes and their relative density is examined. The specimen are even cuboids with the dimension of 5 x 5 x 5 mm. The single track cuboids are directly connected to the build plate and the solid cubes are connected with a 1 mm line support structure.

The first series of investigations regarding the single tracks is divided into four blocks, depending on the atmospheric conditions as shown in table 1.

Table 1. Atmospheric conditions of the single track experiment.

Block	Inert gas	Build plate temperature in $^{\circ}\text{C}$
I	100 % Argon	40
II	100 % Argon	200
III	98 % Argon; 2 % Hydrogen	40
IV	98 % Argon; 2 % Hydrogen	200

Each block is divided into four different laser exposure strategies, resulting in 16 groups:

- outer contour line
- an inner contour line
- a double outer laser line exposure
- outer and inner contour line

Within these groups, hollow cuboids with six different parameter sets are produced (Table 2). This results in a total number of 96 samples in the first study. The parameters are given by the statistic software JMP and originate from a preliminary test, with the aim to have a lower (20 W) und upper (100W) energy density boundary.

The expected result of these parameters is a non-melting of the powder at low power and a much wider melting than the laser spot diameter at high power. To get more statistical significance, the parameter with a medium energy density is fabricated twice. The ideal result of the melting process is a dense rectangular wall with the width of the laser spot. The adhesion of one particle layer is expected and so results up to 150 μm are targeted. Results above a wall thickness of 196 μm (i.e. adhesion of the largest particle diameter of 63 μm on both sides of the 70 μm spot) are not desired in this experiment, as an ideal thin structure is to be produced first.

Table 2. Laser parameters of the cuboids.

Number	Laser power in W	Scanning speed in $\frac{\text{mm}}{\text{s}}$
I	20	100
II	20	900
III	60	500
IV	60	500
V	100	100
VI	100	900

The second series of investigations regards the relative density of solid cubes with identical atmospheres according to the blocks in table 1. It considers two hatching strategies:

- chess pattern
- line pattern

Table 3 shows the investigated laser parameters. There is a full factorial experiment within a narrow interval. The hatch distance is set to 45 μm . The resulting total amount of the investigated cubes is 72.

Table 3. Laser parameters for the cubes.

Number	Laser power in W	Scanning speed in $\frac{\text{mm}}{\text{s}}$
I	75	400
II	80	400
III	85	400
IV	75	450
V	80	450
VI	85	450
VII	75	500
VIII	80	500
IX	85	500

3. Experimental Results

3.1. Results of the first investigation

The results of the first investigation show the influence of laser parameters, different hatching strategies and atmospheric condition. The figure 2 shows an exemplary build plate with unextracted specimen and the table 4 shows the overall results, differentiated by laser parameter, forming averages over all atmospheric conditions and exposure strategies. Figure 2 illustrates the evaluation. Three specimens with good and two with undesirable structures can be identified. One of these specimens has too thin and the other too thick structures.

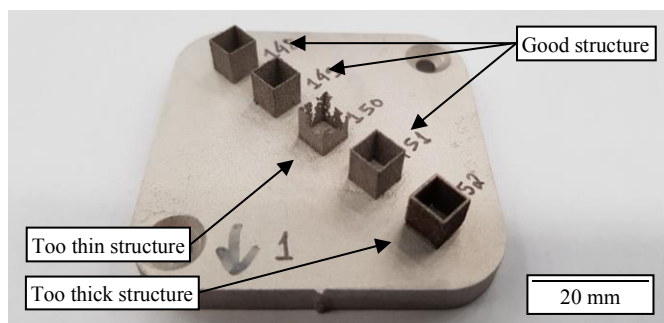


Fig. 2. Single track specimen

Figure 3 shows cross sections of wall structures. The one on the left is too thin, is middle is desirable and the one on the right is too thick. The ideal wall thickness is between 100 to 140 μm , forming a solid wall with the thickness of the laser spot (70 μm) with some adhering particles.



Fig. 3. Cross sections of different wall structures, left too thin (65.2 μm), middle desirable (115.2 μm), right too thick (203.1 μm)

The evaluation is shown in the table 4. Only the parameter III and IV (which are the same) resulting in a thin consistent structure. Thus, 32 desirable test specimens were selected in order to evaluate the influence of the exposure strategy and the atmospheric conditions in the next steps.

Table 4. Averaged results of the cuboids, differentiated by laser parameter

No.	Mean width in μm	Mean standard deviation in μm	Evaluation of the structure
I	84.8	38.7	Too thin & inconsistent
II	-	-	Powder did not melt
III	137.4	24.4	Thin & consistent
IV	140.8	27.0	Thin & consistent
V	590.1	16.8	Too thick & consistent
VI	158.0	33.8	Thin & slightly inconsistent

Table 5 shows the averaged results of the 32 most desirable selected cuboids in structure width and standard deviation differentiated by exposure strategy, averaging the atmospheric conditions. It is displayed that the exposure strategy has no influence on the mean width or the standard deviation.

Table 5. Averaged results of the best cuboids, differentiated by exposure strategy

Exposure strategy	Mean width in μm	Standard deviation in μm
Outer contour	138.7	25.0
Outer contour double	139.0	25.6
Inner contour	139.5	26.9
Double contour	139.3	25.5

The mean values of the wall thickness of the selected cuboids, differentiated by atmospheric conditions are shown in table 6. It is displayed, that the addition of hydrogen in the inert gas decreased the width by 20.3 % and the standard deviation by 20.6 %. There is an influence of the build plate temperature, but it is not systematic.

Table 6. Averaged results of the best cuboids, differentiated by atmospheric condition

Block	Mean width in μm	Standard deviation in μm
I (Ar – 40 °C)	148.9	27.9
II (Ar – 200 °C)	160.8	29.5
III (H ₂ – 40 °C)	119.7	23.3
IV (H ₂ – 200 °C)	127.2	22.3

3.2. Results of the second investigation

The following results display the influence of the build plate preheating temperature, the hatching strategy and the hydrogen addition in the inert gas on the relative density on solid cubes. Figure 4 displays the analyzed cross sections as examples with two different relative densities. These cubes were fabricated with identical parameters except for scanning speed.

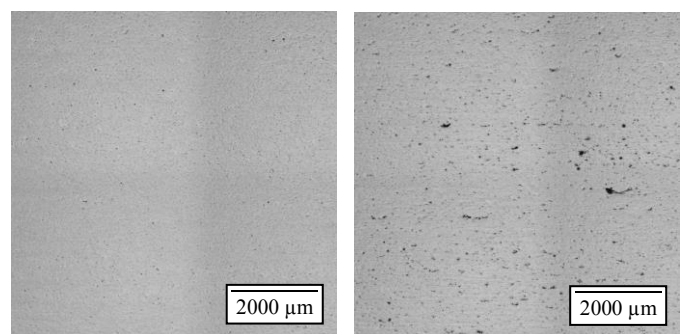


Fig. 4. Cross sections of cubes (H₂, 200 °C, 75 W and 45 μm chess hatching). Left 99.86 % (400 mm/s) and right 98.99 % (450mm/s) relative density

Table 7 shows the mean relative densities of the cubes differentiated by build plate preheating. The difference in median is below the standard deviation, thus negligibly small.

Table 7. Averaged results of the cubes, differentiated by heating temperature

Parameter	Rel. density at 40 °C in %	Rel. density at 200 °C in %
I	99.84	99.91
II	99.70	99.85
III	99.53	99.76
IV	99.57	99.64
V	99.91	99.88
VI	99.65	99.80
VII	99.52	99.35
VIII	99.61	99.60
IX	99.75	99.65
Median	99.67	99.72
Std. deviation	0.13	0.17

The influence of the hatching strategy is displayed in table 8. The mean values over all samples show a difference in 0.25 % density and the standard deviation is reduced by a factor of 4.

Table 8. Averaged results of the cubes, differentiated by hatching strategy

Parameter	Rel. density with chess hatching in %	Rel. density with line hatching in %
I	99.86	99.88
II	99.67	99.88
III	99.51	99.78
IV	99.42	99.79
V	99.89	99.91
VI	99.63	99.83
VII	99.04	99.84
VIII	99.49	99.73
IX	99.61	99.75
Median	99.57	99.82
Std. deviation	0.24	0.06

The table 9 shows the results differentiated by inert gas. It is shown that the difference in density is below the standard deviation and therefore the hydrogen shows no significant influence on mean value. However, eight of the ten specimen with the highest density are fabricated with hydrogen.

Table 9. Averaged results of the cubes, differentiated by inert gas

Parameter	Rel. density Ar in %	Rel. density H ₂ in %
I	99.86	99.89
II	99.74	99.82
III	99.57	99.73
IV	99.63	99.58
V	99.85	99.94
VI	99.70	99.75
VII	99.44	99.43
VIII	99.62	99.60
IX	99.69	99.69
Median	99.68	99.71
Std. deviation	0.12	0.15

4. Conclusion

This investigation shows the influence of a 2 % hydrogen addition in a pure argon inert gas on the production of hollow cuboids and solid cubes in the PBF-LB with the magnesium alloy WE43. The first investigation determined the influence of the inert gas on single track structures in hollow cuboids. Different laser exposure strategies were applied but no impact occurred. A decrease of 20.3 % in structure width and a 20.6 % decrease in the associated standard deviation was shown, due to the addition of hydrogen in the inert gas. Which is a significant improvement and shows the potential of the research in atmospheric parameters in the PBF-LB process.

The second investigation carried out a series of experiments to determine the influence of the inert gas on the relative density of solid cubes. The admixture of hydrogen and the build plate preheating showed no significant influence in terms of mean values of the density. Nevertheless, eight out of the best ten results were fabricated with hydrogen and five of these eight were fabricated with 200 °C plate temperature. It is shown that the line hatching improves the density and significantly reduces the standard deviation. It is suspected that there will be a noticeable difference in a wider process parameter interval, due to the major improvements in the first investigation.

The next steps will be a series of investigations to determine if the hydrogen addition causes a shift of optimal process parameters of the relative density. This should improve the robustness of the process and increase the volume generation rate. The influence on surface roughness of the generated geometries, the microstructure of the building specimen and the tensile properties should be determined.

Acknowledgements

The authors gratefully acknowledge the funding by the German Research Foundation (DFG) within the priority program (SPP) 2122 “Materials for Additive Manufacturing (MATframe)”.

References

- [1] Manakari et al., V., Selective Laser Melting of Magnesium and Magnesium Alloy Powders: A Review, Department of Mechanical Engineering, Nation University of Singapore, Journal Metals, 2017.
- [2] Ng et al., C.C., Selective Laser Melting of Magnesium Alloys, Rapid Prototyping Journal, Vol. 17, 2011.
- [3] Gieseke et al., M., Selective Laser Melting of Magnesium and Magnesium Alloys, Rapid Tech 2015, Erfurt, Trade forum “Science”, 2015.
- [4] Wessarges et al., Y, Selective Laser Melting of Magnesium Alloys for Biomedical Applications, Proceedings of 6th International Conference on Additive Manufacturing, Nürnberg, 2016.
- [5] Jauer et al., L., Selective Laser Melting of Magnesium Alloys, Fraunhofer Institut for Laser Technology ILT, AKL2016, Aachen, 2016.
- [6] Gieseke et al., M., Selective Laser Melting of Magnesium Alloys for Manufacturing Individual Implants, DDMC 2014 Fraunhofer Direct Digital Manufacturing Conference, Berlin, 2014.
- [7] Tandon et al., R., Emerging applications using magnesium alloy powders: A feasibility study, Magnesium Technology 2014, The Minerals, Metals & Materials Society, 2014.
- [8] Gieseke et al., M., Challenges of processing Magnesium and Magnesium Alloys by Selective Laser Melting, World PM2016, Proceedings, 2016

11th CIRP Conference on Photonic Technologies [LANE 2020] on September 7-10, 2020

Snapshot hyperspectral imaging for quality assurance in Laser Powder Bed Fusion

N. Gerdes^{a,*}, C. Hoff^a, J. Hermsdorf^a, S. Kaierle^a, L. Overmeyer^a

^aLaser Zentrum Hannover e.V., Hollerithallee 8, 30419 Hannover, Germany

* Corresponding author. Tel.: +49 511 2788-348; fax: +49 511 2788-100. E-mail address: n.gerdes@lzh.de

Abstract

Laser Powder Bed Fusion (LPBF) is widely considered a key enabling technology of the future. In order to realize its full potential, however, reproducibility and in-process quality inspection capabilities have to meet industrial requirements. The application of novel sensor technologies such as hyperspectral cameras and intelligent data evaluation methods like machine learning models will allow more reliable manufacturing processes.

This article discusses the value of snapshot hyperspectral imaging as a means to predict process states and defects with the help of machine learning algorithms. The imaging technology is presented and its characteristic advantage of providing spectral as well as spatial resolution is weighed against the drawbacks of low temporal resolution and reduced spatial resolution. Besides, different methods and configurations for in-process data acquisition and subsequent data labeling are explained. Finally, the utilization of this monitoring approach to the LPBF-processing of magnesium alloys is discussed and results are presented.

© 2020 The Authors. Published by Elsevier B.V.

This is an open access article under the CC BY-NC-ND license (<http://creativecommons.org/licenses/by-nc-nd/4.0/>)
Peer-review under responsibility of the Bayerisches Laserzentrum GmbH

Keywords: Laser Powder Bed Fusion, Additive Manufacturing, Process Monitoring, Hyperspectral Imaging, Machine Learning

1. Introduction

The technological benefits of Laser Powder Bed Fusion (LPBF, also Metal PBF-LB) have sparked bold visions of a future without conventional manufacturing. Although this is exaggerated, the technology does hold tremendous potential especially for lightweight applications or biomedical implants. The complexity of the process along with the completely different nature of crystal structure formation compared to traditional forging or casting techniques, however, still pose a significant challenge in terms of reproducibility and quality assurance [1].

In-process quality assurance approaches aim to monitor process quality on-line during the process. There are two ways to integrate the sensor into the machine setup: on-axially (also called co-axially) or off-axially. The on-axis approach is suited for high-frequency observation of the melt pool that allows

closed-loop control of laser parameters. The off-axis approach, on the other hand, makes it possible to monitor the entire build platform and thus allows geometry-based analysis.

Spatially integrated on-axis sensors like photodiodes or pyrometers are the most widely adapted monitoring tools on the market [2]. Reference signals are gathered for certain parts and materials and compared to the signals measured in the process at hand. Besides, spatially resolved sensors like high-speed or bolometric cameras have been applied as well, both on- and off-axially [3, 4]. The process emissions could be linked to material properties and pore formation. There are yet other approaches providing spectral information about the process zone [5], but sacrificing temporal and spatial information.

This article presents a further approach for powder bed monitoring using a sensor that combines both spatial and spectral resolution in what is called snapshot hyperspectral

imaging. The sensor specifications are explained in section 2 along with characteristic benefits and drawbacks. Section 3 describes the integration of the camera into the LPBF process and section 4 provides insight into how to evaluate the data using methods of machine learning as has been used already in LPBF for conventional cameras [6]. The conclusion finally gives an evaluation of the findings and the potential benefits of future application of this monitoring technique.

2. Snapshot hyperspectral imaging

Table 1 gives an overview of the most important features that the camera used in this work offers. Each pixel is coated with one of 25 different Fabry-Pérot interference filters that each has a different spectral transmittance. Each spectral transmittance peak is accompanied by a second harmonic, necessitating the use of spectral filters. In this work, an 875 nm shortpass filter was used to protect the camera from direct reflections of the laser light at 1070 nm. The 25 spectral bands therefore lie between 600 and 875 nm.

The Fabry-Pérot filters are spread over the CMOS sensor in 5 x 5 patterns, also called mosaics, resulting in a resolution of 409 x 217 x 25 channels from the initial 2048 x 1088 pixels. Fig. 1 illustrates the mosaics on the CMOS sensor chip. The height of the Fabry-Pérot interference filters correlates with the wavelength they are transmissive to.

Table 1. Overview of camera characteristics.

Specification	Ximea MQO22HG-IM-SM5X5-NIR
Resolution	Original: 2048 x 1088 Spatial: 409 x 217
Spectral range	600 – 975 nm; 25 bands
Sensor	2/3" CMOS
Frame rate	170 fps at full resolution
Dimensions	26 x 26 x 31 mm ³
Weight	32g

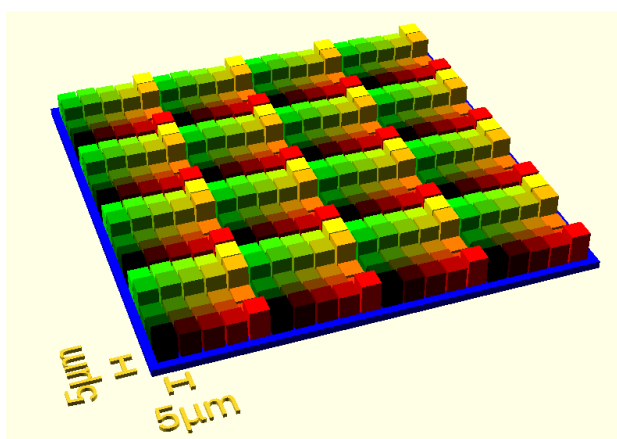


Fig. 1. Illustration of CMOS sensor chip with 5 x 5 mosaic patterns of Fabry-Pérot filters.

This configuration is prone to noise from crosstalk induced by non-parallel light beams. Further noise is caused by dark current, vignetting effects as well as chromatic aberration of the optical setup. Besides, the sensitivity in one pixel is not

confined to one narrow wavelength band around the peak, but has several minor peaks at other wavelengths. This latter effect can be accounted for by a so-called correction matrix.

The major benefit of this sensor technology, namely the combination of spectral as well as spatial resolution, comes with certain costs: comprehensive correction/calibration, reduced spatial and temporal resolution when compared to high-speed cameras and reduced spectral resolution when compared to spectrometers. Table 2 lists the advantages and drawbacks of different sensor technology that has been used for process monitoring in Laser Powder Bed Fusion. Snapshot hyperspectral imaging fulfills a niche whose potential shall be discussed in the remainder of this article.

Table 2. Overview of sensor technology for LPBF process monitoring.

Sensor	Advantage	Drawback
Photodiode	+High temporal resolution	-No spatial resolution
	+Little data size	-No spectral resolution
	+Easy to integrate	-Low cost
High-speed camera	+High spatial resolution	-Amount of data
	+High temporal resolution	-No spectral resolution
Bolometer	+LWIR-sensitivity	-Low Temporal resolution
Camera	+Good spatial resolution	-Require specialized optics
Spectrometer	+Excellent spectral and good temporal resolution	-No spatial resolution
		-Prone to chromatic aberrations
Snapshot hyperspectral camera	+Good spatial and spectral resolution	-Correction/Calibration necessary
		-Amount of data

3. LPBF process and sensor integration

The laser melting experiments were done using the magnesium alloy WE43 as powder material. The main characteristics of the powder are shown in table 3. The alloy contains rare-earth elements and its main application area are biomedical implants. The build platform consisted of the magnesium alloy AZ31 substrate with a diameter of 50 mm.

Table 3. Powder properties.

Powder material: magnesium alloy WE43		Measurement technique
Composition	Mg: 92.2; Y: 4.3; Nd: 3.4 (in wt.%)	EDX
Particle size distribution	D10: 13.6; D50: 31.4;	Dynamic Particle Image Analysis
	D90: 58.5 (in µm)	
Sphericity	SHP < 0.8: 15.3 %; SHP < 0.9: 53.1 %	
Hausner ratio	1.26	ISO 3953
H ₂ O-content	0.05 %	Karl Fischer Titration

The hyperspectral camera was integrated into a laboratory LPBF machine setup, as can be seen in Fig. 2 (a). The objective's working distance is fixed at 190 mm, the magnification 1,0x and its field of view (FOV) thus

corresponding to the sensor size. Fig. 2 (b) shows the orientation of the manufactured part on the build platform. One rectangular layer was built with the dimensions $14 \times 10 \text{ mm}^2$ with the camera's FOV in the center with dimensions of $10 \times 6 \text{ mm}^2$. This way, a maximum number of frames is collected from the center of the scan vectors.

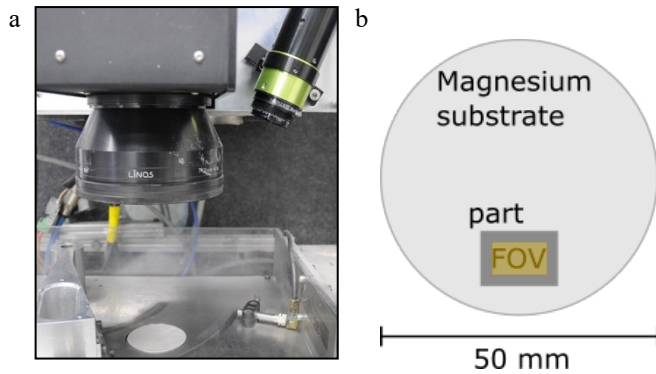


Fig. 2. (a) Laboratory machine setup with off-axis camera integration; (b) magnesium AZ31 substrate with laser melted part and field of view of the camera.

For data acquisition, a script was programmed to only save images during laser exposure in the FOV. To improve data handling, the saved images were post-processed directly after exposure of the layer was done. The 2048×1088 images were reduced to 100×100 images by determining the original image's maximum pixel value and defining it as the center. The cropping was then done such that the spectral bands' pixel locations were identical for each post-processed frame.

Fig. 3 shows an example of a post-processed image during laser melting of WE43 powder. The 100×100 image is converted into a 20×20 image with 25 different spectral bands. The peaks of the 25 spectral bands lie between 600 and 875 nm, with a FWHM between 3 and 12 nm. The exposure time of the camera was set to 4 ms for the entirety of the experiments.

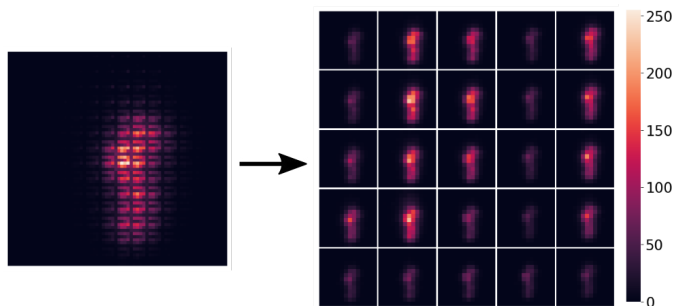


Fig. 3. Example of image acquired during laser melting of WE43 powder. The 100×100 image is converted into a 20×20 image with 25 channels. The colorbar shows gray values from 0 – 255.

In order to determine suitable laser process parameters, reference values were taken from literature [7]. All parameters except laser power and scan speed were kept constant. These parameters and the corresponding values are listed in table 4.

Table 4. Laser process parameters.

Process Parameter	Value
Laser type	CW fibre laser, 1070 nm
Laser spot size	$19 \mu\text{m}$
Hatch distance	$10 \mu\text{m}$
Scan pattern	Stripe pattern
Blade type	Carbon fibre
Atmosphere	Ar with crossjet; $< 1000 \text{ ppm O}_2$
Layer thickness	$40 \mu\text{m}$

4. Data evaluation

The target value of the investigations was the surface roughness of additively manufactured WE43 alloy. In order to keep ambient conditions as reproducible as possible, only one layer was manufactured while the process was monitored with the hyperspectral camera. Three parameter combinations of laser power and scan speed were selected from literature [7]. One was reported to lead to dense parts and good reproducibility (50 W ; 75 mm/s), one to too much energy input (50 W ; 40 mm/s) and the final one to too little energy input (20 W ; 75 mm/s). For every parameter set, two samples were manufactured and its roughness was determined. Table 5 presents an overview of the samples, the roughness R_z and the number of frames acquired from that sample.

Table 5. Overview of samples processed and monitored.

Sample	Laser Power; Scan Speed	Roughness R_z [μm]	Number of frames
1.	50 W ; 75 mm/s	30.5	3581
2.	50 W ; 75 mm/s	31.0	3607
3.	50 W ; 40 mm/s	28.6	6644
4.	50 W ; 40 mm/s	43.4	6678
5.	20 W ; 75 mm/s	69.1	802
6.	20 W ; 75 mm/s	70.0	2788

The roughness R_z was measured according to DIN EN ISO 4288 using a Keyence VK X1050 confocal microscope. The cut-off wavelengths λ_c and λ_s were set to 2.5 mm and $8 \mu\text{m}$, respectively. The measuring section l_n was therefore 12.5 mm long. Fig. 4 shows the confocal image of the first sample and the location of five measuring sections that all lie in the FOV of the camera. The average of the five roughness values was taken as the final value that was used as a label for all the camera images taken at the respective sample. The exact same procedure was repeated for all six samples.

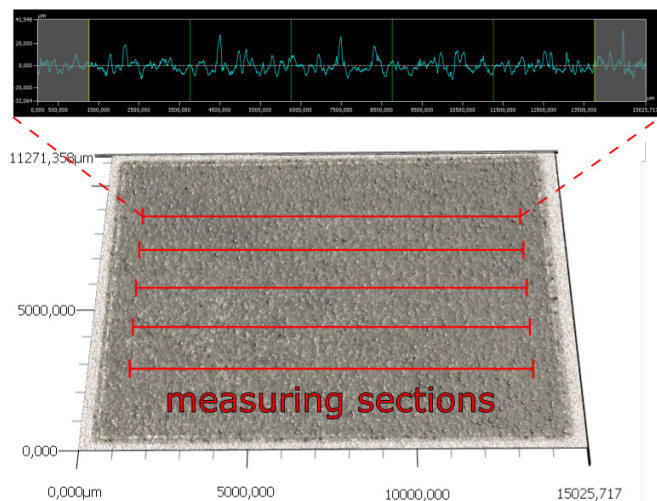


Fig. 4. Image of first WE 43 sample taken with a confocal microscope. The roughness R_z was determined at five measuring sections.

To predict the roughness from a hyperspectral image of the process zone, a simple convolutional neural network (CNN) was designed and trained with the labeled images. The open source machine learning framework Keras was used to set up the network architecture shown in table 6. The table shows how the data from the input images is processed and passed through the layers of the neural network. The images have a large number of channels (25), but are otherwise very small (20×20), which is why no max-pooling layers were applied. Of the data available, 60 % served as training set, 20 % as validation set and another 20 % as test set data.

Table 6. Network topology of CNN designed to predict roughness R_z .

Layer	Output Shape	Trainable Parameters
1. Input images	$20 \times 20 \times 25$	0
2. Conv-2D-layer	$18 \times 18 \times 32$	7,232
3. Conv-2D-layer	$16 \times 16 \times 64$	18,496
4. Conv-2D-layer	$14 \times 14 \times 128$	73,856
5. Conv-2D-layer	$12 \times 12 \times 128$	147,584
6. Flatten	18432	0
7. Dropout (rate = 0.4)	18432	0
8. Dense-layer	32	589,856
9. Dense-layer	1	33

The metric to be optimized was chosen to be mean absolute error (MAE). The deviation between predicted and actual surface roughness shall thus be minimized. Fig. 5 shows the evolution of the metric during training for the training and validation data sets. Even though a dropout layer with a dropout rate of 0.4 was implemented, a slight overfitting can be observed towards the end of the training process.

The final mean absolute error of the roughness R_z that was achieved for the test data set was $2.1 \mu\text{m}$. For the smallest roughness measured, $28.6 \mu\text{m}$, this corresponds to a deviation of 7.3 %.

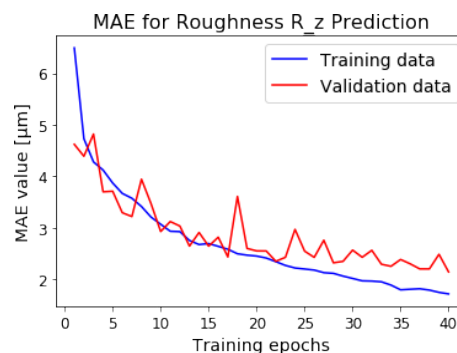


Fig. 5. Evolution of mean absolute error for training and validation set during training of the CNN.

5. Conclusion

Snapshot hyperspectral imaging is a novel sensor technology with characteristic advantages (combination of spatial and spectral resolution) and drawbacks (data handling and low temporal resolution). The first results show that it has potential for beneficial use in process monitoring of laser powder bed fusion, since the surface roughness R_z of additively manufactured magnesium alloy WE43 could be predicted within a reasonable error range of at most 7.3 % using convolutional neural networks.

Due to the small number of samples manufactured, these results should be regarded preliminary. Investigations with larger sample numbers are necessary to validate the findings statistically.

To further improve monitoring with this sensor technology in the future, the laser scanner mirror position shall be correlated with the acquired images, spectral correction algorithms shall be enhanced and further network topologies shall be applied to the data.

Acknowledgements

The authors gratefully acknowledge the funding by the German Research Foundation (DFG) within the priority program (SPP) 2122 “Materials for Additive Manufacturing (MATframe)”.

References

- [1] Schmidt M, Merklein M, Bourell D, Dimitrov D et al. 2017. Laser based additive manufacturing in industry and academia. *Cirp Annals*, 66(2), 561-583.
- [2] Spears TG, & Gold SA. 2016. In-process sensing in selective laser melting (SLM) additive manufacturing. *Integrating Materials and Manufacturing Innovation*, 5(1), 16-40.
- [3] Clijsters S, Craeghs T, Buls S, Kempen K et al. 2014. In situ quality control of the selective laser melting process using a high-speed, real-time melt pool monitoring system. *The International Journal of Advanced Manufacturing Technology*, 75(5-8), 1089-1101.
- [4] Krauss H, Zeugner T, Zäh MF. 2014. Layerwise monitoring of the selective laser melting process by thermography. *Physics Procedia*, 56, 64-71.
- [5] Staudt T, Tenner F, Klämpfl F, Schmidt M. 2017. Development of a hyperspectral imaging technique for monitoring laser-based material processing. *Journal of Laser Applications*, 29(2), 022601.
- [6] Zhang B, Liu S, Shin YC. 2019. In-process monitoring of porosity during laser additive manufacturing process. *Additive Manufacturing*, 28, 497-505.
- [7] Gieseke M, Noelke C, Kaierle S, Wesling V, Haferkamp H. Selective laser melting of magnesium and magnesium alloys. In *Magnesium Technology 2013*, pp. 65-68. Springer, 201

11th CIRP Conference on Photonic Technologies [LANE 2020] on September 7-10, 2020

Experimental investigations on the influence of temperature for Laser Metal Deposition with lateral Inconel 718 wire feeding

Thomas Bergs^b, Sebastian Kammann^{a*}, Gabriel Fraga^a, Jan Riepe^a, Kristian Arntz^a

^aFraunhofer Institute for Production Technology IPT, Steinbachstraße 17, Aachen 52074, Germany

^bLaboratory for Machine Tools and Production Engineering (WZL) of RWTH Aachen University, Campus-Boulevard 30, Aachen 52074, Germany

* Corresponding author. Tel.: +49 241 8904-565; fax: +49 241 8904-6565. E-mail address: sebastian.kammann@ipt.fraunhofer.de

Abstract

In the present work, the thermal history influence on Inconel 718 thin-wall structures fabricated by wire-based Laser Metal Deposition (LMD-w) was analyzed. To perform the depositions, a novel processing head with wire force and gas nozzle temperature monitoring was employed. Based on the thermal radiation a temperature threshold for a stable process could be defined. General process trends and typical defects as cracks, pores and lack of fusion are also discussed. Additionally, Scanning Electron Microscope (SEM) images and Energy Dispersive Spectroscopy (EDS) were employed to verify the influences of different cooling rates and the deposition strategy on the microstructure. Finally, to verify the resulting mechanical properties, hardness measurements were performed on each sample. It was found that, for thin-wall fabrication by LMD-w, heat accumulation can adversely affect the build-up. Therefore, cooling of interlayers is suggested as a strategy to mitigate such a problem.

© 2020 The Authors. Published by Elsevier B.V.

This is an open access article under the CC BY-NC-ND license (<http://creativecommons.org/licenses/by-nc-nd/4.0/>)

Peer-review under responsibility of the Bayerisches Laserzentrum GmbH

Keywords: wire-based Laser Metal Deposition (LMD-w); Inconel 718; Thermal radiation; Thin-walled structures; Laser additive manufacturing

1. Introduction

In view of the increasingly pronounced demand in the aerospace industry for a more sustainable footprint, manufacturing processes capable of reducing material waste are required, particularly in the production of components and spare parts for gas turbines. In this context, the machining of superalloys for high performance applications remains a technological challenge due to the inherent high temperature stresses within the manufactured specimen, which can lead to premature tool wear and increased machining costs. [1].

Within the last five years, both industry and science have shown an increased interest in Additive Manufacturing (AM) processes. This is mainly due to its potential for the fabrication of complex geometries, short product lead time and design freedom [2].

One of the possibilities for repair and fabrication of aerospace components is the wire-based Laser Metal Deposition (LMD-w) process, classified under the physical principle of Directed Energy Deposition (DED) [3]. In the LMD-w process, a laser beam is used as a heat source to continuously melt wire feedstock material into a melt pool. Due to the high-cooling rate weld beads can be deposited. Furthermore it is possible built complex structures by the subsequent deposition of beads in a layer-wise manner [4].

The advantages of using wire as feeding material include benefits of an established supply chain for welding equipment as well as the contamination-free handling of the filler material. Furthermore, Arrizubieta et al. observed that for geometrically simple components, the LMD-w process has an advantage against the powder based LMD process when higher deposition rates are required for the repair or manufacture of bigger parts [5].

However, the LMD-w technology has also got some drawbacks. The process is sensitive to the wire position and orientation relative to the melt pool [6]. In addition, high throughput deposition is often limited by considerable heat accumulation, insufficient surface quality and a coarse solidification structure. [7].

In the existing literature, the influence of several cooling regimes on LMD-w thin-walled deposits and the associated feasibility problems in the application of constant process parameters such as grain formation and the formation of a unidirectional microstructure are recognized. [8]. Furthermore, crack formation, part distortion and residual stresses are intrinsically connected with the heat input in the process. Due to the small laser spot size the heat input of the LMD-w process is rather low compared to the WAAM process. Despite those advantages, there are still challenges with the LMD-w process. Freund et al. have observed macroscopic crack formation while they were setting up thin-walled structures [9].

Therefore the mechanisms and the influences of the building strategy, regarding the thermal history, in parts fabricated by LMD-w are yet not fully understood. Also, to increase the industrial readiness level of the LMD-w technology it is important to adapt the manufacturing strategy and process parameters to local instabilities [10]. In order to understand the influences of the temperature on thin walled structures two different approaches are compared within this publication. Based on these results it is possible to set up specific process strategies regarding the resulting microstructure and defects for the manufacturing of thin-walled structures with the LMD-w process.

2. Experimental Setup

To perform the thin-wall depositions, the recently developed laser processing head LMD-W-20-L (see Fig. 1A) was used [11]. The modular design utilizes commercially available optical components and wire feeding systems. In the actual configuration, the relative position of the optical system (OTS 5, Laserline) and the Wire Feeding System (MF1 30, Abicor Binzel) have some degree of freedom and can be adjusted according to the process requirements. Such an adjustment is conducted with the support of a coaxial camera image (see Fig. 1C). The wire is fed laterally at 20° relative to the beam central

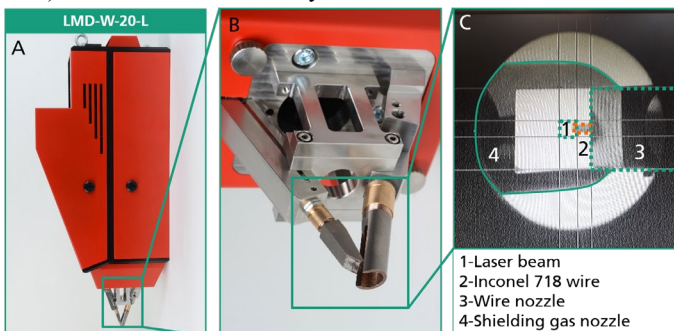


Fig. 1. A- LMD-W-20-L processing head. B- Wire nozzle for lateral feeding and shielding gas nozzle. C- Wire-beam adjustment by coaxial camera.

axis. For the conducted experiments the distance of the solid wire to the center of the laser beam was 0.63 mm (Fig. 1B).

Additionally, the LMD-W-20-L is equipped with the following sensors: Wire force (strain-gage concept), wire contact tip temperature (thermocouple), shielding gas flow and laser activation. The sensor data is acquired and the process can be monitored online. In order to avoid peripherals damage the process can be stopped manually, whenever the force on the wire or the temperature on the contact tip are above a certain threshold.

Further equipment in the experimental setup included a continuous-wave multimode diode laser source (LDF 4500-30 VGP, Laserline) with nominal power up to 4,5 kW within the experiments the wavelengths: 940 nm, 980 nm, 1020nm and 1064 nm were used.

The motion was provided by a Cartesian machine, controlled via numerical control (NC) (840D, Siemens). Argon 4.6 (purity 99.996 vol. %) was used as shielding gas. For convenient process parameters, a process window, based on a full factorial design of experiments, i.e. based on different machine feeding rates and laser power, was examined in advance. Within the setup the ratio of machine and wire-feedrate was kept constant at 1.1. Unsuitable process parameters were identified on the basis of the occurrence of smoke trails, waviness structure, macroscopic pores and cracks or the formation of droplets (Table 1). A laser beam, with a non-real Gaussian beam distribution and a 1.9 mm spot size was used. The Intensity I in the process zone can be expressed by Eq. (1) [7].

$$I = P_L/A \quad (1)$$

P_L is the laser power and A is the laser beam focal spot area.

Table 1. LMD-w process parameters

Parameter	Value
Laser Power (P_L) [W]	1200
Travel Speed [mm/min]	900
Wire Speed [mm/min]	990
Shielding Gas Flow Rate [l/min]	20
Irradiance [W/mm ²]	199.57
Focal spot area (A) [mm ²]	6.01

For the LMD-w process Inconel 718 wire (diameter of 1.2 mm) was used as a feedstock and S355J2+N Steel was used as a substrate.

Table 2. Typical chemical composition of Inconel 718 wire (EN 2.4668).

Element	Ni	Cr	Fe	Nb	Mo	Ti
Percentage by weight (wt %)	54	18	18	5	3	1

To better understand the effect of the heat input and thermal history in the overall LMD-w process stability, thin-wall structures were manufactured using two build-up strategies:

- Beads deposited subsequently, without cooling step between layers (Strategy 1)
- Interlayer cooling: The temperature of the structure was reduced to 21 ° prior of the deposition, by the usage of compressed air (Strategy 2). To ensure comparable cladding conditions the temperature was measured with a thermocouple before each step.

The height difference of each toolpath layer was established as 0.65 mm and kept constant throughout the depositions.

Several thin walled structures were cladded with both strategies, within the paper the two (representative) specimen are compared, since both of them had the same process parameters and toolpath. In other samples, adjustments were made to the tool path planning and waiting times for melt pool formation, making a detailed comparison not feasible.

To track the heat input evolution into the part in progress, both depositions strategies were recorded with an infrared thermal camera (FLIR S65, FLIR Systems). To calibrate the camera, the emission was determined in advance with the combined usage of a thermocouple and the camera. Thermal radiation was subsequently analyzed with the camera supplier software (ThermaCAM Researcher Pro 2.8, FLIR Systems). In order to examine the effects of the thermal radiation on the entire component, the evaluation was carried out with the frames that were recorded one second after deactivating the laser. The relevant parameters of the thermal camera are summarized in Table 3.

Table 3. Thermal camera parameters employed in the measurements

Parameter	Value
Emissivity	0.10
Spectral range [μm]	7.5 - 13
Temperature range [°C]	150 – 550
Resolution [pixel]	640 x 480
Frequency [Hz]	60

The schematic of the overall experimental setup is shown in Fig. 2.

After the deposition of thin-walled samples, three different cross-sections of each sample were prepared by conventional metallographic technique. The etching was performed with 160 mL HNO₃ and 6 mL HF per sample.

In the sequence, the samples were analyzed by optical light microscopy (Axio Imager 2, ZEISS). Scanning electron microscopy (SEM) (Neon 40 EsB, ZEISS) and energy dispersive X-ray spectrometry (EDS) (Inca, Oxford Instrument) were used for the microstructural analysis.

Finally the micro hardness of each strategy was measured to correlate the effect of the different strategies to the mechanical properties. Hence, Vickers indentations with a contact time of 5 s and applied load of 0.1 kg were performed (durometer M-400-H, Akashi Corp.). The measurements were taken vertically on the wall, in the bottom-up direction (see Fig. 3).

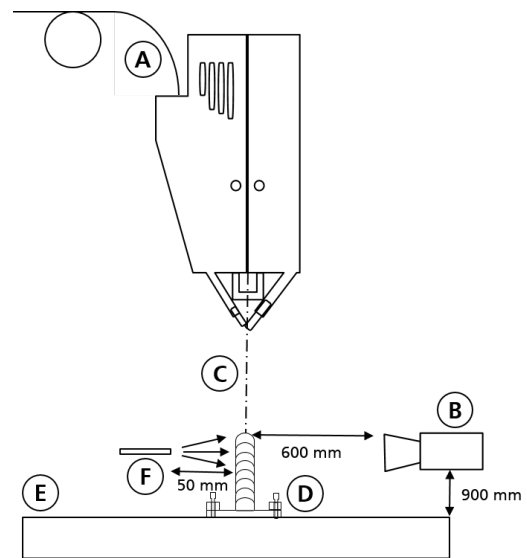


Fig. 2. Schematic of experimental apparatus. A - LMD-W-20-L processing head. B - Infrared camera. C - Deposited thin-wall structure. D - Clamping device. E - CNC working table. F - Compressed air for inter layer cooling

3. Results and Discussion

For the depositions without cooling (Strategy 1), the process was stable throughout seven layers (4.5 mm). In the eighth layer, an unstable process was observed, with a globular metallic transfer. This results in the formation of waves and droplets, which prevented further cladding progress (see Fig. 3A).

The wall-like structures deposited with interlayer cooling (Strategy 2) did not present defects. Thus, a total of twenty layers (12.5 mm) were deposited by a stable process, but the second specimen has a strongly sloping contour towards the end of the clad, which is a result of a non-optimized G-Code (see Fig. 3B). Both specimens had an average width of 2.5 mm. Macroscopically visible pores or cracks, which indicate a

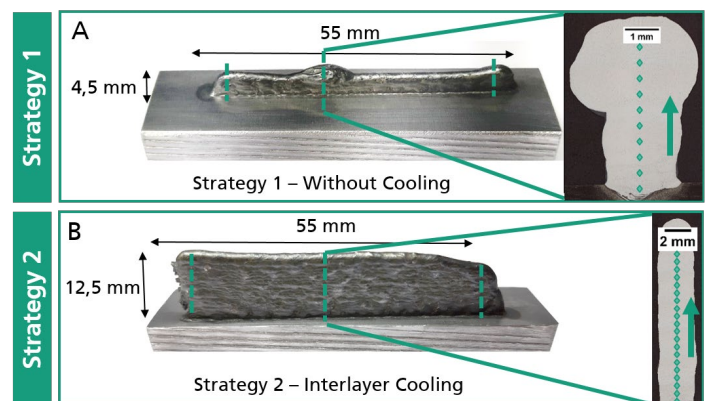


Fig. 3. Inconel 718 thin-wall structures fabricated through LMD-w with different build-up strategies. Samples for metallographic analysis were taken along the dashed lines. The positions of the hardness measurements are indicated in the cross sections by dots. A - Without cooling stage between layers. B - Interlayer cooling through air forced convection.

crucial manufacturing failure, could not be detected on any manufactured specimen .

The SEM images show a pore-free structure for both the processes (see Fig. 4A and Fig. 4C). Besides this, in both manufactured specimen no crack formation was detected. In addition, both samples contain a fine distribution of carbides, as can be expected for Inconel 718 (see Figure 4B and Figure 4D). The microstructure of both specimens presents columnar grain growth, typical of high-cooling rate and unidirectional processes [12]. Therefore, it can be expected that the resulting manufacturing strategy of the thin-walled structures does not influence the microstructure in a critical aspect. Nevertheless, the formation of small oxide particles was observed for both strategies (see Fig. 4B and Fig. 4D). In order to overcome this issue, further adjustments regarding the shielding gas flow need to be considered.

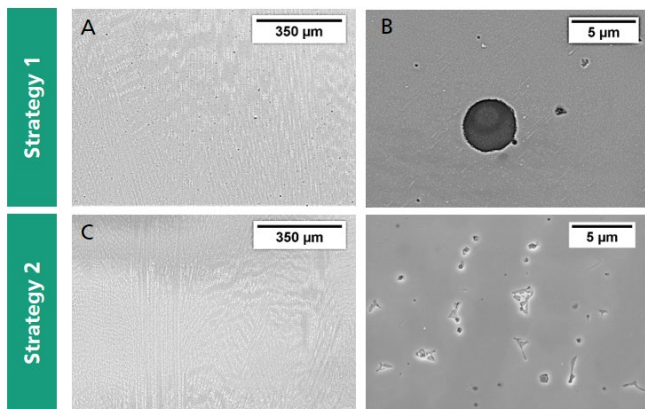


Fig. 4. SEM images from the cross-section of Inconel 718 thin-wall structures. Both deposition strategies resulted in dendritic microstructure (A and C), with small oxidized surfaces (B and D).

To verify the resulting microstructure regarding its element distribution, an EDS analysis was performed on a small surface of a specimen fabricated with the second strategy (see Fig. 5). Inconel 718 has around 1% content of titanium (see Table 2), which rapidly reacts under oxygen presence [13]. Hence, the presence of oxygen and titanium indicates a surface oxidation. On the other hand, the presence of niobium and molybdenum are characteristic from the Inconel 718 alloy composition.

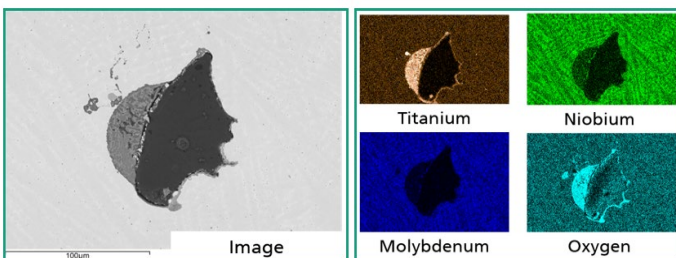


Fig. 5. EDS analysis of an oxidized surface of the specimen produced with the second strategy. The oxidized surface can be clearly identified by the presence of oxygen and titanium. The presence of niobium and molybdenum indicates the Inconel 718 composition.

It can be observed that there are small oxidized pores (< 100 µm) in the sample. Therefore, it is necessary to make adjustments in the shielding gas supply to overcome these defects.

The thermal radiation distribution along the deposited layers, is shown in Fig. 6. The absence of a cooling stage between the

different layers (Strategy 1) led to a gradual increase in the profile, as evidenced by the comparatively higher values of maximum of 203 °C in the first layer and 495 °C in the seventh layer. As a result of the excessive heat input the process failed and it was not possible to deposit further layers on the specimen, as depositions at high temperatures result in a poor surface quality and part distortion [8,14,15].

As for the usage of Strategy 2, the result is a uniform thermal radiation of the welding beads. The first cladbed bead shows an increase of the temperature, based on the thermal radiation, at the end of each bead with maximum of 180 °C. The overall temperature, based on the thermal radiation, of the specimen, welded with strategy 2, remained continuously below 200 °C, even for the twentieth layer. This result indicates that above a certain height, there is steady heat flow, which could prevent the process stability and part fabrication of being affected by a three-dimensional heat conduction behavior [16]. However, it needs to be noted, that the melting pool emission changes abruptly during the solidification process and the transition time from liquid to a solid state is below 0.5 seconds [8]. Therefore it is not possible to make statements about the specific temperature within the melt pool, nor of the molten wire. Consequently, only statements about the temperature

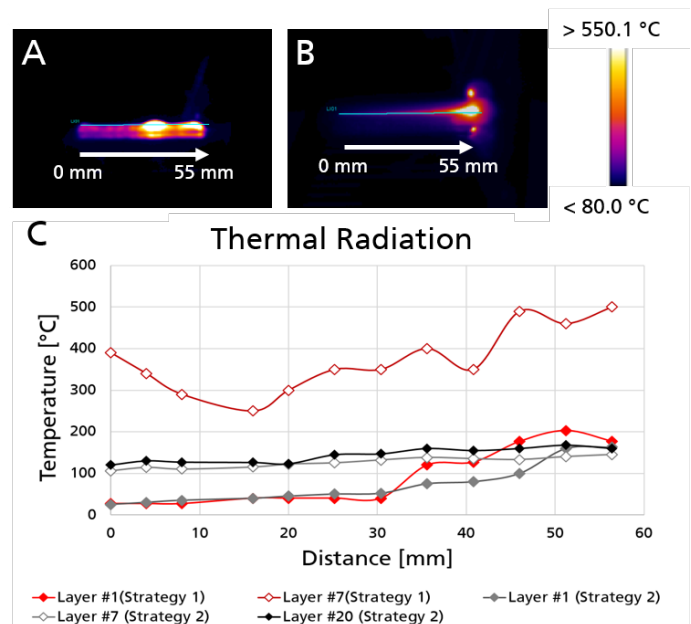


Fig. 6. A - Thermographic data of the process at 4.5 mm of strategy 1 which lead to a process stop. B - Thermographic image of the process at 4.5 mm for strategy 2, the process could be continued. C - Thermal Radiation along the bead for the two different build-up strategies, showing a higher heat accumulation for Strategy 1 (without cooling).

distribution within the specimen can be made and are presented within this work. Further emission analysis and thermocouple-aided temperature profile assessments are presented in the literature [7].

The Vickers microhardness measurements, shown in Fig. 7, aim to compare the specimens' mechanical properties with each other. Measurements were made in the direction of the arrow, with the initial measurement at the level of the substrate (Fig. 3). For Strategy 1 (without cooling), no significant hardness variation is observed throughout the deposition direction, with an overall mean value of 257 ± 20.56 HV 0.1. Results from Strategy 2 (interlayer cooling) have an overall mean value of 259 ± 10.34 HV 0.1. Both mean values are comparable to micro hardness values of Inconel 718 deposits via LMD before a heat treatment [17].

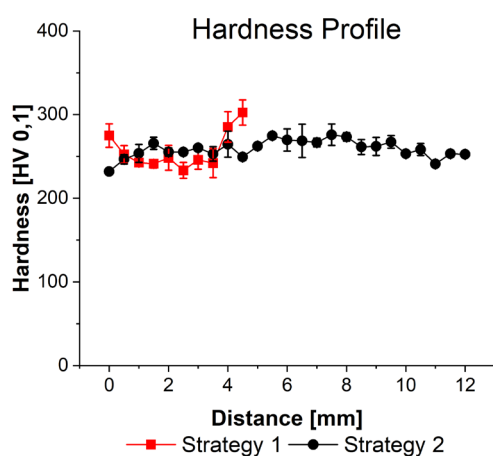


Fig. 7. Vickers micro hardness measurements for thin-wall structures at the as-deposited condition. Both specimens show values which are expected for non-heat-treated Inconel 718 alloys [17].

Moreover, the interlayer cooling approach enabled the fabrication of multiple thin-wall-based structures, as shown in Fig. 8. As the component is at room temperature before deposition, the layer-specific heat input has no influence on the overall thermal properties. This enables the development of taller and more complex structures. This is exemplified in the thin-wall structure of Fig. 8A, where 53 layers were deposited.

Multidirectional deposition of thin-walled parts was also possible (Fig. 8B). In Fig. 8C a prototype of a conformal cooling channel is shown. The part completion was made possible by both the cooling strategy and the CNC machine's kinematics adaptation to perform complex trajectories.

4. Conclusions

This experimental study has identified that the excessive heat input generated by successive depositions leads to collapse of Inconel 718 thin-walled structures fabricated by LMD-w. Such a correlation between thermal history and process stability is in good agreement with the LMD-w process trends for other alloys [6, 7].

Additionally, it was found that interlayer cooling using compressed air enables the deposition of thin-wall components without adversely affecting the hardness values and microstructural characteristics. The captured thermal radiation

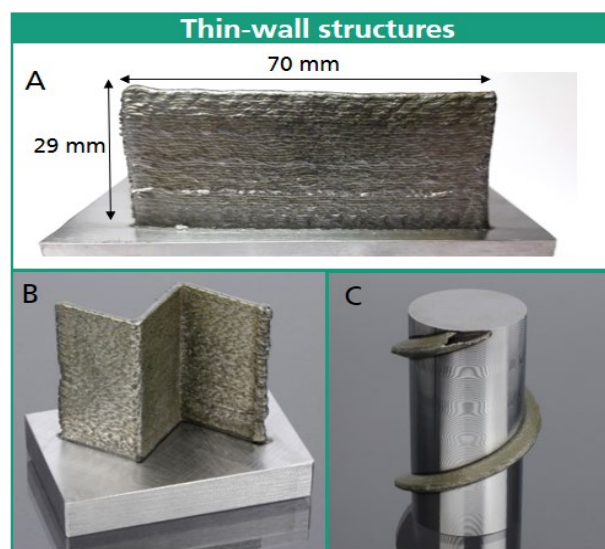


Fig. 8. Inconel 718 thin-wall structures fabricated by LMD-w with interlayer cooling strategy. A - Single wall. B - Rectangular wall configuration. C - Prototype of a conformal cooling channel.

indicates that the overall temperature of the last clad bed should be below 200 °C in order to ensure a stable process.

As further steps the influence of the energy input on the substrate should also be considered. Due to an increased thermal input the substrate could bend resulting in a crack formation within the deposited structures.

Besides the existing EDS imaging, further studies regarding the temperature distribution within each built specimen in correlation to the microstructural phase should be taken into account. Another important aspect is the surface oxidation regardless of the employed strategy. This can be mitigated with an improved shielding gas flow.

Further studies must be carried out to understand whether the interlayer cooling strategy affects the part mechanical properties (i.e. Ultimate Tensile Strength and fatigue strength).

Another major aspect to be analyzed is the positioning of the wire within the melting pool of the laser beam. Kotar et al. have shown that an adapted workpiece-wire irradiation proportion (WIP) can effectively control the process. Accordingly, the process stability, the welding contours and the dilution of the deposited layer are significantly influenced [18]. Yu et al. have also successfully shown that, depending on the positioning of the wire, the formation of droplets, corresponding to the feed direction, can be effectively influenced during the process [19]. As a consequence, further experiments with the LMD-W-20-L should look more closely at the positioning of the wire within the laser spot. With the correct alignment of the WIP, it may be possible to weld omnidirectional, which in turn enables further options of complex geometries.

Finally, to increase the technology's industrial readiness level, proper process optimization is required to manage the compromise between the time-consuming cooling stage and process stability. At this stage, the specimen must be cooled down for about 30-50 seconds before it is possible to set up another. To bridge this time, several samples could be constructed one after another, where the previous one can cool

down in the meantime. An adaptive process (i.e. closed-loop control) is seen as a suitable alternative for achieving this goal.

Overall, these findings strengthen the potential of the LMD-w process for the aerospace industry to fabricate near-net-shape components without the formation of cracks or macroscopic pores and no significant differences within the resulting micro hardness in comparison to values from literature [17].

References

- [1] Klocke, F., Schmitt, R., Zeis, M., Heidemanns, L., Kerkhoff, J., Heinen, D., & Klink, A. (2015). Technological and Economical Assessment of Alternative Process Chains for Blisk Manufacture. In *Procedia CIRP* (Vol. 35, pp. 67–72).
- [2] R. Liu et.al. (2017) Aerospace applications of laser additive manufacturing, in M. Brandt (ed) *Laser Additive Manufacturing*, Woodhead Publishing, 351-371.
- [3] International Organization for Standardization. (2015). Standard Terminology for Additive Manufacturing (ISO/ASTM Standard No. 52900).
- [4] Scott M. Thompson, Linkan Bian, Nima Shamsaei, Aref Yadollahi, An overview of Direct Laser Deposition for additive manufacturing; Part I: Transport phenomena, modeling and diagnostics, *Additive Manufacturing*, Volume 8, 2015, Pages 36-62, ISSN2214-8604.
- [5] Arrizubieta, J., Klocke, F., Klingbeil, N., Arntz, K., Lamikiz, A. and Martinez, S. (2017), Evaluation of efficiency and mechanical properties of Inconel 718 components built by wire and powder laser material deposition, *Rapid Prototyping Journal*, Vol. 23 No. 6, pp. 965-972.
- [6] Heralić, A. (2012). Monitoring and control of robotized laser metal-wire deposition. Chalmers University of Technology.
- [7] M. Froend, V. Ventzke, N. Kashaev, B. Klusemann, J. Enz, Thermal analysis of wire-based direct energy deposition of Al-Mg using different laser irradiances, *Additive Manufacturing*, Volume 29, 2019, 100800, ISSN 2214-8604.
- [8] Froend, M., Bock, F. E., Riekehr, S., Kashaev, N., Klusemann, B., & Enz, J. (2018). Experimental investigation of temperature distribution during wire-based laser metal deposition of the al-mg alloy 5087. *Materials Science Forum*, 941 MSF, 988–994.
- [9] Froend, M., Ventzke, V., Dorn, F., Kashaev, N., Klusemann, B., & Enz, J. (2019). Microstructure by design: An approach of grain refinement and isotropy improvement in multi-layer wire-based laser metal deposition. *Materials Science and Engineering: A*, 138635.
- [10] Hagqvist, P., Christiansson, A. K., & Heralić, A. (2015). Automation of a laser welding system for additive manufacturing. *IEEE International Conference on Automation Science and Engineering*, 2015-October, 900–905.
- [11] Fraunhofer IPT, Smart processing module for wire-based laser deposition welding, accessed February 15 2020. <https://www.ipt.fraunhofer.de/en/Competencies/processstechnology/non-conventional-manufacturing-processes-and-technology/integration/welding-head-lmd-w-20-l.html>
- [12] S. Sun et.al. (2017) Powder bed fusion process: an overview, in M. Brandt (ed) *Laser Additive Manufacturing*, Woodhead Publishing, 351-371.
- [13] Titanium. *Columbia Encyclopedia* (6th ed.) New York: Columbia University Press. 2000-2006. ISBN 978-0-7876-5015-5
- [14] Geng, H., Li, J., Xiong, J., & Lin, X. (2017). Optimisation of interpass and heat input for wire and arc additive manufacturing 5A06 aluminium alloy. *Science and Technology of Welding and Joining*, 22(6), 472–483.
- [15] Heilemann, M., Beckmann, J., Konigorski, D., & Emmelmann, C. (2018). Laser metal deposition of bionic aluminum supports: Reduction of the energy input for additive manufacturing of a fuselage. *Procedia CIRP*, 74, 136–139.
- [16] Wu B., Pan Z., van Duin S., Li H. (2019) Thermal Behavior in Wire Arc Additive Manufacturing: Characteristics, Effects and Control. In: Chen S., Zhang Y., Feng Z. (eds) *Transactions on Intelligent Welding Manufacturing*. Springer, Singapore
- [17] Nils Klingbeil. (2018). Untersuchung des Drahtsystems zur Prozessstabilisierung für das drahtbasierte Laserauftragschweißen in der additiven Fertigung. Rheinisch-Westfälischen Technischen Hochschule Aachen .
- [18] Kotar, M., Fujishima, M., Levy G., Govekar E., (2019). Initial transient phase and stability of annular laser beam direct wire deposition. *CIRP Annals – Manufacturing Technology*, 68, 233-236.
- [19] Yu Y., Huang W., Wang G., Meng X., Wang C., Yan F., Hu X., Yu S. (2013), Investigation of melting dynamics of filler wire during wire feed laser welding. *Journal of Mechanical Science and Technology* 27 (4), Springer,

11th CIRP Conference on Photonic Technologies [LANE 2020] on September 7-10, 2020

Processing of 316L hybrid parts consisting of sheet metal and additively manufactured element by Powder Bed Fusion using a laser beam

Thomas Papke^{a,*}, Marion Merklein^a

^aInstitute of Manufacturing Technology (LFT), Friedrich-Alexander-Universität Erlangen-Nürnberg, Egerlandstraße 13, 91058 Erlangen, Germany

* Corresponding author. Tel.: +49-9131-85-27956; fax: +49-9131-85-27141. E-mail address: thomas.papke@fau.de

Abstract

The approach of 316L hybrid parts consisting of sheet metal with additively manufactured element is investigated regarding relative density, warpage and bonding strength between additively manufactured element and sheet metal. Process parameters for manufacturing hybrid parts with relative density of 99.9 % are identified. Warpage is a critical aspect for hybrid parts, which increases with increasing volume energy density. Regarding a proper part design, knowledge of dependencies of bonding strength is essential. The bonding strength is influenced by relative density of the additively manufactured element and remains on one level for increasing volume energy density.

© 2020 The Authors. Published by Elsevier B.V.

This is an open access article under the CC BY-NC-ND license (<http://creativecommons.org/licenses/by-nc-nd/4.0/>)

Peer-review under responsibility of the Bayerisches Laserzentrum GmbH

Keywords: Additive Manufacturing; PBF-LB/M; Hybrid Part; Sheet Metal; Stainless Steel; Part Characterization;

1. Introduction

In the industry, a trend towards customized products in high numbers is prevalent [1]. Due to high geometric flexibility, additive manufacturing (AM) processes are widely used to manufacture individualized components. However, compared to conventional manufacturing processes, as sheet metal forming the process times are long. In order to reduce process time in additive manufacturing, one approach is the combination of sheet metal forming and additive manufacturing by powder bed fusion of metal using a laser beam (PBF-LB/M) [2]. Regarding this approach, time for additive manufacturing is limited to a minimum, because only individual part areas are manufactured by AM, whereas geometric simple part sections are realized by sheet metal forming. The result is a hybrid part consisting of a formed sheet metal body with additively manufactured elements. The process chain is based on subsequent steps, where forming can be conducted before or after the AM process [3]. A potential application of the hybrid approach is manufacturing of a gear component, which consists of a sheet metal with discrete additively manufactured tooth

Nomenclature

σ_{HBS}	hybrid shear bonding strength
A_{AE}	area of additively manufactured element
d	initial diameter of additively manufactured element
E_v	volume energy density
$F_{s,max}$	maximum punch force
h	initial height of additively manufactured element
h_s	scan line spacing
l_z	layer thickness
P_L	laser power
s	quantified warpage of sheet metal
t_0	initial sheet thickness
v_s	scan speed

geometries. The process chain of additive manufacturing and forming as well as a hybrid gear component are shown in Fig. 1. These parts are conventionally manufactured by forming operations using a sheet metal or tailored blanks [4]. However, the formability and material flow, in the latter cases, are limited. Therefore, one approach is to build the tooth geometry by

PBF-LB/M. For a proper part design, the impact of process parameters on relative density, warpage and bonding strength between sheet metal and additively manufactured element are essential. In this work, the processing of hybrid parts is investigated fundamentally using a simplified hybrid part geometry represented by a cylindrical additively manufactured element on a sheet metal. In this context the process parameters laser power P_L and scan speed v_s in PBF-LB/M are varied on different stages to analyze its impact on the relative density of the AM structure. Based on the relative density of the parts, proper process parameters for manufacturing 316L hybrid components are derived. Beside the relative density, the warpage is investigated, which is quantified by tactile measurements of the curvature of the sheet metal after PBF-LB/M. Finally, the impact of the process parameters on the bonding strength is evaluated by shear tests.

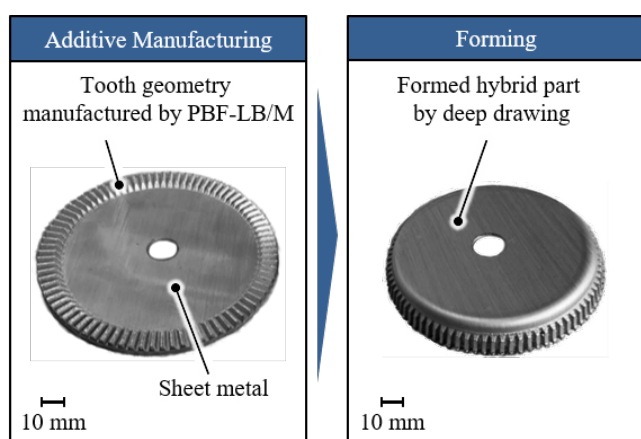


Fig. 1. Process chain and potential application of hybrid part.

2. State of the art

The austenitic stainless steel 316L is developed for parts with high corrosion resistance at room temperature [5] and is applied in different fields like the automotive sector [6], for medical products [7] and the aeronautical industry [8]. 316L is an appropriate material for processing in PBF-LB/M.

Regarding hybrid parts the metallographic structure, mechanical properties and formability of additively manufactured material 316L is different compared to conventionally manufactured material. The yield stress of AM material at room temperature under compressive load is slightly higher than for conventionally manufactured material and depends on the build direction [9]. This indicates different formability of AM material and should be considered for characterization and forming of hybrid parts.

The process parameters for receiving AM parts with high relative density are well-established [10]. According to VDI 3405 [11] the relative density of parts manufactured by PBF-LB/M should be at least 99%. Since the technology matured densities of 99.7% [12] or even 99.9% [13] are achievable. This should be considered when manufacturing hybrid parts and represents the benchmark. The relative density strongly depends on volume energy density E_v , which is calculated by laser power P_L divided by scan speed v_s , layer thickness l_z and scan line spacing h_s according to equation (1) [11].

$$E_v = \frac{P_L}{v_s \cdot h_s \cdot l_z} \quad (1)$$

According to early publications on PBF-LB/316L with machines of maximum laser power of 100 W a relative density of at least 99% is achievable for $E_v = 40 \text{ J/mm}^3 - 90 \text{ J/mm}^3$ [14]. Recent investigations with higher laser power until 400 W lead to this relative density at comparable volume energy densities of $E_v = 50 \text{ J/mm}^3 - 80 \text{ J/mm}^3$ [12]. However, the production of dense parts depends also on several other factors like powder properties, machine setup, scanning strategy, time of scanning one point or spot size [15]. Hence, the range for volume energy densities is an initial point for identifying proper process parameters. Beside the relative density, residual stresses are challenging in PBF-LB/M, which originate from the high cooling rates during the process. The stresses resulting from process heat promote warpage [16]. Therefore, preheating of the build plate is beneficial to decrease the thermal gradient during the building process [17]. Even though the fundamentals for processing PBF-LB/316L parts are well known, the approach of hybrid parts consisting of a sheet metal with additively manufactured elements is more challenging. In addition to relative density, residual stresses influence the warpage of the sheet metal and a proper design of the bonding zone between the additively manufactured element and the sheet metal is essential. Furthermore, no additional support structures for reducing warpage and controlling heat transfer from the part into the build plate are used. Schaub [18] investigated the approach of hybrid parts made of Ti6Al4V especially regarding the characterization of the bonding strength of cylindrical additively manufactured elements, the interaction zone and forming of parts with sheet thicknesses of 1.0 mm to 1.5 mm. However, 316L possesses fundamentally different mechanical and physical properties compared to Ti6Al4V. For example, thermal conductivity of 316L is higher whereas the yield strength is lower compared to Ti6Al4V [17]. Beside others, these properties have a strong impact on residual stresses and warpage, also known from laser forming [19]. Therefore, the approach of hybrid parts made of 316L will be investigated regarding achievable relative density, warpage and bonding strength by variation of volume energy density.

3. Experimental setup and methodology

3.1. Additive manufacturing of 316L hybrid parts

Regarding a fundamental analysis of 316L hybrid parts, the specimen geometry in this work consists of an additively manufactured element with a diameter $d = 5 \text{ mm}$ and a height $h = 5 \text{ mm}$. The initial thickness of the sheet metal is 1.5 mm. The part geometry is illustrated in Fig. 2. For processing additively manufactured elements on the sheet metal a Lasertec 30 SLM from DMG Mori is used. The machine is equipped with a fibre laser with a maximum laser power of 600 W, Gaussian beam profile and has a spot size (d_{1/e^2}) of approximately $70 \mu\text{m}$. To reduce residual stresses the heating of the build plate is set to $200 \text{ }^\circ\text{C}$. The powder is delivered by LPW Technology Ltd. with a powder size distribution between

19 μm and 43 μm . The layer thickness l_z is set to 50 μm . For manufacturing hybrid parts, the sheet metal with a size of 277 x 277 mm^2 is clamped by 14 countersunk screws on the build plate. Using this setup, 24 cylindrical elements are manufactured on one sheet metal. In this work the impact of different volume energy densities on the part properties is investigated. Therefore, the parameters being changed are laser power P_L and scan speed v_s , which are main factors of impact on the relative density. In order to keep the number of experiments small, layer thickness l_z and scan line spacing h_s are kept constant. For identifying proper parameters for 316L hybrid parts volume energy densities between 27 J/mm^3 and 111 J/mm^3 are investigated. The range includes volume energy densities from the state of the art for PBF-LB//316L specimens [12] and is extended in order to receive a broad process knowledge, since the impact of volume energy on the properties of hybrid parts is not investigated yet. The laser power P_L is changed on 8 stages from 150 W to 500 W and the scan speed v_s is investigated on the stages 900 mm/s , 1000 mm/s and 1100 mm/s resulting in 24 sets of parameters. After additive manufacturing, the specimens with a size of 20 x 56 mm^2 are extracted from the sheet metal by laser cutting. The final shape of the sheet metal is based on former investigations on bending hybrid parts [20]. After additive manufacturing, hybrid parts are analyzed regarding warpage.

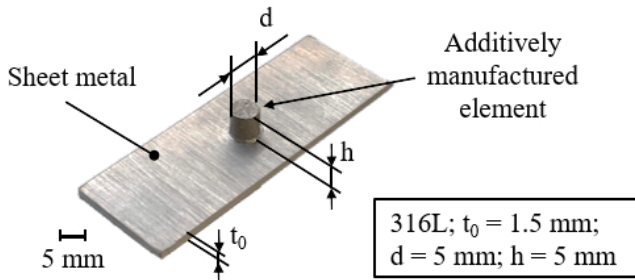


Fig. 2. Specimen geometry for analyzing hybrid parts.

3.2. Evaluation of warpage by tactile geometry measurement

In order to evaluate the warpage of the sheet metal, the curvature of the sheet metal is measured with a tactile geometry measurement system MarSurf XCR 20 by Mahr. Within the measuring procedure a tactile tracer is drawn over the surface of the sheet metal at the opposite side of the additively manufactured element. The result is a surface profile for a single line measurement over the center of the cylindrical element, which is compared to the ideal geometry. In order to receive a sufficient surface profile, a measurement length of 25 mm is used. This represents five times the diameter of the additively manufactured element and ensures the measurement of warpage and undeformed sheet metal areas. An exemplary evaluation is shown in Fig. 3. In this work, the warpage is quantified by the maximum distance s from the highest peak of the profile to the reference plane of the undeformed sheet. For receiving a broad process understanding, the warpage is evaluated over a wide range of volume energy densities from 30 J/mm^3 to 111 J/mm^3 .

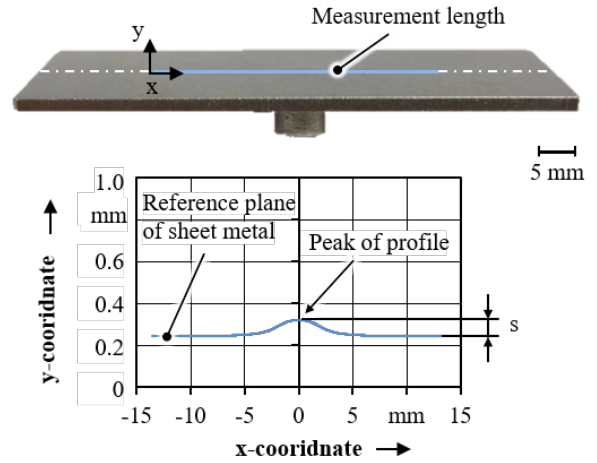


Fig. 3. Exemplary evaluation of warpage s.

3.3. Characterization of relative density

The relative density of the additively manufactured cylinder is investigated using metallographic analysis. In this context the specimens are separated in the middle cross section of the cylinder. Based on image analysis [11], the distribution of pores is evaluated and the relative density is determined.

3.4. Characterization of mechanical properties

The shear bonding strength is measured using a tool developed by Schaub [18], which is mounted in a universal testing machine from Walter+Bai with a maximum load of 300 kN. The setup is schematically illustrated in Fig. 4a. The specimen is clamped vertically in the tool and the shear punch is moved with a constant velocity of 5 mm/min along the surface. During the test, force and displacement are recorded. After the test, the additively manufactured element is separated from the sheet metal as shown exemplarily in Fig. 4b. The shear bonding strength σ_{HBS} can be calculated using equation (2), where the maximum punch force $F_{s,max}$ is divided by the initial area A_{AE} of the cylindrical element [18]. The shear tests are conducted for hybrid parts manufactured with volume energy densities between 30 J/mm^3 and 111 J/mm^3 .

$$\sigma_{HBS} = \frac{F_{s,max}}{A_{AE}} \quad (2)$$

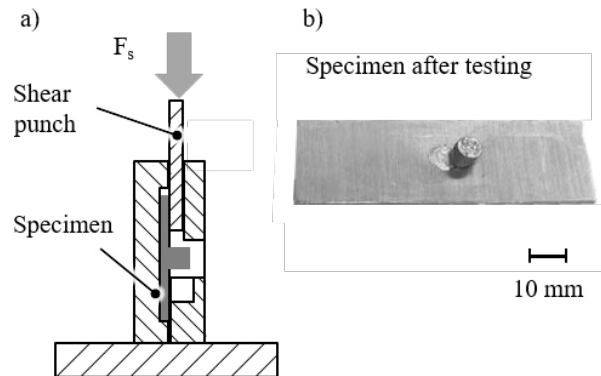


Fig. 4. a) Schematic setup for shear test of hybrid part b) Exemplary specimen after testing.

4. Results

4.1. Investigation of relative density of 316L hybrid parts

In a first step the achievable relative density is evaluated for a wide range of volume energy densities. The results for relative density of the parameter study are presented in Fig. 5a.

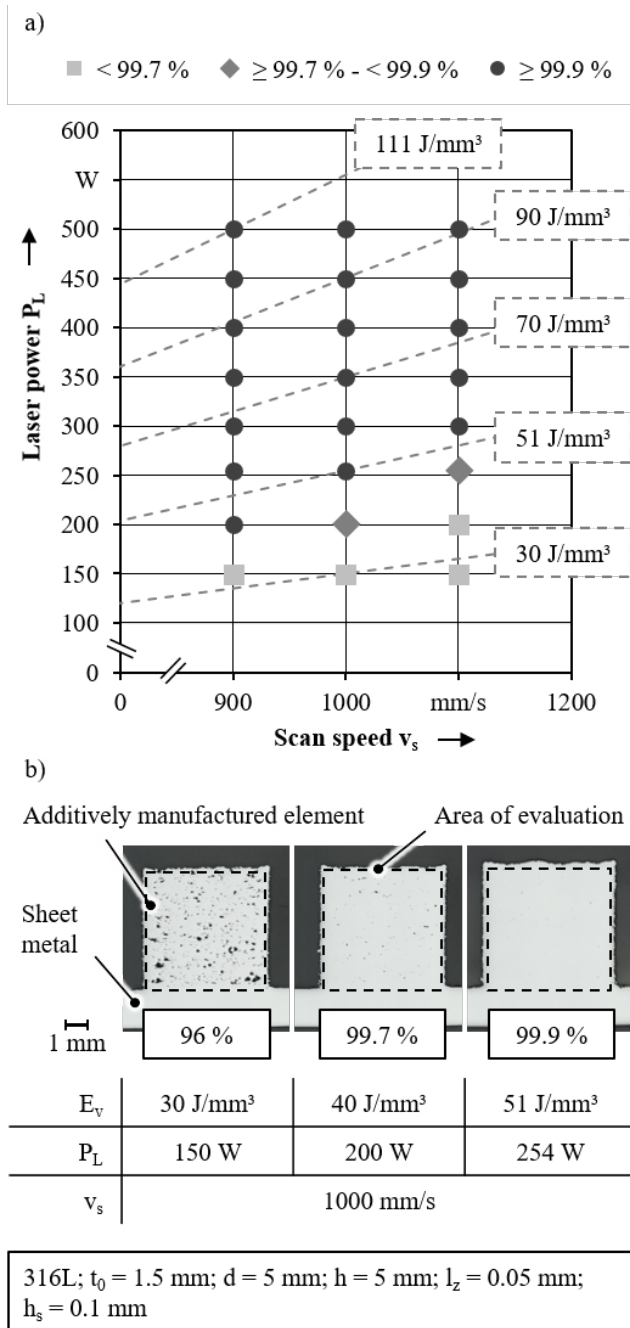


Fig. 5. a) Relative density of hybrid parts b) Metallographic images for different volume energy densities.

Following the state of the art, the relative densities are divided in three groups: $< 99.7\%$, $\geq 99.7\% - < 99.9\%$ and $\geq 99.9\%$. Within the range of parameters investigated a laser power of $P_L = 150$ W and the combination of $P_L = 200$ W and $v_s = 1100$ mm/s result in a relative density below 99.7%. However, a lower scan speed at $P_L = 200$ W lead to increasing relative density due to increasing volume energy density. At

$P_L = 254$ W and $v_s = 1100$ mm/s ($E_v = 46$ J/mm³) the relative density is lower than for the combination $P_L = 200$ W and $v_s = 900$ mm/s ($E_v = 44$ J/mm³) even though the volume energy density is higher. This can be explained by process deviations over the build space, which is present in PBF-LB/M machines and not investigated in this work. Volume energy densities above $E_v = 51$ J/mm³ result in relative density $\geq 99.9\%$. Regarding the selected parameter combinations this volume energy density represent the border to high relative density. For illustrating the differences in relative densities exemplarily, images from metallographic analysis for $E_v = 30$ J/mm³, $E_v = 40$ J/mm³ and $E_v = 51$ J/mm³ are shown in Fig. 5b. The parameters distinguish in laser power ($P_L = 150$ W, $P_L = 200$ W and $P_L = 254$ W) and the scan speed is kept constant at $v_s = 1000$ mm/s. A volume energy density of $E_v = 30$ J/mm³ results in severe porosity. Comparing the relative density for $E_v = 40$ J/mm³ (99.7 %) and $E_v = 51$ J/mm³ ($\geq 99.9\%$) the porosity is diminished for increasing volume energy density. Assuming that a relative density of 99.7 % is sufficient, the selected volume energy density for manufacturing 316L hybrid parts of this geometry should be at least 40 J/mm³. These findings correlate with the state of the art for PBF-LB/316L structures [12]. Regarding relative density in this range of parameters, an upper limit of volume energy density is not identified. The results indicate a broad process window for hybrid parts over several volume energy densities leading to high relative density. However, for hybrid parts beside relative density, warpage of the sheet metal and bonding strength are crucial part properties. Therefore, the process window is evaluated in this context and the impact of volume energy density on these properties is analysed in order to identifying proper process parameters for 316L hybrid parts.

4.2. Evaluation of warpage regarding the impact of volume energy density

For hybrid parts, a relative density higher than 99.7 % is achievable over a wide range of volume energy densities. However, the manufacturing process results in warpage of the sheet metal. In order to avoid an unintended change in geometry of the sheet metal caused by PBF-LB/M, the warpage should be as small as possible. The results of quantified warpage are illustrated in Fig. 6. As expected, the warpage increases for higher volume energy density. The lowest warpage is reached for $E_v = 30$ J/mm³, which is approximately 0.08 mm. Even though this volume energy density is not high enough to produce parts with sufficient relative density, the conduction of heat into the sheet metal material still leads to plastic deformation. This indicates that the energy input results in stresses above the yield strength of the material. For higher volume energy density, the warpage increases to 0.15 mm for $E_v = 111$ J/mm³, which is the highest value in this study. For all volume energy densities, the warpage is represented by a concave curvature of the sheet metal to the opposite side relative to the laser input side. This shape indicates, that the warpage is caused by the phenomenon of temperature gradient mechanism, which is fundamentally investigated for laser forming in [19] and analysed by numerical modelling in [21]. The phenomenon is based on different temperatures over the

sheet thickness due to the input of heat using a laser beam [19]. In case of forming, the phenomenon of temperature gradient mechanism leads to bending of the sheet metal when the input of heat is high enough [19]. Beside other parameters, the grade of forming depends on the line energy, which is defined as the ratio of P_L and v_s [19]. A higher laser power leads to increasing bending angles [19]. Applying the fundamentals of laser forming to hybrid parts the increase of warpage for a higher volume energy density can be explained, while h_s and l_z are kept constant. The distribution of values in Fig. 6 indicate a non-linear relation, which is similar to the fundamentals of laser forming. However, the impact of scan speed is not investigated yet. In contrary to laser forming of sheet metals, in PBF-LB/M several more factors of influence like powder properties or melting of additional material exist [22]. Also the scan strategy should be considered, which has an impact on warpage of hybrid parts [23]. Therefore, the fundamentals of laser forming remain, but the application to manufacturing of hybrid parts should be investigated further. Regarding the results presented, the volume energy density should be high enough to produce parts with sufficient relative density. However, to reduce warpage, the volume energy should be as low as possible.

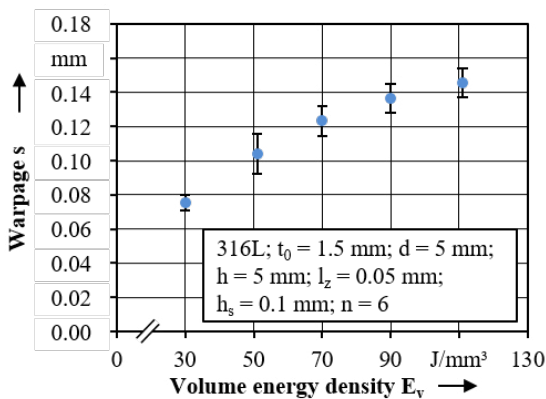


Fig. 6. Warpage depending on volume energy density.

4.3. Investigation of mechanical properties

Beside the warpage, the mechanical properties of hybrid parts like the bonding strength are of special interest for a proper part design. The bonding strength is investigated by shear tests. Based on the maximum shear force and the initial area of the additively manufactured element the shear bonding strength σ_{HBS} is calculated according to equation (2). The results are presented in Fig. 7. The shear bonding strength of parts of volume energy density $E_v = 30$ J/mm³ (444 ± 67 MPa) is significantly lower than for $E_v = 51$ J/mm³ (563 ± 28 MPa). The difference indicates that the shear bonding strength depends on the relative density. This is supported by the fact that the shear bonding strength remains on almost the same level for volume energy densities between 51 J/mm³ and 111 J/mm³, which result in structures with sufficient relative density. Regarding the standard deviation, a clear trend cannot be identified, even though the shear bonding strength seem to decrease for higher volume energy densities. More important is that a higher volume energy density does not result in higher shear bonding strength. Hence, a volume energy density of

51 J/mm³ is sufficient since further increase of volume energy does not improve the bonding strength but increase the warpage. Beside the bonding strength, mechanical properties and formability should be considered when designing hybrid parts. Prior investigations on forming of additively manufactured elements indicate differences to conventionally manufactured material in upsetting tests [9]. These differences can have an impact on the forming behaviour of hybrid parts in subsequent forming operations.

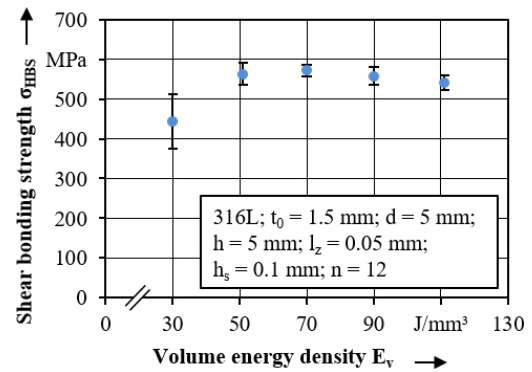


Fig. 7. Shear bonding strength depending on volume energy density.

5. Conclusion

Regarding the results on relative density, warpage and bonding strength of 316L hybrid parts, the volume energy density should be at least 40 J/mm³ to receive a relative density of $\geq 99.7\%$ and $E_v \geq 51$ J/mm³ for a relative density $\geq 99.9\%$. Within the parameter combinations investigated, higher volume energy density does not result in higher relative density, but the warpage increases. Therefore, the volume energy density should be as low as possible to reduce warpage. The bonding strength depends on the relative density and remains on one level even for higher volume energy densities. Hence, for processing hybrid parts with high relative density, low warpage and sufficient bonding strength a suitable volume energy density is $E_v = 51$ J/mm³ regarding the investigated parameter sets.

6. Summary and outlook

This work focuses on processing 316L hybrid parts consisting of a sheet metal with an additively manufactured element. One application of this approach is a hybrid gear component with discrete tooth geometries on the surface of a sheet metal, which is formed subsequently by deep drawing. These kind of hybrid parts combine the advantages of additive manufacturing and forming. A semi-finished product can replace simple part geometries, which is individualized by additive manufacturing technologies. PBF-LB/M is a promising process to manufacture additive elements on a sheet metal due to high structure resolution and surface quality compared to other AM processes. Regarding the state of the art, a relative density of 99.9% is achievable for PBF-LB/316L structures, which is also desirable for hybrid parts. However, the approach of hybrid parts is challenging because of warpage of the sheet metal and a proper design of the bonding zone.

Therefore, the relative density, warpage and bonding strength are investigated in this work.

In a first step the relative density of additively manufactured elements is investigated for volume energy densities between $E_v = 27 \text{ J/mm}^3$ and $E_v = 111 \text{ J/mm}^3$. Based on the parameter sets investigated, a relative density of at least 99.9 % can be reached for $E_v \geq 51 \text{ J/mm}^3$, which is in accordance with the state of the art for PBF-LB/316L. This indicates process ability over a wide range of volume energy densities. However, higher volume energy density results in increasing warpage of the sheet metal due to higher energy input. This behavior can be explained by the phenomenon of temperature gradient mechanism also known from laser forming. Therefore, to avoid unintended deformation of the sheet metal body, low volume energy density is desirable. Regarding the bonding strength, a strong impact of relative density can be seen. For a volume energy of $E_v = 30 \text{ J/mm}^3$, which leads to parts with severe porosity, the shear bonding strength is significantly lower than for parts with a relative density of at least 99.9 % ($E_v \geq 51 \text{ J/mm}^3$). However, the shear bonding strength does not increase for higher volume energy density. Hence, the volume energy density selected for manufacturing hybrid parts should be high enough to produce parts with sufficient density but not higher in order to reduce warpage of the sheet metal to a minimum.

Even though a wide range of parameters for processing parts with sufficient relative density is identified, the impact of the position of the additively manufactured element in the build space on the relative density is not investigated yet. Therefore, further research should be done regarding the variation of additively manufactured element position and achievable relative density to evaluate deviations over the build space. In addition, it would be beneficial to consider the impact of volume energy density on part properties for identifying an upper limit of the process window. Regarding the fundamentals of temperature gradient mechanism, the influence of scan speed on warpage should be part of future work. Further investigations will focus on analyzing the formability of functional hybrid components consisting of sheet metal with additively manufactured tooth geometries.

Acknowledgements

The authors acknowledge the Deutsche Forschungsgemeinschaft (DFG, German Research Foundation) within the Gottfried Wilhelm Leibniz Prize (DFG ME2043/38-1) and the SFB 814 - „Additive Manufacturing“ (Project-ID 61375930) – TP B05 for the financial support.

References

[1] Tseng M M, Hu S J, Wang Y. Mass Customization. CIRP Encyclopedia of Production Engineering 2014. p. 836-843

- [2] Schaub A, Ahuja B, Karg M, Schmidt M, Merklein M. Fabrication and Characterization of Laser Beam Melted Ti-6Al-4V Geometries on Sheet Metal. DDMC 2014. p. 1-5
- [3] Merklein M, Dubjella P, Schaub A, Butzhammer L, Schmidt M. Interaction of Additive Manufacturing and Forming. iCAT 2016. p. 309-316
- [4] Schulte R, Hildenbrand P, Vogel M, Lechner M, Merklein M. Analysis of fundamental dependencies between manufacturing and processing Tailored Blanks in sheet-bulk metal forming processes. Proc Eng 2017;207:305-10
- [5] Peckner D, Bernstein I M. Handbook of Stainless Steels. 1977
- [6] Podder S, Bhanja A. Applications of Stainless Steel in Automobile Industry. Adv Mater Res 2013;794:731-740
- [7] Lodhi M J K, Deen K M, Greenlee-Wacker M C, Haider W. Additively manufactured 316L stainless steel with improved corrosion resistance and biological response for biomedical applications. J Add Man 2019;27:474-84
- [8] Cianett F, Ciotti M, Palmieri M, Zucca G. On the Evaluation of Surface Fatigue Strength of a Stainless-Steel Aeronautical Component. Metals 2019;9:455
- [9] Papke T, Merklein M. Characterization of Work Hardening Behavior of Additively Manufactured Stainless Steel 316L (1.4404) Using Bulk Metal Forming at Elevated Temperature. LIM 2019
- [10] Zitelli C, Flogarait P, Di Schino A. Laser Powder Bed Fusion of Stainless Steel Grades: A Review
- [11] VDI 3405-2. Additive manufacturing processes, rapid manufacturing – beam melting of metallic parts – qualification, quality assurance and post processing. 2013
- [12] Tucho W M, Lysne V H, Austbo H, Sjolyst-Kverneland A, Hansen V. Investigation of effects of process parameters on microstructure and hardness of SLM manufactured SS316L. J Alloys a Compounds 2018;740:910-25.
- [13] Liverani E, Toschi S, Ceschini L, Fortunato A. Effect of Selective Laser Melting (SLM) process parameters on microstructure and mechanical properties of 316L austenitic stainless steel. J Mat Proc Tech 2017;249:255-63.
- [14] Meier H, Haberland C. Experimental studies on selective laser melting of metallic parts. Mat-wiss u Werkstofftech 2008;39:8
- [15] Kurzynowski T, Chlebus E, Kuznicka B, Reiner J. Parameters in Selective Laser Melting for processing metallic powders. SPIE 2012.
- [16] Vrancken B, Study of residual stresses in selective laser melting. Dissertation KU Leuven 2016
- [17] Yadroitsev I, Yadroitsava I. Evaluation of residual stresses in stainless steel 316L and Ti6Al4V samples produced by selective laser melting. J Virt a Phys Prototyping 2015;10-2:67-76
- [18] Schaub A. Grundlagenwissenschaftliche Untersuchung der kombinierten Prozesskette aus Umformen und Additive Fertigung. Dissertation FAU Erlangen-Nürnberg 2018
- [19] Vollertsen F. Laserstrahlumformen – Lasergestützte Formgebung: Verfahren, Mechanismen, Modellierung. Habilitation FAU Erlangen-Nürnberg 1996
- [20] Papke T, Dubjella P, Butzhammer L, Huber F, Oleksandra P, Klose D, Schmidt M, Merklein M. Influence of a bending operation on the bonding strength for hybrid parts made of Ti-6Al-4V. Proc CIRP 2018;74:290-4
- [21] Merklein M. Laserstrahlumformen von Aluminiumwerkstoffen – Beeinflussung der Mikrostruktur und der mechanischen Eigenschaften. Dissertation FAU Erlangen-Nürnberg 2001
- [22] King W E, Anderson A T, Ferencz R M, Hodge N E, Kamath C, Khairallah S A, Rubnchik A M. Laser powder bed fusion additive manufacturing of metals; physics, computational, and materials challenges. J App Phy Rev 2015;2:041304
- [23] Hagedorn-Hansen D, Bezuidenhout M B, Dimitrov D M, Oosthuizen G A. The effect of selective laser melting scan strategies on deviation of hybrid parts. South Af J Ind Eng 2017;28:200-12

11th CIRP Conference on Photonic Technologies [LANE 2020] on September 7-10, 2020

Effect of nanoparticle additivation on the microstructure and microhardness of oxide dispersion strengthened steels produced by laser powder bed fusion and directed energy deposition

C. Doñate-Buendia^a, R. Streubel^a, P. Kürnsteiner^b, M. B. Wilms^c, F. Stern^d, J. Tenkamp^d, E.Bruder^e, S. Barcikowski^a, B. Gault^b, K. Durst^e, J. H. Schleifenbaum^c, F. Walther^d, B. Gökce^{a,*}

^aTechnical Chemistry I and Center for Nanointegration Duisburg-Essen (CENIDE), University of Duisburg-Essen, 45141 Essen, Germany

^bDepartment Microstructure Physics and Alloy Design, Max-Planck-Institut für Eisenforschung GmbH, 40237 Düsseldorf, Germany

^cChair for Digital Additive Production, RWTH Aachen University and Fraunhofer Institute of Laser Technology, 52074 Aachen, Germany

^dDepartment of Materials Test Engineering, TU Dortmund University, 44227 Dortmund, Germany

^ePhysical Metallurgy, Materials Science Department, Technische Universität Darmstadt, 64287 Darmstadt, Germany

* Corresponding author. Tel.: +49-201-183-3146; fax: +49-201-183-3049. E-mail address: bilal.goekce@uni-due.de

Abstract

In this contribution, the effect of nanoparticle additivation on the microstructure and microhardness of oxide dispersion strengthened steels (ODS) manufactured by laser powder bed fusion (L-PBF) and directed energy deposition (DED) additive manufacturing (AM) is studied. The powder composites are made of micrometer-sized iron-chromium-alloy based powder which are homogeneously decorated with Y_2O_3 nanoparticles synthesized by pulsed laser fragmentation in water. Consolidated by L-PBF and DED, an enhanced microhardness of the AM-built ODS sample is found. This increase is related to the significant microstructural differences found between the differently processed samples.

© 2020 The Authors. Published by Elsevier B.V.

This is an open access article under the CC BY-NC-ND license (<http://creativecommons.org/licenses/by-nc-nd/4.0/>)

Peer-review under responsibility of the Bayerisches Laserzentrum GmbH

Keywords: Oxide dispersion strengthened steel, ODS, Powder modification, Laser based powder bed fusion, Directed energy deposition, Laser metal deposition, Nanoparticles

1. Introduction

The manufacturing of steel components represents a pillar of the industrial development due to their high demand in fundamental areas like construction, automation or aeronautics [1,2]. In that sense, the aim to develop steel parts with complex geometries and specific properties requires the development and employment of different manufacturing technologies. Powder and laser based additive manufacturing (powder LAM) englobes the techniques based on the processing of powders by high power lasers to manufacture the final pieces based on the melting and solidification of the base material [3]. The flexibility of the technique for the employment of a wide library of base materials relies on the possibility of optimizing the laser

and processing parameters for each specific material [4]. The scanning methodology and the layer by layer deposit and growth procedure leads to an enhanced versatility when complex geometries are desired [5]. Inside the general term powder LAM, two main technologies can be highlighted due to their standard use in metal powders processing, i.e. directed energy deposition (DED) and laser powder bed fusion (L-PBF). While both are based on the same general principle, their differences rely on the depositing methodology of the powder material, which can affect the dynamics of the process [6]. Both techniques are conventionally applied in the processing of metallic powders. Consequently, their comparison is necessary to select the optimum technique for all individual processing conditions.

There exist a wide library of processable powders, even more, if modifications for enhanced performance are taken into account [7]. In this context, the controlled addition of oxide nanoparticles to the steel powders has been proved to modify the properties of the generated steel pieces, giving rise to oxide dispersion strengthened (ODS) steels [8]. Yttrium based oxides have been extensively employed in the modification of steel powders due to their proven mechanical reinforcement [9] and radiation sink effect [10]. Generally, due to their lattice mismatch with the metal matrix they act as dispersoids, hindering dislocation propagation and acting as sinks for radiation-induced defects [11]. The most common route for their fabrication is reactive ball milling and annealing [12,13]. Nevertheless, achieving control over nanoparticle dispersion and size is important as it influences the performance of the final pieces [14]. Consequently, a fabrication route based on the synthesis of colloidal nanoparticles by laser fragmentation in liquids (LFL), followed by their pH-controlled dielectrophoretic supporting on the steel powder has been proposed for an enhanced control of the nanoparticle dispersion and size evolution during the different steps towards the development of ODS steel samples [15–17].

In the present study, the achieved control over nanoparticle features during the processing steps for ODS steel preparation by the LFL synthesis route is explored. To do so, the nanoparticle size, dispersion, and composition is analyzed after fragmentation, supporting on the steel micro-powder and processing by DED and L-PBF. This way, nanoparticle evolution during the complete additive manufacturing process of an ODS steel sample is monitored for a better understanding of the influence of each technique over the nanoparticle distribution, microstructure of the fabricated piece, and hence over the ODS steel final properties.

2. Materials and methods

The materials employed for the ODS steel manufacture by DED and L-PBF are Y_2O_3 nanoparticles and a PM2000 ferritic steel powder. The raw Y_2O_3 nanoparticles are commercially acquired from Sigma Aldrich and dispersed in ultrapure deionized water (pH adjusted to 3.5 for stability) for deagglomeration and size reduction by laser fragmentation in liquids (LFL) employing an $f=100$ mm cylindrical lens, Fig. 1 top part [18]. This technique offers numerous advantages for the preparation of colloidal nanomaterials as it yields a wide library of processable materials [19–21], reduced waste generation and high nanoparticle output [22,23]. The supporting of the generated nanoparticles on the steel powder is achieved by the addition of the PM2000 to the colloidal Y_2O_3 nanoparticles and the modification of the pH to a value between the isoelectric point of both materials, Fig. 1 bottom part, by NaOH addition [24].

The prepared powder material is then processed by DED and L-PBF, respectively. In the first case, Fig. 2a, the powder is directly sent to the laser beam by a nozzle, the interaction with the high power laser beam melts it and gets the powder material deposited on the workpiece.

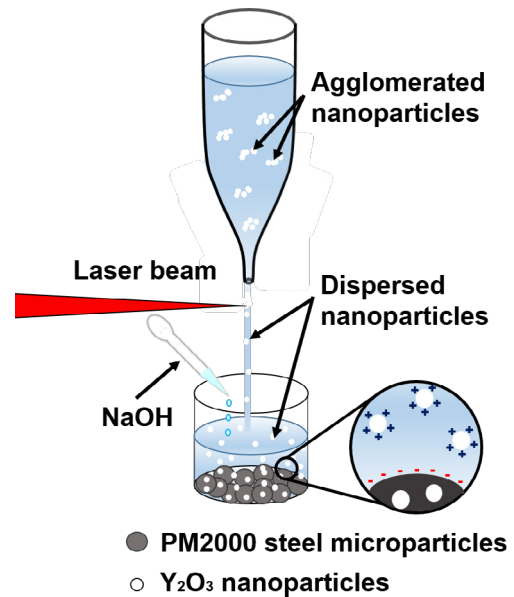


Fig. 1. Schematic illustration of the passage reactor LFL setup and dielectrophoretic nanoparticle adsorption on the steel powder by pH control.

Then the material solidifies, obtaining the final ODS steel samples and controlling the sample geometry by a scanning system. In the case of the L-PBF, Fig. 2b, the powder is spread over a substrate and the laser beam controlled by a scanning system melts the interacting areas. Again, the melted material solidifies forming the ODS steel sample. The non-irradiated powder material can be removed and reutilized.

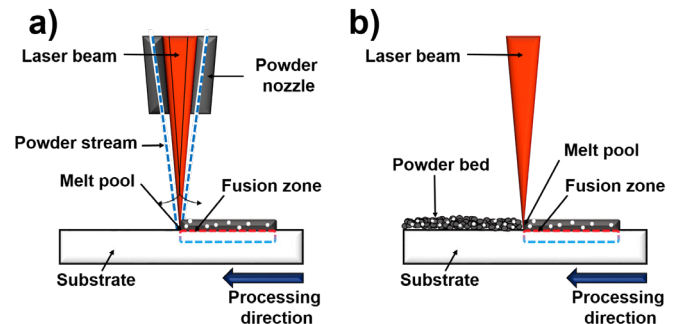


Fig. 2. Representative scheme of the (a) DED and (b) L-PBF laser additive manufacturing technologies.

Different analytical techniques are employed to characterize the nanoparticle size at the different stages of the process as well as their dispersion. After LFL, transmission electron microscopy (TEM) measurements are performed to evaluate the nanoparticle size, Fig. 3a. When the Y_2O_3 nanoparticles are supported on the steel powder, scanning electron microscopy (SEM) images are acquired to visualize nanoparticle size and dispersion on the surface of the steel powder, Fig. 3b. It should be noted that SEM is needed to visualize the nanoparticles on the steel surface, however, the spatial resolution achievable is lower than TEM and small nanoparticles may not appear. Finally, after processing the samples by DED and L-PBF, are analyzed by SEM-energy dispersive X-ray spectroscopy (EDS) and electron backscatter diffraction (EBSD). Microhardness measurements (HV0.1) are conducted with an applied load of

0.9807 N. The mean hardness is calculated by performing at least five indents.

3. Results and discussion

The evolution of the nanoparticles during LAM processing is compared from the Y_2O_3 nanoparticles synthesized by LFL. The TEM image in Fig. 3a displays that a bimodal distribution is found, a smaller population of 3.2 ± 0.6 nm and larger particles with a 28 ± 8 nm size distribution. The presence of two differentiated particle populations is potentially beneficial to observe the effect of the manufacturing process for both nanoparticle sizes. Besides, nanoparticle size is reported to influence the strengthening mechanism in ODS steels [25]. In particular, for small particles, dislocation cutting is the predominant effect, while for larger ones dislocation looping around the particle is the main strengthening mechanism [26].

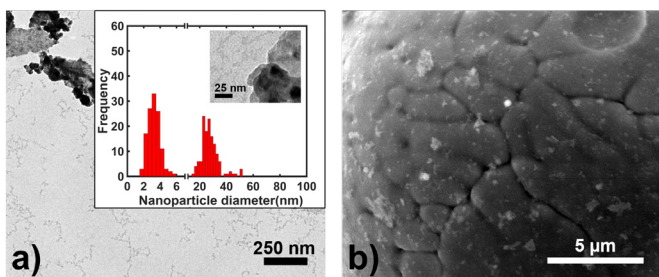


Fig. 3. (a) Y_2O_3 nanoparticle size distribution after LFL measured by TEM. (b) Dispersion and size of the Y_2O_3 nanoparticles supported on PM2000 powder by electrostatic deposition.

After deposition of the nanoparticles on the PM2000 steel powder, the SEM image, Fig. 3b, demonstrates a fine dispersion on the surface with the addition of only a 0.08 wt% of Y_2O_3 nanoparticles. It should be noted that SEM images are limited by the spatial resolution of the technique, and so smaller nanoparticles could be present in the steel surface, lowering the average nanoparticle size and reducing the interparticle distance.

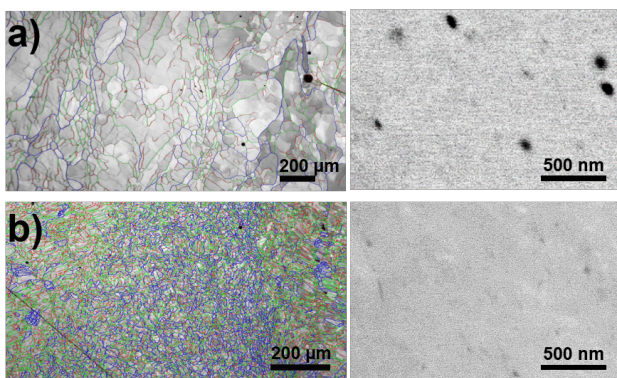


Fig. 4. Image quality (band contrast) maps with superimposed grain boundaries (misorientation: 2-5° green, 5-15° red, >15° blue), left, detailed view of nanoinclusions, right (backscatter electron micrograph), of the ODS steel pieces manufactured by (a) DED and (b) L-PBF.

After parts were printed with the nano-decorated powder by DED and L-PBF, the distribution and size of the resulting nanoinclusions are characterized by SEM and EBSD, Fig. 4.

The manufacturing method is shown to influence the grain size, which is known to have a fundamental impact on the mechanical properties of the metal [25,26]. It is visible that the grain size is significantly bigger in the DED sample, Fig. 4a, than in the L-PBF sample, Fig. 4b. The differences are attributed to the higher cooling rate in L-PBF and suggest a superior mechanical strength of the L-PBF sample due to the smaller grain size [27]. Besides, higher magnification images of the samples show the presence of larger particles in the DED piece. To investigate which elements might be contained in these particles, EDS analysis is performed, Fig. 5.

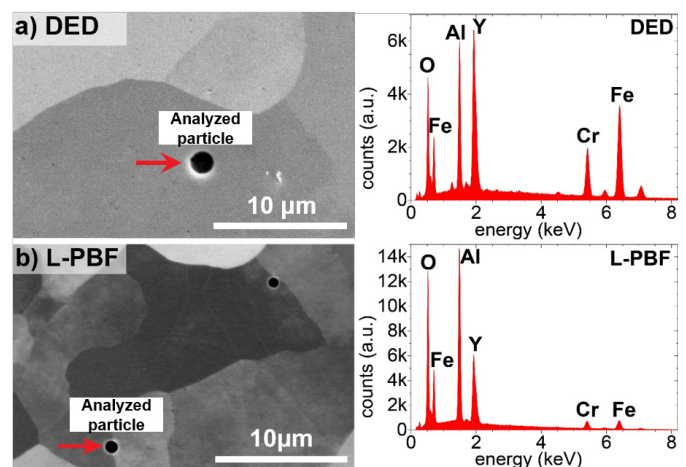


Fig. 5. Backscatter electron SEM images of the nanoinclusions, left, and EDS analysis of the particles marked by the arrow, right, of the ODS steel pieces manufactured by (a) DED and (b) L-PBF. Note that the spectrum is not exclusively from the particle itself but might contain some contribution from the matrix as the excitation volume in SEM-EDS might be larger than the particle.

The measurements reveal the presence of Y, O and Al in the particle and its surrounding, Fig. 5a and Fig. 5b. This result, together with the differences in particle size observed in Fig. 4, suggests that stronger agglomeration and particle size growing of the initial Y_2O_3 nanoparticles occurs during DED manufacturing, while these effects are reduced by L-PBF processing. The presence of Al in both samples is associated to its precipitation during processing.

Microhardness measurements (HV0.1) of the cross-sections show different hardness values depending on the processing route. The results are given in Table 1. As evident, processing with L-PBF results in a slightly higher hardness compared to DED. A possible explanation for this variation can be found in the higher cooling rates in L-PBF resulting in a finer microstructure compared to the DED [28] process as can be seen in Fig. 4a) and b), thus, causing differing hardness values. Additionally, the larger size of nanoinclusions as shown in Fig. 4a) in the DED steel specimens leads to a potentially lower effect of dispersion strengthening. However, the amount of nanoinclusions inherited in the steel is considerably low so that a considerable influence of the dispersion strengthening on the measured microhardness is not to be expected, especially at

room temperature [29]. Nevertheless, it is expected that a significant difference in terms of material strength at high temperatures due to the two processing routes will be identifiable.

Table 1. Microhardness (HV0.1) of the DED and L-PBF samples

Microhardness	DED	L-PBF
HV0.1	223 ± 9	247 ± 8

4. Conclusions

A study of the evolution and effect of nanoparticles in powder LAM of an ODS steel has been performed. The influence of the processing technique has been studied by comparing the microstructure and composition of DED with L-PBF manufactured parts. Regarding the microstructure, L-PBF processing is shown to reduce the grain size and increase grain boundaries compared to DED, which is expected to result in an enhanced strengthening of the built parts.

Concerning the evolution of the initially added 0.08 wt% Y_2O_3 nanoparticles, a fine dispersion is achieved on the steel powder decoration process by electrostatic deposition. After processing, an enrichment of Y, O and Al in the particles and its surrounding is shown by EDS analysis. The composition analysis together with SEM visualization of the nanoinclusions indicates that L-PBF is reducing agglomeration of the Y_2O_3 particles. During DED processing, apparently agglomeration of the nanoparticles is taking place. Since a fine dispersion and small nanoparticles are desired to enhance the strengthening effect due to the Orowan mechanism, L-PBF is potentially a more suitable technique compared to DED for the manufacturing of ODS steels from Y_2O_3 nanoparticle decorated PM2000 powder.

Acknowledgements

The authors acknowledge the funding by the Deutsche Forschungsgemeinschaft (DFG, German Research Foundation) within the priority program (SPP) 2122 “Materials for Additive Manufacturing” and within the CRC/TRR 270 Project-ID 405553726.

References

- [1] N.R. Baddoo, Stainless steel in construction: A review of research, applications, challenges and opportunities, *J. Constr. Steel Res.* 64 (2008) 1199–1206. <https://doi.org/10.1016/j.jcsr.2008.07.011>.
- [2] Y. Inoue, M. Kikuchi, Present and Future Trends of Stainless Steel for Automotive Exhaust System, 2003.
- [3] D.D. Gu, W. Meiners, K. Wissenbach, R. Poprawe, Laser additive manufacturing of metallic components: Materials, processes and mechanisms, *Int. Mater. Rev.* 57 (2012) 133–164. <https://doi.org/10.1179/1743280411Y.0000000014>.
- [4] N. Shamsaei, A. Yadollahi, L. Bian, S.M. Thompson, An overview of Direct Laser Deposition for additive manufacturing; Part II: Mechanical behavior, process parameter optimization and control, *Addit. Manuf.* 8 (2015) 12–35. <https://doi.org/10.1016/j.addma.2015.07.002>.
- [5] M. Alkhatay, E. Khavkin, A. Gasser, W. Meiners, I. Kelbassa, Comparison of geometrical properties of parts manufactured by powder bed based (SLM) and powder fed based (LMD) laser additive manufacturing technologies, in: *Int. Congr. Appl. Lasers Electro-Optics*, Laser Institute of America, 2018: pp. 740–745. <https://doi.org/10.2351/1.5063125>.
- [6] S. Li, H. Xiao, K. Liu, W. Xiao, Y. Li, X. Han, J. Mazumder, L. Song, Melt-pool motion, temperature variation and dendritic morphology of Inconel 718 during pulsed- and continuous-wave laser additive manufacturing: A comparative study, *Mater. Des.* 119 (2017) 351–360. <https://doi.org/10.1016/J.MATDES.2017.01.065>.
- [7] B.M. Arkhurst, J.-J. Park, C.-H. Lee, J.H. Kim, Direct Laser Deposition of 14Cr Oxide Dispersion Strengthened Steel Powders Using Y_2O_3 and HfO_2 Dispersoids, *Korean J. Met. Mater.* 55 (2017) 550–558. <https://doi.org/10.3365/KJMM.2017.55.8.550>.
- [8] M. Brocq, B. Radiguet, S. Poissonnet, F. Cuvilly, P. Pareige, F. Legendre, Nanoscale characterization and formation mechanism of nanoclusters in an ODS steel elaborated by reactive-inspired ball-milling and annealing, *J. Nucl. Mater.* 409 (2011) 80–85. <https://doi.org/10.1016/J.JNUCMAT.2010.09.011>.
- [9] J.S. Benjamin, Dispersion strengthened superalloys by mechanical alloying, *J. Nucl. Mater.* 1 (1970) 2943–2951. <https://doi.org/10.1007/BF03037835>.
- [10] V.V. Sagaradze, V.I. Shalaev, V.L. Arbutov, B.N. Goshchitskii, Y. Tian, W. Qun, S. Jiguang, Radiation resistance and thermal creep of ODS ferritic steels, *J. Nucl. Mater.* 295 (2001) 265–272. [https://doi.org/10.1016/S0022-3115\(01\)00511-6](https://doi.org/10.1016/S0022-3115(01)00511-6).
- [11] K.E. Knipling, B.W. Baker, D.K. Schreiber, Mechanisms of Particle Coarsening and Phase Transformation in Oxide Dispersion Strengthened Steels During Friction Stir Welding, in: *Proceeding Microsc. Microanal.*, 2016: pp. 676–677.
- [12] B. AlMangour, D. Grzesiak, J.-M. Yang, Selective laser melting of TiB₂/H13 steel nanocomposites: Influence of hot isostatic pressing post-treatment, *J. Mater. Process. Technol.* 244 (2017) 344–353. <https://doi.org/10.1016/J.JMATPROTEC.2017.01.019>.
- [13] B. AlMangour, D. Grzesiak, J.-M. Yang, Nanocrystalline TiC-reinforced H13 steel matrix nanocomposites fabricated by selective laser melting, *Mater. Des.* 96 (2016) 150–161. <https://doi.org/10.1016/J.MATDES.2016.02.022>.
- [14] H.J. Chang, H.Y. Cho, J.H. Kim, Stability of Y-Ti-O nanoparticles during laser melting of advanced oxide dispersion-strengthened steel powder, *J. Alloys Compd.* 653 (2015) 528–533. <https://doi.org/10.1016/j.jallcom.2015.08.273>.
- [15] R. Streubel, M.B. Wilms, C. Doñate-Buendía, A. Weisheit, S. Barcikowski, J.H. Schleifenbaum, B. Gökce, Depositing laser-generated nanoparticles on powders for additive manufacturing of oxide dispersed strengthened alloy parts via laser metal deposition, *Jpn. J. Appl. Phys.* (2018). <https://doi.org/10.7567/JJAP.57.040310>.
- [16] C. Doñate-Buendía, F. Frömel, M.B. Wilms, R. Streubel, J. Tenkamp, T. Hupfeld, M. Nachev, E. Gökce, A. Weisheit, S. Barcikowski, F. Walther, J.H. Schleifenbaum, B. Gökce, Oxide dispersion-strengthened alloys generated by laser metal deposition of laser-generated nanoparticle-metal powder composites, *Mater. Des.* 154 (2018) 360–369. <https://doi.org/10.1016/j.matdes.2018.05.044>.
- [17] M.B. Wilms, R. Streubel, F. Frömel, A. Weisheit, J. Tenkamp, F. Walther, S. Barcikowski, J.H. Schleifenbaum, B. Gökce, Laser additive manufacturing of oxide dispersion strengthened steels using laser-generated nanoparticle-metal composite powders,

- Procedia CIRP. 74 (2018) 196–200.
<https://doi.org/10.1016/J.PROCIR.2018.08.093>.
- [18] P. Wagener, S. Barcikowski, Laser fragmentation of organic microparticles into colloidal nanoparticles in a free liquid jet, *Appl. Phys. A*. 101 (2010) 435–439. <https://doi.org/10.1007/s00339-010-5814-x>.
- [19] T. Schmitz, U. Wiedwald, C. Dubs, B. Gökce, Ultrasmall Yttrium Iron Garnet Nanoparticles with High Coercivity at Low Temperature Synthesized by Laser Ablation and Fragmentation of Pressed Powders, *ChemPhysChem*. 18 (2017) 1125–1132. <https://doi.org/10.1002/cphc.201601183>.
- [20] C. Doñate-Buendia, R. Torres-Mendieta, A. Pyatenko, E. Falomir, M. Fernández-Alonso, G. Mínguez-Vega, Fabrication by Laser Irradiation in a Continuous Flow Jet of Carbon Quantum Dots for Fluorescence Imaging, *ACS Omega*. 3 (2018) 2735–2742. <https://doi.org/10.1021/acsomega.7b02082>.
- [21] D. Zhang, Z. Ma, M. Spasova, A.E. Yelsukova, S. Lu, M. Farle, U. Wiedwald, B. Gökce, Formation Mechanism of Laser-Synthesized Iron-Manganese Alloy Nanoparticles, Manganese Oxide Nanosheets and Nanofibers, *Part. Part. Syst. Charact.* 34 (2017) 1600225. <https://doi.org/10.1002/ppsc.201600225>.
- [22] T. Hupfeld, T. Laumer, T. Stichel, T. Schuffenhauer, J. Heberle, S. Barcikowski, B. Gökce, A new approach to coat PA12 powders with laser-generated nanoparticles for selective laser sintering, *Procedia CIRP*. 74 (2018) 244–248. <https://doi.org/10.1016/J.PROCIR.2018.08.103>.
- [23] S. Kohsakowski, A. Santagata, M. Dell'Aglio, A. de Giacomo, S. Barcikowski, P. Wagener, B. Gökce, High productive and continuous nanoparticle fabrication by laser ablation of a wire-target in a liquid jet, *Appl. Surf. Sci.* 403 (2017) 487–499. <https://doi.org/10.1016/J.APSUSC.2017.01.077>.
- [24] G. Marzun, C. Streich, S. Jendrzey, S. Barcikowski, P. Wagener, Adsorption of Colloidal Platinum Nanoparticles to Supports: Charge Transfer and Effects of Electrostatic and Steric Interactions, *Langmuir*. 30 (2014) 11928–11936. <https://doi.org/10.1021/la502588g>.
- [25] M. Ratti, D. Leuvrey, M.H. Mathon, Y. de Carlan, Influence of titanium on nano-cluster (Y, Ti, O) stability in ODS ferritic materials, *J. Nucl. Mater.* 386–388 (2009) 540–543. <https://doi.org/10.1016/J.JNUCMAT.2008.12.171>.
- [26] M.N. SHETTY, *Dislocations and Mechanical Behaviour of Materials*, 2013.
- [27] A. Lasalmonie, J.L. Strudel, Influence of grain size on the mechanical behaviour of some high strength materials, *J. Mater. Sci.* 21 (1986) 1837–1852. <https://doi.org/10.1007/BF00547918>.
- [28] D. Herzog, V. Seyda, E. Wycisk, C. Emmelmann, Additive manufacturing of metals, *Acta Mater.* 117 (2016) 371–392. <https://doi.org/10.1016/j.actamat.2016.07.019>.
- [29] I. Bogachev, A. Yudin, E. Grigoryev, I. Chernov, M. Staltsov, O. Khasanov, E. Olevsky, Microstructure Investigation of 13Cr-2Mo ODS Steel Components Obtained by High Voltage Electric Discharge Compaction Technique, *Materials (Basel)*. 8 (2015) 7342–7353. <https://doi.org/10.3390/ma8115381>.

11th CIRP Conference on Photonic Technologies [LANE 2020] on September 7-10, 2020

Laser additive manufacturing of hot work tool steel by means of a starting powder containing partly spherical pure elements and ferroalloys

A. Taruttis^{a,*}, C. Hardes^b, A. Röttger^b, V. Uhlenwinkel^a, A. B. Chehreh^c, W. Theisen^b, F. Walther^c,
H. W. Zoch^a,

^aLeibniz Institute for Materials Engineering, Badgasteiner Straße 3, 28359 Bremen, Germany

^bRuhr-University Bochum, Chair of Materials Technology, Universitätsstr. 150, 44780 Bochum, Germany

^cTU Dortmund University, Department of Materials Test Engineering, Baroper Str. 303, 44227 Dortmund

* Corresponding author. Tel.: +49-421-218-51327; fax: +49-421-218-513333. E-mail address: taruttis@iwt-bremen.de

Abstract

Until now, additive manufacturing of high-performance materials such as martensitic hardenable tool steels is rarely investigated. This work addresses the introduction of an alternative alloying strategy for hot work tool steel powder, provided for laser powder bed fusion (L-PBF). The focus is on the question whether a powder mixture of spherical iron powder mixed with mechanically crushed ferroalloy particles can be processed by L-PBF, instead of using cost-intensive pre-alloyed gas-atomized powder, and to investigate the material properties associated with it. The particle morphology, packing density and flowability of this L-PBF powder feedstock is compared to gas-atomized spherical pre-alloyed steel powder and the results are correlated to the defect density, the resulting microstructure and the chemical homogeneity. Finally the resulting surface hardness is compared to a conventionally casted material as a reference state. It shows that the L-PBF fabrication of high-dense parts by means of both starting powders is technically feasible. Even though the alternative alloying concept promotes local chemical inhomogeneities within the microstructure, the overall porosity and the appearance of micro cracks are reduced.

© 2020 The Authors. Published by Elsevier B.V.

This is an open access article under the CC BY-NC-ND license (<http://creativecommons.org/licenses/by-nc-nd/4.0/>)

Peer-review under responsibility of the Bayerisches Laserzentrum GmbH

Keywords: Powder mixing; New alloying strategies for additive manufacturing; Hot work tool steels; Laser powder bed fusion (L-PBF); Martensitic transformation

1. Introduction

Nowadays, the fabrication of individualized components made out of important engineering materials is possible with the help of Laser Additive Manufacturing (LAM), building-up a preferably dense part layer-by-layer [1]. In this context, LAM of metallic materials is a fast-growing economy field and of increasing interest e.g. in the automotive industry, aerospace sector, consumer products or health care [2]. Especially with respect to environmental responsibility, LAM technologies can improve the sustainability of products by enabling repair,

refurbishment and remanufacturing such as on-demand replacement of components [3].

Powder bed additive manufacturing techniques, such as Laser Powder Bed Fusion (L-PBF), use a powder feedstock, deposited on a powder bed of a certain size, which is selectively fused by a computer-controlled laser beam [4]. After the distribution of a new powder layer, this process is repeated until the part is completely manufactured [4]. A variety of different process parameters such as laser power, scan speed, building direction and layer thickness etc. influence the component's properties [5].

Moreover, Dowling et al. pointed out that the powder morphology is a critical factor concerning the reproducibility and quality of the as-built specimen [6]. This is due to the influence of the flowability, the bulk density of the powder layer applied and the powder particle shape on the melt pool characteristics, the thermal conductivity, and the resulting laser energy input [5, 6]. Common materials used as powder feedstock are gas-atomized pre-alloyed powders or wires of established functional alloys [4]. However, fewer investigations focus on the LAM fabrication of metal alloys mixed with pure elemental powders [7-9]. Roberts et al. showed that L-PBF processing of elemental mixtures containing spherical aluminum and aspherical silicon powder particles with fractured surfaces is technically feasible [9].

Steel powders used for LAM processes are typically produced by means of gas-atomization, further described in [11]. This could be expensive due to the additional added value and involve a high experimental effort. In addition, there is the problem that many materials cannot be processed with LAM due to the formation of defects, thus causing component failure during the built-up process. This reduces the amount of commercially available materials for LAM-processing. Among the most frequently used materials in LAM are stainless steels, especially grade 316L, nickel-, aluminum-, and titanium-based alloys [10]. Additive manufacturing of high performance materials, like hot work tool steels, important for highly-stressed parts used in hot-working applications like forging, die casting, mold-making and cutting, has not been extensively investigated so far [2].

Even though LAM is promising with respect to innovative tool concepts, LAM of tool steels is still complex, due to crack-inducement during the martensitic transformation [12]. The aim of this study is to highlight an approach to find alloying techniques that enable higher flexibility with respect to the individual fabrication of materials using iron powder as a base and adding need-orientated alloying elements. This shall contribute to a reduction in manufacturing costs and a decrease of raw element waste in the long-term perspective. The following scientific questions are addressed:

- Does mixing of pure spherical Fe powder with aspherical ferroalloys allows the L-PBF fabrication of nearly defect-free samples? Does this improve the local crack occurrence?
- To what extent can we achieve a homogeneous chemical composition of a complex hot work tool steel in the as-built specimen?
- How does this affect the hardness of the material?

2. Materials and Methods

Specimen Nomenclature

AdPre	L-PBF of gas-atomized, pre-alloyed powder
AdEle	L-PBF of gas-atomized Fe-powder and broken elements and ferroalloys
Cast	Casted reference sample

The alloys to be compared are called AdPre and AdEle in the following, which are based on the condition of the powder: pre-alloyed and element powder.

2.1. Chemical composition

In this work, a tool steel alloy is considered that, despite of the formation of carbon martensite, can be processed using L-PBF without additional process adjustments with regard to the exposure strategy or preheating of building platform. A carbon content in the range of 0.35 to 0.45 mass% was targeted for the martensitic hardening. The remaining element contents were alloyed with regard to the adjustment of the martensite start temperature, so that a certain residual austenite content forms, which counteracts the formation of cold cracks.

The chemical composition of both additively manufactured alloys AdPre and AdEle (EDS), the reference cast and the target is shown in Table 1. Apart from the increased carbon content, the alloys achieve the targeted chemical composition in a good approximation and only show slight differences among each other. However, the local spot-wise chemical composition shows more significant variations.

Table 1. Chemical composition of AdPre and AdEle (Due to experimental restrictions concerning light-weight elements, the C-content was separately measured with carrier gas hot extraction and set as 0.41 mass% (AdPre) and 0.47 mass% (AdEle). The chemical composition of the casted reference sample (Cast) was measured by means of sparc spectrometry.)

	Fe	C	Cr	Si	Mn	Ni	Mo	Ti	V	W
AdPre	Bal.	0.41	11.04	0.68	0.69	1.71	3.22	0.21	0.2	1.92
AdEle	Bal.	0.47	9.89	0.73	0.67	1.95	3.36	0.13	0.29	2.17
Cast	Bal.	0.32	9.84	0.87	0.68	1.69	3.06	0.11	0.3	2.02
Target	Bal.	0.36	10.00	0.70	0.60	1.7	3.00	0.20	0.3	2.00

2.2. Gas-atomization

Both starting powders were synthesized by means of nitrogen gas atomization in a close-coupled atomizer (Indutherm, AU 1000 Prototype). To fabricate the pre-alloyed powder, raw elements and ferro-alloys were melted and superheated to 1,710 °C using an indirect inductive melting system. To prevent oxidization, the melting chamber was evacuated and subsequently flooded with argon. For the atomization nitrogen was used. A close coupled atomizer, with a melt mass flow of 290 kg/h was used to achieve spherical particle with mass median diameters in the range of 40-50 µm.

The fabrication of the iron powder, serving as a base for the manually mixed alloy, was performed in the same manner, using a superheat temperature of 1,710 °C to melt the bulk iron (99.9 mass% purity) and had a melt mass flow of 430 kg/h. Further details of the gas atomization are reported in a previous publication of the authors [13].

2.3. Alternative alloying strategy

The new alloying strategy implies the mixing of gas atomized, pure iron powder with mechanically milled element powders and ferroalloys:

Cr, Ni, Mn, FeCrC (22/70/8), FeMo (70/30), FeV (20/80), FeTi (30/70), FeSi (25/75), FeW (80/20) (numbers in brackets correspond to the element contents in mass%).

To further reduce the ductility, some of the raw elements have been cryogenically frozen in advance of the milling process. The individual ferroalloys were sieved in the fraction 20–63 μm and then mixed in the correct mass% by a 3D shaker mixer (WAB Group, Turbula).

2.4. Powder characterization

The gas-atomized powders were sieved by an air jet sieve (Hosokawa Alpine AG, Air Jet Sieve e200LS) in the fraction 25–63 μm . The particle size distributions of all powders were analyzed with a diffraction spectrometer (Malvern Panalytical Ltd, Mastersizer 2000). The particle shape distribution and sphericity were measured with dynamic image analysis (Sympatec GmbH, QICPIC/R).

The carbon content of the starting powders was identified by means of carrier gas hot extraction (Bruker, IR07). The measuring results of each five powder portions with a mass of 500–600 mg were averaged.

The flowability was measured in different ways. Hall Flow was measured according to DIN EN ISO 4490 with a 5 mm nozzle. For the angle of repose a prototype machine (prototype built by Leibniz IWT) and ImageJ by NIH Image was used. The tap density, for the Hausner ratio, was measured according to ISO 3953.

2.5. L-PBF fabrication

The cubic samples with an edge length of 5 mm each, were built-up on a cylindrical base plate without support structures under argon gas atmosphere by means of Laser Powder Bed Fusion (L-PBF) (Aconity GmbH, AconityMINI) using a checkerboard strategy. All relevant scanning parameters are given in Table 2.

Table 2. L-PBF process parameters (Aconity GmbH, AconityMINI)

Laser power	Scanning speed	Spot size	Hatch distance
250 W	600 mm/s	0.05 mm	0.08 mm
Layer thickness	Strategy	Tilt angle	Gas
0.05 mm	Checkerboard	12°	Argon

2.6. Microscopy

In advance of the microscopical analysis, all specimen were embedded into conductive resin, mechanically ground with SiC abrasive paper (320, 800 and 1000 mesh size) and polished with a diamond suspension with a final particle size of 1 μm . To

further smoothen the polished surfaces, oxide polishing suspension (SiO_2) with a particle size of 0.25 μm was finally applied.

We conducted optical microscopy using light microscopes with brightfield mode (Olympus, BX60M and CarlZeiss, Axiotech) using the 50-fold and 500-fold magnification lenses. We analyzed optical porosity with the help of computer-aided image analysis (ImageJ, Version 1.52n). The powder morphology was determined with the help of a scanning electron microscope (Tescan, Mira) using the SE-detector, an acceleration voltage of 30 kV and a working distance of 25 mm. Electron dispersive spectroscopy (EDS) was carried out for a duration of at least 12 hours using an additional EDS-detector (Oxford, XMaxN) assessing $\text{K}_{\alpha 1}$ - and $\text{L}_{\alpha 1}$ -radiation.

2.7. Hardness testing

Hardness testing was performed according to DIN EN ISO 6507-1:2018-07 using a Vickers-hardness tester (KB-Prüftechnik GmbH, KB30 S) with a load of 9.807 N (HV1). The results were averaged from 25 randomly distributed hardness imprints on the top surface of the additively manufactured specimen. The hardness of the conventionally fabricated reference specimen was averaged from 10 different hardness imprints.

3. Results and Discussion

3.1. Powder properties and powder morphology

Table 3 depicts the most important characteristic powder properties. Additionally, the values of the spherical, gas-atomized pure iron powder are given for comparison. As described in the table, the powders do not show major differences with respect to the particle size distribution, the particle shape distribution, the sphericity and the flowability.

The table clarifies that in terms of the flowability the milled particles in AdEle have an apparent positive effect on the angle of repose, while the particle size distribution and Hall flow appears to have a negative influence.

Table 3. Powder characteristics

	AdPre	AdEle	Pure Fe
Characteristic particle sizes [μm]			
d (0.1)	24.7	29.1	25.2
d (0.5)	41.8	46.0	42.4
d (0.9)	69.1	72.3	69.4
Characteristic particle shapes			
d (0.1)	0.70	0.66	0.71
d (0.5)	0.86	0.85	0.86
d (0.9)	0.93	0.92	0.93
Sphericity			
s (0.5)	0.86	0.85	0.86
Flowability			
Hall flow [s/50 g]	3.2	3.6	3.0
Angle of repose [°]	62	44	58
Hausner ratio	1.15	1.16	1.15

Additional to these characteristic properties the morphology of the AdPre and AdEle is shown in Fig. 1. The powder particles of AdPre are highly spherical, with a low amount of satellites, which is consistent to the sphericity values, given in Table 3. As visible on the right picture, the spherical iron powder particles are surrounded by randomly distributed sharp-edged ferroalloy particles in the AdEle alloy.

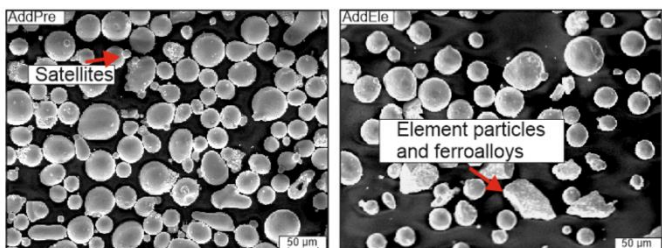


Fig. 1. Morphology of AdPre and AdEle

3.2. Microstructure of the as-build specimen

Figure 2 compares the porosity of the additively manufactured specimen, analyzed by means of optical image analysis. Both alloys show a high density >99%. Therefore, the processability of these two alloys is technically feasible.

As obvious in Fig. 2, AdPre shows an increased number of pores and also micro cracks, whereas in AdEle there are unmelted powder particles, which are evenly distributed across the area. Hence, the porosity and the appearance of cracks is slightly reduced in the AdEle alloy. Therefore, it can be assumed that the powder was applied evenly during the coating process.

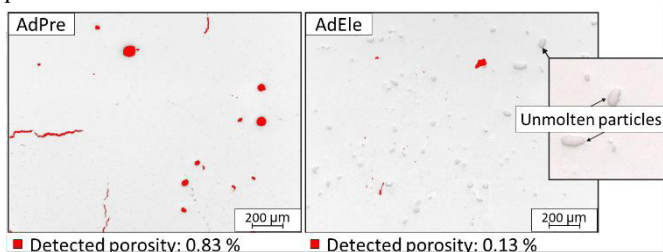


Fig. 2. Microscopical image analysis of the optical porosity of AdPre and AdEle (the as porous detected areas are highlighted in red)

As described in [14, 15, 16], the condition of the powder and the atomization process directly influence the density and mechanical properties of the additively manufactured components. As shown by Attar et al. [16], the porosity of L-PBF manufactured parts is increased in the case of underlying round powder grains, compared to irregularly shape non-

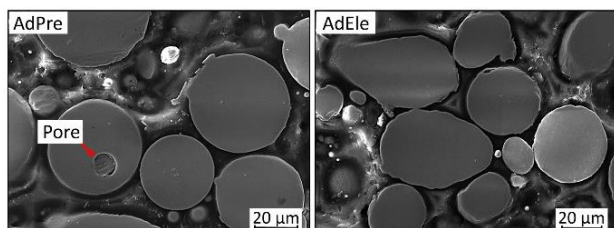


Fig. 3. SEM-micrographs of cross- sections of the AdPre and AdEle powder particles

spherical powder grains, which are more difficult to apply during the L-PBF process. Although the alloy AdEle contains a small number of non-spherical particles, the processability and relative density is still higher.

To investigate the origin of these porosities and the reason behind the differences in the density of the as-built parts, both powders were analyzed by means of SEM. As can be seen in Fig. 3, AdEle powder particles are mostly dense with almost no porosity. Small number of inherent gas pores can be found in several AdPre powder particles. These small pores (maximum 10 µm in diameter) are most likely evoked by the atomization gas, trapped in the powder particles during the atomization process [17]. These pores are often able to survive the L-PBF process and remain as unwanted artefacts in the produced parts [18].

However, the maximum size of porosity seen in the AdPre parts (Fig. 2) is larger than any porosity seen in the powder. This will therefore not be the decisive reason for the increased porosity of the alloy. Therefore, further investigations, for example a powder CT, will follow to determine whether the porosity that has occurred is due to possible pores in the powder, oxide layers or other causes.

Fig. 4 shows the microscopical local segregation of elements. Position 1 and Position 2 (Fig. 4 a) are two different measurement spots in the vicinity of a tungsten-rich particle. The change in the element concentration in wt.% is depicted in the bar chart below the figure. Close to this unmelted particle, at Position 2, the mass% is more than 10% higher than at Position 1, which is located a few microns from the tungsten-rich particle. However, even if the W-content is highly increased in close proximity to an unmelted tungsten-rich particle (Position 2), in a distance of a few micrometer away from the tungsten particle (Position 1), the chemical composition is far more homogeneous even though the local tungsten concentration is still reduced.

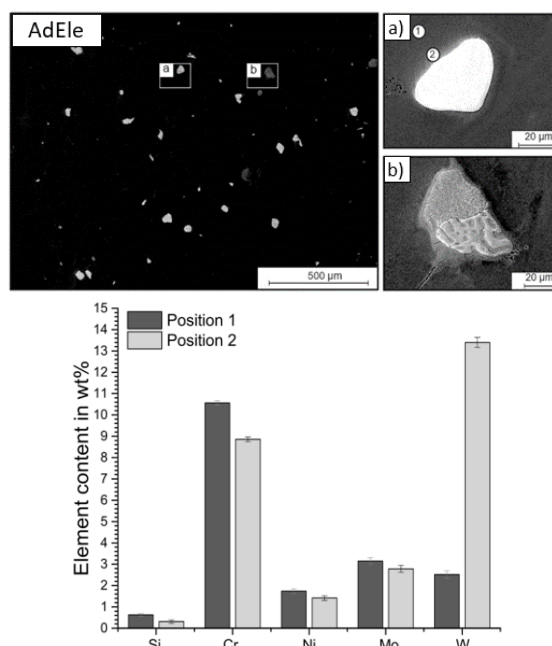


Fig. 4. SEM-image of the AdEle microstructure and local chemical decomposition in the vicinity of unmolten particles

In order to have a closer look at this distribution, an EDS mapping (Fig. 5) shows the local tungsten concentration in mass% in the vicinity of such a particle. It looks like the local decomposition follows the melting traces of the laser spot. Corresponding to the flow, a streamline with increased W-content compared to the matrix can be seen.

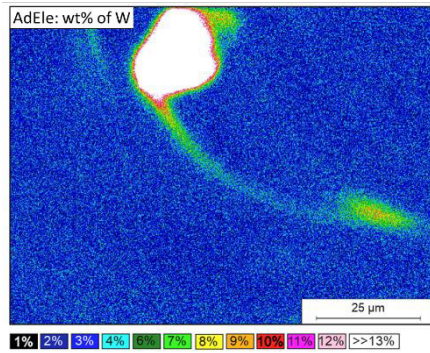


Fig. 5. W content [wt.%] of AdEle

Due to the higher melting temperatures of e.g. FeW (2,111 – 2,723 K) and FeMo (1,790 K), the fast process and short retention times of the L-PBF process, such particles can be explained. The flow and melting time were not sufficient to melt the tungsten-rich particle completely. Only the surface was dissolved and mixed with the surrounding melt pool. This could possibly be avoided if smaller particle fractions are used. Based on the investigations in [23], it is more likely that unmelted ferroalloys are more likely to melt in L-PBF if a smaller particle size is used.

Another influencing factor on such particles is, as described in [20], tungsten has a lower absorption capacity than steel. This means that due to the high proportion of these tungsten-rich particles, a larger portion of the laser light is reflected, and the energy density is lower for the same scanning parameters. As known from the literature [14, 21, 22] the energy density and the scanning strategy is an essential influencing factor regarding the quality of additively manufactured components.

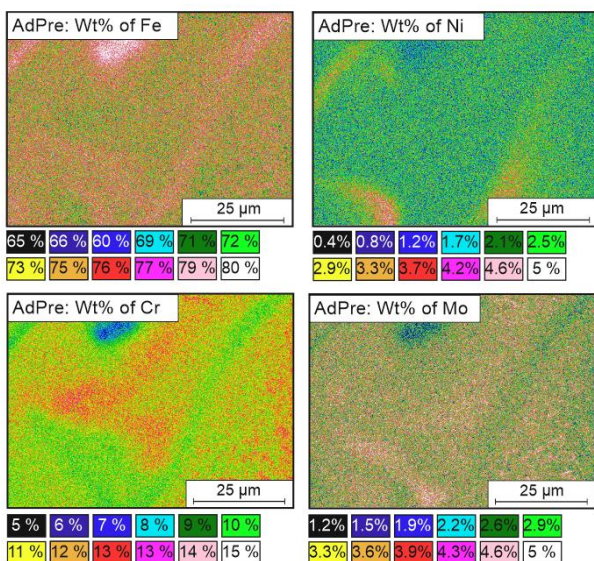


Fig. 6. L-PBF caused segregation of alloying elements in AdPre

However, as shown in Fig. 6, even in the pre-alloyed powder AdPre, where all elements have been melted and atomized together, element segregations, as a result of the constitutional super cooling and the consequent accumulation of elements such as W, Mo and Cr in the residual melt, are visible. This is highlighted in detail in Fig. 7. The etched light-microscopical image highlight the segregation-caused cellular substructure, which typically appears in L-PBF fabricated components.

Furthermore, Fig. 7 shows martensite and retained austenite as well as preferred cracking locations within the microstructure. Since the cracks in AdPre have mainly formed along the martensite needles, this confirms that the production of tool steel with LAM is still complex, due to crack-formation during the martensitic transformation [12].

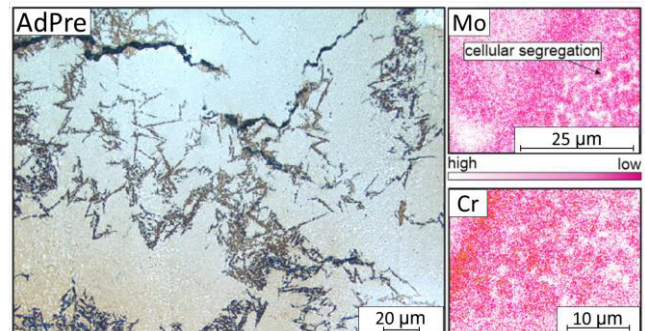


Fig. 7. Etched microstructure of AdPre alloy containing martensite and retained austenite (left) and preferred hot-cracking locations

3.3. Hardness

Fig. 8 depicts the achieved hardness of both additively manufactured specimen compared to a conventionally casted reference sample. As illustrated in the bar diagram, the hardness of AdPre is more or less reduced by a quarter compared to the other specimen AdEle and the cast.

One influencing factor on the decreased hardness is the increased number of pores and micro cracks, as shown by several investigations [21, 22, 24]. Possible other influencing factors on the hardness, like the retained austenite or the C content, are investigated in detail in the future.

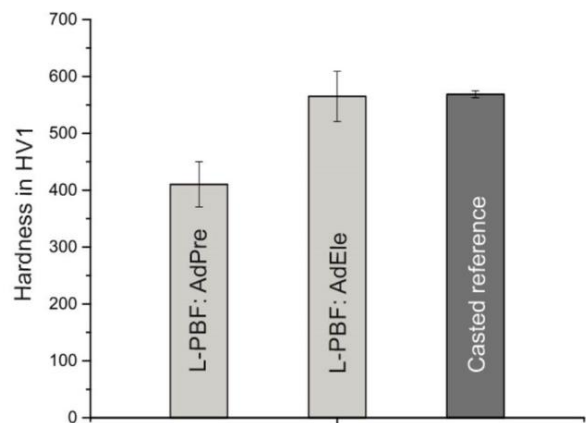


Fig. 8. Micro hardness of L-PBF processed alloys AdPre and AdEle compared to conventionally cast reference sample

4. Conclusions and Outlook

This study has successfully shown that it is technically possible to mix gas-atomized powder with mechanically milled ferroalloys (AdEle) to produce a hot work tool steel alloy usable for the L-PBF process. Furthermore, the following conclusions can be drawn:

- The flow properties of the two powders AdPre and AdEle were evaluated contradictorily by the Hall flow measurement and the dynamic angle of repose. Both powders show similar Hausner ratios and could be processed in the L-PBF process.
- The relative density of the AdEle alloy is slightly improved compared to the fully gas-atomized alloy. This can be most likely traced back to a higher portion of gas pores in the powder grains. Due to the "admixed" alloying elements, the AdEle alloy contains a lower proportion of gas-atomized powder and thus a lower proportion of gas.
- The structure of the alloy AdEle contains unmelted particles of various ferroalloys, which locally inhomogenize the chemical composition on the microscale. Achieving a complete melting of this particles during the L-PBF process or with the help of a subsequent post-treatment requires further prospective investigations.
- The higher density and the reduced number of micro cracks, among others, contributes to an increased hardness, which is within the regime of a conventionally manufactured reference alloy.

The results show that the L-PBF processing of ferro alloy particles is basically possible. However, further questions arise regarding the achievement of a homogeneous element distribution. In further investigations, the influence of the L-PBF process parameters (double exposure), the selected particle size and post-processing on the element distribution will be investigated.

Acknowledgements

The authors gratefully acknowledge the funding by the German Research Foundation (DFG) of project 409651875 within the priority program (SPP) 2122 "Materials for Additive Manufacturing (MATframe)". Furthermore, we highly appreciate the technical support of P. Jadzinski and J. Borkowski.

References

- [1] Herzog, D.; Seyda, V.; Wycisk, E.; Emmelmann, C. Additive manufacturing of metals, *Acta Materialia*, Vol. 117, pp. 371-392, 2016.
- [2] Klocke, F.; Arntz, K.; Teli, M.; Winands, K.; Wegener, M.; Oliari, S.; State-of-the-art laser additive manufacturing for hot-work tool steels, *Procedia CIRP* 63, p. 58–63, 2017.
- [3] Leino, M.; Pekkarinen, J.; Soukka, R.; The role of laser additive manufacturing methods of metals in repair, refurbishment and remanufacturing – enabling Circular Economy, *Physics Procedia* 83, p. 752–760, 2016.
- [4] Fisher, D.J.; Additive manufacturing of metals, Vol. 67 of Materials Research Foundations, Materials Research Forum LLC, 2020.
- [5] Brandt, M.; *Laser Additive Manufacturing: Materials, Design, Technologies and Applications*, Woodhead Publishing, 2017.
- [6] Downing, L.; Kennedy, J.; O'Shaughnessy, S.; Trimble, D.; A review of critical repeatability and reproducibility issues in powderbed fusion, *Materials and Design* Vol. 186 (108346); 2020.
- [7] Schwendner, K. I.; Banerjee, R.; Collins, P. C.; Brice, C.A.; Fraser, H.L.; Direct Laser Deposition of alloys from elemental powder blends; *Scripta Materialia* 45, p. 1123-1129; 2001.
- [8] Clayton, R. M.; The use of elemental powder mixes in laser-based additive manufacturing; Master Thesis; Missouri University of Science and Technology; 2013.
- [9] Roberts, C. E.; Bourell, D.; Watt, T.; Cohen, J.; A novel processing approach for additive manufacturing of commercial aluminum alloys, *Physics Procedia* 83, p. 909–917; 2016.
- [10] Niu, X.; Singh, S.; Garg, A.; Singh, H.; Panda, B.; Peng, X.; Zhang, Q.; Review of materials used in additive manufacturing processes to produce metallic products, *Front. Mech. Eng.* 14 (3), p. 282 – 298, 2019.
- [11] Lawlay, A.; Atomization, *Encyclopedia of Materials: Science and Technology*, p. 387-392, 2001.
- [12] Krell, J.; Röttger, A.; Geenen, K.; Theisen, W.; General investigations on processing tool steel X40CrMoV5-1 with selective laser melting, *Journal of Materials Processing Technology*, Vol. 255, p. 679-688, 2018.
- [13] Ciftci, N.; Ellendt, N.; Coultard, G.; Soares Barreto, E.; Mädler, L.; Uhlenwinkel, V.; Novel cooling rate correlations in molten metal gas atomization, *Metallurgical and Materials Transactions* 50B, p. 666-677, 2019.
- [14] Rashida, R.; Masooda, S.H.; Ruana, D.; Palanisamy, S.; Rahman Rashid, R.A.; Brandt, M.; Effect of scan strategy on density and metallurgical properties of 17-4PH parts printed by Selective Laser Melting (SLM), *Journal of Materials Processing Tech*, p. 502-511, 2017.
- [15] Irrinki, H.; Dexter, M.; Barmore, B.; Enneti, R.; Pasebani, S.; Badwe, S.; Stitzel, J.; Malhotra, R.; Atre, S.V.; Effects of powder attributes and laser powder bed fusion (L-PBF) process conditions on the densification and mechanical properties of 17-4 pH stainless steel. *JOM* 68 (3), p. 860–868, 2016.
- [16] Attar, H.; Prashanth, K.G.; Zhang, L.-C.; Calin, M.; Okulov, I.V.; Scudino, S.; Yang, C.; Eckert, J.; Effect of powder particle shape on the properties of in situ Ti-TiB composite materials produced by selective laser melting. *J. Mater. Sci. Technol.* 31 (10), p. 1001–1005, 2015.
- [17] Sun, Z.; Tan, X.; Tor, S. B.; Yeong, W. Y.; Selective laser melting of stainless steel 316L with low porosity and high build rates, *Materials & Design* Vol 104, p. 197–204, 2016.
- [18] Cunningham, R.; Narra, S. P.; Ozturk, T.; Beuth, J.; Rollett, A. D.; Evaluating the effect of processing parameters on porosity in electron beam melted Ti-6Al-4V via synchro-tron X-ray microtomography, *JOM* 68, p. 765–771, 2016.
- [19] Ng, G. K. L.; Jarfors, A. E. W.; Bi, G.; Zheng, H. Y.; Porosity formation and gas bubble retention in laser metal deposition, *Applied Physics A* 97, p. 641–649, 2009.
- [20] Trappa, J.; Rubenchikb, A.M.; Gussb, G.; Matthews, M.J.; In situ absorptivity measurements of metallic powders during laser powder-bed fusion additive manufacturing, *Applied Materials Today* 9, p. 341–34, 2017.
- [21] Lu, Y.; Wu, S.; Gan, Y.; Huang, T.; Yang, C.; Junjie, L.; Lin, L.; Study on the microstructure, mechanical property and residual stress of SLM Inconel-718 alloy manufactured by differing island scanning strategy, *Optics & Laser Technology* Vol 75, p. 197–206, 2015.
- [22] Tucho, W.M.; Lysne, V.H.; Austbø, H.; Sjølyst-Kverneland, A.; Hansen, V.; Investigation of effects of process parameters on microstructure and hardness of SLM manufactured SS316L, *Journal of Alloys and Compounds*, Volume 740, p. 910-925, 2018.
- [23] Buchbinder, D.; Meiners, W.; Brandl, E.; Palm, F.; Müller-Lohmeier, K.; Wolter, M.; Over, C.; Moll, W.; Weber, J.; Skrynecki, N.; Gradl, J.; Neubert, V.; Generative Fertigung von Aluminiumbauteilen für die Serienproduktion – AluGenerativ Abschlussbericht, Förderkennzeichen BMBF 01RI0639A-D, 2010.
- [24] Chen, J.; Hou, W.; Wang, X.; Chu, S.; Yang, Z.; Microstructure, porosity and mechanical properties of selective laser melted AISi10Mg, *Chinese Journal of Aeronautics* (In Press), 2019.

11th CIRP Conference on Photonic Technologies [LANE 2020] on September 7-10, 2020

A comparison of material models for the simulation of selective beam melting processes

Christian Burkhardt^{a,*}, Dominic Soldner^a, Julia Mergheim^a

^a*Institute of Applied Mechanics (LTM), Friedrich-Alexander-Universität Erlangen-Nürnberg, Egerlandstr. 5, 91058 Erlangen*

* Corresponding author. Tel.: +49 9131 85-20972; fax: +49 9131-85-28503. E-mail address: christian.burkhardt@fau.de

- Invited Paper -

Abstract

The focus of this contribution lies on the comparison of different material models for the thermo-mechanical simulation of selective laser melting (SLM) processes. A Finite Element (FE) framework for the analysis of residual stresses and distortions in laser beam melting processes is introduced. The FE solver for the thermo-mechanical problem uses a staggered algorithm, is based on the open source finite element library deal.ii and makes use of heavy parallelization. The most important aspects to be investigated here are the mechanical material behavior and stress relaxation in the range of the melting temperature. Material models, which reset certain variables as stress and plastic strain to zero at a critical temperature are compared to a thermo-viscoplastic constitutive law. Simulations, related to the SLM process of Ti-6Al-4V, are performed to compare the residual stresses and plastic strains predicted by different models after melting and cooling. Furthermore, the validity of geometrically linearized material model is analyzed.

© 2020 The Authors. Published by Elsevier B.V.

This is an open access article under the CC BY-NC-ND license (<http://creativecommons.org/licenses/by-nc-nd/4.0/>)

Peer-review under responsibility of the Bayerisches Laserzentrum GmbH

Keywords: SLM process; Finite Element simulations; residual stresses; viscoplastic material models; melting and solidification;

1. Introduction

Additive manufacturing offers almost unlimited design freedom in the construction of components. In particular, very filigree structures can be produced. In selective laser beam melting (SLM), parts are produced by locally melting metal powder together. The highly concentrated energy input by a laser leads to huge temperature gradients during the manufacturing process. As a consequence, process parameter dependent residual stresses and distortions occur. These cause a reduction in dimensional accuracy and have a negative influence on the fatigue strengths of components [1]. If the distortions increase during the manufacturing process, the occurring warpage can even lead to a premature process termination [2].

A powerful tool to predict these effects are thermo-mechanical finite element (FE) simulations [3]. Due to the high computing power required for thermo-mechanical process simulations, a heavy parallelized staggered approach has proven to be particularly suitable. The nonlinear thermal problem is solved first and the computed temperatures serve as input for the following mechanical simulation. While the assumptions of thermal modeling and their effects are well understood, the same is not true for the influences of mechanical model assumptions [4]. A main aspect is the modeling of stress and plastic strain relaxation during melting and re-melting, but also the validity of geometrically linear material models.

Ganeriwala et al. [5] used a rate-independent elastoplastic material model for lower temperatures and a rate-dependent

constitutive law for medium temperature regions. In the temperature range near the melting point a viscoelastic material model was used to account for stress and strain relaxation. Furthermore, the plastic strains were set to zero in this high temperature range. Denlinger et al. [6] used a geometrically linearized incremental elasto-plastic model. They modelled the relaxation of plastic strains and stresses by resetting these quantities to zero when a prescribed critical temperature is exceeded.

In this paper, these common mechanical modelling approaches are investigated for the SLM process of Ti-6Al-4V. Therefore, a modelling framework is presented that allows to easily switch between the geometrically nonlinear and linear setting and different relaxation models. The plastic strains and stresses predicted by the various models are compared by means of numerical simulations of melting and re-melting processes.

2. Numerical model

Nomenclature

T	temperature
λ	thermal conductivity
H	enthalpy
Q	heat source
$\boldsymbol{\varepsilon}$	linearized total strain
$\boldsymbol{\varepsilon}^{th}$	linearized thermal strain
$\boldsymbol{\varepsilon}^{pl}$	linearized viscoplastic strain
\mathbf{E}	total Hencky strain
\mathbf{E}^{th}	thermal Hencky strain
\mathbf{E}^{pl}	viscoplastic Hencky strain
\mathbf{F}	deformation gradient
\mathbf{u}	displacements
α	hardening variable
$\boldsymbol{\sigma}$	Cauchy stress
η	viscosity

2.1. Thermal model

The temperature field in the selective beam melting process is derived by solving the nonlinear heat equation

$$\dot{H} = \text{div}(\lambda(T)\nabla T) + Q, \quad (1)$$

using a two-step Runge-Kutta S-DIRK [7] method. The heat source Q represents the energy input by the laser beam and is modelled as a volumetric Gaussian distribution around the beam center and pre-integrated in time [8]. A change in the enthalpy H accounts for the latent heat during solidification. For a more detailed description of the thermal simulations, the reader is referred to [9].

2.2. Mechanical model

The temperature fields obtained from the thermal analysis are included in the mechanical simulation as thermal loads. The

balance of linear momentum is solved to derive plastic strains, stresses and distortions

$$\text{div}(\boldsymbol{\sigma}) = 0. \quad (2)$$

Boundary conditions on the displacements or forces are prescribed. The Cauchy stress is related to the deformation (history) by means of constitutive models, which will be introduced in the following.

2.2.1. Constitutive Model

The mechanical simulations shall be compared for a geometrically linear and nonlinear setting. A unifying description is given by the formulation in the logarithmic strain space [10]. The same constitutive equations can be used, but in the finite strain setting a pre- and post-processing step is required, transferring the results in or from the logarithmic strain space. As a finite strain measure the Hencky strain

$$\mathbf{E} = \frac{1}{2} \ln(\mathbf{F}^T \mathbf{F}) \quad (3)$$

is used. It is decomposed into an elastic, a viscoplastic and a thermal part

$$\mathbf{E} = \mathbf{E}^e + \mathbf{E}^{pl} + \mathbf{E}^{th}. \quad (4)$$

The thermal strain \mathbf{E}^{th} follows from the thermal loads, applying a temperature dependent coefficient of thermal expansion (CTE), see Fig. 1. A von Mises type yield criterion with isotropic hardening is used, in which the yield stress and the hardening parameter are also temperature dependent. The viscoplastic strains follow a Perzyna-type evolution equation, which accounts for rate-dependent effects. When setting the viscosity parameter $\eta=0$ a rate independent thermo-elastoplastic material model is obtained.

In order to account for the nonlinearities due to temperature dependencies and to allow for a resetting of particular variables, as described in detail in section 2.2.3, an incremental formulation is used to update the stresses in each time step, according to the incremental change in the strains and the temperatures.

$$\boldsymbol{\sigma}_{n+1} = \boldsymbol{\sigma}_n + \Delta\boldsymbol{\sigma} = \boldsymbol{\sigma}_n + \frac{\partial\boldsymbol{\sigma}}{\partial\mathbf{E}} : \Delta\mathbf{E} + \frac{\partial\boldsymbol{\sigma}}{\partial T} \Delta T. \quad (5)$$

2.2.2. Material Parameters

The thermal and mechanical material parameters are modelled to be temperature dependent. A distinction is made for the different material states such as powder, solid and melt. The powder is modelled as elastic. The Young's modulus of the powder at room temperature is assumed to be one tenth of that of the solid. Additionally, the powder does not expand or contract due to temperature changes.

All relevant parameters of Ti-6Al-4V for the mechanical simulations are shown in Fig. 1. Smooth curves are fitted to experimentally measured temperature-dependent parameters taken from [11]. The solid and melt phases are represented in

black and the powder state in green. Experimental data is indicated by red crosses.

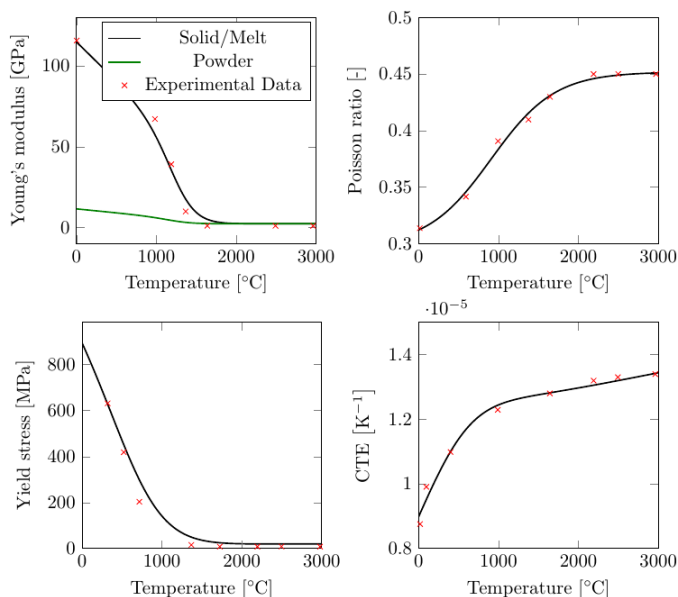


Fig. 1: Temperature dependent mechanical properties of Ti-6Al-4V. The colours of the lines indicate the state of material: black (solid/melt) and green (powder). The underlying experimental data [11] is represented with red crosses. The Poisson's ratio is assumed to be state independent and the thermal expansion coefficient (CTE) of powder is set to 0. The powder is modelled to be elastic and therefore no yield stress is given.

2.2.3. Relaxation during melting

One way to account for the relaxation of stresses during the melting phase is by means of an increasing viscosity parameter η in the viscoplastic material model for higher temperatures. This approach is compared to models in which the stress relaxation is approximated by resetting certain variables to zero. Here, the thermal strain, the plastic strain, the hardening variable and the stresses are adjusted to zero when a certain critical temperature is exceeded

$$\boldsymbol{\varepsilon}^{th} = \mathbf{0}, \quad \boldsymbol{\varepsilon}^{pl} = \mathbf{0}, \quad \boldsymbol{\sigma} = \mathbf{0}, \quad \alpha = 0 \quad \text{if } T > T^{crit}. \quad (6)$$

Another approach [5] uses a viscoplastic model together with a reset of only the hardening variable and the plastic strain for high temperatures. One critical aspect which is common for these approaches is the determination of suitable values for either the viscosity parameter η or the critical temperature T^{crit} . In the present comparison, literature values are used, which were shown to predict stresses which are in good agreement with experimental results. The viscosity parameter is taken from [5] and the critical temperature is set to be 80% of the melting temperature, which denotes the beginning of the mushy zone for metallic materials [12]. For Ti-6Al-4V with a melting temperature of 1674°C, the critical temperature is taken as 1339°C.

3. Results

In this section, numerical results for the material models with different approximations of the stress relaxation during melting are compared for a single melting point example. The

stresses and plastic strains obtained with small and large strain viscoplastic models are contrasted to those of elastoplastic and viscoplastic models with resetting various variables to zero. Additionally, a single-layer example is presented and the stress and plastic strain formation for a cross-snake hatching is analyzed.

3.1. Single melting point example

In the first example, the stresses and plastic strains for two cycles of melting and solidification are simulated, with no movement of the laser beam. The initial material state is powder and the powder bed has the size 1 x 1 x 0.8 mm³. The powder bed is modelled to be mechanically constrained at the bottom plate and stress free at the beginning of the simulation. In the thermal simulation the bottom and side faces are insulated. Convection and radiation is accounted for at the top face. The simulation setting is shown in Fig. 2 and further simulation parameters are summarized in Tab. 1.

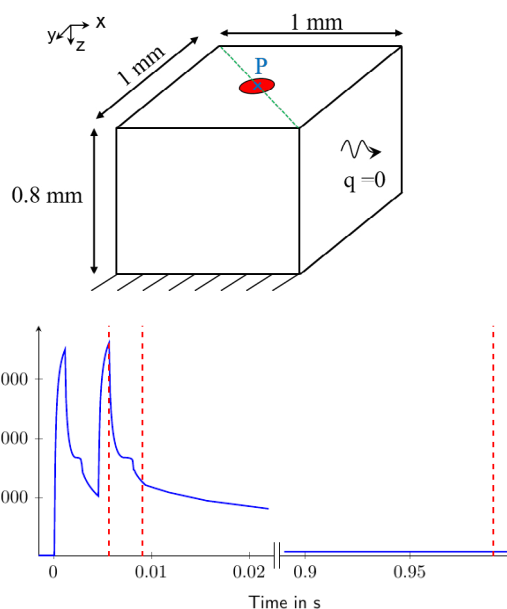


Fig. 2: Schematic illustration of the single melting point example. The green line indicates the position at which the stresses and plastic strains are evaluated (top); Temperature history at point P. The temperature exceeds the melting temperature twice before the material is cooled down to room temperature. The red lines indicate the points in time when the plastic strains and stresses are evaluated (bottom).

The geometry is meshed with 152864 hexahedral elements, using a fine mesh in the area near the laser spot and coarser elements for the remaining areas. The same mesh is used for the thermal and the mechanical simulation. For the thermal simulation tri-linear and for the mechanical simulation tri-quadratic shape functions are applied.

Table 1. Process parameters single melting point example

Laser power	100	W
Laser radius	100	μm
Absorption coefficient	1.0	
Initial temperature	20	°C

The laser exposes the centre point of the powder bed for

1.1 ms, is then switched off for 3.4 ms, and then exposes the same spot again for 1.1 ms. The powder material melts, solidifies, melts, solidifies again and is cooled down to room temperature afterwards. The thermal fields are simulated once and used within a staggered approach for the mechanical simulations with the different material models. The resulting plastic strains and von Mises stresses are compared in the following.

The results obtained for the thermo-viscoplastic model in the geometrically linear setting are compared to those of the geometrically nonlinear setting. As shown in Fig. 3, the differences for the von Mises stress after cooling are negligible for the current example. This can be explained by the small maximum values of the total strain of about 4.8%. The small strain assumption is still valid here, but should be verified for other examples, e.g. multi-layer simulations. Due to these small differences, all further simulations are made using the geometrically linear setting.

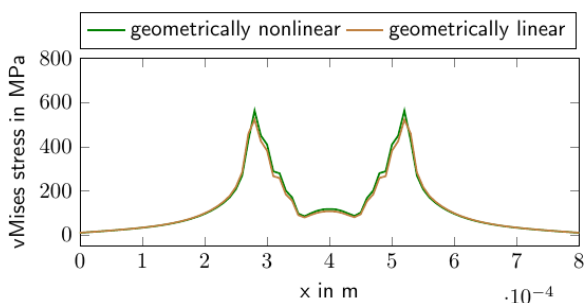


Fig. 3: Final distribution of the von Mises stress for the geometrically linear and non-linear case.

The evaluation of the plastic strains along a diagonal line on the top surface of the geometry is illustrated in Fig. 4 for three points in time. The formation of plastic strains is related to the thermal gradients. During the first melting phase, nearly no stresses and plastic strains arise due to the powder properties, which allow an almost unhindered thermal expansion of the material. During the second melting phase, the now solid material restricts the thermal expansion of the melting material. At this stage, the thermal gradient is the highest at the interface between melt and solid. Therefore, negative plastic strains ϵ_{11}^{pl} arise in these regions for the viscoplastic material model without resetting. The same holds for the material model with resetting, but as the temperature exceeds the critical temperature all plastic strains are zeroed. In the following solidification phase the plastic strains increase further for the viscous case. Since the temperatures in this region are still above the critical temperature, no plastic strains remain for the elastoplastic material model with resetting. With the exception of the boundary of the previously molten region, which shows positive plastic strains ϵ_{11}^{pl} due to the limited thermal contraction during cooling. Similar plastic strains are also observed for the viscoplastic model in the remaining cooling phase to room temperature. The results of the viscoplastic model which resets the hardening variable and the plastic strains to zero show similar plastic strains as the model with the reset of all variables. A reset of only the hardening variable leads to similar results as the viscoplastic model with no resetting.

Most of the plastic strains, by which the approaches differ, see Fig. 4 c), result from plastic deformations in the mushy or

molten material state. These do not lead to large differences in the stresses as is shown in Fig. 5. The stresses arise mostly during the cooling period to room temperature. The largest stresses appear at the outer boundary of the previously molten material due to the inhomogeneous temperature field and the restricted thermal contraction in this region. The stress values decrease towards the beam centre as the thermal gradients decrease. For all approaches, the temperature gradient along the x-direction is zero in the center, due to the symmetry of the problem, resulting in no plastic strains and small stresses.

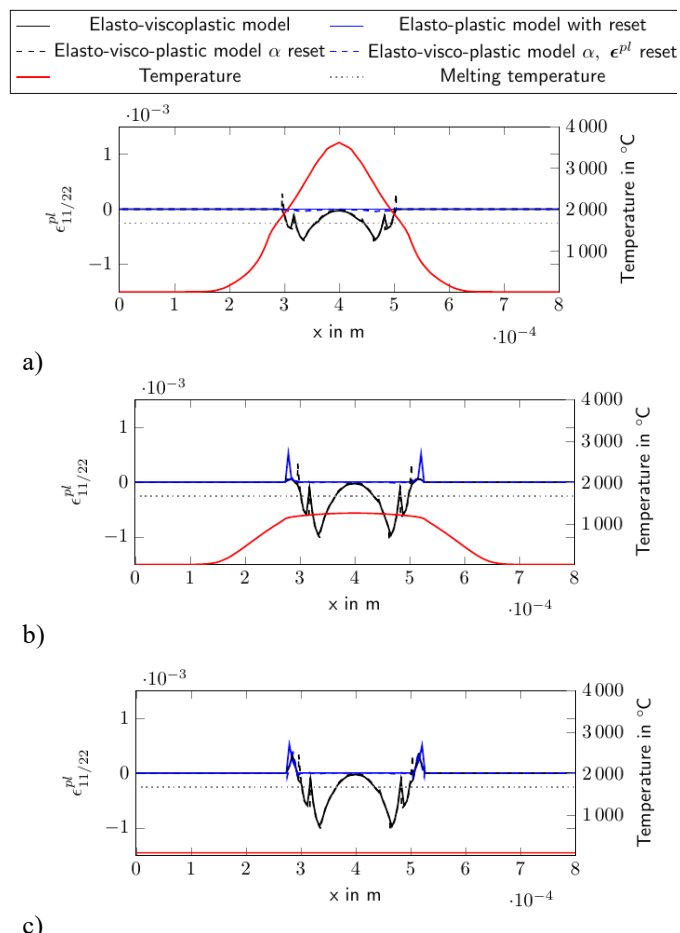


Fig. 4: Plastic strain after the second melting phase (a), after the second cooling phase (b) and after cooling down to room temperature (c), evaluated on the surface along a diagonal line through the laser centre.

The maximum von Mises stresses for the different models are reached at the same locations ($x=0.28$ mm and 5.2 mm, due to symmetry) and are given in Tab. 2. The maximum difference is about 15 MPa or 2.8%, which is negligible, considering the uncertainties of the parameters and residual stress measurements.

Table 2. Maximum von Mises stresses

	MaxValue [MPa]	AbsDif [MPa]	RelDif [%]
Elasto-viscoplastic model no resetting	522		
Elasto-plastic model with reset	508	-14	-2.7
Elasto-viscoplastic model α reset	507	-15	-2.8
Elasto-viscoplastic model α and ϵ^{pl} reset	524	+2	+0.4

The material modelling approaches are sensitive to the

choice of the viscosity or the critical temperature. When the viscosity parameter is increased, smaller stresses are computed. A similar behaviour results from decreasing the critical temperature.

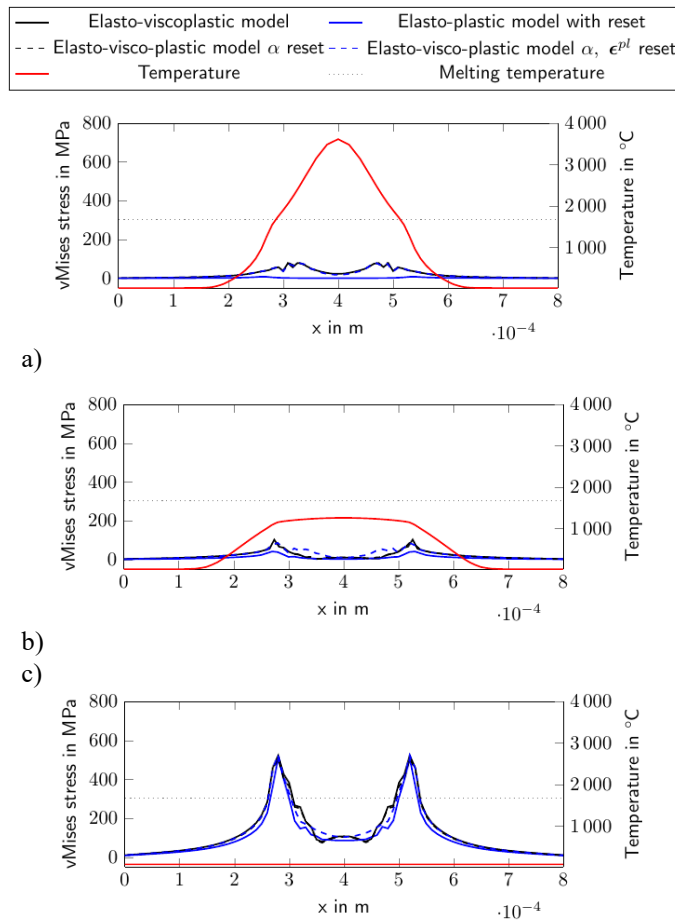


Fig. 5: Von Mises equivalent stress after the second melting phase (a), after the second cooling phase (b) and after cooling down to room temperature (c), evaluated on the surface along a line through the laser centre.

The final stress distribution after cooling to room temperature evaluated along the z-direction is shown in Fig. 6. It is visible that the results of the different models are also in good agreement. The highest stresses are reached at the boundary of the former melt pool, which is similar as for the stress evaluation along the x-axis.

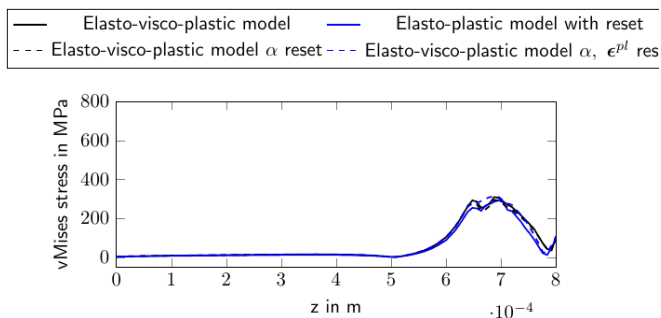


Fig. 6: Von Mises equivalent stress after cooling down to room temperature; evaluated along the z-axis through the laser centre; top surface: $z=0.8$ mm.

3.2. Single layer example

In the second example the viscoplastic model without resetting is used to simulate the stress and plastic strain formation during the melting and solidification of a five line cross-snake hatch pattern for a single layer of 20 μm height, as shown in Fig. 7. The lines are melted on top of a 1.58 mm thick Ti-6Al-4V base plate. Each scanning line is 2.0 mm long and the hatch distance is 120 μm . The dimensions of the simulation box are 5 x 3 x 1.6 mm^3 . The temperature of the base plate is set to 160°C. The simulation parameters are summarized in Tab. 3.

Table 3. Simulation parameters single layer example

Laser power	400	W
Laser velocity	0.9	m/s
Laser radius	110	μm
Absorption coefficient	0.3	
Initial temperature	20	°C
Bottom temperature base plate	160	°C

A static mesh consisting of 187160 hexahedral cells is used with coarse elements at the bottom of the base plate and finer elements in the powder bed. Near the scan path, an additional local mesh refinement results in an element edge length of approximately 15 μm . The same mesh was used for the thermal and the mechanical simulation. As in the first example, tri-linear shape functions are applied for the thermal simulation and tri-quadratic ones for the mechanical simulation.

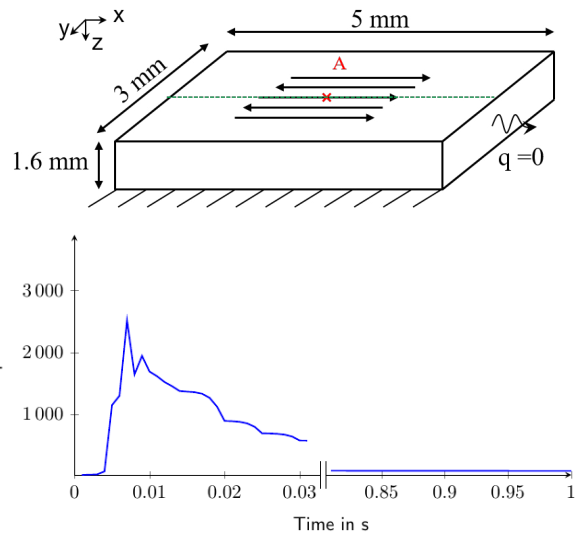


Fig. 7: Schematic illustration of the single layer example. The green line indicates the position at which the stresses and plastic strains are evaluated (top); Temperature history at point A. The temperature exceeds the melting temperature while being scanned and again when the next line is scanned. After 1 s of cooling a constant temperature of approximately 85°C is reached (bottom).

The resulting plastic strains and von Mises stresses evaluated along the green dashed line in Fig. 7, at the end of the simulation, when a uniform temperature is reached, are shown in Fig. 8. In this example, the formation of stresses and plastic strains is influenced by several additional factors as compared to the first example. The thermal and mechanical boundary conditions change due to the movement of the beam, and the thermal volume change of the base plate is also

important. At first sight, the results show large differences in the plastic strains and stresses as compared to the single melting point example. But if the scan line is regarded as a continuous sequence of melting points, the influence of the positive plastic strains, which are formed at the edge of the solidifying melt in each case, predominates. This results in almost constant plastic strains ϵ_{11}^{pl} and ϵ_{22}^{pl} and stresses along the x-direction, compare Fig. 8. The fluctuations can be explained by the inhomogeneous temperature histories, which differ at every point. Furthermore, the solid base plate has a significant influence on the plastic strain evolution, since it allows less thermal expansions than the powder bed from the first example.

The stress curve shows an almost uniform stress distribution close to the maximum of 903 MPa in the previously molten region. This higher value, as compared to the single melting point example, results from the different mechanical boundary conditions due to the base plate and the non-simultaneous solidification of the larger melt pool.

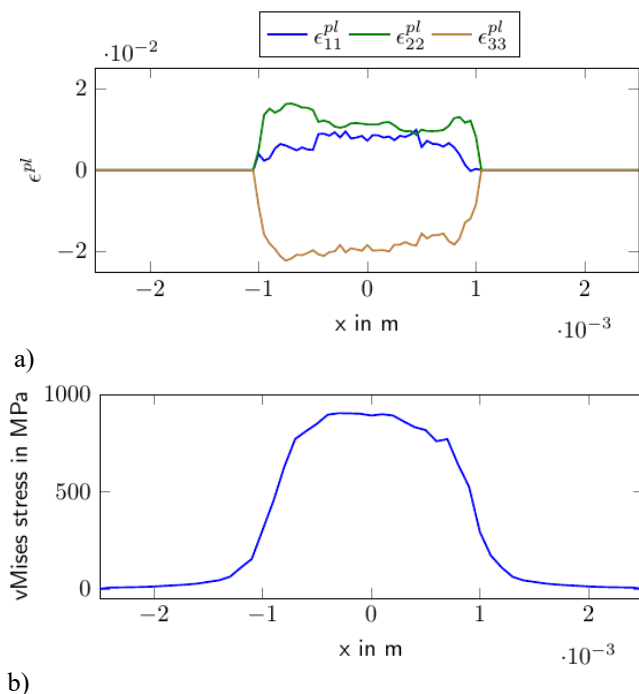


Fig. 8: Viscoplastic strain (a) and equivalent von Mises stress (b) after reaching a constant temperature, evaluated along the dashed green line as shown in Fig 7.

4. Conclusion

In the current contribution, the predicted plastic strains and stresses of different material models are compared for melting and re-melting processes, similar to the SLM process. The focus is on the influence of various approximations of the stress relaxation in the melt phase. A viscoplastic model is compared to models in which the stresses and plastic strains are reset to zero at a critical temperature. The differences are illustrated by means of a single melting point example, in which powder is melted and solidified twice, before cooling down to room temperature. While the plastic strains derived by a material model with resetting of variables develop only at the outer region of the solidified material, the viscoplastic material model results in the formation of higher plastic strains within

the previously molten region. However, since the stresses primarily arise during final cooling to room temperature, the residual stress distributions of the models are very close. The differences in the results for the geometrically linear and geometrically nonlinear case are negligible, which is due to the small overall strains with a maximum of 5%. However, it is emphasized that this is not a general rule for the simulation of SLM processes, but further comparisons for multi-layer or part scale examples are required to confirm the validity of the small strain assumption. The simulation of an example with multiple scan lines shows the strong influence of the inhomogeneity of the temperature field on the results. Solid materials such as the building plate have a large influence on the resulting plastic strains and stresses.

Future investigations will include the simulation of multiple-layer examples and small parts. This will also allow comparison with experimental data.

Acknowledgements

Funded by the Deutsche Forschungsgemeinschaft (DFG, German Research Foundation) – Project-ID 61375930 – SFB 814 - „Additive Manufacturing“ TP C03.

References

- [1] Leuders S, Thöne M, Riemer A, Niendorf T, Tröster T, Richard HA, Maier HJ, On the mechanical behaviour of titanium alloy TiAl6V4 manufactured by selective laser melting: Fatigue resistance and crack growth performance, *International Journal of Fatigue* 48 (2013) 300-307
- [2] Chen Z, Cao S, Wu X, Davies CHJ, Surface roughness and fatigue properties of selective lasermelted Ti-6Al-4V alloy, *Additive Manufacturing for the Aerospace Industry* (2019) 283-299
- [3] Bartlett JL, Li X, An overview of residual stresses in metal powder bed fusion, *ADDMA* 27, 2019.
- [4] King WE, Anderson AT, Ferencz RM, Hodge NE, Kamath C, Khairallah SA, Rubenchik AM. Laser powder bed fusion additive manufacturing of metals; physics, computational, and materials challenges. *Applied Physics Reviews* 2, 2015.
- [5] Ganeriwala RK, Strantz M, King WE, Clausen B, Phan TQ, Levine LE, Brown DW, Hodge NE. Evaluation of a thermomechanical model for prediction of residual stress during laser powder bed fusion of Ti-6Al-4V, *ADDMA* 688, 2019.
- [6] Denlinger ER, Heigel J, Michaleris P. Residual stress and distortion modeling of electron beam direct manufacturing Ti-6Al-4V. *Proceedings of the Institution of Mechanical Engineers, Part B: Journal of Engineering Manufacture*, 2015.
- [7] Ellsiepen P, Hartmann S. Remarks on the interpretation of current non-linear finite element analyses as differential-algebraic equations. *Int. J. Numer. Meth. Engng*, 2001. **51**:679-707
- [8] Irwin J, Michaleris P, A Line Heat Input Model for Additive Manufacturing, *J. Manuf. Sci. Eng* 138 (11), 2016.
- [9] Soldner D, Mergheim J. Thermal modelling of selective beam melting processes using heterogeneous time step sizes. *Computers & Mathematics with Applications*, 2018. **78**(7), 2183-2196
- [10] Miehe C, Apel N, Lambrecht M. Anisotropic additive plasticity in the logarithmic strain space: Modular kinematic formulation and implementation based on incremental minimization principles for standard materials. *Comput. Methods Appl. Mech. Engrg*. **191**, 2002.
- [11] Hodge NE, Ferencz RM, Solberg JM. Implementation of a thermomechanical model for the simulation of selective laser melting. *Comput Mech*, 2014. **54**:33-51
- [12] Goldak JA, Akhlaghi M, *Computational Welding Mechanics*, Springer US, New York, 2005.

11th CIRP Conference on Photonic Technologies [LANE 2020] on September 7-10, 2020

Scaling melt pool geometry over a wide range of laser scanning speeds during laser-based Powder Bed Fusion

Markus Döring^{a,c,*}, Guillaume Boussinot^b, Jan Frederik Hagen^{a,c}, Markus Apel^b, Stefanie Kohl^{a,c}, Michael Schmidt^{a,c}

^a*Institute of Photonic Technologies (LPT), Friedrich-Alexander Universität Erlangen-Nürnberg, Konrad-Zuse-Str. 3-5, 91052 Erlangen, Germany*

^b*Access e.V., Intzestraße 5, 52072 Aachen, Germany*

^c*Erlangen Graduate School in Advanced Optical Technologies (SAOT), Paul-Gordan-Str.6, 91052 Erlangen, Germany*

* Corresponding author. Tel.: +49-9131-85-23367; fax: +49-9131-85-23234; E-mail address: markus.doering@lpt.uni-erlangen.de

Abstract

Generating dense parts from laser-based Powder Bed Fusion of metals often requires the adaption of laser scanning speed. Thereby, scanning speed is lost as a degree of freedom for tailoring the microstructure. This paper addresses this issue by using an analytical model from literature to achieve equal melt pool width and depth for a range of factor 12 for laser scanning speeds and by examining the resulting specimen densities for this range of scanning speeds. The melt pool width and the melt pool depth of a dense reference specimen are measured. The measured melt pool width and melt pool depth are defined as the target sizes of the melt pool for all examined scanning speeds, as this is expected to result in dense specimens from a geometrical point of view. The target size shall be achieved by using an analytical model from the literature. This strategy is chosen to estimate the necessary energy input for creating dense specimens while avoiding incomplete fusion and keyholing. Defects mechanisms like splatters and cracks are excluded from this initial examination.

© 2020 The Authors. Published by Elsevier B.V.

This is an open access article under the CC BY-NC-ND license (<http://creativecommons.org/licenses/by-nc-nd/4.0/>)

Peer-review under responsibility of the Bayerisches Laserzentrum GmbH

Keywords: PBF; Normalized enthalpy; Line energy, Volume energy density; Melt pool geometry, Melt pool depth

1. Introduction

The resulting microstructure of metallic alloys processed by laser-based Powder Bed Fusion of metals (PBF-LB/M) is strongly dependent on the conditions during solidification [1]. The laser scanning speed is a crucial factor for the conditions during solidification, as it influences the solidification velocity of the melt pool [2]. Hence, scanning speed should be treated as a useful degree of freedom when optimizing the microstructure as this also has implications on the mechanical properties as well as the tearing behavior of a distinct material system [3, 4].

The approach of this paper is generating dense geometries while turning the scanning speed from a parameter that has to be optimized to a variable for the adaption of the microstructure during PBF-LB/M. This shall be achieved by controlling the width and depth of the melt pool for a wide range of scanning speeds. The length of the melt pool is neglected. The goal is to tailor the microstructure of a given material system while reducing the effort necessary for finding suitable process parameters.

An analytical model from literature is used to predict the size of the melt pool depending on the process and material parameters [2]. In order to gain sufficient specimen quality, it is necessary to adapt process parameters for each material

system individually. An advantage of using this analytical model is that it incorporates the material parameters enthalpy at melting temperature $h_s = \rho CT_m$, thermal diffusivity D and absorptivity A , which establish a connection to the real process and possibly enabling analytical process optimization independent of the used material system.

2. Materials and methods

For the experimental procedure, an aluminum alloy with nominally 6.1 wt% nickel was used. The used spherical powder particles had an average diameter of 35.8 μm . The particle size ranged between 20 and 63 μm . For all sub-studies, an SLM®280 powder bed fusion machine from SLM Solutions Group AG utilizing a laser wavelength of 1070 nm was used. The building plate was pre-heated to a temperature of 423 K. Argon was used as shielding gas. A hatch distance of 135 μm and a powder layer height of 50 μm were used unless stated otherwise. The beam diameter was measured to be 68.5 μm . The actual laser power of the machine was calibrated to match the nominal power.

For all specimens described within the scope of this paper, the scanning direction from layer to layer was not rotated. The meandering scanning pattern was not shifted laterally, so each melt track was aligned in parallel and placed directly on top of the respective melt track of the previous layer. Hence, a “worst-case” scanning strategy was used. The reason for using this scanning strategy is to separate the physical relationships in the region of the melt pool from the process strategy of the whole specimen. The examination focuses on the energy input and the accompanying consequences on the density of the specimens, e.g., avoiding incomplete fusion and porosity due to keyholing. The created specimens are 10x10x15 mm in size. The specimens were placed directly onto the building platform to guarantee homogenous heat conduction undisturbed by variations of the support structure and to increase overall heat conduction to the building plate. Thereby the amount of heat accumulated over multiple layers of the specimen should be reduced.

An additional powder layer was added to create single tracks on top of the specimens with a hatch distance of 1 mm. These single tracks were generated to receive the size of the melt pool while not experiencing heat accumulation during the creation of a layer due to the energy input of previous tracks of the same layer. Also, the specimens have time to cool during the application of the powder layer and the absolute energy input during the generation of the single tracks is low compared to scanning with the usual hatch distance of the specimen. The melt pool width and depth later described were measured from these single tracks.

In a pre-study a dense specimen was built. This specimen is shown in figure 1. This specimen was built using a scanning speed of 1400 mm/s and a laser power of 383 W. The specimen was analyzed for its melt pool width and melt pool depth, as

well as for its relative density. The specimen exhibits a relative density of 99.93 % and is treated as the reference for the described studies.

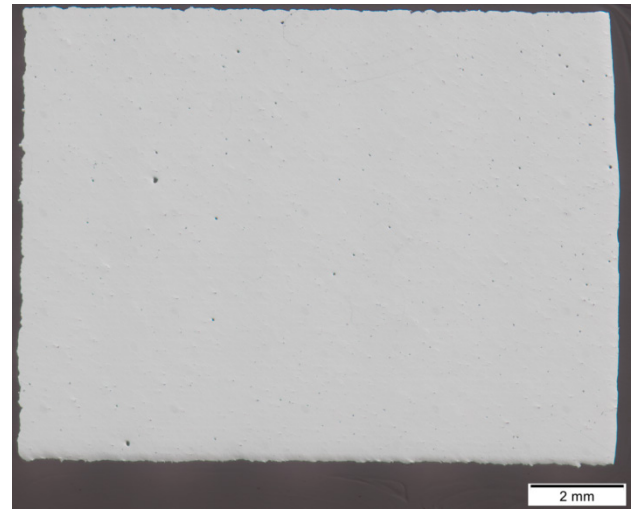


Fig. 1. Polished cross-section (scanning direction perpendicular to the plane of the cross-section, top layer at the left side of the specimen) of the reference specimen scanning directions was perpendicular to the 1400 mm/s, 383 W

3. Experimental procedure

The reference specimen was embedded and polished, such that the single tracks are perpendicular to the polished surface. The relative density, the melt pool width and the melt pool depth were analyzed by optical microscopy. The analysis was conducted, so the cross-section lies in the center of the specimen. Thereby, the influence of edge-induced effects is reduced, and the melt pool is expected to exhibit its steady-state geometry. The relative density was calculated by determining the area of porosity within the prepared surface. The width and depth of the single tracks on top of the specimen were measured after etching the specimen.

The hypothesis is that if the hatch distance and the layer height are kept constant for decreasing scanning speeds, using the same size of the melt pool as the reference specimen's size of the melt pool results in a dense specimen. This statement is derived from a purely geometric point of view and excludes considering effects like balling, cracks and defects resulting from splatters.

For this reason, an analytical model from Rubenchik et al. was chosen, which can estimate melt pool geometry depending on the process and material parameters [2]. As the model incorporates material parameters, it offers the possibility to be transferable to other materials when developing process parameters for a new alloy system, especially the necessary energy input to achieve distinct sizes of the melt pool.

To maintain analytical solvability, the model makes several assumptions and simplifications, e.g. not considering the powder layer, melt motion and evaporation. The model enables the calculation of the melt pool geometry depending on the two parameters ρ and B .

The parameter p is defined by

$$p = \frac{D}{ua}. \quad (1)$$

In this equation, D represents the thermal diffusivity, a the beam width and u the laser scanning speed. B is connected firmly to the normalized enthalpy introduced by Hann et al.

$$\frac{\Delta H}{h_s} = \frac{AP'2^{3/4}}{h_s\sqrt{\pi D}ua^3}, \quad (2)$$

where A represents the absorptivity, P' is the laser power, while the enthalpy at melting h_s is ρCT_m [5, 6]. The normalized enthalpy $\Delta H/h_s$ describes the energy input in multiples of the enthalpy at melting. The heat of fusion is not included. B is given by

$$B = \frac{\Delta H}{2^{3/4}\pi h_s}. \quad (3)$$

B can be thought of as a process parameter directly stating the corresponding temperature increase of the material; a value of $B = 2$ states that the peak temperature of the melt pool is two times the melting temperature of the material. The size of the melt pool is calculated by p and B using the chosen model. Later on, the results are described in normalized enthalpy to stay compatible with earlier publications based on normalized enthalpy [5, 6, 7, 8, 9]. For the calculation of the size of the melt pool, the interpolation functions presented by Rubenchik et al. are used [2]. The width of the melt pool is calculated by

$$w(B, p) = \frac{a}{Bp^3} \begin{bmatrix} 0.0021 - 0.047p + 0.34p^2 \\ -1.9p^3 - 0.33p^4 + B(0.00066 \\ -0.007p - 0.00059p^2 + 2.8p^3 \\ -0.12p^4) + B^2(-0.0007 + 0.15p \\ -0.12p^2 + 0.59p^3 - 0.023p^4) \\ + B^3(0.00001 - 0.00022p \\ + 0.002p^2 - 0.0085p^3 + 0.0014p^4) \end{bmatrix},$$

while the depth is calculated by

$$d(B, p) = \frac{a}{\sqrt{p}} \begin{bmatrix} 0.008 - 0.0048B - 0.047p - 0.099Bp \\ + (0.32 + 0.015B)p \ln p \\ + \ln B(0.0056 - 0.89p + 0.29p \ln p) \end{bmatrix}.$$

The selected model claims to be valid if the values of B are between 1 and 20 and the values of p are between 0.1 and 5. This range of validity regarding p and B is stated by the authors of the model to be representative of the PBF-LB/M process [2]. When the actual dimensions of the melt pool are calculated, the power P' in equation 2 includes the influence of the pre-heating of the building plate. This is described by equation 4 [2]:

$$P' = \frac{PT_m}{(T_m - T_0)} \quad (4)$$

The calculated power P' must be divided by 1.86 to receive the laser powers P as the melting temperature $T_m = 913 \text{ K}$ and the temperature of the building plate is $T_0 = 423 \text{ K}$. The respective laser powers P corrected for the influence of the pre-heating are shown in table 1.

From the reference specimen, a target melt pool width of $210 \mu\text{m}$ and a target melt pool depth of $140 \mu\text{m}$ were

determined for a hatch distance of $135 \mu\text{m}$. Besides testing the hypothesis for a hatch distance of $135 \mu\text{m}$ used for the reference specimen, the target size of the melt pool is scaled down proportionally for a hatch distance of $100 \mu\text{m}$. This was done by reducing melt pool width and afterwards calculating the corresponding depth with the selected analytical approach for the scanning speed of 1400 mm/s . A target width of $160 \mu\text{m}$ and a depth of $84 \mu\text{m}$ for a hatch distance of $100 \mu\text{m}$ were used. To examine the initial hypothesis, these melt pool geometries were to be realized for laser scanning speeds from 100 mm/s to 1200 mm/s in steps of 100 mm/s . For each scanning speed at both hatch distances, the necessary laser powers were calculated to match the respective target values of the melt pool dimension.

Table 1. Process parameters used in the respective sub-studies

u	ID100	IW100	ID135	IW135
100 mm/s	235 W	167 W	294 W	212 W
200 mm/s	177 W	155 W	237 W	205 W
300 mm/s	173 W	161 W	238 W	217 W
400 mm/s	178 W	169 W	250 W	232 W
500 mm/s	186 W	178 W	265 W	247 W
600 mm/s	194 W	187 W	282 W	262 W
700 mm/s	204 W	195 W	299 W	277 W
800 mm/s	213 W	203 W	317 W	292 W
900 mm/s	223 W	211 W	335 W	306 W
1000 mm/s	233 W	218 W	352 W	318 W
1100 mm/s	242 W	226 W	372 W	333 W
1200 mm/s	252 W	232 W	388 W	348 W

For the calculation of the laser power, the absorptivity was assumed to be 0.15 [9]. The enthalpy at melting temperature $h_s = 1.184 \text{ J/mm}^3$ and the thermal diffusivity $D = 57 \text{ mm}^2/\text{s}$ were derived from the commercial software JMatPro®. As the melt pool width and melt pool depth do not scale proportionally to each other for decreasing laser speed, there were two studies conducted for each hatch distance. The goal of the first two studies was to maintain the same melt pool depth (Iso-depth: ID100 and ID135) while the second pair of studies aims to keep the melt pool width constant (Iso-width: IW100 and IW135). The letter indicates whether depth or width was kept constant and the number indicates the hatch distance in μm . Table 1 lists the calculated laser powers for these sub-studies for the respective scanning speeds. The increasing power for low scanning speeds seems to be counterintuitive, as the power is expected to approach a plateau when scanning speed is decreasing. This will be considered in future studies, where the powers for low scanning speeds are substituted by values

approaching a plateau value for low scanning speeds. The increase in power could be explained by the fact that we are operating at the lower limit of the validity regime of the analytical model, as the values for p exceed 5.

4. Results and discussion

The resulting melt pool depths and widths from the nine single tracks per specimen were measured. Furthermore, the resulting specimen density was determined. Figure 2 shows the relative melt pool width w and Figure 3 shows the relative melt pool depths d for the four different sub-studies. The figures show the measured values divided by the calculated ones for both depth and width. Hence, Figures 2 and 3 represent the deviation of the measured from the calculated values. The red line signifies the target value. For the sub-studies with a hatch distance of 100 μm , the depth of the melt pool is in good agreement with the calculated depth, while the width is underestimated slightly.

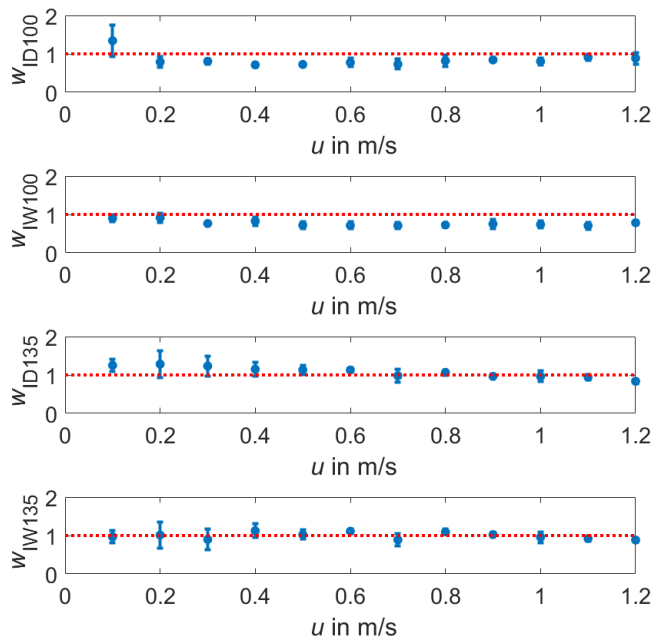


Fig. 2. Relative melt pool width over scanning speed

The situation is reversed for the studies conducted for the hatch distance of 135 μm . In this case, the measured width values are in good agreement with the calculated values, while the depth values are higher than expected. This trend indicates that the assumed absorptivity of 0.15 is too low for the studies conducted for the hatch distance of 135 μm . This is explained by the higher laser powers used in these studies as we have the same scanning speeds but want to achieve bigger melt pools. The higher laser power results in a higher vapor pressure above the melt pool and thereby in a deeper melt pool depression that can result in multiple reflections more easily and lead to a higher absorptivity. In general, the values are in good agreement with the target values considering the fact that the

power was predicted analytically for scanning speeds spanning over a factor of 12.

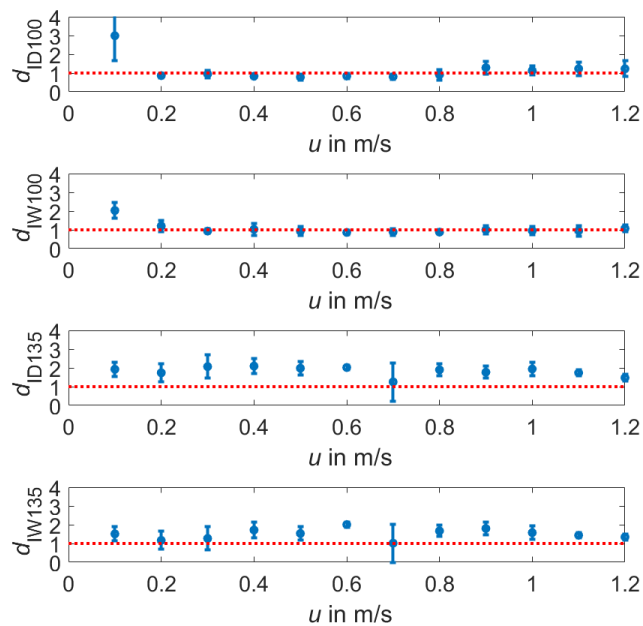


Fig. 3. Relative melt pool depth over scanning speed

Figure 4 shows the relative energy input per melted area in the transverse cross-section of a single track over scanning speed to examine the parameter B from the analytical model for its suitability as a tool of characterizing processing conditions.

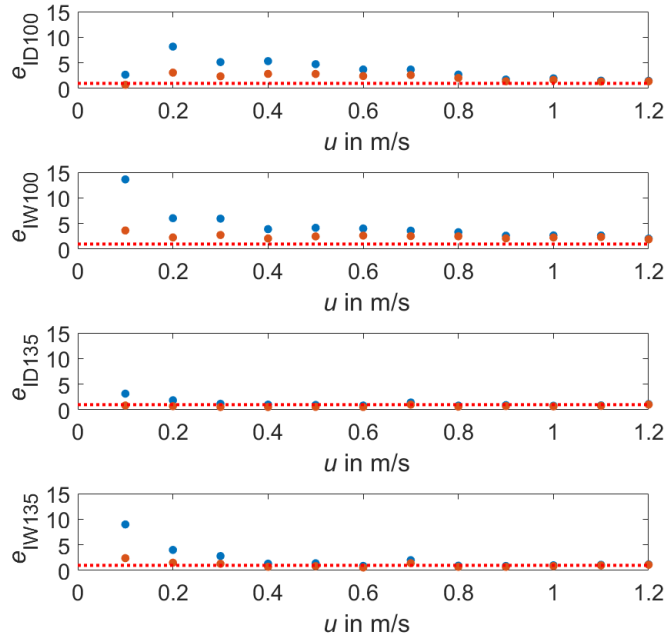


Fig. 4. Relative melting energy density over scanning speed (blue: line energy, red: B)

The line energy P/u and B of the reference specimen, as well as for the generated specimens, are calculated. Afterwards, these values are divided by the area of the transverse section of the single tracks of each specimen. The area of the transverse section is approximated to be the area of a semi-ellipse with half the melt pool width and the melt pool depth as radii for the

calculation. This calculation of energy, respectively B per melted area of the single tracks, was done for all sets of parameters. Afterwards, the results of the experimental study were divided by the values of the reference specimen, receiving a factor called relative melting energy density e . Therefore, a value of $e = 2$ means that twice the energy is necessary for melting the same area of metal when compared with the reference specimen. The calculated value represents the relative melting energy density. It can be stated that B is a significantly better descriptor than line energy in regards to the melted area of a melt track, especially for low scanning speeds. The normalized enthalpy (respectively B), as defined by equation 2, also incorporates the thermal diffusivity and heat capacity. The line energy only states how much energy is applied as none of the parameters that scale the heat release from the energy input region are included. From this point of view, it is advised to use B instead of line energy for describing process parameters for materials with high thermal conductivity. For materials with low thermal diffusivity, the impact should be less significant, but still noticeable.

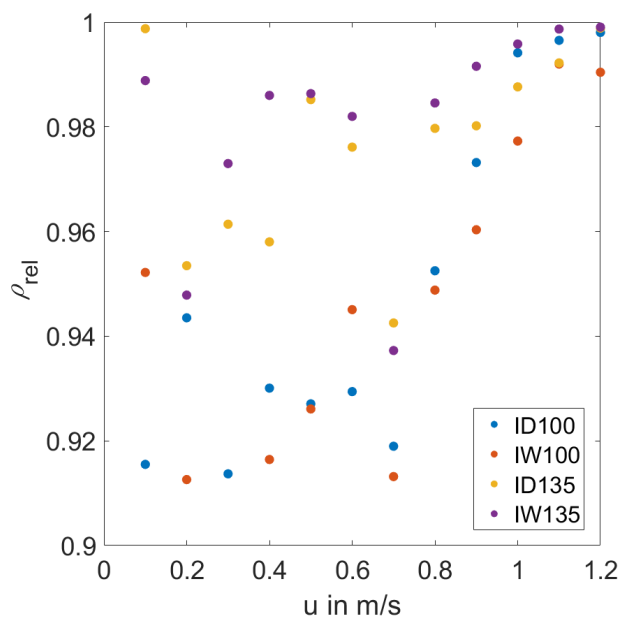


Fig. 5. Relative density over laser scanning speed

After looking at the influence of energy input on melt track size, the influence of the energy input on part density is investigated. Therefore, in figure 5 the relative specimen density depending on laser scanning speed is shown. The values for relative density are decreasing for all sub-studies, but the relative densities for the studies conducted with a hatch distance of 100 μm are experiencing a more pronounced decline with decreasing scanning speed than the studies conducted at 135 μm . This could be explained by a differing heat accumulation occurring at a hatch distance of 100 μm , when compared with a hatch distance of 135 μm . Therefore, the relative volume energy density and its influence on specimen density is examined. Figure 6 depicts the relative density ρ_{rel} of the specimens over the relative volume energy density. The volume energy density is calculated by $P/(hut)$.

The hatch distance is denoted by h , the layer height by t . For decreasing scanning speeds, the relative volume energy density is increasing in figure 6.

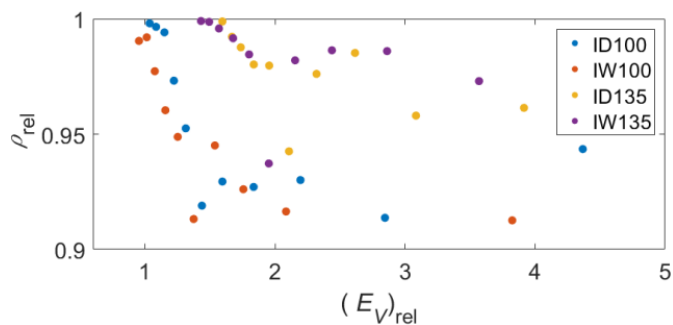


Fig. 6. Relative density over relative volume energy density

On the one hand, figure 6 seems to indicate that we operate at the upper limit of the process window, as only the lowest values of relative volume energy density deliver specimens with high relative densities. This seems especially the case for the studies conducted at 100 μm hatch distance, as they decrease more sharply with increasing relative volume energy densities, which would point to higher heat accumulation in the 100 μm specimens. On the other hand, the size of the melt pool for the 100 μm hatch distance studies is overestimated, while the size of the melt pool for the 135 μm is underestimated in figure 2 and figure 3 by the used analytical model. Therefore, we should expect that the studies conducted with a hatch distance of 135 μm should be more susceptible to the porosity resulting from excessive heat accumulation in the specimen, as we already stated that the absorptivity is underestimated for these studies. It also has to be accounted for the longer time necessary to finish one layer. The powers used for the 100 μm studies are overall lower than the power used for the 135 μm studies, but this effect is mostly compensated for by the additional number of scanned tracks. One way of resolving this issue is by acknowledging the fact that for higher scanning speeds, the thermal diffusion length during the laser dwell time is small, so the heat is localized during the dwell time of the laser. This is not the case for low scanning speeds where the conducted heat away from the laser-material interaction zone becomes more dominant and the heat thereby becomes delocalized. This could explain the steeper decrease in relative density when the heat becomes delocalized during the laser dwell time.

In figure 7, the relative melt pool width and depth are normalized by their respective target value. The influence of the relative melt pool dimensions on specimen density is examined in figure 7. When looking at the influence of melt pool depth and melt pool width on part density, the parameters resulting in the predefined target size of the melt pool for both hatch distances delivers the highest densities. When comparing both, the melt pool depth seems to be the better indicator for dense specimens because, for the melt pool width, there are specimens that result in the target width while showing low relative

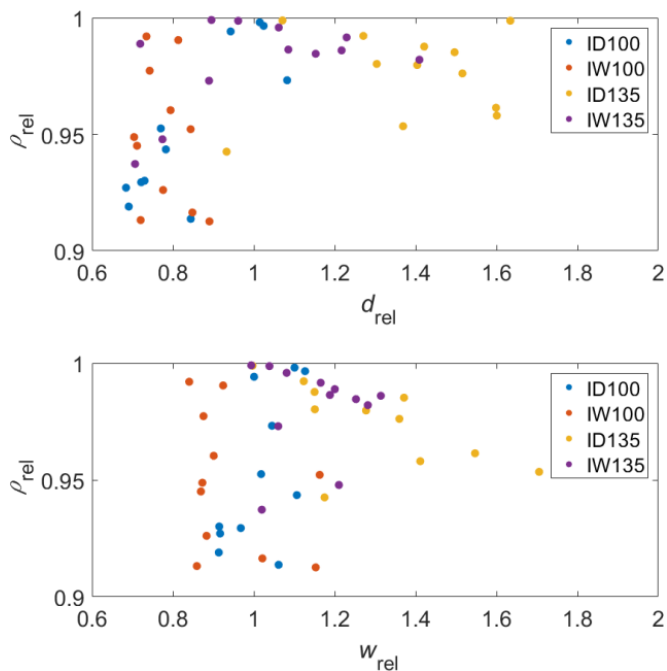


Fig. 7. Relative density over relative melt pool depth and width

densities. This, however, does not occur when looking at the melt pool depth. This seems plausible, as it is known that building dense specimens with PBF-LB/M is – beside other mechanisms – depending on controlling melt pool depth [9]. It is noteworthy that there are many melt pool depths and widths below the target value, while the porosity is increasing with relative volume energy density. The context of this has already discussed for figure 6. There we argued for a too low heat accumulation for the 100 μm studies, which results in a high porosity. This nevertheless has to be proven with additional examinations as another explanation could also be too high heat accumulation, which results in material ejection from the melt pool and the powder layer, resulting in smaller melt pools than expected, while showing low relative densities.

5. Conclusion

The initial examination of the stated hypothesis – achieving distinct melt pool geometry regarding width and depth for a defined hatch distance and layer thickness should result in dense specimens – seems promising. Nevertheless, this relation has to be examined more closely in the future as the role of the heat accumulations has to be estimated to receive specimens with higher densities through this strategy

For low laser scanning speeds, the analytical approach shows increasing laser powers when reducing laser scanning speed, which seems to be physically unjustified. This has to be taken into account when adapting the process parameters.

The sub-studies with a hatch distance of 135 μm show better results and are less susceptible to process defects.

Controlling melt pool depth is significantly more critical than controlling the melt pool width in order to obtain dense specimens.

The parameter B , respectively the normalized enthalpy, is a much better descriptor of the melted volume of a single track than line energy is, especially for materials with high thermal diffusivity and at low scanning speeds.

Acknowledgements

The authors gratefully acknowledge the funding by the German Research Foundation (DFG) within the priority program (SPP) 2122 “Materials for Additive Manufacturing (MATframe)”. The authors gratefully acknowledge funding of the Erlangen Graduate School in Advanced Optical Technologies (SAOT) by the German Research Foundation (DFG) in the framework of the German excellence initiative.

Furthermore, we want to acknowledge Florian Huber and Michael Rasch for their support.

References

- [1] Plotkowski A, Rios O, Sridharan N, Sims Z, Unocic K, Ott RT, Dehoff RR, Babu SS. Evaluation of an Al-Ce alloy for laser additive manufacturing, *Acta Materialia* 2017;126:507–519
- [2] Rubenchik AM, King WE, Wu SS. Scaling laws for the additive manufacturing, *Journal of Materials Processing Tech.* 2018;257:234-243
- [3] Farag MM, Latif MH. An Analysis of the Mechanical Behavior of Al-Ai₃Ni Composites, *Metallurgical Transactions A*, 1975;6A:1354
- [4] Rappaz M, Drezet, Gremaud M. A new hot-tearing criterion, *Metall and Mat Trans A* 1999;30:449–455
- [5] Hann DB, Iammi J, Folkes J. A simple methodology for predicting laser-weld properties from material and laser parameters. *Journal of Physics D-Applied Physics* 2011; 44, 445401
- [6] Hann DB, Iammi J, Folkes J. Keyholing or Conduction? Prediction of Laser Penetration Depth. *Laser Eng* 2012;22:309–317
- [7] Trapp J, Rubenchik AM, Guss G, Matthews MJ, In situ absorptivity measurements of metallic powders during laser powder-bed fusion additive manufacturing, *App. Materials Today* 2017;9:341-349
- [8] Fabbro R. Scaling laws for the laser welding process in keyhole mode, *Journal of Materials Processing Tech.* 2019;264:346-351
- [9] King WE, Barth HD, Castillo VM, Gallegos GF, Gibbs JW, Hahn DE, Kamath C, Rubenchik AM. Observation of keyhole-mode laser melting in laser powder-bed fusion additive manufacturing, *Journal of Materials Processing Tech.* 2014;214:2915-2925

11th CIRP Conference on Photonic Technologies [LANE 2020] on September 7-10, 2020

Eutectic solidification in Al-Ni for L-PBF conditions: a phase-field simulation study

M. Apel^{a,*}, G. Boussinot^a, M. Döring^{b,c}, M. Schmidt^b

^aAccess e.V., Intzestr. 5, Aachen, 52072, Germany

^bInstitute of Photonic Technologies (LPT), Friedrich-Alexander Universität Erlangen-Nürnberg, Konrad-Zuse-Str. 3-5, 91052 Erlangen, Germany

^cErlangen Graduate School in Advanced Optical Technologies (SAOT), Paul-Gordan-Str.6, 91052 Erlangen, Germany

* Corresponding author. Tel.: +49-2418098009. E-mail address: m.apel@access-technology.de

Abstract

Two-phase solidification microstructures of regular binary eutectic alloys are composed of lamellar or rod-like pattern. The corresponding characteristic length scale λ is the spacing between lamellae or rods and results from an interplay between lateral diffusion and capillary, i.e. interfacial curvature. The basic theory had been developed by Jackson and Hunt (JH) in the 1960's and has been proven successfully for "slow" solidification. It leads to a scaling relation $v \cdot \lambda^2 = \text{const.}$ with v the growth velocity. In this work, we investigated eutectic solidification in Al-Ni for the faster growth rates in L-PBF processing by means of phase-field simulations. The consequences of the fast solidification on the deviation from the JH-scaling and the appearance of new features in the growth pattern are shown. Simulation results are confronted with microstructures seen in L-PBF build samples. Eventually, we discuss the opportunity to derive the local solidification speed from microstructure analysis.

© 2020 The Authors. Published by Elsevier B.V.

This is an open access article under the CC BY-NC-ND license (<http://creativecommons.org/licenses/by-nc-nd/4.0/>)

Peer-review under responsibility of the Bayerisches Laserzentrum GmbH

Keywords: eutectic solidification; phase field simulations; L-PBF additive process; strongly out-of-equilibrium conditions

1. Introduction

Additive manufacturing (AM) of metallic alloys is currently receiving great attention due to its promises for the 3D-printing of components presenting complex geometries. In particular, laser-based AM takes advantage of the modern developments of laser technologies, allowing for a sub-millimeter precision and building rates that may be suitable for industrial production.

The melting and solidification of the deposited material then takes place on time scales that are several orders of magnitude smaller than for conventional manufacturing such as casting or welding. Indeed, finite element calculations on the scale of the melt pool, i.e. the material that is locally melted owing to the energy of the laser, suggest cooling rates

possibly reaching a million Kelvin per second with thermal gradients as large as hundred thousand Kelvin per cm [1]. Depending on the melt pool geometry and in particular on whether a keyhole develops when the evaporation temperature is reached, solidification velocities are typically in a range between 10^{-1} cm/s and 10^2 cm/s. These high solidification rates challenge the commonly accepted theories about the solidification microstructure evolution, which plays an important role for defect formation and eventually for the mechanical properties of the as build material.

In a recent study [2], dendritic growth under "conventional" slow solidification conditions has been compared to dendritic growth under conditions typical for L-PBF. Slow solidification corresponds to a weakly out-of-equilibrium (WOE) regime leading to columnar dendrites with

pronounced side arm branches, being spatially arranged in a rather ordered network. Solidification at velocities between 1 cm/s and 10 cm/s corresponds to a strongly out-of-equilibrium (SOE) regime leading to disordered networks of unbranched columnar dendrites. These qualitative differences between the WOE and SOE regimes pertain to the relations between the different length scales characterizing the microstructure, i.e. dendrite tip radius, diffusion length and dendrite spacing. While in the WOE regime, the tip radius is much smaller than the two other length scales, the three length scales are of the same order in the SOE regime, inhibiting the development of side arms and the phase diffusion process responsible for the ordering of the dendritic network.

In this work, we are interested in AM for eutectic alloys, especially Al-Ni. In eutectics, solidification at small velocities usually takes place through the coupled growth of two solid phases, which are thermodynamically stable below the eutectic temperature. The corresponding microstructure consists in a lamellar structure or fibers of one of the solid phases embedded in a matrix of the other one. The creation of ultrafine eutectic microstructures by AM processes is of general interest in view of the potential improvement of mechanical material properties due to the small length microstructure scales. In this respect, we simulate the solidification of binary Al-Ni alloys under L-PBF conditions using the phase field method. Phase field methods are the tools of choice when one aims at describing the microstructure evolution at the scale of the solid/liquid interface [3]. We use the software MICRESS that has already demonstrated its capabilities in describing eutectic-like structures at higher undercooling (see for example [4]).

The paper is organized as follows. We first present the Al-Ni phase diagram and the phenomenology of eutectic solidification. Second, we present results of phase field simulations at a growth velocity $V = 1$ cm/s. Then, we compare our simulations results with slow solidification simulations in order to estimate the validity of existing theories. Finally, we compare simulation results with real microstructures from samples build by Laser Powder Bed Fusion.

2. Al-Ni phase diagram and weakly out-of-equilibrium eutectic solidification

Fig.1 shows the Temperature-Concentration phase diagram of Al-Ni calculated by ThermoCalc using the TCAL4 database. The eutectic point is at $T_E = 920$ K and $C_E = 6$ wt% Ni. The eutectic temperature corresponds to a temperature at which a three-phase equilibrium exists between the liquid, the solid fcc α -Al phase (with a very small Ni solubility) and the solid orthorhombic β -Al₃Ni phase (at 42 wt% Ni). As mentioned in the introduction, when the liquid at eutectic composition is cooled down in a temperature gradient at a slow rate, a coupled growth occurs, producing lamellae or fibers of α and β phases and an almost flat solidification front. The characteristic length scale λ associated with this microstructure is the inter-lamellae or inter-fibers distance. It is the scale on which the exchange of solute atoms actually takes place, and is much smaller than the so-called diffusion

length $l = D/V$ where D is the diffusion coefficient in the liquid phase, and V is the growth velocity of the solidification front.

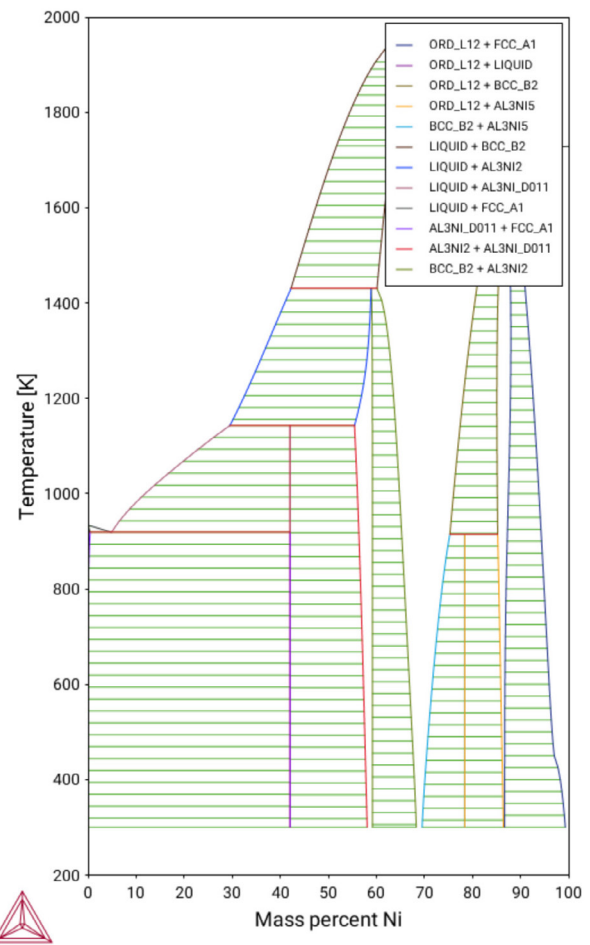


Fig. 1. Al-Ni phase diagram calculated using the TCAL4 ThermoCalc database.

The relations between λ , l and the front temperature T_0 , smaller than T_E , has been theoretically analyzed by Jackson and Hunt (JH) in their seminal paper [5]. For a given λ , they consider a periodic steady-state and find l and T_0 such that a balance exists between the contributions to the diffusion flux provided by capillary effects, parametrized by the capillary length d (comparable to the atomic distance), and the difference in liquid-solid equilibrium composition whether considering the liquid- α or liquid- β equilibria. It has been shown that only a certain interval $\delta\lambda$ around the periodicity, called λ_0 , leading to the largest T_0 , yields stable steady-state solutions (note that this selection of periodicity is soft in the sense that $\delta\lambda/\lambda_0 \sim 1$). Without giving details, one should note that:

$$\Delta = (T_E - T_0)/\Delta T \sim d/\lambda_0 \sim \sqrt{d/l}$$

where ΔT is the characteristic temperature interval, linked to liquidus slopes and the concentration interval on the eutectic plateau, here around 40 wt%. In slow solidification conditions, the undercooling verifies $\Delta \ll 1$, yielding a separation of length scales $d \ll \lambda \ll l$. The coupled growth described by the JH theory may also take place in a certain interval of nominal concentrations around C_E called the

‘coupled zone’, although in this case, an additional long range diffusion field on the scale of l playing a minor role in the determination of the pattern, i.e. in the relations between Δ , λ and l . Beyond the boundaries of the coupled zone, a single-phase growth can be observed forming dendrites of the solid phase that presents the higher liquidus temperature, i.e. α for nominal compositions that are smaller than C_E (hypo-eutectic compositions) and β for nominal compositions that are larger (hyper-eutectic compositions).

3. Strongly out-of-equilibrium solidification: phase field simulations

When the cooling rate reaches values such that Δ becomes of order unity, the phenomenology corresponding to the JH theory does not hold anymore, especially because the Péclet number $P = \lambda/l$ becomes also of order unity. Then, deviations from equilibrium at the interfaces or changes in the boundaries of the coupled zone occur [6].

As mentioned in the introduction, we have made phase field simulations at a prescribed growth velocity $V=1\text{cm/s}$. In order to reproduce thermal conditions typical for L-PBF experiments, a thermal gradient $G = 10^5\text{K/cm}$ (yielding a cooling rate $\dot{T} = GV = 10^5\text{K/s}$) is superimposed on the simulation domain (the so called “frozen temperature approximation”). The phase field model is linked to the thermodynamic database for the computation of the driving forces and the element partitioning at the interfaces, which also provides the temperature dependent liquidus slopes [7]. In Fig. 2, the solidification front for a simulation with a nominal alloy composition Al-10.2 wt%Ni is shown.

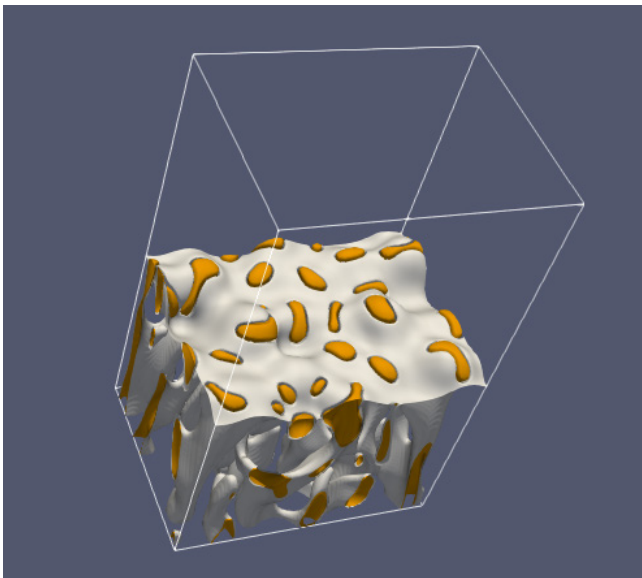


Fig. 2. Coupled eutectic growth at $V = 1\text{ cm/s}$ and $G = 10^5\text{ K/cm}$. The Al₃Ni phase is drawn in orange, fcc-Al in grey.

The result corresponds to a coupled growth structure. Perpendicularly to the growth direction, the box dimensions are $L_x \times L_y = 0.288\ \mu\text{m} \times 0.4\ \mu\text{m}$. A moving frame algorithm allows following the solidification along much larger distances along the growth direction. Orange and white colors represent the β -liquid and α -liquid interfaces, respectively.

In order to apprehend the qualitative differences between the microstructures inherited from the SOE and the WOE regimes, we represent in Fig. 3 also the growth front in the WOE regime. In the WOE regime, the shape and size of the β -fibres are much more regular in comparison to the SOE regime. Moreover, the solid/liquid front is significantly more flat in the case of WOE compared to SOE. These effects are due to the qualitative change of Δ from the WOE to the SOE regime ($\Delta \ll 1$ in the WOE regime and $\Delta \sim 1$ in the SOE regime) and are related to the inhibition of the so-called phase diffusion process in the SOE (see [2]) and to the emergence of a flat front single-phase solution, here α .

Let us now confront these observations with the JH theory. We first note that, although our nominal composition (10.2 wt%Ni) deviates from the eutectic one (6 wt%Ni), this may not alter significantly the relations between undercooling, spacing and diffusion length, since the eutectic plateau corresponds to a much wider concentration interval (around 40 wt% Ni). The front undercooling of about 40K is about two times the difference between T_E and the melting temperature of pure Al (verifying indeed a regime $\Delta \sim 1$). In order to quantify the inter- β distance in the simulation, we measure the number N of β domains and define $\lambda = \sqrt{N/(L_x L_y)}$ for which we find a value close to 80 nm. Within the JH theory, a velocity $V = 1\text{ cm/s}$ provides an undercooling about 7 times smaller and a spacing about 2 times smaller than found in the simulation. Conversely, if one uses the undercooling found in the simulation to derive the growth velocity and the spacing, one finds a velocity 50 times larger than in our simulation and a spacing 7 times smaller. If instead we use the spacing λ resulting from the simulation, we find a velocity 4 times smaller than the one that is prescribed and we find an undercooling 2 times smaller than the one we obtain.

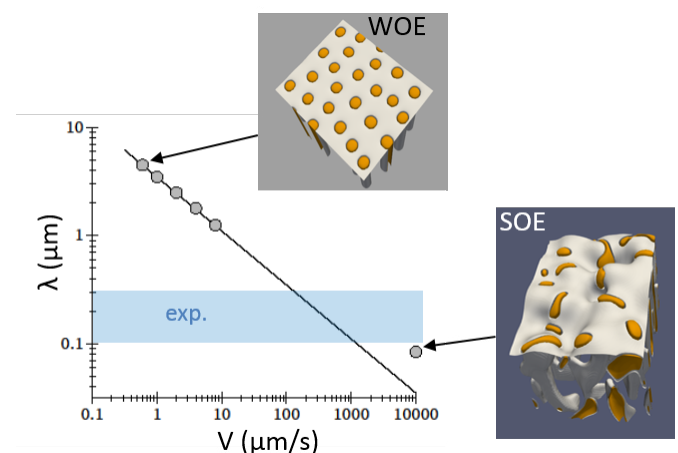


Fig. 3. Plot of the simulated spacing λ as a function of the growth velocity V with corresponding microstructure (box dimensions: $L_x = 18.5\ \mu\text{m}$, $L_y = 24.5\ \mu\text{m}$ for WOE, $L_x = 0.288\ \mu\text{m}$, $L_y = 0.4\ \mu\text{m}$ for SOE). Circles: phase field simulations. Line: scaling corresponding to the JH theory (see text); blue color: interval corresponding to the L-PBF experiment in Fig. 4.

Thus, we see that a substantial deviation from the JH theory occurs. In order to illustrate the deviation, in Fig. 3 the spacing obtained from a simulation at $V = 1\text{ cm/s}$ is plotted together with results for different velocities in the WOE regime. While

in the WOE regime the spacing follows the JH scaling, i.e. $\lambda \propto V^{-1/2}$, the result for the SOE regime deviates significantly from the extrapolation made using the data in the WOE regime (that corresponds quite faithfully to the JH theory). The deviation from the JH theory in the SOE regime is of course related, as mentioned above, to the breakdown of its assumptions, i.e. $\Delta \sim 1$, but also the steadiness and flatness of the growth front (in our simulation the waviness of the growth front is accompanied by a perpetual motion of the β -domains perpendicularly to the growth direction).

4. L-PBF experiment vs. Jackson-Hunt theory

We now present results from an L-PBF build sample. The SEM image in Fig. 4 shows the microstructure for a transversal section (perpendicular to the build direction) of a sample additively built at a laser scanning speed of 50 cm/s.

The dark regions correspond to Ni-poor material and the bright regions correspond to Ni-rich one. We observe a rather irregular structure that does not resemble a dendritic one (in other samples one may find dendritic-like structures). One may interpret dark regions as α and bright regions as β (thereby neglecting the possible formation of a metastable phase such as Al₉Ni₂). The irregularity of this eutectic-like microstructure is rather in line with our simulations. The typical distance between bright regions falls into an interval between 100 nm and 300 nm. Hence our simulated inter- β distance around 80 nm is close to the lower bound of this interval, which supports not only the thermal conditions that are used but also the phase field model itself, owing to the deviation from equilibrium at the interfaces in the SOE regime.

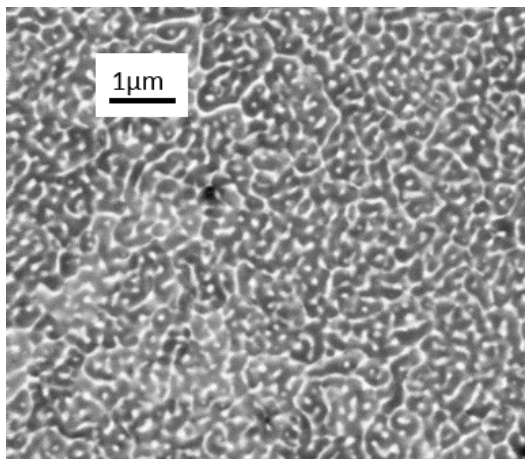


Fig. 4. SEM image of a transversal section in a L-PBF processed Al_{6.2}wt%Ni_{0.5}wt%Si alloy at laser scanning velocity 500mm/s.

In Fig. 3, we have highlighted this interval in blue color in order to confront this experimental result also with the JH theory. We see that, in the frame of the JH theory, this interval of spacing corresponds to growth velocities in the interval 0.01-0.1 cm/s. In comparison with the laser scanning velocity (50 cm/s), such a growth velocity is extremely small and would probably only correspond to solidification speeds that one finds at the interlayer boundaries between additive layers, where the cooling rate almost vanishes. In the bulk of the

layers, no reason exists for having several orders of magnitude differences between scanning and growth velocities.

Thus, we can conclude that, also in experiments a significant deviation from the predictions given by the JH theory is observed. The deviations caused by the departure from the WOE regime ($\Delta \ll 1$, equilibrium at the interfaces) should be necessarily taken into account when the eutectic microstructure is related to the thermal conditions, and especially the growth velocity. A straightforward derivation of the growth velocity from spacing measurements according to the JH-model leads to significantly wrong results.

5. Conclusion

We have performed phase field simulations of the solidification of an eutectic Al-Ni alloy under conditions that are typical for L-PBF experiments, i.e. with a prescribed growth velocity $V = 1 \text{ cm/s}$. We obtain α - β coupled eutectic growth and we find a significant deviation from the Jackson-Hunt theory. In particular, the simulation leads to a solidification front undercooling 7 times larger and a spacing 2 times larger than predicted by the theory. When analyzing a L-PBF processed Al-Ni alloy, we also find that the JH theory is not adequate for describing its microstructure. These deviations pertain to the different mechanisms operating in the strongly out-of-equilibrium (SOE) regime, inherent for the thermal conditions in L-PBF experiments, compared to the weakly out-of-equilibrium (WOE) regime, within which the JH theory is developed. In particular, the diffusion length is in the order of the spacing in the SOE regime, while it is much larger in the WOE regime. More investigations are needed to understand the qualitative differences between eutectic solidification in the SOE and in the WOE regimes. Especially, in view of our first simulations, the limits of the coupled zone should be determined with respect to the emergence of the flat front solution for the solidification of α phase.

Acknowledgements

We acknowledge the financial support provided by the Deutsche Forschungsgemeinschaft (DFG) in the framework of the Priority Program SPP2122.

References

- [1] Keller T, Lindwall G, Ghosh S, Ma L, Lane BM, Zhang F, Kattner UR, Lass EA, Heigel JC, Idell Y, Williams ME, Allen AJ, Guyer JE, Levine LE. Application of finite element, phase-field and CALPHAD-based methods to additive manufacturing of Ni-based alloys. *Acta Mater* 2017;139:244.
- [2] Boussinot G, Apel M, Zielinski J, Hecht U, Schleifenbaum JH. Strongly Out-of-Equilibrium Columnar Solidification During Laser Powder-Bed Fusion in Additive Manufacturing. *Phys Rev Applied* 2019; 11:014025.
- [3] Provatas N, Elder K. *Phase-Field Methods in Materials Science and Engineering*. Wiley-VCH Verlag GmbH & Co. KGaA: 2010.
- [4] Nakajima K, Apel M, Steinbach I. The role of carbon diffusion in ferrite on the kinetics of cooperative growth of pearlite: A multi-phase field study. *Acta Mater* 2006; 54:3665.
- [5] Jackson KA, Hunt JD, *Trans Soc Min Eng AIME* 1966; 236:1129.
- [6] Kurz W, Trivedi R, Eutectic growth under rapid solidification conditions. *Metall Trans A* 1991; 22A:3051.

- [7] Eiken J, Böttger B, Steinbach I. Multiphase field approach for multicomponent alloys with extrapolation scheme for numerical application. *Phys Rev E* (2006); 73:066122.

11th CIRP Conference on Photonic Technologies [LANE 2020] on September 7-10, 2020

Additive manufacturing of binary Al-Li alloys

Burak Yürekli^{a,*}, Lisa Schade^a, Tobias Ullsperger^a, Brian Seyfarth^a, Hagen Kohl^a,

Gabor Matthäus^a, Dongmei Liu^b, Markus Rettenmayr^b, Stefan Nolte^{a,c}

^a*Institute of Applied Physics, Friedrich-Schiller-Universität Jena, Albert-Einstein-Straße 15, 07745 Jena, Germany*

^b*Otto Schott Institute of Materials Research, Friedrich-Schiller-Universität Jena, Löbdergraben 32, 07743 Jena, Germany*

^c*Fraunhofer Institute for Applied Optics and Precision Engineering, Albert-Einstein-Straße 7, 07745 Jena, Germany*

* Corresponding author. Tel.: +49 364 194 7825; fax: +49 364 194 7802. E-mail address: burak.yurekli@uni-jena.de

Abstract

Laser assisted additive manufacturing using binary Al-Li with increased Li content is presented. Al-Li alloys show high potential for future lightweight constructions due to increased stiffness at decreased mass. In particular, the elastic modulus significantly increases with increasing Li content. However, up to now, precipitation of the δ -AlLi limits the Li fraction to approximately 2 wt. %. In our approach, ultrashort laser pulses are used for powder fusion yielding increased cooling rates. As a result 3D printed parts of binary Al-Li with a Li content of 4 wt. % can be successfully demonstrated for the first time.

© 2020 The Authors. Published by Elsevier B.V.

This is an open access article under the CC BY-NC-ND license (<http://creativecommons.org/licenses/by-nc-nd/4.0/>)

Peer-review under responsibility of the Bayerisches Laserzentrum GmbH

Keywords: Additive Manufacturing; Laser Powder Bed Fusion; Selective Laser Melting; Ultrashort Laser Pulses; Al-Li Alloys

1. Introduction

During the last two decades additive manufacturing (AM) evolved from a process used exclusively for rapid prototyping to an established fabrication method in industry worldwide [1,2]. Laser based powder bed fusion (LPBF) is one of the best-known representatives regarding the fabrication of sophisticated metal parts [3-5]. Nevertheless, considering available materials for metal AM, still a comparatively limited range of traditional alloys exists.

Recently, ultrashort laser pulses were investigated as an alternative heating source for LPBF [6-8]. Ultrashort laser pulses are well-known for their advantages in subtractive manufacturing like cutting and drilling, often termed “cold ablation”. This term refers to the feature of ultrashort interaction between matter and radiation with minimal thermal effects. Using ultrashort laser pulses at fluences well above the ablation threshold, the irradiated material can be

vaporized without transferring significant heat to the surrounding area.

However, ultrashort pulse lasers can also be used for confined heating. In this case, the applied fluence must be chosen below the ablation threshold yielding a transformation of the absorbed energy into heat. Moreover, the heat distribution can be easily controlled via adapted pulse repetition rates and the heat accumulation effect, respectively [9]. This feature together with extremely high peak power allows the additive manufacturing of special materials like tungsten, glass, hypereutectic alloys or copper [6-8].

Some of the most popular AM materials today, are aluminium alloys such as Al6061, Al7005 or Al7020. Recently, newer alloys based on Al-Si with different fractions of silicon were used during LPBF due to their

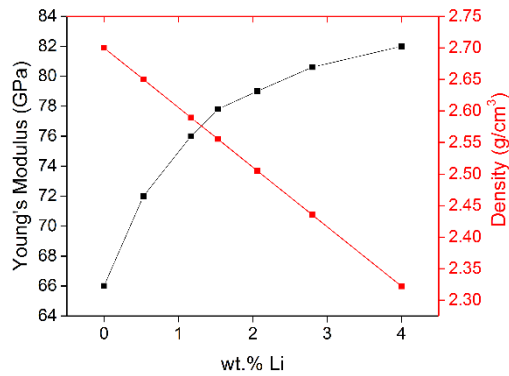


Fig. 1 Relation between the density, Young's modulus and Li content in binary Al-Li alloys [10].

excellent compatibility with Ni-P coatings [7].

A new candidate for lightweight constructions is Al-Li. This material exhibits a significant increase of the elastic modulus accompanied with a decrease in density with increasing Li fraction, as depicted in Fig. 1 up to 4 wt. % [10]. So far, the Li content in commercially available Al-Li alloys is limited to approximately 2 wt. % due to the precipitation of brittle δ -AlLi phase during conventional casting processes [11], resulting in deteriorated mechanical properties. In order to avoid pronounced precipitation, a significantly increased cooling rate is one of the key elements during processing.

With the help of ultrashort pulses the cooling rate within the melt pool can be significantly increased due to the reduced interaction time between matter and radiation. This effect was already demonstrated on hypereutectic Al-Si [12]. As a consequence, the application of ultrashort pulse lasers shows the potential to allow single phase Al-Li alloys of higher Li content even beyond the maximal Li solubility. In addition, ultrashort pulses are suitable for precise control of the melt pool temperature, which is a critical parameter to avoid excessive evaporation of Li during laser fusion.

In this paper, we present the additive manufacturing of binary Al-Li for the first time to the best of our knowledge. The process is based on the laser powder bed fusion (LBPF) method. In particular, ultrashort laser pulses were applied for selective laser melting of the primary material. This approach allows the fabrication of Al-Li parts with a significantly increased Li content (4 wt. %).

2. Experimental Method

Due to the high reactivity of Li, Al-Li with an increased Li content is not commercially available. Hence, the investigated material was produced in-house. Therefore, melting and casting of Al-Li 4 wt. % alloy from high-purity Al and Li (99.99%) was carried out in a glove box under protective argon atmosphere. A steel crucible lined with graphite foil was used for melting in order to prevent reaction between the melt and the crucible and the contamination of the Al-Li ingots, respectively. The as-cast structure of Al-Li 4 wt. % alloy consists of primary bright α -Al phase and dark δ -AlLi phase at the grain boundaries as seen in Fig. 2.

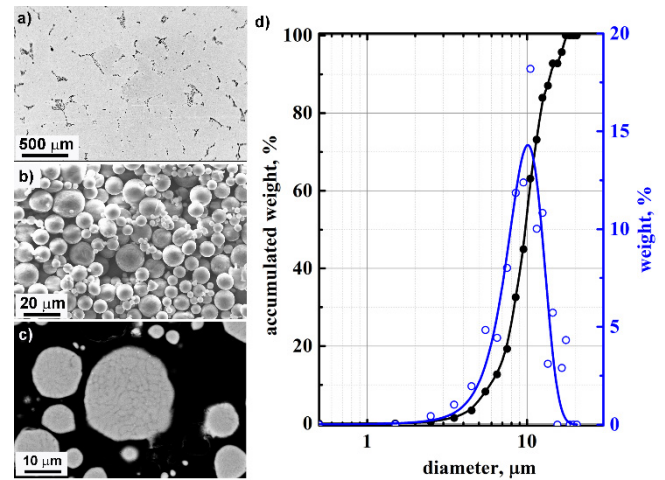


Fig. 2 (a) SEM (BSE) image of the microstructure of as-cast Al-Li 4wt. % ingot, (b) powder of Al-Li 4 wt. % alloy from gas atomization, and (c) cross section of the powder. (d) Grain size distribution of Al-Li 4 wt. % powder used in experiments.

Afterwards, gas atomization was applied by NANOVAL (Germany) to produce Al-Li 4 wt. % powder. The size distribution of the powder was analyzed using a scanning electron microscope (SEM) which was equipped with a back-scattered electron (BSE) detector.

For analyzing the microstructure, the powder was mounted in resin and grounded using a series of SiC papers up to a grit size of 1200. After polishing with 3 μ m and 1 μ m Al₂O₃ powder and finally polishing with 50 nm colloidal silica, the microstructure was characterized by SEM (BSE). The results as well as the grain size distribution within the powder can be seen in Fig. 2. The powder exhibits a particle diameter distribution between 1 μ m and 20 μ m, with a mean value of 13.3 μ m.

For the additive manufacturing process a typical setup for LBPF was used (see Fig. 3). It was based on a femtosecond fiber laser (Active Fiber Systems) as irradiation source. The laser delivers ultrashort pulses (USP) of a minimum pulse duration of 500 fs at a central wavelength of 1030 nm and maximum average power of 30 W. By employing an acousto-optic modulator (AOM) during the experiments, repetition rates of 10 MHz and 20 MHz were applied. For

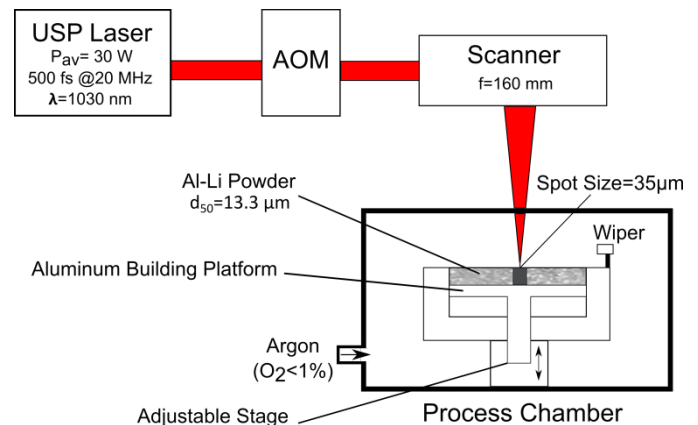


Fig. 3 Schematic of the experimental setup for LBPF.

irradiation an optical scanner (SCANLAB, intelliSCAN III 14) was used together with an f-theta objective. The corresponding focusing length was 160 mm yielding a focal diameter of $35 \mu\text{m}$ ($1/e^2$).

In order to avoid oxidation, the process chamber was sealed and flooded with argon. During LBPF the measured oxygen concentration was below 1 %.

Cubic samples with edge length in the range of a few millimeters were additively manufactured for different process parameter. Within this feasibility study the focus was on laser power of 30 W, repetition rate of 10 MHz and 20 MHz, scanning speed from 0.1 m/s to 0.7 m/s, hatch distance from $30 \mu\text{m}$ to $60 \mu\text{m}$ and layer thickness from $20 \mu\text{m}$ to $40 \mu\text{m}$.

After fabrication, the surfaces of the generated samples were analyzed by optical microscopy to evaluate the laser process parameters with respect to the achieved melt characteristics. For a deeper insight into the microstructure, the samples were prepared metallographically and then analyzed by SEM. In addition, the Brinell hardness of the as-cast ingot and additively manufactured parts was characterized using a ball size of 2.5 mm and a maximal load of 196 N.

3. Results

At first, a parameter study was performed in order to generate robust samples. During our investigations the pulse length was kept constant at 500 fs. Fig. 4 shows different surface morphologies obtained at different pulse energies and scanning speeds while keeping the average laser power at 30 W. The other parameters were repetition rate = 20 MHz, hatching distance = $30 \mu\text{m}$ and layer thickness = $40 \mu\text{m}$. It can be seen that samples with higher pulse energy exhibit pronounced balling effects (Fig 4. (a, b)). This is due to the fact that the melt pool on the surface enlarges when the pulse energy is increased and attracts surrounding powder into the melt pool. In general, this mechanism negatively affects the filling factor and surface quality.

Fig. 5 (a) shows solid bodies generated with 20 MHz repetition rate and a pulse energy of $1.5 \mu\text{J}$ at four different scanning speeds. The layer thickness and hatching distance was set to $40 \mu\text{m}$ and $30 \mu\text{m}$, respectively. The influence of scanning speed can be seen in the corresponding subfigures (b) and (c). Scanning speeds of 0.3 m/s (Fig. 5 (b)) and below resulted in rippled surfaces due to an increased melt track

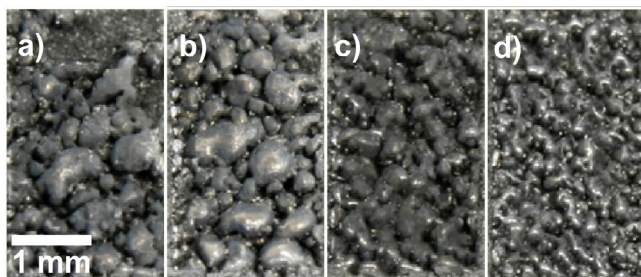


Fig. 4 Influence of scanning speed, repetition rate and pulse energy on the surface morphology: (a) 0.1 m/s at 10 MHz and $3 \mu\text{J}$; (b) 0.2 m/s at 10 MHz and $3 \mu\text{J}$; (c) 0.1 m/s at 20 MHz and $1.5 \mu\text{J}$; (d) 0.2 m/s at 20 MHz and $1.5 \mu\text{J}$.

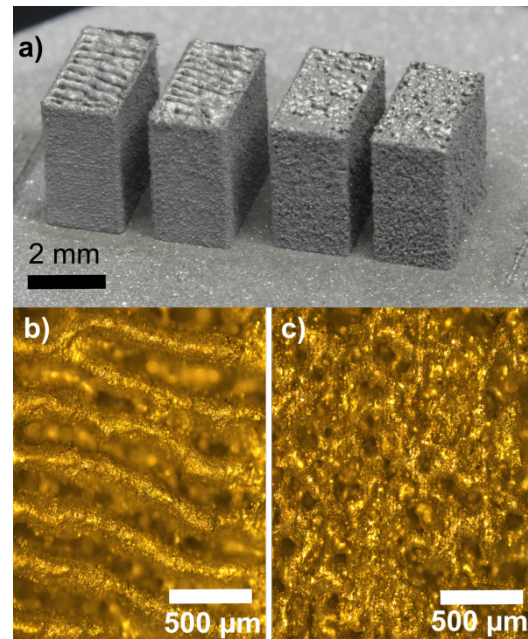


Fig. 5 (a) Typical samples built using four different scanning speeds (0.2, 0.3, 0.5, 0.7 m/s; from left to right). Microscope images of the sample surface built with a scanning speed of (b) 0.3 m/s and (c) 0.7 m/s.

yielding balling effects. Hence, for further investigations, the parameters applied in Fig. 5 (c) were chosen. In order to prove the feasibility of the process, a gear wheel was fabricated as an example for a complex 3D printed object (see Fig. 6).

The laser processed samples were embedded in epoxy resin and the microstructures of the bulk samples were investigated by SEM with BSE. Fig. 7 (a) shows an SEM image of the Al-Li ingot with 4 wt. % Li content. The δ -AlLi phase can be identified as dark regions. In Fig. 7 (b) it can be seen, that the δ -AlLi phase is significantly decreased when ultrashort laser pulses are applied for melting.

In order to measure the corresponding Brinell hardness, samples with a cubic shape were built. The corresponding dimensions were $6 \times 6 \times 6 \text{ mm}^3$. Some of these samples can be seen in Fig. 8 (a). They were fabricated using different hatching distances in the range from 30 to $60 \mu\text{m}$ (repetition rate = 20 MHz, pulse energy = $1.5 \mu\text{J}$, scanning speed =

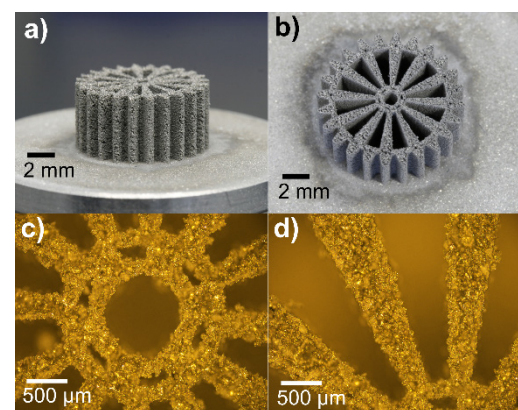


Fig. 6 (a, b) Images of a gear wheel fabricated at 20 MHz repetition rate with a pulse energy of $1.5 \mu\text{J}$ and a scanning speed of 0.7 m/s. (c, d) Light microscope images at different locations on the gear.

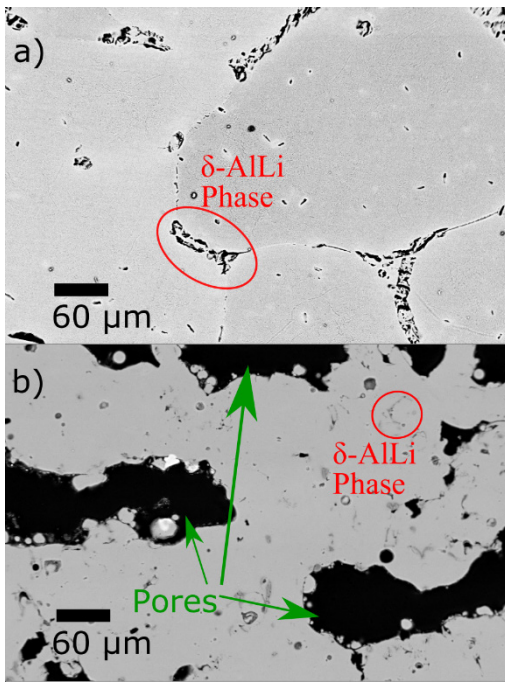


Fig. 7 (a) SEM image of as-cast Al-Li 4 wt. % alloy (b) SEM image of LPBF processed Al-Li 4 wt. % alloy

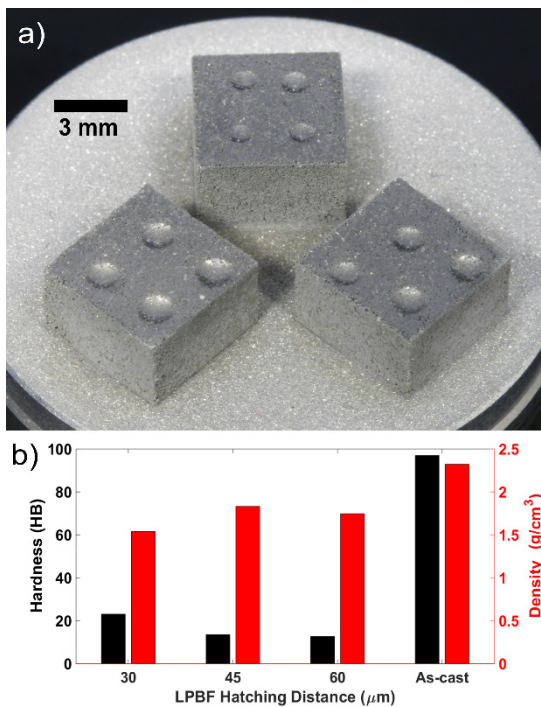


Fig. 8 (a) Indentations created during Brinell hardness tests (b) Comparison of USP-LPBF processed and as-cast structures in terms of Brinell hardness and density

0.7 m/s, layer thickness = 40 μm). The results obtained can be seen in Fig. 8 (b). Here, the corresponding densities were estimated by measuring the individual weights.

One can see, that at the current stage the produced samples exhibit a reduced hardness compared to the ingot reference hardness of 96 HB. The main reason was most likely the reduced relative density. This property must be optimized in the future.

In particular, the average power of the laser system was

limited to 30 W. During the experiments it was obvious, that higher values would have improved the process significantly. The study revealed that using 30 W was the absolute minimum of average power to realize mechanically stable structures.

4. Conclusion

This work demonstrates the additive manufacturing of binary Al-Li parts for the first time. In particular, Al-Li with an increased Li content of 4 wt. % was used. This alloy is one of the most promising candidates for future high stiffness, lightweight materials. One of the biggest challenges regarding Li-rich Al-Li is the precipitation of the δ-AlLi phase yielding an inhomogeneous microstructure and degraded mechanical properties, respectively. In order to minimize this behaviour, increased cooling rates and short solidification times must be achieved, respectively. In this respect, ultrashort laser pulses for LPBF were used. The observations support this approach, by measuring a decreased fraction of brittle δ-AlLi within the fabricated parts.

During the investigation feasible processing parameters were identified to generate solid bodies and sophisticated 3D structures. However, an achieved relative density of approximately 75 % accompanied with reduced hardness reflected the limitation in available laser power so far. Further optimization will be done by performing a more extensive parameter study, however the bottleneck during the investigations was the limited output power of about 30 W. Today, high-repetition rate ultrafast laser systems with a few hundred W average power are commercially available. Hence, achieving higher densities should be straightforward.

Acknowledgements

The authors gratefully acknowledge the funding by the German Research Foundation (DFG) within the Priority Program (SPP) 2122 “Materials for Additive Manufacturing (MATframe)” (grants NO462/13-1 and Re1261/23–1). Brian Seyfarth likes to acknowledge the Center of Excellence in Photonics of the Fraunhofer Institute for Applied Optics and Precision Engineering (IOF).

References

- [1] Santos EC, Shiomi M, Osakada K, Laoui T. Rapid manufacturing of metal components by laser forming. *International Journal of Machine Tools and Manufacture* 2006;46(12-13):1459-68.
- [2] Attaran M. The rise of 3-D printing: The advantages of additive manufacturing over traditional manufacturing. *Business Horizons* 2017;60(5):677-88.
- [3] Kruth JP, Froyen L, Van Vaerenbergh J, Mercelis P, Rombouts M, Lauwers B. Selective laser melting of iron-based powder. *Journal of Materials Processing Technology* 2004;149(1-3):616-22.
- [4] Nie B, Huang H, Bai S, Liu J. Femtosecond laser melting and resolidifying of high-temperature powder materials. *Appl. Phys. A* 2015;118:37–41.

- [5] Olakanmi EO, Cochrane RF, Dalgarno KW. A review on selective laser sintering/melting (SLS/SLM) of aluminium alloy powders: Processing, microstructure, and properties. *Progress in Materials Science* 2015;74:401-77.
- [6] Kaden L, Matthäus G, Ullsperger T, Engelhardt H, Rettenmayr M, Tünnermann A, Nolte S. Selective laser melting of copper using ultrashort laser pulses. *Applied Physics A* 2017;123(9):596.
- [7] Ullsperger T, Matthäus G, Kaden L, Engelhardt H, Rettenmayr M, Risse S, Tünnermann A, Nolte S. Selective laser melting of hypereutectic Al-Si40-powder using ultra-short laser pulses. *Applied Physics A*. 2017;123(12):798.
- [8] Nie B, Yang L, Huang H, Bai S, Wan P, Liu J. Femtosecond laser additive manufacturing of iron and tungsten parts. *Appl. Phys. A* 2015;119(3):1075-80.
- [9] Bauer F, Michalowski A, Kiedrowski T, Nolte S. Heat accumulation in ultra-short pulsed scanning laser ablation of metals. *Opt. Express* 2015;23(2):1035-43.
- [10] Noble B, Harris SJ, Dinsdale K. The elastic modulus of aluminium-lithium alloys. *J Mater Sci* 1982;17:461–8.
- [11] Rioja RJ, Liu J. The Evolution of Al-Li Base Products for Aerospace and Space Applications. *Metall and Mat Trans A* 2012;43:3325–37.
- [12] Ullsperger T, Matthäus G, Kaden L, Seyfarth B, Liu D, Rettenmayr M, Nolte S. Laser assisted powder bed fusion of hypereutectic Al-Si using ultra-short laser pulses at different pulse durations (Conference Presentation). In *Laser 3D Manufacturing VII 2020 Mar 9* (Vol. 11271, p. 112710M). International Society for Optics and Photonics.

11th CIRP Conference on Photonic Technologies [LANE 2020] on September 7-10, 2020

Particle-based simulation, dimensional analysis and experimental validation of laser absorption and thermo-viscous flow during sintering of polymers

Claas Bierwisch^{a*}, Shoya Mohseni-Mofidi^a, Bastien Dietemann^a, Torsten Kraft^a,
Johannes Rudloff^b, Marieluise Lang^b

^aFraunhofer IWM, Wöhlerstraße 11, 79108 Freiburg, Germany

^bSKZ – German Plastics Center, Friedrich-Bergius-Ring 22, 97076 Würzburg, Germany

* Corresponding author. Tel.: +49 761 5142 347; fax: +49 761 5142 510. E-mail address: claas.bierwisch@iwm.fraunhofer.de

Abstract

Smoothed Particle Hydrodynamics simulations are used to study the thermo-viscous flow on the powder particle length scale. The effects of laser absorption, latent heat, thermal diffusion, melting and re-solidification, viscous diffusion, surface tension, Marangoni currents and gravity are considered in the model. Influences of varied laser scanning parameters are analyzed. The strongly different time scales of laser absorption, heat conduction and viscous flow as well as the transient behavior of temperature and strain rate observed in the simulations are predicted with good accuracy by a dimensional analysis. The simulation results for the transient surface temperature are validated by infrared camera measurements.

© 2020 The Authors. Published by Elsevier B.V.

This is an open access article under the CC BY-NC-ND license (<http://creativecommons.org/licenses/by-nc-nd/4.0/>)

Peer-review under responsibility of the Bayerisches Laserzentrum GmbH

Keywords: PA12; grain scale; mesh free simulation; smoothed particle hydrodynamics; dimensionless numbers

1. Introduction

Early sintering models are provided by Frenkel [1] and Mackenzie & Shuttleworth [2] describing the behavior of metal particles. In both models the material properties particle diameter, viscosity and surface tension are used to quantify differences in the sintering behavior. The model of Frenkel is later used for the rotation sintering process and modified for the inclusion of viscoelastic effects [3]. The early models are modified and used by Schultz to describe the selective laser sintering (SLS) process of polycarbonate and polyethylene-oxide [4]. Schultz validates his models with a self-built SLS machine and finds a basic agreement between calculated and measured part densities. Riedlbauer *et al.* model the heat transfer in laser sintering of polyamide 12 (PA12) using a homogenized finite element analysis [5]. They predict the width and depth of a melt track and find good agreement with experimental measurements. Wohlgemuth & Alig study the physical modelling of the additive sintering processes for

polymer materials including viscoelasticity [6]. All models taking viscoelastic effects into account incorporate a relaxation time which can be measured in a rheometer. Osmanlic *et al.* develop a ray tracing model for the laser beam absorption in the powder bed [7]. They find that the effective laser penetration depth in the powder can be lower than in bulk material. Mokrane *et al.* provide homogenized simulations of the temperature field of a series of melt tracks [8]. They also predict spatial distributions of the porosity and of the degree of crystallization, however, without experimental validation. Balemans *et al.* model the laser sintering of two particles with high spatial resolution in 2D [9]. They also carry out a dimensional analysis of the system and vary several process parameters such as, e.g., laser power or ambient temperature to study the influence on the sintering behavior.

In summary within this brief survey, several works [3, 4, 6] show that the models by Frenkel or Mackenzie & Shuttleworth can be used to describe the influence of some relevant material parameters on the sintering process. Yet to gain a deeper

understanding of the SLS process, more sophisticated material models are necessary which include process parameters [5, 9], consider the granular nature of the powder bed [7] and link model predictions to part quality [8].

Our research aims ultimately at a profound understanding of the physical processes taking place in the melt pool during selective laser sintering. It shall clarify origins of remaining porosity after re-solidification and quantify the resulting surface roughness. As practical benefit, processability windows shall be predicted based on material properties and process parameters. These windows would also enable an accelerated development of new materials for SLS.

In the present work simulations of the melt pool dynamics by means of Smoothed Particle Hydrodynamics (SPH) [10] are presented. These simulations of polymeric powders on the particle scale yield detailed insights in the dynamics of the process. Theoretical analyses of the melt pool temperature, the melt viscosity and the strain rate are used to normalize the data obtained from the simulations yielding dimensionless master curves. Such master curves provide the basis for the envisioned processability windows as they reveal the relations between process parameters and material properties on the one hand and the thermo-viscous process dynamics on the other hand. Measurements of the transient surface temperature are used to validate the respective simulation results.

2. Numerical Simulation Model

The melt pool dynamics is analyzed by solving the continuity equation,

$$\frac{D\rho}{Dt} = -\rho \nabla \cdot \mathbf{u} , \quad (1)$$

as well as the Navier-Stokes momentum equation,

$$\rho \frac{D\mathbf{u}}{Dt} = -\nabla p + \mu \nabla^2 \mathbf{u} + \mathbf{f}_\Sigma + \rho \mathbf{g} . \quad (2)$$

Here, \mathbf{u} is the velocity, ρ is the mass density, p is the hydrostatic pressure, μ is the dynamic viscosity, \mathbf{f}_Σ is the volumetric surface tension force and $\mathbf{g} = -g\hat{\mathbf{z}}$ is the acceleration due to gravity. Bold face symbols denote vector quantities.

The hydrostatic pressure is given by an equation of state,

$$p = \rho_0 s^2 \left[\frac{1}{\gamma} \left[\left(\frac{\rho}{\rho_0} \right)^\gamma - 1 \right] + d \beta (T - T_a) \right] , \quad (3)$$

where ρ_0 is the equilibrium solid density, s is the speed of sound, γ is the isentropic exponent, d is the number of spatial dimensions and β is the linear thermal expansion coefficient. T is the temperature and T_a is the ambient temperature.

The melt rheology is modeled by means of a temperature-dependent viscosity. The viscosity μ changes depending on the state of matter of the material. Here, we differentiate three states: fully solid (S) below the solidus temperature T_S , fully liquid (L) above the liquidus temperature T_L and an intermediate state in between,

$$\mu(T) = \begin{cases} \mu_L \exp \left[\frac{E_a}{R} \left(\frac{1}{T} - \frac{1}{T_L} \right) \right] , & T \geq T_L , \\ \mu_S + (\mu_L - \mu_S) \frac{T - T_S}{T_L - T_S} , & T_S < T < T_L , \\ \infty , & T \leq T_S . \end{cases} \quad (4)$$

Above the liquidus temperature, the viscosity is modeled by an Arrhenius law using the activation energy E_a and the universal gas constant R . Below the solidus temperature the material is spatially fixed. The asymmetry between heating and cooling of polymers is considered by subtracting an offset temperature θ from T_S and T_L if the material is cooling and has reached T_L during the process,

$$T_S^{\text{cool}} = T_S - \theta , \quad T_L^{\text{cool}} = T_L - \theta . \quad (5)$$

The surface tension force,

$$\mathbf{f}_\Sigma = (-\sigma_N \kappa \mathbf{n} + \sigma_T \nabla_\Sigma T) \delta_\Sigma , \quad (6)$$

is composed of a contribution normal to and a contribution tangential to the local surface. Here, σ_N is the surface tension, κ the surface curvature and \mathbf{n} the surface unit normal vector. σ_T is the Marangoni coefficient describing the variation of surface tension with temperature and $\nabla_\Sigma T$ is the gradient of the surface temperature field. δ_Σ is a delta function marking the location of the surface in space [11].

The evolution for the thermal energy per unit mass e ,

$$\rho \frac{De}{Dt} = k \nabla^2 T + 2 \mu \underline{E} : \underline{E} - \varepsilon \sigma_B (T^4 - T_a^4) \delta_\Sigma + \frac{dI}{dz} \quad (7)$$

is influenced by contributions from heat conduction, viscous heating, Stefan-Boltzmann radiation and absorbed laser radiation. Here, k is the thermal conductivity of both powder and molten phase, \underline{E} is the strain rate tensor, ε is the emissivity, σ_B is the Stefan-Boltzmann constant and I is the local intensity of the laser radiation.

The strain rate tensor is defined as

$$\underline{E} = \frac{1}{2} [\nabla \mathbf{u} + (\nabla \mathbf{u})^T] , \quad (8)$$

while the effective strain rate is given by

$$E = \sqrt{2 \underline{E} : \underline{E}} . \quad (9)$$

The absorption of the laser radiation along the vertical coordinate z is described by the Lambert-Beer law with an attenuation coefficient a ,

$$\frac{dI}{dz} = a I . \quad (10)$$

The relation between temperature T and thermal energy per unit mass e is given by the following expression which takes into account the specific heat capacity c and the latent heat of melting H [12],

$$T(e) = \begin{cases} T_L + \frac{e - e_L}{c} , & e \geq e_L , \\ T_S + \frac{e - e_S}{c + \frac{H}{T_L - T_S}} , & e_S < e < e_L , \\ \frac{e}{c} , & e \leq e_S . \end{cases} \quad (11)$$

Here, $e_S = c T_S$ is the solidus thermal energy per unit mass and $e_L = c T_L + H$ is the liquidus thermal energy per unit mass. For the cooling phase, $e_S^{\text{cool}} = e_S - c \theta$ and $e_L^{\text{cool}} = e_L - c \theta$ apply.

The laser radiation is described by a Gaussian intensity profile in 2D [13],

$$I(x) = \frac{P}{\sqrt{2\pi} w h} \exp\left[-\frac{(x-x_0)^2}{2w^2}\right], \quad (12)$$

with power P , characteristic spot size w , hatch distance h and the variable laser spot center coordinate x_0 .

An overview of all used simulation parameters is given in Table 1. The process parameters are based on a working set for the present experimental setup (EOS FORMIGA P 110 CO₂ laser system using PA2200 powder).

All simulations are carried out using the SimPARTIX® simulation software developed at the Fraunhofer IWM (<http://www.simpartix.com>).

Table 1. Simulation parameters.

Quantity	Symbol	Value
Powder particle radius	r	25 μm
Powder area fraction	ϕ	0.77
Solid density	ρ_0	1020 kg/m ³
Speed of sound	s	1 m/s
Isentropic exponent	γ	7
Heat capacity	c	2.8 kJ/(kg K)
Thermal conductivity	k	0.24 W/(m K)
Thermal expansion	β	$1.71 \cdot 10^{-4}$ / K
Latent heat	H	100 kJ/kg
Attenuation coefficient	a	$1.3 \cdot 10^4$ / m
Emissivity	ε	0.5
Liquidus temperature	T_L	463.15 K; 190 °C
Solidus temperature	T_S	443.15 K; 170 °C
Offset temperature	θ	40 K
Activation energy	E_a	22.6 kJ/mol
Liquidus viscosity	μ_L	14.26 kPa s
Solidus viscosity	μ_S	35 kPa s
Surface tension	σ_N	35 mN/m
Marangoni coefficient	σ_T	$-1.2 \cdot 10^{-4}$ N/(m K)
Laser power	P	18 W; 21.5 W; 25 W
Laser spot diameter	$4w$	240 μm
Laser hatch distance	h	200 μm ; 250 μm ; 300 μm
Laser scan speed	v	2.6 m/s; 3 m/s; 3.4 m/s
Ambient temperature	T_a	442.15 K; 169 °C
Stefan-Boltzmann constant	σ_B	$5.67 \cdot 10^{-8}$ W/(m ² K ⁴)
Universal gas constant	R	8.31 J/(mol K)
Gravitational acceleration	g	9.81 m/s ²
Number of dimensions	d	2
Surface layer	Δz	5 μm

$$T(t_0, z) = \frac{a P \exp(-\phi a z)}{\rho_0 c h v} - \frac{H}{c} + T_a. \quad (13)$$

By solving $T(t_0, z_m) = T_L$ one obtains the initial depth z_m of the melt pool,

$$z_m(t_0) = \frac{1}{\phi a} \log\left(\frac{a P}{\rho_0 c h v (T_L - T_a + \frac{H}{c})}\right). \quad (14)$$

Integrating over the vertical coordinate z along the melt pool and normalizing by the pool depth yields the initial average melt pool temperature

$$\langle T \rangle = \frac{P}{\rho_0 c h v \phi z_m(t_0)} - \frac{T_L - T_a + \frac{H}{c}}{\phi a z_m(t_0)} - \frac{H}{c} + T_a. \quad (15)$$

By integrating only over a shallow surface layer Δz the initial surface temperature is obtained,

$$\langle T_{\text{surf}} \rangle = P \frac{1 - \exp(-\phi a \Delta z)}{\rho_0 c h v \phi \Delta z} - \frac{H}{c} + T_a. \quad (16)$$

An average viscosity of the melt pool is obtained by integrating the viscosity over the vertical coordinate z along the melt pool,

$$\langle \mu \rangle = \frac{\mu_L}{z_m(t_0)} \int_0^{z_m(t_0)} \exp\left[\frac{E_a}{R} \left(\frac{1}{T(t_0, z)} - \frac{1}{T_L}\right)\right] dz. \quad (17)$$

A normalization of the strain rate during the process is assumed to be given by multiplication with the Frenkel time scale $\mu r / \sigma_N$ [1],

$$E^* = \frac{E \mu r}{\sigma_N}. \quad (18)$$

In order to complete the analysis of the thermal behavior of the melt pool, the relevant thermal process time scales need to be identified. For the thermal diffusion within the melt pool the length scale of the initial pool depth $z_m(t_0)$ and the length scale of attenuation $1/(\phi a)$ are combined with the thermal diffusivity $k/(\rho_0 c)$ yielding a time scale

$$t_{\text{pool}} = \frac{z_m(t_0) \rho_0 c}{\phi a k}. \quad (19)$$

For the thermal diffusion on the melt pool surface the particle radius r is considered as the relevant length scale instead of the pool depth yielding a time scale

$$t_{\text{surf}} = \frac{r \rho_0 c}{\phi a k}. \quad (20)$$

3. Theoretical analysis of laser energy absorption and thermo-viscous properties of the SLS process

As the time scale of laser energy absorption is much smaller than the thermal diffusion time scale, it is reasonable to assume the initial temperature distribution at time $t_0 = 0$ to be an exponential function of the powder bed depth z according to the Lambert-Beer law,

4. Results

4.1. Numerical simulation of a melt track

Figures 1 and 2 show snapshots from simulations using a vertical laser source of $P = 25\text{ W}$ power moving with constant scan speed $v = 3\text{ m/s}$ along a random arrangement of PA12 particles. The 2D sample is 2 mm long and has periodic boundary conditions. The hatch distance is implicitly given by setting $h = 250\text{ }\mu\text{m}$ in the laser intensity formulation. The six subfigures show the system at different times. The left part of each subfigure shows results from a simulation with adiabatic boundary conditions at the substrate while the right part shows results with a thermally conductive substrate which is held at ambient temperature T_a . Note that the length of the simulation domain for each case corresponds to the total figure width, i.e. the left column shows only the left half of the adiabatic simulations while the right column contains only the right half of the simulations with the conductive substrate.

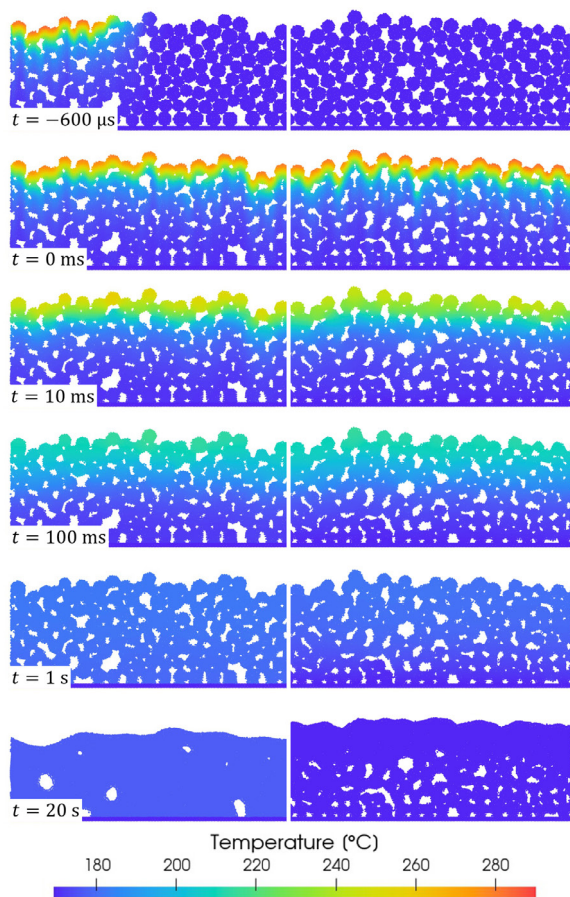


Fig. 1. 2D SLS energy deposition and melt process simulation with color-coded temperature field using either adiabatic (left column) or cooling (right column) boundary conditions at the substrate.

The laser moves until $t = 0\text{ s}$ and is then turned off. While the laser traverses the particles negligible thermal diffusion occurs. Then, the temperature field becomes more and more homogeneous. On the largest time scale densification due to fusion of the particles becomes apparent. The particles already start melting once they are irradiated. However, because of the

large viscosity of polymers in the SLS process the viscous flow leading to densification happens on a much larger time scale than the heat flow. Differences between the thermal boundary conditions at the substrate are initially negligible but pronounced in the end. In both cases the thickness of the fully liquid layer (green in Fig. 2) is comparable. The melting layer (blue in Fig. 2) reaches for the adiabatic case down to the substrate until the end of the simulation. For the cooling substrate, however, all of the material below the liquid pool becomes solid again for large times (purple in Fig. 2). This difference explains why strong densification can be observed in the adiabatic case throughout the powder bed while in the cooling case only in a surface layer. Furthermore, some pores between the particles do not completely vanish even in the adiabatic case. A surface roughness profile at the final stage can to some extent be related to the initial particle positions.

From these simulations it can be deduced that three distinct time scales are relevant. First, a laser irradiation time scale of the order of hundreds of microseconds, second, a thermal diffusion time scale of the order of hundreds of milliseconds, and third, a viscous flow time scale of the order of seconds exist.

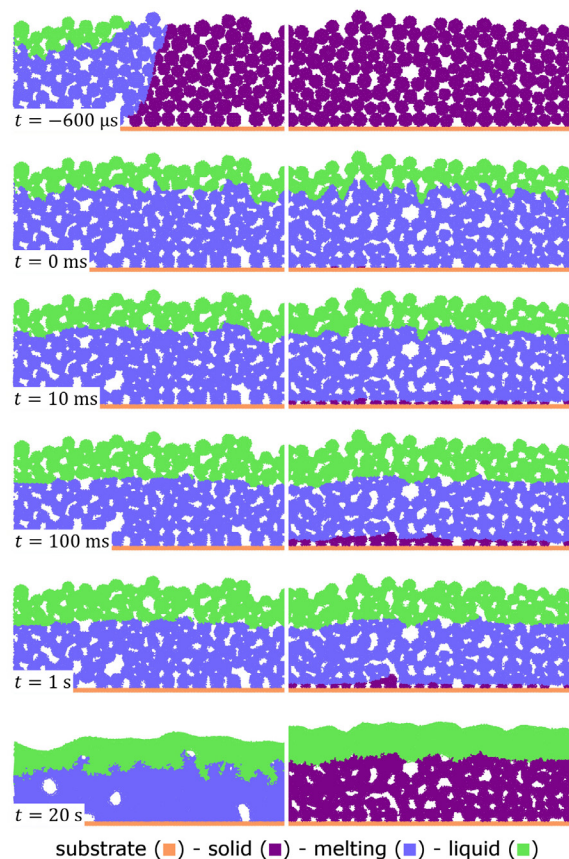


Fig. 2. Like Fig. 1 but with color-coded state of matter: solid ($T \leq T_s$), melting ($T_s < T < T_L$) or liquid ($T \geq T_L$).

With respect to the experiment we assume that the adiabatic thermal boundary condition underestimates the cooling from the substrate or from lower powder layers, respectively. The thermally conductive substrate, on the other hand, probably causes an overestimation of the cooling due to its constant temperature.

4.2. Dimensional analysis of laser energy absorption and thermo-viscous properties of the SLS process

In order to test the analytical models for the melt pool temperature, the reference 2D melt track simulation with adiabatic substrate is repeated with varied process parameters. In each simulation only one parameter is changed with respect to the reference case. The varied parameter is mentioned in the figure legend for each respective simulation. Note that melt pool refers to the fully liquid material (green in Fig. 2).

The average melt pool temperature obtained from the simulations is shown in Fig. 3 using dimensional units. The spread of the initial temperature is about 30 °C. The same data collapses on a single master curve if the average melt pool temperature is scaled using Equation (15) and the time is scaled using Equation (19) as can be seen in Fig. 4. This observation strongly supports the relevance and validity of the analytically derived scales.

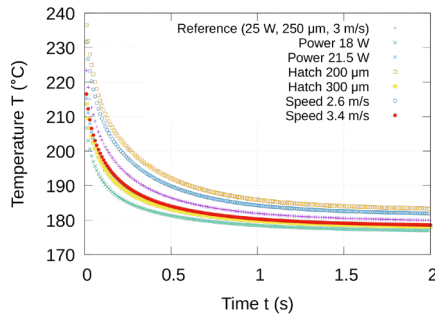


Fig. 3. Transient behavior of the average melt pool temperature from 2D simulations using various process parameters.

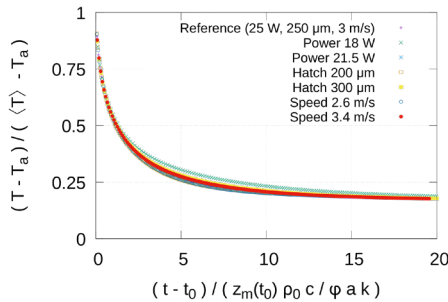


Fig. 4. Like Fig. 3 but using a dimensionless scaling for melt pool temperature and time.

Complementary to the average melt pool temperature the immediate surface temperature is analyzed. Figure 5 shows the obtained data from the simulations. In comparison to the average pool temperature the initial temperature spread is now significantly larger, namely about 70 °C. In order to validate the numerical results, the surface temperature is measured in SLS experiments (EOS FORMIGA P 110 system) with PA12 powder (EOS PA2200) using an infrared camera. In the experiment a 10 x 10 mm² monolayer is created. The measurement spot of the camera has a size of 0.8 x 0.8 mm². The experimental data is shown in Fig. 6. More details on the experimental procedures can be found in the paper by Rudloff et al. in this issue [14].

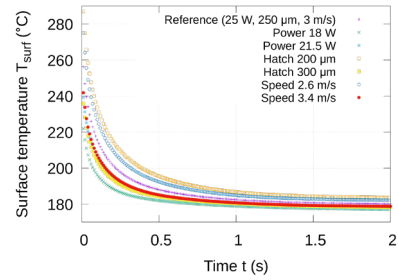


Fig. 5. Like Fig. 3 but for the surface temperature of the melt pool.

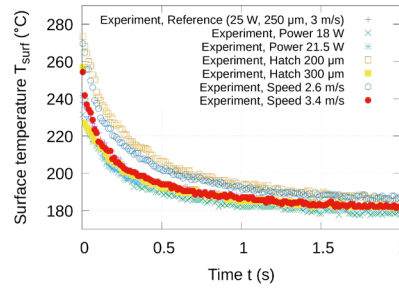


Fig. 6. Like Fig. 5 but for experimental data using an infrared camera.

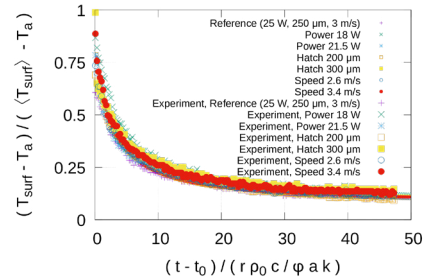


Fig. 7. Data of Figs. 5 and 6 combined and normalized.

A data collapse of both the experimental and numerical data is achieved by using Equation (16) to scale the surface temperature and using Equation (20) to scale the process time as can be clearly observed in Figure 7. Note that the volume fraction in the experiments is different than the area fraction in the simulations and, thus, $\phi = 0.45$ is used to normalize the experimental data. The quantitative agreement between theory, simulation and experiment is very good.

The transient evolution of the average viscosity in the melt pool is shown in Fig. 8. Due to the decrease of viscosity with increasing temperature the average viscosity starts from small values and approaches large values over time. Again, a satisfactory data collapse is obtained by scaling the average viscosity using Equation (17) and scaling the process time using Equation (19) as shown in Fig. 9.

Finally, the average effective rate of strain in the melt pool is analyzed. The data from the numerical simulations is shown in Fig. 10. Initially the strain rate is largest which is caused by the decreased viscosity at high temperature. Then the strain rate decreases during the process. The scaling of the effective strain rate using the Frenkel time scale according to Equation (18) works rather well as shown in Fig. 11. The normalized strain rates are not perfectly constant but vary only in a small window roughly between 0.5 and 0.6. This result proofs the applicability of the Frenkel scaling.

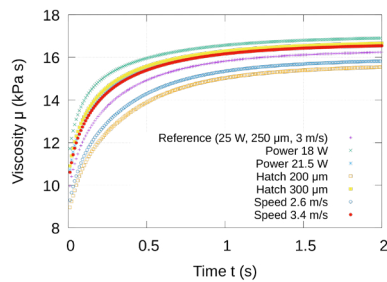


Fig. 8. Transient behavior of the average melt pool viscosity.

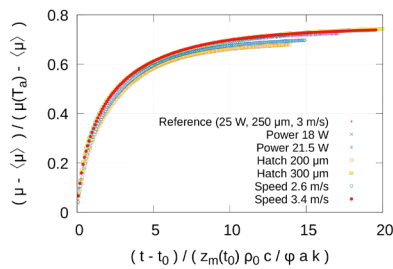


Fig. 9. Like Fig. 8 but using a dimensionless scaling.

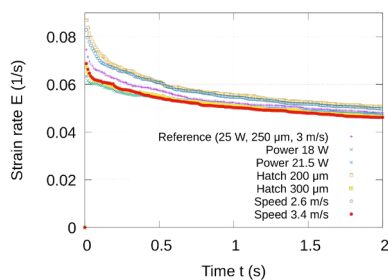


Fig. 10. Transient behavior of the average strain rate in the melt pool.

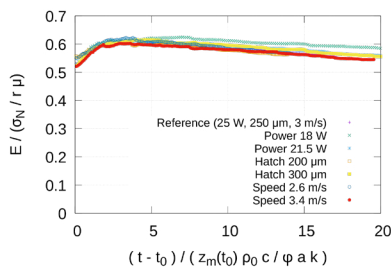


Fig. 11. Like Fig. 10 but using a dimensionless scaling.

5. Conclusions

Particle-based simulations of the SLS process reveal that the laser irradiation and subsequent polymer flow can be divided into three temporal regimes: (1) laser motion, (2) thermal diffusion and (3) viscous flow. The actual choice of the thermal boundary conditions at the substrate is found to be of minor importance during the initial phase of the process while it is crucial for the long term densification behavior.

Analytical models for the transient behavior of the surface temperature, melt pool temperature and viscosity enable a collapse of all gathered numerical data from simulations with different process parameters on single master curves. The strain rate in the system follows the scaling proposed by Frenkel. These master curves enable quantitative predictions of the

temperature, viscosity and strain rate in the melt pool for any set of material properties and process parameters. Hereby, they form the basis for predicting the transient densification rate which in turn is a key ingredient for the assessment of processability of an SLS material.

The numerical predictions of the transient surface temperature of the melt pool are validated by measurements. The agreement between numerical and experimental data is remarkable. Yet, further validations of other results of the numerical simulations are required in future work. Obvious candidates for this purpose are the thickness and the porosity of the sintered layer.

Acknowledgements

Financial support by the Deutsche Forschungsgemeinschaft (DFG, German Research Foundation) under grants number BI 1859/2-1 and LA 4328/1-1 within the priority program 2122 *Materials for Additive Manufacturing* is greatly acknowledged.

References

- [1] Frenkel, J. Viscous flow of crystalline bodies under the action of surface tension. *J. Phys.* (1945) 9(5):385–391.
- [2] Mackenzie, J.K. and Shuttleworth, R. A Phenomenological Theory of Sintering. *Proc. Phys. Soc. B* (1949) 62(12):833–852.
- [3] Bellehumeur, C.T., Kontopoulou, M. and Vlachopoulos, J. The role of viscoelasticity in polymer sintering. *Rheol. Acta* (1998) 37(3):270–278.
- [4] Schultz, J.P. Modeling Heat Transfer and Densification during Laser Sintering of Viscoelastic Polymers. PhD Thesis, Virginia Polytechnic Institute and State University (2003).
- [5] Riedlbauer, D., Drexler, M., Drummer, D., Steinmann, P. and Mergheim, J. Modelling, simulation and experimental validation of heat transfer in selective laser melting of the polymeric material PA12. *Comput. Mater. Sci.* (2014) 93:239–248.
- [6] Wohlgenuth, F. and Alig, I. Physikalische Modellbildung für das Additive Sintern von Kunststoffmaterialien. In: *Additive Fertigung von Bauteilen und Strukturen*. Richard, H.A. (Ed.). Springer Fachmedien, Wiesbaden, Germany (2017) 121–136.
- [7] Osmanlic, F., Wudy, K., Laumer, T., Schmidt, M., Drummer, D. and Körner, C. Modeling of Laser Beam Absorption in a Polymer Powder Bed. *Polymers* (2018) 10:784.
- [8] Mokrane, A., Boutaous, M. and Xin, S. Process of selective laser sintering of polymer powders: Modeling, simulation, and validation. *C. R. Mecanique* (2018) 346:1087–1103.
- [9] Balemans, C., Jaensson, N.O., Hulsen, M.A. and Anderson, P.D. Temperature-dependent sintering of two viscous particles. *Additive Manufacturing* (2018) 24:528–542.
- [10] Gingold, R.A. and Monaghan, J.J. Smoothed Particle Hydrodynamics: Theory and Application to Non-Spherical Stars. *Mon. Not. R. Astron. Soc.* (1977) 181:375–389.
- [11] Bierwisch, C. A surface tension and wetting model for the δ -SPH scheme. In: *Proceedings of the 13th SPHERIC International Workshop 2018*. Quinlan, N.J., Tong, M., Moghimi, M.H. and McLoone, M. (Eds.). National University of Ireland, Galway, Ireland (2018) 95–102.
- [12] Körner, C., Attar, E. and Heintz, P. Mesoscopic simulation of selective beam melting processes. *J. Mater. Process. Technol.* (2011) 211:978–987.
- [13] Körner, C., Bauereiß, A. and Attar, E. Fundamental consolidation mechanisms during selective beam melting of powders. *Modelling Simul. Mater. Sci. Eng.* (2013) 21:085011.
- [14] Rudloff, J., Lang, M., Mohseni-Mofidi, S. and Bierwisch, C. Experimental investigations for improved modelling of the laser sintering process of polymers. In: *Proceedings of the 11th CIRP Conference on Photonic Technologies – LANE 2020*. Fürth, Germany (2020).

11th CIRP Conference on Photonic Technologies [LANE 2020] on September 7-10, 2020

Experimental investigations for improved modelling of the laser sintering process of polymers

Johannes Rudloff^{a*}, Marieluise Lang^a, Shoya Mohseni-Mofidi^b, Claas Bierwisch^b,

^aSKZ – German Plastics Center, 97076 Würzburg, Germany

^bFraunhofer IWM, 79108 Freiburg, Germany

* Corresponding author. Tel.: +49-931-4104-528; fax: +49-931-4104-707. E-mail address: j.rudloff@skz.de

Abstract

For laser sintering the knowledge about which material properties are important for the process and the product quality is insufficient. This causes significant difficulties in developing new materials. To address this problem, a link between material data, process parameters and component quality is necessary. This link can be achieved by a combination of experimental investigations and theoretical considerations to develop dimensionless characteristic numbers. As a first step to derive such numbers, this paper presents experimental methods to determine temperature development and sintered volume during the sintering process. These methods are used to investigate different process parameter settings during the sintering of polyamide 12. The measurement results are then compared with simulated results.

© 2020 The Authors. Published by Elsevier B.V.

This is an open access article under the CC BY-NC-ND license (<http://creativecommons.org/licenses/by-nc-nd/4.0/>)

Peer-review under responsibility of the Bayerisches Laserzentrum GmbH

Keywords: Simulation, Modelling, Laser Sintering, Polyamide 12, Thermal Imaging

1. Introduction

There is a high growth of additively manufactured parts in the polymer industry [1]. Nevertheless, especially for laser sintering (LS) the material selection is very limited in comparison to other polymer production processes like, for example, extrusion or injection molding. One major reason for that problem is that there is almost no knowledge which material properties are important for the process and how the material parameters affect the product quality. This is particularly disadvantageous because there are many potential influencing factors for polymer sintering. Thus, developing new materials for the LS is a complex process. Even a specification of limit values for powder properties to classify new powders as "definitely suitable" or "definitely not suitable" for LS cannot be carried out 100 % reliably at present. In some cases, "worse" property values can be compensated by plant options and process parameters via - extremely time-consuming "trial and error" experiments [2, 3].

In order to develop and qualify a polymer powder suitable for the LS process, various properties - both intrinsic and extrinsic - have to be investigated. These are determined on the one hand by the basic chemical structure and on the other hand by the method of production and processing [4]. The influencing factors can be divided in material and process parameters, but in order to predict the behavior of a material during laser sintering, both types of parameters must be linked together.

This link can be achieved by a combination of experimental investigations, numerical simulations and analytical considerations to develop dimensionless characteristic numbers (DCN). As a first step to derive such numbers, this paper presents experimental methods to determine temperature development and sintered volume during the sintering process. These methods are used to investigate different process parameter settings during the sintering of polyamide 12 (PA12). The measurement results are then compared with simulated results.

Nomenclature

d_s	Layer thickness (process parameter)
E_A	Surface energy density
E_V	Volume energy density
h_S	Hatch distance
P_L	Laser power
v_s	Scan speed
T_B	Part bed temperature

2. Material Properties

In the past, there have been various efforts to examine the most important material properties, especially for PA12, individually for their influence on the LS process and on the quality properties of components. Mielicki et al. dealt, for example, with the melt viscosity [5]. Schmid and Drummer et al. dealt with the particle geometry and the resulting powder flowability [4,6], also at elevated temperatures [7]. Sutton et al. investigated the "powder chemistry" and the thermal properties [8]. Laumer et al. analyzed the absorption behavior [9]. However, no weightings or correlations among each other were evaluated. This is problematic because an ideal interplay of several material properties must exist in order to be able to process a material successfully in the LS process [10].

The interplay of the material properties can be investigated in numerical simulations. Therefore, a set of material data suitable for simulations is necessary. This material data was determined for PA12 type EOS PA2200 with a mixture of 50 % virgin powder and 50 % recycled powder (compare Table 1).

Table 1. Material data

Quantity	Symbol	Value
Powder particle radius	r	25 μm
Solid density	ρ_0	1020 kg/m^3
Powder bulk density	ρ_B	436 kg/m^3
Heat capacity	c	2.8 $\text{kJ}/(\text{kg K})$
Thermal conductivity	k	0.24 $\text{W}/(\text{m K})$
Thermal expansion	β	$1.71 \cdot 10^{-4} / \text{K}$
Latent heat	H	100 kJ/kg
Melting / Liquidus temperature	T_L	463.15 K; 190 $^\circ\text{C}$
Solidus temperature	T_S	443.15 K; 170 $^\circ\text{C}$
Offset temperature	θ	40 K
Activation energy	E_a	22.6 kJ/mol
Liquidus viscosity	μ_L	14.26 kPa s
Solidus viscosity	μ_S	35 kPa s
Surface tension	σ_N	35 mN/m

The viscosity was measured in a plate-plate rheometer in oscillation mode at 195, 215 and 235 $^\circ\text{C}$ and shear rates from 0,6 to 450 $1/\text{s}$ and extrapolated to a shear rate of 0,1 with a Carreau Modell. An Arrhenius model describes the temperature dependency. The bulk density of the powder was measured according to DIN EN ISO 60 at room temperature. The solid density and thermal expansion was determined with

a pressure-volume-temperature measurement in a high-pressure capillary rheometer. The thermal conductivity was measured with a laser flash system, the specific heat capacity, the latent heat, the liquidus and solidus temperature with differential scanning calorimetry for a temperature range of 0 - 250 $^\circ\text{C}$. Surface tension was determined with sessile drop method on sintered and injection-moulded plates at room temperature.

3. Process Parameter

In addition to the material properties, process parameters have a major influence on surface qualities (e.g. roughness) and the mechanical properties (e.g. tensile strength, surface hardness and density) of parts produced by LS. The most important process parameters are the part bed temperature T_B , the laser power P_L , the scan spacing or hatch distance h_S , the scan speed v_s and the layer thickness d_s [11].

During the laser sintering process, the powder bed is heated up to just below its melting temperature to enable sintering and reduce thermal stress and thus distortion of the parts. The temperature is achieved by several heating elements inside the process chamber in order to get an even temperature distribution on the powder surface. The laser beam then liquefies this preheated powder bed at defined points and fuses the particles of the material [12,13,14].

To get the temperature of the powder to a level over the melting temperature T_m of the material in a short period of time the laser power P_L is used. At a temperature above melting temperature T_L the polymer is able to flow because of its liquid state. As a result of this flowability the porosity is reduced and the mechanical properties of the part are improved [11].

The scan speed v_s describes the speed at which the scanner directs the laser beam over the powder bed. A high speed is preferable, as this results in a shorter construction time. The hatch distance h_s is the distance between the sintering lines (perpendicular to the direction of the laser spot movement). This determines the overlapping of the nearby tracks, which results in their connection strength. The layer thickness d_s indicates the height of each powder layer and, thus, is a major influence parameter of the morphology and density of final parts. The minimum possible layer thickness depends on the material. The standard layer thickness for PA 12 material is 0.1 mm [13]. On the laser-sintering system FORMIGA P 110 from EOS GmbH, additional layer thicknesses of 0.06 mm and 0.12 mm can be realized [15].

For the description of the energy introduced by the laser, the surface energy density E_A as energy input into a layer, is often used. It represents the ratio, according to equation 1, of the laser power P_L , the scan speed v_s and the hatch distance h_s . Furthermore, the volume energy density E_V is often used (equation 2). The layer thickness d_s is also taken into account here. These equations are nowadays used to describe the energy input and the correlation of process contexts of laser sintering [10,16].

$$E_A = \frac{P_L}{v_s h_s} \quad (1)$$

$$E_V = \frac{P_L}{v_s \cdot h_s \cdot d_s} \quad (2)$$

Numerically the same values for each, E_A or E_V , can be obtained using different input parameters. As a result, even if, e.g., E_A is kept constant by reducing P_L and reducing v_s by the same factor, different sintering results will be generated. However, parts built with higher scan speeds tend to exhibit lower mechanical properties, although the energy density remains constant through compensation with the laser power. One assumption for this is that the time dependency of energy absorption has not been taken into account. Since the materials used in LS have a limited specific energy absorption capacity per unit of time, compensation cannot be achieved by increasing the laser power. Therefore, a low laser power with low scan speed of the laser is desirable in terms of mechanical properties. However, this approach conflicts with economical consideration of LS in which high laser speeds and thus short construction times are aimed at [10]. Furthermore, to use the energy density as a quality parameter for material development, a link to material properties as melting enthalpy, particle geometry and density is necessary.

4. Experimental and numerical Investigations

To achieve a better understanding of the energy input and distribution during laser sintering, experimental investigations on an EOS Formiga P110 with a CO₂ laser were conducted. Thereby, 10 x 10 mm monolayer plates were printed. The material PA2200 50/50, the layer height of 0.1 mm and the laser spot diameter of 0.24 mm were kept constant. The varied parameters are shown in Table 2. When a given parameter was varied, the bold written values of the other parameters were kept constant.

Table 2. Experimental design

Parameter	Values	Unit
Laser power	18.0, 21.5, 25.0	W
Hatch distance	0.20, 0.25 , 0.30	mm
Scan speed	2600, 3000 , 3400	mm/s
Part bed temperature	164, 169 , 174	°C

In order to measure the temperature during the sintering process, an infrared camera type TIM 400 from MICRO-EPSILON was used. The resolution of this camera is 0.8 x 0.8 mm per pixel. The camera was calibrated with LS machine pyrometer. To enable a measurement when the laser is active, a special wave length filter was installed. Furthermore the thickness of the printed monolayer plates was determined with a dial gauge and on microscopy images.

Parallel to the experimental investigations, the process was analysed numerically. For this purpose, simulations based on the Smoothed Particle Hydrodynamics (SPH) method [17] were conducted. Thereby, the LS of a 2D system of randomly positioned PA12 particles was simulated. Material and process parameters were selected according to the experimental studies [18].

5. Results and Discussion

First, the results of the experimental investigations are considered. Afterwards they are compared with numerical determined results.

5.1. Experimental Results

Images of the infrared camera for three time steps during the printing of a monolayer plate with the bold parameter values of table 2 are shown in Fig. 1. It can be seen that the temperature of the whole monolayer plate is above 225 °C after complete exposure. Furthermore there is a slight temperature gradient of approximately 25 °C across the plate width, wherein the temperature across the plate length is approximately constant.

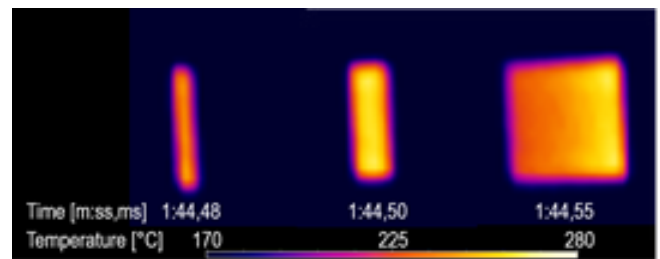


Fig. 1. Images of the infrared camera for three time steps during sintering

The temperature development after exposure in the center of the plate for different P_L values is shown in Fig. 2. It is noticeable that the curves are very similar for all three P_L values. In the first 50 ms a rapid temperature rise to temperatures above 250 °C can be seen. With increasing P_L the maximum temperature increases as well. It should be noted that due to the resolution of the thermal camera no single exposure process can be recorded here. The laser moves over the pixel about 4 times until a complete exposure of the pixel is achieved. For a single exposure process, the measured temperature rise would probably be even more pronounced. After reaching the maximum temperature, the temperature drops continuously and approaches T_B . During the cooling process, thermal energy is probably released into the powder bed by heat conduction. This leads to a further melting of powder.

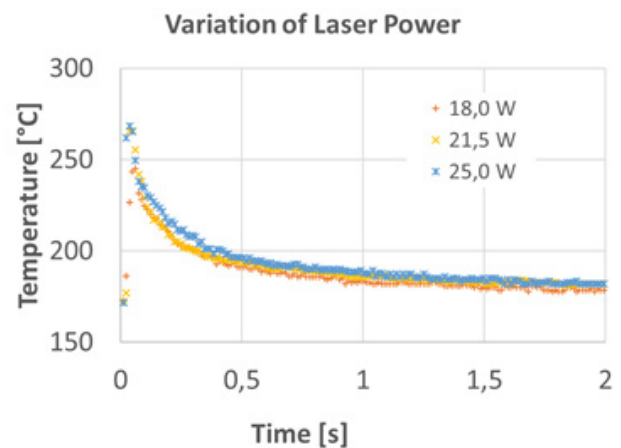


Fig. 2. Measured temperature as a function of time and set laser power of EOS Formiga P110

A similar behavior could also be determined for the other process parameters. This is shown as an example for v_s in Fig. 3. With decreasing v_s the maximal temperature increases due to a higher E_A .

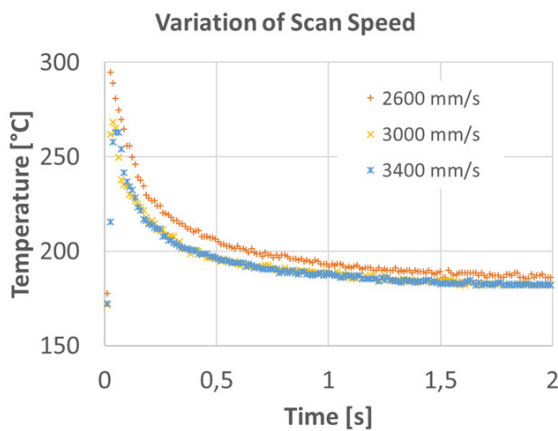


Fig. 3. Measured temperature as a function of time and scan speed

In order to be able to completely evaluate the process from an energetic point of view, not only the temperature development but also the volume or mass into which the energy is introduced is relevant. Figure 4 shows the measured thickness of the monolayer plates as a function of E_A for the experiments performed. For both measuring methods a clear increase of the monolayer thickness with increasing E_A can be detected. This means that the mass to which the introduced energy is distributed increases with increasing introduced energy. It is noticeable that the measured thickness differs significantly depending on the measuring method. For the measurements with the dial gauge, a linear increase with a slope of ten can be seen and the straight line cuts the abscissa close to the origin. The values determined from microscopic images scatter more strongly and the straight line runs much flatter. The standard deviation for the dial gauge values, at an average of 5 μm , was also significantly lower than for the microscopy values, at an average of 20 μm . This can partly be attributed to the fact that the interpretation of the microscopic images is difficult, especially with regard to the differentiation of melted powder that is not located in the plane to be measured. In addition, the dial gauge had a flattened tip so that unevenness could not be determined. This value therefore probably corresponds to a maximum thickness of the plates.

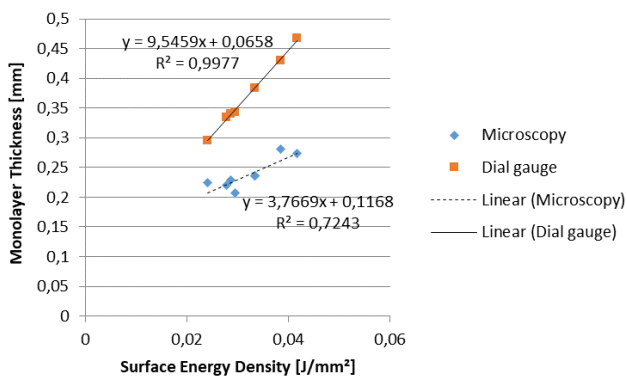


Fig. 4. Measured monolayer thickness as a function of surface energy density

5.2. Numerical Results

The numerical calculated temperature development over time for a variation of laser power and scan speed is shown in Fig. 5 and Fig. 6. The curve progressions correspond very well with the experimentally determined values. This suggests that the real temperature development during LS can be well represented by SPH simulations.

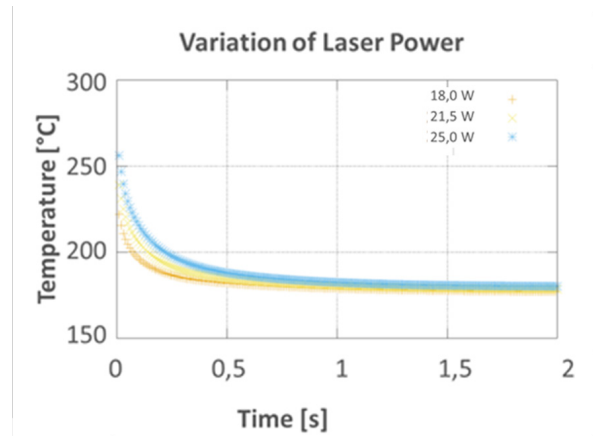


Fig. 5. Numerically calculated temperature as a function of time and laser power

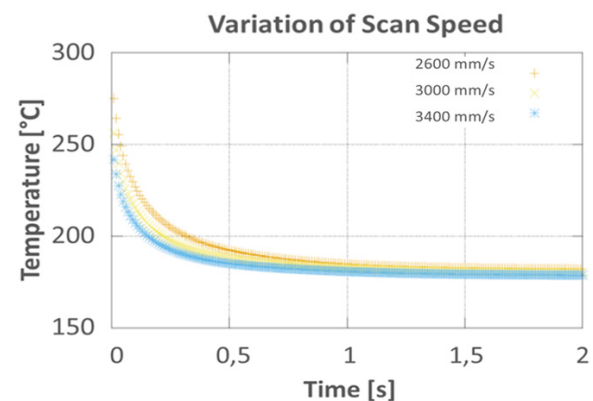


Fig. 6. Numerically calculated temperature as a function of time and scan speed

The simulated thickness of the sintered material is shown in Fig. 7. As with the experimental determination of the thickness, there are different possibilities to determine this value. The Maximum Thickness is best compared to a dial gauge with a flattened tip. Here, the difference between the highest and lowest point of the simulation area was formed, which each exceeded the liquidus temperature. The local thickness is more comparable to values determined under a microscope or with a dial gauge with a fine tip. To determine this value, the difference between the highest and lowest points was determined at 40 positions and then averaged over these values.

Although the four curves shown in Fig. 4 and Fig. 7 differ significantly in their gradient and absolute values, it can nevertheless be stated, that the sintered thickness increases linear with increasing surface energy density. The deviation between experiment and simulation can be explained, among other things, by the fact that in experiments unsintered powder can stick to the sintered plate, which cannot be considered in

the simulation. In addition, more monolayers were printed in one experimental run, so that plates were arranged above each other and separated by several layers of unexposed powder. This leads to unexposed powder on the top of the plate that adheres to them. Here, experimental and numerical procedures must be better harmonized in order to be able to make a statement about which absolute thicknesses occur.

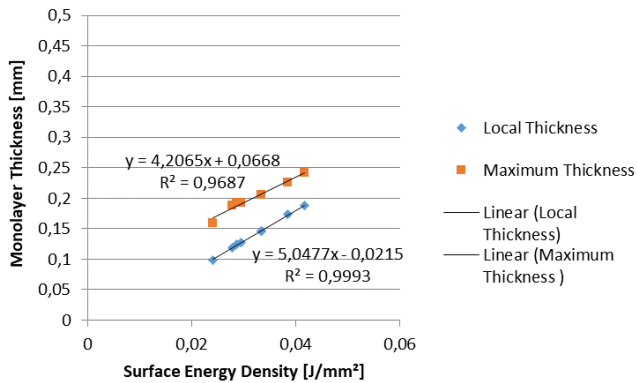


Fig. 7. Simulated monolayer thickness as a function of surface energy density

6. Conclusion

The temperature development over time during laser sintering was recorded with a thermal camera. The differences between different energy inputs are much less pronounced than expected. This can be attributed to the fact that the thickness of the molten material and thus the volume into which energy is introduced also increases with increasing energy input. This is shown by an increase of monolayer thickness with increasing surface energy density. The experimentally determined behavior could also be observed in numerical 2D simulations. This confirms that both the numerical and the experimental methods provide valid results. Further work in the project will concentrate on presenting the results for both methods in a dimensionless form. Furthermore, the investigations will be extended to other material systems such as polypropylene.

Acknowledgements

Financial support by the Deutsche Forschungsgemeinschaft (DFG, German Research Foundation) under grants number BI 1859/2-1 and LA 4328/1-1 within the priority program 2122 Materials for Additive Manufacturing is greatly acknowledged. All simulations are carried out using the SimPARTIX® software developed by Fraunhofer IWM (<http://www.simpartix.com>).

References

- [1] Wohlers T, Caffrey T. 3D Printing and Additive Manufacturing State of the Industry. Wohlers Report; 2014
- [2] Schmid M, Amado F, Levy G, Wegener K. Flowability of Powders for Selective Laser Sintering (SLS) investigated by Round Robin Test. ETH Zürich; 2014
- [3] Handlungsfelder Additive Fertigungsverfahren. VDI-Publikation; 2016
- [4] Amado A, Schmid M, Levy G. Advances in SLS powder characterization. Proceedings of the international Solid Freeform Fabrication Symposium. Austin; 2011
- [5] Mielicki C, Wegner A, Gronhoff B, Wortberg J, Witt G. Prediction of PA12 melt viscosity in Laser Sintering by a Time and Temperature dependent rheological Model. Uni Duisburg-Essen; 2012
- [6] Lexow M, Drummer D. New Materials for SLS: The use of antistatic and flow agents, Institute of polymer technology. Journal of powder Technology 2016
- [7] Amado A, Schmid M, Wegener K. Flowability of SLS powders at elevated temperatures. Proceedings Rapid Tech. Erfurt; 2013
- [8] Sutton A, Kriewall C, Leu M, Newkirk J. Powders for additive manufacturing processes: Characterization techniques and effects on part properties. Proceedings of the 27th annual international Solid Freeform Fabrication Symposium. Austin; 2016
- [9] Laumer T, Stichel T, Bock T, Amend P, Schmidt M. Characterization of temperature-dependent optical material properties of polymer Powders. AIP Conference Proceedings 2015; 1664
- [10] Schmid M. Selektives Lasersintern (SLS) mit Kunststoffen. Munich: Hanser Verlag; 2015
- [11] Gibson I, Shi D. Material properties and fabrication parameters in selective laser sintering process. Rapid Prototyping Journal 1997;3:4
- [12] Caulfield B, McHugh PE, Lohfeld S. Dependence of mechanical properties of polyamide components on build parameters in the SLS process. Journal of Materials Processing Technology 2007;182:1-3
- [13] Kaddar W. Die generative Fertigung mittels Laser-Sintern: Scanstrategien, Einflüsse verschiedener Prozessparameter auf die mechanischen und optischen Eigenschaften beim LS von Thermoplasten und deren Nachbearbeitungsmöglichkeiten. Universität Duisburg-Essen; 2010
- [14] Singh S, Sachdeva A, Sharma V. Optimization of selective laser sintering process parameters to achieve the maximum density and hardness in polyamide parts. Progress in Additive Manufacturing 2017;1-2
- [15] System Data Sheet Formiga P110. Kraling: EOS GmbH; 2017
- [16] Wegner A. Theorie über die Fortführung von Aufschmelzvorgängen als Grundvoraussetzung für eine robuste Prozessführung beim Laser-Sintern von Thermoplasten. Universität Duisburg-Essen; 2015
- [17] Gingold RA, Monaghan JJ. Smoothed Particle Hydrodynamics: Theory and Application to Non-Spherical Stars. Mon. Not. R. Astron. Soc. 1977;181:375–389
- [18] Bierwisch C, Mohseni-Mofidi S, Dietemann B, Kraft T, Rudloff J, Lang M. Particle-based simulation, dimensional analysis and experimental validation of laser absorption and thermo-viscous flow during sintering of polymers. 11th CIRP Conference on Photonic Technologies LANE; 2020

11th CIRP Conference on Photonic Technologies [LANE 2020] on September 7-10, 2020

Experimental determination of scattering processes in the interaction of laser radiation with polyamide 12 powder

Thomas Schuffenhauer^{a,c,d,*}, Thomas Stichel^{a,c}, Michael Schmidt^{a-d}

^a*Bayerisches Laserzentrum GmbH (blz), Konrad-Zuse-Straße 2-6, 91052 Erlangen, Germany*

^b*Institute of Photonic Technologies (LPT), Friedrich-Alexander-Universität Erlangen-Nürnberg, Konrad-Zuse-Straße 3-5, 91052 Erlangen, Germany*

^c*Collaborative Research Center (CRC) 814 “Additive Manufacturing”, 91058 Erlangen, Germany*

^d*Erlangen Graduate School in Advanced Optical Technologies (SAOT), 91052 Erlangen, Germany*

* Corresponding author. Tel.: +49-9131-97790-28; fax: +49-9131-97790-11. E-mail address: t.schuffenhauer@blz.org

Abstract

Energy density, scanning strategy and laser spot size are some of the parameters influencing the optical energy input during laser-based powder bed fusion of polymers. For newly developed polymer powders, such parameters must still be determined empirically. Understanding the complex mechanisms underlying the beam-matter interaction, including absorption characteristics or multiple scattering behavior, is crucial to predict material processability and to improve interlayer fusion for enhanced final part properties.

A measurement system based on two integrating spheres is employed to analyze the scattering processes during the interaction of a CO₂ laser beam with polymeric powder materials. The setup is used to measure total reflection from the sample surface as well as unscattered and diffuse transmission through the sample. The resulting optical properties of polyamide 12 powder are evaluated and compared to those of thin films of the same base material. Thus, the influence of particle interfaces on the energy deposition characteristics can be analyzed qualitatively.

© 2020 The Authors. Published by Elsevier B.V.

This is an open access article under the CC BY-NC-ND license (<http://creativecommons.org/licenses/by-nc-nd/4.0/>)

Peer-review under responsibility of the Bayerisches Laserzentrum GmbH

Keywords: powder bed fusion; laser sintering; optical properties; polymers; polyamide 12; integrating spheres

1. Introduction

During laser sintering or laser-based powder bed fusion of polymers (PBF-LB/P), the interaction between the incident laser beam and the powder material significantly influences the building process and final part properties [1]. While a certain amount of radiation is reflected from the surface, the main part should penetrate deeper regions where it can either be absorbed by or transmitted through the powder layer. The relation between total reflectance (R), total transmittance (T) and absorbance (A) is given in equation 1 [2].

$$R + T + A = 1 \quad (1)$$

R and T can be subdivided into diffuse and unscattered portions which, depending on the experimental setup, can be measured separately. The separate detection of diffuse and unscattered radiation can contain valuable information about material properties such as microstructural features [3,4].

For the case of a CO₂ laser with a wavelength λ of 10.6 μm interacting with PBF-LB/P powders with particle sizes ranging roughly from 1 μm to 150 μm and sub-micron sized intraparticle features, also scattering phenomena on multiple scales may occur, as proposed by Wegner [1]. However, the effect of scattering in the PBF-LB/P context has not yet been studied experimentally and has very rarely been considered in the modelling of the beam-matter interaction [1,5-7]. Hence, the influence of scattering phenomena on the absorption characteristics of PBF-LB/P powders is still unknown.

Understanding such scattering mechanisms and correlating these to the underlying powder material properties could potentially lead to an improved energy deposition and ultimately resolve some of the remaining limitations of PBF-LB/P parts such as lacking interlayer fusion due to insufficient (unmolten powder particles) or excessive (formation of pores as a result of degradation) energy input [8].

The aim of this contribution is the successful employment and adaptation of a previously described measurement system based on two integrating spheres for the characterization of PBF-LB/P powders [9–11] to analyze scattering processes during the interaction of a CO₂ laser beam with polyamide 12 (PA12) powder and solid films. By separately measuring the diffuse and the unscattered transmittance, information about scattering processes is extracted and evaluated, thus deepening the understanding of the beam-matter interaction during PBF-LB/P.

2. Materials and methods

2.1. Double-integrating-sphere setup and optical measurements

The setup used for measurement of the optical properties is depicted in Fig. 1.

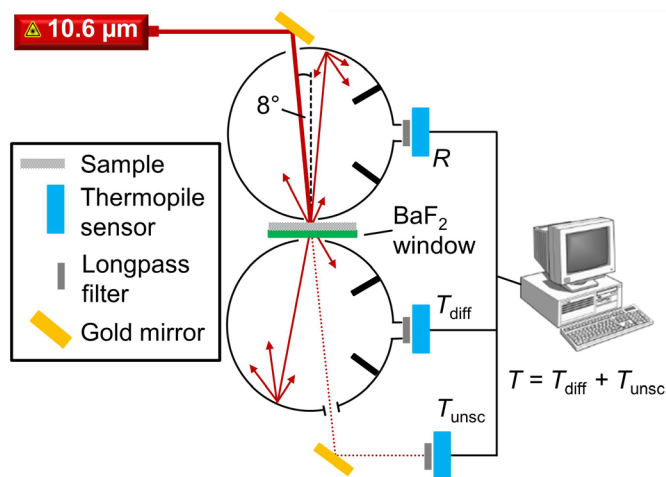


Fig. 1. Double-integrating-sphere setup for reflectance and transmittance measurements.

Both integrating spheres possess a highly reflective, diffuse gold coating on the interior and several ports for light entrance or detection of either integrated (R , T , T_{diff}) or direct (T_{unsc}) radiant power. Highly sensitive thermopile sensors were used for power detection and longpass filters were placed in front of each sensor to minimize power fluctuations due to variations of thermal conditions inside the laboratory. It should be mentioned that in case of a sealed T_{unsc} -port, the T_{diff} -sensor then measured the total transmittance T instead of only the diffuse portion.

For measurement of the optical properties, the collimated CO₂ laser beam (firestar-ti60, Synrad, USA) was directed into the top sphere via gold mirrors, irradiating the sample under an angle of 8° in accordance with DIN 5036-3. The analyzed samples were placed between reflection (top) and transmission

(bottom) sphere, on top of a 3-mm-thick barium fluoride (BaF₂) infrared (IR) window. Besides its excellent transmission behavior (T at 10.6 μm > 90 %, low reflective loss < 10 %), BaF₂ was selected due to its hazard-free application (in contrast to e. g. zinc selenide) and its high robustness against atmospheric humidity (compared to e. g. sodium chloride or potassium chloride).

To prevent laser-induced changes of the samples such as partial sintering or a phase transition, which would in turn alter the absorption characteristics, all experiments were conducted with a low laser power of 4 W and a short irradiation time of 0.5 s.

Prior to sample analysis, reference measurements for both spheres were performed. A diffusive gold reflectance standard and the empty BaF₂ window were used for referencing the reflection and the transmission sphere, respectively. These reference measurements also take the inherent reflectance and transmittance properties of BaF₂ into account. Referring the subsequently conducted sample measurements to these references gave the values of R , T and T_{unsc} . Finally, the values of T_{diff} and A were calculated.

All measurements were conducted at room temperature and performed 10 times. Mean values and measurement uncertainties (calculated via error propagation) are shown in the figures as data points and error bars, respectively. If no error bars are visible, the uncertainties are too low to display.

2.2. Sample preparation

PA12 powder (PA2200, EOS GmbH, Germany) was used for all samples. For optical measurements, powder layers and solid thin films were prepared. Powder layers were coated directly onto the BaF₂ window using a quadruple film applicator (Erichsen GmbH & Co. KG, Germany) with gap heights of 150 μm, 200 μm, 250 μm and 300 μm. Thin films were prepared by melting of powder layers of varying thickness in an industrial oven. The layers were allowed to fully melt at 200 °C and were either slowly cooled to room temperature (cooling rate 20 K/h) or rapidly quenched in air to facilitate the correlation of the measured optical properties to the different microstructural characteristics.

For microscopic analysis, a defined amount of PA12 powder was poured into ceramic crucibles and the same melting/solidifying strategy was applied to generate bulk specimens. From these, thin sections were cut and prepared for optical microscopy.

2.3. Microstructural characterization

The microstructure of the thin sections was characterized by means of polarized transmitted light microscopy.

3. Results and discussion

3.1. Optical properties of powder layers compared to solid thin films

To evaluate the influence of particle interfaces on beam propagation within PBF-LB/P powder layers, the measured

optical properties of powder layers are compared to the solidified thin film samples. The resulting values of PA12 powders and thin films (slowly cooled) are shown in Fig. 2 and Fig. 3, respectively.

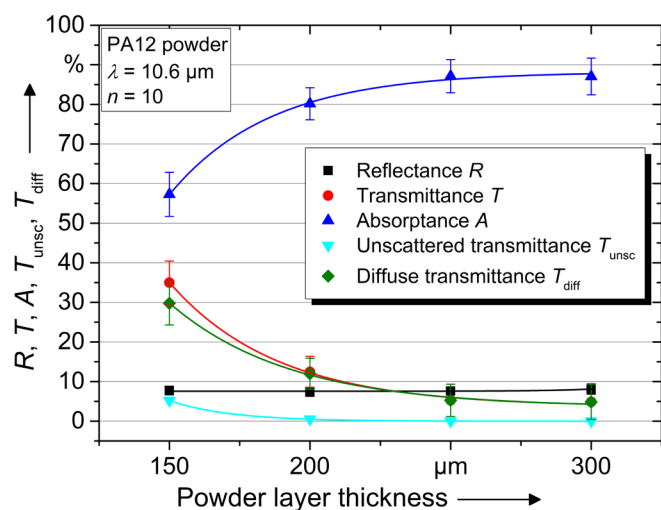


Fig. 2. Optical properties of PA12 powder of varying layer thickness.

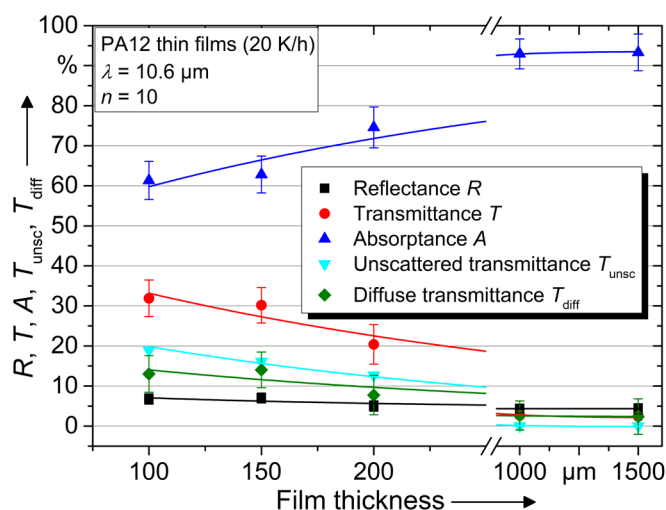


Fig. 3. Optical properties of PA12 thin films (slowly cooled at a rate of 20 K/h) of varying film thickness.

As shown, in both cases the trend of R is independent of sample thickness. However, powder layers exhibit a slightly increased overall R compared to the thin films. This is due to the increased surface roughness of powder layers compared to molten and solidified films [12], leading to diffuse back scattering of photons from the powder surfaces [1] which is not the case for the smooth film surfaces.

The measured portions of transmitted laser power differ significantly between powdery and solid samples. While T mainly consists of T_{diff} in the former (i. e. most of the transmitted radiation is diffusely scattered), the latter exhibits higher values of T_{unsc} . This behavior can be attributed to the effect of multiple scattering through a powder material due to particle-air interfaces and therefore refractive index changes [13], which is not the case in the solid thin films. For a thickness of 150 μm , this leads to an effective increase of T_{diff}

by approximately 15 % for powder compared to thin films. During the PBF-LB/P process, this reduces the probability of the laser beam penetrating into deeper regions of the powder bed. Hence, most of the absorption is considered to take place in near-surface regions [14].

It can furthermore be observed from Fig. 2 that the values of A increase as the powder layer thickness increases until a constant value between 83 % and 91 % is reached. This range of A is in good agreement with values for PA12 powder reported throughout literature [1].

3.2. Correlation of optical properties and microstructure of solid thin films

Fig. 4 depicts the optical properties of the rapidly quenched thin films.

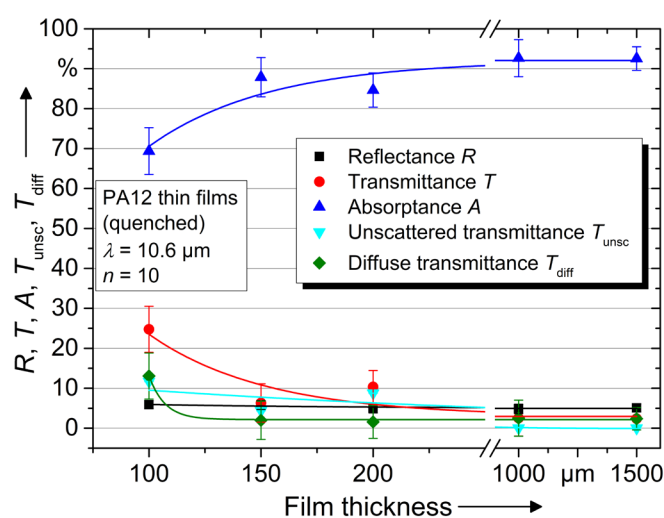


Fig. 4. Optical properties of PA12 thin films (quenched) of varying film thickness.

Since the R -values are the same as in the slowly cooled samples (cf. Fig. 3), the cooling rate does not seem to affect the thin films' reflective properties. This is reasonable since in both cases the polymer was melted completely which determined the resulting surface roughness of the thin films.

On the contrary, the amount of transmitted laser light is strongly influenced by the thermal history (i. e. cooling rate). Regardless of film thickness, the values of both T_{unsc} and T_{diff} (and therefore T) are significantly higher in the case of slowly cooled thin films compared to the quenched samples. This is particularly interesting since the quenching of the molten polymer is expected to lead to (a) the suppression of crystallization, therefore to (b) a low degree of crystallinity (or high degree of amorphousness) [15,16] and ultimately to (c) a higher transmittance than in the case of slowly cooled films.

Still, the observed behavior can be correlated to the applied cooling rate and thus to the resulting microstructural features (see Fig. 5 and the subsequent text passage).

The absorptance values which are therefore mainly determined by the degree of transmission (since reflectance is unaffected by the cooling rate) are higher in the case of quenched thin films.

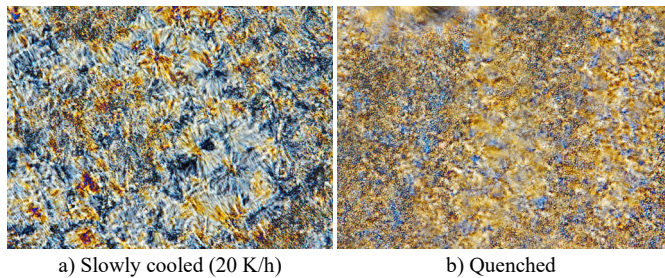


Fig. 5. Polarization microscopy images of PA12 thin sections (scale bars equal 40 μm).

The influence of the cooling rate is reflected in the microscopic structure by the different sizes of spherulites (clearly visible as radially symmetrical lamellae in Fig. 5a). While a low cooling rate leads to a coarsely grained morphology with spherulite sizes of up to about 40 μm (Fig. 5a), the air-quenched samples exhibit a much finer spherulitic structure (Fig. 5b). This observation agrees very well with the measured optical properties: During quenching, the crystallization process is interrupted after a few seconds rather than completely suppressed. After initial nucleation and growth, the quenching results in many small spherulites. Since the number of scattering interfaces (crystalline/amorphous) is higher in these quenched samples, the measured T is lower. On the contrary, if controlled cooling is applied, spherulites can further grow until they impinge on each other. Thus, the effective number of scattering interfaces is reduced and the transmittance increases again.

This effect of increased multiple scattering in the finer microstructure compared to the coarser one leads to an effective increase of A by more than 10 % (cf. Fig. 3 and Fig. 4) depending on the film thickness. These correlations between optical behavior and morphological features are supported very well by theoretical studies found in literature such as [16].

4. Conclusion

The presented experimental results show the suitability of the adapted double-integrating-sphere setup for the analysis of scattering processes during the interaction of a CO_2 laser beam with PBF-LB/P powders.

By measurement of diffuse and unscattered transmittance, scattering mechanisms both within powder layers and inside thin films of different microstructures can be detected and qualitatively evaluated. This can be extremely useful for the optimization of energy deposition during PBF-LB/P and ultimately for enhanced part properties.

A practical example can be the identification of different intraparticle morphologies, since usually a mixture of aged and new powder is processed in PBF-LB/P build jobs. For different ageing histories or varying mixing ratios this could lead to different scattering properties, penetration depths and ultimately process parameters.

In future works, the gained knowledge will be extended by temperature-dependent measurements to obtain insights into the change of scattering properties during phase transitions, which is essential for the development of a process-adapted powder characterization and qualification technique.

Acknowledgements

The authors gratefully acknowledge funding of the Collaborative Research Center 814 (CRC 814), sub-project A3, and of the Erlangen Graduate School in Advanced Optical Technologies (SAOT) by the German Research Foundation (DFG) in the framework of the German excellence initiative.

References

- [1] Wegner A. Theorie über die Fortführung von Aufschmelzvorgängen als Grundvoraussetzung für eine robuste Prozessführung beim Laser-Sintern von Thermoplasten. Dissertation Universität Duisburg-Essen; 2015.
- [2] Poprawe R. Lasertechnik für die Fertigung – Grundlagen, Perspektiven und Beispiele für den innovativen Ingenieur. Springer-Verlag; 2005.
- [3] Pickering JW, Moes CJM, Sterenborg HJCM, Prah SA, van Gemert MJC. Two integrating spheres with an intervening scattering sample. *J Opt Soc Am A* 1992;9:621-31.
- [4] Pickering JW, Prah SA, van Wieringen N, Beek JF, Sterenborg HJCM, van Gemert MJC. Double-integrating-sphere system for measuring the optical properties of tissue. *Appl Opt* 1993;32:399-410.
- [5] Steinberger J. Optimierung des Selektiven-Laser-Sinterns zur Herstellung von Feingußteilen für die Luftfahrtindustrie. Dissertation Technische Universität München; 2001.
- [6] Liu X, Boutaous M, Xin S. Scattering effect in radiative heat transfer during selective laser sintering of polymers. *AIP Conf Proc* 2016;1769.
- [7] Liu X. Numerical modeling and simulation of selective laser sintering in polymer powder bed. Dissertation University of Lyon; 2017.
- [8] Bourell DL, Watt TJ, Leigh DK, Fulcher B. Performance limitations in polymer laser sintering. *Phys Procedia* 2014;56:147-156.
- [9] Laumer T, Stichel T, Sachs M, Amend P, Schmidt M. Qualification and modification of new polymer powders for laser beam melting using Ulbricht spheres. *Proc 6th Int Conf Adv Res Rapid Prototyping* 2013;255-260.
- [10] Laumer T, Stichel T, Nagulin K, Schmidt M. Optical analysis of polymer powder materials for Selective Laser Sintering. *Polym Test* 2016;56:207-213.
- [11] Heint M, Laumer T, Bayer F, Hausotte T. Temperature-dependent optical material properties of polymer powders regarding in-situ measurement techniques in additive manufacturing. *Polym Test* 2018;71:378-383.
- [12] Delfs P, Schmid HJ. Areal Surface Characterization of Laser Sintered Parts for Various Process Parameters. *Proc 28th Ann Int Solid Free Fabr Symp* 2017;2624–2631.
- [13] Papini M. Study of the relationship between particle sizes of polymer powders and their radiative properties. *Infrared Phys* 1993;34:607–619.
- [14] Osmanlic F, Wudy K, Laumer T, Schmidt M, Drummer D, Körner C. Modeling of Laser Beam Absorption in a Polymer Powder Bed. *Polymers* 2018;10:784.
- [15] Nojima S, Marubayashi H. Crystalline Morphology of Homopolymers and Block Copolymers. In: Guo Q, editor. *Polymer Morphology: Principles, Characterization, and Processing*. John Wiley & Sons, Inc; 2016. p. 166.
- [16] Lamberti G, Titomanlio G. Interaction between light and crystallizing polymer: a simulation study. *Eur Polym J* 2005;41:2055-2066.

11th CIRP Conference on Photonic Technologies [LANE 2020] on September 6-10, 2020

Infrared monitoring of modified hatching strategies for laser sintering of polymers

Sandra Greiner^{a,b,*}, Dietmar Drummer^{a,b}

^aCollaborative Research Center 814 - Additive Manufacturing (CRC 814), Am Weichselgarten 9, 91058 Erlangen, Germany

^bInstitute of Polymer Technology (LKT), Am Weichselgarten 9, 91058 Erlangen, Germany

* Corresponding author. Tel.: +49-(0)9131-85-29724; fax: +49-(0)9131-85-29709. E-mail address: sandra.greiner@fau.de

Abstract

In laser sintering of polymers, the exposure strategy, consisting of hatching strategy, laser power and scan speed determines the final properties. In polymer processing, mainly the meander hatching strategy is applied, which leads to geometry-dependent part properties at supposedly identical processing parameters due to overlay effects of temperature fields. Within this work, different hatching strategies, originating from laser beam melting of metals are investigated to overcome the limitations of laser sintering of polymers. The processability is evaluated characterizing single- and multi-layer parts. A direct correlation between the predominant temperature fields resulting from different hatching strategies and the resulting part properties, such as surface topology or part height, could be evidenced. These results contribute to the understanding of the impact of hatching strategy on the laser sintering process and should be considered in the future development of geometry-invariant processing strategies.

© 2020 The Authors. Published by Elsevier B.V.

This is an open access article under the CC BY-NC-ND license (<http://creativecommons.org/licenses/by-nc-nd/4.0/>)

Peer-review under responsibility of the Bayerisches Laserzentrum GmbH

Keywords: Additive Manufacturing, Laser Sintering, Exposure Strategy, Thermography, PA12

1. Introduction

Laser sintering of polymers (LS) allows for the direct fabrication of individualized geometrical structures without the need of support structures. However, the reproducibility of part properties is limited, due to the complexly interacting thermal fields during processing [1,2]. Besides the fundamental thermal influences during the repeating sub-process steps powder coating, exposure and consolidation, the geometry of the exposed cross section affects the resulting temperature fields within the melt [3-5]. Infrared (IR) thermographic investigations, as shown in [6] and [7], allow for the correlation of temperature fields resulting from exposure to the final part properties, which is necessary for the generation of a basic understanding of the LS process. The variation of the exposure parameters, such as laser power, scan speed, hatch distance and the resulting energy density is essential for the optimum part properties and therefore in the focus of most studies [8-10]. In addition to that, the

delay time or laser return time plays a crucial role for the resulting temperature fields and mechanical part properties [11]. In LS, the laser return time can be varied by changing to orientation of the standard meander scan pattern.

In laser beam melting of metals (LBM), a wide range of more elaborate hatching strategies, which can be described as the spatial layout of scan vectors has been under scientific investigation. The impact of spiral [12] or island hatching strategies [13,14], which are similar to a chessboard structure, on temperature distribution, microstructure or part mechanics was studied. Furthermore, fractal hatching strategies based on mathematical area filling curves [15,16] were implemented for LBM. The aim of these strategies is to reduce the scan vector length in order to homogenize the temperature distribution of the melt. The modification of the hatching strategies allows for homogenous melting of the metal material, the processability of new materials and the avoidance of process defects like hot cracks or splatters [17]. However, the potential of a modified

hatching strategy has not been exploited in LS of polymers. A more homogenous temperature distribution as induced by island or fractal hatching strategies bears the potential to improve the reproducibility of part properties. Within this work, different hatching strategies, such as spiral or fractal strategies, originating from laser melting of metals are investigated using IR thermography to study the impact of the temperature fields on part properties and to reveal new potentials for increasing reproducibility of part properties in LS.

2. Experimental

2.1. Material system

Polyamide 12 (PA12) powder (PA 2200, EOS GmbH, Krailling, Germany) is used for the shown LS experiments and the production of single- and multi-layer parts. A refreshed powder mixture of a 50:50 percentage of virgin and used powder was applied. The used powder was taken from overflow containers. Prior to fabrication, the powder system was characterized. Measurements of the bulk density ($0.43 \pm 0.01 \text{ g/cm}^3$) and the viscosity number ($55.3 \pm 2.9 \text{ ml/g}$) of the powder system were performed, indicating a low aging influence compared to virgin powder [18]. Hence, it can be assumed that the fabrication process and the thermographic measurements are largely unaffected.

2.2. Laser sintering system

The experiments were carried out using a freely parameterizable laser sintering system. The build height of the system is 500 mm, the maximum build width and length is 350 mm, respectively. For setting a homogeneous thermal basis for processing, the system is equipped with eight individually controllable infrared quartz radiator arrays. For local energy input, a 50 W CO₂ laser with a focus diameter d_f of 0.4 mm was applied. The exposure strategy, consisting of laser power P_L , scan speed v_s and hatching strategy is openly variable, which is a necessary condition for the present experiments.

2.3. Infrared camera

The measurement of the temperature fields during processing, which were caused by different hatching strategies was performed using the IR thermographic system Velox 1310k SM from IRCAM GmbH (Erlangen, Germany). The camera is capable to detect IR-radiation in a wavelength range of 1.5 μm to 5.5 μm . A sapphire glass window, which is impermeable for the wavelength of the CO₂-laser, but permeable for short wave and medium wave IR, is mounted in front of the camera to prevent the detector from damage. The camera was calibrated according to the manufacturer's specifications and focused on the level of the powder bed surface. The assembly situation and the measured data evaluation was introduced in [5] and is schematically depicted in Fig. 1. The vertical viewing angle of the IR camera was significantly smaller than 30 degree. According to [19], the measurement error originating from viewing angle is accentuated for vertical viewing angles of above 45 degree. The measuring position within the surface of the build chamber and an exemplary thermogram is shown in Fig. 2.

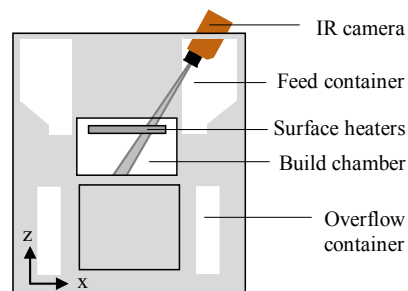


Fig. 1. Schematic depiction of the assembly situation of the IR monitoring system.

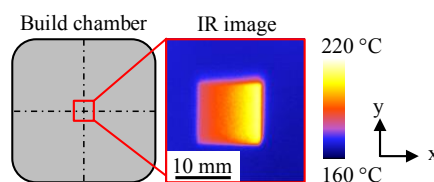


Fig. 2. Schematic depiction of the measuring position for the IR thermograms.

3. Design of experiments

3.1. Exposure experiments

Two different sample geometries were fabricated, varying the underlying hatching strategy. For thermographic investigations, monolayers with a cross-section of 20 x 20 mm² were prepared to study the temperature fields during exposure. In addition, cuboid multilayer parts were prepared with the same cross-section and a height of 2.5 mm to investigate the processability and the resulting part properties, e. g. dimensional accuracy or part density. For all experiments, the basic exposure parameters, such as laser power, scan speed and hatch distance were kept constant. The processing parameters are listed in table 1.

The contours of the samples were fabricated using the same parameters to avoid influences from varied processing parameters of the scan vectors in the samples interior. Four different hatching strategies, partially originating from laser beam melting of metals were applied to study the potential for reproducible part fabrication. In Fig. 3, the four hatching strategies, consisting of differently oriented hatches (or scan vectors) and the outline contours, are schematically depicted. Two different superordinate hatching strategies were applied. On the one hand, standard hatching strategies, like meander or spiral hatching strategies, were analyzed. On the other hand, fractal strategies, which are structurally organized like chessboards, were investigated.

Table 1. Constant processing parameters for monolayer and part fabrication.

Process parameter	Value
Laser power P_L	16 W
Scan speed v_s	2,000 mm/s
Hatch distance h_s	0.2 mm
Contour offset h_c	0.2 mm
Build chamber temperature T_B	172 °C

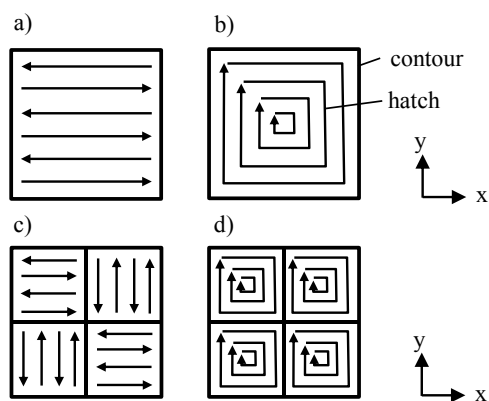


Fig. 3. Standard hatching strategies: (a) meander hatching and (b) spiral hatching; fractal hatching strategies: (c) fractal meander hatching and (d) fractal spiral hatching.

In general, it is possible to assign different properties like hatching strategies to the white or the black fields of the chess-board. In this study, meander and spiral strategies were applied to black and white fields with dimensions of $0.4 \times 0.4 \text{ mm}^2$. Furthermore, different chronological orders of field exposure are possible. In Fig. 4, two different exposure sequences are exemplarily shown for fractal hatching strategies. The sequence in Fig. 4 a) was applied for the following investigations.

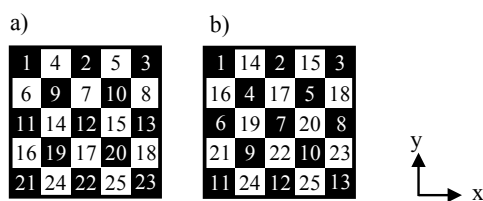


Fig. 4. Exemplary exposure sequences for fractal hatching strategies: (a) line-by-line and (b) field-by-field exposure sequence.

3.2. Thermographic experiments

For the detection of the thermal radiation during processing, the recording format was set to 288 to 288 pixels, which represents an area of around $25 \times 25 \text{ mm}^2$ within the build chamber. The data acquisition rate was adjusted to 355 Hz. The emission coefficient was adapted to the temperature of the powder bed surface, resulting in a value of 0.9 for all experiments. After phase transition from powderous solid to molten material, a reduction of the emissivity is expected and the measured temperatures are lower than the actual temperatures. Within these investigations, this influence was neglected, as the results can be interpreted as parametrically correct because different radiation intensities have been detected. All thermographic measurements were repeated three times. The maximum temperature (T_{max}) during exposure of the fill area, the mean temperature (T_{mean}) at the end of exposure and the duration of exposure t_{exp} were evaluated.

3.3. Part characterization

As the influence of hatching strategy on the resulting part properties has not been object of investigation yet, especially basic part characterization was performed. For documentation

of the monolayer formation, photographs were taken. Scanning electron microscopy (CamScan C20) at 20-x magnification was executed to investigate the appearing surface phenomena. For geometric characterization the multilayer parts' dimensions height, length and width were determined by outside micrometer in the center of each particular site. Furthermore, CT measurements (sub μ -CT, Fraunhofer Institut, Germany) were performed to measure the parts' porosity and to visualize the interior of the sample. CT allows for the porosity evaluation of complexly shaped parts or samples with geometrical or surface defects. The viscosity number (VN) was determined by Ubbelohde viscometer to study the thermal impact of exposure strategy on part aging, using concentrated sulphuric acid as solvent. These measurements were repeated three times.

4. Results and discussion

4.1. Thermographic results

IR measurements were performed to study the thermal household within the monolayers. In Fig. 5, thermograms of the monolayers at half exposure time are depicted and the values for T_{mean} and T_{max} are listed in Table 2. For the standard meander strategy, a thermal gradient can be observed perpendicular to the direction of the scan vectors, which can be assigned to the temporal offset and the cooling of the first scan vectors already taking place. The temperature at exposure site is affected by the laser absorption on the surface of the powder particles, the temperature increase induced by previous scan vectors and heat conduction into the surrounding powder bed.

T_{mean} of the meander hatching strategy is determined to $207 \text{ }^\circ\text{C}$, whereas T_{max} is measured to $219 \text{ }^\circ\text{C}$ at the end of exposure. The spiral hatching strategy leads to a temperature gradient from part outside to part center. Furthermore, hot spots can be detected in the corner points of the spiral, which can be explained by deceleration and acceleration processes due to the direction change of scan vectors. Moreover, the decrease in laser return time leads to higher temperatures with progressing exposure time due to extensive overlapping of thermal fields. On the one hand, this leads to an elevated T_{mean} of $209 \text{ }^\circ\text{C}$, but on the other hand to a significantly higher T_{max} of $285 \text{ }^\circ\text{C}$ in the center of the sample.

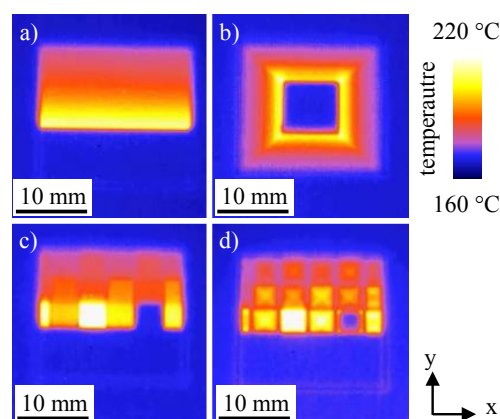


Fig. 5. Thermographic mappings of the different hatching strategies: (a) meander hatching and (b) spiral hatching; fractal hatching strategies: (c) fractal meander hatching and (d) fractal spiral hatching.

Table 2. Results of the thermographic measurements at the end of exposure.

Hatching strategy	T_{mean}	T_{max}	t_{exp}
Meander	206.7 ± 1.7 °C	219.6 ± 1.0 °C	1.6 s
Spiral	209.1 ± 2.5 °C	284.9 ± 2.6 °C	1.6 s
Fractal meander	216.0 ± 0.9 °C	239.5 ± 3.2 °C	1.9 s
Fractal spiral	237.0 ± 1.6 °C	271.4 ± 2.9 °C	1.7 s

The thermograms of the fractal strategies can be seen in Fig. 5 c) and 5 d). In contrast to the standard exposure strategies, no linear gradient is visible along the sample due to the fragmentation of scan vectors, but the influence of the basic hatching strategy, meander or spiral, is still visible. In addition to that, the shorter scan vectors result in higher T_{mean} values of 216 °C and 237 °C and in T_{max} of 240 °C and 271 °C for fractal meander and fractal spiral hatching strategy, respectively. Notably, T_{max} of the fractal spiral hatching strategy is lower than that of the basic strategy, which can be assigned to a lower impact of overlapping scan vectors and cooling processes occurring during exposure of the small fields. For the shown hatching strategies, a significantly differing thermal influence during exposure of single layers is visible.

4.2. Part characterization

Within this section, the influence of thermal fields on the resulting part properties will be discussed. Processability of monolayers and multilayer parts could be ensured. In Fig. 6, photographic images of the fabricated monolayers are shown. To a certain extent, the appearance of the monolayers resembles the thermal structures of the thermograms. The most homogeneous monolayer was prepared by meander hatching, whereas an x-shaped structure is visible for spiral hatching. This structure is corresponding to the hot spots in the corner of the spiral, which is caused by the direction change of scan vectors. In the picture of the sample prepared by the fractal meander hatching, the chessboard structure is clearly visible. Within the field of the chessboard, the sample is homogeneously structured.

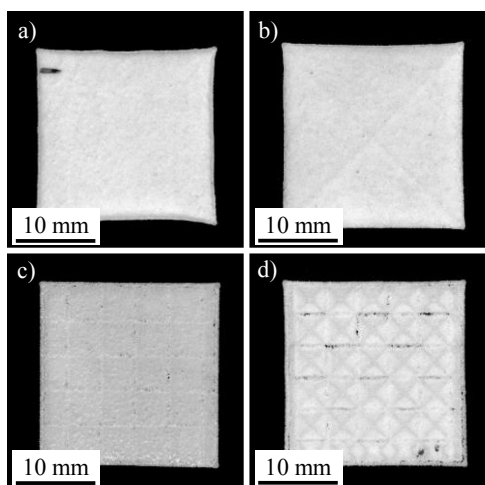


Fig. 6. Photographs of the monolayers fabricated by different hatching strategies: (a) meander hatching and (b) spiral hatching; fractal hatching strategies: (c) fractal meander hatching and (d) fractal spiral hatching.

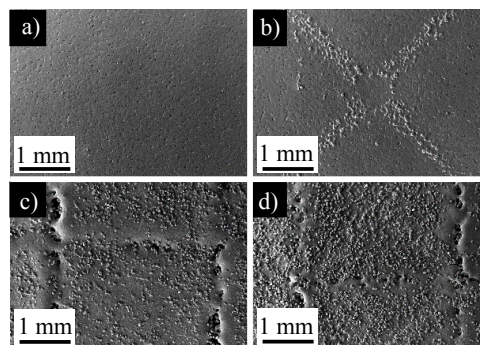


Fig. 7. SEM images of the monolayers fabricated by different hatching strategies: (a) meander hatching and (b) spiral hatching; fractal hatching strategies: (c) fractal meander hatching and (d) fractal spiral hatching.

In contrast to that, the fields of the sample prepared by fractal spiral hatching are characterized by small x-shaped textures, which can be assigned to the local thermal fields. It could be shown, that the morphology of monolayers is corresponding to the prevalent thermal fields and therefore is depending on the hatching strategy.

The SEM images of the part surfaces are shown in Fig. 7. In Fig. 7 a) the surface resulting from meander hatching strategy is depicted and a homogeneous, smooth and slightly porous topology can be observed. The spiral hatching leads to an x-shaped artefact at the location of direction change of the laser beam. At these points, a greater amount of powder is molten onto the surface due to locally higher temperatures. For the fractal strategies, this observation can be confirmed, as the number of particles on the sample surface is significantly higher, which can be correlated to the higher thermographically determined temperature values. Therefore, a link between mean temperature and powder adhesion can be found. In addition, inconstant layer formation can be seen at the overlapping sites of the different exposure areas, which can be correlated to locally delayed material shrinkage at comparably high laser return times. The variation of the contour offset or the overlap distance of the chessboard fields could avoid this phenomenon.

The results of the geometric characterization are summarized in Table 3. Especially the increase in height dimension can be correlated to an increasing T_{mean} as more material is molten. However, for the geometric differences of cross-sectional area, the total temperature level and the temperature difference between T_{max} and T_{mean} could be made responsible as it might affect the shrinking behavior. CT measurements of the samples are depicted in Fig. 8.

Table 3. Results of the geometric characterization, the porosity and V/N .

Hatching strategy	Height in mm	Cross section in mm	Porosity in %	V/N in ml/g
Meander	2.50 ± 0.08	396.5 ± 2.5	4.9	70.3 ± 0.6
Spiral	2.53 ± 0.09	390.4 ± 5.7	5.2	74.3 ± 1.2
Fractal meander	2.61 ± 0.07	400.7 ± 8.2	4.9	74.0 ± 1.0
Fractal spiral	2.76 ± 0.08	406.0 ± 7.4	3.0	77.7 ± 2.5

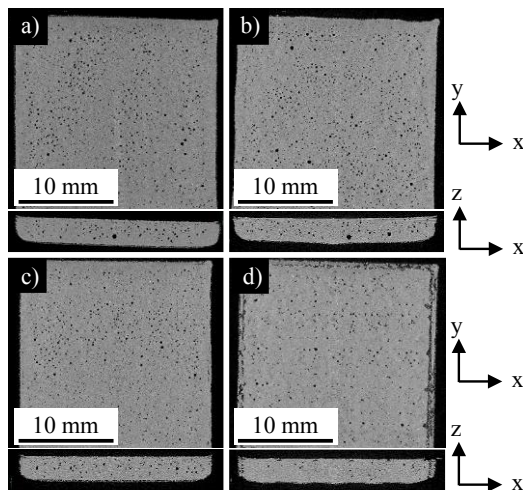


Fig. 8. CT slice planes of the samples fabricated by different hatching strategies: (a) meander hatching and (b) spiral hatching; fractal hatching strategies: (c) fractal meander hatching and (d) fractal spiral hatching.

Shrinkage induced geometric deviations in x-y-plane can be observed for the samples, whereas in x-z-plane especially for the spiral strategies local geometric deviations due to heat accumulations can be observed. The resulting porosities are ranging between 3.0 % and 5.2 %, with the lowest porosity for the sample with the highest T_{mean} . For the other samples, comparable porosity values can be observed. Besides geometric characterization, the results for the measurement of the viscosity number can be found in Table 3. It can be seen, that compared to the VN value of the powder mixture, the VN is increasing for all of the samples. In addition to that, spiral hatching strategies result in higher VN values, and especially comparing standard to fractal hatching strategies, the latter result in higher values, respectively. An increase of the VN value can be an indicator for post condensational aging of PA12, which is dependent on a temperature-time relation. However, for an assessment of the change of the molecular weight distribution, gas chromatography measurements should be performed [20].

5. Conclusion and outlook

Within these investigations, processability of different hatching strategies, originating from LBM, could be proven. These hatching strategies greatly determine the prevalent temperature fields of the monolayers and the resulting part properties. Furthermore, different topological structures are originating from different hatching strategies and their temperature fields, respectively. This could either be used for surface structuring, locally graded part properties or be avoided by varying the overlap distance between the fields of the fractal strategies. Especially for extensive cross sections and for avoiding thermal overlapping, fractal hatching strategies can be expedient, whereas for small cross sections, they are not applicable. However, in contrast to LBM, no mayor impact of the hatching strategy on the morphologic structure within the sample is visible, indicating a limited transferability of the LBM findings to LS of polymers due to different material and process characteristics.

Prospectively, optimization of processing parameters and the assessment of mechanical properties depending on the applied hatching strategies will be performed. Furthermore, the combination of different hatching strategies and the development of new strategies for layer dependent and geometric optimization will be in the focus of the authors future work, in order to drive LS towards a geometry invariant technology.

Acknowledgements

Funded by the Deutsche Forschungsgemeinschaft (DFG, German Research Foundation)-Project-ID 61375930- SFB 814 „Additive Manufacturing“ TP B03.

References

- [1] Rietzel D, Drexler M, Kühnlein F, Drummer D. Influence of temperature fields on the processing of polymer powders by means of laser and mask sintering technology. Proceedings of the Solid Freeform Fabrication Symposium 2011;252-62.
- [2] Josupeit S. On the influence of thermal histories within part cakes on the polymer laser sintering process, Dissertation, Forschungsberichte des Direct Manufacturing Research Centers, ISBN: 978-3-8440-6720-0, 2019.
- [3] Drummer D, Greiner S, Zhao M, Wudy K. A novel approach for understanding laser sintering of polymers, Additive Manufacturing 2019;27:379-88.
- [4] Wegner A. Theorie über die Fortführung von Aufschmelzvorgängen als Grundvoraussetzung für eine robuste Prozessführung beim Laser-Sintern von Thermoplasten, Dissertation, Universität Duisburg-Essen, 2015.
- [5] Greiner S, Wudy K, Wörz A, Drummer D. Thermographic investigation of laser-induced temperature fields in selective laser beam melting of polymers. Optics & Laser Technology 2019;109:569-76.
- [6] Wegner A, Witt G. Understanding the decisive thermal processes in laser sintering of polyamide 12. AIP Conference Proceedings. 2015;1664:160004.
- [7] Walker Wroe W, Gladstone J, Phillips T, Fish S, Beaman J, McElroy A. In-situ thermal image correlation with mechanical properties of nylon-12 in SLS, Rapid Prototyping Journal 2016;22:5:832-846.
- [8] Wörz A, Drummer D. Understanding hatch-dependent part properties in SLS. Proceedings of the 29th Annual International Solid Freeform Fabrication Symposium 2018:1561-69.
- [9] Caulfield B, McHugh PE, Lohfeld S. Dependence of mechanical properties of polyamide components on build parameters in the SLS process. J Mater Process Technol 2007;182:477–88.
- [10] Pilipovic A, Brajliah T, Drstvenšek I. Influence of processing parameters on tensile properties of SLS polymer product, Polymers 2018; 10(11):1208.
- [11] Jain PK, Pandey PM, Rao PVM. Effect of delay time on part strength in selective laser sintering, Int J Adv Manuf Technol 2009;43:117-26.
- [12] Jhabvala J, Boillat E, Antignac T, Glardon R. Study and simulation of different scanning strategies in SLM, Innovative Developments in Design and Manufacturing, 2009.
- [13] Yanjin L, Wu S, Gan Y, Huang T. Study on the microstructure, mechanical property and residual stress of SLM Inconel-718 alloy manufactured by differing island scanning strategy, Optics & Laser Technology 2015;75:197-206.
- [14] Carter NC, Martin C, Withers PJ, Attallah MM. The influence of the laser scan strategy on grain structure and cracking behaviour in SLM powder-bed fabricated nickel superalloy, Journal of Alloys and Compounds 2014;615:228-47.
- [15] Catchpole-Smith S, Aboulkhair N, Parry L, Tuck C, Ashcroft I A, Clare A. Fractal scan strategies for selective laser melting of ‘unweldable’nickel superalloys, Additive Manufacturing 2017;15:113-22.
- [16] Yang J, Bin H, Zhang X, Liu Z. Fractal scanning path generation and control system for selective laser sintering (SLS), International Journal of Machine Tools & Manufacture 2003;43:293-300.

- [17] König-Urban K, Uhlmann E. Additive Fertigung von Nickelbasis-Superlegierungen mittels Laserstrahlschmelzen am Beispiel von Diamalloy 4004NS, Dissertation, Berichte aus dem Produktionstechnischen Zentrum Berlin, ISBN 978-3-8396-0978-1, 2016.
- [18] Wudy K. Alterungsverhalten von Polyamid 12 beim selektiven Lasersintern. Dissertation, Friedrich-Alexander Universität Erlangen-Nürnberg; ISBN: 978-3-931864-72-9, 2017.
- [19] Muniz PR, Cani SPN, Magalhães R da S. Influence of field of view of thermal imagers and angle of view on temperature measurements by infrared thermovision, IEEE Sensors Journal 2014;14:3:729-733.
- [20] Wudy K, Drummer D. Aging effects of polyamide 12 in selective laser sintering: Molecular weight distribution and thermal properties. Additive Manufacturing 2019;25:1-9.

11th CIRP Conference on Photonic Technologies [LANE 2020] on September 7-10, 2020

On the Development of Polymer Particles for Laser Powder Bed Fusion via Precipitation

Maximilian A. Dechet^a, Jochen Schmidt^{a,*}

^a*Institute of Particle Technology, Friedrich-Alexander-Universität Erlangen-Nürnberg, Cauerstraße 4, D-91058 Erlangen, Germany*

^b*Interdisciplinary Center for Functional Particle Systems, Friedrich-Alexander-Universität Erlangen-Nürnberg, Haberstraße 9a, D-91058 Erlangen, Germany*

* Corresponding author. Tel.: +49-9131-85-29404; fax: +49-9131-85-29402. E-mail address: jochen.schmidt@fau.de

Abstract

In this contribution, some aspects of the development of powder bed fusion (PBF) feedstock powders via the solution-dissolution process, also known as precipitation, are exemplarily addressed based on the authors' own work. The development is based on the selection of an appropriate polymer-solvent system, followed by the investigation of the cloud point diagram. After identification of a polymer-solvent system for precipitation, process-product relations, i.e. the influence of stirring, concentration and thermal regime on particle size distribution and shape, can be assessed. Via thorough product characterization concerning, amongst others, flowability and thermal properties, not only applicable PBF process parameters, but also necessary in-situ additive-enhancement with thermal stabilizers or post-processing with flow aids can be derived.

© 2020 The Authors. Published by Elsevier B.V.

This is an open access article under the CC BY-NC-ND license (<http://creativecommons.org/licenses/by-nc-nd/4.0/>)

Peer-review under responsibility of the Bayerisches Laserzentrum GmbH

Keywords: Additive Manufacturing; Powder bed fusion; Particles, Polymers, Precipitation, Feedstock

1. Introduction

Additive manufacturing via powder bed fusion (PBF) of polymers yields parts of high mechanical strength, while offering large freedom of design. In PBF, the powder feedstock is spread as a homogeneous layer onto a building platform. Then, the contours of the part cross-section to be built are selectively fused by a CO₂ laser. Finally, the platform is lowered and the process is repeated. The process is run at elevated temperature (c.f. building chamber temperature), which typically lies between the onset of melting and the onset of crystallization, i.e. the so-called process window [1]. However, the powder feedstock applicable in PBF needs to be tailor-made for the application. The polymers need to exhibit a narrow particle size distribution, high flowability (spreadability), suitable rheological properties, high crystallinity for good detail precision (c.f. sharp solid melt transition), moderate isothermal crystallization kinetics at the building chamber temperature to prevent curling, a sufficiently

wide enough process window and PBF relevant optical properties (c.f. laser absorption), to only name a few [2,3]. Due to these rigid and demanding requirements, the choice of commercially available PBF feedstock materials is still limited. The market was and is dominated [4] by polyamide 12 (PA12) and its additive-enhanced variants, which are manufactured via the precipitation process in ethanol [5]. Other processes yielding PBF feedstocks include cryo-milling [6], co-extrusion [7], (thermal) rounding [8] and melt-based processes like emulsification [9] or fiber decomposition [10]. While there are other materials available, e.g. polypropylene, thermoplastic urethanes or other polyamides, they often appear less optimized for PBF as the PA12 material [1,2]. This can lead to diminished processability, resulting in build-jobs with low reproducibility and deviating part properties and tolerances, rendering such feedstock materials problematic for industrial applications [1,2,4]. Therefore, there is still a need for research on PBF feedstock materials and on processes to obtain them. For this purpose, we focused on the precipitation process, which is well-

known for PA12, with the aim to make it applicable to other thermoplastics. Interestingly, reports in the open literature on the application of liquid-liquid phase separation and precipitation for production of polymer PBF feedstock powders are scarce and virtually limited to the work of the authors and some other groups [1,10–17]. Though, in an academic environment, contrary to large chemical corporations, the full development control starting from petro or renewable raw feed material, over the polymerization, additive-enhancement and post-processing is lacking, there are still many insights able to be gained. In the following, we want to showcase important aspects of the PBF feedstock development, based on our own results. Starting from the selection of an appropriate polymer-solvent system, followed by the investigation of the cloud point diagram, the process-product dependencies, i.e. the influence of stirring, concentration and thermal regime on particle size distribution (PSD) and shape can be investigated. PBF process parameters, but also the possible need for in-situ additive-enhancement with e.g. thermal stabilizers or post-processing with flow aids can be derived, based on thorough powder characterization.

2. Identification of Polymer-Solvent Systems

First, a polymer, or to be more precise, a plastic has to be selected for PBF feedstock manufacturing. While, as outlined above, the formulation of a tailor-made PBF-grade plastic is most probably not an option, some reports suggest, that injection molding grade plastics are a good enough choice for the feed material [13,18]. The precipitation or solution-dissolution process requires so called ‘moderate’ solvents, which only act as solvents for the appropriate polymer at elevated temperatures. Upon cooling, the moderate solvent does not act as a solvent anymore. Fundamental to the process is the exploitation of a miscibility gap in the system [19]. After the polymer is fully dissolved, the system is cooled down and reaches the miscibility gap characterized by a binodal and a spinodal [20]. For the PBF feedstock production, especially the metastable area enclosed by the binodal and the spinodal is important, as, after a temperature-dependent induction time, liquid-liquid phase separation (LLPS) and subsequent nucleation and growth set in [21]. Small, polymer-rich droplets are forming and grow. The droplets are furthermore affected by coalescence, Ostwald ripening and, via stirring, shear-induced droplet breakup or collision [13]. Consequently, polymer solidification or crystallization begins in the polymer-rich droplets and micro particles are precipitated. In order to identify suitable moderate solvents, solubility parameters, especially Hansen solubility parameters [22] have proven to be useful as a criterion for the pre-selection of solvents prior to a screening study. The Hansen parameters give information on the interaction of the polymer with the solvent with respect to dispersion forces (c.f. dispersive Hansen parameter, δ_d), polar interactions (δ_p) and hydrogen bond interactions (δ_h). Based on these single contributions, the total Hansen parameter δ_t can be calculated and the difference in total Hansen parameter $\Delta\delta_t$ between the polymer and the respective solvent can be assessed. Based on this assessment, a threshold value for $\Delta\delta_t$ can be assigned, where polymer-solvent pairings outside this

threshold are ruled out. While e.g. a threshold of $\Delta\delta_t \leq 2.5 \text{ MPa}^{1/2}$ proved viable for poly(L-lactide) (PLLA) [23], the PA12-ethanol system exhibits a $\Delta\delta_t$ of $4.3 \text{ MPa}^{1/2}$. Furthermore, solvents known to act as a good solvent, i.e. dissolving the polymer at room temperature, should be ruled out. Additionally, the solvent hazardousness, cost, recyclability and vapor pressure should be considered. Since in the precipitation process, the particles need to be dried, higher volatility of the solvent renders the drying process more efficient. Considering these aspects, ethanol is a superb solvent for PA12, as, except for its high flammability, it is non-toxic, cheap, evaporates easily and can be re-used after purification via rectification. Each of the pre-selected potential solvents is then tested in a screening study, e.g. in autoclaves [23], and assessed according to whether particles are obtained. As an example, a TEAS plot of a screening study for polyvinylidene difluoride (PVDF), adapted from [17], with successful and non-successful solvents is displayed in Figure 1. Each solvent and PVDF are depicted in the ternary TEAS plot based on their Hansen parameters according to Eq. 1.

$$f(\delta_x) = 100 * \frac{\delta_x}{(\delta_d + \delta_p + \delta_h)} \quad (1)$$

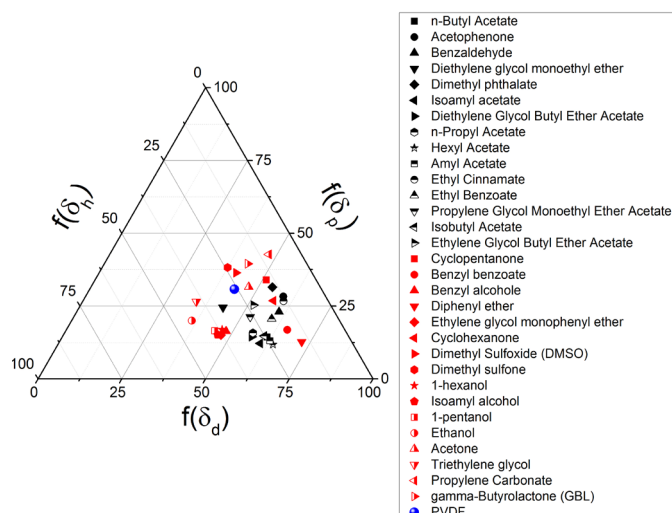


Fig. 1. TEAS plot for the screening study of moderate solvents yielding PVDF particles in the precipitation process; adapted from [17]. PVDF (blue symbol) particles could be successfully obtained from the solvents with black symbols, while the solvents with red symbols did not yield appropriate particles. Complete overview of displayed solvents is listed in [17].

This solubility parameter approach has been successfully reported for the manufacture of particles comprising polypropylene (PP) [11], polyethylene terephthalate (PET) [16], polybutylene terephthalate (PBT) [16], PLLA [23], polycarbonate (PC) [14], polyoxymethylene (POM) [12] and will most probably also work for other polymers, e.g. polyetherimide (PEI) and many more.

3. Cloud Point Diagram

Once a suitable solvent is identified, knowledge on the temperature of dissolution and the cloud point, i.e. the temperature where LLPS sets in, depending on the system composition is needed, in order to transfer the process to a

reactor or autoclave system. The knowledge on the system behavior is important to derive suitable process temperature profiles and process control. While of course, also the full exploration of the phase diagram, which deviates strongly from the ideal binary phase diagram due to the heterogeneity in molecular weight of technical polymers, for a polymer-solvent system is possible (c.f. polystyrene / cyclohexane [20]), it is very tedious and cumbersome. Depending on the boiling point of the solvent, cloud points can be easily determined in open systems, e.g. in a beaker [23] or it might be necessary to investigate them in a pressure resistant optical cell as demonstrated for the PA11-ethanol system [13]. As an example, in Fig. 2, the cloud points and the approximate dissolution temperatures are given for PBT (Ultradrur B4520, BASF) in propylene carbonate, γ -butyrolactone and cyclopentanone.

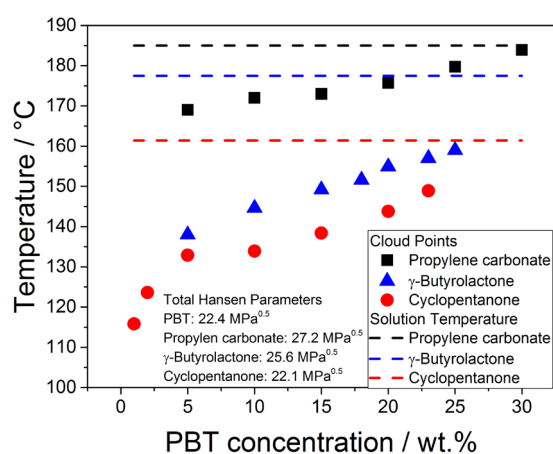


Fig. 2. Cloud points and approximate dissolution temperatures in dependence of PBT concentration in propylene carbonate, γ -butyrolactone and cyclopentanone. Dissolution temperatures indicate full dissolution of PBT feed granules. Also displayed are the δ_i values of the components.

It can be clearly observed, that dissolution temperatures and cloud points are a function of the respective solvent, i.e. these characteristic temperatures are directly linked to the compatibility of the polymer-solvent system as expressed by $\Delta\delta_i$. Higher compatibility results in lower temperatures of dissolution and, subsequently, lower cloud-points, which is well reflected for PBT in cyclopentanone, γ -butyrolactone and propylene carbonate with $\Delta\delta_i$ of 0.3 MPa^{1/2}, 3.2 MPa^{1/2} and 4.8 MPa^{1/2}. Another point, which should be considered as well, is the effect of the precipitation process on the molecular weight distribution (MWD). The solvent itself, potential contaminations and water, in combination with the minimum dissolution temperature predefined by the solvent, could contribute towards polymer chain degradation. For the systems depicted in Fig. 2 with the highest and lowest compatibility, a MWD degradation, assessed via gel permeation chromatography, from 43.39 kDa for the PBT feed material to 41.23 kDa and 17.99 kDa could be determined for PBT particles precipitated from cyclopentanone and propylene carbonate, respectively [16]. Therefore, cyclopentanone appears as a very favourable solvent for PBT PBF feedstock production, as it requires low dissolution temperatures, is non-toxic, shows no significant chain degradation, is obtainable in

large quantities and can be easily evaporated during particle drying.

The cloud-point measurements are typically performed with continuous cooling after dissolution of the polymer. Therefore, the observed cloud points are close to the spinodal, i.e. the lower boundary of the metastable area. However, when the precipitation process is scaled up to several cubic meters of reactor volume, continuous cooling seems impractical. In this case, after dissolution of the polymer, it might be more reasonable to approach a certain temperature in the metastable area, or even two, where one acts as nucleating step [24]. There, LLPS sets in after a temperature dependent induction time, which is shorter for temperatures closer to the spinodal and longer for temperatures closer to the binodal. Above the binodal, no LLPS takes place. Knowledge of the induction times yields time-efficient process operation and can be obtained by isothermal cloud point experiments. In Fig. 3 (a), the cloud point diagram of a PA11-ethanol system, including isothermal cloud points and an estimate of the binodal is depicted. In Fig. 3(b) the obtained induction times are plotted and interpolated according to [21] for different PA11 concentrations. Via this plot, induction times for different concentrations at different temperatures in the metastable area can be approximated.

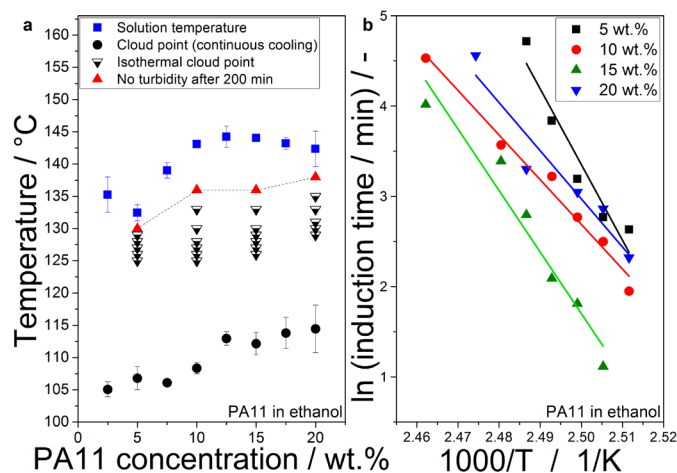


Fig. 3. (a) Cloud point diagram of a PA11-ethanol system, depicting cloud points obtained from continuous cooling, isothermal cloud points, an estimate of the binodal, where after waiting for 200 min no turbidity, i.e. cloud point, could be observed and, the dissolution temperature. (b) Plot of the determined induction times from the isothermal cloud point measurements.

4. Process-Product dependencies

Based on the cloud point diagram, the process can now be transferred to an autoclave or reactor system. Important process parameters governing the particle properties, c.f. PSD, shape, porosity etc., are stirring, temperature profile and initial polymer concentration. While many implications of the process parameters on the LLPS process, the formed droplets and subsequently the obtained particles, are discussed in detail in [13] and references therein, in this contribution we want to focus on the stirring conditions and give an example for a PBT-cyclopentanone system. The stirring conditions strongly affect the obtained PSD, as intense stirring leads to smaller particles. In Fig. 4, the PSDs of PBT particles precipitated from

cyclopentanone under varying stirrer speeds are displayed. Additionally, also the mean particle size $x_{50,3}$ and the distribution width, given as span, calculated according to Eq. 2, are displayed.

$$\text{span} = \frac{x_{90,3} - x_{10,3}}{x_{50,3}} \quad (2)$$

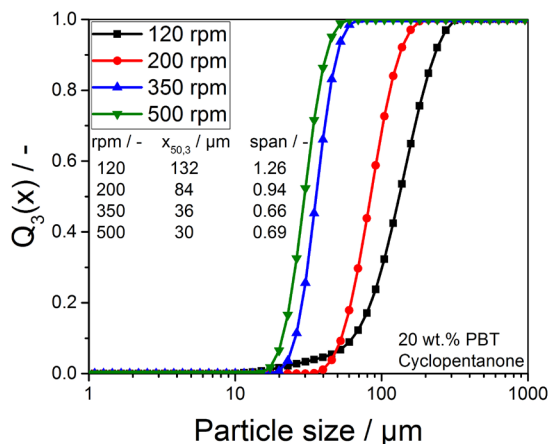


Fig. 4. PSDs of PBT particles precipitated from cyclopentanone under varying stirring conditions. Also given are the mean particle size $x_{50,3}$ and the span of the particles. The employed PBT concentration was 20 wt.%. The experiments were conducted in a 3L autoclave system (versoclave Typ 3E/3.0 lt., 200 bar, 300°C)

As can be seen, depending on the stirring conditions, larger, broader distributed particles or smaller, narrowly distributed particles can be obtained. Typically, particles in the size range 30 μm to 90 μm with a span below 1 are favored for PBF, as they exhibit high packing density and ensure homogeneously spread layers [2].

5. Particle characterization

In order to assess the suitability of the precipitated particles, thorough characterization is needed. Next to the PSD, imaging of the particles via electron microscopy gives insight on the particle shape and especially the particle surface and morphology. Fig. 5 (a-d) shows exemplary PBT particles, PET particles precipitated using PET beverage bottles as feed material [16], PVDF particles and PLLA particles, respectively. In addition to the relative spherical particle shape, the precipitation process yields particles with very high degrees of crystallinity [13,23] and can yield even semi-crystalline particles for polymers which are typically hard to crystallize, as e.g. PC [14].

This high crystallinity, which can be determined by the melt enthalpy or solid density [23], is often unmatched by cryo-milled feedstock. However, it offers a sharp transition from solid to melt, which leads especially at the boundaries of the part to fewer sticking particles, which increases the surface properties and the detail precision. Further characterization should include measurement of flowability, by e.g. a ring shear tester [13], a powder tensile strength tester [23] or a rotating drum. Also, amongst others, the thermal properties, i.e. process window and isothermal crystallization kinetics, the mass-specific surface area and structural properties, e.g. obtainable

via X-ray diffraction, should be assessed. A comprehensive characterization of a precipitated PBF feedstock is outlined in [13].

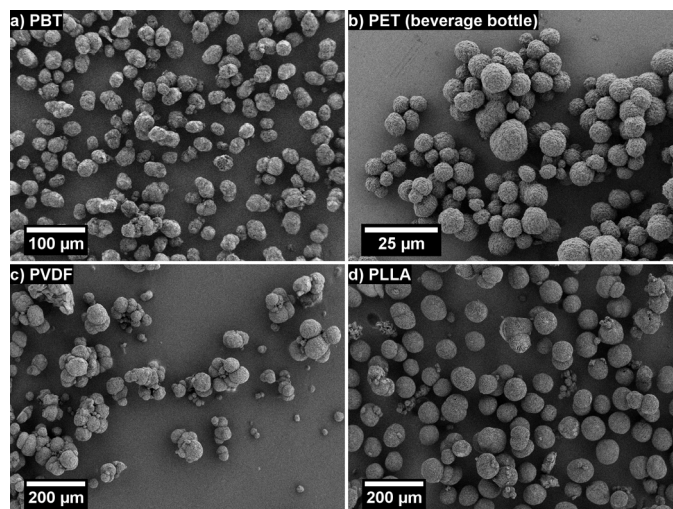


Fig. 5. (a) PBT particles precipitated from cyclopentanone [16]. (b) PET particles precipitated from cyclopentanone using a PET beverage bottle as feed material [16]. (c) PVDF particles precipitated from diethylene glycol n-butyl ether acetate [17]. (d) PLLA particles precipitated from triacetin [23].

6. Post-processing and PBF application

Based on the performed characterization, the need for post-processing and a range of suitable PBF parameters can be derived. The most widespread post-processing operations for PBF feedstock are sieving and classifying of the particles in order to optimize the PSD and dry coating with nanoparticles to increase the flowability [2]. Especially dry coating can drastically enhance powder flowability and spreadability in the PBF process, which is why commercial PBF feedstocks are typically dry coated [13]. Suitable PBF process parameters, which can be easily obtained from the powder characterization, are e.g. the layer height, which is reflected in the PSD, the building chamber temperature, which can be derived from the determined process window, the isothermal crystallization kinetics, and, to some degree, the laser power or energy input, which should in any case surpass the melt enthalpy to ensure full melting of the powder. Further details on the PBF processing itself are not addressed here, but can be found elsewhere, see e.g. [25].

7. Additive-enhancement and functionalization

Lastly, we want to address the unique possibilities the precipitation process offers concerning the additive-enhancement and in situ functionalization of the particles, i.e. during the precipitation process. By adding fibers, e.g. glass [26] or carbon, to the plastic feed material and the moderate solvent, manufacturing of fiber filled particles for PBF [15], yielding fiber-reinforced parts, is possible. Furthermore, also nanoparticle-filled particles are obtainable, via addition of dispersed nanoparticles to the moderate solvent [27]. Depending on the choice of nanoparticles, a wide range of functionalization is accessible, e.g. enhanced mechanical properties, whitening or increased thermal stability. Another

very interesting possibility is the addition of specific plastic additives to the process. Fig. 6 shows exemplary the effect of added antioxidants to the precipitation. Naturally, also the addition of flame retardants, anti-static agents, pigments, colors and many more, solely or together, can be imagined.

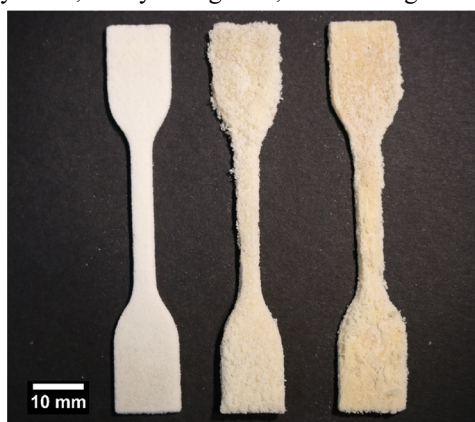


Fig. 6. Image of PA11 tensile test specimens manufactured via PBF with a Sharebot SnowWhite desktop device using PA11 feedstock with 0.5 wt.% primary and 2 wt.% secondary antioxidant (left), 0.05 wt.% primary and 0.2 wt.% secondary antioxidant (middle), without any antioxidants (right).

8. Conclusion

In this contribution, we highlighted important aspects of the development of PBF polymer feedstocks, based on the precipitation process investigated in our group. From solvent selection, cloud point determination, process-product dependencies, product characterization, functionalization and application, the precipitation process offers huge possibilities to produce tailor-made PBF feedstock materials.

Acknowledgements

We thank the German Research Foundation (DFG) for funding this work in the framework of the priority program 2122 “Materials for Additive Manufacturing”, grant SCHM3230 1-1, project-ID 409808524.

References

- [1] Ligon SC, Liska R, Stampfl J, Gurr M, Mülhaupt R. Polymers for 3D Printing and Customized Additive Manufacturing. *Chem Rev* 2017;**117**:10212–90.
- [2] Schmid M. *Laser Sintering with Plastics* München: Carl Hanser Verlag GmbH & Co. KG; 2018.
- [3] Schmid M, Amado A, Wegener K. Polymer powders for selective laser sintering (SLS). *Proc PPS-30 30th Int Conf Polym Process Soc – Conf Pap* 2015:160009.
- [4] Wohlers TT. *Wohlers Report 2016* Fort Collins, Col.: Wohlers Associates; 2016.
- [5] Monsheimer S, Grebe M, Baumann F-E, von der Bey E. DE102004010160 (A1) — 2005-09-15 2005.
- [6] Gayer C, Ritter J, Bullemer M, Grom S, et al. Development of a solvent-free polylactide/calcium carbonate composite for selective laser sintering of bone tissue engineering scaffolds. *Mater Sci Eng C* 2019;**101**:660–73.
- [7] Kleijnen R, Schmid M, Wegener K. Production and Processing of a Spherical Polybutylene Terephthalate Powder for Laser Sintering. *Appl Sci* 2019;**9**:1308.
- [8] Schmidt J, Sachs M, Fanselow S, Zhao M, et al. Optimized polybutylene terephthalate powders for selective laser beam melting. *Chem Eng Sci* 2016;**156**:1–10.
- [9] Fanselow S, Emamjomeh SE, Wirth KE, Schmidt J, Peukert W. Production of spherical wax and polyolefin microparticles by melt emulsification for additive manufacturing. *Chem Eng Sci* 2016;**141**:282–92.
- [10] Zhou Y, Xi S, Huang Y, Kong M, et al. Preparation of near-spherical PA12 particles for selective laser sintering via Plateau-Rayleigh instability of molten fibers. *Mater Des* 2020;**190**:108578.
- [11] Wang S-J, Liu J-Y, Chu L-Q, Zou H, et al. Preparation of polypropylene microspheres for selective laser sintering via thermal-induced phase separation: Roles of liquid-liquid phase separation and crystallization. *J Polym Sci Part B Polym Phys* 2017;**55**:320–29.
- [12] Dechet MA, Baumeister I, Schmidt J. Development of Polyoxymethylene Particles via the Solution-Dissolution Process and Application to the Powder Bed Fusion of Polymers. *Materials (Basel)* 2020;**13**:1535.
- [13] Dechet MA, Goblirsch A, Romeis S, Zhao M, et al. Production of polyamide 11 microparticles for Additive Manufacturing by liquid-liquid phase separation and precipitation. *Chem Eng Sci* 2019;**197**:11–25.
- [14] Kloos S, Dechet MA, Peukert W, Schmidt J. Production of spherical semi-crystalline polycarbonate microparticles for Additive Manufacturing by liquid-liquid phase separation. *Powder Technol* 2018;**335**:275–84.
- [15] Yan C, Hao L, Xu L, Shi Y. Preparation, characterisation and processing of carbon fibre/polyamide-12 composites for selective laser sintering. *Compos Sci Technol* 2011;**71**:1834–41.
- [16] Dechet MA, Kloos S, Schmidt J, Peukert W. WO2019185582 2019.
- [17] Dechet MA, Kloos S, Schmidt J, Peukert W. WO2019185583 2019.
- [18] Haworth B, Hopkinson N, Hitt D, Zhong X. Shear viscosity measurements on Polyamide-12 polymers for laser sintering. *Rapid Prototyp J* 2013;**19**:28–36.
- [19] van de Witte P, Dijkstra PJJ, van den Berg JWAW a, Feijen J. Phase separation processes in polymer solutions in relation to membrane formation. *J Memb Sci* 1996;**117**:1–31.
- [20] Rehage G, Möller D, Ernst O. *Entmischungerscheinungen in Lösungen von molekularuneinheitlichen Hochpolymeren*. *Die Makromol Chemie* 1965;**88**:232–55.
- [21] van Emmerik PT, Smolders CA. Liquid-liquid phase separation by nucleation and growth in solutions of poly(2,6 dimethyl-1,4 phenylene oxide) in toluene. *Eur Polym J* 1973;**9**:931–40.
- [22] Hansen CM. *Hansen Solubility Parameters*, 2nd ed. Boca Raton: Taylor & Francis; 2007.
- [23] Dechet MA, Demina A, Römling L, Gómez Bonilla JS, et al. Development of poly(L-lactide) (PLLA) microspheres precipitated from triacetin for application in powder bed fusion of polymers. *Addit Manuf* 2020;**32**:100966.
- [24] Baumann FE, Wilczok N. DE19708946 1998.
- [25] Drummer D, Rietzel D, Kühnlein F. Development of a characterization approach for the sintering behavior of new thermoplastics for selective laser sintering. *Phys Procedia* 2010;**5**:533–42.
- [26] Dechet MA, Lanzl L, Werner Y, Drummer D, et al. Manufacturing and Application of PA11-Glass Fiber Composite Particles for Selective Laser Sintering. *Proc 30th Annu Int Solid Free Fabr Symp* 2019:1022–30.
- [27] Dechet MA, Lanzl L, Wilden A, Sattes M, et al. Manufacturing of Nanoparticle-Filled PA11 Composite Particles for Selective Laser Sintering. *Proc 30th Annu Int Solid Free Fabr Symp* 2019:1031–40.

11th CIRP Conference on Photonic Technologies [LANE 2020] on September 7-10, 2020

Production of PBT/PC multi-material particles via a combination of co-grinding and spray-agglomeration for powder bed fusion

F.Riedel^a, B.Düsenberg^a, J.Schmidt^a, A.Bück^a, W.Peukert^{a,*}

^a*Institute of Particle Technology, Friedrich-Alexander-Universität Erlangen-Nürnberg, Cauerstraße 4, Erlangen 91052, Germany*

* Corresponding author. Tel.: +49 9131 85-29400. E-mail address: wolfgang.peukert@fau.de

Abstract

Polybutylene terephthalate (PBT) – polycarbonate (PC) multi-materials with a PBT mass content of 25% to 75% were produced for the powder bed fusion process by the means of co-grinding and spray agglomeration. The influence of the PC content and the process parameters on the thermal properties of the obtained powders are discussed in detail. Compared to pure PBT powder, the PBT/PC multi-materials crystallize at lower temperatures, which improves the handling during the additive manufacturing process.

© 2020 The Authors. Published by Elsevier B.V.

This is an open access article under the CC BY-NC-ND license (<http://creativecommons.org/licenses/by-nc-nd/4.0/>)

Peer-review under responsibility of the Bayerisches Laserzentrum GmbH

Keywords: multi-material particles; polycarbonate; polybutylene terephthalate; comminution; spray agglomeration

1. Introduction

Additive manufacturing offers the possibility of producing completely new structures that cannot be realized with traditional technologies like subtractive manufacturing [1]. In particular, powder-based processes such as powder bed fusion (PBF) are in the focus of the industry [2,3,4]. During the PBF process, the polymer powder is heated near its melting point. A powder deposition unit, typically either a doctor-blade or a roller coater is used to evenly distribute the layer with a defined powder height. Next, a laser is used as energy source to melt the powder locally. These steps are repeated until the desired part is finished. A major challenge in PBF is the limited choice of available materials. Mainly polyamides, such as PA 12 and PA 11 or filled systems based on these polymers (e.g. PA12 - glass, PA12 - aluminum powder) are on the market [5,6]. Pure PC or PBT, with their very specific material properties, are currently not commercially available for the PBF process. PBT/PC blends should have high dimensional stability, attrition resistance and impact strength as well as high chemical resistance and are, therefore, suitable for various applications [7].

In order to extend the range of materials, the approach of co-grinding [4,8] and spray drying of PBT and PC was chosen and demonstrated in this work to produce a multi-material of both aforementioned polymers. In addition to the proof-of-concept, the materials were thermally examined by means of differential scanning calorimetry (DSC) to draw conclusions about the mixing ratio and crystallinity. Furthermore, Fourier-transform infrared spectroscopy (FTIR) was performed to monitor changes of the materials along the process chain.

Nomenclature

PBT	polybutylene terephthalate
PC	polycarbonate
$d_{10,3}$	10 % percentile of the volume sum distribution
$d_{50,3}$	mass-median-diameter
$d_{90,3}$	90 % percentile of the volume sum distribution
T_M	melting temperature
ΔH_M	enthalpy of fusion
T_C	crystallisation temperature
ΔH_C	enthalpy of crystallisation
SW	sinter window

2. Isothermal crystallization

It is important to know about the crystallization kinetics of the powder to prevent crystallization effects during the additive manufacturing process. Furthermore, a too fast crystallization after the process, which leads to distortion in the finished part, must be avoided.

The isothermal crystallization measurement is a special method of DSC measurement. In contrast to dynamic measurements, where the sample is measured with a fixed heating / cooling ramp, in isothermal crystallization measurements, the sample is (i) first melted and (ii) then cooled to the isothermal temperature as quickly as possible. It is reported that cooling rates of at least 60 K/min should be used to avoid crystallization during the cooling phase. Additionally, the cooling rate should not be too high to ensure a stable measuring program [13]. The stability of the measuring program can be evaluated on the basis of the temperature dip when reaching the isothermal temperature, which should be a minimum. During this holding phase (iii), temperature-dependent crystallization takes place (see Figure 1).

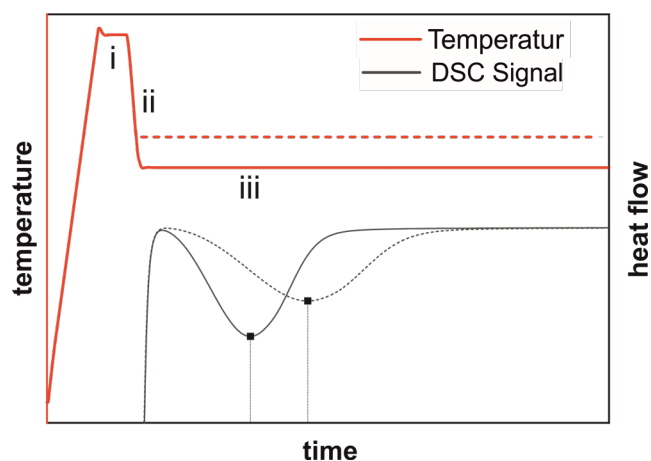


Fig. 2. Schematic of isothermal crystallisation measurements.

3. Co-grinding

The wet grinding [14] of PBT RXP 7103 Natural (Resinex) with a $d_{90,3} = 1065 \mu\text{m}$ and PC RXP 1201 Natural (Resinex) with a $d_{90,3} = 658 \mu\text{m}$ took place in the stirred media batch mill PE 075 (Netzsch) at ambient temperature (20°C). The polymer mass concentration was about 20%; the solvent was denatured ethanol (96%, VWR). The PBT to PC mass ratio was varied from 25/75 to 75/25. The stirrer speed was set to 2000 rpm and 2 mm ZrO_2 grinding beads ($\rho_{\text{GM}} = 6.050 \text{ kg/m}^3$) were used. This results in a stress energy of $\text{SE} = \rho_{\text{GM}} d_{\text{GM}}^3 v_{\text{tip}}^2$ of about $550 \mu\text{J}$ [9]. After a process time of 7 h, the ground polymer was separated from the grinding media by sieving with a mesh of 1 mm. Particle size distributions were measured with the Mastersizer 2000 Hydro S (Malvern Instruments) five times over a time span of 15 seconds and an average was calculated. The standard deviation for all measurements of the $x_{50,3}$ were less than $0.3 \mu\text{m}$.

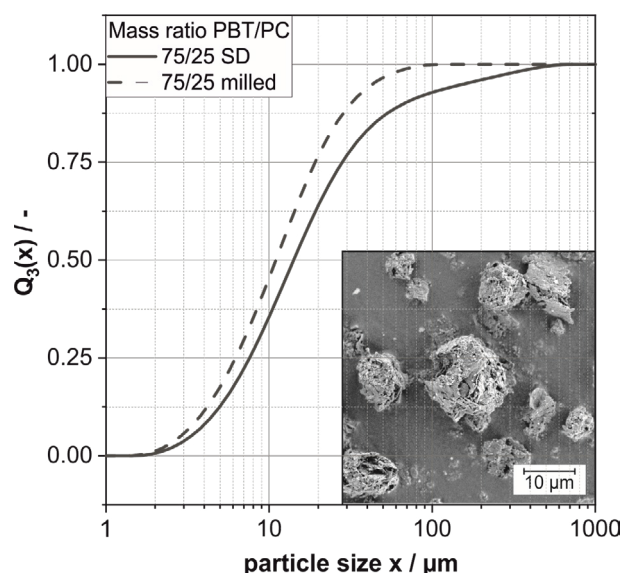


Fig. 1. Particle size distribution of PBT/PC particles with a mass ratio of 75/25 before and after the spray agglomeration step with SEM image of agglomerated particles.

Plate-shaped PBT / PC particles with a $d_{10,3}$ of about $4,5 \mu\text{m}$, a $d_{50,3}$ of $14 \mu\text{m}$ and a $d_{90,3}$ of $50 \mu\text{m}$ were obtained, which were spray-dried in the next step. The comminution kinetic followed an exponential trend. However, no dependence on PBT/PC mass ratio and comminution kinetics was observed.

4. Spray-drying

A Buchi B-290 Mini Spray Dryer with Inert Loop B-295 was used to dry the suspension. The spray device consists of a two-component nozzle with a 1.4 mm nozzle cap and the peristaltic pump installed at the spray dryer. The chosen parameters were an inlet temperature of 140°C , a feed rate of 3.5 ml/min and drying gas volume flow of 360 l/h .

After spray drying, the particles showed a $d_{10,3}$ of about $5 \mu\text{m}$, a $d_{50,3}$ of $15 \mu\text{m}$ and a $d_{90,3}$ of $62 \mu\text{m}$. A particle size distribution before and after the spray agglomeration step for a PBT/PC mass ratio of 75/25 is shown in Figure 2 representatively. In order to increase the size of the particles further, the use of a chemical binder, such as an acrylate, should be considered in the future work. As expected, the particle size distributions after spray drying do not differ significantly from each other under constant process conditions. The structure of the comminuted particles and obtained spray agglomerates was determined by SEM imaging. Plate-like (cohesive) particles obtained by comminution could be successfully combined to more compact agglomerates (see Fig. 2). The flowability was evaluated using a modified Zimmermann tensile strength tester ($n=6$). The PBT/PC powder showed a tensile stress of $17.7 \pm 0.8 \text{ Pa}$, which could be improved to $12.0 \pm 0.7 \text{ Pa}$ by dry coating the powder with 0.1 wt.% Aerosil R200. Most likely, a subsequent thermal rounding step must be selected in future work [8] to further optimize the flow and packing properties of the material and thus, facilitate powder application during additive production. To identify the polymers used, the bands shown in Table 1 were used [10,11,12].

Table 1. Functional groups and mode of vibration from FTIR spectra of the evaluated polymers.

Polymer	Wavenumber [cm^{-1}]	Assignment
PBT	1260	C – O – C
	1510	α - Phase
	1710	C = O; Carbonyl
PC	1235	O – C – O
	1505	C = O; Aromat
	1770	C = O; Carbonyl

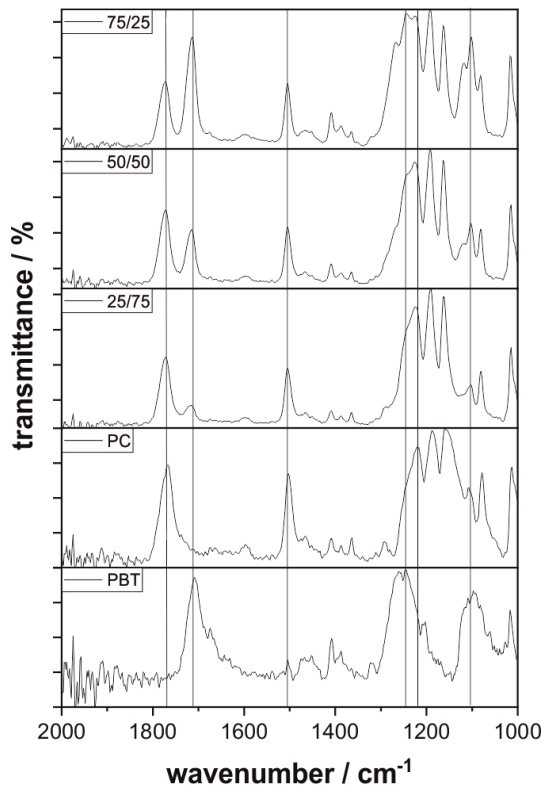


Fig. 3. FTIR measurements of pure PBT and PC powder in comparison with the processed PBT/PC multi-materials at different mass ratios.

Fig. 3 shows the spectra of the pure substances (PBT and PC) as well as the spray-dried mixtures at the adjusted ratios. The material-specific bands of the polymers can be found in the mixtures. Additionally, the ratio between PBT and PC was evaluated by the glass transition of polycarbonate (see Table 2, for discussion please refer to Section 5.1).

Table 2. Change in heat capacity (Δc_p) at glass transition and calculated PC content for different PBT/PC ratios.

label	$\Delta c_p / \text{J g}^{-1} \text{K}^{-1}$	adjusted PC content	calculated PC content
PBT/PC (75/25)	0.0514	25 %	23.1 %
PBT/PC (50/50)	0.1124	50 %	50.5 %
PBT/PC (25/75)	0.1641	75 %	73.7 %
Pure PC	0.2226	100 %	100.0 %

5. Thermal analysis

The thermal behaviour of the powder has a considerable influence on the choice of parameters during the powder bed fusion process. For example, the powder bed temperature should be within the sintering window (SW) of the material, which is defined by the onset of the melting and crystallization peak.

5.1. Dynamic scanning calorimetry (DSC)

For dynamic calorimetry measurements, a Polyma 214 (Netzsch) was used with a constant heating and cooling rate of 10 K/min. All measurements were carried out twice in order to rule out the possibility of outliers. Built-in functions of the analysis software Proteus were used to evaluate the enthalpy of fusion and crystallization and the change in heat capacity at the glass transition. For the enthalpy of fusion and crystallization a tangent to the points to the right of the peak was chosen as baseline. The glass transition was determined using the direct method.

Table 3. Thermal parameters of processed PBT/PC multi-material.

	PBT	PBT/PC 75/25	PBT/PC 50/50	PBT/PC 25/75
T_M °C	225.3	223.5	222.9	224.6
$T_{M,On}$ °C	216.8	214.3	214.5	218.2
ΔH_M J/g	55.0	22.8	12.9	6.4
T_C °C	180.5	177.8	177.7	177.3
$T_{C,On}$ °C	192.2	186.0	184.5	183.5
ΔH_C J/g	-55.1	-19.0	-9.7	-2.5
SW K	24.6	28.3	30.0	34.7

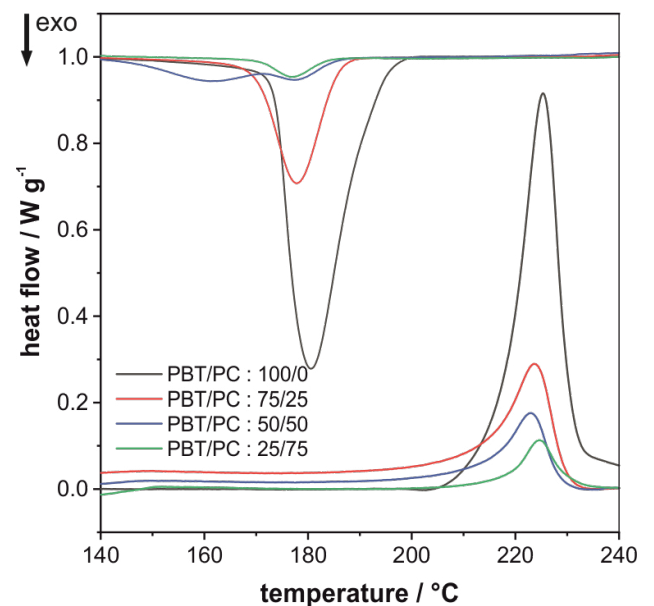


Fig. 4. DSC measurements of different PBT/PC mass ratios with a heating rate of 10 K/min.

As shown in Figure 4 and Table 3, wet grinding and spray-drying have little effect on the location of the melting peak, as both, the peak temperature and the onset temperature, remain almost the same. However, the crystallinity, which is proportional to the enthalpy of the fusion, of the PBT is reduced by the process. For example, raw PBT has a heat of fusion of 55.0 J/g. Theoretically, a physical blend of PBT/PC with a mass ratio of 50/50 should have half (27.5 W/g) of the enthalpy of fusion of the raw PBT material, which was proven by DSC measurements. The processed PBT/PC 50/50 powder however, has an enthalpy of fusion of 12.9 J/g. Therefore, the glass transition of polycarbonate was used to calculate the PBT/PC ratio. Also, the onset temperature of crystallization shifts to lower temperatures with increasing PC content, which results in an enlargement of the sintering window. The sintering window was increased from 24.6 K for pure PBT powder to 34.7 K for a processed PBT/PC 25/75 powder. The two crystallisation peaks at a PBT/PC mass ratio of 50/50 indicate a fractional crystallisation into two different phases, which happens at PBT/PC mass ratios of around 50/50 [15].

5.2. Isothermal crystallization behavior

To further investigate the effects of processing on the crystallization behaviour, isothermal crystallization measurements of the powder were carried out at different stages of the process. Besides, isothermal measurements can be used to allow accurate predictions about the crystallization effects of the powder during the PBF process. Isothermal measurements better represent the thermal conditions, which the powder is facing during the manufacturing process.

For the isothermal crystallization measurements, the sample was cooled to the isothermal temperature at a cooling rate of 180 K/min. This resulted in a temperature dip of 0.2 °C, which indicates a stable measuring program. The maximum time of the isothermal segment was 1h, which was used at higher temperatures. As an example, the thermogram of the processed PBT/PC powder with a mass ratio of 75/25 is shown in Figure 5 for a temperature range of 175 °C – 187 °C.

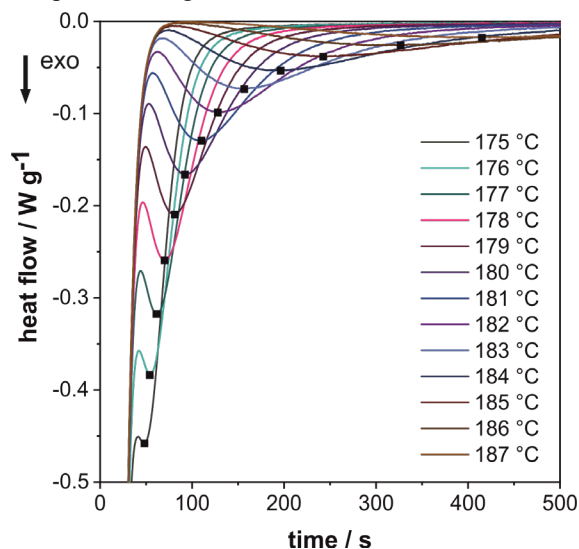


Fig. 5. Thermogram of isothermal DSC measurements of processed PBT/PC powder with a mass ratio of 75/25.

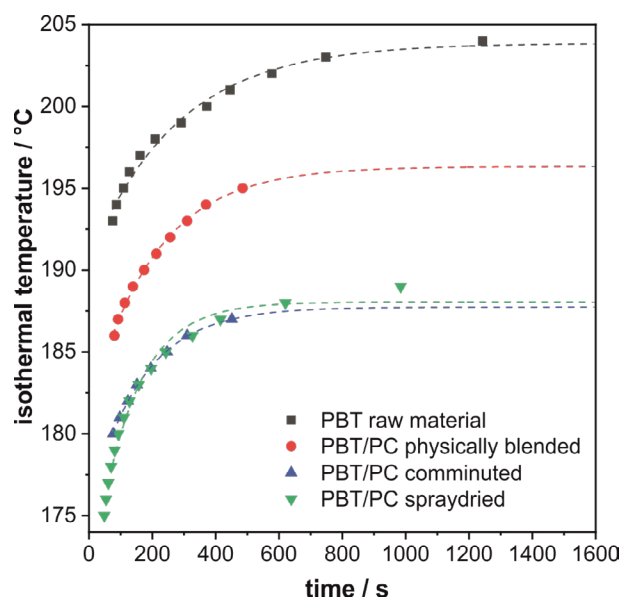


Fig. 6. Time dependency of the crystallization peak for different isothermal temperatures for the used PBT raw material, a physically blended PBT/PC powder with a mass ratio of 75/25 material and the processed PBT/PC powder with a mass ratio of 75/25.

The samples were measured over a wide temperature range to get enough data points for a good fit and to see if and how fast crystallization still takes place within the sintering window, as this is the temperature range used for the powder bed fusion process.

For better comparison, the time at which the maximum of the crystallization peak was reached, is plotted against the isothermal temperature at different stages during the process chain. In Figure 6 it can be seen that as the temperature increases, crystallization proceeds more slowly until an upper limit temperature is reached at which crystallization no longer occurs during the isothermal segment (1h). It cannot be excluded that crystallization can still take place during longer isothermal segment times, but this should no longer be relevant for the powder bed fusion process. The limit temperature T_{Lim} can be calculated by fitting an exponential function to the curves with A and B as further fitting parameters (see Table 4).

$$T = T_{Lim} - A \cdot e^{\left(\frac{-t}{B}\right)} \quad (1)$$

Table 4. Fitting parameters of the isothermal crystallization data.

Sample	$T_{lim} / ^\circ\text{C}$	A / $^\circ\text{C}$	B / s
PBT raw	203.9	13.3	208
PBT/PC blended	196.3	14.9	203
PBT/PC grinded	187.3	12.4	160
PBT/PC processed	188.0	18.1	124

By physically blending PBT/PC in a ratio of 75/25, the exponential function becomes steeper and crystallization starts at lower temperatures compared to the PBT raw material. After wet grinding of the physical blend, this trend becomes even more pronounced, which is favorable for the PBF process due to the enlargement of the sintering window. The crystallization limit temperature of the processed PBT/PC powder is 188 °C, 16 °C lower than the PBT raw material. Spray drying was

observed to have no detrimental influence on the thermal behavior of the powder.

Furthermore, the crystallization limit temperature is above the onset temperature of the crystallization peak of 186.0 °C, which is often chosen for the determination of the sintering window. However, the powder bed temperature should be above the crystallization limit temperature to avoid crystallization effects during the PBF process.

6. Conclusion

Wet grinding and spray drying has been studied for producing PBT/PC multi-material powders for additive manufacturing was presented. The particle size of the agglomerated powder showed a $x_{50,3} = 15 \mu\text{m}$, which was measured with laser diffraction particle sizing. The influence of the process, as well as the mixing ratio on the thermal properties of the powder, was measured by dynamic and isothermal DSC measurements. It was shown that the wet grinded and spray dried PBT/PC powder crystallizes at lower temperatures than pure PBT powder or physically blended PBT/PC powders, causing a broadening of the sintering window, which may improve the handling during the powder bed fusion process.

Acknowledgements

Funded by the Deutsche Forschungsgemeinschaft (DFG, German Research Foundation) – Project-ID 61375930 – SFB 814 - „Additive Manufacturing“ TP A01 and TP A02

References

- [1] I. Gibson, D.W. Rosen, B. Stucker, Additive manufacturing technologies, Springer, 2014.
- [2] I. Campbell, O. Diegel, J. Kowen, T. Wohlers, Wohlers report 2018: 3D printing and additive manufacturing state of the industry: annual worldwide progress report, Wohlers Associates, 2018.
- [3] M. Schmid, Laser Sintering with Plastics: Technology, Processes, and Materials, Carl Hanser Verlag GmbH Co KG, 2018.
- [4] Schmidt, J., Romeis, S., & Peukert, W. (Ed.), Polymer powders for selective laser sintering (SLS), AIP Publishing LLC, 2015.
- [5] R.D. Goodridge, C.J. Tuck, R.J.M. Hague, Laser sintering of polyamides and other polymers, Progress in Materials science 57 (2012) 229–267.
- [6] D. Bourell, J.P. Kruth, M. Leu, G. Levy, D. Rosen, A.M. Beese, A. Clare, Materials for additive manufacturing, CIRP Annals 66 (2017) 659–681.
- [7] S. Fakirov, Handbook of condensation thermoplastic elastomers, John Wiley & Sons, 2006.
- [8] M.A. Dechet, J.S. Gómez Bonilla, L. Lanzl, D. Drummer, A. Bück, J. Schmidt, W. Peukert, Spherical Polybutylene Terephthalate (PBT)—Polycarbonate (PC) Blend Particles by Mechanical Alloying and Thermal Rounding, Polymers 10 (2018) 1373.
- [9] A. Kwade, Wet comminution in stirred media mills — research and its practical application, Powder Technology 105 (1999) 14–20
- [10] D. Delimoy, C. Bailly, J. Devaux, R. Legras, Morphological studies of polycarbonate - poly (butylene terephthalate) blends by transmission electron microscopy, Polymer Engineering & Science 28 (1988) 104 - 112.
- [11] I. Hopfe, G. Pompe, K.-J. Eichhorn, Ordered structures and progressive transesterification in PC/PBT melt blends studied by FT ir spectroscopy combined with dsc and nmr, Polymer 38 (1997) 2321–2327.
- [12] G.-P. Lin, L. Lin, X.-L. Wang, L. Chen, Y.-Z. Wang, PBT/PC Blends Compatibilized and Toughened via Copolymers in Situ Formed by MgO-Catalyzed Transesterification, Ind. Eng. Chem. Res. 54 (2015) 1282–1291.
- [13] A. T. Lorenzo, M. L. Arnal, J. Albuérne, A. J. Müller, DSC isothermal polymer crystallization kinetics measurements and the use of the Avrami equation to fit the data: Guidelines to avoid common problems, Polymer Testing, 26 (2007) 223–231
- [14] J. Schmidt, M. Plata, S. Tröger, W. Peukert, Production of polymer particles below 5 μm by wet grinding, Powder Technology, 228 (2012) 84–90
- [15] H.-J. Radusch, R. Androsch, Die Kristallisation von Polybutylenterephthalat (PBT) und Polycarbonat (PC) im Polymerblend PBT/PC, Die Angewandte Makromolekulare Chemie, 214 (1994) 179–196

11th CIRP Conference on Photonic Technologies [LANE 2020] on September 7-10, 2020

Enhancement of polyamide laser sinter powder reusability by acid catalyzed hydrolysis

Nicolas Hesse^a, Wolfgang Peukert^a, Jochen Schmidt^{a,*}

^a*Institute of Particle Technology (LFG), Friedrich-Alexander-Universität Erlangen-Nürnberg (FAU), Cauerstraße 4, D-91058 Erlangen, Germany*

* Corresponding author. Tel.: +49 9131 85-29404; fax: +49 9131 85-29402. E-mail address: jochen.schmidtt@fau.de

Abstract

This contribution introduces a method to reverse the deterioration in melt rheological behaviour ('ageing') of polyamide 12 that has previously been used in powder bed fusion processing by reduction of the polymers molecular weight via acid catalysed hydrolysis. Chosen hydrolysis conditions allow for a reconditioning below melting temperature and therefore leave the particulate nature of the powder intact while significantly improving the polymers rheological properties. The influences of different temperatures, acids and pH-values are investigated and the processability of recycled powders is assessed by melt rheological, optical and thermal characteristics.

© 2020 The Authors. Published by Elsevier B.V.

This is an open access article under the CC BY-NC-ND license (<http://creativecommons.org/licenses/by-nc-nd/4.0/>)

Peer-review under responsibility of the Bayerisches Laserzentrum GmbH

Keywords: powder bed fusion; selective laser sintering; polyamide 12; powder reusability; hydrolysis; molecular chain length; zero shear viscosity

1. Introduction

Additive Manufacturing (AM) is a rapidly growing market for the production of highly customized metal, ceramic and plastic components [1]. Among the wide variety of AM methods established in recent years, the powder bed fusion (PBF) processing of metals and polymers shows great promise for the industrial production of parts with good mechanical properties [2]. The process consists of several repetitive steps. First, a fine powder layer is applied onto a building platform by a blade or roller coater. Secondly, the powder is exposed to a laser or electron beam in accordance to the pattern of the part that is supposed to be built. In a third step the building platform is lowered to allow the application of a new powder layer. This way, a part can be build layer by layer, while the surrounding, non-molten powder acts as supporting structure and allows for the production of elements with a high geometrical freedom unmatched by classical subtractive manufacturing methods [3]. When processing

polymer materials in PBF, an additional step consists of heating the newly applied powder layer to a temperature closely below its melting region by infrared radiation. Additionally, the building chamber is heated during the whole process [3] to minimize warpage. One challenge arising from those boundary conditions is the ageing of the non-molten powder material. Typically, only fifteen to thirty mass percent of the powder used in the process ends up in the finished part [4]. Therefore, reusing the previously processed powder is crucial from an ecologic and economic point of view and is usually performed by blending with virgin powder [5]. However, commonly applied mixing ratios and processing strategies still lead to the accumulation of used powder, which has to be utilized either thermally or by downcycling of the otherwise highly engineered materials.

The most widespread polymers used in PBF processes are the polyamides 11 and 12 (PA11 and PA12) in their pure or glass fiber reinforced form [1]. While their thermal properties are excellent for PBF processing, reusability of previously processed powders poses a challenge. Long processing times

at elevated temperatures in the continuously flushed nitrogen atmosphere of the building chamber are ideal conditions to promote solid-state post-condensation in polyamides. This reaction results in the connection of multiple polymer chains and therefore a linear chain growth [6]. The accompanying increase in molecular weight improves some mechanical properties like the tensile strength [7], but it also causes a raise in polymer melt viscosity, which affects the coalescence of melt droplets and the sintering kinetics of the polymer. Consequently, an extensive increase in melt viscosity has shown to be disadvantageous during processing and can result in poor part quality due to insufficient layer junction, part density or the generation of an orange peel surface structure [8].

However, the molecular chain length of polyamide can be reduced under suitable conditions [9-11]. While technical applications in polymer synthesis are focused on increasing a polymers chain length, it is known that hydrolysis in the condensation - hydrolysis equilibrium is favoured in humid and in particular acidic environments, which results in a decrease in molecular mass [9-11]. This effect is usually seen as an unwanted deterioration of the material when used over a long time, since it can lead to unfavorable mechanical properties. Additionally, exposure to an oxygen-rich atmosphere can lead to radical chain scission and a multiplicity of secondary reactions, which are often associated with a discoloration of the polymer [12-15]. Application of these effects for an enhancement of polymer powder recyclability in the context of AM presents a novel approach to deal with the widespread problem of PBF process related feedstock material ageing.

Aim of this study is the adjustment of the molecular chain length dependent melt rheological properties of PA12 to allow an efficient recycling of previously processed laser sinter powder. This is achieved by acid catalyzed hydrolysis at temperatures above 100°C. For this reason, a variety of different acidic solutions and the influence of their pH value on the reaction as well as the temperature dependency is investigated.

2. Methodology

2.1. Materials

PA12 (PA2200) laser sinter powder was provided by EOS GmbH. Besides virgin powder, materials with two different thermal histories have been used in this study. Powders denoted as “used #1” went through a 15.5 hour building process with a withdrawal chamber temperature of 150°C on an EOS Formiga P110 machine, while the ones labeled as “used #2” were exposed to a shorter build job.

For the adjustment of the pH value of the hydrolysis aqueous solutions gallic acid, ascorbic acid or phenylphosphonic acid was used. Carl Roth GmbH + Co. KG supplied all reagents. Water used in experiments was purified

and deionized with a Purelab Ultra device by ELGA LabWater to exhibit a resistivity of 16.8 MΩ·cm.

2.2. Hydrolysis

All experiments were conducted in autoclave reactors with a fixed amount of aqueous solution of different pH values and used PA12 powder. Ascorbic, gallic and phenylphosphonic acid have been used to investigate their effect on the rheological, thermal and optical properties of treated powders and the hydrolysis reaction kinetics. In the case of ascorbic and phenylphosphonic acid, the concentration was adjusted by titration at ambient temperature and continuously monitored via SenTix HW glass electrode by WTW GmbH until the desired pH value was reached. Due to the low solubility of gallic acid at ambient conditions, the pH values of respective solutions were adjusted at 60°C. Furthermore, experiments in purified water without the addition of any catalyst were conducted in a temperature range of 100°C to 150°C. Autoclave reactors were either sealed in ambient atmosphere or in nitrogen atmosphere in a glovebox for the investigation of oxidative degradation during hydrolytic processing. Reaction vessels were deposited on heating plates with appropriate sheathings to minimize heat loss and were stirred continuously at 600 rounds per minute. If not stated otherwise, reaction conditions were maintained for 24 hours at 125°C, including a short heating-up and a one-hour cooling-down period. Afterwards, the powders were purged with deionized water multiple times and dried at 70°C and 10% relative humidity for at least two days.

2.3. Rheology

Rheological properties of the polymer melt were analyzed by frequency sweep tests in a Discovery Hybrid Rheometer 2 with the electrically heated plates mount system by TA Instruments. Specimen were prepared by pressing 25 mm diameter pellets with a weight of 600 mg. Measurements were performed at 200°C with 1% oscillatory strain in a frequency range of 100 Hz to 0.01 Hz. To ensure a measurement within the linear viscoelastic region, amplitude sweep tests have been performed for a few meaningful spot samples. Zero shear viscosities have been calculated by fitting of frequency sweep test data according to the Carreau-Yasuda model [16] with a coefficient of determination R^2 of 0.998 or higher.

2.4. Optical spectroscopy

Optical material properties in the visible wavelength range were analyzed using a Lambda 950 UV/Vis spectrometer with an 150 mm integrating sphere module by PerkinElmer. All spectra were calibrated against a Zenith polymer diffuse reflectance standard by SphereOptics GmbH for 100% reflectance and a light trap for 0% reflectance. Analogue to rheological measurements, samples have been prepared by pressing 25 mm diameter pellets.

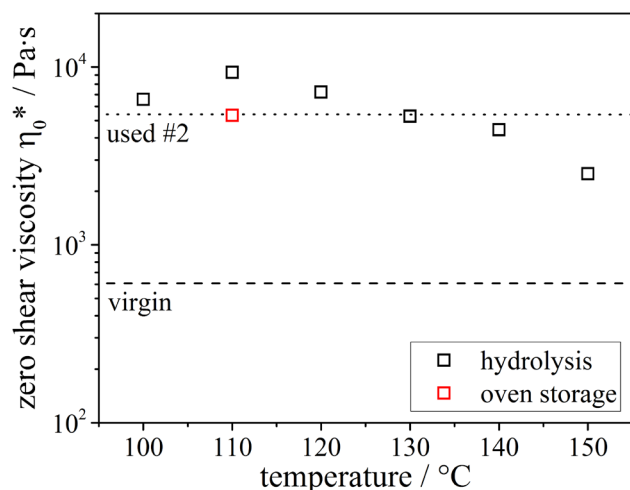


Fig. 1. Zero shear viscosity of used powder after hydrolysis for 24 hours in pure water at different temperatures. Initial state of used powder before hydrolysis and virgin material properties are given by the dotted and dashed line.

2.5. Differential scanning calorimetry

Thermal material properties were analyzed by differential scanning calorimetry (DSC) with a Polyma DSC 214 system by Netzsch. The heating and cooling rates for dynamic measurements were set to 10 K/min. Isothermal crystallization measurements were performed with a cooling rate of 180 K/min prior to the isothermal holding step. The specimen weight was approximately 5 mg.

3. Results and Discussion

A multiplicity of factors potentially influences the polymer's reaction during hydrolysis. Not only the composition of the hydrolysis solution but also the processing time, temperature, pressure and the presence of oxygen, which promotes oxidative degradation, play an important role. Therefore, the temperature range that enables hydrolysis without damaging the polymer material excessively has been investigated. The results of melt rheological measurements for experiments in pure water and ambient atmosphere with varying temperatures are shown in figure 1. The zero shear viscosity of the feed material that has been used in a building process earlier is marked as dotted line and the virgin powder as dashed line respectively. For lower temperatures an increase in viscosity with respect to the feed material can be observed. Powder treated at 110°C yields the highest value, while a further increase in temperature leads to a declining viscosity. Storing used powder #2 samples in an oven in air for 24 hours at 110°C does not lead to a comparable increase in viscosity as the hydrolysis at the same conditions. Therefore, it can be concluded, that the raise in viscosity does not stem from the solid-state post-condensation typically observed in heated gaseous atmospheres, but must be attributed to other effects unique to the treatment in a hydrolytic environment.

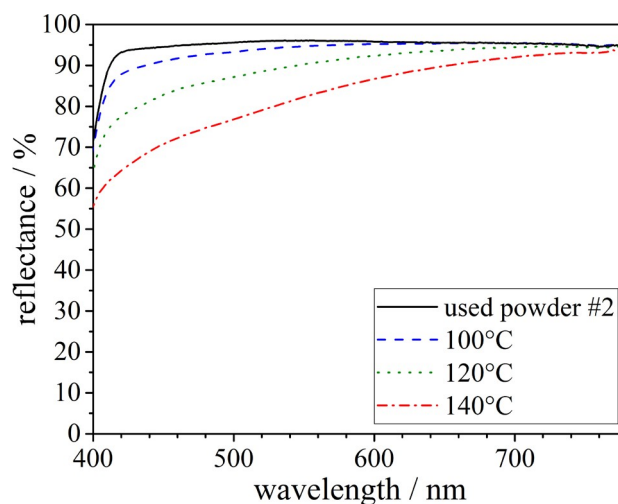


Fig. 2. Reflectance of light in the visible spectrum for used powder before and after hydrolysis in pure water.

However, the melt rheological behaviour is only one aspect important for the processing during PBF and the resulting part properties. A treatment at higher temperatures also leads to a gradual change in optical properties of the powders. While this does not necessarily lead to worse mechanical properties of parts built, the characteristic brownish tint is usually not desirable. To quantify the perception of colour, reflectance spectra in the range of visible wavelengths have been recorded and are shown in figure 2. An increase in hydrolytic treatment temperature leads to a decline in reflectance of light, especially in the lower region of the observed spectrum.

According to the temperature dependent deterioration effects observed in reflectance measurements, a reduced hydrolysis temperature of 125°C is an appropriate trade-off between rheological and optical properties, due to acidic conditions potentially leading to both, an enhanced decline in optical properties and an amplified reduction in melt viscosity. Since it is known that some chromophores resulting in discolouration stem from oxidative degradation [14,15], autoclaves were also sealed in nitrogen-flushed atmosphere. Additionally, the selected acids used for the catalytic hydrolysis have been chosen due to their anti-oxidative nature. Furthermore, sterically hindered phenolic antioxidants are often used for the thermal stabilization of plastics. These act as primary antioxidants by converting peroxy radicals to hydroperoxides and therefore inhibit autooxidation of the polymer [17]. The reactive hydrogen of the phenolic stabilizer is abstracted and transferred to the polymer, leaving behind an oxytoluene radical. Due to the electron delocalization and the steric hindrance, this compound is more stable than a peroxy radical in the polymer chain [17]. Moreover, phosphites are used as secondary antioxidants to further decompose hydroperoxides. While it is not possible to add these stabilizers to the hydrolysis solution directly due to their low solubility and high melting point caused by the sterically hindering molecule chains, a stabilization due to radical scavenging and electron delocalization might be achievable. Therefore, gallic acid and phenylphosphonic acid have been chosen as low molecular, non-toxic aromatic compounds with free hydroxy groups and an acid functionality.

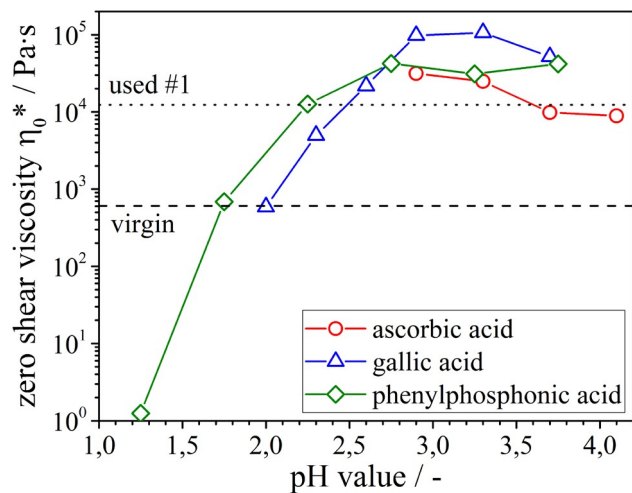


Fig. 3. Zero shear viscosity of polymer powders hydrolysed for 24 hours at 125°C with different acids and pH values. Initial state of used powder before hydrolysis and virgin material properties are given by the dotted and dashed line.

Figure 3 shows the pH dependency of the zero shear melt viscosity of used PA12 powder hydrolysed for one day at 125°C for all acids utilized. Analogous to the measurements with varying temperatures, it can be seen for all measurement series that there is a range in which the melt viscosity increases rather than declines. This effect is most pronounced for gallic acid between pH 2.9 and 3.3, whereas phenylphosphonic acid exhibits a broader range of pH 2.75 to 3.75 in which the hydrolysis results in an increased zero shear viscosity that is independent of the acid concentration within this range. By further increasing the concentration and therefore lowering the pH, a rapidly declining melt viscosity can be observed. It is possible to reduce the zero shear viscosity to the virgin powder level for both gallic and phenylphosphonic acid at a pH of 2.0 and 1.75, respectively. Ascorbic acid shows a slight reduction in viscosity at pH 3.5 and above and an increase towards lower pH values. A further reduction below pH 2.9 leads to the destruction of the polymer material. Rheological measurements for these powders have been omitted due to strong discolouration of the polymer and odour development during melting.

The excessive degradation of the ascorbic acid treated polymer is also noticeable in results obtained from optical spectroscopy depicted in figure 4. Even for comparably mild conditions with a pH of 3.3, the reflectance of the powder declines significantly. For reasons of clarity, values for powders treated with ascorbic acid at lower pH values are not depicted, however these show a further deteriorating reflection behaviour. While it is possible to reach rheological characteristics comparable to those of the virgin polymer by gallic acid catalysed hydrolysis the optical properties of the treated powders are dissatisfactory. However, the perception of colour for the powders treated in experiments with phenylphosphonic acid is only slightly tinted due to a lower reflection of light among the lower wavelength of the visible spectrum.

As third criterion, the thermal properties of the powders that yield the most advantageous rheological behaviour have been investigated. The thermograms for virgin, used and

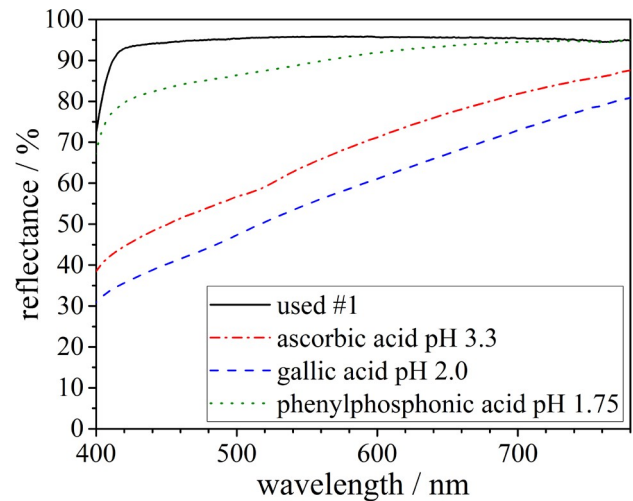


Fig. 4. Reflectance of light in the visible spectrum for used powder before and after hydrolysis. Depicted hydrolysis conditions are the ones that yield melt rheological behaviour closest to virgin material.

recycled powders are depicted in figure 5. The most important thermal property of a PBF polymer material is its sinter window, which is defined as the range between the onset of the melting and the onset of the crystallization measured by DSC. A broad sintering window allows for a wide operational range during processing. While a high machine temperature may lead to the sintering in unsolicited parts of the powder bed, a temperature too low can lead to warpage or curling and consequently the abortion of the building process. In the case of gallic acid treated powders, the sinter window is reduced mainly due to the shift of the melting peak towards lower temperatures and to a lower degree by an increase in the recrystallization temperature. However, the recrystallization peak for this powder is close to the one observed for virgin powder, which should enable simple processing. For powders treated with phenylphosphonic acid, a less pronounced shift of the melt peak towards lower temperatures can also be observed, whereas the onset of the recrystallization is elevated to 156.5°C, which is a considerable increase when compared

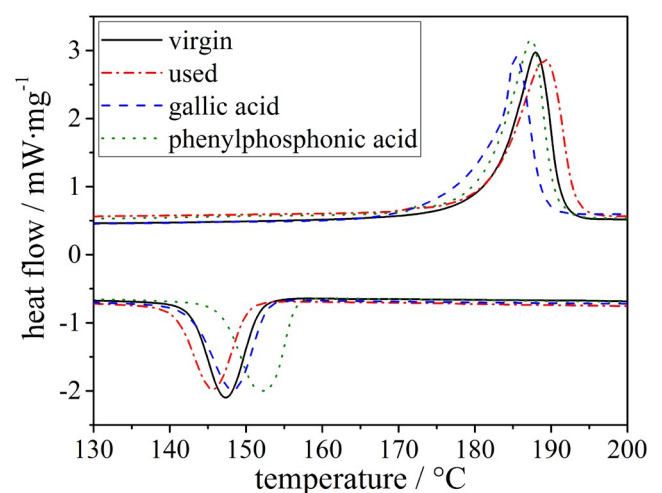


Fig. 5. Thermograms of investigated powders for dynamic DSC measurements at 10 K/min heating and cooling rate. Depicted hydrolysis conditions are the ones that yield melt rheological behaviour closest to virgin material.

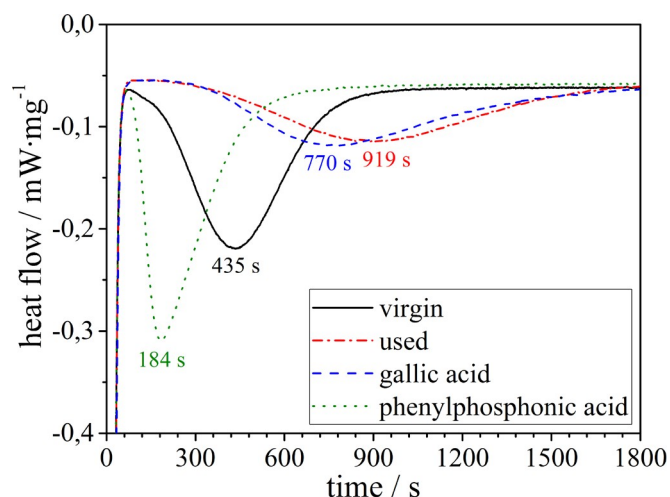


Fig. 6. Isothermal crystallisation time for investigated powders at 164°C. Depicted hydrolysis conditions are the ones that yield melt rheological behaviour closest to virgin material.

to virgin powder with an onset temperature of 151.9°C. However, due to the beneficial properties of PA12 and its comparatively broad sintering window in general, the treated powders still exhibit a thermal window that allows PBF processability.

Furthermore, not only the crystallization temperature but also the speed of the advancing crystallization is decisive. To evaluate this, isothermal crystallization measurements were taken at 164°C and are shown in figure 6. In comparison to the used powder, the crystallization for both recycled powders investigated advances in a shorter time. While this increase in crystallization speed is only minor for gallic acid, which does still have a longer crystallization time than virgin powder, the reduction for powders hydrolysed in phenylphosphonic acid solution is considerable. In consequence, the accelerated crystallization, which can be expected shortly after laser exposition and therefore in the upmost powder layers of the building chamber can be a challenge for PBF processing.

4. Conclusion

It has been shown that it is possible to restore melt rheological properties of previously processed PA12 laser sinter powder by acid catalysed hydrolysis. Gallic and phenylphosphonic acid enable the recovery of the polymers rheological behaviour during the low shear stress conditions associated with the PBF processing, while phenylphosphonic acid allows for a treatment that mostly maintains the colour of the polymer. In either case the sinter window of the recycled powder shrinks. For phenylphosphonic acid, the isothermal crystallisation kinetic is accelerated, while the treatment with gallic acid only leads to a minor reduction in crystallisation time when compared to used powder. Studies on the PBF processability of the recycled powders will be subject to future work.

Acknowledgements

The German Research Foundation (DFG) is acknowledged for funding of this study within the framework of CRC814 “Additive Manufacturing” (project-ID 61375930, subproject T1).

References

- [1] Associates, Wohlers (2019): Wohlers report 2019. 3D printing and additive manufacturing state of the industry. Fort Collins (Colo.): Wohlers Associates.
- [2] Kotlinski, Jaroslaw (2014): Mechanical properties of commercial rapid prototyping materials. In: Rapid Prototyping Journal 20 (6), S. 499–510. DOI: 10.1108/RPJ-06-2012-0052.
- [3] Ligon, Samuel Clark; Liska, Robert; Stampfl, Jürgen; Gurr, Matthias; Mülhaupt, Rolf (2017): Polymers for 3D Printing and Customized Additive Manufacturing. In: Chemical reviews 117 (15), S. 10212–10290. DOI: 10.1021/acs.chemrev.7b00074.
- [4] Dotchev, Krassimir; Yusoff, Wan (2009): Recycling of polyamide 12 based powders in the laser sintering process. In: Rapid Prototyping Journal 15 (3), S. 192–203. DOI: 10.1108/13552540910960299.
- [5] M. Schmid, Selektives Lasersintern (SLS) mit Kunststoffen - Technologie, Prozesse und Werkstoffe, Carl Hanser Verlag, 2015.
- [6] Wudy, Katrin; Drummer, Dietmar (2019): Aging effects of polyamide 12 in selective laser sintering. Molecular weight distribution and thermal properties. In: Additive Manufacturing 25, S. 1–9. DOI: 10.1016/j.addma.2018.11.007.
- [7] Wegner, Andreas; Mielicki, Christoph; Grimm, Tobias; Gronhoff, Burkhard; Witt, Gerd; Wortberg, Johannes (2014): Determination of robust material qualities and processing conditions for laser sintering of polyamide 12. In: Polym Eng Sci 54 (7), S. 1540–1554. DOI: 10.1002/pen.23696.
- [8] Kruth, J - P.; Mercelis, P.; van Vaerenbergh, J.; Froyen, L.; Rombouts, M. (2005): Binding mechanisms in selective laser sintering and selective laser melting. In: Rapid Prototyping Journal 11 (1), S. 26 – 36. DOI: 10.1108/13552540510573365.
- [9] Hocker, Samuel; Rhudy, Anne K.; Ginsburg, Gregory; Kranbuehl, David E. (2014): Polyamide hydrolysis accelerated by small weak organic acids. In: Polymer 55 (20), S. 5057–5064. DOI: 10.1016/j.polymer.2014.08.010.
- [10] Merdas, I.; ThomINETTE, F.; Verdu, J. (2003): Hydrolytic ageing of polyamide 11—effect of carbon dioxide on polyamide 11 hydrolysis. In: Polymer Degradation and Stability 79 (3), S. 419–425. DOI: 10.1016/S0141-3910(02)00358-0.
- [11] Chaupart, N.; Serpe, G.; Verdu, J. (1998): Molecular weight distribution and mass changes during polyamide hydrolysis. In: Polymer 39 (6-7), S. 1375–1380. DOI: 10.1016/S0032-3861(97)00414-X.
- [12] Zhang, Jie; Adams, Alina (2016): Understanding thermal aging of non-stabilized and stabilized polyamide 12 using 1H solid-state NMR. In: Polymer Degradation and Stability 134, S. 169–178. DOI: 10.1016/j.polymdegradstab.2016.10.006.
- [13] El-Mazry, C.; Ben Hassine, M.; Correc, O.; Colin, X. (2013): Thermal oxidation kinetics of additive free polyamide 6-6. In: Polymer Degradation and Stability 98 (1), S. 22–36. DOI: 10.1016/j.polymdegradstab.2012.11.002.
- [14] Karstens, Ties; Rossbach, Volker (1990): Thermo-oxidative degradation of Polyamide 6 and Polyamide 6,6. Structure of UV/VIS-active Chromophores. In: Makromol. Chem. 191 (4), S. 757–771. DOI: 10.1002/macp.1990.021910404.
- [15] Li, Rongfu; Hu, Xingzhou (1998): Study on discoloration mechanism of polyamide 6 during thermo-oxidative degradation. In: Polymer Degradation and Stability 62 (3), S. 523–528. DOI: 10.1016/S0141-3910(98)00037-8.
- [16] Yasuda, K.: Investigation of the analogies between viscometric and linear viscoelastic properties of polystyrene fluids. Thesis (Ph.D.) – Massachusetts Institute of Technology, Dept. of Chem. Engineering, 1979
- [17] Shahidi, F.; Wanasundara, P. K. (1992): Phenolic antioxidants. In: Critical reviews in food science and nutrition 32 (1), S. 67–103. DOI: 10.1080/1040839920952758

11th CIRP Conference on Photonic Technologies [LANE 2020] on September 7-10, 2020

Scaling up colloidal surface additivation of polymer powders for laser powder bed fusion

Tim Hupfeld^a, Carlos Doñate-Buendía^a, Matthias Krause^b, Alexander Sommereyns^{c,d}, Andreas Wegner^e, Thorsten Sinnemann^b, Michael Schmidt^{c,d}, Bilal Gökce^a, Stephan Barcikowski^{a*}

^aTechnical Chemistry I and Center for Nanointegration Duisburg-Essen (CENIDE), University of Duisburg-Essen, Universitaetsstrasse 7, 45141 Essen, Germany

^bFachhochschule Dortmund, Department for mechanical engineering, Sonnenstrasse 96, 44139 Dortmund, Germany

^cInstitute of Photonic Technologies (LPT), Friedrich-Alexander Universität Erlangen-Nürnberg, Konrad-Zuse-Str.3-5, 91052 Erlangen, Germany

^dErlangen Graduate School in Advanced Optical Technologies (SAOT), Paul Gordan Straße 6, 91052 Erlangen, Germany

^eChair for Manufacturing Technology, University of Duisburg-Essen, Lotharstrasse 1, 47057 Duisburg, Germany

* Corresponding author. Tel.: +49-201-183-3150; fax: +49-0201-183-3049. E-mail address: stephan.barcikowski@uni-due.de

Abstract

Nanoadditivation of polymer materials has high potential to meet the needs of material modification for laser powder bed fusion (PBF-LB/P), e.g. by tuning optical or mechanical properties. Colloidal additivation of polymer powders has proven to avoid aggregation of nanofillers on the polymer surface during additivation. In our study, we demonstrate kg-scale, continuous colloidal surface additivation of polymer powders to generate sufficient amounts for PBF-LB/P process development and manufacturing of test specimens. Furthermore, colloidal additivation achieves a high surface coverage even at low wt% and allows PBF-LB/P with CO₂ and diode lasers to form parts preserving the superior nanoparticle dispersion within TPU and PA12.

© 2020 The Authors. Published by Elsevier B.V.

This is an open access article under the CC BY-NC-ND license (<http://creativecommons.org/licenses/by-nc-nd/4.0/>)

Peer-review under responsibility of the Bayerisches Laserzentrum GmbH

Keywords: nanocomposites; laser powder bed fusion (PBF-LB); selective laser sintering (SLS); Laser synthesis and processing of colloids; upscaling, colloidal additivation; deposition

Introduction

Laser powder bed fusion (PBF-LB/P, according to ISO/ASTM DIS 52900:2018) has become an important prototyping and manufacturing technique over the last years [1]. Extending the variety of polymer powder feedstock materials is an important step to unlock PBF-LB/P's potentials for industrial applications [2], e.g. in fields of aerospace and automotive. Developing new materials, however, is challenging, due to the complex processing conditions during PBF-LB/P [3]. Additivation of polymer powders with nanomaterials for PBF-LB/P has proven to be a versatile approach for enhancing the powder processability and to

introduce new part properties and functionalization [4–7]. A high dispersion and homogeneous distribution of nanoparticles in/on the polymer matrix poses a key feature for the fabrication of nanoparticle-composites, but cannot be reached easily by conventional additivation methods like dry coating [8–10]. Colloidal additivation can overcome this challenge and can lead to extraordinary dispersion of nanoparticles on the polymer surface [11–13]. Nanoparticles are generated by flexible and scalable laser synthesis and processing of colloids (LSPC) [14] in aqueous solution and adsorbed onto the polymer surface by pH-controlled mixing with the polymer powder, followed by filtration and drying. This process is also well known for fabrication of heterogeneous catalysts [15–17]

and additivation of steel powders for additive manufacturing [18,19].

In order to generate sufficient amounts of nanoparticle-polymer composite powders for statistically validated PBF-LB/P experiments and process developments (> 3 kg), upscaling of the colloidal additivation process is of central importance. Hence, laser-generated nanoparticles in the gram-scale will be needed for each experiment, e.g. 3 g of colloidal nanoparticles are necessary to fabricate 3 kg of polymer composite powder with 0.1 wt% loading. The scalability of laser synthesis, namely the employed technique laser ablation in liquids (LAL), can be achieved by using a flow chamber setup in combination with high power, high repetition rate lasers and advanced scanning strategies [20] to result in a productivity of more than 1 g/h. Since the colloidal additivation of polymer powders is governed by colloidal stability and is therefore dependent on the interplay of particle concentration, electrostatic forces and mixing conditions [11,13], upscaling requires precise control of these parameters.

Our study focuses on upscaling of colloidal additivation towards kg-scale for fundamental PBF-LB/P studies and the influence of different upscaling strategies on the overall process duration as well as on the reproducibility and quality of the composite powders. Examples will be given for the PA12 (Evonik Vestosint 1115) and TPU (AM POLYMERS Rolaserit PB01) polymer powders decorated with silver nanoparticles as model systems, since optical powder analysis can be used on the surface plasmon resonance (SPR) peak to investigate the dispersion quantity and quality of nanoparticles on the polymer surface [13].

Strategies for upscaling

The process of colloidal additivation can be divided into five steps. LSPC, mixing, and filtration represent the “liquid part” in which the nanoparticle adsorption onto the powder takes place, whereas drying and sifting represent the “dry part”. A long duration for a specific process step, however, does not automatically mean that it is labor intensive, e.g. compared to the liquid part, the dry part requires a relatively small number of man-hours, although it makes up most of the overall process duration (Figure 1). Moreover, process duration and man-hours required for drying and sifting of a specific amount of polymer powder are independent of the individual batch size. However, several parameters with high influence on the liquid part and the overall process duration can be identified. For a certain mass of composite powder, the nanoparticle load governs the LSPC process duration. The higher the targeted nanoparticle load (wt%), the more nanoparticles are needed and the longer lasts the LSPC process. With increasing batch size, process duration of colloidal additivation decreases, because fewer batches are necessary for the same powder mass, resulting in fewer cleaning and preparation cycles (Figure 1a). For example, batches with 50 g each result in a total process duration of 11 hours for the liquid part, corresponding to 12 man-hours for preparation and operating the setup, whereas mixing in a 1 kg batch reduces the process duration and the required man-hours in the liquid part to 3 h and 4 h, respectively.

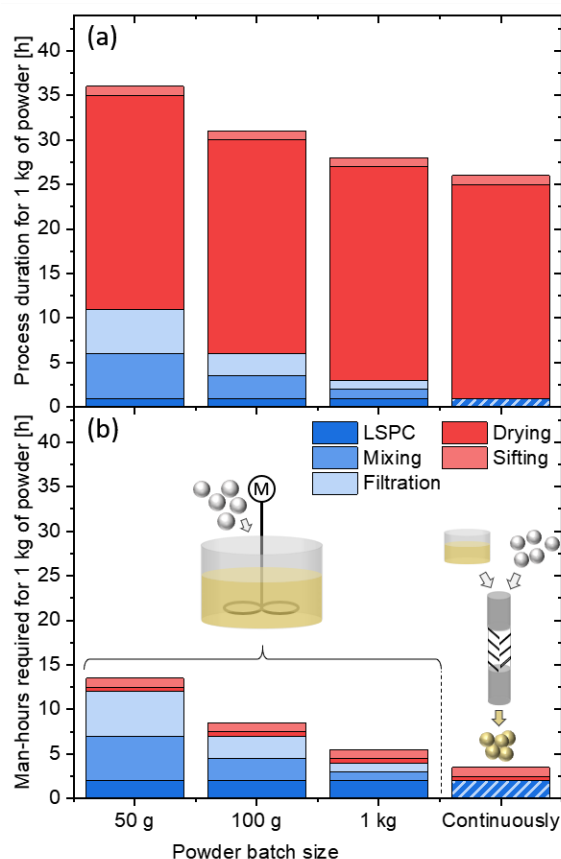


Fig. 1. Processing steps (liquid part and dry part) for colloidal additivation. Share of each process step on (a) the overall process duration and on (b) the required man-hours. The example is given for processing of 1 kg of polymer powder with 0.1 wt% of nanoparticles for different powder batch sizes compared to continuous processing. Fluid volumes scale linearly with the polymer amount and range from 1 l to 20 l for batch sizes of 50 g to 1 kg.

Either the colloid can be collected during LSPC and mixed with the polymer afterwards (Figure 2a), or a semi-continuous process can be established to support the nanoparticles on the polymer in parallel to LSPC (Figure 2b). In both cases stirring of the suspension is required for 60 minutes after adding the last portion of colloid to ensure complete mixing and high supporting efficiency (depending on the stirring conditions and material system).

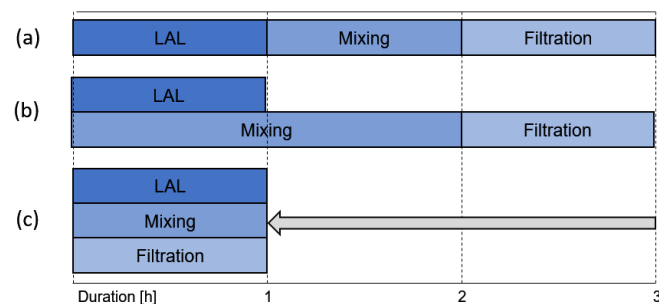


Fig. 2. Different procedures for upscaling towards 1 kg of polymer powder at 0.1 wt% of silver. (a) Batch wise and (b) Semi-continuous colloidal additivation in a stirred-tank reactor (1 kg batch) and (c) continuous processing with a static mixer.

Up-scaling of a stirred-tank process always needs adaption of the stirring conditions (geometry and rotation speed) for turbulent flow (high Reynolds number Re) and fast mixing to minimize the size of single fluid elements and to shorten the necessary diffusion length between polymer and nanoparticle. In order to decrease the mixing time and increase the process control, a static mixer can be utilized instead of a stirred-tank reactor. This also enables shortening the overall process duration (Figure 2c) by fully continuous operation of LSPC, mixing/supporting and filtration in parallel. Variation of reactor geometry and volume flow would also require further adaption to the colloidal additivation process for various nanoparticle-polymer systems and nanoparticle loadings. As a disadvantage, the more complex setup for continuous processing might not be useful for small batch fabrication with just a few grams of material.

Results and discussion

1.1. Batch wise colloidal additivation in a stirred-tank reactor

100 g batches in a stirred-tank reactor are the first step towards upscaling, since it delivers a sufficient amount for powder characterization, e.g. measurement of Hausner ratio, powder spreading tests on a PBF-LB/P machine or for first PBF-LB/P experiments.

As it was shown for silver nanoparticles on commercial PA12 powder (Evonik Vestosint 1115), the dispersion of PA12 powder in water induces a significant decrease in pH (buffer effect) during colloidal additivation in a stirred-tank reactor [13]. The longer the mixing duration and residence time, the lower the pH value of the suspension. This will affect the colloidal stability and the adsorption process. Moreover, different polymer-nanoparticle systems require different procedures for pH adjustment to perform colloidal additivation. Whereas the used PA12 powder comes with an intrinsic pH shift caused by the buffer effect, the TPU powder (AM POLYMERS Rolaserit PB01) does not change the pH of the suspension and needs external pH adjustment for successful colloidal additivation with silver nanoparticles [11]. If further pH-adjustment is needed during mixing, stirring conditions become even more important, because a long stirring time at a low pH close to the isoelectric point increases the probability for aggregation of the nanoparticles. This is not an issue for small batches of up to 100 g, where the mixing time for complete supporting of the nanoparticles on the polymer is still in the range of minutes to reach high supporting efficiency, as it is shown in Figure 3 for TPU microparticles additivated with silver nanoparticles. After stirring for 15 minutes under constant shifting of the pH by addition of hydrochloride acid (1 ml/min of 1 mol/l, total volume: 5 ml), the surface plasmon resonance (SPR) peak intensity of the permeate completely vanishes (Figure 3a), corresponding to a reproducible supporting efficiency of $99.80 \pm 0.12\%$. This is confirmed by UV-Vis absorption analysis of the powder (Figure 3c). The SPR peak of silver was successfully transferred to the polymer powder (Figure 3b) and the SPR peak position only slightly changes for upscaling from 1 g to 50 g or 100 g batches (Figure 3d). However, 100 g batches show a 20 % reduced SPR peak absorption with higher fluctuations, indicated by larger error

bars. The influence of long mixing time becomes even more obvious when increasing the batch size to 1 kg of TPU powder. As expected, this results in much longer stirring time and a higher risk for complete aggregation of silver and loss of plasmonic properties of the powder (Figure 3c,d). After 60 minutes of stirring, the supporting efficiency is reduced and powder and permeates tend to a green/grey color, instead of yellow color of non-aggregated Ag nanoparticles. Although this issue might be less pronounced for PA12-Ag, which does not need external pH adjustment and is a more robust system with less degree of freedom, these experiments highlight the potential problems during upscaling in a stirred-tank.

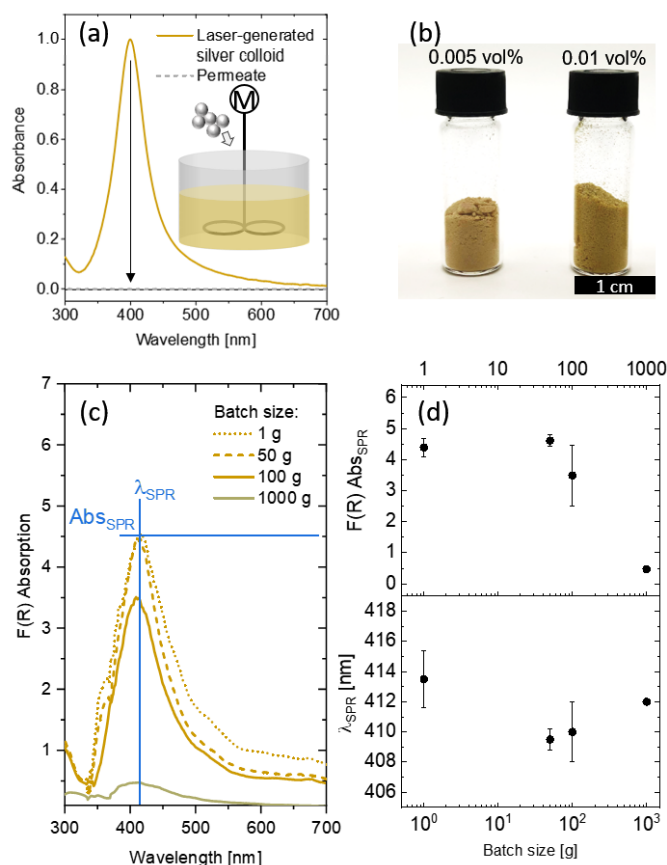


Fig. 3. (a) UV-Vis absorbance spectra of a silver colloid and the permeate before/after colloidal additivation in a 100 g batch of TPU, (b) exemplary powders, (c) absorption spectra of the functionalized powders made in different batch sizes and (d) corresponding SPR peak intensity ($F(R)$ absorption) and SPR peak wavelength. For the 1 kg batches, permeates come with high instability, which makes exact determination of supporting efficiency impossible

1.2. Continuous colloidal additivation with a static mixer

In order to shorten the mixing time and increase the process control, a static mixer can be utilized instead of a stirred-tank reactor for larger batch sizes. It also enables shortening the overall process duration as it was shown in Figure 2c by fully continuous operation of LSPC, mixing/supporting and filtration in parallel. To prove the concept for continuous colloidal additivation, a static mixer cascade was constructed based on the requirements regarding the necessary residence time as well as the polymer powder and nanoparticle

concentrations given for the PA12-silver-system [13]. 2 m of tubing (inner diameter 13 mm) were mounted on a base plate and filled with static mixer elements (ESSKA, PTFE elements) to create a static mixer with a total volume of 350 ml (Figure 4a,b). The volume flow of the colloid ($c = 50 \text{ mg/l}$) and the microparticle suspension ($c = 50 \text{ g/l}$) were both 250 ml/min. Operating at a total volume flow rate of 500 ml/min, equivalent to an average residence time of 40 s. The laser-generated silver colloid and the polymer suspension were stored in reservoirs of 2 l, which were refilled regularly. With respect to the previous experiments and under assumption of good mixing quality, a dwell time of 40 s is expected to achieve at least 90 % of supporting efficiency [13]. After the whole tubing was filled with suspension, samples of the suspension at the output of the static mixer cascade were taken every 2 minutes and directly filtered to allow calculations of supporting efficiency from the remaining SPR peak intensity of the permeate. The process runs for ten minutes in total and the complete product suspension was filtered directly at the output of the mixer.

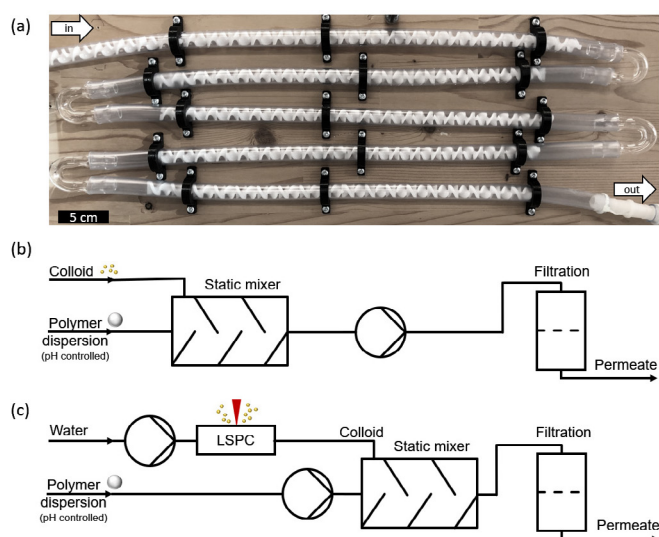


Fig. 4. (a) Image of the static mixer setup. (b) Schematic illustration of the used set-up operating with one sucking pump and (c) illustration of the proposed additivition system with two pumps, one of them directly attached to the LAL setup with further potential for fully automated continuous colloidal additivition of nanoparticles on polymer powders.

As expected, the SPR peak intensity of the permeate decreases significantly compared to the educt colloid and the supporting efficiency is constantly between 90 and 95 % throughout the process (Figure 5a). After filtration and drying, the homogeneously yellow-colored powders were investigated by diffuse reflectance spectroscopy, where a pronounced SPR peak can be observed (Figure 5b). The intensity at the SPR peak as a function of time in Figure 5b confirms only minor fluctuations and a steady state of the process. The SPR peak position at around 400 nm and the SPR intensity are similar to batch-wise processed silver-functionalized PA12 powder [12]. Compared to TPU powder, the SPR peak position is blue-shifted by 10-15 nm, indicating an even better dispersion of the nanoparticles on the PA12. Within 10 min a total liquid volume of 5 l flowed through the setup, equivalent to a productivity of 750 g/h (3 kg in 4 h), proving the concept of downstream

colloidal supporting. To increase productivity to an even higher extend, the volume flow rate and the length of the static mixer could be increased, resulting in a similar residence time but a more intense mixing. An increase of the reactor diameter is also an option but comes with decreasing velocity and therefore a less turbulent flux (lower Re), which should be avoided to ensure good mixing quality at the given residence time [21].

In future studies, the setup schematically illustrated in Figure 4c directly attached to a LSPC setup could allow even better control over the separate volume flows, for example to allow adjustment of pH values and nanoparticle load. Inline process monitoring, e.g. UV-Vis spectrometer, flowmeter, and pH-meter would allow full automatization and further increase of productivity and process stability. In order to influence the nanoparticle size, the setup could further be extended with inline centrifugation of the colloids before entering the static mixer [22].

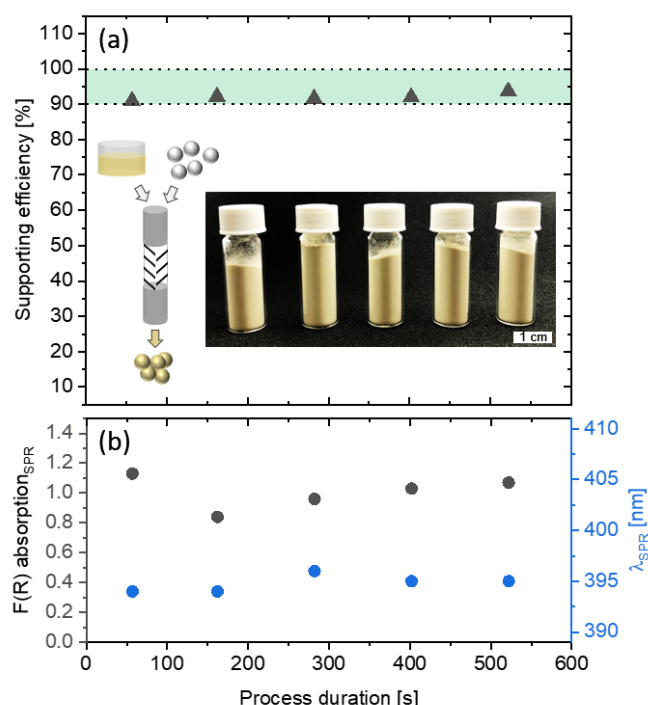


Fig. 5. (a) Supporting efficiency as a function of process duration during continuous colloidal supporting of colloidal nanoparticles on polymer powders with a static mixer at a volume flow rate of 500 ml/min and a powder throughput of 750 g/h (0.1 wt% silver). The inset shows dried functionalized powders collected during the process. (b) Exemplary F(R) absorption spectra of a functionalized powder and corresponding SPR peak absorption as a function of process duration.

1.3. Nanoparticle dispersion and powder processability

Colloidal additivited powders were sifted (125 μm) after drying. In addition, TPU powder was additivited with a flow aid (0.4 wt%, AM POLYMERS AC1) to enhance flowability. The functionalized powders showed a Hausner ratio of 1.14 (TPU-Ag with flow aid) and 1.13 (PA12-Ag) according to VDI 3405 sheet 1.1 norm, with matches the Hausner ratio of the base polymer powders without silver nanoparticle additivition (Table 1). Finally, both feedstock materials were successfully

processed through PBF-LB/P. TPU-Ag was processed on a diode laser machine (Sintratec S1, $\lambda = 445$ nm, more information in Table 2), whereas PA12 powder was processed on a Sharebot Snowwhite ($\lambda = 10.6$ μm , layer height of 300 μm , building platform temperature of 192 $^{\circ}\text{C}$). An overview of the materials and resulting parts is given in Figure 6. The preservation of the yellow color caused by the SPR of silver nanoparticles proves the outstanding nano-dispersion of silver along the whole process chain, which is the key feature of colloidal additivation and is also supported by TEM images of the final PA12 part (inset Figure 6f)

Table 1. Hausner ratio of the silver functionalized powders (0.01 vol%) compared to the powders without silver functionalization.

	Hausner ratio
TPU + flow aid	1,20
TPU-Ag + flow aid	1,14
PA12	1,15
PA12-Ag	1,13

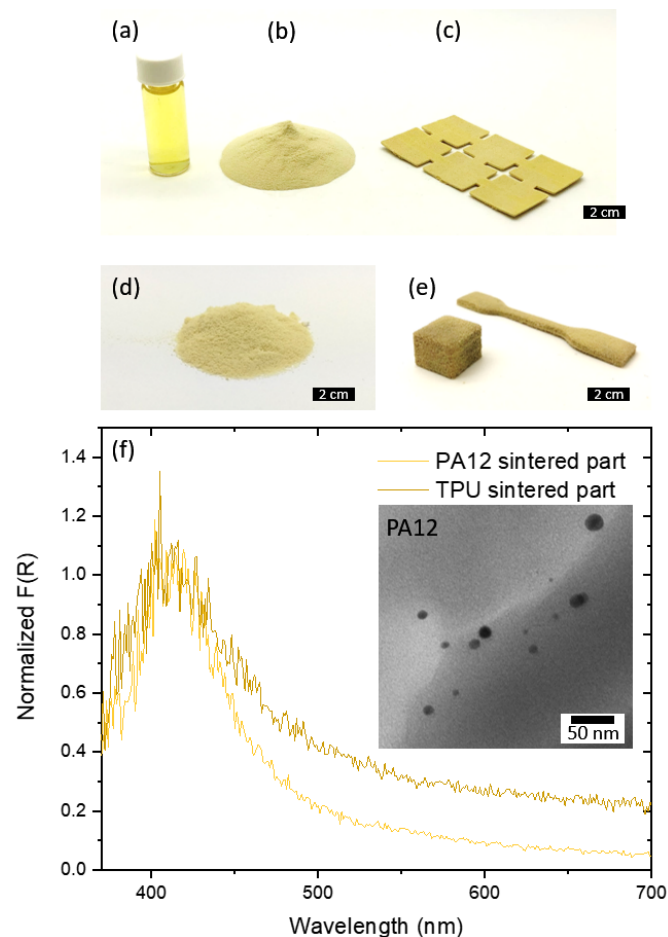


Fig. 6. Conservation of the surface plasmon resonance along the process chain for colloidal additivation of PA12 and TPU powders with silver nanoparticles, indicated by its characteristic yellow color. (a) Laser-generated silver colloid, (b) silver additivated PA12 powder, (c) test structures built from PA12-Ag powder by CO₂-laser PBF-LB/P and (d) TPU powder with (e) corresponding TPU-Ag test structures built by diode laser PBF-LB/P, exploiting the enhanced powder absorption by the plasmon resonance at the diode laser wavelength of 445 nm. (f) Absorption measurement of printed parts with the inset showing a TEM image of a sliced PA12 part.

Table 2. Parameters for diode laser PBF of silver functionalized TPU powder with a silver nanoparticle loading of 0.01 vol%.

	Powder bed temperature [$^{\circ}\text{C}$]	Laser power [W]	Hatch distance [mm]	Scan speed [mm/s]	Volume energy density [J/mm^3]
Sintratec S1 (445 nm laser)	94	2	0.05	200	2.0

Conclusion

In conclusion, the process of colloidal additivation of nanoparticles on polymer powders was successfully scaled-up towards kg-scale. Since drying and sifting are relatively easy to scale to kg/day, the liquid-phase processing is identified as the current bottleneck with highest optimizing potential to reduce the amount of man-hours/kg. For small batch sizes of up to 100 g of functionalized powder, a batch process in a stirred-tank reactor is a feasible method, whereas a continuous processing with a static mixer leads to high throughput in the kg-scale, which is necessary for using the nanoparticle-functionalized powder for PBF-LB/P part fabrications. Besides, along the whole process chain, nanoparticle properties are preserved. Whilst productivity is enhanced by this continuous approach, process control could profit from it as well. The fast mixing and narrow residence time distribution of a static mixer could enable precise control over nanoparticle adsorption and dispersion on the polymer particle surface by fine tuning pH values, volume flow rates and concentrations of the mixed fluids. Nanoparticles could be supported just a few seconds after LSPC under constant conditions. Encouraged by the results presented here, future studies should focus on process optimization and investigation of the deposition yield, kinetics and nanoparticle dispersion in steady state conditions for various polymer-nanoparticle systems. Through automatization, this continuous colloidal additivation approach has high potential to meet the needs for upscaling towards the multi-kg and thus increasing the technology readiness level (TRL), which is a common measure for evaluation of the technology development status [23] and was demonstrated by Maurer et al. for laser-based nanoparticle-polymer composite fabrication [24].

Acknowledgements

Tim Hupfeld thanks Vladyslav Sharov for his help during experiments. Tim Hupfeld also acknowledges Evonik Industries for financial support of his work. Alexander Blaszcyk gratefully acknowledges funding of the Erlangen Graduate School in Advanced Optical Technologies (SAOT) by the German Research Foundation (DFG) in the framework of the German excellence initiative. The authors gratefully acknowledge the funding by the German Research Foundation (DFG) within the priority program (SPP) 2122 “Materials for Additive Manufacturing (MATframe, BA 3580/27-1 + SCHM 2115/78-1).

References

- [1] Wohlers Associates, Wohlers Report 2019, (2019) 369.
- [2] Nationale Akademie der Wissenschaften Leopoldina, Deutschen Akademie der Technikwissenschaften Acatech, Additive Fertigung, Munich, 2017.
- [3] A. Wegner, New polymer materials for the laser sintering process: Polypropylene and others, *Phys. Procedia*. 83 (2016) 1003–1012. doi:10.1016/j.phpro.2016.08.105.
- [4] S. Yuan, F. Shen, C.K. Chua, K. Zhou, Polymeric composites for powder-based additive manufacturing: Materials and applications, *Prog. Polym. Sci.* 91 (2019) 141–168. doi:10.1016/j.progpolymsci.2018.11.001.
- [5] S.R. Athreya, K. Kalaitzidou, S. Das, Processing and characterization of a carbon black-filled electrically conductive Nylon-12 nanocomposite produced by selective laser sintering, *Mater. Sci. Eng. A*. 527 (2010) 2637–2642. doi:10.1016/j.msea.2009.12.028.
- [6] A.W. Powell, A. Stavrinadis, I. De Miguel, G. Konstantatos, R. Quidant, White and Brightly Colored 3D Printing Based on Resonant Photothermal Sensitizers, *Nano Lett.* 18 (2018) 6660–6664. doi:10.1021/acs.nanolett.8b01164.
- [7] M.M. Lexow, D. Drummer, New Materials for SLS: The Use of Antistatic and Flow Agents, *J. Powder Technol.* 2016 (2016) 1–9. doi:http://dx.doi.org/10.1155/2016/4101089.
- [8] H.C. Kim, H.T. Hahn, Y.S. Yang, Synthesis of PA12/functionalized GNP nanocomposite powders for the selective laser sintering process, *J. Compos. Mater.* 47 (2012) 501–509. doi:10.1177/0021998312441812.
- [9] C. Blümel, M. Sachs, T. Laumer, B. Winzer, J. Schmidt, M. Schmidt, W. Peukert, K.E. Wirth, Increasing flowability and bulk density of PE-HD powders by a dry particle coating process and impact on LBM processes, *Rapid Prototyp. J.* 21 (2015) 697–704. doi:10.1108/RPJ-07-2013-0074.
- [10] J. Yang, A. Sliva, A. Banerjee, R.N. Dave, R. Pfeffer, Dry particle coating for improving the flowability of cohesive powders, *Powder Technol.* 158 (2005) 21–33. doi:10.1016/j.powtec.2005.04.032.
- [11] T. Hupfeld, A. Wegner, M. Blanke, C. Doñate-Buendía, V. Sharov, S. Nieskens, M. Piechotta, M. Giese, S. Barcikowski, B. Gökce, Plasmonic seasoning: Giving color to desktop laser 3D-printed polymers by highly dispersed nanoparticles, *Adv. Opt. Mater.* (2020). doi:10.1002/adom.202000473.
- [12] T. Hupfeld, T. Laumer, T. Stichel, T. Schuffenhauer, J. Heberle, M. Schmidt, S. Barcikowski, B. Gökce, A new approach to coat PA12 powders with laser-generated nanoparticles for selective laser sintering, *Procedia CIRP*. 74 (2018) 244–248. doi:10.1016/j.procir.2018.08.103.
- [13] T. Hupfeld, A. Blasczyk, T. Schuffenhauer, E. Zhuravlev, M. Krebs, S. Gann, O. Keßler, M. Schmidt, B. Gökce, S. Barcikowski, How colloidal surface additivation of polyamide 12 powders with well-dispersed silver nanoparticles influences the crystallization already at low 0.01 vol%, *Submitt. to Addit. Manuf.* (2020).
- [14] D. Zhang, B. Gökce, S. Barcikowski, *Laser Synthesis and Processing of Colloids: Fundamentals and Applications*, *Chem. Rev.* 117 (2017) 3990–4103. doi:10.1021/acs.chemrev.6b00468.
- [15] S. Reichenberger, G. Marzun, M. Muhler, S. Barcikowski, Perspective of Surfactant-Free Colloidal Nanoparticles in Heterogeneous Catalysis, *ChemCatChem*. 11 (2019) 4489–4518. doi:10.1002/cctc.201900666.
- [16] D. Zhang, J. Liu, P. Li, Z. Tian, C. Liang, Recent Advances in Surfactant-Free, Surface-Charged, and Defect-Rich Catalysts Developed by Laser Ablation and Processing in Liquids, *ChemNanoMat*. 3 (2017) 512–533. doi:10.1002/cnma.201700079.
- [17] J. Zhang, M. Chaker, D. Ma, Pulsed laser ablation based synthesis of colloidal metal nanoparticles for catalytic applications, *J. Colloid Interface Sci.* 489 (2017) 138–149. doi:10.1016/j.jcis.2016.07.050.
- [18] C. Doñate-Buendía, F. Frömel, M.B. Wilms, R. Streubel, J. Tenkamp, T. Hupfeld, M. Nachev, E. Gökce, A. Weisheit, S. Barcikowski, F. Walther, J.H. Schleifenbaum, B. Gökce, Oxide dispersion-strengthened alloys generated by laser metal deposition of laser-generated nanoparticle-metal powder composites, *Mater. Des.* 154 (2018) 360–369. doi:10.1016/j.matdes.2018.05.044.
- [19] R. Streubel, M.B. Wilms, C. Doñate-Buendía, A. Weisheit, S. Barcikowski, J.H. Schleifenbaum, B. Gökce, Depositing laser-generated nanoparticles on powders for additive manufacturing of oxide dispersed strengthened alloy parts via laser metal deposition, *Jpn. J. Appl. Phys.* 57 (2018). doi:10.7567/JJAP.57.040310.
- [20] R. Streubel, S. Barcikowski, B. Gökce, Continuous multigram nanoparticle synthesis by high-power, high-repetition-rate ultrafast laser ablation in liquids, *Opt. Lett.* 41 (2016) 1486–1489. doi:10.1364/OL.41.001486.
- [21] M.H. Pahl, E. Muschelknautz, Einsatz und Auslegung statischer Mischer, *Chemie Ing. Tech.* 51 (1979) 347–364. doi:10.1002/cite.330510504.
- [22] S. Kohsakowski, F. Seiser, J.P. Wiederrecht, S. Reichenberger, T. Vinnay, S. Barcikowski, G. Marzun, Effective size separation of laser-generated, surfactant-free nanoparticles by continuous centrifugation, *Nanotechnology*. 31 (2020). doi:10.1088/1361-6528/ab55bd.
- [23] M. Héder, From NASA to EU: The evolution of the TRL scale in Public Sector Innovation, *Innov. J.* 22 (2017).
- [24] E. Maurer, S. Barcikowski, B. Gökce, Process Chain for the Fabrication of Nanoparticle Polymer Composites by Laser Ablation Synthesis, *Chem. Eng. Technol.* 40 (2017) 1535–1543. doi:10.1002/ceat.201600506.

11th CIRP Conference on Photonic Technologies [LANE 2020] on September 7-10, 2020

Evaluation of essential powder properties through complementary particle size analysis methods for laser powder bed fusion of polymers

A. Sommereyns^{a,b,*}, T. Hupfeld^c, B. Gökce^c, S. Barcikowski^c, M. Schmidt^{a,b}

^aInstitute of Photonic Technologies (LPT), Friedrich-Alexander-Universität Erlangen-Nürnberg, Konrad-Zuse-Str. 3-5, 91052 Erlangen, Germany

^bErlangen Graduate School in Advanced Optical Technologies (SAOT), Paul Gordan Straße 6, 91052 Erlangen, Germany

^cTechnical Chemistry I and Center for Nanointegration Duisburg-Essen (CENIDE), University of Duisburg-Essen, Universitätsstrasse 7, 45141 Essen, Germany

* Corresponding author. Tel.: +49-913-185-64102; fax: +49-913-185-23234. E-mail address: alexander.blaszczyk@lpt.uni-erlangen.de

Abstract

The resolution of complex parts produced by laser powder bed fusion of polymers (PBF-LB/P) is defined significantly by the shape and size distribution of the feedstock powder. Its analysis is usually performed by optical measurement systems such as laser diffraction or image analysis. In this study, the most relevant particle size parameters will be extracted from a set of different measuring methods, as well as the Hausner ratio and finally discussed regarding safe and successful processability. Extracted data include the sphericity, fine fraction, volume- and number-weighted diameter distributions, and statistical significance analysis, including comparison of PA12 and carbon-black-additivated PA12. The presented results should give researchers a first impression about the suitability of polymer powders for PBF-LB/P, based on powder feedstock characterization.

© 2020 The Authors. Published by Elsevier B.V.

This is an open access article under the CC BY-NC-ND license (<http://creativecommons.org/licenses/by-nc-nd/4.0/>)

Peer-review under responsibility of the Bayerisches Laserzentrum GmbH

Keywords: polymer powders; laser beam melting; PBF-LB/P; particle size distribution; flowability; image analysis; laser diffraction, selective laser sintering

1. Introduction

The ability to create fine structures and precise geometries with a resolution close to the feedstock powder particle sizes is one of the advantages of laser powder bed fusion of polymers (PBF-LB/P) [1,2]. Through a layer by layer principle, three-dimensional structures can be created without the need of subtractive machining [3]. Besides important thermal and optical material properties, the particle shape and its distribution affects the powder processability, specifically the recoating process during powder application, and thus influence the quality and performance of the produced parts [4–8].

As a first estimation of the provided powder quality (VDI 3405 Part 1.1), datasheets of powder manufacturer typically provide the quantile particle diameters $x_{10,3}$, $x_{50,3}$, and $x_{90,3}$ of the cumulative volume-weighted size distribution (Q_3). In this

arrangement, larger particles have a more significant impact on the distribution than small ones [9]. However, a high amount of finer particles increases the cohesion among the powder particles [6,10], which impairs the powder flowability and thus the powder application during PBF-LB/P [11–13]. Consequently, the cumulative number-weighted particle size distribution (Q_0) needs to be addressed as well, where every particle is equally weighted relative to the total number of particles [14,15].

Being able to evaluate small particles also allows the examination of particle sizes smaller than 10 μm , which are inhalable and thus can affect the circulatory system of heart and lungs of the human body [16–19]. However, round particles can be more easily removed by alveolar macrophages through phagocytosis than fibrous particles which exhibit an increased

length in one dimension [20,21]. These conditions of particle size and shape also apply for polymer particles [22,23].

The particle morphology is not only relevant regarding human health but also important for the spreadability of the powder by the coater in a PBF-LB/P machine. Typically, spherical or potato shapes are considered the most suitable forms for PBF-LB/P powders due to their achievable high powder density and good flowability [6,14,24–28]. Up to now, there is still a lack of measuring systems to accurately examine the spreadability of PBF-LB/P powders in such a way to emulate the recoating mechanisms under realistic process conditions [12,29]. Currently, most instruments rely on measuring the flowability of loose powders at room temperature (e.g. angle of repose, powder rheometer, revolution powder analyzer, bulk and tapped volume [6,12,30]). Despite its simplicity, one of the most commonly used technique is the empirical calculation of a flow index via the Hausner ratio H_R . The main advantages are the fast procedure and its high reproducibility for thermoplastic powders even among different work spaces and operators [6,31,32]. Modified annular ring shear cells, which can determine the flowability under high temperatures, show the potential to replace the Hausner ratio measurement [33–35]. However, ring shear test measurements are more time consuming and the powder is not recyclable afterwards due to thermal aging. The spreading process of the ring shear cell still doesn't replicate the recoating process of PBF-LB/P, but comes closer to it than any other method so far.

Frequently used methods for particle analysis are laser diffraction measurements (ISO 8130-13) [36–40] as well as static (ISO 13322-1) [41–45] and dynamic image analysis (ISO 13322-2) [45–48]. Depending on the utilized particle size analysis method, the obtained results may show large discrepancies due to different physical measuring principles and mathematical calculations [49].

Among the vast amount of available particle analysis techniques, this study aims to provide an overview of the effect of different measuring principles on the results of examined powder particles and which parameters are important for a first assessment of the suitability of polymer powders for PBF-LB/P.

Nomenclature

CB	carbon black
LM	light microscopy
PA12	polyamide 12
PBF-LB/P	laser powder bed fusion of polymers
$Q_{0/3}$	cumulative particle distribution, weighted by number (0) or volume (3) of particles
rpm	rounds per minute
SEM	scanning electron microscopy
x_{area}	particle diameter calculated by the area of a particle, assuming a spherical shape
$x_{Fe\ max}$	longest Feret diameter of a particle

2. Materials and methods

Polyamide 12 powders (PA12; Evonik Vestosint 1115) were used for the particle analyses. To evaluate the effect of adhesion of additives on the particle morphology and size, 1 wt% Carbon Black (CB; Origin "Lamp Black") were added to the surface of the PA12 powders through mechanical mixing (milling with 50 g steel balls at a rotation speed of 60 rpm for 2 h).

Automated analyses via static laser diffraction were conducted in air and in a wet state (Sympatec HELOS equipped with RODOS and SUCCELL), based on x_{area} . In the wet state, 20 mg of polymer particles were dispersed in water by ultrasonic treatment. In air, the analysis required at least 200 g of powder for measurements. The range of detectable particles was between 0.5/0.9 μm and 175 μm .

For the dynamic image analysis, a few grams of PA12 powder, which corresponds to approximately 500,000 detectable particles, were analyzed via the Camsizer X2 with compressed air of 50 kPa through the X-Jet extension to get rid of possible agglomerations. The range of detection went from 0.8 μm to 8 mm. The system allowed the simultaneous measurement of number- and volume-weighted particle size distributions using a two-camera system. Respectively, the particle diameter x_{area} and the longest Feret diameter $x_{Fe\ max}$ have been recorded for comparison between the different particle analysis methods. The sphericity (ISO 9276-6) was calculated by using volume-weighted data and was based on the measurements of x_{area} .

Approximately 1000 PA12 powder particles were analyzed by light microscopy at 20-fold magnification (one pixel corresponds to 0.33 μm) by applying a single powder layer on a microscope slide. The ImageJ plugin ParticleSizer [50,51] has been used for the semi-automatized particle size ($x_{Fe\ max}$) measurements and all images were checked manually on misinterpretation of agglomerated particles.

SEM images were taken after applying a powder layer on an adhesive carbon tape and removing loose powder particles. A 3 nm layer of platinum was sputtered on the powder layer. Images (one pixel corresponds to 9.93 μm) of about 100 PA12 powder particles were analyzed manually ($x_{Fe\ max}$), since the contrast was not suitable for automated analysis.

In order to get an impression of the general flowability of the powder, the Hausner ratio H_R was measured according to VDI 3405 Part 1.1 with a 100 mL plastic measuring cylinder. The procedure was repeated five times for the same powder for statistical analysis. For maintaining the same prerequisites, the powders have been analyzed as received within a short time span by the same operator.

For the statistical evaluation of available datasets, analyses of significance ($p \leq 0.05$) have been conducted.

3. Results and discussion

When considering a typical powder layer in PBF-LB/P of 100 μm , firstly, the median value ($x_{50,3}$) should be represented by at least two particles [52]. Assuming perfectly spherical particles, an $x_{50,3}$ value of around 50 – 59 μm should be ideal considering stacking two particles on each other (worst case) and an optimal dense powder layer (best case) in z-direction of the powder bed (Fig. 1). The radius of the best case was calculated by (1):

$$2r + \sin 45^\circ \cdot 2r = 100 \mu\text{m} \quad (1)$$

Secondly, at least 90 % of the particles ($x_{90,3}$) should measure less than 100 μm in size to ensure that one particle doesn't exceed the typical layer height and thus parts with lower accuracy and resolution are produced [6].

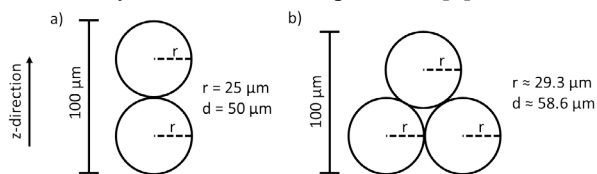


Fig. 1. A layer of 100 μm , achieved by (a) stacking two 50 μm particles onto each other and (b) by close-packing of equal spheres, but with larger diameter; displayed as two-dimensional images.

For all particle measurements it is important to know which kind of particle diameter they are based on. The differences between particle diameters measured by laser diffraction and image analysis can be clearly distinguished for PA12 in Fig. 2 a.

Despite the wider availability of static image analysis systems, the amount of analyzable particles is much smaller than with dynamic image analysis and thus comes with weaker statistics. LM and SEM would declare the analyzed powder as suitable for PBF-LB/P when considering only the second criterion, as they show an $x_{50,3}$ value of 72 μm with LM and 74 μm with SEM, while their $x_{90,3}$ values are at 92 μm . Accordingly, dynamic image analysis of $x_{Fe\ max}$ display an $x_{50,3}$ value of 67 μm and an $x_{90,3}$ value of 91 μm .

SEM, LM and Camsizer measurements coincide, among a few outliers, at the important particle quantiles. The overestimation of certain particle sizes can be explained by existing agglomerated particles, which cannot be completely avoided in the microscopic setups. Especially small polymer particles below 40 μm are underestimated due to agglomeration and adhesion on larger particles. Nevertheless, the relatively large overlap between the results of the automatic dynamic image analysis and the microscopic methods proves that the manual or semi-automatized measurement is feasible to represent our powder batch. However, determining only the Feret diameter would not be sufficient to define the shape of particles, since it only depicts one size.

Automatic analysis methods (dynamic image analysis and laser diffraction), which base their calculations of particle sizes on x_{area} can examine higher amounts of powder in a short time, leading to better statistics. In this regard, Camsizer measurements exhibit an $x_{50,3}$ of 59 μm and an $x_{90,3}$ of 77 μm . Meanwhile, laser diffraction measurements in air result in an

$x_{50,3}$ of 58 μm and an $x_{90,3}$ of 89 μm . Surprisingly, measurements in water deliver larger particle sizes with an $x_{50,3}$ of 61 μm and an $x_{90,3}$ of 108 μm , even though particles were dispersed in water by ultrasound. The particles seem to be less dispersed in water than in air due to a possible lack of wetting of smaller particles, resulting in agglomerations. Measurements in Ethanol instead of water could improve the accuracy of the results. Only the Camsizer and laser diffraction measurements in air would declare the analyzed powder as suitable for PBF-LB/P, when considering the aforementioned two criteria. While there is a certain agreement at $x_{50,3}$, the cumulative distribution curve measured with dynamic image analysis has a steeper slope than the one of static laser diffraction (Fig. 2 a, c), which increases the total range of measured particle sizes with static laser diffraction.

The cumulative distribution curves of each method show overall similar characteristics in their slope and course. A closer look reveals that the dynamic image analysis seems to measure a higher amount of smaller particles than the laser diffraction and the microscopic methods below 5 % due to their different measuring principles (Fig. 2 b, c).

Furthermore, the curves of x_{area} and $x_{Fe\ max}$ of the dynamic image analysis match below 32 μm , providing useful data on the ratio of length to width of the powder particles. An overlap of x_{area} and $x_{Fe\ max}$ data would refer to spherical particles, while larger $x_{Fe\ max}$ values would indicate irregular, elongated shapes. In our study, this becomes especially apparent for particles > 32 μm , where $x_{Fe\ max}$ displays an up to 13 μm shift to higher values than x_{area} . This difference indicates the potato-shape of the PA12 powders over 32 μm , while smaller particles have a more spherical character. Analyzing both x_{area} and $x_{Fe\ max}$ can be useful to estimate the overall shape of the particles, depending on how well the x_{area} and $x_{Fe\ max}$ values coincide.

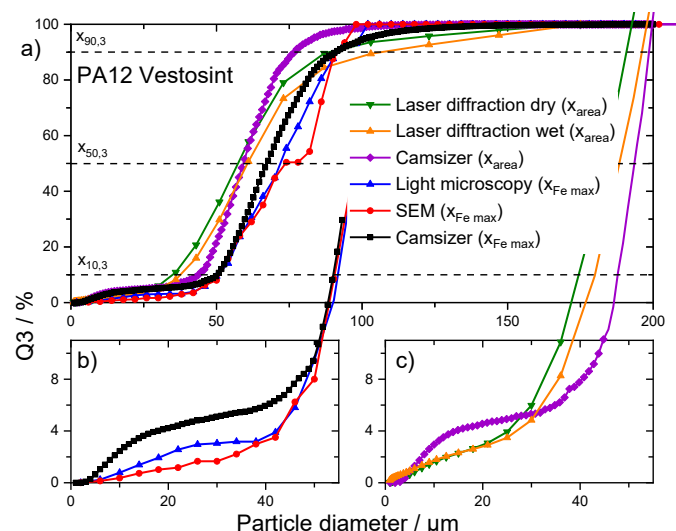


Fig. 2. Comparison of PA12 Vestosint 1115 between the different particle diameters (Q_3) through various methodologies with (a) the complete particle size distribution of every method and their values below $x_{10,3}$ (b) for $x_{Fe\ max}$ and (c) for x_{area} .

In order to avoid misinterpretations, the particles must have a chance to deagglomerate during the analyzing process. Applying a powder layer on a microscopic slide or letting particles fall down a shaft by gravity are not suitable approaches to adequately represent the distribution of powders for PBF-LB/P. Analysis methods which base their calculations on χ_{area} should be used preferably as first estimation. This diameter depicts particles as close to a sphere as possible, including their length and width, while others measure only one size [53]. This way, particles with different morphologies can be compared more easily with a perfect sphere, which is an optimal geometrical shape for PBF-LB/P [5,13,54]. Even when the particle diameter is the same by definition, each method uses its own mathematical calculations and assumptions based on different physical processes. Despite similar tendencies and characteristics, results of different particle size analysis methods can have significant differences, even when the same methodology has been applied.

Accordingly, further investigations of important particle parameters were carried out for this study with dynamic image analysis (Camsizer X2) and repeated three times for statistical analysis. The relevant findings can be transferred to other methods analogously.

To understand how many fine particles ($< 10\mu\text{m}$) are within the powder batch, the typically displayed $\chi_{10,3}$ values don't give conclusive results due to the overall particle volume outweighing individual particle sizes (Fig. 2 b, c). Instead, the analysis of fine particles should be done via the number-weighted distribution Q_0 . A certain amount of fine particles may even be useful for PBF-LB/P, as they fill the gaps between bigger particles and thus lead to denser parts [11,28,55,56]. The difference between the volume- and number-weighted distributions of the used polymer powders can be seen in Fig. 3 a.

In this study, based on the volume-weighted distribution, only 3 % of the PA12 particle diameters are below $10\mu\text{m}$ (Fig. 3 a). The addition of 1 wt% CB shows a small effect on the volume-weighted particle size distribution with an increase of $\chi_{90,3}$ from 74.90 ± 1.20 to 78.10 ± 1.31 , while the other quantile diameters remain within the range of the standard deviations (Fig. 3 b).

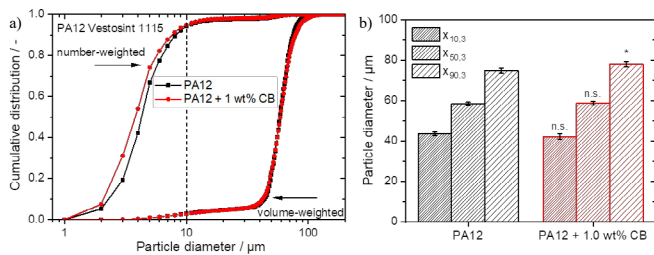


Fig. 3. (a) Distribution curves depicting the difference between the cumulative number- and volume-weighted particle size distribution of PA12 and its addition with 1 wt% CB, resulting in (b) averaged volume-weighted particle sizes. The significance levels ($p \leq 0.05$) are depicted with an asterisk (*); a declaration of "n.s." will be used in case of no significant differences.

On the other hand, when considering the number-weighted distribution, 94 % of PA12 particles and 95 % of PA12 + 1 wt% CB particles are smaller than $10\mu\text{m}$ (Fig. 3 a). At the same time, the values of PA12 significantly decrease for $\chi_{10,0}$ from 2.45 ± 0.10 to 2.10 ± 0.06 , for $\chi_{50,0}$ from 4.28 ± 0.05 to 3.80 ± 0.06 and for $\chi_{90,0}$ from 8.15 ± 0.19 to 7.57 ± 0.15 due to the addition process of CB through mechanical forces during milling (Fig. 4 a). The sphericity below $10\mu\text{m}$ for PA12 is between 0.82 and 0.91, while it lies between 0.79 and 0.89 for PA12 + 1 wt% CB. These values correlate to ellipsoidal particles that can be removed from the respiratory system by alveolar macrophages [22,23].

Next to this, the average sphericity of particles represents an important parameter for the spreadability in PBF-LB/P. The values should be between 0.79 (potato shape) and 0.99 (spherical shape) [57,58], while a perfect sphericity of 1 can hardly be achieved during powder manufacturing. This parameter becomes especially relevant if the good flowability of already optimally shaped particles has to be maintained by adhesion of additives to their surface. In our study, the particles retained their average sphericity of 0.80 by adding 1 wt% of CB onto the PA12 particles.

The particle size evaluations on a microscopic level may also macroscopically affect the powder spreadability during the recoating process. When combining the resulting data of Q_0 with the H_R , it becomes apparent that the ball milling process reduces the particle sizes of PA12 significantly (**; $p \leq 0.01$) by up to $0.5\mu\text{m}$, increasing the H_R value from 1.10 ± 0.03 to 1.18 ± 0.02 (Fig. 4). This means that the flowability worsened due to an increase in inter-particle cohesion of more available smaller particles, which were formed through impact and attrition during the ball milling process. Note that Hausner ratio can only be a first indication of flowability, but is often considered to be inappropriate to predict an accurate PBF-LB/P processing behavior [12,59,60].

Nevertheless, the overall good flowability (< 1.25) is still maintained. Smaller particles don't per se worsen the flowability in such a way that they are not spreadable anymore during the recoating process. First PBF-LB/P runs under elevated temperatures showed that the recoating process was not affected by the addition of 1 wt% CB to the PA12 surface.

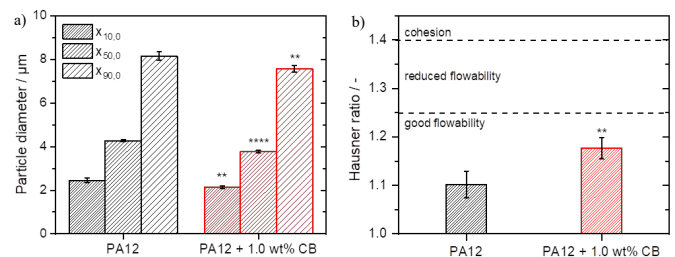


Fig. 4. (a) The particle diameters (χ_{area}) of PA12 powders based on the number-weighted Q_0 and (b) the powder flowability. The significance levels ($p \leq 0.05$) are depicted with an asterisk (*); the higher the significant difference to the reference, the more asterisks are appointed.

4. Conclusion

The availability of different particle size analysis methods can be overwhelming due to a large amount of possible analysis options. In this article, we summarized the most important parameters for a first on-site evaluation of the suitability of feedstock powders for PBF-LB/P.

Measurements of particle sizes, distributions and shapes should be conducted by automated measuring systems (e.g. dynamic image analysis and laser diffraction) due to their high reproducibility and representativeness for the whole powder batch. To break-up agglomerations, particles should be analyzed with compressed air or dispersed in an appropriate solvent. It is important to clearly indicate which particle analysis methodology has been used to avoid misinterpretations. Choosing the particle parameter x_{area} allows the comparison of spheres with differently shaped particles, as it normalizes different particle morphologies to its projection surface. Contrary to what is often prescribed by powder manufacturers and listed in the VDI 3405 Part 1.1, not only the volume- but also the number-weighted distributions need to be calculated to have a better understanding of the amount and characteristics of fine particles in the powder batch. Volume-weighted distributions should be used to extract the particle diameters $x_{50,3}$ and $x_{90,3}$ as well as the average sphericity of the powder particles to give a first indication of their ability to form precise layers during the recoating process of PBF-LB/P, as it is driven by powder volume. Number-weighted distributions are essential to indicate the content of fine particles ($< 10 \mu\text{m}$) in the feedstock powder and to estimate the effect of additivation processes on the base powder properties. Besides the size, the sphericity of fine particles is also relevant for occupational safety. In combination with the obtained particle properties, determining the Hausner ratio should provide a straightforward estimation of the flowability of thermoplastics in powder form.

Acknowledgements

The authors thank Marc Labusch for size measurements of the polymer powder particles via static laser diffraction. We thank Smal Boukercha (AK Eppele, University of Duisburg-Essen) for SEM imaging of the powders. Alexander Sommereyns would like to thank Tobias Kolb (Robert Bosch GmbH Nürnberg) for providing the possibility of powder measurements with the Camsizer X2. The authors acknowledge Evonik industries for the provision of PA12 powders. Tim Hupfeld thanks Evonik industries for funding. Alexander Sommereyns gratefully acknowledges funding of the Erlangen Graduate School in Advanced Optical Technologies (SAOT) by the German Research Foundation (DFG) in the framework of the German excellence initiative. The authors also gratefully acknowledge the funding by the German Research Foundation (DFG) within the priority program (SPP) 2122 “Materials for Additive Manufacturing (MATframe, BA 3580/27-1 + SCHM 2115/78-1).

References

- [1] O. Ojogba Spencer, Additive Manufacturing Technology Development: A Trajectory Towards Industrial Revolution, *Am. J. Mech. Ind. Eng.* 3 (2018) 80. doi:10.11648/j.ajmie.20180305.12.
- [2] A. Dawood, B.M. Marti, V. Sauret-Jackson, A. Darwood, 3D printing in dentistry, *Br. Dent. J.* 219 (2015) 521–529. doi:10.1038/sj.bdj.2015.914.
- [3] J. Kietzmann, L. Pitt, P. Berthon, Disruptions, decisions, and destinations: Enter the age of 3-D printing and additive manufacturing, *Bus. Horiz.* 58 (2015) 209–215. doi:10.1016/J.BUSHOR.2014.11.005.
- [4] S. Dadbakhsh, L. Verbelen, O. Verkinderen, D. Strobbe, P. Van Puyvelde, J.P. Kruth, Effect of PA12 powder reuse on coalescence behaviour and microstructure of SLS parts, *Eur. Polym. J.* 92 (2017) 250–262. doi:10.1016/j.eurpolymj.2017.05.014.
- [5] S. Vock, B. Klöden, A. Kirchner, T. Weißgärber, B. Kieback, Powders for powder bed fusion: a review, *Prog. Addit. Manuf.* 4 (2019) 383–397. doi:10.1007/s40964-019-00078-6.
- [6] M. Schmid, *Laser Sintering with Plastics - Technology, Processes, and Materials*, Carl Hanser Verlag GmbH & Co. KG, München, 2018. doi:10.3139/9781569906842.
- [7] L. Verbelen, S. Dadbakhsh, M. Van den Eynde, J.-P. Kruth, B. Goderis, P. Van Puyvelde, Characterization of polyamide powders for determination of laser sintering processability, *Eur. Polym. J.* 75 (2016) 163–174. doi:10.1016/j.eurpolymj.2015.12.014.
- [8] S. Dadbakhsh, L. Verbelen, T. Vandeputte, D. Strobbe, P. Van Puyvelde, J.-P. Kruth, Effect of Powder Size and Shape on the SLS Processability and Mechanical Properties of a TPU Elastomer, *Phys. Procedia.* 83 (2016) 971–980. doi:10.1016/J.PHPRO.2016.08.102.
- [9] D.J. Burgess, E. Duffy, F. Etzler, A.J. Hickey, Particle size analysis: AAPS workshop report, cosponsored by the Food and Drug Administration and the United States Pharmacopeia, *AAPS J.* 6 (2004) 23–34. doi:10.1208/aapsj060320.
- [10] H. Shi, R. Mohanty, S. Chakravarty, R. Cabisco, M. Morgeneyer, H. Zetzener, J.Y. Ooi, A. Kwade, S. Luding, V. Magnanimo, Effect of Particle Size and Cohesion on Powder Yielding and Flow, *KONA Powder Part. J.* 35 (2018) 226–250. doi:10.14356/kona.2018014.
- [11] D. Drummer, D. Rietzel, F. Kühnlein, Development of a characterization approach for the sintering behavior of new thermoplastics for selective laser sintering, *Phys. Procedia.* 5 (2010) 533–542. doi:10.1016/J.PHPRO.2010.08.081.
- [12] C.A. Chatham, T.E. Long, C.B. Williams, A review of the process physics and material screening methods for polymer powder bed fusion additive manufacturing, *Prog. Polym. Sci.* 93 (2019) 68–95. doi:10.1016/j.progpolymsci.2019.03.003.
- [13] M. Schmid, A. Amado, K. Wegener, Polymer powders for selective laser sintering (SLS), *AIP Conf. Proc.* 1664 (2015). doi:10.1063/1.4918516.
- [14] M. Schmid, M. Vetterli, K. Wegener, Polymer powders for laser-sintering: Powder production and performance qualification, *AIP Conf. Proc.* 2065 (2019). doi:10.1063/1.5088258.
- [15] O. Molerus, Effect of interparticle cohesive forces on the flow behaviour of powders, *Powder Technol.* 20 (1978) 161–175. doi:10.1016/0032-5910(78)80045-X.
- [16] R.M. Harrison, J. Yin, Particulate matter in the atmosphere: Which particle properties are important for its effects on health?, *Sci. Total Environ.* 249 (2000) 85–101. doi:10.1016/S0048-9697(99)00513-6.
- [17] M. Alias, Z. Hamzah, L.S. Kenn, Pm 10 and Total Suspended Particulates (Tsp) Measurements in Various Power Stations, *Malaysian J. Anal. Sci.* 11 (2007) 255–261.
- [18] de Jong, Drug delivery and nanoparticles: Applications and hazards, *Int. J. Nanomedicine.* 3 (2008) 133. doi:10.2147/IJN.S596.
- [19] R.J. Thomas, Particle size and pathogenicity in the respiratory tract, *Virulence.* 4 (2013) 847–858. doi:10.4161/viru.27172.
- [20] R. Toy, P.M. Peiris, K.B. Ghaghada, E. Karathanasis, Shaping cancer nanomedicine: the effect of particle shape on the in vivo journey of nanoparticles, *Nanomedicine.* 9 (2014) 121–134. doi:10.2217/nmm.13.191.
- [21] K. Donaldson, C.A. Poland, F.A. Murphy, M. MacFarlane, T. Chernova, A. Schinwald, Pulmonary toxicity of carbon nanotubes and asbestos — Similarities and differences, *Adv. Drug Deliv. Rev.* 65 (2013) 2078–2086. doi:10.1016/j.addr.2013.07.014.

- [22] N.J. Hallab, K. McAllister, M. Brady, M. Jarman-Smith, Macrophage reactivity to different polymers demonstrates particle size- and material-specific reactivity: PEEK-OPTIMA® particles versus UHMWPE particles in the submicron, micron, and 10 micron size ranges, *J. Biomed. Mater. Res. - Part B Appl. Biomater.* 100 B (2012) 480–492. doi:10.1002/jbm.b.31974.
- [23] J.A. Champion, S. Mitragotri, Role of target geometry in phagocytosis, *Proc. Natl. Acad. Sci.* 103 (2006) 4930–4934. doi:10.1073/pnas.0600997103.
- [24] C. Huang, X. Qian, R. Yang, Thermal conductivity of polymers and polymer nanocomposites, *Mater. Sci. Eng. R Reports.* 132 (2018) 1–22. doi:10.1016/j.mser.2018.06.002.
- [25] A.B. Spierings, M. Voegtlin, T. Bauer, K. Wegener, Powder flowability characterisation methodology for powder-bed-based metal additive manufacturing, *Prog. Addit. Manuf.* 1 (2016) 9–20. doi:10.1007/s40964-015-0001-4.
- [26] S. Singamneni, R. Velu, M.P. Behera, S. Scott, P. Brorens, D. Harland, J. Gerrard, Selective laser sintering responses of keratin-based bio-polymer composites, *Mater. Des.* 183 (2019) 108087. doi:10.1016/J.MATDES.2019.108087.
- [27] S. Yang, J.R.G. Evans, Metering and dispensing of powder; the quest for new solid freeforming techniques, *Powder Technol.* (2007). doi:10.1016/j.powtec.2007.04.004.
- [28] S.E. Brika, M. Letenneur, C.A. Dion, V. Brailovski, Influence of particle morphology and size distribution on the powder flowability and laser powder bed fusion manufacturability of Ti-6Al-4V alloy, *Addit. Manuf.* 31 (2020) 100929. doi:10.1016/J.ADDMA.2019.100929.
- [29] Z. Snow, R. Martukanitz, S. Joshi, On the development of powder spreadability metrics and feedstock requirements for powder bed fusion additive manufacturing, *Addit. Manuf.* 28 (2019) 78–86. doi:10.1016/j.addma.2019.04.017.
- [30] J. Clayton, An Introduction to Powder Characterization, *Handb. Pharm. Wet Granulation.* (2019) 569–613. doi:10.1016/B978-0-12-810460-6.00021-X.
- [31] I. Akseli, J. Hilden, J.M. Katz, R.C. Kelly, T.T. Kramer, C. Mao, F. Osei-Yeboah, J.C. Strong, Reproducibility of the Measurement of Bulk/Tapped Density of Pharmaceutical Powders Between Pharmaceutical Laboratories, *J. Pharm. Sci.* 108 (2019) 1081–1084. doi:10.1016/J.XPHS.2018.10.009.
- [32] M. Schmid, F. Amado, G. Levy, K. Wegener, Flowability of powders for Selective Laser Sintering (SLS) investigated by Round Robin Test, in: *High Value Manuf. Adv. Res. Virtual Rapid Prototyp.*, CRC Press, 2013; pp. 95–99. doi:10.1201/b15961-19.
- [33] D. Schulze, *Powders and Bulk Solids - Behavior, Characterization, Storage and Flow*, Springer Berlin Heidelberg, Berlin, Heidelberg, 2008. doi:10.1007/978-3-540-73768-1.
- [34] I. Tomasetta, D. Barletta, M. Poletto, The High Temperature Annular Shear Cell: A modified ring shear tester to measure the flow properties of powders at high temperature, *Adv. Powder Technol.* 24 (2013) 609–617. doi:10.1016/j.apt.2012.11.007.
- [35] R. Chirone, D. Barletta, P. Lettieri, M. Poletto, Bulk flow properties of sieved samples of a ceramic powder at ambient and high temperature, *Powder Technol.* 288 (2016) 379–387. doi:10.1016/j.powtec.2015.11.040.
- [36] J.A. Slotwinski, E.J. Garboczi, P.E. Stutzman, C.F. Ferraris, S.S. Watson, M.A. Peltz, Characterization of metal powders used for additive manufacturing, *J. Res. Natl. Inst. Stand. Technol.* 119 (2014) 460–493. doi:10.6028/jres.119.018.
- [37] P.J. Loveland, *Principles, Methods and Application of Particle Size Analysis*, Cambridge University Press, 1991. doi:10.1017/CBO9780511626142.
- [38] A. Rawle, Basic of principles of particle-size analysis, *Surf. Coatings Int. Part A, Coatings J.* 86 (2003) 58–65.
- [39] H.G. Merkus, G.M.H. Meesters, W. Oostra, *Particles and Nanoparticles in Pharmaceutical Products*, Springer International Publishing, Cham, 2018. doi:10.1007/978-3-319-94174-5.
- [40] G.S. Upadhyaya, German R.M., *Powder metallurgy and particulate materials processing*, Metal powder industries federation, Princeton, USA, 2005, pp. 522, isbn 0-9762057-1-8, *Sci. Sinter.* 38 (2006) 95–95. doi:10.2298/SOS0601095U.
- [41] A.P. Tinke, A. Carnicer, R. Govoreanu, G. Scheltjens, L. Lauwerysen, N. Mertens, K. Vanhoutte, M.E. Brewster, Particle shape and orientation in laser diffraction and static image analysis size distribution analysis of micrometer sized rectangular particles, *Powder Technol.* 186 (2008) 154–167. doi:10.1016/j.powtec.2007.11.017.
- [42] M.L. Hentschel, N.W. Page, Selection of Descriptors for Particle Shape Characterization, *Part. Part. Syst. Charact.* 20 (2003) 25–38. doi:10.1002/ppsc.200390002.
- [43] E. Olson, Particle shape factors and their use in image analysis - part 1: theory, *J. GXP Compliance.* 3 (2011) 85–96.
- [44] R.K. Dhamoon, H. Popli, G. Aggarwal, M. Gupta, Particle Size Characterization- Techniques, Factors and Quality-by-design Approach, *Int. J. Drug Deliv. Technol.* 10 (2018) 01–11. doi:10.5138/09750215.2204.
- [45] A. Strondl, O. Lyckfeldt, H. Brodin, U. Ackelid, Characterization and Control of Powder Properties for Additive Manufacturing, *Jom.* 67 (2015) 549–554. doi:10.1007/s11837-015-1304-0.
- [46] N.A. Miller, J.J. Henderson, Quantifying Sand Particle Shape Complexity using a Dynamic, Digital Imaging Technique, *Agron. J.* 102 (2010) 1407–1414. doi:10.2134/agronj2010.0097.
- [47] Optimising the measurement of fine particles, *Met. Powder Rep.* 68 (2013) 34–37. doi:10.1016/S0026-0657(13)70128-0.
- [48] K. Patchigolla, D. Wilkinson, Crystal Shape Characterisation of Dry Samples using Microscopic and Dynamic Image Analysis, *Part. Part. Syst. Charact.* 26 (2009) 171–178. doi:10.1002/ppsc.200700030.
- [49] H. Choi, W. Lee, D.-U. Kim, S. Kumar, J. Ha, S. Kim, J. Lee, A comparative study of particle size analysis in fine powder: The effect of a polycomponent particulate system, *Korean J. Chem. Eng.* 26 (2009) 300–305. doi:10.1007/s11814-009-0052-7.
- [50] C.A. Schneider, W.S. Rasband, K.W. Eliceiri, NIH Image to ImageJ: 25 years of image analysis, *Nat. Methods.* 9 (2012) 671–675. doi:10.1038/nmeth.2089.
- [51] M. Frei, F.E. Kruis, Image-based size analysis of agglomerated and partially sintered particles via convolutional neural networks, *Powder Technol.* 360 (2020) 324–336. doi:10.1016/j.powtec.2019.10.020.
- [52] R.D. Goodridge, C.J. Tuck, R.J.M. Hague, Laser sintering of polyamides and other polymers, *Prog. Mater. Sci.* 57 (2012) 229–267. doi:10.1016/j.pmatsci.2011.04.001.
- [53] H. Umhauer, A. Gutsch, Particle Characterization by Projected Area Determination, *Part. Part. Syst. Charact.* 14 (1997) 105–115. doi:10.1002/ppsc.199700023.
- [54] R. Goodridge, S. Ziegelmeier, Powder bed fusion of polymers, in: *Laser Addit. Manuf.*, Elsevier, 2017; pp. 181–204. doi:10.1016/B978-0-08-100433-3.00007-5.
- [55] G. Egger, P.E. Gygax, R. Glardon, N.P. Karapatis, Optimization of powder layer density in selective laser sintering, 10th Solid Free. Fabr. Symp. (1999) 255–263. doi:http://dx.doi.org/10.26153/tsw/746.
- [56] L. Benedetti, B. Brulé, N. Decraemer, K.E. Evans, O. Ghita, Evaluation of particle coalescence and its implications in laser sintering, *Powder Technol.* 342 (2019) 917–928. doi:10.1016/J.POWTEC.2018.10.053.
- [57] C. Mielicki, B. Gronhoff, J. Wortberg, Effects of laser sintering processing time and temperature on changes in polyamide 12 powder particle size, shape and distribution, in: *AIP Conf. Proc.*, 2014; pp. 728–731. doi:10.1063/1.4873880.
- [58] E.D. Bain, E.J. Garboczi, J.E. Seppala, T.C. Parker, K.B. Migler, AMB2018-04: Benchmark Physical Property Measurements for Powder Bed Fusion Additive Manufacturing of Polyamide 12, *Integr. Mater. Manuf. Innov.* 8 (2019) 335–361. doi:10.1007/s40192-019-00146-3.
- [59] J. Schmidt, M.A. Dechet, J.S.G. Bonilla, N. Hesse, A. Bück, W. Peukert, Characterization of Polymer Powders for Selective Laser Sintering, *Proc. 30th Annu. Int. Solid Free. Fabr. Symp.* (2019) 779–789.
- [60] M. Van den Eynde, L. Verbelen, P. Van Puyvelde, Assessing polymer powder flow for the application of laser sintering, *Powder Technol.* 286 (2015) 151–155. doi:10.1016/j.powtec.2015.08.004.

11th CIRP Conference on Photonic Technologies [LANE 2020] on September 7-10, 2020

Investigation of the electrophotographic powder deposition through a transfer grid for efficient additive manufacturing

Sebastian-Paul Kopp^{a,c,d*}, Thomas Stichel^{a,c}, Stephan Roth^{a,c,d}, Michael Schmidt^{a-d}

^a*Bayerisches Laserzentrum GmbH (blz), Konrad-Zuse-Straße 2-6, 91052 Erlangen, Germany*

^b*Institute of Photonic Technologies (LPT), Friedrich-Alexander-Universität Erlangen-Nürnberg, Konrad-Zuse-Straße 3-5, 91052 Erlangen, Germany*

^c*Collaborative Research Center (CRC) 814 “Additive Manufacturing”, 91058 Erlangen, Germany*

^d*Erlangen Graduate School in Advanced Optical Technologies (SAOT), 91052 Erlangen, Germany*

* Corresponding author. Tel.: +49-9131-97790-27; fax: +49-9131-97790-11. E-mail address: s-p.kopp@blz.org

Abstract

Until today, the electrophotographic transfer of toner powders has been applied successfully in common printing technology for many years. Utilizing the electrophotographic principle for the transfer of polymer powders in the context of additive manufacturing can give a variety of advantages like e.g. the possibility of generating multi-material components or a reduced consumption of powder. Here, the multiple depositions of powder particle-layers via electrostatic forces to create 3D objects have turned out to be a major challenge. Therefore, a new strategy based on the usage of a grounded transfer grid is examined. Due to its positioning above the generated layers, it makes the powder deposition independent of the already produced part height. For improving the particle transfer, geometrical properties of the grid are analyzed with respect to their influence on the efficiency of the powder deposition. Here, particular attention is paid to the manipulation of the electric transfer field, which is applied for accelerating the charged powder particles. The aim is to enhance the coverage and dimensional accuracy of the deposited powder layers by finding a new transfer structure.

© 2020 The Authors. Published by Elsevier B.V.

This is an open access article under the CC BY-NC-ND license (<http://creativecommons.org/licenses/by-nc-nd/4.0/>)

Peer-review under responsibility of the Bayerisches Laserzentrum GmbH

Keywords: selective laser melting, electrophotography, polymer powder transfer, multi-material deposition, electric field

1. Introduction

The utilization of additive manufacturing techniques such as selective laser melting of polymer powder enables almost arbitrary design flexibility [1,2]. However, conventional powder application methods do not allow the simultaneous and selective deposition of different materials and thus render the generation of multi-material components impossible [3]. Nevertheless, being able to fabricate multi-material parts by means of additive manufacturing offers a variety of benefits for many different areas such as the medical industry [4].

A promising approach is to use the electrophotographic principle for generating tailored powder layers [5,6]. At this, it becomes apparent that the powder deposition, which must be

reproducible, dimensionally accurate and has to feature a high coverage, remains a major challenge.

Here, the spatial distribution of the electric transfer field, which develops between the photoconductive plate and the respectively applied transfer structure, significantly affects the powder deposition. The influence of an electric field on charged particles is determined by the Coulomb force, which moves the charged particles against the viscous drag air force described by the Stokes law [7]. Depending on the applied charging strategy [8,9], different phenomena lead to the overall charge. In case of the herein presented corona charging, the charge consists of ions as well as induced dipoles, which result from deformation polarization. Apart from that, triboelectric charging merely causes the latter [10].

On the one hand in this paper the manipulation of the electric transfer field by applying different transfer structures is investigated in order to enhance the powder deposition. This is done by employing a simulative analysis of the spatial distribution of the electric transfer field. At this, the simulation allows the evaluation of the ratio between field components, which point into the desired movement direction of the powder particles, and parasitic transversal field components. The latter lead to a distraction of powder particles from their straight movement direction and thus impair the powder deposition.

On the other hand the experimental analysis, which is presented in this paper, is used for validating the simulative results and hence is focused on the behavior of the charged powder particles within the applied electric transfer field. For this purpose the deposited powder layers are studied with respect to their coverage and dimensional accuracy.

The state of the art transfer grid [3] exhibits two major drawbacks. First, the grid wires act as physical barriers at which the powder particles are scattered. Second, these wires introduce substantial transversal field components deflecting the particles from their linear motion. Therefore, a new transfer structure is to be found which does not act as a physical barrier for powder particles being deposited and furthermore features decreased parasitic transversal field components. In order to quantify the ratio between parasitic transversal and the intended longitudinal field component in the direction of particle movement, the spatial field distribution of the transfer grid is first simulated. The thereby obtained quantitative spatial field distribution is subsequently used for designing a new transfer structure which features reduced transversal field components and thus increases the efficiency of the powder deposition. The simulative results are then compared with experimental results utilizing the new transfer structure.

Ultimately, the charge accumulation within the part as a consequence of the multiple depositions of charged powder layers on top of each other also has to be taken into account. That is because the accumulation of charges may lead to a weakening of the electric transfer field [9]. Consequently, this could significantly decrease both the motive forces responsible for the powder transfer and thus the coverage of the deposited powder layers. Therefore, the influence of the part height on the transfer field is simulated.

2. Simulative and experimental investigations

2.1. Methodology

The conducted simulations of the spatial distributions of resulting electric transfer fields for various transfer structures presented in this paper were performed with COMSOL Multiphysics 5.2a. The simulations are based on numerical solutions of Maxwell's equations. Within the conducted simulations the assumption of purely electrostatic processes is made, i.e. excluding any kind of charge flow. This assumption is valid for the investigation of electric transfer fields of different transfer structures because except for the negligibly short (relating to the inertia of the powder particles) duration of the switch-on or switch-off process of the electric transfer field, there is no charge flow present [7]. In case of the analyzed

influence of the part height on the attenuation of the electric transfer field as a matter of fact charge flow might occur within the built part and between the part and surrounding air. However, since the built part consists of dielectric material, this effect most probably is of subordinate importance. Fig. 1 shows the applied layer geometry representing an exemplary test part for the powder deposition both for the simulative as well as experimental examination. Due to comparability with previous work [3], the presented experiments were conducted with a negatively charged powder mixture of 99.0 wt. % of polypropylene PP PD0580 DuPont with a particle size distribution $X_{50} = 113.6 \mu\text{m}$ and 1.0 wt. % of Aerosil (R106, Evonik).

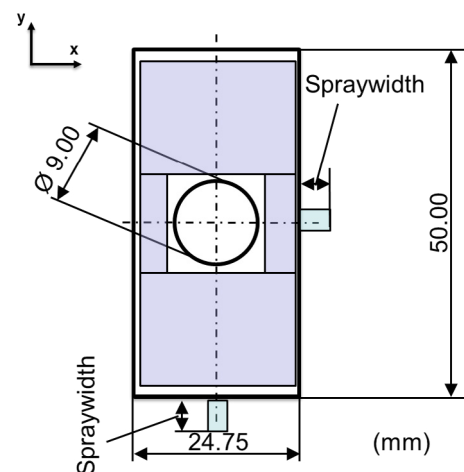


Fig. 1. Utilized test geometry for the simulative and experimental analysis; the four areas for experimental determination of the coverage are colored.

As initially mentioned, the primary quality criteria in the context of powder pattern deposition are reproducibility, dimensional accuracy and a high coverage. The aim is to achieve coverage close to 100 %, which is comparable to conventional powder application methods. Furthermore, the spraywidth should tend to 0 mm for a preferably high dimensional accuracy.

For the experimental analysis regarding coverage and spraywidth the powder is initially charged by applying a distinct powder charge voltage and subsequently developed onto a photoconductive plate [3]. At this, the test geometry depicted in Fig. 1 is used. Hereinafter, an electric transfer field is established between the photoconductive plate and the transfer structure for depositing the powder particles onto the substrate plate.

The determination of the coverage is conducted within the four highlighted areas visualized in Fig. 1. It can be calculated with the number of white pixels n_{white} and the number of black pixels n_{black} using a cut-off threshold of 50 % for the discrimination between white and black pixels as follows:

$$\text{Coverage} = \frac{n_{\text{white}}}{n_{\text{white}} + n_{\text{black}}} 100 \% \quad (1)$$

2.2. Simulative analysis of electric field distributions for different transfer structure geometries

The simulation model for the state of the art transfer grid as well as the transfer frame, which is introduced as a new transfer structure for achieving reduced transversal field components, is visualized in Fig. 2. This transfer frame does not show any physical barrier for the powder particles moving from the photoconductive plate towards the substrate plate anymore. Moreover, due to the absence of grid wires it has reduced parasitic transversal field components. The simulation model is based on the experimental setup, which already has been reported in previous work [3,6].

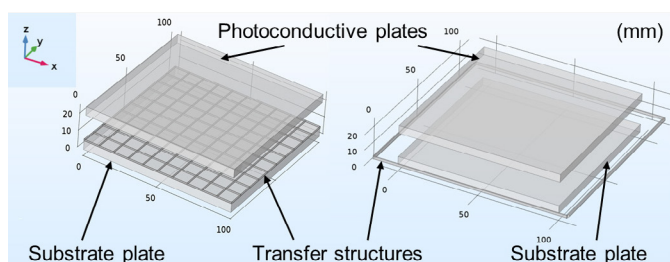


Fig. 2. Simulated transfer structure geometries; grid (left), frame (right).

The simulation setup consists of an aluminum plate representing the photoconductive plate and a polyamide 6 substrate plate on which the powder layers are deposited. Here, the center of the test geometry (cf. Fig. 1) coincides with the center of the substrate plate. Furthermore, the transfer structures are made of copper and are grounded whereas a voltage of 1000 V is assigned to the photoconductive plate. By contrast, no voltage is assigned to the substrate plate enabling the investigation of the influence of the part height on the transfer field. That is possible because the charge of every powder layer is conserved in this way.

Both the transfer grid and the transfer frame are positioned at a z -position directly above the deposited powder layer or the substrate plate in case of the first layer, respectively. In accordance with the state of the art grid [3] a wire diameter of 1 mm with a row spacing of 10 mm and an overall length of 100 mm is chosen for the simulation depicted in Fig. 3. However, it has shown that in case of a transfer frame good results can be achieved with a wire diameter of 1.5 mm and a wire length of 120 mm. This configuration, which is used in the presented paper, gives a reasonable compromise between preferably strong field components of approximately 12500 V/m in negative z -direction and relatively weak parasitic transversal field components of approximately 1500 V/m (cf. Fig. 3). These values are valid when limiting the used area to a square of 25 mm · 25 mm centered in the middle of the photoconductive plate.

Fig. 3 visualizes the spatial distribution of the electric field strength for the used transfer grid along a line directly above the substrate plate at $y = 55$ mm (cf. Fig. 2). This position was chosen for reasons of clarity since here the transversal field components in y -direction cancel out for symmetry reasons within a grid mesh. As opposed to this, the transfer frame was analyzed at $y = 50$ mm since no intermediate grid wires are

present and thus the transversal field components in y -direction cancel out here for symmetry reasons. The mentioned symmetry reasons arise from the fact that at equidistant positions relative to both sides of grid or frame elements, the electric field spreads equally towards these elements and thus cancels out at the center line.

As expected, the grid causes substantial transversal field components, which increase with decreasing distance to the grid wires. The electric field strength in transversal direction reaches up to 25 % of that in z -direction leading to significant spray at the edges of the powder pattern. This is aggravated by the fact that the grid wires serve as physical barriers, which reduce the coverage. Therefore, the maximum coverage with the above-mentioned state of the art transfer grid lies in the range of 70 % [3].

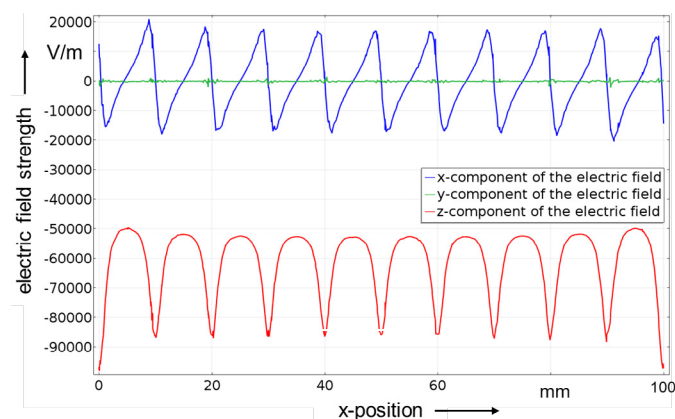


Fig. 3. Simulated electric field strength at $y = 55$ mm directly above the substrate plate in case of a transfer grid.

Since there are no intermediate grid wires present at a transfer frame, it can be expected that in case of the frame the transversal field components are considerably less pronounced than for the transfer grid. In fact, this can be seen in Fig. 4. When limiting the used area to a square of 25 mm · 25 mm centered in the middle of the photoconductive plate (i.e. $37.5 \text{ mm} < x < 62.5 \text{ mm}$ and due to symmetry reasons of the rectangular frame $37.5 \text{ mm} < y < 62.5 \text{ mm}$), the transversal field components can be limited to less than 12 % of those in z -direction. However, because the distance to the framework is maximal in this area, the electric field components in z -direction exhibit a minimum.

Beyond that, the absence of physical barriers should positively influence the achievable coverage. Nevertheless, the electric field strength in z -direction in case of the transfer frame is significantly lower compared to the transfer grid. At this, the experimental analysis has to evince whether the electric field is still strong enough to move the charged particles from the photoconductive plate to the substrate plate.

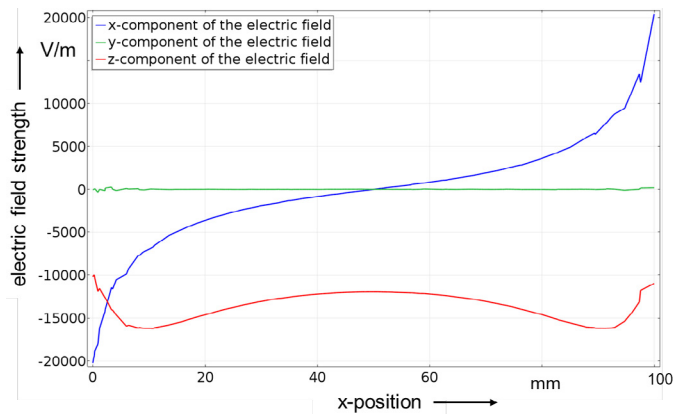


Fig. 4. Simulated electric field strength at $y = 50$ mm directly above the substrate plate in case of a transfer frame.

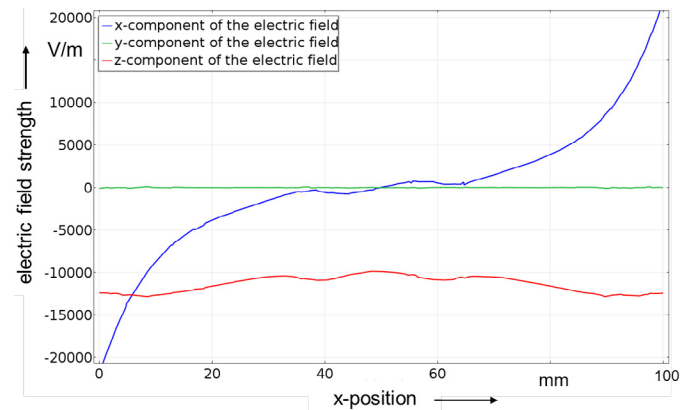


Fig. 5. Simulated electric field strength at $y = 50$ mm directly above a test part with a thickness of 10 mm (100 deposited powder layers) and an accumulated charge of $1.5 \cdot 10^{-10}$ C in case of a transfer frame.

2.3. Simulative analysis of the influence of the part height on the electric transfer field

So far the electric field distribution in case of depositing a powder layer directly onto the substrate plate has been investigated. The simulated electric field distribution only holds true for the first powder layer, though. For including the influence of the part height on the electric transfer field, the accumulation of charges within the part has to be considered. The charge of every single powder layer can be estimated by initially calculating the gravitational force F_g acting on that layer using a density of ca. 1000 kg/m^3 . By knowing the field strength of the electric field E , which is applied for attracting a powder layer to the photoconductive plate during powder development (approx. 660 kV/m) [3], the charge q within a single powder layer can be calculated yielding [7]:

$$q = \frac{F_g}{E} = 1.5 \cdot 10^{-12} \text{ C} \quad (2)$$

Furthermore, for the simulation a particle diameter of $100 \mu\text{m}$ and a relative permittivity of the built part of 2.5 were applied.

According to the Coulomb potential, the potential of a point charge increases with growing charge [7]. Thus, the potential of a part will also increase with growing number of layers due to the accumulation of charges within the part. Since the voltage between two points is defined by their potential difference [11], the voltage between the photoconductive plate and the part surface will therefore decrease with growing number of layers. This results in an attenuation of the electric transfer field. Fig. 5 displays the lateral distribution of electric field strength (in x -direction) directly above 100 powder layers of the test geometry depicted in Fig. 1.

At this, the distance between the part surface and the photoconductive plate is kept constant to 15 mm as is the case with the powder deposition directly to the substrate plate (cf. Fig. 4). Interestingly, according to the simulation, the effect of field attenuation outlined above only weakens the electric field in z -direction by approximately 8 %, which can be compensated by slightly increasing the voltage at the photoconductive plate if necessary.

The small deflections visible in Fig. 5 (contrary to Fig. 4) arise from the fact that there is no potential assigned to the substrate plate whereas the deposited powder layers have a distinct potential originating from their charge and therefore lead to a disturbance of the electric transfer field.

2.4. Experimental results for various transfer structure geometries

The resulting powder layers deposited through a transfer grid and a transfer frame, respectively, can be seen in Fig. 6. However, in case of the transfer frame the electric field strength in z -direction is not sufficient for overcoming the strong adhesive forces like the van der Waals force as long as the powder particles are attached to the photoconductive plate. Only a small mechanical excitation pulse acting on the photoconductive plate, which slightly increases the distance between the single particles and thus decreases the intermolecular interactions, allows the powder particles to follow the electric transfer field.

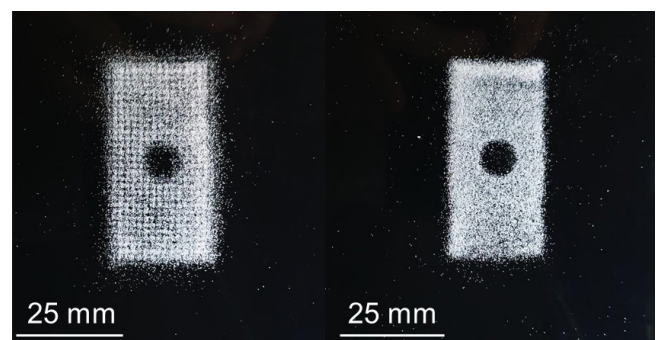


Fig. 6. Single test layers of a powder mixture of 99.0 wt. % PP PD0580 DuPont and 1.0 wt. % Aerosil (R106, Evonik) deposited through a transfer grid (left) and a transfer frame (right).

It is evident from Fig. 6 that the usage of a transfer frame leads to an increased coverage, which is quantitatively depicted in Fig. 7. According to that, the coverage reaches more than 90 % with a distinct reduction in case of a lower powder charge voltage. This behavior can be explained by the relatively weak z -component of the electric transfer field of the transfer frame. By contrast, the powder charging does not have a significant impact on the coverage in case of the grid. For referencing reasons the powder deposition was also conducted without any kind of transfer structure (“blank”). Especially for a transfer voltage of -3.5 kV the coverage values without a transfer structure are comparable to those of the transfer grid. This behavior can be explained by the fact that in the experimental setup the surrounding components like the formwork are grounded for safety reasons.

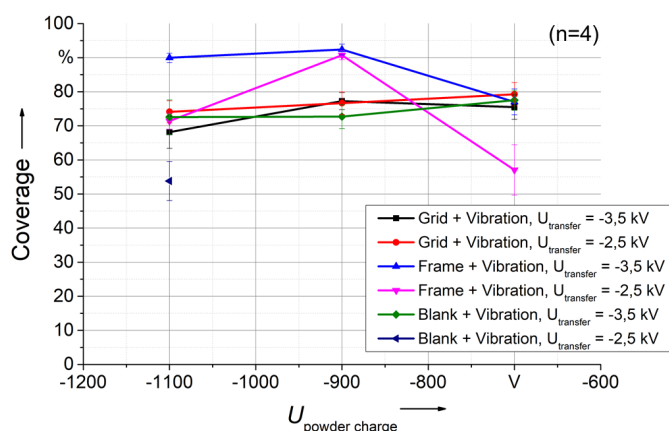


Fig. 7. Coverage values for different powder charge voltages and transfer structure geometries.

However, this also introduces some kind of electric field between the photoconductive plate and the surrounding components. Apparently, this field is strong enough to move the charged powder particles to the substrate plate in the event of a small induced mechanical excitation pulse as long as the powder charge voltage is high enough. Otherwise no measurable powder transfer takes place anymore (cf. missing values for “blank + vibration” at a transfer voltage of -2.5 kV in Fig. 7 and Fig. 8)

Fig. 8 shows that by applying a transfer frame the mean spray can be reduced to approximately 0 mm, which corresponds to a reduction by up to 90 % compared to the state of the art transfer grid. The comparably high spray values of the transfer grid are caused by relatively strong transversal field components and scattering effects, which arise from collisions of powder particles at grid wires.

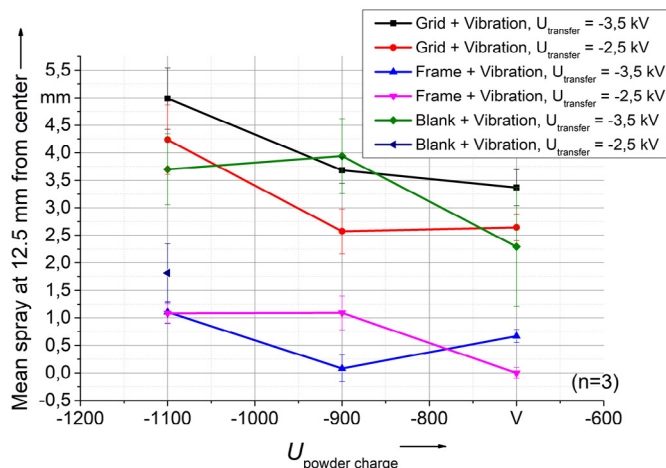


Fig. 8. Mean spray for different powder charge voltages and transfer structure geometries at a distance of 12.5 mm from center.

Interestingly, the mean spray in case of no applied transfer structure is similar to that of the transfer grid. This is most probably caused by the transversal field components of the mentioned electric field between the photoconductive plate and grounded surrounding components.

3. Conclusion

The powder deposition through a state of the art transfer grid exhibits two main drawbacks. These are the existence of grid wires acting as physical barriers and very strong parasitic transversal field components, which deflect the powder particles from their linear motion. By applying the newly introduced improved transfer frame these grid wires are avoided. Furthermore, the transversal field components can be significantly reduced. At this, the simulative investigation reveals that in case of the transfer frame the ratio between transversal field components and field components in z -direction can be reduced by a factor of two compared to the transfer grid. The subsequent experimental analysis has shown that this results in a significant reduction of the spraywidth of up to 90 %. Furthermore, the coverage could be enhanced by approximately 17 % by applying the new transfer frame in combination with an induced mechanical excitation pulse onto the photoconductive plate. For a further improvement of the coverage, future investigations should employ a piezo-induced mechanical excitation and additionally investigate the impact of different particle size distributions on the powder deposition behavior. Since the particle size distribution among others influences the charge distribution [8,9], it might affect the electrophotographic powder pattern deposition and could help to improve the coverage even further.

Moreover, the conducted simulative analysis has shown that the accumulation of charges within deposited powder layers only slightly attenuates the electric transfer field. This can be compensated by slightly adjusting the voltage at the photoconductive plate if necessary.

It has been shown that a detailed analysis of the simulated spatial electric field distribution can help to understand the movement of charged powder particles within an applied electric field. Although the similarly charged particles may

exhibit forces of repulsion to each other, the influence of an external electric field on their behavior can be predicted in a reasonable way. Thus, the transfer frame could be introduced for improving the dimensional accuracy as well as the coverage. Therefore, it helps to advance towards the superior aim of the presented investigations, which is the implementation of the electrophotographic powder deposition into the process of selective laser melting.

Acknowledgements

The authors gratefully acknowledge funding of the Collaborative Research Center 814 (CRC 814), sub-project B6, and of the Erlangen Graduate School in Advanced Optical Technologies (SAOT) by the German Research Foundation (DFG) in the framework of the German excellence initiative.

References

- [1] Kruth JP, Wang X, Laoui T, Froyen L. Lasers and materials in selective laser sintering. *Assembly Automation* 2003;23(4):357-371.
- [2] Kruth JP, Levy G, Klocke F, Childs THC. Consolidation phenomena in laser and powder-bed based layered manufacturing. *CIRP Annals* 2007;56:730-759.
- [3] Stichel T, Brachmann C, Raths M, Dechet MA, Schmidt J, Peukert W, Frick T, Roth S. Electrophotographic Multilayer Powder Pattern Deposition for Additive Manufacturing. *JOM* 2020;72:1366–1375.
- [4] Bandyopadhyay A, Heer B. Additive manufacturing of multi-material structures. *Materials Science and Engineering: R: Reports* 2018;129:1–16.
- [5] Kumar A, Dutta A, Fay J. Electrophotographic printing of part and binder powders. *Rapid Prototyping Journal* 2004;10(1):7-13.
- [6] Stichel T, Brandl T, Hauser T, Geißler B, Roth S. Electrophotographic multi-material powder deposition for additive manufacturing. *Procedia CIRP* 2018;74:249–253.
- [7] Pai DM, Springett BE. Physics of electrophotography. *Reviews of Modern Physics* 1993;65(1):163–211.
- [8] Shahin MM. Nature of Charge Carriers in Negative Coronas. *Appl Opt Suppl Electr Photog* 1969;82:106-110.
- [9] Matsusaka S, Masuda H. Electrostatics of particles. *Advanced Powder Technology* 2003;14(2):143–166.
- [10] Shahin MM. Mass-spectrometric Studies of Corona Discharges in Air at Atmospheric Pressures. *J Chem Phys* 1966;43:2600-2605.
- [11] Itakura T, Masuda H, Ohtsuka C, Matsusaka S. The contact potential difference of powder and the tribo-charge. *Journal of Electrostatics* 1996;38(3):213–226.

11th CIRP Conference on Photonic Technologies [LANE 2020] on September 7-10, 2020

Directed Energy Deposition of PA12 carbon nanotube composite powder using a fiber laser

Yunus Kutlu^{a*}, Yannick L. Wencke^b, Gerrit A. Luinstra^b, Cemal Esen^a, Andreas Ostendorf^a

^aApplied Laser Technologies, Ruhr University Bochum, Universitätsstr.150, 44801 Bochum, Germany

^bInstitute for Technical and Macromolecular Chemistry, University of Hamburg, Bundesstr.45, 20146 Hamburg, Germany

* Corresponding author. Tel.: +49-234-32 23306; fax: +49-234-32 14259. E-mail address: kutlu@lat.rub.de

Abstract

Directed Energy Deposition (DED) an AM-technology that is widely known for its applications with metals was adapted for use with thermoplastics. A drop-in approach was used based on a DED setup for metal powders consisting of a Yb fiber laser with a wavelength of 1075 nm and a powder feed from a coaxial powder nozzle. The possibility of manufacturing items with simple geometries from a polyamide 12 multi-walled carbon nanotube composite starting material is described as a proof of concept. Tensile properties of samples are reported for measurements perpendicular and parallel to the generating direction, showing still a low strength compared to Bulk PA12 or SLS sintered PA12 specimens.

© 2020 The Authors. Published by Elsevier B.V.

This is an open access article under the CC BY-NC-ND license (<http://creativecommons.org/licenses/by-nc-nd/4.0/>)

Peer-review under responsibility of the Bayerisches Laserzentrum GmbH

Keywords: Additive Manufacturing; Directed Energy Deposition; Laser Polymer Deposition; Drop-in approach; Polymer composites

1. Introduction

With the growing advancement in Additive Manufacturing (AM), it has become clear, that access to and testing of novel and adapted materials is a major factor in widening the scope of this technology. While the intrinsic idea of looking for new materials itself is rather common, the basic material type (metals, polymers, ceramics, etc.) typically is unaltered in each specific AM technology. Powder-based laser AM is a field which is dominated by two technologies: Powder Bed Fusion – Laser Beam (PBF-LB) and Directed Energy Deposition – Laser Beam (DED-LB) [1]. While the former technology is feasible with metallic and polymeric materials, the latter finds applications mostly with metals and hence is often referred to as Laser Metal Deposition (LMD). Laser Polymer Deposition (LPD), or DED-LB with polymeric materials, is a method of AM that has marginally been researched. It was demonstrated that wear resistant polymer coatings can be manufactured with DED-LB. These coatings were produced with a diode laser with

a wavelength of 940 nm and polyamide 11 (PA11) powder which was mixed with poly(tetrafluoro ethylene) (PTFE) or molybdenum disulphide (MoS₂) respectively, resulting in deposited polymer coatings with a reduced friction coefficient [2–6]. More recently, it was further demonstrated that pristine polyamide 12 (PA12) powder can also be used in a manual deposition process using a thulium laser with a wavelength of 1940 nm, generating porous structures [7].

Based on these observations, it was decided to investigate PA12 powders as it holds a promise for reaching an economically viable drop-in solution, i.e. using a DED-LB setup that was originally designed for metallic materials. PA12 is the most commonly used polymer powder in laser based AM with a market share of 90% [8]. Its mechanical properties makes it also an attractive material for DED-LB [9]. Pristine PA12 powder, however, suffers from being a poor absorber in the near-infrared (NIR) regime [10], in which the most common DED-LB lasers operate.

Nomenclature

AM	Additive Manufacturing
DED-LB	Directed Energy Deposition – Laser Beam
LMD	Laser Metal Deposition
LPD	Laser Polymer Deposition
NIR	Near-infrared
MWCNT	Multi-walled carbon nanotubes
PBF-LB	Powder Bed Fusion – Laser Beam
PA12	Polyamide 12

In order to increase the absorption of laser energy by PA12 powder it can be modified with specific additives. The additives may range from inorganic pigments to organic dyes or even carbonaceous additives [11], such as multi-walled carbon nanotubes (MWCNT). CNTs are an interesting option in that regard as already low quantities lead to almost complete absorption of visible and NIR radiation [12]. Apart from their application as IR-absorbing agent, the high electric conductivity and the low percolation threshold of the MWCNTs leads to antistatic polymer powders with the application of already small amounts of MWCNTs compared to carbon black [13–15]. Decorating MWCNT onto the polymer powder can readily be achieved by means of high energy mixing. This work thus aims to establish a proof of concept for the feasibility of AM with a PA12/MWCNT composite in a DED-LB setup.

2. Experimental Procedure

DED-LB was performed with a Yb doped fiber laser with a central emission wavelength of $1075 \text{ nm} \pm 7 \text{ nm}$ (redPOWER® QUBE, SPI Lasers, Southampton, United Kingdom). It was utilized in a 3-axis DED-LB setup, including a processing head which focuses the laser beam onto the substrate with a focusing optic of a focal length of 150 mm, while simultaneously feeding the melt pool with a coaxial powder nozzle. The overall work distance was set to 164 mm to increase the spot diameter up to a size of 2 mm to approximately adapt the powder track width. The powder feed to the nozzle was achieved by a rotary disc powder feeder, which fluidizes the powder with a nitrogen gas stream. An additional vibrating module was installed inside the powder feeder to further ensure consistent powder flow. DED-LB substrates were prepared by coating a steel substrate with a $500 \mu\text{m}$ layer of the composite powder and heating it up at 180°C for 20 minutes. As pristine PA12 powder does not flow well enough in this setup and is prone to agglomeration, nanosized silica was employed as a flow additive. MWCNTs were employed as an additional optical absorber and antistatic aid to overcome the inadequate energy absorption of PA12 in the spectral range of the fiber laser used and to decrease the static powder buildup in the machine.[10] For the powder preparation, pristine PA12 powder (PA2200, EOS, Kraling, Bavaria, Germany) was mixed with MWCNT with an average diameter of 9.5 nm and an average length of $1.5 \mu\text{m}$ (NC7000, Nanocyl SA, Sambreville, Namur, Belgium) and additionally silicon dioxide nanoparticles with an average diameter of 70 nm (Ionic Liquids Technologies GmbH, Heilbronn, Baden-

Württemberg, Germany). Additives were added in a one to one ratio (50/50), amounting to a total of 1.25 wt% with respect to PA12. To establish an intimate contact between the polymer powder and the additives, the combination was subjected to mechanical stirring with a speed mixer. The nanoparticulate additives were thus mechanically fixated to the polymer particles. Mixing was performed separately for each additive, using a Speedmixer DAC 400 (Hauschild & Co KG, Hamm, North Rhine-Westphalia, Germany), switching between a cooling step, where the mixing container is cooled with ice water to 0°C , and a mixing step with 2500 rpm for one minute, for a total of five cycles for each additive.

As the mixing process involves high mechanical energy input, the particles size distribution was determined before and after the mixing (Figure 2, 3 and Table 2). Particle size distribution was measured with a HELOS KR, a laser diffraction-based sensor equipped with a RODOS/GRADIS dry dispersion setup of the company Sympatec (Clausthal-Zellerfeld, Lower Saxony, Germany).

The generating strategy consisted of generating single tracks with a width of approximately 2 mm on top of each other, overall resulting in 2 mm by 20 mm by 90 mm wall structures. Laser and DED parameters were optimized iteratively and kept constant for this study (see table 1) and only non-recycled powder was used. The usage of recycled powder and the influence on part properties is topic of ongoing research. The DED-LB process operated smoothly during the building process. Powder efficiency during processing was found to be at approximately 10%. This was expected with the design of the powder nozzle, originally optimized for metal powder with a different fluid mechanical behavior than the less dense polymer powder.

Parts built by AM often exhibit anisotropic behavior depending on the building direction of the generated parts.[16] Layer to layer adherence is frequently less strong than inline layer adherence. To test if this applies to the developed system, two generating strategies (perpendicular and parallel) were used. Two types of wall structures were produced: one with its long axis perpendicular to the deposition direction (see Fig. 1. (a)) and one parallel to the deposition direction (Fig 1. (b)).

Table 1. Laser and DED parameters.

Parameter	Value
Peak power [W]	150
Pulse width [μs]	40
Pulse Frequency [kHz]	1
Duty Cycle [%]	4
Carrier Gas Pressure [bar]	2
Feed speed [mm/min]	400

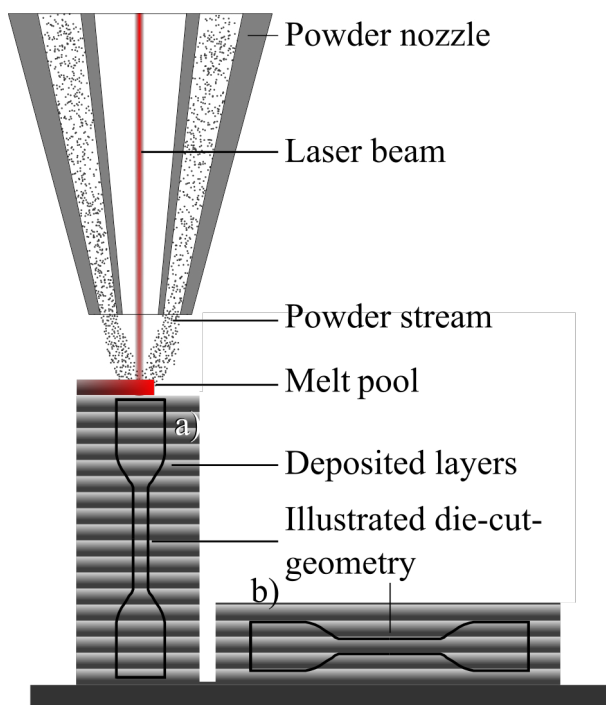


Fig. 1. Schematic DED-LB process and the two building strategies for generating parts (a) DED-LB part with illustrated die-cut geometry tensile specimen with perpendicular layers; (b) DED-LB sample with illustrated die-cut geometry tensile specimen with parallel layers.

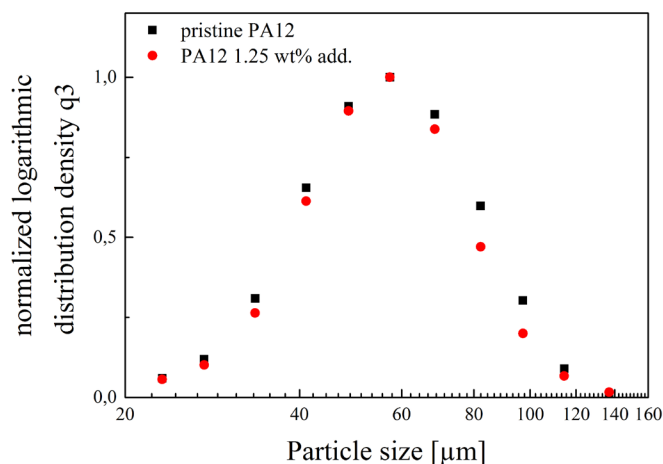


Fig. 2. Particle size distribution for PA12 powder for pristine PA12 powder and after high energy mixing with 1.25 wt% additives

Table 2. Particle size distribution of pristine PA12 powder and PA12 powder with 1.25 wt% additives.

	X _{10,3} [μm]	X _{16,3} [μm]	X _{50,3} [μm]	X _{84,3} [μm]	X _{90,3} [μm]	X _{99,3} [μm]
Pristine PA12	33.49	38.55	56.01	79.10	86.48	115.5
PA12 1.25wt% additives	33.33	38.62	55.20	75.01	83.66	117.1

Die cutting was chosen to generate comparable test specimens out of the center of the build structures to mitigate the effect of incomplete melting towards the edges. No preselection towards non-marred or non-cracked appearances were made. Specimens were die cut from the built parts as received. Only one tensile test specimen could be die cut per built part due to geometric constraints. As die cutting effects the mechanical properties only intra series comparability is given. Larger or DIN-according test specimens could not be fabricated directly due to the geometric constraints of the build setup, the low quantity in the powder reservoir and the – as of yet – inability to generate overhanging structures. Tensile test specimens (type 5A DIN EN ISO 527)) were die-cut using a ZCP 020 die-punch of ZwickRoell (Ulm, Baden-Württemberg, Germany). Tensile testing was performed on a Zwicki-Line Z1.0 (ZwickRoell) with a test speed of 50 mm/min. Five samples were tested in the case of perpendicular generated method, and four samples were tested in the case of the parallel generated method. Laser scanning microscopy was performed on a VKX250 of the company KEYENCE (Osaka, Osaka Prefecture, Japan).

3. Results and Discussion

It is found that the particle size distribution does not change significantly (Fig. 2). These results suggest no agglomeration or particle fractures takes place. Laser scanning microscope analysis performed before and after the mixing process show approximately the same results. The PA12 particles exhibit a rough surface with a round “potato”-shaped morphology. No agglomeration or broken particles could be detected (Fig 3).

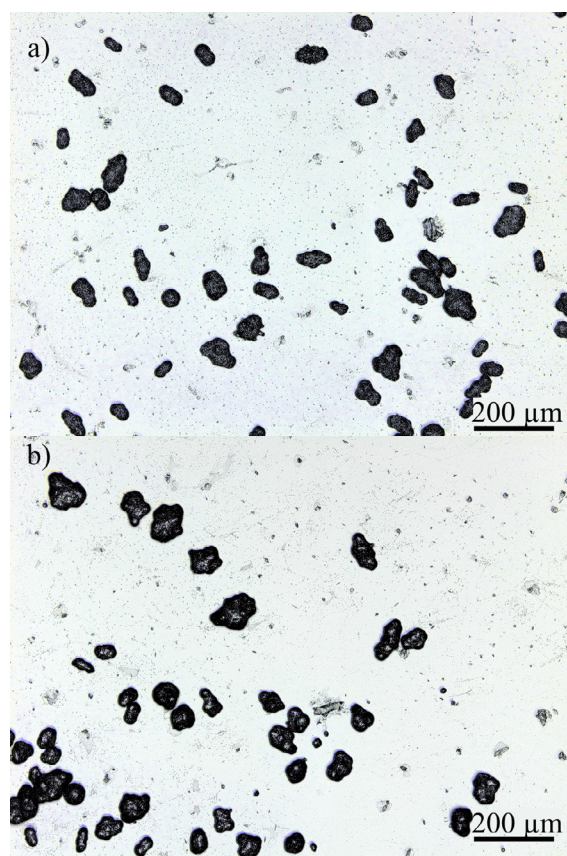


Fig. 3. Laser scanning microscope images of PA12 particles a) prior to coating with MWCNT and silica and b) following the addition of MWCNTs and silica

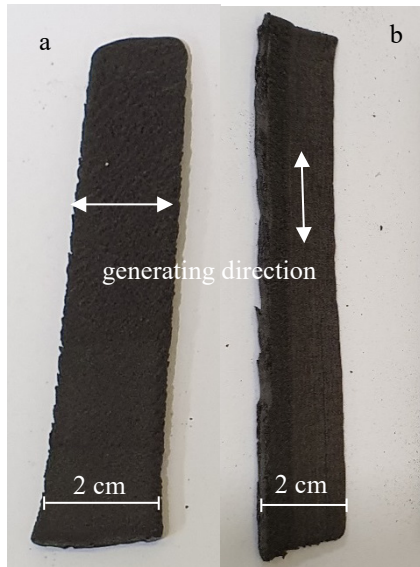


Fig. 4. DED specimens with a) perpendicular generating and b) parallel generating operation

The obtained parts are mechanically stable and have a rough surface with partially molten particles onto it (Fig. 4). Parts can be broken apart from the substrate leaving behind a minor fractured surface. The specimens show a uniform melting line in the middle, while on the outside areas polymer particles are only partially melted to each other.

Laser scanning microscopy analysis of fractured unused tensile test specimens of both perpendicular and parallel generating show a solidified but porous melt along the z-axis (Fig. 5). The surfaces of the melt line on top of the build parts shows complete homogenous melting with minor imperfections (Fig. 6b). The fracture surfaces of used tensile test specimens with perpendicular building direction are rough with a surface reminiscent of loosely bound PA12 particles (Fig. 6a). This suggest that minor parameter fluctuations in the production process might lead to incomplete interlayer adhesion. These areas of loosely bound particles act as weak links and determine the overall result in the tensile testing.

These results suggest that the building process has the potential to create smooth pore-free polymer melts but has needs to operate perfect at every step to create smooth melts (Fig. 6b).

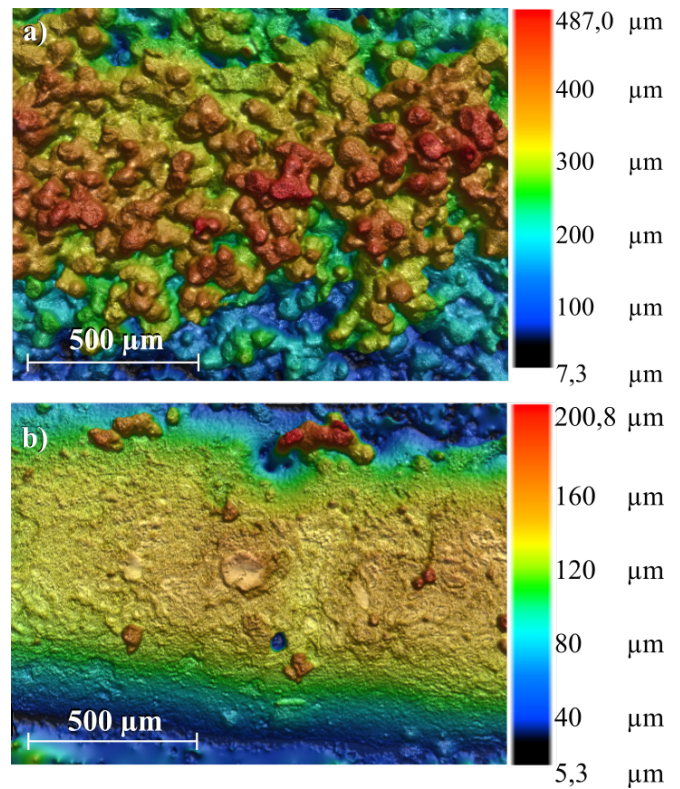


Fig. 6. Laser scanning microscopy analysis of the surface of a) the fracture surface of a used tensile test specimen with parallel generating and b) the melt line. Generating direction perpendicular to observation plane.

The resulting stress strain diagram is depicted in Figure 7. The ultimate stress and the resulting Young's moduli are collected in Table 3. Perpendicularly built samples show a lower ultimate stress and a lower Young's modulus than the built parts in the parallel mode, it should be noted that one of the given perpendicular samples has one outlying performance, as can be seen in Fig. 7. The higher performance is presumably due to the influence of interlayer bonding for the different generating strategies. Since faulty inter layer bonding might pose as a weak link, it would be expected that parts written with perpendicular strategy have lower ultimate tensile stresses. Given the low number of samples with high standard deviations, no statistically significant trend could yet be

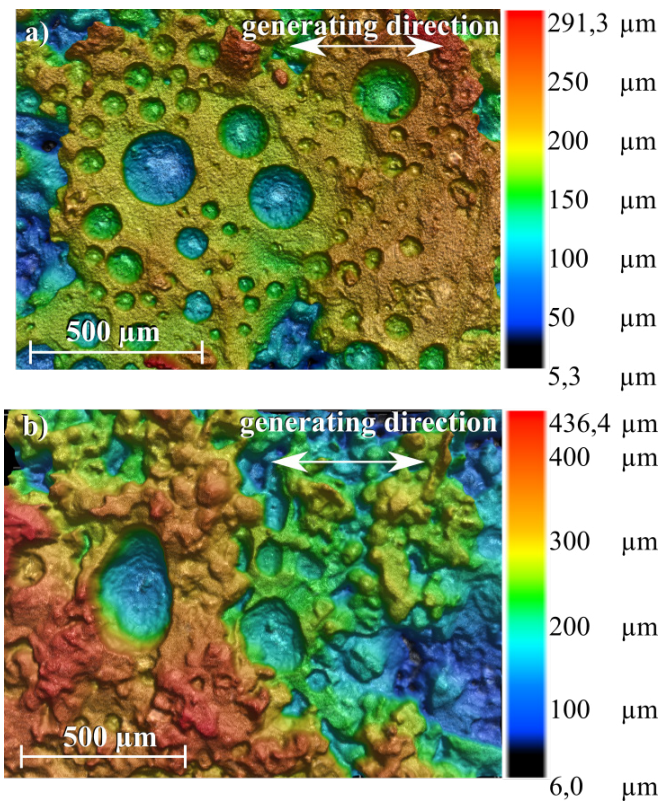


Fig. 5. Laser scanning microscopy analysis of the fracture surface perpendicular to the building direction a) parallel and b) perpendicular generating.

observed and will be part of further investigations. A literature comparison to injection molded or SLS prepared tensile test specimens out of PA12 loaded with 4 wt% carbon black shows that the LPD generated structures reach ~10% of the reported values for Young's modulus and ultimate tensile stress [17]. This is possibly due to two reasons. Firstly, the high degree of porosity in the specimens weakens the part overall strength and secondly the die-cutting process generates inhomogeneous cracked surfaces around the edges of the specimen, which can act as additional weak points for the tensile testing.

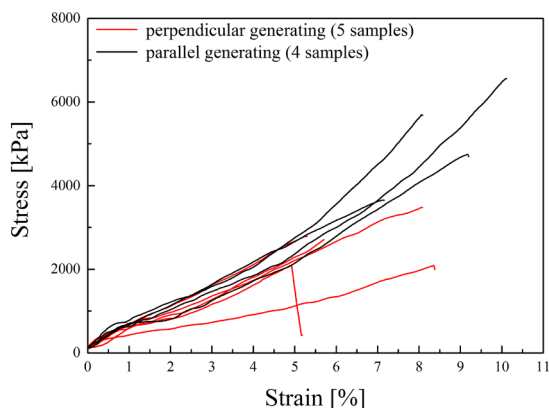


Fig. 7. Tensile diagrams of DED built specimens of PA12 with 1.25 wt% additives with different generating and processing strategies

Table 3. Young's modulus and ultimate tensile stress of laser-built specimens of PA12 with 1.25 wt% additives with different writing strategies.

	Young's modulus [MPa]	Ultimate tensile stress [MPa]
perpendicular generating	55.7 ± 12.4	4.2 ± 0.2
parallel generating	73.5 ± 18.1	5.1 ± 1.2

4. Conclusion

Tailor made PA12/MWCNT composite powder could be prepared by a facile high energy mixing technique without affecting the particle size distribution. The building of simple structures of PA12/MWCNT composites showcase a feasibility to use a DED setup with an Yb doped fiber laser. It was found that the generating direction has effects on the resulting mechanical properties of the built parts, albeit these trends have to be viewed cautiously as the results suffer from a high standard deviation. The low performance compared to injection molded or SLS prepared PA12 specimen are most probably due to the high porosity of the samples.

This drop-in approach showcases the potential of the combination of DED with PA12/MWCNT composites. With a careful finetuning of the powder properties and improved generating strategies, DED-LB with polymeric materials can become a valuable additional technique in the AM portfolio.

Acknowledgements

The authors would like to express their gratitude to the

German Research Foundation (DFG) for funding this study within the priority program 2122 "Materials for Additive Manufacturing".

References

- [1] Additive manufacturing - General principles - Terminology (ISO/ASTM DIS 52900:2018), 2018. <https://doi.org/10.31030/2842544>.
- [2] J. Kruth, P. Mercelis, J. Van Vaerenbergh, L. Froyen, M. Rombouts, Binding mechanisms in selective laser sintering and selective laser melting, *Rapid Prototyp. J.* 11 (2005) 26–36. <https://doi.org/10.1108/13552540510573365>.
- [3] B. Verheyde, M. Rombouts, Laser cladding of a thermoplastic powder on plastics, 2011.
- [4] M. Rombouts, M. Canales, A. Vanhulsel, R. Persoons, The production of polymer composite coatings by laser cladding, *Proc. LANE 2007*. (2007) 815–823.
- [5] B. Verheyde, M. Rombouts, A. Vanhulsel, D. Havermans, J. Meneve, M. Wangenheim, Influence of surface treatment of elastomers on their frictional behaviour in sliding contact, *Wear*. 266 (2009) 468–475. <https://doi.org/10.1016/j.wear.2008.04.040>.
- [6] M. Rombouts, A. Vanhulsel, A. Komp, J. Gedopt, W. Engelen, R. Persoons, Production of low-friction coatings by laser cladding, *ICALEO 2008 - 27th Int. Congr. Appl. Lasers Electro-Optics, Congr. Proc.* 2101 (2008) 759–764. <https://doi.org/10.2351/1.5061295>.
- [7] S. Böhm, M. Schmidt, T. Stichel, M. Kahlmeyer, I. Kryukov, N. Sommer, Single-step Laser Plastic Deposition (LPD) using a near-infrared Thulium fiber-laser, *Polym. Test.* 81 (2020) 106185. <https://doi.org/10.1016/j.polymertesting.2019.106185>.
- [8] R.D. Goodridge, C.J. Tuck, R.J.M. Hague, Laser sintering of polyamides and other polymers, *Prog. Mater. Sci.* 57 (2012) 229–267. <https://doi.org/10.1016/j.pmatsci.2011.04.001>.
- [9] W. Griehl, D. Ruestem, Nylon-12-Preparation, Properties, and Applications, *Ind. Eng. Chem.* 62 (1970) 16–22. <https://doi.org/10.1021/ie50723a005>.
- [10] V. Mamuschkin, C. Engelmann, A. Olowinsky, Improvement of energy deposition in absorber-free laser welding through quasi-simultaneous irradiation, *Phys. Procedia*. 83 (2016) 472–482. <https://doi.org/10.1016/j.phpro.2016.08.049>.
- [11] R. Klein, Laser Welding of Plastics, Wiley-VCH Verlag GmbH & Co. KGaA, Weinheim, Germany, 2011. <https://doi.org/10.1002/9783527636969>.
- [12] K. Mizuno, J. Ishii, H. Kishida, Y. Hayamizu, S. Yasuda, D.N. Futaba, M. Yumura, K. Hata, A black body absorber from vertically aligned single-walled carbon nanotubes, *Proc. Natl. Acad. Sci. U. S. A.* 106 (2009) 6044–6047. <https://doi.org/10.1073/pnas.0900155106>.
- [13] M.B. Bryning, M.F. Islam, J.M. Kikkawa, A.G. Yodh, Very low conductivity threshold in bulk isotropic single-walled carbon nanotube-epoxy composites, *Adv. Mater.* 17 (2005) 1186–1191. <https://doi.org/10.1002/adma.200401649>.
- [14] W. Bauhofer, J.Z. Kovacs, A review and analysis of electrical percolation in carbon nanotube polymer composites, *Compos. Sci. Technol.* 69 (2009) 1486–1498. <https://doi.org/10.1016/j.compscitech.2008.06.018>.
- [15] T. Deplancke, O. Lame, S. Barrau, K. Ravi, F. Dalmas, Impact of

- carbon nanotube prelocalization on the ultra-low electrical percolation threshold and on the mechanical behavior of sintered UHMWPE-based nanocomposites, *Polymer (Guildf)*. 111 (2017) 204–213. <https://doi.org/10.1016/j.polymer.2017.01.040>.
- [16] I. Gibson, D.W. Rosen, B. Stucker, *Additive Manufacturing Technologies*, Springer Berlin Heidelberg, Berlin, Heidelberg, 2019.
- [17] S.R. Athreya, K. Kalaitzidou, S. Das, Mechanical and microstructural properties of Nylon-12/carbon black composites: Selective laser sintering versus melt compounding and injection molding, *Compos. Sci. Technol.* 71 (2011) 506–510. <https://doi.org/10.1016/j.compscitech.2010.12.028>.

11th CIRP Conference on Photonic Technologies [LANE 2020] on September 7-10, 2020

Laser polishing as a new post process for 3D-printed polymer parts

Karsten Braun^{a*}, Edgar Willenborg^a, Johannes Henrich Schleifenbaum^a

^a*Fraunhofer Institute for Laser Technology ILT, Steinbachstrasse 15, 52074 Aachen, Germany*

* Corresponding author. Tel.: +49 241 8906-645; fax: +49 241 8906-121. E-mail address: karsten.braun@ilt.fraunhofer.de

Abstract

A process strategy – a quasi-top-hat scanning strategy with closed-loop temperature control – for laser polishing of additively manufactured polymer parts is developed to reduce the process to its two main process parameter, polishing temperature and melt duration. A study for SLS-printed PA12 results in an achievable roughness reduction from an initial roughness of $S_a = 10.2 \mu\text{m}$ to $S_a = 0.61 \mu\text{m}$. Further investigations are performed for PP, TPU, ABS and PEEK.

© 2020 The Authors. Published by Elsevier B.V.

This is an open access article under the CC BY-NC-ND license (<http://creativecommons.org/licenses/by-nc-nd/4.0/>)

Peer-review under responsibility of the Bayerisches Laserzentrum GmbH

Keywords: Laser; Polishing; Surface finish; Roughness; Polymers; Plastics; Additive manufacturing; 3D-printing; SLS; FDM;

1. Introduction

Despite their great potential for individualization, 3D-printing processes for polymer parts such as SLS (Selective Laser Sintering) and FDM (Fused Deposition Modeling) have the particular disadvantage of a high surface roughness; therefore, surface finishing is often necessary. However, current finishing procedures often have deficits such as low flexibility, long processing times or the incorporation of abrasives into the component. Therefore, a non-contact, laser-based polishing process for additively manufactured polymer parts is being developed. Previous works have already shown that the laser polishing of polymers is possible. For example it was shown that a turned polycarbonate surface can be polished using CO₂-Laser radiation in combination with a Quasi-Line scanning strategy. [1] For additively manufactured polymer parts laser polishing of various materials was performed successfully by Layher et al. [2] and Kumbhar et al. [3]. It was also shown that the laser polishing can have a positive effect on mechanical properties of 3D-printed parts by Chen et al. [4, 5]. Further studies were performed by Dewey et al. [6] and Chai et al. [7].

Although the process principle does work a general knowledge of the requirements for a smoothing of the material in the polishing process is not yet developed. In this work a new process strategy for laser polishing of additively manufactured polymer parts is presented with which a more basic understanding of the polishing process can be achieved.

2. Experimental Setup

The experimental setup contains a CO₂-laser with a maximum output power in continuous wave mode of about 200 W. The laser radiation is guided through a 2D galvanometer scanner and a focal lens with 200 mm focal length (see Fig. 1). The beam diameter in the focal plane is about 350 μm . For the process the laser beam is defocused to a beam diameter of 2 mm. A closed-loop temperature control is realized using a pyrometer and a laser power control. The setup is integrated in a 3 axis machine.

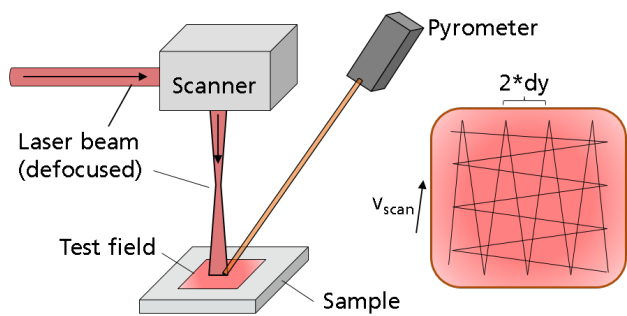


Fig. 1. Scheme of the processing setup (left) and the laser path (right) for a quasi-top-hat scanning strategy

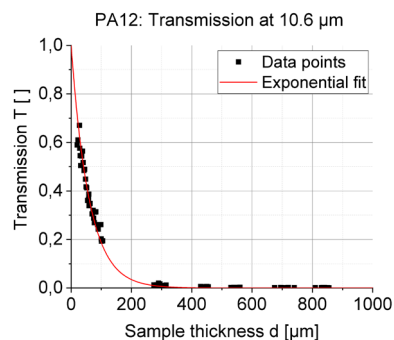


Fig. 3. Measurement of the optical transmission of 3D printed PA12 samples at 10.6 μm wavelength for different sample thicknesses

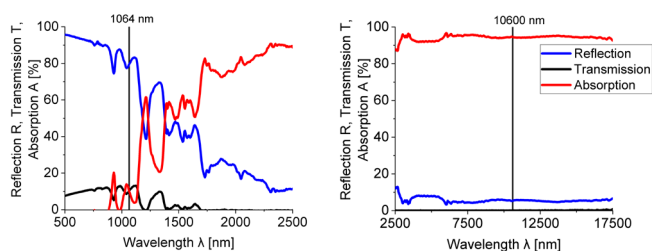


Fig. 2. Optical spectrum of SLS manufactured PA12 with a sample thickness of 5 mm using a UV-VIS (left) and an FTIR (right) spectrometer

4. Development of a quasi-top-hat scanning strategy

Polymers typically have a low heat conductivity compared to other material classes. Also the CO₂-laser radiation is absorbed within a few 10 to 100 μm. These properties can be used to generate extended melt pools at the surface. To realize such extended melt pools a new scanning strategy is developed, the so called quasi-top-hat scanning strategy. With a rapid movement of the defocused laser beam across the material surface and a closed-loop temperature control that regulates the laser power the processed area of the material surface can be heated up and melted simultaneously (see Fig. 4).

3. Preparative experiments

For laser processes the knowledge of the basic interaction between the laser light and the material is important. Therefore a spectral analysis of the used material is done (see Fig. 2).

Due to the typical porosity of additively manufactured materials the optical spectrum and especially the optical penetration depth of different wavelengths may vary slightly from that of the solid bulk material. For SLS manufactured PA12 the absorption of CO₂-Laser radiation ($\lambda = 10.6 \mu\text{m}$) is 94.6%. In the visible range the reflection is >90%, leading to the white appearance of the material.

It is advantageous for the laser polishing process that the laser light is absorbed near the surface of the material. To determine the optical penetration depth d_{opt} – the reciprocal of the absorption coefficient – the optical spectrum is measured for several thin slices of the sample material with a thickness ranging from 20 μm to 839 μm. The slices are cut from a 30x30x5 mm³ sized sample with a microtome. The transmission as a function of the sample thickness follows an exponentially decaying curve (Beer-Lambert law). By determining the slope of this curve the optical penetration depth can be calculated. For the wavelength of CO₂-Laser radiation and the SLS printed PA12 material the optical penetration depth is calculated to $d_{opt,10.6} = 60 \mu\text{m}$ at room temperature (see Fig. 3)

For the experiments also the optical penetration depth of the measurement wavelength of the used pyrometer ($\lambda = 3.9 \mu\text{m}$) is important and can be determined with the same method to $d_{opt,3.9} = 102 \mu\text{m}$.

Here, the scanning speed v_{scan} of the laser beam movement is 5-10 m/s and it is moved across the processed area in a bidirectional way with a track distance dy of 100-300 μm (see Fig. 1). The area size can be between 1x1 mm² and 30x30 mm². After each pass the orientation of the movement is rotated by 90° and a slight random offset of the tracks is calculated to avoid a direct overlap of tracks from different passes. Within each pass the processed area is slightly heated up. This is repeated as often as required until a certain surface temperature is reached which can then be maintained for an arbitrary amount of time. Using a pyrometer the surface temperature of the processed area is tracked and with a closed-loop control the laser power is regulated to achieve the desired temperature-time curve on the material surface (see Fig. 5). The temperature distribution is similar to that of a top-hat intensity distribution, leading to its name (see Fig. 4).

This process strategy has the particular advantage of reducing the laser polishing process to its two main influencing quantities, temperature and polishing time. In addition to the polishing time the actual process also has a heat up phase of a few seconds that is included in the interaction time between laser radiation and material surface that is used in the following as parameter.

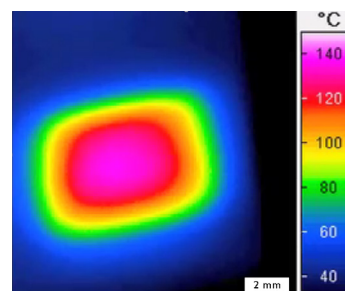


Fig. 4. Temperature distribution on the sample surface using a quasi-top-hat scanning strategy with a size of 10x10 mm² on a 30x30x5 mm³ sample

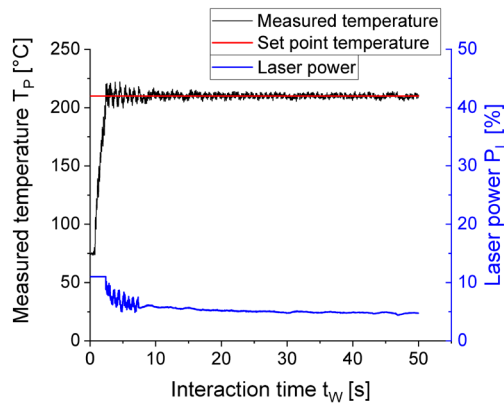


Fig. 5. Temperature curve for the closed-loop control and curve of the regulated laser power

5. Results

The main result parameter for the evaluation of the experiments is the surface roughness of the processed area. The roughness is measured in the center of each processed area using white light interferometry. The resolution of the surface measurements in this work is $1.1 \mu\text{m}$ in lateral dimensions and about 1 nm in vertical dimension. The measurement area is $1 \times 1 \text{ mm}^2$. To remove the form from the surface measurements and to consider the resolution of the measurement an FFT band pass filter from $8 \mu\text{m}$ to $320 \mu\text{m}$ spatial wavelength is applied to each measurement. The initial surface topography of the SLS printed PA12 samples is shown in Fig. 6 and its areal arithmetic mean roughness S_a is determined to $S_a = 10.2 \mu\text{m}$. However, the peak-valley value can reach up to $PV = 100 \mu\text{m}$.

Using the quasi-top-hat scanning strategy and the closed-loop temperature control a 2-dimensional experimental design can be setup in which the polishing temperature and the interaction time are varied. For the choice of the parameter range the thermal material properties, especially the melting temperature, of PA12 are taken into account (see Table 1).

PA12 is a semi-crystalline material. Although the glass transition temperature is quite low, the polishing temperature must exceed the melting temperature.

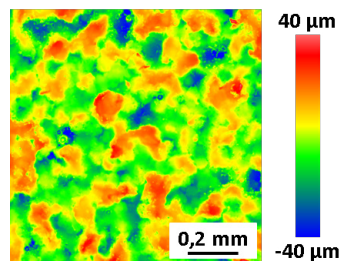


Fig. 6. White light interferometric measurement of an SLS printed PA12 sample – Band pass filter $8 - 320 \mu\text{m}$

Table 1. Material properties of PA12 [8]

Material properties	Value
Melting temperature	180°C
Glass transition temperature	37°C

Thermal conductivity	0.23 W/mK
Specific heat conductivity	2.4 kJ/kgK
Absorption of water at room temperature	$0.7 - 1.1 \%$

Only above the melting temperature the crystalline parts of the material become flexible and a polishing effect due to melting can occur.

In the experiments it is important to note that the temperature measured with the pyrometer for the closed-loop control is not necessarily the actual temperature at the material surface. This has two reasons. First, the emission coefficient is not known for the material and might even change with temperature. However, for many polymers and glasses the emission coefficient is very high and is thus set here to $\epsilon = 0.95$. Second, the measurement wavelength of the pyrometer has an optical penetration depth of $102 \mu\text{m}$ and the temperature of the bulk material decreases the further away it is from the surface. This leads to an averaging effect in the measured heat radiation and thus to an uncertainty in the calculated temperature. Therefore the polishing temperature is referred to as *measured temperature*.

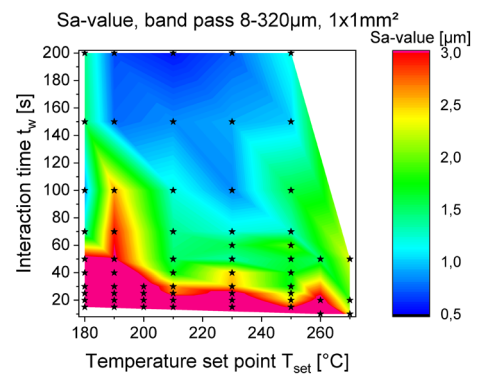


Fig. 7. Roughness of PA12 sample surfaces for various polishing parameters

In the experimental design for the laser polishing of PA12 with the quasi-top-hat scanning strategy the polishing temperature set point T_{set} for the closed-loop control is varied from 180°C to 270°C and the interaction time t_w from 5 s to 200 s . The roughness of each test field is then measured (see Fig. 7).

The surface roughness is decreased for most of the tested polishing parameters, although there are different degrees of smoothing. There is a large parameter field where the resulting surface roughness is below $S_a = 1 \mu\text{m}$. The lowest measured roughness is $S_a = 0.61 \mu\text{m}$ at a temperature set point of 210°C and an interaction time of 200 s . An example of a white light interferometric measurement of a laser polished test field is shown in Fig. 8 for two different color scales. Although the surface topography is significantly smoother than in the initial state there is a noticeable structure left on the surface. This might be smoothed at longer interaction times, which can be interpreted from Fig. 7.

If the temperature set point and thus the polishing temperature is too high a thermal degradation of the polymer material occurs. This leads to a yellow discoloration of the

material surface and appears for temperature set points of 220°C or higher. The longer the interaction time or the higher the temperature, the stronger the discoloration (see Fig. 9).

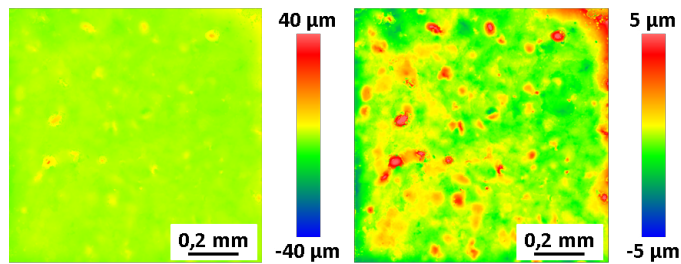


Fig. 8. White light interferometric measurement of an SLS printed PA12 sample after laser polishing with two different color scales. The left picture can be compared to the state before polishing (Fig. 6) and in the right picture the remaining roughness is visible. – Band pass filter 8 – 320 μm, $T_{set} = 210^{\circ}C, t_w = 200s$

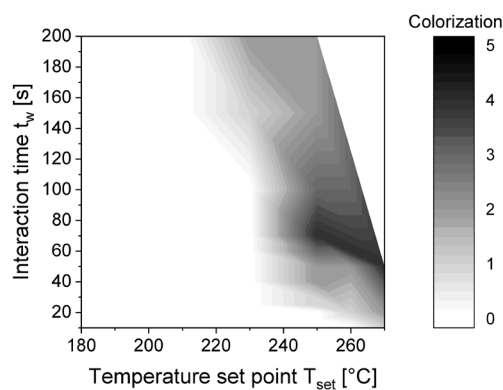


Fig. 9. Discoloration of PA12 sample surfaces for various polishing parameters on a subjective scale from 0 (no discoloration) to 5 (strong discoloration)

6. Transfer to other materials

In additive manufacturing many materials are used for different applications. For most applications and materials a post processing is necessary. The developed process strategy can be used to simplify the parameter search for laser polishing of other materials and to get a basic understanding of the materials behavior during melting.

To test this a parameter study similar to the one for SLS printed PA12 is applied to further 3D printed materials: SLS printed Polypropylene (PP), SLS printed thermoplastic Polyurethane (TPU), FDM printed Acrylonitrile butadiene styrene (ABS) and FDM printed Polyether ether ketone (PEEK).

The areal arithmetic mean surface roughness of the used samples after 3D printing and thus in the initial state for the laser polishing is listed in Table 2 for each material and also the investigated parameter range. The used samples have the same dimensions as the used PA12 samples (30x30x5 mm³) and the process strategy and the evaluation method for the laser polishing study is also the same.

A variation of the polishing temperature set point and the interaction time result in a basic correlation between the

process parameters and the roughness. The lowest achieved roughness of this parameter variation is given in Table 3. It is noted that there is also a significant smoothing of the surface for polishing parameters near the parameters given in Table 3. Although, the exact range is still to be determined with more detailed parameter studies and robustness tests.

Although the polishing temperature set point is not necessarily exactly the actual surface temperature, the temperature set point typically is slightly above the melting temperature of the processed material. The interaction time to achieve a low roughness depends on the temperature set point and especially on the viscosity and surface tension of the material in the melted state.

Besides the roughness reduction of the surface topography there can occur various side effects like discoloration of the material or bubble formation. These effects typically occur for higher temperature set points and can be explained with either thermal degradation of the material or evaporation of contained water. The latter can be avoided with a drying or pre heating of the samples before laser polishing to reduce the moisture. A more detailed analysis of the material behavior in the laser polishing process with drying or pre heating is still to be performed.

Table 2. 3D printing method and initial roughness of various materials measured with a band pass filter at 8-320 μm spatial wavelength

Material	Printing method	Roughness after printing	T_{set} inspected range	t_w inspected range
PA12	SLS	10.2 μm	180 - 270°C	10 - 200 s
PP	SLS	16.9 μm	120 - 200°C	20 -160 s
TPU	SLS	39.5 μm	170 - 220°C	20 - 240 s
ABS	FDM	18.5 μm	180 - 220°C	20 - 140 s
PEEK	FDM	7.7 μm	300 - 370°C	600 - 1800 s

Table 3. Achieved roughness for various laser polished materials measured with a band pass filter at 8-320 μm spatial wavelength

Material	Temperature set point for laser polishing	Interaction time for laser polishing	Roughness after laser polishing
PA12	210°C	200 s	0.61 μm
PP	180°C	60 s	0.59 μm
TPU	200°C	40 s	0.12 μm
ABS	220°C	60 s	0.24 μm
PEEK	340°C	1800 s	0.13 μm

With the developed process strategy and determined parameter sets various demonstration samples are produced. For the demonstration parts the size of the processed area is extended to a larger area up to the size of the whole sample. Simple 3D geometries like cubes or pyramids can be aligned like a flat sample and thus be processed with the same strategy. Demonstration parts are made from PA12, PP and PEEK (Fig. 10)

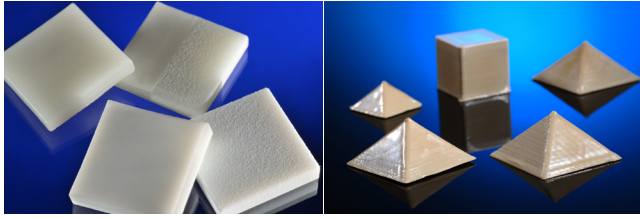


Fig. 10. Demonstration parts with the materials PA12 (left, bottom), PP (left, top) and PEEK (right).

7. Conclusion and Outlook

In this work a new approach to improve the basic understanding of the laser polishing process of additively manufactured polymer parts is presented. With the process strategy used – a quasi-top-hat scanning strategy with closed-loop temperature control – the basic temperature-time-roughness relation can be observed for different materials. For each investigated material a parameter range with a significant smoothing of the material surface can be determined. The minimum roughness achieved is between $Sa = 0.12 \mu\text{m}$ and $Sa = 0.61 \mu\text{m}$ depending on the material. Concluding from the conduction of the experiments it is assumed that a drying step of the material before laser polishing has a significant influence on the process, but this is still to be analyzed in detail.

The results can either be used as an orientation for the choice of polishing parameters or can directly be used to polish whole sample surfaces. A particular advantage of the quasi-top-hat scanning strategy is the flexibility regarding the geometry of the generated melt pool. By scanning, different melt pool

geometries can be created, which are potentially more advantageous for the polishing of larger areas. A suitable scanning strategy to move the quasi-top-hat scanning area across larger surfaces has to be developed in the next step.

References

- [1] Richmann A. Polieren von Gläsern und Kunststoffen mit CO₂-Laserstrahlung. Aachen; 2013
- [2] Layher M, Hopf A, Eckhardt L, Bliedtner J. Laser Beam Polishing of Polymers. *PhotonicsViews* 16 (3); 2019. p. 83–87
- [3] Kumbhar N N, Mulay A V. Finishing of Fused Deposition Modelling (FDM) Printed Parts by CO₂ Laser. *Proceedings of 6th International & 27th All India Manufacturing Technology, Design and Research Conference*; Pune, Maharashtra; 2016. p. 63-67
- [4] Chen L, Zhang X, Gan S. Effects of laser polishing on surface quality and mechanical properties of PLA parts built by fused deposition modeling. *J. Appl. Polym. Sci.* 137 (3); 2020. p. 48288
- [5] Chen L, Zhang X. Modification the surface quality and mechanical properties by laser polishing of Al/PLA part manufactured by fused deposition modeling. *Applied Surface Science* Vol.492, 2019, p. 765-775
- [6] Dewey M P, Ulutan D. Development of laser polishing as an auxiliary post-process to improve surface quality in fused deposition modeling parts. *ASME 2017 12th International Manufacturing Science and Engineering Conference, MSEC 2017 collocated with the JSME/ASME 2017 6th International Conference on Materials and Processing*, 2017, Vol.2
- [7] Chai Y, Li R W, Perriman D M, Chen S, Qin Q H, Smith P N. Laser polishing of thermoplastics fabricated using fused deposition modelling. *International Journal of Advanced Manufacturing Technology* Vol.96(9-12), 2018, p. 4295-4302
- [8] Domininghaus H, Elsner P, Eyerer P, Hirth T. *Kunststoffe. Eigenschaften und Anwendungen*. Springer. 2008

11th CIRP Conference on Photonic Technologies [LANE 2020] on September 7-10, 2020

Laser Transmission Welding of additive manufactured parts: process modifications to reduce cavities inside the weld seam

Julian Kuklik*, Verena Wippo, Peter Jaeschke, Stefan Kaieler, Ludger Overmeyer

Laser Zentrum Hannover e.V., Holerithallee 8, 30419 Hanover, Germany

* Corresponding author. Tel.: +49-511-2788-269; fax: +49-511-2788-100. E-mail address: j.kuklik@lzh.de

Abstract

For small batches, prototypes, and customized mass production, additive manufacturing is a prominent technology in the production of complex thermoplastic parts. A frequently used process is Fused Deposition Modeling (FDM). For more and more applications, additive manufactured components have to be joined in order to form larger functional assemblies. Laser transmission welding (LTW) of thermoplastics is an industrial established technique, e.g. for joining injection molded parts in the automotive sector.

Compared to injection molding, the FDM process itself results in an inhomogeneous structure with a significant amount of air inside a component. Because the part is built up layer by layer, it supports the formation of cavities inside the weld seam and thus a reduction in the weld seam strength.

To optimize the weld seam quality, new strategies for the design of FDM parts for LTW are being investigated. Welded parts are being analyzed with tensile testing and cross sections.

© 2020 The Authors. Published by Elsevier B.V.

This is an open access article under the CC BY-NC-ND license (<http://creativecommons.org/licenses/by-nc-nd/4.0/>)

Peer-review under responsibility of the Bayerisches Laserzentrum GmbH

Keywords: Laser transmission welding; fused deposition modeling; Cavities; Polylactide;

1. Introduction

In recent years, additive manufacturing has developed into technology that can produce customized parts in small and large volumes. The first additive manufactured part that was qualified for aerospace applications is a nose bracket gear made of titanium for the Airbus A350 XWB [1]. The automotive sector also increasingly produced metallic and thermoplastic parts with additive manufacturing. In 2018, BMW announced it had produced more than 1 million parts in the last ten years with additive manufacturing [2]. The market volume for additive manufacturing equipment and services is expected to grow from 4 billion USD in 2014 to 44 billion USD in 2025 [3].

A popular additive manufacturing process for thermoplastics is Fused Deposition Modeling (FDM). To prepare a 3D-CAD part for the deposition process, it must be converted into a file format that encodes the surface geometry of the part, such as the STL format. In the next step, software cuts the surface

model into defined layers with a description of each layer infill and generates machine-readable code such as G-code. Within this process, deposition parameters such as layer thickness, layer infill pattern, print velocity, and line width are defined. Finally, the FDM printer uses the G-code to form the 3D object. The thermoplastic material in filament form is melted by the print head and extruded through a fine nozzle line-by-line to form a layer in the XY plane. After solidification, the Z-axis moves and the print head deposits the next layer on top. These stacked layers form the 3D object.

A single layer of an FDM part has an anisotropic mechanical behavior based on the deposition direction [4, 5]. Along the axes of deposition, the load capacity of the filaments is higher than in their radial direction that is where the filaments are fused together on the touching surfaces. Because the deposited filaments have a circular cross section, they create voids in between the adjacent filaments of an FDM part. In recent years, many authors have investigated the influence of process

parameters and manufacturing strategies on the anisotropic material behavior and voids [6-9]. To increase the bonding strength between line intersections, Torres et al. used annealing for FDM parts made of polylactide. The parts had increased strength after the annealing but a decreased ductility [8]. Rodriguez et al. investigated the influence of FDM process parameters on the void formation. [9]

Laser transmission welding (LTW) is an established industrial technique to join thermoplastic parts. It is based on the optical transmittance of thermoplastic material for near-infrared radiation (NIR). To join two parts, see Fig. 1, the radiation must pass through the transparent part (LT) to reach the surface of the second part (LA), which absorbs the radiation to a certain depth. By absorbing the radiation, the optical energy transforms into thermal energy. Heat conduction transfers the heat to the transparent part, resulting in both parts melting at their interface. After cooling and solidification, the two parts form a bond. A good surface contact requires constant joining pressure and a smooth surface at the parts' interface [10].

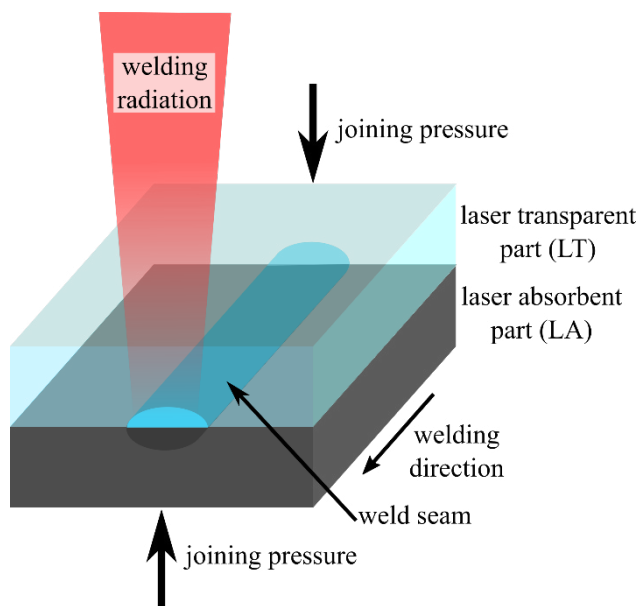


Fig. 1. Schematic laser welding process

In 2019, Kuklik et al. demonstrated a fundamental study of laser transmission welding for additively manufactured parts. They investigated the influence of additive manufacturing process parameters on the transmissivity as well as the weldability of natural polylactide parts. For the highest weld seam strength, an energy per unit length of $E_l = 4 \text{ J/mm}$ at a weld velocity of $v = 2.5 \text{ mm/s}$ was recommended. Cross sections discovered cavities inside the weld seam, which resulted in an unpredictable weld seam width and connected area in the joint. This was also reflected in the high standard deviation of the weld seam strength. The authors suggested that voids caused these cavities during the additive manufacturing process and that surface roughness resulted in small gaps between the parts [11].

In this study, intermediate layers in the form of bars are applied between the parts in order to provide additional material for the weld seam. The hypothesis is that during the welding process, the bar melts and the molten material fills the cavities

in the weld seam that would cause the voids inside the additive manufactured parts. The authors assume that the weld seam without cavities increases the weld seam strength while decreasing the standard deviation. A weld seam with constant width and without cavities is required for a high-quality laser transmission welding of additive manufactured parts.

Nomenclature

E_l	energy per unit length
LA	laser absorbent part
LT	laser transparent part
λ	wavelength
P	laser power
v	scanning velocity

2. Experimental Set-up

In this study of laser transmission welding of additive manufactured components, parts were manufactured with a 3rd generation Ultimaker FDM desktop printer. This printer has a heated glass build plate and a resolution of $12.5 \mu\text{m}$ in the X- and Y-axes and $2.5 \mu\text{m}$ in the Z-axis. The utilized nozzle has a diameter of 0.4 mm .

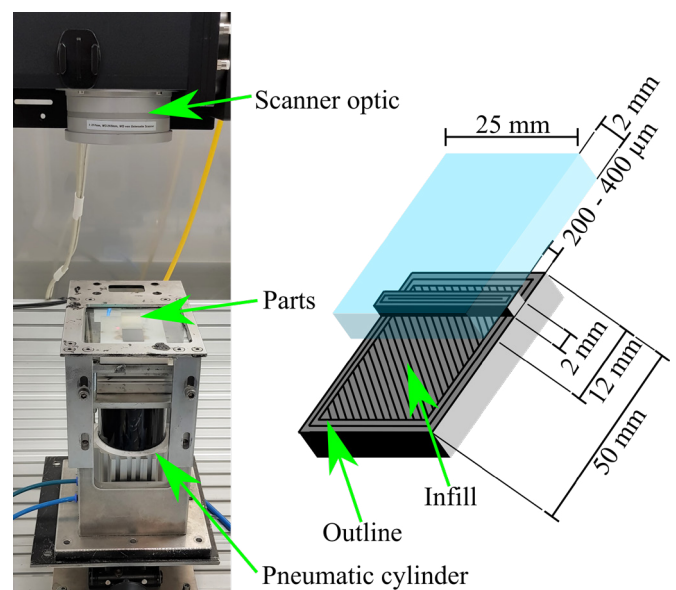


Fig. 2. Experimental setup with the laser scanner optic and the clamping device. The parts were aligned with an overlap of 12 mm and the bar in the middle of the overlap.

The materials for the transparent and the absorbent parts are natural and black polylactide respectively from Filamentworld. Cura, the software from Ultimaker, was used for slicing the CAD models in $200 \mu\text{m}$ thick layers. A layer has an outline that consists of three filaments. The layer infill consist of filaments aligned in the 45° direction to the outline (cf. Fig. 2). The orientation of the layer infill changes by 90° every layer. For the laser welding experiments, transparent and absorbing parts with 50 mm length, 25 mm width, and 2 mm thickness were produced. To reduce cavities inside the weld seam, bars of 2 mm width and 200 μm or 400 μm height respectively were

added onto the top layer of the absorbing parts in order to provide additional material in the welding zone (cf. Fig. 2). The printing direction of the bar was parallel to the weld seam. For the laser transmission welding, Laserline's diode laser LDM-300-40 with a maximum power of $P_{\max} = 300$ W and a wavelength of $\lambda = 940$ nm was used. The laser beam was guided by an optical fiber to a scanner equipped with a focusing optic. This optic generated a focal diameter of 2 mm.

The parts were aligned with an overlap of 12 mm, see Fig. 2 right. To generate the required clamping pressure, a pneumatic cylinder pressed the parts against a glass plate with a pressure of 0.2 MPa, see Fig. 2 left. With the parameters for the contour welding process recommended in an earlier study [11], the bars overheat. Therefore, in this investigation the parts were fused by contour welding with scanning velocities ranging from $v = 5$ mm/s to $v = 20.0$ mm/s and a laser power range of $P = 10.0$ W to $P = 20.0$ W.

3. Results and discussion

The absorbent parts with the intermediate layers in form of bars on top were fused in overlap to transparent parts. To study the influence of the different amount of additional material on cavities inside the weld seam, welds were performed with different scanning velocities and laser powers.

For each parameter set, cross sections were made from welded samples at three different positions of the weld. Only a few cross sections are shown in this study, but the details described also appear at other positions of the weld seams.

Fig. 3 A – C show the cross sections of parts without a bar (A), with a 200 μm (B), and a 400 μm (C) high bar that were fused together with a laser power of $P = 10$ W and a scanning velocity of $v = 5$ mm/s. Figures 3 A and B show a large cavity in the middle of the weld seam. In both cases, the parts were completely melted from the first layer of the additively manufactured transparent part (LT) to the second layer of the absorbent part (LA). Fig. 3 C shows that the former bar height of 400 μm reduced to 200 μm during the welding process and the width extended to 3 mm. Also, the first manufacturing layer of the bar was melted and squeezed to the sides. The absorbent and transparent parts were melted until to the third manufacturing layer and a weld seam was formed with a clear contour and without cavities.

A weld seam cross section of an experiment with a higher scanning velocity of $v = 10$ mm/s and a 400 μm high bar is seen in Fig. 3 D. The laser power was kept constant at $P = 10$ W. The absorbent part was melted until the third layer but only the top layer of the 400 μm high bar was melted and squeezed slightly to the sides. The transparent part was melted until the second additively manufactured layer. The welding process formed a weld seam without cavities and with a clear contour.

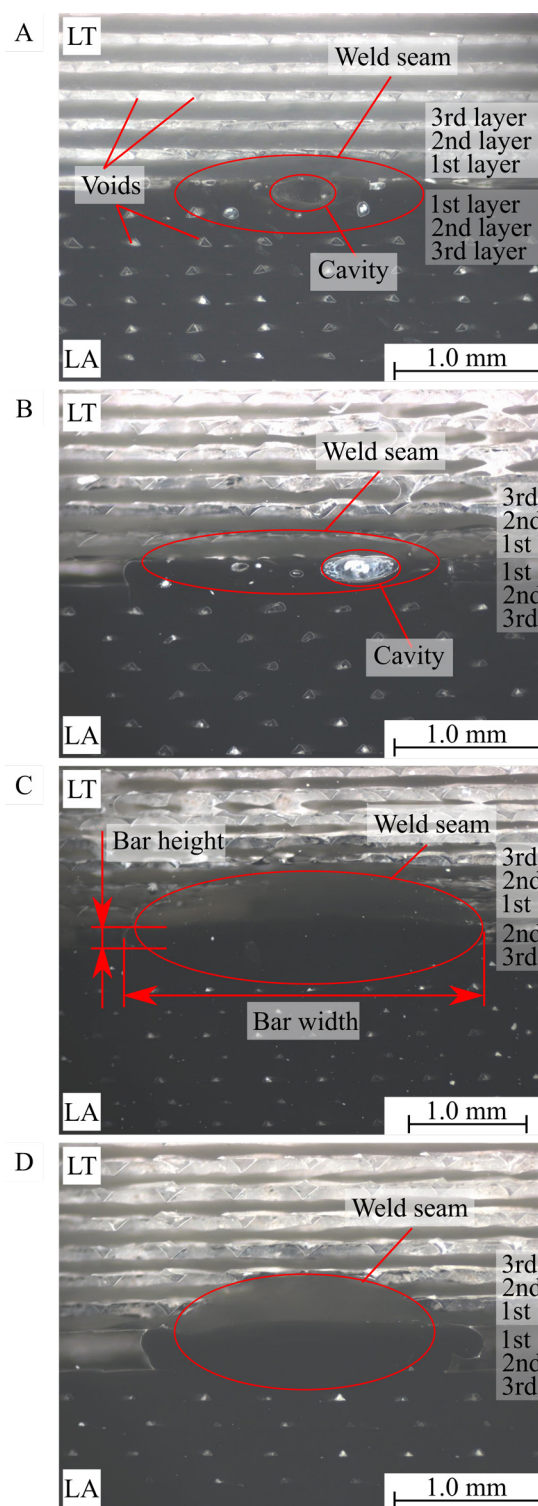


Fig. 3. Cross sections of weld seams with no bar (A), a 200 μm high bar (B), and a 400 μm high bar (C). Welding parameter: $P = 10$ W, $v = 5$ mm/s. Cross section D shows a weld seam with a 400 μm high bar and welding parameter: $P = 10$ W, $v = 10$ mm/s.

The analysis of the weld seam cross sections shows that the bars on top of the absorbent part are necessary for the cavity reduction. The authors conclude from the voids inside the additively manufactured parts that the absorbent material melts and sinks down during the welding process. Without an intermediate layer, the transparent part was also in contact with the absorbent part on both sides of the weld seam during the

welding process. When the absorbent part was melted and sank down to fill the voids, the transparent part could not yield. Therefore, the heat transfer was prevented from the absorbent to the transparent part. With the bar on top of the absorbent part, the constant pressure of the clamping device results in a six times higher clamping force, because of the smaller surface in contact. When the bar melts and yields to the pressure, the transparent part follows and the heat transfer to the transparent part improves. However, there are still cavities in the parts with a 200 μm high bar. Providing material for the weld seam and increasing the clamping force could not eliminate all cavities. Comparing Fig. 3 B with C that has a higher bar, the transparent part was melted until the third layer with the same welding parameters. It is assumed that the air at the sides of the bar isolate the heat and support the heat transfer to the transparent part.

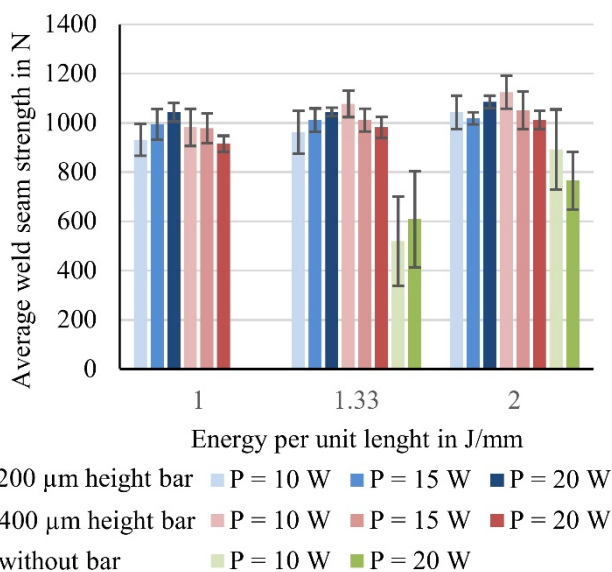


Fig. 4. Results of the average weld seam strength of welded parts with 200 μm and 400 μm high bars at different energy per unit length in comparison to welding experiments without a supporting bar from [11].

In order to determine the influence of the intermediate layers on the weld seam strength, parts with 200 μm and 400 μm high bars were fused with transparent parts using different laser powers and scanning velocities. The scanning velocities were chosen to observe equivalent energy per unit length between $E_1 = 1 - 2 \text{ J/mm}$ at laser powers of $P_1 = 10 \text{ W}$, $P_2 = 15 \text{ W}$ and $P_3 = 20 \text{ W}$. For each parameter set, the weld seam strength of four welded samples were tested with a tensile lap-shear test. Fig. 4 shows the weld seam strength tests' result. The result of the tests demonstrate that with the 200 μm and 400 μm high bar the maximum weld seam strength increases in comparison to the parts without a bar. The difference in the weld seam strength is very low for the experiments with the bars. The average weld seam strength decreases with less energy per unit length. Nevertheless, the standard deviation of the experiments overlaps, so the result is not entirely clear. For the parts with a 400 μm high bar, the average weld seam strength decreases for higher laser power. The opposite behavior is observed for the parts with 200 μm high bars. This could be explained by an

overheating of the absorbent part during the welding with the 400 μm high bar and a laser power of $P = 20 \text{ W}$.

However, during the weld seam strength tests of the parts with the bars, not all of them broke in the weld seam. The absorbent part broke directly at the edge of the bar (cf. Fig. 5 A) or the formed weld seam was ripped off from the transparent part, (cf. Fig. 5 C) in contrast to the parts without a bar (Fig. 5 B), which all broke in the weld seam.

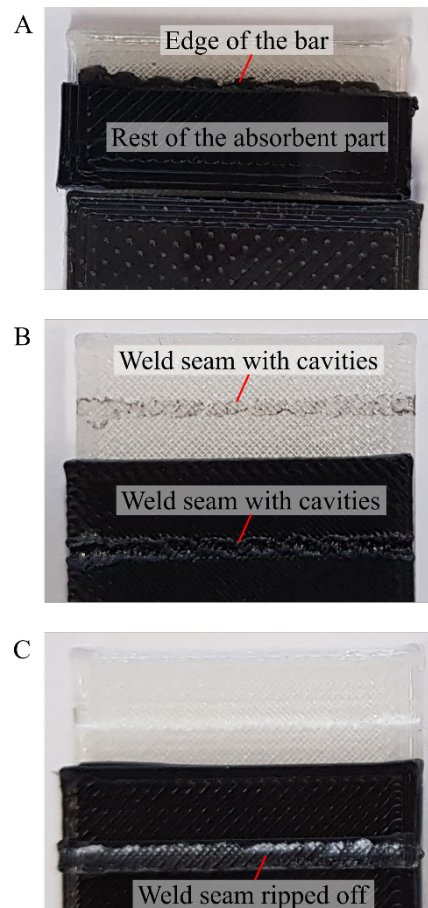


Fig. 5. Different failure types of the weld seam strength tested parts. A and C: Parts with a 400 μm high bar, B: without a bar.

During the weld seam strength tests, the parts bend around the weld seam. This momentum results in high stress at the edge of the bar. The material broke inside the part, but not in the weld seam. Therefore, an influence of the different bar heights on the weld seam strength could not be determined. However, it is determined that the weld seams have a higher strength than the additively manufactured parts themselves for the load case.

4. Conclusion

This study enhanced the process knowledge of the laser transmission welding for additively manufactured components made using a FDM process with polylactide. The cavities inside the weld seam were reduced by providing additional material in form of bars with different heights for the welding process. Contour welding with various laser power and velocity values was tested.

Cross sections of the parts without and with a 200 μm high bar show cavities in the middle of the weld seam. Only with a 400 μm high bar, cavities were prevented in the weld seam. The transparent part was melted until the third layer and a weld seam was formed with a clear contour.

An average weld seam strength of $F = 1123 \text{ N}$ was reached with absorbent parts with a 400 μm high bar on top, using a laser power of $P = 10 \text{ W}$ and a scanning velocity of $v = 5 \text{ mm/s}$. However, during the weld seam strength tests of the parts with a bar, they failed in the additively manufactured material. The influence of the different bar heights on the weld seam strength could not be determined.

In further studies, the temperature in the weld seam should be measured with a pyrometer to identify the heat dynamics with different bar heights on top of the absorbing part. New shapes should be investigated for the bars to prevent high loads during the weld seam strength test in the material at the root of the bar. Because of superior gap bridgeability, a quasi-simultaneous welding process should be tested as well.

References

- [1] <https://fon-mag.de/industry-news/news-plus-2019/template-news/?L=1> (Status: 09.03.2020).
- [2] <https://www.press.bmwgroup.com/global/article/detail/T0286895EN/a-million-printed-components-in-just-ten-years-bmw-group-makes-increasing-use-of-3d-printing?language=en> (Status: 09.03.2020).
- [3] <https://www.alliedmarketresearch.com/3d-printing-market> (Status: 09.03.2020).
- [4] Ahn, S.-H., Montero, M., Odell, D., et al., (2002) Anisotropic material properties of fused deposition modeling ABS, *Rapid prototyping journal*, v. 8, n. 4, 248-257.
- [5] Ahn, S.-H., Baek, C., Lee, S., et al., (2003) Anisotropic Tensile Failure Model of Rapid Prototyping Parts - Fused Deposition Modeling (FDM), *International Journal of Modern Physics B*, Vol. 17, No. 08, 1510-1516.
- [6] Giannatsis, J., Sofos, K., Canellidis, V., et al., (2012) Investigating the influence of build parameters on the mechanical properties of FDM parts, In *proceedings of the 5th International Conference on Advanced Research and Rapid Prototyping*, 525–529.
- [7] Tarko, J., Vladić, G., Pál, M., et al., (2017) Influence of printing speed on production of embossing tools using FDM 3D printing technology, *Journal of graphic engineering and design*, v. 8, n. 1, 19-27.
- [8] B. M. Tymrak, B. M., Kreiger, M., Pearce, J. M. (2014) Mechanical Properties of Components Fabricated with Open-Source 3-D Printers Under Realistic Environmental Conditions, In *Materials & Design*, v. 58, 242-246.
- [9] Rodriguez, J.F., Thomas, J.P., Renaud, J.E. (2000), Characterization of the mesostructure of fused - deposition acrylonitrile - butadiene - styrene materials, *Rapid Prototyping Journal*, Vol. 6, No. 3, pp. 175-186.
- [10] Potente, H. (2004) *Fügen von Kunststoffen. Grundlagen, Verfahren, Anwendung*, Carl Hanser Verlag, München, Wien.
- [11] Kuklik, J., Henkel, C., Wippo, V., et al., (2019) Laser transmission welding of additive manufactured components, In *Proceedings of the 38th International Congress on Applications of Lasers & Electro-Optics (ICALEO 2019)*, Laser Institute of America.

11th CIRP Conference on Photonic Technologies [LANE 2020] on September 7-10, 2020

Improving property consistency and reliability for polyamide processed using powder bed fusion

David L. Bourell^{a*}, David K. Leigh^b

^aUniversity of Texas at Austin, 204 E. Dean Keeton St., Austin TX USA 78712

^bEOS North America, 3813 Helios Way, Suite B298, Pflugerville TX USA 78660

* Corresponding author. Tel.: +01-512-471-3170. E-mail address: dbourell@mail.utexas.edu

Abstract

An historic obstacle to widespread application of polymer powder bed fusion in structural applications is the reliability, consistency and repeatability of part service properties between builds. This is discussed in the context of data from a service bureau representing over 80,000 ASTM D638 tension tests of additive manufactured laser sintered polyamide 11. It is shown that the usual method for relating process parameters to part properties, the energy density, is valid when considering part service strength but is not adequate when considering part ductility. A solution approach is presented based on thermal modeling during the build process.

© 2020 The Authors. Published by Elsevier B.V.

This is an open access article under the CC BY-NC-ND license (<http://creativecommons.org/licenses/by-nc-nd/4.0/>)

Peer-review under responsibility of the Bayerisches Laserzentrum GmbH

Keywords: polyamide; laser sintering; reliability; strength; ductility; thermal model

1. Introduction

Laser-based powder bed fusion of polymers is a widespread application area for additive manufacturing (AM). According to the Wohlers Report [1], polymeric powder for laser-based powder bed fusion (PBF-LB/P) represents over 25% of all feedstock for AM, and polyamide is by far the most popular polymer in this class.

Polyamide 11 has very good mechanical properties as produced using PBF-LB/P, but a primary issue with open acceptance for structural applications is the reliability and consistency of mechanical properties from one build to the next. This is illustrated in Fig. 1 for almost 4000 ASTM D638 tension test results for polyamide 11 PBF-LB/P in a commercial setting. The strength values are reasonably constant over a large range of feedstock lots and machines. However, the ductility varies widely independent of the testing direction for the build, varying from ~1% elongation to over 50%. The low ductility, coupled with an intrinsic defect structure associated with porosity and limited inter-layer strength, can create a shift in

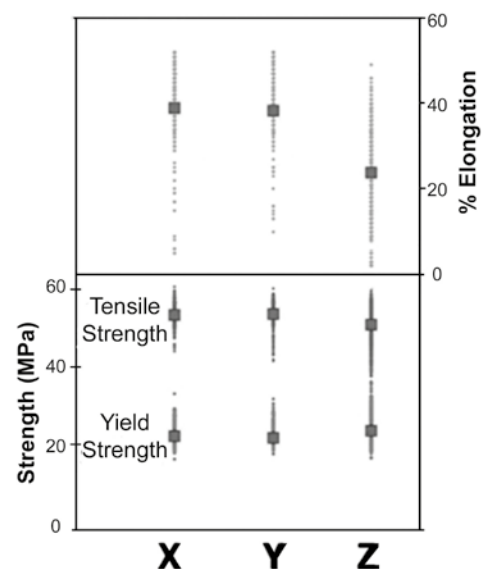


Fig. 1. ASTM D638 tension test results PBF-LB/P polyamide 11, commercial builds [2]



Fig. 2. PBF-LB/P polyamide 11 prosthetic foot which shattered a low load [3]. The green marks on the main piece are spaced at 25 mm.

deformation mode from the usual yield/plasticity mode to a brittle fracture-mechanics failure mechanism. This is illustrated in Fig. 2 which shows a polyamide 11 prosthetic foot which, when loaded in bending by hand, shattered in a brittle mode [3].

A major issue then is to understand the conditions resulting in low ductility and toughness. By doing so, one might set the build conditions in a way to avoid these deleterious results. It is the goal of this work to describe the manufacturing conditions leading to limited ductility and to provide a model for assessing the manufacturing conditions leading to acceptable service mechanical properties.

2. Experimental Methods

Polyamide 11 was obtained from two providers: ALM FR-106 and Arkema Rilsan D80. The number of ASTM D638 tension tests from each provider was 68,000 and 16,700, respectively. An MTS Insight 10 tension tester was used for all tests. Tests covered commercial builds at Stratays Digital Manufacturing (formerly Harvest Technologies) over a ten-year period, across approximately 15 different PBF-LB/P machines and over a large number of machine operators. 3D Systems SPro 60s or equivalents by the same company. For all builds, the machine parameter set included 46 Watts power, 0.25 mm hatch spacing, 10.2 m/s scan speed, 0.1 mm layer thickness and 180°C part bed temperature.

The variation in ductility was assessed using a single AM fabricator over a large number of commercial batches. The average value of elongation to fracture and the standard deviation were obtained for Z-oriented polyamide 11 test specimens gathered in the middle of the build chamber (138 specimens, 126 separate builds, Z distance 175-300 mm, over a four-year period), and also for Z-oriented test specimens built on the same machine at the back left corner (63 specimens, 52 separate builds, Z distance 75-100 mm, over a nine-year period).

3. Results

Figs. 3 and 4 show summary results of the average strength and elongation at break, respectively, for ASTM D638 samples

tested parallel to the build (Z) direction. It is seen that the strength is rather uniform across the build volume, but the elongation suffers as the testing location approaches the sidewalls of the build volume.

A common manufacturing parameter for PBF-LB/P polymers is the energy density ED. Over the years, investigators have reported at least five different forms for polymer energy density [5]. The form best reflecting actual measurements is

$$ED = \frac{P}{vHt} \quad (1)$$

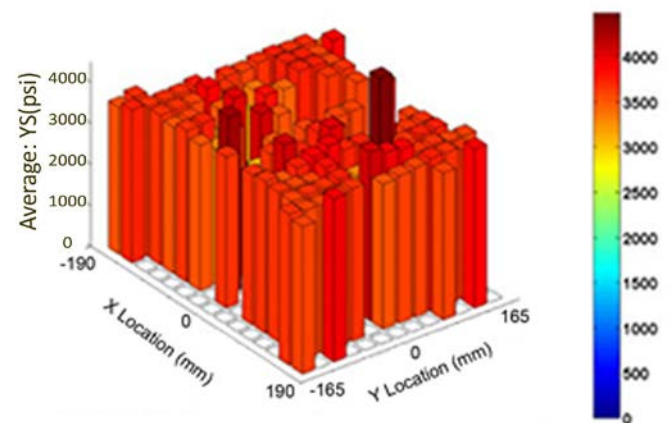


Fig. 3. Average yield strength of ~68,000 ASTM D638 tension specimens built using ALM FR-106 polyamide 11 and tested in the Z-direction. [4]

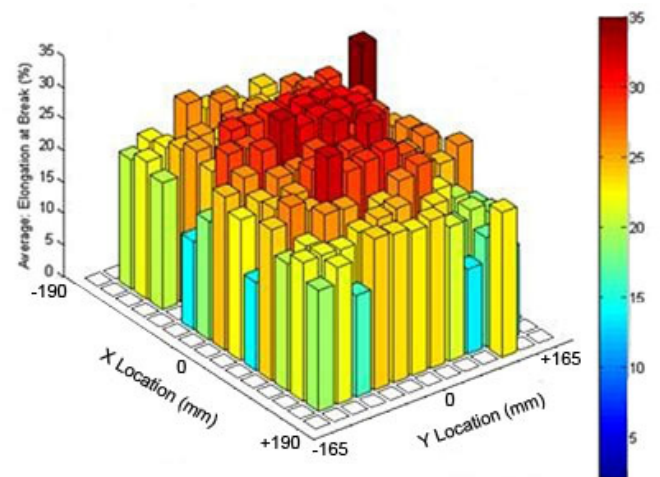


Fig. 4. Average elongation at break for ~17,000 ASTM D638 tension specimens built using Arkema Rilsan D80 polyamide 11 and tested in the Z-direction. [4]

where P = laser power, v = scan speed, H = hatch spacing and t = layer thickness. For the data presented, the energy density was 0.18 J/mm^3 . It is seen in Fig. 3 that the strength is rather uniform for all specimens which have the same energy density. Lowering the energy density below about 0.12 J/mm^3 results in a loss of strength due to creation of fusion errors and porosity [6]. However, the ductility results in Fig. 4 show that the energy density term is not a good indicator of acceptable ductility,

since the energy density for all samples tested and reported in Fig. 4 have the same energy density of 0.18 J/mm^3 .

The average elongation to fracture for polyamide 11 tension specimens from a single machine over numerous builds was $39.1 \pm 7.1\%$ for specimens built in the center of the build chamber. At the outside area near the back left corner, the elongation to fracture was $15.4 \pm 5.3\%$.

4. Discussion and Thermal Model

The authors believe that the reduction in ductility illustrated in Fig. 4 for specimens built near the build chamber wall is due to a reduced thermal exposure from the time the powder is first heated prior to lasing to the time at which the part is cooled to room temperature after the build is complete [4,7]. Of importance is the dwell time of the lased feedstock in the build chamber after it becomes molten until the part cools to room temperature. For parts in the center of the build chamber, this dwell time at high temperature is long, whereas for parts built near the sidewalls (or X- or Y-oriented samples built at the top or bottom of the build), the time at temperature is short. Several binding mechanisms may be at play for the part after lasing which may improve the ductility of the final part. This includes a traditional Frenkel viscous sintering during which porosity is reduced [8]. Another possible mechanism is long chain diffusion or reptation which yields similar results [9]. Using the Frenkel model, the rate of pore closure is given by

$$\frac{da}{dt} = -\frac{2\sigma}{a^2} \frac{\delta^3}{kT} D \quad (2)$$

where a = pore radius, t = elapsed time, σ = interfacial tension of the molten polymer, δ = crystal lattice constant, k = Boltzmann's Constant, T = absolute temperature and D = diffusivity. An incremental decrease in pore volume for a spherical pore is

$$dV = d\left(\frac{4\pi a^3}{3}\right) = 4\pi a^2 da \quad (3)$$

Solving Equation 1 for $a^2 da$ and substituting into Equation 2, the following differential equation is obtained:

$$dV = \left[\frac{8\pi\sigma\delta^3}{k}\right] \left[\frac{D}{T}\right] dt \quad (4)$$

Knowing that the diffusivity D has an Arrhenius relationship $D = A \exp(-Q/kT)$, the relation is substituted into Equation 4 to produce:

$$dV = \left[\frac{8\pi\sigma\delta^3 A}{k}\right] \left[\frac{\exp\left(-\frac{Q}{kT}\right)}{T}\right] dt = \left[\frac{8\pi\sigma\delta^3 A}{k}\right] [f(t, T)] dt \quad (5)$$

The temperature-independent term in Equation 5 is effectively a constant given a specific feedstock material. Assuming that the ductility becomes acceptable once a pore shrinks past some

critical size or volume, then the integral F of the $f(t, T)$ term over time will also cross over a critical value F_{cr} . In principle, one might calculate the integral of $f(t, T) dt$ for every point in the build chamber from the start of part bed heating until the entire chamber is cooled after the build. The integrated value F will be smallest at the build walls and at the top and bottom of the build chamber, and it will be largest in the middle of the build chamber [4,7]. A value of the integral may be selected for which smaller values are associated with unacceptable ductility and for which higher values cause full ductility.

The authors have earlier experimentally probed feedstock/part cooling rates of various points within the build chamber [4,7]. The thermal conductivity of the powder bed is extremely low, approximately 0.1 W/mK [10], so there is a large difference in time-at-temperature between feedstock near the build chamber sidewalls and feedstock located near the center of the build chamber. From this earlier work, the initial cooling rate in the center of a build chamber was $\sim 5^\circ\text{C/hr}$, while near the build chamber wall, it measured about 15°C/hr [4]. The integrated value of $f(t, T) dt$ for the center of the build chamber is over twice the value near the chamber sidewalls.

This is illustrated in Fig. 5, an ANSYS simulation of the build chamber temperature of a polyamide full-chamber build after 30 min [4]. It is seen that the center of the chamber remains at the build temperature 180°C , whereas the material near the chamber sidewalls has cooled to below 150°C .

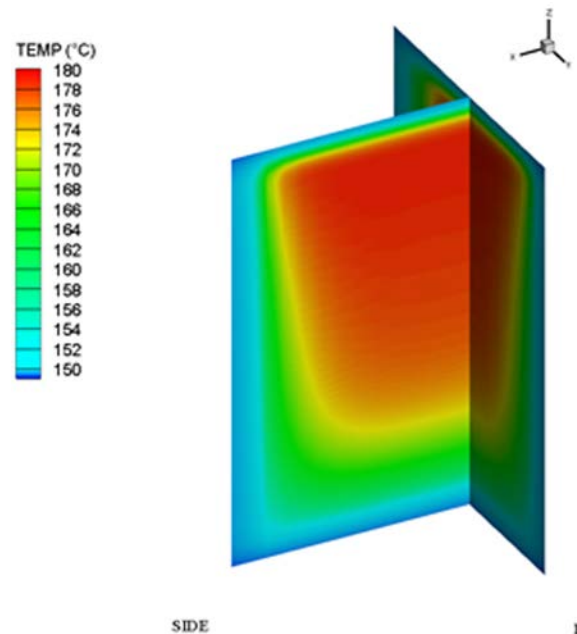


Fig. 5. ANSYS simulation of a full-chamber polyamide build 30 min after the end of the build. [4] “Side” is the x or left direction in the build chamber; “F” denotes the y direction or front of the build chamber.

The temperature profile of the build chamber after 40 min of cool-down time is shown in Fig. 6. It is seen that material near the center of the chamber remains at 180°C , but cooling has progressed over 100 mm away from the sidewalls.

A topic of commercial interest then is how to expand the volume within the build chamber where parts with high

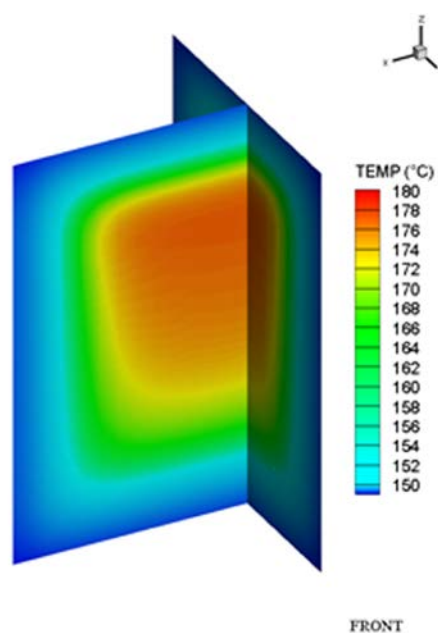


Fig. 6. ANSYS simulation of a full-chamber polyamide build 40 min after the end of the build. [4] “FRONT” denotes the y direction or front of the build chamber.

ductility are produced. There are several approaches that may produce this desirable result. Perhaps the most obvious is to install sidewall heaters on the build chamber sidewalls which would slow the cooling rate laterally (cf., Figs. 5 and 6). Some pre-commercial PBF-LB/P fabricators once had sidewall heaters. Alternatively, some PBF-LB/P fabricators have removable build chambers to enhance productivity, including the current EOS P700, Integra P450 and 3D Systems sPro 140 and sPro 230. All these fabricators currently require cooling to $\sim 100^\circ\text{C}$ prior to enabling removal. Placing the removable build chamber in an oven immediately at the end of the build with minimal cooling rather than ambient cooling would likewise slow the cooling rate and improve final part ductility. Issues of oxidation must be considered in this implementation. Lowering the intrinsic powder bed thermal conductivity would slow the cooling rate as well, but this could have a deleterious effect on productivity.

The authors speculate that taking cooled polyamide 11 parts and oven soaking them at the build temperature, 180°C , will not result in improved ductility. The main reason is that the parts in the build chamber during the PBF-LB/P process are liquid, whereas cooled parts once crystallized will remain solid upon heating to the build chamber temperature. This is illustrated by the differential scanning calorimeter run of polyamide 11, Fig. 7 [4]. Here, on heating, the powder melts at $\sim 190^\circ\text{C}$ and on cooling crystallizes at $\sim 160^\circ\text{C}$. During a build, the powder is heated to the part bin temperature, $\sim 180^\circ\text{C}$, which is below the melting temperature. Once it is lased, the powder melts and flows to form a small portion of the part. In the build chamber, it rather quickly cools back to the build temperature, $\sim 180^\circ\text{C}$, which is above the crystallization temperature. Hence, the part in the build chamber remains molten until it cools below $\sim 160^\circ\text{C}$. This typically occurs at the end of the build during the overall build chamber cooling process. The point then is that the thermal exposure resulting in ductility improvement during the build and associated cool down operates on liquid polyamide, whereas a post-build

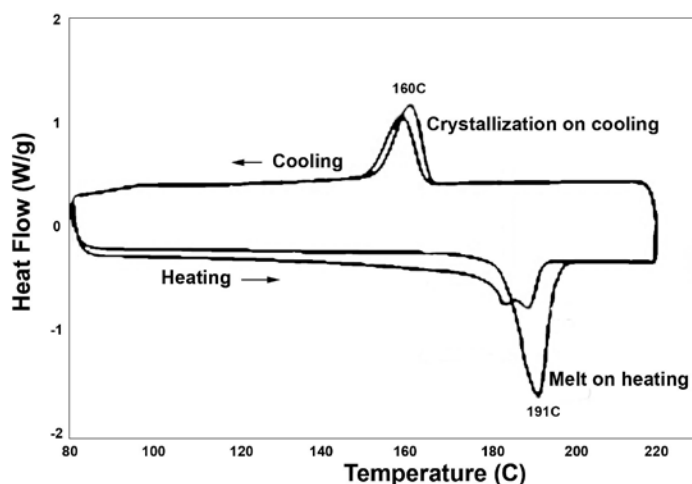


Fig. 7. Experimental Differential Scanning Calorimeter plot for Polyamide 11. [4]

thermal processing of the part would operate on solid polyamide.

5. Conclusions

This work is based on analysis of approximately 85,000 ASTM D638 tension specimens built over ~ 10 years on multiple machines in a commercial setting using polyamide 11 feedstock from two manufacturers. It is observed that the specimen strength correlates to the energy density, but the ductility does not. Further, variations in ductility can be traced to the location of the tension specimen within the build chamber. Specimens located near the center of the build chamber exhibited high ductility, elongations to break exceeding 20%, but the ductility decreased as the location shifted toward the build chamber sidewalls.

A thermal model was derived to define the location within the build chamber where parts with acceptable ductility could be produced. Based on the Frenkel theory of viscous sintering, the model confirms that locations away from the build chamber sidewalls have the best opportunity to exhibit acceptable ductility. Because the time at temperature after the build is a significant contribution to the overall thermal exposure of the part, the part cooling rate is important in defining the final ductility. Part cooling rate in turn is strongly affected by how far the part is away from the build chamber sidewalls. The most effective approach to expanding the build chamber volume where parts with acceptable ductility are obtained is to install sidewall heaters as a fabricator modification.

References

- [1] Wohlers Report 2019: 3D Printing and Additive Manufacturing State of the Industry Worldwide Progress Report, Wohlers Associates, Ft. Collins CO USA 2019.
- [2] Bourell DL, Leigh DK. The Development of Mechanical Properties in Laser Sintered Polyamide, 5th International Conference PMI2012, Ghent, Belgium, September 14, 2012, p. 25-30.
- [3] Leigh DK, Bourell DL. Powder Bed Fusion of Polymers, ASM Handbook Vol. 24 Additive Manufacturing, Materials Park OH USA, 2020, in press.
- [4] Leigh DK. Improving Process Stability and Ductility in Laser sintered Polyamide. Doctoral Dissertation, The University of Texas at Austin, Austin TX USA, 2019.

- [5] Bourell DL, Coholich J, Chalancon A, Bhat A. Evaluation of energy density measures and validation for powder bed fusion of polyamide”, *CIRP Annals Manufacturing Technology* Vol. 1, 66 (Aug. 2017), p. 217-220.
- [6] Starr TL, Gornet TJ, Usher JS. The effect of process conditions on mechanical properties of laser-sintered nylon, *Rapid Prototyping Journal*, 17#6, 2011, p. 418-423.
- [7] Bourell DL, Leigh DK. Improvements in Ductility and Reliability of Mechanical Properties of Polyamide 11 Produced Using Laser-Based Powder Bed Fusion. *JOM*, 72#3, (Mar. 2020) in press.
- [8] Ristic M, Milosevic. *Sci Sinter*, 7 (2006).
- [9] Kim KD, Sperling L, Klein A. *Macromolecules*, 27 (1994) p. 6841.
- [10] Yuan M, Bourell D. Thermal Conductivity of Polyamide 12 Powder for Use in Laser Sintering, *Rapid Prototyping Journal*, 19#6 (2013) p. 437-445.

11th CIRP Conference on Photonic Technologies [LANE 2020] on September 7-10, 2020

Microstructure and mechanical properties of selective laser melting of hydrogen embrittlement resistance stainless steel HR-2

Xianfeng Shen*, Guowei Wang, Zhiyao Cheng, Shengwang Zhang, Qin Yang, Shuke Huang

Institute of Machinery Manufacturing Technology, China Academy of Engineering Physics, No.64 Mianshan Road, Mianyang 621900, China

* Corresponding author. Tel.: +86-816-248-4292; fax: +86-816-248-7614. E-mail address: xianfeng_shen@163.com, shenxianfeng@caep.cn

Abstract

HR-2 is a single-phase austenitic stainless steel with excellent hydrogen embrittlement resistance and a wide range of applications in hydrogen storage pressure vessels. During the powder preparation and additive manufacturing process, burning nitrogen deteriorates its hydrogen embrittlement resistance and mechanical properties. In this paper, HR-2 stainless steel powder was prepared by vacuum induction melting atomization (VIGA), and the HR-2 powder with acceptable nitrogen content was obtained in a nitrogen atmosphere. The effects of process parameters in selective laser melting, including laser energy density on the part density, microstructure, and mechanical properties of the formed specimens, were investigated. The results show the density of the formed samples first increase and then decrease as the energy density increases. With the optimization of process parameters, the density of the parts fabricated by SLM formed HR-2 with low nitrogen can reach more than 99.5%, the tensile strength can reach 735 ± 5 MPa, the yield strength can reach 415 ± 10 MPa, the percentage elongation of $43 \pm 5\%$, and percentage reduction of $44 \pm 5\%$, while the tensile strength of HR-2 with high nitrogen can reach 720 ± 10 MPa, the yield strength can reach 603.5 ± 10 MPa, the percentage elongation of $45 \pm 5\%$, and percentage reduction of $60 \pm 5\%$, which are comparable with the base material of forged HR-2.

© 2020 The Authors. Published by Elsevier B.V.

This is an open access article under the CC BY-NC-ND license (<http://creativecommons.org/licenses/by-nc-nd/4.0/>)

Peer-review under responsibility of the Bayerisches Laserzentrum GmbH

Keywords: "Insert 5 to 10 keywords here, separated by semicolons ;"

1. Introduction

Selective laser melting (SLM) is an eruptive technology of additive manufacturing or three-dimensional (3D) printing that can be used to produce 3D metal parts directly from a CAD model by the selective laser melting of successive thin layers of metallic or pre-alloyed powders. SLM is becoming a significant method in various industries, including aerospace, consumer products, healthcare, energy, automotive, and marine [1], due to the unique advantage in direct manufacturing of customized metal function parts, lack of constraints regarding complicated structures and for eliminating the expensive time-consuming pre- and post-processing steps, compared with

indirect laser sintering or other conventional manufacturing processes.

Moreover, as hydrogen is regarded as a clean and efficient energy resource, researchers and engineers focus on hydrogen storage containers produced by hydrogen embrittlement resistance stainless steels. Such containers are becoming complicated for better performance, more functions and compacter volume of products in many applications, such as nuclear plants. Therefore, the demand for additive manufacturing of hydrogen embrittlement resistance stainless steels is growing.

Hydrogen embrittlement resistance stainless steels refer to the alloys with the ability to resist hydrogen embrittlement damage and corrosion. They have many important applications

in the petrochemical, nuclear, aerospace, energy and related industries [2]. HR-2 is a single-phase austenitic steel developed by the Institute of Metal Research (IMR), Chinese Academy of Science with excellent resistance to hydrogen embrittlement performance, and with a minimum tensile strength of 650 MPa, yield strength of 390 MPa, percentage elongation of 40% and percentage area reduction of 50% [3], which is superior to 316L.

So far, most of the research has been focused on mechanical properties of SLM of 316L [4, 5] or particle-reinforced 316L [6]. High-density dislocations obtained by the SLM of 316L contributes significantly to high-yield strength [7]. Heat treatment stress relieving at 800°C for 5 h decreases the yield strength with no significant changes to the ultimate tensile strength and elongation of SLM processed 316L [8]. The anisotropy in the microstructure and the mechanical property of SLM processed 316L can be eliminated after recrystallization during heat treatment, which is related to the reduction in dislocation density and stress status [9]. However, research on higher strength hydrogen embrittlement-resistant stainless steels, such as HR-2, are limited. HR-2 contains nitrogen of 0.20%–0.36% for better tensile and yield strengths, and the nitrogen element tends to easily burn out during powder preparation and selective laser welding since these processes involve melting and solidification at high temperatures. Such burning loss of nitrogen in HR-2 will degrade the mechanical performance of SLM. Therefore, it is significant to investigate the mechanical properties of SLM of higher tensile strength HR-2.

Evaluation of microstructure and mechanical properties of SLM of hydrogen embrittlement resistance stainless steels HR-2 were performed in this investigation. Effects of processing parameters on densities and tensile strength of selective laser melted samples were also studied. The burning losses of N content during powder preparation and selective laser melting have also been addressed.

2. Materials and Experimental Procedures

2.1. Material

Two kinds of hydrogen embrittlement resistance stainless steel HR-2 powders were used in this investigation, that is, HR-2 with low nitrogen of 0.080% and HR-2 with high nitrogen of 0.209%. Their compositions are shown in Table 1, and the range requirement for HR-2 chemical compositions with the Institute of Metal Research according to Chinese Standard is also presented in Table 1. The HR-2 powder was prepared by vacuum induction melting atomization (VIGA). It is evident that the HR-2 powder with low nitrogen of 0.08% cannot meet the requirements of the standard compared with the nitrogen ranging from 0.20% to 0.34%. This low nitrogen content in the HR-2 powder is caused by the evaporation of N during the melting process of the base material under vacuum and low-pressure atmosphere, since the vapor pressure of nitrogen is low. This problem can be solved with a nitrogen atmosphere during powder fabrication and raising the nitrogen content from 0.080% to 0.209%. The powder with a satisfactory

nitrogen content was obtained using appropriate pressure of N₂ gas in the smelting furnace.

Table 1. Chemical composition of HR-2 powder with low N and high N, and range requirement (wt.%).

	C	Si	Mn	P	S	H
HR-2 Low N	0.034	0.22	8.97	0.012	0.0021	0.0033
HR-2 with High N	0.037	0.22	9.26	0.0066	0.0016	0.0026
HR-2 Requirement	≤0.04	≤1.0	8~10	≤0.025	≤0.015	
	Ni	Cr	N	O	H	
HR-2 Low N	7.54	20.06	0.080	0.114	0.0033	
HR-2 with High N	7.48	19.92	0.209	0.070	0.0026	
HR-2 Requirement	5.5~8.0	19~21.5	0.20~0.34			

Scanning electron microscope photographs, particle size distribution and sphericity of the low nitrogen HR-2 powder are shown in Fig. 1(a)–(c), respectively. The particle size of powder D10 is 13.82 μm, D50 is 22.87 μm, D90 is 36.74 μm, and the sphericity is 96%. The corresponding characteristics of high nitrogen content HR-2 powder are shown in Fig. 2. The particle size of the powder D10 is 18.37 μm, D50 is 30.83 μm, D90 is 50.26 μm, and the sphericity is 96%.

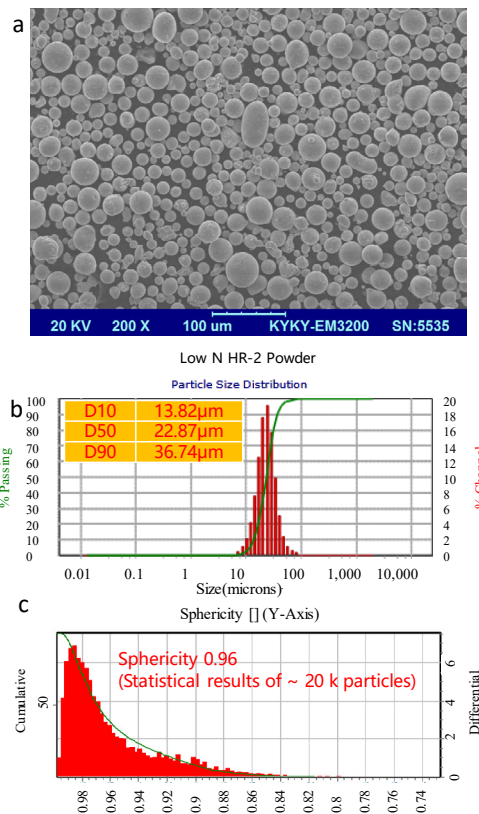


Fig. 1. Powder characteristic of HR-2 with low N content: (a) morphology with SEM, (b) particle size distribution, and (c) sphericity.

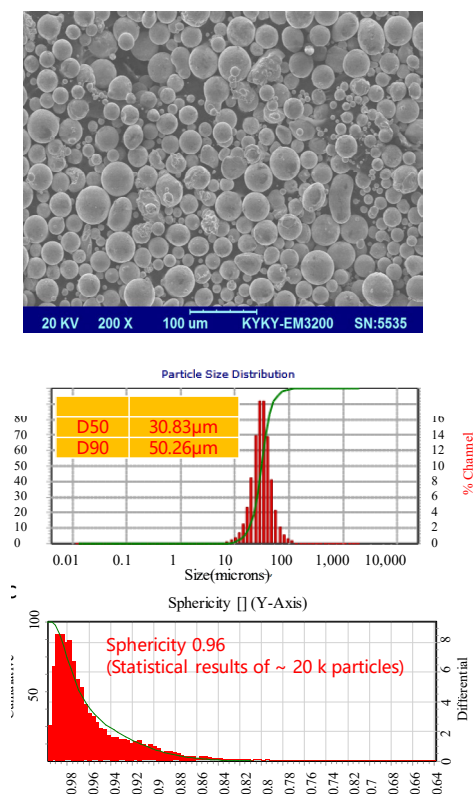


Fig.2. Powder characteristic of HR-2 with high N content: (a) morphology with SEM, (b) particle size distribution, and (c) sphericity.

A2	220	1050	0.11	63.5
A3	195	1050	0.11	56.3
A4	195	755	0.11	78.3
B1	275	1050	0.1	87.3
B2	275	1250	0.1	73.3
B3	250	1050	0.1	79.4
B4	250	1250	0.1	66.7
C1	285	960	0.11	90.0
C2	285	1150	0.11	75.1
C3	315	960	0.11	99.4
C4	315	1150	0.11	83.0
D1	220	755	0.11	88.3
D2	220	650	0.11	102.6
D3	220	1350	0.11	49.4
D4	220	1550	0.11	43.0
E1	195	1083	0.09	66.7
E2	195	812	0.09	88.9
E3	360	1250	0.09	106.7
E4	195	1083	0.09	66.7

The surfaces of the SLM-ed HR-2 metallurgical test pieces were first subjected to sandblasting and shot blasting. The densities of test pieces were then measured using Archimedes' drainage method expressed as follows:

$$\rho = \frac{m_a \times \rho_w}{m_a - m_w} \quad (2)$$

In the formula, m_a is the mass of the test specimen in air, m_w is the mass of the test specimen in water, and ρ_w is the water density.

A metallographic specimen was cut out by EDM, grounded on a grinding and polishing machine, and was then electrolytically corroded. The electrolyte used for electrolytic corrosion was oxalic acid plus hydrofluoric acid composite electrolyte. The metallographic sections were observed under Zeiss optical microscope. A scanning electron microscope machine KYKY-EM3200 was employed with an acceleration voltage of 20 kV. The powder particle sizes were tested using the laser interference method. Chemical compositions of SLM samples were inspected with laser direct reading spectrum detection (SPECTRO). Tensile strength tests were performed on a universal tensile testing machine with a strain rate of 1×10^{-3} /S.

3. Results and discussion

3.1. N Content of SLM samples with HR-2 of Low N

Chemical composition of SLM manufactured samples with HR-2 of Low N were inspected with laser direct reading spectrum detection (SPECTRO). The results show that the nitrogen content of SLM formed samples ranged from 0.0795% to 0.0848%. This indicates that N content has no evident burning loss when compared with the 0.80% N content of

2.2. Experimental Procedures

The SLM machine used in the experiments was EOS M290. It was using a 400W IPG fiber laser with a wavelength of 1.064 μm , a spot diameter of 76 μm , a maximum forming size of $250 \times 250 \times 325 \text{ mm}^3$, a layer thickness of 20–100 μm , and a maximum scanning speed of 7000 mm/s. The size of the metallographic test block is 10 mm * 10 mm * 10 mm, and the size of the tensile samples is $\Phi 12 \text{ mm} \times 68 \text{ mm}$ with a gauge distance of 30 mm. In addition, the preheating temperature of substrates is 100°C with a layer thickness of 30 μm . To prevent denitrication of HR-2 during 3D printing, nitrogen is chosen as the protective chamber atmosphere of the SLM machine. Horizontal samples were fabricated in this investigation. The process parameters of SLM HR-2 with low nitrogen used in the experimental scheme are shown in Table 2, where laser power, scanning speed and hatch distance are single parameters, while energy density (E) is a combined parameter presented as follows:

$$E = \frac{P}{V \times \tau \times h} \quad (1)$$

where P is the laser power, V is the scanning speed, τ is the layer thickness, and h is the hatch distance. The layer thickness was constant at 30 μm in Table 2.

Table 2. Experimental scheme of SLM of HR-2 with low nitrogen

Sample No.	Laser power (W)	Scanning speed (mm/s)	Hatch distance (mm)	Energy density (J/mm ³)
A1	220	755	0.11	88.3

powder during SLM, which attributes to the N₂ chamber protective atmosphere.

3.2. Effects of Processing Parameters on Density of SLM Parts

Densities of twenty samples corresponding to experimental scheme in Table 2 were measured using Archimedes' drainage method. Effect of energy density on relative density of SLM samples is shown in Fig.3. From the fitted curve in this figure, the sample's density generally increases with the increase in energy density, then reaches a maximum point, and then decreases with the further increase in energy density. Occurrence of turning point on the curve can be related to the occasional presence of unstable keyhole mode during SLM when the energy density is too high. Such occasional unstable keyhole vapor leads to entrapped pores, and then will result in higher porosity, deteriorating part density. This changing trend in samples' density with energy density is consistent with the literature [10] and such trend can be deduced from the influence of processing parameters on samples' porosity.

The changing trend contour of samples' density with scanning speed and laser power is shown in Fig. 4. Sample density generally increases with the increase in laser power. It first decreases, then increases and finally decreases with the rising scanning speed. Generally, a wide optional processing parameter window of SLM of HR-2 with density greater than 99% can also be obtained, that is, the laser power is greater than 220 W, the scanning speed is lower than 1200 mm/s, and the energy density is 70~100 J/mm³, according to the screening experimental results.

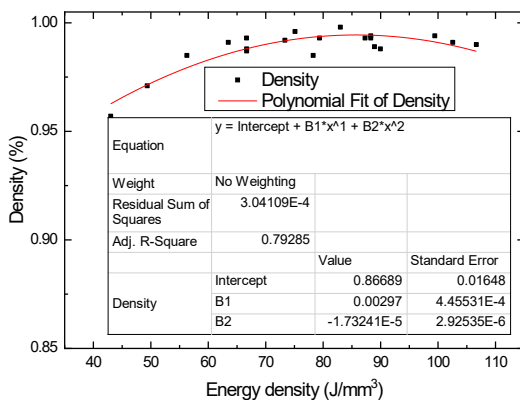


Fig.3. Scatter plot of energy density - relative density of SLM samples.

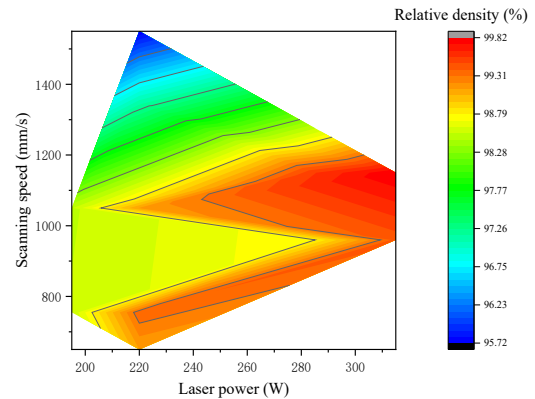


Fig.4. Contour of density with laser power and scanning speed (hatch distance is 0.11)

3.3. Microstructure of SLM Parts of HR-2 with Low N

The microstructure of different sections of SLM-formed HR-2 is presented in Fig. 5. A cross-section (XOY) plane microstructure is shown in Fig.5a, where several molten pools of different passes stand side by side. Figure 5b illustrates a metallographic diagram of the longitudinal section of the SLM formed HR-2 stainless steel. Columnar austenite grains locate competitive grows, and a single grain with a large size can continuously grow across several layers of molten pool. Figure 5c gives a high magnification view of the molten pool in the longitudinal section. It can be observed that the dendrites continuously grow between the molten pools. The growth direction of the dendrites stretches along the greatest temperature gradient, and directionally solidifies towards the center of the molten pool. Compared with cast-forged HR-2 stainless steel, SLM-formed HR-2 stainless steel is composed of austenitic stainless steel, but the metallographic structure of cast-forged austenitic stainless steel is usually a regular polygonal equiaxed crystal with a slightly larger size. SLM is epitaxially grown columnar crystals with a slightly smaller size.

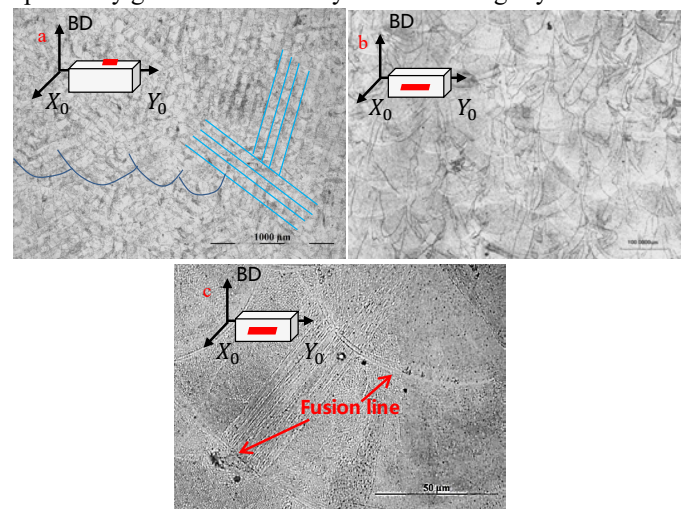


Fig.5. Microstructure of the XOY plane and longitudinal section of SLM HR-2 samples.

3.4. Mechanical properties of SLM parts of HR-2 with low N

Six groups of tensile tests on SLM processed samples of HR-2 with low N were performed with three samples in each group, and the results are shown in Fig.6. The performance requirements of HR-2 products are ultimate tensile strength $UTS \geq 650$ MPa, percentage elongation $A \geq 45\%$ and percentage reduction of area $\geq 50\%$. The experimental samples formed by SLM can meet the strength requirements, but the ductility and plasticity of most tests are weaker than the requirement. The tensile strength of as-build SLM samples of HR-2 with low N using optimized parameters can reach 735 ± 10 MPa, the yield strength can reach 415 ± 10 MPa, the percentage elongation of $43\% \pm 5\%$, and percentage reduction of $44\% \pm 5\%$. Heat treatment can be helpful to improve the ductility performance of samples.

Contours of UTS and elongation with laser power and scanning speed are presented in Fig.7 a) and b), respectively. The relationship between strength and process parameters is not easy to discover. It seems that the highest UTS can be obtained with a laser power of 270–330 W and a scanning speed of 1100–1200 mm/s, but the highest percentage elongation can be obtained with a laser power of about 200 W and a scanning speed of about 1100 mm/s. Therefore, suitable parameters should be selected according to the target mechanical properties.

The minimum mechanical performance of forged HR-2 samples is as follows: tensile strength of 650 MPa, yield strength of 390 MPa, and percentage elongation of 45%. Compared to mechanical properties of forged samples, the tensile strength and yield strength of SLM formed samples are better, but the ductility is inferior. This trend is similar to that of SLM formed 316L [2]. Furthermore, heat treatment is required for better ductility of HR-2 samples fabricated by SLM.

Resilience, including elasticity modulus, is also required to be tested in the future.

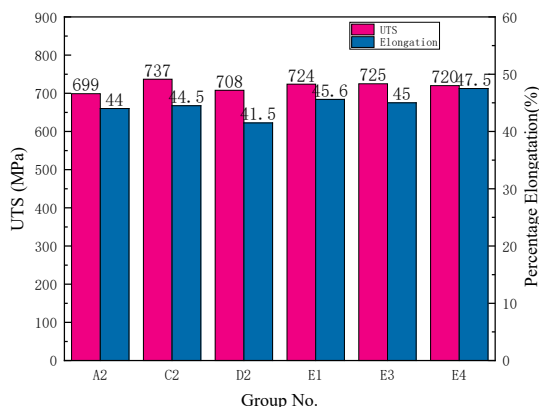


Fig.6. Ultimate tensile strength and percentage elongation of SLM samples of HR-2 with low nitrogen.

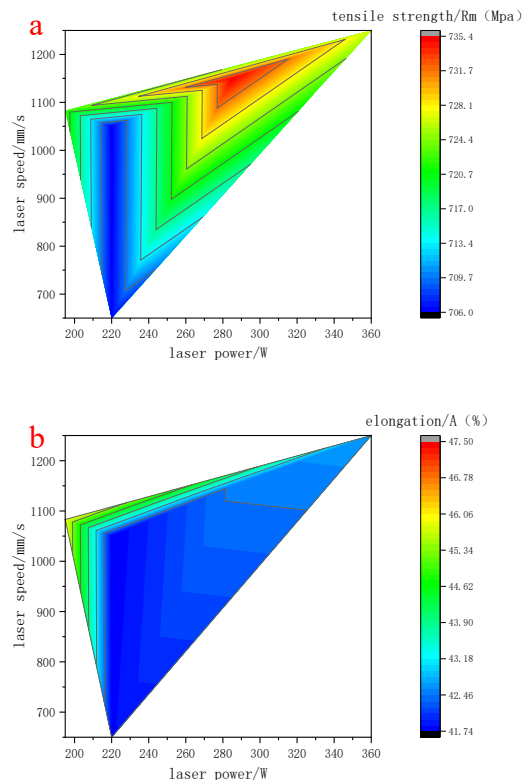


Fig.7. Contour of (a) UTS and (b) elongation with laser power and scanning speed in SLM of HR-2 with low nitrogen.

3.5. Comparison of Stress–Strain Curves of As-build SLM Samples Between HR-2 with Low N and High N

Several initial tensile tests of SLM processed samples of HR-2 with high N were performed. The results show that the tensile strength can reach 720 ± 10 MPa, the yield strength can reach 603.5 ± 10 MPa, the percentage elongation of $45\% \pm 5\%$, and percentage reduction of $60\% \pm 5\%$. The mechanical properties of HR-2 samples with high N are comparable with those of low N. The bigger difference between them lies in the higher yield strength of HR-2 with high N while with the other mechanical properties which are shown in stress-strain curve are similar, as shown in Fig. 8. The microstructure needs to be further investigated to discover the above mechanism.

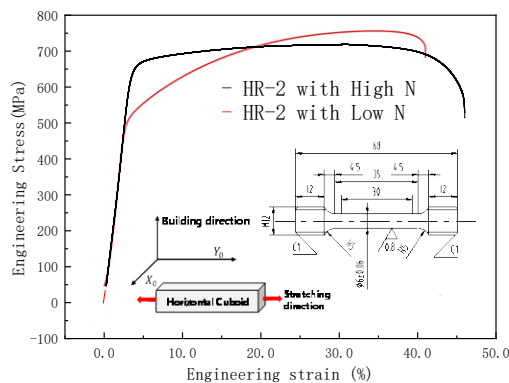


Fig.8. Engineering stress-strain curves of as-build SLM samples.

3.6. Fracture Morphology of SLM Parts

Fracture morphology of additively manufactured HR-2 is shown in Fig. 9. It is a typical ductile fracture with more dimples and smaller size. Furthermore, there were no big pores, voids or second-phase particles found on the interface, and there were no precipitated phases or impurities at the grain boundaries that reduce the matrix performance. These facts illustrate that the fracture belongs to a continuous dislocation slip ductile fracture.

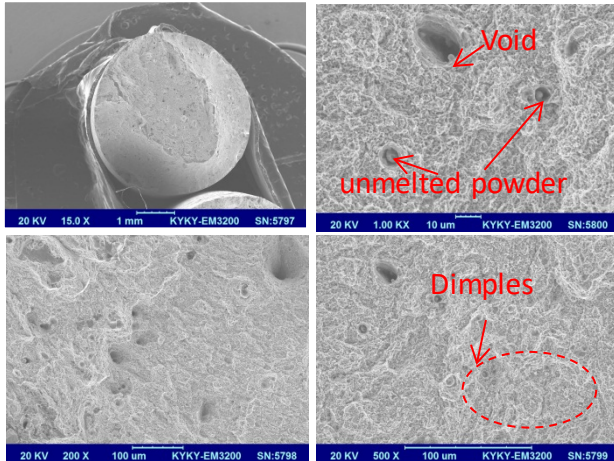


Fig.9. Tensile fracture morphology of SLM samples.

4. Conclusion

The effects of SLM processing parameters, including energy density, scanning speed, and laser power, on density and mechanical properties of HR-2 hydrogen embrittlement resistance stainless steel samples have been investigated. The following conclusions can be drawn.

Loss of nitrogen in HR-2 during powder preparation and SLM can be minimized under an optimized atmosphere. HR-2 stainless steel powder which meets the standard of N content was obtained using the vacuum induction melting atomization method (VIGA), where N_2 instead of Ar is used as the atmosphere with the suitable N_2 gas pressure in the smelting furnace. Comparison of N content of HR-2 powder and SLM parts shows no obvious loss of N content during SLM under a nitrogen atmosphere.

The density of the SLM formed samples first increases with the increase in energy density, then reaches a maximum point, and then decreases with the further increase in energy density. The occurrence of turning point on the curve can be related to the occasional presence of unstable keyhole mode during SLM when the energy density is too high, which leads to a higher porosity.

The microstructure formed by SLM of HR-2 is composed of large irregular columnar grains that grow continuously across several layers of powder. Dendrites within the columnar grains grow epitaxially along the edge of the molten pool towards the center. The microstructure of SLM-formed HR-2 is composed

of a single phase of austenite, which is similar to the forged microstructure.

The density of the parts fabricated by SLM formed HR-2 with low nitrogen and with optimized process parameters can reach more than 99.5%, the tensile strength can reach 735 ± 5 MPa, the yield strength can reach 415 ± 10 MPa, the percentage elongation of $43 \pm 5\%$, and the percentage reduction of $44\% \pm 5\%$, while the tensile strength of HR-2 with high nitrogen can reach 720 ± 10 MPa, the yield strength can reach 603.5 ± 10 MPa, the percentage elongation of $45\% \pm 5\%$, and percentage reduction of $60 \pm 5\%$, which are comparable with the base material of forged HR-2.

Acknowledgements

The authors are grateful to the financial support of the project from the NSAF (grant No.1930207) under and the key project of Science & Technology Plan of Sichuan Province of China under (grant No.2018GZ0535).

References

- [1] DebRoy T, Wei HL, Zuback JS, Mukherjee T, Elmer JW, Milewski JO et al. Additive manufacturing of metallic components – Process, structure and properties. *Progress in Materials Science*. 2018;92:112-224.
- [2] Li Y, Fan C, Rong L, Yan D, Li X. Hydrogen embrittlement resistance of austenitic alloys and aluminium alloys. *Acta Metallurgica Sinica*. 2010; 46, 1335-1346.
- [3] Shen X, Teng W, Zhao S, He W. Microstructure and porosity of laser-welded dissimilar material joints of HR-2 and J75. In: Schmidt M, Vollertsen F, Arnold CB, editors. *Laser Assisted Net Shape Engineering 9 International Conference on Photonic Technologies Proceedings of the Lane 20162016*. p. 406-16.
- [4] Larimian T, Kannan M, Grzesiak D, AlMangour B, Borkar T. Effect of energy density and scanning strategy on densification, microstructure and mechanical properties of 316L stainless steel processed via selective laser melting. *Materials Science and Engineering: A*. 2020;770:138455.
- [5] Liu J, Song Y, Chen C, Wang X, Li H, Zhou Ca et al. Effect of scanning speed on the microstructure and mechanical behavior of 316L stainless steel fabricated by selective laser melting. *Materials & Design*. 2020;186:108355.
- [6] Zhao S, Shen X, Yang J, Teng W, Wang Y. Densification behavior and mechanical properties of nanocrystalline TiC reinforced 316L stainless steel composite parts fabricated by selective laser melting. *Optics and Laser Technology*. 2018;103:239-50.
- [7] Yin YJ, Sun JQ, Guo J, Kan XF, Yang DC. Mechanism of high yield strength and yield ratio of 316 L stainless steel by additive manufacturing. *Materials Science and Engineering: A*. 2019;744:773-7.
- [8] Kurzynowski T, Gruber K, Stopyra W, Kuźnicka B, Chlebus E. Correlation between process parameters, microstructure and properties of 316 L stainless steel processed by selective laser melting. *Materials Science and Engineering: A*. 2018;718:64-73.
- [9] Kong D, Ni X, Dong C, Zhang L, Man C, Cheng X et al. Anisotropy in the microstructure and mechanical property for the bulk and porous 316L stainless steel fabricated via selective laser melting. *Materials Letters*. 2019;235:1-5.
- [10] Oliveira JP, LaLonde AD, Ma J. Processing parameters in laser powder bed fusion metal additive manufacturing. *Materials & Design*. 2020;193.

11th CIRP Conference on Photonic Technologies [LANE 2020] on September 7-10, 2020

In situ heat accumulation by geometrical features obstructing heat flux and by reduced inter layer times in laser powder bed fusion of AISI 316L stainless steel

Gunther Mohr^{a,b,*}, Nils Scheuschner^a, Kai Hilgenberg^{b,a}

^aFederal Institute for Materials Research and Testing (BAM; Bundesanstalt für Materialforschung und prüfung), Unter den Eichen 87, 12205 Berlin, Germany

^bInstitute of Machine Tools and Factory Management, Chair of Processes and Technologies for Highly Loaded Welds, Technische Universität Berlin, Straße des 17. Juni 135, 10623 Berlin, Germany

* Corresponding author. Tel.: +49-30-8104-4865; fax: +49-30-8104-74865. E-mail address: gunther.mohr@bam.de

Abstract

Material qualification for laser powder bed fusion (L-PBF) processes are often based on results derived from additively manufactured (AM) bulk material or small density cubes, although it is well known that the part geometry has a tremendous influence on the heat flux and, therefore, on the thermal history of an AM component. This study shows experimentally the effect of simple geometrical obstructions to the heat flux on cooling behavior and solidification conditions of 316L stainless steel processed by L-PBF. Additionally, it respects two distinct inter layer times (ILT) as well as the build height of the parts. The cooling behavior of the parts is in-situ traced by infrared (IR) thermography during the built-up. The IR signals reveal significant differences in cooling conditions, which are correlated to differences in melt pool geometries. The acquired data and results can be used for validation of computational models and improvements of quality assurance.

© 2020 The Authors. Published by Elsevier B.V.

This is an open access article under the CC BY-NC-ND license (<http://creativecommons.org/licenses/by-nc-nd/4.0/>)

Peer-review under responsibility of the Bayerisches Laserzentrum GmbH

Keywords: selective laser beam melting; thermography; inter layer time; geometry; heat accumulation; preheating temperature; melt pool depth

1. Introduction

Laser powder bed fusion (L-PBF) is the most prevalent additive manufacturing (AM) technology to produce metallic components [1, 2]. Selective Laser Melting (SLM) and Laser Beam Melting (LBM) are widespread synonyms for L-PBF [3, 4]. The process offers huge potentials for the production of complex and lightweight structures and the integration of functional designs as well as the potential for mass customization and lead time reduction [4-6].

Nomenclature

L-PBF laser powder bed fusion
ILT inter layer time
RAE ratio of area exploitation

Recently, concerns about inconsistent or inhomogeneous mechanical properties of AM parts produced by L-PBF of the same material could be noticed in the relevant literature [3, 7]. Variability in microstructure of AM components as well as variability in defect existence and characteristics has been identified as a major challenge, especially for safety-critical

components [8]. The comparability between L-PBF real part components which have often complex geometries containing different sized cross sections as well as volume leaps and standard test specimens is controversial [6, 8, 9]. There are many factors which are able to significantly affect the thermal history of a L-PBF component: not only variations in processing parameters, scanning strategies and support design affect the thermal history, also geometrical variations itself and variations in number of parts per build process do, which directly affects the ratio of area exploitation (RAE) and in turn the inter layer time (ILT) [6, 7, 10].

The thermal history of a part governs the development of the microstructure and is able to affect the occurrence and distribution of defects as well as residual stresses [6, 7, 11]. Hence, the mechanical properties depend on the thermal history during manufacturing [7, 12]. Temperature gradients and melt pool sizes as “inherent characteristics” of the L-PBF process depend on thermal behavior [13]. Consequently, the call for reliable and well documented relationships between process and properties, which includes the consideration of the real part geometry or structure, is expressed by many authors [3, 6, 9, 14, 15]. Additionally, small ranges of variations of process parameters in many studies, attempting to investigate the correlations between parameters and microstructure evolution, were criticized as they limit the process-microstructure correlations to a narrow band [16]. There are many studies focusing on the influence of process parameters and/or scanning strategies or post processing treatments on defect densities, microstructural development and mechanical properties [17–19]. However, only very few respect further aspects during manufacturing as inter layer times and part geometry on a large scale in terms of relevant built height for L-PBF processes.

To extend the existing picture of the process-property-relationship of the widely used and intensively studied stainless steel AISI 316L, this study investigated the rarely considered aspect of ILT and heat flux obstructing variations in geometry at still tall and massive specimens at once. The in-situ usage of an infrared (IR) camera gave valuable insights into the thermal history of the growing parts.

2. Material and methods

2.1. Material and L-PBF processing conditions

A commercial AISI 316L stainless steel powder of spherical morphology in a sieving fraction of approx. 10 μm to 45 μm was processed on a commercial L-PBF single laser system SLM280 HL (SLM Solutions Group AG, Lübeck, Germany). The system was equipped with a 400 W continuous wave ytterbium fiber laser emitting at a wavelength of 1070 nm. The spot size was approximately 80 μm in focal position. The laser melting process ran in argon gas atmosphere with oxygen content below 0.1%. All parts were manufactured on a stainless steel substrate plate at a platform preheating temperature of 100 °C. Detailed information about the L-PBF system and the powder properties can be taken from [7], as the same configurations were used in this study.

2.2. Thermographic measurement set-up

The processes were partially monitored by a mid-wave infrared (MWIR) thermographic camera of type ImageIR8300 (InfraTec GmbH, Dresden, Germany) through a sapphire window in the ceiling of the building chamber and two gold coated mirrors. The measurement set-up is illustrated in Fig. 1.

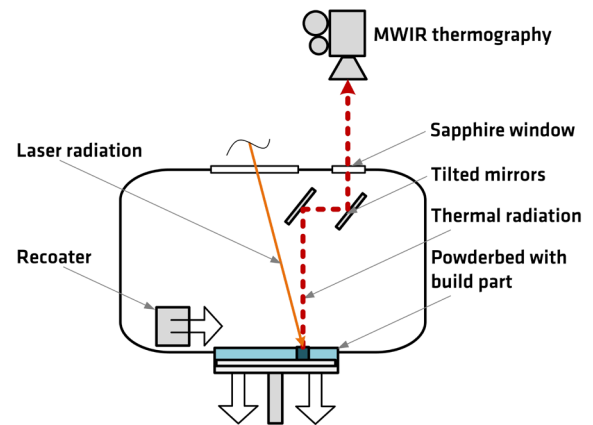


Fig. 1. Schematic of the thermographic measurement set-up.

The IR camera used a cooled InSb-focal-plane-array as detector and was sensitive in a spectral range from 2 μm to 5 μm . It was calibrated for blackbody radiation by its vendor. No additional filters were used. All optical elements were chosen to provide minimal and constant optical losses over the whole detection range of the camera; e.g., according to supplier’s information, the transmission of the commercial sapphire glass (Edmund Optics Inc., Barrington, USA) was constantly greater than 90% in the detection range of the camera. Due to these losses and the low emissivity of the build part surface or the recoated powder, the observed specimens showed less intensity than a blackbody would do at the same surface temperature. As a result, the apparent temperature values indicated by the camera underestimated the real temperatures systematically. As a correction could not be derived from the available data, the focus was set on a qualitative analysis in this work. To underline the fundamental distinction to the real temperatures the uncorrected apparent temperature values of the camera were referred as IR-signal values in this work. Nevertheless, as the real temperatures could only be underestimated, the real temperatures must be larger than the IR-signal values presented here. This discrepancy was discussed in more detail in [20]. The used camera calibration ranges varied between 125 °C – 300 °C, 300 °C – 600 °C and 450 °C – 1000 °C. Using a 25 mm objective a spatial resolution of approx. 420 $\mu\text{m}/\text{pixel}$ was achieved. Using a frame rate of 600 Hz, and a region of interests of 160 pixels x 224 pixels, the observed field was approx. 68 mm x 94 mm large.

2.3. Specimen geometry, scanning strategy and selection of part sections for analysis

As specimen geometry, three types of cuboids of the outer hull dimensions (13 x 20 x 114.5) mm^3 were built perpendicular to the build plate using an alternating meander

stripe scanning strategy. The scan vectors proceeded parallel to the edges of the cuboid over the full length of the part without being split into different sections. The scanning pattern was rotated by 90° from layer to layer. The three specimens differed in the lower 30 mm of their build height with regard to their connection to the base plate, as can be taken from Fig. 2. Regarding the size of the cross section of the connection to the base plate the specimens are called “small connection” (1.3 mm x 2 mm), “medium connection” (3.9 mm x 6 mm) and “full connection” (13 mm x 20 mm) throughout the document.

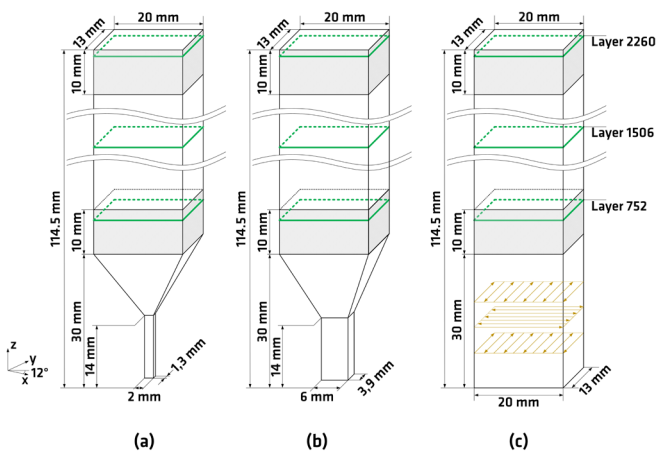


Fig. 2. Specimens' geometry: (a) small connection to the base plate; (b) medium sized connection to the base plate; (c) full connection to the base plate. Yellow arrows sketch the scanning vectors and scanning strategy. Grey parts were taken for metallographic analysis. Green layers were taken for thermographic analysis.

All specimens were heat treated at 450°C for 4 h under argon gas atmosphere in order to relieve stresses. The specimens were cut into different parts, from which the grey parts (Fig. 2) were taken for metallographic analysis. Fig. 2 also highlights three layers in green color, for which comparisons of thermographic intensity measurements were analyzed in the results chapter.

The scanning parameters (laser power $P_L = 275$ W, scanning velocity $v_s = 700$ mm/s and hatch distance $h_s = 0.12$ mm) as well as layer thickness (50 μ m) were kept constant for all specimens and built processes. The three types of specimens were built in two series: The first one was built in a process, which had an ILT of approx. 65 s. This ILT will be called intermediate ILT. The second series was built in a process, which had an ILT of approx. 18 s. This ILT will be called short ILT. Apart from the differences in ILT between distinct build processes, a constant ILT over the entire build height of the specimens was ensured, despite the difference in RAE caused by the geometry. This was realized by scanning so called dummy parts using $P_L = 0$ W. The three specimens fitted into the field of view of the IR camera. Thermography data was analyzed by using the software IRBIS 3 (InfraTec GmbH, Germany) and Origin 2019 (OriginLab Corporation, USA). IR-signal-time-curves were able to serve as comparison mean between the respective conditions. The average values of five manually chosen pixels located in the center line of the respective cross section were used for each layer of investigation. Within each part, IR-signal-time-data were

analyzed at three distinct layers (layer 752, layer 1506, layer 2260) which represented different build heights during the process. More information on this evaluation method can be found in [7].

2.4. Metallography

For each specimen two parts were prepared for metallographic analysis (grey parts in Fig. 2), hereafter called upper and lower part. By cutting these cuboids into three sections (first cut: bisection; second cut: bisection of the left half, illustrated in [7]) two metallographic planes of each part were prepared for light-microscopy (embedding, grinding, polishing). Polished but unetched cross sections were taken for optical light microscopy in order to determine porosity by grey value analysis using the software IMS Client V17Q1 (Imagic Bildverarbeitung AG, Glattbrugg, Switzerland). A threshold value of 115 was chosen for all cross sections. Cross sections were then color etched using Beraha II etching detergent for 10 s to 30 s. Melt pool depths were determined at the upper part of the specimens, by measuring ten melt pools of the last exposed layer. To get information about melt pool depths in lower sections of the specimens, further production of these respective specimens is planned.

3. Results

3.1. Macroscopic results

Tempering colors on the upper surface of the specimens were noticed for the specimens of small connection and medium connection in the short ILT process during the manufacturing of the specimens. These effects varied in intensity (color and time of glowing after laser exposing) during the process, which was observed qualitatively by the machine operator. Additionally, the depowdered specimens showed tempering colors in different characteristics at their surfaces. The upper surface of the specimens manufactured with intermediate ILT did not show visible tempering colors. However, the full connection specimen manufactured at short ILT showed a brownish color and the small and medium connection specimens showed a grey-bluish color. Variations in tempering colors over the built height were noticeable.

3.2. Thermographic results

Fig. 3 show the IR-signal-time-curves for all specimen geometries and ILT. For comparability the illustrated IR-signal-time-curves of each individual specimen were shifted in the manner, that the measured maximum IR-signal value (for short ILT) or the first value of the maximum value plateau (for intermediate ILT) were set as $t = 0$. The following trends could be observed: Reducing the ILT led to a strong increase of the IR-signal values for all analyzed layers and specimens. With increasing size of the connection lower IR-signal values were measured, whereby the effect decreased with increasing layer number. An increase of IR signal values of the full connection specimen could be observed over the complete build height.

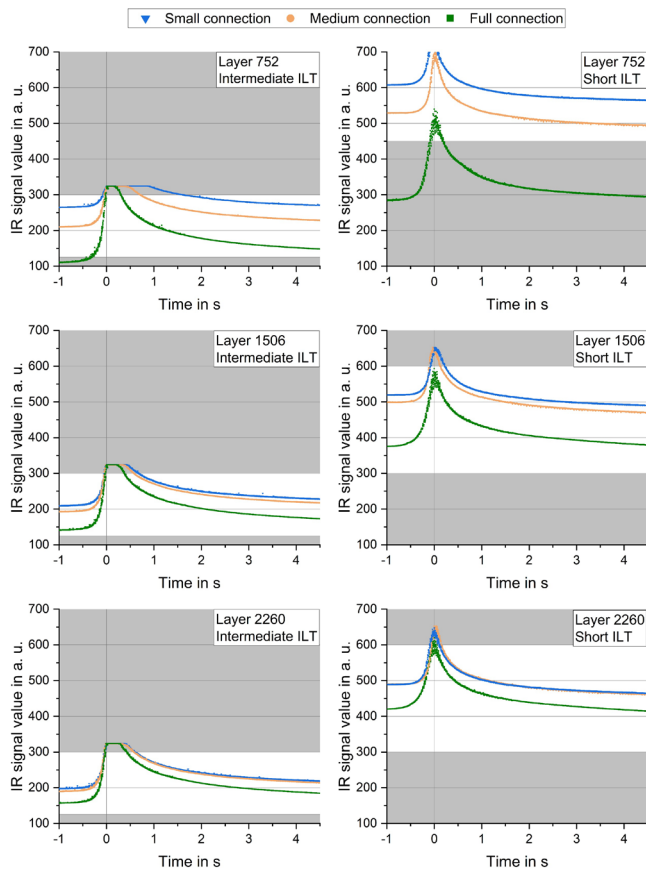


Fig. 3. IR-signal-time-plots of complete parameter matrix. Three lines indicate the three different geometries: small connection (blue), medium connection (yellow), full connection (green). Values of three different build heights are presented for two different ILT (left: intermediate ILT, right: short ILT). Grey (white) areas indicate temperatures outside (inside) the used calibration range.

3.3. Metallographic results

Differences in melt pool geometries of the top layer were observed as exemplified in Fig. 4. The mean values of the depth of ten measured melt pools per specimen were plotted in Fig. 5.

For intermediate ILT no significant differences in melt pool depth between the distinct specimens were measured. However, for short ILT specimens, the melt pool depth varied significantly in comparison to the intermediate ILT specimens. Furthermore, within the short ILT specimens a significant variation between the geometrical different specimens was revealed. No clear difference could be noticed between small and medium connection but a huge increase in melt pool depth in comparison to the full connection specimen.

The porosity determination by grey value analysis at two cross sections per part indicated for nearly all parts a very low level of 0.1 % porosity. Only the porosity value in the lower part of the small connection type specimen manufactured at short ILT showed a slightly increased porosity of 0.5 %. Detailed analysis by micro computed tomography will be conducted in a subsequent study.

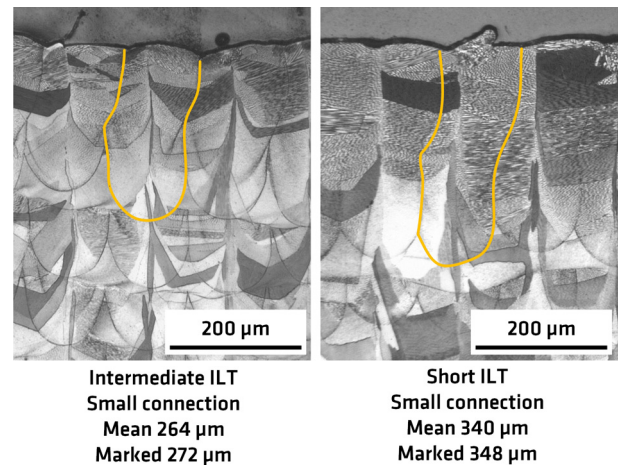


Fig. 4. Color etched cross sections showing melt pool geometries at the topmost layer for the small connection specimen at intermediate ILT (left) and short ILT (right).

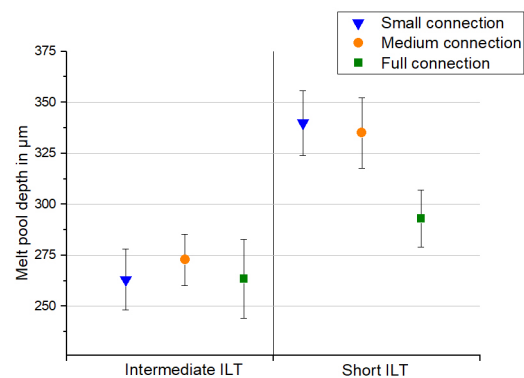


Fig. 5. Measured melt pool depth at the topmost layer, i.e. at built height of 114.5 mm.

4. Discussion

The analysis of the manufactured specimens by means of melt pool measurements, porosity determination and in-situ IR measurements clearly stressed the influence of part geometry and ILT, and as worst case scenario a combination of detrimental conditions of both factors combined, on the thermal history of parts manufactured with a type of standard processing parameters. The heat accumulation could be qualitatively retraced in the tempering colors already. However, inner surfaces of complex real parts cannot be visually analyzed.

When considering the IR-signals as apparent surface temperatures in °C of the observed solidified parts as in [20], which would be assumed to underestimate the real temperatures, the process inherent preheating effect of the growing part for the short ILT got obvious. As could be seen from IR-signal-time-plots, the parts did not cool down to a level of the pre-set platform temperature in the respective build heights, as the IR-signal values prior to exposing are well above the starting values in these cases. This consideration neglected any differences in emissivity of powder and solidified bulk AM

material. However, the general aspect of an elevated surface temperature prior to recoating and prior to exposing remained valid. A quantification is planned in calibration experiments by the authors. As variations in emissivity are one of the most important sources of measurement uncertainty in thermographic measurements [21] and are highly dependent on surface condition [22], the comparison of the IR-signal-time-plots had to be considered very carefully. The observed tempering colors as a result of oxidation might have influenced the emissivity. However, under the assumption of higher emissivity values of oxidized steel surfaces compared to non-oxidized surfaces [23], the revealed differences in apparent temperature would get even increased, as the degree of underestimation would be higher for higher emissivity values.

The observed preheating effect increased by geometrical heat flux obstructions as the small and medium connection geometries constituted. The resulting changes in melt pool sizes represented most likely not the maximum variation within these parts, as the melt pool sizes could be measured only at the topmost layer, which was not the layer of the maximum preheating temperature as indicated by the thermographic results from the two other layers of analysis. The occurrence of more spherical pores in the lower part of the small connection specimen manufactured with short ILT was an additional indicator that the melt pool sizes were probably even stronger increased in these regions. This will also be analyzed in detail in a subsequent study.

Moreover, according to [7], it can be assumed that a change in melt pool size went along with a change in sub grain sizes. This can be explained with changes in constitutional undercooling of the melt during solidification, which changes with varying preheating temperature [24]. A grain size decrease for higher cooling rates was reported by Zitelli et al. [25]. Bertoli et al. [26] pointed out that the size and morphology of the resulting microstructure is a function of temperature gradient within the liquid phase and velocity of the solidification front. At least the former will, therefore, be influenced by preheating temperatures. A detailed analysis of microstructure will be conducted in a subsequent study.

The authors of this study were aware of industrial partners who do not want to conduct recrystallization heat treatments for AISI 316L components. Seifi et al. reported the industrial desire (aerospace and biomedical) for as-built materials even in high cycle fatigue (HCF) critical applications [15]. These industrial inputs emphasized the importance of knowledge about the presumed microstructural variations within a L-PBF part and opportunities of monitoring. Furthermore, recent research goals in L-PBF regarding tailored materials by control of microstructure during the built up of an AM part could be noticed [5, 27-29]. The knowledge about the current surface temperature of the growing part is mandatory for any kind of pre-calculations in this direction. For these examples variations over build height and through changing ILT or geometries has to be taken into account as the results of this study clearly indicated.

Lastly, off-axis thermographic measurements of surface IR radiation of already solidified material seems to be a valuable mean for the definition of critical locations within a part. They do not require a high temporal resolution, which can reduce

costs for equipment and computational time as well as data storage. Seifi et al. [15] considered the potential impact of in-situ process monitoring and control as extremely high for qualification and certification of AM parts. In addition, they considered the lack of adequate process monitoring methods as a bottleneck for more widespread applications of AM technologies [15].

The IR thermography appeared to be a useful tool for retracing the thermal history of a part and to give answers to questions regarding the characterization of location-specific properties and the relationship of properties between small laboratory specimens and large real part components. The answers are key for the application of safety critical AM components, as Shresta et al. [12] and Gorelik [9] stated very clearly. Numerical models can be helpful for this duty [13]. Optimization of the manufacturing process as well as quality control are both related to a sufficient determination of temperature profiles and melt pool sizes. The acquired data can assist with the validation of computational models.

5. Conclusions

In this study, the relevance of the interplay between part geometry, build height and ILT for properties and quality of the resulting product was highlighted. A process inherent preheating effect of the growing part, which increased with geometrical heat flux obstruction was experimentally shown. The occurring heat accumulation resulted in raising surface temperatures and affected the melt pool sizes significantly. Some indications of effects on defect density (porosity) were also presented. Assumptions of effects on the microstructure, especially on the sub-grain sizes, were discussed. The knowledge about the current surface temperature of the growing part appeared to be mandatory for a quality assurance. In-situ thermographic imaging demonstrated its ability to retrace the thermal history of a part. Further research questions were identified.

Acknowledgements

The authors would like to thank Susanna Nowakowski for her very helpful support during the L-PBF experiments and in the metallography laboratory.

This research was funded by BAM within the focus area Materials.

References

- [1] M. Schmidt, M. Merklein, D. Bourell, D. Dimitrov, T. Hausotte, K. Wegener, L. Overmeyer, F. Vollertsen, G.N. Levy, Laser based additive manufacturing in industry and academia, *CIRP Annals* 66(2) (2017) 561-583.
- [2] T. Wohlers, I. Campbell, O. Diegel, J. Kowen, T. Caffrey, Wohlers Report. 3d printing and additive manufacturing state of the industry, Fort Collins: Wohlers Associates 2017.
- [3] T. DeRoy, H.L. Wei, J.S. Zuback, T. Mukherjee, J.W. Elmer, J.O. Milewski, A.M. Beese, A. Wilson-Heid, A. De, W. Zhang, Additive manufacturing of metallic components – Process, structure and properties, *Progress in Materials Science* 92 (2018) 112-224.
- [4] D. Herzog, V. Seyda, E. Wycisk, C. Emmelmann, Additive manufacturing of metals, *Acta Materialia* 117 (2016) 371-392.
- [5] R. Piticescu, A. Katz-Demyanetz, V.V. Popov, A. Kovalevsky, D. Safranchik, A. Koptyug, I. Vlaicu, Powder-bed additive manufacturing for aerospace application: Techniques, metallic and metal/ceramic composite

- materials and trends, *Manufacturing Review* 6 (2019).
- [6] M. Seifi, M. Gorelik, J. Waller, N. Hrabe, N. Shamsaei, S. Daniewicz, J.J. Lewandowski, Progress Towards Metal Additive Manufacturing Standardization to Support Qualification and Certification, *Jom* 69(3) (2017) 439-455.
- [7] G. Mohr, S.J. Altenburg, K. Hilgenberg, Effects of inter layer time and build height on resulting properties of 316L stainless steel processed by laser powder bed fusion, *Additive Manufacturing* 32 (2020).
- [8] N. Sanaei, A. Fatemi, N. Phan, Defect characteristics and analysis of their variability in metal L-PBF additive manufacturing, *Materials & Design* 182 (2019).
- [9] M. Gorelik, Additive manufacturing in the context of structural integrity, *International Journal of Fatigue* 94 (2017) 168-177.
- [10] R. Ranjan, C. Ayas, M. Langelaar, A. van Keulen, Towards design for precision additive manufacturing: A simplified approach for detecting heat accumulation, *ASPE*, 2018.
- [11] L.A. Parry, I.A. Ashcroft, R.D. Wildman, Geometrical effects on residual stress in selective laser melting, *Additive Manufacturing* 25 (2019) 166-175.
- [12] R. Shrestha, N. Shamsaei, M. Seifi, N. Phan, An investigation into specimen property to part performance relationships for laser beam powder bed fusion additive manufacturing, *Additive Manufacturing* 29 (2019) 100807.
- [13] M.J. Ansari, D.S. Nguyen, H.S. Park, Investigation of SLM Process in Terms of Temperature Distribution and Melting Pool Size: Modeling and Experimental Approaches, *Materials (Basel)* 12(8) (2019).
- [14] M. Mahmoudi, A. Elwany, A. Yadollahi, S.M. Thompson, L. Bian, N. Shamsaei, Mechanical properties and microstructural characterization of selective laser melted 17-4 PH stainless steel, *Rapid Prototyping Journal* 23(2) (2017) 280-294.
- [15] M. Seifi, A. Salem, J. Beuth, O. Harrysson, J.J. Lewandowski, Overview of Materials Qualification Needs for Metal Additive Manufacturing, *Jom* 68(3) (2016) 747-764.
- [16] P. Köhnen, M. Létang, M. Voshage, J.H. Schleifenbaum, C. Haase, Understanding the process-microstructure correlations for tailoring the mechanical properties of L-PBF produced austenitic advanced high strength steel, *Additive Manufacturing* 30 (2019).
- [17] J.W. Xie, P. Fox, W. O'Neill, C.J. Sutcliffe, Effect of direct laser re-melting processing parameters and scanning strategies on the densification of tool steels, *Journal of Materials Processing Technology* 170(3) (2005) 516-523.
- [18] H. Choo, K.-L. Sham, J. Bohling, A. Ngo, X. Xiao, Y. Ren, P.J. Depond, M.J. Matthews, E. Garlea, Effect of laser power on defect, texture, and microstructure of a laser powder bed fusion processed 316L stainless steel, *Materials & Design* 164 (2019).
- [19] T. Kurzynowski, K. Gruber, W. Stopyra, B. Kuźnicka, E. Chlebus, Correlation between process parameters, microstructure and properties of 316 L stainless steel processed by selective laser melting, *Materials Science and Engineering: A* 718 (2018) 64-73.
- [20] B. Lane, E. Whitenon, V. Madhavan, A. Donmez, Uncertainty of temperature measurements by infrared thermography for metal cutting applications, *Metrologia* 50(6) (2013) 637-653.
- [22] B. Lane, S. Moylan, E. Whitenon, L. Ma, Thermographic Measurements of the Commercial Laser Powder Bed Fusion Process at NIST, *Rapid Prototyp J* 22(5) (2016) 778-787.
- [23] J.R. Howell, M.P. Menguc, R. Siegel, Thermal radiation heat transfer, CRC press, London, 2010.
- [24] P. Krakhmalev, G. Fredriksson, K. Svensson, I. Yadroitsev, I. Yadroitsava, M. Thuvander, R. Peng, Microstructure, Solidification Texture, and Thermal Stability of 316 L Stainless Steel Manufactured by Laser Powder Bed Fusion, *Metals* 8(8) (2018).
- [25] Zitelli, Folgarait, S. Di, Laser Powder Bed Fusion of Stainless Steel Grades: A Review, *Metals* 9(7) (2019).
- [26] U.S. Bertoli, B.E. MacDonald, J.M. Schoenung, Stability of cellular microstructure in laser powder bed fusion of 316L stainless steel, *Materials Science and Engineering: A* 739 (2019) 109-117.
- [27] G. Mohr, J. Johannsen, D. Knoop, E. Gärtner, K. Hummert, C. Emmelmann, Processing of a high-strength Al-Fe-Ni alloy using laser beam melting and its potential for in-situ graded mechanical properties, *Lasers in Manufacturing Conference*, Munich, Germany, 2017.
- [28] R. Shi, S.A. Khairallah, T.T. Roehling, T.W. Heo, J.T. McKeown, M.J. Matthews, Microstructural control in metal laser powder bed fusion additive manufacturing using laser beam shaping strategy, *Acta Materialia* 184 (2020) 284-305.
- [29] T. Niendorf, F. Brenne, M. Schaper, Lattice Structures Manufactured by SLM: On the Effect of Geometrical Dimensions on Microstructure Evolution During Processing, *Metallurgical and Materials Transactions B* 45(4) (2014) 1181-1185.

11th CIRP Conference on Photonic Technologies [LANE 2020] on September 7-10, 2020

Characterization of part deformations in laser powder bed fusion of stainless steel 316L

Niko Riikonen^{a,*}, Heidi Piili^a

^aLUT University, School of Energy Systems, Department of Mechanical Engineering, Research Group of Laser Material Processing and Additive Manufacturing, Yliopistonkatu 34, Lappeenranta 53850, Finland

* Corresponding author. Tel.: +358 503386230. E-mail address: niko.riikonen@lut.fi

Abstract

Laser powder bed fusion (L-PBF) is a suitable manufacturing method for end-use complicated metal parts. However, cyclic thermal load belongs to the nature of the process and it creates residual stresses in the parts due to their subsequent thermal expansions and contractions. These residual stresses make the parts exposed to deformations. Aim of this study was to recognize why deformations occur in parts made by L-PBF. Deformations of stainless steel 316L parts were examined experimentally. As a conclusion, building orientation is crucial factor in generation of deformations in L-PBF. Each test sample that had deformation, could be manufactured without deformation by adjusting the orientation. Parts built horizontally flat were the most vulnerable to have deformation.

© 2020 The Authors. Published by Elsevier B.V.

This is an open access article under the CC BY-NC-ND license (<http://creativecommons.org/licenses/by-nc-nd/4.0/>)

Peer-review under responsibility of the Bayerisches Laserzentrum GmbH

Keywords: Additive manufacturing; 3D printing; powder bed fusion; stainless steel; 316L; deformation; residual stress

1. Introduction

Additive manufacturing (AM) industry is strongly growing due to the possibilities that AM technologies offer [1]. AM is making large steps towards becoming a serious option for manufacturing end-use parts in a serial production enabling to manufacture structures that have not been able to be manufactured by conventional manufacturing methods [1, 2, 3]. The most popular metal AM technology, laser powder bed fusion (L-PBF), can produce strong, high quality and high-performance parts having complex shapes [1, 2]. However, L-PBF has its limitations due to the cyclic heat delivery that is inherent in this technology. Cyclic heat delivery leads to subsequent expansion and contraction of the material, which creates stresses in the part during the build. These stresses can rise higher than the yield strength of the material, which causes deformations in the parts. [4, 5, 6]

Aim of this study was to recognize why deformations occur in parts made by L-PBF and what is the deformation type and shape. Experiments were performed to study this. L-PBF may induce imperfections such as undesired microstructure, residual stresses, deformations and porosity in parts [7]. The imperfections examined in this study relate to geometrical errors in the outer shape of the part and do not include internal defects such as porosity or microstructure faults.

Nomenclature

AM	Additive manufacturing
L-PBF	Laser powder bed fusion
TGM	Temperature gradient mechanism

1.1. Background

Metal aims to expand or contract as a response to the temperature changes. When expansion or contraction of metal is restricted, thermal stresses occur in the material. [8] The generation of thermal stresses can be explained with temperature gradient mechanism (TGM), see Fig. 1 [8, 9].

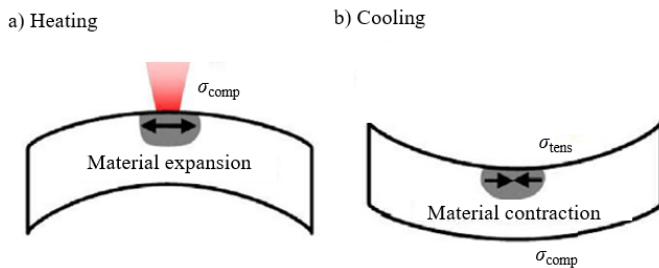


Fig. 1. Schematic of TGM, (a) heating; (b) cooling [10].

When the laser beam interacts with powder bed, the powder melts and the surface of the part is strongly heated. During this heating cycle, surface of the part pursues to expand due to strong heating but the expansion of the heated top layer is limited due to surrounding solid material, which creates compressive stress σ_{comp} on the upper surface (Fig. 1 (a)). When the occurred compressive stress exceeds yield strength of the material, the top surface will experience plastic deformation that pursues to bend the material towards the laser (Fig. 1 (a)). When cooling of the material begins, the material starts to contract. Now contraction of the surface is limited due to surrounding solid material, which ends up in tensile stress σ_{tens} on the top surface. When the tensile stress exceeds yield strength of the material, the top surface pursues to bend into the opposite direction (Fig. 1 (b)). [8, 9]

Based on earlier studies of Yang et al., Li et al. and Wu et al. [4, 11, 12], expected deformation of metal parts made by L-PBF obeys the TGM, which aims to bend the edges of parts upwards from the building platform (Fig. 1 (b)). In the study of Yang et al. [4], deformation shape of a vertically build Inconel 718 bridge sample was modeled as represented in Fig. 2.

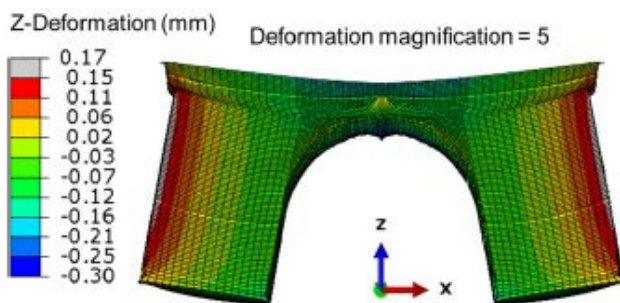


Fig. 2. Prediction of deformation of a bridge sample manufactured by L-PBF [4].

In Fig. 2 the original flat surface on top of the bridge is bent down in the middle and bridge legs have spread and raised, due to the residual stresses caused by cyclic heat [4].

In the study of Wu et al. [12], deformation magnitudes of a horizontally build stainless steel 316L prism sample were modeled as represented in Fig. 3.

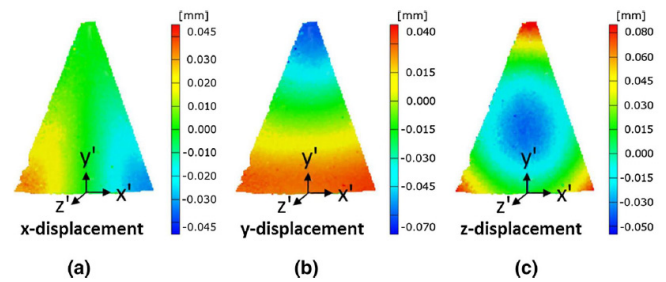


Fig. 3. Deformation magnitudes of a horizontally build prism sample, (a) x-displacement; (b) y-displacement; (c) z-displacement. Local z-axis indicates building direction. [12]

It can be noted in Fig. 3 (a) that the displacement along x-axis locates in the lower corners of the prism, being equal on both sides (maximum 0.045 mm). The corners have contracted towards the center of the prism. Displacement along y-axis (Fig. 3 (b)) can be observed in the bottom and top regions of the prism, again contracting them towards the center of the prism. Displacement along z-axis (Fig. 3 (c)) indicates the deformation along building direction in which the prism has spherically deflected in a way that the corners of the prism have bent upwards while the center of the prism has bent downwards. [12] Based on Fig. 3 it seems that the largest deformations occur in the building direction (Fig. 3 (c)) [12]. Exaggerated view of the total deformation shape of the prism sample is represented in Fig. 4 [12].

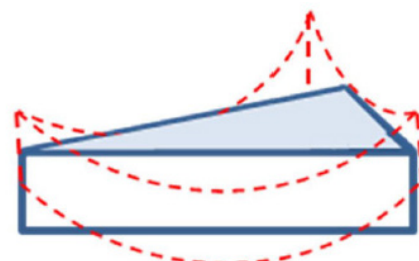


Fig. 4. Expected deformation of a prism sample manufactured by L-PBF [12].

It can be observed in Fig. 4 that the prism has spherically deflected in a way that the corners of the prism have bent upwards [12].

In the study of Li et al. [11], deformation of a cantilever sample printed of AlSi10Mg, was demonstrated as shown in Fig. 5.

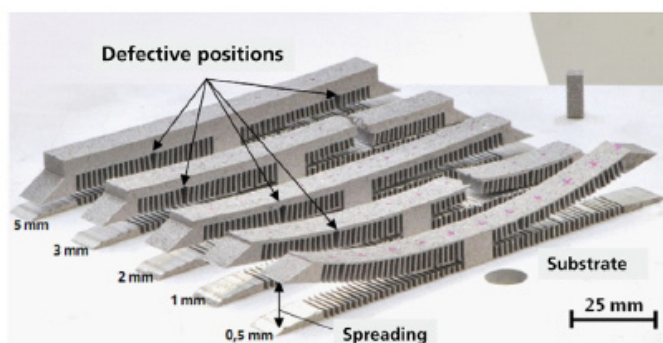


Fig. 5. Deformations of cantilever samples with varying thicknesses. Manufactured by L-PBF of AlSi10Mg. [11]

It can be observed in Fig. 5 that the thickest cantilever (5.0 mm) shows the least deformation while the thinnest (0.5 mm) shows the greatest deformation. Because thicker cantilever has more material to endure the stresses and is stiffer, it is less prone to bend.

2. Experimental setup

The test samples in this study were modeled with SolidWorks 2018 CAD software and the test samples were manufactured by EOS Finland Oy, in Turku, with EOS M 290 L-PBF machine. Machine specifications for the experiments are represented in Table 1.

Table 1. Specifications of EOS M 290.

Machine	EOS M 290
Build area	250 × 250 × 325 mm ³
Layer thickness	40 μm
Shielding gas	Argon
Focal point diameter	70–80 μm
Platform temperature	80 °C

The test samples were manufactured of EOS StainlessSteel 316L of which material properties are represented in Table 2 [13].

Table 2. Material properties of parts made of EOS StainlessSteel 316L [13].

Material property	Value
Density	7.9 g/cm ³
Ultimate tensile strength	590 MPa
Yield strength	500 MPa
Elongation at break	46.7 %

The tensile test values represented in Table 2 are determined in parts made with vertical and horizontal orientations and the numbers are average values of them. Tensile test values are determined according to ISO 6892 / ASTM E8M. [13]

Test sample dimensions and building orientations are represented in Table 3.

Table 3. Test sample dimensions and building orientations.

Test sample	Dimensions (mm)	Orientation
A1	20 × 20 × 20	horizontal
B1	20 × 5 × 20	vertical
B2	20 × 20 × 5	horizontal
B3	20 × 20 × 5	45°
C1	60 × 5 × 20	horizontal
C2	60 × 20 × 5	horizontal
C3	20 × 5 × 60	vertical
C4	60 × 20 × 5	45°
C5	60 × 5 × 20	45°
D1	60 × 20 × 20	horizontal
D2	20 × 20 × 60	vertical
D3	60 × 20 × 20	45°

Deformations were analyzed with Keyence VR-3200 microscope at LUT University in Lappeenranta, by taking macrographs of the side profiles of the test samples.

2.1. Experimental procedures

Rectangular shapes were built in different orientations to study which shapes and orientations cause deformations and which kind of deformation. The test samples have differences in layer number and scanning areas which result in different magnitudes of thermal stresses. Standard parameter set used to manufacture the test samples was EOS 316L 40μm FlexLine.

All the test samples were built in one batch together and the layout of the samples on the building platform is shown in Fig. 6.

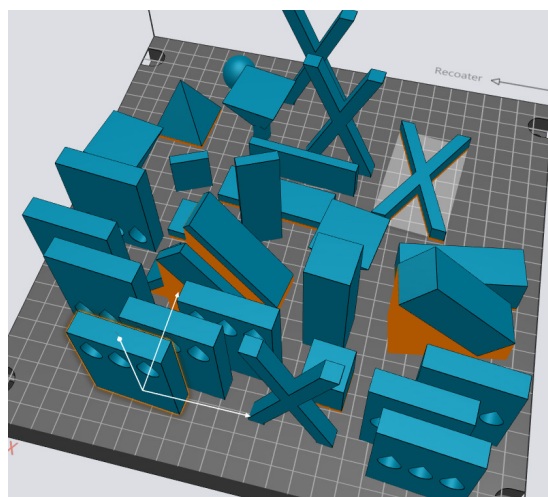


Fig. 6. Layout of the test samples on the building platform. Solid rectangular shapes are involved in this study.

The test samples of this study were located mainly to the central area of the building platform while there were simultaneously some other parts printed, locating on the outer regions of the building platform (Fig. 6).

Test samples were removed from the building platform as built, with no post-processing performed. No thermal stress relief was performed. The test samples were cut from the building platform and the support structures were removed and

since no post-processing operations were performed. The effect of machine parameters (such as laser power, scanning speed, focal point size, hatch spacing, scanning strategy, scan length, layer thickness), powder properties (such as packing efficiency and particle size) and support structure parameters, were neglected, as they all were constant during the experiments. This leaves the geometry and orientation of the part to be the variable parameters.

3. Results and discussion

Results observed in the experiments of this study are represented in this section. Fig. 7 represents test samples A1, B1, B2 and B3.

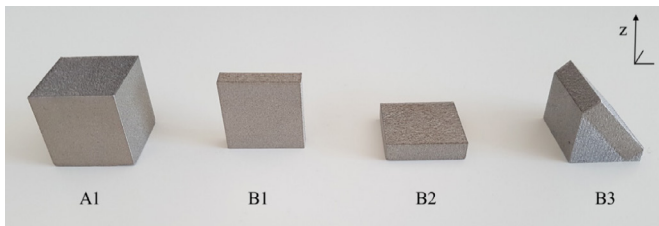


Fig. 7. Test samples A1, B1, B2 and B3 (with support structures). Building direction along z-axis.

No deformation could be observed in macrographs of test samples represented in Fig. 7.

Test samples C1, C2, C3, C4 and C5 are represented in Fig. 8.

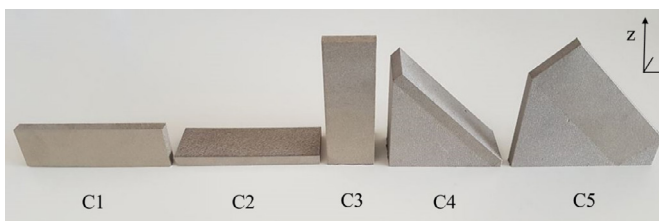


Fig. 8. Test samples C1, C2, C3, C4 (with support structures) and C5 (with support structures). Building direction along z-axis.

Test sample C2 is the only one to have evident deformation of test samples represented in Fig. 8. Fig. 9 represents test sample C2 closer.



Fig. 9. Test sample C2, building direction along z-axis.

It can be seen in Fig. 9 that the edges of test sample C2 have bent upwards (indicated with arrows) which obeys the TGM.

Macrographs of test samples C1, C2, C3, C4 and C5 are represented in Fig. 10.

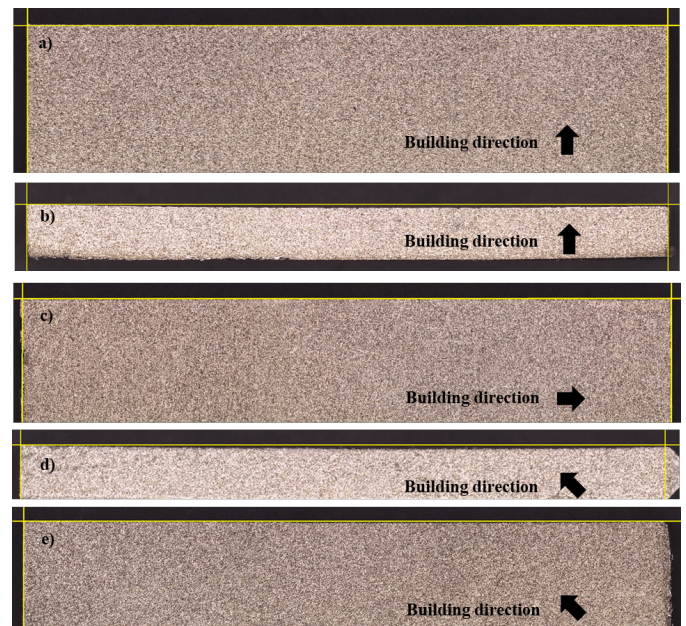


Fig. 10. Macrographs of test samples, (a) C1; (b) C2; (c) C3; (d) C4; (e) C5 (support structures removed from C4 and C5). Side view, building direction is indicated with arrow.

Test samples C1, C2, C3, C4 and C5 are dimensionally equal and only their building orientation was varied. However, test samples C2 and C4 have top surface warping, as it can be seen in Fig. 10 (b) and (d). The deformation shapes of test samples C2 and C4 are similar and they obey the TGM. It is notable that test samples C1 and C2 were both built horizontally but only C2 has deformation. Test sample C2 was orientated flat whereas test sample C1 was orientated on its side (see Fig. 8). Test sample C1 is higher and stiffer in the building direction to resist the deformation compared to test sample C2. This is illustrated in Fig. 11.

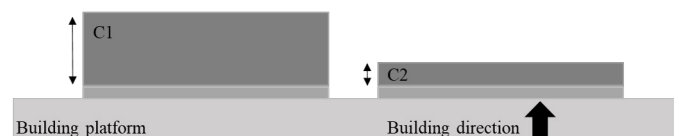


Fig. 11. Schematic of test samples C1 and C2 on the building platform.

Test sample C1 has more material in the building direction and more stiffness, as observed in Fig. 11. The scanning area of a single layer is also smaller in test sample C1. Smaller scanning area contracts less than larger one [14]. This same result and conclusion can be observed between test samples C4 and C5 represented in Fig. 10 (d) and (e) of which both were built in 45° angle and only C4 has deformation. C4 was orientated flat and C5 on its side (see Fig. 8).

Test samples D1, D2 and D3 are represented in Fig. 12.

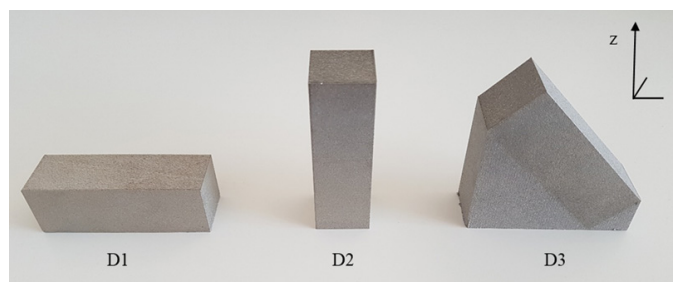


Fig. 12. Test samples D1, D2 and D3 (with support structures). Building direction along z-axis.

Test samples D1, D2 and D3 did not show any deformation in the macrographs.

In the experiments, each geometry was successfully manufactured without deformation by adjusting the part orientation. The most vulnerable part orientation for having deformations is horizontal especially when part is positioned flat, which indicates that thin parts with large surface area are prone to have deformation when orientated horizontally. It is notable that test sample B2 was orientated in such a way, but it did not have any deformation like sample C2 had. Test sample B2 has much smaller area than C2 and because smaller area contracts less, it is more difficult to notice the possible deformation even with a microscope. Fig. 13 demonstrates the situation.

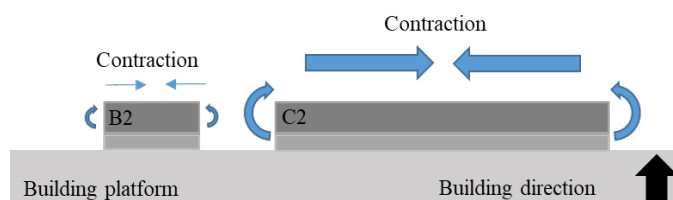


Fig. 13. Demonstration of the contraction of test samples B2 and C2.

It can be noted in Fig. 13 that test sample C2 will contract more due to larger area and thus giving more noticeable deformation.

It must be carefully considered when choosing suitable building orientation that the parts have different mechanical properties depending on the orientation they are built, due to the layer wise manufacturing [1, 16, 17]. Tensile strength properties and surface roughness values are affected by the orientation of the part. Horizontally built parts have higher tensile strength compared to vertically built parts and sloped surfaces suffer from rough surface due to stair-step effect. [13, 17] Also building time and the need and location of support structures are affected by the orientation of part. Vertical orientation requires more recoating time due to higher number of layers. [1]

Support structures are needed to support the overhanging features of the part and to fix the part to the building platform. Therefore, by changing the orientation of the part, it is possible to affect the need of support structures. It is also important to

notice that the surfaces where support structures are attached, have rougher surface compared to surfaces without support structures. [1, 17] Also capacity of the build can be affected by choosing orientation to allow building as many parts as possible in one build.

Deformation of parts is a common problem in L-PBF due to the cyclic heat delivery and residual stresses [1, 2, 6]. There are some ways to reduce the causes of cyclic heat, such as by preheating the building platform which enables lower thermal gradients to occur due to lower temperature difference between bottom and top regions of the part [15, 18]. Also support structures have an impact on the resistance of deformations. Higher amount of support structures have more volume to transfer heat away from the part and fix the part more strongly to the building platform, in order to avoid warping. [1] However, support structures are removed from the part after build which limits the usage of them as they can be challenging and costly to remove [1, 17]. Residual stresses of parts can also be reduced by thermal stress relief that can be performed after build once the loose powder has been removed from the parts, but the parts are still attached to the building platform [1, 14, 17].

4. Conclusion

Based on the experiments executed in this study, horizontally built parts are more vulnerable to have deformations compared to parts built vertically (see Fig. 10). Especially the parts that were built horizontally flat were the ones to have deformation in the experiments whereas the parts that were built horizontally on their sides, did not have deformation. The test samples built horizontally on their sides are taller in the building direction and they have more stiffness in the building direction to resist the deformation, as demonstrated in Fig. 11. Also, part dimensions have an effect on the amount of deformation as smaller parts may not show noticeable deformation when built horizontally flat (Fig. 13).

No evident deformations could be observed in most of the test samples manufactured. In fact, test samples C2 and C4 (see Fig. 10 (b) and (d)) were the only ones of all test samples to show evident deformation. The deformation shape of test samples C2 and C4 obey the TGM which pursues to bend the edges of the parts upwards from the building platform [8, 9]. This behaviour is observed also in the studies of Yang et al., Li et al., Li et al. and Wu et al. [4, 10, 11, 12].

Acknowledgements

Authors of this article are grateful for the help of the personnel of EOS Finland Oy for manufacturing the test samples investigated in this study, especially Antti Seppälä who operated the powder bed fusion machine and Juha Kotila who organized the experiments. Authors would also like to acknowledge the staff of LUT Laser & AM of making it possible to conduct this study.

References

- [1] Wohlers T, Campbell I, Diegel O, Kowen J, Huff R. Wohlers report 2019. Fort Collins: Wohlers Associates Inc; 2019.
- [2] Brandt M. Laser additive manufacturing: Materials, design, technologies, and applications. Amsterdam: Elsevier; 2017.
- [3] Yang L, Hsu K, Baughman B, Godfrey D, Medina F, Menon M, Wiener S. Additive Manufacturing of Metals: The Technology, Materials, Design and Production. Cham: Springer; 2017.
- [4] Yang YP, Jamshidinia M, Boulware P, Kelly SM. Prediction of microstructure, residual stress, and deformation in laser powder bed fusion process. *Computational Mechanics* 2017;61:599-615.
- [5] Masoomi M, Thompson SM, Shamsaei N. Laser powder bed fusion of Ti-6Al-4V parts: Thermal modeling and mechanical implications. *International Journal of Machine Tools & Manufacture* 2017;118-119:73-90.
- [6] Mukherjee T, Wei HL, De A, DebRoy T. Heat and fluid flow in additive manufacturing – Part II: Powder bed fusion of stainless steel, and titanium, nickel and aluminum base alloys. *Computational Materials Science* 2018;150:369–380.
- [7] Kurzynowski T, Gruber K, Stopyra W, Kuźnicka B, Chlebus E. Correlation between process parameters, microstructure and properties of 316 L stainless steel processed by selective laser melting. *Materials Science and Engineering* 2018;718:64–73.
- [8] Simson T, Emmel A, Dwars A, Böhm J. Residual stress measurements on AISI 316L samples manufactured by selective laser melting. *Additive Manufacturing* 2017;17:183-189.
- [9] Kruth JP, Froyen L, Van Vaerenbergh J, Mercelis P, Rombouts M, Lauwers B. Selective laser melting of iron-based powder. *Journal of Materials Processing Technology* 2004;149:616-622.
- [10] Li C, Fu CH, Guo YB, Fang FZ. A multiscale modeling approach for fast prediction of part distortion in selective laser melting. *Journal of Materials Processing Technology* 2015;229:703-712.
- [11] Li C, Liu JF, Fang XY, Guo YB. Efficient predictive model of part distortion and residual stress in selective laser melting. *Additive Manufacturing* 2017;17:157-168.
- [12] Wu AS, Brown DW, Kumar M, Gallegos GF, King WE. An experimental investigation into additive manufacturing-induced residual stresses in 316L stainless steel. *Metallurgical and Materials Transactions A* 2014;45A:6260-6270.
- [13] EOS. Material data sheet. EOS StainlessSteel 316L 2017. Available: https://cdn0.scrvt.com/eos/7d9518b6b150de07/2e8cde1098a2/SS-316L_M290_Material_data_sheet_FlexLine_40_12-16_en.pdf.
- [14] Liu Y, Yang Y, Wang D. A study on the residual stress during selective laser melting of metallic powder. *International Journal of Advanced Manufacturing Technology* 2016;87:647-656.
- [15] Mercelis P, Kruth JP. Residual stresses in selective laser sintering and selective laser melting. *Rapid Prototyping Journal* 2006;12:254-265.
- [16] Gibson I, Rosen D, Stucker B. *Additive Manufacturing Technologies: 3D Printing, Rapid Prototyping, and Direct Digital Manufacturing*. Second Edition. New York: Springer; 2015.
- [17] Saunders M. Design for metal AM 2017. Available: <https://resources.renishaw.com/en/details/--101490>.
- [18] Metal Additive Manufacturing. Fraunhofer ILT showcases VCSEL pre-heating for additive manufacturing. *Metal Additive Manufacturing* 2018;4:55.

11th CIRP Conference on Photonic Technologies [LANE 2020] on September 7-10, 2020

Influence of metal powder cross-contaminations on part quality in Laser Powder Bed Fusion: copper alloy particles in maraging steel feedstock

Max Horn^{a,*}, Lukas Langer^a, Mario Schafnitzel^a, Simone Dietrich^a, Georg Schlick^a,
Christian Seidel^{a,b}, Gunther Reinhart^{a,c}

^a Fraunhofer Institute for Casting, Composite and Processing Technology IGCV, Am Technologiezentrum 10, 86159 Augsburg, Germany

^b Department of Applied Sciences and Mechatronics, University of Applied Sciences Munich, Lothstr. 34, 80335 Munich, Germany

^c Institute for Machine Tools and Industrial Management of Technical University of Munich, Boltzmannstr. 15, 85748 Garching b. München, Germany

* Corresponding author. Tel.: +49 821 90678-187. E-mail address: max.horn@igcv.fraunhofer.de

Abstract

Metal powder cross-contaminations are a hindrance in powder-based additive manufacturing (AM). Foreign particles can enter the powder feedstock when two different materials are processed on a single machine – either successively through material changes or simultaneously during multi-material AM. In order to evaluate the criticality of named powder impurities, this study investigates the influence of foreign particle inclusions on part quality during laser powder bed fusion of a material combination commonly processed in multi-material AM: copper alloy CW106C particles in maraging steel 1.2709 feedstock. Different contamination levels are examined regarding metallurgical structure, defect formation, and mechanical strength. It is observed that copper inclusions are dissolved and do not cause cracks, porosity or other defects below three particle percent. Furthermore, ultimate tensile strength and fracture elongation show a slight negative trend for increasing contamination levels.

© 2020 The Authors. Published by Elsevier B.V.

This is an open access article under the CC BY-NC-ND license (<http://creativecommons.org/licenses/by-nc-nd/4.0/>)

Peer-review under responsibility of the Bayerisches Laserzentrum GmbH

Keywords: multi-material additive manufacturing; powder quality; powder purity; foreign particles; cross-contamination; recycling; reuse;

1. Introduction

1.1. Initial situation

Short lead-times, economic production of prototypes, and small lot sizes as well as a high degree of design freedom have made additive manufacturing (AM) technologies key processes for manufacturing of complex parts. For the production of metal (M) components, powder bed fusion (PBF) via laser beam (LB), together PBF-LB/M) is the dominating solution [1]. In accordance with ISO 52900, PBF-LB/M facilitates a laser beam to melt and fuse selected areas of a powder bed layer by layer [2]. Therefore, powder property characterization and feedstock quality control are key for the final part performance of this AM process [4–6,3]. Extensive research has been conducted about

the influences of powder properties on part quality in PBF-LB/M. Vock et al. have given an overview of recent activities [3]. One quality aspect, which has not yet been studied in detail is the influence of foreign particle contaminations, mostly from other powder material, referred to as cross-contaminations. However, foreign particles can enter the powder feedstock when two different materials are processed on a single AM machine – either subsequently through material changes or simultaneously during multi-material AM. The same applies to powder production and powder handling equipment [7]. In multi-material PBF-LB/M especially, where cross-contaminations cannot be fully avoided, foreign particles are found to be a key challenge and reconditioning solutions, such as powder purification, for contaminated feedstock need to be developed [9–11,8].

Irrespective of the source of contamination, Lutter-Guenther et al. and Kilburn found foreign particles of Ni-base alloy Inconel® 718 in AlSi10Mg feedstock to cause swirl-like inclusions and micro cracks [12,7]. The latter can be explained due to the formation of the brittle Ni₃Al and Al₃Ni phases in the melt pool [12]. Brandão et al. investigated the influence of tungsten contamination in Ti6Al4V specimens. Mostly unmelted spherical tungsten inclusions led to a larger variation in yield and tensile strength and caused a decrease in fracture elongation [13]. Jamshidinia et al. found tungsten particles in Inconel® 625 feedstock to cause material delamination [14]. Gatto et al. detected trace particles of a Ti-Al-alloy with high oxygen content in maraging steel 1.2709 feedstock and studied the influence of the cross-contamination on static and fatigue tensile strength. Although the contamination level was low enough that the average chemical composition of the feedstock powder was within nominal ranges, partially melted inclusions had a strong negative effect on fatigue life [15]. Horn et al. investigated the influence of copper alloy CuCr1Zr foreign particles on metallurgical structure and tensile strength of Al-alloy AlSi10Mg [17,16]. A contamination level of 0.5 weight percent (wt.%) caused material embrittlement due to Al₂Cu formation. Additionally, a basic concept of foreign particle behavior in the melt pool was derived.

In summary, cross-contaminations can have negative effects on part quality in PBF-LB/M. In order to secure quality-assured components, particle inclusions of foreign material need to be taken into consideration.

1.2. Material combination

Appearance of contamination-related defects and their influence on part properties are versatile and have to be studied on a single case basis. One particular material combination often used in recent multi-material PBF-LB/M investigations is maraging steel 1.2709 (X3NiCoMoTi18-9-5) and copper alloy CW106C (CuCr1Zr) [18,19,9]. Mechanical properties of the steel combined with high thermal conductivity of the Cu-alloy make it a suitable material combination for, e.g., casting or molding tools with integrated copper cooling elements. As 1.2709 serves as a structural, load-bearing material in the named example it will be the focus of this investigation.

In order to evaluate CW106C contamination-related defect evolution in maraging steel, introductory information about the material system is provided. The Fe-Cu binary system can be characterized by a peritectic reaction for the Fe-rich side, a flat liquidus line, and full solid state immiscibility. γ -Fe shows the highest solubility of Cu of more than 11% at roughly 1450 °C. Furthermore, Cu can be an alternative to nickel to support austenite creation [20]. Liquid-phase separation that occurs during rapid solidification processes is a peculiarity of the material combination. The liquefied material mixture separates into dispersed droplets of both components. Depending on element concentration and cooling rates, secondary and tertiary phase separation can occur, leading mainly to the presence of discrete Fe-rich and Cu-rich zones. This effect is also used to increase mechanical properties of stainless steel 1.4542 and other chromium-nickel-copper steels through precipitation of the face-centered cubic (fcc) ϵ -Cu phase [24,25,23,21,22].

The fusion zones of dissimilar metal joints of low-alloy, stainless, and tool steels with Cu-alloys manufactured by laser welding are also dominated by the presence of discrete ϵ -Cu and γ -Fe or α -Fe zones, respectively. Furthermore, accumulation of liquefied copper along already solidified grain boundaries of the steel materials can lead to hot cracking [24,26,22,27]. Due to the similarity of laser welding and PBF-LB/M, comparable observations are expected for this study.

1.3. Problem statement and approach

Maraging steel 1.2709 and copper alloy CW106 are a relevant material combination in multi-material PBF-LB/M [18,19,9]. However, during the process both powder materials get mixed to some extent and occurring cross-contaminations can lead to inferior part properties [9,10,8]. In order to evaluate reusability of contaminated 1.2709 steel powder and to approximate powder purity thresholds for the studied material combination, metallurgical and mechanical properties of systematically contaminated steel specimens manufactured by PBF-LB/M were analyzed.

2. Experimental methods

Contaminated powder samples were created by manual mixing and tumbling for more than 20 minutes in order to achieve a homogenous distribution of foreign particles. In order to achieve desired contamination levels, necessary material weights were calculated. Details about the mixing procedure are given in chapter 3.1. Table 1 gives information about the processed powder materials, where particle size distribution (PSD) data was generated via laser diffraction with wet dispersion facilitating a Mastersizer 3000 from Malvern Panalytical Ltd.

Specimens were manufactured on a SLM 250^{HL} PBF-LB/M machine from SLM Solutions Group AG equipped with an ytterbium fiber laser having a nominal wavelength of 1060 nm and a nominal spot diameter of 150 μ m. All powder variations were processed using the following standard parameters for pure metal alloy 1.2709: layer thickness of 30 μ m, hatch distance of 105 μ m, laser power of 200 W, and scan speed of 600 mm/s. For each contamination level, cubes with an outline of 10 x 10 x 10 mm³ were manufactured directly on the build plate without using support structures and subsequently cut in x-y- and y-z-planes for metallurgical analysis. Cross-sections were polished and etched using V2A etchant for 60-120 s at room temperature. Additionally, rods for tensile strength analysis were produced and machined according to DIN 50125 – B4 x 20 [28]. Six rods per build orientation were manufactured and tested in accordance with DIN EN ISO 6892-1 [29]: 90° (vertical), 45° (inclined), and 0° (horizontal). Specimens, which either broke eccentrically or did not fully break were excluded from the analysis. For each orientation and contamination degree a minimum of three samples was available for evaluation. Appendix A gives the overall number of analyzed specimens per contamination level and test piece type. A Hitachi TM3030Plus scanning electron microscope (SEM) equipped with an energy-dispersive x-ray spectroscopy (EDS) module from Bruker Nano as well as an Olympus

BX53M upright metallurgical light microscope were used for qualitative and quantitative analysis of the metallurgical cross-sections and fracture surface inspection. Furthermore, X-ray diffraction analysis (XRD) was conducted for phase identification using a PANalytical X'Pert PRO MRD diffractometer facilitating a θ -2 θ -geometry and Cu-K α -radiation.

Table 1. Powder materials and particle size distribution percentiles.

Material	Supplier	d _{10,3}	d _{50,3}	d _{90,3}
1.2709 (X3NiCoMoTi18-9-5)	NMD GmbH	24 μm	34 μm	49 μm
CW106C (CuCr1Zr)	Schmelzmetall GmbH	20 μm	32 μm	45 μm

3. Results and discussion

3.1. Creation of contaminated powder samples

For mixtures of materials, e.g., in alloying, weight percentage (wt.%), or atomic percentage (at.%) are common. In the underlying study however, each foreign particle can be the source of a defect. Thus, particle percentage (part.%) is used as the unit for the purposes of this investigation. In order to enable comparability between wt.% and part.%, median diameters d_{50} of the materials' PSDs are used as approximation for the conversion of units. Hereinafter indices A and B stand for the two components of the mixture. They can either be 1.2709 or CW106C in this investigation respectively. Equation 1 was derived from basic relations given in DIN 1310 [30]. If particles are assumed to be perfectly spherical, it gives the particle percentage for one material $part.\%_A$ for a desired weight percentage $wt.\%_A$ and given material densities ρ_A and ρ_B as well as median diameters of both materials $d_{50;A}$ and $d_{50;B}$.

$$part.\%_A = \frac{1}{1 + \frac{(1 - wt.\%_A)}{wt.\%_A} \cdot \frac{\rho_A}{\rho_B} \cdot \left(\frac{d_{50;A}}{d_{50;B}}\right)^3} \quad (1)$$

In order to examine defect evolution of metallurgical structure for rising CW106C contents in 1.2709, initially five different powder variations were prepared to manufacture cubic specimens for metallographic analysis as described in Chapter 2. Table 2 shows desired part.% and corresponding wt.% calculated using Equation 1. Additionally, Cu content in processed specimens was measured via SEM EDS and is used as an approximation for Cu-alloy CW106C. This is allowable due to the high Cu percentage 99.1 wt.%. Despite being an approximation, the small differences between calculated and measured Cu wt.% validates the described samples preparation procedure for this particular material combination and respective PSDs.

Table 2. Calculated and measured CW106 wt.% in 1.2709 for defined part.% exemplary shown for cubic specimens for metallographic analysis.

Part.% CW106C	0.5	2	5	10	20
Wt.% calculated	0.47	1.87	4.69	9.41	18.94
Wt.% measured	0.46	1.73	4.24	9.91	18.17

3.2. Metallurgical structure and defect formation

Initially, for metallographic analysis, the following contamination levels were chosen. Zero part.% CW106C in 1.2709 serve as references, 0.5 part.% refer to the remaining contamination after multi-material powder sorting processes [10], and 5 part.% were chosen in accordance with the maximum Cu content found in commercially available alloys, such as 1.4548. Furthermore, 2 part.% were chosen as the intermediate step to account for nonlinear material variations between 0.5 and 5 part.%. Lastly, 10 and 20 part.% were processed to study the influence of contamination levels at and above the maximum solubility of Cu in Fe. Fig. 1 shows vertical cross-sections of the processed powders with different contamination levels.

Up to 2 part.% samples reveal metallurgical structures with columnar grain growth from noticeable melt pool borders towards the melt pool centers and in build direction, typical for PBF-LB/M. All samples show little porosity and no material deterioration. From 5 part.% onwards cracks start appearing as indicated by arrows for 5 and 10 part.% in Fig.1. Due to their presence along grain boundaries and melt pool borders, especially noticeable for 20 part.% CW106C, these defects can be identified as hot cracks. As observed in laser welding, the lower-melting Cu-alloy tends to collect or precipitate at solidifying grain and melt pool borders where it remains in liquid state longer than Fe-phases, as also observed in previous studies [24,22]. During further solidification Fe-phase grains cannot fully coalesce and hot cracks appear. It should be noted that a single hot crack, smaller than all cracks observed for higher contamination levels, was also found in a sample contaminated with 2 part.% CW106C. A total cross-section surface of 3 cm³ was analyzed and only one conspicuity was



Fig. 1. Light microscopy images of etched cross-sections of the y-z-plane of cubic specimens, where z indicates the build direction and arrows mark cracks at 5 and 10 part.%.

found. This can most likely be explained by randomly increased concentration of foreign particles. It should therefore be considered a deviation within expectable statistical range and should be excluded from further analysis.

As shown in Fig. 2, for 20 part.% CW106C, EDS element mapping does not reveal Cu enrichment nor Fe depletion along the crack edges. Fig. 3 shows the results of the XRD analysis for the reference sample and a specimen contaminated with 5 part.% CW106C. Peaks identified as the CaCO_3 phase can be explained by the compound material, in which specimens were embedded. The Bakelite used appears to show a similar crystallographic structure. These peaks may therefore be ignored for further analysis. Comparing the remaining peaks, both graphs show high similarity. The major difference is an increased signal for the austenitic phase. Peak positions of $\gamma\text{-Fe}$ and $\varepsilon\text{-Cu}$ however, are almost identical. Thus, it cannot be fully distinguished whether the Cu phase is prevalent, Cu is solved in supersaturated austenitic crystals, or a combination of both exists, although a split peak at $\sim 43.5^\circ$ of Fig. 3 and hot cracks along grain boundaries of Fig. 1 make an increase in $\varepsilon\text{-Cu}$ more probable.

It can be concluded that below 2 part.% CW106C in 1.2709 no significant negative influence on metallographic structure is observed. Higher Cu contents appear to either lead to increased $\gamma\text{-Fe}$ creation or $\varepsilon\text{-Cu}$ formation along grain and melt pool boundaries. A combination of both phenomena cannot be excluded. At 5 part.% CW106C hot cracks start appearing and the 1.2709 feedstock cannot be used further without purification. Thus, somewhere in between contamination levels of 2 and 5 part.%, a sudden drop in part quality occurs. Given the fact that a single crack was observed at 2 part.% CW106C, the critical contamination level is expected to be closer to the lower boundary.

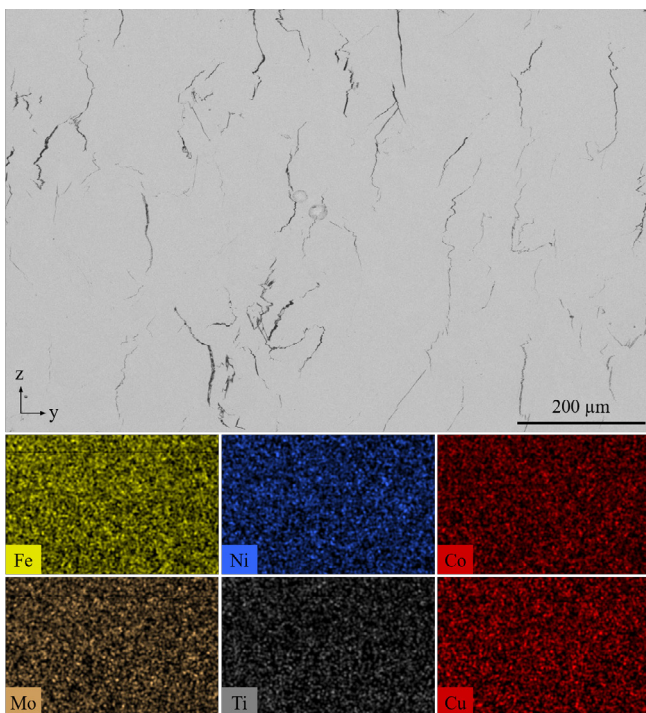


Fig. 2. SEM image and main elements' EDS maps of the y-z-plane of a cubic test piece contaminated with 20 part.% CW106C.

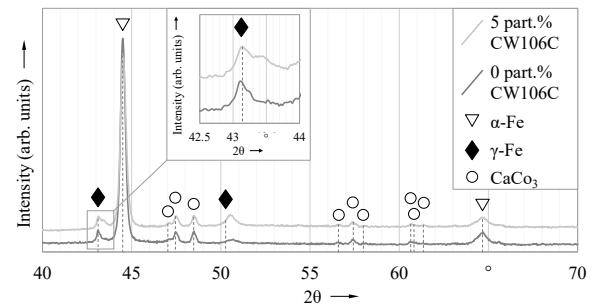


Fig. 3. Results of the X-ray diffraction analysis for zero and 5 part.% CW106C in 1.2709.

3.3. Tensile strength and fractography

Based on findings from the metallographic analysis, 3 part.% are set as the maximum foreign particle percentage for ultimate tensile strength (UTS) tests. Uncontaminated reference samples are again built for comparison and 0.5 part.% contamination are chosen in accordance with samples built in this chapter. Additionally, a foreign particle content of 1 part.% is chosen as the intermediate step between 0.5 and 3 part.%. Fig. 4 shows the results of the tensile strength tests for a set of reference samples and the described contamination levels. Despite vertically built samples with a contamination degree of 0.5 part.%, all build directions show a monotonic decrease of UTS and yield strength (YS) as indicated by second degree

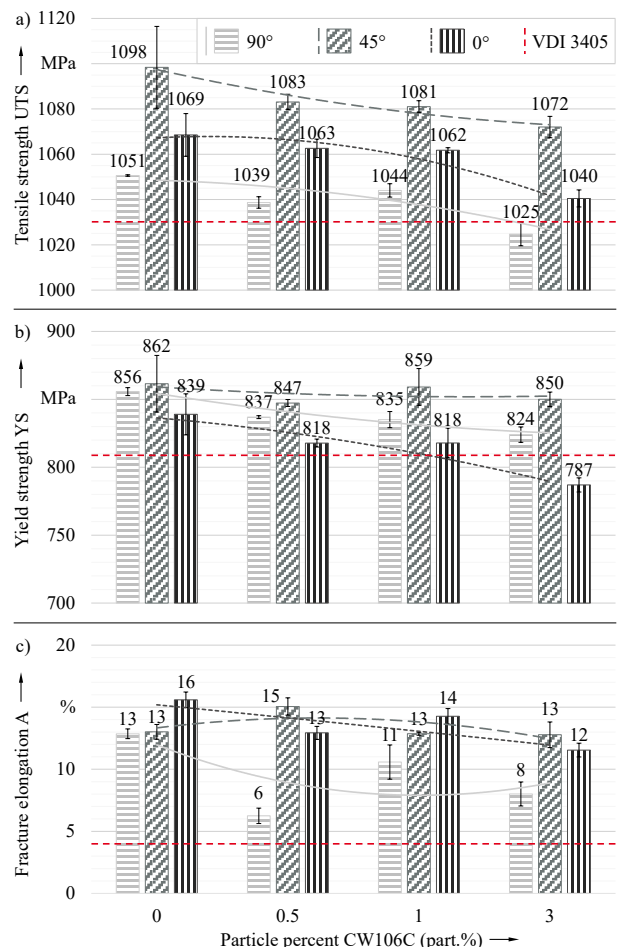


Fig. 4. Ultimate tensile strength, yield strength, and fracture elongation for different contamination levels of CW106C in 1.2709.

polynomial trend lines. Low variation within upright samples contaminated with 0.5 part.% could indicate a discrepancy of the build job itself. These specimens should therefore be excluded from further analysis. For zero, 0.5 and 1 part.% CW106C, UTS and YS are mostly constant for all build directions with only a slight negative tendency. Measured values are above the minimum threshold suggested by VDI guideline 3405 [31]. Between 1 and 3 part.% a sudden drop in part quality can be observed and UTS as well as YS fall below suggested limits for at least one build direction. Excluding vertical samples containing 0.5 part.% contamination, fracture elongation shows some more variation, but in total constant values between 0 and 1 part.%. Also, despite revealing negative trends for vertical and inclined samples for increasing contamination levels, fracture elongation (A) does not drop as significantly from 1 to 3 part.% as do UTS and YS. Assuming measured values for 0.5 part.% CW106 would lie between 13% and 11%, vertical samples showed a significant deterioration in fracture elongation. For inclined samples, rising Cu levels do not seem to influence A at all. In total however, fracture elongation does not fall below the limits suggested by VDI guideline 3405 for any build direction or contamination degree.

Decreases in UTS and YS are expected to occur due to the presence of cracks. To validate this, fracture surfaces are examined. Fig. 5 shows representative examples of the highest and lowest contamination levels of each build direction. Across all samples, foremost ductile failure mechanics are examined leading to cup and cone fractures. Surfaces are dominated by fine cellular dimple structures indicating transgranular failure. Some porosity can be observed for all test pieces. Mainly vertically built specimens show some surfaces indicating intergranular fractures. Percentage of intergranular failure appears to increase with rising contamination levels. Single cracks, as depicted for the vertical sample, can be observed for all specimens containing 3 part.% foreign particles. Significant numbers of cracks are only found in vertical samples. However,

crack surfaces do not show smooth dendritic structures as observed in previous studies [17]. Thus it remains unclear whether identified cracks opened during tensile strength tests or if they formed during material solidification. An additional defect type found foremost in vertically built contaminated specimens is weakened inter-layer bonding. Furthermore, larger defects containing unmelted powder particles are observed in vertical specimens containing 0.5 part.% CW106C. Defects are not caused by foreign particles and can be seen as process deviations independent from investigated contamination. Altogether, fractography is unobtrusive for most samples. Only vertical samples contaminated with 3 part.% CW106C reveal significant conspicuities.

It can be concluded that tensile strength, yield strength, and fracture elongation appear to be only slightly influenced by CW106C foreign particles up to contamination levels of 1 part.%. Above this threshold Cu appears to weaken grain boundaries and melt pool borders, leading to a significant drop in material strength.

4. Conclusion and outlook

In this study, the influence of CW106C foreign particles in 1.2709 feedstock that occurs during material changes on PBF-LB/M machines or during multi-material PBF-LB was investigated. Results can be summarized as follows:

- Below 2 part.% CW106 in 1.2709, foreign particles seem to have no negative effect on part quality of metallurgical cross-sections. Above this threshold hot cracks start to form.
- Due to high cooling rates of the PBF-LB/M process, large percentages of Cu contamination remain dissolved in super saturated solid solutions of Fe phases, foremost in austenite.
- Results from the XRD analysis are ambiguous. Cu either supports austenite creation or exists as finely dispersed ϵ -Cu. Either way, rising contamination levels lead to the weakening of grain and melt pool boundaries, and thus part quality deterioration.
- Above 1 part.% CW106C tensile strength and yield strength of 1.2709 partly decrease below minimum values suggested by VDI guideline 3405 [31]. Therefore, feedstock contaminated above this threshold must be purified during powder recycling processes.

Looking at further research demands, the following topics need to be investigated in greater detail to enable the transfer to industrial applications:

- Part properties were studied as built, without prior thermal treatment. Behavior of Cu contamination during maraging steel heat treatment processes and their influence on part properties should be studied.
- Fatigue strength of contaminated feedstock should be investigated.

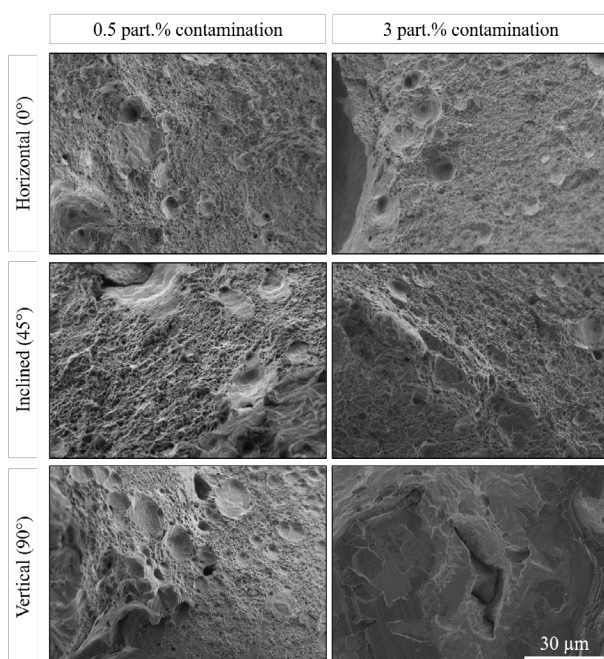


Fig. 5. Fracture surfaces of the lowest and highest contamination levels of each build direction.

Acknowledgements

The authors express their sincere thanks to the State of Bavaria and its Bavarian Ministry of Economic Affairs, Regional Development and Energy StMWi for funding the "MULTIMATERIAL-Zentrum Augsburg" (English: "Multi-material Center Augsburg"). Furthermore, the authors thank Norbert Zimmer and Kurt Hartmann for their support while conducting the experiments.

Appendix A. Overview of analyzed specimens

Table 3. Number of specimens per contamination level and test piece type analyzed for this study.

Part.% CW106C	0	0.5	1	2	3	5	10	20
Cubic specimens	3	3	-	3	-	3	3	3
UTS specimens 0°	6	6	6	-	3	-	-	-
UTS specimens 45°	4	4	3	-	4	-	-	-
UTS specimens 90°	3	3	6	-	5	-	-	-

References

- [1] Wohlers, T., Campbell, R.I., Huff, R., Diegel, O., Kowen, J., 2019. Wohlers Report 2019: 3D printing and additive manufacturing: state of the industry. Wohlers Associates, Fort Collins, Colo., 369 pp.
- [2] DIN EN ISO ASTM 52900: Additive Manufacturing - General Principles - Terminology. Berlin: Beuth 2015., 26 pp.
- [3] Clayton, J., Millington-Smith, D., Armstrong, B., 2015. The Application of Powder Rheology in Additive Manufacturing. JOM 67 (3), 544–548.
- [4] Slotwinski, J.A., Garboczi, E.J., Stutzman, P.E., Ferraris, C.F., Watson, S.S., Peltz, M.A., 2014. Characterization of Metal Powders Used for Additive Manufacturing. Journal of research of the National Institute of Standards and Technology 119, 460–493.
- [5] Strondl, A., Lyckfeldt, O., Brodin, H., Ackelid, U., 2015. Characterization and Control of Powder Properties for Additive Manufacturing. JOM 67 (3), 549–554.
- [6] Vock, S., Klöden, B., Kirchner, A., Weißgärber, T., Kieback, B., 2019. Powders for powder bed fusion: a review. Prog Addit Manuf 4 (4), 383–397.
- [7] Lutter-Günther, M., Schwer, F., Seidel, C., Reinhart, G., 2016. Effects on Properties of Metal Powders for Laser Beam Melting Along the Powder Process Chain. DDMC 2016: Fraunhofer Direct Digital Manufacturing Conference.
- [8] Binder, M., Anstaett, C., Horn, M., Herzer, F., Schlick, G., Seidel, C., Schilp, J., Reinhart, G., 2018. Potentials and Challenges of Multi-Material Processing by Laser-Based Powder Bed Fusion. Proceedings of the 29th Annual International Solid Freeform Fabrication Symposium.
- [9] Horn, M., Prudzilko, P., Anstaett, C., Lutter-Guenther, M., Seidel, C., Reinhart, G., 2018. Powder Separation Strategies for Recycling in Multi-Material AM. Proceedings of the EuroPM2018 Congress & Exhibition.
- [10] Santeccchia, E., Mengucci, P., Gatto, A., Bassoli, E., Denti, Gheorghiu, B., Barucca, G., 2019 (In Press). Enhancing The Quality Of Metal Powder Feedstock For Laser PBF Through Cross-contamination Removal. Proceedings of the Euro PM2019 Congress & Exhibition.
- [11] Vaezi, M., Chianrabutra, S., Mellor, B., Yang, S., 2013. Multiple material additive manufacturing – Part 1: a review. Virtual and Physical Prototyping 8 (1), 19–50.
- [12] Kilburn, P., 2016. LPW Technology – Intelligence in Metal. Company Presentation. http://www.advantageaustria.org/gb/events/LPWTechnologies_PhilKilburn_3011_2.pdf [Accessed 2018/05/25].
- [13] Brandão, A.D., Gerard, R., Gumpinger, J., Beretta, S., Makaya, A., Pambaguian, L., Ghidini, T., 2017. Challenges in Additive Manufacturing of Space Parts: Powder Feedstock Cross-Contamination and Its Impact on End Products. Materials 10 (5).
- [14] Jamshidinia, M., Boulware, P., Marchal, J., Mendoza, H., Cronley, L., Kelly, S., Newhouse, S., 2016. In-Process Monitoring of Cross Contamination in Laser Powder Bed Fusion (L-PBF) Additive Manufacturing (AM). Proceedings of the 27th Annual International Solid Freeform Fabrication Symposium.
- [15] Gatto, A., Bassoli, E., Denti, L., 2018. Repercussions of powder contamination on the fatigue life of additive manufactured maraging steel. Additive Manufacturing (24), 13–19.
- [16] Horn, M., Schlick, G., Lutter-Günther, M., Anstaett, C., Seidel, C., Reinhart, G. Metal powder cross-contaminations in multi-material laser powder bed fusion: Influence of CuCr1Zr particles in AlSi10Mg feedstock on part properties. Proceedings of the Lasers in Manufacturing LiM Conference 2019.
- [17] Horn, M., Schlick, G., Wegner, F., Seidel, C., Anstaett, C., Reinhart, G., 2018. Defect formation and influence on metallurgical structure due to powder cross-contaminations in LPBF. Proceedings of 7th International Conference on Additive Technologies (iCAT).
- [18] Anstaett, C., Seidel, C., Reinhart, G., 2017. Fabrication of 3D Multi-material Parts Using Laser-based Powder Bed Fusion. Proceedings of the 28th Annual International Solid Freeform Fabrication Symposium.
- [19] Anstaett, C., Seidel, C., Reinhart, G., 2018. Multi-Material Fabrication of Copper-Chrome-Zirconia and Tool Steel 1.2709 by Powder Bed Based Laser Beam Melting. DDMC 2018: Fraunhofer Direct Digital Manufacturing Conference.
- [20] Weißbach, W., 2010. Werkstoffkunde: Strukturen, Eigenschaften, Prüfung, 17., überarb. und aktualisierte Aufl. ed. Vieweg + Teubner, Wiesbaden, 447 pp.
- [21] Chen, S., Huang, J., Xia, J., Zhang, H., Zhao, X., 2013. Microstructural Characteristics of a Stainless Steel/Copper Dissimilar Joint Made by Laser Welding. Metall and Mat Trans A 44 (8), 3690–3696.
- [22] Kauss, N., Halle, T., Rosemann, P., 2018. Age-hardening behaviour, microstructure and corrosion resistance of the copper alloyed stainless steel 1.4542. IOP Conf. Ser.: Mater. Sci. Eng. 373, 12020.
- [23] Lu, X.Y., Cao, C.D., Wei, B., 2001. Microstructure evolution of undercooled iron–copper hypoperitectic alloy. Materials Science and Engineering: A 313 (1-2), 198–206.
- [24] Munitz, A., 1987. Liquid separation effects in Fe–Cu alloys solidified under different cooling rates. MTB 18 (3), 565–575.
- [25] Phanikumar, G., Manjini, S., Dutta, P., Chattopadhyay, K., Mazumder, J., 2005. Characterization of a continuous CO₂ laser-welded Fe–Cu dissimilar couple. Metall and Mat Trans A 36 (8), 2137–2147.
- [26] Mai, T.A., Spowage, A.C., 2004. Characterisation of dissimilar joints in laser welding of steel–kovar, copper–steel and copper–aluminium. Materials Science and Engineering: A 374 (1-2), 224–233.
- [27] Yao, C., Xu, B., Zhang, X., Huang, J., Fu, J., Wu, Y., 2009. Interface microstructure and mechanical properties of laser welding copper–steel dissimilar joint. Optics and Lasers in Engineering 47 (7-8), 807–814.
- [28] DIN 50125: Testing of metallic materials - Tensile test pieces. Berlin: Beuth 2016.
- [29] DIN EN ISO 6892-1: Metallic materials - Tensile testing: Method of test at room temperature. Berlin: Beuth 2017.
- [30] DIN 1310-2: Composition of (gaseous, liquid and solid) mixtures; concepts, symbols. Berlin: Beuth 1984.
- [31] VDI 3405, Blatt 2.1: Additive manufacturing processes, rapid manufacturing - Laser beam melting of metallic parts; Material data sheet aluminium alloy AlSi10Mg. Düsseldorf: Beuth 2015.

11th CIRP Conference on Photonic Technologies [LANE 2020] on September 7-10, 2020

Influence of the process parameters on the absorptance during Laser-Based Powder Bed Fusion of AlSi10Mg

Artur Leis^{*a,b}, Rudolf Weber^a, Thomas Graf^a

^aInstitut für Strahlwerkzeuge (IFSW), 70569 Stuttgart, Germany

^bGraduate School of Excellence advanced Manufacturing Engineering (GSaME), 70569 Stuttgart, Germany

* Corresponding author. Tel.: +49711-685 60428; fax: +49711-685 66842. E-mail address: artur.leis@ifsw.uni-stuttgart.de

Abstract

Knowledge of the absorptance during Laser-Based Powder Bed Fusion of metals (PBF-LB/M) is essential in order to investigate the interaction of the laser beam with the powder particles and the substrate of AlSi10Mg. A calorimetric measurement was performed to determine the absorptance of the laser beam. Using additively manufactured samples, the absorptance was investigated as a function of the powder layer, the laser power, and the laser beam diameter. The absorptance varied between 28% and 73% depending on the process parameter and configuration used with the minima at line powers between 1800 W/mm and 2800 W/mm for different beam diameters.

© 2020 The Authors. Published by Elsevier B.V.

This is an open access article under the CC BY-NC-ND license (<http://creativecommons.org/licenses/by-nc-nd/4.0/>)

Peer-review under responsibility of the Bayerisches Laserzentrum GmbH

Keywords: PBF-LB/M; Absorptance; Additive Manufacturing; Calorimetric; AlSi10Mg

1. Introduction

Laser-Based Powder Bed Fusion of metals (PBF-LB/M) allows for the generation of complex parts [1]. The process is very time-consuming due to the use of small gaussian laser beam diameters in the order of 100 μm at $1/e^2$ of the maximum intensity in combination with small layer thicknesses [2,3]. In laser materials processing, the interaction between the laser beam and the material is essential [4–6] and is defined by the absorptance of the laser beam. Factors particularly influencing the absorptance are the optical properties of the processed material, the temperature, the roughness of the sample surface, and the wavelength of the laser beam [7–9]. Furthermore, at PBF-LB/M in the regime of heat-conduction the laser beam is absorbed only once, whereas in case of PBF-LB/M with a capillary multiple reflection of the laser beam may lead to an absorptance of up to nearly 100% [4,5].

Previous investigations by Trapp et al. and Ye et al. to determine the absorptance with calorimetric measurements of the absorptance at PBF-LB/M on machined samples of

aluminum 1100 alloy, tungsten [10], Ti-6Al-4V, Inconel 625 [11] and stainless steel 316L [10,11]. Other groups have also published the calculation of the absorptance recording the time-resolved reflections of the laser beam inside an Ulbricht-sphere during PBF-LB/M [12–14].

This work presents the results of the calorimetric measurements of the absorptance during PBF-LB/M of the aluminum alloy AlSi10Mg on *additively manufactured* sample substrates. Different process configurations were investigated to determine the influence of varying the process parameters laser power, feed rate, and laser beam diameter on the sample surface. On the one hand, the absorptance was investigated on samples with additional powder layer of approximately 80 μm to represent the single melt process of PBF-LB/M, and on the other hand, samples without additional powder layer were used representing the so-called double melting process of one layer during PBF-LB/M.

Nomenclature		
η_A	Absorptance	in %
P	Laser power	in W
d_b	Laser beam diameter on the sample surface	in mm
P/d_b	Line power	in $\frac{W}{mm}$
t	Time	in s
T	Temperature	in K
m	Mass	in kg
c_P	Mass specific heat capacity	in $\frac{J}{kg \cdot K}$

2. Methods

2.1. Determination of the absorptance η_A

For the determination of the absorptance, calorimetric measurements according to the standard EN ISO 11551:2018 were performed [15]. The irradiation times were below 1 s, corresponding to the recommended pulsed procedure. Fig. 1 shows a recorded temperature increase (black) in Kelvin over the time in s. The fit is in red. The sample was heated and the temperature increase was recorded until the sample cooled down. The cooling curves are fitted with

$$T(t) = A_c + B_c \cdot e^{-\gamma_c t}, \quad (1)$$

where the fit parameters A_c , B_c and γ_c were determined for each curve.

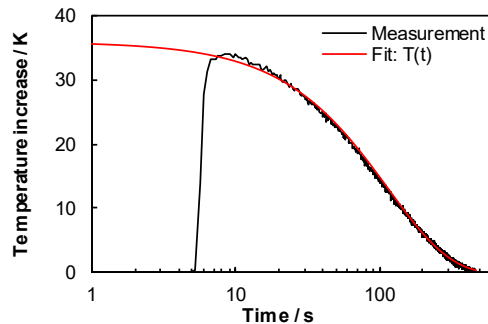


Fig. 1. Example for a recorded temperature increase in Kelvin (black) of a sample with the fit of the cooling curve (red) over the time in s.

From the recorded temperature increase and decrease of the processed samples, the absorptance η_A was calculated using

$$\eta_A = \frac{T_{ext} \sum_i (m_{Cu} \cdot c_{P,Cu} + m_{Al} \cdot c_{P,Al})}{P \cdot t_{weld}} \cdot \frac{0.5 \cdot \gamma_c \cdot t_{weld}}{\sinh(\gamma_c \cdot \frac{t_{weld}}{2})}, \quad (2)$$

where T_{ext} represents the extrapolated temperature of the cooling curve to the mean time of the heating at $t = \frac{t_2 - t_1}{2}$ with Eq. (1), where t_1 represents the start of heating and t_2 is the end point of heating with the maximum temperature.

In Eq.(2), m_{Cu} represents the mass of the copper base plate, whereas $c_{P,Cu} = 385 \text{ J}/(\text{kg} \cdot \text{K})$ is the mass specific heat capacity of it [16]. The mass of each sample m_{Al} was obtained by weighing, which were in the range of $0.969 \text{ g} \pm 0.022 \text{ g}$ for all samples and $c_{P,Al} = 910 \text{ J}/(\text{kg} \cdot \text{K})$ represents the mass

specific heat capacity of AlSi10Mg [17]. The laser power P multiplied with the irradiation time t_{weld} represent the applied laser energy. The mass of the copper base plate was determined before the experiments and was 3.240 g.

2.2. Experimental setup for calorimetric measurement

The setup used for the calorimetric measurements is shown in Fig. 2. The sample is linked with heat sink paste to the copper base plate. The copper base plate is fixed horizontally with three insulating screws and vertically with one on the bottom side. This allowed easy change of the sample. The resistance temperature detector (RTD) is linked to the copper base plate and to the data acquisition system. Nitrogen was used as shielding gas to prevent an exothermic reaction during irradiation. No shielding gas was used during cooling to avoid influence on the measurement.

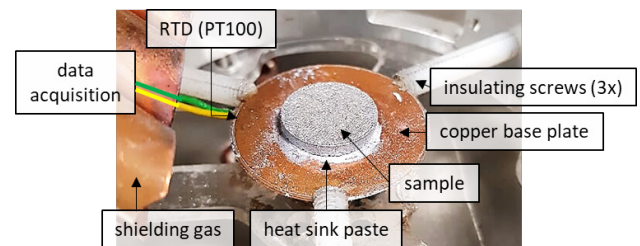


Fig. 2. Photography of the experimental setup for calorimetric measurement of the absorptance of additively manufactured samples.

A fiber laser with a core diameter of $25 \mu\text{m}$ was used for the experiments. The wavelength of the laser was $1,075 \text{ nm} \pm 2 \text{ nm}$. A Scanlab intelliSCAN 30 scanner was used to move the laser beam in spiral shapes on top of the sample's surface. The optical design of the scanner with a 200 mm collimating length and 340 mm focusing length lead to a minimum measured beam diameter of $35 \mu\text{m}$ at $1/e^2$ of the maximum intensity of the laser beam. The measured beam quality M^2 behind the scanning system was 1.2. Due to the high beam quality, the laser beam diameter on the sample's surface d_b can be increased by defocusing while maintaining the gaussian intensity distribution.

2.3. Sample preparation

The samples were manufactured by means of PBF-LB/M in a TruPrint3000 with the provided standard parameter set for the used powder AlSi10Mg-A LMF with a powder grain distribution of 20 – 63 μm . This was done to ensure PBF-LB/M process conditions at the experiments. The last layers during the generation of the samples were not used to smooth the top surface. Thus, the surface roughness was $S_a = 22.3 \mu\text{m} + 4.7 \mu\text{m} - 7.3 \mu\text{m}$. The surface of one sample is shown in Fig. 3. The individual vectors and their combination to the square hatch can be seen. In addition, individual small balls can be identified on the sample's surface, which are marked with black arrows.

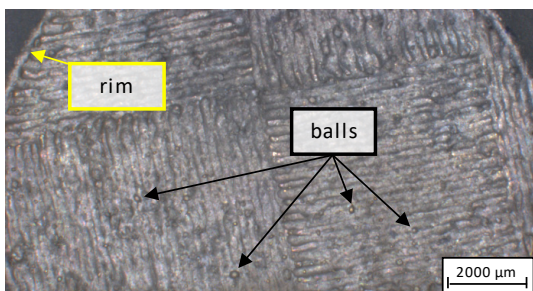


Fig. 3. Example surface of an additively manufactured sample without re-melting the last layers used for the experiments.

A rim of 80 μm height (marked with the yellow arrow in Fig. 3) was manufactured additively serving as a gauge for the thickness of the powder layers ensuring identical powder layer thicknesses. The powder layer was applied manually using the edge of an aluminium sheet as a scraping coater.

2.4. Experimental procedure

The samples were weighed before every experiment. The recording of the temperature started before the irradiation, and was stopped when the temperature reached the ambient temperature. The laser power was varied between 12 W and 2000 W. The feed rates used were 0.7 m/s, 1.0 m/s, and 1.3 m/s. The laser beam diameter on the sample surface used were $d_b = 35 \mu\text{m}$, $d_b = 100 \mu\text{m}$, and $d_b = 200 \mu\text{m}$. The quantity P/d_b referred to as line power is useful to illustrate the results as it represents the resulting surface temperature created by a moving laser beam as shown by Cline and Anthony [18] and Graf et. al. [19].

3. Results

For better visibility, the results for the respective d_b are displayed separately. Each figure shows the absorptance with (red) and without (blue) the additional powder layer. Three areas with different behaviours of the absorptance can be distinguished: I. for low line power up to 500 W/mm, II. for medium line power between 500 W/mm and ~2800 W/mm, highlighted in light-red and III. for high line power above of ~2800 W/mm, which is highlighted in red.

Fig. 4 shows the absorptance η_A as a function of the line power P/d_b for $d_b = 100 \mu\text{m}$. The data points are the mean values of both the absorptance and the line power. The absorptance values were averaged over an interval, which is indicated by the horizontal error bars. The error bars in the vertical direction show the minimum and maximum values of the absorptance in the considered line power range.

In area I., the results of the absorptance without and with the additional powder layer are similar. Without the additional powder layer, the absorptance was 45% at a line power of 430 W/mm and with the additional powder layer the absorptance was 49%. At this line power, only heating without melting of the sample surface was detected.

In area II., the absorptance without additional powder layer decreased to 30%. The absorptance with additional powder layer kept a constant value of $48\% \pm 1\%$ up to the line power of 2400 W/mm, shown with the red arrow in Fig. 4. The

biggest difference in the results with and without the additional powder layer is seen in area II, when the absorptance without the additional powder layer reached the minimum. Above the line power of 1600 W/mm and without additional powder layer the absorptance increased again, whereas the minimum measured values were constant up to the line power of 2800 W/mm, as shown with the blue arrow in Fig. 4. The maximum mean absorptance of 67% was reached at a line power of 11800 W/mm. The range of the values increased significantly due to the combination of different feed rates.

In the transition from area II. to area III., beginning with the line power of 2500 W/mm, the results of the experiments with and without additional powder layer were similar.

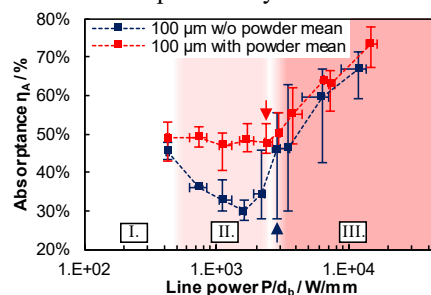


Fig. 4. Absorptance η_A as function of the line power P/d_b for $d_b = 100 \mu\text{m}$.

In Fig. 5, the absorptance is shown for $d_b = 35 \mu\text{m}$. Without additional powder layer the absorptance was between 30% and 40% up to the line power of about 1800 W/mm. With a line power between 1800 W/mm and 2500 W/mm, the range of the minimum and maximum values dropped to $\pm 2\%$ around the absorptance of 31%. At the line power of 2500 W/mm the minimum absorptance of 30% is seen, which shows the beginning of the transition from area II. to area III, as depicted with the blue arrow in Fig. 5. Further increase of the line power lead to an increase of the absorptance up to 64% at the line power of 5500 W/mm, which is seen in area III.

With additional powder layer, the absorptance was $45\% \pm 1\%$ up to the line power of 1800 W/mm in both, area I. and area II. The transition of the line power into area III. lead to an increase of the absorptance up to 60% at the line power of 5000 W/mm or higher, as seen in area III. The increase of the absorptance with an additional powder layer, beginning at the line power of 1800 W/mm (red arrow), was less as in the experiments without an additional powder layer. In area III. no significant influence of the additional powder layer is seen.

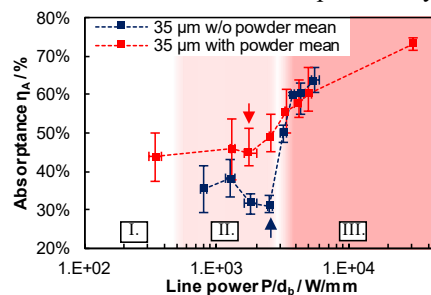


Fig. 5. Absorptance η_A as function of the line power P/d_b for $d_b = 35 \mu\text{m}$.

Fig. 6 shows the absorptance at $d_b = 200 \mu\text{m}$. The absorptance was 50% for the experiments without a powder

layer and was 48% with an additional powder layer at a line power of 280 W/mm, represented in area I.

In area II., the absorptance at experiments without additional powder layer decreased to the minimum of 28% with increased line power up to 2800 W/mm, as shown with the blue arrow. With additional powder layer the absorptance was constant up to the line power of 880 W/mm. Above the line power of 880 W/mm the absorptance slightly decreased to 41% at the line power of 2800 W/mm, as shown with the red arrow.

In the transition to area III., the absorptance increased for both with and without additional powder layer, with further increase of the line power. For a line power of 8400 W/mm the absorptance was $57\%_{-12\%}^{+9\%}$ without an additional powder layer and was $59\%_{-7\%}^{+5\%}$ with an additional powder layer.

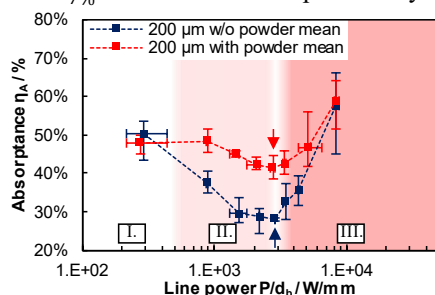


Fig. 6. Absorptance η_A as function of the line power P/d_b for $d_b = 200 \mu\text{m}$.

4. Discussion

The results with different beam diameters indicate that the influences of the process parameters on the absorptance η_A are comparable.

As clearly seen in Fig. 4, Fig. 5, and Fig. 6 the process can be separated in three regimes of applied line power. In area I. no melt pool was formed and the material was only heated. In area II. the material started to melt without the formation of a capillary. In area III. the line power lead to the formation of a capillary which resulted in an increased absorptance.

In any case, the absorptance with additional powder layer is higher than without additional powder layer. This is very pronounced in area II., where the results without additional powder layer showed the minimum absorptance. The decrease of the absorptance in area II. is probably due to the smoothing of the rough additively manufactured sample surface. With higher line power, a greater melt pool is generated and the ratio between molten and still solid material increases and the surface becomes smoother.

A strong increase of the absorptance for line powers exceeding about 2500 W/mm can be seen, as shown in area III. This most probably occurs because a capillary is formed, as described in the introduction. Up to this line power, the absorptance with an additional powder layer remains mainly constant. For the beam diameter of 200 μm , the absorptance slightly decreases from 48% to 41% when the line power increases from 880 W/mm to 2800 W/mm. This could be an indicator of the decreasing influence of the powder particle size with increasing beam diameter, and the better smoothing of the

surface with an additional powder layer due to the increasing size of the melt pool.

With a line power below 500 W/mm, the difference between the absorptance with and without additional powder layer diminished, as seen in area I. in Fig. 4, Fig. 5, and Fig. 6, as no material was molten.

Acknowledgements

The authors would like to thank Trumpf GmbH + Co. KG for supplying the TruPrint3000 at ARENA 2036 for manufacturing the test samples and SPI Lasers UK Ltd for supplying the test laser system for the experiments.

References

- [1] Gebhardt, Andreas. Generative Fertigungsverfahren: Additive Manufacturing und 3D-Drucken für Prototyping - Tooling - Produktion. 5th ed. München: Hanser; 2016.
- [2] Kruth, J - P, et al. Binding mechanisms in selective laser sintering and selective laser melting. Rapid prototyping journal 2005; 11:1 p. 26 - 36.
- [3] Louvis, Eleftherios, Fox, Peter & Sutcliffe, Christopher J. Selective laser melting of aluminium components. Journal of Materials Processing Technology 2011; 211:2 p. 275–284.
- [4] Hügel, Helmut & Graf, Thomas. Laser in der Fertigung: Grundlagen der Strahlquellen, Systeme, Fertigungsverfahren. 3rd ed. Wiesbaden: Springer; 2014.
- [5] Dausinger, F. Strahlwerkzeug Laser: Energieeinkopplung und Prozesseffektivität, Habilitationsschrift. Stuttgart; 2006.
- [6] Hecht, Eugene & Ganesan, A. R. Optics. 4th ed. Chennai: Pearson; 2012.
- [7] Ordal, M. A, et al. Optical properties of fourteen metals in the infrared and far infrared: Al, Co, Cu, Au, Fe, Pb, Mo, Ni, Pd, Pt, Ag, Ti, V, and W. (eng) Applied optics 1985; 24:24 p. 4493.
- [8] Wen, Chang-Da & Mudawar, Issam Emissivity characteristics of roughened aluminum alloy surfaces and assessment of multispectral radiation thermometry (MRT) emissivity models. International Journal of Heat and Mass Transfer 2004; 47:17-18 p. 3591–3605.
- [9] Ordal, M. A, et al. Optical properties of Al, Fe, Ti, Ta, W, and Mo at sub-millimeter wavelengths. (eng) Applied optics 1988; 27:6 p. 1203–1209.
- [10] Trapp, Johannes, et al. In situ absorptivity measurements of metallic powders during laser powder-bed fusion additive manufacturing. Applied Materials Today 2017; 9 p. 341–349.
- [11] Ye, Jianchao, et al. Energy Coupling Mechanisms and Scaling Behavior Associated with Laser Powder Bed Fusion Additive Manufacturing. Adv. Eng. Mater. 2019; 21:7 p. 1900185.
- [12] Gunenthiram, Valérie, et al. Analysis of laser–melt pool–powder bed interaction during the selective laser melting of a stainless steel. Journal of Laser Applications 2017; 29:2 p. 22303.
- [13] Simonds, B. J, et al. Dynamic and absolute measurements of laser coupling efficiency during laser spot welds. Procedia CIRP 2018; 74 p. 632–635.
- [14] Tolochko, Nikolay K, et al. Absorptance of powder materials suitable for laser sintering. Rapid prototyping journal 2000; 6:3 p. 155–161.
- [15] DIN EN ISO 11551; 2018. Optics and photonics - Lasers and laser-related equipment - Test method for absorptance of optical laser components.
- [16] Stevens, Rebecca & Boerio-Goates, Juliana Heat capacity of copper on the ITS-90 temperature scale using adiabatic calorimetry. The Journal of Chemical Thermodynamics 2004; 36:10 p. 857–863.
- [17] Raffimetal S.p.a. Leghe di alluminio in colata. Continuous casting aluminium alloys: AlSi10Mg. Available: http://www.raffimetal.com/scarica_file.asp?c=/dati/SearchAlloy/ENG/&f=EN43000.pdf (2020, Feb. 18)
- [18] Cline, H. E. & Anthony, T. R. Heat treating and melting material with a scanning laser or electron beam. Journal of Applied Physics 1977; 48:9 p. 3895–3900.
- [19] Graf, Thomas, et al. Analytical expressions for the threshold of deep-penetration laser welding. Laser Phys. Lett. 2015; 12:5 p. 56002.

11th CIRP Conference on Photonic Technologies [LANE 2020] on September 7–10, 2020

Analysis of the phase transformation of AlSi10Mg during Laser Powder Bed Fusion

Andreas Wimmer^{a,*}, Maja Lehmann^a, Adrian Schuler^a, Michael F. Zaeh^a

^aTechnical University of Munich, TUM Department of Mechanical Engineering, Institute for Machine Tools and Industrial Management, Boltzmannstr. 15, 85748 Garching, Germany

* Corresponding author. Tel.: +49 89 289 16586; E-mail address: andreas.wimmer@iwb.tum.de

Abstract

The characteristics of the process zone during Laser Powder Bed Fusion (LPBF) are decisive for the quality of additively manufactured parts. Thermographic measurements give an insight into the temperatures of the melt pool and its surroundings. Particularities in the temperature field can be attributed to the process dynamics or the alteration of the alloy composition during LPBF. This study presents a method for the analysis of the phase transformation during the process. It is demonstrated that thermographic measurements allow a detailed investigation of the liquidus and the solidus temperature. Experiments with AlSi10Mg revealed a direct interaction between the energy input and the resulting constitutional undercooling. Based on this finding, process parameters can be adjusted during LPBF to control the phase transformation process of the alloy.

© 2020 The Authors. Published by Elsevier B.V.

This is an open access article under the CC BY-NC-ND license (<http://creativecommons.org/licenses/by-nc-nd/4.0/>)

Peer-review under responsibility of the Bayerisches Laserzentrum GmbH

Keywords: Laser Powder Bed Fusion; Thermography; Undercooling; Cooling Curve; Phase Transformation

1. Introduction

Laser Powder Bed Fusion (LPBF) is a powder-based additive manufacturing process. A laser is used to expose the area of the component cross-section in each powder layer leading to local melting and subsequent solidification. This allows to generate parts with complex geometries [1]. The process is characterized by a local heat input and a small volume of molten material resulting in rapid solidification. By controlling the energy input with the process parameters (i. e. laser power or scanning velocity), the solidification behavior and the cooling rates can be adjusted [2]. Furthermore, the microstructure formation is determined by the energy input. Due to rapid solidification and due to high cooling rates non-equilibrium solidification during the LPBF process and undercooling in front of the solid-liquid interface occur [3, 4]. This means that the elements on the solidification front start to segregate. Consequently, the first solid formed has a lower Si content than the remaining liquid. During the ongoing solidification process, the liquid is further enriched with Si, since the crystallization occurs faster than the diffusion

can take place in the solid. Simultaneously, the liquidus temperature of the residual liquid decreases. For its solidification, an additional reduction of the temperature is necessary, which lies below the nominal solidus temperature of the alloy [5]. The undercooling is affected by the cooling rate: A higher cooling rate results in greater undercooling, which leads to finer grains [3]. Consequently, the cooling rate and the undercooling determine the size of the solidification structure and the mode of solidification (planar, cellular, columnar dendritic or equiaxed dendritic) [6]. The undercooling also increases the temperature difference ΔT between liquidus and solidus.

A large ΔT often results in hot tearing. When the material reaches the solidus or the eutectic temperature during cooling, the remaining liquid can fill the interdendritic areas or the resulting cracks in the solid. The larger ΔT is, the less liquid is available to fill the cracks that form during solidification [7].

Thermographic process monitoring provides insight into the temperature distribution of each layer over time and can be used to determine the cooling rate during the process. It can

also be utilized to investigate the above-mentioned aspects related to rapid solidification, i.e. the solidification structure and the mode of solidification [2, 6]. The cooling rate gives information about the microstructure, but not about the undercooling and the phase transformation during the process. Until now, it has only been possible to detect a discontinuity in the temperature profile during phase transformation [8]. Due to the limited spatial resolution (i.e. the large size of a pixel), the exact liquidus and solidus temperature could not yet be determined.

Differential Scanning Calorimetry (DSC) has been used to study the detailed phase transformation during heat treatment [9] and Differential Fast Scanning Calorimetry (DFSC) was applied to achieve a better understanding of the rapid solidification of powders during simulated additive manufacturing conditions [10]. Both methods are unsuitable for in-situ measurement of the phase transformation and the undercooling, because the experiments cannot be performed inside the LPBF machine during the process.

This paper provides an experimental method for investigating the undercooling of a material during the LPBF process. Thereby, a detailed analysis of the phase transformation is possible and a ΔT between the solidus and the liquidus temperature can be determined and employed to quantify the undercooling.

With the presented in-situ method, it is possible to better understand the rapid solidification during LPBF and correlate the results with process parameters.

2. Experimental set-up and method

2.1. Experimental set-up

For all experiments, AlSi10Mg powder (EOS GmbH) was used and the processing of the powder was performed on an EOSM270Xtended (EOS GmbH). During the experiments, the chamber was filled with argon while the oxygen content was below 2000 ppm. The door of the EOSM270Xtended was modified to allow for high-speed thermographic imaging (Figure 1). The thermographic images were recorded employing a FLIR X6901 sc (Flir Systems GmbH) with a spectral range of 3.0 – 5.0 μm . The high-speed thermographic camera is able to record up to 9762 fps. For the experiments a FLIR Precision

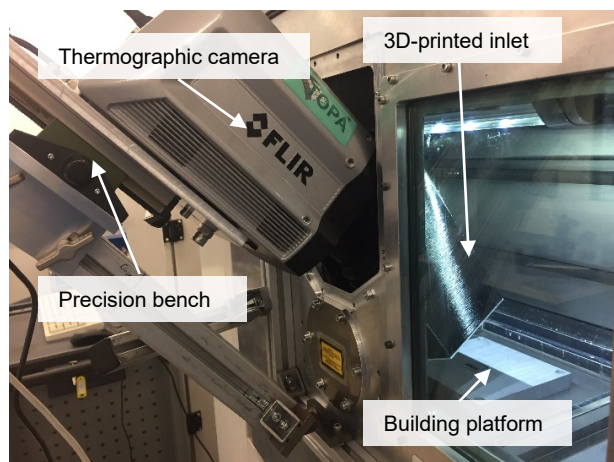


Fig. 1. Experimental set-up for the thermographic measurements of the melt pool during LPBF

optics with 100 mm focal length and 63.5 mm extension rings was used. The high frame rate allows measurements in a very short time window and a scanning track length of a few millimeters. This ensures a reduction of several disturbance variables, e.g. a variation of the laser spot size, the process gas flow, the heat distribution of the building platform and the layer thickness.

For a detailed analysis of the melt pool, the high-speed thermographic camera had to be positioned at a distance of a few millimeters from the melt pool. For this purpose, an inlet with a mounted precision bench was designed and built in-house. The set-up enabled a repositioning of the camera without contact to the building chamber as well as a collision-free movement of the recoater, and preserved the process gas flow.

For the measurements, the scanning velocity was varied to achieve different energy inputs. The process parameters and the energy inputs are shown in Table 1. Hereby, the energy input E is calculated according to

$$E = \frac{P}{d \cdot h \cdot v} \quad (1)$$

with the laser power P , the layer thickness d , the hatch spacing h , and the scanning velocity v .

Table 1. Process parameters and calculated energy input

P in W	h in μm	d in μm	v in mm/s	E in J/mm^3
120	90	20	735	91
120	90	20	588	113
120	90	20	490	136

2.2. Calibration of the high-speed thermographic camera

The high-speed thermographic camera was calibrated for temperatures up to 1500 $^{\circ}\text{C}$ by Flir. Spatial calibration for the horizontal and the vertical axis was performed on the building platform inside the EOSM270Xtended with a thermographic

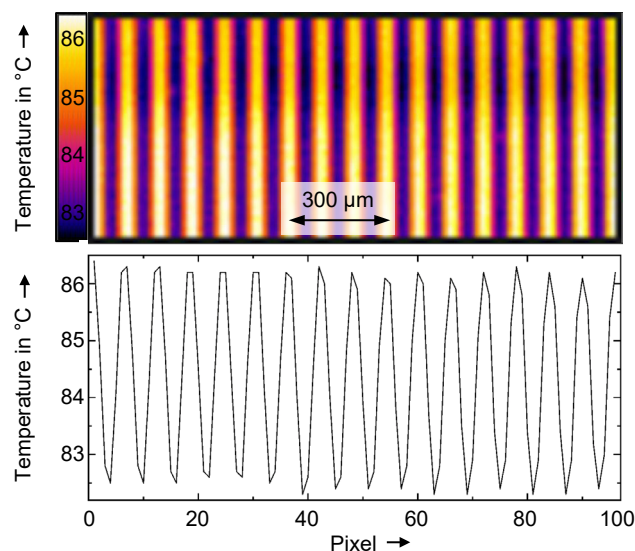


Fig. 2. Thermographic image of a glass scale to determine the exact pixel size

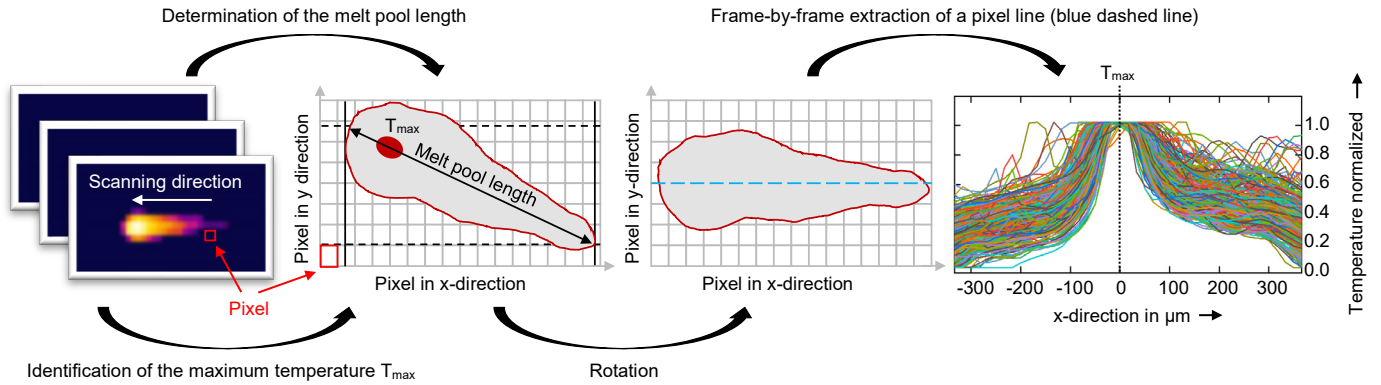


Fig. 3. Schematic representation of the algorithm for the frame-by-frame extraction of the thermographic images; to identify the phase transformation exactly, the calibration range of the camera was adjusted to the melting point of AlSi10Mg. For this reason, temperatures above the liquidus temperature are cut off.

image of a glass scale. This is shown in Figure 2. The correlation between the thermographic image and the known length of the glass scale results in a pixel width of 16.7 μm for the horizontal axis and a pixel height of 25.0 μm for the vertical axis.

The recorded data was evaluated with the software ResearchIR 4.40.9. The software settings include the distance to the test object (160 mm), the temperature of the preheated building platform (80 °C), the atmospheric temperature (20 °C), the relative humidity (0 %), the transmission of the atmosphere (100 %), the temperature of the external optics (20 °C), the emissivity (0.3 [11]), and the transmission of the optics (95 %).

According to [12] the infrared spectrum of several metals is constant for different wavelength and temperatures in the solid phase. However, due the unstable emissivity of liquid AlSi10Mg and the unknown emissivity during the phase transition, the recorded temperature values were only considered relatively.

The high frame rate of the thermographic camera results in a large amount of data being recorded. Hence, a special evaluation algorithm was required, which permits the automatic evaluation of the data.

2.3. Data analysis algorithm

Figure 3 shows the data-processing procedure schematically. The goal of this algorithm was to extract a single pixel line that represents the melt pool length. This ensured equal conditions when comparing different melt pool images.

In the experiment, both scanning directions (right-to-left and left-to-right) were applied. Hence, the images were mirrored by the algorithm to enable the use of data from both scanning directions. Subsequently, the thermographic images were analyzed with regard to the maximum temperature. Around this point, the dimensions of the melt pools were calculated.

To bring all images into a horizontal alignment, the pixel line of each melt pool with the longest melt-pool length was extracted and all pixel lines were shifted to their maximum temperature.

3. Results and discussion

With the above presented method, the data from 364 individual melt pools were extracted for the energy input

$E = 136 \text{ J/mm}^3$. Figure 4 a) depicts all pixel lines within the solidification process. After averaging, Figure 4 b) shows the mean temperature curve with the corresponding 90 % confidence interval. The mean temperature is further used to analyze the phase transformation process and determine the value of ΔT between the solidus and the liquidus.

The effect of cooling in the liquid and the solid phase can be described with physical models depending on an exponential decay function. Therefore, the data in Figure 4 b) was fitted with an exponential decay function in the corresponding range, which is presented in Figure 5. The phase transformation was present between 130 μm and 300 μm. This area deviates from the exponential function and indicates the points at which the exponential model differs from the mean temperature curve. These points are assigned to the liquidus and the solidus temperature of AlSi10Mg.

During equilibrium solidification of AlSi10Mg a ΔT of 39 K was expected [11]. This ΔT is marked in Figure 6. In case of

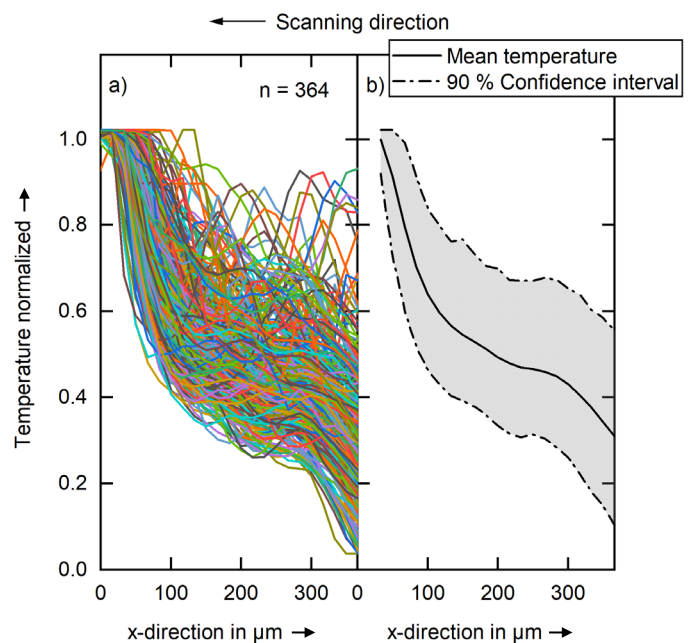


Fig. 4. a) Solidification of AlSi10Mg with the energy input of 136 J/mm³ during LPBF; the diagram shows pixel lines of 364 individual melt pool images. For comparison, all lines are shifted to their maximum temperature value. b) Mean temperature with corresponding confidence interval

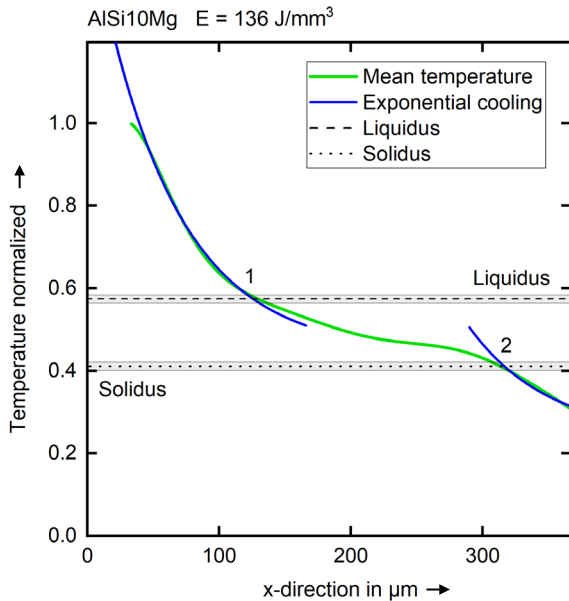


Fig. 5. Mean temperature of 364 individual melt pools with fitted exponential cooling (fitting coefficients are listed in appendix A). The points 1 and 2 – at which the exponential cooling models deviate from the mean temperature – are designated to liquidus and solidus of AlSi10Mg.

non-equilibrium solidification, the solidus temperature decreases and consequently ΔT increases. Hence, in Figure 6 the solidus temperature is shifted from point 2 to a lower temperature (point 3).

Figure 7 shows the dependence of ΔT on three different energy inputs. Due to the unknown emissivity of the liquid and the solid phase, the value of ΔT is calculated for relative comparison between different energy inputs. A low energy input results in a higher undercooling during the non-equilibrium solidification process.

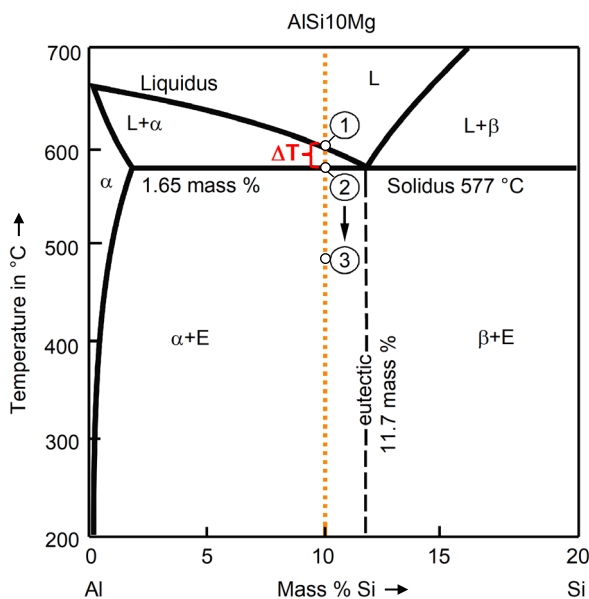


Fig. 6. Al-Si binary phase diagram (data from ref. [13]); the orange dotted line indicates the equilibrium solidification process. The points 1 and 2 are designated to the liquidus and the solidus temperature of AlSi10Mg. During non-equilibrium solidification, point 2 is shifted to lower temperatures (point 3).

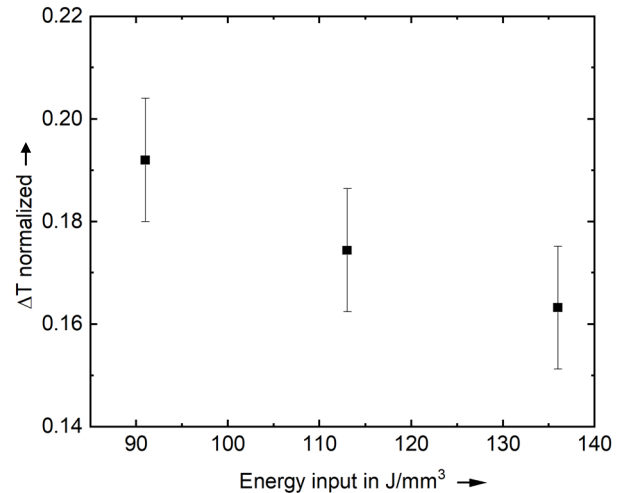


Fig. 7. Temperature difference between the liquidus and the solidus temperatures for different energy inputs during LPBF of AlSi10Mg; the normalization is equal to the one of Figure 4 and Figure 5.

The calculated energy input depends only on the scanning velocity. At slow scanning velocities, the melted and then solidified areas stay at higher temperatures for a longer period of time. Due to the slower resulting crystallization temperature, the remaining time for the diffusion-based solidification process is longer, and thus less undercooling occurs. It can therefore be assumed that the non-equilibrium solidification can be counteracted by reducing the scanning velocity.

4. Conclusion

This paper shows a method to gain better insight into the solidification process of AlSi10Mg during LPBF. The experimental setup enables pixel sizes that are smaller by a factor of two compared to the state of the art and enables a detailed determination of the phase transformation. This difference between the liquidus and the solidus temperatures was determined by high-speed thermographic imaging using a novel data analysis algorithm. By a variation of the scanning velocity, the energy input is influenced. It is shown that the scanning velocity has a major effect on undercooling during solidification. The method provides an option for controlling the undercooling and thereby influencing the resulting microstructure.

Further investigations regarding the microstructure formation must be conducted. A validation of the method is necessary in order to draw conclusions about the microstructure without the need for elaborate metallurgical investigations, and thus further increase the understanding of the LPBF process. By determining the emissivity of the equilibrium solidification, it is possible to calibrate the cooling curves and identify absolute values for the temperatures of the non-equilibrium solidification. Besides, a semi-empirical model for the undercooling can be used as input for the simulation of the microstructure during LPBF. In order to enable a hierarchical simulation of LPBF, the model could also serve as a connection between process simulation and structure simulation.

Acknowledgements

This research was supported by the Deutsche Forschungsgemeinschaft, DFG, project number ZA 288/68-1.

Appendix A.

Table 1. Exponential cooling in the liquid phase for an emissivity of 0.3 [11]

Model:	$y = A \cdot \exp(-x/t) + c$
c in K	160.52 ± 1.59
A in K	269.16 ± 5.95
t in μm	60.00 ± 0.00
R ²	0.99

Table 2. Exponential cooling in the solid phase for an emissivity of 0.3 [11]

Model:	$y = A \cdot \exp(-x/t) + c$
c in K	110.21 ± 3.61
A in K	8311.84 ± 978.94
t in μm	60.00 ± 0.00
R ²	0.97

References

- [1] J. P. Kruth, P. Mercelis, J. van Vaerenbergh, L. Froyen, and M. Rombouts, Binding mechanisms in selective laser sintering and selective laser melting, *Rapid Prototyping Journal*, vol. 11, no. 1, pp. 26–36, 2005.
- [2] S. Greiner, K. Wudy, A. Wörz, and D. Drummer, Thermographic investigation of laser-induced temperature fields in selective laser beam melting of polymers, *Optics & Laser Technology*, vol. 109, pp. 569–576, 2019.
- [3] E. O. Olakanmi, R. F. Cochrane, and K. W. Dalgarno, A review on selective laser sintering/melting (SLS/SLM) of aluminium alloy powders: Processing, microstructure, and properties, *Progress in Materials Science*, vol. 74, pp. 401–477, 2015.
- [4] X. Liu, C. Zhao, X. Zhou, Z. Shen, and W. Liu, Microstructure of selective laser melted AlSi10Mg alloy, *Materials & Design*, vol. 168, pp.1–9, 2019.
- [5] R. Trivedi and W. Kurz, Dendritic growth, *International Materials Reviews*, vol. 39, no. 2, pp. 49–74, 1994.
- [6] M. H. Farshidianfar, A. Khajepour, and A. P. Gerlich, Effect of real-time cooling rate on microstructure in Laser Additive Manufacturing, *Journal of Materials Processing Technology*, vol. 231, pp. 468–478, 2016.
- [7] B. Fulcher, D. Leigh, T. Watt, Comparison of AlSi10Mg and Al6061 processed through DMLS, In: *Proceedings of the solid freeform fabrication symposium*, Austin (TX, USA), pp. 404–419, 2014.
- [8] B. Cheng, J. Lydon, K. Cooper, V. Cole, P. Northrop, and K. Chou, Melt pool sensing and size analysis in laser powder-bed metal additive manufacturing, *Journal of Manufacturing Processes*, vol. 32, pp. 744–753, 2018.
- [9] C. Rowolt, B. Milkereit, M. Gebauer, C. Seidel, B. Müller, and O. Kessler, In-Situ Phase Transition Analysis of Conventional and Laser Beam Melted AlSi10Mg and X5CrNiCuNb16-4 Alloys, *HTM*, vol. 73, no. 6, pp. 317–334, 2018.
- [10] B. Yang, S. Malz, E. Zhuravlev, B. Milkereit, C. Schick, and O. Kessler, Differential Fast Scanning Calorimetry as analytical tool for mimicking melting and solidification in additive manufacturing, In: *Additive Manufacturing Meets Medicine 2019*, 2019.
- [11] H. Hu, X. Ding, and L. Wang, Numerical analysis of heat transfer during multi-layer selective laser melting of AlSi10Mg, *Optik*, vol. 127, no. 20, pp. 8883–8891, 2016.
- [12] J. Kopitz and W. Polifke, *Wärmeübertragung: Grundlagen, analytische und numerische Methoden*, 2nd ed.: Pearson, 2009.
- [13] T. B. Massalski and H. Okamoto, *Binary alloy phase diagrams*, 1st ed. Materials Park, Ohio: ASM International, p.164, 1990.

11th CIRP Conference on Photonic Technologies [LANE 2020] on September 7-10, 2020

Effects of process interruptions on the microstructure and tensile properties of AlSi10Mg parts manufactured by Laser-Based Powder Bed Fusion

Maximilian Binder^{a*}, Cheechau Leong^a, Christine Anstaett^a, Georg Schlick^a, Christian Seidel^{a,b}, Gunther Reinhart^{a,c}

^aFraunhofer IGCV (Research Institute for Casting, Composite and Processing Technology), Am Technologiezentrum 10, 86159 Augsburg, Germany

^bDepartment of Applied Sciences and Mechatronics, University of Applied Sciences Munich, Lothstr. 34, 80335 Munich, Germany

^cTechnical University of Munich, Institute for Machine Tools and Industrial Management, Boltzmannstr. 15, 85748 Garching, Germany

* Corresponding author. Tel.: +49 821 90678-192; fax: +49 821 90678-199. E-mail address: maximilian.binder@igcv.fraunhofer.de

Abstract

During the metal-based additive manufacturing process “laser-based powder bed fusion” (short: PBF-LB/M) interruptions can occur throughout the build job. These interruptions may be planned to produce hybrid parts, e.g., to insert components or electronics into the part or to adapt the manufacturing process itself. But interruptions can also be fault-induced, which can occur due to system failures, insufficient available powder quantities or poor component and process characteristics. Depending on duration, temperature and ambient atmosphere, these interruptions can have major influences on the component’s properties. The effects of a process interruption on the microstructure and the tensile properties for the material AlSi10Mg are to be presented within this work. In addition the impact of process interruptions on the mechanical properties of the tested components is shown.

© 2020 The Authors. Published by Elsevier B.V.

This is an open access article under the CC BY-NC-ND license (<http://creativecommons.org/licenses/by-nc-nd/4.0/>)

Peer-review under responsibility of the Bayerisches Laserzentrum GmbH

Keywords: process interruptions, change of microstructure and tensile properties, additive manufacturing, metal, laser-based powder bed fusion,

1. Introduction

In laser-based powder bed fusion (short: PBF-LB/M) metal powder is applied layer by layer and is locally solidified by utilizing a laser. This iterative process is usually carried out until the component is finished. However, the process can be interrupted for various reasons, also unplanned and unintentionally. The manufacturing can stop due to insufficient powder quantities, faulty build data, sensor measuring errors or because a component to be produced has been pulled up into the area of coater contact due to thermal deformation and has been wedged in with it. However, interruptions can also be planned and intentional and can be associated with the loss of the protective gas atmosphere. This can be the case, for example, in hybrid production [1], by integrating sensors [2] or radio-frequency identification tags [3] in manufactured

components or by general adjustments to the production process.

If interruptions occur, it needs to be investigated whether the build job can be continued without loss of component quality or needs to be aborted. In general, interruptions to the build job are dealt with differently, depending on the cost pressure, application and industry sector. However, if it can be proven that interruptions in the building process do not have a negative impact on the manufactured components, this would bring economic advantages. Partially manufactured components would no longer have to be disposed of, but could be completed and installed as planned, despite interruptions in the production process. The influence of an interruption will be investigated within this work.

2. State of the art

2.1. Influence of process interruptions

Stoll proved that an interruption of a build job during 316L processing resulted in a reduction of strength (change > 15%) and elastic modulus [1]. In another study [4], the influence of a process interruption on the microhardness and tensile strength of AlSi10Mg samples was investigated. Samples without interruption had microhardness values and a tensile strength 10% greater than those samples whose process was interrupted. However, the interruption was accompanied by a removal of the platform, including the components from the chamber and a subsequent re-insertion of the platform [4]. The probability is therefore high that, in addition to the influence of an interruption to a build job, other additional influences will come into effect: contamination of the components in the disassembled state, changed position of the parts after re-insertion into the building chamber or similar.

If a build job is interrupted, oxidation of the component may occur (opening of the process chamber or failure to maintain the inert gas atmosphere). Such oxidation of the component surface can, according to Yap et al., impede the bonding between layers. Liquid metals generally cannot contact an oxidized surface in the absence of a chemical reaction, which leads to balling [5]. If such balling effects can be detected during process interruptions, this would be one explanation for reduced tensile strength.

2.2. Change of layer thicknesses over the process

Spierings et al. calculated in his work of 2009 that the effective layer thickness during PBF-LB/M is practically greater than the actual layer thickness parameter. At a powder layer density of 60% and a solid material density of 99%, a preset powder start layer of 30 μm results in a 18.2 μm layer of solid material. If 30 μm powder is applied again, this value is added to the 18.2 μm material shrinkage of the previous layer and so on. After 10 layers, a layer thickness of 49.5 μm is achieved that remains constant throughout the process [6]. This theoretical approach to layer thickness calculation must be extended and verified in the context of this work to include interruptions to build jobs.

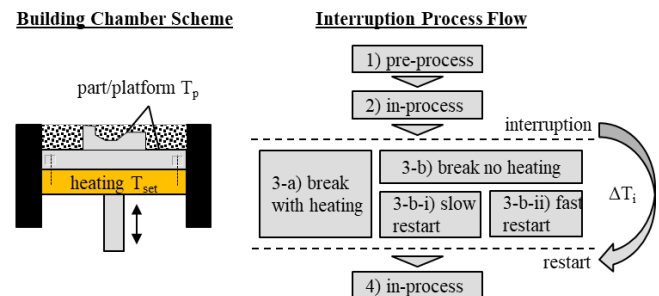
2.3. Measuring of melting paths

Manufactured melt paths can be analyzed by measurement. Width b and welding depth t of welds with deep penetration are determined using the equation: $\varphi = b/t$ while φ has to be < 1 [7]. Such approaches in general welding metallurgy can also be transferred to PBF-LB/M, in particular for measuring single tracks during material qualification. By measuring the keyhole, the optimal process parameters can be determined, which lie between a conduction mode melting and an unstable process melting [8]. These approaches to measure melt pool dimensions within PBF-LB/M are to be extended and deepened within the scope of this work.

3. Material and scientific methods

Within this contribution, material AlSi10Mg was used in all of the tests. Temperature measurements were carried out to analyze the temperature drop in case of a process interruption. In Figure 1, the temperatures at different times of an PBF-LB/M process, including an interruption, are recorded. Measurements via thermocouples were taken on the manufactured components and on the platform. Since these results differ by a maximum of 1 $^{\circ}\text{C}$, these values were combined.

At the start (1), the platform temperature T_{set} was set from room temperature to 200 $^{\circ}\text{C}$. The platform then reached a temperature T_p of 111 $^{\circ}\text{C}$ (equilibrium on the upper side of the platform) after 35 min (duration $d = 35$ min). Next a build job was performed (2) until it was interrupted after $d = 113$ minutes ($T_p = 130$ $^{\circ}\text{C}$). Then 3 cases were considered: In the first case (3-a), the heating remained at 200 $^{\circ}\text{C}$, so that the platform only cooled down during the interruption by $\Delta T_i = -13$ $^{\circ}\text{C}$. However, if the heating was switched off (3-b) and then switched on again, a much larger temperature gradient was created. If the building chamber is given $d = 80$ minutes to allow the 200 $^{\circ}\text{C}$ substrate platform heating to take effect (3-b-i, new temperature equilibrium), this corresponded to a cooling down of $\Delta T_i = -26$ $^{\circ}\text{C}$ compared to the value before the interruption. However, if the build job is resumed immediately after the substrate platform temperature of 200 $^{\circ}\text{C}$ is restored (3-b-ii), $d = 3$ min for building temperature to take effect, the same temperature difference is $\Delta T_i = -70$ $^{\circ}\text{C}$ (4).



Temperature measurements										
all undimensioned values in $^{\circ}\text{C}$, room temperature = 25										
step	1)	2)	3-a)	3-b)	3-b-i)	3-b-ii)	restart		4)	
T_{set}	200	200	200	no heating	200	200			200	
T_p	111	130	117*	54	104	60			130	
d in min	35	113	-	41	80	3			113	
ΔT_p	86	19	-13	-76	50	6	a)	+13, bi)	+26, bii)	+70
ΔT_i			-13		-26	-70				

*value averaged from in-process 2) and slow restart 3-b-i)

Fig. 1. Temperature profile of manufactured components and the substrate platform under three different building process interruption scenarios. The time of the restart is the moment when the first layer starts to be exposed.

The process parameters shown in Table 1 below were used in this study (laser spot diameter of about 85 μm).

Test specimens manufactured with these parameters achieved a density determined using Archimedes' principle of

Table 1. Process parameters used in this study for AlSi10Mg

laser power	laser velocity	hatch distance	layer thickness	platform temperature
330 W	1250 mm/s	0.17 mm	50 μm	200 $^{\circ}\text{C}$

99.95% with an assumed material density of 2.67 g/cm^3 . The powder had a measured particle size distribution of $D_{10} = 19.9$ μm , $D_{50} = 35.0$ μm and $D_{90} = 60.3$ μm . The flowability

of the powder was determined with unexpectedly high flowability differences in the measurements, resulting in a flowability energie of 244.6 mJ (mean value) with a standard deviation of 40.9 mJ (rheometer measurement). The particle morphology, analysed by SEM, was spherical throughout.

Scenario for all tests described in the following: the interruption of the build job was 40 min for all tests and was connected with an opening of the process chamber. Previous tests have shown that a process interruption of 40 min is a good reference value for a manual integration of several sensors into manufactured components on an SLM 125 HL system. For the specimens considered in this paper, the real temperature drop during an interruption is between 3-b-i and 3-b-ii (Figure 1), so that a temperature drop (40 min/(80°min-3 min)) assumed to be linear leads to a ΔT_{ir} of 36 °C. This value was assumed in the further calculations as the temperature gradient by interruption.

In this paper, it is assumed that the last process step before an interruption is always the melting by the laser and the first step after process resumption is the application of a new powder layer.

4. Theoretical approach to the influence of process interruptions

In the following, the approach by Spierings [6] regarding layer thickness changes will be extended by the theory of temperature change during process interruptions (surface roughness not considered). The first step is to determine a density factor δ , which indicates the density change of the powder d_p to the solidified material of the component d_c :

$$\delta\delta = 1 - (dd_{cc} - dd_{pp}) \tag{1}$$

Assuming that $d_p = 59\%$ (according to [9] between 55-63%) and $d_c = 100\%$, δ can be calculated to be 59%. When the building process is resumed, the component slowly returns to its equilibrium temperature due to the laser energy input (see chapter 3). This factor should be taken into account. The behavior must be described by the following linear approximation, where h_t describes the thermally induced height change per layer, h_i the thermally induced height change in total and l_t the number of layers until thermal equilibrium is restored:

$$h_{tt} = \frac{h_i}{l_t} = \tag{2}$$

Based on the temperature measurements made, it can be said that the temperature equilibrium of 130 °C is restored after approx. 15 min, which, assuming a process time of 23 s per layer, leads to a l_t of 39. h_i still has to be calculated as follows (α = coefficient of thermal expansion, h_b = current build job height including platform height, ΔT_i = temperature change in the component due to process interruption):

$$h_{ii} = -(\alpha\alpha * h_{bb} * \Delta\Delta T_{ii}) \tag{3}$$

Assuming $\alpha = 20.5 * 10^{-6} \text{ K}^{-1}$ [10], $h_b = 27 \text{ mm}$ and $\Delta T_i = 36 \text{ K}$, h_i is calculated to $-20 \text{ }\mu\text{m}$. This results in a h_t of 0.5 μm per layer. These calculated values can now be combined with the following formula, where h_c represents the height of the component, the index n stands for the current layer number, counted in the build-up direction. $h_{s,n}$ stands for the position of the substrate platform in the building chamber, depending

on the current layer n . k_i and k_f form factors which assume the value 1 or 0 depending on the current layer.

$$h_{cc,n} = \underbrace{h_{cc,n-1} + h_{ss,n} - h_{cc,n-1}}_{\text{component height after melting the new layer}} * \delta\delta - \underbrace{h_{ii} * k_{k_{ii,n}}}_{\text{height change through interruption}} + \underbrace{h_{tt} * k_{k_{tt,n}}}_{\text{height read-justment after interruption}} \tag{4}$$

The effective layer thickness t_{eff} can thus be calculated:

$$t_{eff,n} = h_{ss,n} - h_{cc,n-1} \tag{5}$$

t_{eff} was now calculated for each layer and is shown in the following Figure 2. It can be seen how the effective layer thickness increases to its equilibrium value within the first 10 layers at the beginning. From the process interruption onwards, there is an increase in layer thickness of 20 μm under the given parameters. After the first new layer, this increase changes into a reduction of the layer thickness, since the component expands due to the thermal input. If, as in case 3-b-ii) from chapter 3, the substrate platform temperature has been switched on only with a very short lead time, this effect increases considerably. The temperature-related height changes presented here are doubled, for example, at a temperature range of 72 °C or a job height (including platform) of 54 mm.

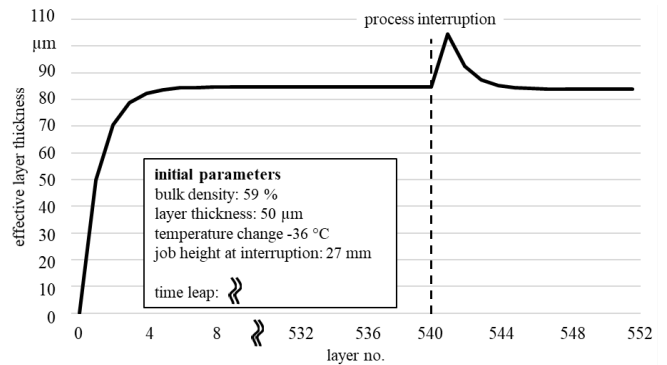


Fig. 2. Influence of a process interruption on the effective layer thickness for the material AISi10Mg

5. Proof of process interruptions on the component

A build job interruption results in different, measurable changes to the component. The following section provides evidence of an interruption to the build job. For this purpose, the untreated outer surface of the test specimens is analyzed photographically and by means of a laser microscope. Afterward the component is examined in the microsection and after an etching process, the melting paths are measured. Finally, the influence on mechanical parameters is verified by tensile tests.

5.1. Analysis of the outer surface

After completing of the build job with interruption, the test specimens are photographed under uniform lighting. The position of the build job interruption is usually quickly visible to the observer by means of an "interruption line". This

supposedly subjective impression can also be translated into quantitatively analyzable values. For this purpose, the image is converted to its gray values and the threshold value is set to e.g. 100 (see Figure 3). The interruption is thus also made easily visible by automated analysis programs by a deflection of the graph due to a rapid change in the proportion of white pixels.

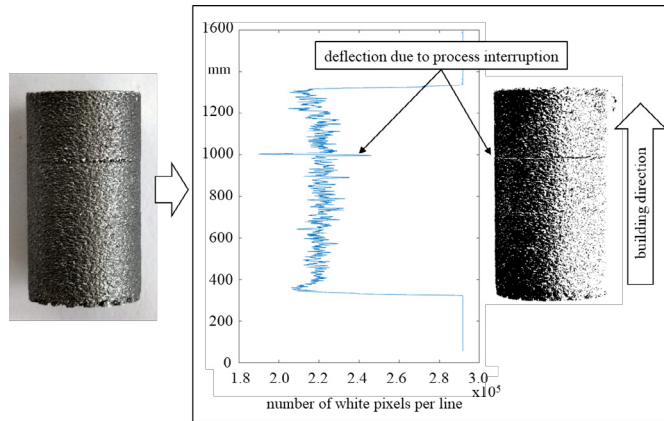


Fig. 3. Proof of a building job interruption due to colour change (converted to gray values) of the surface

In addition to a purely photographic analysis, the sample is also subjected to a roughness analysis using a laser microscope. Here too, the interruption is easily detected by a jump in the surface contour of about 150 μm (see Figure 4). The "roughness discontinuity" shown in the graph can be attributed to the temperature that has not been restored after the process has been restarted, but only a part can be explained by a pure temperature difference. A further potential influence on the edge in the component can also be a displacement of the substrate platform in the installation space due to cooling and reheating. The screw connection loosens when cooling down and can induce a displacement of the platform during reheating. A similar effect could appear due to thermal fluctuation of the laser optic.

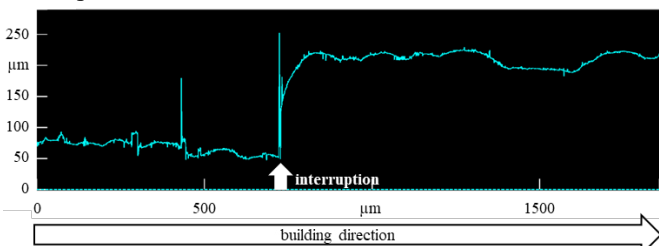


Fig. 4. Proof of a building job interruption due to change in surface roughness

5.2. Analysis of the microsection

In the next step, the interruption must be detected in the microsection of the sample. For this purpose, the sample is etched after polishing (macro etching, etchant: 60 ml distilled water, 10 g sodium hydroxide, 5 g potassium ferricyanide, reaction time 20 s). The analysis of the etching is shown in Figure 5. The microsection is also transferred to its grey values in a first analysis approach. A threshold value of 98 is then applied. The interruption layer is also visible in this view. The dark discolouration of the layer is conspicuous here, as well as the overlying layers. This effect could be related to an oxidation of the interruption layer, which is "pulled" into the overlying layers by repeated melting.

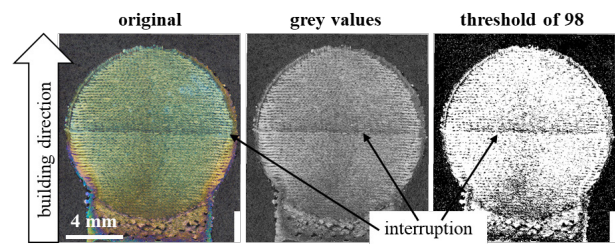


Fig. 5. Visibility of the interruption layer in the etched microsection of a sample (horizontal interruption line can be seen in the middle)

For a better quantitative analysis, specially defined characteristic values are to be determined for the melt paths. The values will be measured for an observation window with a width of 2 mm (width of Figure 6). In relation to the interruption layer every 4th layer (and their relations to each other) is measured, which is plane-parallel to the microsection plane through a pattern rotation angle of 45° per layer. Only every 4th layer is measured in relation to each other and not every single one, since evaluation graphs for all layer-values show a result which is very difficult to interpret. The following characteristic values are determined (measured values always recorded in the direction of build-up, compare Figure 6):

- 1) **Minimum distance** between the melt pools: the highest point of the lower melt pool to the lowest point of the upper melt pool
- 2) **Maximum melt pool height**: lowest point of the melting pool to the uppermost point of the same path
- 3) **Melt pool distance (measured from the top)**: highest point of the lower melt pool to the highest point of the upper melt pool
- 4) **Melt pool distance (measured from the bottom)**: lowest point of the lower melt pool to the lowest point of the upper melt pool

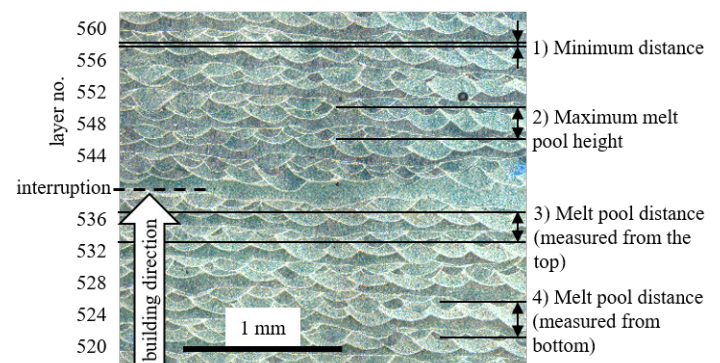


Fig. 6. Proof of a process interruption in the etched section by recording quantitative melt pool parameters (labelling of the characteristic values 1-4) only shown as an example)

The characteristic values were determined for 4 different "viewing windows" of 2 mm width (Figure 6 shows one of them) in different microsection planes and the mean value of the characteristic values 1) to 4) was calculated $((4 \cdot 4 \cdot (576 - 504)) / 4 = 288$ single measurements). Thus, outliers can be compensated better and the analysis receives an improved statistical load capacity. The following graphs show the analyses for the 4 characteristic values (Figure 7). The horizontal lines in the graphs form the supposedly stable process window in which the respective characteristic value moves until the process is interrupted. For all recorded

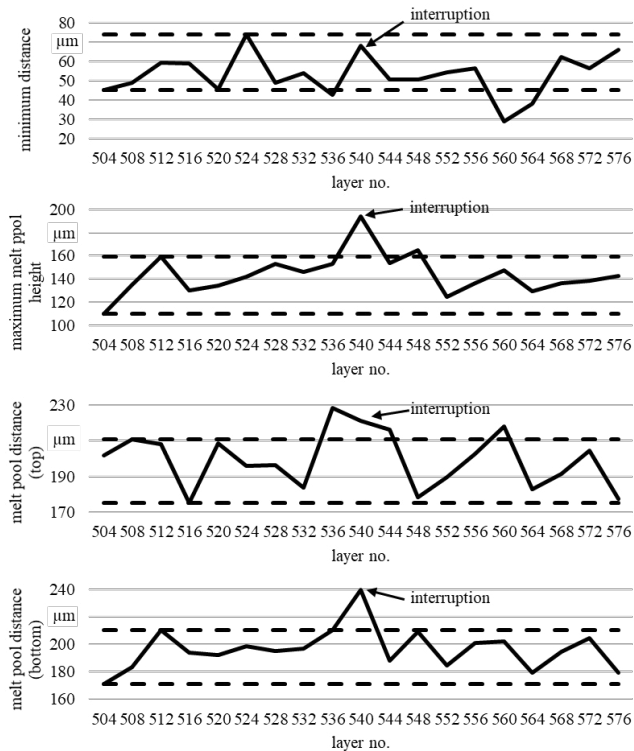


Fig. 7. Detection of the process interruption (layer 540) by deflection of the graphs over the process window (dashed lines) in which the values have moved before the interruption

characteristic values, except the minimum melt path distance, a clear change can be seen in the interruption layer. The zigzag course, which can be seen in every graph, is caused by the 45° pattern rotation and the fact that every 4th layer is parallel, but slightly shifted (the preparation software starts the calculation of the single vectors from the other side of the component, so that exposure vectors every 4th layer are parallel to each other, but not exactly on top of each other.) to the micrograph surface, so that the melting paths are only every 360° similarly oriented (i.e., every 8th layer).

According to the theory presented in chapter 4, it makes sense that the melt path of the interruption is largest in the microsection (35 μm above the process window for the maximum height difference). A thermally induced component length change due to a build job interruption thus seems to be detectable in the change of melt pools.

5.3. Analysis of the mechanical properties

In the following section, a tensile test according to DIN EN ISO 6892-1 is carried out with a round specimen form according to DIN 50125 - B4 x 20. As shown in Figure 8 a), vertical and horizontal tension rods are manufactured. Components with or without interruption are manufactured to allow comparability of the values. An interruption in the tests lasted 40 minutes and was connected with the opening of the process chamber door. The substrate platform heating was switched off during this time. In order to compensate for potential negative effects of the process interruption on the strength of some samples, a simple remelting using the same exposure parameters as for the build-up is performed after the interruption on a new layer of powder. The various tensile test variations are abbreviated as follows: v. = vertical, n.i. = no

interruption, i. = with interruption, r. = with remelting, h. = horizontal. The following number of tensile samples was considered in this work: 7x v.n.i., 7x v.i., 6x v.i.r., 7x h.n.i., 4x h.i., 3x h.i.r. in. The combined results for yield strength $R_{p0.2}$, ultimate tensile strength R_m and elongation at break ϵ_f are given in Figure 8 b).

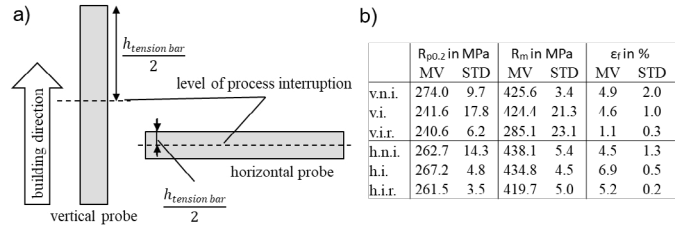


Fig. 8. a) Interruption of build job during the production of tensile specimens for vertical and horizontal samples, b) Results of the tensile test (MV= mean value, STD = standard deviation)

All tested samples are brittle fractured. The vertical specimens without interruption are broken in equal proportions at 45° and 90° angles, partly in the middle and partly off-center. Vertical specimens with interruption, on the other hand, are broken in 12 of 13 cases centrally and with a 90° fracture surface. Horizontal samples show 90° fracture surfaces without interruption. With interruption the failure changes to 45° fracture surfaces. The fracture planes of the horizontal specimens were distributed from fracture areas from top to bottom with no discernible trend.

Figure 9 shows the ultimate tensile strength and yield strength of the samples. It can be seen that vertical and horizontal samples behave very similar. The interruption of the building process does not seem to have any influence unless it is associated with remelting. In this case, R_m decreases by 34% from 425.6 MPa in the uninterrupted state to 285.1 MPa.

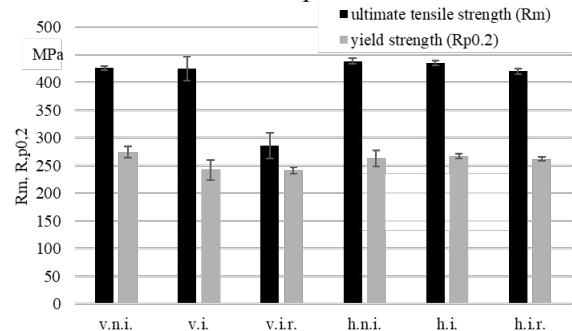


Fig. 9. Ultimate tensile strength and yield strength of the tested tensile samples (v = vertical, n.i. = no interruption, i. = interruption, r = with remelting, h = horizontal)

Figure 10 shows that interruptions seem to be associated with a slight increase in young's modulus, especially if this is associated with remelting. A strong decrease in ϵ_f can be seen in standing samples with remelting compared to standing samples with and without interruption.

The strongly negative effect of a process interruption reported by Hammond et al. could not be reproduced. It can be assumed that during the execution of the experiment further unreported influences were also present, which did not come to bear in our experiments. It is also possible that with a 40-minute interruption and just little gas circulation through an open process chamber door the component can hardly oxidize.

In previous own tests, which will not be discussed in detail in this paper, the influence of post heat treatment (standard T6-

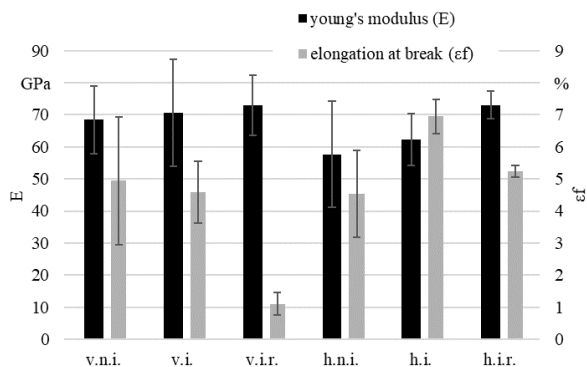


Fig. 10. Young's modulus and elongation at break of the tested samples (v = vertical, n.i. = no interruption, i = interruption, r = with remelting, h = horizontal)

cycle) was also considered. Except for the strength changes typical for post heat treatment, no differences between samples with and without interruption could be detected.

In Table 2, the mechanical characteristic values determined were compared with empirical values from the literature to ensure their reliability [4,5,11–14]. The results are comparable with the literature values and the VDI 3405 [14] standard.

Table 2. Literature review of the mechanical strength of AlSi10Mg samples produced by PBF-LB/M without process interruption (v = vertical, h = horizontal) [4,5,11-14]

literatur reference	$R_{p0.2}$ in MPa	R_m in MPa	ϵ_f in %	considering process interruptions
Binder et al. 2020 (v/l)	274.0/262.7	425.6/438.1	5.0/4.5	yes
Hammond et al. 2019 (v/l)	295.8/276.0	449.7/447.8	3.3/5.4	yes
Kempen et al. 2012 (v/l)		396/391	3.47/5.55	no
Li et al. 2016	322.2	434.3	5.3	no
Li et al. 2017 (v/l)	340/350		11.2/13.4	no
VDI 3405, Part 2.1	210-292	353-473	2-7	no
Yap et al. 2015	220	400	11	no

6. Conclusion and outlook

In this study it could be shown that the processing of AlSi10Mg only has an effect on the mechanical properties due to an interruption of the building process if it is combined with remelting. The opposite has already been proven in the literature for AlSi10Mg or 316L under other conditions [1,4]. It must be more thoroughly checked under which circumstances either no influences or influences on the strength can be expected. In particular, varying melt pool depths, depending on process parameters, could be the cause of this effect (use of 350 W and 930 mm/s at 50 μ m by Hammond [4] versus 330 W and 1250 mm/s at 50 μ m in this work). Parameters with a greater melt pool depth should be able to compensate for thicker powder layer thicknesses. To what extent this is the case here must still be examined. Hammond was able to record effects during the interruption. This probably happened because he mapped the "remelting effect" introduced in Figure 9 by applying a new starting layer. In addition, it must be said that if an interruption is made at a late stage in the building process and thus a higher building height is reached, the theoretical thermal shrinkage is greater. This means that a greater influence should be detectable for larger, standing tensile specimens or tensile specimens which are only interrupted shortly before completion of the component.

Furthermore, it could be shown how build job interruptions affect melt pool sizes or the outward appearance of specimens and can be verified. The described mathematical approach to

calculate changes in layer thickness could be used in the future to automatically compensate for job interruptions. Depending on temperature change (e.g., tracked by a monitoring system) and interruption time, the height of the substrate platform can be adjusted before the restart. With such an interruption compensation, components could be used in the future, as a negative influence on the mechanical properties can be minimized. By a strategy, by which parts with interruption demonstrably do not bring any disadvantages, the component scrap can be minimized considerably in the future and also the subsequent use of failure critical components can be guaranteed. High personnel, plant time and material costs can thus be saved.

Acknowledgments

The authors express their sincere thanks to the State of Bavaria and its Bavarian Ministry of Economic Affairs, Regional Development and Energy StMWi for funding the "MULTIMATERIAL-Zentrum Augsburg. Furthermore, the authors would like to thank Martina Fischer, Georg Edelman, Mario Schafnitzel, Kurt Hartmann and Christina Aust for their support in the performance of experiments and data collection.

References

- [1] P. Stoll, A. Spierings, Impact of a process interruption on tensile properties of SS 316L parts and hybrid parts produced with selective laser melting, *Int J Adv Manuf Technol* 103 (2019) 367–376.
- [2] M. Binder, L. Kirchbichler, C. Seidel, C. Anstaett, G. Schlick, G. Reinhart, Design Concepts for the Integration of Electronic Components into Metal Laser-based Powder Bed Fusion Parts, *Procedia CIRP* 81 (2019) 992–997.
- [3] M. Binder, F. Schönfeld, C. Anstätt, G. Schlick, C. Seidel, Radio-Frequency Identification of Metal-AM Parts, Weinheim, 2019.
- [4] V. Hammond, M. Schuch, M. Bleckmann, The influence of a process interruption on tensile properties of AlSi10Mg samples produced by selective laser melting, *RPJ* 25 (2019) 1442–1452.
- [5] C.Y. Yap, C.K. Chua, Z.L. Dong, Z.H. Liu, D.Q. Zhang, L.E. Loh, S.L. Sing, Review of selective laser melting: Materials and applications, *Applied Physics Reviews* 2 (2015) 41101.
- [6] A. Spierings, G. Levy, Comparison of density of stainless steel 316L parts produced with Selective Laser Melting using different powder grades, 20th Annual International Solid Freeform Fabrication Symposium, SFF 2009 (2009).
- [7] G. Schulze, Die Metallurgie des Schweissens: Eisenwerkstoffe - Nichteisenmetallische Werkstoffe, 4th ed., Springer-Verlag Berlin Heidelberg, Berlin, Heidelberg, 2010.
- [8] C. Tenbrock, F.G. Fischer, K. Wissenbach, J.H. Schleifenbaum, P. Wagenblast, W. Meiners, Influence of keyhole and conduction mode melting for top-hat shaped beam profiles in laser powder bed fusion, *Journal of Materials Processing Technology* 278 (2020) 116514.
- [9] N. Karapatis, G. Egger, Gygax, P. Glardon, R., Optimization of powder layer density in selective laser sintering (1999).
- [10] Renishaw plc, AlSi10Mg-0403 powder for additive manufacturing: Data sheet, 2015.
- [11] K. Kempen, L. Thijs, J. van Humbeeck, J.-P. Kruth, Mechanical Properties of AlSi10Mg Produced by Selective Laser Melting, *Physics Procedia* 39 (2012) 439–446.
- [12] W. Li, S. Li, J. Liu, A. Zhang, Y. Zhou, Effect of heat treatment on AlSi10Mg alloy fabricated by selective laser melting: Microstructure evolution, mechanical properties and fracture mechanism, *Materials Science and Engineering: A* 663 (2016) 116–125.
- [13] X. Li, J. Ni, Q. Zhu, H. Su, J. Cui, Y. Zhang, J. Li, Structure and Mechanical Properties of the AlSi10Mg Alloy Samples Manufactured by Selective Laser Melting, *IOP Conf. Ser.: Mater. Sci. Eng.* 269 (2017) 12081.
- [14] VDI 3405 Part 2.1, Laser beam melting of metallic parts: Material data sheet aluminium alloy AlSi10Mg, Beuth Verlag, 2015.

11th CIRP Conference on Photonic Technologies [LANE 2020] on September 7-10, 2020

Influence of isolated structural defects on the static mechanical properties of PBF-LB/M components

Stefan Kleszczynski^{*}, Arno Elspaß^a

University of Duisburg-Essen, Chair of Manufacturing Technology, Lotharstr. 1, 47057 Duisburg, Germany

^{*} Corresponding author. Tel.: +49 203 379 1268; fax: +49 203 379 1530. E-mail address: stefan.kleszczynski@uni-due.de

Abstract

Since the microstructure of components made by Laser-based powder bed fusion of metals (PBF-LB/M) is directly affected by the melting and solidification, mechanical properties are very sensitive to deviating process conditions. If deviations occur, local defects may remain within the microstructure. The impact of isolated defects on the resulting mechanical properties is only poorly understood. Since PBF-LB/M processes are increasingly used in industrial applications, fundamental systematic studies on the effects of structural defects on the mechanical properties are necessary to ensure quality. Thus, single defined structural defects of different dimensions are reproducibly placed in PBF-LB/M samples and used for static-mechanical tests. The results of tensile testing are compared with structural mechanical simulations, which provide insights into the prevailing stress and strain distributions. The achieved results show that isolated internal defects have only a minor influence on static strength parameters. Particularly with larger defect sizes, the values determined for tensile strength and yield strength showed only minor impairment.

© 2020 The Authors. Published by Elsevier B.V.

This is an open access article under the CC BY-NC-ND license (<http://creativecommons.org/licenses/by-nc-nd/4.0/>)

Peer-review under responsibility of the Bayerisches Laserzentrum GmbH

Keywords: “Additive Manufacturing, Laser Beam Melting, Laser Powder Bed Fusion, Mechanical Properties, Pores, Voids”

1. Introduction

Laser Powder Bed Fusion (PBF-LB/M) is currently finding its way into industrial series production. The resulting mechanical properties meet the requirements of industrial applications in principle. With regard to the reproducibility of quality-relevant component properties, however, more work is required, since slight fluctuations in process control or in the process boundary conditions can lead to defects during the layered build-up of the components [1]. The special feature compared to conventional manufacturing processes is that the high number and interaction of process parameters and process boundary conditions have a decisive influence on the resulting component quality. The exact number of quality-decisive factors varies in the technical literature: *Sehrt* [2] names 218 in his work, *Rehme* [3] even names 299. In most PBF-LB/M processed materials a certain residual porosity is detectable

[2,4,5]. The pores can be caused by Lack-of-Fusion (LOF) [1], where the layer and track connection is not sufficiently formed during melting, or by keyhole welding [1,4-6]. In the latter case, the pores have a spherical structure, while a non-spherical pore shape can usually be observed with LOF-defects. Additionally cracks are another important defect category for some alloy systems [7]. *Sehrt* [2] characterized the anisotropic behavior in the static strength of laser-melted components. He showed that the tensile strength of specimens made from horizontally oriented GP1 (X5CrNiCuNb16-4) cylinders was about 8 % higher than that of vertically oriented specimens. This is explained by the compound of the individual material layers. *Niendorf et al.* [8] could also demonstrate strong texturing and a preferential direction in the microstructure of 316L stainless steel, which is also expected to cause anisotropic mechanical properties.

In a published round-robin study by *Ahjuja et al.* [9] not only the known anisotropy but also a strong variation of the strength

properties was determined. A similar observation is given in the review article by *Bourell et al.* [1] for the material Ti6Al4V. This shows that the PBF-LB/M process apparently tends to form local pores, defects or cracks when fluctuations occur during the process, which can in combination with the anisotropy of microstructure presumably lead to a strong scattering of the mechanical properties. In principle, such defects could be detected in-situ by process monitoring systems or ex-situ with expensive non-destructive testing like computer tomography (CT). Besides the detection of such defects it is necessary to be able to describe their influence on mechanical properties. Recently some work in this field has been carried out. A good overview is given by *du Plessis et al.* [10]. Here it is stated that the impact of small defects (the authors focus on pores) are mainly presented to be harmless for quasi-static strength properties. Further the authors mention, that the impact of larger pores and the variations of pore manifestations might be detrimental to the mechanical properties and are not well understood. Especially LOF defects on a larger scale (> 500 μm) are reported to reduce strength and ductility. Studies by *Fieres et al.* [11] focus on a combination of CT measurements, static mechanical testings and mechanical simulations to demonstrate that the crack initiation on PBF-LB/M fabricated parts from AlSi10Mg strongly depends on the position of defects. Here CAD models of test specimens (standard tensile rod and an aeronautic part geometry) were modified by implementing defined pore-like cavities within the material volume and the specimens' surface. Number and size of pores were not specified, but vary in three different modifications. The implemented information about the approximate positions of the pores within the CAD model allows to predict the locations where material failure occurs during the mechanical testing. This work presents a useful approach for application related quality control, but demands a hundred percent CT-testing. Furthermore the pore size were in the order of millimeters, randomly distributed within the CAD volume and allow no systematic insight in the dependence of single structural defects on mechanical properties of PBF-LB/M manufactured materials. Additionally, it is unclear how the occurrence of smaller defects within the solidified material is process inherently remelted during the layer-wise build-up of PBF-LB/M.

Wang et al. [12] investigated the effect of geometrical defects on the surface and in form of voids (pore diameters from 0.01 mm to 0.107 mm) on the tensile strength of AlSi10Mg components, fabricated by PBF-LB/M. Therefore, experimental results of tensile tests were compared with uniaxial FEM simulations based on CAD models. The CAD data was modelled as a reconstruction of CT images. The material parameters for the FEM model were taken from the tensile tests, which do not consider the anisotropic behaviour of PBF-LB/M manufactured components. It is shown that the uniaxial simulation performed with this approach matches the experimental results quite accurately, even if the anisotropic material behaviour is disregarded. A comparison of the FEM simulation with the designed and the reconstructed CAD model has shown that process-induced defects decreased the ultimate tensile strength, Young's modulus and yield strength of PBF-LB/M components. *Biswal et al.* [13] developed a isotropic simulative approach for fatigue life prediction of additive manufactured Ti-6Al-4V considering ideal spherical and oblate spherical pore geometries with diameters between 45 μm up to

240 μm . Based on the results of the simulation they concluded that the shape and position of voids are more important to the mechanical properties than the size. The results were not confirmed by real experiments.

Summarized, the known works mostly focus on pores as defects in different numbers and sizes and point out that the shape and form of defects plays a crucial role for the resulting mechanical properties. One main challenge to systematically analyse the effect of structural defects is to categorise and measure the dependencies of different defect types and the macroscopic mechanical response. Up to now no experimental studies on the influence of single isolated structural defects are known. For the sake of in-situ monitoring and control of the process the impact of single, detectable defects is important to derive strategies for in-situ healing by cyclic remelting. This contribution aims to generate first insights in this field.

2. Method

2.1. LBPF manufacturing and testing of tensile specimen

The investigations presented here were carried out with an EOSINT M 270 PBF-LB/M system and the powder material GP1 (X5CrNiCuNb16-4), both distributed by eos GmbH. All tested specimen were manufactured with the PBF-LB/M parameters given in Table 1.

Table 1. Used PBF-LB/M process parameters

Laser Power	Hatch distance	Scanning velocity	Layer height
165 W	0.1 mm	800 mm/s	20 μm

To clarify the question of the behaviour of single local defects during cyclic remelting, defined structural defects in the form of cuboid cavities, are placed in the CAD model of a more cuboid test specimen (see Fig. 2). The cavities are extruded through the CAD model and can therefore be identified on the penetrated sample surface by optical inspection. For this purpose, an Olympus BX 51 light microscope and Stream Essentials software were used. The modified CAD model of the cuboid provides an exact description of the position and size of the inserted cavity and can therefore serve as a reference for optical investigations. The inserted cavities have a rectangular shape and are varied in width and height. Width and height of the square edges were varied between 0.02 mm and 1 mm in steps of different increments (see Table 2).

Table 2. Parameters of the defined structural defects

Parameter	Description	Value range [mm]	Increment [mm]
Δx	defect width	0.02 – 0.1	0.02
		0.2 – 1	0.2
Δz	defect height	0.02 – 1	0.02

To avoid mutual influences of the defects within the component structure, a distance of 0.5 mm is maintained between the individual defects in x -direction and a distance of 0.2 mm in z -direction. In addition, an offset in the x - and z -directions is provided. In order to bring similar thermal loading cycles to the test body's upper defects, a material impact of 2 mm (corresponds to one hundred layers) above the defect is provided. All specimen in this work were built with identical

process parameters. The defect height z is kept constant for each specimen built. The defect width x is varied. For statistical verification, each defect geometry is inserted three times. Thus, a total of 10 cuboid test objects with 3×10 defects are examined. The remaining of defects is investigated by light microscopy. In this way, the deviations from the original defect shape caused by the cyclical re-melting can be determined and estimated. This provides information about the possibility of healing individual defects by re-melting.

Based on these findings, a test design for the production of defined faulty tensile specimens is created. For these investigations only horizontally oriented tensile test specimens are built (polar angle 90°). Anisotropy effects are therefore not investigated. According to the previous method for placing structural defects into PBF-LB/M specimen, defined cavities are placed in the middle of the tensile specimens' CAD model. In contrast to the cuboids previously considered, isolated cube-shaped defects with an varying edge length are now inserted into the center of the CAD model. Additionally, to the defined faulty tensile rods, reference rods without any structural defects were produced and tested in the same way. The placement of the samples within the build chamber and the PBF-LB/M production is carried out according to VDI 3405-2 [14]. For statistical validation, the faulty tensile specimens are set up in three identical PBF-LB/M processes. The tensile rods produced in this way are machined into the tensile test specimen form according to DIN 50125 - B 5 x 25. The tensile tests were carried out in accordance with DIN EN ISO 6892-1. In the evaluation of the tensile tests, the cross-sectional reductions caused by the structural defects introduced were not taken into account. The diagrams obtained from the tests thus show the technical strain rather than the true strain. It can therefore be assumed that the cross-sectional reduction of the faulty samples in comparison to the reference sample has led to tendentially lower stress curves, which was not considered in the evaluations. The determined strength values thus tend to be too low and are significantly higher in reality, especially for larger defect sizes.

2.2. Quasi static simulation of tensile tests

The uniaxial static mechanical simulation was performed using the FEM software ANSYS 19R2. The material parameters for the multilinear isotropic solidification model were determined within tensile testing of specimen without defects (E-Modulus: $E = 178 \text{ GPa}$, tensile strength: $R_m = 956 \text{ MPa}$, yield strength: $R_{eH} = 676 \text{ MPa}$). Poisson's ratio of 0.3 [11,15] as a common choice for steels and density of $7,8 \text{ g/cm}^3$ [15] were taken from literature to complete the model. The known anisotropy of PBF-LB/M components was not considered in order to keep model complexity and computational time low. In this case the results of the simulation are dependent on the building direction of the examined tensile rods and can therefore not be transferred to other sample orientations. A CAD model of the faulty and the reference tensile specimens was created for each simulation carried out. Tetrahedron geometries in size of 3 mm were used to mesh the model. Starting from the symmetry plane (B), where the defects are located, mesh density was enhanced to an element size of 0,15 mm with $C = 3.5 \text{ mm}$ (Fig. 1). In order to optimize the calculation time and due to symmetry, only half

of the symmetrical tension rods were simulated. As in the tensile testing, a constant shift ($A = 3,36 \text{ mm}$) was applied on the thread of the tensile rod in X-direction (see Fig. 1). The shift was calculated using the elongation at break which was determined in the tensile testing. Thus, the applied displacement corresponds to the real movement until failure in the tensile test. For the simulation of the equivalent stress and the main stress vector the sparse direct solver (SDS) was used.

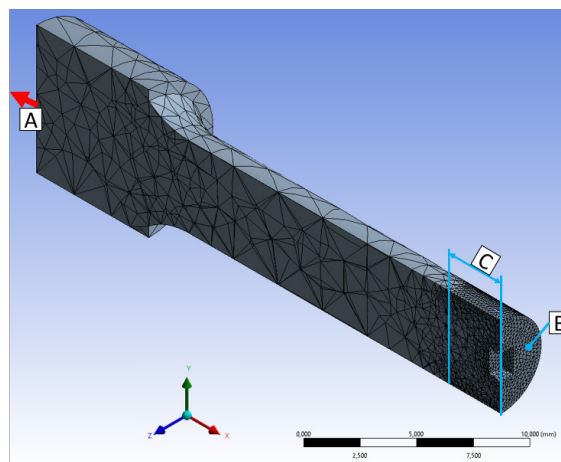


Fig. 1. Sectional view along the axis of the simulation model "1.5", A: Shift in x-direction, B: symmetry plane, C: Area with adjusted element size

3. Results

3.1. Influence of the PBF-LB/M layer build-up on the remaining of defined defects

Fig. 2 shows a section of a prepared test body with a defect height $z = 0.2 \text{ mm}$ compared to the underlying CAD model. The lower defects, up to a width of $x = 0.06 \text{ mm}$, are remelted by the further layer structure and are no longer detectable in the component structure (not shown in Fig. 2). Only from a width of $x = 0.1 \text{ mm}$ can at least one of the three defects still be detected in the microsection. As the width of the defect increases, ever larger, contiguous pore structures become visible, which, however, are also remelted and closed in partial areas. It should also be noted that the previously rectangular defect geometry has shrunk as a result of the further layer build-up and no longer has sharp edges. In all defects, a rounded shape forms, which can be seen in the microsection as a single pore or as a series of two or more pores, which is comparable to known LOF defects. The resulting pore shape is also different for defects with the same geometric dimensions. Looking at the scale and the marked defect in Fig 2, it is noticeable that the visible defect width is only about 60 % of the previously applied defect width.

The light microscopic evaluation of the remaining test objects shows that up to a defect height of $z = 0.06 \text{ mm}$, no remaining porosity can be detected in the microsection. It can therefore be assumed that up to 0.06 mm of unmelted material can be remelted inherently during PBF-LB/M and solidify to a defect-free material composite.



Fig. 2. Comparison of a section of the prepared test specimen (left side) with the volumetric cavities placed in the CAD model (right side).

On the basis of the light microscopic images taken, the remaining severity of the defects can be qualitatively assessed by a system of indicators. Here, the defect characteristic is valuated with a number from 1 to 10, where 10 represents the highest remaining characteristic and the defect at 1 can no longer be recorded optically. This subdivision is shown as a false colour representation in Fig. 3 and shows that the whereabouts of the defects can be divided into three different categories.

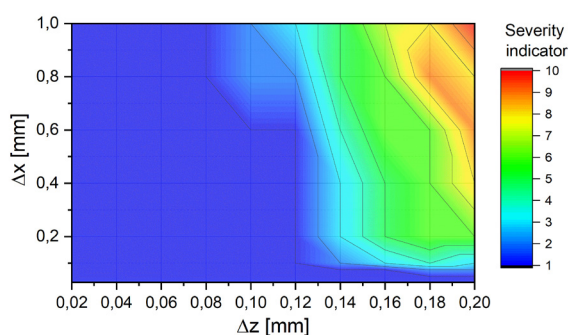


Fig. 3. False colour representation of the severity indicator system used to describe the defect remaining as a function of the defect width Δx and height Δz .

The defects are completely healed in the blue area (category 1, severity 1 to 3). This is the case for a defect height of up to $z = 0.06$ mm (corresponds to three layers). For larger defect heights (up to $z \leq 0.1$ mm, corresponds to five layers), no impairment of the material compound can be detected up to a defect width of $x = 0.6$ mm. Only when the parameters of the defects exceed $x = 0.6$ mm and $z = 0.12$ mm they can be detected in the light microscope as LOF pores with diameters from $5 \mu\text{m}$ to $20 \mu\text{m}$. These are assigned to an indicator range of 2 to 5 and are remelted in a transition area (category 2, light blue to green area in Fig. 3) such that the resulting defect size within the microstructure is significantly smaller than the previously introduced geometric defect. If the defect parameters continue to increase, larger, contiguous pores in the microstructure are recognizable, which deviate from the introduced geometric defect by less than 50 % in terms of their area and are partially filled with powder. Those kinds of LOF defects are assigned to an indicator range greater than 5 (category 3, yellow to red area in Fig. 3).

3.2. Influence of defect categories on static strength

As described in section 2.1 the influence of isolated defects on tensile strength is investigated by placing cube-shaped structural defects into the center of cylindrical tensile rods. The previously determined error categories are utilized in 4 tensile specimens, each with different gradations of the error dimensions. For specimen 1 to 4 defect edge length was varied from 1.5 mm to 0.75 mm in steps of 0.25 mm (category 3). Specimens 5 to 8 contained defects with an edge length of 0.5 mm to 0.2 mm with an increment of 0.1 mm (category 2). For specimens 9 to 12 the smaller defects in the order of 0.1 mm to 0.025 mm were applied, providing an increment of 0.025 mm (category 1). Fig. 4 shows the determined mean tensile strength R_m values as a function of the defect edge length.

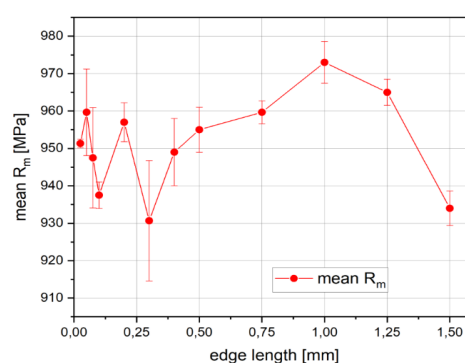


Fig. 4. Determined tensile strength values R_m as a function of the defect edge length of the geometric defect inserted in the center. The diagram shows the mean values and standard deviations from each of the three test series

For defect categories 1 and 2 no certain course of the R_m value data points can be seen. The values vary between 915 MPa and 972 MPa, and thus within the value range of 930 ± 50 MPa specified in the material data sheet [15]. From a defect edge length of 0.75 mm, a slight increase in the tensile strength values and a simultaneous decrease in the scattering can be seen. The spread of the measured values is now between 6 MPa and 12 MPa. At a defect volume of 1 mm^3 , the highest mean tensile strength value ($R_m = 978$ MPa) was determined for the specimen from the third build process V03. The two further samples with a defect volume of 1 mm^3 from the build processes V02 and V01 also achieve high values for tensile strength. Only with the largest defect edge length of 1.5 mm is a significant reduction in tensile strength observed, with still low standard deviation. However, the values determined here remain within the range specified in the material data sheet.

Fig. 5 presents the upper yield strength values R_{eH} determined from the same test series. Since X5CrNiCuNb16-4 has a pronounced upper and lower yield point, the transition from elastic to plastic material behavior can be determined using the upper yield point R_{eH} . The results show R_{eH} values in the range of 680 MPa with some lower scattering for category 1 and category 2 samples (edge length between 0.025 mm and 0.5 mm). With increasing edge length a significant decrease of R_{eH} can be observed. The reference value for R_{eH} given in the eos datasheet is 586 ± 50 MPa [15].

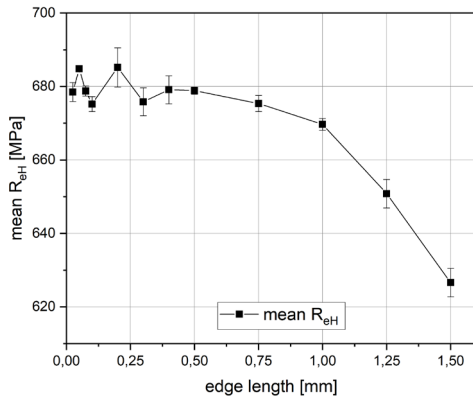


Fig. 5. Determined upper yield strength values R_{eH} as a function of the defect edge length of the geometric defect inserted in the center. The diagram shows the mean values and standard deviations from each of the three test series

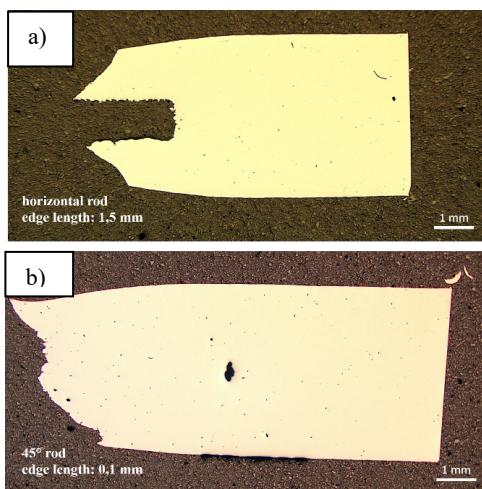


Fig. 6. Prepared test specimens from the fracture point of the tensile specimens. a) defect with an edge length of 1.5 mm is elongated by the plastic deformation and lies within the fracture surface. b) fracture near a defect of 0.1 mm edge length.

An examination of the fracture surfaces showed that not all samples are torn at the defect. Through a cutting and grinding preparation of the fragments it could be shown that especially with a defect length greater than 1 mm the fracture occurred within the inserted defect (Fig. 6a). In that case the defect zone showed strong plastic deformation. For category 1 and 2 samples are torn in the immediate vicinity of the defect (see Fig. 6b). Here most specimen showed a flat or 45° sloped fracture surface, which indicates moderate ductile fracture behavior. Some specimens of these categories also showed cup and cone fracture manifestations.

3.3. Results of the quasi-static simulation of tensile tests

Fig. 7 shows selected results from quasi-static mechanical simulations. From top to bottom the respective results of a defect length of 0.1 mm, 0.3 mm, 1 mm and 1.5 mm are shown. In column a) the calculated von Mises equivalent stress distribution is displayed. Here it can be seen that with increasing defect size, a stronger notch effect emanates from the structural defects introduced, which leads to locally increased equivalent stresses in the area of the structural defect. The spatial distribution of equivalent stress is highest directly

next to the inserted defect. Above the defect, respectively in tension direction only low equivalent stresses are computed.

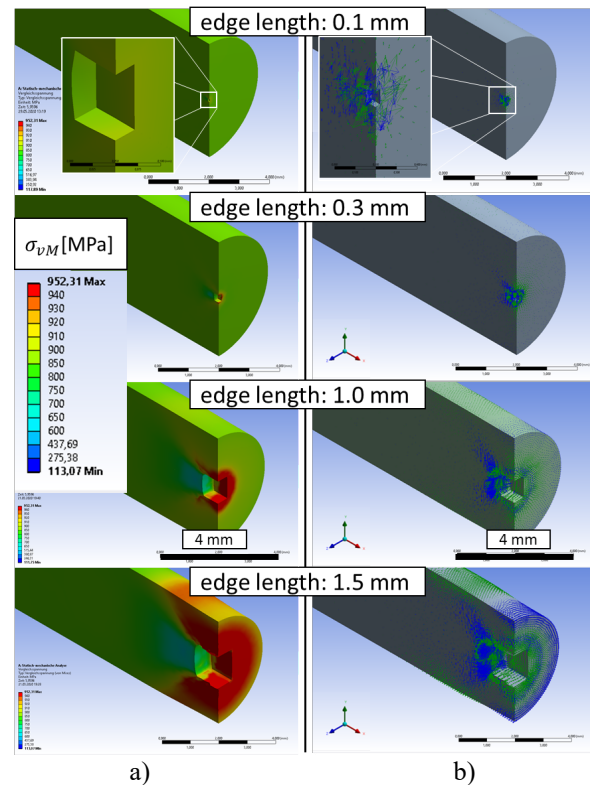


Fig. 7. Results from quasi-static mechanical simulation, displayed after a defined time of 5.96 s for selected defect edge lengths. a) von Mises equivalent stress distribution in the vicinity of the structural defects. b) main stress vectors in y- (blue) and z-direction (green)

Column b) of Fig. 7 shows the computed main stress vectors in y- (blue) and z-direction (green). The main stress direction was the x-direction in the chosen coordinate system. X-direction tension vectors are not shown in Fig. 7b for the sake of overview. The existence of structural defects in the centre of the tension specimens, which is where the highest plastic strains and stress components occur during tensile testing, causes additional stress components in different directions. This phenomena is also known from theory of notch effects.

4. Discussion

The presented experimental results from tensile tests show that single defined structural defects have only a low impact on R_m and R_{eH} . The results of the simulation suggests that the defects introduced have an effect on the expression of the stress states. During tension load of metal alloys with a distinct upper and lower yield strength the materials plastification starts when R_{eH} is reached. The fact that R_{eH} does not significantly change for increasing edge length of defect categories 1 and 2, but decreases for bigger defects (category 3) shows that plastic deformation behavior starts at an earlier timestep during the tension load for larger isolated LOF deftees. This might result in a deviating plastification process. Tensile specimens without structural defects achieve maximum stress and strain manifestation values in the center. As the center of the sample has a structural defect, stress and strain maxima might be shifted to other material regions. According to the FEM results the location of the stress and strain load within these regions

varies in dependence of defect size. For smaller defects (< 1 mm) the region of local stress and strain maxima is shifted above the defect location and is oriented in 45° direction towards the specimens surface (compare row 3 in Fig. 7 and Fig. 6 b). For defects with an emergence above an edge length of 1 mm stress and strain maxima are extended to the sample surface. The FEM studies carried did not consider the real defect shape after remelting or inner powder material, so that slightly different maxima will appear in reality. Anyway, this may induce that material strengthens within the entire cross section under high flow stresses with high plastic deformation, resulting in a slight increase in the determined tensile strength. Furthermore for tensile tests a uniaxial stress state exists until necking occurs. At this point, very different strains and stress distributions occur within the sample. The increase in plastic deformation and the resulting increase in yield stress is generally referred to as strain hardening and can be pronounced differently depending on the material properties. For PBF-LB/M materials the strain hardening phenomena are not well investigated and may be a crucial requirement for understanding the observed values for R_m and R_{eH} . Additionally the structural conditions caused by the defined defects inside the PBF-LB/M material and the resulting complex stress states can provide an explanation for the strength values determined. However, the explanation of the exact failure mechanisms and the statistically verified confirmation of these first explanation approaches require further experimental and numerical investigations, which should also examine if the anisotropic material behavior or trapped powder material contributes to the plastic deformation processes during tension load.

5. Conclusion

Metallographic investigations of cuboid PBF-LB/M geometries with defined structural defects have shown that these are remelted and healed by the cyclic thermal layer build-up to a height of 0.1 mm. Based on the optical inspection of defined faulty cross sections three categories of defects were defined. Based on this categorization defined faulty tensile specimens were built for each category and tested. The results of the tests have shown that the individual geometric defects in the tensile specimens do not lead to a drastic reduction in tensile strength. The values determined were all within the range specified in the material data sheet. In addition, it was found that the upper yield strength only decreases for huge defects (> 1mm edge length). First explanation approaches for these observations were proposed: The determined yield strength values show that plastic material behavior starts earlier for structural defects > 1 mm. It is assumed that additionally the structural defects inside the specimen significantly influence the strain and stress distributions and result in complex multi-axial stress states. These may influence strengthening mechanisms in the area of uniform elongation and exert to affect necking. The combination of those effects may be the cause of the resulting strength values. Further studies are needed to determine the PBF-LB/M specific strain strengthening laws. The mechanical simulation model does not consider PBF-LB/M typical anisotropic properties and should therefore be improved in future works. A combination of the

presented methodology with CT-investigations could provide a deeper insight into the real geometric manifestation of structural defects.

Acknowledgements

The authors thank the student assistants Jannik Bäcker, Eduard Hulm and Lukas Pieper for conducting the experimental investigations.

References

- [1] Bourell D, Kruth JP, Leu M, Levy G, Rosen D, Beese AM, Clare A (2017) Materials for additive manufacturing. CIRP Annals - Manufacturing Technology.
- [2] Sehr J (2010) Static Strength Analysis of Beam Melted Parts Depending on Various Influences. in Bourell et al., (Ed.). Proceedings of the 20th international Solid Freeform Fabrication Symposium, pp. 407–414.
- [3] Rehme O (2010) Cellular Design for Laser Freeform Fabrication. Schriftenreihe Lasertechnik.
- [4] Carlton HD, Haboub A, Gallegos GF, Parkinson DY, MacDowell AA (2016) Damage evolution and failure mechanisms in additively manufactured stainless steel. Materials Science and Engineering: A 651:406–14.
- [5] Dai D, Gu D (2015) Effect of metal vaporization behavior on keyhole-mode surface morphology of selective laser melted composites using different protective atmospheres. Applied Surface Science 355:310–9.
- [6] Ly S, Rubenchik AM, Khairallah SA, Guss G, Matthews MJ (2017) Metal vapor micro-jet controls material redistribution in laser powder bed fusion additive manufacturing. Sci Rep 7(1):127.
- [7] Carter, L. N., Martin, C., Withers, P. J., Attallah, M.M., The influence of the laser scan strategy on grain structure and cracking behaviour in SLM powder-bed fabricated nickel superalloy, in Journal of Alloys and Compounds 615 2014, pp. 338-347
- [8] Niendorf T, Leuders S, Riemer A, Richard HA, Tröster T, Schwarze D (2013) Highly Anisotropic Steel Processed by Selective Laser Melting. Metall and Materi Trans B 44(4):794–6.
- [9] Ahuja B, Schaub A, Junker D, Karg M, Tenner F, Plettke R, Merklein M, Schmidt M (2016) A ROUND ROBIN STUDY FOR LASER BEAM MELTING IN METAL POWDER BED. SAJIE 27(2).
- [10] du Plessis A, Yadroitsava I, Yadoitsev I, Effects of defects on mechanical properties in metal additive manufacturing: A review focusing on X-ray tomography insights, in Materials and Design, 2019, <https://doi.org/10.1016/j.matdes.2019.108385>
- [11] Fieres, J; Schumann, P; Reinhart, C; Predicting failure in additively manufactured parts using X-ray computed tomography and simulation. Fatigue Design. 2017, 69-78.
- [12] Wang, P.; Lei, H.; Zhu, X.; Chen, H.; Influence of manufacturing geometric defects on the mechanical properties of AlSi10Mg alloy fabricated by selective laser melting. Journal of Alloys and Compounds 789 2019 pp. 852-859
- [13] Biswal R, Syed A. K., Zhang X, Assessment of the effect of isolated porosity defects on the fatigue performance of additive manufactured titanium alloy, in Additive Manufacturing, 2018, <https://doi.org/10.1016/j.addma.2018.08.024>
- [14] Verein Deutscher Ingenieure e.V. (2013) VDI 3405 Blatt 2, Additive Fertigungsverfahren: Strahlschmelzen metallischer Bauteile - Qualifizierung, Qualitätssicherung und Nachbearbeitung. Beuth Verlag GmbH, Berlin.
- [15] N.N. Materialdatenblatt GP1. www.eos.info (accessed on 25.11.2017)

11th CIRP Conference on Photonic Technologies [LANE 2020] on September 7-10, 2020

Metallographic study of denudation in laser powder-bed fusion

R. S. Khmyrov^a, R. R. Ableeva^a, A. V. Gusarov^{a,*}

^aLaboratory of 3D Structural and Functional Engineering, Moscow State University of Technology STANKIN, Vadkovsky per. 3a, 127055 Moscow, Russia

* Corresponding author. Tel.: +7-499-973-3961. E-mail address: av.goussarov@gmail.com

Abstract

Recent experiments on laser powder-bed fusion (L-PBF) revealed intensive transport of powder particles in the gas phase and on the surface due to a gas flow indicating that it is the key mass-transfer process, understanding of which is important for optimizing and controlling the L-PBF. In the present work, the width of the so-called denuded zone formed around the fused bead as the result of powder transport is measured as function of the powder material and particle size. An original technique is proposed to fix non-consolidated particles on the substrate surface to visualize the denuded zone in the cross-section. To understand the influence of the gravity force, two materials of different specific mass are compared, cemented carbide and aluminum bronze. A theoretical analysis of inter-particle forces explains the measured dependencies of the denuded width versus the particle size.

© 2020 The Authors. Published by Elsevier B.V.

This is an open access article under the CC BY-NC-ND license (<http://creativecommons.org/licenses/by-nc-nd/4.0/>)

Peer-review under responsibility of the Bayerisches Laserzentrum GmbH

Keywords: additive manufacturing; evaporation; heat and mass transfer; laser powder-bed fusion; selective laser melting

1. Introduction

Powder-bed additive manufacturing has found industrial use. However, detailed physical mechanisms governing the process have not been completely understood, which restricts our possibilities for optimizing and controlling it. For example, in 2007 Yadroitsev *et al.* [1] first described the denudation effect in the interaction of a laser beam with a powder bed. Further studies, see [2,3], indicated that the denudation is very common in laser powder-bed fusion (L-PBF). For about a decade, the existing theoretical approaches could not explain why the melt pool attracts powder particles from the distance of several particle diameters. Over the years, it has become clear that spatter formation and two-phase gas-particle flow above the melt pool are also common in L-PBF [4]. In 2016 Matthews *et al.* [5] observed a motion of powder particles toward the melt pool. They supposed that a vapor jet emerging from the laser spot induces an entrainment flow in the ambient gas, which drags powder particles around the melt pool. Such a gas-phase flow can naturally explain both the denudation and the spattering [6].

Recent experimental and theoretical studies confirm the hypothesis of the evaporation-induced gas flow. Zhirnov *et al.* [7] could measure the velocity of powder particles on the substrate and estimate the velocity of the vapor jet. Podrabinnik *et al.* [8] used interferometry to visualize the jet. Gunenthiram *et al.* [9] visualized the zone of spatter formation and showed how the gas flow captures powder particles. Bidare *et al.* [10,11] comprehensively analyzed the influence of L-PBF parameters on spatter transport. Numerical simulation of laser evaporation and vapor and ambient gas flow at L-PBF [5,8,10,12] gives the flow fields consistent with the experimentally observed velocities of particles on the substrate [7] and in the gas phase [9-11] and the jet flow velocity [7,8]. Gusarov [13,14] found a similarity solution of the Navier-Stokes equations for a jet emerging into a half-space and validated it for the conditions of L-PBF. In summary, the above-mentioned works demonstrate the importance of the evaporation-induced two-phase gas-particle flows in mass transfer in the laser-interaction zone at L-PBF.

The acquired knowledge indicates that the evaporation-induced gas flow is not very sensitive to such process

parameters as the laser beam power and the scanning speed. A slight widening of the denuded zone with the energy density was only noticed [1,2]. The experiments in various gas atmospheres [10] and at low [5] and high [11] pressure revealed a significant impact of the ambient-gas parameters. In particular, the denuded zone widens considerably with decreasing the ambient pressure [5]. This result seems to be paradoxical because the denudation, which is the result of a gas flow, increases with the decrease of the gas density. However, the similarity law of viscous jet flows explains it. It is known that the physical values with the dimension of pressure are proportional to [15]

$$\eta^2/(\rho r^2), \quad (1)$$

where η is the dynamic viscosity of the gas, ρ the gas density, and r the distance from the jet source. This law is applicable to the shear stress arising on the powder bed surface due to the ambient gas flow induced by the evaporation jet [13,14] (see Fig. 1). Note that the dynamic viscosity of gases is practically independent of pressure [16]. Thus, one can obtain from Eq. (1) that the shear stress increases with the decrease of pressure because density ρ is proportional to the pressure. This is why the drag force applied to a powder particle on the top of the powder bed increases with decreasing the ambient pressure. Therefore, the denudation increases with decreasing the pressure too.

The gravity, Van der Waals adhesion and friction forces are the principal ones governing rearrangement in powder beds [17]. They normally balance the gas-flow drag force applied to the particles on the top of the powder bed. According to Eq. (1), the drag force sharply increases with approaching to the evaporation spot. At a certain distance, it can overcome the sum of the gravity, adhesion, and friction forces, which hold particles in their places. This distance determines the denuded width. The mentioned inter-particle forces depend on the particle size and shape and the material density, Hamaker constant, and friction coefficient [18]. Thus, the denuded width should depend on the material properties and particle granulometry and morphology and can characterize the inter-particle forces in the given powder. The influence of powder parameters on the denudation in L-PBF have not been systematically studied. The present work attempts to bridge this gap. The aim is to compare denudation for powders with quite different mean particle size and for materials with quite different density.

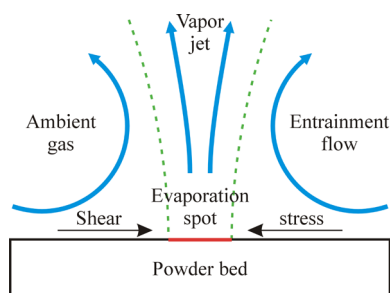


Fig. 1. Vapor jet induces an entrainment flow in the ambient gas, which tends to drag the top of the powder bed toward the evaporation spot.

2. Materials and methods

Table 1 lists two powder materials, aluminum bronze and cemented carbide, produced by Oerlikon Metco [19], which are chosen for the present study because of a considerable difference in density [20]. The different density and chemical composition imply a different ratio between the gravity and the adhesion forces. Each powder was sieved to obtain a fine and a coarse size fractions (see the last column in Table 1). Figure 2 shows the four selected powders. According to the images, each powder has a narrow size distribution, a high content of spherical particles, and a low content of satellites and dust.

Table 1. Powder materials.

Material	Composition, wt%	Density, g/cm ³	Particle size (μm)
Bronze	Cu 10Al [19]	7.5 [20]	Fine:0-20; Coarse:50-63
WC-Co	WC 12Co [19]	14.3 [20]	Fine:0-20; Coarse:50-63

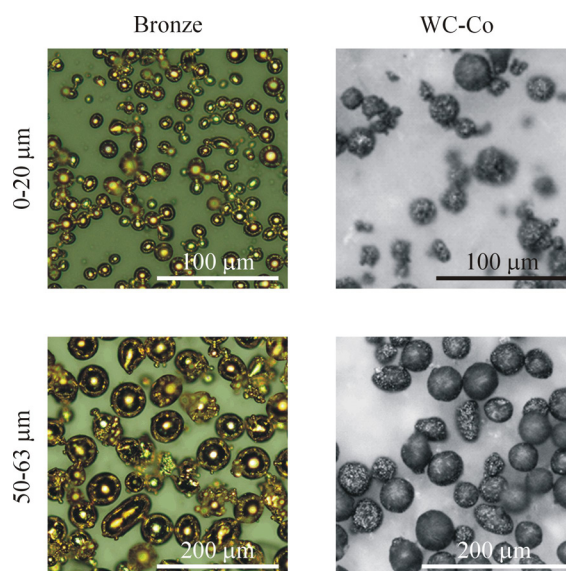


Fig. 2. Four studied powders of bronze (left) and cemented carbide (right) with particle size in the range of 0-20 μm (top) and 50-63 μm (bottom).

Table 2. Laser processing parameters.

Wavelength	Spot diameter	Beam power	Scanning speed
1064 nm	100 μm	170 W	50 mm/s

Substrates of low-carbon steel are covered with 100 μm thick powder layers in an L-PBF machine. Laser beam with the parameters listed in Table 2 scan the powder/substrate sample to obtain separated tracks. The same laser parameters and substrate material assure similar thermal conditions in the laser/interaction zone and, hence, similar flow field in the gas phase. The present work aims to obtain cross sections of the single tracks visualizing not only the substrate and the fused bead but also the distribution of the non-treated powder over the substrate surface. That is why the powder is fixed with hot melt glue just after the laser processing. Then, the samples are cut to obtain cross-sections. The laser tracks are often non-uniform in lengths. To gather more objective information, several cross-sections of a track are studied. They are prepared

by consecutive grinding of the initial sample with the increment in depth of around 0.5 mm. The cross-section micrographs are taken by an optical microscope.

3. Results

Figure 3 shows typical top views of the laser-processed samples. One can distinguish the fused bead, the non-treated powder, and the bright-contrast substrate visible through the denuded zones on the sides of the bead. The fused beads are uniform in length while the denuded zones are not. It can be explained by highly variable inter-particle forces depending on the size and the morphology of particles. Visually, the denuded zone of the coarser powder is wider than that of the finer powder. However, there are qualitative differences. The boundary between the denuded zone and the powder layer is sharp for fine powders 0-20 μm and diffuse for coarse powders 50-63 μm . The coarse powder can rearrange due to the gravity force after removal of its portion by the gas flow. This is why it is better to speak about the volume of the removed powder but not about the denuded width. Figure 4 shows the cross sections of the laser-processed samples, which visualize the volume of removed powder.

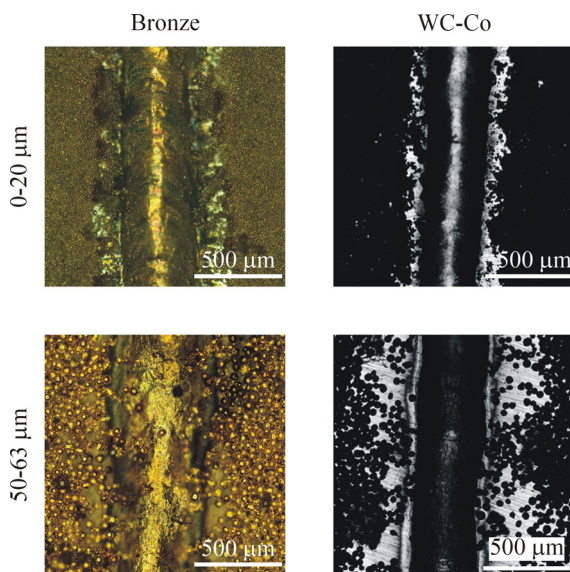


Fig. 3. Top views of the tracks obtained with powders of bronze (left) and cemented carbide (right) with the particle size indicated on the left.

To analyze the cross sections, they are divided into small vertical bands as shown in Fig. 5. Figure 6 shows the number of powder particles n (left axis) in every band as function of the lateral coordinate y . The linear number density of particles ν (right axis in Fig. 6) is calculated as the number of particles per unit length in the lateral direction. The obtained profile $\nu(y)$ quantifies powder redistribution around the laser track. In particular, the profile shown in Fig. 6 confirms that the denuded zone has no well-defined boundaries in the considered case of 50-63 μm WC-Co powder. The particle density gradually changes in the interval 0.5 mm $< |y| < 1$ mm. No powder redistribution is observed at $|y| > 1$ mm. The mean particle density in this domain ν_0 estimates the density of the powder layer before laser processing. For example, a value ν_0

$= 42.5 \text{ mm}^{-1}$ is obtained from the data of Fig. 6. One can estimate the number of removed particles N as integral

$$N = \int (\nu_0 - \nu) dy, \quad (2)$$

over the interval including the domain disturbed by laser processing, $-1 \text{ mm} < y < 1 \text{ mm}$ in the considered case.

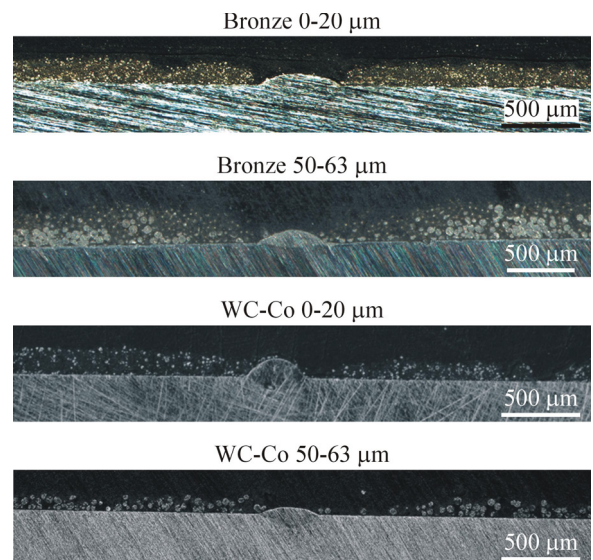


Fig. 4. Cross sections of the laser track visualizing the substrate, the fused bead, the denuded zone, and the non-treated powder.

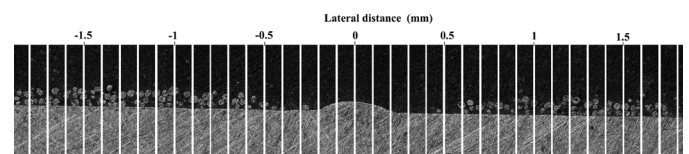


Fig. 5. Vertical grid superposed on the cross section of a laser-processed sample with 50-63 μm WC-Co powder. The grid step is 100 μm .

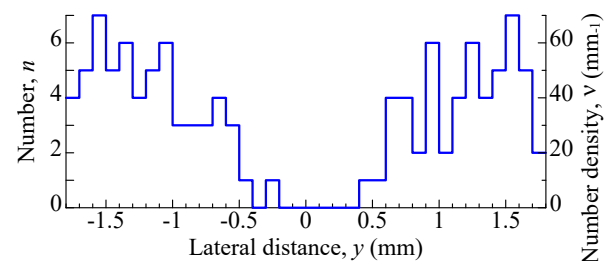


Fig. 6. Lateral profile of powder: number of particles in a 100 μm band n and linear number density ν .

Note that the introduced number of removed particles N depends not only on the impact of the laser processing but also on the powder layer thickness and the particle size. To exclude the influence of the two latter factors, we define the effective denuded width as

$$w = N / \nu_0. \quad (3)$$

It would be the distance between the opposite boundaries of the denuded zone if they were sharp. This definition does not distinguish the denuded domains on the left of the fused bead and on the right of it (see Fig. 3). The denuded width is

measured from the left boundary of the left domain to the right boundary of the right one over the fused bead. Table 3 lists the results of the analysis for the four studied powders. The denuded width is calculated for 6-7 different cross-sections of laser-processed sample. The last two rows of Table 3 show the mean width and its mean-squared deviation for each powder. Figure 7 plots the denuded width versus the particle size. For bronze powder, the observed variation of the width with the particle size is within the confidence interval of a measurement (see the vertical bars in Fig. 7). For WC-Co powder, denuded width confidently increases with the particle size.

Table 3. Effective denuded width, w (μm).

Number of cross section	Bronze 0-20 μm	Bronze 50-63 μm	WC-Co 0-20 μm	WC-Co 50-63 μm
1	402	657	529	771
2	702	800	610	814
3	771	608	680	1088
4	475	645	792	1042
5	736	843	617	1005
6	749	719	540	800
7	-	684	677	-
Mean	639	708	635	920
Mean squared error	159	86	91	140

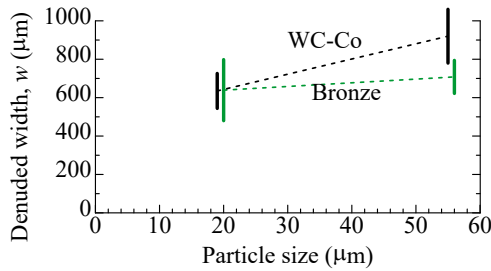


Fig. 7. Measured denuded width versus particle size for WC-Co (black) and bronze (green) powders. Vertical bars show the mean square deviation.

4. Discussion

Consider forces applied to a spherical powder particle on a substrate as shown in Fig. 8. This idealized sketch neglects the interactions of a particle with other particles of the powder bed. Such interactions are similar to the interaction of a particle with the substrate. Therefore, this approach is useful to understand the force balance. The gravity force is

$$F_g = g\rho_p \frac{\pi d^3}{6}, \quad (4)$$

where g is the gravity acceleration, ρ_p the mass density of particle material, and d the particle diameter. The adhesion force is [21]

$$F_a = \frac{Ad}{12\varepsilon^2}, \quad (5)$$

where A is the Hamaker constant and ε the gap between the sphere and the substrate. Both the gravity and the adhesion

forces are directed downwards (see Fig. 8). The normal reaction force balances their sum.

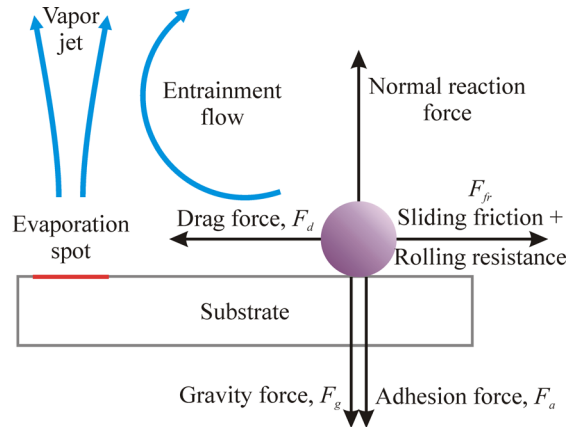


Fig. 8. Forces applied to a powder particle at L-PBF.

The drag force arises due to the entrainment flow of the gas toward the evaporation spot (see Fig. 8). It is estimated as the projected area of the particle $\pi d^2/4$ multiplied by the shear stress τ on the substrate surface due to the gas flow,

$$F_d = \tau \frac{\pi d^2}{4}. \quad (6)$$

The drag force is directed toward the evaporation spot and balances the friction force (see Fig. 8). The shear stress on the surface is given by the similarity solution for a point-source jet emerging into a half space [13,14] as

$$\tau = c \frac{\eta^2}{\rho r^2}, \quad (7)$$

where η is the dynamic viscosity of the gas, ρ the gas density, r the distance between the evaporation spot and the particle, and c the dimensionless constant of the similarity solution, which increases from zero to its limit value $c_0 \approx 15.2894$ when the Reynolds number Re of the vapor jet increases from zero to infinity [13].

The Reynolds number of the vapor jet in L-PBF is of the order of $Re = 10^3$ or greater [5-7]. At such high values of Re , constant c is very close to its maximum possible value c_0 , the deviation being estimated as [13]

$$c_0 - c = \frac{2450}{Re^2}. \quad (8)$$

If the energy density increases at L-PBF, evaporation becomes more intensive and the Reynolds number can considerably increase. However according to Eqs. (6)-(8), the drag force remains practically constant around its limit value. The issue is that with the increase of the jet Reynolds number, the entrainment flow saturates [22]. It was experimentally proven [23]. That is why the stress on the surface saturates too. The saturation of the entrainment flow explains, in particular, why the denudation is not sensitive to the laser power and the scanning speed in L-PBF. A slow widening of the denuded zone with the power density observed [1,2] is rather due to the widening of the evaporation spot.

For the saturated entrainment flow, combining Eqs. (6)-(8) gives the drag force independent on the process parameters,

$$F_d = c_0 \frac{\eta^2 \pi d^2}{\rho r^2 4} . \quad (9)$$

This equation shows that the drag force sharply increases with approaching to the evaporation spot. At a certain distance r , the drag force becomes greater than the combined friction and rolling resistance force F_{fr} that holds the particle on its place. The gas flow removes all particles within this critical distance, which determines the denuded width.

The considerable redistribution of the coarse powder particles over the denuded zone shown in Fig. 3 suggests that they can roll under the convective forces. In the combined translational/rotational motion, one should account for both the sliding friction and the rolling resistance. The both components are proportional to the normal force while the rolling resistance coefficient can be much less than the sliding friction coefficient [24]. The maximum force holding the particle on its place is a fraction of the normal force,

$$F_{fr} = \mu(F_g + F_a) , \quad (10)$$

where μ is the effective coefficient taking a value somewhere between the rolling resistance and sliding friction coefficients. Therefore, the balance equation $F_d = F_{fr}$ to find the critical value of r becomes

$$F_d = \mu(F_g + F_a) . \quad (11)$$

Note that the adhesion force F_a , Eq. (5), is proportional to the particle diameter d , the drag force F_d , Eq. (9), is proportional to the particle diameter squared d^2 , and the gravity force F_g , Eq. (9), is proportional to the particle diameter cubed d^3 . Therefore, at small d , the gravity force is negligible in Eq. (11), and the critical distance r is essentially determined by the balance between the drag force and the adhesive force. At great d the adhesive force is negligible in Eq. (11), and the critical distance r is essentially determined by the balance between the drag force and the gravity force.

One can obtain from Eq. (11) that for fine powders with small d , the critical distance in the denuded zone r is

$$r^2 = 3\pi \frac{c_0 \eta^2 \varepsilon^2}{\mu \rho A} d . \quad (12)$$

Similarly, for coarse powders with great d ,

$$r^2 = \frac{3 c_0 \eta^2}{2 \mu g \rho \rho_p} \frac{1}{d} . \quad (13)$$

Thus, the critical distance r increases proportional to the square root of d at small d and decreases inversely proportional to the square root of d at great d . One can suppose that it attains maximum at intermediate values of d where the adhesive force is comparable with the gravity force. In the framework of the point-source similarity approach, the experimentally measured denuded width w is estimated as double critical distance r . However, the evaporation spot size can be not negligible in L-PBF. The comparison of the similarity point-source approach with numerical calculations

for finite-size evaporation spot [14] indicates that in the latter case Eq. (7) is still applicable but distance r in Eq. is rather the distance from the border of the evaporation spot. In view of the above, Fig. 9 presents the structure of the denuded zone. According to this structure, the denuded width is

$$w = S + 2r , \quad (14)$$

where S is the evaporation spot diameter. Term S contributes to the dependence of the denuded width on the laser power and scanning speed. The critical distance r is essentially independent of the laser parameters but depends on the particle size d and the parameters of inter-particle interaction according to Eqs. (9) and (10).

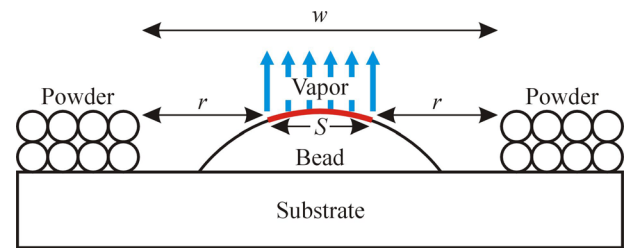


Fig. 9. Denudation zone structure: evaporation spot diameter S , critical distance r , and denuded width w .

The experimentally observed widening of the denuded width with the particle size for WC-Co (see Fig. 7) qualitatively corresponds to Eq. (12) obtained in assumption that the gravity force is considerably lower than the adhesive force. Therefore, one can conclude that in the studied WC-Co powders the adhesive force is more important than the gravity one. No clear dependence of the denuded width versus the particle size is found for the bronze powder (see Fig. 7). According to the above theoretical consideration, this may indicate that the adhesive force is comparable with the gravity force in the considered bronze powders. The accomplished experimental study of the denudation and the theoretical analysis reveals the contribution of various inter-particle forces and the influence of the particle size and material parameters. The measurement and the theoretical prediction of the denuded width are useful to quantify the transport of powder particles by the gas flow, which considerably contributes to the mass transfer in the laser-interaction zone at L-PBF. Understanding of such basic physical processes is necessary for optimising L-PBF and adaptation of the processing parameters for specific powder materials.

5. Conclusions

An original metallographic technique is developed to measure the distribution of powder in the cross section of a single track. Transversal profiles of powder density are obtained for the fine and coarse powders of two materials, aluminium bronze and WC-Co cemented carbide. The effective denuded width is calculated from these profiles. The denuded width increases with the particle size for the WC-Co powders. No confident variation of the denuded width with the particle size is observed for the bronze powders.

The balance of forces applied to a powder particle is theoretically analyzed. The gravity, adhesion, drag, sliding friction, and rolling resistance forces are considered. The drag force due to the entrainment flow of a vapor jet is calculated by means of a similarity solution for a jet emerging into a half space. The theory reveals two limit regimes for the influence of the particle size on the denuded width: the denuded width increases with the particle size for finer powders and decreases for coarser powders. The experimentally observed behavior of the WC powders corresponds to the former case where the adhesion force is considerably greater than the gravity one. The observed behavior of the bronze powders may indicate that the adhesive force is comparable with the gravity one.

The measurement and the theoretical prediction of the denuded width quantify the transfer of powder particles by the gas flow. This transfer considerably contributes to the overall mass transfer in the laser-interaction zone at L-PBF. Understanding of such a basic physical process is useful to choose the processing regimes for specific powders and to optimize the technology.

Acknowledgements

This work was supported by the Ministry of Science and Higher Education of the Russian Federation under project 0707-2020-0034.

References

- [1] Yadroitsev I, Bertrand Ph, Smurov I. Parametric analysis of the selective laser melting process. *Appl. Surf. Sci.* 2007; 253:8064-69.
- [2] Yadroitsev I, Gusarov A, Yadroitsava I, Smurov I. Single track formation in selective laser melting of metal powders. *J. Mater. Process. Technol.* 2010; 210:1624-31.
- [3] Gunenthiram V, Peyre P, Schneider M, Dal M, Coste F, Fabbro R. Analysis of laser-melt pool-powder bed interaction during the selective laser melting of a stainless steel. *J. Laser Appl.* 2017; 29:022303.
- [4] Liu Y, Yang Y, Mai A, Wang D, Song C. Investigation into spatter behavior during selective laser melting of AISI 316L stainless steel powder. *Mater. Design* 2015; 87:797-806.
- [5] Matthews MJ, Guss G, Khairallah SA, Rubenchik A, Anderson AT, Depond PJ, King WE. Denudation of metal powder layers in laser powder bed fusion processes. *Acta Mater.* 2016; 114:33-42.
- [6] Ly S, Rubenchik AM, Khairallah SA, Guss G, Matthews MJ. Metal vapor micro-jet controls material redistribution in laser powder bed fusion additive manufacturing. *Sci. Rep.* 2017; 7:4085.
- [7] Zhimov I, Kotoban DV, Gusarov AV. Evaporation-induced gas-phase flows at selective laser melting. *Appl. Phys A* 2018; 124:157.
- [8] Podrabinnik PA, Shtanko AE, Khmyrov RS, Korotkov AD, Gusarov AV. Interferometry of gas-phase flows during selective laser melting. *Appl. Sci.* 2020; 10:231.
- [9] Gunenthiram V, Peyre P, Schneider M, Dal M, Coste F, Koutiri I, Fabbro R. Experimental analysis of spatter generation and melt-pool behavior during the powder bed laser beam melting process. *J. Mater. Process. Technol.* 2018; 251:376-386.
- [10] Bidare P, Bitharas I, Ward RM, Attallah MM, Moore AJ. Fluid and particle dynamics in laser powder bed fusion. *Acta Mater.* 2018; 142:107-120.
- [11] Bidare P, Bitharas I, Ward RM, Attallah MM, Moore AJ. Laser powder bed fusion in high-pressure atmospheres. *Int. J. Adv. Manuf. Technol.* 2018; 99:543-555.
- [12] Mayi YA, Dal M, Peyre P, Bellet M, Metton C, Moriconi C, Fabbro R. Laser-induced plume investigated by finite element modelling and scaling of particle entrainment in laser powder bed fusion. *J. Phys. D* 2020; 53: 075306.
- [13] Gusarov AV. Analytic similarity solutions of the Navier-Stokes equations for a jet in a half space with the no-slip boundary condition. *Phys. Fluids* 2020; 32:053104.
- [14] Gusarov AV. Entrainment flow of emerging jet in a half-space with the no-slip boundary condition. *arXiv e-prints* 2020; arXiv:2001.02406.
- [15] Landau LD, Lifshitz EM. *Fluid Mechanics*. New York: Pergamon; 1959.
- [16] Ferziger JH, Kaper HG. *Mathematical Theory of Transport Processes in Gases*. Amsterdam: North-Holland; 1972.
- [17] Meier C, Weissbach R, Weinberg J, Wall W.A., John Hart A. Critical influences of particle size and adhesion on the powder layer uniformity in metal additive manufacturing. *J. Mater. Process. Technol.* 2019; 266:484-501.
- [18] Kovalev OB, Gusarov AV. Modeling of granular packed beds, their statistical analyses and evaluation of effective thermal conductivity. *Int. J. Thermal Sci.* 2017; 114:327-341.
- [19] Oerlikon Metco. www.oerlikon.com 2020.
- [20] Grigoriev IS, Meilikhov EZ. *Handbook of Physical Quantities*. New York: CRC Press; 1997.
- [21] Leite FL, Bueno CC, Da Róz AL, Ervino Ziemath EC, Oliveira Jr. ON. Theoretical models for surface forces and adhesion and their measurement using atomic force microscopy. *Int. J. Mol. Sci.* 2012; 13:12773-856.
- [22] Schneider W. Flow induced by jets and plumes. *J. Fluid Mech.* 1981; 108:55-65.
- [23] Zauner E. Visualization of the viscous flow induced by a round jet. *J. Fluid Mech.* 1985; 154: 111-119.
- [24] Hibbeler RC. *Engineering Mechanics: Statics and Dynamics*. New York: Pearson; 2016.

11th CIRP Conference on Photonic Technologies [LANE 2020] on September 7-10, 2020

Controlling melt pool shape, microstructure and residual stress in additively manufactured metals using modified laser beam profiles

M. J. Matthews^{a,*}, T. T. Roehling^a, S. A. Khairallah^a, T. U. Tumkur^a, G. Guss^a, R. Shi^a, J. D. Roehling^a, W. L. Smith^a, B. K. Vrancken^a, R. K. Ganeriwala^a, J. T. McKeown^a

^a Lawrence Livermore National Laboratory, 7000 East Avenue, Livermore 94550 CA, USA

* Corresponding author. Tel.: +1-925-424-6762. E-mail address: ibo@llnl.gov

Abstract

Laser powder bed fusion has proven to be an effective additive manufacturing technology for the manufacture of complex metal components. However, the local thermal history associated with Gaussian beam, raster scan processes produces heterogeneous and spatially non-uniform microstructures that differ from those produced from conventional manufacturing and often lack optimized mechanical properties. Steep thermal gradients and high cooling rates produce large thermal strains driving residual stress fields that can negatively affect the dimensional accuracy of the as-built component. Here, we present experimental and simulation methods for controlling microstructure and residual stress through tailored laser beam profiles. Elliptical and Bessel beam profiles are shown to produce more equiaxed microstructures as compared to those of Gaussian beams, while distributed diode-based illumination profiles allow for reduced residual stresses. These experimental results are supported by high-fidelity powder-scale simulation models coupled to the cellular automata and thermomechanical models that account for macroscale residual stress.

© 2020 The Authors. Published by Elsevier B.V.

This is an open access article under the CC BY-NC-ND license (<http://creativecommons.org/licenses/by-nc-nd/4.0/>)

Peer-review under responsibility of the Bayerisches Laserzentrum GmbH

Keywords: additive manufacturing, beam shaping, microstructure, residual stress, simulation

1. Introduction

Control of local thermal histories in laser powder bed fusion that dictate microstructure, phase fraction, morphology, and residual stress begins with understanding the laser energy coupling mechanisms involved. The steep thermal gradients ($\sim 10^7$ K/m) and fast scanning speeds (~ 1 m/s) involved lead to rapid solidification, large thermal stresses, and significant surface roughness due to the parasitic behavior of loose powder particles under the action of evaporation-induced gas flow. Although typical laser powder bed fusion (LPBF) systems use circular Gaussian intensity profiles operated in continuous mode, we have recently shown that simple modifications (i.e., an elliptical beam, multiple lasers) can result in significant changes in the microstructure and stress state of LPBF material [1,2]. While encouraging, the exact mechanisms involved were not completely understood. The work presented here seeks to expand this

initial effort to understand the physics of local beam shaping for micro-structural control, while exploring longer-scale (\sim mm to cm) photonic sources that can result in distributed, low-gradient heating. Surface morphology can be affected by the spatial distribution of laser energy, for example, through hatch spacing optimization and remelting [3]; temporal formatting, however, has been shown to be more decisive in enabling so-called “micro-SLM” or micron-scale LPBF [4,5]. To fully optimize the LPBF process it is necessary to develop a deeper understanding of the mechanisms involved in pulsed-format LPBF in order to push the limits of low surface roughness, which will enable yet finer-scale (\sim μm) features to be created while controlling microstructure. Other temporally-driven approaches have involved the use of laser shock peening to impart mechanical work and tune the local strain field in situ with the goal of producing optimized-stress-state materials with unique properties. In the currently work however we focus on spatially modifying the laser energy to

demonstrate microstructure, morphological, and stress state control of steel alloys and compare with simulated predictions for optimization of parameters. Furthermore, tuning the alloy composition in addition to modifying the laser source presents an opportunity to harness the full potential of LPBF technologies. In summary, we will present efforts to:

- Tailor photonic sources, guided by thermal measurements and modelling (custom beam shaping for controlled energy deposition profiles)
- Demonstrate spatial modulation for modification of thermal gradients, solidification rates, and cooling rates to control macro- and microstructure
- Employ multiple laser beam sources or distributed photonic sources (e.g., optically address-able light valves with kW-scale diode lasers)
- Optimize laser beam formats for specific alloy sets and part geometries to improve AM part performance and leverage topology optimization tools

Figure 1 displays the conceptual idea of co-designing energy sources and alloy composition to achieve tailored materials.

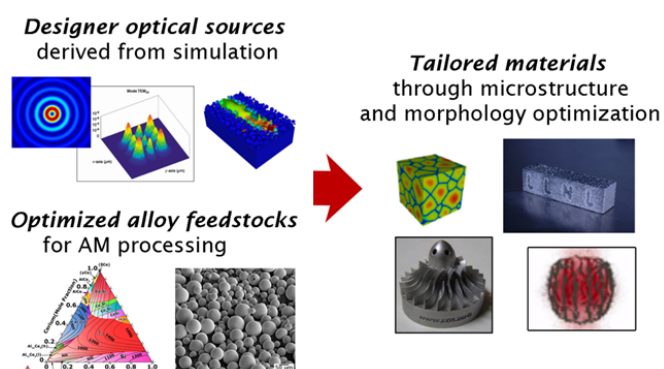


Fig. 1. Conceptual schematic describing the tuning of additively manufactured material properties using designer light sources and new alloys.

To demonstrate microstructure, morphological, and stress state control of alloys through spatial formatting of incident laser energy in LPBF processes we describe both local beam shaping and dual laser approaches. We characterize the microstructures produced by non-Gaussian laser intensity profiles at different length scales (tens of μm to $\sim\text{cm}$ scale), laser powers, and scan speeds. Analyses of our experimental results will be accompanied by finite element modeling (ALE3D). To date, demonstration of microstructure control in metal AM has been somewhat limited to electron beam melting [6,7]. For example, control of the solidification texture in an Inconel 718 alloy during electron beam additive manufacturing was demonstrated by developing a customized melt scanning strategy guided by numerical predictions of the fraction of equiaxed grain formation as a function of electron beam spatial distributions [7]. Localized tailoring of microstructure in LPBF using “complex” laser beams was recently demonstrated by Huang et al. using an “optical engine” comprised of a focused Gaussian beam and a rectangular, lower-intensity beam [8]. However, material

ductility was increased at the expense of strength and a clear connection with thermal histories was not shown.

Our goal is to locally tune laser beam shape using simple optics such as anamorphic prism pairs and polarization multiplexers of dual beams to control microstructure, building on initial work our group has performed [2]. Large-scale, distributed laser sources will also be used, with our demonstrated diode-based additive manufacturing system [9] providing a convenient means to extend irradiation over $\sim\text{mm}$ to $\sim\text{cm}$ scales. Similar “direct diode” approaches were recently demonstrated by the Mumtaz group at Sheffield University [10].

Nomenclature

P	laser power [W]
v	scan speed [mm/s]
H	hatch spacing [μm]
λ	wavelength [nm]
Q	volumetric energy density [J/mm^3]

2. Materials & Methods

LPBF experiments were completed using 316L stainless steel powder (Concept Laser) on 316L stainless steel substrates (McMaster-Carr). Prior to use, the $\sim 27\text{-}\mu\text{m}$ powders were vacuum dried at 623 K and stored in a desiccator thereafter. The surfaces of build substrates were bead blasted prior to use in the experiments.

2.1. Microstructure control using spatially-shaped laser beams

An Aconity Lab system (Aconity3D, Germany) was used to build 1-cm^3 test cubes of 316L stainless steel from powder (Additive Metal Alloys, Ohio) in an Ar atmosphere. An elliptical beam ($1/e^2$ diameters = $110\ \mu\text{m} \times 474\ \mu\text{m}$) was formed using cylindrical lenses and was scanned along the direction of its minor axis for all experiments presented here. In this configuration, we refer to the beam as a transverse elliptical (TE) beam, as opposed to a longitudinal elliptical (LE) beam which is scanned along the direction of its major axis. For comparison, cubes were also built using a defocused circular Gaussian (CG) beam ($1/e^2$ diameter = $228\ \mu\text{m}$) of approximately equivalent area. Laser power (P) was varied from 150 to 400 W, and volumetric energy density (Q) was varied from 80 to 380 J/mm^3 . Volumetric energy density is reported as $Q=P/(vtw)$ where P is laser power, v is scan speed, t is powder layer thickness and w is $1/e^2$ laser beam diameter. For elliptical beams, the laser beam diameter is taken as the geometric average of major and minor axes.

A powder layer thickness (t) of $50\ \mu\text{m}$ and a hatch spacing (H) of $100\ \mu\text{m}$ were initially selected for 0.5-cm test cubes. In the experiments, which duplicated parameters used in our single-track study [2], metallographic examination indicated that at $P < 350\ \text{W}$ and $Q < 260\ \text{J}/\text{mm}^3$, the average vertical spacing between fusion boundaries is much smaller than the powder layer thickness for samples built using an elliptical beam, especially compared to those built using a Gaussian

beam ($L_z = 26.6\text{--}45.4 \mu\text{m}$). These low melt depths correlate to low sample densities, indicating a need to use higher laser powers and lower speeds to achieve consistent layer remelting.

2.2. Residual stress reduction through in situ diode laser annealing

The experimental setup for the residual stress reduction experiments is described in [1]. To build simple bridge samples that can be cut to evaluate stress through deflection, four semiconductor laser diodes ($\lambda=1000 \text{ nm}$, 1.25 kW) are focused and combined into a spatial homogenizer. The intensity profile masked with two distinct patterns using 2 mm thick aluminum apertures for building (1) the bridge supports and (2) the bridge top (i.e., supports + overhang). The diode light is then reflected from a dichroic mirror onto the build-plate. Illumination from a second, focused scanning laser (IPG Photonics, $\lambda=1070 \text{ nm}$, 1 kW) passes through the dichroic to be coincident with the diode light. The diode power could be controlled in any arbitrary temporal profile desired, up to a total of 5 kW. A maximum of 1.2 kW was used in this work and the masks transmitted 18 and 27% of the power to the build surface.

The bridges were 5 mm tall, 20 mm long and 11 mm wide on build plates that were 25.4 mm in diameter and 6.35 mm thick. The bridge overhang section was nominally 1.5 mm thick (30 layers). The hatch spacing for the focused laser was 100 μm with a 50 μm layer thickness. The focused beam $1/e^2$ diameter was 80 μm . Maximum density was achieved using a scan speed of 278 mm/s. The zigzag scan strategy was rotated 90° between layers, with the scanning vectors angled 45° with respect to the long axis the bridge.

For the bridges that were annealed in situ, the diodes illuminated the bridge before or after the focused melting laser finished its scan. Each layer was illuminated with the diode, except for the first five layers of the bridge overhang sections to avoid dross formation on the down-facing surface. The maximum diode powers used for bridges subjected to in situ annealing were: 400, 800, 1000, and 1200 W. The masks used for (1) the bridge supports and for (2) the bridge top (i.e., supports + overhang) let through 18% and 27%, respectively, of the maximum power.

2.3. Beam shaping simulations

Several different beam shapes were simulated in single-track configurations. Details of the ALE3D code and the 316L material properties used in the simulations are published elsewhere [11,12]. Briefly, the simulation used the actual particle size distribution, and random particle packing (40 % density) was modeled using the ALE3D utility code, ParticlePack. A laser ray tracing algorithm was used to simulate laser interaction with the powder bed. The three-dimensional model was addressed using a hybrid finite element and finite volume formulation on an unstructured grid. Simulations were run using each beam shape at Size S for P = 550 W. To conserve computational time, the scan velocity was set at 1800 mm/s, resulting in an energy density

of 61 J/mm³. This energy density is slightly lower than the minimum value used in the experiments (80 J/mm³), and for the sake of drawing qualitative connections to the experiment about beam shape effects does not affect our conclusions.

3. Results and Discussion

3.1. Microstructure control using spatially-shaped laser beams

When comparing the Gaussian and Elliptical beams, higher power and energy densities were found necessary for full densification when an elliptical beam is used compared to when a Gaussian beam is used. Cubes built using an elliptical beam at a hatch spacing $H=100 \mu\text{m}$ did not demonstrate the prototypical “scalloped” fusion boundary patterns found in LPBF metals. Instead, the layers appeared thin and continuous in the x and y lateral directions, where z is the build direction (BD). This suggests that, in a single plane, each new track is deposited before its immediately preceding neighbor has fully solidified. This effect is lessened with increasing part size, increasing scanning speed (or increasing solidification rate), and increasing hatch spacing. In contrast, cubes built using a Gaussian beam demonstrated fusion zone dimensions that directly reflect the hatch spacing and laser power used.

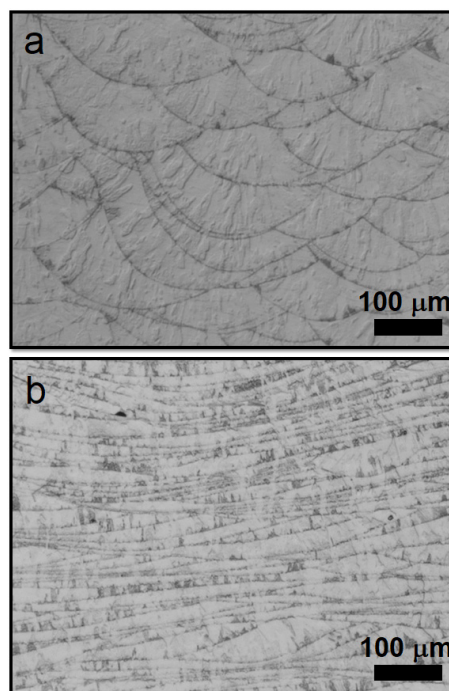


Fig. 2. Melt pool morphology for LPBF 316L steel produced using (a) Gaussian and (b) elliptical laser beams. The build direction is along the vertical direction from bottom to top of the figures. The scan direction is roughly out of the plane of the image with no cross hatching. The elliptical beam resulted in shallower melt depths, and consequently, a higher density of fusion boundaries.

It was also observed that, as with the single track study [2] previously reported, the microstructure of the elliptical beam samples was notably refined and more equiaxed as compared to the Gaussian beam samples, consistent with lower thermal

gradients predicted by the finite element simulations reported previously [13] and also shown below. Further details of the microstructure arising from full builds using elliptical beams will be reported in a forthcoming publication.

3.2. Residual stress reduction through *in situ* diode laser annealing

Results of several different *in situ* annealing treatments are shown in Fig. 3. The residual stress in test bridges built with *in situ* diode annealing are reduced above a critical temperature, while no changes were noticed for insufficiently high diode power input. The critical temperature was found to be above 625 °C. These findings correlate well with the yield stress of austenitic stainless steels, which decreases sharply above this temperature. Along with 5 or 10 s ramp-down in laser diode energy at the end of each layer, a pre-heat step was also performed. As reported in [1], the pre-heat step was not very effective and could be dropped from the treatment to save processing time.

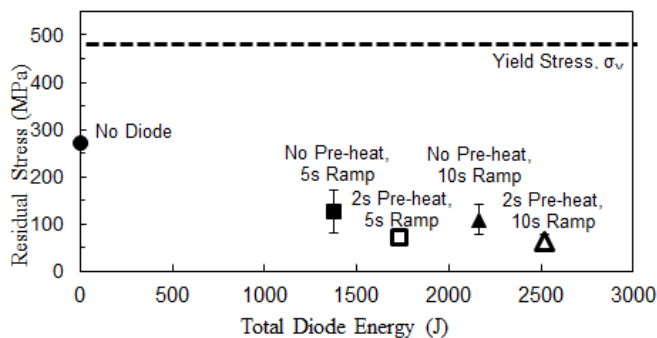


Fig. 3. Reduction of residual stress in 316L steel bridges printed using *in situ* diode laser annealing. Samples were exposed to a ramp down in diode laser energy with or without an initial pre-heating step.

The results suggest that a significant reduction in residual stress is possible by simply reaching the desired temperature. While diode annealing was applied to nearly every layer in this study, less frequent *in situ* annealing steps could be comparably effective. In this study we wanted to ensure the entire volume of material reached the desired temperature but the frequency of the *in situ* anneal could be reduced to skip multiple layers, given that the desired temperature could be still be reached in unannealed underlying layers (a temperature drop into previous layers is unavoidable). The power ramp-down rate could be optimized. A faster cooling rate could still achieve lowered residual stress, but there could be a critical point at which increasing the cooling rate would introduce new thermal stresses and thus become the controlling factor in the final residual stress state.

3.3. Beam shaping simulations

Modelling laser-material interactions using LLNL's ALE3D code allowed beam shape effects on track macro- and microstructures to be further investigated. Details of the simulation can be found in [13]. The simulated thermal profiles and histories can then be combined with cellular

automata [14] which is beyond the scope of the present work. Melt track simulations for five different beam shapes – Gaussian, Elliptical (transverse, longitudinal), annular and Bessel – are shown in Fig. 4 and indicate a wide variety of melt pool response and temperature fields. For example, as compared to the standard Gaussian beam, the transverse elliptical and annular beams have much wider melt pools which lead to shallower temperature gradients. The Bessel beam showed similarly shallow melt pools but owing to the sharp central peak in the profile, the temperature distribution was more confined along the surface. The longitudinal elliptical beam had only a modest effect on the melt pool shape and was found to also affect the grain structure moderately in our previous study [2].

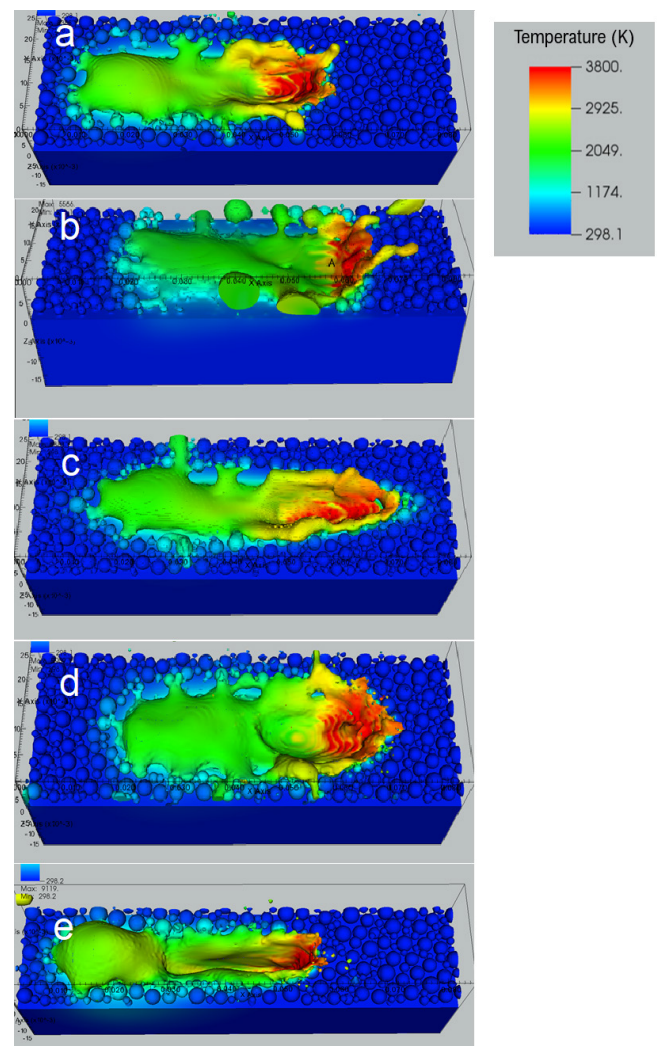


Fig. 4. Finite element simulations using ALE3D. The domain size for the simulations was $250 \times 250 \times 750 \mu\text{m}^3$. Gaussian (a), transverse elliptical (b), longitudinal (c), annular (d) and Bessel (e) beams were simulated using a mean beam diameter of $100 \mu\text{m}$ and laser power $P = 550 \text{ W}$. To conserve computational time, the scan velocity was set at 1800 mm/s . The pseudo-colors correspond to temperature linearly, where red is 3200 K and blue is room temperature.

Conclusions

In conclusion, we present here novel process laser modifications to enhance the microstructure and stress properties and processability of AM metals. The effects of Gaussian and tailored laser intensity profiles on single-track microstructures were investigated using finite element simulations. Beam ellipticity demonstrated a strong effect on solidification microstructure in full 3D builds. These results indicate that grain morphology can be tailored by varying beam intensity spatial profile with the potential to optimize final mechanical properties. Finally, residual stress was shown to be reduced when employing a multiple laser solution with an *in situ* diode laser as the second laser. These approaches, guided by simulation, show promise in accelerating acceptance of additively manufactured parts and improving overall design flexibility and part performance.

Acknowledgements

This work was performed under the auspices of the U.S. Department of Energy by Lawrence Livermore National Laboratory under Contract No. DE-AC52-07NA27344. This work was funded by the Laboratory Directed Research and Development Program at LLNL under project tracking code 18-SI-003.

References

- [1] J. D. Roehling, W. L. Smith, T. T. Roehling, B. Vrancken, G. M. Guss, J. T. McKeown, M. R. Hill, M. J. Matthews, Reducing residual stress by selective large-area diode surface heating during laser powder bed fusion additive manufacturing, *Additive Manufacturing* 28 (2019) 228.
- [2] T.T. Roehling, S.S.Q. Wu, S. Khairallah, J.D. Roehling, S.S. Soezeri, M.F. Crumb, M.J. Matthews, Modulating laser intensity profile ellipticity for microstructural control during metal additive manufacturing, *Acta Materialia* 128 (2017) 197.
- [3] K. Alrbaey, D. Wimpenny, R. Tosi, W. Manning, A. Moroz, On optimization of surface roughness of selective laser melted stainless steel parts: A statistical study, *Journal of Materials Engineering Performance* 23 (2014) 2139.
- [4] K. A. Mumtaz, N. Hopkinson, Selective Laser Melting of thin wall parts using pulse shaping, *Journal of Material Processing Technology* 210 (2010) 279.
- [5] A. Diatlov, D. Buchbinder, W. Meiners, K. Wissenbach, J. Bultmann, Towards surface topography: Quantification of Selective Laser Melting (SLM) built parts, *Innovative Developments on Virtual and Physical Prototyping* (2012) 595.
- [6] K. Hagihara, T. Nakano, M. Suzuki, T. Ishimoto, Suyalatu, S.-H. Sun, Successful additive manufacturing of MoSi₂ including crystallographic texture and shape control, *Journal of Alloys and Compounds* 696 (2017) 67.
- [7] M.M. Kirka, K.A. Unocic, N. Raghavan, F. Medina, R.R. Dehoff, S.S. Babu, Microstructure development in electron beam-melted Inconel 718 and associated tensile properties, *JOM* 68 (2016) 1012.
- [8] W.-C. Huang, K.-P. Chang, P.-H. Wu, C.-H. Wu, C.-C. Lin, C.-S. Chuang, D.-Y. Lin, S.-H. Liu, J.-B. Horng, F.-H. Tsau, 3D printing optical engine for controlling material microstructure, *Physics Procedia* 83 (2016) 847.
- [9] M.J. Matthews, G. Guss, D.R. Drachenberg, J.A. Demuth, J.E. Heebner, E.B. Duoss, J.D. Kuntz, C.M. Spadaccini, Diode-based additive manufacturing of metals using an optically-addressable light valve, *Optics Express* 25 (2017) 11788.
- [10] M. Zavala-Arredondo, N. Boone, J. Willmott, D.T.D. Childs, P. Ivanov, K.M. Groom, K.A. Mumtaz, Laser diode area melting for high speed additive manufacturing of metallic components, *Materials & Design* 117 (2017) 305.
- [11] S. A. Khairallah et al., "Controlling interdependent meso-nanosecond dynamics and defect generation in metal 3D printing," *Science*, 368 (2020) 660
- [12] S. A. Khairallah, A. T. Anderson, A. Rubenchik, and W. E. King, "Laser powder-bed fusion additive manufacturing: Physics of complex melt flow and formation mechanisms of pores, spatter, and denudation zones," (in English), *Acta Materialia*, 108 (2016) 36
- [13] R. Shi, S. A. Khairallah, T. T. Roehling, T. W. Heo, J. T. McKeown, and M. J. Matthews, Microstructural control in metal laser powder bed fusion additive manufacturing using laser beam shaping strategy, *Acta Materialia*, 184 (2020) 284.

11th CIRP Conference on Photonic Technologies [LANE 2020] on September 7-10, 2020

Influence of process gas during powder bed fusion with laser beam of Zr-based bulk metallic glasses

Jan Wegner^{a*}, Maximilian Frey^b, Stefan Kleszczynski^a, Ralf Busch^b, Gerd Witt^a

^a Chair of Manufacturing Technology, University Duisburg-Essen, Lotharstraße 1, 47057 Duisburg, Germany

^b Chair of Metallic Materials, Saarland University, Campus C6.3, 66123 Saarbrücken, Germany

* Corresponding author. Tel.: +492033793075; fax: +492033791530. E-mail address: jan.wegner@uni-due.de

Abstract

Zr-based bulk metallic glasses offer a unique combination of hardness, high strength, and high elastic limits. Yet, manufacturable size and complexity are limited due to the required cooling rates. Short laser-material interaction times together with layer-wise and selective energy input allows the laser powder bed fusion process to largely overcome those restrictions. Still, the complex process-material interactions inhere numerous uncertainties. In the present work, additively manufactured Zr-based bulk metallic glasses produced under three different process gases are investigated by calorimetry, x-ray diffraction, and bending tests. A strong dependence between the thermophysical properties, flexural strength, and the applied atmosphere is found.

© 2020 The Authors. Published by Elsevier B.V.

This is an open access article under the CC BY-NC-ND license (<http://creativecommons.org/licenses/by-nc-nd/4.0/>)

Peer-review under responsibility of the Bayerisches Laserzentrum GmbH

Keywords: Laser powder bed fusion; bulk metallic glasses; process gas; mechanical properties; crystallization

1. Introduction

Additive manufacturing is steadily emerging as a production method in the recent decade. Among the different techniques, the powder bed fusion of metals using a laser beam (PBF-LB/M) established as the most promising process for the efficient fabrication of highly complex and customized shapes. The design freedom is especially desirable in the medical, automotive, and aerospace industries, driving PBF-LB/M-manufactured components to series production [1, 2]. Such applications often demand advanced material performance. Apart from new geometrical possibilities, the layer-wise build-up process combined with highly dynamic laser exposure favors the creation of non-equilibrium microstructures, hence creating further potential for functional parts and material design [3, 4]. In this context, the PBF-LB/M process inaugurates new opportunities in the fabrication of bulk metallic glasses (BMGs). High cooling rates between

10^4 - 10^6 K/s combined with the layer-wise energy input allows for largely suppressed crystallization and thus surpasses the current possibilities given by casting methods [5–7]. The amorphous microstructure of Zr-based BMGs leads to high strength, elastic limits of 2 % or more, and high corrosion resistance [8]. Furthermore, the isotropic and homogenous mechanical properties of BMGs are especially desirable for additively manufactured parts [9]. However, the PBF-LB/M process is featured by complex multi-physical laser-material interactions. Respectively, the processing of BMGs inhere additional challenges, since not only lack of fusion but also crystallization must be prevented through a careful parameter selection to retain the aspired mechanical properties of BMGs [6, 10, 11]. The crystallization of Zr-based BMGs during PBF-LB/M is strongly related to increased energy inputs applied by the process parameters. The detrimental phase formations not only consist of primary crystalline phases such as Zr_2Cu but also oxide phases [11, 12]. Oxygen impurities, therefore, play a

crucial role for the glass-forming ability (GFA) of Zr-based BMGs regarding PBF-LB/M. Bordeenithikasem et al. for instance report in [13] that crystallization, and hence the resulting mechanical properties, are strongly affected by the oxygen content within the fabricated material. Further, Pacheco et al. investigated the thermal stability of PBF-LB/M manufactured AMZ4 and observed the formation of nanocrystalline oxides [12]. Respectively deteriorated mechanical properties in dependence on the oxygen contamination were also reported in [14]. This further leads to questions about the impact of the applied shielding gases during PBF-LB/M. In this context, not only the influence of residual oxygen contamination within the process atmosphere but also the gas-material interactions may play a crucial role regarding the resulting mechanical properties and the economic aspects, since laboratory-grade gases can be a non-negligible cost driver. Studies addressing the atmosphere during laser powder bed fusion are rare [15, 16]. The established shielding gases in PBF-LB/M are N₂ and Ar [17]. While argon as a noble gas is inert, N₂ can dissolve, react, and form nitrides [18]. Liu et al. report in [19] that the GFA of Zr-based BMGs is promoted by nitrogen-doping between 1000 and 3000 appm during casting in a Cu₄₉Zr₄₄Al₇ alloy by suppressing the formation of the primary Zr-Cu-phase, inhering potential benefit for the application in PBF-LB/M-process. Conventional welding techniques on the other hand often apply gas mixtures subjecting the particular requirements, for instance by H₂ addition. Due to its high thermal conductivity and oxygen-reducing chemical activity, the influence of H₂ doped gases in the PBF-LB/M of BMGs appears promising in order to reduce nano-crystalline oxide formation during the process and potentially be beneficial to increase local cooling rates [20]. Regarding the material properties, microalloying of H₂ is reported to enhance GFA and plasticity in casted Zr-based BMGs. Dong et al. report that additions of 10 - 30 % H₂ led to increased free volumes and enhanced plastic strain [21]. This study aims to evaluate the possibilities for process optimization of PBF-LB/M fabrication of Zr-based BMGs regarding the used process gas. Therefore, PBF-LB/M-manufactured samples are systematically analyzed in terms of their microstructure, thermophysical properties, and mechanical performance. Specimens produced under high-purity argon are compared to samples produced under less expensive, commercial purity N₂ process gas as well as a commercial purity argon-hydrogen mixture.

2. Experimental procedure

2.1. PBF-LB/M process

Argon atomized powder with a nominal chemical composition of Zr_{59.3}Cu_{28.8}Al_{10.4}Nb_{1.5} (in at. %) and an average particle size x_{50} of 23.65 μm was provided by Heraeus GmbH. The material was processed on an M100 PBF-LB/M system (eos GmbH) equipped with a 1064 nm wavelength fiber laser and a nominal spot-size d of 40 μm. Three different shielding gases were investigated: N₂ “N40” with 99.99 vol.% purity, “ARCAL prime” 99.998 vol.% Ar by Air Liquide GmbH, and the argon-hydrogen mixture “Varigon® H2” containing

2 vol.% hydrogen (Ar₉₈H₂) provided by Linde with a purity of 99.95 vol.% were investigated in three PBF-LB/M processes. The residual oxygen level was held below 0.05 ± 0.02 vol.%, as measured by the integrated oxygen sensor of the PBF-LB/M machine. Cubes with an edge length of 5 mm were processed to determine the influence of the respective gas on the processable parameter windows. Based on King et al. [22] a quantification of the energy deposition during PBF-LB/M dependent on the process parameters laser power P and scan speed v for the conduction and keyhole mode during melting can be given by (1):

$$\frac{\Delta H}{h_s} = \frac{A \cdot P}{h_s \cdot \pi \cdot \sqrt{\alpha \cdot v} \cdot d^3} \quad (1)$$

The absorptivity A , the melting enthalpy h_s , and the thermal diffusivity α are considered as given intrinsic material properties throughout the experimental procedure of this study. Therefore, the energy deposition is proportional to the ratio of the applied laser power and the root of the scan speed [22,23] (2):

$$\Delta H \sim \frac{P}{\sqrt{v}} \quad (2)$$

In contrast to other approaches, such as line energy density (P/v), here the laser power is considered to have a stronger impact on the energy deposition than the scan speed. This is in accordance with Tsai et al., who showed that the peak temperatures originating from exposure with a gaussian laser beam are proportional to the ratio of P/\sqrt{v} [23, 24]. Therefore, the applied process parameters are further represented by e_i as the ratio of P/\sqrt{v} . In this context, e_i was varied between 894 and 1375 $mW/\sqrt{ms^{-1}}$. Volumetric process parameters were kept constant at a layer thickness $d_s = 20$ μm and hatch distance $h = 40$ μm. For the mechanical characterization, four bending beams were fabricated in horizontal alignment to the bending direction. The beams were built with a length of 25.2 mm, a height 2.8 mm, and a width of 1.9 mm, with respect to the built orientation and evaluated by three-point bending. The process parameters were set based on Wegner et al. in [14], applying an e_i of $894 mW/\sqrt{m \cdot s^{-1}}$.

2.2. Structural and mechanical analysis

After processing, the cubic samples were cut in half along the building direction and prepared for further analysis. To conduct microscopy and hardness indentation, one half of each cube was embedded in epoxy and further ground and polished down to 1 μm diamond suspension. The intrinsic porosity was then determined through optical density measurements using a BX50M light microscope together with the stream essential software by Olympus GmbH. Hardness indentation was performed according to DIN EN ISO 6507-1 (HV5) on polished cross-sections and was averaged over five measurements per sample. Bending beams were sanded and tested via three-point flexural bending with a Shimadzu testing machine as explained in detail in [14].

2.3. Thermophysical analysis

In order to analyze the influence of the shielding gas on the thermophysical properties, the remaining half of each cube was analyzed by means of x-ray diffraction (XRD) and differential scanning calorimetry (DSC). An X'Pert Pro MPD (Panalytical) diffractometer was used, equipped with a copper tube emitting K_{α} radiation with a wavelength of 1.5406 Å. The angular angle 2θ (Bragg angle) was scanned from 20° to 50° . DSC scans were performed with a Perkin Elmer Diamond DSC applying a heating rate of 60 K/min from 323 K to 753 K. The samples were measured in aluminum crucibles under argon flow.

3. Results and discussion

3.1. Influence on the structural properties

The application of the Ar and Ar_{98}H_2 atmosphere enabled stable processing of the entire range of investigated parameter range. On the contrary, the N_2 atmosphere led to a narrowed processable range. Here, samples processed with an e_i -value above $1230 \text{ mW}/\sqrt{\text{m}} \cdot \text{s}^{-1}$, had to be excluded from exposure during the process, due to the collision of the samples with the recoater blade. The reduced process stability of samples processed under N_2 was the result of distinctive stress-induced cracking along the contour surfaces and occasionally in the boundary surface towards the substrate, as exemplarily shown in (Fig. 1).

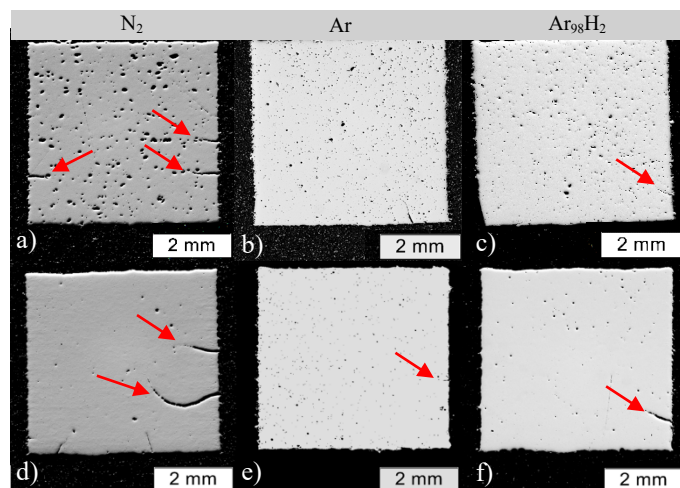


Fig. 1. Exemplarily cross sections of samples processed under N_2 , Ar and Ar_{98}H_2 comparing e_i (a)-(c): 894 and (d)-(e): $1125 \text{ mW}/\sqrt{\text{m}} \cdot \text{s}^{-1}$. Cracks are marked with red arrows.

As illustrated in Fig. 2, the relative density of the investigated parameter window resulted in relative densities above $\sim 99\%$ throughout the sample series. With increasing energy input, a further decreasing porosity was observed. Voids occur as mostly spherical gas pores and lack of fusion for energy levels below $1000 \text{ mW}/\sqrt{\text{m}} \cdot \text{s}^{-1}$, while with increasing energy input only spherical gas pores remain (compare Fig. 1). Among the compared gases, Ar led to a slightly increased relative density compared to N_2 and Ar_{98}H_2 . At ambient conditions (300 K and 100 kPa), Ar inheres with

$17.9 \text{ mW}/\text{mK}$ the lowest thermal conductivity compared to N_2 ($26 \text{ mW}/\text{mK}$) and Ar_{98}H_2 ($\sim 21.18 \text{ mW}/\text{mK}$), which contributes to increased temperatures within the melt pool and the heat-affected zone [25], hence decreased lack of fusion is expected [26]. However, the influence is subordinated compared to the energy input, since the heat convection through the gas has a minor influence on the melt pool temperature of the PBF-LB/M process and the relative density [15, 27].

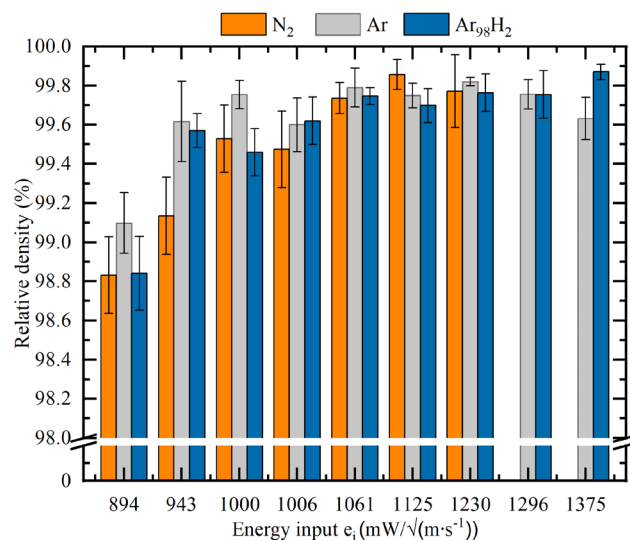


Fig. 2. Optically measured relative density in dependence of the energy input e_i for N_2 , Ar, and Ar_{98}H_2 -shielding gas. N_2 samples processed with an $e_i > 1230 \text{ mW}/\sqrt{\text{m}} \cdot \text{s}^{-1}$ had to be excluded from further exposure

3.2. Influence on the thermophysical properties

Exemplary DSC-scans of three samples produced under N_2 , Ar, and Ar_{98}H_2 with identical parameter sets, thus equivalent energy inputs of $894 \text{ mW}/\sqrt{\text{m}} \cdot \text{s}^{-1}$ are shown in Fig. 3a). At first glance, all curves show, in principle, the typical behavior of amorphous AMZ4 [14, 28]. A glass transition occurs at about 673 K as a rise of the heat flow from the glassy state level to the supercooled liquid (SCL) state level. At about 730 K, the SCL starts to crystallize as indicated by a massive exothermal event in the heat flow curve. The enthalpy of crystallization ΔH_x is defined by the integration over the respective exothermal event that starts at the end of the supercooled liquid state, as illustrated by the dotted lines in Fig. 3a). Fig. 3b) compares the obtained ΔH_x values for the fabricated samples. The usage of Ar and Ar_{98}H_2 resulted in ΔH_x values in the order of 4300–4600 J/mol, which is a typical value for amorphous PBF-LB/M-processed AMZ4 samples [14]. Here, ΔH_x only decreases for e_i values above $1230 \text{ mW}/\sqrt{\text{m}} \cdot \text{s}^{-1}$ using Ar_{98}H_2 and $1375 \text{ mW}/\sqrt{\text{m}} \cdot \text{s}^{-1}$ in Ar. Thus, a relative density of $\sim 99,8\%$ can be achieved without distinct crystallization within the samples. Different behavior is found for samples produced under N_2 . Here, ΔH_x only reaches about 4100 J/mol for low energy inputs and further decreases for growing e_i values, indicating partially crystalline samples after the PBF-LB/M process. Therefore, within the investigated framework of this study, the usage of “N40” N_2 does not allow the fully amorphous processing of AMZ4.

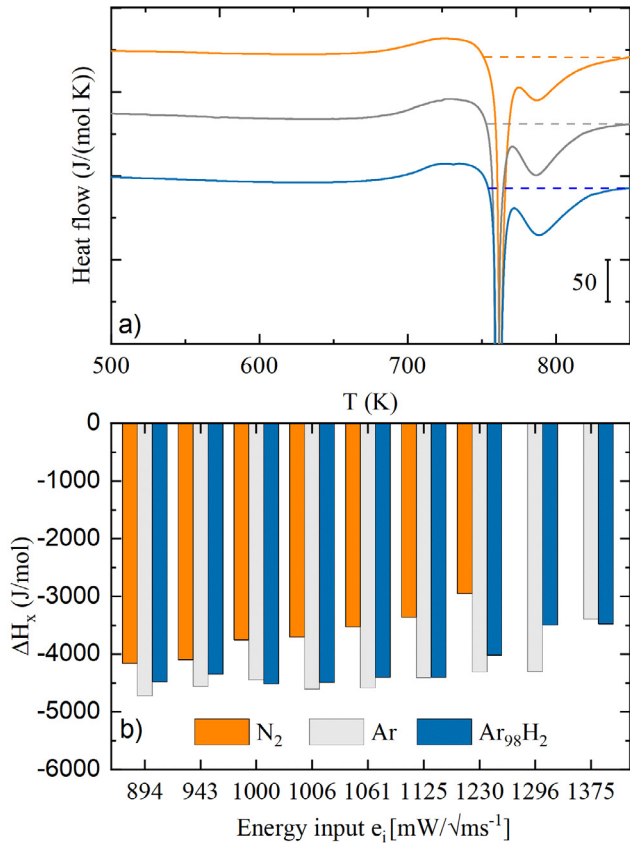


Fig. 3. (a) exemplary DSC measurements, the dotted lines indicate the integration interval (b) Enthalpy of crystallization H_x in dependence of e_i and the introduced gases N₂, Ar, and Ar₉₈H₂

Three representative XRD results are pictured in Fig. 4. For $e_i = 894 \text{ mW}/\sqrt{\text{m} \cdot \text{s}^{-1}}$, the diffractogram of the sample formed under Ar shows an amorphous halo without crystalline reflexes, indicating a glassy microstructure within the detection limits. In comparison, the usage of N₂ and Ar₉₈H₂ led to crystalline reflexes, which corresponds well to those of the Cu₂Zr₄O phase reported in the literature [11, 12]. With increasing e_i , the amount and intensity of crystalline reflexes increase for all process gases whereas N₂-formed samples feature the most distinct peaks over the entire e_i range. [11, 12]. As the energy input increases, the size and dwell time of the melt pool increases. Thus, the interaction time and reactive area between the molten material and shielding gas is enhanced, fostering reactions with the surrounding atmosphere. [29] Consequentially, also the heat-affected zone grows, and the effect of heat treatment in the subsequent layers increases the timespan for nucleation and growth of Cu-Zr-phases and oxides in the material. It is noticeable that despite the rather high reactivity of N₂, the formation of oxides is predominant compared to the formation of nitrides. Since the residual oxygen contamination within the chamber ($0.05 \pm 0.02 \text{ vol.}\%$) was held constant and the powder material was not reused over the different processes, an additional oxygen uptake resulting from the N₂ flow is concluded. Compared to that, samples built under Ar-based (Ar, Ar₉₈H₂) shielding gases exhibited minor crystalline fractions. Although the amount of impurities in the Ar₉₈H₂ gas mixture is within the same

scale as the investigated N₂, the oxide formation is significantly reduced. This might be attributed to an oxygen reduction caused by the hydrogen content. However, the effect vanishes compared to the high-purity Ar gas used in this study.

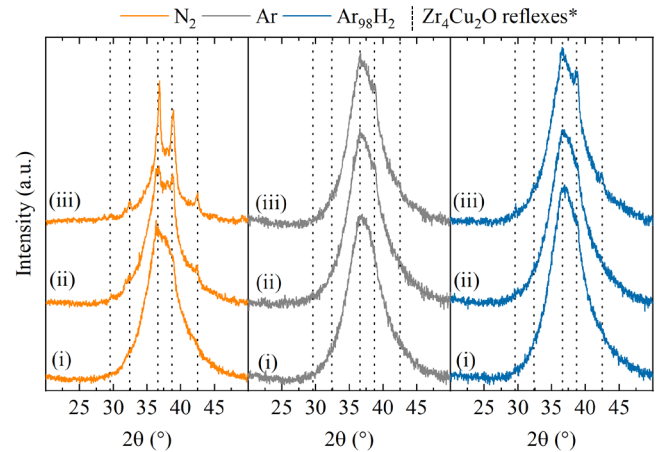


Fig. 4. X-ray diffractograms of under (a) N₂, (b) Ar, and (c) Ar₉₈H₂ processed samples with e_i of: (i) 894 (ii) 1061 (iii) 1230 $\text{mW}/\sqrt{\text{ms}^{-1}}$, with θ as glancing angle (Bragg-angle). The dotted lines represent the reflexes of Zr₄Cu₂O (*as reported in [11, 12])

3.3. Influence on the mechanical properties

The observed increase of the crystalline fraction accompanied by the usage of N₂ processed samples was accompanied by enhanced mean hardness values as illustrated in Fig. 5. The hardness further rises with the energy input under N₂ from 451 ± 8 to $496 \pm 9 \text{ HV5}$.

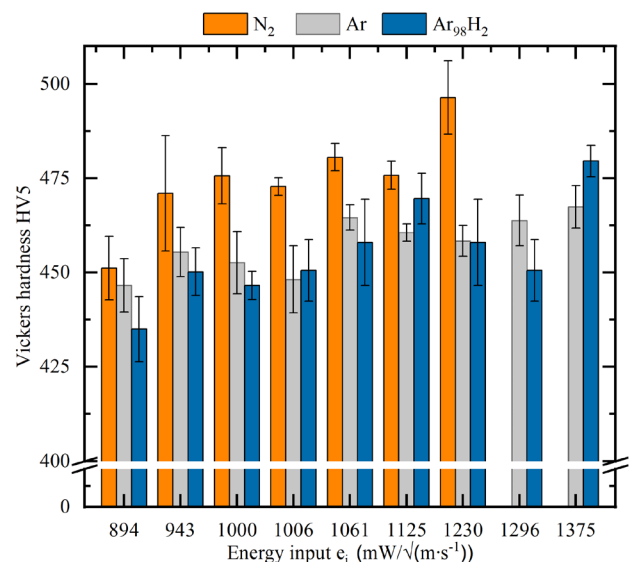


Fig. 5. (a) Mean Vickers hardness in dependence of the energy input e_i and the used shielding gases N₂, Ar, and Ar₉₈H₂.

The correlation between energy input and hardness with argon-based shielding gases is distinctive with higher e_i where a significant hardness increase is observed with $1375 \text{ mW}/\sqrt{\text{ms}^{-1}}$, corresponding to the decrease of the

crystallization enthalpy and formation of $\text{Cu}_2\text{Zr}_4\text{O}$ -oxides as seen in Fig. 3 and Fig. 4. Further fluctuating hardness values are also attributed to the varying relative densities.

The impact of the microstructural condition on the flexural strength is illustrated in Fig. 6. All investigated bending beams exhibited brittle fracture without plastic deformation and comparable young's modulus of ~ 82 GPa. Bending beams built in Ar showed a flexural strength of 1684.3 ± 115.5 MPa which is in good correspondence with the observations from Wegner et al in [14]. In comparison, beams processed under Ar_{98}H_2 exhibited a slightly increased flexural strength of 1692.7 ± 49.7 MPa. The N_2 -atmosphere led to a severe reduction of flexural bending strength of $\sim 30\%$ to 1167.3 ± 107.9 MPa. Since the relative density values of the Ar_{98}H_2 and N_2 samples are equal at the applied energy input level of $894 \text{ mW}/\sqrt{\text{m} \cdot \text{s}^{-1}}$, the significant weakening is

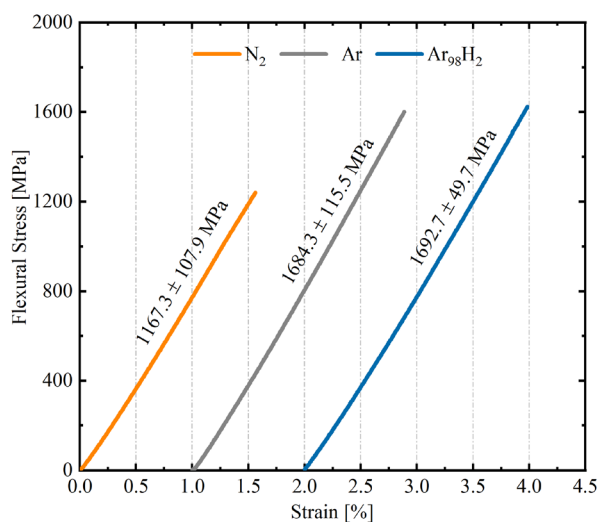


Fig. 6. Mean stress-strain curves averaged over four measurements for each applied shielding gas. The samples are processed with an e_i of $894 \text{ mW}/\sqrt{\text{m} \cdot \text{s}^{-1}}$.

attributed to the increased crystalline fraction in this context. One can conclude that the present residual porosity of $\sim 1\%$ has a minor influence on the flexural strength, compared to the microstructural weakening through the crystalline fraction [14]. It is noteworthy, that although the applied parameter set revealed first signs of crystallization within the XRD and DSC-measurements in the material processed under Ar_{98}H_2 , no distinct weakening of the material was present. However, measuring the hydrogen and oxygen uptake during the process is further necessary to quantify the impact of hydrogen addition in the process gas.

5. Conclusion

The influence of three different shielding gases (N_2 , Ar, and Ar_{98}H_2) on the PBF-LB/M-process and the resulting structural, mechanical, and thermophysical properties of $\text{Zr}_{59.3}\text{Cu}_{28.8}\text{Al}_{10.4}\text{Nb}_{1.5}$ were investigated. Applying high purity Ar as shielding gas led to fully amorphous processing with a relative density of 99.8%. The usage of N_2 -shielding gas led to a reduction of the processable parameter range

accompanied by severe cracking and crystallization. However, no reaction of nitrogen with the alloy was observed, instead the formation of $\text{Zr}_4\text{Cu}_2\text{O}$ was observed as the primary phase formation for all investigated gases. Despite a similar impurity as the applied N_2 the introduced Ar_{98}H_2 as shielding gas led to comparable results as Ar. Introducing hydrogen as a reducing element, therefore, appears as a promising approach to reduce the influence of oxygen impurities in the introduced gases. Therefore, further investigations with lower impurities within the gas mixture and higher H contents will be performed.

Acknowledgements

The authors would like to thank Dr.-Ing. Stefanie Hanke from the Chair of Materials Engineering at the University of Duisburg-Essen for their extensive support in carrying out metallography. We also want to thank Nico Neuber, Patrick Stiglmaier, and Martina Stemmler from the Chair of Metallic Materials for help in sample preparation, analysis, and fruitful discussions. Further thanks also go to Moritz Stolpe from Heraeus GmbH and Dominik Bauer from Linde AG for the provision of the powder material and gas. The research was conducted within the Industrial Community Research (IGF) project 19927 N of the Association for Research in Precision Mechanics, Optics and Medical Technology (F.O.M), Werderscher Markt 15, 10117 Berlin. The project is funded by the German Federal Ministry of Economics and Energy within the framework of the AiF's Programme for the Promotion of Industrial Community Research (on the basis of a resolution passed by the German Bundestag).

References

- [1] Wohlers Associates. Wohlers report 2019: 3D printing and additive manufacturing state of the industry. Fort Collins, Colorado: Wohlers Associates; 2019.
- [2] Yap CY, Chua CK, Dong ZL, Liu ZH, Zhang DQ, Loh LE et al. Review of selective laser melting: Materials and applications. *Applied Physics Reviews* 2015;2(4):41101
- [3] Chen S, Tong Y, Liaw P. Additive Manufacturing of High-Entropy Alloys: A Review. *Entropy* 2018;20(12):937.
- [4] Li XP, Ji G, Chen Z, Addad A, Wu Y, Wang HW et al. Selective laser melting of nano-TiB 2 decorated AlSi10Mg alloy with high fracture strength and ductility. *Acta Materialia* 2017;129:183–93.
- [5] Li XP, Roberts MP, O'Keeffe S, Sercombe TB. Selective laser melting of Zr-based bulk metallic glasses: Processing, microstructure and mechanical properties. *Materials & Design* 2016;112:217–26.
- [6] Pauly S, Schricker C, Scudino S, Deng L, Kühn U. Processing a glass-forming Zr-based alloy by selective laser melting. *Materials & Design* 2017;135:133–41.
- [7] Yang C, Zhang C, Xing W, Liu L. 3D printing of Zr-based bulk metallic glasses with complex geometries and enhanced catalytic properties. *Intermetallics* 2018;94:22–8.
- [8] Inoue A, Shen B, Koshiba H, Kato H, Yavari AR. Cobalt-based bulk glassy alloy with ultra high strength and soft magnetic properties. *Nature Materials* 2003;2(10):661–3.
- [9] Kok Y, Tan XP, Wang P, Nai MLS, Loh NH, Liu E et al. Anisotropy and heterogeneity of microstructure and mechanical properties in metal additive manufacturing: A critical review. *Materials & Design* 2018;139:565–86.
- [10] Jung HY, Choi SJ, Prashanth KG, Stoica M, Scudino S, Yi S et al. Fabrication of Fe-based bulk metallic glass by selective laser melting: A parameter study. *Materials & Design* 2015;86:703–8.
- [11] Marattukalam JJ, Pacheco V, Karlsson D, Riekehr L, Lindwall J, Forsberg F et al. Development of process parameters for selective laser

- melting of a Zr-based bulk metallic glass. *Additive Manufacturing* 2020;33:101124.
- [12] Pacheco V, Karlsson D, Marattukalam JJ, Stolpe M, Hjärvarsson B, Jansson U et al. Thermal stability and crystallization of a Zr-based metallic glass produced by suction casting and selective laser melting. *Journal of Alloys and Compounds* 2020;825:153995.
- [13] Bordeenithikasem P, Stolpe M, Elsen A, Hofmann DC. Glass forming ability, flexural strength, and wear properties of additively manufactured Zr-based bulk metallic glasses produced through laser powder bed fusion. *Additive Manufacturing* 2018;21:312–7.
- [14] Wegner J, Frey M, Stiglmair P, Kleszczynski S, Witt G, Busch R. MECHANICAL PROPERTIES OF HONEYCOMB STRUCTURED ZR-BASED BULK METALLIC GLASS SPECIMENS FABRICATED BY LASER POWDER BED FUSION. *SAJIE* 2019;30(3).
- [15] Wang XJ, Zhang LC, Fang MH, Sercombe TB. The effect of atmosphere on the structure and properties of a selective laser melted Al–12Si alloy. *Materials Science and Engineering: A* 2014;597:370–5.
- [16] Dai D, Gu D. Effect of metal vaporization behavior on keyhole-mode surface morphology of selective laser melted composites using different protective atmospheres. *Applied Surface Science* 2015;355:310–9.
- [17] King WE, Anderson AT, Ferencz RM, Hodge NE, Kamath C, Khairallah SA et al. Laser powder bed fusion additive manufacturing of metals; physics, computational, and materials challenges. *Applied Physics Reviews* 2015;2(4):41304.
- [18] Pazuon C, Hryha E, Forêt P, Nyborg L. Effect of argon and nitrogen atmospheres on the properties of stainless steel 316 L parts produced by laser-powder bed fusion. *Materials & Design* 2019;179:107873.
- [19] Liu Z, Li R, Wang H, Zhang T. Nitrogen-doping effect on glass formation and primary phase selection in Cu–Zr–Al alloys. *Journal of Alloys and Compounds* 2011;509(16):5033–7.
- [20] Brezovnik A. J. Tušek, M. Suban: Influence of hydrogen in argon as a shielding gas in arc welding of high-alloy stainless steel.
- [21] Dong F, Su Y, Luo L, Wang L, Wang S, Guo J et al. Enhanced plasticity in Zr-based bulk metallic glasses by hydrogen. *International Journal of Hydrogen Energy* 2012;37(19):14697–701.
- [22] King WE, Barth HD, Castillo VM, Gallegos GF, Gibbs JW, Hahn DE et al. Observation of keyhole-mode laser melting in laser powder-bed fusion additive manufacturing. *Journal of Materials Processing Technology* 2014;214(12):2915–25.
- [23] Scipioni Bertoli U, Wolfer AJ, Matthews MJ, Delplanque J-PR, Schoenung JM. On the limitations of Volumetric Energy Density as a design parameter for Selective Laser Melting. *Materials & Design* 2017;113:331–40.
- [24] T.W. Eagar N-ST. Temperature fields produced by traveling distributed heat sources. *Welding Journal* 1983(62):346–55.
- [25] Pooriya Dastranjy Nezhadfar, Mohammad Masoomi, Scott Thompson, Nam Pham, and Nima Shamsaei. Mechanical Properties of 17-4 Ph Stainless Steel Additively Manufactured Under Ar and N₂ Shielding Gas.
- [26] Masmoudi A, Bolot R, Coddet C. Investigation of the laser–powder–atmosphere interaction zone during the selective laser melting process. *Journal of Materials Processing Technology* 2015;225:122–32.
- [27] Masoomi M, Pegues JW, Thompson SM, Shamsaei N. A numerical and experimental investigation of convective heat transfer during laser-powder bed fusion. *Additive Manufacturing* 2018;22:729–45.
- [28] Heinrich J, Busch R, Nonnenmacher B. Processing of a bulk metallic glass forming alloy based on industrial grade Zr. *Intermetallics* 2012;25:1–4.
- [29] Na T-W, Kim WR, Yang S-M, Kwon O, Park JM, Kim G-H et al. Effect of laser power on oxygen and nitrogen concentration of commercially pure titanium manufactured by selective laser melting. *Materials Characterization* 2018;143:110–7.

11th CIRP Conference on Photonic Technologies [LANE 2020] on September 7-10, 2020

Laser Powder Bed Fusion of NdFeB and influence of heat treatment on microstructure and crack development

Nicole Emminghaus^{a,*}, Christian Hoff^a, Jörg Hermsdorf^a, Stefan Kaieler^a

^aLaser Zentrum Hannover e. V., Hollerithallee 8, 30419 Hannover, Germany

* Corresponding author. Tel.: +49-511-2788-355 ; fax: +49-511-2788-100. E-mail address: n.emminghaus@lzh.de

Abstract

This work follows up on the influence of the processing parameters and a subsequent heat treatment on the resulting properties of magnetizable neodymium-iron-boron (NdFeB) parts produced by Laser Powder Bed Fusion. Highly dense (> 95 %) cubes were built up and an uneven distribution of neodymium- and iron-rich phases was observed. It could be shown that internal stresses leading to crack development represent the main challenge. According to the experimental results, this can be approached more effectively through successive optimization of the processing parameters and therefore adjustment of the energy input rather than heat treatment of the built parts.

© 2020 The Authors. Published by Elsevier B.V.

This is an open access article under the CC BY-NC-ND license (<http://creativecommons.org/licenses/by-nc-nd/4.0/>)
Peer-review under responsibility of the Bayerisches Laserzentrum GmbH

Keywords: Additive manufacturing; laser powder bed fusion; NdFeB magnets; rare-earth magnets; microstructure

1. Introduction

As electric mobility and renewable energy production become more important, demands for high performance permanent magnets (e.g. for electrical motors) with adapted geometries come up. With Laser Powder Bed Fusion (LPBF), geometric limitations are overcome and new microstructures can be achieved. In addition, the high material utilization and thus resource efficiency is a further advantage, which contributes to a growing market share within the manufacturing technologies [1].

Numerous industrially relevant materials like steel or titanium can already be processed using LPBF [2, 3, 4]. They show a process-specific fine-grained microstructure that depends on the process parameters selected, as well as changed mechanical properties, e.g. anisotropy in tensile strength, compared to conventional manufacturing processes [5, 6].

A material group that, despite of geometric limitations for conventional processing techniques, has hardly been considered in connection with LPBF are materials for

permanent magnets, especially NdFeB that takes over half of the market for permanent magnets due to its outstanding magnetic properties [7]. By Jacimovic *et al.* a spherical powder was processed by LPBF for the first time using a pulsed laser system leading to magnets with very fine microstructure providing grain sizes of around 1 μm and superior magnetic performance at elevated temperatures compared to conventionally processed NdFeB magnets [8]. The fine-grained microstructure, which is favorable for a high coercivity, was also described by Goll *et al.* and Kolb *et al.* and is caused by rapid solidification during the building process [9, 10]. Furthermore, different phases, mainly divided into the Nd-rich and the Fe-rich phase in which the Nd-rich phase has essential importance for the materials coercivity [11], could be detected [9, 10]. Beneath Kolb *et al.* also Urban *et al.* provided a parameter study for processing an NdFeB alloy indicating that with less porosity, the specimens become prone for cracking [12].

Former publications focused on the achievable magnetic properties and either lack in a sufficient number of processed

specimens for a statistical analysis or they look on the microstructure and especially the occurring cracks only superficially without taking into account different phase distributions within the samples or the influence of processing parameter variation. Additionally, in none of the papers dealing with LPBF of NdFeB heat treatment was applied.

This paper therefore aims to provide a closer look on the microstructure in dependence of the applied processing parameters and partly, a subsequent heat treatment. The occurrence of cracks and possible ways to prevent them are taken into account and influences of processing parameters on the relative density as well as their interaction effects are investigated.

2. Materials and Methods

2.1. Experimental Materials

As in some of the aforementioned publications [8, 10, 12], the gas-atomized and therefore spherical commercial NdFeB powder (commercial name MQP™-S-11-9-20001-070) supplied by Magnequench GmbH (Tübingen, Germany) was used in this work. The material has the chemical composition $\text{Nd}_{7.5}\text{Pr}_{0.7}\text{Zr}_{2.6}\text{Ti}_{2.5}\text{Co}_{2.5}\text{Fe}_{75}\text{B}_{8.8}$ with a theoretical density of 7.43 g/cm^3 and a median particle diameter d_{50} of $38.99 \mu\text{m}$ with a standard deviation in particle size of $17.25 \mu\text{m}$ according to the manufacturers' datasheet [13]. Scanning electron microscopy (SEM) was employed to analyze the powder morphology. As Fig. 1 shows, the morphology was mainly spherical with a high proportion of small particles and also some agglomerates. Both may impede the flowability and spreadability of the material.

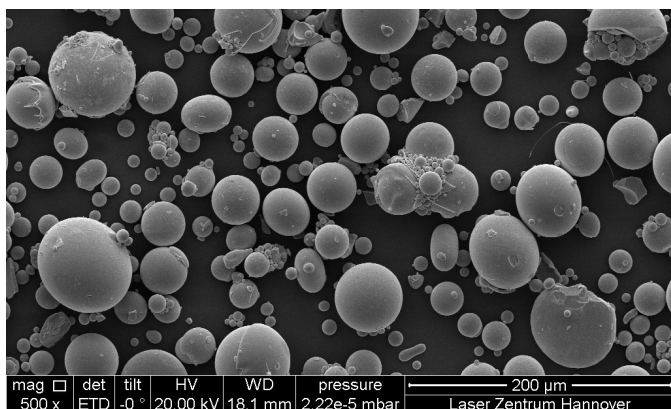


Fig. 1. SEM image of the NdFeB powder.

2.2. Experimental Equipment

The experiments were executed on the industrial machine Lasertec 12 SLM by DMG MORI Bielefeld GmbH (Bielefeld, Germany) that is equipped with an ytterbium fiber laser (single mode, continuous wave, wavelength 1070 nm) operating at a maximum laser power of 400 W. It supplies a beam quality factor of $M^2=1.05$ and a minimum beam diameter of $35 \mu\text{m}$. Especially when working with highly oxygen sensitive materials, as it is the case with NdFeB, filling the processing chamber with argon gas is necessary to prevent oxidation.

Thereby the mentioned machine can reach a minimum residual oxygen content of 0.13 to 0.15 vol%.

For the subsequent heat treatment, the oven Top 16/R by Nabertherm GmbH with a maximum heating temperature of $1300 \text{ }^\circ\text{C}$ was used.

2.3. Experimental Methods

For the investigations, rectangular specimens were built directly on the substrate plate. The plate was made of stainless steel (1.4404), sandblasted and preheated ($200 \text{ }^\circ\text{C}$) to ensure a good bond between plate and specimens. The specimens were built with a side length of 5 mm and a height of 6.4 mm to provide a sufficient volume reserve when being cut off the substrate plate. Because former publications indicated that small layer thicknesses would be advantageous [10, 12], a constant layer thickness of $30 \mu\text{m}$ was chosen for all experiments. The beam diameter was kept at the minimum of $35 \mu\text{m}$ and a cross-hatching strategy with a rotation angle of 67° between adjacent layers was employed.

Laser power, scanning speed and hatch distance are the basic processing parameters that influence the process outcomes in LPBF according to literature [10, 12] and former experiments, therefore they were chosen as the three parameters to be varied in the conducted experiments.

Preliminary tests showed that for single linescans, high energy inputs and in particular high laser powers are desirable for good line qualities, means uniformly built and smooth lines. First cubic samples were built with scanning speeds up to 1300 mm/s and laser powers up to 150 W resulting in a high amount of failures especially for high energy inputs, in contrary to the linescans, due to extensive crack development.

Consequently, for the 3 experimental runs conducted in this work relatively low laser power and low scanning speed were implemented to reduce thermal stress. The chosen parameter settings of run 2 and 3 were based on the outcomes of run 1 and 2 respectively. Table 1 provides an overview of all parameter settings in the conducted experimental runs. It also shows how many of the planned samples of each run could be successfully built and evaluated.

Table 1. Parameter settings in experimental runs.

Parameter	1 st run	2 nd run	3 rd run
Laser power P_L in W	40 / 60	20 / 30 / 40 / 50 / 60	20
Scanning speed v_s in mm/s	150 / 300	100 / 200 / 300 / 400 / 500 / 600	100 / 200
Hatch distance d_H in μm	20 / 40	30	30 / 45 / 60 / 75 / 100
Heat treatment	2 h / $650 \text{ }^\circ\text{C}$	2 h / $500 \text{ }^\circ\text{C}$	none
Specimens	16	20	20
Evaluable specimens	12	14	20

The chosen settings for the subsequent heat treatment were based on literature on conventionally processed NdFeB magnets (e.g. [14]) and experiments were carried out in normal atmosphere using the aforementioned oven. After two hours at the given temperature, the specimens cooled down in the closed

oven and were taken out at room temperature. Due to failed built ups of some specimens not all parameter combinations could be submitted to a subsequent heat treatment.

2.4. Methods for Analysis

After processing respectively subsequent heat treatment, the specimens were taken off the substrate plate manually. Parts from run 1 were directly embedded in epoxy resin and polished. To enable further characterization of the porosity, the Archimedes method with isopropanol as measuring liquid was employed in run 2 and 3 prior to embedding and polishing. After polishing, pores and cracks were analyzed by light microscopy (Olympus BX60 by Olympus, Europa SE & Co. KG). The images were transformed into black and white images and the relative density was evaluated by calculating the ratio between black and white pixels. For each specimen three cross sections were made to calculate the mean relative density, which was then evaluated statistically with the statistics software JMP by SAS Institute GmbH. Afterwards the specimens were etched (1 % Nital for 10 s) to investigate the microstructure. For high magnification images, the confocal laser scanning microscope VK-X1000 by Keyence Deutschland GmbH was employed. The element distribution in the phases observed in the microstructure were examined by EDX (energy dispersive x-ray spectroscopy).

3. Results and Discussion

As mentioned before, not all specimens could be built up as successfully as the cubes shown in Fig. 2 a). Some specimens failed due to extensive cracks and the resulting brittleness (Fig. 2 b)). Only successfully built specimens or ones with minor defects were analyzed.

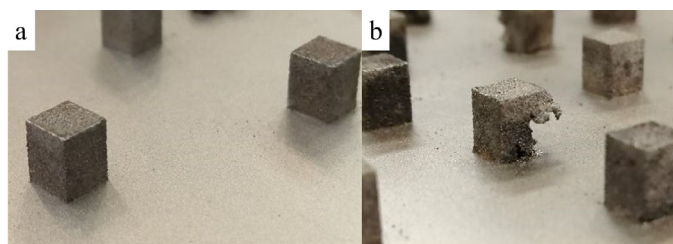


Fig. 2. (a) Successfully built specimens; (b) failed specimens.

The first and second experimental runs showed that specimens with higher laser power and especially higher scanning speed exhibit larger cracks, as it can be seen in Fig. 3, and were more likely to fail during building. This observation can be attributed to the increasing cooling rates accompanying increasing scanning speeds. The occurring high temperature gradients lead to internal stresses and consequently induce cracks. As pores are likely to impede crack propagation and therefore might improve mechanical stability of the cubic specimens, the aim of the third run was to shift the examined parameter settings towards lower energy inputs to generate pores and specimens with less cracks. As a result, all planned specimens could be built up successfully. A detailed evaluation of porosity, crack development and the observed microstructure will be given in the following.

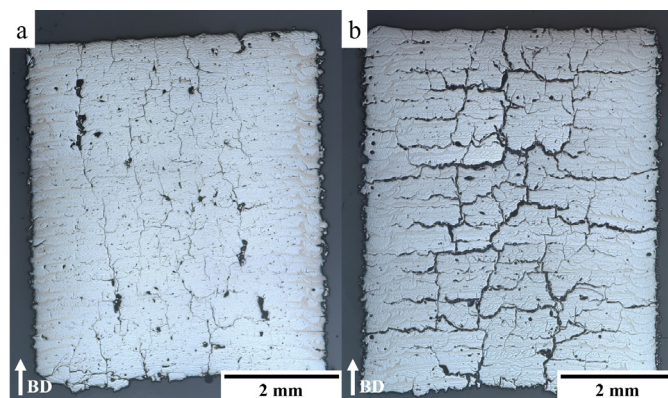


Fig. 3. Cross sections of built specimens without heat treatment and with (a) P_L : 20 W, v_S : 100 mm/s, d_H : 30 μm ; (b) P_L : 50 W, v_S : 300 mm/s, d_H : 30 μm .

3.1. Porosity

The comparison of the two methods for measuring the relative density, the Archimedes method and image analysis of metallographic cross sections, indicates that both lead to different results which, however, roughly show the same trends. For both methods, the results become more similar for high relative densities while for low relative densities the Archimedes method leads to much higher values than the image analysis. This is due to the increasing open porosity with a decreasing relative density. The open pores and cracks can be detected as such in the image analysis but using the Archimedes method, they become filled with liquid and cannot be measured.

In general, the Archimedes method can only be used to achieve a rough estimate of the results but cannot replace the image analysis method, which therefore should be regarded in the following results.

The maximum mean relative density measured by image analysis was 95.71 % (P_L : 40 W, v_S : 200 mm/s, d_H : 30 μm), the minimum relative density was 62.28 % (P_L : 20 W, v_S : 200 mm/s, d_H : 100 μm). The influences and interactions between the three varied processing parameters were evaluated and were found to all have a significant influence on the processing result. As Fig. 4 presents, high relative density, or in other words low porosity, occurs for low scanning speed and low hatch distance.

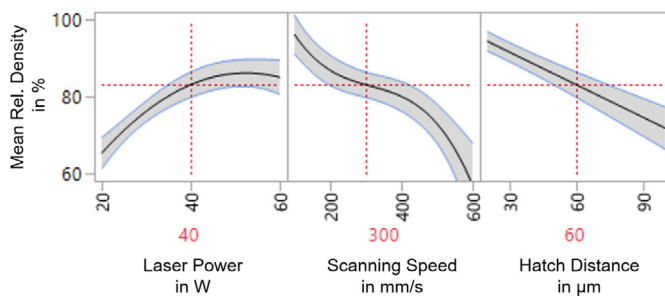


Fig. 4. Prediction profiler for varied parameters.

The prediction profiler (Fig. 4) enables predictions of the response values in dependence of the factors, the varied processing parameters. The grey areas around the graphs represent the confidence intervals. While the dependency on

the hatch distance is linear, for the scanning speed also a cubic influence can be observed, that is, however, less pronounced than the linear effect. For the laser power with a quadratic influence there is a maximum that depends on the chosen scanning speed as it can be seen in the interaction plot (Fig. 5).

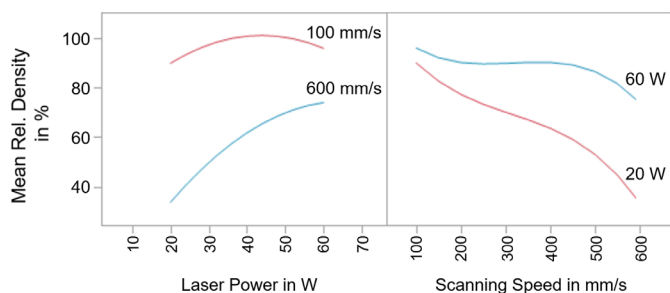


Fig. 5. Interaction plot.

The higher the chosen scanning speed the higher the value of the laser power that should be chosen for a maximum relative density. Additionally, for a high scanning speed, the laser power has a stronger influence on the result. This can be seen in the much steeper graph for 600 mm/s than for 100 mm/s in Fig 5. The other way round, it can be stated that for low laser power, the scanning speed has a stronger influence.

The parameters and their effects can also be summed up by calculating the energy input. Fig. 6 presents the mean relative density in dependence of the applied volume energy density. In addition, the hatch distance is marked in color in this graph. As the effects of the single parameters already predicted, a higher energy density leads to a higher mean relative density.

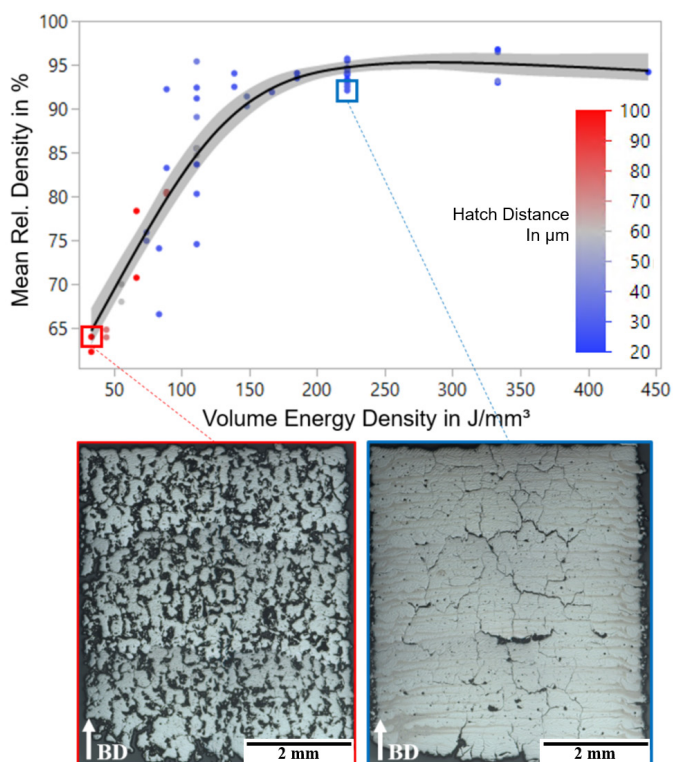


Fig. 6. Relative density dependent on volume energy density with smooth line (cubic spline, $\lambda = 1$) and corresponding cross sections.

The higher amount of pores especially for high hatch distances and low energy density is caused by the insufficient energy input for melting the material. A lack of fusion between the layers results and therefore irregular shaped pores occur, as Fig. 6 illustrates. Additionally, a high hatch distance can lead to unmelted material between the scan lines.

A difficulty that should be kept in mind is that for the image analysis cracks also count as porosity as their color is darker than the surrounding dense material. The calculated densities therefore contain an error if only the pores count for porosity. Furthermore, the pores and thus the porosity are only reproducible within large constraints and should consequently always be regarded critically.

The partly applied subsequent heat treatment did not change the porosity. The pores remained in the specimens and did not change their size or geometry because the applied temperatures were below the melting point and no pressure was applied to the specimens.

3.2. Crack Development

Cracks occurred in all specimens but there were differences in the size of them. Since the specimens showed an extensive crack network, it was not possible to measure the length of single cracks. The diameter of cracks as a measure for the crack size increased for increasing scanning speed with maximum values of around 60 μm . The resulting brittleness of the specimens together with the internal stresses was the main cause of failure during processing. In the middle of the specimens, the cracks had larger diameters than near the surface (see Fig. 3, 6 and 7). The stresses that develop in the center of the specimens during building are tensile stresses caused by the material shrinkage when the material cools down and solidifies. NdFeB in general is a brittle material and so the internal stresses lead to material failure in the form of cracking. The few cracks that started on the side surface proceeded perpendicular to the building direction (BD) while in the center there was also a high amount of cracks running in building direction.

A subsequent heat treatment could not reduce the amount of cracks. A possible reason for this observation are the different coefficients of thermal expansion of substrate plate and specimens. The one of the steel substrate plate is around 3 times higher than the one of NdFeB. Accordingly, the heat treatment induced additional tension in the specimens due to the higher expansion of the built plate. Nevertheless, there was a difference in the crack appearance between specimens with and without heat treatment (Fig. 7). For specimens from the first run treated with 650 $^{\circ}\text{C}$ for 2 hours the cracks appear lighter and seem to have a smaller diameter.

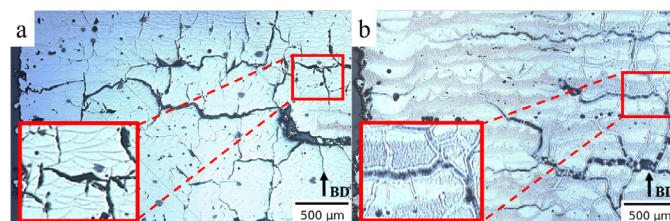


Fig. 7. Cracks (a) without heat treatment; (b) after heat treatment (2h/650 $^{\circ}\text{C}$).

A closer look on the cross section reveals a thin light layer on the crack surfaces. An element analysis of this layer will be given in the next section. Specimens treated with 500 °C however did not show a comparable image. No difference of the cracks for samples with and without heat treatment could be detected for the specimens in the second experimental run.

3.3. Microstructure

Etching of the metallographic cross sections revealed different phases within the bulk material. The melt tracks were clearly visible as they were darker at the edge than in the middle. Near the surface of the specimens, the melt pools were much larger than in the center. This was caused by the decreased heat conduction at the interface of bulk material and powder bed that leads to an accumulation of heat and thus deeper melt pools that can be seen in Fig. 8.

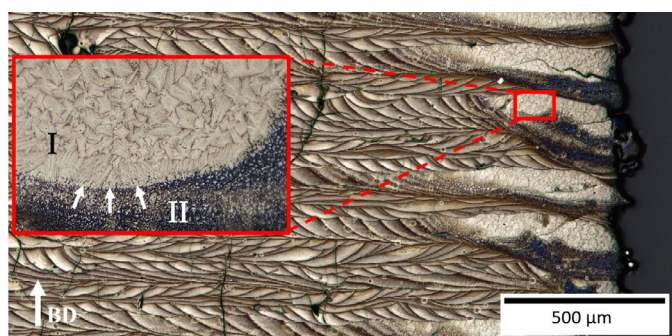


Fig. 8. Cross section after etching without heat treatment and with P_L : 20 W, v_S : 100 mm/s, d_H : 30 μm .

Some of the specimens showed finely granulated, dark regions especially near the surface where the heat accumulation led to deep melt pools. The amount of these dark regions increased with increasing energy input. As the close up in Fig. 8 reveals, there were lighter zones (I) in between the granulated dark zones (II) containing a dendritic grain structure. Near the former interface of melt pool and solid material, the dendrites show a more directional growth (arrows, Fig. 8) than in the middle of the melt pool attributed to the direction of the heat flow and the grain growth in the opposite direction.

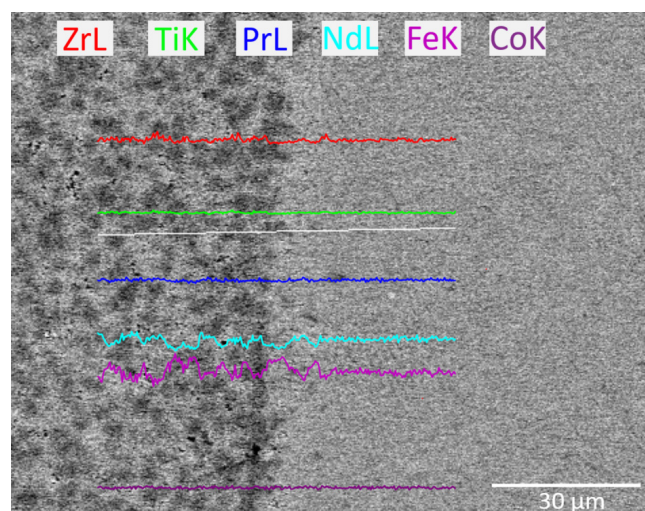


Fig. 9. EDX analysis of different phases (scan line in white).

To further investigate the different phases observed in the etched specimens, an EDX analysis was conducted (Fig. 9) for the interface between the dendritic light and the finely granulated dark zone that was marked by the arrows in Fig. 8. As the lines for the different elements show, there are only few fluctuations in element composition within the light zone on the right. Within the granulated dark zone, the lines show varying contents of zirconium (Zr), iron (Fe) and neodymium (Nd). Thereby Zr shows the smallest fluctuations that also cannot be connected to the fluctuations of the other elements or the differences in color. On the other hand, Nd and Fe (turquoise and purple line) show strong fluctuations in content within the dark zone that are also connected to the different colored constituents of this zone. The dark parts are rich in Fe and poor in Nd while for the lighter parts the opposite is the case. This indicates that the dark phase is formed by magnetically soft α -iron and the light phase within the dark zone is formed by the desired hard magnetic $\text{Nd}_2\text{Fe}_{14}\text{B}$ that is essential for the achievable magnetic properties. The light zone on the right seems to consist completely of $\text{Nd}_2\text{Fe}_{17}\text{B}_x$ (with $x \sim 1$ [15]) according to Sridharan *et al.* [16], which is a soft magnetic non-equilibrium phase. Under equilibrium conditions, $\text{Nd}_2\text{Fe}_{14}\text{B}$ develops in the peritectic reaction $L + \gamma \rightarrow \text{Nd}_2\text{Fe}_{14}\text{B}$ [17]. In the case of LPBF, solidification takes place under non-equilibrium conditions with rapid cooling rates that can induce critical undercooling of the melt. According to David & Titek, the solidification mode can change to $\text{Nd}_2\text{Fe}_{17}\text{B}_x$ instead of $\text{Nd}_2\text{Fe}_{14}\text{B}$ or γ -Fe when there is an undercooling of over 60 K that is likely to take place in additive manufacturing [18]. The nucleation of magnetically soft $\text{Nd}_2\text{Fe}_{17}\text{B}_x$ then becomes favorable [19]. With scanning speeds over 0.1 m/s and therefore high interface velocities in the conducted experiments, this could be a possible explanation for the observed light zones consisting presumably of $\text{Nd}_2\text{Fe}_{17}\text{B}_x$. Furthermore, the dark zones occurring especially in regions with heat accumulations can be explained by the cyclic reheating, remelting and slower solidification in this area and therefore near equilibrium conditions leading to the formation of the equilibrium phases. Nevertheless, the EDX analysis does not provide sufficient information to clearly identify the present phases and should be supplemented by other methods like EBSD (electron backscatter diffraction).

Apart from the general microstructure, etching revealed additional information about the effect of heat treatment on the cracks. The layers that formed inside of the cracks during heat treatment in the first experimental run could be seen more clearly after etching (Fig. 10 a)).

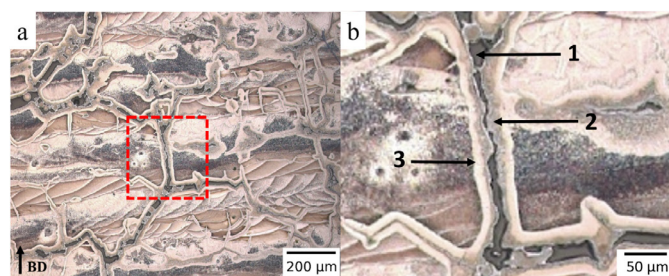


Fig. 10. (a) Etched cross section after heat treatment (2h/650 °C) and with P_L : 60 W, v_S : 300 mm/s, d_H : 20 μm ; (b) close up of crack with different zones.

In general, it can be differentiated between three different zones: (1) the open crack in the middle, (2) the dark zone directly surrounding the crack and (3) the light zone in between the dark zone and the bulk material. For these zones, different element contents could be detected by EDX analysis (Fig. 11)). Both zones around the open crack, especially the inner zone, show a high oxygen content. The darker inner zone (2) is rich in neodymium and poor in iron whereas the outer lighter zone (3) provides the opposite elemental distribution. As the oven only allowed heat treatment in normal atmosphere, this leads to the assumption, that due to the missing argon for inertisation, oxidation within the cracks took place leading to a reduction of the crack diameter. Thereby, different oxides developed, a neodymium-rich and an iron-rich oxide phase, leading to the observed layers filling up the cracks.

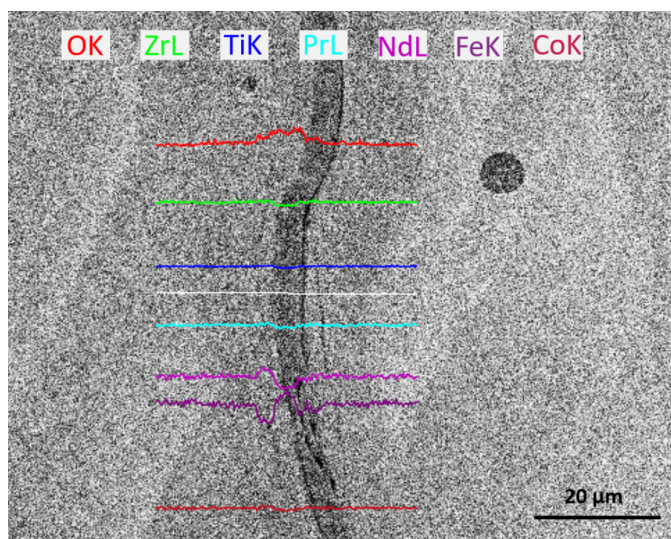


Fig. 11. EDX analysis of a crack after heat treatment (2h/650 °C) (scan line in white).

4. Conclusion

In this work, the influence of different processing parameters and their interactions as well as a subsequent heat treatment on the resulting properties of NdFeB parts produced by LPBF were investigated. This first time statistical analysis could show that all three varied parameters have a significant influence on the process outcome with a significant interaction effect of laser power and scanning speed. Summed up it can be stated that the energy input as a calculated measure containing all of the varied parameters can be used to adapt the porosity of additively manufactured NdFeB parts specifically. It is more effective than a subsequent heat treatment that could not decrease the amount of pores or cracks. Cracks caused by internal stresses were the main cause of specimen failure during the building process and could be attributed most effectively by increasing the porosity through implementing higher hatch distances and therefore a lower volume energy density. Microstructural analysis revealed different phases indicating a non-equilibrium solidification due to rapid cooling rates and a change in solidification mode presumably leading to the formation of soft magnetic phases and therefore weakened magnetic properties. Furthermore, the formation of oxide phases around the cracks after heat treatment could be detected.

With regard to this, further investigation of heat treatment methods under argon atmosphere or hot isostatic pressing (HIP) are of future interest. Nevertheless, a further microstructural analysis is inevitable to clearly identify the observed phases and as NdFeB is used for high performance permanent magnets, the magnetic properties in dependence of the processing parameters and the resulting microstructure will be part of future research.

References

- [1] Sapate KD, Apte TU. Metal fabrication by additive manufacturing. *International Journal of Current Engineering and Technology* 2019;7:9-14.
- [2] Gieseke M, Albrecht D, Nölke C, Kaierle S, Suttman O, Overmeyer L. Laserbasierte Technologien. In: Lachmayer R, Lippert RB, Fahlbusch T, editors. 3D-Druck beleuchtet: Additive Manufacturing auf dem Weg in die Anwendung. Berlin, Heidelberg: Springer-Verlag; 2016. p. 132.
- [3] Herzog D, Seyda V, Wycisk E, Emmelmann C. Additive manufacturing of metals. *Acta Materialia* 2016;117:371-392.
- [4] Schmidt M, Merklein M, Bourell D, Dimitrov D, Hausotte T, Wegener K, Overmeyer L, Vollertsen F, Levy GN. Laser based additive manufacturing in industry and academia. *CIRP Annals* 2017;66:561-583.
- [5] Song B, Zhao X, Li S, Han C, Wei Q, Wen S, Liu J, Shi Y. Differences in microstructure and properties between selective laser melting and traditional manufacturing for fabrication of metal parts: A review. *Frontiers in Mechanical Engineering* 2015;10:111-125.
- [6] Liu S, Shin YS. Additive manufacturing of Ti6Al4V alloy: A review. *Materials and Design* 2019;164:107552.
- [7] Gutfleisch O, Willard MA, Bruck E, Chen CH, Sankar SG, Liu JP. Magnetic materials and devices for the 21st century: Stronger, lighter, and more energy efficient. *Advanced Materials* 2011;23:821.
- [8] Jacimovic J, Binda F, Herrmann LG, Greuter F, Genta J, Calvo M, Tomse T, Simon RA. Net Shape 3D Printed NdFeB Permanent Magnet. *Advanced Engineering Materials* 2017; 1700098.
- [9] Goll D, Vogelgsang D, Pflanz U, Hohs D, Grubesa T, Schurr J, Bernthaler T, Kolb D, Riegel, H, Schneider G. Refining the Microstructure of Fe-Nd-B by Selective Laser Melting. *Physica status solidi (RRL)-Rapid Research Letters* 2019;13:1800536.
- [10] Kolb T, Huber F, Akbulut B, Donocik C, Urban N, Maurer D, Franke J. Laser Beam Melting of NdFeB for the production of rare-earth magnets. 6th International Electric Drives Production Conference (EDPC). IEEE 2016. p. 34-40.
- [11] Vial F, Joly F, Nevalainen E, Sagawa M, Hiraga K, Park KT. Improvement of coercivity of sintered NdFeB permanent magnets by heat treatment. *Journal of magnetism and magnetic materials* 2002;242:1329-1334.
- [12] Urban N, Huber F, Franke J. Influences of process parameters on Rare Earth Magnets produced by Laser Beam Melting. 7th International Electric Drives Production Conference (EDPC). IEEE 2017. p. 1-5.
- [13] neo Magnequench, Datasheet MQP-S-11-9-20001-070 isotropic powder.
- [14] Brown D, Ma BM, Chen Z. Developments in the processing and properties of NdFeB-type permanent magnets. *Journal of magnetism and magnetic materials* 2002;248:432-440.
- [15] Schneider G, Henig ET, Petzow G, Stadelmaier HH. The binary system iron-neodymium. *Zeitschrift fuer Metallkunde* 1987;78: 694-696.
- [16] Sridharan N, Cakmak E, List FA, Ucar H, Constantinides S, Babu SS, McCall SK, Paranthaman MP. Rationalization of solidification mechanism of Nd-Fe-B magnets during laser directed-energy deposition process. *Scripta Metallurgica* 2018. doi:10.1007/s10853-018-2178-7.
- [17] Schneider G, Landgraf FJ, Missell FP. Additional ferromagnetic phases in the Fe-Nd-B system and the effect of 600 °C annealing. *Journal of Less common Metals* 1989;153:169-180.
- [18] David SA, Vitek JM. Correlation between solidification parameters and weld microstructures. *International Materials Reviews* 1989;34:213-245.
- [19] Gao J, Volkmann T, Herlach DM. Undercooling-dependent solidification behavior of levitated Nd₁₄Fe₇₉B₇ alloy droplets. *Acta materialia* 2002;50:3003-3012.

11th CIRP Conference on Photonic Technologies [LANE 2020] on September 7-10, 2020

Mechanical properties of NiCrBSi self-fluxing alloy after LPBF with additional heating

Igor Shishkovsky^{a,*}, Nina Kakovkina^b, Vladimir Sherbakof^a

^aCenter for Design, Manufacturing and Materials (CDMM), Skolkovo Institute of Science and Technology, Moscow 121205, Russia

^bLebedev Physics Institute (LPI) of Russian Academy of Sciences, Samara 443011, Russia

* Corresponding author. Tel.: +7-495-280-1481 ext 3455; fax: +7-495-280-1481. E-mail address: I.Shishkovsky@skoltech.ru

Abstract

The study was devoted to a detailed experimental study of the implementation conditions of the laser powder bed fusion (LPBF) process of special-purpose products from self-fluxing powdered high-temperature NiCrBSi composite. Optimal regimes of LPBF for the 3D part of the simplest shape were experimentally determined. We recommended laser power $P = 100$ W, the laser scanning velocity is $v = 10$ cm / s, the beam diameter is $70 \mu\text{m}$, process gone in argon. Additional efforts were made to evaluate the effect of additional heating the base platform up to 500 °C. Optical and scanning electron microscopy, the X-ray diffraction analysis and EDS microanalysis were used for describing the sequence of structure formation in the created 3D samples. We conducted mechanical and tribological testing allowed to evaluate the relationship between the laser PBF parameters and data on linear wear, roughness, fracture rupture for 3D from NiCrBSi superalloy after the laser PBF process. Possible causes of increase crack formation during the LPBF of the NiCrBSi powder system are considered and revealed.

© 2020 The Authors. Published by Elsevier B.V.

This is an open access article under the CC BY-NC-ND license (<http://creativecommons.org/licenses/by-nc-nd/4.0/>)

Peer-review under responsibility of the Bayerisches Laserzentrum GmbH

Keywords: laser powder bed fusion (LPBF); nickel-chrome super alloy; additional heating.

1. Introduction

PGSR-4 is a Ni-base superalloy which can be used in laser additive manufacturing (powder bed fusion (PBF) and direct metal deposition (DMD)) [1-3]. Self-fluxing nickel superalloy PGSR-4 (16 % Cr, 2 % B, 3 % Si, <5 % Fe, 1% C, 0.04% P, 0.04 % S, Ni bal.,% wt) is considered to be six-component, hot resistant and refers to multiphase systems. The alloy is mixture of low-melting eutectic based on Ni, a solid solution of Cr, B, and Si in nickel with carbide inclusions, which makes it attractive for aerospace applications [2-6]. It is known that the distribution of carbide, boride, and silicide inclusions in the main phase with a Ni-based solid structure with an fcc (γ -phase) lattice has a complex character [2, 5, 6]. However, NiCrBSi alloy prone to microcracking during the LPBF process [2, 3]. Low ductility is explained by the conditions of cross-boundary grain cracking at the temperature range from

$0.5T_m$ to $0.7T_m$ [2], where pinning by carbides, borides and silicides by boundaries play important role. So, we strongly recommended to significantly raise the temperature (up to 500 – 700 °C) in the synthesis chamber in order to improve the manufacturability and reproducibility of 3D products and also to avoid the tendency to cracking [5, 6].

Influence of additional heating during the LPBF process was the goal of this study. Microstructure, phase structure, mechanical and tribological properties of the NiCrBSi alloy fabricated through LPBF are carried out.

2. Materials and methods

Powder of the NiCrBSi alloy was chosen with a dispersion of 60 – $80 \mu\text{m}$. The distribution of all the aforementioned powders by size was analyzed by means of an optical granulometer ALPAGA 500NANO (OCCHIO s.a.,

Belgium). The LPBF was performed on the ILM-100B ytterbium laser (IPG, Frazino, RF). Our SLM laboratory setup at the LPI was equipped with a high-temperature chamber, the temperature in which could reach 500-800 °C due to symmetrically arranged ceramic heaters. The temperature was measured by a thermocouple method. The LPBF setup was described earlier in [3, 6].

The optimized hatching distance was equal to the laser beam diameter $d_b = 70 \mu\text{m}$, layer thickness H was $\sim 0.2 \text{ mm}$. The laser scan velocity V ranged from 0.5 to 10 cm/s, laser power P - from 10 to 100 W. Two regimes of manufacturing have been studied on the substrate - chamber additional heating up to 500 °C and without it. Each second layer was formed on the bottom layer after its turning by 90 degrees (L – longitudinal, T – transversal). The laser melting process was conducted in Ar gas-filled chamber in order to protect the samples against oxidation and nitration.

After the etching, cross sections of the multi-layered melting samples were subjected to microstructural analysis with the optical microscope (Neophot 30M, Carl Zeiss, Germany) equipped with a digital camera. The 3D samples obtained under the optimized regimes were analyzed by PMT-3M (OKB SPECTR Ltd., St. Petersburg, Russia), microhardness testing and scan electron microscopy LEO 1450 (Carl Zeiss Company) equipped with an energy-dispersive x-ray microanalyzer (INCA Energy 300, Oxford Instruments, UK). The phase composition of the SLM parts was determined by XRD using a DRON-3M (Bourestnik Inc., St. Petersburg, RF) diffractometer in $\text{Co-K}\alpha$ radiation.

The universal complex Universal-1B (Samara-Balance Ltd., RF) was used for the tribomechanical tests, which included roughness behavior and wear fatigue by scheme (ring-plate sliding friction). As the material for the control sample, high-speed steel P6M5 (in the tempering state HRC65) was selected. Opportunities of Universal-1B setup were described precisely in [7].

3. Results and discussion

Previously, we experimentally determined the optimal LPBF regimes for individual passages of the NiCrSiB alloy, the regime of layerwise fabrication during scanning with a laser beam along the meander and a meander rotation by 90° on each subsequent layer [5, 6]. However, now, all of the above scanning techniques were carried out but with the platform heated up to $T = 500 \text{ }^\circ\text{C}$. The results of the obtained structures were compared when the treatment was carried out without heating.

Figure 1 shows the sample (disk) appearance from the NiCrBSi alloy after the LPBF (laser regime was $P = 100 \text{ W}$; $v = 10 \text{ cm/s}$; powder layer thickness $s = 0.1 \text{ mm}$; track distance $l = 0.2 \text{ mm}$; beam diameter 0.2 mm). Additive manufacturing process was realized in argon and the chamber with the powder composition was warmed up to 500 °C.

The surface roughness of the 3D printed samples after combining LPBF with heating is different from the LPBF without heating. The external shape of the products practically does not change, however, after 3D printing without heating, we clearly fixed the shrinkage of the 3D part in height. In

addition, the edges of the disk had a smoothed character due to high-temperature heating.



Fig. 1. LPBF of the NiCrBSi alloy (top view)

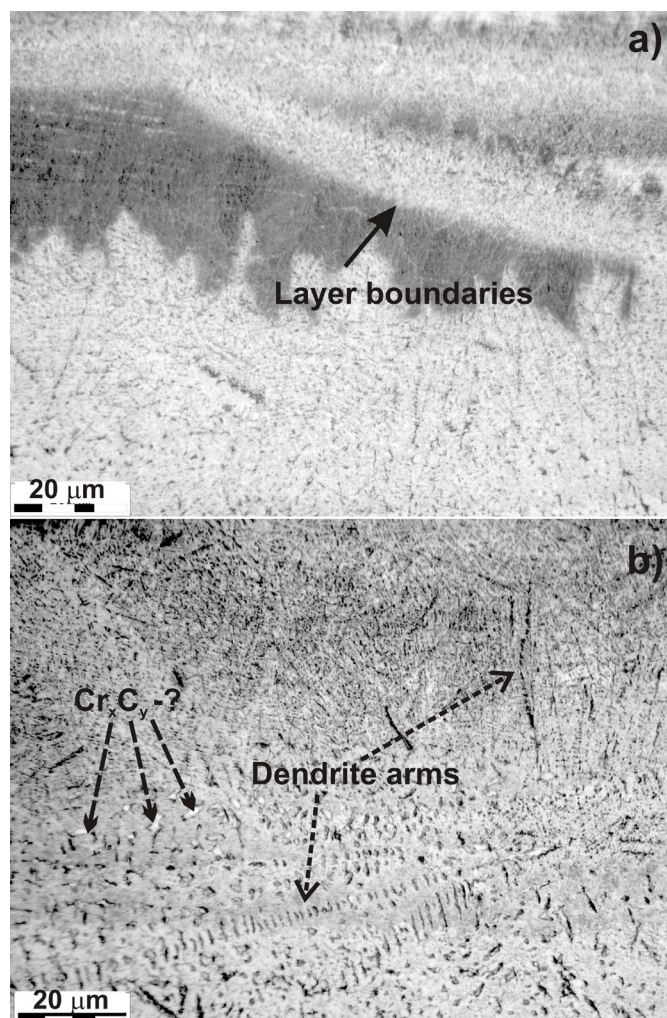


Fig. 2. OM after the LPBF without heating (a) and with heating (b) for NiCrBSi alloy

The LPBF process proceeds by nonequilibrium crystallization, which is due to the nature of the deposition and redistribution of the molten powder particles, specifically changes the phase-structural composition, and also affects the removal of part of the fluxing components (silicon and boron) with low-melting slags. The optical microscopy (OM) images of the upper layers is shown in Fig. 2. It can be argued that additional heating contributes to some homogenization of the structure of all the phases studied in NiCrSi alloy.

We clearly observe the interface between the laser remelted layers of alloy in Fig. 2a. Below and under the interface line, the darker section could be considered the slag zone that precipitated on the surface of the previous layer. In Fig. 2b, the long dendrite branch with size ~ 0.6 mm is visible. The growth direction of this dendrite is not corresponded to the direction of thermal transfer into substrate. Dendrite did not give secondary branches. Hence, the crystallization process was very fast. At the edges of the dendritic segregation the white inclusions are visible, which are the carbide phase.

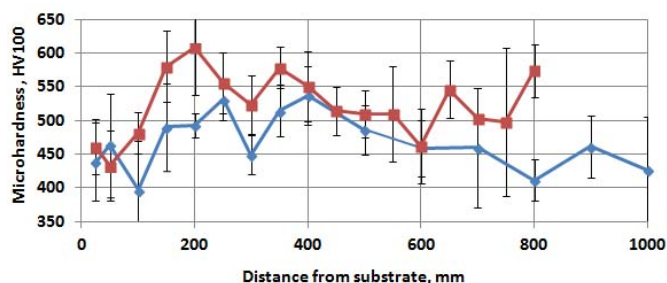


Fig. 3. Microhardness after the LPBF without heating and with additional heating for NiCrBSi alloy

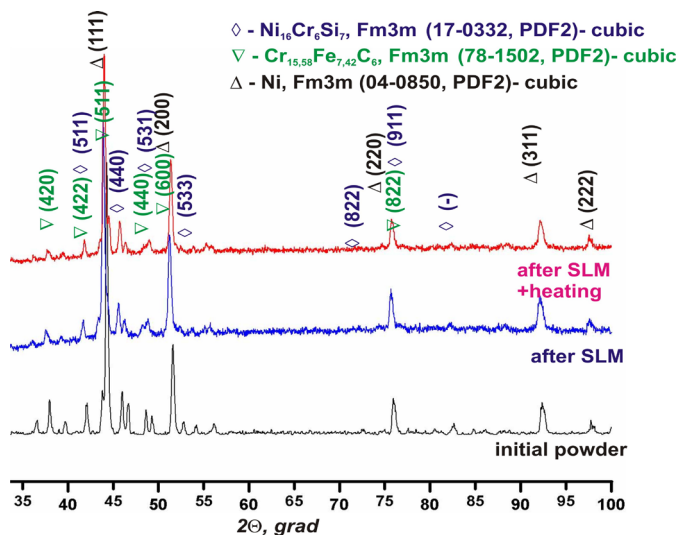


Fig. 4. XRD patterns after the LPBF and LPBF + heating for NiCrBSi alloy

These inclusions have different chemical compositions based on binary crystalline structures Me_xC_y phases (Cr_7C_3 , $Cr_{23}C_6$, Cr_3C_2) borides (CrB or Fe_2B) and complex borides Cr_3NiB_6 or $Cr_2Ni_3B_6$, silicides (τ_1 , τ_2 , σ , π) and Ni_2Si intermetallide [5,6]. This is evidenced by triple diagrams of the Cr-Ni-B, Cr-Ni-Si and Cr-Ni-C systems [8-10].

The microhardness measurements of the studied alloys are shown in Fig. 3. In almost all cases, we observe an increase in the microhardness of 3D parts after heat-producing LPBF process. The possibility of improving the microstructure and controlling the hardness in the 3D products allows us to hope for the applicability of NiCrBSi alloy in the aerospace or nuclear industry. We associate the increase and decrease in microhardness with the presence in the γ -Ni solid solution - carbides, borides or silicides inclusions. The low plasticity and increasing of crack formation after LPBF process during rapid cool are connected with different behavior of precipitates into intervals of Temperature Interval Fragility (TIF).

At the next stage, X-ray analysis of the 3D printed samples based on nickel super alloy after LPBF were carried out and the effect of additional heating was studied.

Figure 4 shows the results of the XRD patterns of NiCrBSi alloy after the selective laser melting (SLM - blue curve) and the SLM process together with heating to 500 °C (red curve). The lower diffraction pattern corresponds to the initial NiCrBSi powder before laser irradiation. The interpretation shows that the main phases, without any undesirable inclusions, remain after the SLM, including under additional heating, with virtually no changes.

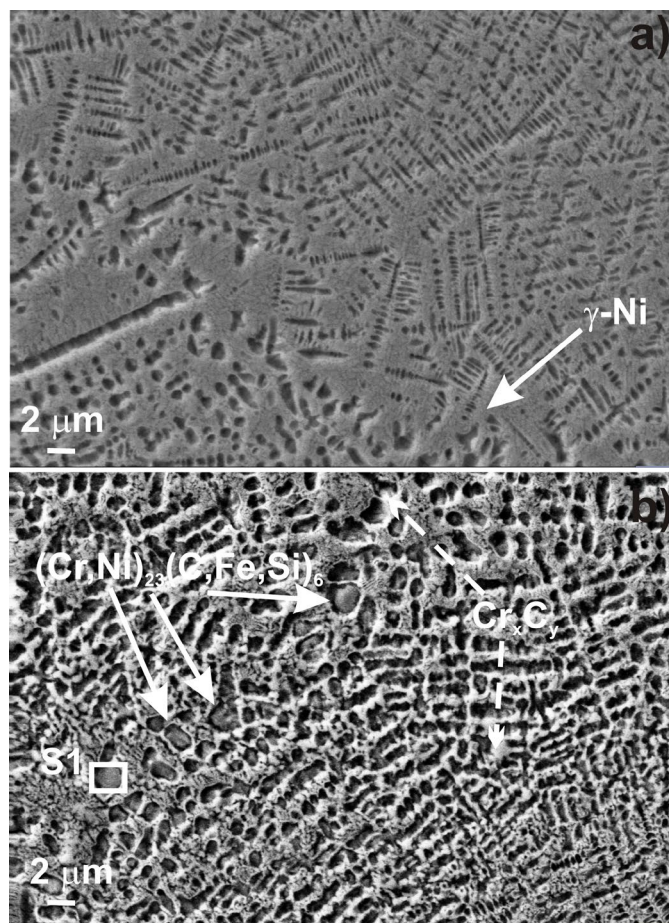


Fig. 5. The SEM images after the LPBF without heating (a) and with heating (b) for NiCrBSi alloy

Intense Bragg lines (111), (220), (311) and (222) are observed on all X-ray diffraction patterns, from the fcc lattice based on the γ - (Ni,Cr) solid solution. After laser influence a

slight increase of the lattice parameter is observed. At the same time, the redistribution of the content of secondary phases occurs. XRD patterns allowed to establish that the main phase is the γ - (Ni,Cr) solid solution with a low content of carbides, borides and silicides (below 8%).

The typical submicrostructures is shown in Fig. 5 and correspond to the above OM results (see, Fig. 2). We can again repeat that heating makes the microstructure more homogenously. The NiCrBSi alloy microstructure as a whole did not change as a result of additional heating.

The EDX microanalysis (Table 1) from the entire area of the presented images (Fig. 5) gives the following information. The element analysis data repeats the NiCrBSi chemical content of self-fluxing powder (see Introduction). Comparison with the XRD data allows to conclude, the possibility of the formation of the Ni₁₆Cr₆Si₇ phase (17-0332, PDF2) and the Cr_{15.58}Fe_{7.42}C₆ phase (78-1502, PDF2) is observed.

Table 1.EDS microanalysis by Fig. 5

Elements, % wt.	All Fig. 5a	All Fig. 5b	S1 (Fig.5b)
O	1.84	--	--
Si	1.94	1.83	2.84
Fe	2.86	3.45	23.63
Cr	13.72	13.62	10.57
Ni	79.63	81.10	62.96
Totals	100.00	100.00	100.00

The next reasons could be proposed for explanation of increase crack formation during LPBF of the NiCrBSi powder system. The first reason can be associated with the formation of a complex boride-silicide eutectic of the type (Ni + Ni₃B + Ni₃Si) with a melting point of 950 °C, which, located along the boundaries of the dendrites the γ -solid Ni based solution, leads to brittle destruction. The second reason can be explained on the basis of the possible separation of strengthening phases due to the decay of a non-equilibrium γ -solid solution based on Ni. Such precipitates are carbide particles Me₂₃C₆ and borides of chromium. The third reason may be associated with the presence of carbon from 0.4 % by weight up to 0.8 % by weight, significantly affecting the plastic properties of the metal during deformation [3, 6].

Also, we conducted a quantitative assessment of the 3D printed sample roughness after the LPBF and LPBF with heating. Figure 6 shows the OM surface of the investigated alloys under low magnifications (x10).

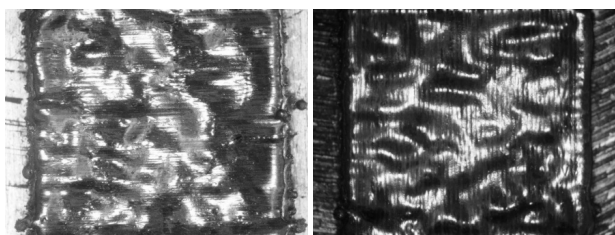


Fig. 6. General view of the rough surface for 3D printed samples made of the NiCrBSi after PLBF (left) and LPBF with heating to 500 OC (right).

Visually, we observed the roughness decrease after the heating-based LPBF. The color of the surface also changed,

which indicates an appearance of some surface precipitations (slags) after the LPBF with heating.

The microgeometry assess of the 3D samples obtained by the LPBF method, a profilograph - profilometer was used. The results for the studied samples from Fig. 7 were summarized in the Table. 2

Table 2. Microgeometry data

Name	NiCrBSi	NiCrBSi+ heating
Roughness , R _a (μm)	116,0	39,7
Running-in wear, R _{pk} (μm)	167,0	69,0
Surface 'contamination', R _{vk} (μm)	174,0	57,4

It can be noted that after the LPBF, a rather high surface roughness of R_{max}, often exceeding 100-116 μm, is formed. However, additional heating reduces the surface roughness after LPBF for all the alloys in 3-4 times we have studied. The R_{pk} value characterizes the running-in wear of the material. The use of 3D-printed samples with high values of the parameter R_{vk}, characterizing the surface oil consumption, provides good conditions for retaining the lubricant in the cracking zone.

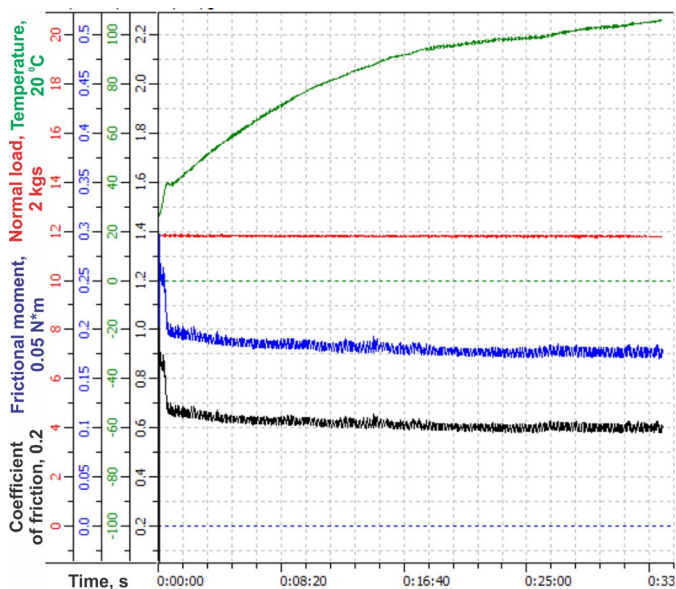


Fig. 7. Tribotechnical diagram of 3D samples from NiCrBSi alloy after LPBF with additional heating

For the tribomechanical tests, a ring-plane sliding friction scheme was used. Steel 41Cr4 (in the state of quenching and tempering HRC 45) was chosen as the material (a cylinder with a diameter of 10 mm) of the counter-part. The test objective was to evaluate the tribological properties of 3D parts of the material and analyze the frictional compatibility of the friction pair. Below, the example of tribotechnical diagram of normal load, temperature and friction moment during wear tests (Fig. 8) are presented for the case of the LPBF + heating to 500 °C, only.

During the tests, the friction moment stability is observed, which indicates that the studied friction pair has frictional compatibility under the specified conditions of friction. As it can be seen from Fig. 8, during the test, some heating of the

sample to temperatures up to ~ 100 °C was observed for NiCrBSi alloy, which, apparently, is not essential for these materials, because their melting points are significantly higher than these temperatures.

It was determined that the wear debris has been generated mainly from carbide, boride and/or silicide type ceramics as counter bodies, are filled in the pits on NiCrBSi surface. It provides formation of tribocouple which further prevents severe damages of NiCrBSi contact surface.

4. Conclusions

The mechanical properties of the NiCrBSi alloy after the PBF are investigated. Possible causes of increase crack formation during LPBF of the NiCrBSi powder system are considered and revealed. It is established that in the process of cooling the low ductility could be connected with some reasons. The following results were obtained also:

- The ability of the LPBF technology to create functional structures and to fabricate 3D parts of the NiCrBSi superalloy has been studied. The optimal regime for the layerwise LPBF in argon environment demands additional heating and the laser influence regime $P = 100$ W, $v = 10$ cm/s.
- By the methods of OM, SEM combined with EDX microanalysis, XRD patterns, the morphology and structural phase transformations in the studied materials were investigated.
- The mechanical properties of the fabricated 3D parts were evaluated: microhardness was measured, product roughness was determined, wear and fracture were estimated and the nature of friction was determined.

A fundamentally important result of the completed study is the experimental implementation of additional high-temperature heating during the LPBF process up to 500 °C, which was done for the first time in principle for the NiCrBSi superalloy, and for specific materials promising in aerospace applications - in particular.

Acknowledgments

This study was supported by the Russian Foundation of Basis Researches (grants 17-48-630290 Povolzh'ye_a).

References

- [1] Chang Z, Wang W, Ge Y, Zhou J, Cui Z. Microstructure and mechanical properties of Ni-Cr-Si-B-Fe composite coating fabricated through laser additive manufacturing. *J. of Alloys and Compounds* 2018;747: 401-07.
- [2] Boswell JH, Clark D, Li W, Attallah MM. Cracking during thermal post-processing of laser powder bed fabricated CM247LC Ni-superalloy. *Materials and Design* 2019;174: 107793.
- [3] Shishkovsky I. Aerospace applications of the SLM process of functional and functional graded metal-matrix composites based on NiCr superalloys. In: F. Froes, R. Boyer (Eds.) *Additive Manufacturing for the Aerospace Industry*. Elsevier Publ.; 2019. p. 265-80. doi: 10.1016/B978-0-12-814062-8.00014-5
- [4] Vilar R, Almeida A. Repair and manufacturing of single crystal Ni-based superalloys components by laser powder deposition—A review, *J. Laser Appl.* 2015; 27: S17004.
- [5] Shishkovsky I, Kakovkina N., Scherbakoff W. Layerwise fabrication refractory NiCrSiB composite with gradient grow of tungsten carbide

- additives by selective laser melting. *Optics and Laser Technology* 2019; 120: 105723.
- [6] Shishkovsky I, Kakovkina N., Scherbakov V. Fabrication of heat-resisting nickel composite gradient structures with TiC nano additive during powder bed fusion process. *Procedia CIRP* 2018; 74: 68-71.
- [7] Shishkovsky I, Scherbakov V., Ibatullin I, Volchkov V., Volova L. Nano- size ceramic reinforced 3D biopolymer scaffolds: tribomechanical testing and stem cell activity. *Composite Structures* 2018; 202: 651-59.
- [8] Velikanova T.Ya., Bondar A.A., Grytsi, A.V. The Chromium-Nickel-Carbon (Cr-Ni-C) PhaseDiagram. *J. Phase Equilib.* 1999; 20(2): 125-147.
- [9] Gladyshevsky E.I., Borusevich L.K. The Ternary System Cr-Ni-Si., *Russ. J. Inorg. Chem.* 1963; 8(8): 997-1000.
- [10] Chepiga M.V., Krivutskii V.P., Kuzma Yu.B., The System Cr-Ni-B. *Inorg. Mater.* 1972; 8(6): 928-932.

11th CIRP Conference on Photonic Technologies [LANE 2020] on September 7-10, 2020

Surface integrity factors influencing fatigue crack nucleation of laser powder bed fusion Ti6Al4V alloy

A.M.Vilardell^{a,*}, G.Fredriksson^a, F.Cabanettes^b, A.Sova^b, P.Krakhmalev^a

^aKarlstad University, Department of Engineering and Physics, Karlstad SE-651 88, Sweden.

^bUniversity of Lyon, ENISE, LTDS CNRS UMR 5513, 58 rue Jean Parot, 42023 Saint-Etienne, France.

* Corresponding author. Tel.: +8152-789-3358; fax: +8152-789-5348. E-mail address: amvilardell.research@gmail.com

Abstract

The quality of the surface influences remarkably the fatigue life of additive manufactured components. This work proposes to study the influence of surface integrity on the bending fatigue life of Ti6Al4V manufactured by laser powder bed fusion. Rectangular specimens were manufactured horizontally and the last printed layer had laser track scanning directions ($\alpha=30^\circ, 60^\circ, 90^\circ$) in relation to the specimen length. The top surface 3D-roughness average was similar for all the specimens. The specimens were studied under as-built and heat-treated conditions. A correlation between laser track scanning direction, 2D-roughness parameters, and fatigue life for as-built specimens was found. The as-built specimens with 90° and 30° direction showed the shortest and the longest fatigue life, respectively. Heat-treated specimens showed a shorter fatigue life independently of the surface roughness. This could be explained by other surface integrity factors influencing fatigue performance of the material, such as the presence of subsurface porosity and surface oxygen enrichment.

© 2020 The Authors. Published by Elsevier B.V.

This is an open access article under the CC BY-NC-ND license (<http://creativecommons.org/licenses/by-nc-nd/4.0/>)

Peer-review under responsibility of the Bayerisches Laserzentrum GmbH

Keywords: Laser powder bed fusion; Ti6Al4V; Heat-treatment; Surface topography; Fatigue test; crack nucleation;

1. Introduction

Ti6Al4V alloy is one of the most recognized titanium alloys due to its high strength, low density, high fracture toughness and excellent corrosion resistance. There is a big Ti6Al4V demand in industrial applications due to its lightweight and high strength. Conventional manufacturing methods for Ti6Al4V material require extensive further machining to obtain the desired shapes and dimensions of the part [1]. Thus, the fabrication of Ti6Al4V parts by additive manufacturing (AM) methods is convenient due to its multiple advantages, such as freedom in design, no component-assembly requirements and less waste of material during production in comparison with conventional technologies. Laser powder bed fusion (L-PBF) is an AM process that uses digitized information from computer-aided design software to guide a laser to melt or partially melt,

metal feedstock powder. However, the high cooling rates lead to the transformation of Ti6Al4V from β -phase to α' martensitic phase, which is well-known for its superior strength but also for its low ductility. Nonetheless, the properties of Ti6Al4V can be controlled by heat treatment (HT). Heat treatment of Ti6Al4V, leads to a diverse number of microstructures, having a critical impact on the mechanical properties. Normally, the regime used for HT stands within $\alpha+\beta$ phase region, although it can be also performed in β -phase region. By HT, the amount and morphology of α and β phases are controlled to provide good strength, ductility, as well as fatigue life.

Fatigue failure is one of the main reasons for mechanical failure in engineering components. Microstructure and especially surface topography have been reported to have significant influence on fatigue life. Numerous investigations have been performed to achieve longer fatigue life of a

component by decreasing the surface roughness. Post-processing treatments, such as machining, are required to decrease crack initiation and enhance fatigue life [2]. However, a post-processing treatment cannot be applied to all AM parts (e.g. components with inner surfaces, cavities or holes), thus the influence of surface topography on fatigue needs to be carefully understood. Most of the literature is focused on the optimization of process parameters to understand surface topography by means of surface roughness [3,4,5]. In a previous research, the influence of surface topography on fatigue behavior of the top and side surfaces of L-PBF Ti6Al4V was studied [6]. Differences between top and side surfaces were found to be due to (i) different surface roughness, but also (ii) the staircase effect inherent to AM surfaces. Therefore, it is of importance to understand how surface integrity, e.g. surface morphology, texture, roughness, defects, etc., affects fatigue properties.

The present study focuses on the influence of surface topography by means of different surface patterns on fatigue life. Ti6Al4V specimens were obtained by L-PBF, and the last layer was modified to have different laser track scanning directions ($\alpha=30^\circ$, 60° and 90°). Bending fatigue life was evaluated for as-built, but also heat-treated conditions, to analyze the combined influence of surface topography and microstructure.

2. Materials and methods

Ti6Al4V alloy powder was obtained from TLS Technik GmbH (Germany). The powder had a spherical morphology and a particle size distribution of $d_{10}=7.6\ \mu\text{m}$, $d_{50}=28.6\ \mu\text{m}$ and $d_{90}=41.9\ \mu\text{m}$. The production of the specimen plate was performed with a ProX® DMP 200 L-PBF machine. The following parameters were set and correspond to optimal parameters in terms of volume density: laser power 300W, laser scan speed 1800 mm/s, beam diameter $70\ \mu\text{m}$, hatch spacing $85\ \mu\text{m}$, layer thickness $30\ \mu\text{m}$. Concerning the scanning strategy, each layer was scanned with back and forth tracks and the scan direction was shifted of 90° from one layer to the other. No contour strategy was performed [7]. The construction chamber was filled with argon gas. The samples were divided on two building plates, to test the fatigue life in (i) as-built (AB) and (ii) heat-treated (HT) conditions. Both building plates had the same process parameters, giving a sample density higher than 99.5%. The direction of the last printed layer had laser track scanning directions of $\alpha=30^\circ$, 60° , 90° in relation to the length of the specimen (Fig. 1). The AB specimens from the first plate were detached by wire EDM, meanwhile the second plate was HT in argon atmosphere (2h at 940°C followed by furnace cooling, then 2h at 650°C also followed by furnace cooling) before being detached. All the sides of the specimens were milled in order to calibrate their dimensions ($8\times 8\times 60\ \text{mm}$), except the top surface with different laser track scanning directions.

Top surface topographies were measured with a focus variation microscope (Alicona Infinitfocus G5): one measurement per process ($2.9\times 2.9\ \text{mm}$ area with a lateral resolution of $2\ \mu\text{m}$ and a vertical resolution of $0.1\ \mu\text{m}$). A polynomial filter of order 1 was used to remove the form but no further filter was applied as proposed in [8].

Three-point bending fatigue tests were performed with an Instron 8801 equipment with load cell capacity of 50 kN. The tests were carried out with a maximum stress of $\sigma_{\text{max}}=700\ \text{MPa}$, stress ratio of $R=0.1$ and a frequency of $f=8\ \text{Hz}$, until failure (Fig.1). The specimens tested were designated as: AB-30, AB-60, AB-90 (AB specimens), and HT-30, HT-60 and HT-90 (HT specimens) according to the laser track scanning directions on the top surface layer ($\alpha=30^\circ$, 60° , 90°). Fatigue tests were performed in such a way that the highest tensile stresses were applied on the top surfaces to evaluate influence of laser track scanning direction on fatigue properties. 4 samples were tested for each condition. Fracture surface analyses and microstructural characterization were carried out by scanning electron microscopy (SEM) LEO 1350 FEG, operated at 20 kV and equipped with Oxford EDX INCA-sight system and Oxford EBSD (C-Nano detector), and optical microscopy (Olympus CZH10 research stereo microscope). Cross-sections were prepared by recommended metallographic procedure by grinding up to 4000 SiC paper and then polishing with colloidal silica. The cross-section areas were etched in Kroll's reagent for microstructural investigations.

3. Results

3.1. Surface topography measurements

No differences between the surface topography of AB and HT conditions were found (in agreement with [7]). The roughness computed from the surface topography measurements is presented in table 1 as a function of the laser track scanning direction angle α . Both 2D (Ra , average roughness, and Rdq , root mean square slope) and 3D parameter (Sa , Areal average roughness,) were analyzed.

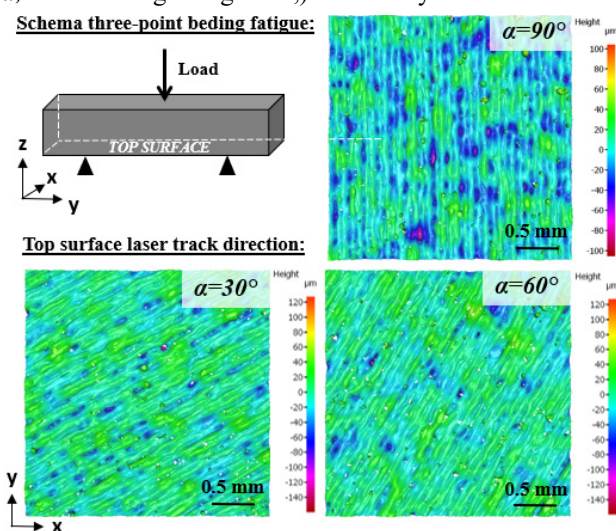


Fig 1. Schema of fatigue test performance, as well as top surface topography of specimens with a laser track scanning direction at 30, 60 and 90° .

Based on results from Table 1, it was observed that the areal average roughness, Sa , and average roughness, Ra , were rather constant for different α values (7.5% and 7.9% of variation, respectively). However, the Rdq value rose by 35% as the α value increased from 30° to 90° .

Table 1. Surface roughness measurements of AB and HT specimens

	Sa (μm)	Ra (μm)	Rdq ($\mu\text{m}/\mu\text{m}$)
$\alpha=30^\circ$	11.9	11.8 ($\sigma=1.6\mu\text{m}$)	0.54 ($\sigma=0.24$)
$\alpha=60^\circ$	11.6	10.9 ($\sigma=2.0\mu\text{m}$)	0.70 ($\sigma=0.28$)
$\alpha=90^\circ$	12.5	11.6 ($\sigma=1.4\mu\text{m}$)	0.73 ($\sigma=0.21$)

3.2. Microstructural analyses

Figure 2 shows the microstructures of the L-PBF Ti6Al4V samples before and after HT. In the AB conditions, an α' -martensitic phase of a sharp needle-like morphology was observed. After the HT, α' was transformed to a coarsened and slightly rounded lamellar α -phase. AB material showed the presence of β -phase (<2 vol.%) between α' needles, which is increased after the HT to ~ 2 vol.%).

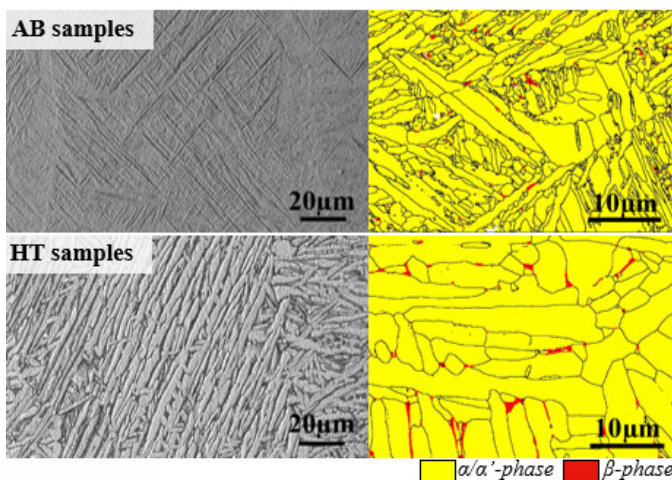


Fig 2. Cross-section optical micrographs of L-PBF AB and HT Ti6Al4V samples, as well as EBSD phase mappings.

3.3. Fatigue life

Figure 3 shows the fatigue life of the tested specimens versus laser track scanning direction of the last printed layer. In the AB specimens, a decrease in fatigue life from 26209 ± 1789 down to 11269 ± 1364 cycles as laser track scanning direction changed from 30° to 90° was observed. Contrary to that behavior, HT specimens (1st HT batch) did not show close correlation between fatigue life and laser track scanning direction. Additionally, HT showed shorter fatigue life in comparison with AB specimens. Fracture analysis of the fatigue specimens revealed the presence of subsurface porosity (Fig. 3, inset), mainly causing a promptly subsurface fatigue crack initiation and reducing fatigue life. The reasons for formation of subsurface porosity were not clearly identified. It could be related to the powder aging but this could not be verified. As a consequence, a 2nd HT batch of specimens was manufactured. No subsurface porosity was observed on this new batch, and crack initiation occurred at surface irregularities. However, fatigue life for all HT conditions ($\alpha=30^\circ$, 60° and 90°) was shorter than for the AB specimens. HT did not improve fatigue life and, no clear correlation was found between the fatigue life and the laser track scanning directions.

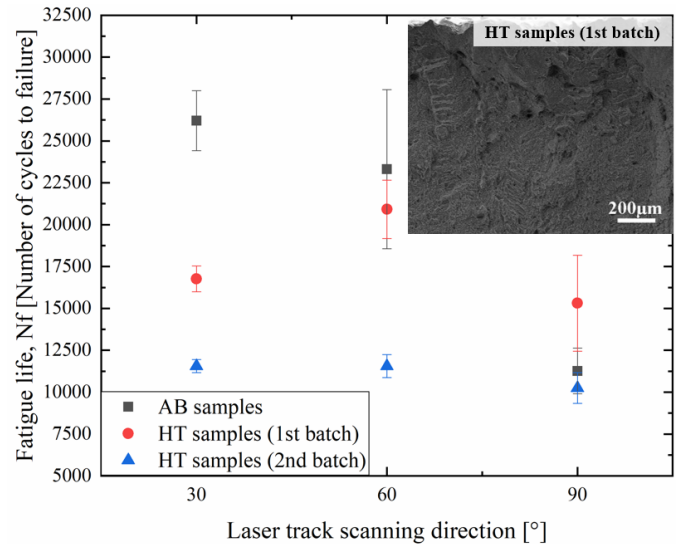


Fig 3. Fatigue life of the studied specimens [$\sigma_{\text{max}}=700\text{MPa}$; $R=0.1$; $f=8\text{Hz}$]; SEM micrograph of fatigue fractured surface of 1st HT batch.

3.4. Fatigue behavior

Figure 4 shows the top surfaces of AB and HT specimens with laser track scanning direction of 30° , 60° and 90° on the last printed layer. AB specimens showed several cracks following grooves on the surface originating from the laser scanning. On the other side, HT specimens did not show any such crack pattern related to the laser track scanning direction, except for HT- 90° condition where the crack path matches with the direction of grooves on the surface.

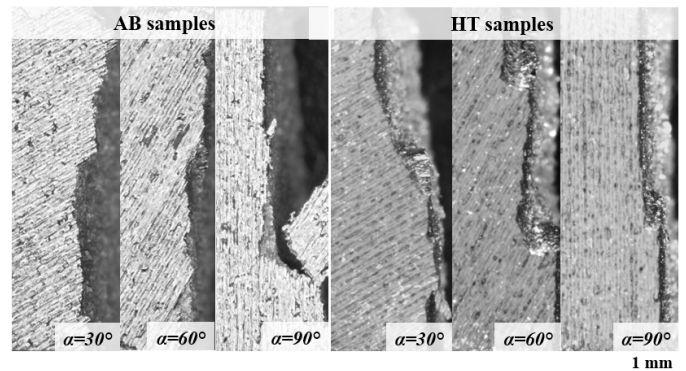


Fig 4. Top surface of fractured fatigue of L-PBF AB and HT Ti6Al4V samples with laser track scanning directions at $\alpha=30^\circ$, 60° and 90° .

4. Discussion

Fatigue is a failure mechanism where cracks are formed due to the cyclic loading of the component. The failure is divided in two steps: crack nucleation and propagation, in which crack nucleation is the main part of the fatigue life time (>70%). Several factors such as, microstructure, surface roughness, internal defects and residual stresses influence fatigue life of Ti6Al4V [2].

Surface defects and high surface roughness, have been identified to be the most critical for fatigue performances [8]. In a previous study, it has been demonstrated that L-PBF AB surfaces have shown to give lower fatigue life than milled surfaces [6]. Rough surfaces are detrimental for fatigue life,

since surface valleys act as notches concentrating high stresses and causing crack nucleation. Surface roughness parameters Ra and Rz , as well as the valleys' depth Svk , were found to determine fatigue life [6, 9]. In the present study, profiles taken in the fatigue stress direction presented steeper slopes (higher Rdq value) as the laser track scanning direction changes from 30° to 90° . As a consequence, higher stress concentration could be reached during fatigue tests, as was observed for AB specimens. Furthermore, when larger surface valley areas (or laser track pattern) were oriented along the fracture direction of the specimen (matching with 90° pattern), they concentrated higher stresses leading to shorter fatigue life in comparison with lower angles (AB-30 and AB-60 specimens).

In the 1st HT batch specimens, the influence of subsurface porosity was detrimental. The position, size and concentration of defects are crucial in determining the fatigue crack initiation. Tammis-Williams et al. [10] showed by fractography and microCT analysis that subsurface pores which lay within a diameter from the surface led to critical fatigue cracks, where the rise in the local elastic stress concentration (Kt) was the most significant. Thus, it was reported that the increase in stress concentration near a surface is an important contributor to the propensity of fatigue cracks to initiate at surface pores. Therefore, an increase in Kt was noticeable when pores were separated from the surface by less than one diameter, and significant when were closer than half a diameter. In the present study, it was observed that the 1st HT batch of specimens had shorter fatigue life than AB specimens, and that fatigue cracks initiated at the subsurface pores. These observations suggest that the combination of influence of subsurface porosity and surface roughness can be more detrimental than the surface roughness itself. Additional post-treatments such as HIP can therefore be useful to increase fatigue resistance, as well as fatigue life, due to the decrease in porosity, but also enhanced ductility due to the growth of α grains [8].

HT is expected to relieve residual stresses, modify microstructure and improve mechanical properties [11]. A 2nd HT batch of specimens was manufactured. No subsurface porosity was observed for those samples, and fatigue crack initiation started at the top of surface irregularities. However, the 2nd HT batch of specimens showed shorter fatigue life than AB specimens too. For Ti6Al4V, it has been reported that at temperatures exceeding 480°C , oxidation of the surface and formation of a hard and brittle layer enriched with oxygen, called alpha-case [12] is possible. In the present study EDX surface analyses showed a thin oxygen-enriched layer beneath the top surface of 2nd HT batch of specimens, which was not found in AB condition. The layer was about 2-3 μm thin, which is below the resolution limit of SEM EDS at 20 kV acceleration voltage, and because of that the concentration of oxygen in the layer was not defined accurately. It is known that high concentrations of interstitials in Ti-alloys usually leads to an increase in strength and a decrease in ductility. Additionally, diffusion of oxygen may result in the formation of an α -case, although, microscopy carried out in the present investigation did not reveal any clear α -phase grains at the surface. Nevertheless, multiple nucleation of cracks at the surface of the 2nd HT batch of specimens at bending fatigue tests suggested embrittlement of the surface, which can be a result of oxygen

enrichment. Thus, changes in chemical composition near surface region after post HT needs to be considered for the performance of the printed part. A need of vacuum treatment instead of argon protective atmosphere could avoid the oxygen enrichment. If not, post machining needs to be considered to improve the final fatigue performance of the AM parts.

5. Conclusions

Ti6Al4V specimens were manufactured by L-PBF to study the factors influencing fatigue life and fatigue crack nucleation. Not only surface topography but also subsurface porosity and surface chemistry were found to influence fatigue performance.

L-PBF AB Ti6Al4V specimens showed a correlation between fatigue life and laser track scanning direction. Fatigue life was 26209 ± 1789 cycles at $\alpha=30^\circ$ and it decreased down to 11269 ± 1364 cycles at $\alpha=90^\circ$. This can be due to the fact of: (i) larger area of valleys oriented parallel to the fracture direction that concentrated higher stresses, and (ii) the increase of Rdq values with the increase in angle from 30° to 90° .

HT led to changes in microstructure, nevertheless, a comparison between AB and HT conditions was challenging due to issues with surface integrity factors. The presence of subsurface porosity in the 1st HT batch of specimens led to a substantial decrease in fatigue life compared to AB specimens where only surface topography governed fatigue crack nucleation at the surface. The 2nd HT batch of specimens had even shorter fatigue life than AB and 1st HT batch. This can be explained by a surface oxygen enrichment during HT. In addition to the influence of surface topography, the formation of a thin oxygen-enriched layer resulted in shorter fatigue life, Fig. 3. Therefore, a strong need to control surface topography but also other factors influencing surface integrity, e.g. surface contamination and subsurface porosity is required for AM components.

Acknowledgements

The authors wish to thank Mehmet Cici from LTDSSENISE for the SLM production. The authors are grateful to the Program "Investissements d'Avenir"- labelled by the French Government and operated by the National Research Agency (ANR) – for financial support to the LabEx MANUTECH-SISE of Université de Lyon (France) within ADDISURF Project. The authors also want to thank the Swedish Agency for Economic and Regional Growth, Grant No20201144, ATLAB - additive manufacturing laboratory at Karlstad University, and Region Värmland for financial support.

References

- [1] Liu S et al. Additive manufacturing of Ti6Al4V alloy: A review, Mater Des 2019;164:107552
- [2] Li P et al. Critical assessment of the fatigue performance of additively manufactured Ti-6Al-4V and perspective for future research. Int J Fatigue 2016;85:130–143.
- [3] Safdar A et al. Effect of process parameters settings and thickness on surface roughness of EBM produced Ti-6Al-4V, Rapid Prototyping J 2012;18:401–408.
- [4] Strano G et al. Surface roughness analysis, modelling and prediction in selective laser melting, J Mater Process Technol 2013;213:589–597.

- [5] Beard M.A et al. Using Raman spectroscopy to monitor surface finish and roughness of components manufactured by selective laser sintering. *J Raman Spectrosc* 2011;42:744–748.
- [6] Vilardell A.M et al. Influence of surface topography on fatigue behavior of Ti6Al4V alloy by laser powder bed fusion, *Procedia CIRP*. 2018;74:49–52.
- [7] Cabanettes F et al. Topography of as built surfaces generated in metal additive manufacturing: A multi scale analysis from form to roughness. *Precis Eng* 2018;52:249–265.
- [8] Chastand V, Tezenas A, Cadoret Y, Quaegebeur P, Maia W, Charkaluk E. Fatigue characterization of Titanium Ti-6Al-4V samples produced by Additive Manufacturing. *Procedia Structural Integrity* 2016;2:3168–3176.
- [9] Pegues J et al. Surface roughness effects on the fatigue strength of additively manufactured Ti-6Al-4V. *I J Fatigue* 2018;116:543–552.
- [10] Tammam-Williams S et al. The Influence of Porosity on Fatigue Crack Initiation in Additively Manufactured Titanium Components. *Sci Rep* 2017;7:7308.
- [11] Leuders S et al. On the mechanical behaviour of titanium alloy TiAl6V4 manufactured by selective laser melting: Fatigue resistance and crack growth performance. *Int J Fatigue* 2013;48:300–307.
- [12] Gaddam R et al. Study of alpha-case depth in Ti-6Al-2Sn-4Zr-2Mo and Ti-6Al-4V. *IOP Conf. Ser.: Mater Sci Eng* 2013;48:012002.

11th CIRP Conference on Photonic Technologies [LANE 2020] on September 7-10, 2020

Characterization of IN718 recycling powder and its effect on LPBF manufactured parts

S.Sendino^{a,*}, S.Martinez^a, A.Lamikiz^a

^a*Aerospace Advance Manufacturing Research Center - CFAA, P. Tecnológico de Bizkaia, Edificio 202, 48170 - Zamudio, Spain.*

* Corresponding author. Tel.: 946018470; E-mail address: sara.sendino@ehu.eus

Abstract

The quality of the powder is a key aspect in the Laser Powder Bed Fusion (PBF-LB/M) process to guarantee manufacturability and quality of the manufactured parts. However, the powder is reused several times and its quality changes during the manufacture process, which affects the quality of the manufactured parts. Throughout this article, the powder and the final part properties will be studied during 25 manufacturing process. Specifically, morphology, granulometry and flowability of the powder were studied, and these results were related with the roughness and the porosity of the manufactured parts. Thanks to this research, it was found that the size of the particles increases when the powder is reused. And this directly affects the flowability of the powder which increases. Furthermore, it has also been shown that this increase in particle size distribution causes an increase in the porosity and roughness of the manufactured parts.

© 2020 The Authors. Published by Elsevier B.V.

This is an open access article under the CC BY-NC-ND license (<http://creativecommons.org/licenses/by-nc-nd/4.0/>)

Peer-review under responsibility of the Bayerisches Laserzentrum GmbH

Keywords: “PBF-LB/M; Flowability; Recycled powder; Granulometry; Small particles; Roughness; Porosity”

1. Introduction

PBF -LB/M technology is one of the most popular technologies for manufacturing complex parts [1]. However, nowadays this technology still presents several challenges compared to others, even so, due to the great advantages it shows, as the ability to manufacture very complex parts, it is one of the most developed additive manufacturing (AM) technologies. Especially because of the great interest that this technology presents to the aeronautical and medical sector [1].

One of these challenges is the reduction of the price of the raw material, since this powdered material must have a specific PSD (Particle size distribution), composition and morphology, which makes it an expensive material. A common practice to reduce this cost is to reuse the powder and even mix it with virgin powder to recover its properties

Nonetheless, the powder during the recycling process can be affected by various changes in its morphology and composition, due to partial fusion of the particles, agglomerations, contamination...

Different studies show how the particle size increases when the powder is reused [2][3][4] in addition to losing its sphericity [3].

It has also been studied how the flowability of the powder changes when is reused and many studies have concluded that this flowability improves when the powder is reused [3][4] due to the absence of satellite particles and the removal of moisture because of the repeated long exposures to vacuum at elevated temperatures (>550 C) in the AM chamber [3]. However, studies such as the one carried out by Ahmed et al. [5] detected

that the flowability of the powder decreased due to the lower sphericity of the reused powder particles.

In addition, several studies have been carried out to check how these changes in the morphology of the powder affect the final characteristics of the part [3][5][6], and the study made by Tang et al. [3] determined that UTS (ultimate tensile strength) and the roughness increased in the case of recycled powders [5].

Other studies [7] [8] have also analyzed the effect of spatters on the powder bed, since these spatters generated during the process lands into the powder bed, and may fall into a part that has not yet melted. In addition, these spatters usually have different morphology and size, which means that some of these spatters are not filtered on the sieving process and are used as powder particles in the next manufacturing process. This can affect the characteristics of the manufactured part, and greater defects and porosity can appear in the part.

Consequently, a proper recycling process is necessary for the development of this technology. For this reason, it is necessary not only to know the changes that occur in the powder itself, it is also necessary know the effects that these changes can have on the final parts manufactured using this technology. These variations in the powder itself and the final parts will be analyzed throughout this study.

2. Methodology

During this work Inconel 718 powder samples will be analyzed from virgin powder every 5 manufactures up to 25 manufactures.

First the characteristics of the powder such as morphology and PSD (particle size distribution) will be studied in order to relate these characteristics to the flowability results obtained using 3 different methods. Then, the different properties of the final part will analyzed. And finally, the results obtained by analyzing the roughness and porosity of the parts will be related to the characteristics obtained from the powder

2.1. Powder analysis

2.1.1. Particles granulometry and morphology

To determinate the PSD, the powder samples were analysed using different sieves. According to the B214-15 standard 90g of each powder samples were sieved during 15 minutes at 280 rotation per minute.

For this analysis, 5 sieves of different spans have been used, in particular these spans were: 63µm, 40µm, 32µm, 25µm and 20µm. After sieving the powder, the quantity of powder on each of the sieves was measured to obtain the PSD.

To carry out this analysis, images of the powder particles had been taken using SEM-EDX (Scanning Electron Microscopy - Energy Dispersive X-ray spectroscopy) 250X scanning electron microscopy at different magnifications.

2.1.2. Flowability

Flowability is a critical factor to validate the powder. This factor limits the ability of the powder to obtain a homogenous powder layer in the manufacture platform [9].

Due to the great importance of flowability, three different tests have been carried out: Analysis based on funnels, Hausner ratio analysis and repose angle analysis. Two of them are standardized tests, and the other one is not a standardized but is a very usual analysis in powder for other applications [10].

In addition, due to the results obtained from the different flowability tests, the three tests were repeated using another batch of powder that showed a lower initial flowability to check if the trend of both powders flowability is similar.

A) ANALYSIS BASED ON FUNNELS

To carry out this test, the time it takes for a certain amount of powder to pass through a funnel of known diameter is measured. These analyses were made using a static method based on standards: ASTM B213-13 (Using the Hall funnel of 2.54 mm diameter) and ASTM B964-16 (Using the Carney funnel of 5.04mm diameter).

For both tests, Qualtech's QPI-HFM1800 equipment has been used, using in each case the funnel specified in the standard, using 150g for the Carney funnel and 50g for the Hall funnel. Each test with each of the powder samples has been repeated 5 times with an error of less than 0.5 seconds between these measurements, as specified in the standard.

A) HAUSNER RATIO ANALYSIS

This ratio is calculated by relating the tapped bulk density and freely settled bulk density of the powder, as can be seen in equation (1).

This factor is related to the flowability, and ensures a correct and homogeneous distribution of the powder in each layer of the bed.

$$\text{Hausner Ratio} = \frac{\text{Tap density}}{\text{Freely settled density}} \quad (1)$$

The tests have been carried out based on ASTM B527-15 standard. Using: 1500 taps, amplitude= 3mm amplitude, frequency= 250 tap/min and a mass of 100±0.5g in each case.

C) REPOSE ANGLE ANALYSIS

The last flowability test was the measurement of the repose angle. This is the only non-standardized method used to measure the flowability.

In this test the powder flows through the Carney funnel and dropped into a cylinder of known diameter (D=35mm). Then two images are taken, one from the top and the other from the

front. From these images and knowing the diameter of the cylinder, the repose angle is calculated.

2.2. Manufactured parts analysis.

The parts were manufactured using the AM400 manufacturing system with the RBV (Reduced Build Volume) system installed. The parameters and the scanning strategy were determined using QuantAM V4, a layer height of 60 μm , a power of 200W, exposure time of 70 μs and a distance point and hatch distance of 80 μm has been set for all the manufactures.

2.1.1. Roughness

Roughness is a key factor to ensure an acceptable quality of the final part. This roughness affects the surface quality and the appearance of the final part, but its affects also to the fatigue resistance. Parts with high roughness obtain a lower resistance in fatigue tests [11].

To measure surface roughness according to the ISO 4287-1997 standard (with an $L_c=2.5\text{mm}$, No. of samples= 5 and 0.8 gaussian filter), a 13mm high cubic parts were manufactured. This part has been manufactured in the central part of the platform to avoid the effects of laser incidence angle, which seems to be one of the main sources of the high roughness of the parts manufactured using PBF -LB/M technology [12].

The surface roughness was measured by an optical method with Infinite Focus Microscope (Alicona Infinite Focus Microscope model Control ServerFP G1 Vf2). These images have been taken in the surfaces ZX and ZY (Fig.5), always taking measurements with a surface area of 13mmx2mm. Using these images it also was possible to analyze the surface topography and analyzed the particles partially molten to the surface.

2.1.2. Porosity

To analyze the porosity, three 1 cm^3 cubic parts have been manufactured with each powder sample to be able to analyze the porosity in the XY, ZX and ZY plane.

For this study, the parts have been encapsulated and polished to a mirror finish. Then, using the infinite focus microscope, images of the surface were taken at 50X magnification.

For the analysis of these images, a software based on image processing algorithms has been used. In this software the images are binarized, leaving the pores as black elements while the piece remains white. By studying the ratio between the black and white area, the porosity of the final part has been calculated.

3. Results and discussion

3.1. Powder analysis

3.1.1. Particles granulometry and morphology

After sieving the powder, the quantity of powder on each of the sieves was measured to obtain the particle size distribution shown in Fig.1.

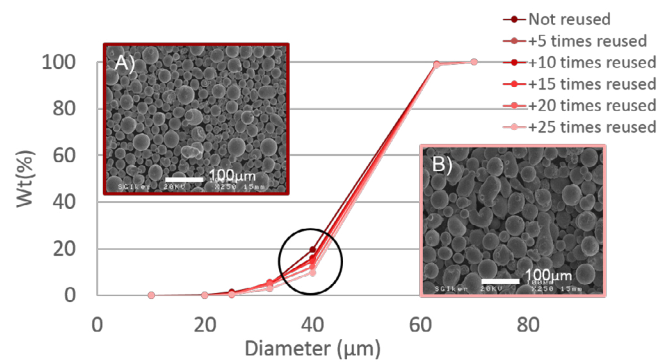


Fig. 1. Particle-size distribution determined by selective sieving based on ASTM B214-15 and powder samples analyzed by SEM (250X). (A) Virgin powder (without reuses) (B) After 25 reuses.

As can be seen in Fig.1 the particle size of the distribution increases with the number of reuses of the powder.

The morphology of the powder has also been studied, to determine if this morphology changes considerably after several reuses.

Fig. 1 shows two images taken by SEM-EDX at 250X. On the left, it can be seen the powder sample without reuses Fig. 1 (A), and on the right the sample after 25 reuses Fig. 1 (B).

Analyzing the images obtained, it has been verify that the particles' morphology changes considerably. It can be seen how after several reuses the particles lose their sphericity and many particles appeared with satellites attached to their surface or completely molten with other particles.

3.1.2. Flowability

B) ANALYSIS BASED ON FUNNELS

The results obtained in these analyses are shown in Fig.2. Here is shown how the results obtained with the two funnels are opposite. On the one hand, the results obtained with Hall funnel shows how the flowability improves when the powder is reused. On the other hand, the results obtained with the Carney funnel shows an opposite tendency, the flowability is lower when the powder is reused several times.

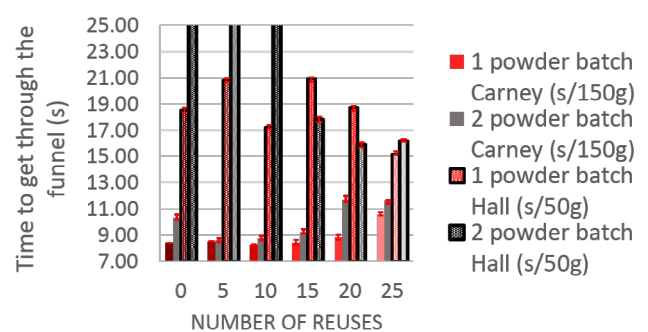


Fig. 2. Flowability values based on funnel tests.

These results were related with the results obtained in section 3.1.1, where the morphology and granulometry were analyzed. It has been determined that this opposite trend on flowability is due to changes in the particles of each powder sample when

they are reused. On the one hand, due to reuses, the particles size increase and due to this increase, the adhesion and friction forces between the particles decrease, improving the flowability results. On the other hand, the results obtained analyzing the morphology shows how the sphericity of the particles decreases after several reuses, and this causes a decrease in the flowability values.

The flowability analyses carried out have been repeated with another powder batch (2. Powder batch) that initially showed a lower flowability to check if these opposite effects were repeated and as Fig. 2 shows the trend seen with the two batches of powder is similar.

C) HAUSNER RATIO ANALYSIS

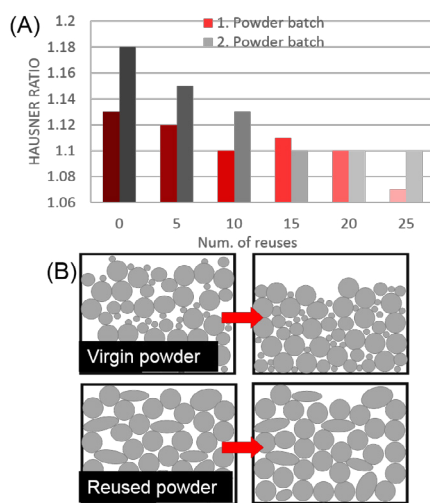


Fig. 3. (A) Hausner ratio obtained. (B) Comparison of the powder compaction mechanism between virgin powder (without reuse) and reused powder.

The results shown in Fig. 3 (A) show that the virgin powder had an acceptable Hausner ratio, using both batches of powder. The powders that have a Hausner Ratio equal or less than 1.25 are considered as freely flowing, and cohesive and non-flowing powders show a bigger ratio than 1.40 [13].

Furthermore, this ratio decreased with the reuses of the powder, which indicates a better flowability. These results contradicts the results obtained using the Hall funnel and the study carried out by Ahmed et al [5]. However, this ratio shows the same trend as the results obtained when the Carney funnel is used. This trend can be show also in other flowability studies [3][4][14].

Hausner ratio indicates the compacting capacity of the powder, and when the powder is not compactable de value of the ratio will be one. Consequently, it seems logical that the value of this ratio decreases when the powder is reused:

When the reused powder is studied, the smaller particles are attached to larger particles and therefore cannot get into the gaps between the particles to compact. Therefore, this reused powder not only shows a more homogeneous distribution of powder granulometry, also has particles with less sphericity and this makes the arrangement more complicated, because the

movement between particles is more difficult. This effect can be seen schematically in the Fig.3 (B).

C) REPOSE ANGLE ANALYSIS

As the Fig. 4 shows, the lowest repose angle was obtained, in the case of the two batches of powder, with the sample with the highest number of reuses. Therefore, as the Hausner ratio showed, the flowability seems to improve when the powder is reused.

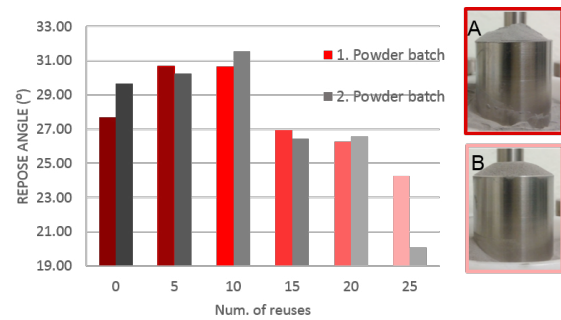


Fig. 4. Results of the repose angle obtained. Button) images obtained with the powder with: (A) 10 reuses and (B) 25 reuses.

This indicates that the repose angle is mainly influenced by particle size. When the powder is reused, its particle size increases, for that the frictional forces decreases, which causes an increase in flowability.

Therefore, after analyzing the flowability by three different methods, the results can be summarized according to two opposite effects:

- On the one hand, when the PSD decreases, the interparticle forces increase [15], due to the Van der Waals forces, which can represent 80-90% of these interparticle forces [10]. Furthermore, these smaller particles tend to agglomerate as can be determined by the Hausner Ratio [16]. Taking into account these phenomena it would be logical to think that the flowability of the powder will increase due to the increase in particle size.

- But on the other hand the particles lose their sphericity, which causes this flowability and packing capacity to decrease [17].

Throughout this study it has been possible to verify how the flowability obtained by the different methods has shown an increase in flowability, in the recycle powder. This trend has been seen in all the tests made, except the one carried out using the Carney funnel.

3.1. Manufactured parts analysis

3.1.1. Roughness

As shows Fig.5 the roughness is higher in the parts manufactured with reused powder. The increase in roughness has been most significant on the ZY surface.

This roughness is related to the granulometry of the powder. During the PBF-LB/M process, many particles melt partially to the part surface, as can be seen in Fig.6. If the particle size distribution has larger particles the partially molten particles in the surface will be larger, and due to these particles, roughness will be higher.

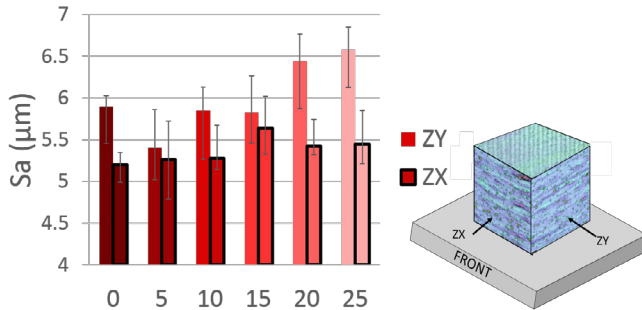


Fig. 5. Results of surface roughness Sa obtained in ZX and ZY surfaces.

These partially adhered particles are shown in Fig.6, where the surface analyzed can be seen in the cases of virgin powder and the most reused powder.

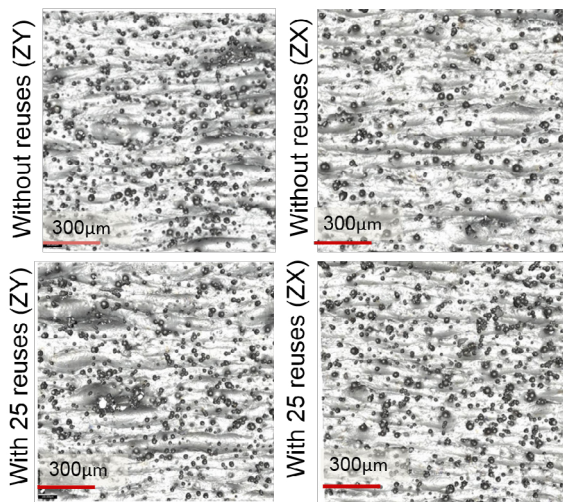


Fig. 6. Surface topography of the part manufactured with virgin powder and with the powder with 25 reuses.

As can be seen in Fig.6 on the ZY surface, a greater number of particles are molten, which is consistent with the results obtained for roughness.

3.1.2. Porosity

Fig. 7 shows an increase in the porosity of the parts when the powder is reused.

According to several previous studies the porosity of the manufactured parts can vary for different reasons depending on the powder characteristics. On the one hand, porosity is affected by the composition of the particles and the amount of oxide or spatters [18] [19]. Since these spatters can jump into the melting zone increasing the porosity, in addition the smaller oxide particles cannot be sieved out, so the quantity of these spatters increase when the powder is reused.

On the other hand, other studies have shown how this porosity

increases increasing particle size [5] [18] [20]. Since an increase in the particle size affects the compaction of the layer generated in the powder bed, which can result in an uneven distribution of heat during the deposition of the laser energy that can create pores in the parts [21]. In the same way, for a given input laser energy, an increase in the size of the powder can cause an increase in porosity due to incomplete melting of the particles [5].

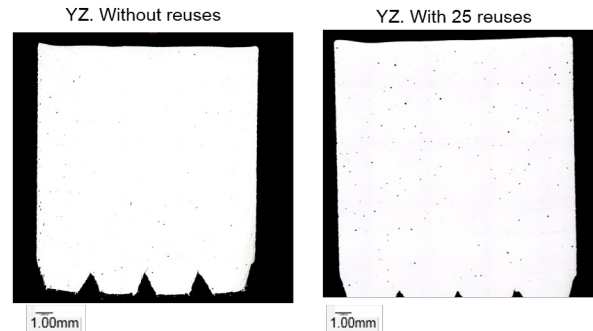
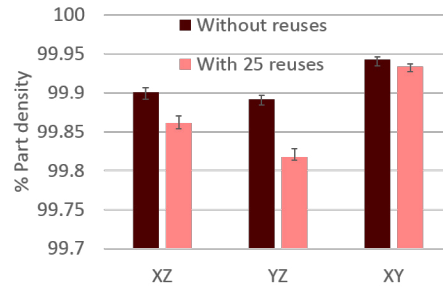


Fig. 7. Parts porosity, (LEFT: without reuses and RIGHT: with 25 reuses). (A) XY surface (B) ZY surface.

Therefore, the increase in porosity that could be seen after this study is coherent with the study seen in the literature, since the recycled powder shows a higher particle size than the virgin one as well as a higher quantity of spatters.

In consequence, it seems to be necessary to adjust the parameters after reusing the powder several times.

4. Conclusion

Throughout this study, the properties of the powder during 25 manufacture processes have been analyzed. This study shows how the morphology of the particles is worse when the powder is reused, appearing satellites attached to the larger particles. Besides, as far as granulometry is concerned, the particle size increases due to this adhesion between particles.

These variations in morphology and particle size affect the flowability of the powder samples, but in an opposite way. The increase in particle size causes an improvement in flowability, while the lack of sphericity of the particles causes a flowability decrease. This effect has been seen using two different powder batches.

Once the powder has been characterized, some of the properties of the final part have been analyzed, and it has been possible to see how the roughness increases when the powder is reused due to the increase in particles size. The same effect was detected

when the porosity was studied, the porosity has also increased due to the increase in particle size.

5. Acknowledgements

This research has received funding from the Basque Government through the nG18 project, under Grant Elkartek-KK000001. The authors also thank for technical and human support provided by the SGiker Laboratory (UPV/EHU) and the support provided by the members of RENISHAW Ibérica.

6. References

- [1] Wang Z., Guan K., Gao M., Li X., Chen X., Zeng X., The microstructure and mechanical properties of deposited IN718 by selective laser melting, (2012) *Journal of alloys and compounds* 513; P.518-523. <https://doi.org/10.1016/j.jallcom.2011.10.107>
- [2] Asgari H., Baxter C., Hosseinkhani K., Mohammadi M., On microstructure and mechanical properties of additively manufactured AlSi10Mg_200C using recycled powder. (2017) *Materials Science Engineering: A* .707: P. 148–158. <https://doi.org/10.1016/j.msea.2017.09.041>
- [3] Tang HP, Qian M, Liu N, Zhang XZ, Yang GY, Wang J, Effect of Powder Reuse Times on Additive Manufacturing of Ti-6Al-4V by Selective Electron Beam Melting (2015) *JOM*, 67(3):555-563 DOI: 10.1007/s11837-015-1300-4
- [4] Cordova L, Campos M, Tinga T, Revealing the effects of powder reuse of selective laser melting by powder characterization. (2019) 71:3, 1062-1073, <https://doi.org/10.1007/s11837-018-3305-2>
- [5] Ahmed F., Ali U., Sarker D., Marzbanrad E., Choi K., Mahmoodkhani Y., Toyserkani E., Study of powder recycling and its effect on printed parts during laser powder-bed fusion of 17-4 PH stainless steel, (2020) *Journal of Materials Processing Tech.* 278:P.116522 <https://doi.org/10.1016/j.jmatprotec.2019.116522>
- [6] Nguyena Q. B., Nai M. L. S., Zhu Z., Sun C., Weia J., Zhou W., Characteristics of Inconel Powders for Powder -Bed Additive Manufacturing, (2017) *Engineering*, 3: P.695–700 <http://dx.doi.org/10.1016/J.ENG.2017.05.012>
- [7] Gasper AND, Szost B, Wang X, Johns D, Sharma S, Clare AT, Ashcroft IA, Spatter and oxide formation in laser powder bed fusion of Inconel 718 (2018) *Additive manufacturing* 24:446-456. <https://doi.org/10.1016/j.addma.2018.09.032>
- [8] Gasper AND, Hickman D, Ashcroft I, Sharma S, Wang X, Szost B, Johns D, Clare AT, Oxide and spatter powder formatios during laser powder bed fusion of Hastelloy X (2019) *powder technology* 354: 333-337 <https://doi.org/10.1016/j.powtec.2019.06.004>
- [9] Spierings A.B., Voegtlin M., Bauer T., Wegener K., Powder flowability characterisation methodology for powder-bedbased metal additive manufacturing, (2016) *Prog Addit Manuf* 1:9–20. DOI 10.1007/s40964-015-0001-4
- [10] Krantz M., Zhang H., Zhu J., Characterization of powderflow: Static and dynamic testing (2019), *Powder technology*, V.194, P239-245, <https://doi.org/10.1016/j.powtec.2009.05.001>
- [11] Afkhami S., Piili H., Antti S., Björk T., Effective parameters on the fatigue life of metals processed by powder bed fusion technique, (2019) *Procedia Manufacturing* V36 3-10. DOI: 10.1016/j.promfg.2019.08.002
- [12] Kleszczynski S., Ladewig A., Friedberger K., Zur Jacobsmühlen J., Merhof D., Witt G. Position dependency of surface roughness in parts from laser beam melting systems. (2015) *Solid freeform fabrication symposium*
- [13] Abdullah EC, Geldart D The use of bulk density measurements as flowability indicators. (1999) *Powder Technology*, 102(2): p. 151-165. [https://doi.org/10.1016/S0032-5910\(98\)00208-3](https://doi.org/10.1016/S0032-5910(98)00208-3)
- [14] Strondl A., Lyckfeldt O., Brodin H., Ackelid U. Characterization and Control of Powder Properties for Additive Manufacturing, V.67, 2015, P.549-554 DOI: 10.1007/s11837-015-1304-0
- [15] Karapatis NP A sub-process approach of selective laser sintering. Dissertation, (2002) Ecole Polytechnique fédérale de Lausanne EPFL, Lausanne. Doi 10.5075/epfl-thesis-2506
- [16] Yu AB, Hall JS Packing of fine powders subjected to tapping. (1994) *Powder Technology* 78(3):p.247–256. doi:10.1016/0032-5910(93)02790-H
- [17] Spierings AB, Herres N, Levy G Influence of the particle size distribution on surface quality and mechanical properties in additive manufactured stainless steel parts, (2011) *Rapid Prototyping Journal*, 17: .p. 195 - 202. DOI: 10.1108/13552541111124770
- [18] Tan JH, Wong WLE, Dalgarno KW, An overview of powder granulometry on feedstock and part performance in the selective laser melting process, (2017) *Additive Manufacturing*, .18, P. 228-255 <http://doi.org/10.1016/j.addma.2017.10.011>
- [19] Vock S, Klöden B, Kirchner A, Weibgärber T, Kieback B, Powders for powder bed fusion: a review, (2019) *Progress in Additive Manufacturing* 4:383–397 <https://doi.org/10.1007/s40964-019-00078-6>
- [20] Ali, U., Mahmoodkhani, Y., Imani Shahabad, S., Esmailzadeh, R., Liravi, F., Shaydain, E., Huang, K.Y., Marzband, E., Vlasea, M., Toyserkani, E., (2018). On the measurement of relative powder-bed compaction density in powder-bed additive manufacturing processes. *Mater. Des.* 155, 495–501. <https://doi.org/10.1016/J.MATDES.2018.06.030>.
- [21] Esmailizadeh, R., Ali, U., Keshavarzkermani, A., Mahmoodkhani, Y., Marzbanrad, E., Toyserkani, E., 2019. On the effect of spatter particles distribution on the quality of Hastelloy X parts made by laser powder-bed fusion additive manufacturing. *J. Manuf.Process.* 37, 11–20. <https://doi.org/10.1016/j.jmapro.2018.11.012>

11th CIRP Conference on Photonic Technologies [LANE 2020] on September 7-10, 2020

Influence of contaminants on part quality during Laser-Based Powder Bed Fusion of nickel base alloys

Mathias S. Palm^{a,b,*,*}, Max Horn^{c,=}, Andreas Bachmann^a, Georg Schlick^c, Michael F. Zaeh^a,
Gunther Reinhart^{a,c}

^aInstitute for Machine Tools and Industrial Management of Technical University of Munich, Boltzmannstr. 15, 85748 Garching b. München, Germany

^bArianeGroup GmbH, Robert-Koch-Straße 1, 82024 Taufkirchen, Germany

^cFraunhofer Research Institution for Casting, Composite and Processing Technology IGCV, Am Technologiezentrum 10, 86159 Augsburg, Germany

* Corresponding author. Tel.: +49-89-6000-24738 ; fax: +49-89-6000-25233. E-mail address: mathias.palm@iwb.tum.de

= These authors contributed equally to this work

Abstract

Laser-based Powder Bed Fusion (LPBF) has become a key Additive Manufacturing (AM) technology for the production of complex metallic components within a short lead-time. Contaminated powder feedstock is a major challenge in LPBF due to the uncertain influence of contaminations on part quality. This study investigates the effects of different contaminants inside the feedstock on material density and metallurgical structure in order to evaluate their implications for serial production. Pieces of rubber gloves, human, and recoater brush hair as well as five more substances were applied manually at a defined layer during the manufacturing process of Hastelloy® X (HX) specimens. The part densities were 99.9% for all contaminated specimens. Cross-sections did not show increased porosity. For some contaminants, inclusions of foreign material residue were observed. The results for HX were evaluated and implications for comparable materials were derived. Lastly, the criticality of the investigated contaminants on part quality was analyzed.

© 2020 The Authors. Published by Elsevier B.V.

This is an open access article under the CC BY-NC-ND license (<http://creativecommons.org/licenses/by-nc-nd/4.0/>)

Peer-review under responsibility of the Bayerisches Laserzentrum GmbH

Keywords: Additive Manufacturing; powder quality; foreign particles; contamination; HastelloyX

1. Introduction

Additive Manufacturing (AM) is increasingly used for the fabrication of complex parts. Freedom of design, the considerable reduction of part numbers, and the shortened time to market make AM technologies a game changer for industries such as aerospace [1]. Laser-based Powder Bed Fusion (LPBF) of metals is an AM technology, which enables the production of fully dense metal components with material properties comparable to those of conventionally manufactured parts [2].

The LPBF process is characterized through a high number of influencing factors [3]. Quality assurance of additively manufactured parts is a major challenge for the industrial application of AM technologies [4]. Post-process quality evaluation

through non-destructive inspection leads to massive increase of cost and lead time. Consequently, the quality of the parts has to be evaluated in-process by means of process monitoring to exploit the full potential of LPBF. The layer-wise character of the technology enables the monitoring of each layer during the production process [5].

Optical Tomography (OT) is a layer-wise monitoring technology used for quality assurance of the LPBF process [6]. Near-infrared emission from the process zone is captured by a camera inside the process chamber. Through a filter, the wavelength of the captured light is reduced to a narrow band around 900 nm. All signals reaching the camera chip during the exposure of one layer are integrated over time and depicted in one

image. This procedure is similar to long time exposure photography [7].

During LPBF, the formation of various defects can occur. The interaction between the laser and process by-products, such as spatter or welding fumes, can lead to lack-of-fusion defects [8]. Furthermore, the process parameters and the exposure strategy have a strong influence on the resulting microstructure and on the formation of cracks [9, 10]. Porosity is primarily caused by inadequate energy input into the powder material [11]. OT has successfully been used for in-process detection of lack-of-fusion defects and increased porosity [12].

Along with the influence of process by-products and the energy input, the properties of the powder material have a major impact on the resulting part properties and the creation of defects [13–15]. One particular material property that has not yet been explored in detail is powder purity or the lack thereof due to contaminants [15]. Lutter-Guenther et al. conducted a failure mode and effects analysis (FMEA) of LPBF powder properties and found feedstock contaminations to be a relevant quality risk along the entire LPBF process chain [16]. Particulate impurities can be divided into cross-contamination resulting from other LPBF powders and further contaminations, such as rubber glove pieces, human hair, or any other matter that can enter the feedstock along the process chain. While both categories have not yet been investigated extensively, some results are available for the cross-contamination [17–21]. In particular, the influence of other contaminants on part quality has not yet been analyzed. External contaminants, which can enter the powder during LPBF machine preparation and powder recycling were chosen to be investigated during the described study.

2. Experimental methods

In order to evaluate the impact of different contaminants on the resulting manufactured parts, a test build job was performed on an EOS M 290 LPBF system with an Ytterbium fiber laser, emitting light with a wavelength of 1064 nm, which arrives to the build plane with a Gaussian intensity profile. The machine was equipped with an OT process monitoring system from EOS GmbH. The in-process evaluation of the impact of the different contaminants was performed through the analysis of OT images and images from an optical camera inside the process chamber. Hastelloy® X (HX) powder from Aubert & Duval S.A. with a particle size between 10 µm and 53 µm was fused with a parameter setting characterized through an energy density of 2.699 J/mm², which was calculated with the laser power divided through the product of scan speed and hatch distance according to Song et al. [22]. The layer thickness was 40 µm. HX is a solid solution hardening nickel base alloy consisting of 0.5–23% Cr, 17–20% Fe, 8–10% Mo, 0.5–2.5% Co, 0.2–1% W, maximum 1% Si and Mn, maximum 0.5% Al and Cu and several trace elements in lower concentration [23].

18 rectangular specimens with a square base of 2 cm x 2 cm were distributed evenly across nine zones of the build platform. The process was stopped at a build height of 3.08 mm and the process chamber door was opened to apply different types of contamination onto the surface of the specimens (see Fig. 1). Each contaminant was applied on the surface of two specimens in different zones within the build area. No contamination was

applied on the surface of two reference samples. For the other samples, typical contaminations from powder handling and part marking were added (see Table 1). Furthermore, Inconel® 718 recoater brush hair was added as contaminant to represent a soft recoater suitable for nickel base alloys. The particles from the suction lance and from both sieves had a diameter in the range between 60 µm and 120 µm. Paper particles and nitrile rubber glove shreds with a maximum size of 0.5 cm were added. Both the Inconel® 718 recoater brush hair and the human hair were cut to pieces with a length of approximately 0.5 cm before they were applied onto the specimens. For each specimen to which a contaminant was applied, about half of the specimen's surface was covered with the contaminant (see Fig. 1). The build process was continued through lowering the build platform by the height of one layer and recoating the next layer after the process chamber door was closed and a suitable argon atmosphere inside the machine was achieved. The interruption of the LPBF process took 35 minutes including flooding of the machine with argon. During the nominal LPBF process prior to the layer, in which contaminants were applied, and following this layer, no additional contaminants were added. The test build job was performed to evaluate the influence of contaminants, which were applied to a single layer within the specimens.

After the LPBF manufacturing process, specimens 2b, 3b, 4a, 5b, 6b, 7b, 8a and 9b were scanned in a Computed Tomography (CT) system. These specimens contained one sample for each contaminant. The reference samples were not examined. The measurement was performed with 290 kV acceleration voltage, 250 µA current, and an exposure time of 2.2 s, resulting in a voxel size of 65 µm.

Density measurements of manufactured test pieces were conducted using the Archimedes' principle in Isopropanol.

Table 1. List of investigated contaminants

Specimens	Contaminants	Abbreviation
1a,b	Uncontaminated reference samples	Reference
2a,b	Oversize particles from suction lance	Lance
3a,b	Edding® permanent marker	Marker
4a,b	Paper cloth snippets	Paper
5a,b	Nitrile rubber glove shreds	Rubber
6a,b	Oversized particles from the 1 st sieve	Sieve 1
7a,b	Oversized particles from the 2 nd sieve	Sieve 2
8a,b	Inconel® 718 recoater brush hair	Brush hair
9a,b	Human hair	Human hair

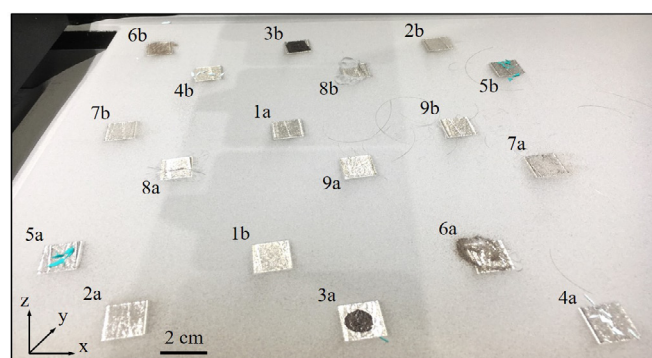


Fig. 1. Positioning of the contaminants during the build process in the x-y-plane of the specimens

Cross-sections of y-z-planes of all specimens were etched using Adler's reagent for approximately 10 s at room temperature. Cross-sections were examined using an Olympus BX53M upright metallurgical light microscope, as well as a Hitachi TM3030Plus Scanning Electron Microscope (SEM) equipped with an Energy-dispersive X-ray Spectroscopy (EDS) module from Bruker Nano. After a second grinding and polishing step, the porosity of all samples was measured using a 3D laser scanning confocal microscope from Keyence's VX-R series. For this purpose, three sets of 1 x 8 images in horizontal arrangement were captured. For subsequent comparison, one set of images was acquired directly at the contaminated layer and two sets were taken above the interruption line in uncontaminated sections. In total, three sets of images, each having a length of 9.99 cm and a height of 0.91 cm, were acquired per test piece.

3. Results and discussion

3.1. Process monitoring

The optical image showed recoating issues in the layer after addition of contaminants (see Fig. 2, left). These recoating issues are a clear evidence that some of the added contaminants were moved by the recoater. The recoating issues were observed in three layers following the layer with the added contaminants. The OT image of the first exposed layer with contaminants did not show any indications (see Fig. 2, right). Within the OT analysis performed, no higher or lower emission

intensity values could be observed within the next layer and the one that followed.

3.2. Defect analysis

CT scanning did not reveal any defects larger than the detection boundary of approximately 200 μm . Furthermore, Table 2 depicts the results of the density measurement via Archimedes' principle and optical porosity analysis. The average density across all specimens is 8.35 g/cm^3 . The specimens showed a low standard deviation and all values are well within the overall variance. No specimen exhibited significant decreased density or increased variance. Values given in the column "Porosity *uncontaminated*" display values for uncontaminated areas of the analyzed specimens, whereas "Porosity *contaminated*" gives values for the contaminated specimens' layers. The overall average porosity was identical for contaminated as well as for uncontaminated layers and showed similar standard deviations. Again, no specimen deviated due to increased porosity. The porosity difference in percent corresponds to the porosity of uncontaminated areas subtracted by the porosity of the contaminated area of each specimen. Three specimens showed increased porosity for the contaminated layers. The highest difference was observed for brush hair. However, it is comparable with deviations measured in the reference samples and can be attributed to the normal variance. On average, contaminated layers show 0.06% less porosity than uncontaminated layers, which can also be seen as normal process variance. Thus, from CT scans as well as density and porosity measurements, it can be concluded that the examined contaminants do not have a negative influence on the physical part quality. A relation between powder impurities and increased porosity, crack formation, or lack-of-fusion defects was not observed.

3.3. Metallurgical analysis

Although, the cause-effect relationship between impurities and physical defects could not be confirmed, contaminants could still have a negative influence on the metallurgical struc-

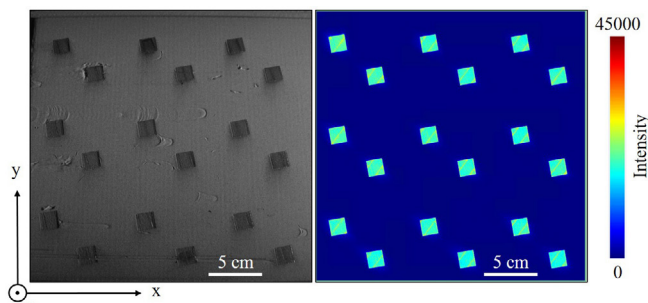


Fig. 2. Optical camera image (left) and OT image (right) at 3.12 mm build height

Table 2. Density and porosity for examined specimens

Samples	Abbreviation of contaminant acc. to Table 1	Density and its standard deviation in g/cm^3	Porosity <i>uncontaminated</i> and its standard deviation in %	Porosity <i>contaminated</i> and its standard deviation in %	Porosity difference in %
1a,b	Reference	8.35 (± 0.013)	0.04 (± 0.032)	0.03 (± 0.001)	0.014
2a,b	Lance	8.34 (± 0.013)	0.04 (± 0.024)	0.04 (± 0.027)	0.006
3a,b	Marker	8.35 (± 0.010)	0.05 (± 0.017)	0.05 (± 0.042)	-0.003
4a,b	Paper	8.35 (± 0.010)	0.06 (± 0.014)	0.06 (± 0.018)	-0.002
5a,b	Rubber	8.35 (± 0.006)	0.04 (± 0.035)	0.03 (± 0.025)	0.012
6a,b	Sieve 1	8.34 (± 0.005)	0.05 (± 0.028)	0.03 (± 0.011)	0.015
7a,b	Sieve 2	8.35 (± 0.007)	0.03 (± 0.006)	0.03 (± 0.012)	0.002
8a,b	Brush hair	8.34 (± 0.010)	0.03 (± 0.013)	0.05 (± 0.018)	-0.015
9a,b	Human hair	8.34 (± 0.007)	0.06 (± 0.048)	0.04 (± 0.031)	0.025
Average across all samples		8.35 (± 0.010)	0.04 (± 0.022)	0.04 (± 0.020)	0.006

ture or chemical composition through inclusion of foreign material. Consequently, etched cross-sections were examined employing a light microscope and SEM (EDS). For comparison, Fig. 3 shows the structure of uncontaminated reference samples. Hereby, the dark u-shaped lines were attributed to the melt pool borders. The metallurgical structure showed columnar grains reaching over several build layers, which is commonly observed for LPBF of HX [24]. Within the interruption area, a horizontal line with slight deviations in melt pool color, size, and regularity is visible (Fig. 3 a). Magnification of the interruption line, however, does not reveal any defects or inclusions. The different appearance can be explained by higher overlapping of the melt pools and a slight variance in the melt pool sizes. The interruption line appearance of specimens 1a and 1b was considered as the benchmark. Deviations found in other specimens were attributed to process irregularities caused by the contaminants as described below.

Fig. 4 a) depicts the contamination line of specimen 5a that shows high irregularity in the melt pool dimensions, which have not been observed for any other sample. A possible explanation is that increased fumes due to rubber glove vaporization widened the laser beam and caused larger melt pools [8]. But this would also mean less focused energy, which could in turn result in lack-of-fusion defects. To the contrary, no further defects along with irregular melt pool shapes were found.

Both samples contaminated with marker (3a and b) showed a clear interruption line containing dark inclusions inside the melt pools as shown in Fig. 4 b) and c). The marker most likely burnt incompletely during laser exposure and the remaining residue was included in the solidified part. It should be noted that the marker was still visible after the second laser scanning process subsequent to the manual contamination. SEM EDS element mappings of discontinuities found within the contaminated area revealed carbon enrichment as well as Ni-, Fe- and Mo-depletion as depicted in Fig. 5. Cr and Co remained unchanged.

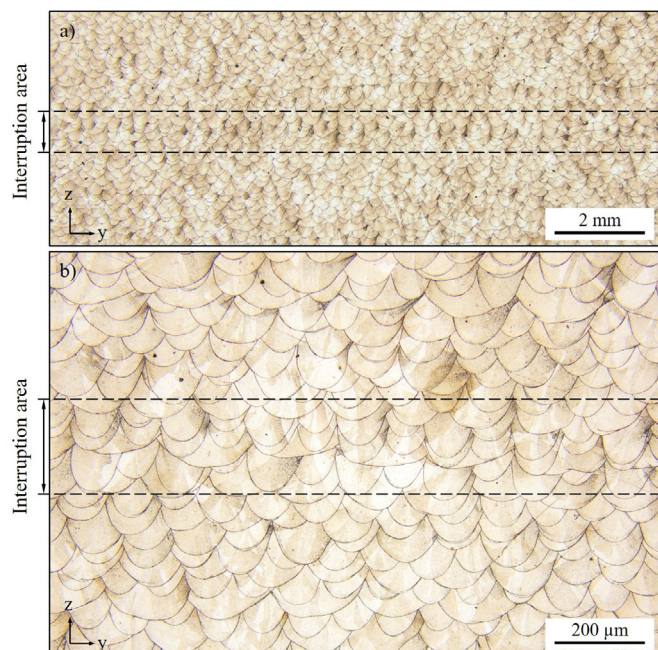


Fig. 3. Light microscope images of uncontaminated reference samples

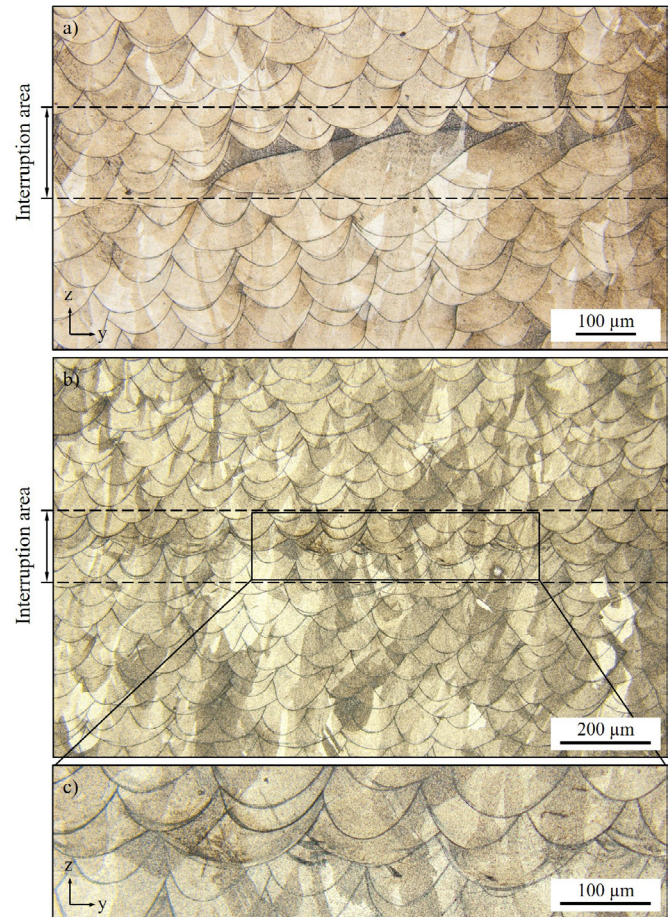


Fig. 4. Light microscope images of contaminated samples 5a and 3b showing irregularities in the metallurgical structure

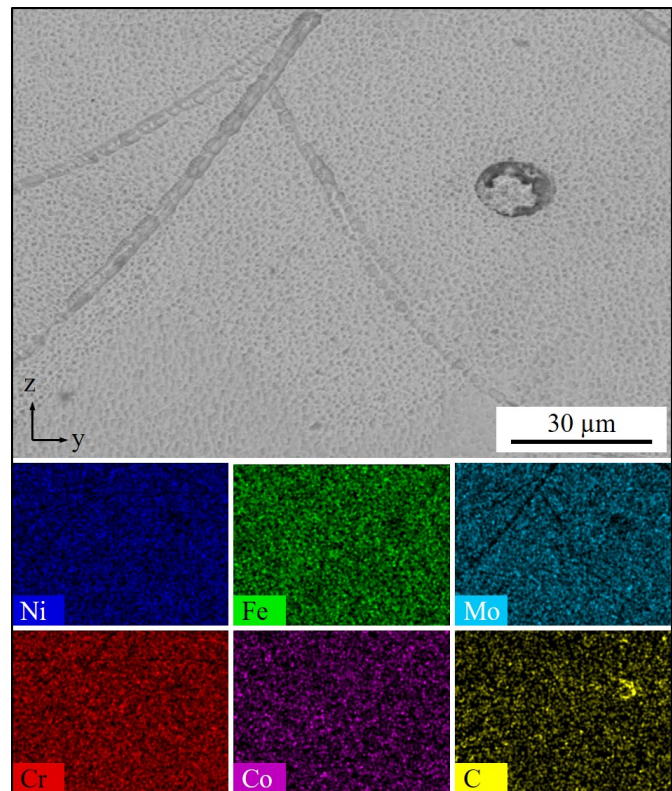


Fig. 5. SEM image (left) and EDS element mapping (right) of sample 3b contaminated with permanent marker showing a carbon inclusion

No further irregularities or deteriorations were observed while examining the interruption layers of all test pieces employing a light microscope and SEM EDS. It can be summarized that despite potential laser beam defocusing due to rubber vaporization and inclusion of marker residue, no negative influence of contaminants on the metallurgical structure or the chemical composition was detected.

4. Conclusion and outlook

This study explored the influence of relevant contaminants in LPBF on the part quality. The results can be summarized as follows:

- Neither CT scans nor density measurements by the Archimedes' principle or optical porosity measurements have shown a negative influence of the examined contaminants.
- The specimens contaminated with rubber gloves revealed some irregularities with respect to the melt pool dimensions, possibly caused by the defocusing of the laser beam by escaping fumes.
- No inclusions of contamination residues were found in the test pieces, except for permanent marker.

It can be concluded that all investigated contaminants either fully melted and were included in the final parts (in the case of oversize particles), or the contaminants vaporized due to high process temperatures and did not leave any residue in the metallurgical structure. Thus, process temperatures and physical properties of the molten material appear to be essential in determining material vulnerability to contaminants in LPBF. Therefore, similar observations made during this study are expected for other nickel base super-alloys. Due to the different chemical composition leading to a different melting behavior, other materials, which have lower melt pool temperatures, such as aluminum base alloys, might have a different response to the investigated contaminants. The high melting temperature of the examined Ni-base alloy probably causes the majority of contaminants to vaporize during LPBF. Lower melt pool temperatures could lead to delayed burning of the foreign material and thus more inclusions from residue material.

Consequently, further research is necessary to investigate the influence of foreign matter in LPBF. According to the authors, these are the most relevant topics:

- Higher resolution CT scans are necessary to detect smaller defects.
- The influence of the heat treatment on the residue inclusions needs to be studied.
- The effects of the observed defect types on the mechanical part properties, e.g. static and fatigue tensile strength, need to be explored.
- Internal contaminants, which can enter the powder feedstock during the process, such as lubricants or abraded particles, e.g. from the recoater blade, need to be examined.
- The investigations need to be extended to other material systems.
- Contamination in several following layers cannot be evaluated from the results of this study. Therefore, additional

tests with increased amounts of contaminants, applied to specimens in several consecutive layers, have to be performed.

- Additionally, specific thresholds for examined contaminants need to be developed and measuring methods for powder purity control need to be qualified.

References

- [1] Zaeh, M.F., 2006. *Wirtschaftliche Fertigung mit Rapid-Technologien*. Carl Hanser Verlag GmbH & Co. KG, Muenchen.
- [2] Gibson, I., Rosen, D., Stucker, B., 2015. *Additive manufacturing technologies: 3D printing, rapid prototyping and direct digital manufacturing*, 2nd edn. Springer, New York, NY.
- [3] van Elsen, M., 2007. *Complexity of selective laser melting: A new optimisation approach*, PhD thesis KU Leuven.
- [4] Krauss, H., 2016. *Qualitätssicherung beim Laserstrahlschmelzen durch schichtweise thermografische In-Process-Überwachung*, PhD thesis TU Muenchen.
- [5] Everton, S.K., Hirsch, M., Stravroulakis, P., Leach, R.K. et al., 2016. Review of in-situ process monitoring and in-situ metrology for metal additive manufacturing, *Materials & Design* 95: pp. 431–445. doi:10.1016/j.matdes.2016.01.099.
- [6] Zenzinger, G., Bamberg, J., Ladewig, A., Hess, T. et al., 2015. Process monitoring of additive manufacturing by using optical tomography, In: *Proceedings of the 41st Annual Review of Progress in Quantitative Nondestructive Evaluation held 20–25 July 2014 in Boise, USA*: pp. 164–170.
- [7] Carl, V., 2015. Monitoring system for the quality assessment in additive manufacturing, In: *Proceedings of the 41st Annual Review of Progress in Quantitative Nondestructive Evaluation held 20–25 July 2014 in Boise, USA*: pp. 171–176.
- [8] Ladewig, A., Schlick, G., Fisser, M., Schulze, V. et al., 2016. Influence of the shielding gas flow on the removal of process by-products in the selective laser melting process, *Additive Manufacturing* 10: pp. 1–9. doi:10.1016/j.addma.2016.01.004.
- [9] Cloots, M., Uggowitzer, P.J., Wegener, K., 2016. Investigations on the microstructure and crack formation of IN738LC samples processed by selective laser melting using Gaussian and doughnut profiles, *Materials & Design* 89: pp. 770–784. doi:10.1016/j.matdes.2015.10.027.
- [10] Carter, L.N., Martin, C., Withers, P.J., Attallah, M.M., 2014. The influence of the laser scan strategy on grain structure and cracking behaviour in SLM powder-bed fabricated nickel superalloy, *Journal of Alloys and Compounds* 615: pp. 338–347. doi:10.1016/j.jallcom.2014.06.172.
- [11] Kasperovich, G., Haubrich, J., Gussone, J., Requena, G., 2016. Correlation between porosity and processing parameters in TiAl6V4 produced by selective laser melting, *Materials & Design* 105: pp. 160–170. doi:10.1016/j.matdes.2016.05.070.
- [12] Palm, M.S., Chandelle, A., Riss, F., Zaeh, M.F., 2019. Overview and Classification of Defects occurring during Laser Beam Melting of Nickel-base Alloys, In: *Production at the leading edge of technology*, Springer Berlin, Heidelberg, pp. 379–388. doi:10.1007/978-3-662-60417-5_38.
- [13] Slotwinski, J.A., Garboczi, E.J., Stutzman, P.E., Ferraris, C.F. et al., 2014. Characterization of Metal Powders Used for Additive Manufacturing, In: *Journal of Research of the National Institute of Standards and Technology* 119, pp. 460–493. doi: 10.6028/jres.119.018
- [14] Clayton, J., Millington-Smith, D., Armstrong, B., 2015. The Application of Powder Rheology in Additive Manufacturing, *JOM* 67(3), p. 544.
- [15] Vock, S., Kloeden, B., Kirchner, A., Weißgaerber, T. et al., 2019. Powders for powder bed fusion: a review, In: *Progress in Additive Manufacturing* 4, p. 383.
- [16] Lutter-Guenther, M., Schwer, F., Seidel, C., Reinhart, G., 2016. Effects on Properties of Metal Powders for Laser Beam Melting Along the Powder Process Chain, In: *Proceedings of the Fraunhofer Direct Digital Manufacturing Conference DDMC2016*.

- [17] Horn, M., Schlick, G., Lutter-Guenther, M., Anstaett, C. et al. Metal powder cross-contaminations in multi-material laser powder bed fusion: Influence of CuCr1Zr particles in AlSi10Mg feedstock on part properties, In: Proceedings of the Lasers in Manufacturing Conference 2019.
- [18] Horn, M., Schlick, G., Wegner, F., Seidel, C. et al., 2018. Defect formation and influence on metallurgical structure due to powder cross-contaminations in LPBF, In: Proceedings of the 7th International Conference on Additive Technologies iCAT2018 .
- [19] Jamshidinia, M., Boulware, P., Marchal, J., Mendoza, H. et al., 2016. In-Process Monitoring of Cross Contamination in Laser Powder Bed Fusion (L-PBF) Additive Manufacturing (AM), In: Proceedings of the 26th Annual International Solid Freeform Fabrication Symposium SFF2016.
- [20] Brandão, A.D., Gerard, R., Gumpinger, J., Beretta, S. et al., 2017. Challenges in Additive Manufacturing of Space Parts: Powder Feedstock Cross-Contamination and Its Impact on End Products, *Materials* 10(5), p. 522. doi: 10.3390/ma10050522
- [21] A.Gatto, E. Bassoli, L. Denti, 2018. Repercussions of powder contamination on the fatigue life of additive manufactured maraging steel, *Additive Manufacturing* 24, pp. 13–19.
- [22] Song, Y.-A., Koenig, W., 1997. Experimental Study of the Basic Process Mechanism for Direct Selective Laser Sintering of Low-Melting Metallic Powder, *CIRP Annals* 46(1): pp. 127–130. doi:10.1016/S0007-8506(07)60790-2.
- [23] Aubert & Duval S.A. Pearl@Micro HX powder for Additive Manufacturing datasheet: <https://www.aubertduval.com/alloy/776/>, accessed on 9th of March 2020.
- [24] Montero-Sistiaga, M.L., Pourbabak, S., van Humbeeck, J., Schryvers, D. et al., 2019. Microstructure and mechanical properties of Hastelloy X produced by HP-SLM (high power selective laser melting), *Materials & Design* 165, Article 107598

11th CIRP Conference on Photonic Technologies [LANE 2020] on September 7-10, 2020

Impact of laser irradiation on microstructure and phase development of tungsten carbide - cobalt

Tobias Schwanekamp^{a*}, Joachim Gussone^b, Martin Reuber^a

^aInstitute of Manufacturing and Tooling Technology (iWFT), University of Applied Sciences (RFH) Cologne, Vogelsanger Str. 295, 50825 Cologne, Germany

^bGerman Aerospace Center (DLR), Institute of Materials Research, Linder Hoehe, 51147, Cologne, Germany

* Corresponding author. Tel.: +49-221-54687-743; fax: +49-221-54687-36. E-mail address: tobias.schwanekamp@rfh-koeln.de

Abstract

Previous studies on Laser Powder Bed Fusion of tungsten carbide-cobalt (WC-Co) revealed several defects in the laser molten microstructures. To analyze the defect formation mechanisms and the fundamental impact of laser energy input on phase development and microstructure of WC-Co, single-pulse and single-track analogy experiments are conducted. Conventional WC-Co is used as substrate. Variations in cobalt content and processing conditions are investigated. It is found that a single laser exposure can be enough to induce decomposition of microstructure, WC grain growth, formation of non-equilibrium phases and thermal cracking. Based on the results, defect formation mechanisms and countermeasures are discussed.

© 2020 The Authors. Published by Elsevier B.V.

This is an open access article under the CC BY-NC-ND license (<http://creativecommons.org/licenses/by-nc-nd/4.0/>)

Peer-review under responsibility of the Bayerisches Laserzentrum GmbH

Keywords: Cemented Carbides, Tungsten Carbide-Cobalt, WC-Co, Laser Melting, Laser Powder Bed Fusion, L-PBF, Non-Equilibrium Phase, Metastable Phase

1. Introduction

Tungsten carbide-cobalt (WC-Co) is widely used for manufacturing of cutting tools. The conventional manufacturing of WC-Co in a liquid phase sintering process is characterized by a well-controlled and homogeneous input of thermal energy and processing times in the order of several hours. Controlled diffusion processes along the grain boundaries between the WC hard phase and the Co binder ensure the formation of the desired material microstructure. After sintering, the solid carbide blanks are contoured using CNC-grinding machines to achieve the final tool shape.

In contrast to the conventional cutting tool fabrication process, Laser Powder Bed Fusion (L-PBF) offers significant potential for manufacturing of innovative tool geometries [1]. However, previous studies indicate that laser molten WC-Co is impaired by characteristic defects, which corrupt the material properties. The laser generated microstructures exhibit increased porosity and WC grain growth, thermal cracks and

undesired changes in the composition of elements and phases [1]. A summary of studies conducted on L-PBF of WC-Co at different research institutions was given by Uhlmann et al. [2]. The conditions of melting and solidification during L-PBF are completely different from the conventional liquid phase sintering process. Therefore, microstructure and mechanical properties similar to conventionally sintered WC-Co are still not achieved by L-PBF.

Further optimization requires a better understanding of the defect formation mechanisms. To achieve a more differentiated consideration of the mechanisms, the impact of powder layer characteristics is excluded in this study. Single-pulse and single-track analogy experiments are conducted on conventional solid WC-Co substrate under variation of the cobalt content and the processing conditions. Thereby, the fundamental impact of laser energy input on phase development and microstructure of WC-Co is analyzed. Based on the results, different measures to reduce the material defects are discussed.

2. Materials and methods

The experiments were conducted on a Renishaw AM250 L-PBF system under inert gas atmosphere (nitrogen 5.0). The machine is equipped with a modulated Ytterbium fiber laser (cw) with a focal diameter of $d_f = 70 \mu\text{m}$ (Gaussian mode, TEM₀₀). Single pulses with pulse durations $t_p \geq 20 \mu\text{s}$ can be achieved by modulation. The scan velocity v_s is approximated by $v_s = d_p / t_p$. The local distance d_p between two exposure points is set to a constant value of $d_p = 45 \mu\text{m}$ in all tests. The maximum platform temperature in the standard configuration of the AM 250 machine is limited to 170°C. For the realization of higher platform temperatures, a lab scale pre-heating module is used. This module can heat up a build area of 25 mm width and 50 mm length to approx. $T_{PH} = 800^\circ\text{C}$. The temperature can be monitored with thermocouples and pyrometry.

Different conventional WC-Co grades with variations in the Co-content from 6 wt.-% to 24 wt.-% were used. The WC grain size of the tested materials increases with the Co-content from “fine” to “coarse” (classification according to ISO 4499). The surfaces of the samples were ground and polished. Variations in scan velocity ($25 \text{ mm/s} \leq v_s \leq 200 \text{ mm/s}$) and laser power ($50 \text{ W} \leq P \leq 200 \text{ W}$) were chosen according to the process windows of previous studies on L-PBF of WC-Co [2]. For the single-track experiments, the variations in P and v_s result in a specific energy per unit length $E_s = P / v_s$ between $0.25 \text{ J/mm} \leq E_s \leq 8 \text{ J/mm}$. The range of v_s results in pulse durations $t_p = d_p / v_s$ between 0.225 ms and 1.8 ms ($d_p = 45 \mu\text{m}$), which are applied for the single-pulse experiments. For the single pulses, the chosen range of P and t_p result in a pulse energy $E_p = P \cdot t_p$ between $11.25 \text{ mJ} \leq E_p \leq 360 \text{ mJ}$.

The heat affected zones were inspected by top view and polished cross sections of the scan tracks. Optical microscopy and scanning electron microscopy (SEM) were applied. Microstructure was investigated by secondary electron (SE) and backscattered electron (BSE) contrast. The proportion of the elements in the heat affected zones provides a clue for possible phases and is measured by energy dispersive X-ray spectroscopy (EDX). To minimize contamination during sample preparation, some of the microstructural areas were ablated using focused ion beam (FIB). Emphasis of the analysis was on the dimensions of the heat affected zones, the formation of microstructure and the occurrence of thermal cracks.

3. Results and discussion

The first single-track experiments were conducted without pre-heating of the substrate. The results indicate a significant impact of laser energy on the given WC-Co microstructure for all tested parameter combinations and materials. The temperature gradient dT/ds along the distance s from the center of the melt pool causes different microstructural zones. These are shown schematically in Fig. 1. In sufficient distance to the melt pool (zone D), the material is unaffected by the laser energy (E_s, E_p). Summarizing the tendencies seen in all parameter settings, the following microstructural observations have been made. Full decomposition of the WC microstructure is observed in the center of the melt pool (zone C), where the highest temperature can be expected. At the border of the melt

pool (zone B), WC grain growth is observed. Between the border (B) and the unaffected material (D), a heat affected zone is detected, where increased amounts of W are measured in the Co phase (zone C). The described zones occur for each parameter setting and tested Co-content, but are most obvious for high energy inputs. Therefore, the typical zones are explained in detail by example of the scan track, that was generated with $E_s = 8 \text{ J/mm}$.

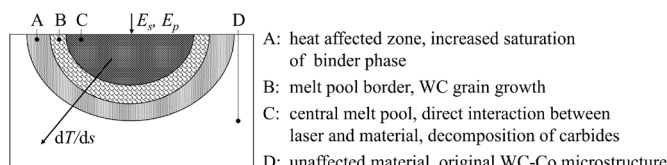


Fig. 1. Schematic view and description of microstructural zones in the cross section of a laser scan track on WC-Co

Fig. 2 shows the cross-sections of scan tracks generated with WC-Co 76/24 and WC-Co 90/10. Comparison of zone A to the original material in zone D indicates that a significant impact of laser energy input on the carbide structure is not evident. The light-grey WC grains are homogeneously embedded in the dark-grey Co matrix in both regions. However, EDX analysis of this region indicates a gradient in the mole fraction of W (x_W) dissolved in the Co-matrix. In the unaffected zone D a mole fraction of $x_W \approx 1.5 \text{ at.-%}$ is measured. Getting closer to the melt pool, the mole fraction increases up to $x_W \approx 20 \text{ at.-%}$. This can be explained by the gradient dT/ds , since the solubility of W in Co increases with increasing temperature [3]. The high cooling rates lead to supersaturated solidification. The dissolved tungsten affects the density of the binder phase and thereby the material contrast in the BSE image. For higher Co-contents, filamentary precipitations are observed in the Co-matrix, which are rich in tungsten (detail zone A). These structures suggest not only solid state diffusion but a transition of the binder phase into liquid state. For lower Co-contents, reliable measurement of the mole fraction x_W in the Co matrix was not possible due to the small amount of Co between the WC grains. However, the saturation gradient is visible by the slight decrease in brightness of the binder phase outwards the melt pool. The width of zone A generally increases with the Co-content of the substrate material.

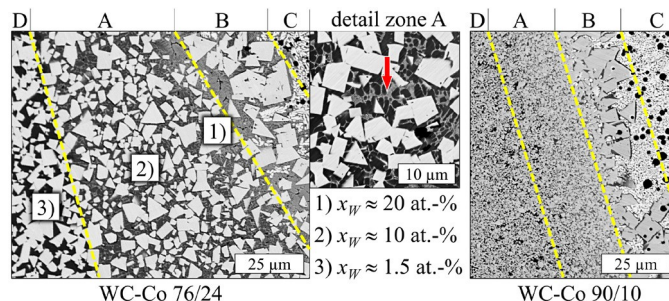


Fig. 2. Scan track cross-sections of zone A (SEM-BSE) with binder phase saturation gradient, $E_s = 8 \text{ J/mm}$, WC-Co 76/24 (left), WC-Co 90/10 (right)

In the border region B between the central melt pool (zone C) and the heat affected zone A, significant WC-grain growth is observed (Fig. 3). The formation mechanisms are basically known from conventional sintering processes [4]. High temperature leads to increased dissolution of carbides in the liquid binder and a highly saturated melt phase. During solidification and cooling, the dissolved W and C precipitates

at the grain boundaries of the undissolved carbides at the border to zone A, causing grain growth. In addition, the minimization of surface energy leads to partial or full coalescence of grains. In some of the enlarged grains, black inclusions can be identified. These are also observed in the central melt pool and contain high amounts of carbon (Fig. 5). The carbon is enclosed in the WC grains during coalescence and grain growth.

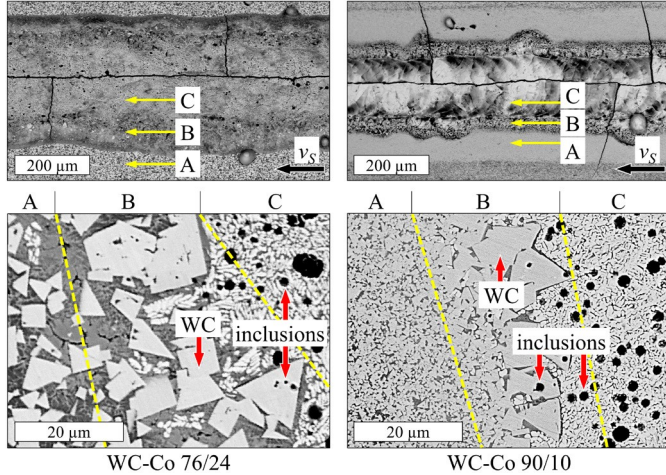


Fig. 3. Scan track top views (top, SEM-BSE) and cross-sections of zone B (bottom, SEM-BSE), $E_s = 8 \text{ J/mm}$, WC-Co 76/24 (left), WC-Co 90/10 (right)

In the central interaction zone (C) between the laser radiation and the material, the highest laser intensity, melt pool temperature and temperature gradients exist [5]. Global EDX analysis of these regions is conducted for both Co-contents as shown in Fig. 4 (red frames). The results indicate residual Co contents of approx. 15 wt.-% (WC-Co 76/24) respectively 5 wt.-% (WC-Co 90/10). Hence, a single laser exposure is enough to reduce the initial Co content by up to 50 %. Co evaporation is also known from L-PBF [2]. This indicates, that the evaporation temperature of Co (2900°C) is locally exceeded during laser exposure. According to the W-C-Co phase diagram, given e.g. by Bondar et al. [6], WC is in liquid state at 2900°C . WC melts incongruently, which implies decomposition into W-rich liquid phase and solid graphite (C). Due to rapid cooling, diffusion processes are inhibited. Non-equilibrium conditions can cause meta-stable solidification of the melt. Dependent on the energy input and the Co-content of the substrate, lamellar or cellular microstructures similar to cast material with spheroidal graphite are observed (Fig. 4).

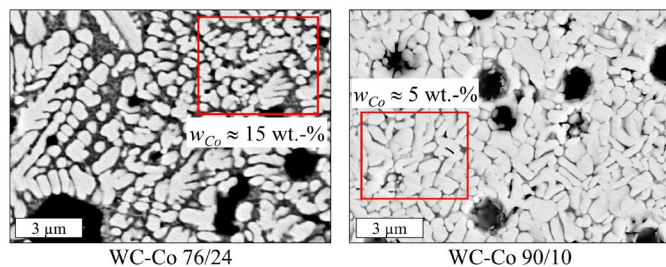


Fig. 4. Scan track cross-sections of zone C (SEM-BSE) with fully decomposed WC, $E_s = 8 \text{ J/mm}$, WC-Co 76/24 (left), WC-Co 90/10 (right)

More detailed analysis of this region is conducted by means of EDX mapping on a section prepared by FIB (Fig. 5). Almost 100 % carbon is measured inside the black inclusions. Due to the high cooling rates, the dissolved carbon and tungsten do not precipitate as WC but instead the C remains enclosed in the

microstructure as graphite leading to a carbon deficiency in the surrounding material. The light grey regions around the C-inclusions contain high amounts of tungsten. BSE indicates a higher Z-contrast (mean atomic number) and thereby higher material density compared to WC. Hence, potential phases are W_2C , WC_{1-x} (γ) or W. The dark grey matrix is rich in cobalt. The compositions, measured by EDX, most likely suggest supersaturated $\text{Co}(\text{W,C})$ or Co_3W .

Microstructures as they are observed in zone C are not known from conventional sintering processes but are sporadically described in beam based surface treatment of hard metal tools. In this context, Xu et al. also confirmed Co-loss due to evaporation and, depending on the energy input, meta-stable phases such as WC_{1-x} and $\text{Co}_3\text{W}_9\text{C}_4$ (κ) [7]. Zhang et al. detected $\text{W}_3\text{Co}_3\text{C}$ (η) and graphite (C), in addition [8].

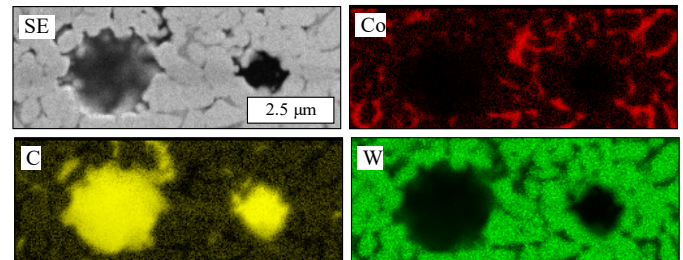


Fig. 5. EDX mapping of the microstructure in the central melt pool region ($E_s = 8 \text{ J/mm}$, WC-Co 90/10)

Measurement of the melt pool dimensions indicated, that the width and depth of zone C increase exponentially with the laser energy input. High laser power $P \geq 150 \text{ W}$ in combination with low scan velocity $v_s < 200 \text{ mm/s}$ leads to keyhole effect and keyhole pores. Furthermore, thermal cracks are detected in most of the generated scan tracks. The extent of cracking increases with the induced laser energy. For low E_s , most of the cracks are oriented perpendicular to the scan direction. Additional cracks in longitudinal direction occur for higher E_s . This phenomenon is known from laser welding and is related to the dominating direction of thermally induced tensile stress. Dependent on Young's modulus E , thermal expansion coefficient α , Poisson's ratio ν and temperature difference ΔT , the thermal stress σ_{th} can be approximated by Eq. (1).

$$\sigma_{th} = \frac{E \alpha}{1 - \nu} \Delta T \quad (1)$$

With increasing Co-content, the Young's modulus of WC-Co hard metals decreases [9], resulting in a decrease of thermal stress. For hard and brittle materials such as WC-Co, rapid transient temperature changes are most critical, since this thermal shock can cause stress peaks, resulting in instant crack initiation and propagation. The thermal shock resistance increases with the fracture toughness K_{IC} of the material [10] and thereby with increasing Co-content and WC-grain size [9]. The experiments indicate that even a single pulse with low energy induces thermal cracking for low Co contents (Fig. 6). The central melt pool region is most prone to crack formation due to the high temperature gradients and the embrittlement caused by Co-evaporation and phase transformation. For low Co-content, additional cracks occur around the melt pool in zone A.

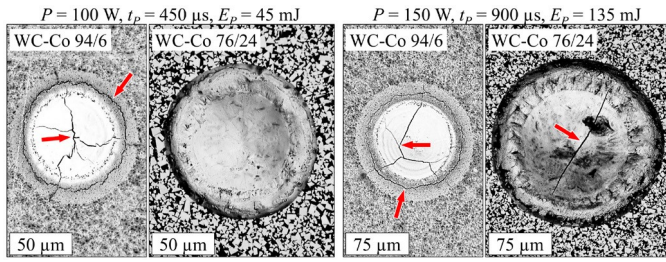


Fig. 6. Single pulses on WC-Co substrate with minimum and maximum Co content and varying pulse energy E_p (top view, SEM-BSE)

The formation of cracks depends on thermal gradients, affected by laser energy input, and on fracture toughness, affected by material ductility. Teppernegg et al. have shown, that the ductility of a given WC-Co composition increases at a temperature around 800°C , resulting in a sudden increase in K_{IC} [11]. An increase in the WC-Co substrate temperature level also reduces ΔT and, according to Eq. (1), the thermal stress. To verify this assumption, similar experiments are conducted at an increased pre-heating temperature $T_{PH} \approx 800^\circ\text{C}$. With this temperature, cracks can be prevented in a wide parameter range, even for WC-Co 94/6 and for the highest pulse energy as shown in Fig. 7 (a). With pre-heating, the melt pool dimensions increase. The higher substrate temperature reduces cooling rates. Consequently, it affects the formation of phases. The impact of reduced cooling rates on the microstructure is most distinct for high Co-content as shown in Fig. 7 (b). Taking into account the scheme given in Fig. 1, $T_{PH} \approx 800^\circ\text{C}$ leads to enlargement of the regions A (solution of W in Co) and B (WC-grain growth). Increased and distorted WC grain growth is observed in zone B for most of the tested parameter settings at $T_{PH} \approx 800^\circ\text{C}$. In the central melt pool region (zone C) the lower cooling rates lead to coarser microstructure. Increased porosity is observed in some melt pools, indicating evaporation due to a higher melt pool temperature.

In contrast to the single laser exposure applied in these experiments, the repetitive layer-wise laser exposure during L-PBF increases overall temperature level and reduces cooling rates. Overlapping of scan-tracks, continuous re-melting and re-heating affects the L-PBF-made material below and beside the current track and creates a heterogeneous microstructure, most similar to zone B in the single-track experiments, as shown in previous studies [1].

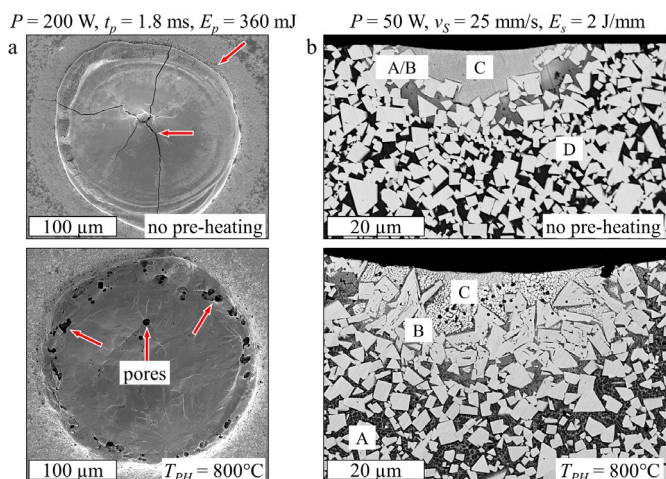


Fig. 7. (a) SEM (SE) images of single pulses on WC-Co 94/6, (b) SEM (BSE) images of single-track cross sections on WC-Co 76/24

4. Conclusion

Single-track and single-pulse experiments on WC-Co with varying Co-content between 6 and 24 wt.-% revealed, that a single laser exposure is already sufficient to induce decomposition of microstructure, WC grain growth, formation of non-equilibrium phases and thermal cracking. The parameter range used in relevant studies on L-PBF of WC-Co [2] was applied. It was found that the decomposition of carbide microstructure in the central interaction zone between the laser beam and the material is inevitable in the tested range of P and v_s . Increased substrate temperature of 800°C reduces thermal gradients and increases material ductility. At $T_{PH} \approx 800^\circ\text{C}$, thermal cracking, which is the most critical defect in L-PBF of WC-Co, can successfully be prevented for a wide range of parameters and WC-Co compositions. Melt pool dimensions and heat affected zones are larger at $T_{PH} \approx 800^\circ\text{C}$. Consequently, laser energy input and thereby the negative impact on the microstructure should be reduced in the L-PBF process at $T_{PH} \approx 800^\circ\text{C}$. Furthermore, the higher temperature level in the substrate leads to enlarged regions with increased saturation of binder. $T_{PH} \approx 800^\circ\text{C}$ leads to reduction of cooling rates and consequently to increased WC grain growth. Despite these drawbacks, pre-heating is highly recommended for L-PBF of WC-Co to reliably prevent thermal cracking. Beyond a reduction of laser energy input, further measures, such as grain growth inhibitors, additives or alternative binders, should be investigated. For deeper understanding of solidification phenomena and phase development, future research should be supported by thermodynamic simulations and transmission electron microscopy (TEM).

References

- [1] Schwaneckamp, T. and Reuber, M. (2016) Additive Manufacturing of application optimized tungsten carbide precision tools. in: Proc. 6th Int. Conf. Addit. Technol., Interesansa - zavod, Ljubljana, Nürnberg, Germany, pp. 100–114.
- [2] Uhlmann, E., Bergmann, A., and Gridin, W. (2015) Investigation on Additive Manufacturing of Tungsten Carbide-cobalt by Selective Laser Melting. *Procedia CIRP*. 35 8–15.
- [3] Okamoto, H. (2008) Co-W (Cobalt-Tungsten). *Journal of Phase Equilibria and Diffusion*. 29 (1), 119–119.
- [4] Spriggs, G.E. (1995) A history of fine grained hardmetal. *International Journal of Refractory Metals and Hard Materials*. 13 (5), 241–255.
- [5] Hooper, P.A. (2018) Melt pool temperature and cooling rates in laser powder bed fusion. *Additive Manufacturing*. 22 548–559.
- [6] Bondar, A., Bocharov, N., Dobatkina, T., Krendelsberger, N., Effenberg, G., and Ilyenko, S. (2010) Carbon – Cobalt – Tungsten, Landolt-Börnstein - Group IV Physical Chemistry 11E2 (Refractory metal systems). 41.
- [7] Xu, Y., Zhang, Y., Hao, S.Z., Perroud, O., Li, M.C., Wang, H.H., et al. (2013) Surface microstructure and mechanical property of WC-6% Co hard alloy irradiated by high current pulsed electron beam. *Applied Surface Science*. 279 137–141.
- [8] Zhang, Y., Yu, F., Hao, S., Dong, F., Xu, Y., Geng, W., et al. (2017) Evolution of Nanostructure and Metastable Phases at the Surface of a HCPEB-Treated WC-6% Co Hard Alloy with Increasing Irradiation Pulse Numbers. *Coatings*. 7 (11), 178.
- [9] Spriggs, G.E. (2002) Properties of hardmetals and cermets. in: Powder Metall. Data Refract. Hard Intermet. Mater., Springer, pp. 86–117.
- [10] Hasselman, D.P.H. (1969) Unified Theory of Thermal Shock Fracture Initiation and Crack Propagation in Brittle Ceramics. *Journal of the American Ceramic Society*. 52 (11), 600–604.
- [11] Teppernegg, T., Klünsner, T., Kremsner, C., Tritremmel, C., Czettel, C., Puchegger, S., et al. (2016) High temperature mechanical properties of WC-Co hard metals. *International Journal of Refractory Metals and Hard Materials*. 56 139–144.

11th CIRP Conference on Photonic Technologies [LANE 2020] on September 7-10, 2020

Features of structure-sensitive hard magnetic alloy Fe – 25 wt. % Cr – 15 wt. % Co manufactured by Laser Powder Bed Fusion

A.S. Zhukov^{a,*}, B.K. Barakhtin^a, A.V. Kamynin^b, I.S. Gavrikov^b, P.A. Kuznetsov^a

^aNRC "Kurchatov Institute" – CRISM "Prometey", 49 Shpalernaya str., St. Petersburg, 191015, Russian Federation

^bJSC "S-Magnet", 58 Dmitrovskoe sh., Moscow, 127238, Russian Federation

* Corresponding author. Tel.: +7-812-335-5843; fax: +7-812-710-3756. E-mail address: jouan2@gmail.com

Abstract

It was studied the structure of alloy manufactured on the RussianSLM FACTORY unit by laser powder bed fusion. The powder was produced by gas atomization from ingots on a HERMIGA 75/3VI unit. By constructing a hysteresis loop, data were obtained that indicate an increase in the magnetic characteristics (Br, Bd, Hcb, Hcm and BHmax) in additive samples in comparison with similar ones obtained by foundry technologies.

© 2020 The Authors. Published by Elsevier B.V.

This is an open access article under the CC BY-NC-ND license (<http://creativecommons.org/licenses/by-nc-nd/4.0/>)

Peer-review under responsibility of the Bayerisches Laserzentrum GmbH

Keywords: selective laser powder bed fusion; additive technologies; metal powders; multifractal analysis; magnetic properties

1. Introduction

Manufacturing of magnets of complex geometric shapes according to the designed digital models is of practical and scientific interest (Fig. 1a). One of the promising methods for their manufacture is the laser powder bed fusion (LPBF), variety of additive technologies [1-3].

A feature of this process is the interaction of solid and liquid phases during short-term exposure to a laser beam.

The local melting events and structural-phase transformations realized under conditions of thermodynamic nonequilibrium are not well understood, although they are widespread in various technological applications with transient conditions [4].

The aim of the present work is to try the LPBF for the manufacture of permanent magnets from the Fe – 25 wt. % Cr – 15 wt. % Co powder, produced by gas atomization.

2. Materials and Experimental Methods

LPBF was carried out in the laboratory of the research center of the NRC "Kurchatov Institute" – CRISM "Prometey" on the RussianSLM FACTORY unit with a solid-state laser (Fig. 1b). This unit implements the melting process in a protective atmosphere of nitrogen. To select the best melting mode, the laser power and scanning speed were varied in the ranges of 150–195 W and 800–1000 mm / s so that the energy input for melting the metal in the laser spot was maintained at ~ 0.18 W·s / mm. The powder with the chemical composition shown

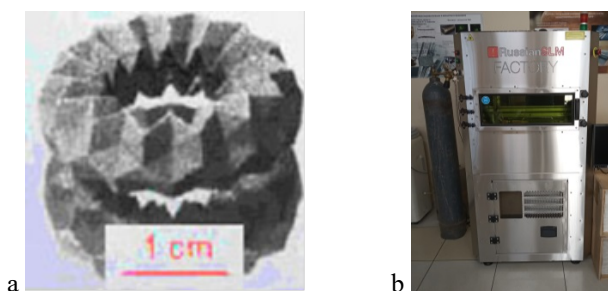


Fig. 1. (a) Magnet layout; (b) RussianSLM FACTORY unit.

in Table 1 was obtained by gas atomization on a HERMIGA 75/3VI unit with induction heating of the crucible.

Table 1. Chemical composition of powder.

Alloy	Basic alloying elements, wt. %							
Elements	Fe	Cr	Co	Nb	V	Ni	Ti	Cu
ingot	56.0	23.0	16.5	1.2	1.2	0.5	0.2	0.2
powder	57.0	24.5	15.6	1.1	1.0	0.5	0.2	0.2

The particles morphology of the manufactured powder is demonstrated in Fig. 2a. It can be concluded that the particles have a shape close to spherical, with no particles of irregular shape, which makes the powder suitable for using in the LPBF. Powder size distribution of two samples of powders manufactured was measured by laser diffraction using the Fraunhofer approximation on the Malvern Mastersizer 2000 unit. According to the results of particle size analysis (Fig. 2b), powder fractions of more than 80 μm were excluded, because they are not suitable for using in LPBF. The share of raw materials suitable for melting was 73 %. To sieve powder, a sieve system on a shaker table was used.

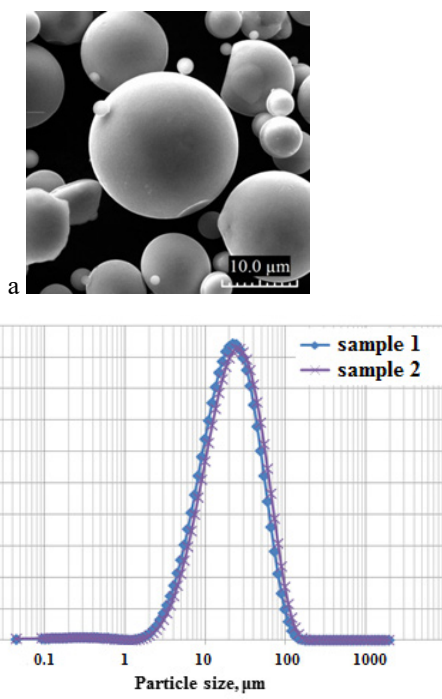


Fig. 2. (a) the particles morphology of the manufactured powder Fe – 25 wt. % Cr – 15 wt. % Co; (b) powder size distribution.

To control chemical composition of powders and LPBF samples, the X-ray fluorescence method on a Thermo Niton XL3t unit was used. Volatilization of some light elements was negligible.

Structural studies were performed on thin sections by X-ray diffraction analysis using a Rigaku Ultima multipurpose X-ray diffractometer and multifractal image processing metallography. The plastic deformation resistance was estimated on the DIL 805 deformation dilatometer platform according to the methodology [5] by uniaxial compression of samples with velocities of 10^{-3} and 10^{-1} s^{-1} at 700 °C. The

reason for the plastic deformation resistance studies is that near the melting zone, relaxation of elastic distortions occurs at different velocities (where is hotter – relaxation is faster). Specific velocities were determined by the capabilities of the equipment (DIL 805).

According to X-ray diffraction analysis, the additive samples present a body-centered-cubic Fe-Co-Cr matrix with ~10 wt. % FeO. X-ray diffraction analysis spectra characterize the phase composition of the LPBF samples after melting with a different laser power (Fig. 3a). As it has a protective atmosphere of nitrogen inside the LPBF unit, it can be concluded that this oxide is a result of oxidation of the powder.

The experiments showed that an increase in laser power up to 195 W is accompanied by an improvement in the metallurgical quality of the metal with a small number of discontinuities (Fig. 3b). The traces of recrystallization in the form of alternating cellular and columnar structures are distinguishable in the images.

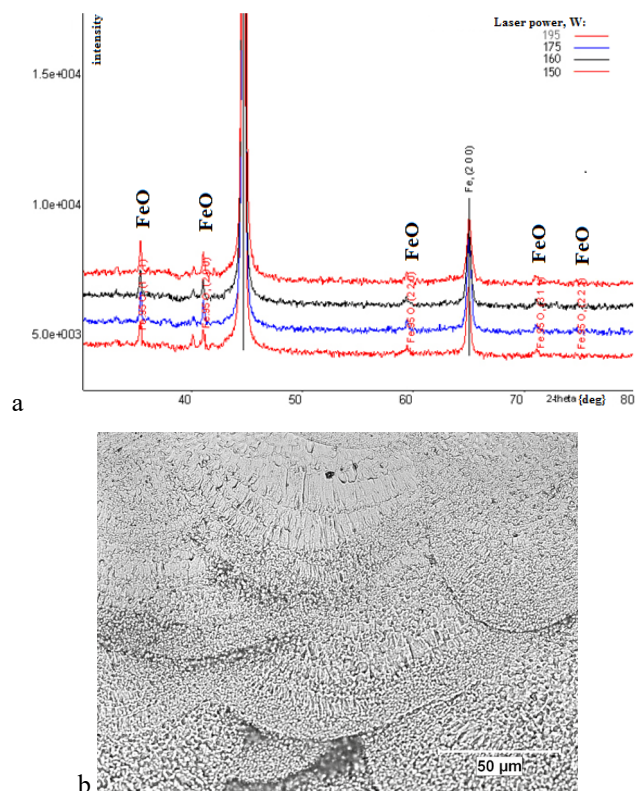


Fig. 3. (a) X-ray diffraction analysis spectra of the obtained additive samples; (b) example of a structure on a thin section of a sample after melting at 195 W power.

A parallel can be drawn between the methods of representing continuous functions in the form of convergent series and multifractal analysis of images. If on a finite interval of existence a continuous differentiable function can be represented by a convergent series or Fourier integral, then the results of the obtained expansions can be used in solving physical problems. When analyzing a digitized image in a field of finite size, arrays of points (pixels 0 and 1) are considered in the form of a statistical set. By analogy with the expansion of continuous functions in series, the original set is represented as the sum of statistical subsets included in the original sum with

its own statistical weight. A feature of the procedure is that each subset is generated by a self-similar algorithm with its fractional (fractal) dimension q . The results of such a transformation in the form of a Renyi distribution have a probabilistic-statistical meaning [6, 7]. The feasibility of multifractal analysis largely depends on the physical content of the obtained probabilistic-statistical assessment.

Considering the scale and interconnection of structural transformations in short-term and fast acts of melting and solidification, when analyzing the results of the study with digital image processing of structures, a systematic approach with multifractal analysis was used.

Multifractal analysis of grayscale images of structures was carried out according to their black and white (binary) maps, which are mathematically considered in the form of statistical sets of different dimensions [8, 9]. From the Renyi spectrum, the values of the dimensions D_q were calculated: the spatial dimension D_0 , the ordering measure $\delta = D_1 - D_q$, and the periodicity measure $K = D_{-q} - D_{+q}$. Here q is the dimension of the statistical binary subsets in the interval $(-40 \div +40)$ from which the binary display of the initial grayscale image is composed.

The spatial dimension D_0 is a quantitative estimate of the investigated image, characterizing the filling of the image field. The value of δ is sensitive to symmetry breaking for the structure as a whole. The larger the value of δ (modulo), the more ordered the structure. The tendency of δ to zero is a sign of disorder. An increase in K values indicates an increase in the periodic component in the display of structures. The results of multifractal analysis have a statistical meaning and are calculated with an accuracy of 5 %.

Magnetic properties with the determination of B_r (residual induction), B_d (working point by induction), H_{cb} (coercivity by induction), H_{cm} (coercivity by magnetization) and BH_{max} (maximum energy product, or maximum amount of magnetic energy stored in a magnet) were obtained on hysteresisgraphs and milliteslameter in measuring device.

3. Experimental Results and Discussion

In the alternation of the influxes, a two- and three-level homogeneous oriented structure was observed, formed by dendrites from 12 to 24 μm length with wavy boundaries and grains up to 4 μm in size, formed in the process of recrystallization. Within the boundaries of the influxes, quasiperiodicity with a wavelength of $26 \pm 1 \mu\text{m}$ and 2 μm was recorded due to diffusion of chemical elements in the molten pool. These facts were an indirect justification for using multifractal analysis [6, 7, 10, 11].

The results of multifractal parametrization (Fig. 4a) of the additive structures showed that, despite the short exposure times of the laser beam, an ordered periodic structure dominates in the volumes of the solid-liquid state of the metal, which is characteristic of crystallization. The scatter in the D_0 , δ and K values suggests that grains and crystals form under different conditions and are characterized by different morphologies. For example, in grains one can detect signs of a disordered (amorphous) state, which is indicated by pores (where D_0 and δ are small); signs of ordering (growth of δ) with

a simultaneous increase in periodicity (decrease of the K scatter) and a decrease in porosity (increase of D_0). A decrease of δ can be considered as a sign of the reaction volume localization with partial or complete amorphization of the structure. In this case, a simultaneous increase in the scatter of K values may indicate an oscillating transformation in the melt zones with different degrees of crystallinity. An increase in δ indirectly indicates the tendency of the mass transformation with a preferred frequency in the additive metal.

It was established that the non-uniform state of the structure varies depending on the conditions of temperature exchange with the environment. For example (Fig. 4b), the values of the parameter δ , sensitive to disorder, decrease with distance from the edge of the sample and an increase in the laser beam power. This fact indirectly indicates a greater heating of the central zones of the sample and a possible increase in the tendency to structural changes. The value of D_0 indicates satisfactory filling of the image field ($D_0 = 1.998 \pm 0.001$), and the value of K indicates the presence of quasiperiodicity in the structures ($K = 0.46 \pm 0.04$).

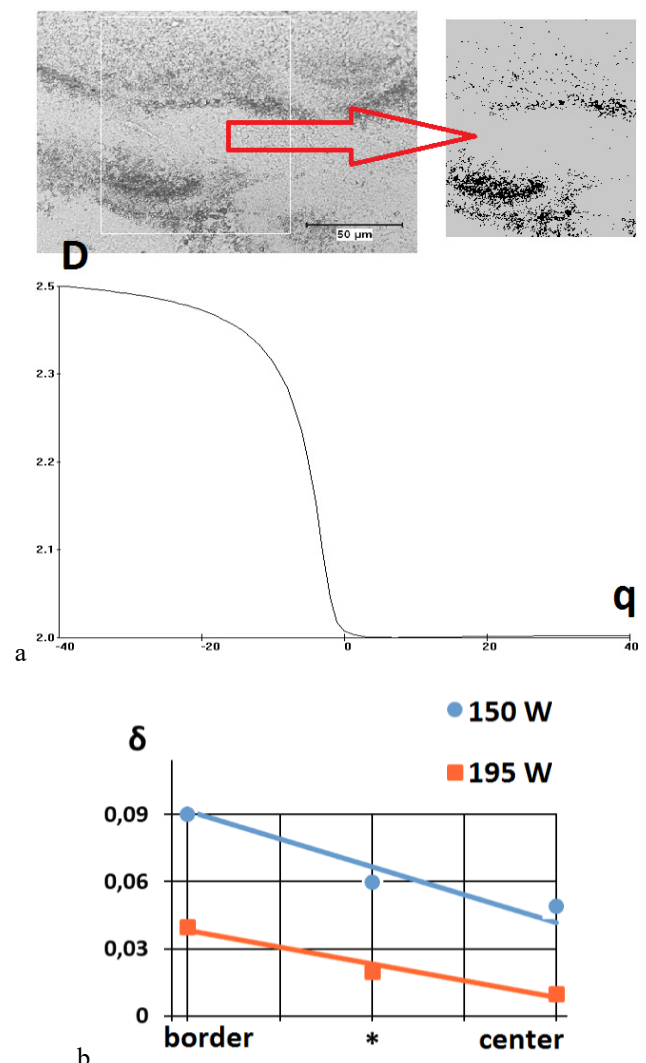


Fig. 4. (a) fragment of multifractal analysis with the construction of the Renyi function and the calculation results after laser melting at a power of 150 W; (b) the places of variation in the structure ordering parameters δ .

Since local micro-volumes are heated and cooled during LPBF, it was of interest to investigate how the elastoplastic properties of the samples change under conditions of heating and deformation.

On the thin sections of the samples, bands of a dark color indicate accumulations of FeO oxides, the presence of which can be the additive metal hardening factor. This does not contradict the fact that after melting at the power of 195 W, the strength of the metal is higher than after melting at the power of 150 W (Fig. 5a) [12]. The shape of the σ - ϵ curves is typical of metals in which the mechanisms of dislocation hardening are activated at $\dot{\epsilon} = 10^{-1} \text{ s}^{-1}$ and dynamic recrystallization at $\dot{\epsilon} = 10^{-3} \text{ s}^{-1}$ [13].

The experiments with hot plastic deformation made it possible to qualitatively assess the fraction of energy stored in the compression process. Thus, according to [14], in the σ - $\dot{\epsilon}$ coordinates, the part of the area lying above the curve (shaded on Fig. 5b) corresponds to the energy stored in the latent form during structural rearrangements. The graphs show that when samples are compressed to $\epsilon = 0.1$ at 700 °C, the introduced mechanical energy is not only transformed into heat, but also scattered in the structure in the form of uniformly distributed objects of the substructure, in which s and d electron shells responsible for the formation of magnetic properties interact [15]. It can be seen that melting at the power of 195 W leads to a more complete supply of internal energy.

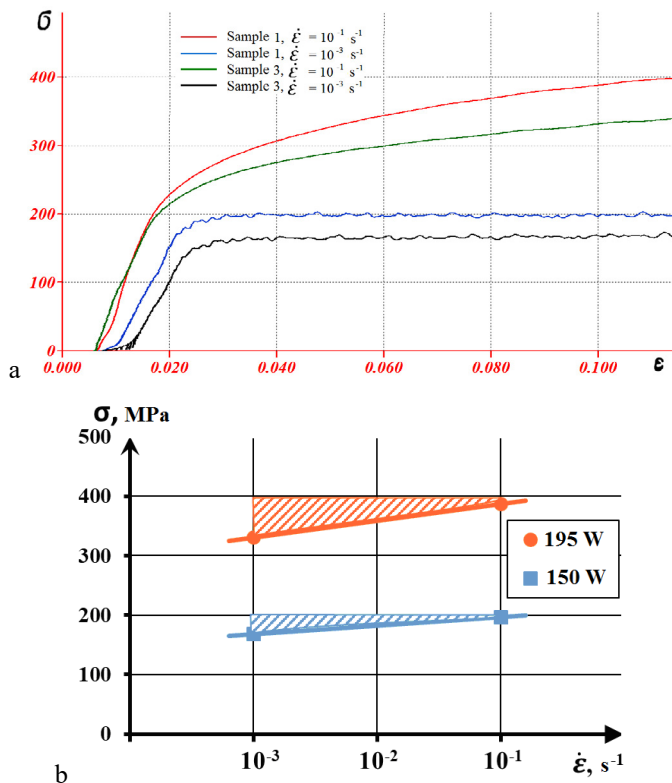


Fig. 5. (a) deformation resistance of specimens under compression with the indicated rates at 700 °C; (b) scheme for estimating the shares of stored energy during compression of samples.

Magnetic measurements showed (Fig. 6, Table 2) that the LPBF allows one to produce a composite whose magnetic

parameters are not lower to samples obtained by traditional founding.

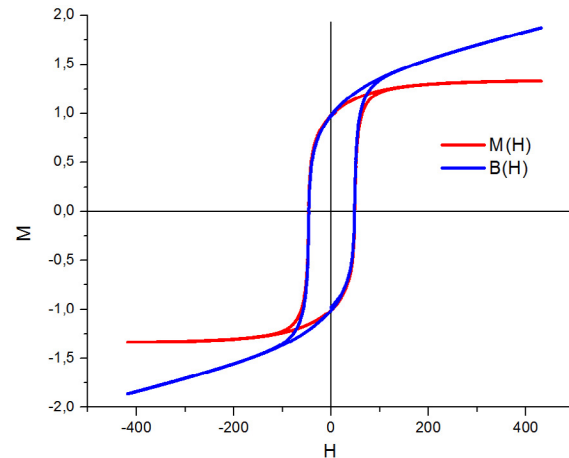


Fig. 6. Typical magnetic loops of additive samples.

Table 2. Magnetic properties of materials.

Characteristic	B_r	BH_{max}	B_d	H_d	H_{cb}	H_{em}
additive sample	10.2 kG	3.02 MGOe	6.83 kG	0.44 kOe	0.57 kOe	0.58 kOe
founding sample	12.9 kG	4.62 MGOe	—	—	0.53 kOe	0.53 kOe

4. Conclusions

It has been established that using the laser powder bed fusion of Fe – 25 wt. % Cr – 15 wt. % Co powder, produced by gas atomization, it is possible to form a monolithic magnet with properties not lower to the same obtained by traditional founding.

Melting is accompanied by structural changes, the intensity of which is proportional to the power of laser beam.

Acknowledgements

This work was supported by the Ministry of Education and Science of the Russian Federation (a unique identifier for subsidies – RFMEFI62519X0046).

References

- [1] Brandt M et al. Laser Additive Manufacturing. Materials, Design, Technologies and Applications. Sawston, Cambridge: Woodhead Publishing, 2016
- [2] Krishnamurthy N, Gupta CK. Extractive Metallurgy of Rare Earths. Boca Raton: CRC Press, 2015
- [3] Krakhmalev P et al. Manufacturing of intermetallic Mn-46%Al by laser powder bed fusion. Procedia CIRP 2018; 74:64–67
- [4] Kuznetsov P et al. Structure and Properties of the Bulk Standard Samples and Cellular Energy Absorbers. Rieka: IntechOpen, 2018
- [5] Schroers J et al. Thermoplastic blow molding of metals. Materials Today 2011; 14:14-19
- [6] Hutchinson J.E. Fractals and self-similarity. Indiana University Mathematics J. 1981; 30:713-747
- [7] Mandelbrot B. The Fractal Geometry of Nature. New York: W. H. Freeman & Company, 2002

- [8] ImageJ n.d., Image Processing and Analysis in Java, accessed 31 May 2020, <<https://imagej.nih.gov/ij/>>
- [9] Barakhtin B, Chashnikov V. Computer program for multifractal analysis of images of structures of metals and alloys. *Materials Science Issues*. 2001; 28 vol.4:5-8
- [10] Coniglio A, De Arcangelis L, Herrmann HJ. Fractals and multifractals: applications in physics. *Physica A: Statistical Mechanics and its Applications*. 1989; 1 vol.157:21-30
- [11] Zhukov A et al. Nanodispersing and Hardening in Technology of Selective Laser Melting of Metallic Powders. *IOP Conference Series: Earth and Environmental Science* 2019; 272:022233
- [12] Zhang J, Jung Y-G. Additive Manufacturing: materials, processes, quantifications and applications. Oxford: Butterworth-Heinemann, 2018
- [13] Korznikova G.F. Structure formation under hot compression deformation of hard magnetic alloy Fe-30% Cr-8% Co. *Physical Mesomechanics*. 2015; 2 vol.18:89-94
- [14] Prasad YVRK, Rao KP, Sasidhara S. Hot Working Guide. A Compendium of Processing Maps. Bangalore: Department of Metallurgy Indian Institute of Science, 2004
- [15] Hofstadter D.R. Energy levels and wave functions of Bloch electrons in rational and irrational magnetic fields. *Physical Review*. 1976; 14:2239-2249

11th CIRP Conference on Photonic Technologies [LANE 2020] on September 7-10, 2020

Additive manufacturing of soft and hard magnetic materials

D. Goll^{a*}, J. Schurr^a, F. Trauter^a, J. Schanz^b, T. Bernthaler^a, H. Riegel^b, G. Schneider^a

^aAalen University, Materials Research Institute, Beethovenstr. 1, 73430 Aalen, Germany

^bAalen University, LaserApplicationCenter, Beethovenstr. 1, 73430 Aalen, Germany

* Corresponding author. Tel.: +49-7361-576-1601; fax: +49-7361-576-2329. E-mail address: dagmar.goll@hs-aalen.de

Abstract

For laser powder bed fusion (L-PBF) processing of powders sensitive to oxidation (e.g. hard magnetic Fe-Nd-B) or powders of various compositions (e.g. soft magnetic Fe-Si) or multilayer composites, special processing chambers have been developed. For soft magnetic materials with reduced losses, L-PBF allows to develop (1) optimized alloy compositions of increased content of alloying elements, (2) novel topological structures and (3) multilayer composites of alternating electrical insulating and soft magnetic materials similar to the principle of electrical steel. For hard magnetic materials, L-PBF allows to develop very fine microstructures of Fe-Nd-B alloy with directed crystal growth and finely dispersed Nd-rich phase.

© 2020 The Authors. Published by Elsevier B.V.

This is an open access article under the CC BY-NC-ND license (<http://creativecommons.org/licenses/by-nc-nd/4.0/>)

Peer-review under responsibility of the Bayerisches Laserzentrum GmbH

Keywords: Additive manufacturing; laser powder bed fusion; soft magnetic materials; hard magnetic materials; FeSi; NdFeB; electric motor

1. Introduction

For efficient electric motors, established soft magnets in the stator are electrical steel (Fe-Si) and established hard magnets in the rotor are rare earth (RE) based magnets (Fe-Nd-B).

Additive manufacturing of soft magnetic materials and components based on laser powder bed fusion (L-PBF) may provide new opportunities for soft magnetic core materials in efficient energy converters [1-3]. I.e. maximum magnetic induction B for high engine torques and minimum magnetic losses P for high rotational frequencies. L-PBF allows to develop [2]: (1) optimized alloy compositions of increased content of alloying elements such as Si or Al and direct fabrication of soft magnetic components thereof, regardless of their mechanical properties, (2) novel topological structures like inner slits and high design flexibility of components, and (3) multilayer composites of alternating layers of electrical insulating materials (high electrical resistivity) and high performance soft magnetic materials (high saturation polarization) to copy the principle of conventional electrical steel. Additive manufacturing of hard magnetic materials based on L-PBF

allows to develop very fine microstructures of Fe-Nd-B based alloys with directed crystal growth and a finely dispersed Nd-rich phase [4-6]. For effective reduction of critical raw materials such as heavy rare earths, finest microstructures are required. These model experiments can show possibilities to design and further improve the alloy microstructure. E.g. the additively manufactured fine and textured microstructure leads to large coercivity in sintered Fe-Nd-B magnets [5]. Additive manufacturing of multilayer composites of different materials, of small powder volumes for effective materials development and of powders sensitive to oxidation requires special equipment. Special lab-scale processing chambers for L-PBF have been built up [2, 5].

In this paper, for soft magnetic materials a feasibility study is performed to combine the described three strategies in one component for eddy current loss reduction and to develop better electrically insulating layers. For hard magnetic materials the influence of processing parameters of L-PBF on the microstructure development of Fe-Nd-B is investigated.

2. Processing set-up and procedures

For additive manufacturing based on laser powder bed fusion (L-PBF), two different lab scale process chambers have been developed (Fig. 1). Both chambers allow fabrication of layered structures of two different materials. The manual lab scale chamber (mLPC, Fig. 1a) enables manual coating operation and processing of small powder volumes ($< 350 \text{ mm}^3$). It can be loaded and operated under pure Ar atmosphere. The automated lab scale chamber (aLPC, Fig. 1b) facilitates automated coating operation and processing of larger powder volumes (20–100 g) under inert gas atmosphere. It was mainly designed for the realization of more complex sample geometries such as ring-shaped samples and larger construction volumes. It consists of three main components – (1) lifting table system, (2) recoating system and (3) housing for inert gas management. In both systems, two different metal powders can be stored inside of two lifting tables. Depending on which material is necessary, one lifting table with powder is moved and a recoater applies a new layer of powder on the work plate. Both powder-supply lifting tables have their own scraper system, which intersect at the work place position. To keep the oxygen content below 60 ppm, a measuring system has been installed, that monitors the atmosphere. Additionally, a ventilator system has been integrated, which circulates the inert gas atmosphere inside the chamber. Particles from process-exhaust fumes are removed by filtration. For a better heat dissipation, a turbulent gas flow is provided. It reaches the interaction zone of laser and alloy powder from two sides. The mLPC and aLPC can be used in common laser process cells. The aLPC is connected with the laser cell for synchronize the automated recoating and laser exposure steps. The remelting of the powder was realized with a Trumpf TruFiber 1000 (wavelength $\lambda = 1075 \text{ nm}$, maximum power $P_L = 1000 \text{ W}$) and a Scanlab intelliSCAN 30 2D scanner with a spot size of $s = 46 \text{ }\mu\text{m}$ and a maximum scan velocity $v_s = 6000 \text{ mm/s}$. Both systems can be alternatively used with a disk laser (Trumpf TrueDisk 4002) of larger spot size ($s = 430 \text{ }\mu\text{m}$). Different optical measurement equipment such as thermography and high-speed cameras can be utilized to observe and visualize the ongoing laser process in-situ.

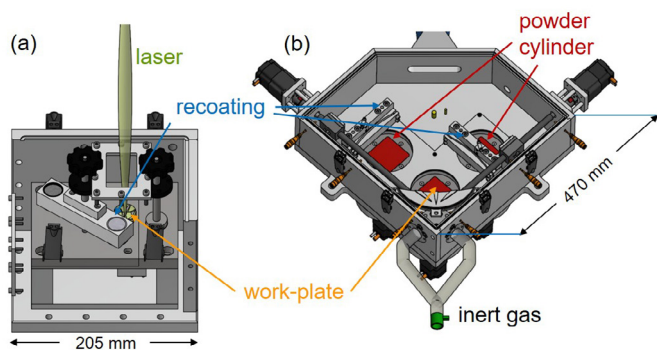


Fig. 1. Lab-scale process chambers for L-PBF additive manufacturing. The chambers allow processing of small powder volumes and of layered structures of different materials. Also powders sensitive to oxidation can be processed. (a) Chamber for manual operation (mLPC). (b) Chamber for automated operation (aLPC).

For L-PBF processing of soft and hard magnetic materials commercially available alloy powders (Fe-Si and Fe-Al based powders and powder mixtures) and in-house developed alloy powders (Fe-Nd-B) have been used: For FeSi6.7, powders of gas-atomized pre-alloyed Fe-Si (Höganäs AB, particle size $< 45 \text{ }\mu\text{m}$, Si content 6.7 wt%, spherical shape and smooth surface) has been used. For FeSi50, gas-atomized ferrosilica powder (Höganäs AB, particle size $< 45 \text{ }\mu\text{m}$) has been utilized. For Fe, water-atomized Fe powder (MG metal powders, CHEMICAL 45, particle size: $45 \text{ }\mu\text{m}$, spattered shape) has been used. For FeAl16, a mixture of the Fe powder and Al powder of ECKA (99.8%, particle size $< 63 \text{ }\mu\text{m}$) has been chosen. For dry mixing of the alloy, a tumble mixer (Turbula WAB) has been used. The flow-rates measured by Carney method (hopper opening 5 mm) yielded 3.5 (FeSi6.7), 10 (FeSi50), 6 (Fe) and 8 (FeAl16) s / 50 g, respectively. The bulk density was given by 4.0 (FeSi6.7), 2.13 (FeSi50), 3.3 (Fe) and 1.54 (Al) g/cm^3 , respectively. An Fe75-Nd18-B7 pre-alloy was produced by book-mold-casting [5]. The pre-alloy was mechanically pre-shredded and ball-milled under Ar atmosphere ($\text{O}_2 < 1 \text{ ppm}$). Subsequently, the powder was mechanically sieved. For L-PBF, the powder fraction $\leq 63 \text{ }\mu\text{m}$ was selected. More details on the powder characteristics (e.g. scanning electron microscopy images) are given in [2, 5]. For all alloy powders the influence of processing parameters such as laser power P_L , scan velocity v_s , and annealing parameters on the microstructure and resulting material properties has been studied and the process optimized accordingly (Fig. 2). Further, different laser exposure strategies have been tested. The parameters chosen for realizing fully dense samples are specified for each prototype in the following chapter.

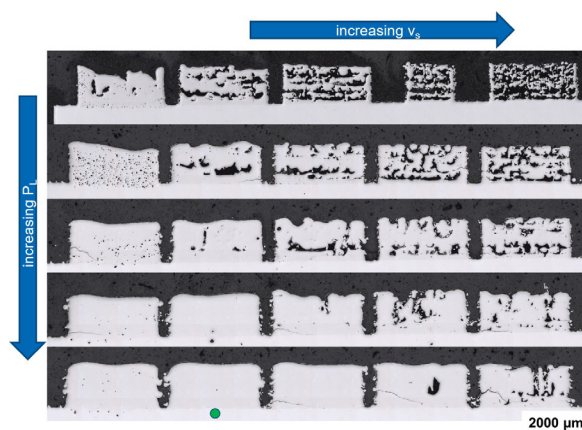


Fig. 2. Example of parametric study (P_L : laser power, v_s : scan velocity) for realizing fully dense specimen for Fe-Si6.7. For lower P_L and v_s , the degree of porosity increases. For higher P_L and v_s , the tendency for residual stresses and therefore towards crack formation is enhanced. The best choice ($P_L = 300 \text{ W}$, $v_s = 200 \text{ mm/s}$) is marked. For the study Ar atmosphere under slight overpressure has been used. Starting value of oxygen content was 100 ppm.

The microstructure was characterized in an optical microscope (ZEISS Axio Imager.Z2m). For the investigations polished microsections of the samples have been produced using metallographic techniques (Struers RotoPol-31). For texture analysis, EBSD (electron backscatter diffraction) analysis, EDAX camera and software (EDAX Hikari, OIM v7.3.1

orientation imaging microscopy) were used in combination with scanning electron microscopy (ZEISS Sigma 300 VP).

3. Application to magnetic materials

The following feasibility studies and research experiments on soft and hard magnetic materials can only be performed by using the special processing chambers developed for L-PBF.

3.1. Soft magnetic materials

A favorable structure for additively manufactured soft magnetic components is to combine the three different strategies mentioned in the introduction. This is shown in Fig. 3. Eddy currents are narrowed down to well-defined small areas. Here, FeSi6.7 base material with increased Si-content and large saturation polarization is combined with horizontal separation layers of an FeAl alloy with higher specific electrical resistivity. Using the dryly mixed alloy with 22 wt% of Al for printing the FeAl layers, the result after the printing process shows an FeAl alloy with 16 wt% Al (FeAl16) due to mixing effects. Both, the FeSi6.7 (thickness 600 μm) and FeAl16 (thickness 140 μm) layers are stacked in an alternating manner. Additionally, slits shall guarantee good electrical insulation in the remaining vertical direction. To realize the slits, ring-shape samples have been fabricated by helical movement of the laser beam and defined track pitch between the helical tracks.

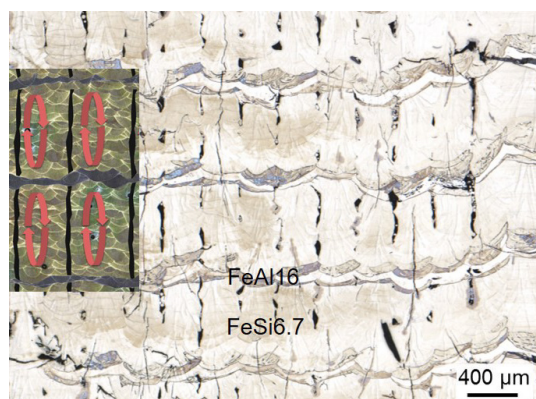


Fig. 3. Combination of three strategies in a single component to realize soft magnets with lower eddy current losses: Optimized composition FeSi6.7, multilayers of FeSi6.7 and FeAl16 in horizontal direction and slits in vertical direction. Processing parameters: $P_L = 225 \text{ W}$, $v_s = 80 \text{ mm/s}$, $s = 300 \mu\text{m}$. The optical microscopy image shows the ring cross-section. For processing the multilayer structure, 10 layers Fe-Si (80 μm) and 2 layers Fe-Al (70 μm) have been printed.

The helical exposure strategy combines a focal diameter of the laser beam of 200 μm with the chosen hatch distance (Fig. 4a). A further feasibility study has been performed on Fe-FeAl16 to investigate the influence of the hatch distance on the slit quality. Hatch distances of up to 200 μm result in unbonded lines, where the individual exposed tracks are connected to each other only slightly. For larger hatch distances of 300 μm and 400 μm , some continuous separations occur between the individual laser tracks. Thus, with increasing hatch distance, slits appear between the individual tracks of the laser. Due to the helical exposure strategy, the slits are arranged radially in the ring sample. As shown in Fig. 4b, the slits result in a

significant reduction of eddy current losses. The effectivity of the slits on loss reduction depends on the thickness. Influencing parameters are the wetting of the melt during printing and remaining particles in the slits. More detailed studies are necessary to quantitatively clarify these relationships.

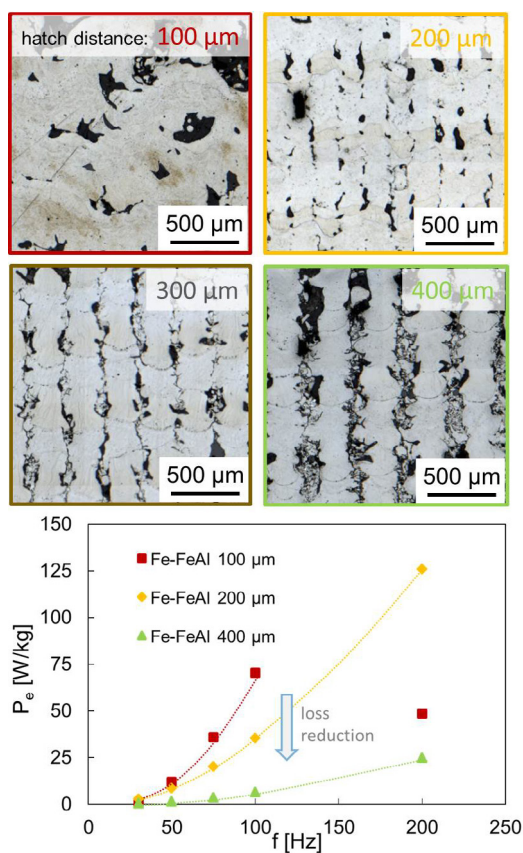


Fig. 4. Adjustment of hatch distance between 100 μm and 400 μm to design vertical slits in Fe-FeAl16 multilayer components. Processing parameters: $P_L = 200 \text{ W}$, $v_s = 83 \text{ mm/s}$, $s = 200 \mu\text{m}$. Top: Microstructure of the cross-section of ring samples. Optical microscope image. Bottom: Related eddy current losses P_e . The frequency of the alternating field has been changed between 30 and 200 Hz. The magnetic field strength used has been 0.3 T. For processing 8 layers Fe (75 μm) and 2 layers FeAl (100 μm) have been printed.

Soft magnetic materials require an annealing treatment to reduce hysteresis losses. Fig. 5 shows, that it is possible to subject alternating layered components to an annealing treatment of up to 900 $^\circ\text{C}$ for 1 h without losing the positive effect of the higher-resistance separation layers. For higher temperatures, however, increased diffusion of Al within the separation layers takes place. As a result, the effectiveness of the separation layers deteriorates and the sample shows significantly higher eddy current losses. In the next step, focus will be put on optimizing the magnetic properties by annealing.

The extent of reduction of eddy current losses further depends significantly on the presence of continuous separating layers and their specific electrical resistivity. In the feasibility test above, the specific electrical resistivity amounts to 1.0 $\mu\Omega\text{m}$ for FeAl16 and to 0.85 $\mu\Omega\text{m}$ for FeSi6.7. This is 8 to 10 times higher compared to Fe (0.1 $\mu\Omega\text{m}$) [2]. To use the same L-PBF process for the two different layers, more promising candidates for the “insulating”

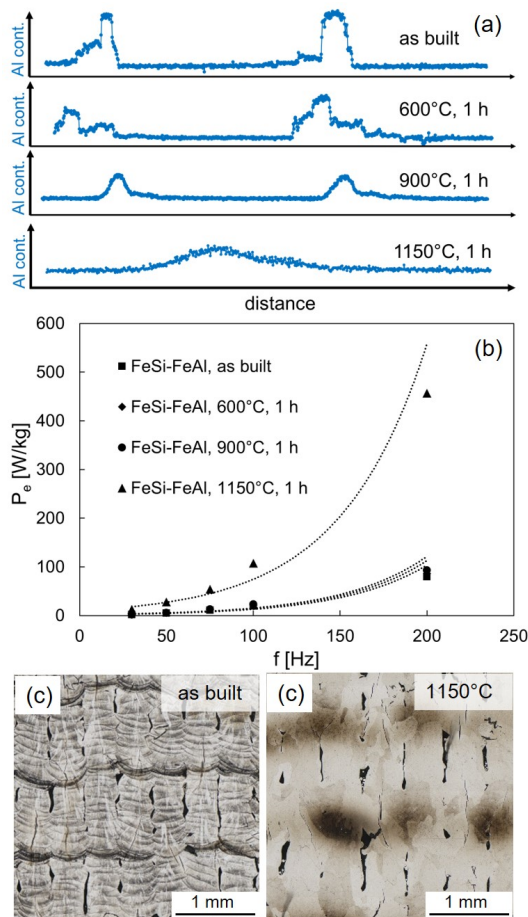


Fig. 5. For recovery of stresses or deformations during the L-PBF process post-annealing treatments are required. They are possible up to temperatures of 900 °C. Then intermixing of the multilayers by diffusion starts and eddy current losses significantly increase. (a) EDS analysis of horizontal Fe-Al separation layers compared to the as built state after different post-annealing treatments. (b) Related eddy current losses P_e . The frequency f of the alternating field has been changed between 30 and 200 Hz. The magnetic field strength used has been 1 T. (c) Sample in as built and 1150 °C state, i.e. before and after intermixing of the multilayers starts. For processing 10 layers Fe-Si (80 μm) and 2 layers Fe-Al (70 μm) have been printed. A hatch distance of 350 μm and spot size of 300 μm have been used.

layer material are FeSi with a higher Si content or intermetallics like FeSi₂ (1000 μm) [2, 7]. However, with increasing Si content, the brittleness of the materials is significantly increasing. Here, additive manufacturing provides the opportunity to manufacture thin sheets of brittle alloys. Alternated stacking of FeSi6.7 with such brittle insulating layers has been tested for ferrosilica (FeSi50, EDX measurement Si 41 wt%). For suitable laser processing parameters (double exposure, $P_L = 400$ W, $v_s = 573$ mm/s) very good connectivity of the ferrosilica layer to FeSi6.7 was achieved in parts of up to 6 x 6 mm² base area (Fig. 6a). Also, only few cracks formed in the body. In the test specimen, a layer thickness of 75 μm has been chosen (4 layers of ferrosilica, 75 μm each). In Fig. 6b, the microstructure of the cross-section of the specimen is shown in more detail. The ferrosilica layer shows a eutectic structure of FeSi and FeSi₂. On both interfaces, it is connected to the FeSi6.7 bulk material by thin mixing zones of intermediate Si content (~ 20 wt%) and thickness 30 μm . In the next step, the focus will be on optimizing the physical properties of these interlayers.

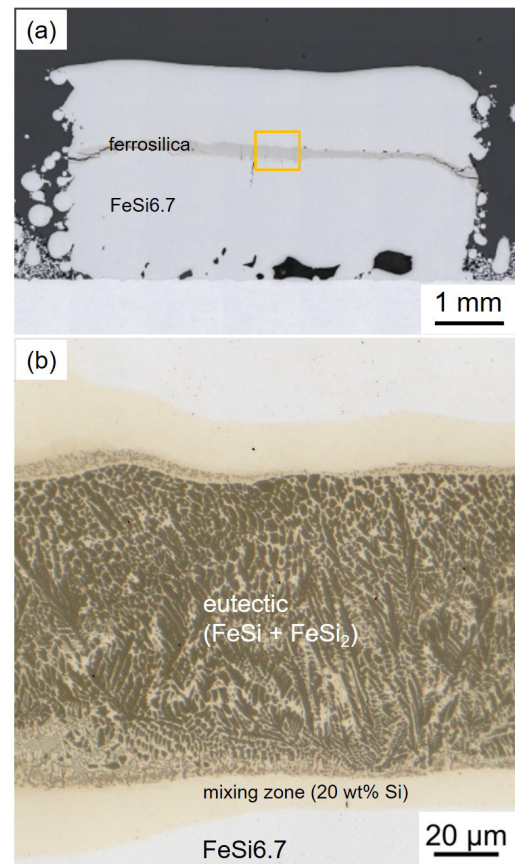


Fig. 6. Ferrosilica as interlayer anticipates higher specific electrical resistivity. However, the material is extremely brittle. By means of parametric study optimization (double exposure, $P_L = 400$ W, $v_s = 573$ mm/s), crack free layers of good connectivity have been realized: (a) cross-section overview, (b) cross-section of the interlayer in more detail. Optical microscope image. For processing 20 layers FeSi6.7 (75 μm) and 4 layers FeSi50 (75 μm) have been printed.

3.2. Hard magnetic materials

In Fig. 7 the Fe75-Nd18-B7 powder used in the L-PBF process is shown using scanning electron microscopy. The aspherical shape of the Fe-Nd-B powder particles may restrict flowability during the L-PBF process. However, using mLPC, parts with high relative density of 98 to 99 % could be realized. This shows the qualification of the powder for lab scale processing.

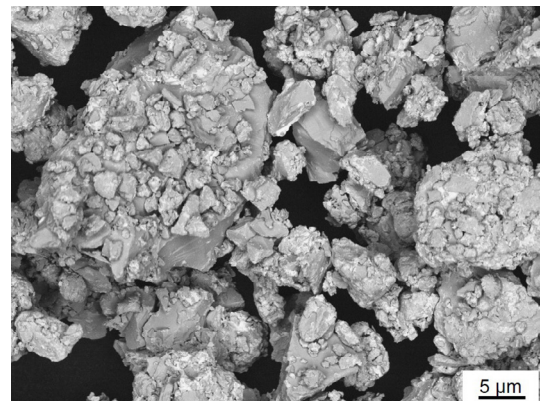


Fig. 7. Fe75-Nd18-B7 powder used in the L-PBF process (mLPC). Scanning electron microscopy (SEM) image.

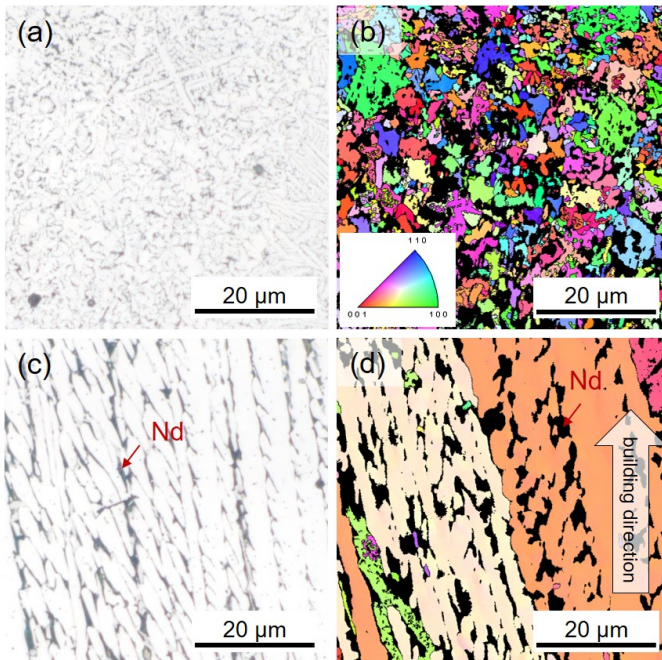


Fig. 8. Different microstructures for Fe75-Nd18-B7 by L-PBF ($v_s = 400$ mm/s). (a, b) Fine-granular isotropic microstructure for lower laser power ($P_L = 150$ W). (c, d) Fine microstructure with a directed crystal growth and finely dispersed Nd-rich phase for higher laser power (450 W). Optical microscope image (a, c). EBSD analysis (inverse pole figure) (b, d).

In Fig. 8 the influence of the laser power P_L on the microstructure is shown. The scan velocity has been kept constant ($v_s = 400$ mm/s). For lower laser power a fine-granular isotropic microstructure is obtained. This is due to the related high cooling rates. The isotropic character of the structure has been confirmed by EBSD analysis. For higher laser power, and therefore higher energy input, the solidification structure changes. A fine microstructure with a directed crystal growth and finely dispersed Nd-rich phase is obtained. The preferred direction of primary crystallized $\text{Fe}_{14}\text{Nd}_2\text{B}$ (tetragonal unit cell of 68 atoms and lattice parameters $a = 8.8 \text{ \AA}$ and $c = 12.2 \text{ \AA}$ [8]) is oriented along the crystallographic a -axis.

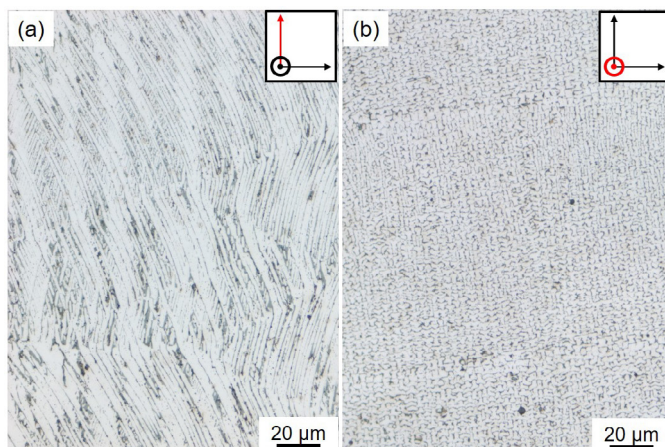


Fig. 9. Large-scale microstructure of 3D-printed (L-PBF) Fe75-Nd18-B7 material ($P_L = 450$ W, $v_s = 400$ mm/s) (a) parallel and (b) perpendicular to building direction (building direction is indicated by red arrow). Optical microscope image.

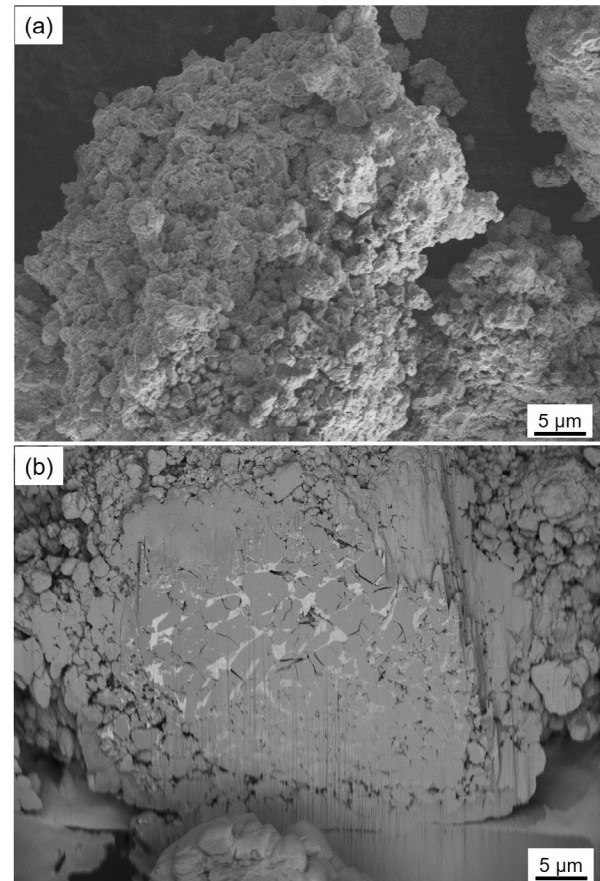


Fig. 10. Re-milled Fe75-Nd18-B7 material which has been 3D-printed (L-PBF mLPC, $P_L = 450$ W, $v_s = 400$ mm/s). (a) Powder particle. (b) Particle after ion beam milling (FIB). Scanning electron microscopy (SEM) image.

Due to heat flow in work-plate direction, therefore, the a -axis is aligned to the building direction. This orientation information was revealed by EBSD measurements. As a consequence of the temperature gradient in the part, it is further assumed, that during solidification the $\text{Fe}_{14}\text{Nd}_2\text{B}$ grains grow in a lamellar or columnar way. In Fig. 9 the microstructure parallel and perpendicular to the building direction is shown. By choosing a suitable scanning structure, e.g. parallel lines in the same scanning direction, a further temperature gradient may be implemented. This can be used to adjust preferred alignment of the magnetocrystalline easy c -axis (texture). The preferred magnetization direction is directed along the c -axis of the tetragonal crystal structure.

Re-milling of the additively manufactured sample with its fine and textured microstructure results in significantly finer powders compared to the powder fabricated from book-mold-cast material (Fig. 10). After ion beam milling (FIB), it becomes obvious, that particles consisting of lamellar/columnar structure with finely dispersed Nd rich phase are still present. As shown in [5], these ultrafine structured particles could lead to an ultrafine grain structure in sintered magnets, thus, resulting in significantly higher coercivity. In the next step, the processing parameters have to be optimized to receive even finer microstructures. Subsequently, economic ways to process such fine microstructures have to be realized.

4. Conclusions

To sum up, special lab-scale processing chambers for L-PBF have been built-up to enable additive manufacturing of small powder volumes for materials development, of material sensitive to oxidation as well as for processing multilayer composites of different materials. The chambers have been used for three different feasibility studies based on additive manufacturing of soft and hard magnetic materials:

- The combination of soft magnetic material with topological structures and composite structures of alternating electrical insulating and soft magnetic material is promising for eddy current loss reduction. The feasibility of such components has been demonstrated using Fe and FeSi_{6.7} soft magnetic material. It could be shown, that inner slits in vertical direction by hatch distances > 200 µm and FeAl₁₆ layers of higher specific electrical resistance (compared to pure Fe) reduce losses. Annealing of such composite structures for reduction of hysteresis losses is possible up to 900 °C for 1 h without losing the positive effect of the higher-resistance separation layers.
- Better electrical insulating layers (similar to the principle of electrical steel) in such soft magnetic components may be obtained by intermetallics like FeSi₂ which however are comparably brittle. The feasibility of additively manufactured composites with brittle materials has been demonstrated for FeSi_{6.7}-FeSi₅₀. The ferrosilica layer shows a eutectic structure of FeSi and FeSi₂ and mixing zones of intermediate Si content (~ 20 wt%) and thickness 30 µm at the interfaces.
- By an appropriate choice of processing parameters of L-PBF, very fine microstructures can be developed in hard magnetic materials. The feasibility of very fine microstructures has been demonstrated for Fe-Nd-B alloy resulting in directed crystal growth and finely dispersed Nd-rich phase. This can be used to adjust the texture for preferred magnetization orientation. Furthermore, fine structured powder particles thereof may lead to a fine grain structure in sintered magnets.

Acknowledgements

The authors would like to thank for assistance during preparation, processing and analysis of the samples and for fruitful discussions (all Aalen University): D. Hohs, L. Lang, R. Loeffler, D. Kolb, T. Kunert, S. Muerdter, U. Pflanz and T. Schubert. The work was funded by the German BW-Stiftung and the State Ministry of Baden-Wuerttemberg for Sciences, Research and Arts (MWK) (within the scope of the projects AddLAS and Admiral, respectively).

References

- [1] Garibaldi M, Ashcroft I, Hillier N, Harmon SAC, Hague R. Relationship between laser energy input, microstructures and magnetic properties of selected laser melted Fe-6.9%wt Si soft magnets. *Mater. Charact.* 2018; 143; 144-151.
- [2] Goll D, Schuller D, Martinek G, Kunert T, Schurr J, Sinz C, Schubert T, Bernthaler T, Riegel H, Schneider G. Additive manufacturing of soft magnetic materials and components. *Add. Manufact.* 2019; 27; 428-439.
- [3] Plotkowski A, Pries J, List F, Nandwana P, Stump B, Carver K, Dehoff RR. Influence of scan pattern and geometry on the microstructure and soft-magnetic performance of additively manufactured Fe-Si. *Add. Manufact.* 2019; 29; 100781.
- [4] Jacimovic J, Binda F, Herrmann LG, Greuter F, Genta J, Calvo M, Tomse T, Simon RA. Net shape 3D printed NdFeB permanent magnet. *Adv. Eng. Mater.* 2017; 19; 1700098.
- [5] Goll D, Vogelgsang D, Pflanz U, Hohs D, Grubesa T, Schurr J, Bernthaler T, Kolb D, Riegel H, Schneider G. Refining the microstructure of Fe-Nd-B by selective laser melting. *Phys. Stat. Sol. RRL* 2019; 13; 1800536.
- [6] Skalon M, Görtler M, Meier B, Arneitz S, Urban N, Mitsche S, Huber C, Franke J, Sommitsch C. Influence of melt-pool stability in 3D printing of NdFeB magnets on density and magnetic properties. *Materials* 2020; 13;139.
- [7] Kloc C, Arushanov E, Wendl M, Hohl H, Malang U, Bucher E. Preparation and properties of FeSi, α -FeSi₂ and β -FeSi₂ single crystals. *J. Alloys Comp.* 1995; 219; 93-96.
- [8] Herbst JF, Croat JJ, Pinkerton FE, Yelon WB. Relationships between crystal structure and magnetic properties in Nd₂Fe₁₄B. *Phys. Rev. B* 1984; 29; 4176-4178.

11th CIRP Conference on Photonic Technologies [LANE 2020] on September 7-10, 2020

Benchmark parts for the evaluation of optimized support structures in Laser Powder Bed Fusion of metals

Katharina Bartsch^{a,b,*}, Joost Ohrenberg^b, Claus Emmelmann^{a,b}

^aHamburg University of Technology, Institute of Laser and System Technologies, Denickestr. 17, 21073 Hamburg, Germany

^bFraunhofer Research Institution for Additive Manufacturing Technologies IAPT, Am Schleusen graben 14, 21029 Hamburg, Germany

* Corresponding author. Tel.: +49-40-484010-648; fax: +49-40-484010-999. E-mail address: katharina.bartsch@tuhh.de

Abstract

Laser powder bed fusion (PBF-LB/M) of metals belongs to the advanced additive manufacturing processes on the brink of industrialization. Successful manufacturing often requires the utilization of support structures to support overhangs, dissipate heat, and prevent distortion due to residual stresses. Since the support structures result in increased costs, research, as well as industry, aim at optimizing the application of those or the support structures themselves. New approaches are validated with individual use cases, though, preventing an objective comparison of optimization strategies. This paper contributes to the advance of support structure optimization by providing a benchmark strategy including part geometries, which enables to evaluate technical as well as economical aspects of support structures or support strategies. The benchmark process is demonstrated with the help of the currently most used block and pin support structures.

© 2020 The Authors. Published by Elsevier B.V.

This is an open access article under the CC BY-NC-ND license (<http://creativecommons.org/licenses/by-nc-nd/4.0/>)

Peer-review under responsibility of the Bayerisches Laserzentrum GmbH

Keywords: support structures; optimization; benchmark; laser powder bed fusion (PBF-LB/M); selective laser melting (SLM)

1. Introduction

With additive manufacturing exhibiting market growth rates above 26% over the last 30 years, laser powder bed fusion of metals (PBF-LB/M), also known as selective laser melting, being the leading manufacturing process in the field of final production of metal parts plays an important role in the establishment of additive manufacturing in industry [1]. To successfully manufacture metal parts, PBF-LB/M often requires support structures to support overhangs, dissipate heat, and prevent distortion due to residual stresses. Because support structures do not belong to the final part and hence need to be removed, they increase the overall costs of the parts. For this reason, numerous approaches on optimizing support structures are found in literature, which can be categorized according to their overall goal [2]: (1) Reduction or avoidance of support structures, (2) Optimization of existing support types, and (3) Creation of new support structures. To reduce or even

completely avoid the use of support structures, the design process offers several possibilities. While the compliance with design rules, either manually or by utilizing topology optimization [3-5], is the most obvious approach, the correct choice of the part orientation on the build platform [6-8] is an essential tool given that the geometry of the part is fixed. Other studies aim at incorporating finite element method to properly choose the sections in need of support as well as the appropriate amount of support [9,10]. Mumtaz et al. [11] explored the possible combination of eutectic alloys and specific process parameters in order to avoid the use of support structures. Nonetheless the efforts put into this category of support structure optimization, until a product is designed completely for additive manufacturing, there will always be a need for support structures, though.

With regard to already existing support types, a lot of research is done to optimize the geometry of those by determining the limits of manufacturability [12] or introducing

new features such as perforation or additional material for improved heat dissipation [13-15]. Furthermore, support structures can be built using specific process parameters [16] to tailor them to the expected loads. Lefky et al. [17] as well as Hildreth et al. [18] take the first steps to transfer the multi-material approach common in polymer additive manufacturing to metal processing. Despite the extensive research done within this approach of support structure optimization, the success is limited to use cases ideal to the already existing support types.

The creation of completely new support structures has been becoming increasingly popular during the last years. The design of unit cells, especially lattice structures, is a promising approach in terms of support volume reduction that is capable of keeping the needed computational resources at a reasonable level [19-22]. Because of the overall space the unit cells occupy this approach is limited to the support of surfaces. To design completely individual support structures, algorithms such as topology optimization [2,23-25] or other computational algorithms [26,27] are employed.

A major issue in support structure optimization, though, is the lack of standardized part geometries for validation, hampering the objective assessment of the different approaches. While in the field of polymer material extrusion (MEX/P) certain models such as the minotaur, gymnast, or rabbit [28-30] have been somewhat established as commonly used validation geometries (even though they do not allow a systematic technical assessment) there is no such geometry in PBL-LB/M besides the cantilever beam [2]. The cantilever beam represents a simple use case to quantify residual stresses and is not fit to thoroughly examine support structures, though. Jiang et al. [31] addressed issue of standardized geometries in the field of polymer material extrusion (MEX/P) by designing a single benchmark part. Since MEX/P support structures are only needed to support overhangs, the developed benchmark part focuses on features related to overhangs. This is not sufficient for PBF-LB/M, leaving a need for benchmark parts for the evaluation of optimized support structures in PBF-LB/M.

This study aims at creating a standardized procedure for PBF-LB/M to assess the performance of support structures and general support strategies because the way of the utilization of currently applied support structures can also influence the manufacturability of a part [12]. Therefore, the benchmark parts do not characterize support structure properties such as tensile strength directly but provide a set of common features testing the overall performance of the support structures regarding those. To ensure the wide applicability of the benchmark procedure, care has been taken to integrate measurement methods that are broadly available. Additionally, all files required for a quick and reliable implementation of the benchmark procedure (CAD files, evaluation sheet, manual) are provided under CC BY-SA license via the research data repository of Hamburg University of Technology [32].

2. Development of the benchmark procedure

In the first step, the criteria suitable to evaluate the performance of support structures are determined. On the one hand, the criteria have to meet the general requirements of a benchmark to create a valid comparison: benchmarks need to

be objective, valid (criteria not influencing each other), reliable (measured variations are significant), and reproducible. On the other hand, several technical as well as economical details shall be assessed, which are representative of the overall task of support structures. To define relevant criteria, the consequences of a poor support structure performance are considered (see Tab. 1), since they provide identifiable characteristics of support structure performance.

Table 1. Consequences of poor support structure performance.

Task	Consequence of poor performance
Supporting overhangs	Overhangs not build, dross formation, distortion, delamination
Dissipating heat	Discoloration, distortion
Counteracting residual stresses	Distortion, cracks, support structure detachment, part detachment from the substrate

Based on the characteristics displayed in Tab. 1, a two-phase procedure for the technical performance assessment is proposed. First, a qualitative visual inspection of the benchmark parts is carried out. Here, the existence of cracks, notches, distortions, discolorations, delamination, edge errors and any detachment of either part or support structure is noted. Second, criteria that can be quantified are assessed in detail. To keep the benchmark procedure simple, the second phase is restricted to geometrical means, since they can be measured via images and coordinate measuring machines (CMM) with no need for complex laboratory setups.


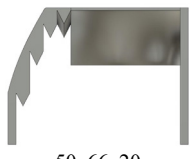



Besides the technical performance of support structures, the economic point of view due to the increase in costs is also of interest. Therefore, a dedicated third phase is added to the benchmark procedure. Here, the focus lies on three aspects that greatly influence the support structure costs [33]: material consumption, ease of support structure removal, and the influence on the surface quality. To determine the material consumption, the benchmark parts are weighted before and after support structure removal, because the volume of the digital support structures does not include possibly entrapped powder. The ease of removal is assessed according to the scale proposed by Gralow et al. [3]: (1) Close to no resistance/very easy to remove, (2) low resistance/easy to remove, (3) medium resistance/moderate effort to remove, and (4) high resistance/hard or impossible to remove. Here, the resistance of the structure against removal respectively the necessary effort for removal is judged by the responsible person. Only manual support removal is considered. Additionally, the time needed to remove any residuals of the support structures is measured. The goal of the post-processing is a state where the effect of the support structures on the surface does not influence further surface finishing by sandblasting.

In regard of the surface quality, which is influenced by material residuals or even craters, the supported features are visually inspected and rated applying the following scale: (1) residuals can be removed by sandblasting (commonly applied post-processing method, no further effort due to support structures), (2) Residuals need to be removed by files, and (3) pitting (existence of craters).

To develop the benchmark procedure, the criteria and measurement methods defined in the first step are mapped to

common geometrical features found in parts manufactured by PBF-LB/M. Support structures are generally used for overhanging features, which can be planes or edges. Furthermore, the planes and edges can be straight or curved. A special case is the merging of two structures into one. Paying attention to the results of step one and the identified geometrical features, five benchmark parts are designed, whose features are summarized in Tab. 2. The exact dimensions of each respective feature, which are based on many years of experience in determining and optimizing process parameters for a broad range of metal alloys within the research group, can be taken from the CAD files [32]. In general, the size of the benchmark parts is kept at 50mm height and 20mm thickness as a compromise of cost and reliable measurement of geometrical features. Additionally, to avoid that interfacing features of the support structures, e.g. tooth geometries, influence each other, a minimal support height of 30mm is planned for.

Table 2. Benchmark parts and their features.

Part No.	h x w x d [mm]	Features
1	 52.5x52x30	<ul style="list-style-type: none"> • Straight surfaces with 0°, 10°, 20°, 30° inclination • min. support height: 30 mm
2	 50x66x20	<ul style="list-style-type: none"> • Straight edges with support heights of 15 mm, 30 mm, 40 mm • Edge with curvature in horizontal direction • Edge with curvature in vertical direction
3	 57x90x20	<ul style="list-style-type: none"> • Holes (curved surface) with 56 mm, 36 mm diameter
4	 50x25x20	<ul style="list-style-type: none"> • Structural transition, edge • min. support height: 33 mm
5	 50x25x20	<ul style="list-style-type: none"> • Structural transition, curved • min. support height: 33 mm

Part no. 1 includes overhanging planes. Since surfaces with an inclination angle of 0° to 30° (with regard to the build plate) need support [34], this interval is covered with a step size of 10°, leading to four respective planes. To allow for a representative plane, the size of the part is slightly altered from

the general dimensions described earlier in terms of height and thickness. Part no. 2 integrates the edge overhangs. On the one hand, the ability to build the support structure over various heights is tested by incorporating straight edges with different distances to the ground. Furthermore, two edges with a varying contour in vertical (continuous arch) as well in horizontal direction (wavy curve) challenge the support structures ability to follow an edge. With holes as the key feature, part no. 3 represents the case of curved planes. Two different diameters allow for the interpretation of different curvatures. Part no. 4 and 5 tackle the special case of the merging of two structures, in this case the merging of two thin walls. While part no. 5 integrates the continuous merging via an arch, also adding a third (smaller) diameter to part no. 3, part no. 4 features the discontinuous merging by an inverted edge, challenging the support structures ability to prevent distortion of the thin walls while manufacturing the upper area of the part.

In terms of geometrical aspects that are measurable, the following features are integrated: At the overhangs of part no. 1, the angle deviation as an indicator of residual stresses as well as the edge deviation as a mean of heat dissipation (particle sinter on the edges when temperatures are too high) are measured. Part no. 3 provides holes where dross formation can occur at the top of the holes if not properly supported, therefore the deviation in diameter is evaluated. Last, the levelness of the side surfaces of part no. 4 and 5 indicate how well the structural transition has been held in place, so the deviation of the upper and lower edges is measured. Part no. 2 is only evaluated in the first step and does not include any measurable features.

3. Validation of the benchmark concept

To validate the developed benchmark procedure, it is applied to common support structures, whose general performance is well known. The block support consists of thin, perforated walls, which are positioned in a two-dimensional grid. Block supports are considered non-solid support structures [3] and mainly applied to surfaces because of their 2D appearance. Pin supports have opposite characteristics compared to the block supports. Their geometry is represented by columns, which are not connected to each other. That is why pin supports are categorized as solid support structures [3]. Pin supports are mainly applied to edges and where high residual stresses are expected since the volumetric nature results in higher strength. Evaluating [3] with regard to the characteristics of block and pin supports, the following results of a direct comparison are expected by the authors:

- Supporting overhangs: block supports will perform better on surfaces, pin supports on edges
- Dissipating heat: pin supports will dissipate more heat than block supports because of the volumetric geometry compared to the single scan, perforated walls of the block support, even though the overall volume may be smaller
- Counteracting residual forces: pin supports will be more effective than block supports because of their higher strength

- Material consumption: pin supports have a greater individual volume, but block supports are connected and prone to powder entrapment, therefore block supports will have higher material consumption
- Removability: block supports will be easier to remove and leave fewer residuals than pin supports because of their non-solid nature and comparatively small interface cross-section

The data preparation, i.e. generation of support structures as well as slicing, is done using the software Materialise Magics (Version 20.01). The production system for the manufacturing of the benchmark parts is the SLM500HL (SLM Solutions AG, Lübeck, Germany). The build chamber employing a build platform of 500x280mm² allows distancing the respective benchmark parts in a way that they do not influence each other.

The material of the benchmark parts is Ti6Al4V. A standard set of process parameters (see Tab. 3) as well as argon atmosphere is applied. For the benchmark, each of the five parts is manufactured once, all together in the same build job and slightly scaled down in size to meet material availability. An alternating scan pattern is chosen. After manufacturing, the parts are manually cleaned and detached from the build platform by wire electrical discharge machining. Geometrical measurements are performed using the CMM type Wenzel LH87 (WENZEL Group GmbH & Co. KG, Wiesthal, Germany) equipped with an optical measurement device.

Table 3. Process parameter applied in validation.

Parameter	Value
Laser power [W]	240
Scan velocity [mm/s]	1200
Hatch distance [μm]	100
Layer thickness [μm]	60

The results of the visual inspection of all five parts are shown in Fig. 1 and summarized in Tab. 4. All parts have been successfully manufactured regardless of the support type. The block supports resulted in more cracks (e.g. as seen in Fig. 1a), occurring in part no. 1, 2 & 3. In terms of discoloration, the block support is more severely affected than the pin support: part no. 3-5 show light discoloration in areas with large volumes, part no. 2 even strong discoloration, whereas for the pin supports part no. 2 is only slightly discolored (Fig. 1b&d). Furthermore, some of the outer block supports detached in part no. 3. On the other side, the pin supports resulted in a notch at the bottom of the 50mm diameter hole of part no. 3. Since the notch is localized at the bottom of the hole, the notch is attributed to the manufacturing system though, not to the pin support.

Tab. 5 displays the measurements of the CMM. Overall, the pin supports result in greater deviations compared to the block supports, nearly doubling the values of the block supports.

The data gathered for the economic evaluation is presented in Tab. 6. Here, the data of all five parts for material consumption as well as the time needed for removal is summed up, while the rating of the removal of the supports is averaged. The block supports consumed more material and took

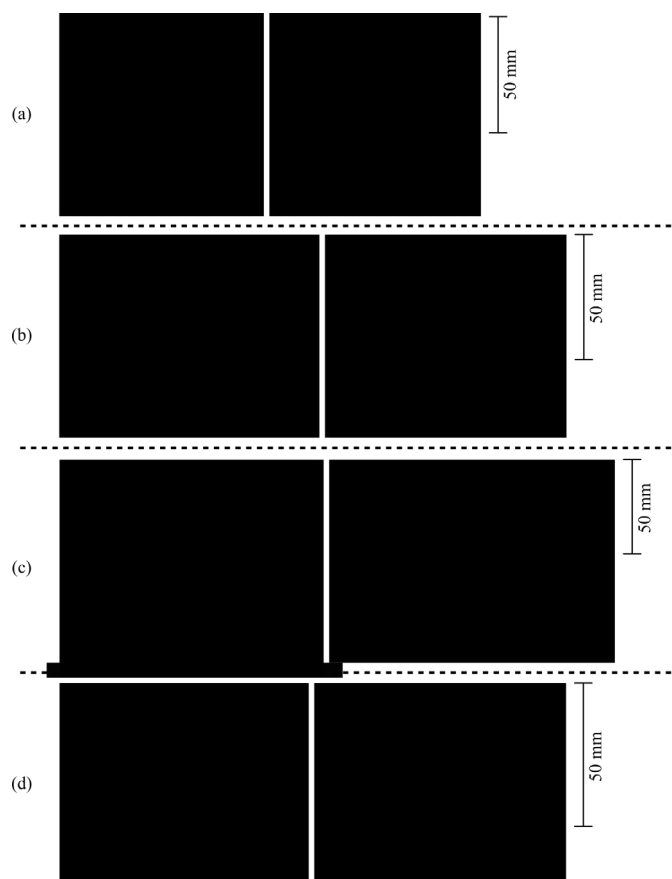


Fig. 1. Benchmark parts (left: block support, right: pin support) prior to support removal, with indicated visual issues. (a) Part no. 1, (b) part no. 2, (c) part no. 3, (d) part no. 4 and 5.

significantly longer to be removed, although they were easier to remove than pin supports. In terms of material consumption, the weighting result for both support types was 5% higher than the theoretical material calculation from the volume of the digital support structures, highlighting the need for weighting. The pin supports resulted in a surface quality worse than the block supports, see Fig. 2. This also shows in the time needed for the post-processing of the surface, which is nearly triple the amount necessary for the block supports. The detailed data that is shown summarized in Tab. 4 – 6 is available in the Excel sheet of [32].

Considering the results of all three benchmark evaluation steps, the following statements regarding the differences between block and pin supports are made: (1) Pin supports have a higher tensile strength than block supports. This is mainly



Fig. 2. Benchmark part no. 1 (left: block support, right: pin support) after support removal.

evident in the increased number of parts with cracks and detached support structures. (2) Block supports have higher shearing resistance than pin supports. The grid layout of the block supports creates a stable structure in terms of shear forces. In the benchmark, this is visible in the geometric deviations, especially in the smaller edge deviation of side surfaces compared to the pin support. (3) Pin supports dissipate more heat than block supports. The lower discoloration of the benchmark parts indicates that a lower temperature was reached faster than within the benchmark parts with the block supports. (4) Pin supports require less material than block supports. (5) Block supports are easier to remove and result in a higher surface quality than block supports. Even though the time necessary solely for the removal of the support structures is higher compared to the pin supports, the post-processing time is significantly lower, and the ease of removal is slightly better.

Table 4. Results of the qualitative inspection (step 1).

Criterion	Block support	Pin support
No. of parts successfully built	5	5
No. of cracks	5	3
No. of notches	0	1
No. detached support structures	1	0
No. of parts with light discoloration	3	4
No. of parts with strong discoloration	1	0

Table 5. Results of the quantitative evaluation (step 2).

Criterion	Block support	Pin support
Edge deviation of overhangs [mm]	0.41	0.72
Angle deviation of overhangs [°]	0.90	1.60
Edge deviation of side surfaces [mm]	0.28	0.43
Diameter deviation of holes [mm]	0.22	0.15

Table 6. Results of the economic evaluation (step 3).

Criterion	Block support	Pin support
Material consumption [g]	88.89	71.24
Time for removal [h:min:s]	00:32:30	00:17:00
Time for post-processing [h:min:s]	00:25:00	00:65:00
Ease of removal [-]	1.8	2.0
Surface quality after removal [-]	1.2	2.2

Reviewing the formulated expectations of the benchmark (see beginning of Section 3), it is concluded that the results meet the expectations. Only the first thesis regarding the preference of the support structures towards either surface or edge supporting is not confirmed: Both support types were able to successfully support every feature. This may be due to the small distance of the pin supports (maximum distance of 2 mm), which allowed for the support structures to effectively support a surface. In terms of the block supports performing on the edges, the block supports were positioned at the edge as well as a small zone beneath the edge. This makes it possible for block supports to act on edges, but increases the post-processing effort significantly if any residuals are present after the removal of the support structures. Additionally, this

concept is only possible due to the broadening of the edge with increasing height; if the edge represents the beginning of a small overhanging wall, block supports might not be able to sufficiently support the edge.

One issue, which became apparent during the evaluation period, lies with the interpretation of cracks. Cracks can occur due to stresses perpendicular or parallel to the build platform. Only the perpendicular stresses indicate a fault in the support structure layout, they are not able to counteract stresses in the build plane. Therefore, caution and experience are necessary for a correct interpretation of cracks and a decision whether to include them in the benchmark result.

4. Conclusion

In PBF-LB/M, the optimization of support structures is important to the successful manufacturing at minimal costs. Current optimization approaches do employ their own use cases for validation though, hindering the objective comparison of the approaches. In this paper, a benchmark procedure was developed to enable the direct comparison of different support structures or strategies. The procedure includes a qualitative inspection, the quantitative evaluation of geometrical key factors, and the evaluation of economic aspects. All tasks of support structures, namely the support of overhangs, heat dissipation, and the counteracting of residual stresses, are considered in five distinct benchmark parts. The validity and significance of the procedure are demonstrated with the help of two common support structures, the block and the pin support. The benchmark results meet the expectations derived from experience:

1. Pin supports have a higher tensile strength than block supports.
2. Pin supports have a lower shear resistance than block supports.
3. Pin supports dissipate more heat than block supports.
4. Pin supports require less material than block supports.
5. Pin supports are harder to remove and result in a lower surface quality than block supports.

Today, the cost due to support structures are displayed indirectly by the material consumption as well as the time needed for removal and post-processing. To gain more insight into the cost evolution, the development of a cost model for PBF-LB/M support structures is a goal of future work.

Furthermore, the benchmark procedure can be extended by a quantitative characterization of the support structure performance. Possible experimental setups include tensile tests, or bending tests to evaluate the effort necessary for the support structure removal, substituting the subjective assessment by the operator. Additionally, while the dimensional and shape accuracy is already evaluated by the optical measurements of the CMM, the surface quality is not assessed in detail. Optical measurement of the surface roughness via microscopy could provide insights into the processing of the material as well as the heat dissipating capability of the support structures. The integration of such experimental measures requires thoughtful design of the

specimen as well as the experimental setup, though, to ensure a fair comparison of support structures designed for specific applications; e. g. testing a support structure optimized for surfaces with only a single line or vice versa may lead to wrong or imprecise conclusions. Also, to conduct those experiments, one must have access to a broad range of testing equipment.

Benchmark procedures are only useful if adapted by as many studies as possible. To help other parties with their development of optimized support structures or support strategies, the files necessary to perform the presented benchmark are freely available under CC-BY SA license [32]. This includes the CAD files of the benchmark parts, an Excel sheet for the evaluation of the benchmark results as well as a short tutorial with aids for the interpretation of the results, e.g. the categorization of the discoloration as “light” or “strong”.

References

- [1] Wohlers Associates, Inc. Wohlers Report 2018. 3D Printing and Additive Manufacturing State of the Industry. Fort Collins: Wohlers Associate, 2018.
- [2] Bartsch K, Lange F, Gralow M, Emmelmann C. Novel approach to optimized support structures in laser beam melting by combining process simulation with topology optimization. *Journal of Laser Applications* 2019, 30-022302.
- [3] Gralow M, Blunk H, Imgrund P, Herzog D, Emmelmann C. Design guidelines for adequate support types with regards to different use cases in the field of laser beam melting – Leading towards automated support generation. *Proceedings of the 15th Rapid.Tech Conference*, 2018, p. 95-110.
- [4] Murphy C, Meisel N, Simpson TW, McComb C. Predicting part mass, required material, and build time via autoencoded voxel patterns. *Proceedings of the 29th Annual International Solid Freeform Fabrication Symposium* 2018, p. 1660-1674.
- [5] Gaynor T, Guest J. Topology optimization considering overhang constraints: Eliminating sacrificial support material in additive manufacturing through design. *Structural and Multidisciplinary Optimization* 2016, 54, p. 1157-1172.
- [6] Das P, Chandran R, Samant R, Anand S. Optimum Part Build Orientation in Additive Manufacturing for Minimizing Part Errors and Support Structures. *Procedia Manufacturing* 2015, 1, p. 343-354.
- [7] Cheng L, To A. Part-scale build orientation optimization for minimizing residual stress and support volume for metal additive manufacturing. Theory and experimental validation. *Computer-Aided Design* 2019, 113, p. 1-23.
- [8] Chen N, Frank MC. A method for metal AM support structure design to facilitate removal. *Proceedings of the 28th Annual International Solid Freeform Fabrication Symposium* 2017, p. 1516-1524.
- [9] Kober C, Bergmann S, Ploshikhin V. Minimierung des Stützvolumens in LBM Prozessen durch einen simulationsbasiert-, adaptiven Ansatz. *Werkstoffe und Additive Fertigung* 2018, p. 146-152.
- [10] Umer U, Ameen W, Abidi MH, Moiduddin K, Alkhalefah H, Alkahtani M, Al-Ahmari A. Modeling the Effect of Different Support Structures in Electron Beam Melting of Titanium Alloy Using Finite Element Models. *Metals* 2019, 9, 806.
- [11] Mumtaz K, Vora P, Hopkinson N. A method to eliminate anchors/supports from directly laser melted metal powder bed processes. *Proceedings of the Solid Freeform Fabrication Symposium* 2011, p. 55-64.
- [12] Calignano F. Design optimization of supports for overhanging structures in aluminum and titanium alloys by selective laser melting. *Materials and Design* 2014, 64, p. 203-213.
- [13] Huang J, Kwok TH, Zhou C, Xu W. Surfel convolutional neural network for support detection in additive manufacturing. *The International Journal of Advanced Manufacturing Technology* 2019, 105:9, p. 3593-3604.
- [14] Zhang Z, Wu C, Li T, Liang K, Cao Y, Campbell RI, Gibson I. Design of internal branch support structures for selective laser melting. *Rapid Prototyping Journal* 2018, 24:4, p. 764-773.
- [15] Zhang K, Fu G, Zhang P, Ma Z., Mao Z., Zhang DZ. Study on the Geometric Design of Supports for Overhanging Structures Fabricated by Selective Laser Melting. *Materials* 2018, 12, 27.
- [16] Morgan D, Agba E, Hill C. Support Structure Development and Initial Results for Metal Powder Bed Fusion Additive Manufacturing. *Procedia Manufacturing* 2017, 10, p. 819-830.
- [17] Lefky CS, Zucker B, Wright D, Nassar AR, Simpson TW, Hildreth OJ. Dissolvable Supports in Powder Bed Fusion-Printed Stainless Steel. *3D PRINTING AND ADDITIVE MANUFACTURING* 2017, 4:1, p. 3-11.
- [18] Hildreth OJ, Nassar AR, Chasse KR, Simpson TW. Dissolvable Metal Supports for 3D Direct Metal Printing. *3D PRINTING AND ADDITIVE MANUFACTURING* 2016, 3:2, p. 91-97.
- [19] Gan MX, Wong CH. Practical support structures for selective laser melting. *Journal of Materials Processing Technology* 2016, 238, p. 474-484.
- [20] Hussein A, Hao L, Yan C, Everson R, Young P. Advanced lattice support structures for metal additive manufacturing. *Journal of Materials Processing Technology* 2013, 213:7, p. 1019-1026.
- [21] Vaissier B, Pernot JP, Chougrani L, Veron P. Genetic-algorithm based framework for lattice support structure optimization in additive manufacturing. *Computer-Aided Design* 2019, 110, p. 11-23.
- [22] Cheng L, Liang X, Bai J, Chen Q, Lemon J, To A. On utilizing topology optimization to design support structure to prevent residual stress induced build failure in laser powder bed metal additive manufacturing. *Additive Manufacturing* 2019, 27, p. 290-304.
- [23] Langelaar, M. Integrated component-support topology optimization for additive manufacturing with post-machining. *Rapid Prototyping Journal* 2019, 25:2. P. 255-265.
- [24] Zhou M, Liu Y, Lin Z. Topology optimization of thermal conductive support structures for laser additive manufacturing. *Computer Methods in Applied Mechanics and Engineering* 2019, 35, p. 24-43.
- [25] Allaire G., Bihl M., Bogosel B. Support optimization in additive manufacturing for geometric and thermo-mechanical constraints. *Structural and Multidisciplinary Optimization* 2020, 30:5, 343.
- [26] Leary M, Mazur M, Watson M, Boileau E, Brandt M. Voxel-based support structures for additive manufacture of topologically optimal geometries. *The International Journal of Advanced Manufacturing Technology* 2019, 105, p. 1-26.
- [27] Zhu L, Feng R, Xi J, Li P, Wei X. A Lightweight Design of Tree-shaped Support Structures for SLM Additive Manufacturing.
- [28] Jiang J, Stringer J, Xu X, Zheng P. A benchmarking part for evaluating and comparing support structures of additive manufacturing. *Proceedings of the 3rd International Conference on Progress in Additive Manufacturing* 2018, p. 196-201.
- [29] Zhang N, Zhang LC, Chen Y, Shi YS. Local Barycenter Based Efficient Tree-Support Generation for 3D Printing. *Computer-Aided Design* 2019, 115, p. 277-292.
- [30] Qiu J, Wu L, Mao Y. A novel supporting structure generation scheme to 3D printing. *Proceedings of the 7th International Conference on Internet Multimedia Computing and Service* 2015, 69.
- [31] Hu K, Jin S, Wang CL. Support slimming for single material based additive manufacturing. *Computer-Aided Design* 2015, 65, p. 1-10.
- [32] Bartsch K. Benchmark parts for the evaluation of optimized support structures in laser powder bed fusion of metals (data set). TUHH Universitätsbibliothek, 2020. <https://doi.org/10.15480/336.2658>.
- [33] Oter ZC, Coskun M, Akca Y, Surmen O, Yilmaz MS, Ozer G, Tarakci G, Khan HM, Koc E. Support optimization for overhanging parts direct metal laser sintering. *Optics* 2019, 181, p. 575-581.
- [34] Kranz J, Herzog D., Emmelmann, C. Design guidelines for laser additive manufacturing of lightweight structures in Ti6Al4V. *Journal of Laser Applications* 2015, 27-S14001.

11th CIRP Conference on Photonic Technologies [LANE 2020] on September 7-10, 2020

Parameter identification approach for support structures in laser powder bed fusion and analysis of influencing factors

Matthias Schmitt^{a,*}, Bernhard Kempter^a, Georg Schlick^a, Gunther Reinhart^a

^aFraunhofer Research Institute for Casting, Composite and Processing Technology IGCV, Beim Glaspalast 5, 86153 Augsburg, Germany

* Corresponding author. Phone: +49 821 90 678 147. Fax: +49 821 90 678 199. Email address: matthias.schmitt@igcv.fraunhofer.de

Abstract

Additive manufacturing, especially laser powder bed fusion (LPBF), enables the build-up of complex parts. LPBF is a technology with high geometric degrees of freedom, but there are production restrictions, e.g. with regard to overhangs. One strategy to produce these components despite the restrictions is the use of support structures.

Parameter determination for support structures is strongly neglected in contrast to component parameters. In this paper, a methodology for determining parameters for support structures is presented. Test geometries for the determination of mechanical properties (tensile and torsional properties) are developed. Subsequently, the influence of the manufacturing parameters (e.g. laser power) on the properties of the widely used lattice support are determined for the case-hardening steel 16MnCr5. It can be shown that shear and tensile strength of the support structures are influenced by the applied manufacturing parameters. Furthermore, the influence of geometrical parameters such as grid spacing and perforation on the tensile strength is investigated.

© 2020 The Authors. Published by Elsevier B.V.

This is an open access article under the CC BY-NC-ND license (<http://creativecommons.org/licenses/by-nc-nd/4.0/>)

Peer-review under responsibility of the Bayerisches Laserzentrum GmbH

Keywords: Laser powder bed fusion; support structure; parameter development; 16MnCr5; case-hardening steel

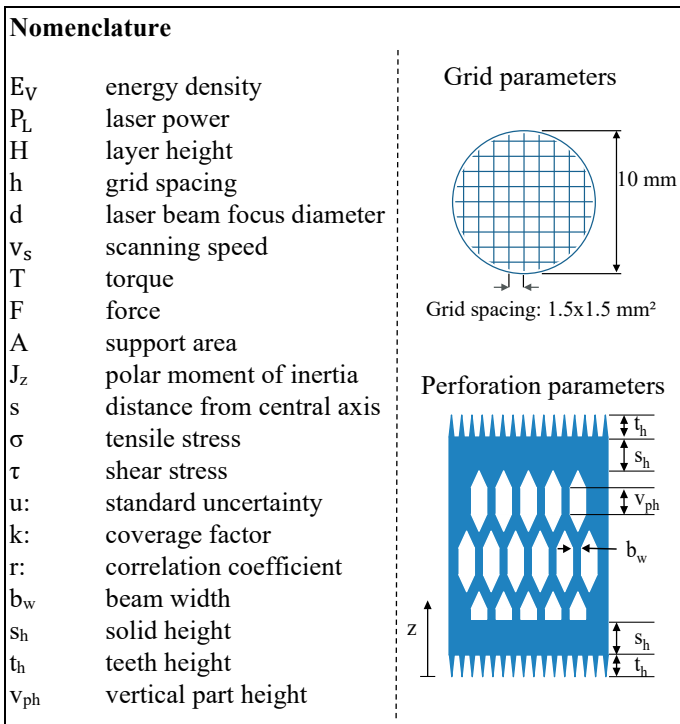
1. Introduction

Additive manufacturing technologies are characterized by a build-up of layers and offer great freedom with respect to part designs, e.g. lightweight structures or integrated cooling channels [1]. With these technologies, part designs formerly impossible to build and new business models are evolving that include spare part supply and individualization [2]. Laser powder bed fusion (LPBF) is an additive manufacturing technology which melts powder particles using a laser beam and possesses the possibility of achieving high part density [3]. Even though a high degree of design freedom is achieved as compared to traditional manufacturing processes (e.g. forging or milling), geometrical limits prevail due to the characteristic of the LPBF process. The rapid cooling of the melt pool leads to the formation of residual stresses which can lead to curling and warping of the part [4]. One strategy to prevent this is to

design parts within specific geometrical boundaries where these effects are limited. Many studies have been conducted to specify such design rules in general as well as for specific materials [5,6]. Another strategy is the use of support structures that anchor the manufactured part into the building platform and dissipate heat into the building platform [7]. Other functions are to elevate the part above the building platform for easy removal and increase the part stiffness of tall and thin parts to prevent plastic deformation during recoater interactions [8]. All in all, it can be concluded that support structures are necessary in many complex parts and play an important role in the LPBF process.

2. Literature Review

Many studies have been conducted to develop specific process parameters for certain materials, such as tungsten, case-



hardening steel and copper [9–12]. In comparison, however, the development of support structure parameters has been neglected. Morgan et al. developed support structure parameters for 17-4 PH steel by visually rating the bead straightness, consistency and spatter of single tracks [13]. No further approaches for quantification were implemented, resulting in limited repeatability and accuracy.

Hussein et al. compared the manufacturability of support structure geometries derived from minimum surface area bodies such as the Schwartz diamond and the Schoen gyroid, showing that low volume support is possible but large unsupported areas increase the surface roughness of the part [8]. Two geometric variants of line support were assessed on the basis of their removability by applying a semi-quantitative grading system from 0-5, and it was concluded that the interface connection has a strong influence [14]. Tensile tests were conducted on Ti-6Al-4V lattice support structures at very small grid sizes (0.35 and 0.7 mm), showing a dependency of tensile strength and grid density [15]. Lindecke et al. derived guidelines for Ti-6Al-4V support structures with the emphasis on the connection elements to the solid material, showing that with doubled interface area (achieved through an increase in

support structure tooth width), absolute connectivity strength increased by 12% [16].

In conclusion, it becomes clear that there is currently no general approach for the parameter development for support structures. Using normal material parameters proves to be insufficient because the optimization goal applied is predominantly part density or surface roughness. The requirements for support structures vary and high density may not be needed. Support structures should be easy to remove by hand and usually torsion is applied when using pliers or a similar tool. At the same time, warpage of the part due to residual stresses needs to be prevented, and therefore the support structures should have a high tensile strength. These two requirements may be contradictory. However, only the tensile properties have been investigated to date. Torsion properties are not available. In addition, geometric parameters for wide grids, which reduce build time, and perforation of the support for better powder removal are not considered in this context. The focus of this contribution is the development of a methodology for general support parameter development and the analysis of the main influencing factors (manufacturing and geometric parameters), as depicted in Figure 1.

3. Methods and approach

3.1. Scientific Method

First, the specimens for the methodology are defined. To examine the removability, the maximum shear stress before rupture is quantified by measuring the maximum tolerable torque. The proposed specimen consists of a fully dense base, 10-mm support, and a 6-mm top containing a 6-mm hexagonal key as shown in Figure 2. The testing is conducted on the build plate without part removal with a releasing torque wrench in accordance with DIN EN ISO 6789-1. Accuracy of the used torque wrench is given with $\pm 4\%$ by the supplier. Stepwise testing is carried out. If the torsion does not lead to rupture, the torsion moment is increased until rupture occurs. To examine

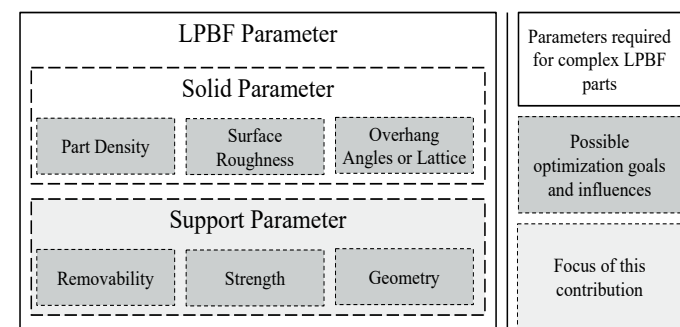


Fig. 1. Structure of a LPBF parameter

	Specimen	Testing method	Variation
Procedure of the method	Removability	Torsion test Stair tread method	<ul style="list-style-type: none"> Laser power Scan speed Layer thickness
	Strength	Tensile test	<ul style="list-style-type: none"> Laser power Scan speed Layer thickness
	Geometry	Tensile test	<ul style="list-style-type: none"> Lattice density Tooth connection Perforation

Fig. 2. Defined specimen and procedure for the proposed methodology to develop support structure parameters

the tensile strength of the support, tensile tests are performed according to DIN EN ISO 6892-1 with a Zwick Roell Z050 (accuracy $\pm 0.1\%$) testing device. A detailed description of the specimens and the testing methods is presented in Fig. 2. A lattice support is applied as the support structure geometry. The support area is filled with a grid of single tracks with a spacing in xy-plane (build direction z) and is closed by a single track along the perimeter (c.f. drawing in the nomenclature). Table 1 describes the detailed lattice support parameters.

Table 1. Standard support structure characteristics. (MoI: Moment of Inertia)

Type	Spacing	Perforation	Base area	Support area	Support density	Polar MoI
Lattice	1.5 x 1.5 mm ²	no	78.5 mm ²	10.31 mm ²	13 %	75.22 mm ⁴

The specimens are manufactured using an EOS M290 under argon atmosphere. To minimize recoating interruptions, a carbon brush is used, since a wide parameter window for the support structures is screened. Instead of applying the hatch distance the laser beam focus diameter is used to calculate the resulting energy density since the support is composed of many individual thin walls. The energy density varies from 13.7 to 171.23 J/mm³ according to:

$$E_V = \frac{P_L}{d \cdot v_s \cdot H} \quad (1)$$

The following parameters are varied to achieve different energy densities:

- Laser power (P_L): 75-300 W
- Scanning speed (v_s): 800-1250 mm/s
- Layer height (H): 0.03-0.06 mm.

Laser beam focus diameter (d) is not varied and is given with 0.073 mm. Full material parts of the specimens are built with a layer height of 0.03 mm and a parameter set with an energy density of 100 J/m³ [9]. The occurring tensile (σ) and shear (τ) stresses in the support structures are calculated with the applied force (F), support area (A), applied torque (T), distance from the central axis (s) and the polar moment of inertia (J_z) according to the following equations:

$$\sigma = \frac{F}{A} \quad (2) \quad \tau = \frac{T \cdot s}{J_z} \quad (3)$$

During the torsion test great care was taken not to cause additional bending of the specimen. Therefore the occurrence of pure shear is expected and the maximum shear stress at the boundary ($s = 5$ mm) is calculated. Each test specimen is built three times and the mean value of the tensile or shear strength is displayed whereas the strength is defined as the ultimate bearable stress of the specimen. The standard deviation of the measurements and the measurement uncertainty are represented by the error bars. The standard uncertainties $u(x)$ are determined by method B of the Guide of uncertainty of measurement (Part 3) through manufacturer's specification and calibration [17]. For the measurements performed it can be assumed that the probability distribution of the measurements and the uncertainties is approximately normal and the effective degrees of freedom is of significant size (INC-1 (1980)). By assigning $k = 2$ an interval of the measurement values having a level of confidence of approximately 95% is displayed.

3.2. Material

For the experimental studies, 16MnCr5 (1.7131) is used, since no support structure parameters are currently available for the material. 16MnCr5 is a low-alloy steel with case-hardening capabilities and is widely used in drivetrain parts such as gears. The chemical composition of the powder is

shown in Table 2. The processed powder lies within the range specified by DIN EN 10084 and was atomized with argon gas. Particle size distribution is of approximately normal distribution, with a D10 of 28 μ m, D50 of 47 μ m, and D90 of 72 μ m.

Table 2. Chemical composition of 16MnCr5 in % by mass: 1) DIN EN10084 2) supplier certificate

	C	Mn	Cr	Si	P	S	Fe
1)	0.14-0.19	1.0-1.3	0.8-1.1	≤ 0.4	≤ 0.025	≤ 0.035	Res.
2)	0.15	1.05	0.9	0.19	-	-	Res.

4. Parameter development for the support structure

As the first step, the torsion specimens were built on the EOS M290 machine with varied process parameters. Figure 3 depicts parts on the build plate, including specimens with damaged support. Nevertheless, the top parts of the specimens could be built successfully. Specimens with damaged support were excluded from the trial, since a torque could not be measured. Failed specimens occurred predominantly at very low energy densities and more frequently at a layer height of

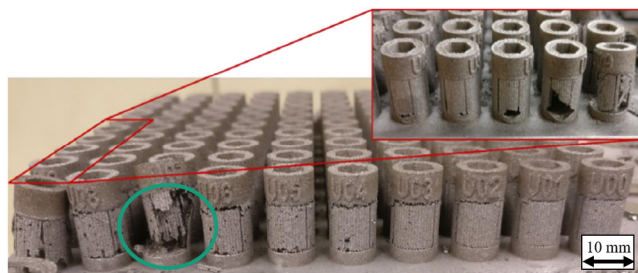


Fig. 3. Torsion specimens built with varied energy densities at 0.06 layer height. Markings show failed specimens which were not tested.

0.06 mm. The shear strength was examined using the stair tread method as described in the previous section. The tests were started with a minimal torque of 5 Nm, as that was the lower resolution limit of the torque wrench used. The torque was increased in increments of 1 Nm until rupture occurred. The resulting torques were in a range from 5 to 13 Nm, showing that manufacturing parameters have a high influence on the removability of support structures. Derived from the torque data, the ultimate shear stress was calculated (c.f. Eq. 3) with the polar moment of inertia and the maximum diameter of the support structures. Table 3 shows the resulting correlation matrix of the ultimate shear stress and the manufacturing parameters of the specimen to identify linear correlation. It becomes clear that the energy input during manufacturing has the greatest influence. The influence of applied energy

Table 3. Correlation matrix of ultimate shear stress and manufacturing parameters; the correlation coefficient r is represented. r has no unit.

r	τ	P_L	v_s	E_V	H
τ	1	0.7	-0.4	0.9	-0.4
P_L	0.7	1	0	0.7	0
v_s	-0.4	0	1	-0.26	0
E_V	0.9	0.7	-0.26	1	-0.6

density on the shear strength is illustrated in Fig. 4, showing a linear correlation ($r = 0.9$). At the same time, the disadvantage

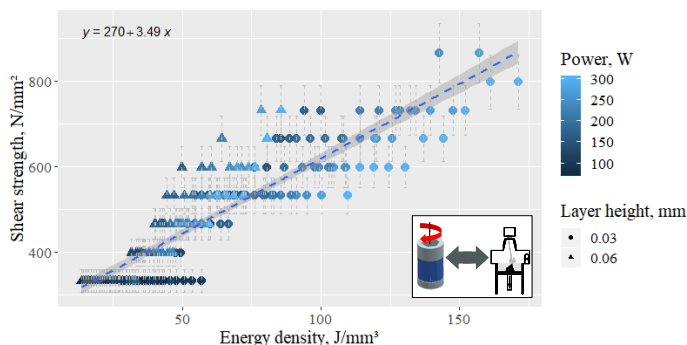


Fig. 4. Correlation of shear strength and energy density of applied manufacturing parameter

of the discrete testing method becomes clear, since many data points appear at the same shear strength level. Nevertheless, it can be concluded that with increasing energy density and laser power, the shear strength increases. Laser speed and layer height only have smaller influences on the shear stress as the low correlation coefficients show. Nevertheless, the highest shear strength is seen at layer heights of 0.03 mm.

As a next step, the number of specimens was reduced, since tensile testing involves higher effort compared to torsion testing. The tensile specimens were built on the EOS M290 machine. In-process conditions and finished specimens are depicted in Fig. 5. The markings on part a) show bulges at the

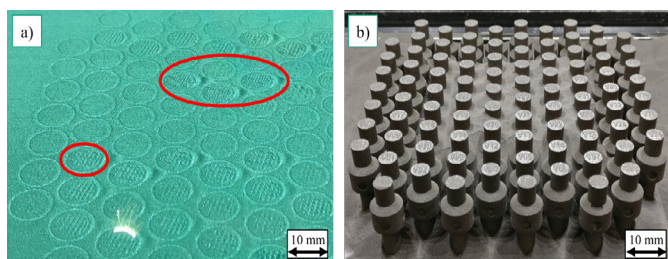


Fig. 5. Tensile specimen a) process conditions showing bulges and powder pile ups b) specimens in build chamber before powder removal

crossing of the single tracks and powder pileups in front of the specimens. These flaws predominantly occurred during the manufacturing process at a layer height of 0.06 mm, but none of them led to a process interruption because a soft recoating with a carbon brush was used. Tensile tests were conducted after removing the loose powder and wire cutting the specimens off the build plate. Nearly no elastic deformation was seen during the tests and a brittle failure behavior occurred. With the support area in Table 1 the tensile stress was calculated and the maximum bearable tensile stress was used

Table 4. Correlation matrix of ultimate tensile stress and manufacturing parameters; the correlation coefficient r is represented. r has no unit.

r	σ	τ	P_L	v_s	E_v	H
σ	1	0.7	0.2	-0.49	0.65	-0.6
τ	0.7	1	0.7	-0.4	0.9	-0.4
P_L	0.2	0.7	1	0	0.64	0
v_s	-0.49	-0.4	0	1	-0.38	0
E_v	0.65	0.9	0.64	-0.38	1	-0.6

as the decisive value to determine the tensile strength of the specimens. The resulting correlation matrix of the ultimate tensile stress, the ultimate shear stress and the manufacturing parameters is shown in Table 4. A weak correlation is seen with the applied energy density ($r=0.65$). A slightly higher correlation is seen with the ultimate shear stress of the specimens manufactured with the same parameters. In general the correlation to the manufacturing parameters is lower compared to the shear stress. Figure 6 shows the interaction of

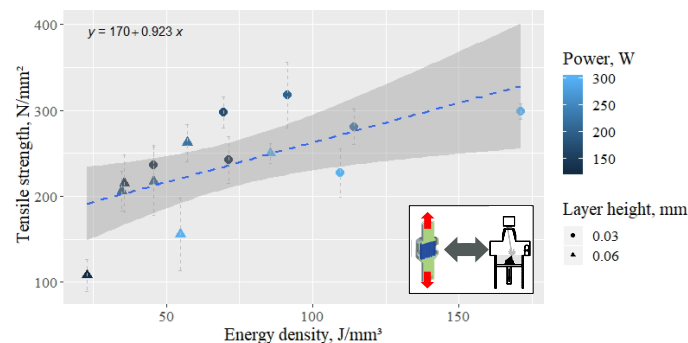


Fig. 6. Tensile strength of support structures in dependency of energy density and the tensile strength. Tensile strength increases slightly with energy density. At the same time, higher tensile strength is achieved when the lower layer height of 0.03 mm is used. When comparing the shear strength with the tensile strength (see Fig. 7), a low linear correlation can be seen. However, measurement uncertainty and measurement scatter make a more detailed statement difficult. Tensile strength ranges between minimum 113 to maximum

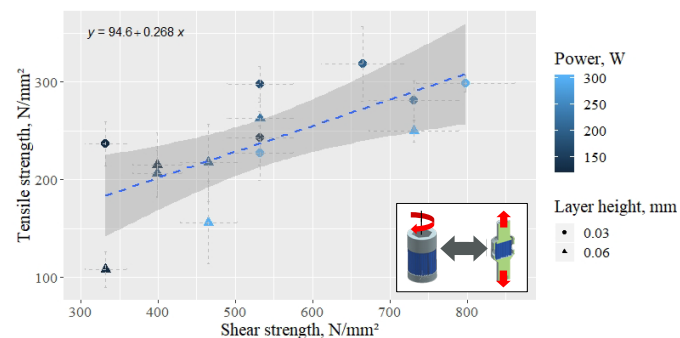


Fig. 7. Dependency of shear strength and tensile strength of support specimen

316 N/mm² whereas the shear strength, spans from minimum 305 to maximum 861 N/mm². The ratio between maximum and minimum strength indicates the possible change in properties by altering the manufacturing parameters. The ratio is almost the same for tensile strength (2.80) and shear strength (2.82) showing that a wide range of strength can be achieved. At a tensile strength of around 250 N/mm² three shear strength levels of 320, 530 and 740 N/mm² can be adjusted. This option shows the low level of linear correlation and the high uncertainty. Nevertheless, such an independent adjustment between shear and tensile strength is not possible for most of the data. Suitable support parameters can be selected with the aid of Figure 7. High tensile strength is preferable in order to counteract the warpage of parts. At the same time, shear strength should be minimized for better support removal. In a

trade-off between these properties, good combinations can be found at a torsion strength of 530 N/mm², resulting in tensile stresses of 250 to 300 N/mm², which is only slightly below the maximum achievable strength.

5. Influence of geometric support parameters

Up to this point, the geometric properties of the lattice support were not altered. To obtain further insights into the behavior of tensile properties as most relevant parameter to prevent part warpage, the lattice density and the perforation of the support structures are varied. With increasing lattice density, the support area as well as the connection with the solid material increases. Figure 8 presents the experimental results of varied lattice densities manufactured with constant parameters ($P_L=200$ W, $v_s=1100$ mm/s, $E_{v,0.03}=83$ J/mm³ and $E_{v,0.06}=41.5$ J/mm³). Layer heights of 0.06 mm show no

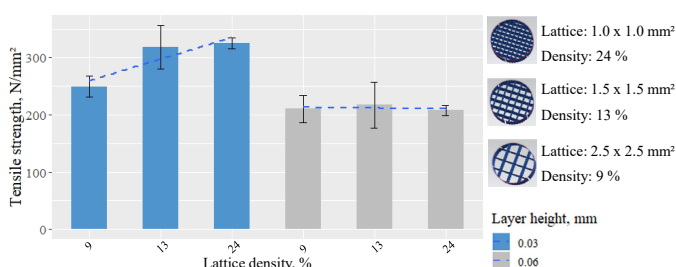


Fig. 8. Effect of lattice support density on the tensile strength

influence of the lattice density on the tensile strength. The change in support area results in an equal change in tensile force that leads to the same tensile strength of the specimens. In contrary, the specimens manufactured at 0.03 mm layer height show an increased tensile strength with increased lattice density. Similar findings are reported by Bobbio et al. [15]. One possible explanation is the size effect where voids and geometrical deviations show a higher influence on small structures. Dong et al. showed this effect in small struts of AlSi10Mg samples produced with LPBF [18]. This leads to the assumption that the 0.03 mm layer height parameter generates a higher number of defects than the 0.06 mm layer height parameter. However, in order to verify this hypothesis, further investigations such as determining the real density of the single tracks must be carried out.

Perforation of the support structures prevents trapped powder and allows easy powder removal. The effect on the tensile strength of the support structures is unknown. Specimens with four grades of perforation (no, low, medium,

Table 5. Perforation geometry regarding specification given in nomenclature

	Perforation	T_h	v_{ph}	S_h	b_w
Standard	-	0.7 mm	-	-	-
Low	60°	0.7 mm	1 mm	3 mm	0.6 mm
Medium	60°	0.7 mm	1 mm	3 mm	1.2 mm
High	60°	0.7 mm	1 mm	1.5 mm	1.2 mm

and high) were tested and the geometric variations are given in Table 5. Contradicting the expectations a low perforation leads to an increase (+1% and +18%) in tensile strength for both layer heights compared to no perforation (c.f. Fig. 9). A further increase in perforation (medium) leads to a decrease in tensile

strength of 11% and 14% compared to no perforation. At 0.03 mm layer height the tensile strength is decreased by 113% when a high perforation is applied. On the other hand, at 0.06 mm layer height tensile strength only decreases by 31% at a high perforation compared to no perforation. This shows that perforation is significantly influencing the tensile strength. However, the influence of a high perforation is greater at lower layer heights. Perforation up to a medium level show the ability to increase powder removability while keeping comparable tensile strength.

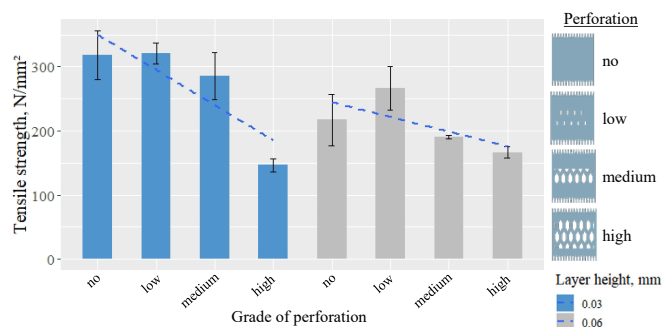


Fig. 9. Dependency of tensile strength and grade of perforation

6. Discussion

All in all, the proposed methodology proved suitable for developing support structure parameters. The torsion testing was able to screen many different parameters in a short time and quantify the removability of the structures. However, due to the stepwise increase in torque, only discrete values were obtained and the accuracy is limited, which can complicate the selection process. The subsequent tensile tests provided important data regarding the tensile strength of the support structures. When comparing tensile strength and shear strength, a part or build job specific tradeoff can be executed in order to select a suitable support structure manufacturing parameter. Together with the analysis of lattice density and perforation, a comprehensive support design can be chosen. For further insight the tensile strength is compared to the ultimate tensile strength of full material specimen (c.f. Table 6). Depending on the applied manufacturing parameter 10-30% of the UTS can be achieved. Support geometry shows the ability to alter tensile strength in a comparable range of 15-30% of the UTS. This is predominately because of the low density which is expected in

Table 6. Tensile properties of full material specimen. (UTS: ultimate tensile strength; elongation: elongation at break)

Specimen	Layer height	UTS	Elongation
Full material	30 μm	1,079±1.5 N/mm ²	10.9±0.9 %

the single tracks and the high amount of defects. The proposed methodology can be used for different materials. However, the resulting tensile and shear properties will differ. The ratio of support tensile strength to full material tensile strength lies in a similar range derived from TiAl6V4 (~20%) [16].

7. Conclusion and outlook

Applying the proposed methodology is an effective way to determine support structure parameters. The study has led to the following conclusions:

- Manufacturing parameters have an influence on the shear and tensile strength of support structures.
- Suitable combinations of shear and tensile strength can be chosen depending on the part requirements.
- Lattice density can be varied depending on the expected residual stresses and part geometry. Tensile strength increases for a layer height of 0.03 mm whereas tensile strength remains approx. without change for a layer height of 0.06 mm. Further studies have to be carried out to understand the underlying effects.
- A low perforation should be used to improve powder removal since tensile strength is slightly improved. An increase in perforation leads to a decrease in tensile strength and is dependent on the layer height.
- Depending on the manufacturing parameters only 10–30% of the tensile strength of full material is achieved. Further investigations have to be conducted to determine if this value can be generalized to other materials.

To simplify the tradeoff between removability and tensile strength, specific geometric structures combining a low polar moment of inertia and high tensile properties can be selected. Additionally, the influence of the interface has to be investigated in depth, since the results of the increased perforation showed the importance of this feature. AM engineers can use the results of this work as guidelines and rules for support design for 16MnCr5. This ensures that supports with sufficient tensile strength are selected, which increases process reliability and reproducibility in LPBF. At the same time, good removability can be adjusted, which has the potential to increase the economic efficiency. Furthermore, the use of contact-free support structures has to be explored in detail and an additional section should be added to the proposed methodology [19].

Acknowledgements

We would like to extend our sincere thanks to the German research Foundation (DFG) for providing the financial means for this research within the RE 1112/50-1 project: “Integrational lightweight design for gears by laser beam melting”.

References

- [1] Thompson MK, Moroni G, Vaneker T, Fadel G, Campbell RI, Gibson I, Bernard A, Schulz J, Graf P, Ahuja B, Martina F (2016) Design for Additive Manufacturing: Trends, opportunities, considerations, and constraints. *CIRP Annals* 65(2):737–60.
- [2] Lutter-Guenther M, Seidel C, Kamps T, Reinhart G (2015) Implementation of Additive Manufacturing Business Models. *Applied Mechanics and Materials*:547–54.
- [3] Meiners W, Poprawe R (1999) Direktes selektives Laser-Sintern einkomponentiger metallischer Werkstoffe, Dissertation, Aachen, RWTH University Aachen.
- [4] Kruth J-P, Deckers J, Yasa E, Wauthlé R (2012) Assessing and comparing influencing factors of residual stresses in selective laser melting using a novel analysis method. *Proceedings of the Institution of Mechanical Engineers, Part B: Journal of Engineering Manufacture* 226(6):980–91.
- [5] Kranz J, Herzog D, Emmelmann C (2015) Design guidelines for laser additive manufacturing of lightweight structures in TiAl6V4. *Journal of Laser Applications* 27(S1):S14001.
- [6] Adam GAO, Zimmer D (2014) Design for Additive Manufacturing—Element transitions and aggregated structures. *CIRP Journal of Manufacturing Science and Technology* 7(1):20–8.
- [7] Gao W, Zhang Y, Ramanujan D, Ramani K, Chen Y, Williams CB, Wang CCL, Shin YC, Zhang S, Zavattieri PD (2015) The status, challenges, and future of additive manufacturing in engineering. *Computer-Aided Design* 69:65–89.
- [8] Hussein A, Hao L, Yan C, Everson R, Young P (2013) Advanced lattice support structures for metal additive manufacturing. *Journal of Materials Processing Technology* 213(7):1019–26.
- [9] Schmitt M, Schlick G, Seidel C, Reinhart G (2018) Examination of the Processability of 16MnCr5 by Means of Laser Powder Bed Fusion. *Procedia CIRP* 76-81:8.
- [10] Müller Av, Schlick G, Neu R, Anstätt C, Klimkait T, Lee J, Pascher B, Schmitt M, Seidel C (2019) Additive manufacturing of pure tungsten by means of selective laser beam melting with substrate preheating temperatures up to 1000 °C. *Nuclear Materials and Energy* 19:184–8.
- [11] Lykov PA, Safonov EV, Akhmedjanov AM (2016) Selective Laser Melting of Copper. *MSF* 843:284–8.
- [12] Kamps T (2018) Leichtbau von Stirnzahnrädern aus Einsatzstahl mittels Laserstrahlschmelzen, Munich, Technical University Munich.
- [13] Morgan D, Agba E, Hill C (2017) Support Structure Development and Initial Results for Metal Powder Bed Fusion Additive Manufacturing. *Procedia Manufacturing* 10:819–30.
- [14] Järvinen J-P, Matilainen V, Li X, Piili H, Salminen A, Mäkelä I, Nyrhilä O (2014) Characterization of Effect of Support Structures in Laser Additive Manufacturing of Stainless Steel. *Physics Procedia* 56:72–81.
- [15] Bobbio LD, Qin S, Dunbar A, Michaleris P, Beese AM (2017) Characterization of the strength of support structures used in powder bed fusion additive manufacturing of Ti-6Al-4V. *Additive Manufacturing* 14:60–8.
- [16] Johannes Lindecke PN, Blunk H, Wenzl J-P, Möller M, Emmelmann C (2018) Optimization of support structures for the laser additive manufacturing of TiAl6V4 parts. *Procedia CIRP* 74:53–8.
- [17] ISO/IEC Guide 98-3:2008 (2009) Uncertainty of measurement - Part 3: Guide to the expression of uncertainty in measurement (GUM:1995).
- [18] Dong Z, Zhang X, Shi W, Zhou H, Lei H, Liang J (2018) Study of Size Effect on Microstructure and Mechanical Properties of AlSi10Mg Samples Made by Selective Laser Melting. *Materials (Basel, Switzerland)* 11(12).
- [19] Cooper K, Steele P, Cheng B, Chou K (2018) Contact-Free Support Structures for Part Overhangs in Powder-Bed Metal Additive Manufacturing. *Inventions* 3(1):2.

11th CIRP Conference on Photonic Technologies [LANE 2020] on September 7-10, 2020

Improving the quality of up-facing inclined surfaces in laser powder bed fusion of metals using a dual laser setup

Jitka Metelkova^{a,*}, Daniel Ordnung^{a,b}, Yannis Kinds^a, Ann Witvrouw^a, Brecht Van Hooreweder^a

^a Department of Mechanical Engineering, KU Leuven - Member of Flanders Make, Celestijnenlaan 300, 3001 Heverlee, Belgium

^b Institute of Photonic Technologies, Friedrich-Alexander-Universität Erlangen-Nürnberg, Konrad-Zuse-Straße 3/5, 91052 Erlangen, Germany

* Corresponding author. Tel.: +32 16379004. E-mail address: jitka.metelkova@kuleuven.be.

Abstract

Surface quality of parts produced by laser powder bed fusion (LPBF) is often insufficient for their final application. Up-facing inclined surfaces are among the major challenges, due to the combination of elevated edges (edge effect) and the staircase effect. This work presents a novel methodology to enhance the quality of inclined surfaces using a dual laser PBF setup. In the first step called “selective powder removal”, powder is blown away from undesired areas using shock waves produced by a nanosecond pulsed wave laser. Consequently, the newly exposed inclined surfaces can be remelted with a continuous wave laser, reducing significantly the surface texture.

© 2020 The Authors. Published by Elsevier B.V.

This is an open access article under the CC BY-NC-ND license (<http://creativecommons.org/licenses/by-nc-nd/4.0/>)

Peer-review under responsibility of the Bayerisches Laserzentrum GmbH

Keywords: additive manufacturing; laser powder bed fusion; staircase effect; surface quality; laser ablation; shock waves; maraging steel.

1. Introduction

Laser Powder Bed Fusion (LPBF) is an additive manufacturing technique used in many industrial sectors requiring high level of customization (e.g. medical sector) or a high performance-to-weight ratio (e.g. aeronautical or aerospace sector) [1]. In LPBF, a thin layer of metal powder is deposited, followed by selective laser melting of powder particles at locations corresponding with a cross-section of the part being produced. Combining low layer thicknesses with small laser focus diameters allows a high degree of freedom in designing the component. However, the surface quality is often insufficient for the final application. Up-facing inclined surfaces present a substantial challenge, mostly because of the combination of elevated edges (also called “edge effect”) and the “staircase effect” [2, 3]. The latter is related to the part shape discretization due to layer-wise manufacturing.

The quality of horizontal surfaces can be improved by in-situ remelting (laser polishing) [4]. However this is impossible for inclined surfaces as the surface is still covered with powder.

Nomenclature

d_p	pulse-to-pulse distance, in μm
DOE	design of experiments
E_p	pulse energy, in μJ
h	hatch spacing, in μm
l_s	length of the scan vector, in mm
$L_i (L_o)$	inner (outer) powder bed disturbance length, in mm
LPBF	laser powder bed fusion
P	laser power, in W
Pa	arithmetic mean height on the primary profile, in μm
PRR	pulse repetition rate, in kHz
v	scanning speed, in mm/s
τ	pulse duration, in ns

Therefore, the only option to enhance the quality of such a surface is to proceed to time consuming and often expensive post-processing steps such as machining or laser post-processing [5-8].

During the laser ablation process, high intensity pulses are emitted towards the target material. This results in temperatures above the material melting temperature which leads to its evaporation. The interaction of this vapor with the laser beam may generate plasma which by expanding can create a shock wave [9]. Laser induced shock waves appear in the literature mainly in relation with laser shock peening [10], film deposition methods or adhesion tests [11, 12], foil forming [13] and laser induced breakdown spectroscopy [9]. However, in the field of LPBF, shock waves have been reported by many authors as an undesired phenomenon to be avoided [14-18]. This is due to the fact that shock waves blow away the surrounding powder which makes the building process impossible.

This work presents a novel methodology to enhance the quality of the inclined surfaces using a dual-laser setup. In the first step called “selective powder removal”, shock waves produced by a nanosecond pulsed wave (PW) laser are used to blow away the powder from the undesired areas (e.g. inclined up-facing surfaces). The influence of selected process parameters on the powder removal efficiency is investigated (pulse energy, pulse-to-pulse distance, pulse duration, hatch spacing, scanning vector length), in order to maximize the generated shock waves. In the second step, the surface of the newly exposed surfaces is remelted with a continuous wave (CW) laser, in order to reduce the surface texture. This step can be also combined with laser ablation of new features such as grooves and holes below the resolution of the LPBF process or surface texturing.

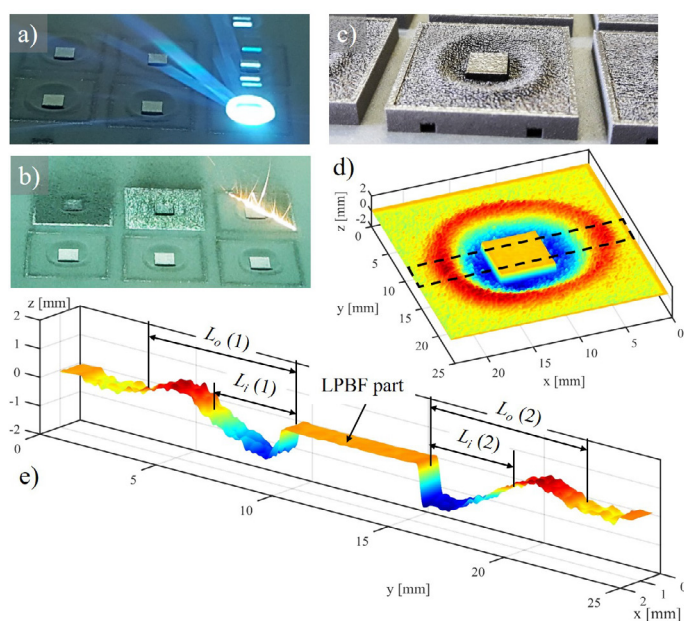


Fig. 1 Illustration of the methodology to characterize the powder bed disturbance: (a) laser ablation of the part surface resulting in powder bed disturbance, (b) fixation of the disturbed powder bed, (c) fixed powder bed, (d) measurement of the part and consolidated powder bed with a microscope, (e) detail on the measured 3D data, L_i and L_o correspond to the inner and outer disturbance length respectively.

Table 1. Build process parameters (CW laser).

Process parameters	LPBF substrate and frame	Powder fixation	
		(scan 1)	(scan 2)
Laser power, P (W)	150	100	100
Scanning speed, v (mm/s)	1100	1500	1300
Hatch spacing, h (μm)	70	40	40

Table 2. Ablation process parameters (PW laser), fractional L9 DOE at constant $PRR=100\text{kHz}$, $h=40\ \mu\text{m}$, $l_s=6\ \text{mm}$. Corresponding levels (L1/L2/L3): $E_p=200/250/300\ \mu\text{J}$, $d_p=15/10/5\ \mu\text{m}$, $\tau=10/20/30\ \text{ns}$.

Process parameters	Sample number								
	1	2	3	4	5	6	7	8	9
DOE levels									
Pulse energy, E_p	1	2	3	1	2	3	1	2	3
Pulse-to-pulse distance, d_p	1	1	1	2	2	2	3	3	3
Pulse duration, τ	1	2	3	2	3	1	3	1	2

2. Experimental setup and methodology

2.1. Process study

This work was realized on a modified LPBF machine from 3D Systems (DMP ProX320). This machine is equipped with a single scanner and a flipping optic such that both a 500 W CW fiber laser with 60 μm focus spot and a 50 W nanosecond PW laser with 50 μm focus spot can be used consecutively. All samples were designed with 3DXpert software.

To evaluate the powder disturbance by shock waves, 6 mm cubes from maraging steel 300 were built with the CW laser and their top surface was ablated with the nanosecond PW laser. The disturbance of the powder bed surrounding the ablation zone was evaluated using the method described in section 2.2.

The build parameters are given in Table 1. The ablation process study consists of two parts: first varying pulse energy E_p (200-300 μJ), pulse-to-pulse distance d_p (5-20 μm), hatch spacing h (10-100 μm) and length of the scan vector l_s (1-10 mm). In the second part a Taguchi design of experiments (DOE) was performed as detailed in Table 2, aiming to maximize the inner disturbance length L_i as defined below.

2.2. Evaluation method for the process study

In order to quantify the measure of powder bed disturbance when only ex-situ measurement tools are available, the unmolten powder had to be fixed first. For this reason, a frame was built around the part and the loose powder was scanned within the boundaries of this frame (Fig. 1a-c). The scanning was done in two steps (Table 1), under 45° with 90° rotation.

The parts were measured using a high-resolution focus variation microscope Sensofar S-Neox (Fig. 1d,e). The powder bed disturbance was evaluated on 1.3 x 25.4 mm. The measured 3D data were filtered with a Gaussian filter with a 250 μm cutoff length. The mean profile was calculated and the inner and outer limits of the powder bed disturbance were detected (Fig. 1e). The presented results show a mean inner disturbance length L_i and the standard deviation based on $L_i(1)$ and $L_i(2)$.

2.3. Application to inclined surfaces

After the process study, the method could be applied to a 5° inclined surface of 20x8x5 mm. The selective powder removal was performed with a single scan at scanning direction of 0°,

$E_p=420 \mu\text{J}$, $d_p=5 \mu\text{m}$, $PRR=100 \text{ kHz}$, $\tau=30 \text{ ns}$, $h=40 \mu\text{m}$. These correspond to the optimal d_p and τ from the DOE, and E_p closer to the machine limits. After visual check of the powder-free surface, the surface was remelted 10 times under 45° with 90° rotation, using $P=150 \text{ W}$, $v=1100 \text{ mm/s}$, $h=35 \mu\text{m}$.

The surface texture of the parts before and after remelting was evaluated using a tactile profilometer Mitutoyo Formtracer CS3200 (10 profiles of 10-mm evaluation length) and Sensofar S-Neox (3 x 3 mm surface).

3. Results and discussion

3.1. Effect of the ablation on the surrounding powder

Fig. 2 presents the influence of selected ablation process parameters on the inner length of the disturbed powder bed L_i after ablation of a horizontal as-built LPBF surface. The disturbance length increases in a linear trend with increasing pulse energy E_p (Fig. 2a) and with decreasing pulse-to-pulse distance d_p (Fig. 2b). In other words, the shock waves generated by the PW laser appear to be stronger with increasing pulse energy (thus increasing peak power) leading to evaporation of a larger amount of material, which can be then converted into plasma that would subsequently create the shock wave disturbing the powder bed. The influence of the pulse-to-pulse distance is not that straightforward. It might be related to the interaction between the pulses or to the total number of pulses, considering the constant length of the scanned line and variable pulse spacing. The influence of this parameter will be further investigated in future studies.

As shown in Fig. 2c, the disturbed powder bed length increases when decreasing the hatch spacing h . For low hatch spacing, however, the disturbance length seems to level out. The length of the scanning vector does not seem to have a significant influence for the selected parameters (Fig. 2d).

Fig. 3 shows the main effect plots from the L9 Taguchi DOE. The pulse duration seems to have the most significant effect within the range of selected parameters (Fig. 3c). Studies [19] have reported that the shock wave pressure increases with decreasing pulse duration. For shorter pulse durations the peak power increases together with the capacity to evaporate material and create plasma. However for the investigated pulse durations (10, 20 and 30 ns) the shock waves appear to be stronger for the longer durations. This could be due to the amount of influenced material as shown in Fig. 4. For short pulse durations (7 and 10 ns) the amount of ablated material is very low. For longer durations (30 and 50 ns), the ablated depth and volume significantly increase. In future studies the effect of the pulse duration will be further investigated, as the maximal shock wave efficiency might be situated outside the parameter range selected for this study. The main effects of the pulse-to-pulse distance and pulse energy plotted in Fig. 3a,b confirm the observations from Fig. 2a,b.

3.2. Improving the quality of inclined surfaces

The first feasibility tests indicate the possibility to successfully apply the proposed method for selective powder removal (Fig. 5). The powder covering the 5° inclined surface

after the building process (Fig. 5a) could be successfully removed using the shock waves induced by the ablation process (Fig. 5b,c). After remelting of the inclined surface the as-built surface texture could be reduced from $Pa = 12.9 \mu\text{m} \pm 1.2 \mu\text{m}$ to $5.4 \mu\text{m} \pm 0.6 \mu\text{m}$, corresponding to a 58% improvement.

This is a significant achievement because these surfaces are unreachable in-situ, as they are still covered in powder. A representative 2D profile, as well as 3D optical measurement data and a photograph of the as-built and remelted sample are provided in Fig. 6. The staircase effect clearly noticeable in Fig. 6a cannot be observed anymore in Fig. 6b. A certain degree of waviness, however, still remains on the surface.

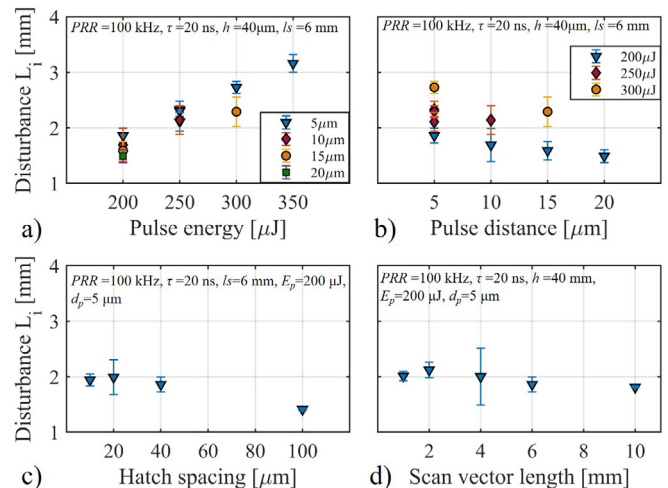


Fig. 2 Effect of (a) pulse energy, (b) pulse-to-pulse distance, (d) hatch spacing, (c) vector length on the powder bed disturbance length L_i .

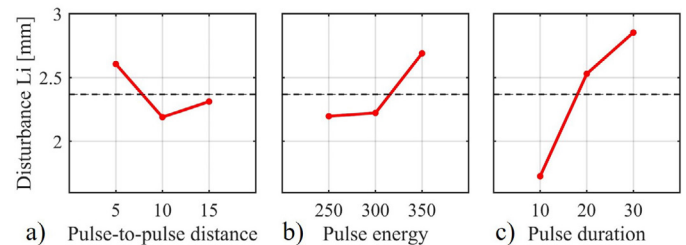


Fig. 3 Main effects plot based on the L9 design of experiments for powder bed disturbance length.

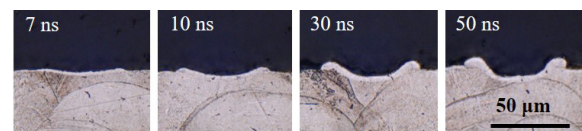


Fig. 4 Effect of the pulse duration on single line scans morphology. $PRR=250 \text{ kHz}$, $E_p=180 \mu\text{J}$, $d_p=5 \mu\text{m}$.

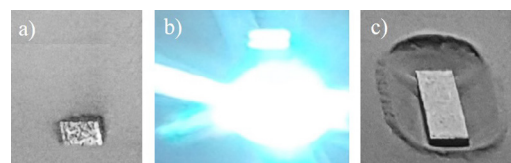


Fig. 5 Selective powder removal process. (a) LPBF part with a small horizontal surface and 5° inclined surface covered with powder after building (b) laser ablation on the part surface, (c) resulting powder-free surface.

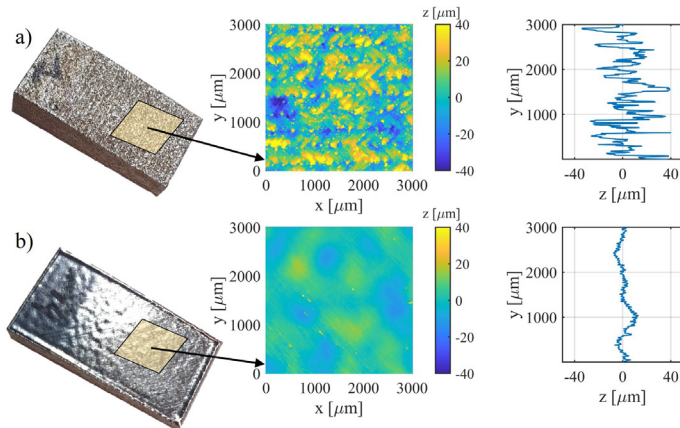


Fig. 6 In-situ improvement of the inclined surface quality: (a) as-built, (b) after 10 times remelting.

Both powder removal and remelting processes are fast, one pass takes approx. 5s. The remelting step could be replaced or followed by another ablation step of surfaces otherwise covered in powder. Also surface texturing after remelting can be possible. The proposed method is not limited to a flat surface, also freeform surfaces could possibly be processed in the same way, as long as steep angles and large depths are avoided. These can create shadow zones which the laser cannot irradiate.

Furthermore the selective powder removal step is expected to be limited by the maximal operational depth of the surface to be cleaned, limited by the Rayleigh length of the laser system. When defocusing, laser fluence (pulse energy per area) decreases rapidly, resulting in a significant drop in the ablation efficiency and thus shock wave generation. The volume of the powder to be relocated is another limiting factor, as at higher volumes it has the tendency to slide back on the already cleaned surface.

4. Conclusion

This study investigated the effect of the nanosecond laser ablation process on metal powder surrounding the ablation zone. An increase of the laser induced shock waves was observed with increasing pulse energy and decreasing pulse-to-pulse distance. The effect of the pulse duration was found to be dominant within the range of the investigated parameters (10–30 ns). The powder removal efficiency also increased with decreasing hatch spacing. The scanning vector length did not seem to have a significant effect in the here described experimental conditions.

As demonstrated in this study, this method to improve in-situ the quality of inclined surfaces has proved to be successfully working on flat inclined surfaces. Selective powder removal followed by a remelting step led to a significant improvement of the surface finish with Pa reduction by 58%, from 12.9 μm to 5.4 μm .

One of the main benefits of this method is that powder removal is fast, selective and accurate, as a single scanner LPBF machine is used. The proposed method should be applicable also to freeform surfaces, within the operating range defined by a maximal depth and powder volume to be relocated.

This work is part of an ongoing study and the efficiency of the selective powder removal technique is still being optimized.

Acknowledgements

This research was funded by The EU Framework Programme for Research and Innovation - Horizon 2020 - Grant Agreement N 721383 within the PAM² (Precision Additive Metal Manufacturing) ITN project, the SBO project CombiLaser (IWT.150521) and the infrastructure platform HyLaForm, funded by the Flemish government (2016). The authors would also like to thank Lars Vanmunster and Bram Lommelen for evaluating the remelted inclined surface and for preparing the metallographic cross-sections, respectively.

References

- [1] Horn JH, Harrysson OLA. Overview of current additive manufacturing technologies and selected applications. *Sci Progress* 2012; 95: 255-282.
- [2] Yasa E, Poyraz O, Solakoglu EU, Akbulut G, Oren S. A study on the stair stepping effect in direct metal laser sintering of a nickel-based superalloy. *Procedia CIRP* 2016;45:175-178.
- [3] Strano G, Hao L, Everson RM, Evans KE. Surface roughness analysis, modelling and prediction in selective laser melting. *J Mater* 2013;213:589-597.
- [4] Yasa E, Kruth JP, Deckers J. Manufacturing by combining Selective Laser Melting and Selective Laser Erosion/laser re-melting. *CIRP Ann-Manuf Techn* 2011;60:263-266.
- [5] Bhaduri D, Penchev P, Batal A, Dimov S, Soo SL, Sten S, Harrysson U, Zhang Z, Dong H. Laser polishing of 3D printed mesoscale components. *Appl Surf Sci* 2017;405:29-46.
- [6] Marimuthu S, Triantaphyllou A, Antar M, Wimpenny D, Morton H, Beard M. Laser polishing of selective laser melted components. *Int J Mach Tool Manu* 2015;95:97-104.
- [7] Hofe M, Schanz J, Burzic B, Lutz S, Merkel M, Riegel H. Laser based post processing of additive manufactured metal parts. *Proc LiM*; 2017.
- [8] Khorasani AM, Gibson I, Goldberg M, Littlefair G. A comprehensive study on surface quality in 5-axis milling of SLM Ti-6Al-4V spherical components. *Int J Adv Manuf Technol* 2018;94:3765-3784.
- [9] Campanella B, Legnaioli S, Pagnotta S, Poggialini F, Palleschi V. Shock waves in laser-induced plasmas. *Atoms* 2019;7.
- [10] Ding K, Ye L. *Laser shock peening*. 1st ed. Sawston: Woodhead Publishing; 2006.
- [11] Li ZH, Zhang DM, Yu BM, Guan L. Characteristics of plasma shock waves in pulsed laser deposition process. *Eur Phys J Appl Phys* 2004;28:205-211.
- [12] Boustie M, Berthe L, de Resseguier T, Arrigoni M. *Laser Shock Waves: Fundamentals and Applications*. Proc 1st Int Symp on Las Ultrason:2008.
- [13] Nagarajan B, Castagne S, Wang Z. Mold-free fabrication of 3D micro-features using laser-induced shock pressure. *Appl Surf Sci* 2013;268:529-534.
- [14] O'Neill W, Sutcliffe CJ, Morgan R, Hon KKB. Investigation of short pulse Nd:YAG laser interaction with stainless steel powder beds. *Proc SFF* 1998.
- [15] Morgan R, Sutcliffe CJ, O'Neil W. Experimental investigation of nanosecond pulsed Nd:YAG laser re-melted pre-placed powder beds. *Rapid Prototyp J* 2001;7:159-172.
- [16] Morgan R, Sutcliffe CJ, O'Neil W. Density analysis of direct metal laser re-melted 316L stainless steel cubic primitives. *J Mater Sci* 2004;39: 1195-1205.
- [17] Ng CC, Savalani M, Man HC. Fabrication of magnesium using selective laser melting technique. *Rapid Prototyp J* 2011;17:479-490.
- [18] Fischer P, Karapatis N, Romano V, Glardon R, Weber HP. A model for the interaction of near-infrared laser pulses with metal powders in SLS. *Appl Phys A* 2002;74:467-474.
- [19] Oros C. Investigations involving shock waves generation and shock pressure measurement in direct ablation regime and confined ablation regime. *Shock waves* 2002;11:393-397.

11th CIRP Conference on Photonic Technologies [LANE 2020] on September 7-10, 2020

Study of the elaboration of high entropy material from powder by laser additive manufacturing

G. Huser^a, I. Demirci^b, P. Aubry^{a*}, I. Guillot^c, L. Perrière^c, E. Rigal^d, H. Maskrot^a

^a Den – Service d'Etudes Analytiques et de Réactivité des Surfaces (SEARS), CEA, Université Paris-Saclay, F-91191, Gif sur Yvette, France, France

^b Arts et Metiers Institute of Technology, MSMP, HESAM Université, Châlons en champagne 51006, France

^c Univ. Paris Est Creteil, ICMPE (UMR 7182), CNRS, F-94320 Thiais, France

^d CEA, LITEN, F-38054 Grenoble Cedex 9, France

* Corresponding author. Tel.: +33169088191 ; *E-mail address*: pascal.aubry@cea.fr

Abstract

If Stellite® 6 is a cobalt base alloy with a hard coating well known for its good wear resistance, its use is not desirable for nuclear installations due to the activation of cobalt under neutron flux which makes maintenances more delicate as, later, decommissioning. If several studies have led to propose certain hard coatings without cobalt, for the moment, none equals the wear properties of Stellite® 6.

The present research aims to explore the recent research area on high entropy alloys or concentrated composition alloys (HEA/CCA) as a new path for the development of innovative hard coatings. The study is based on the use of thermodynamics simulations with CALPHAD in order to predict the compositions of a large number of alloys, after an initial selection of the acceptable elements (NiFeCrMoTi in this study). Then, Laser Metal Deposition (LMD) is used for manufacture walls of graded compositions for a rapid screening of compositions and coatings for later wear tests. The metallurgical analyses of the elaborated samples allow selecting the most promising ones on which wear pin-on-disk tests are finally conducted. The wear tests have evidenced promising behavior for the selected HEA/CCAs.

© 2020 The Authors. Published by Elsevier B.V.

This is an open access article under the CC BY-NC-ND license (<http://creativecommons.org/licenses/by-nc-nd/4.0/>)

Peer-review under responsibility of the Bayerisches Laserzentrum GmbH

Keywords: Laser Metal Deposition, High Entropy Alloy, Concentrated Composition Alloy, Combinatorial Metallurgy, Hardfacing Material, CALPHAD

1. Introduction

1.1. Context of the study

The CEA is leading researches on existing nuclear reactor and innovative nuclear systems called Generation III and Generation IV reactors. They require major technological breakthroughs compared with the previous generation of reactors, particularly on materials and manufacturing processes.

Besides the structural materials, contact areas between moving components require specific wear resistant coatings with a very long lifetime.

Stellite®, a cobalt based alloy is the well-known and widely used hardfacing wear resistance material from Deloro Company. Unfortunately, one major drawback of this type of alloy for nuclear applications is the activation of cobalt under neutron flux in a reaction that generate radioactive ⁶⁰Co. With a period of 5.7 years, the activity of ⁶⁰Co is maximum during operation of the reactor. Thus, it is desirable to avoid these alloys for severe neutron flow and different studies tried to find substitute material without cobalt or in very small quantities.

The requirements are very demanding: tribo-corrosion under sodium, operating temperature from 180 to 500°C, risk of thermal shock and thermal cycling, and life span of over 60 years without binding or degradation. As a consequence, thick

coatings (2-3mm) with little porosity, no crack and metallurgical bond between the coating and the base material are required. This implies to use a high energy fusion process that can be automatized as Plasma Transferred Arc Welding (PTAW) or Laser Metal Deposition (LMD).

If the cobalt base alloy Stellite remains the reference, other alloys have been investigated as cobalt-free alternatives. Base substrates are majorly stainless steel as 304L, 316L or 316L(N).

A large number of Co-free hardfacing materials have been proposed in the literature. Among them, we can consider two main types of materials: the iron and nickel based alloys. If iron base alloys cannot be definitely excluded, the bibliography [1, 2, 3] demonstrates a poor behavior of the iron-based hardfacing coatings at high temperature regardless of the deposition process.

On the opposite, authors have evidenced the interest of using hardfacing nickel based alloys [4,5]. For this reason, two promising nickel base alloys have been studied : NiFeCrSiBC alloys as Colmonoy[®], from Wall Colmonoy Company, presented in previous publications [6-9] or NiFeCrMoSi alloys, as Tribaloy[®] T700, developed by Deloro Company. These materials have been tested but, up to now, none of them have provided equivalent behavior to Stellite[®] [10,11,12].

1.2. Interest for HEA/CCAs

Considering the composition of the alloys that have been previously evaluated (particularly the Tribaloy[®] T700), one idea to extend the research base of innovative substitute can be to consider a new family of alloys and fully new methodology for their formulation by exploring the capabilities of finding cobalt-free high entropy alloys (HEAs) or complex concentrated alloys (CCAs).

HEA is a new type of alloy without a single main constituent. Cantor [14] and Yeh [15] firstly discovered them, and explored the theory of HEAs. They are thought to be promising material in several domains. If HEAs are single solid solutions or eutectics structures of multiple elements in high concentration ($\geq 5\text{at}\%$), a dual phased or multi phased HEA is more properly named Complex Composition Alloy (CCA). Particularly, CCAs can exhibit good tribological behaviors, as precipitation of hard phases can improve hardness and wear resistance [16,17]. Consequently, cobalt-free CCAs could be interesting candidates to stellite[®] substitutes. Very few studies on cobalt-free HEA/CCA coatings for tribological behavior were published, and even less on stainless steel substrates [18].

For this study, Laser Metal Deposition (LMD), a laser additive manufacturing process, is the chosen process to deposit thick CCAs coatings because it is a known to be particularly adapted to deposit thick (several mm) of Stellite[®] coatings [1,2,4,6]. It is also a powerful process to develop new alloys as HEA/CCAs since it is possible to make in-situ alloys by co-projecting different elemental powders and mixing them inside the melt pool [19, 20, 21, 22]. It also allows massive fabrication of samples by making composition gradient and studying several composition in one sample.

CALPHAD (CALculation of PHase Diagram) is a calculation tool of thermodynamic properties of

multi elements material as metallic alloys. It is based on thermodynamics databases of single elements and on the fact that a phase diagram is a manifestation of the equilibrium thermodynamic properties of a system, which are the sum of the properties of the individual phases [23].

CALPHAD has been used on numerous HEA/CCAs [24, 25] with accurate predictions of the microstructure. Addition of Mo and Ti to the three “base elements” NiFeCr promotes the formation of hard phases such as sigma and C14 Laves phase.

CALPHAD allows not only equilibrium but also out-of-equilibrium calculation models, as the Gulliver-Scheil approximation. As high solidification speed and cooling rates result from the LMD process, this will be considered in the study.

At the beginning of the research, it is proposed that CALPHAD calculations could be a tool for an initial selection of composition, avoiding extended experimental investigations. Consequently, a methodology, presented in the next section, is proposed and will be the common thread of this article.

1.3. Methodology

A proposed methodology, sketched in Fig. 1, is applied to our HEA/CCAs developments:

- A first set of alloys is selected from the bibliography analyses and material data.
- Composition of alloys after solidification are forecast by thermodynamic calculations on CALPHAD. It is possible to generate a very large number of compositions.
- After analyses of the simulations, some compositions are selected and achieved by fusion of powder. The microstructure is investigated.
- Following the results of the previous step, some compositions are chosen and coated samples are tested.

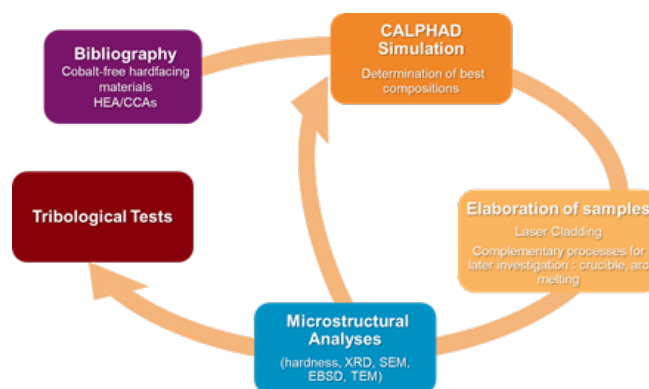


Fig. 1: Proposed methodology for exploring HEA/CCAs

Of course, multiple loops can be necessary to explore different compositions before to converge toward an optimal result. In the next sections, we show the work that has been initiated trying to follow this methodology.

2. Selection of alloys

2.1. Selection of a family of alloys

Considering the bibliography analysis and the targeted applications, considerations can be made to focus our selection of alloy family:

1. As the coating has to be made on stainless steel, it is desired that the chosen alloys should generate a good metallurgical bonding with the substrate. This is in favor of a rich (Fe,Cr,Ni)-rich composition.
2. No cobalt is allowed. Moreover, for the same reason than cobalt, niobium amount should be limited.
3. Hardfacing property implies that the material would have a good compromise between hardness and elasticity. Globally, hardness is usually above 400Hv. Consequently, the alloys should contain hard phases.
4. Good corrosion behavior would be considered. In our study, we consider wear test in Argon gas environment to facilitate the wear tests.

Combining these points, it can be proposed to retain a general formulation as $Fe_{x1}Ni_{x2}Cr_{x3}Mn_{x4}Mo_{x5}Ti_{x6}V_{x7}Zr_{x8}Nb_{x9}Al_{x10}$ with $[x1...x10] \geq 5at\%$.

As combinatorial metallurgy our manufacturing process consists in the fusion process of a mixture of powder, it has been decided to avoid using Mn, due to low boiling point compared to the other elements. Adding cost and powder quality constraints, it has been decided to consider the first alloy family $Fe_{x1}Ni_{x2}Cr_{x3}Mo_{x4}Ti_{x5}$. In this article, we present the results obtained for 3 alloys: $(FeNiCr)_{80}Mo_{10}Ti_{10}$, $(FeNiCr)_{80}Mo_{15}Ti_5$, and $(FeNiCr)_{90}Mo_5Ti_5$.

2.2. Thermodynamics simulations

Thermodynamic calculations using CALPHAD/Thermo-Calc® supported by TCHEA1 database were performed. As said in the introduction, CALPHAD calculation was performed to have an estimation of the phases present and their composition. In the family of alloy FeNiCrMoTi, Fig. 2 shows the solidification curves calculated by CALPHAD at thermodynamical equilibrium for two of the three alloys with the TCHEA1 database: $(FeNiCr)_{90}Mo_5Ti_5$ and $(FeNiCr)_{80}Mo_{10}Ti_{10}$.

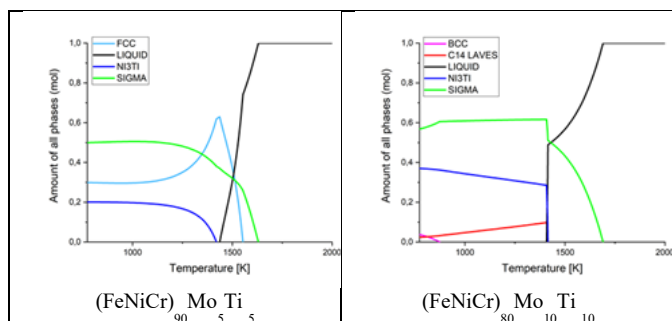


Fig. 2. CALPHAD simulation of solidification of two alloys

Calculations on the $Mo_{10}Ti_{10}$ and Mo_5Ti_{15} alloys predict the presence of four phases: sigma, BCC, Ni_3Ti and C14 Laves phase. BCC phase should be absent of $Mo_{10}Ti_{10}$ because of its low formation temperature, and C14 Laves phases is supposed

to transformed into Ni_3Ti upon cooling. During the cooling of Mo_5Ti_{15} , C14 Laves phases and sigma phase are supposed to transform into Ni_3Ti and BCC phase, respectively. $Mo_{15}Ti_5$ is predicted to have a high sigma phase amount with FCC and Ni_3Ti phase. A small amount of BCC phase is also predicted at low temperature and should not be observed experimentally.

Table1 presents the CALPHAD calculation results with Gulliver-Scheil approximation (as LMD solidification is supposed to lead to an out-of-equilibrium solidification) at the end of solidification on the three alloys with the TCHEA1 database. This hypothesis increases the number of phases predicted in the alloys. FCC and C14 Laves are predicted in all alloys in addition to the equilibrium phase predicted. The only exception is the substitution of Ni_3Ti in by a $D0_{19}$ phase in the Mo_5Ti_5 alloy.

Table 1. CALPHAD calculations for the three alloys with Gulliver-Scheil approximation

Alloy	Phases predicted after cooling CALPHAD + Gulliver-Scheil approximation
$(FeNiCr)_{90}Mo_5Ti_5$	Sigma, FCC, $D0_{19}$, C14 Laves
$(FeNiCr)_{80}Mo_{10}Ti_{10}$	Sigma, FCC, BCC, Ni_3Ti , C14 Laves
$(FeNiCr)_{80}Mo_{15}Ti_5$	Sigma, FCC, Ni_3Ti , C14 Laves

These calculations evidence the possibility to obtain alloys composed of a mixture of medium hard matrix and hard phase, which hardness and fracture toughness has to be determined in the study. This can be related to the Tribaloy T700 microstructure. Now, we present the elaboration of the alloys by LMD and the results obtained.

3. Elaboration of alloys

3.1. Experimental setup

The manufacturing of samples has been achieved on an OPTOMECH machine with four powder feeders (Fig. 3). The laser used is an IPG 3kW CW ($\lambda=1070nm$), a core fiber of 400 μm . A coaxial nozzle has been used.

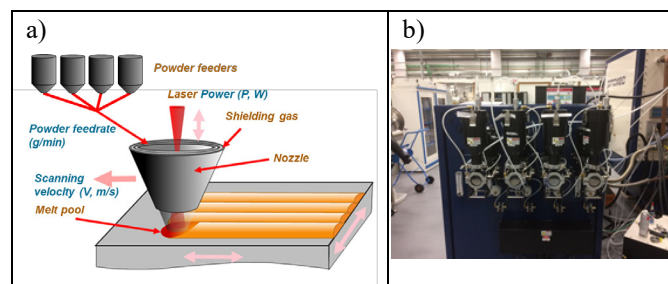


Fig. 3. LMD system: a) LMD principle b) the four powder feeders

It can be difficult to get a homogenous melting of the material from the mixture of powders [26]. Thus, the in situ fusion is better achieved with a relatively large melt pool and low speed. Therefore, the optical configuration has been chosen to provide a defocused laser beam spot size of about 2mm diameter.

3.2. Manufacturing of samples

Following the selection of compositions obtained from CALPHAD calculations, different samples have been prepared.

First, single elements have been provided in powder form: Ni, Fe, Cr, Mn, Mo, Ti, Al, Zr, Si. Moreover, it has been decided to provide a powder of $(\text{Ni}_{100/3}\text{Fe}_{100/3}\text{Cr}_{100/3})$ at% as a basis of our experimental investigation. This powder will be blended with others to generate the samples.

Two types of samples have been elaborated by laser cladding:

- wall structures with or without graded composition, typically of about 30mmx20mmx2mm (example in Fig. 4). They are used for combinatorial investigation purpose. The process parameters used were:
 - ✓ Power (P)=1800W (first layer), 1400W (following layers),
 - ✓ Travel speed (V)=250mm/min,
 - ✓ Powder flow rate (Dp)= 6g/min.

There are mainly used to generate a rapid screening of a selected range of compositions.

- coatings: After a selection of some compositions from their microstructural analysis, some coatings have been achieved for wear tests. Coatings of about 40mmx40mm on about 4mm thickness are elaborated for the alloys to be tested in tribology (example in Fig. 5). The parameters (P,V,Dp) are the same as chosen for the wall structures. Hatching Distance (HD) between two tracks is 1.8mm. The coatings consist in 5 layers of about 0.8mm each.

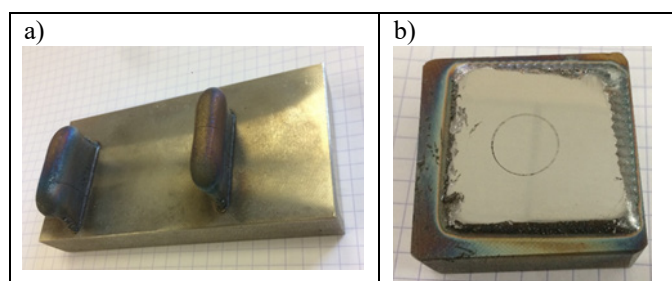


Fig. 4. Example of samples elaborated by laser cladding: a) wall structure with graded composition, b) Laser cladded coatings for wear tests

Two coatings of each composition $(\text{FeNiCr})_{90}\text{Mo}_5\text{Ti}_5$, $(\text{FeNiCr})_{80}\text{Mo}_{10}\text{Ti}_{10}$ and $(\text{FeNiCr})_{80}\text{Mo}_{15}\text{Ti}_5$ have been elaborated for the microstructure analysis and the wear tests.

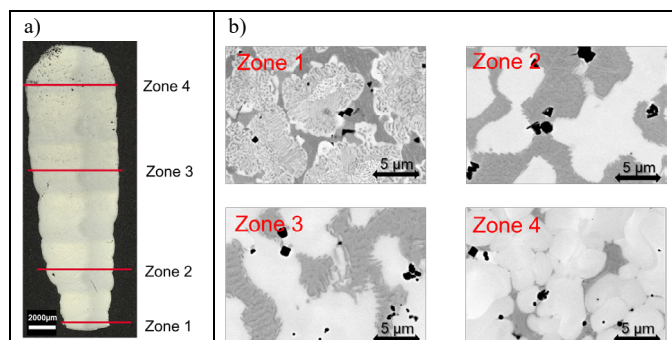


Fig. 5. Example of graded wall in NiFeCr+Mo+Ti : a) Vertical cut macrograph, b) cross-section micrographs in defined zones (BSE)

The composition of each zone of the wall structure is presented in Table 2. It can be seen that the measured composition globally follows the programmed one. The small deviations are most probably due to the dilution of the substrate.

Table 2. Programmed and measured (EDX) composition of the zones of the wall presented in Fig.5.

Zone	Programmed content (%at)			Measured content (%at)		
	$\text{Ni}_{100/3}\text{Fe}_{100/3}\text{Cr}_{100/3}$	Mo	Ti	$(\text{Ni,Fe,Cr})_{\text{total}}$	Mo	Ti
1	85	10	5	88,9	7.3	3.8
2	83	12	5	85.6	10.3	4.1
3	81	14	5	81.0	13.4	5.6
4	79	16	5	77.1	16.2	6.7

The elaborated samples have been analyzed by SEM/SE+BSE, XRD and EBSD and the results compared to the thermodynamically simulations. The results are presented in the next sections.

3.3. $(\text{FeNiCr})_{90}\text{Mo}_5\text{Ti}_5$ sample

The alloy is mainly composed of a FCC matrix containing a medium amount of sigma phase presented in Fig. 6. A small presence of Ni_3Ti and titanium nitride have been detected. Although this is close to TCHEA1 CALPHAD calculation at equilibrium solidification, the proportion of phases slightly differs and TiN has not been predicted. Out of equilibrium calculation does not give more correlated results.

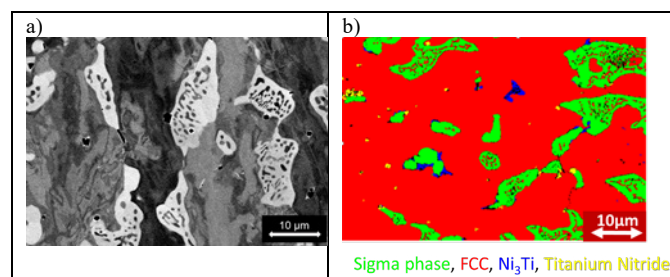


Fig. 6. a) SEM/BSE image and b) EBSD phase determination of $(\text{FeNiCr})_{90}\text{Mo}_5\text{Ti}_5$ sample

Globally, the sample exhibits a microhardness of about 550 HV_{10} (5.40 GPa).

3.4. $(\text{FeNiCr})_{80}\text{Mo}_{10}\text{Ti}_{10}$ sample

The microstructure of this alloy is presented in Fig.7. Due to the high content of Mo, the alloy is mainly composed of a sigma phase surrounded by C14 Laves p.phases and additional Chi phase, Ni_3Ti and TiN in small amount.

This differs significantly from TCHEA1 CALPHAD calculation at equilibrium solidification. Particularly, no BBC phase has been found in the sample. Out of equilibrium calculation does not give more correlated results.

Globally, the sample exhibits a microhardness of about 755 HV_{10} (7.40 GPa). The high content of sigma phase has a clear impact on the increase of hardness compared to $(\text{FeNiCr})_{90}\text{Mo}_5\text{Ti}_5$ sample.

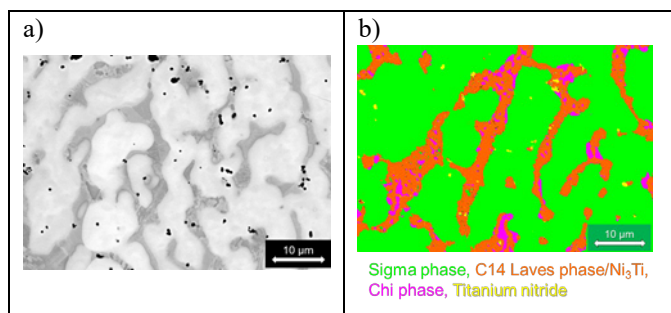


Fig. 7. a) SEM/BSE image and b) EBSD phase determination of $(\text{FeNiCr})_{80}\text{Mo}_{10}\text{Ti}_{10}$ sample

3.5. $(\text{FeNiCr})_{80}\text{Mo}_{15}\text{Ti}_5$ sample

The microstructure of this alloy is presented in Fig. 8.

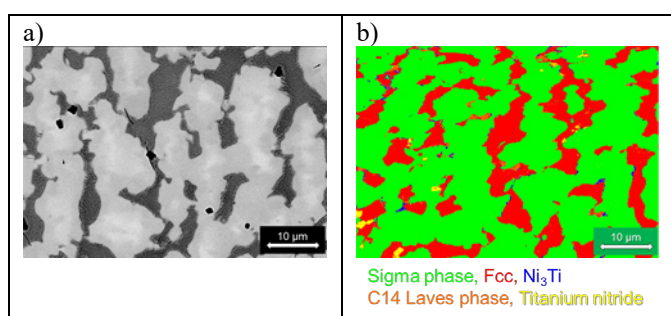


Fig. 8. a) SEM/BSE image and b) EBSD phase determination of $(\text{FeNiCr})_{85}\text{Mo}_{10}\text{Ti}_5$ sample

As for $(\text{FeNiCr})_{80}\text{Mo}_{15}\text{Ti}_5$, the high content of Mo has induced the solidification of the sigma phase as the main phase surrounded by FCC and additional C14 Laves, Ni_3Ti and TiN phases in a very small amount. For this composition, except for TiN, the out of equilibrium calculations globally fits with the experimental results.

Globally, the sample exhibits a microhardness of about 700 HV_{10} (6.9 GPa). This is comparable to the $(\text{FeNiCr})_{80}\text{Mo}_{10}\text{Ti}_{10}$ sample.

Globally, the alloys exhibit a fine a relatively equiaxed microstructure composed, as expected, by a high content of hard phases. It is now necessary to make the wear tests for comparing their tribological behaviors.

4. Tribology tests

4.1. Experimental setup

Pin-on-disk tests were performed on a rotary pin-on-disk tribometer THT from CSM Instrument. In accordance with regular tests previously defined [11,12], tests were performed with a ruby ball of 6mm diameter, a Hertz pressure of 1GPa, rotation speed of 5mm/s for a total distance of 100m under argon atmosphere with constant argon flushing and room temperature. The load and the sliding speed are representative of the conditions that would be encountered in targeted applications. The ruby ball is not worn out during the tests and it does not participate to the formation of a third body, allowing an easiest comparison between different alloys. The goal of the

tribological analysis is to compare the wear behavior of the CCAs with the Stellite reference.

Samples were first surfaced and then gradually polished to finish with a 2400 grade SiC paper. Friction coefficient was measured with two force sensors to minimize errors coming from the temperature changes. Wear rate was estimated by measuring the lost volume with an interferometric microscope.

4.2. Tribology tests

Four samples $(\text{FeNiCr})_{90}\text{Mo}_5\text{Ti}_5$, $(\text{FeNiCr})_{90}\text{Mo}_{10}\text{Ti}_{10}$, $(\text{FeNiCr})_{90}\text{Mo}_{15}\text{Ti}_5$, and Stellite 6 as the reference material have been prepared by laser cladding. The friction coefficients are measured along the wear test and wear rates after 100m driving distance (see Fig. 9 for results).

Globally, the CCAs exhibit similar wear properties. Their friction coefficients stabilize at about 0.4, which remains higher than Stellite 6 (close to 0.2). However, the wear rate of the three tested CCAs remains lower that of Stellite 6.

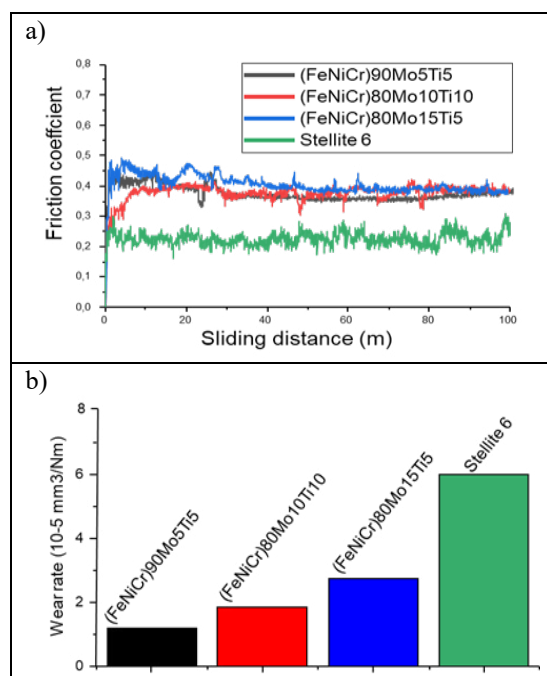


Fig. 9. a) Friction coefficient along wear, and b) wear rate for the 3 alloys

4.3. Discussion

First, the three alloys exhibit a similar abrasive wear. Although a very good argon gas protection, an oxide film is formed by the heat induced by dissipated energy in the contact decreasing the friction coefficient and protecting the alloys by reducing the contact surface between the ball and the coating.

This film is subjected successively to growth, abrasion, formation of cracks and partial delamination. This delamination process results in a significant variation in the friction coefficient. Depending on the alloy, certain variations are visible on the size of the particles generated by the damage to the surface. These oxide particles can contribute to abrasion: the smaller the particles, the more they can be trapped inside the contact and contribute to the abrasion of the surface. The phase composition can clearly lead to different wear behaviors.

So far, it is unclear whether the surface of the samples is damaged differently depending on their composition. In addition, wear tests are planned to assess the repeatability of the measurements.

5. Conclusion and perspectives

In this article, we have proposed a new approach for the elaboration of cobalt free hardfacing coatings. From the bibliography, we have shown that new approaches in metallurgy and material processing is a good opportunity for this purpose. LMD is a very versatile tool for a combinatorial metallurgy approach that can be used for the exploration of the new family alloys of HEA/CCAs material. Moreover, we have proposed an iterative methodology that combines simulations with CALPHAD calculations and combinatorial elaboration of materials by the in-situ laser fusion of powders. This study has recently started and an example has been presented on three alloys.

It is clear that each step has some drawbacks as prediction errors due to incomplete thermodynamic database, uncertainty in melting of powders (impurities, segregation of powders, melting point issue,...). Although this has to be improved, promising results have been obtained for the wear behavior of the proposed CCAs. If their friction coefficients are still higher than Stellite 6, they would be acceptable for a large range of applications. Moreover, the three alloys exhibit a smaller wear rate compared to Stellite 6 and their wear mechanism in mainly abrasive mode are promising characteristics for galling conditions.

The study will be extended on other type of alloys from the initial group, improving simulation and experimental tools for their development.

References

- [1] D.H.E. Persson, S. Jacobson, S. Hogmark, Effect of temperature on friction and galling of laser processed Norem 02 and Stellite 21, *Wear* 255, 2003, pp.498–503
- [2] D. H. E. Persson, Laser processed low friction surfaces, Dissertation for the degree of Licentiate of Philosophy in Materials, Materials Science Division, the Ångström Laboratory, Uppsala University, Sweden, March 2003
- [3] C. B. Bahn, B. C. Han, J. S. Bum, I. S. Hwang, Chan Bock Lee, Wear performance and activity reduction effect of Co free valves, in PWR environment, *Nuclear Engineering and Design* 231, 2004, pp. 51–65
- [4] M. Corchia, P. Delogu., F. Nenci., Microstructural Aspects of Wear-Resistant Stellite and Colmonoy Coatings by Laser Processing, *Wear*, Volume 119, 1987, pp. 137-152
- [5] Kashani, A. Amadeh, & H. Ghasemi, Room and high temperature wear behaviors of nickel and cobalt base weld overlay coatings on hot forging dies. *Wear*, 262(7-8), 2007, pp. 800-806,
- [6] Qian Ming, L.C. Lim, Z.D. Chen, Laser cladding of nickel-based hardfacing alloys, *Surface and Coatings Technology* 106, 1998, pp. 174-182
- [7] D. Kesavan, & M. Kamaraj, The Microstructure and High Temperature Wear Performance of a Nickel Base Hardfaced Coating, *Surface and Coatings Technology*, 204(24), 2010, pp. 4034-4043
- [8] V.D. Tran, P. Aubry, C. Blanc, J. Varlet, T. Malot, Laser Cladding And Tribocorrosion Testing Of Cobalt-Free Hardfacing Coatings For Fast Neutron Reactor, Proc. of ICALEO 2014, 2014, paper #203
- [9] C. Navas, R. Colaço, J. Damborenea, & R. Vilar, Abrasive Wear Behavior of Laser Clad and Flame Sprayed-Melted NiCrBSi Coatings, *Surface and Coatings Technology*, 200(24), 2006, pp. 6854-6862
- [10] K. Komvopoulos, K. Nagarathnam, Processing and Characterization of Laser-Cladded Coating Materials, *J. of Engineering Materials and Technology*, vol. 112, (1990), pp. 131-143
- [11] P.Aubry, C.Blanc, I.Demirci, M.Dal, T.Malot, H. Maskrot, Laser Cladding of Nickel Base Hardfacing Materials: Influence of Process Parameters, Proc. of ICALEO 2016 (2016), San Diego, Paper #303
- [12] P. Aubry, C. Blanc, I. Demirci, M. Dal, T. Malot, and H. Maskrot, Laser cladding and wear testing of nickel base hardfacing materials: Influence of process parameters, *J. Laser Appl.* 29, 022504, 2017, pp. 1-9
- [13] P.Aubry, C.Blanc, I.Demirci, M.Dal, T.Malot, Analysis of nickel based hardfacing materials manufactured by laser cladding for Sodium Fast Reactor, Proc. 9th Int. Conf. Photonics Tech. LANE 2016, Physics Procedia, (2016), Procedia CIRP Volume 74, 2018, pp. 210-213
- [14] B. Cantor, I. T. H. Chang, P. Knight, and A. J. B. Vincent, "Microstructural development in equiatomic multicomponent alloys," *Mater. Sci. Eng. A*, vol. 375–377, no. Supplement C, pp. 213–218, Jul. 2004,
- [15] J.-W. Yeh et al., "Nanostructured High-Entropy Alloys with Multiple Principal Elements: Novel Alloy Design Concepts and Outcomes," *Adv. Eng. Mater.*, vol. 6, no. 5, pp. 299–303, May 2004,
- [16] Y. H. Jo et al., "Utilization of brittle σ phase for strengthening and strain hardening in ductile VCrFeNi high-entropy alloy," *Mater. Sci. Eng. A*, vol. 743, pp. 665–674, Jan. 2019
- [17] H. Abed, F. Malek Ghaini, and H. R. Shahverdi, "Characterization of Fe49Cr18Mo7B16C4Nb6 high-entropy hardfacing layers produced by gas tungsten arc welding (GTAW) process," *Surf. Coat. Technol.*, vol. 352, pp. 360–369, Oct. 2018
- [18] J. Zeisig et al., "Microstructure and abrasive wear behavior of a novel FeCrMoVC laser cladding alloy for high-performance tool steels," *Wear*, vol. 382–383, pp. 107–112, Jul. 2017
- [19] N. Ley, S. S. Joshi, B. Zhang, Y.-H. Ho, N. B. Dahotre, and M. L. Young, "Laser coating of a CrMoTaWZr complex concentrated alloy onto a H13 tool steel die head," *Surf. Coat. Technol.*, Feb. 2018,
- [20] H. Dobbstein, M. Thiele, E. L. Gurevich, E. P. George, and A. Ostendorf, "Direct Metal Deposition of Refractory High Entropy Alloy MoNbTaW," *Phys. Procedia*, vol. 83, no. Supplement C, pp. 624–633, Jan. 2016
- [21] H. Dobbstein, E. L. Gurevich, E. P. George, A. Ostendorf, and G. Laplanche, "Laser metal deposition of a refractory TiZrNbHfTa high-entropy alloy," *Addit. Manuf.*, vol. 24, pp. 386–390, Dec. 2018
- [22] H. Dobbstein, E. L. Gurevich, E. P. George, A. Ostendorf, and G. Laplanche, "Laser metal deposition of compositionally graded TiZrNbTa refractory high-entropy alloys using elemental powder blends," *Addit. Manuf.*, vol. 25, pp. 252–262, Jan. 2019
- [23] The Calphad Methodology, <https://www.thermocalc.com/products-services/databases/the-calphad-methodology/>
- [24] G. Bracq, M. Laurent-Brocq, L. Perrière, R. Pirès, J.-M. Joubert, and I. Guillot, "The fcc solid solution stability in the Co-Cr-Fe-Mn-Ni multi-component system," *Acta Mater.*, vol. 128, pp. 327–336, Apr. 2017
- [25] D. B. Miracle, J. D. Miller, O. N. Senkov, C. Woodward, M. D. Uchic, and J. Tiley, "Exploration and Development of High Entropy Alloys for Structural Applications," *Entropy*, vol. 16, no. 1, pp. 494–525
- [26] Dobbstein H., Thiele M., Evgeny L.GurevichaEaso P. George E.P., Ostendorf, Direct Metal Deposition of Refractory High Entropy Alloy MoNbTaW, *Physics Procedia*, Vol. 83, 2016, pp. 624-633

11th CIRP Conference on Photonic Technologies [LANE 2020] on September 7-10, 2020

Laser glass deposition of spheres for printing micro lenses

K. Rettschlag^{a,b,*}, A. Hohnholz^b, P. Jäschke^b, D. Kracht^b, S. Kaierle^b, R. Lachmayer^a

^aInstitut für Produktentwicklung und Gerätebau, 30823 Garbsen, Germany

^bLaser Zentrum Hannover e.V., 30419 Hannover, Germany

* Corresponding author. Tel.: +49-511-14737; E-mail address: rettschlag@ipeg.uni-hannover.de

Abstract

Similar to components in electronics industry, optical systems are also increasingly miniaturized. The integration of functions as well as the production of optical freeform surfaces, which are not manufacturable with conventional manufacturing processes, are of special interest. One method for additive manufacturing of glass components is the Laser Glass Deposition (LGD) by using a CO₂ laser source (10.6 μm). This allows printing functional waveguides in individual shapes. The process is also able to generate spheres for e.g. a planar lens matrix. In this paper the reproducible controlled deposition of spheres using a fused silica fiber with a diameter of 400 μm is investigated. For this purpose, a parameter variation of the fiber feeding speed and laser power is carried out to produce spheres of different sizes and in different arrangements. Finally, the optical and stress-mechanical properties of the samples are investigated.

© 2020 The Authors. Published by Elsevier B.V.

This is an open access article under the CC BY-NC-ND license (<http://creativecommons.org/licenses/by-nc-nd/4.0/>)

Peer-review under responsibility of the Bayerisches Laserzentrum GmbH

Keywords: "Selective laser melting; Additive manufacturing; 3D printing; Hydrogen embrittlement resistance stainless steel; Nitrogen burning; Mechanical properties; Vacuum induction melting atomization"

1. Introduction

In order to explore new areas of application, additive manufacturing is applied widely for new or significantly modified products. Especially optics as an application area, where high optical surface qualities are required, represent a major challenge for this technology [1]. How selected additive manufacturing processes can be implemented in optics and laser technology and which restrictions apply to these processes is currently a focus of different research projects and industrial developments worldwide. The production of functional transparent optics made of polymers has already been successfully realized [2]. Processes for the additive manufacturing of silicones are also currently developed [2, 3]. However, the printed components are only suitable in low power applications, where the beam quality is not the primary focus. Furthermore, the high absorption rate of the polymer and silicone materials in the UV range may have a negative effect on the beam guidance and lead to an accelerated aging of the

samples, compared to glass materials [1]. For this reason, glass as a base material is still indispensable for high-power applications, since these require good optical light guidance for a broad spectrum. The fabrication of miniaturized optics with free-form surfaces can currently only be realized with conventional glass processing methods (glass blank, blank press, milling, grinding, polishing, qualifying [4]) with a very high expenditure of time and costs. Laser based techniques such as cutting, drilling, re-melting and shaping are no conventional methods in this context [5].

One possible solution for processing free-form optics is the additive manufacturing of glass components by Laser Glass Deposition (LGD) [6,7]. In this paper, the additive manufacturing process of spherical glass lenses with different diameters and sizes is described for the first time. In addition, the manufactured samples are analyzed for their geometric properties, the reproducibility of defined sphere geometries and internal stress.

Different process concepts for the additive manufacturing of glass are considered in research and development. In the processes available so far, additives as binders of the glass particles or a glass powder bed are applied to realize an additive layer structure. Methods such as glassomer technology, selective laser sintering of glass, selective laser melting of glass and stereolithography with glass pastes are based on these approaches [8, 9, 10].

There exist several challenges for the manufacturing of functional spherical lenses. A homogeneous material distribution within the component without inclusions or bubbles is essential [6]. Inhomogeneous material distributions lead to a variation of the refractive index, which influences the propagation of the induced radiation depending on the position. In addition, Inclusions, voids and defects induce internal scattering centers and reduce the optical quality of the component [11, 12]. The LGD process (Fig. 1) can compensate these different influences and is a process that needs no additives. The process based on a fiber extrusion technique.

2. Methods

Due to the high absorption characteristics of fused silica in the IR range, a defocused CO₂ laser beam source (max. 4.5 kW, 10.6 μm) is induced here. For the manufacturing of single layers or spheres are only 100 W up to 150 W needed, whereby a power reduction by two beam splitters is necessary. After a deflecting mirror, the laser radiation is focused by an optical system. In the process zone, a defocused laser beam is generated in order to guarantee a homogeneous intensity distribution on the fiber and not to evaporate the material. The original fiber is fed laterally at a fixed angle of 40° (Fig. 1).

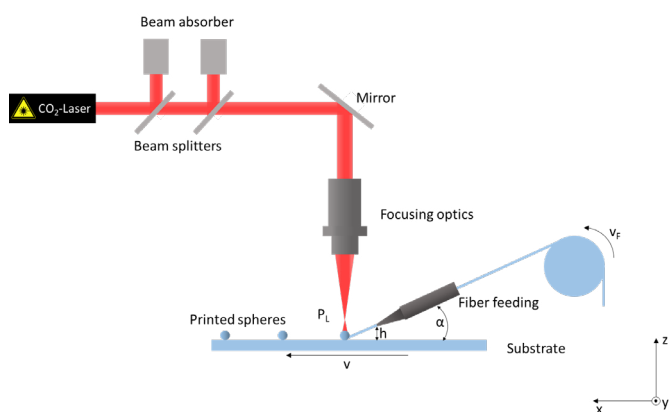


Fig. 1. Schematic illustration of the applied experimental setup.

In this paper, a coreless fused silica fiber with a diameter of 400 μm is chosen. To ensure a breakage-free feeding into the process zone, the fiber is covered with a polymer coating of 50 μm thickness. Due to the high process temperatures of up to over 2000°C (measured with a pyrometer), the coating is burned without any residues during the process. On the fiber surface, no residues of the coating could be detected in an SEM examination [6]. The cross section diameter of the laser beam within the process zone is approx. 4 mm [6, 13]. In order to avoid material losses by evaporation, the original fiber was oriented 1 mm displaced to the center of the beam cross section.

In previous studies, functional waveguides made of fused silica were produced with this process. The functionality was verified by transparency measurements and was compared with the original fiber [6, 14]. To deposit the waveguides, the feeding nozzle and thus the fed fiber is kept at a constant height. In this case one sphere is also formed at the fiber end, when the process starts (Fig. 2). This sphere is formed, because the process is moved above the substrate in order to be able to subsequently finish the fiber ends. For a production of single spheres, only the height is varied from the parameter set for functional waveguides. Therefore, the spheres can be formed during the process. After varying the height, other process parameters such as laser power, feeding speed and the speed of the axes are adapted to find a suitable final parameter set. During the laser irradiation, the spheres are formed at the end of the fiber due to the surface tension of the glass. The fiber is not noticeable bent by the weight of the sphere due to the material stiffness, so that this has no significant influence on the depositing process.

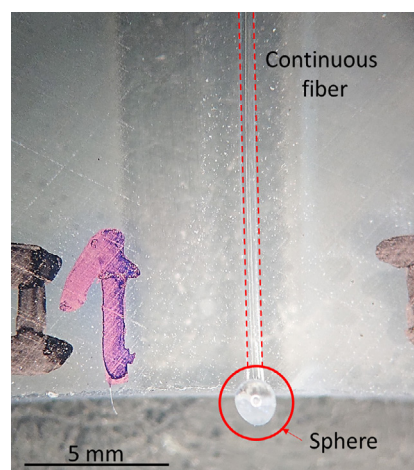


Fig. 2. Continuously deposited waveguide with a diameter of 400 μm and a glass sphere at the fiber end.

Depending on the height of the feeding nozzle, spheres with different diameters are generated. The distance between the single spheres can be adjusted by varying the fiber feeding speed (v_F) or the traverse speed of the axis table (v).

With this method, it is possible to deposit spheres on a fused silica substrate. These spheres are connected to the substrate at one contact area and cannot be removed by minor mechanical impact (e.g. scratching over the surface). All printed glass spheres were produced with a laser power of $P_L = 140$ W as well as an axis and fiber feeding speed of $v = v_F = 100$ mm/min. The height of the feeding nozzle is moved in 0.5 mm steps over a range of 2 mm (Tab. 1).

Table 1. Parameter sets for the additive manufacturing of glass spheres with different resulting diameters on a 50 mm long substrate.

Number	h [mm]	P_L [W]	$v_F = v$ [mm/min]	No. of spheres	Spheres diameter [mm]
1	6.0	140	100	0	-
2	6.5	140	100	13	0.91
3	7.0	140	100	6	1.22
4	7.5	140	100	5	1.47
5	8.0	140	100	4	1.5

In the following chapter, the measurements and results are explained. First, the spheres are analyzed under a microscope to determine their reproducibility. Subsequently, a measurement is made with a polarimeter to investigate whether the process results in thermal induced stress. The final step in this work is to examine the sphere for possible focusing effects with a laser diode.

3. Results and Discussion

For the parameter set number 1, the fiber feeder is with a few millimeters (height: 6 mm) close enough to the substrate that a continuous fiber is deposited. Increasing the distance to the substrate of 0.5 mm results in discontinuous fiber deposition. The feeding fiber is sufficiently higher above the substrate that individual spheres with a diameter of 0.91 mm are formed at the end of the fiber, which are printed on the substrate. The larger the distance between feeder and substrate, the larger spheres are formed at the fiber end. As soon as the sphere surface is in contact with the substrate surface, the sphere is deposited on the substrate and connected in the softened area. As a result, less spheres with a larger diameter are placed on the same substrate length at the same feeding rate.

At a defined feeding height of 10 mm and above, the spheres always have almost the same diameter of approx. 2.1 mm. For the fiber applied here, the 2.1 mm is the maximum achievable diameter of the softened material before the sphere is falling off the fed fiber due to gravity. Subsequently, in this chapter, these samples are evaluate and examine in terms of their internal stress, reproducibility and optical influence on the light guidance.

In the first step after the manufacturing process, the resulting samples are examined under an optical microscope to determine the distance between the spheres (Fig. 3). This distance varies for different sphere diameters, due to the constant axis speed and increases with the size of the spheres (Tab. 2).

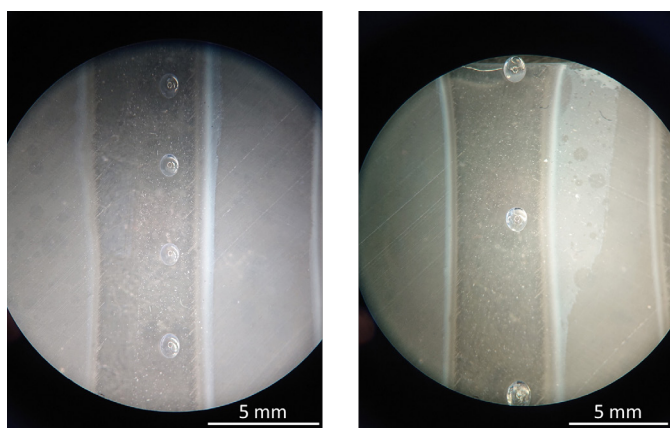


Fig. 3. Left: Four spheres with a middle diameter of 0.91 mm from the parameter set two; Right: Three spheres with a middle diameter of 1.22 mm from the parameter set three.

It was observed that the individual deposited spheres have a preferred direction in the direction of fiber feeding (Fig. 4). The smaller the spheres are the more elliptical is their shape. This can also be observed in Fig. 3. The smaller spheres (0.91 mm,

Fig. 3 left) have a more elliptical shape than the spheres with a diameter of 1.22 mm (Fig. 3 right).

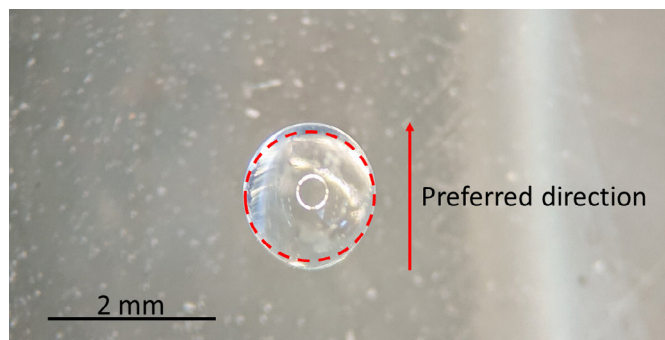


Fig. 4. Elliptical sphere with a middle diameter of 1.22 mm. The preferred direction (printing direction) and the theoretically ideal round shape are marked.

The position of the fiber feeder is identified as a major influencing factor that the spheres results in this shape. During the axial movement the spheres are slightly deformed as they are removed from the fiber end before harden completely. The spheres are deposited because they are more strongly bond to the substrate than to the feeding fiber. For larger diameters above 1.5 mm, the surface tension is almost sufficient to counteract this elliptical tendency.

To evaluate the shape retention, the diameters of the individual spheres of one parameter set are measured horizontally as well as vertically. The result of these measurements shows that the sphere diameter vary in the same process run. The differences are up to half a millimeter (Tab. 2).

Table 2. Diameter and distance between single spheres and the corresponding deviations of the spheres in the different parameter sets.

Number	Diameter [mm]	Tolerance (T_D) [mm]	Distance [mm]	Tolerance (T_{Sp}) [mm]
2	0.91	± 0.025	2.81	± 0.45
3	1.22	± 0.045	7.19	± 0.61
4	1.47	± 0.040	10.24	± 0.71
5	1.50	± 0.045	10.35	

The distance between the individual spheres were also determined. Here the variations within one process run are even more clearly. In further investigations, it is necessary to find a solution in order to control this effect.

Afterwards, the resulting process-related internal stress of the samples are measured using a polarimeter (StrainMatic M4/140, ilis GmbH) (Fig. 5).

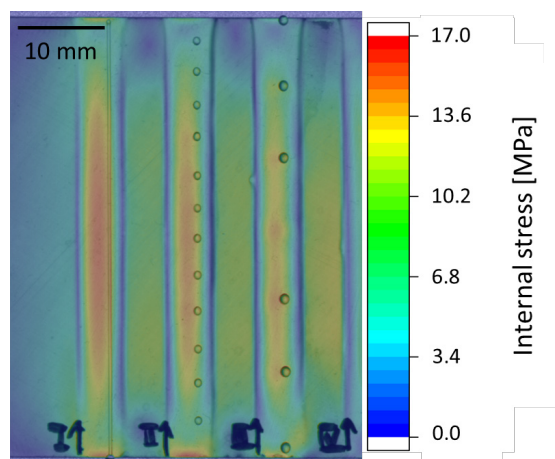


Fig. 5. Results of the measurement of the mechanical stress. Illustration of the internal stress after the deposition process.

A maximum stress of 15.5 MPa exist in the substrate, which corresponds to an optical path difference of 105 nm. The spheres have a maximum internal stress of 12.1 MPa (optical path difference 94 nm).

A more detailed measurement of individual deposited spheres is so far not possible due to the limited resolution of the polarimeter used. This investigation is necessary to obtain a detailed stress distribution inside the optical components. In the case of the continuously deposited fiber (parameter 1 in Fig. 5), the stress distribution is almost uniform. As expected, the maximum stress is in the center of the substrate, since a better heat dissipation is guaranteed to the sides. In the parameter sets of the spheres, especially for parameter set 3, it was observed that at each position of a sphere the stress distribution in the substrate is punctually larger. This is illustrate with an orange coloring in the area of the sphere and a yellow coloring between the single spheres. A local increase of the absorbed energy is assumed, due to the deposition. However, this influence need to be further investigated.

As described in chapter 2, the deposited components are not in the center of the cross-section of the induced laser beam, which is visible in the stress distribution. (Fig. 5). This arrangement was chosen deliberately in order to avoid evaporating the incoming material with a too high-energy input. At lower power levels (less than 140 W in the welding zone) the output power of the laser beam source becomes instable.

To test the focusing property of the deposited spheres, a laser diode (wavelength: 650 nm, output power < 1 mW), was directed onto the spheres. A focusing effect on the radiation can be observed behind the lens (Fig. 6). At a longer distance from to the focal plane, the beam diverges very widely. No specific optical properties were assumed for the manufactured components prior to the process, so that this observation is an essential foundation for the possibility of a parameter-specific adjustment of the optical properties.

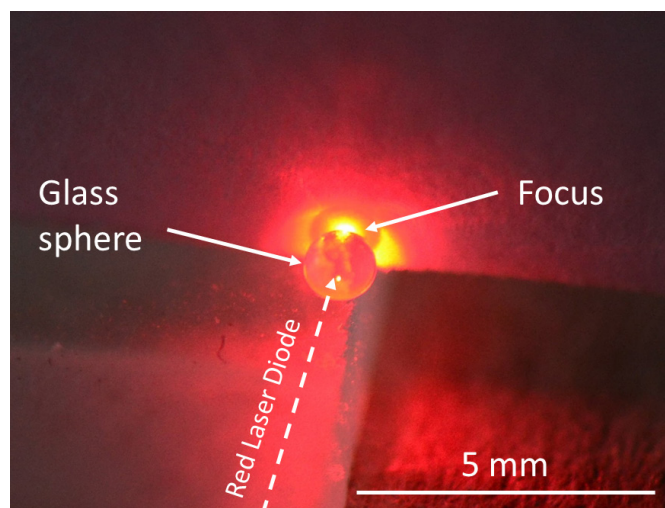


Fig. 6. Illustration of the lens effect of an additive manufactured spherical lens. The focusing effect of the red laser radiation is visible on the white screen behind the sphere.

4. Conclusion and Outlook

In this paper, we showed that the LGD process enables the additive manufacturing of glass spheres of different sizes. Spheres with diameters from 0.91 mm to 1.50 mm and 2.1 mm were generated. Because of the high process temperatures of over partly more than 2000°C, thermal stresses of up to 15.5 MPa occur in the substrate and 12.1 MPa in the spheres. These stresses induce refractive index variations and can influence the optical properties of the spherical lenses. However, the extent to which this effect occurs needs to be further investigated. A path difference of 94 nm in the spheres was detected during this study. Further influences such as the lateral fiber feeding on the shape and reproducibility of the spheres are discussed and identified in this paper. Due to the lateral feeding the spheres have a preferred direction and result in an elliptical shape (e.g.a sphere from parameter 3: diameter in x-direction = 1.05 mm, diameter in y-direction = 1.25 mm). Finally, it could be demonstrated here that the spherical lens has a focusing effect.

Therefore, further investigations will be performed on the base of these preliminary experiments to analyze the reproducibility of different sizes and the optical properties of the spheres, like focal length and transparency. In addition, the shape of the sphere geometry required for a defined optical effect must be determined in advance by a simulated design. The digitally pre-designed optics will be manufacture with the LGD process and analyze in terms of their optical properties. This also includes the investigation of the effects of internal stress on the lens effect and whether these are potentially completely remove from the manufactured components. The simulations described in this section will be carried out in the future. Additionally further studies shall investigate whether the surfaces of the spheres corresponds to an optical quality and whether the lens effect can be utilize and specifically adjust for optical applications.

Further considerations include the feasible applications of printed spherical lenses in the field of optical systems. One

possible application is the direct printing of input and output optics onto a printed waveguide. Core fibers and coreless fibers are then processed and combined for this application in one process. This could avoid the necessary adjustment of the individual components.

Acknowledgements

The experiments were conducted within the framework of the project “GROTESK – Generative Fertigung optischer, thermaler und struktureller Komponenten” funded by EFRE – NBank (ZW6-85018307). All the authors are very grateful for this support.



EUROPÄISCHE UNION
Europäischer Fonds für
regionale Entwicklung



References

- [1] Kloppenburg G, Knöchelmann M, Wolf A. Additive Fertigung transparenter Optiken. In: Lachmayer R, Lippert R (eds), Additive Manufacturing Quantifiziert, Springer Vieweg Verlag, p. 163-174, 2017, 978-662-54113-5.
- [2] Thiel M, Tanguy Y, Lindenmann N, Niesler F, Schmitt M, Quick A. 3D printing of polymer optics. 2017 European Conference on Laser and Electro-Optics and European Quantum Electronics Conference, 2017, 978-1-5090-6736-7/17.
- [3] Heinrich A, Börrer R, Merkel M, Riegel H. Additive Manufacturing of reflective and transmittive optics: Potential and new solutions for optical systems. SPIE Proceeding, Volume 10523, Laser 3D Manufacturing V, 1052302, 2018, <https://doi.org/10.1117/12.2293130>.
- [4] Nollau S, Kunz A, Rübenach O, Pongs G. Innovative Optikdesigns durch Präzisionsblankpressen. Optik&Photonik, WILEY VCH Verlag GmbH & CO. KGaA, p. 30-34, 2011.
- [5] Weingrten C, Schmickler A, Willenborg E, Wissenbach K. Laser polishing and laser shape correction of optical glass. Journal of Laser Application, Volume 29(1), 011702, 2017, doi: <https://doi.org/10.2351/1.4974905>.
- [6] Rettschlag K, Kranert F, Hohnholz A, Wienke A, Suttmann O, Neumann J, Kracht D, Lachmayer R. Laser deposition of fused silica coreless fibers to generate functional waveguides. Laser in Manufacturing Conference, 2019.
- [7] Luo J, Hostetler JM, Gilbert L, Goldstein JT, Urbas AM, Bristoe DA, Landers RG, Kinzel EC. Additive manufacturing of transparent fused quartz. Optical Engineering, Volume 57(4), 041408, 2018, doi: [10.1117/1.OE57.4.041408](https://doi.org/10.1117/1.OE57.4.041408).
- [8] Kotz F, Schneider N, Striegel A, Wolfschläger A, Keller N, Worgull M, Bauer W, Schild D, Milich M, Greiner C, Helmer D, Rapp RB. Glassomer-Processing Fused Silica Glass Like a Polymer. Advanced Materials, Volume 30, Issue 22, WILEY-VCH Verlag GmbH & Co. KGaA, 2018, <https://doi.org/10.1002/adma.201707100>.
- [9] Fateri M, Gebhardt A. Selective Laser Melting of Soda Lime Glass Powder. International Journal of Applied Ceramic Technology, Volume 12, Issue 1, p. 53-61, 2014, <https://doi.org/10.1111/ijac.12338>.
- [10] Kotz F, Bauer AW, Schild D, Keller N, Sachsenheimer K, Nargang TM, Richter C, Helmer C, Rapp BE. Three-dimensional printing of transparent fused silica glass. Nature, Volume 544, p. 337-339, 2017, doi: [10.1038/nature22061](https://doi.org/10.1038/nature22061).
- [11] Pohl L, Von Witzendorff P, Chatzizyrlis E, Suttmann O, Overmeier L. CO₂ laser welding of glass: numerical simulation and experimental study. International Journal of Additive Manufacturing Technology, Volume 90, p. 397-406, 2017.
- [12] Rezaei HS, Hohenhoff G, Jäschke P, Kaierle S, Overmeyer L. Design and fabrication of multilayer GRIN lenses by multi-material additive manufacturing for light coupling applications in planar optoelectronic systems. SPIE Proceeding, Volume 11283, Integrated Optics, Materials and Technologies XXIV, 2020, <https://doi.org/10.1117/12.2545914>.
- [13] Von Witzendorff P, Pohl L, Suttmann O, Heinrich P, Heinrich A, Zander J, Bragard H, Kaierle S. Additive manufacturing of glass: CO₂-laser glass deposition printing. Science Direct Procedia CIRP, Volume 74, p. 272-275, 2018, <https://doi.org/10.1016/j.procir.2018.08.109>.
- [14] Kranert F, Rettschlag K, Wienke A, Hohnholz A, Neumann J, Jäschke P, Kracht D, Lachmayer R. Generation of functional curved waveguides by CO₂-laser based deposition of coreless fused silica fibers. SPIE Photonic Europe Proceedings, Volume 11349, 1134909, 2020, doi: <https://doi.org/10.1117/12.2554516>

11th CIRP Conference on Photonic Technologies [LANE 2020] on September 7-10, 2020

Offline powder-gas nozzle jet characterization for coaxial laser-based Directed Energy Deposition

Zoé Jardon^{a,b,*}, Patrick Guillaume^a, Julien Ertveldt^a, Michaël Hinderdael^a, Galid Arroud^a

^aMechanical Department, Vrije Universiteit Brussel, Pleinlaan, 2, 1050 Elsene, Belgium

^bEnvironmental and Applied Fluid Dynamics Department, von Karman Institute for Fluid Dynamics, Chaussée de Waterloo 72, Belgium

* Corresponding author. Tel.: +32 2 629 23 24. E-mail address: zoe.jardon@vub.be

Abstract

One of the major challenges faced by laser-based Directed Energy Deposition (DED) is the process efficiency. This efficiency is significantly affected by the percentage of blown powder that effectively reaches the spherical metal melt pool. Increasing the powder efficiency would allow to reduce the overall costs of the DED process and consequently reduce the printed part cost. The present work focuses on the experimental characterization of the powder-gas jet in terms of powder stream shape, stand-off distance and powder-jet focus diameter by using 3 different high speed image-based approaches. The powder jet parameters are linked to the blown powder settings (carrier gas, shielding gas, powder feed rate, particle diameter) and optimized to minimize the powder waste. The different approaches give equivalent results and the reduction of the particle diameter turns out to be the most relevant parameter to decrease the powder-jet focus diameter and therefore increase the powder efficiency.

© 2020 The Authors. Published by Elsevier B.V.

This is an open access article under the CC BY-NC-ND license (<http://creativecommons.org/licenses/by-nc-nd/4.0/>)

Peer-review under responsibility of the Bayerisches Laserzentrum GmbH

Keywords: Directed Energy Deposition (DED); Coaxial nozzle; Powder jet; Stand-off distance; Powder-jet focus; Blown powder

1. Introduction

1.1. Additive Manufacturing of Metals

Metal Additive Manufacturing (AM), more commonly known as 3D metal printing, introduces the “imagination is the limit” concept in the manufacturing. 3D printing is a promising technology with maximum design freedom, to which there is often referred to as “rapid prototyping”. Building layer by layer, the technique prints components with highly complex geometries from almost any digital model. Therefore, the determining factor for the cost of a printed component is different with respect to components made by conventional manufacturing techniques. This factor switches from part complexity (conventional) to the size and/or the amount of material used (3D printed).

1.2. Laser-based Directed Energy Deposition

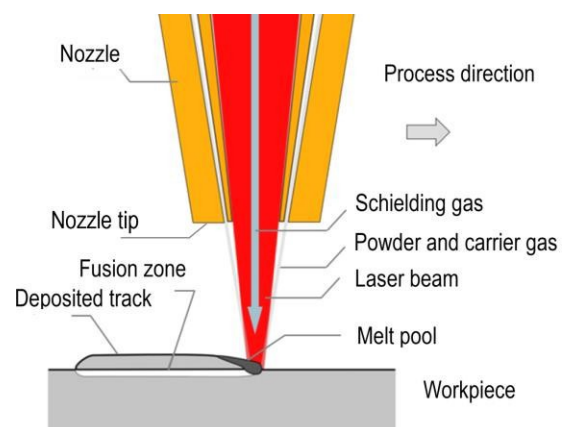


Fig. 1. Laser-based Directed Energy Deposition process principle with continuous coaxial nozzle cross-section.

Presently, a variety of different metal additive manufacturing technologies exist on the market. Directed Energy Deposition (DED) is one of the most known and widespread technologies of 3D metal printing in which focused thermal energy is used to fuse materials by melting as they are being deposited (ISO/ASTM DIS 52900:2018).

The present work is more specifically based on the laser/powder-based DED additive manufacturing technique, characterized by the simultaneous laser and powder delivery. The DED process is used in multiple industries such as the aviation, aerospace, automotive, medical and energy industry. As presented in Fig. 1, metal powder particles are carried by means of a carrier gas through channels inside a nozzle. The laser heat source goes through the inner nozzle cone and locally initiates a liquid metal melt pool on the workpiece surface in which the fine metal powder particles are melted and subsequently fused with the base material. The shielding gas going through the inner nozzle cone is used to minimize oxidation of the workpiece surface with melt pool and to protect the optical system in the nozzle head from any possible damage during the printing process (for example ricocheting heated metal particles). This optical system is needed for the orientation and focus of the laser light and corresponds to the part located above the nozzle itself.

1.3. Powder-gas nozzle jet

During the layer-wise bounding of the material, many complex interconnected physical phenomena take place in a very short time during the DED process (thermal energy transfer, laser/powder/gas interactions, melt pool initiation, localized solidification, ...) [1,2]. Therefore, a first step towards the understanding and quantification of these different physical phenomena, as well as the understanding of their effect on the printed part quality, is the characterization of the powder-gas nozzle jet which is addressed in the present paper.

For the laser-based DED process, different nozzle configurations exist : lateral nozzles, continuous coaxial nozzles and discrete coaxial nozzles [3]. Discrete coaxial powder nozzles, also known as multi-jet nozzles (with a minimum of 3 powder jets), are robust nozzles and are generally used to deposit wider tracks and thicker metal layers. Continuous or multi-directional coaxial powder nozzles on the other hand, are convenient for narrow deposition tracks (and small powder-jet focus diameters) and to obtain a high powder efficiency ϵ_{powder} . Coaxial nozzles are furthermore easier to use and have the advantage to be omni-directional. The present study focuses on coaxial nozzle flow during laser-based DED. Fig. 1 shows a cross section of the considered continuous coaxial nozzle (axisymmetric geometry).

The flow generated by the continuous coaxial nozzle is a 3-dimensional two-phase gas-powder turbulent flow. The parameters influencing the flow behavior, process efficiency and final component quality are the carrier gas volumetric flow rate (in l/min), shielding gas volumetric flow rate (in l/min),

powder mass flow rate (in g/min) and the metal powder characteristics (particle shape, particle size distribution and production technique).

1.4. Objectives and methodology

In comparison with the wire-fed process, laser/powder-based DED allows to deposit finer features and facilitates the real time control of powder dynamics. However, the main drawback is the powder waste and slower print-process in comparison with fire-fed [4].

One of the major challenges faced by laser-based Directed Energy Deposition (DED) is the process efficiency. The process efficiency is significantly affected by the percentage of blown powder that effectively reaches the spherical melt pool. Increasing the powder efficiency, defined as the utilization rate of the fed powder into the build volume, would allow to reduce the overall costs of the DED process and consequently reduce the printed part cost. The powder efficiency is strongly influenced by the choice of the optimal gas and powder settings of the process, which are also essential to obtain good thermo-mechanical properties and a high microstructure quality of the printed parts.

The present work focuses on the experimental characterization of the free flow (without substrate) powder-gas jet in terms of powder stream shape, stand-off distance and powder-jet focus diameter. The stand-off distance represents the distance between the nozzle tip, corresponding to the location at which the particles exit the nozzle (sFig. 1), and the focus of the nozzle jet that coincides with the maximum powder concentration. During the print process itself, the stand-off distance must be set as nozzle tip - melt pool distance in order to optimize the powder efficiency. Logically, an effect of the presence of the substrate with melt pool is expected on the powder jet dynamics, which is deliberately not considered in the present work. The powder-jet focus diameter represents the width of the nozzle jet in the powder focal plane. For an optimal powder efficiency, the powder-jet focus should have a similar or smaller dimension as the melt pool size (that has about the same dimension as the laser spot). Note that the laser spot size is determinant for the printing precision and therefore cannot be enlarged without consequences. The two previously cited parameters are linked to the blown powder settings (carrier gas - CG, shielding gas - SG, powder feed rate - FR) and optimized to maximize the powder efficiency and minimize the powder waste.

To perform this experimental study, different in-situ optical (high-speed) image-based techniques [5-9] are set up and compared in terms of stand-off distance and powder-jet focus diameter. The study is performed for powders with different particle diameter distributions and the effect of powder particle diameter on the powder-gas jet characterization is analyzed. Note that the study is carried out on free nozzle flow, without presence of substrate/melt pool under the nozzle.

2. Experimental study: high speed powder jet visualization and characterization

2.1. Set-up description

An experimental set-up is designed to visualize and characterize the powder gas nozzle jet flow during the Directed Energy Deposition process. The experiments are non-intrusive and are performed on the hybrid MiCLAD DED machine, which was developed in-house by the Additive Manufacturing Research Group of the Vrije Universiteit Brussel. Fig. 2. shows the experimental set-up and identifies every component.

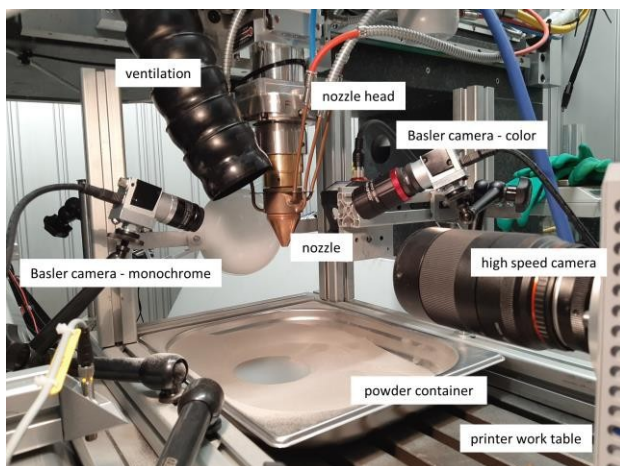


Fig. 2. Set-up description for powder-jet characterization on MiCLAD machine.

The used nozzle is a Fraunhofer ILT COAX-40-S coaxial nozzle with a nozzle tip of outer diameter 7.5mm. Note that the ILT nozzle was particularly adjusted for our print purposes. Argon is used both as carrier and shielding gas and the mass flow can be regulated between 0 and 10 l/min. The metal powder particles used for the experiments are gas atomized 316L stainless steel powders from Carpenter Additive, known to be near-spherical. Powders with two different particle size distributions are used. A powder sieve analysis realized by Additive Carpenter resulted in the following particle size ranges : 15-45 μm and 45-106 μm . Powders of different sizes show both microscopic and macroscopic differences. Microscopic differences between metal powder can among others be seen on Scanning Electron Microscopy (SEM) micrographs. Fig. 3. shows a SEM image of the 316L 45-106 μm powder used for the experiments presented in this study. On the other hand, powders can also show macroscopic differences in terms of flowability, cohesiveness and electric charge that can influence the powder-jet behavior.

A ventilation unit is used to extract the smaller metal particles that are "floating" around the nozzle. An experimental verification was performed to confirm the non-influence of the ventilation on the powder-jet flow. The powder coming from the nozzle is caught by a powder container placed on the printer worktable. Two Basler cameras (acA720-540uc color, acA720-540um monochrome) with adapted objectives are mounted on both sides of the nozzle.

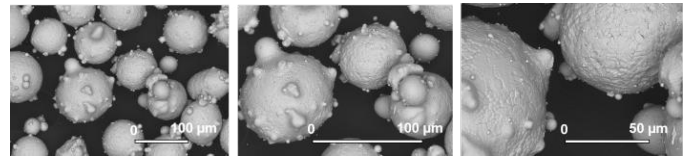


Fig. 3. Scanning Electron Micrograph of 316L powder particles (45-106 μm) with magnification x300, x500, x1000 from Additive Carpenter.

A Photron SA1.1 high speed camera is mounted in the front of the nozzle and used to acquire high speed images of the metal powder flow.

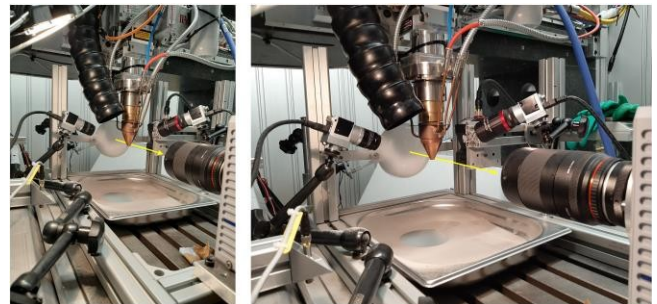


Fig. 4. Back-light illumination set-up (1).

In terms of illumination, 3 configurations are tested and compared. The first configuration, shown in Fig. 4, relies on the maximization of the contrast between the powder particles and background. For this purpose, and for a good detection of the metal particle contours, back-light illumination is used and set by means of a LED lamp (KDP Bulb LED MR16 GU5.3 12V, 2800K, 5W) connected to a DC voltage supply in order to avoid flickering phenomena on the acquired images. A spherical diffuser is placed in front of the light source to have a uniform background on the acquired images.

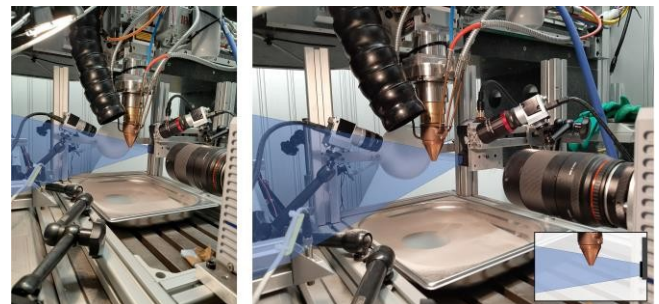


Fig. 5. Vertical laser sheet illumination set-up (2).

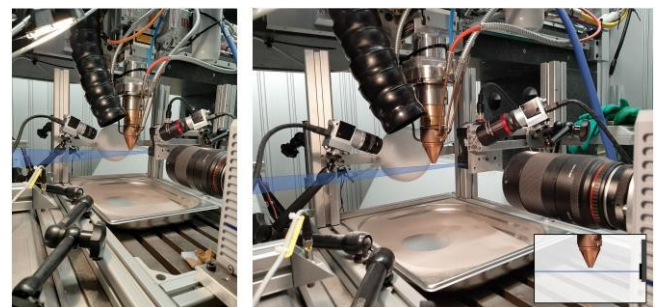


Fig. 6. Horizontal laser sheet illumination set-up (3).

As second light source, a visible line laser of wavelength 405nm with output power of 4.8mW (class 2 laser product) is used for the second and third configuration of the experiments. According to the laser specifications given in the datasheet, the line thickness corresponds to 50 μ m. The line laser is mounted both horizontally and vertically with respect to the nozzle axis. Both configurations are clarified hereunder in Fig. 5 and 6.

For the 3 configurations it is assumed that the light attenuation (conf. 1) or light scattering (conf. 2,3) caught by the camera sensors is linearly proportional to the particle concentration (given in kg/m³), according to Mie's Theory [10,11] :

$$L = \frac{I_{ref} r^2}{A} = \frac{I_{inc} n V}{k^2 A} F(\delta, \varphi)$$

Which relates L , the average luminance of the scattering element, with I_{ref} , the light reflected at distance r by the n particles contained in volume V . I_{inc} stands for the incident light on the particles. k is the wave number, F is a dimensionless function of the orientation of the particle and the state of polarization of the incident light and A is the projected area of the volume. The relative pixel intensity refers to the amount of light or the numerical value of a pixel in the high speed image. The image gray scale levels can therefore directly be used as a representative value for the relative particle concentration, which will be used for the powder characterization. Since only a relative value for the particle concentration is needed to find the powder focal plane (corresponding to the maximum intensity on the image), no calibration is required.

2.2. Results: Powder-gas nozzle jet characterization

2.2.1. Back-light jet characterization

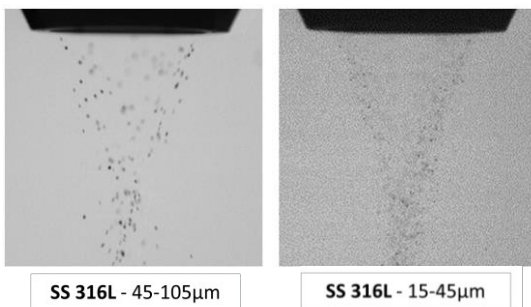


Fig. 7. Raw back-light images : SG 3.5l/min, CG 8l/min, FR 5 g/min (up), zoom raw back-light images (down).

The raw images obtained with the back-light configuration for both powder distributions are shown in Fig. 7. The nozzle tip is visible in black on the top of the images. The powder jet images are acquired with maximal camera aperture in order to reduce the camera focal plane width as much as possible. Care is taken to align the camera focal plane halfway the nozzle depth in order to obtain the largest vertical triangle cross section of the jet cone with the laser light. In this way, the system is optimized to catch non-blurry metal particles only in 1 plane, namely the camera focal plane. The high speed images of the 45-106 μ m particles are acquired at 5400 fps with 25 μ s exposure time.

Note that the images for the 15-45 μ m particles are generally darker and have a lower signal to noise ratio due to the higher fps (9000 fps) and lower exposure time (6.5 μ s) needed to properly catch the particles. This can be explained by their faster travelling speed (reduced mass per unit) and by their smaller diameter that therefore reduces the number of pixels per particle as well as the contrast between particle and background. It is observed in the images that not all the particles are travelling at the same speed due to shape and diameter differences between particles. All the results shown in the present paragraph will be given for the following reference set of gas settings : SG 3.5l/min, CG 8l/min, FR 5 g/min.

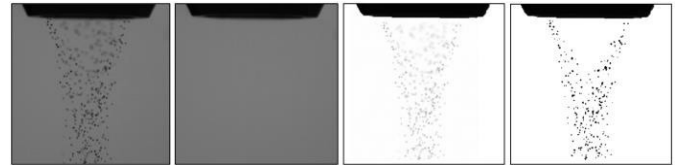


Fig. 8. Image post-processing (256x256px) ((1) raw image, (2) background, (3) background subtraction, (4) final image).

An image post-processing algorithm is set up using the Image Processing Toolbox of the Matlab Mathworks[®] software to improve the quality of the raw high-speed images of the powder jet. For every measurement, a background subtraction is applied on every image to improve the contrast and measurement quality. The contrast of the images is further increased by applying a sequence of image post-processing techniques. The exact location of the nozzle tip is determined by means of image binarization (imbinarize function). This allows to resize the image (256x256px) and only consider the powder jet. Next, the powder jet image intensity is scaled within the interval [0,1] to obtain a relative intensity value (rescale function). The 0-value (black) represents a zero pixel intensity and the 1-value (white) a maximum pixel intensity, corresponding to the maximal powder concentration. Finally, the complement of the image is taken to improve the readability of the results (imcomplement function) and the blurry (out of camera focal plane) particles are discarded by applying image binarization with threshold, see Fig. 8.

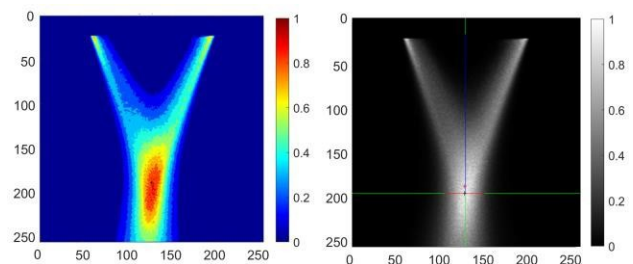


Fig. 9. Particle concentration map (left), stand-off and powder-jet focus diameter identification (right).

The particle concentration or pixel intensity map of the gas-powder cone is then obtained by averaging 30k post-processed images and is shown in Fig. 9. A convergence analysis is completed to find the optimal number of frames needed for the averaging in order to reduce the processing time as much as possible. As can be observed on the particle concentration map, the powder stream diverges into a wider stream from the

moment it exits the nozzle channel. It was noticed from the high speed images that smaller particles travel at higher velocities and therefore diverges less when exiting the nozzle. As stated by Lin [10], an inner stream core with higher powder concentration is observable, which is surrounded by an outer stream shell with lower concentration. This coincides with the typical Gaussian distribution of powder streams.

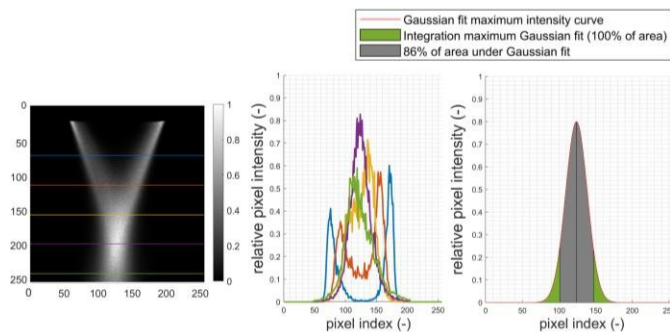


Fig. 10. Scan of post-processed image (left), relative pixel intensity profile at 5 heights under the nozzle (middle), extraction of stand-off distance (right).

Image intensity curves are extracted from the averaged image for every pixel line (horizontal) and pixel column (vertical). An example is given for 5 pixel lines in Fig. 10, left and middle image. A one-term Gaussian fit is applied on all the intensity/concentration profiles (for both lines and columns). The height along the powder cone at which the maximal peak value of the horizontal Gaussian intensity profiles arises, defines the stand-off distance. The powder-jet focus diameter is defined as the minimum width (or diameter) of the particle cone that contains 86% of the total amount of particles at the corresponding stand-off distance, see right graph of Fig. 10. The associated calibration is performed based on the nozzle diameter that can be extracted from the images and has a known measured value. The total processing time required to obtain the values for stand-off distance and powder-jet diameter ≈ 8.5 min per set of gas settings.

The powder-jet focus diameter and stand-off distance are respectively indicated in red and blue on Fig. 9 (right). Both green lines are used to highlight respectively their height and axial position. The same measurement and post-processing is performed for 27 different gas/powder settings chosen within the optimal setting range of the COAX-40-S nozzle. The measurements are carried out for both 45-106 μm (thick lines) and 15-45 μm (thin lines) powder and PF 7 g/min and are shown in Fig. 11. The same set of measurements was performed for PF 3 and 5 g/min but are not shown here. The obtained values for the stand-off distance and powder-jet focus diameter are respectively situated in the ranges [6.3-7.8]mm and [1.5-2]mm for the 45-106 μm particles and [6.9-8.9]mm and [0.63-1.1]mm for the 15-45 μm particles. As can be concluded from the graphs, an increasing SG results in a small increase stand-off distance and powder-jet focus diameter. The SG pushes the powder focal plane down and has a broadening effect on the powder cone. On the other side, a higher CG decreases the stand-off distance and flattens the powder cone due to the higher carrying force applied by the CG on the particles. No effect of the CG on the powder-jet focus diameter seems to be

observable in the present results. Increasing the PF increases both the stand-off and powder-jet focus diameter. This was clearly observable for FR values higher than the one presented here. The effects described above seems to be more pronounced for increasing powder volumetric flow rate (effects more pronounced for 7g/min w.r.t. 3g/min).

To finish, the reduction of the particle diameter of the metal powder reduces the powder-jet focus diameter in a significant way and increases the stand-off distance. The use of smaller metal particles allows a reduction of powder-jet focus diameter up to 50% for the powders used for these experiments. Therefore, to increase the powder efficiency for a given laser spot size, smaller particles should be used carried by CG with higher volumetric flow rate. In this way, more metal particles will be caught by the melt pool, the overall powder efficiency will increase and the powder waste will be reduced.

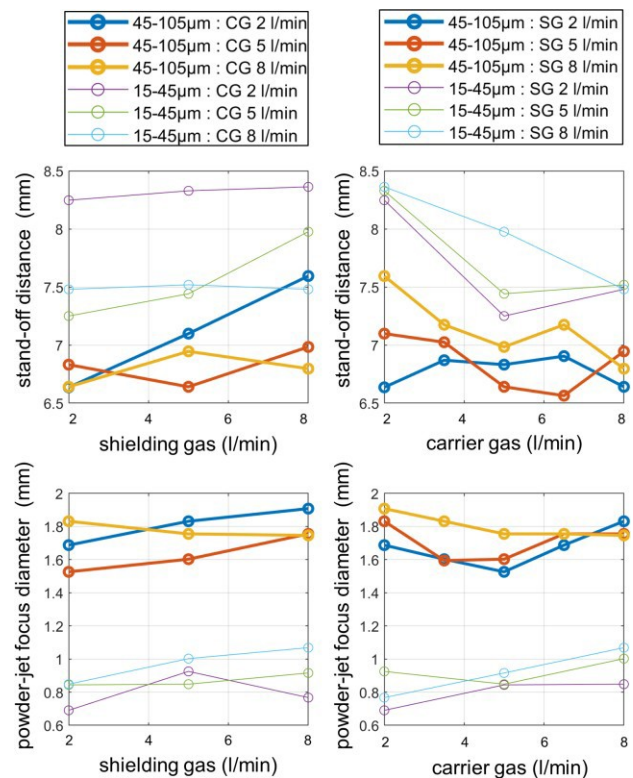


Fig. 11. Back-light results : Effect of shielding gas (left, for constant CG) and carrier gas (right, for constant SG) on stand-off distance (up) and powder-jet focus diameter (down) for FR 7g/min of 15-45 μm (thin lines) and 45- 106 μm 316L powder (thick lines).

2.2.2. Horizontal laser sheet jet characterization

The horizontal laser sheet jet characterization is presented only for the reference set of gas settings (SG 3.5l/min, CG 8l/min, PF 5g/min). The laser sheet has a fixed position during the measurements and the z-position of the nozzle is varied in order to scan the complete powder cone. Fig. 12 (up) gives a superposition of the results at 5 different z-positions of the nozzle (taken with Basler cameras). A lowering of the powder focus diameter is observed for increasing stand-off distance till reaching the focal point, after which the powder cone diverges

again. This corresponds to the observations made in the back-light results. On the high exposure images taken at focal height shown in Fig. 12 (down), the powder cone itself and powder slice at stand-off distance are shown for both particle distributions. A smaller focus diameter is observed for the smaller particles of diameter 15-45 μm .

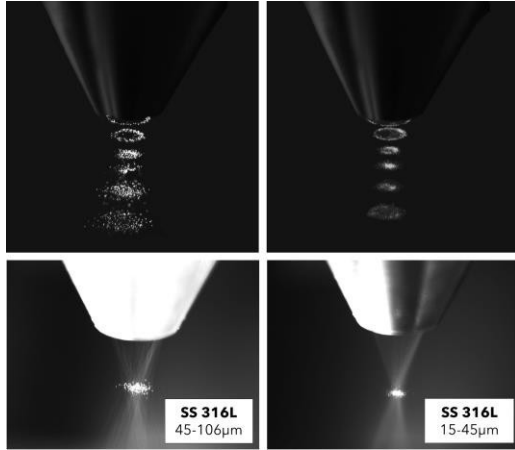


Fig. 12. Side view raw images horizontal laser sheet illumination (up) short exposure at 5 nozzle distances (down) long exposure in powder focal plane.

The corresponding quantitative results shown in Fig. 13. are extracted from the front view high speed camera images. As for configuration 1, a convergence analysis is performed to define the required number of images for averaging. Similar post-processing of the images is applied. The intensity/concentration curves are extracted from the mean image at different stand-off distances (up left), and their local maxima (middle) is used for the powder cone reconstruction (up middle, right). Based on these results, stand-off distance and powder-jet focus diameter are extracted. Note that in comparison to the back-light configuration, several measurements (for different z-positions under the nozzle) are needed to reconstruct the powder cone of 1 set of gas settings. This increases the processing time in an important way.

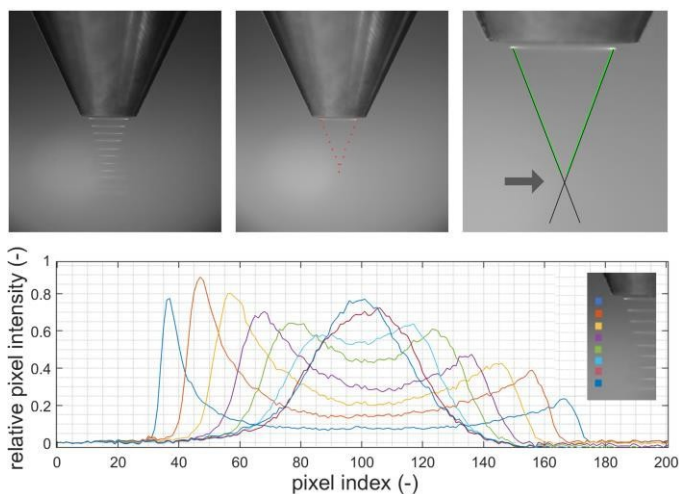


Fig. 13. Superposed front view averaged images (up left), local maxima of intensity Gaussian fits (up middle), stand-off distance definition (up right), relative pixel intensity curves (down).

2.2.3. Vertical laser sheet jet characterization

As for the previous measurements, the same reference settings are considered and similar post-processing techniques are applied. It is clearly observable in Fig. 14. that the smaller particles (15-45 μm) are reflecting less light as the larger ones (45-106 μm) due to their reduced mean diameter. The present optical measurement shows the advantage of only capturing particles in 1 plane, avoiding the need of post-processing to discard particles that are out of camera focal plane (as it is the case for the back-light method). This is clearly visible on the averaged image, in which the inner empty cone (without particles) of the jet is defined more precisely and is deeper w.r.t. the back-light method. Also here, stand-off distance and powder-jet focus diameter are extracted in the same way as described for the back-light method. The processing time is similar to the back-light configuration.

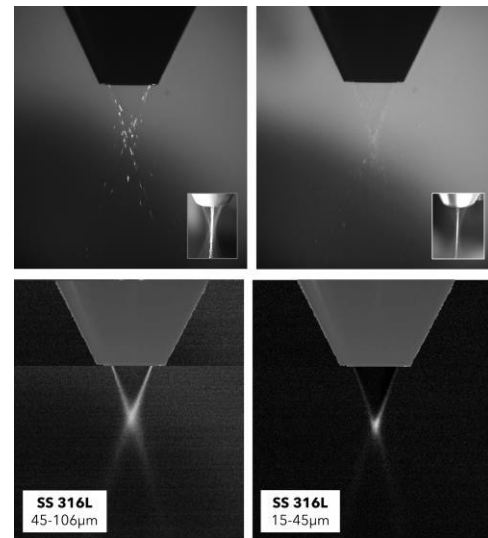


Fig. 14. Front view raw images vertical laser sheet illumination (up), average front view images (down)

2.2.4. Comparison of the optical methods for reference settings

The results (stand-off distance and powder-jet focus diameter) for the 3 experimental configurations given in Table 1 highlights a concordance and similar trend for the different optical methods. The back-light and horizontal laser sheet results are coinciding for both particle diameter ranges (between 2-7% error with respect to the back-light results). For the vertical laser sheet visualization a small overestimation (15-25% error) is observed. This overestimation can be explained by the choice of a slightly to high exposure during the measurements. However, to relatively compare the effect of gas/powder settings on the powder-jet, the 3 techniques/configurations showed their efficiency and can be used separately. The horizontal laser sheet method requires more processing time than the 2 other configurations. On the other hand, the horizontal and vertical laser sheet configurations show the advantage of not needing to discard out of camera focal plane particles.

Table 1. Comparison of optical methods for reference settings : SG 3.5l/min, CG 8l/min, FR 5 g/min.

Optical set-up	Powder diameter range (μm)	Stand-off distance (mm)	Powder-jet focus diameter (mm)
Back-light	45-105	6.90	1.77
	15-45	7.21	0.99
Horizontal laser sheet	45-105	6.99	1.89
	15-45	7.14	0.95
Vertical laser sheet	45-105	6.95	2.27
	15-45	7.44	1.14

2.3. Laser-based DED powder efficiency

The laser-based DED printer on which the experiments are performed is equipped with an invisible (infrared) redPOWER® QUBE fiber laser of 1064nm with power of 2kW. The diameter of the laser beam is theoretically 1mm (considering the optics present in the nozzle head) and follows a near flat-top intensity profile. Fig. 15 shows an image taken with an optical metallographic microscope of a polished cross section of a DED printed track with the reference set of gas settings (SG 3.5l/min, CG 8l/min, FR 5 g/min).

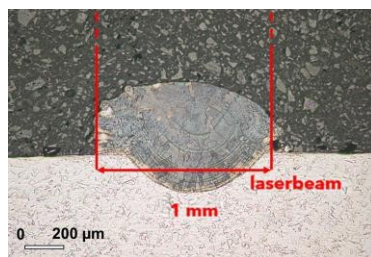


Fig. 15. Optical metallographic microscope image of DED printed track (SG 3.5l/min, CG 8l/min, FR 5 g/min).

The laser spot size is indicated in red and the track width can be extracted based on the observable change in microstructure between built plate and track. From the previously presented measurements, the choice of optimal gas/powder settings is important to decrease the powder-jet focus diameter, in order to have a higher number of metal particles reaching the melt pool. This results in an increasing powder efficiency and therefore in a higher layer thickness. Consequently, the ratio of laser spot size (or melt pool width) and powder focus diameter is a very important parameter that should be maximized to obtain a high powder efficiency and consequently a high process efficiency. Moreover, it was observed that this ratio is also essential to achieve a good printing quality.

$$e_{\text{powder}} \sim \frac{d_{\text{laser beam}}}{d_{\text{powder-jet}}} \sim \text{gas powder settings}$$

3. Conclusion

The results show that the powder-gas jet (in terms of stand-off distance and powder-jet focus diameter) and consequently the powder efficiency are affected by the chosen gas and powder

settings (SG, CG, PF, particle diameter distribution). The three optical methods presented in the study give comparable results and the same trends. However, care should be taken for the choice of the image recording parameters (exposure time and frames per second). The optical measurement with smaller metal particles are less straightforward and require more post-processing since the particles reflect/attenuate less light. A solution would be to increase the light source intensity to make the particles scatter/attenuate more light and to increase the signal-to-noise ratio. Note that the experimental measurements based on high speed imaging techniques are computationally expensive in terms of data storage and post-processing. The powder efficiency can mainly be improved by using metal particles with smaller diameter. In terms of gas settings, a high CG volumetric flow rate combined with a not too high SG volumetric flow rate is reducing the powder-jet focus diameter and therefore has a positive impact on the amount the powder reaching the melt pool, and consequently improves the powder efficiency.

Acknowledgements

This research work was financed by the OZR mandate (No. VOZ/R\&D/2018009) of the Vrije Universiteit Brussel.

References

- [1] S. M. Thompson, L. Bian, N. Shamsaei, A. Yadollahi, An overview of direct laser deposition for additive manufacturing: Part i: Transport phenomena, modeling and diagnostics, *Additive Manufacturing* 8 (2015) 36–62.
- [2] W. Devesse, D. De Baere, P. Guillaume, Modeling of laser beam and powder flow interaction in laser cladding using ray-tracing, *Journal of Laser Applications* 27(S2) (2015) S29208.
- [3] Lamikiz A, Taberero I, Ukar E, Martinez S, de Lacalle LNL, Current designs of coaxial nozzles for laser cladding. *Recent Patents on Mechanical Engineering* 4(1) (2011) 29–36 doi:10.2174/2212797611104010029
- [4] N. Shamsaei, A. Yadollahi, L. Bian, S. M. Thompson, An overview of direct laser deposition for additive manufacturing: Part ii: Mechanical behavior, process parameter optimization and control, *Additive Manufacturing* 8 (2015) 12–35.
- [5] P. Balu, P. Leggett, R. Kovacevic, Parametric study on a coaxial multi-material powder flow in laser-based powder deposition process, *Journal of Materials Processing Technology* 212 (2012) 1598–1610.
- [6] H. Pan, T. Sparks, Y. Thakar, F. Liou, The investigation of gravity-driven metal powder flow in coaxial nozzle for laser-aided direct metal deposition process, *Journal of Manufacturing Science and Engineering* 128(2) (2006) 541–553.
- [7] S. Zekovic, R. Dwivedi, R. Kovacevic, Numerical simulation and experimental investigation of gas-powder flow from radially symmetrical nozzles in laser-based direct metal deposition, *International Journal of Machine Tools & Manufacture*, 47(1) (2007) 112–123.
- [8] Kovalev, O.B., Zaitsev, A.V., Novichenko, D., Smurov, I., Theoretical and experimental investigation of gas flows, powder transport and heating in coaxial laser direct metal deposition (DMD) process, *Journal of Thermal Spray Technology* 20 (2010) 465–478.
- [9] Mann, S., Nottrodt, O., New sensor and system technology for higher process stability in LMD, Conference on Additive Manufacturing Technologies; Bangalore, India, (February 2019) doi: 10.1117/12.2506776
- [10] Lin, J., Concentration Mode of the Powder Stream in Coaxial Laser Cladding, *Opt. Laser Technol.*, 31(3) (1999) 251–257.
- [11] Pinkerton, A. J., and Li, L., Modeling Powder Concentration Distribution from a Coaxial Deposition Nozzle for Laser-Based Rapid Tooling, *J. Manuf. Sci. Eng.* 126(1) (2004) 33–41.

11th CIRP Conference on Photonic Technologies [LANE 2020] on September 7-10, 2020

Concept development for the generation of support structures in the laser metal deposition process

Jan Marx^{a,*}, Magnus Thiele^a, Cemal Esen^a, Andreas Ostendorf^a

^aApplied Laser Technologies, Ruhr University Bochum, Universitätsstr. 150, 44801 Bochum, Germany

* Corresponding author. Tel.: +49-234-32 29083; fax: +49-234-32 14259. E-mail address: marx@lat.rub.de

Abstract

For most additive manufacturing technologies, complex components require a support structure for thermal dissipation and printability. This paper shows for the laser metal deposition process, how weld spot pillars can be used as a support structure for surfaces with large overhangs produced on a three-axis system. A self-written software is used for generating machine and motion sequences, where layered construction of these structures is not mandatory. In the first step, parameters for generating different build strategies of single pillars were found. In a second step, different concepts of combining pillars are presented and compared.

© 2020 The Authors. Published by Elsevier B.V.

This is an open access article under the CC BY-NC-ND license (<http://creativecommons.org/licenses/by-nc-nd/4.0/>)

Peer-review under responsibility of the Bayerisches Laserzentrum GmbH

Keywords: laser metal deposition; support structure; build strategies; lattice structure

1. Introduction

The vision of additive manufacturing (AM) is to produce functionally integrated components faster and faster and with less rework [1]. The laser metal deposition (LMD) technology is a manufacturing process, which allows high deposition rates up to 9000 mm³/min [2]. This is why it has become an established technique for laser cladding. Advanced process control allows generating whole components by using the LMD technology [3]. For creating components with large overhangs, it is necessary to place support structures below the overhanging surfaces. While those structures are commonly used and optimized in the selective laser melting (SLM) process [4], there are only a few approaches for generating slender structures in the LMD process. A first approach for generating LMD lattice structures on a three-axis machine is given by Sharma et al. [5]. The basic elements of these lattice structures are columnar built up pillars, generated by stacking spot welds.

To be used in the support structure, these pillars have to be optimized. Therefore, different requirements are placed on the

design of these structures. The thickness of the pillars is important for connecting them to the surface of the component. For the metal-based AM-processes the constructive parameters of the support structure are also important for stabilizing components against thermomechanical effects [6]. In contrast, filigree structures are desired for easy removal and fast processing. The following concept development aims to find the right balance between these two opposing goals. It is divided into two steps. At first, the design of single pillars is optimized. The second step concerns the combination of the pillars into a single structure.

2. Materials and methods

The experiments are performed on a three-axis processing machine (ORLAS Cube 450, Coherent Laser) equipped with a 1070 nm fiber laser. An external powder feeder conveys 316L stainless steel powder (particle size 53-90 μm). The powder is deposited to the substrate (stainless steel) through a coaxial nozzle. Nitrogen is used as inert gas and is also fed through

the nozzle. At the start of each experiment, the distance between the nozzle and the substrate is set to 8 mm, which is behind the focal spot. The machine and motion sequences are generated by a self-written software. This way a layer-by-layer deposition is not mandatory. The pillars are created by stacking spot welds. For this, the machine repeats a cycle of turning the laser on, exposure, turning the laser off and moving the z-axis upwards by one layer height until the desired total height is reached. The layer height is set to 0.3 mm for all vertical elements of the support structure. For tilted pillars with tilting angles $\geq 30^\circ$ a reduction to 0.15 mm is needed. The exposure time for the last layer is reduced, if the total height cannot be divided by the layer height without remainder. The powder feeding is not stopped during the whole process. If pillars higher than 7 mm are built close to each other, the process has to be divided into two sections. Otherwise there is a risk of a collision between the nozzle and adjacent pillars. An algorithm is used for automatic dividing of large pillars and finding a suitable order for creating a large number of pillars.

3. Results and discussion

3.1. Creating single pillars

In order to precisely adjust the diameter and height of the columns, the influence of the parameters focal spot diameter, powder feeding, laser power and exposure time are examined.

The focal spot diameter is varied from 0.6 to 3.1 mm. In the range from 0.6 to 2.1 mm the differences of height and diameter are below the usual process fluctuations. At higher focal diameters the total height of the pillars is reduced, while the diameter increases. For focal diameters of 3.1 mm or more, the laser power (in these experiments 112.5 W) is not sufficient to melt the substrate. For the aim of creating filigree support structures, the focal diameter is set to 1.6 mm for all further experiments.

The powder feed rate cannot be changed abruptly during the process, so there are efforts to find parameters to keep the feed rate constant during the whole process. In these experiments pillars can be generated by powder feed rates from 2.4 g/min upwards. Higher powder feed does not result in greater pillar diameters, but there are fewer diameter variations over the pillar height. The lateral surface of the pillars is more even. These advantages are of great importance when building highly tilted pillars. For getting high quality results with acceptable material costs, the powder feed rate for further experiments is set to 4.8 g/min. This setting can be used for support structures as well as for the components placed on them.

The influence of the laser power on the pillar geometry is shown in fig. 1. The exposure time for these experiments is set to 1 s. Laser powers below 90 W lead to failed processes in most cases. This is because the distance between nozzle and melting pool rises during the process, until it reaches a distance, where the spot diameter is too great to melt more material. In the range of 90 to 180 W the pillar height is almost constant. Above 180 W the pillar height decreases due to the fact that the top of the pillar melts away.

The diameter of the generated pillars is measured at the bottom and close to the top of the pillar. For the upper measuring point, there is a clear correlation between pillar diameter and laser power. For filigree structures, the laser power should be set as low as possible. For further experiments the laser power is set to 112.5 W, to obtain thin pillars and no risk of process failure due to low laser power. In addition, at this point there is the least process fluctuation.

In every experiment pillars are obtained with their smallest diameter at the connection to the substrate. This leads to low stability at this point, so there is a high risk of breaking connections caused by the inert gas flow or weight forces. As fig. 1 shows, this problem cannot be solved by increasing the laser power. Also, a longer exposure time does not lead to more stable connections. On closer inspection one can see, that the pillar is cooling down very fast at the start of the built process, because of the heat flow into the substrate. For solving this problem an additional design element is required. A grid of weld seams is placed under each support structure. Each line is exposed three times with a feed of 10 mm/s and a powder feed rate of 4.8 g/min. The laser power is set to 315 W. The result is shown in fig. 2. Pillars are set on the intersections. With this connection, pillars are no longer blown away by the inert gas flow and no tipping over under their own weight has been observed.

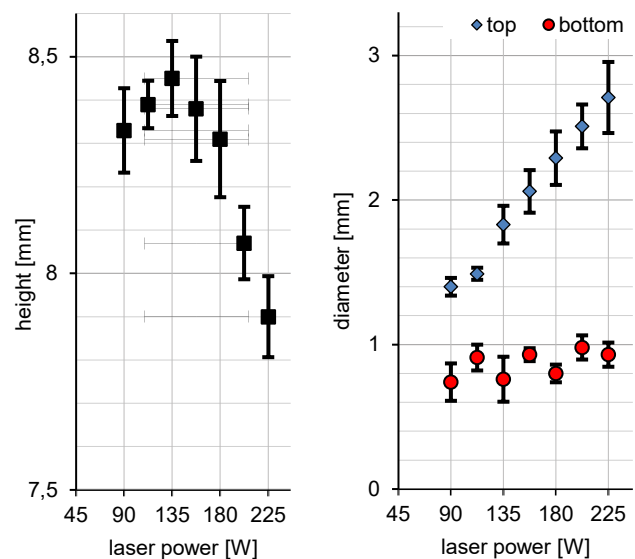


Fig. 1. Height and diameter of pillars at different laser power

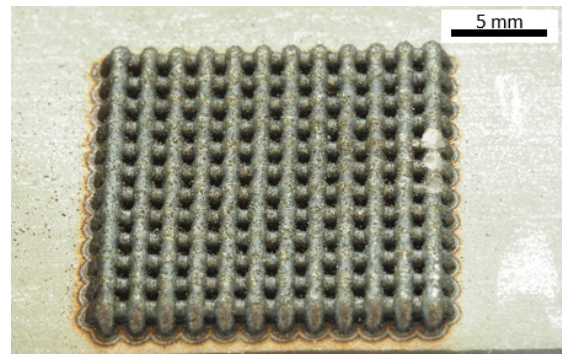


Fig. 2. A three-layer grid on the substrate is used for stabilizing the connection to the support structure

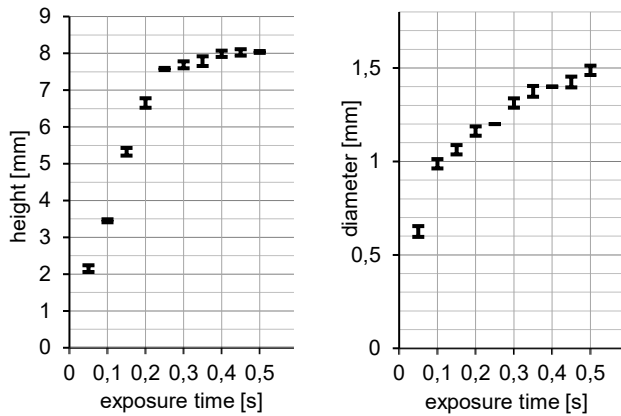


Fig. 3. Height and diameter of pillars at different exposure times

The exposure time of a single spot weld has a large impact on the pillar geometry. For the height, as well as for the diameter longer exposure means higher values (fig. 3). The standard deviation is low for almost all exposure times. Therefore, the adjustment of the exposure time is a suitable method for a specific adjustment of the characteristics of the support structure. The curve in the left diagram can be explained by observing the melting process. During the deposition of a single spot, the gap between nozzle and pillar head decreases. For the first 0.2 seconds, this process is rapid. Afterwards the growth is slowing down due to the fact, that the focal point of the coaxial powder feeding is not in the melting pool anymore. This explains the lower inclining of the curve for values above 0.2 s.

In all experiments described above, the nozzle moves 5 mm upwards. One can see, that the resulting pillar is higher than this value. To still be able to set the desired height, a connection between axis movement and pillar height must be made. The connection varies depending on the chosen parameters. For the exposure times 0.25 s and 1 s, this curve is shown in fig. 4. With this diagram the needed axis movement can be read off easily for different pillar heights. For very high pillars, the deviation between axis movement and pillar height becomes constant. Using the findings from fig. 3 and 4, it is possible to adjust height and thickness of a support structure precisely. Weighing of the samples shows, that the degree of material utilization is 8-9 % for building the support structure.

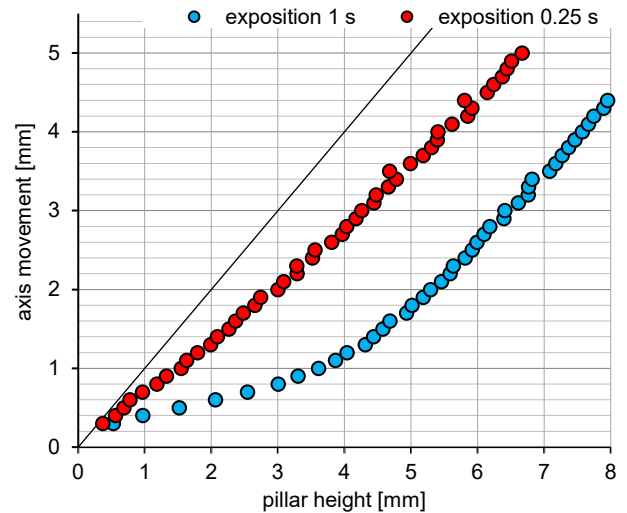


Fig. 4. Correlation between axis movement and pillar height for different exposure times

Table 1. The height of the support influence zone for different exposure times and pillar distances (layer height 0.3 mm, laser power 112.5 W, powder feed rate 4.8 g/min)

No.	Exposure time (s)	Pillar distance (mm)	SIZ
1.	0.25	1.5	5
2.	0.25	2.0	6
3.	0.25	2.5	8
4.	0.25	3.0	11
5.	0.25	3.5	15
6.	0.25	4.0	23
7.	0.25	4.5	23
8.	1	1.5	1
9.	1	2.0	3
10.	1	2.5	8
11.	1	3.0	10
12.	1	3.5	13
13.	1	4.0	15
14.	1	4.5	19

3.2. Connecting pillars to the component

For the examination of the transition between the support structure and the component, lines of parallel pillars were placed on the substrate. On top, welding lines are stacked for building a wall. The distance between the pillars and the exposure time are varied. The results differ in the number of welding lines, that are deposited, until there is a continuous weld seam without any irregularities caused by the gaps between the pillars. In the following, this number is called support influence zone (SIZ). The results are listed in table 1.

The results can be divided into three categories. For components with $SIZ \leq 3$ there is a clear boundary between support structure and component (fig. 5a). For SIZ from 4 to 14 there is an area, where short sections of weld seams form ball-like shapes over each pillar (fig. 5b). The third category is for $SIZ > 14$, where the notches between the pillars cause the failure of the process (fig. 5c).

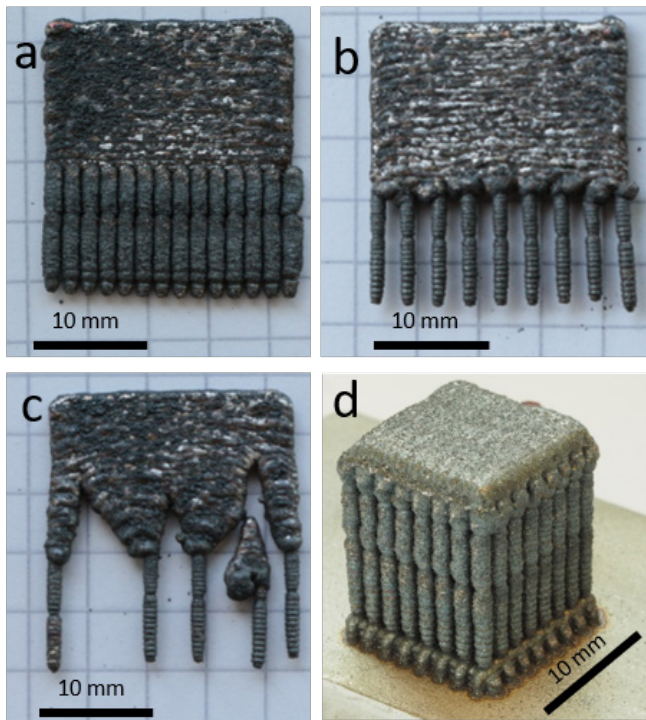


Fig. 5. (a) exposure time 1 s, pillar distance 1.5 mm; (b) exposure time 0.25 s, pillar distance 2.5 mm (c) exposure time 0.25 s, pillar distance 4.0 mm; (d) surface on pillar array

When transferring to the two-dimensional case, the layers of the component are put on a rectangular array of pillars. For the best parameter combination – short pillar distances and long exposure times – the pillar array cannot be built up correctly due to tangential contacts between the pillars. For this reason, only the upper 1 mm of the pillars is processed with the long exposure time of 1 s; below this, the pillar layers are exposed for 0.25 s. With this technique and a pillar distance of 1.5 mm it is possible to create components with $SIZ = 2$ (fig. 5d).

3.3. Design concepts

For complex components, two different types of surfaces have to be supported: The first layer of the component always needs support structure below it (e.g. in fig. 5d). In the following, this surface is defined as base area. The second type of areas are overhanging lateral areas. These are the surfaces, that grow at the side of a component when stacking the layers. Three different pillar-based support structure designs are evaluated for supporting surfaces with different overhanging angles. The surface angle β shall be defined as the angle between the surface normal vector and the horizontal plane. Pillar-based support structures are necessary for surface angles from $\geq 40^\circ$. The first concept is already shown in chapter 3.2 for a surface angle of 90° . As demonstrated in fig. 6a, also for lower surface angle the perpendicular pillars can be used as support. Support structures have a simple motion sequence, so the complete program can be generated from the surface points alone. A disadvantage of this concept is, that the stepped profile of the

different sized pillars supporting a surface with small β is transferred to the components surface.

For reducing this effect, a second concept is developed. Thereby pillars are tilted for keeping them parallel to the surface normal (fig. 6b). The use of those pillars for supporting surfaces is limited to surfaces with $\beta \geq 60^\circ$. Otherwise the melt flows between the pillars. The use of tilted pillars for base areas is not possible due to the fact, that the laser beam exposes the lateral surface of the pillars, which leads to their melting. For the lateral areas of the component, this problem does not exist due to the exposure strategy, so almost stepless surfaces can be generated for $\beta \geq 60^\circ$.

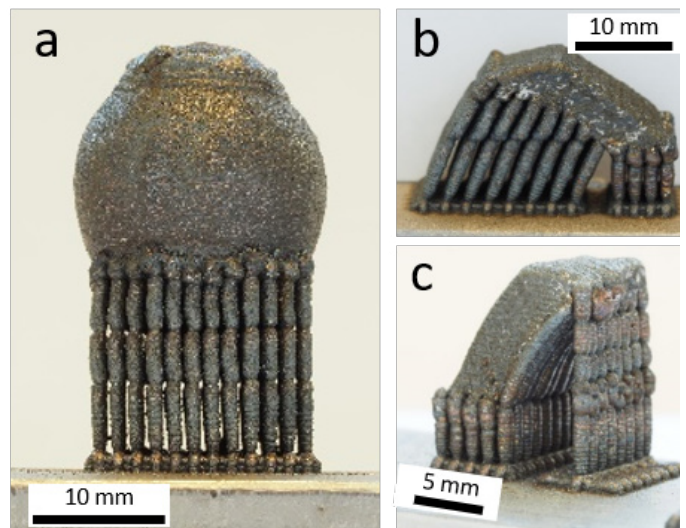


Fig. 6. (a) concept 1: perpendicular pillars; (b) concept 2: tilted pillars; (c) concept 3: pillars parallel to surface

A third concept takes advantage of the fact, that pillars can be tilted further than surfaces. The tilted pillars are fixed at both ends to vertical pillars. The surface of the component is built up on the lateral area of the pillars (fig. 6c). The use of this concept leads to fast processes with easy removal of the component from the support structure. In this case the tilted pillars become a part of the component. The range of application of this concept is limited to β from 40° to 50° . Higher angles lead to high process fluctuations in the tilting angle of the pillars, lower ones cause a collision between nozzle and pillars. Fig. 7 gives an overview; which concept can be used for each particular overhanging surface.

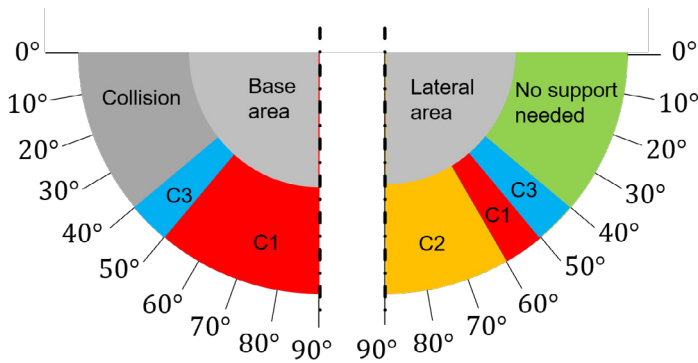


Fig. 7. Recommended use of concepts 1-3 (C1-C3) for different overhanging angles and different surface types

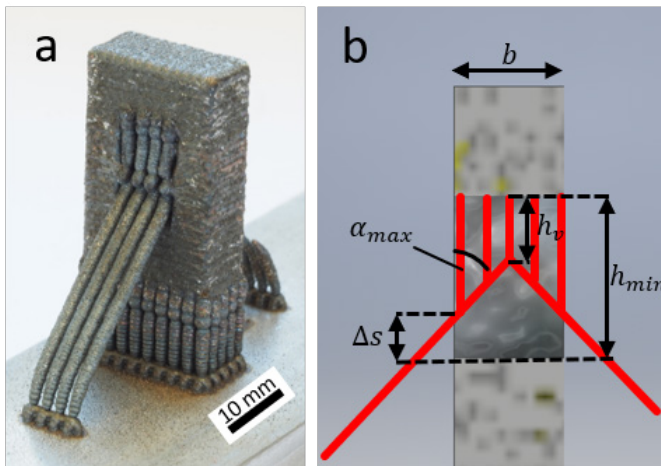


Fig. 8. (a) supported cavity; (b) schematic sectional view of the bridge-structure cavity support

3.4. Combining pillars

To reduce material costs and process time, different approaches were adopted to combine pillars to a lattice structure. Experiments, where more than one pillar is set on the top of the pillar below, failed. Although the tree-formed support structures are built up correctly, the links break up, when trying to deposit the component on top of them. This happens due to thermal stresses. Mostly the last deposited link breaks up first, so we can assume, that pillars must not be set too close to each other for preventing mutual interferences. This cannot be achieved by placing them on the small tops of the lower pillar, but by tilting the lower pillar and placing them on lateral surface. With adding a second counter-tilted pillar and connecting both tops, a bridge-structure is generated.

Another application for bridge-structures is the support of inside surfaces (fig. 8a). The big advantage of these structures is a lateral entry to cavities, which avoids placing them on the surface area below. Due to the maximum pillar tilting angle and the fact, that tilted pillars cannot be used for supporting base areas, there is a minimum cavity height h_{min} , which is

needed for support. It can be calculated by the geometry of the construction (see fig. 8b):

$$h_{min} = h_v + \frac{b}{2 \cdot \tan(\alpha_{max})} + \Delta s \quad (1)$$

α_{max} is the maximum tilting angle, b is the cavity width, h_v is the height of the vertical pillar section, which should be ≥ 5 mm. Δs is a safety factor to avoid welded joints between the tilted pillars and the lower edge of the cavity. It should be at least two times the pillar diameter.

4. Conclusion

There is no single best support method or set of parameters that fits for every support application. Instead the chosen parameters depend on the desired component properties. This paper presents a suitable compromise between the competing objectives of stability, surface quality and process time. It is most useful to adjust the exposure time parameter to adapt to the pillar properties.

It is successfully shown that pillar-based support structures can be used for creating components with large overhangs. This allows creating any geometry with a 3-axis LMD system. Any base area as well as large overhanging sides can be supported by perpendicular pillars. Sides with overhanging angles greater than 60° can be supported by tilted pillars for achieving less rippled surfaces. Surfaces with overhanging angles from 40° to 50° can be supported by pillars that lay parallel to the surface. This method requires high precision in positioning, but it results in components, which are easy to remove from the support structure and have an evenly rippled surface.

References

- [1] Beyer E, Emmelmann C, Overmeyer L, Poprawe, R. Generative Fertigung, WLT-Whitepaper; 2012
- [2] Witzel J, Schrage J, Gasser A, Kelbassa I. Additive manufacturing of a blade-integrated disk by laser metal deposition. In: International Congress on Applications October 23–27; 2011. p. 250-256
- [3] Kaierle S, Barroi A, Noelke C, Hermsdorf J, Overmeyer L, Haferkamp, H. Review on Laser Deposition Welding: From Micro to Macro. In: Physics Procedia 39; 2012. p. 336-345
- [4] Hussein A, Hao L, Yan, C, Everson R, Young P. Advanced lattice support structures for metal additive manufacturing. In: Journal of Materials Processing Technology 213; 2013. p. 1019-1026
- [5] Sharma M, Dobbstein H, Thiele M, Ostendorf A. Laser metal deposition of lattice structures by columnar built-up. In: Procedia CIRP 74; 2018. p. 218-221
- [6] Song J, Chew Y, Jiao L, Yao X, Moon SK, Bi G. Numerical Study of Temperature and Cooling Rate in Selective Laser Melting with Functionally Graded Support Structures. In: Additive Manufacturing 24; 2018. p. 543-551

11th CIRP Conference on Photonic Technologies [LANE 2020] on September 7-10, 2020

LMD coatings as filler material for laser beam welded 30 mm thick plates

Anne StraÙe^{a*}, Ömer Üstündağ^a, Andrey Gumenyuk^a, Michael Rethmeier^{b, a}

^aBundesanstalt für Materialforschung und -prüfung (BAM), Unter den Eichen 87, 12205 Berlin, Germany

^bTechnische Universität Berlin, Pascalstraße 8-9, 10587 Berlin, Germany

* Corresponding author. Tel.: +49 30 8104 4864; E-mail address: anne.strasse@bam.de

Abstract

The development of high energy laser sources enables single-pass welds of thick plates up to 30 mm, but often additional materials are needed to influence the properties of the weld seams. However, the homogenous distribution of filler materials in form of e.g. electrodes is only possible up to 7 mm while the elements are only traceable up to a depth of 14 mm. To overcome this problem a two-step process is used where first the edges of the weld partners are coated with the filler material by laser metal deposition (LMD) and afterwards are welded by laser beam. Single-pass welds with electromagnetic weld pool support of 30 mm thick S355 J2+N-plates with austenitic AISI 316L-coatings were investigated as well as the influence of the coatings to the penetration depth of the laser beam without electromagnetic weld pool support in double-sided joints. The weld seams were tested by X-ray inspection and cross sections.

© 2020 The Authors. Published by Elsevier B.V.

This is an open access article under the CC BY-NC-ND license (<http://creativecommons.org/licenses/by-nc-nd/4.0/>)

Peer-review under responsibility of the Bayerisches Laserzentrum GmbH

Keywords: Laser Metal Deposition (LMD); laser beam welding; filler material distribution; penetration depth

1. Introduction

The development of high energy laser sources opens the market for new applications due to the fact, that plates with higher thicknesses are weldable in a single pass. The advantages of the laser like a low heat input, a high welding speed combined with little distortion are obvious. However, there are two challenges to overcome with this technique and its application for thick plates. The first one relates to a process instability at slower welding velocity, which is required to achieve a full penetration welding with an increasing plates thickness at the limited laser power. This results in a higher volume of molten material and thus a competition of the hydrostatic pressure p_h which is dependent on the plate thickness h with Laplace pressure p_L , which in turn is dependent on the surface tension. If the Laplace pressure cannot compensate the hydrostatic pressure, this results in drop-out on the root side often in combination with melt sagging on the upper side [1]. Common approaches are melt pool support systems or multi-layer welds. Both are time consuming due to

necessary preparations, rework or the higher process times.

Nomenclature

B	Magnetic field in T
F_L	Lorentz force in N
f	Defocussing in mm
f_{AC}	AC-Magnet frequency in Hz
h	Plate thickness in mm
HAZ	Heat affected zone
H LAW	Hybrid laser-arc welding
j	Electric current density in $A \cdot m^{-2}$
LB	Laser beam
LMD	Laser metal deposition
P_{AC}	AC-Magnet power in kW
P_L	Laser power in kW
p_h	Hydrostatic pressure in Pa
p_L	Laplace pressure in Pa
v_s	Welding speed in $m \cdot min^{-1}$

Another, third approach is a non-contact weld pool support system based on electromagnetic compensation of the hydrostatic pressure. It was developed and investigated by Avilov et al. [1] for high power laser welds and further investigated by other authors for the hybrid laser-arc welding (HLAW) process [2]. This compensation works by utilization of an AC-magnet system, which is placed below the specimen and generates an oscillating magnetic field B perpendicular to the welding direction, that in turn induces the electric current density j parallel to the welding direction. The resulting Lorentz force F_L is directed upwards, contrary to the hydrostatic pressure.

The second challenge, which works as a limiting factor at the higher plate thickness is the dilution of the molten material. Many applications need filler materials to influence the weld seam to a certain purpose. A prominent example for this is the usage of filler materials with a higher nickel content for duplex stainless steels laser welding to achieve a higher austenite fraction [3, 4]. Gook et al. [5] showed, that the maximum depth in which the elements of the filler material could be detected is 14 mm and that the distribution through the depth of the weld is uneven for laser hybrid welds, as shown in Fig. 1.

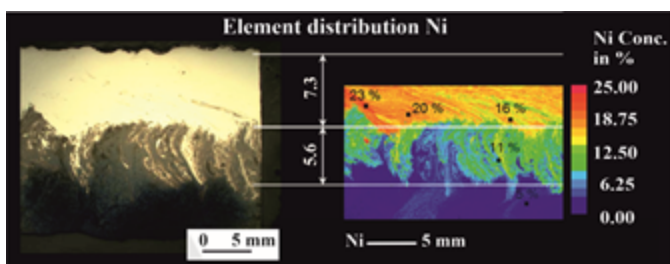


Fig. 1 Element distribution of Ni in length section of laser hybrid welded seam [6]

To overcome this problem different approaches like multi-layer welds with a filler wire or the usage of nickel foils, that were placed between the weld partners were used [3, 7]. For 15 mm thick duplex plates a two-step process was proposed by StraÙe et al. [8], were in the first step the filler material was deposited on the weld partners by laser metal deposition (LMD) and those coated edges were welded by laser beam (LB) afterwards. In this paper two approaches for 30 mm butt joints, single-pass with electromagnetic weld pool support and double-sided joints without the magnetic system are investigated and compared. For both the above described welds a prior coating process by LMD was used.

2. Experimental setup

The base material was a S355 J2+N structural steel with the dimensions of 100 mm x 300 mm x 30 mm. As filler material an AISI 316L-Si austenitic stainless-steel powder with the particle size of 53 μm - 106 μm was used. This material combination has no practical applications. It was chosen, because of the good distinguishability of both phases in microsections and thus to show the effects of both welding approaches. For both materials the chemical composition according to the manufacturers specifications is shown in Table 1.

Table 1. Chemical composition (wt.-%) of the materials

Elements	S355 J2+N (wt.-%)	AISI 316L-Si (wt.-%)
C	0.15	0.01
Si	0.19	2.1
Mn	1.55	0.4
P	0.012	0.01
S	0.003	-
Cr	0.009	17.3
Mo	-	2.5
Ni	-	12.2
Fe	Bal.	Bal.

The coating of the edges was done by LMD with a five-axis Trumpf TruLaser Cell 3000 working station, which is equipped with a 16 kW Trumpf TruDisc 16002 Yb:YAG-disc laser with the wave length of 1030 nm. For the powder distribution a Medicoat Flowmotion Twin powder feeder was used with a powder feed rate of 17 $\text{m}\cdot\text{min}^{-1}$.

The coaxial three-jet nozzle has a working distance of 16 mm with a powder spot diameter of approx. 3.5 mm and the chosen parameters were a laser spot diameter of 2.4 mm, a welding velocity of 1.3 $\text{m}\cdot\text{min}^{-1}$ and a laser power of 1.2 kW. The coating of the edges has been made as a single layer with 21 overlapping tracks with a track width of approx. 2.9 mm and a stepover of 1.38 mm.

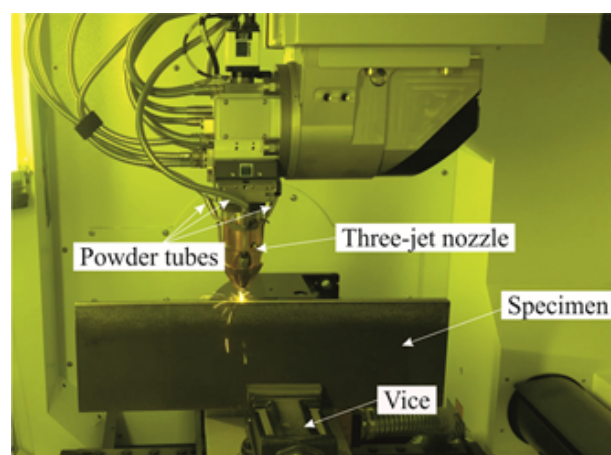


Fig. 2 Experimental setup for the edge coating by LMD

For the laser welding an IPG YLR-20000 fiber laser with a wavelength of 1070 nm, a focus diameter of 0.56 mm and a beam parameter product of 11 $\text{mm}\cdot\text{mrad}$ was used.

The HIGHYAG BIMO HP-Laser processing head with a focal length of 350 mm was mounted on a 6-axis Kuka-robot. The shielding gas (argon) was delivered through a lateral shielding gas nozzle. The experimental setups for the coating and the laser welding are shown in Fig. 2 and Fig. 3, respectively.

For the single-pass welds the AC-magnetic system was installed additionally, with the specimen fixed 2 mm above the magnet poles. Here, instead of the robot with the optical head, the specimen are fixed on a linear axis is moved over the magnetic system.

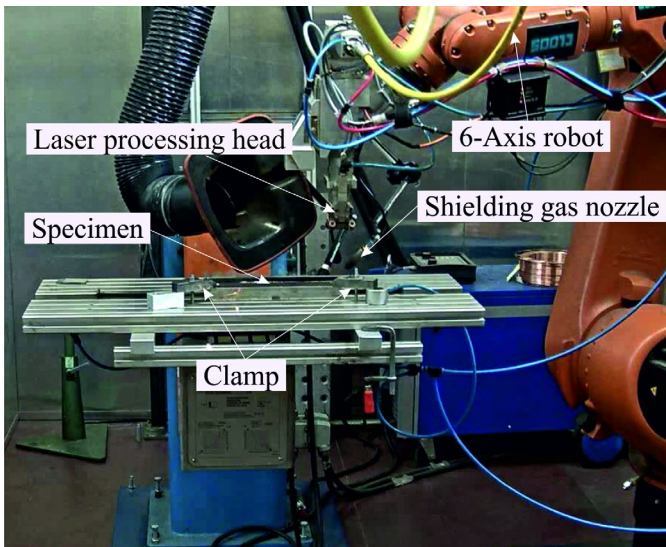


Fig. 3 Experimental setup for the laser welding of the double-sided joints

All weld seams double-sided as well as single-pass were done as butt joints in 1G-position. The welding parameters are listed in Table 2.

Table 2. Welding and AC-magnet parameters

	Single pass welds	Double-sided joints	
		Seam weld	Root weld
Welding speed v_s in $m \cdot min^{-1}$:	0.5	1.6	1.2
Laser power P_L in kW:	18.8	15.6	8.0
Defocussing f in mm:	- 8	- 4	- 4
Magnet power P_{AC} in kW:	2.4	-	-
Frequency f_{AC} in Hz:	1200	-	-

3. Results and discussion

3.1. Edge coating

The outer appearance of the deposition layer of the edges does not perform any obvious oxidation and looks homogenous.

The cross sections display a low dilution (< 20 %) between base material and the filler material, whereas the dilution is defined as the ratio of the volume of the coating material to the volume of the whole molten material and can be deduced from the corresponding areas in the cross sections. Fig. 4 shows a part of the cross section. It is visible, that the upper side is even. The separation between the single tracks is only possible to be recognized by the waviness of the lower section of the coating.



Fig. 4 Cross section of buttered edge

Both mentioned characteristics of the deposited layer, the even upper side as well as the low dilution, are advantageous. The edge evenness is a necessary condition for the following laser welding process for which a technical zero gap is preferred. The thickness of the coating is approx. 0.5 mm and thus sufficient to produce a laser weld within the coated material. In combination with the low dilution, this enables defined weld properties due to a known composition of the filler material, as well as a good connectivity between the base metal and the coating.

3.2. Double-sided joints

The two passes of the double-sided joints showed a good outer appearance with no visible defects. For both passes cross sections were made, to allow an inside impression of the weld's quality (cf. Fig. 5). Those showed solidification cracks and pores for both layers. The formation of hot cracks was investigated by different authors [9-11] and is influenced by a combination of the alloy composition and the welding conditions. The counter pass was done as a partial penetration weld and due to the high cooling rates typical for laser welding the degassing was hindered, which also results in pores and is a known problem for this type of weld seams [12]. Additionally, due to their crystal lattice and thus a lower dissolving ability for low melting elements austenitic stainless steels have a higher susceptibility for hot cracks than mild steels, so cracks were to be expected, but they were not under investigation and thus no efforts were made to prevent them [13].

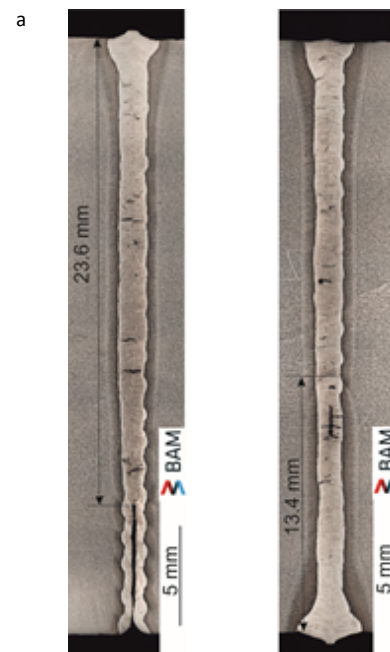


Fig. 5 Cross sections of double-sided joints (a) after the first pass; (b) after the counter pass

Unexpected was the high penetration depth of the first pass. Initially, a welding depth of slightly over half of the material thickness was aspired. With 23.6 mm for the coated edges this value was far higher than expected (< 20 mm [14]) and more than three quarters of the material thickness. This condition can

be explained with the geometry of the coatings. Even though they were quite even, due to the overlapping between single tracks a slight waviness was still evident and thus a wider gap between the valleys of coatings, which allowed for an unhindered passage of the laser beam. The influence of the edge roughness on the penetration depth was also investigated by Sokolov et al. [15] and they confirmed, that a certain roughness as well as a slight increase of the air gap have a positive influence on the penetration depth as well as the weld quality.

This was the reason for an adjustment of the welding parameters to a significant reduction of the laser power for the counter pass. Still the penetration depth was 13.4 mm which resulted in the overlap of approx. 7 mm.

With its slim shape the appearance of the weld seam is typical for laser welds. The low heat input as well as the welding speed allow for only a small volume of molten material. The waviness of the fusion line at the transition to the heat affected zone (HAZ) indicates, that the laser beam only reached the coated areas, as intended to realize known properties in the weld seam, as discussed above.

3.3. Single-pass welds with electromagnetic weld pool support

The single-pass welds also showed a good outer appearance without any visible defects. The cross section is depicted in Fig. 6 and indicates a well-formed weld seam without visible defects apart from a small pore. According to EN ISO 131919-01 the root quality is sorted to the highest evaluation group B.



Fig. 6. Cross section of single-pass weld

The x-ray analysis of the weld seams confirmed that no defects except in the starting and ending region were detected. Those areas are known for defects due a stabilization phase in the beginning and the collapse of the keyhole in the end. Usually this problem is solved by the usage of run-on or run-

off tabs, respectively. Fig.7 shows the x-ray images with the defects highlighted by black circles.

In comparison to the double-sided joints the single-pass welds are wider, with no rest coatings visible. Also, the heat affected zone appears more prominent. This increase of volume of the molten material and the HAZ was to a small part due to the higher laser power of 18.8 kW, but the main reason was the far lower welding speed of $0.5 \text{ m} \cdot \text{min}^{-1}$. Without the electromagnetic support systems such low velocities would result in dropouts in the root region.



Fig. 7. X-ray image of a single-pass weld seam with defects (black circled)

The wider weld seam resulted in a melting of not only the coating but the base material as well. This leads to a change in the composition of the weld seam alloy and thus in a probable change of the properties. To avoid this there are two possible solutions: For one the application of thicker LMD coatings with changed parameters or multiple layers. Another solution is an adjusted element distribution in the powder composition, that reacts to the changed volume of molten material and thus results in the initial aspired properties of the weld seam.

4. Conclusions

The presented two-step process, where the filler material is deposited to the edges of the weld partners by LMD in the first step, prior to the laser beam process as a second step, is a solution to realize a homogenous distribution of the filler material in the weld seam for thick plates.

The double-sided joints showed slim weld seams with a rest coating visible and thus a known element distribution in the molten material but having imperfections like hot cracks and pores.

The single-pass welds with electromagnetic weld pool support allowed for a slower welding velocity. Except for the starting and ending regions, those weld seams were defect free. The weld seams as well as the HAZ were wider due to the higher heat input and all the coating was molten as well as parts of the base material. As a result, the element distribution changed. The knowledge of the geometry and volume of the weld seams enables to adapt the coatings element composition and thus realize the aspired properties in the weld seam. Alternatively, thicker coatings realize the same goal.

Acknowledgements

This work was supported by the Federation of Industrial Research Association (AiF, project number 19.228N) and the German Federal Ministry for Economic Affairs and Energy (BMWi- Bundesministerium für Wirtschaft und Energie) based on a resolution of the Deutscher Bundestag.

References

- [1] V. Avilov, A. Gumenyuk, M. Lammers, and M. Rethmeier, "PA position full penetration high power laser beam welding of up to 30 mm thick AlMg3 plates using electromagnetic weld pool support," *Science and technology of welding and joining*, vol. 17, pp. 128-133, 2012
- [2] Ö. Üstündağ, S. Gook, A. Gumenyuk, and M. Rethmeier, "Hybrid laser arc welding of thick high-strength pipeline steels of grade X120 with adapted heat input," *Journal of Materials Processing Technology*, vol. 275, p. 116358, 2020
- [3] V. Muthupandi, P. Bala Srinivasan, V. Shankar, S. K. Seshadri, and S. Sundaresan, "Effect of nickel and nitrogen addition on the microstructure and mechanical properties of power beam processed duplex stainless steel (UNS 31803) weld metals," *Materials Letters*, vol. 59, pp. 2305-2309, 2005
- [4] A. Karl, "Laserauftragschweißen hochlegierter Duplexstähle," Dissertation, Universität Ilmenau, Ilmenau, 2014
- [5] S. Gook, A. Gumenyuk, and M. Rethmeier, "Hybrid laser arc welding of X80 and X120 steel grade," *Science and technology of welding and joining*, vol. 19, pp. 15-24, 2014
- [6] M. Rethmeier, Gook, S. and Gumenyuk, A., "Einsatz des Laserstrahl-MSG-Hybridschweißverfahrens an längsnahtgeschweißten Großrohren der Güte API-X80/ -X100 zur Steigerung der Zähigkeit und Erhöhung der Wirtschaftlichkeit," Schlussbericht zum Forschungsvorhaben P822 / IGF-Nr. 16415 N2013
- [7] H. C. Wu, L. W. Tsay, and C. Chen, "Laser Beam Welding of 2205 Duplex Stainless Steel with Metal Powder Additions," *ISIJ International*, vol. 44, pp. 1720-1726, 2004
- [8] A. StraÙe, A. Gumenyuk, and M. Rethmeier, "Quality improvement of laser welds on thick duplex plates by laser clad buttering " in *LiM 2019 - Lasers in manufacturing conference 2019, Munich*, pp. 1-6, 2019
- [9] W. S. Pellini, "Strain theory of hot tearing," *Foundry*, vol. 80, pp. 99-125, 1952
- [10] N. N. Prokhorov, "Resistance to hot tearing of cast metals during solidification," *Russian castings production*, vol. 2, pp. 172-175, 1962
- [11] M. Rappaz, J. M. Drezet, and M. Gremaud, "A new hot-tearing criterion," *Metallurgical and Materials Transactions A*, vol. 30, pp. 449-455, 1999
- [12] Z. Yang, X. Zhao, W. Tao, and C. Jin, "Effects of keyhole status on melt flow and flow-induced porosity formation during double-sided laser welding of AA6056/AA6156 aluminium alloy T-joint," *Optics & Laser Technology*, vol. 109, pp. 39-48, 2019
- [13] Masumoto, Tamaki, K., Kutsuna, M., "Hot cracking of austenitic stainless steel weld metal," *Transaction of Japan Welding Society*:1306-1314, 1972
- [14] <https://www.ipgphotonics.com/en/577/Widget/Application+Note+%2311%3A+High+Power+Welding+with+Fiber+Lasers+.pdf>, Last access: 12.03.2020
- [15] M. Sokolov and A. Salminen, "Experimental Investigation of the Influence of Edge Morphology in High Power Fiber Laser Welding," *Physics Procedia*, vol. 39, pp. 33-42, 2012

11th CIRP Conference on Photonic Technologies [LANE 2020] on September 7-10, 2020

The approaches to design and manufacturing of large-sized marine machinery parts by direct laser deposition

Rudolf Korsmik^{a,*}, Igor Tsybulskiy^{a,b}, Aleksander Rodionov^a, Olga Klimova-Korsmik^{a,b}, Maria Gogolukhina^a, Sergei Ivanov^{a,b}, Grigoriy Zadykyan^{a,b}, Ruslan Mendagaliev^{a,b}

^a*Saint-Petersburg State Marine Technical University, Russian Federation*

^b*Peter the Great Saint-Petersburg Polytechnic University, Saint-Petersburg, Russian Federation*

* Corresponding author. Tel.: +7-906-253-62-42; E-mail address: r.korsmik@lrc.ru

Abstract

This article shows several aspects of additive manufacturing via direct laser deposition of machinery parts. The redesigning methods of product manufactured by conventional technologies are considered, taking into account the stress-strain state of a sample manufactured by the DLD-method. Besides modeling methods allow obtaining a product of required geometry, the experience of applying the topological optimization method of structure is demonstrated. The product with optimized design has reliability characteristics close to the original solid version. The differences in the product microstructure obtained by the DLD-method from the structure after casting and thermomechanical processing are shown. The mechanical properties of built-up material are comparable to the same properties after casting and rolling. Economic evaluation of DLD introduction was held. A criterion of advisability replacement to DLD-method of manufacturing is determined. The results prove attractiveness of digital laser technologies application in shipbuilding.

© 2020 The Authors. Published by Elsevier B.V.

This is an open access article under the CC BY-NC-ND license (<http://creativecommons.org/licenses/by-nc-nd/4.0/>)

Peer-review under responsibility of the Bayerisches Laserzentrum GmbH

Keywords: direct laser deposition; distortion prediction; distortion compensation; topological optimization; mechanical properties; economic evaluation

1. Introduction

Until now, the most common method for manufacturing large-sized machinery parts is the cast billets production technology. They are obtained by casting in sand molds, by centrifugal casting in chill molds, and also by investment casting with subsequent time-consuming machining that can remove up to 90% of costly material [1]. With an increase in the accuracy of casting, the volume and cost of subsequent machining decreases, but the costs of producing high-precision castings increase proportionally [2]. The issue of cost reduction is especially relevant in high-tech industries such as aircraft, shipbuilding, engine design, etc [3,4,5]. Additive technologies are replacing the conventional manufacturing methods of joining, casting and milling with decreasing of parts cost. According to experts from The Ulsan

Creative Economy Innovation Center (part of Hyundai Heavy Industries) the replacement of traditional manufacturing techniques for 165 components of marine engineering with additive manufacturing technologies will save \$ 1.8 billion annually [6].

The main development's trend of additive technology is increasing productivity while maintaining required quality of manufactured products. Direct laser deposition is able to satisfy this requirement [7]. Direct laser deposition (DLD, and also known as direct metal deposition – DMD and laser metal deposition - LMD) is the most advanced technology for introducing of large-sized additive manufactured metal products into many industrial areas of mechanical engineering. DLD makes it possible to create parts of complex shape and design in one technological stage without the use of additional equipment [8,9].

The digitalization of production leads to material, time, and cost outgoings to be reduced. Full automation process allows rejecting staff intervention to the process and prevent defects due to lack of its qualifications. That benefits lead to increasing of process efficiency by 10 times and reduces the cost of manufacturing parts by 3 - 5 times. The productivity of process for real products reaches 1.5 - 2.5 kg/h for engineering alloys based on Fe, Co, Ni, Ti and Cu. The typical material utilization rate for large-sized parts is 0.7-0.9. [10,11].

The development of computing technology, the increase in computing power and the emergence of new production technologies leads to changes in approaches to the design of structures. At the forefront is the problem of designing structures under specified quality criteria. This extends the space of using mathematical computational methods during creating new designs and products [12].

Using computer technology, the developer gets a computer model of the part that satisfies all specified operational and technological limitations. At the same time, both traditional engineering and optimization calculations are carried out. The concept formation of the part is carried out using optimization technologies, in particular, topological optimization [13]. Additive technologies as a new class of manufacturing technologies can help reveal the full potential of topological optimization applicability in real parts.

This paper presents authors experience over 3 years of R&D projects with further integration to manufacturing plants of marine machinery parts.

2. Approaches to design

2.1. Distortion prediction and compensation in DLD.

Laser as a concentrated heat source generates a non-uniform temperature field during the build-up of the part. The sharp temperature gradient near the deposited layer causes a non-uniform thermal expansion of the material. Since the adjacent colder metal has a high rigidity the transient compressive longitudinal stress and the plastic strain appear in a heated area [14,15]. The redistribution of the thermal strain during the cooling leads to the compressive stresses are replaced by tensile stresses and the compressive transient plastic strain is partially compensated by the tensile plastic strains. The pattern of residual stresses and distortions depends on part geometry, process parameters, material thermophysical and mechanical properties.

To mitigate residual distortion of built-up parts the different approaches have been proposed. It is shown [16,17] that the level of distortion can be reduced by the development of optimal process parameters or by the use of different toolpath planning strategies. The well-known approaches widely used in welding can be adopted for DLD. For example, welding alternatively on either side of the double V-joint is preferable. The application of this approach in DLD is shown in figure 1. If the part №1 will be completely deposited the cylinder will bend. The subsequent deposition of the part №2 partially compensates distortion. The best practice is

build-up of both components alternatively layer-by-layer on either side.

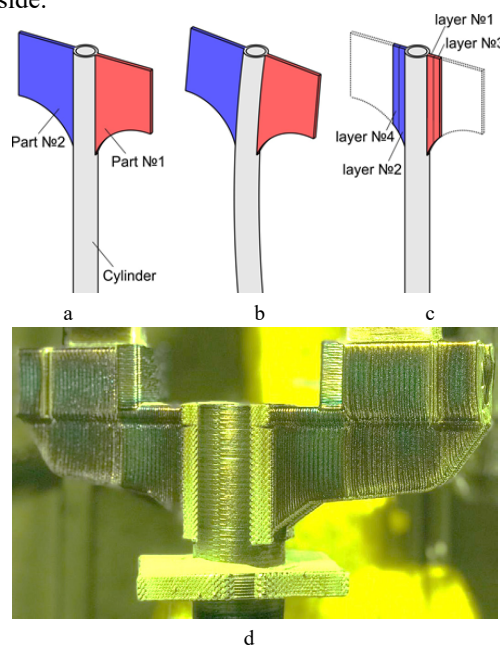


Fig. 1. Schematic of the part (a); one part build-up first (b); alternating build-up (c); built-up product (d).

Required dimensional accuracy of the fabricated part can be ensured by compensation of distortions [18]. To compensate deformations, initial geometry should be pre-distorted. To do this required the final shape of the part manufactured using the original model. The distortion compensation consists of inverting the deformations predicted by FE simulation followed by modifying the original model.

The distortion compensation approach was applied to the hemisphere (figure 2). The simulation of the build-up process for the initial CAD model has been performed using the finite element method. The 4-node axisymmetric elements were employed in 2D model. Deposition of material during DLD was simulated using the so-called element birth technique. The passes geometry was simplified as a cuboid. The obtained distorted shape of the built-up part is shown in figure 3. It is seen that shrinkage of the bulky flange leads to the reduction of the radius by 4 mm near the top of the hemisphere. Radius of curvature in this area is also significantly changed. The flange has a significant deviation from the horizontal axis. In order to obtain part of the required shape and size, the initial CAD model was modified by applying inverted deformations. Comparison of the fabricated part with the initial CAD model is shown a satisfactory agreement.

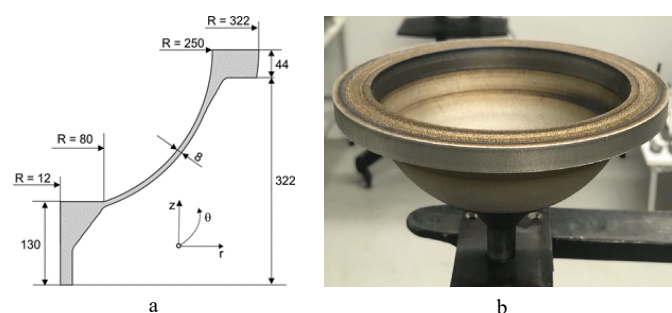


Fig. 2. Schematic of the part (a) and fabricated part (b).

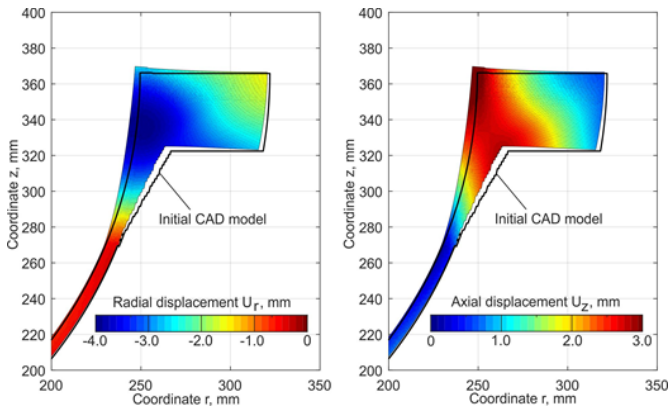


Fig. 3. Simulated radial and axial displacement field during the fabrication of the part using initial CAD model.

2.2. Topological optimization of parts produced via DLD.

As result of topological optimization application in production with help of LMD, the experience of designing and manufacturing of vessel propeller is presented.

The problem of topological optimization, from the point of view of rigidity, is to find the optimal distribution of the material in a given region at given loads. From the condition of stationary total energy of the body in equilibrium state in the possible displacements form principle, minimization of external forces work will correspond to maximization of body rigidity [19].

$$A^{ex}(\delta u) = \delta W(\varepsilon(u)), \quad (1)$$

where A – internal force work, u – displacement, W – potential energy, ε – deformation.

In this case, regions are divided into subdomains of the optimization space and fixed subdomains in which optimization is not performed.

Deformations in the body will be considered quite small, and the volume and surface of the body in the deformed state will be identified by its volume and surface in the undeformed state.

In the process of solving the topological optimization task, for each point of the body, it must be determined whether there is a material in it or not. In the presence of material, the elastic modulus at a point is $E = E_0$. In the absence of material $E = 0$. Thus, the design variables are the elastic properties of the material at each point. Their number is infinite, and they change discretely. The finite element formulation allows us to reduce an infinite number of design variables to a finite number. Further, to apply the methods of mathematical programming, it is necessary to transform the discrete variation of material properties in each finite element to continuous variation. The most popular method is Solid Isotropic Material with Penalization (SIMP) [20], which assumes the presence of an isotropic material at each point of the body, the elastic properties of which are described by a simple relation:

$$E(x) = \rho(x)^p E_0, \quad (2)$$

where ρ is the fictitious density ($0 < \rho < 1$); p is the penalty factor. Thus, if $\rho = 0$, then the elastic properties are also zeroed, which indicates the absence of material. If $\rho = 1$, the elastic properties at the point coincide with the original properties. This method works with isotropic material, and it is accepted as the main method for parameterizing material properties.

To carry out topological optimization of the screw, its finite element model was developed. Since the geometry of the structure is quite complex, a high-precision ten-nodal tetrahedral element was chosen as the main type of the finite element [21], designed to solve various problems of deformable solid mechanics when considering solid-state systems. It is built on a quadratic approximation of displacements and has three degrees of freedom in each node (displacements in the direction of the X, Y, Z axes of the nodal coordinate system).

Optimization calculations were performed separately for the propeller blade and for its hub. When optimizing a rotor blade, it is assumed that the hub is rigidly fixed and, due to the cyclic geometry and external load, optimization of only one blade is considered. When optimizing the screw hub, a complete model is considered, which includes all four blades and the hub itself. Given the accepted system of assumptions, a geometric model suitable for the correct description of finite element method by mathematical models is shown in Figure 4a, 4b.

In order to improve the accuracy of the optimization results, restrictions were adopted on the maximum size of the finite element inside the optimized hub region - 4 mm, for the blade cavity - 2 mm. So the total number of finite elements in the blade model was 332727 pcs, and in the hub model - 1133166 pcs. The results of solving topological optimization task of propeller separately for the blade and hub are shown in Figures 4c, 4d.

The reduction in mass of the blade was 16% relative to its original mass, and 30% for the hub. That allows reducing the weight of the entire propeller by 26%.

Due to the conventionality of calculation methods for assessing the strength characteristics of propellers, using a static distribution of rated pressure, the parameters of the stress-strain state of the optimized version of the propeller were estimated by comparing its stress state with the initial cast version of the solid unit. The von Mises equivalent stress fields in the original and optimized version of the propeller were calculated. It was found that both the character and the general level of the stress-strain state remained practically unchanged. In the optimized version, the maximum stresses are localized on blades' surface near the connection with the hub and increased from 29.3 MPa to 40.7 MPa, i.e. increased by 39%. Thus, we can conclude that propeller with optimized structure has reliability characteristics close to the original solid version.

Figure 4e, 4f, show the manufacturing of hub and blades via DLD. Figure 4g, 4h show built-up propeller before and after CNC-machining and manual polishing.

After all producing stages the propeller was weighted. The weight test showed that the mass is finished product is 105 kg. It is 20% less than original cast design.

Detailed description of design analysis, optimization procedure, properties after optimization and production process are presented in [22].

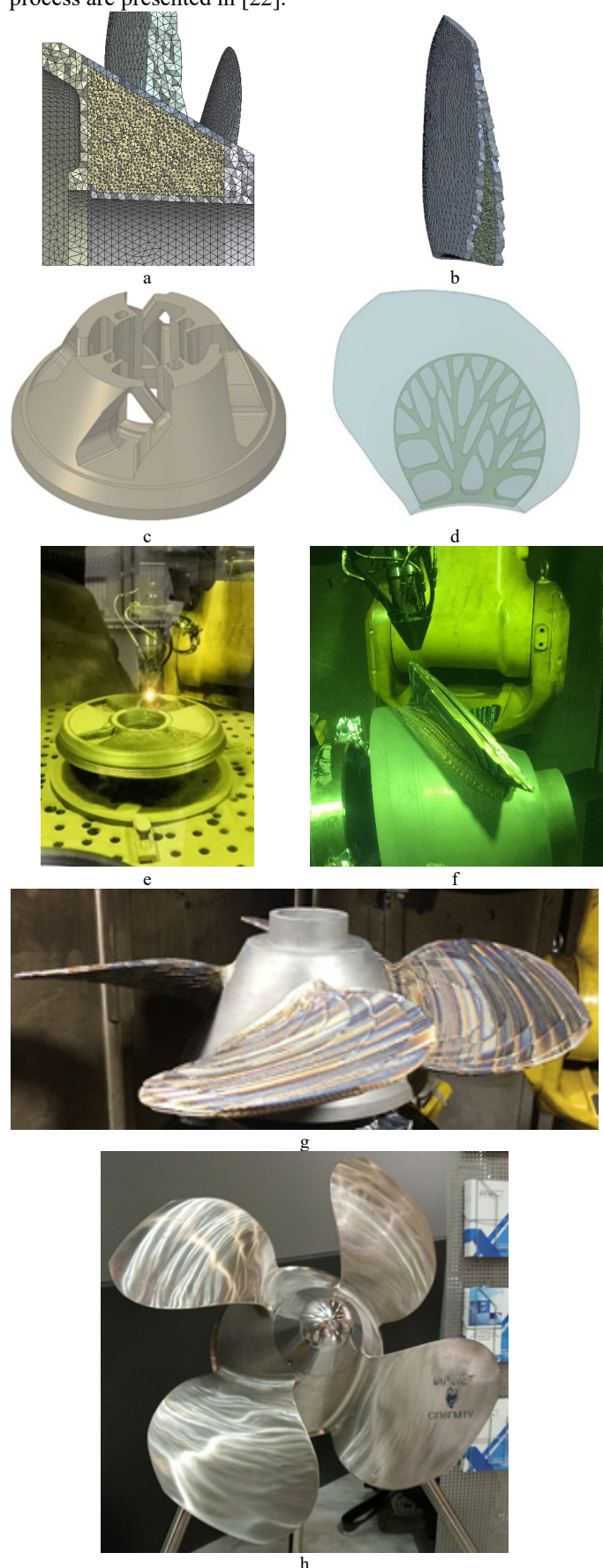


Fig. 4. Stages of topological optimization and manufacturing of vessel propeller.

3. Mechanical properties of DLD of as deposited and heat treated products

Materials used in shipbuilding must have a complex of properties ensuring stable operation at low temperatures. In the manufacturing of products using direct laser deposition technology anisotropy in the structure, and consequently, the properties can be observed in materials. This situation is observed in steels of different classes. This leads to the fact that in the transverse direction plasticity and toughness may be 2-4 times lower in comparison with the longitudinal direction (direction of deposition). In addition, most alloys require heat treatment (HT) to obtain the expected strength and plastic characteristics. Thus, a complete heat treatment is required, which includes homogenization to obtain an isotropic structure and quenching with tempering or aging to obtain the specified mechanical characteristics. Maintenance parameters such as temperature, shutter speed, cooling mode, number of steps are individual for each alloy and require experimental testing. The HT modes from classical metallurgy could be used, but the exposure time and temperature are likely to be different. It is established that the nickel alloy Inconel 625 and titanium alloy TL5 (RU) in the initial state (just after the DLD) have mechanical properties that are not inferior to these alloys in the state of rolled or heat-treated cast. But this is exactly the exception to the rule, which should not be guided. In order to obtain products with the required performance characteristics it is worth initiating the development of a heat treatment process after the DLD. The mechanical properties of as deposited specimens and after HT are summarized in table 1.

Table 1. Mechanical properties after DLD and DLD+HT.

Materials	DLD /HT	Yield	Ultimate	Relative elong., %	Impact tough., J
		strength, MPa	strength, MPa		
06Cr15Ni4-CuMo	Z	858	1093	7,4	12,5
	X	831	1089	8,5	14,8
	HT	766	832	14,5	28,8
08MnCu-NiV	Z	447	524	7,7	21,3
	X	463	550	18,6	44,2
09CrNi2-MoCu [23-25]	Z	563	626	9,7	29,8
	X	515	686	21	57,5
	HT	585	660	23,2	130
In 718	X; Z	339	452	19	63
	HT	1094	1230	16,3	31,5
In 625 [26]	X; Z	479	855	28	-
	Z	742	819	10,5	72,5
Ti5 [27-29]	X	750	826	13,8	75,2
	X; Z	982	1047	10	27,7
Ti-64 [27-29]	X; Z	982	1047	10	27,7
	HT	899	970	10	-

*Z-transverse and X-longitudinal directions of deposited specimen

4. Economic efficiency of DLD

As shown previously, DLD allows manufacturing products with specified geometric dimensions and required operational

and mechanical characteristics. Technically, it means that this method could be applied in fabrication. However, equipment and filler materials for DLD are still quite expensive. This fact affects the production cost of built-up products. Therefore, to assess the feasibility of transition from conventional technological process to DLD-process economic aspects must be evaluated for each product. The production cost of parts manufactured by conventional technologies and DLD-method are compared in this section. Comparing parts, methods of fabrication and using materials are presented in table 2.

Table 2. Comparing data for products, produced by different technologies.

	Material	Weight, kg	Production method	Standard hours	
				Conv. method	DLD
hemisphere	high-strength steel	60	cutting, bending, milling, welding	500	98
propeller	stainless steel	130	casing, milling	150	132
body	Ti-alloy	13	casting	76	26
auger	Ti-alloy	1.5	milling	46	2

Cost of production PC is calculating by equation (3):

$$PC = MC + LIO, \quad (3)$$

where MC = cost of material and LIO = outlay of labour intensity. LIO consists from:

$$LIO = n \times SH + Cost_{SH} + IT + E_A + E_M, \quad (4)$$

where SH = standard hour, n = amount of standard hours, $Cost_{SH}$ = cost of standard hour, IT = insurance taxes, E_A = administrative expense, E_M = manufacturing expense. IT , E_A , E_M are coefficients of $Cost_{SH}$.

Comparing of production cost for conventional technology and DLD is presented in figure 5.

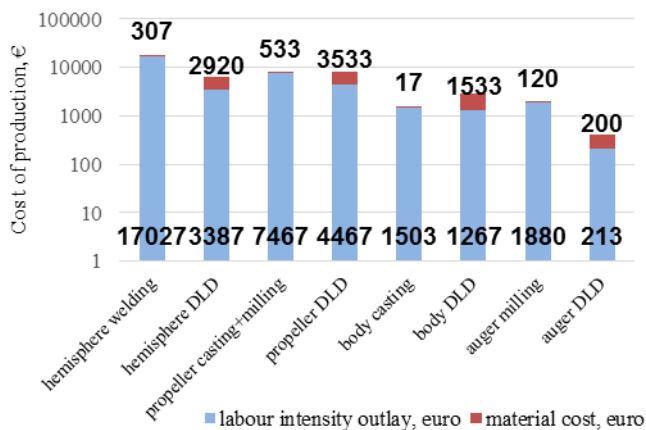


Fig. 5. Cost of production for conventional manufacturing process and DLD. Bottom row – labour intensity outlay, top row – material cost.

As can be seen in figure 1, the production cost of DLD method is lower for the hemisphere and auger by 2.7 and 5.2 times, respectively. For built-up body, on the contrary, production cost is 2 times higher than for conventional technology. For the propeller the ratio of production costs is equal to 1.

Let's consider each indicator for each case more detailed. As can be seen in figure 1, material costs for conventional manufacturing process are several times lower than for DLD-method. Comparison of ratio between material cost and product weight is presented in table 3.

Table 3. The ratio between material cost and product weight for different technology.

	Cost of material, €/kg			
	hemisphere	propeller	body	auger
conventional technology	5.0	4.0	1.5	80.0
DLD technology	49.0	33.5	118.0	133.5

Then let's consider labour intensity outlays. As can be seen in figure 1, labour outlays for DLD-process is lower than for conventional methods. Comparison of ratio between labour intensity outlays and product weight is presented in table 4.

Table 4. The ratio between labour intensity outlays and product weight for different technology.

	Labour intensity outlay, €/kg			
	hemisphere	propeller	body	auger
conventional technology	284.0	57.5	116.0	1253.5
DLD technology	56.0	43.0	97.5	142.0

The DLD production cost almost equally consists material cost (45% - for iron alloys, 55% - for titanium alloys) and labour intensity outlays (55% and 45%, respectively).

Based on data from figure 5 and tables 2 – 4 can be seen, that production cost for conventional technology consists by 94 – 98% of labour intensity outlays. Moreover, material cost is just 2 – 4%. In addition, the material utilization rate in various production processes is more important than the cost of raw material per kg (steel or titanium alloy). In this case material utilization rate increases in further order: auger, hemisphere, propeller, body. In a first approximation, material utilization rate can be used as a criterion for evaluating the feasibility of replacing traditional technology to DLD. Low material utilization rate corresponds to prolonged machining. As a result, high labour outlays and material losses are inherent for the product. For DLD-process the material utilization rate tends to 80% and most of oversprayed powder can be used again after recycling. Some ways, it allows smoothing over the high filling material cost.

Figure 6 shows efficiency of replacing conventional technology by DLD in dependency on material utilization rate.

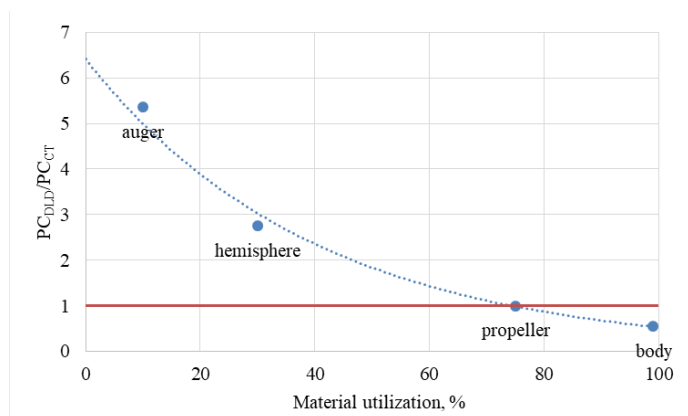


Fig. 6. The efficiency of replacing conventional technology by DLD in dependency on material utilization rate.

Based on data, presented in figure 6, replacement of parts produced with material utilization rate of 75% and higher by casting and insignificant machining to DLD-method is not reasonable. The economic effect of transition to DLD-process increases with increasing of removed material from the billet or with increasing technological operations amount.

5. Conclusions

The direct laser deposition is an advanced production process, which have a big potential of integration many machinery industries including shipbuilding.

The progress in computing technology leads to changes in approaches to the design of structures. This extends the space of using mathematical computational methods during creating new designs and products under specified quality criteria. With help of computational technologies for DLD, it is possible both to design products of required geometry and to create optimized structures of lower weight, ensuring operability under loads.

Subsequent heat treatment is necessary to obtain an isotropic structure and sufficient mechanical properties for the most of products obtained by DLD from metal materials.

The economic effect of replacement conventional manufacturing processes to DLD-process increases with increasing of removed material from the billet or with increasing technological operations amount.

References

- [1] Bogoraz II, Kaufman IM. Handbook of propulsion propeller manufacturing 1978.
- [2] Lysenkov PM, et al. Marine engineering technology. 2016.
- [3] Ageev RV, Kondratov DV, Maslov YV. Polet. Obshcherossiyskiy nauchno-tekhnicheskiiy journal (In Russian). 2013. 6. pp 35 – 39.
- [4] Wilson JM, Piya C, Shin YC, Zhao F, Ramani K. Journal of Cleaner Production. 2014. 80. pp 170-178.
- [5] Dorochoy AF, Abacharev MM Vestnik Astrachanskogo gosudarstvennogo tekhnicheskogo universiteta. Morskaya tekhnika I tekhnologia (In Russian). 2015. 2. pp 42 – 47.
- [6] World's Largest Shipbuilder, Hyundai Heavy, to Focus On 3D Printing Ship Parts Via New Innovation Center. Electronic media. Access mode: <https://3dprint.com/82480/shipbuilder-3d-printing/>.
- [7] Turichin GA, Klimova OG, Zemlyakov EV, et al. Physics Procedia. 15th Nordic Laser Materials Processing Conference “Nolamp 15”. 2015. 78. pp 397 – 406.
- [8] Turichin GA, Somonov VV, Babkin KD, et al. IOP Conf. Series: Materials Science and Engineering. 2016. 125 (Electronic materials) №012009.
- [9] Glukhov V, Turichin G, Klimova-Korsmik O, et al. Key Engineering Materials. 2016. 684. pp 461 – 467.
- [10] Turichin G, Klimova-Korsmik O. Theory and Technology of Direct Laser Deposition // Additive Manufacturing of High-performance Metals and Alloys - Modeling and Optimization 2018. pp 71 – 88.
- [11] Glukhov VV, Turichin GA. Economic efficiency of technology of direct laser deposition in the industry // Theoretical bases of industrial policy formation (In Russian). 2015. pp 176 – 190.
- [12] Rodionov A A Mathematical methods of optimal construction vessel body design (In Russian). 1990.
- [13] Bendsoe MP, Sigmund O. Topology Optimization. Theory, Methods and Applications. 2003
- [14] Ivanov S, Vildanov A, Golovin P, et al. Effect of inter-layer dwell time on distortion and residual stresses of laser metal deposited wall // Key Engineering Materials. 2019.; 822. pp 445-451.
- [15] Gouge M, Michaleris P. Thermo-mechanical modeling of additive manufacturing. Butterworth-Heinemann. 2017.
- [16] Wu Q, Mukherjee T, Liu C, et al. Residual stresses and distortion in the patterned printing of titanium and nickel alloys // Additive Manufacturing. 2019. 29. 100808.
- [17] Nickel AH, Barnett DM, Prinz FB. Thermal stresses and deposition patterns in layered manufacturing // Materials Science and Engineering: A. 2001. 317. pp 59-64.
- [18] Afazov S, Okioga A, Holloway A, et al. A methodology for precision additive manufacturing through compensation // Precision Engineering 2017. 50. pp 269-274.
- [19] Bendsoe, M. P., Sigmund O. Topology Optimization. Theory, Methods and Applications. Springer, 2003.
- [20] Bendsoe MP, Sigmund O. Material interpolation schemes in topology optimization // Archives of Applied Mechanics. 1999. 69 (9-10). pp 635 – 654.
- [21] ANSYS Documentation Release 15.0: SAS IP, Inc.
- [22] Korsmik RS, Rodionov AA, Korshunov V.A., et al. Topological optimization and manufacturing of vessel propeller via LMD-method // Material Today: Proceedings. 2020. DOI:10.1016/j.matpr.2020.01.044.
- [23] Mendagaliyev R., Turichin GA, Klimova-Korsmik OG, et al. Microstructure and Mechanical Properties of Laser Metal Deposited Cold-Resistant Steel for Arctic Application // Procedia Manufacturing. 2019. 36. pp 249-255.
- [24] Mendagaliyev R, Ivanov SYu, Petrova SG. Effect of Process Parameters on Microstructure and Mechanical Properties of Direct Laser Deposited Cold-Resistant Steel 09CrNi2MoCu for Arctic Application // Key Engineering Materials ISSN: 1662-9795, Vol. 822, pp 410-417.
- [25] Bistrova YA, Shirokina EA, Mendagaliev R, et al. Research of Mechanical Properties of Cold Resistant Steel 09CrNi2MoCu after Direct Laser Deposition // Key Engineering Materials, ISSN: 1662-9795, Vol. 822, pp 418-424.
- [26] Turichin GA, Klimova OG, Zemlyakov EV, et al. Technological Aspects of High Speed Direct Laser Deposition Based on Heterophase Powder Metallurgy // Physics Procedia, Vol. 78, 2015, pp. 397-406.
- [27] Shalnova SA, Klimova-Korsmik OG, Sklyar MO, Influence of the roughness on the mechanical properties of Ti-6Al-4V products prepared by direct laser deposition technology // Solid State Phenomena. 2018 pp. 312-318.
- [28] Sklyar MO, Klimova-Korsmik OG, Turichin GA, et al. Influence of technological parameters of direct laser deposition process on the structure and properties of deposited products from alloy Ti-6Al-4V // Solid State Phenomena. 2018. 284 SSP, pp. 306.
- [29] Turichin G.A., Klimova-Korsmik O.G., Gushchina M.O., et al. Features of structure formation in $\alpha+\beta$ titanium alloys // Procedia CIRP, 74. 2018. pp. 188-191.

11th CIRP Conference on Photonic Technologies [LANE 2020] on September 7-10, 2020

Single-crystal height extension by Laser Metal Deposition of CMSX-4

I. Buchbender^{a*}, C. Hoff^a, J. Hermsdorf^a, V. Wesling^a, S. Kaierle^a

^aLaser Zentrum Hannover, Hollerithallee 8, Hannover 30167, Germany

* Corresponding author. Tel.: +49-511-2788-234; fax: +49-511-2788-100. E-mail address: i.buchbender@lzh.de

Abstract

The introduction of directionally solidified and single-crystal nickel-based superalloys have led to a higher thermal efficiency of engines by allowing for an increase in turbine inlet temperatures from 1000°C to 1400°C. These temperatures however lead to higher thermal stress and corrosive environments, resulting in a shorter life span. Previous work has shown the applicability of laser metal deposition (LMD) for the regeneration of these high value components, while maintaining primary crystalline orientation of single-crystal high pressure turbine blades. However, the processing of these materials by LMD poses several challenges, such as susceptibility to cracking, the formation of misoriented grains and low weldability. This paper examines deposition strategies to extend single-crystal height. While a continuous, meandering strategy shows the most promising percentage single-crystallinity results, an additional remelting step increases epitaxial deposition height. Apart from percentage single-crystallinity and deposition height, this study quantifies the effect of these strategies on cracking and the formation of misorientations.

© 2020 The Authors. Published by Elsevier B.V.

This is an open access article under the CC BY-NC-ND license (<http://creativecommons.org/licenses/by-nc-nd/4.0/>)

Peer-review under responsibility of the Bayerisches Laserzentrum GmbH

Keywords: laser cladding; single-crystal; superalloys

1. Introduction

The optimization of the thermal and propulsive efficiencies of modern turbine engines gained importance due to the need for a reduction of fuel costs and compliance with environmental regulations. A significant amount of fuel and maintenance costs can be saved by increasing the efficiency and service interval of these engines [1]. Advancements in gas turbine technology have enabled higher compression ratios, turbine inlet temperatures and combustion that is more efficient. For example, a 50 K increase in turbine inlet temperature leads to a 50 MW increase in power output in a 60 MW engine [2], which in turn reduces the amount of CO₂ and NO_x emitted [3].

1.1. Nickel-based Superalloys

The development of directionally solidified (DS) castings allowed for the elimination of grain boundaries transverse to

the loading axis, while single-crystal (SX) investment castings eliminated grain boundaries almost completely [4]. This allowed for a huge improvement in creep resistance, since grain boundaries are sites of damage accumulation and crack initiation at high temperatures. In the case of high pressure turbine blades, the presence of internal cooling channels and additional thermal barrier coatings has further allowed components made from Nickel-based superalloys to be used at temperatures exceeding their own melting point [5]. While the high performance capabilities of such components result in longer life spans, the repair of these parts still poses a challenge.

1.2. Laser metal deposition

Laser metal deposition (LMD), also known as directed energy deposition (DED), direct metal deposition (DMD), laser-engineered net shape (LENS) or laser metal forming

(LMF) involves the simultaneous deposition of powder material and the melting of said powder material by a heat source, in this case, a laser. The deposition can occur coaxially or laterally in relation to laser beam position. LMD with 3-axis or 5-axis manipulation can be used to build 3D structures by ensuring deposition occurs parallel to the direction of gravity. This enables the deposition of near-net-shape structures onto existing parts, the coating of surfaces and even the manufacture of functionally graded parts. It has established itself as a robust process for the repair of components [6, 7, 8]. In the case of turbine blades, when compared to replacing damaged parts with new ones, additive repair by laser metal deposition results in reduced material costs, reduced energy costs and reduced time to manufacture [1]. Microstructurally, the rapid solidification rates in the melt pool during the LMD process result in small grains [6] with less segregation of alloying elements when compared to casting and conventional arc welding processes. The process also allows for a high degree of control of the heat flow, thereby allowing control over the microstructure [1].

1.3. Challenges in LMD of SX structures

The use of additive-based process to achieve single-crystal microstructure is challenging [8]. The complex chemical composition of these alloys cause several secondary phases to form in the austenitic γ matrix, which has been proven to increase the susceptibility of the material to hot-cracking [4]. Many Ni-based superalloys are considered to have low weldability due to the rapid precipitation of the strengthening phase γ' [9]. An alloy is considered non-weldable if the total Al+Ti content exceeds 4 wt% [10]. In the case of the CMSX-4 powder material used in this study, the Al+Ti content is 6.6 wt% (table 1). The high aluminium and titanium content, while resulting in high γ' volume fractions that improve high temperature performance, makes repair by conventional fusion methods such as welding increasingly difficult [1]. In addition to the Ti+Al content, the Cr+Co content offers yet another approach to the characterization of weldability of superalloys [11]. Both approaches characterize CMSX-4 as non-weldable or difficult to weld. Additionally, the columnar dendritic microstructure of DS and SX material poses a challenge during additive repair. Namely, that this microstructure must be reproduced in the material added during repair. Due to these challenges, these high-value components have high buy-to-fly ratios, high costs and there arises a need for a cost-effective repair process.

Gäumann et al. [6] describe one of the first attempts to deposit multiple layers of epitaxially oriented CMSX-4. René N4 [12] and René N5 [8] have been deposited by DMD, René 142 by electron beam melting [13] and CMSX-4 by selective electron beam melting [14]. Previous work of the authors [15, 16] has shown the applicability of LMD for the deposition of crack-free SX structures with a height of about 1300 μm on CMSX-4 and 775 μm on PWA 1426. Rottwinkel et al. [15] also presented the use of a remelting step to increase epitaxial height. However, the deposition of larger structures of crack-

free, stray-grain-free, epitaxially oriented material remains a challenge.

In summary, CMSX-4 is characterized as difficult to weld, resulting in material that is highly susceptible to cracking during processing. In addition, the columnar dendritic structure of these parts poses a challenge with respect to reproducing the orientation during additive repair. Balancing these requirements with contour fidelity is difficult, as the parameters that result in high single-crystallinity and low cracks, do not necessarily guarantee an optimal shape. Hence, building parts that have the desired geometry (contour fidelity) with the LMD process, while considering single-crystallinity, poses a challenge.

In order to develop a process to build CMSX-4 deposits that are crack-free and have epitaxial orientation, this study evaluates the effect of process parameters and strategies on the deposition of SX structures. Since, with respect to laser speed ($\text{mm}\cdot\text{min}^{-1}$), literature varies as to whether a higher [8] or lower speed [1, 17] delivers better results, first, the optimal laser speed was determined. Subsequently, remelting speed and remelting power were determined, as this has been shown to increase possible single-crystal height [15]. Based on these results, four deposition strategies and two strategies for height extension were evaluated in terms of their ability to deposit multi-layered, crack-free, single-crystal structures, based on their effect on percentage single-crystallinity, the number of cracks, microcracks and misorientations in the deposit.

2. Materials and Methods

2.1. Process technology and materials

The laser metal deposition process was carried out using a diode laser (LDF 400-650, Laserline GmbH) with a beam wavelength of 980 nm and a focus diameter of 800 μm . A maximum power of 340 W was available while using two of the four available stacks. Powder material was deposited coaxially with a powder focus diameter of 2 mm. The Nickel-based superalloy used in this study was CMSX-4 with a powder particle diameter between 25 μm and 45 μm . The substrate material had a similar composition to the powder material, as is shown in table 1. The angle of primary dendrite orientation was between 0° and 5° for the substrate plates and material was always deposited on the (001) plane to maintain primary crystal orientation. In order to carry out the analysis, the builds were cut to visualize the cross-section, embedded, polished, etched and micrographs were obtained.

Table 1. Chemical composition of CMSX-4 powder and substrate material (b. indicates balance wt%)

	Ni	Cr	Co	Mo	W	Ta	Re	Al	Ti	Hf
Powder	b.	6.5	9	0.6	6	6.5	3	5.6	1.0	0.1
Substrate	b.	6.6	9.7	0.6	6.4	6.5	2.9	5.6	1.0	0.1

The process development was carried out as shown in table 2. Deposition parameter laser speed was tested first, followed by the effect of remelting. Subsequently, deposition strategies and remelting parameters were varied.

Table 2. Parameters tested during the process development

Section	2.2	2.3	2.4
Laser power (W)	190	190	190
Laser speed (mm·min ⁻¹)	90, 150, 200	150	150
Strategy	meander	meander	1 to 4
Remelting power (W)	0	0, 90	100, 140, 180
Remelting speed (mm·min ⁻¹)	0	0, 90	50, 100

2.2. Deposition parameter: laser speed

In order to determine the effect of speed on percentage single-crystallinity, the formation of cracks and misorientations, three speeds were tested: 90 mm·min⁻¹, 150 mm·min⁻¹ and 200 mm·min⁻¹. The laser speed, in this study, refers to the speed at which the process head moves across the surface of the work piece. Preliminary work showed that a power of 190 W at a feed rate of 1 g·min⁻¹ delivered optimal results with this particular setup. Hence, a laser power of 190 W with a meander strategy was used, as stated in table 2. Other parameters such as layer thickness (0.25 mm) and deposition width (0.6 mm) were kept constant unless otherwise stated.

2.3. Deposition parameter: remelting

Rottwinkel et al. [15] showed that an additional remelting step involving a single pass of the laser beam allowed for the recrystallization of previously misoriented material within a track. In order to further quantify this and determine its use for the extension of single-crystal height, builds with and without remelting were compared, with the remelting power (P_R) at 90 W and the remelting speed (V_R) at 90 mm·min⁻¹. Laser power, laser speed and strategy were kept constant, as shown in table 2.

2.4. Strategies for deposition

In order to extend single-crystal height, four strategies were chosen, as described in table 3. Thin lines indicate a single-pass of the laser beam, while thick lines indicate a double-pass. Grey lines indicate the ideal geometry of the build. The remelting speed (50 mm·min⁻¹, 100 mm·min⁻¹) and remelting power (100 W, 140 W, 180 W) were varied in order to quantify the effect and optimize the remelting process for further experiments, resulting in 24 builds with 10 layers each and a dimension of approximately 10 mm by 5 mm.

From previous work [15] it is known that the meander strategy or single tracks with a shift, perpendicular to the direction of beam travel every alternating layer, by half the track width allows for material with epitaxial orientation to be deposited.

- Strategy 1: This meander strategy was modified to include a double pass on the first and last tracks during deposition of every alternating layer beginning with the first. This was to aid the horizontal build-up of the walls of the part and maintain contour fidelity of the parts in order to avoid a contour shown in figure 1. The perpendicular shift was also implemented in strategies 1 and 2.

- Strategy 2: This included an additional double-pass remelting step in order to remelt any additional particles or agglomerations adhering to the surface of the part.
- Strategy 3: This involved the meander strategy without a shift every alternating layer. This was tested to evaluate contour fidelity.
- Strategy 4: This entailed a 90° rotation in deposition direction every alternating layer beginning with the second layer, as shown in table 3.

Table 3. Deposition and remelting strategies (- : single pass, - : double pass)

Strategy	Layer	Deposition	Remelting
1	1		
	2		
2	1		
	2		
3	1		
	2		
4	1		
	2		

2.5. Strategies for height extension

Following the determination of the optimal deposition strategy, strategies to double the possible epitaxial height, while reducing crack and misorientation formation were tested. Gäumann et al. [6] drew important conclusions regarding the deposition of SX structures in their work on CMSX-4. These were that the laser power should be reduced as this increases the temperature gradient and that the temperature of the substrate should be as low as possible. Based on this, the following strategies for height extension were tested:

- Waiting time between layers (t_w : 0 seconds – 10 seconds)
- Power reduction every 5 layers (P_{red} : 0 W – 90 W)

In order to evaluate the effect of parameters and deposition strategies, the following factors were quantified (figure 1):

- Percentage single-crystallinity (%-SX): $(\text{single-crystal area}) / (\text{total surface area}) \cdot 100$
- Height of deposit (H_D): measured at three points across the cross-section
- Height difference (H_{diff}): Actual height – desired height
- Number of cracks
- Number of microcracks
- Number of misorientations

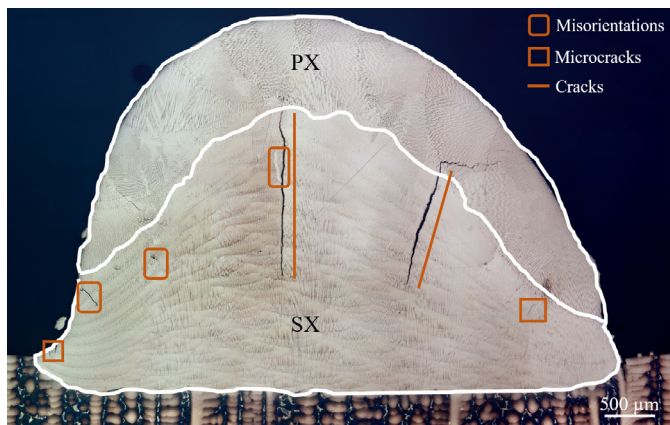


Fig. 1. Cross-sectional micrograph of deposit

Microcracks were defined as those that occurred at misorientation boundaries, as depicted in figure 1. Large cracks (henceforth referred to as just cracks) were identified as those occurring across several deposited layers. Only cracks and misorientations occurring in the SX-area were taken into consideration for the analysis.

3. Results

3.1. Deposition parameter: laser speed

In order to be able to determine a laser speed for further process development, the results of the factors stated above were plotted against the laser speed. $90 \text{ mm} \cdot \text{min}^{-1}$ showed the lowest mean %-SX, $200 \text{ mm} \cdot \text{min}^{-1}$ the widest range of %-SX, while $150 \text{ mm} \cdot \text{min}^{-1}$ showed the highest %-SX as shown in figure 2. Further conclusive evidence for the choice of laser speed was seen in the correlation with the number of cracks. A high and low laser speed resulted in more cracks. Other factors, such as misorientations and deposit height, did not show significant differences in mean values. Based on the results shown in figure 2, a speed of $150 \text{ mm} \cdot \text{min}^{-1}$ was chosen for further experiments.

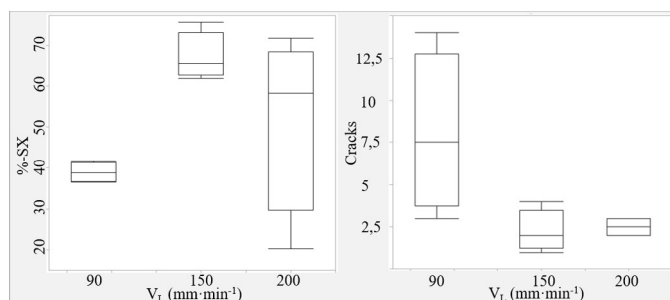


Fig. 2. Effect of laser speed on %-SX and number of cracks

3.2. Deposition parameter: remelting

The results of the remelting analysis is depicted in figure 3. The largest differences between the strategies of remelting (R) and without remelting (X) were seen in the incidence of microcracks and percentage single crystallinity. Deposits built with the remelting strategy showed fewer microcracks and higher percentage single-crystallinity, which are amongst the most influential factors for epitaxial height extension. Hence, the remelting strategy was chosen for further experiments.

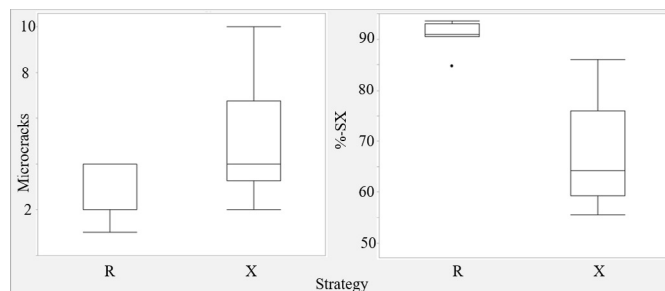


Fig. 3. Effect of remelting strategy (R) and no remelting strategy (X) on microcrack formation and %-SX

3.3. Strategies for deposition

Analysis of the cross-sections of the builds was carried out as stated in section 2.5. An overall improvement across all six criteria was observed. Chosen micrographs of the cross-section of strategies 1 and 2 are shown in figure 4.

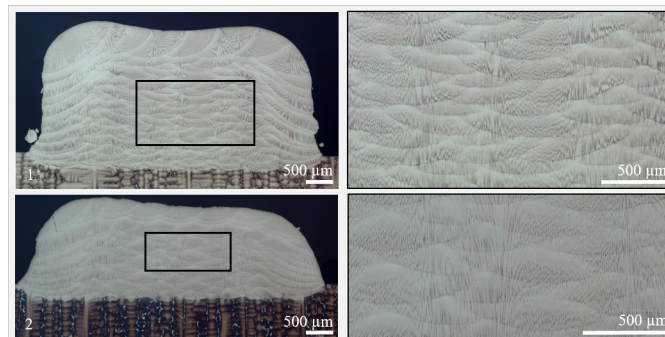


Fig. 4. Selected cross-sectional micrographs of builds from strategies 1 and 2

The results for %-SX, number of cracks, microcracks and misorientations are shown in figure 5. Percentage single-crystallinity was above 80% for all parts, with the highest being 97.9% with strategy 2 at 100 W and $50 \text{ mm} \cdot \text{min}^{-1}$ (remelting parameters). Several builds showed zero microcracks, cracks and misorientations. The mean number of misorientations and microcracks was between one and two and cracks between one and three for all four strategies.

Since the remelting power and speed were also varied, the effects of these changes were also quantified, as shown in figure 6, for all four strategies. In order to extract useful information for further experiments from the analysis, the four strategies were evaluated with respect to the criteria stated in section 2.5 and shown in figure 5. To obtain an overall score for each strategy, a score from 1 (best) – 4 (worst) was given

for each criteria based on the mean value. The results are depicted in table 4. For example, referring to table 4, in the case of percentage single-crystallinity, strategy 2 is scored with the best score (1) due to the best %-SX value. This is followed by strategy 3 with a score of 2, strategy 4 with a score of 3 and strategy 1 with the worst score (4) due to the lowest mean %-SX value. This was carried out for the remaining criteria, resulting in an overall score where the lowest number represents an overall desirable outcome. A similar analysis was carried out to determine the remelting speed and power to be used for further experiments. The overall scores are depicted in table 4.

The overall scores indicate that strategy 2 (double remelting pass) and strategy 3 (meander without shift) result in overall high single-crystallinity and a low number of cracks and misorientations. However, it is evident from figure 5 that strategy 2 results in a higher percentage single-crystallinity than strategy 3 (mean value of 94.2% vs. 87.8%), despite having the same overall score. Hence, strategy 2 was chosen for further experiments. The overall scores for V_R and P_R indicate 100 $\text{mm} \cdot \text{min}^{-1}$ and 100 W are the optimal remelting parameters.

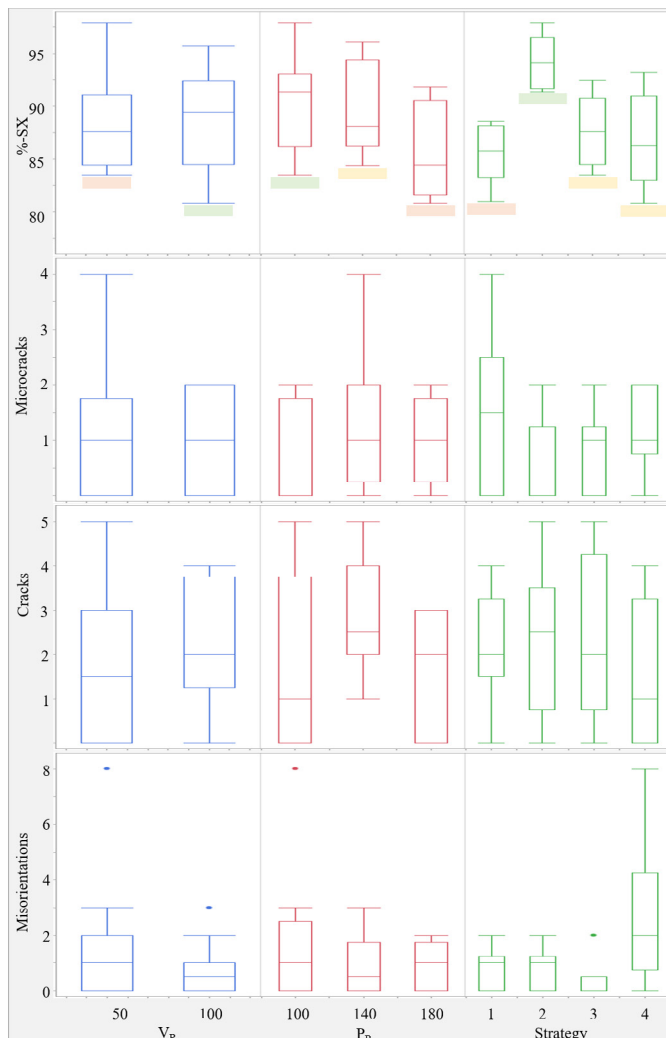


Fig. 5. Effect of remelting speed (V_R), remelting power (P_R) and strategy on %-SX, microcracks, cracks and misorientations as summarized in table 4

Table 4. Overall score for strategies, remelting speed and remelting power

	V_r ($\text{mm} \cdot \text{min}^{-1}$)		P_r			Strategy			
	50	100	100	140	180	1	2	3	4
%-SX	2	1	1	2	3	4	1	2	3
Cracks	1	2	1	3	2	3	4	2	1
Microcracks	2	1	1	3	2	4	1	3	2
Misorientations	2	1	3	1	2	3	2	1	4
Total	7	5	6	9	9	14	8	8	10

3.4. Strategies for height extension

Figure 6 shows the results of the strategies for height extension. The introduction of a waiting time (t_w) between layers to reduce the temperature of the substrate resulted in the lowest percentage single-crystallinity (69.7%), the highest number of microcracks and a wide range of height difference. The gradual reduction of power (strategy P_{red}) showed overall better results. Further analysis of the power reduction strategy showed that a gradual reduction of power to 100 W in layer 15 showed the largest height difference (2.3 mm), indicating that the lowered power was not sufficient to melt powder material, leading to smaller deposits and loss of focus in the higher layers.

In order to compensate for the loss of height and use the power reduction, a third strategy was implemented. From the measurement of H_{diff} (actual height – desired height) of the parts in section 3.3 (strategy 2, V_R : 100 $\text{mm} \cdot \text{min}^{-1}$, P_R : 100 W) an average deposit height difference of -0.5 mm was identified i.e. the builds were 0.5 mm shorter than the desired height. This was taken into consideration to refocus the process head after 10 layers in order to maintain a constant working distance of 9 mm. In addition to this, P_{red} of 0 W – 20 W after layer 10 was also implemented. The results are shown in figure 6 (strategy F).

These show a percentage single-crystallinity of 80.72% (mean value). Deposition with 190 W ($P_{red} = 0$) show the lowest %-SX (80%) and a large number of cracks (11), microcracks (5) and misorientations (4). Deposition with 170 W from layer 10 ($P_{red} = 20$ W) showed promising results with a %-SX of 86.3%, one microcrack, one misorientation and two cracks with a height difference (H_{diff}) of -0.02 mm.

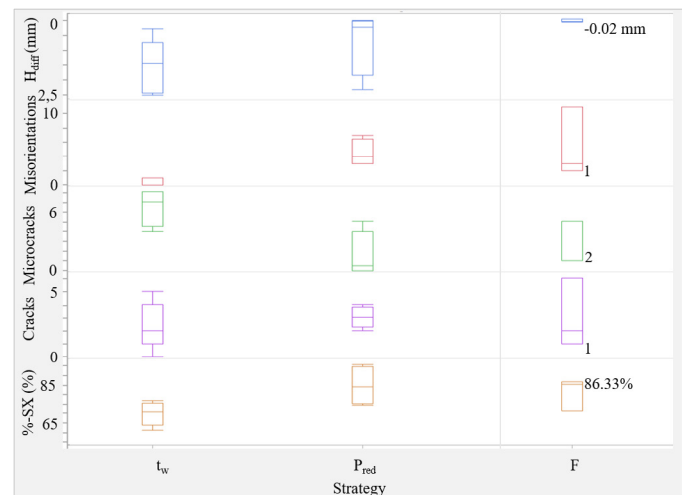


Fig. 6. Strategies for height extension, values for $P_{red}=20$ W are shown for strategy F

4. Conclusion

In this study, parameters and strategies for the deposition of single-crystal structures from CMSX-4 were analyzed. It was determined that for a high percentage single-crystallinity and a low number of cracks, a moderate speed of $150 \text{ mm} \cdot \text{min}^{-1}$ was optimal. Low laser speeds showed a high incidence of cracks and low %-SX, indicating the build-up of excessive heat during the process. High laser speeds showed a low number of cracks, but also a wide range of %-SX, indicating that the reduced laser-material-interaction time was not always sufficient to remelt and recrystallize the material for optimal microstructural orientation. A study of builds with and without an additional remelting pass between layers showed that the former resulted in higher %-SX, fewer microcracks and higher deposition height. A study of deposition strategy was carried out with the chosen parameters. For the four strategies, strategy 2 resulted in the highest %-SX (94.2%), the lowest number of microcracks (0.5) and the best overall score. Strategy 3 also showed promising results, such as low number of misorientations and cracks, but a lower %-SX (87.7%) than strategy 2. Two strategies were tested to extend possible single-crystal height by reducing the laser power and including a waiting time in order to increase the temperature gradient and keep the temperature of the substrate as low as possible. The results showed that the waiting time between layers resulted in a large number of cracks and microcracks with the lowest %-SX. The most promising results were seen with a combination of power reduction ($P_{\text{red}} = 20 \text{ W}$) and resetting of the working distance after 10 layers, which showed high contour fidelity, very few cracks and a deposit height of $4480 \mu\text{m}$. Loss of SX was observed only in the topmost layer of the deposit, indicating that this could be due to colder powder particles adhering to the surface, leading to increased heterogenous nucleation [18].

This combination should be further investigated for a higher number of layers, including a reduction of power every 5 layers. Further work could involve the use of a cooling concept to bring down the temperature of the substrate during the process, reducing the thermal stresses caused by a waiting time. These could speed up overall processing time by increasing the deposit height.

Acknowledgements

This project is funded by the Deutsche Forschungsgemeinschaft (DFG, German Research Foundation) – SFB 871/3 – 119193472.

References

- [1] McNutt PA. An investigation of cracking in laser metal deposited nickel superalloy CM247LC. PhD thesis, University of Birmingham, 2015.
- [2] Czech N, Esser W, Schmitz F. Gas turbine blade materials: the next steps. *Modern Power Systems* 1995;15:43-46.
- [3] Volek A. Erstarrungsmikrostruktur und Hochtemperatureigenschaften rheniumhaltiger, stängelkristalliner Nickel-Basis-Superlegierungen. PhD thesis, Universität Erlangen-Nürnberg, 2002.
- [4] Donachie MJ, Donachie SJ. *Superalloys – a technical guide*. 2nd ed. ASM International; 2002.
- [5] Schneibel JH. Beyond Nickel-Base Superalloys. In: TMS, Charlotte, NC; 2004.
- [6] Gäumann M, Bezencon C, Canalis P, Kurz W. Single-crystal laser deposition of superalloys: processing-microstructure maps. *Acta Materialia* 2001;49:1051-1062.
- [7] Dass A, Moridi A. State of the art in directed energy deposition: from additive manufacturing to materials design. *Coatings* 2019;9:418.
- [8] Basak A, Das S. Additive manufacturing of Nickel-Base Superalloys René N5 through scanning laser epitaxy (SLE) – Material processing, microstructures, and microhardness properties. *Advanced Engineering Materials* 2017;19:3.
- [9] Segerstark A, Andersson J, Svensson L, Ojo O. Effect of process parameters in the crack formation in laser metal powder deposition of alloy 718. *Metallurgical and Materials Transactions A* 2018;59:5042-5050.
- [10] Henderson MB, Arrell D, Heobel M, Larsson R, Marchant G. nickel-based superalloy welding practices for industrial gas turbine applications. *Science and Technology of Welding and Joining* 2004;4:13-21.
- [11] Haafkens MH, Matthey JHG. A new approach to the weldability of nickel-base as-cast and power metallurgy superalloys. *Welding Journal* 1982;61:11.
- [12] Santos EC, Kida K, Carroll P, Vilar R. Optimization of laser deposited Ni-based single crystal superalloys microstructure. *Advanced Materials Research* 2011;154-155:1405-1414.
- [13] Murr LE. Metallurgy of additive manufacturing: examples from electron beam melting. *Additive Manufacturing* 2015;5:40-53.
- [14] Ramsperger M, Roncery LM, Lopez-Galilia I, Singer RF, Theisen W, Körner C. Solution heat treatment of single crystal Nickel-base superalloys CMSX-4 fabricated by selective electron beam melting. *Advanced Engineering Materials* 2015;17:1486-1493.
- [15] Rottwinkel B, Pereira A, Alfred I, Noelke C, Wesling V, Kaieler S. Turbine blade single crystalline clad deposition with applied remelting passes for well oriented volume extension. *Journal of Laser Applications* 2017;29.
- [16] Kaieler S, Overmeyer L, Alfred I, Rottwinkel B, Hermsdorf J, Weidlich N. Single-crystal turbine blade repair by laser cladding and remelting. *CIRP Journal of Manufacturing Science and Technology* 2017;19:196.199.
- [17] Dye D, Hunziker O, Reed RC. Numerical analysis of the weldability of superalloys. *Acta Materialia* 2001;49:683-697.
- [18] Liu Z, Qi H. Effects of processing parameters on crystal growth and microstructure formation in laser powder deposition of single-crystal superalloy. *Journal of Materials Processing Technology* 2015;216:19-27.

11th CIRP Conference on Photonic Technologies [LANE 2020] on September 7-10, 2020

Development of laser metal deposition process for a large IN625 part using small trial samples

Vildanov Artur^{a,*}, Babkin Konstantin^b, Kovchik Anton^b, Arkhipov Andrey^b, Gushchina Marina^b

^a*Peter the Great St. Petersburg Polytechnic University (SPbPU), Polytechnicheskaya, 29, 195251, Russia*

^b*St. Petersburg State Marine Technical University (SMTU), Lotsmanskaya, 10, 190121, Russia*

* Corresponding author. Tel.: +7-812-552-9843; fax: +7-812-552-9843. E-mail address: wildam92@mail.ru

Abstract

The laser metal deposition process is characterized by multiple reheating with high heating and cooling rates, which vary during the deposition process and depend on the size and shape of the part. The development of the process parameters is an essential step in preparing for manufacturing of the real part. As a rule, small trial samples are used for this purpose. Difference in the temperature field during deposition of samples and real part leads to the different microstructure, properties and macrodefects. The aim of this work is to approximate the thermal histories of trial samples and real parts by varying process parameters. It was shown that by varying dwell time and interpass temperature it is possible to obtain similar thermal histories. Metallographic studies showed the absence of defects, the same microstructure and mechanical properties (microhardness) of the samples and real part.

© 2020 The Authors. Published by Elsevier B.V.

This is an open access article under the CC BY-NC-ND license (<http://creativecommons.org/licenses/by-nc-nd/4.0/>)

Peer-review under responsibility of the Bayerisches Laserzentrum GmbH

Keywords: laser metal deposition

1. Introduction

With the implementation of the direct metal deposition technology in various industries, the requirements for deposited parts are being increased [1,2,3,4]. Additive manufacturing technologies are widely developing now in all industrialized countries [5]. In some cases, this approach can significantly reduce energy and material production costs comparing to traditional casting, heat treatment and machining technological process. The most promising technology for manufacturing of large-sized parts from metal is laser metal deposition (LMD). The method is based on geometry forming by 3D cladding of metal powder with laser beam [2,6,7]. The heat-resistant nickel-based alloy Inconel 625 is used in the aviation energy industry. Various experiments show a wide range of mechanical properties of samples deposited by this method [8,9,10,11,12].

The process has to be stable, and the result must meet all the operational characteristics. In a number of papers the effect of the laser power, the speed, the powder flow rate on the structure and the operational properties were defined for trial samples produced from heat resistant nickel alloys was shown. The authors G.P. Dindaa et al. [15] noted that the quality of the deposited samples is highly influenced by the laser scanning direction that should be identical for the deposition of all the layers. In the paper [16], the relationship of thermal cycles with the structure for Inconel 625 and Ti-6Al-4V was evaluated. According to the results, it was found that the morphology of the structure mainly depended on the cooling rate and energy density. As a rule, the mode is worked out on the trial samples, which have smaller dimensions and a different thermal history as well as mechanical tests and structural studies are carried out on samples with dimensions significantly different from the final parts. Therefore, the structure and the mechanical characteristics of the trial samples will differ from the structure

and the mechanical characteristics of the final large size product.

Some large-sized parts have a continuous deposition time (over 100 hours), therefore preparation is a very important step of the LMD process, that also includes the selection of the process parameters. The modes selection for small trial samples does not guarantee the high-quality formation of the large-sized parts, and the process determination of LMD modes using large-sized products is a labor-intensive process that takes a lot of time and resources. Thus, it is very important to take into account the thermal cycles corresponding to large-sized part when selection LMD modes parameters on small trial samples. The thermal cycle on trial samples can be adjusted by varying the waiting time between the layers. Another main parameter of the laser metal deposition process is the width of the deposited track. It determines how much powder must be fed into the melt pool for a stable deposition process.

This paper describes the research on comparing the LMD thermal cycles of the real large-size part with the trial samples. As a build material there will be used the heat-resistant nickel-based alloy Inconel 625. The research significantly simplifies the selection of the process parameters for LMD of the large-sized products with complex geometry.

2. Experimental procedure

2.1. Equipment and materials

The experiments were carried out on a robotic complex for direct metal deposition. The installation includes: a fiber laser with a 3 kW maximum power, a six-axis robot and two axial positioners [17]. As a working tool, a laser-weld head and a four-jet nozzle for feeding powder is used. Fig. 1 shows the robotic complex:

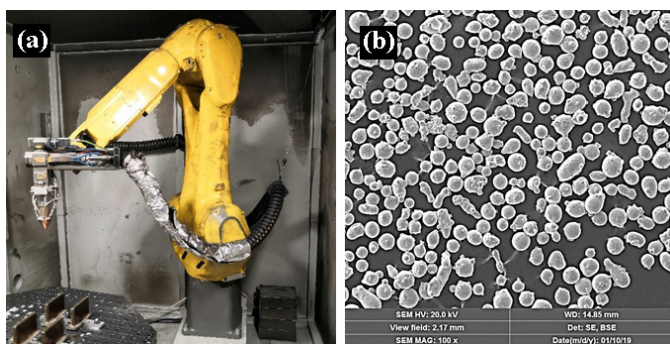


Fig. 1. Robotic complex for direct laser metal deposition (a) Scanning electron microscopy (SEM) images for the Inconel 625 powder used during the experiment (b)

A K-type Cr/Al thermocouple with a wire diameter of 1.2 mm was used for measuring temperatures. The temperature range of the thermocouple is from -200 to 1400°C.

Commercially available, gas atomized Inconel 625 powder (Hoganas) was used for this study. The powder had a composition of 64.61 Ni, 21.25 Cr, 8.45 Mo, 4.65 Nb and 1.06 Fe (in wt.%) with a powder size distribution of 45–135µm diameter (fig. 1b).

2.2. Laser metal deposition process

In this research, a rectangular part with dimensions of 500x200x200 mm and a wall thickness of 2 mm was deposited. The sample was prepared in a spiral trajectory, the transit time of one layer was 56 seconds. A thermocouple was installed during the process at a height of 50 mm from the substrate to reduce its effect on the thermal cycle. During the process, wall thickness was periodically monitored. Fig. 2 shows a photograph of the part deposition:

The part and the samples are deposited with the following technological parameters:

- laser power, 1300 W;
- velocity process 25 mm / s;
- step Δz - 0.6 mm;
- beam diameter - 2 mm.

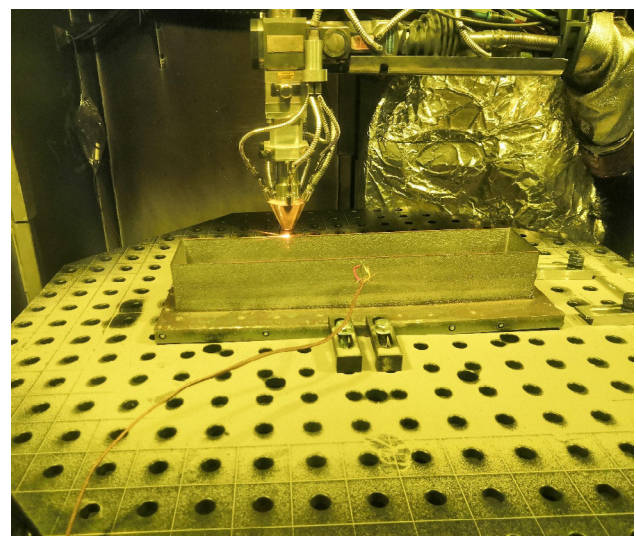


Fig. 2. The temperature measurement during deposition

After the large-sized part deposition the trial samples with dimensions of 50x40x2 mm were made. In order to simulate the technological mode of a large part, a wait was established between small passages on small samples. As a result, 4 trial samples were made with different waits between passes. Fig. 3 shows the trial samples:

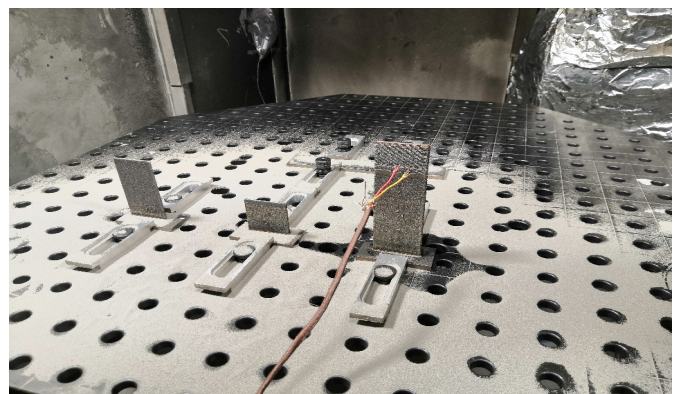


Fig. 3. The trial samples

2.3. The results

Table 1 presents the parameters of the wall thickness and the wait between the layers in the deposited samples:

Table 1. Dependence of the samples thickness on the wait between the layers

Sample	wall thickness, mm	wait between the layers, sec
Part	2	56
Trial sample № 1	1.81	56
Trial sample № 2	1.93	46
Trial sample № 3	2	36
Trial sample № 4	2.08	26

As it can be seen in table 1, the wall thickness of trial samples increases with the decreasing of the wait between the layers. Fig. 4 shows the cooling curves recorded by means of the thermocouple (the second layer after installing the thermocouple):

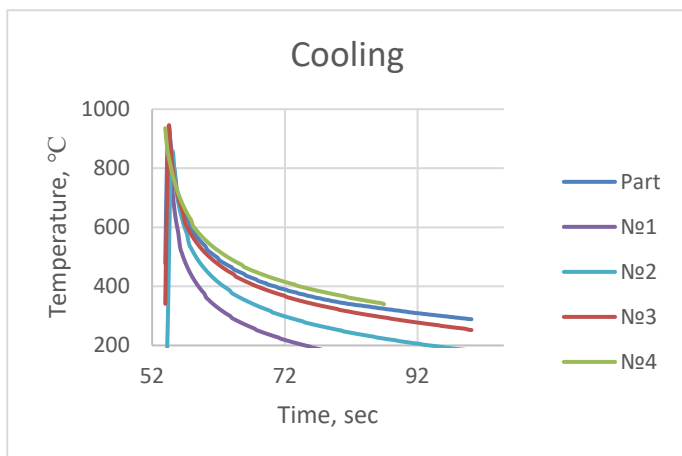


Fig.4. The cooling curves

Fig. 5 shows a graph of the average temperature to which the part (or samples) cools:

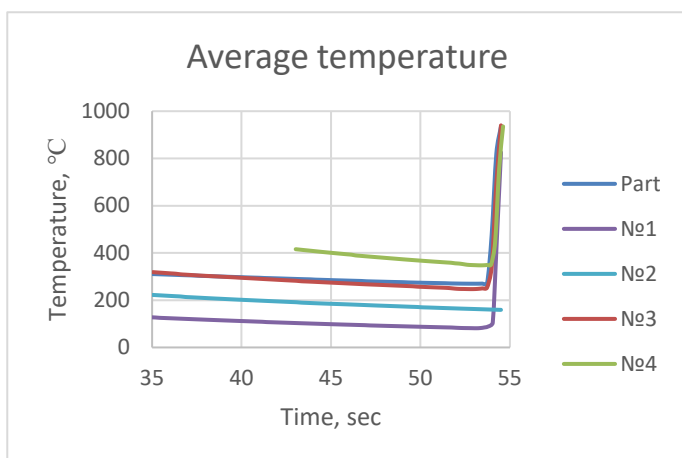


Fig. 5. The average cooling temperature after passing through the layer

According to the data obtained by a thermocouple usage, we can conclude that sample No. 1, which has the same wait between the layers as the part, cools more intensively due to the small dimensions of the sample and has a wall thickness of 0.2 mm less than it is necessary. Trial sample No. 4, with a wait between the layers of 26 seconds, had a larger wall thickness and an average temperature.

As a result, only the trial sample No. 3 has the wall thickness and the thermal cycle as close as it is possible to the part. The wall thickness is determined by the width of the melt pool, which is the one of the main process parameters. In addition to obtaining the necessary geometry, the stability of the process depends on the wall thickness. With an excessive increase of the melt pool, the set value of the powder flow rate may not be enough, as a result, the distance between the working nozzle and the deposited part may increase and the process will become unstable. The width of the melt pool, in its turn, is determined by the temperature of the previous layer, the average temperature of the part and the thermal history.

3. Conclusion

While selecting the process parameters, it is necessary to understand that the correct choice of the technological parameters and the possibility of transferring them to a real part depend on the thermal history. This article shows that the thermal histories of the trial sample №1 and the real part differ from each other, despite the fact that the pause between the layers is the same. This happens because of the different time of exposure of the radiation on the material, different dimensions and different substrates of the part and the trial samples.

The fundamental parameter is the width of the melt pool, as not only the wall thickness depends on it, but the stability of the whole process as well. The next step of the research will be the metallographic studies, mechanical tests and the identification of the correlation of the results and the thermal cycles taken during the process. It is assumed that the changes in thermal cycles will lead to the change of the grain size and phase composition, which in its turn will cause the change in the mechanical characteristics of the deposited parts compared to the deposited trial samples.

Acknowledgments

The reported study was funded by RFBR, project number 19-31-27001

References

- [1] L. E. Murr, S. M. Gaytan, D. A. Ramirez, E. Martinez, J. Hernandez, K.N. Amato, P. W. Shindo, Francisco, R. Medina, R. B. Wicker, Metal Fabrication by Additive Manufacturing Using Laser and Electron Beam Melting Technologies, *J. of Mat. Sci. & Tech.* 28 (2012) 1-14.
- [2] G.A. Turichin, E.V. Zemlyakov, O.G. Klimova, K.D. Babkin, F.A. Shamray, D.Yu. Kolodijniy, Direct laser deposition – perspective additive technology for aircraft engine, *Sv. and Diagn.* 3 (2015) 54-57.
- [3] D. Gu, New metallic materials development by laser additive manufacturing, in: J. Lawrence and D. G. Waugh, *Laser Surface Engineering*, Elsevier Ltd., (2015) 163-180.

- [4] B. Kianiana, S. Tavassoli, T. C. Larsson, The Role of Additive Manufacturing Technology in Job Creation: An Exploratory Case Study of Suppliers of Additive Manufacturing in Sweden, *Procedia in: CIRP, 12th Gl. Conf. Sust. Manuf./ Em. Pot.* 26 (2015) 93–98.
- [5] D. R. Gress, R.V. Kalafsky, Geographies of production in 3D: Theoretical and research implications stemming from additive manufacturing, *Geoforum.* 60 (2015) 43–52.
- [6] L.E. Murr, E. Martinez, S.M. Gaytan, D.A. Ramirez, B.I. Machado, P.W. Shindo, J.L. Martinez, F. Medina, J. Wooten, D. Ciscel, U. Ackelid, R.B. Wicker, Microstructural architecture, microstructures, and mechanical properties for a nickel-base superalloy fabricated by electron beam melting, *Metall. Mater. Trans. A* 42 (11) (2011) 3491 – 3508.
- [7] J. Michael Wilson, C. Piya, Y. C. Shin, F. Zhao, K. Ramani, Remanufacturing of turbine blades by laser direct deposition with its energy and environmental impact analysis, *J. of Clean. Prod.* 80 (2014) 170-178.
- [8] S. M. Thompsona, L. Bianc, N. Shamsaiea, A. Yadollahi, An overview of Direct Laser Deposition for additive manufacturing; Part I: Transport phenomena, modeling and diagnostics, *Add. Manuf.* 8 (2015) 36–62.
- [9] C.P. Paul, P. Ganesh, S.K. Mishra, P. Bhargava, J. Negi, A.K. Nath, Investigating laser rapid manufacturing for Inconel-625 components, *Opt. Laser Technol.* 39 (2007) 800 – 805.
- [10] P. Ganesh, R. Kaul, C.P. Paul, Pragya Tiwari, S.K. Rai, R.C. Prasad, L.M. Kukreja, Fatigue and fracture toughness characteristics of laser rapid manufactured Inconel 625 structures, *Mater. Sci. Eng. A* 527 (2010) 7490 – 7497.
- [11] M. Rombouts, G. Maes, M. Mertens, W. Hendrix, Laser metal deposition of Inconel 625: microstructure and mechanical properties, *J. Laser Appl.* 24 (2012) 052007.
- [12] M.L. Griffith, M.T. Ensz, J.D. Puskar, C.V. Robino, J.A. Brooks, J.A. Philliber, J.E. Smugeresky, W.H. Hofmeister, Understanding the microstructure and properties of components fabricated by laser engineered net shaping (LENS), *Mater. Res. Soc. Proc.* 625 (2000) 9 – 20.
- [13]] M. Rombouts, G. Maes, M. Mertens, W. Hendrix, Laser metal deposition of Inconel 625: microstructure and mechanical properties, *J. Laser Appl.* 24 (2012) 52007.
- [14]]J. Nguejio, F. Szymtka, S. Hallais, A. Tanguy, S. Nardone, M. Godino Martinez Comparison of microstructure features and mechanical properties for additive manufactured and wrought nickel alloys 625 *Materials Science and Engineering: A* Volume 764, 9 September 2019, 138214
- [15] G.P. Dindaa, A.K. Dasgupta, J. Mazumderb Laser aided direct metal deposition of Inconel 625 superalloy: Microstructural evolution and thermal stability *Materials Science and Engineering A* 509 (2009) 98–104
- [16] Thermal and microstructural analysis of laser-based directed energy deposition for Ti-6Al-4V and Inconel 625 deposits Frederick Lia,, Joshua Z. Park, Jayme S. Keist, Sanjay Joshi, Richard P. Martukanitz *Materials Science & Engineering A* 717 (2018) 1–10
- [17] G.A. Turichin, V.V. Somonov, K.D. Babkin, E.V. Zemlyakov, O.G. Klimova. High-Speed Direct Laser Deposition: Technology, Equipment and Materials. *Equip.and Mater.* 125(2016) 012009

11th CIRP Conference on Photonic Technologies [LANE 2020] on September 7-10, 2020

Investigation of cracking causes during multi-pass laser cladding of heat-resistant single crystal nickel alloy

Rudolf Korsmik^{a*}, Olga Klimova-Korsmik^{a, b}, Ekaterina Valdaytseva^{a, b}, Ilia Udin^a

^a*Saint-Petersburg State Marine Technical University, Lotsmanskaya st., 3, Saint-Petersburg, 190121, Russian Federation*

^b*Peter the Great Saint-Petersburg Polytechnic University, Polytechnicheskaya st. 29, 195251, Saint-Petersburg, Russian Federation*

* Corresponding author. Tel.: +7-906-253-62-42;. E-mail address: r.korsmik@ltpc.ru

Abstract

ZhS32 is Ni-based single crystal superalloy has been successfully used in aero and industrial gas turbine applications. Vibrations, shocks, abrasive wear, high temperatures applied to gas turbine blades lead to its damage. Taking into account the complexity of production and the high cost of new blades, after the exploitation of their resource, the blades must be restored. Laser cladding, as one type of DED process, is applicable to repairing operation for machines and mechanisms are subjected to the impact of aggressive environment and surface wear. superalloys with a high γ' -volume fraction are strongly susceptible to crack formation, e.g., strain age or liquidation cracking. The influence of main cladding parameters on the potential defects of deposited metal is considered. Based on the obtained dependencies, the criteria allow obtaining a defect-free clad with controlled structure are determined. As result of investigation, a technological recommendations for restoration laser powder cladding of turbine blades from heat-resistant nickel alloys is developed.

© 2020 The Authors. Published by Elsevier B.V.

This is an open access article under the CC BY-NC-ND license (<http://creativecommons.org/licenses/by-nc-nd/4.0/>)

Peer-review under responsibility of the Bayerisches Laserzentrum GmbH

Keywords: laser cladding; single crystal nickel alloy, solidification cracking; central composite design; cracking initiation criterion

1. Introduction

ZhS32 is a Russian second generation single crystalline superalloy (CMSX-4 analogue) containing 3.5-4 wt % Re with a γ' volume content of about 55-65 %. ZhS32 - Ni-based single crystal superalloy has been successfully used in aero and industrial gas turbine applications. The reliability of gas turbine engines is most dependent on the reliability of the compressor and turbine blades, since they are the most loaded parts. Vibrations, shocks, abrasive wear, high temperatures applied to gas turbine blades lead to its damage. Taking into account the complexity of production and the high cost of new blades, after the exploitation of their resource, the blades must be restored [1].

Direct energy deposition (DED) technology is in potential demand by the companies, which are involved in manufacturing of critical products. The field of these industries

is gas turbine engines, shipbuilding, nuclear power engineering, petrochemical production, mineral resource, metal-working etc. [2; 3]. Laser cladding, as one type of DED process, is applicable to repairing operation for machines and mechanisms are subjected to the impact of aggressive environment and surface wear [4].

Despite all benefits of laser processing compared to an arc welding, it is well known that superalloys with a high γ' -volume fraction such as ZhS32, CMSX-4, IN738LC are strongly susceptible to crack formation, e.g., strain age or liquidation cracking. Therefore, these alloys are considered to be hardly weldable or even non-weldable. This alloy has been developed for very slow cooling technology and subsequent long-term heat treatment. This makes it possible to obtain defect-free products. Thus, processing of these alloys is rather challenging [5].

The use of DED technology for the ZhS32 alloy requires an

understanding of the behavior of the metal during the solidification and subsequent structure formation process. Nonhomogeneous temperature cyclic action "heating↔cooling" leads to thermal stresses in the weld. The presence of this state, along with possible structural changes in the material, local deformation processes, residual stresses, initiates a significant decline of the material properties, i.e. its degradation. Obviously, the achievement degradation level by the material above to the valid value leads to irreversible changes in the material properties. The result is the appearance of cracks and subsequent breakage [6].

The solidification cracking susceptibility of engineering alloys is controlled, in large part, by the solidification temperature range and amount of solute-rich liquid that exists at the end of solidification. The distribution of solute-rich liquid within the low temperature region of the solid + liquid mushy zone is particularly important for controlling cracking susceptibility. These features are, in turn, controlled by the solidification conditions and alloy composition [7].

2. Methodic, materials and equipment

2.1. Identification of mode variables on cladding process

In fact, there are many mode variables that, in one way or another, affect the cladding quality to some extent. Therefore, in the present research, those variables and their interactions that had significant influence on the clad bead geometry were taken into consideration. It was decided to consider as main variables:

- Laser power.
- Traverse speed.
- Powder feeding rate.

2.2. Experimental planning

Choosing an appropriate design in relation to the experiment being undertaken is fundamental for the adequate analysis of data collected at points of the design. In the present work a central composite design (CCD) [8] is used for help to define the minimum number of experiments to achieving this task. The CCD design generates a reasonable distribution of points throughout the whole area of interest using the smallest possible number of experimental points.

Fig. 1 presents a representation of the experimental planning based on CCD for three entrance variables. The CCD counts with a factorial design 2^3 increased with six axial points and a central point; the number of runs to the center and the distance of the axial points (α) were chosen for a rotatable design, where $\alpha=(F)1/4$, being F the number of points of the factorial part, that is, 8. Then $\alpha=(8)1/4=1.682$ [9].

The units presented in Fig. 1 are given in terms of the codified normalized levels (-1, 0, 1) of the entrance variables. The codified levels and the entrance variables with their work ranges are shown in Table 1.

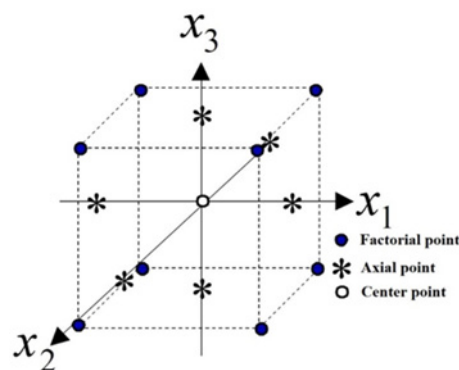


Fig. 1. Central composite design for three input variables

Table 1. The levels and ranges of cladding parameters.

	Factors			
	X_1	X_2	X_3	
	Power, [P], W	Traverse speed, [V], mm/s	Feeding rate of powder, [F], g/min	
Ranges and levels	-1.68	166	3.32	1.77
	-1	200	4	2.12
	0	250	5	2.65
	+1	300	6	3.20
	+1.68	334	6.68	3.53

2.3. Development of experiments

The materials used in the experimental procedure are:

- Metal powder of a heat-resistant nickel alloy ZhS32 with a fraction of 40-100 μm , obtained by the method of plasma rotating electrode process (PREP), was used as feeding material.
- Sliced turbine blade similar type was used as substrate material.
- High purity argon (99.998%) was used as shielding gas to protect a molten pool.
- Shielding gas flow rate: 15 liters/min.
- Spot diameter of laser beam was chosen according to width of repairing element of blade tip and amounted of 0.9 mm.

The cladding of the samples was carried out on a laser cladding technological machine, which includes the industrial robot LRM-200iD_7L, Fanuc; laser radiation source LK-700, IRE-Polus; laser focusing head FLW D30, IPG Photonics with coaxial nozzle COAX-40-S, Fraunhofer ILT; powder feeder Oerlikon Metco Powder Feeder Twin 150 with a groove of the metering disk 5×0.6 mm².

To analyze the samples microstructure, the longitudinal and cross sections were produced. To identify the structure, the surface of polishes was etched with nitromuriatic acid. Metallographic studies were performed using optical microscope Leica DMI 500 and scanning electron microscope Mira3 Tescan.

2.4. Model description

For understanding how temperature and stress distribution during multilayer laser cladding of ZrS-32 affect on cracking the process was simulated by ANSYS multi-physics finite element package. A 2D finite element (FE) model was developed for the numerical simulation. A total number of 4128 elements and 12681 nodes with various cell size were employed in the simulation. The model includes substrate with dimensions 5mm×6mm and cladding part with various dimensions. In the model, the element birth and death method was applied to simulate the multilayers.

The first step involves numerical analysis of thermal phenomena, where temperature distribution is obtained in cladded and substrate part. Results of thermal analysis are then implemented into mechanical analysis where stress and strain is generated by temperature distribution in every simulation time period.

The spatial and temporal distribution of the temperature field analysis is a typical nonlinear transient heat conduction problem, which satisfies the following heat condition equation:

$$\rho C_p \frac{\partial T}{\partial t} = \frac{\partial}{\partial x} \left(k \frac{\partial T}{\partial x} \right) + \frac{\partial}{\partial y} \left(k \frac{\partial T}{\partial y} \right) + Q, \quad (1)$$

where ρ is the material density, C_p is the specific heat capacity, T is the temperature of the model, t is the interaction time between the laser beam and the substrate, k is the thermal conductivity, and Q is the heat generation. The initial condition is $t=0$; $T=T_0$ and boundary conditions of Neumann type with the heat loss due to convection are used to complete equation (1).

In order to increase the efficiency of the simulation results, temperature depending of thermal conductivity and specific heat capacity was used.

The heat flux put on the substrate is high intensity laser energy nearly distributed as Gaussian relationship.

3. Results and discussions

3.1. The influence of laser cladding technological parameters on the cracking formation

During the metallographic studies of manufactured transverse and longitudinal sections, there are cracks, which were found in a number of samples, located mainly along the grain boundaries in the cladded metal (figure 2b, 2c). The typical length of cracks is from first to fourth layer.

Comparing the structure and cladding regimes, it is established that the appearance of cracks is affected by all three parameters expressed by energy amount absorbed by deposited metal volume. Firstly, the parameters corresponding to axial points and center of the plan were analyzed. It was found that defects occur with increasing of irradiation power (positive X_1) and traverse speed (positive X_2), and with decreasing of powder feeding rate (negative X_3). There were not found cracks at the plan' center and in the opposite meaning of axial point. Similar conclusions were also reached by the research of [1]. Secondarily, samples corresponding to factorial points were

examined. As expected, a sample, which was cladded using the regime with worst combination of factors (high laser power, high traverse speed, low feeding rate), had the cracks. Also, cracks were found in the samples which were cladded with two of three factors leading to cracks. There were no cracks in samples produced with combination of low irradiation power, low traverse speed, as well as combination of two of three these factors. There are experimental points (figure 3) showing the parameters leading to presence (red dots) and absence (green dots) of cracks.

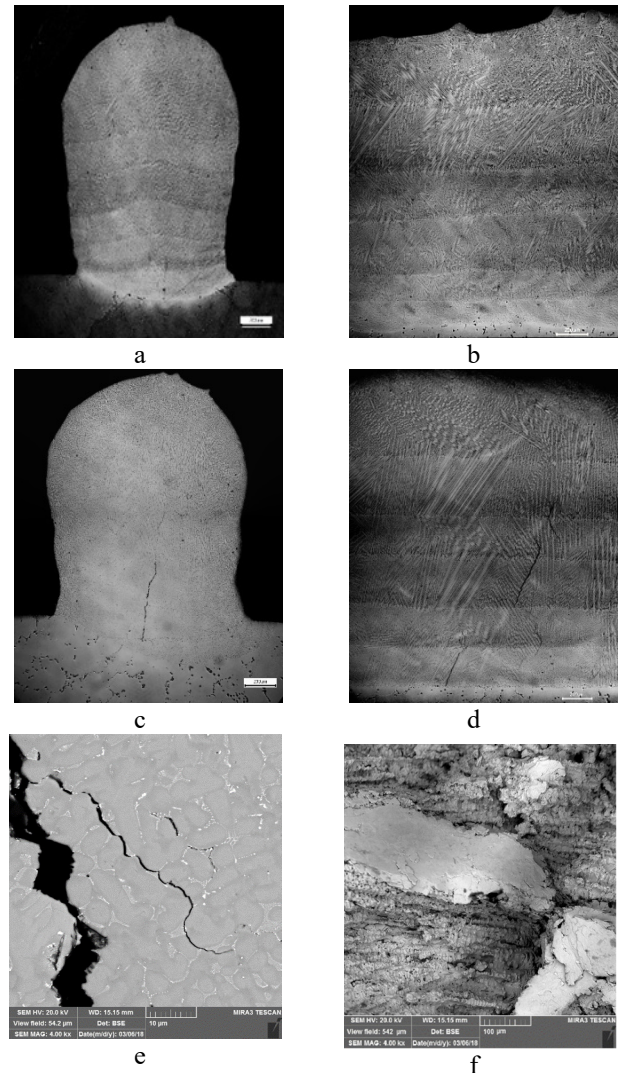


Fig. 2. Photos of cladded layers: a-b) qualitative regime, there are no macrodefects, c-d) regime leading to the cracks formation, e) a crack, and f) fracture of crack

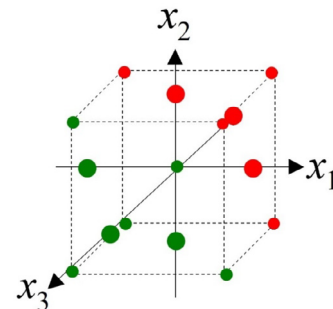


Fig. 3. The experimental regularity of the absence/presence of cracks in the cladded metal depending on the process parameters.

3.2. Cracking phenomena explanation

According to the results of fractographic analysis, these are crystallization cracks, which occur in the semisolid region. Hot cracking during solidification is caused by obstructed shrinkage. In welding and similar processes tensile stresses occurs when shrinkage is obstructed by the rigid or clamped down workpiece. Figure 4 shows stresses caused by thermal cycle during the multilayer cladding.

In view of the fact that cracks have crystallization character, let us consider behavior of the material in the temperature range of crystallization. The semisolid metal has little strength because the grains are not yet bonded together firmly but still separated by the grain boundary liquid. The problem is that the semisolid also has little ductility during the terminal stage of solidification when the fraction of liquid is no longer high enough for the grains to move around and rearrange themselves to accommodate the tensile strain. This phenomenon acts when secondary arms of one dendrites meets secondary arms of another one and closes stream of liquid to compensate shrinkage hollows. Thus, cracking can occur along grain boundaries during the last solidification stage [10; 11].

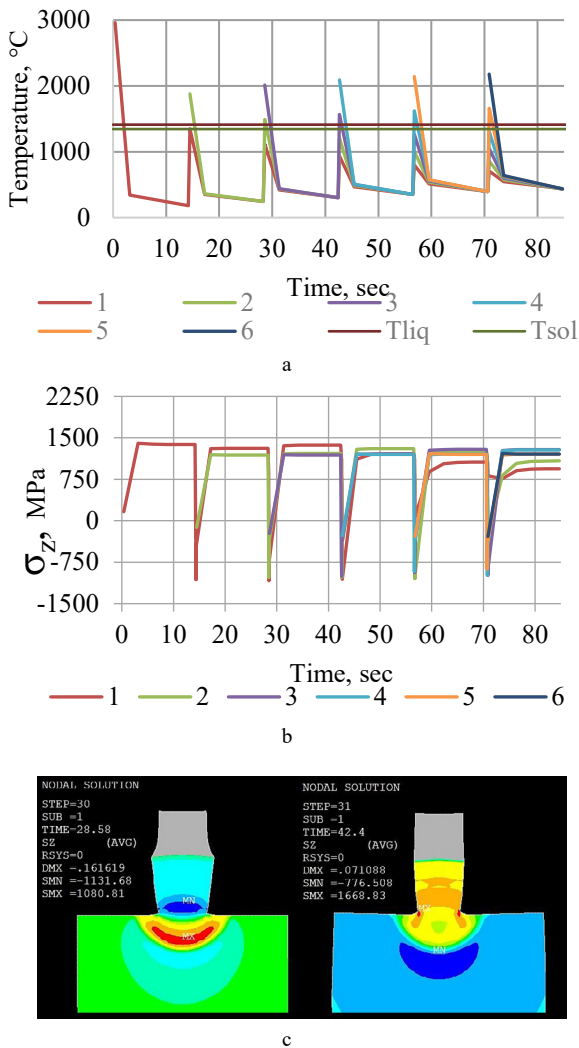


Fig. 4. Temperatures (a) and longitudinal stresses (b, c) occurring in the sample during laser cladding; 1 – 6 are layers. Cladding mode corresponds to center plan. Positive meaning is tensile stresses; negative meaning is compressive stresses

To estimate the probability of cracks, the criterion proposed by Kou [10] (equation 2):

$$\left\{ \frac{d\varepsilon_{local}}{dt} > \sqrt{1 - \beta} \frac{d\sqrt{f_s}}{dT} + \frac{1}{(dT/dt) dz} \left[(1 - \sqrt{1 - \beta} \sqrt{f_s}) v_z \right] \right\}_{\sqrt{f_s} \rightarrow 1} \quad (2)$$

where ε_{local} – local deformation, %, t – time, sec, β – cast shrinkage (2.5% [12]), f_s – fraction solid, T – temperature, z – length of solidified region, v_z – solidification speed. This inequality means that as bigger right side, which consist of two terms – grain growth and liquid feeding, respectively, as bigger strain rate is needed to crack initiation.

dT/dt and v_z depend of regime mode and computed based on thermal cycle. For calculate $d(f_s^{1/2})/dT$, it is necessary to consider the crystallization interval. According to [13] temperature crystallization range of pseudobinary diagram Ni – Σ Al, Ta, Re, Hf is 1412 – 1345 °C. Dependence of amount of fraction solid of temperature is evaluated by the sectional rule (figure 5). According to [14], temperature interval must be taken for $\Delta f_s = 0.9 \div 1$.

When $dT/dt \rightarrow \infty$ or $v_z \rightarrow 0$, then right side consists only grain growth part. And when $dT/dt \rightarrow 0$ or $v_z \rightarrow \infty$, then both terms act in the inequality. In the first approximation, lets mean $v_z = const$ and cooling rate = const for considered range. Then v_z could be proportional to the cladding speed $v_z = k \times v_{cladding}$ and only cooling rate could mostly help us to calculate the meaning of minimal strain rate. Figure 6 shows the typical cooling rate distribution during the multilayer cladding.

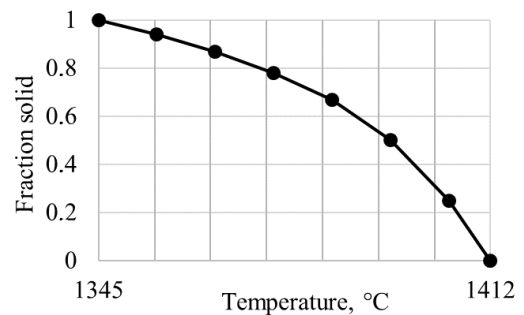


Fig. 5. Quantity of solid phase in the temperature crystallization range of ZhS32 alloy

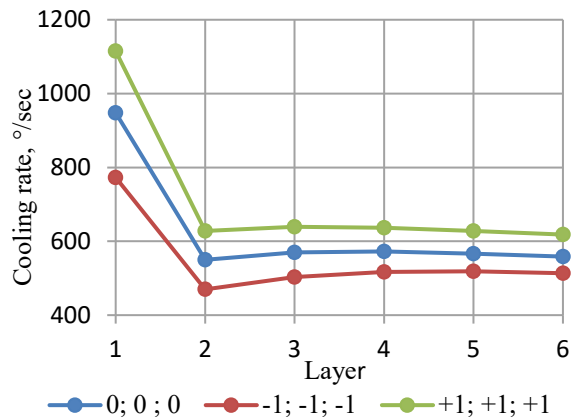


Fig. 6. Cooling rates on the bead surface after each pass

As we can see, the highest cooling rates occur by the first pass of cladding. It means that first pass is the most critical case

for cracking initiation. This sentence correlates with metallographic results, where crack begins from the first layer. In addition, as softer cladding mode (low laser power, low traverse speed, low powder feeding rate – curve “-1; -1; -1” in the figure 6), as lower cooling rates. Figure 7 shows the calculated strain rate distribution for cooling rates of each set of experimental parameters.

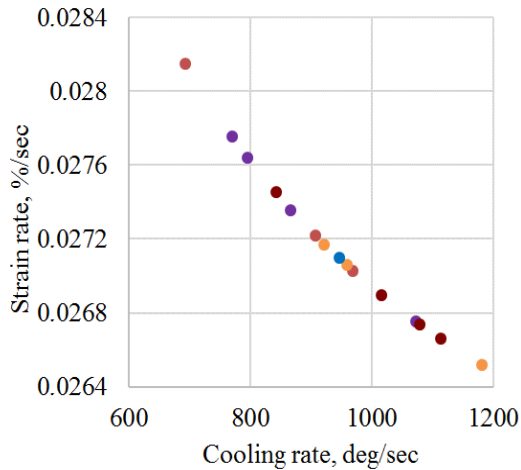


Fig. 7. Strain rate needed to initiate cracking for the different cooling rates. Violet dots – factorial points without cracks; orange dots – axial points without cracks; blue dot – center plan (without cracks); red dots – factorial points with cracks; green dots – axial points with cracks.

The calculated criterion (2) has good correlation with influence of laser power and traverse speed, but does not take into account the effect of powder feeding rate. This explains the experimental point's location mismatch on the curve in the middle part of dependency.

If the traverse speed $v = \text{const}$, then variation of powder feeding rate leads to the changes of layer's height. To investigate the powder feeding influence on the strain rate, let's divide cooling rate by the cladded layer height (figure 8). Figure 8 illustrates that as thicker cladded layer (moving from the right side to the left side), as lower cracking initiation possibility.

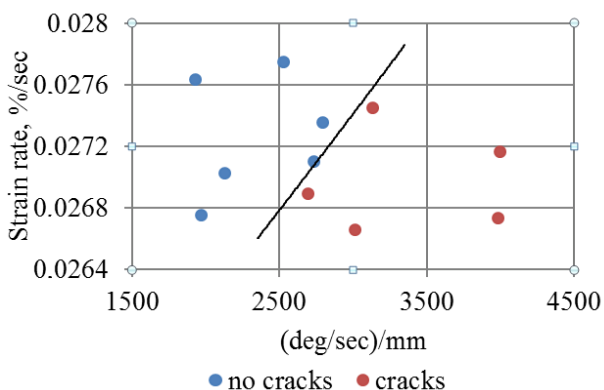


Fig. 8. Dependency of cooling rate divided by layer thickness on the cracking initiation possibility.

The final empiric dependency of regime mode on the cracking formation could look like it's presented in the figure 9.

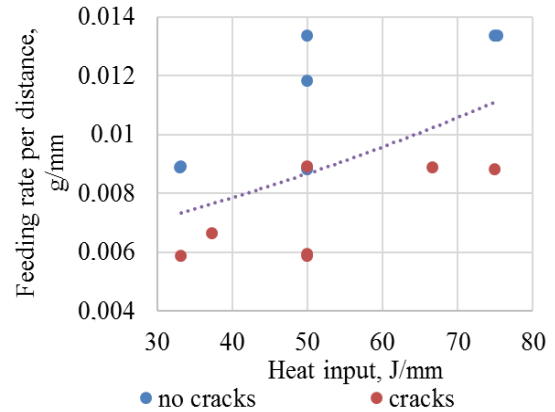


Fig. 9. The experimental regularity of the absence/presence of cracks in the cladded metal depending on the process parameters.

Conclusions

The laser cladding of ZhS32 nickel-based superalloy was carried out using the central composite design. During the metallographic analysis, the areas of experimental planning in which solidification crack formation is observed have been identified. It was found that defects occur with increasing of irradiation power and traverse speed, and with decreasing of powder feeding rate. A sample, which was cladded using the regime with worst combination of factors (high laser power, high traverse speed, low feeding rate), had the cracks. Also, cracks were found in the samples which were cladded with two of three factors leading to cracks.

The criterion which were used to cracking initiation has good correlation with two of three investigated parameters – laser power and traverse speed. However, the dependence for powder feeding rate is not clear enough. This can be explained by the fact that the criterion was created for the welding process, but not for cladding. The study of this parameter influence determined, that increasing of powder feeding rate leads to crack initiation declining. That can be explained by bigger amount of liquid metal, that fills shrinkage hollows during the crystallization process.

Based on the study results, laser cladding with soft regime modes can be recommended. Combination of low laser power, low traverse speed and high feeding rate ensure low cooling rates, low crystallization speed and liquid feeding during the solidification. As results higher strain rate is needed to initiate the crack. The developed criterion will be used to build a phenomenological model of hot crack formation in ZhS32 alloy in DED processes.

References

- [1] Wang S. Welding and repair of single crystal Ni-based superalloys. Master thesis. Ottawa: Carleton University; 2005.
- [2] Magerramova LA, Turichin GA, Nozhnitsky YA, et al. Peculiarities of additive technologies application in the production of gas turbine engine parts. IOP Publishing. InJournal of Physics: Conference Series; 2018. Vol. 1109, No. 1. 012051.
- [3] Turichin GA, Somonov VV, Klimova-Korsmik OG Investigation and modeling of the process of formation of the pad weld and its microstructure during laser cladding by radiation of high power fiber laser. Trans Tech Publications. InApplied mechanics and materials; 2014. Vol. 682, pp. 160-165.

- [4] Zemlykov EV, Babkin KD, Korsmik RS, et al. Prospects of use of laser cladding technology for restoration of compressor blades of gas turbine engines. *Photonics*; 2016. №4 (58). pp. 10-25.
- [5] Körner C, Ramsperger M, Meid C, et al. Microstructure and mechanical properties of CMSX-4 single crystals prepared by additive manufacturing *Metallurgical and materials transactions A.*; 2018. V. 49A. P. 3781 – 3792.
- [6] Derlomenko VV, Yushchenko KA, Savchenko VS et al. Technological strength and analysis of deterioration in weldability and cracking causes. *The Paton Welding Journal*; 2010. №9. pp. 20-24.
- [7] John N. DuPont. Application of Solidification Models for Controlling the Microstructure and Hot Cracking Response of Engineering Alloys // *Hot Cracking Phenomena in Welds III* 265-293 2011.
- [8] Lunev A.V. *Mathematical modeling and experimental design: Educational aid / Saint-Petersburg – SPbPU Publishing*; 2012. 153 p.
- [9] Torres EMM, Cruz JAG, Lopera JEP, et al. Parameter optimization in GMAW process with solid and metal-cored wires. In: *22nd international congress of mechanical engineering (COBEM 2013)*; 2013. pp. 5256-5266.
- [10] Kou S. A criterion for cracking during solidification. *Acta Materialia*; 2015. №88 366–374.
- [11] Coniglio N, Cross CE. Initiation and growth mechanisms for weld solidification cracking. *International materials reviews*; 2013. V. 58 № 7. 375-397.
- [12] Nurgayanova OS. Computer-aided design of casting heat-resistant nickel alloys based on artificial intelligence methods. PhD thesis; Ufa. 2006 (in Russian).
- [13] Azhazha VM, Sverdlov VYa, Ladygin AN, et al. The role of thermophysical conditions in the process of structure formation during directed crystallization of heat-resistant nickel-based alloys. *Voprosy atomnoy nauki i tekhniki*; 2004. № 6. pp. 128-135.
- [14] Cross CE. On the origin of weld solidification cracking. *Hot Cracking Phenomena in Welds*; 2005. pp 3 – 18.

11th CIRP Conference on Photonic Technologies [LANE 2020] on September 7-10, 2020

Comparative analysis of the gamma prime phase formation in nickel alloys in additive manufacturing

Gleb A Turichin^{a,*}, Olga G Klimova-Korsmik^{a,b}, Ekaterina A Valdaytseva^b, Andrey V Alekseev^b, Mariia V Rashkovets^c

^aSt. Petersburg State Marine Technical University, St. Petersburg, Russian Federation

^bPeter the Great St. Petersburg Polytechnic University, St. Petersburg, Russian Federation

^cNovosibirsk State Technical University, Novosibirsk, Russian Federation

* Corresponding author. E-mail address: gleb@ltc.ru

Abstract

The mechanical properties of Ni-based superalloys are based on the hardening gamma-prime phase with an ordered structure. A solution for new phase precipitate growth is suggested for the case of the Ni-based alloys. In accordance with solution a mathematical model of gamma-prime phase precipitates growth during direct laser deposition, which is a type of DED-method, was developed in order to be able to predict the size of the hardening gamma-prime phase grains and thus the mechanical properties of the alloy. A series of experiments on depositing samples using Ni-based superalloys powder was carried out to verify this model.

© 2020 The Authors. Published by Elsevier B.V.

This is an open access article under the CC BY-NC-ND license (<http://creativecommons.org/licenses/by-nc-nd/4.0/>)

Peer-review under responsibility of the Bayerisches Laserzentrum GmbH

Keywords: direct laser deposition; gamma-prime phase; Ni₃Al; mathematical model; precipitate's growth, Ni-based alloys

1. Introduction

Ni-based superalloys are mostly used in the manufacture of aviation gas turbine engines. Details made of Ni-based superalloys are nozzle and working blades that work at high temperatures, as well as turbine rotor disks and other parts of the combustion chamber [1,2]. These alloys occupy a leading position in terms of use and volume among high temperature alloys for constructional purposes.

Ni-based superalloys consist of a heterogeneous disordered γ -solid solution doped with various elements and having a face-centered cubic (FCC) lattice, as well as a strengthening γ' -phase, which is mainly Ni₃Al intermetallics with an ordered FCC lattice of the L1₂ type [3,4,5,6].

It is known that the size of the precipitates of the γ' - phase affects the mechanical properties of the resulting alloys. The phase size depends on the chemical composition of the alloy and its cooling rate [7,8,9,10]. Precipitates of this phase

prevent the movement of dislocations in the process of plastic deformation and thereby strengthening the alloy [11].

Due to the fact that the use of these alloys has found wide application in additive technologies [12,13], the implementation of laser based technology makes possible to control the processing modes with high accuracy and thus the cooling rate, and hence the size of the resulting precipitates of the γ' - phase.

Modeling the processes of heat transfer and growth of precipitates of a new phase allows reducing the labor cost of determining the necessary treatment mode for Ni-based superalloys using laser as the main source of input energy.

In previous articles [14,15], a model for the growth of precipitates of the strengthening gamma-prime phase (in particular, Ni₃Al intermetallics) in the process of direct laser deposition from the powder of the Ni-based superalloys EP741 was described.

In the article [15] was used a method for calculating the pre-exponential factor of the reaction rate constant for the formation of Ni_3Al intermetallide. One of the considered modes was taken as a reference mode. The values of the pre-exponential factor of the reaction rate constant and the limiting value of the size of the precipitate of the new phase are selected so that the size of the precipitates of the new phase is equal to the average value found by metallographic analysis and the concentration of the admixture on the surface of the precipitate is equal to the solubility of the admixture in the solvent at room temperature.

The value of the pre-exponential factor found by this way was used for calculation in other modes. The obtained satisfactory results showed the possibility of using this method for calculating the pre-exponential factor in this model, but it works only in a limited range of cooling speed.

This article tests the possibility of using the previously developed model on another heat resistant Nickel alloy using the previously selected value of the reaction rate constant.

2. Experiment

2.1. An experiment for obtaining a thin-walled sample by direct laser deposition using Ni-based superalloy

An experiment for depositing samples of Ni-based superalloy was carried out using the following equipment: 5 kW IPG YLS-5000 fiber laser, HighYAG BIMO processing head, Sultzer Metco Twin 10-C powder feeder. VV751P powder used as filler material. The VV751P alloy as well as EP741 alloy is used in the manufacture of turbine engine disks. These two alloys are functional analogs. The chemical composition of the VV751P alloy is presented in table 1.

Table 1. Chemical composition of the nickel-base superalloy VV751P.

Element	Ni	Co	Cr	W	Mo	Al	Ti	Nb	C
Average wt., %	56	15	11	3	4.5	4	2.8	3.3	0.06

Three experiments on depositing thin walls were carried out. The power of the laser source was changed (600, 900 and 1200 W) at constant values of the processing speed (45 mm/s), powder feed rate (20 g/min) and the beam diameter in the processing region (1.2 mm) in these experiments.

Hollow cylindrical samples were deposited in the experiment. Thick of the cylinder wall was equal to the single bead width. This experiment was also aimed to test the technology process. Modes were changed in the cylinder height sequentially from bottom to top: 600, 900, 1200 W. On every stage the sample was cooled to the room temperature before changing the power. Ten layers were deposited on each mode.

2.2. Metallographic examination of the deposited samples

The prepared cylinders were cut into specimens in accordance with the set modes. Metallographic analysis was fulfilled on a transmission electron microscopy. We assume that if a previous layer wasn't melted during reheating

process, size of the precipitates didn't change because of the reaction was finished. So, reheating didn't influence on the final structure significantly and lower layer could give the true information.

Microstructure images of the deposited sample are presented in Fig. 1.

The image clearly shows the crystals of the γ' -phase. Based on the obtained images, the average sizes of the γ' -phase precipitates of samples obtained by direct laser deposition at power of 600, 900 and 1200 W were determined. The average radius of the grains amounted to 18.20, 22.31 and 15.58 nm, respectively.

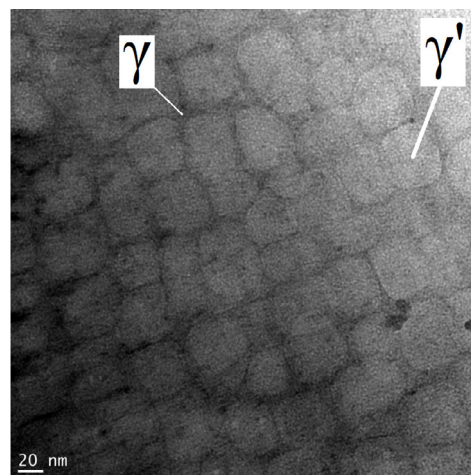


Fig. 1. Microstructure of the sample obtained at 600 W.

3. Simulation results

A model developed earlier [14,15] was used to calculate temperature field created by the laser source during direct laser deposition and growth of precipitates of the new phase.

The examined model is based on self-consistent solution of diffusion problem and kinetic equation of a chemical reaction.

This article will test the possibility of using the reaction rate constant value selected in article [15] for another heat-resistant Nickel alloy.

3.1. Results of the heat transfer solution

The calculations used the part of the thermal cycle responsible for cooling the alloy below the crystallization temperature of Ni_3Al intermetallide (1395 °C). Calculations were made for the layer whose alloy temperature last reached the melting point of the gamma-prime phase. This allows us to take into account the thermocyclicity of the direct laser deposition process, which involves multiple melting and crystallization of the alloy. Preheating from previous layers represents as an additional temperature in the thermal cycle of the examined layer. Initial temperature is 25 °C.

The resulting thermal cycles in examined areas are represented in Fig. 2.

Data processing of the graph in Fig. 2 shows that the higher the power of the laser source, the lower the cooling rate of the solid solution in the case when all other parameters are equal.

The cooling speed for modes at 600, 900, and 1200 W was 4176, 2743, and 2054 °C/s, respectively.

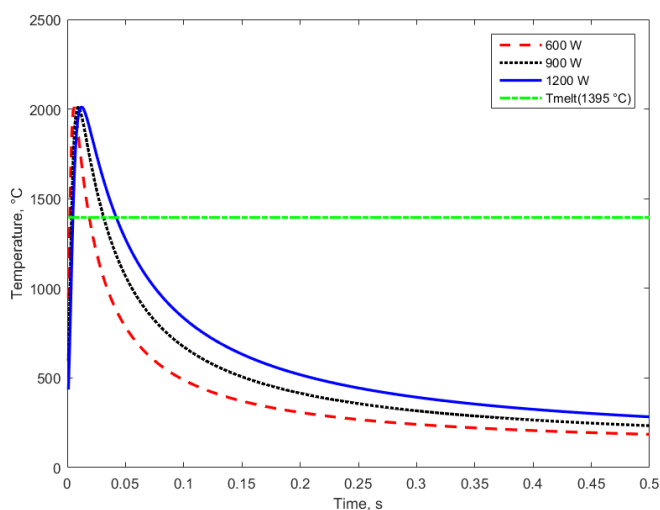


Fig. 2. Thermal cycles in the examined area.

3.2. Results of the new phase precipitate's growth solution

Having solved the heat transfer equation, a thermal cycle was found in the examined area. The resulting temperature-time dependence was used as an input parameter in the equation of the growth of a new phase. The solution of the last equation allows you to determine the size of the growing precipitates. The growth curves of gamma prime phase Ni_3Al precipitates is presented in Fig. 3.

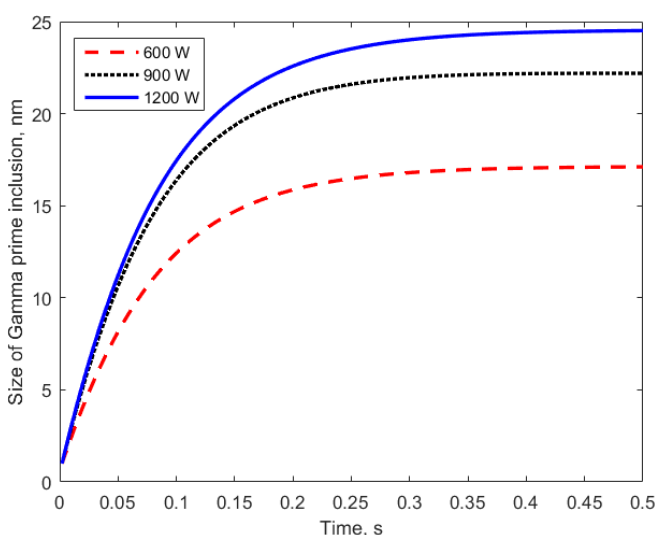


Fig. 3. Growth of new phase precipitates over time.

The graph of changes in the concentration of admixture (Al) on the surface of the growing precipitate is shown in Fig. 4.

The calculated and measured sizes of Ni_3Al intermetallic precipitates, cooling rates for each mode, as well as a comparison of the obtained data are presented in table 2.

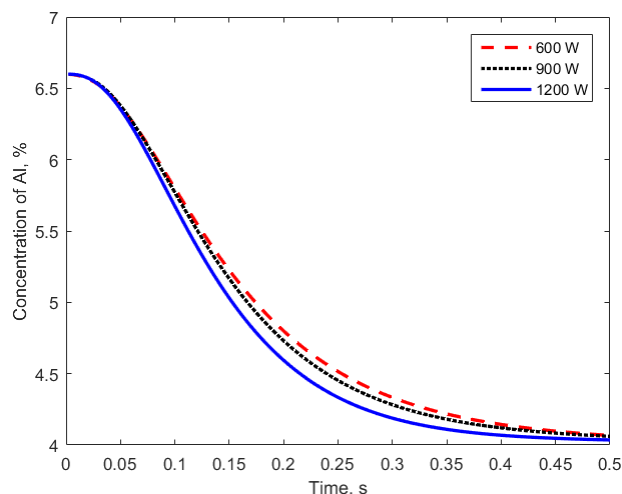


Fig. 4. Concentration of Al on the surface of the growing precipitate.

Table 2. Comparative table.

Power, W	600	900	1200
Cooling rate, °C/s	4176	2743	2054
Measurement size, nm	18.2±0.74	22.31±0.94	15.58±0.66
Calculated size, nm	17.17	22.41	24.59
Difference, %	5.65	0.45	58

4. Discussion

It is obvious from the table 2 that the experimentally measured average value of the precipitate size for the case with 1200 W mode is less than ones for other two cases.

This deviation may be due to the fact that the alloy is subjected to greater heating in modes with higher capacities. At higher temperatures, conditions are created for active growth of carbides, in particular TIC titanium carbides. Carbides formed in the γ -solid solution prevent the growth of intermetallics of the γ' - phase by influence on Ti concentration. A similar pattern was noted in the article [15], where an increase in the power of the laser source over 900 W led to a suspension of the growth of precipitates.

Microstructure images of the deposited specimens at 450 and 1200 W are shown in Fig. 5 and Fig. 6 respectively. These pictures were made using scanning electron microscope. The formed carbides circled in the pictures.

In the pictures we can see that the quantity and the size of carbides at 450 W much less that at 1200 W. This can indirectly confirm the theory that higher temperatures create more favorable conditions for the growth of carbides, which affects the growth of inclusions of gamma prime phase.

Thus, a significant deviation of the calculated and experimentally obtained sizes of precipitates at power 1200 can be explained by the difficult formation of precipitates of the γ' -phase due to the presence of natural obstacles in the γ -solid solution, represented as various carbides. This feature is not taken into account in the developed model, which take into account formation only one new phase, that imposes restrictions on the scope of its application.

The deviation of the calculated size from the average value of the experimentally measured size in the mode with a laser

source power of 600 W is insignificant and amounted to 5.65 %.

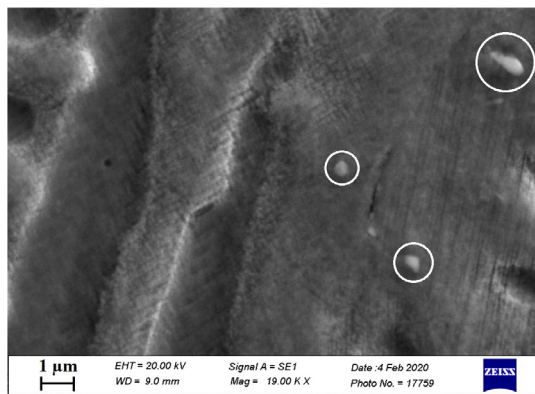


Fig. 5. Microstructure of the sample obtained at 450 W.

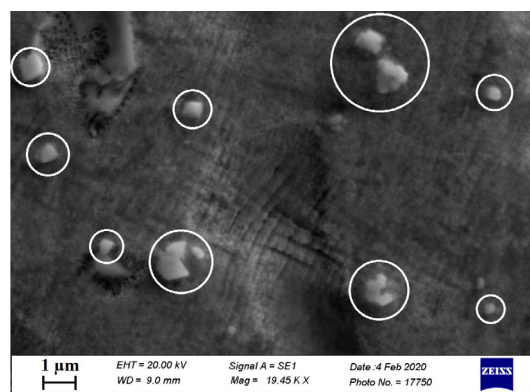


Fig. 6. Microstructure of the sample obtained at 1200 W.

The difference in size in the mode with the power of the 900 W laser source was 0.45 %, which is within the measurement error.

Thus, it was shown that this model can be used to calculate the size of the γ' -phase precipitates that occur in heat-resistant Nickel alloys during direct laser deposition. But for increases of modelling precision it is necessary to include into the model description of formation of several different phases with mutual influence through concentration of impurities in solid solution.

5. Conclusion

Size of the γ' -phase precipitates was calculated using the developed model. The model combines the solution of the heat transfer problem of the direct laser deposition process and the analytical solution of the growth problem of the precipitate of a new phase thermodynamically different from the original one.

Comparison of the results of metallographic research and calculated data showed that the calculated value of the size of the precipitates of the γ' -phase and the experimentally found value agree with each other with a fairly high accuracy.

The limits of applicability of the currently developed model related to the formation of carbide phases at high

temperatures due to the features of the selected mode were revealed.

Thus, it is necessary to refine the existing model and apply a more comprehensive approach to solving the problem, which would take into account the mutual influence of the elements included in the alloy.

References

- [1] Pollock T M и Tin S 2006 Nickel-based superalloys for advanced turbine engines: Chemistry, microstructure, and properties J. Propuls. Power.
- [2] Korsmik R S, Turichin G A, Klimova-Korsmik O G, Alekseeva E V. и Novikov R S 2018 Development of laser powder cladding technology for restoration of heat-resistant nickel alloys turbine blades Journal of Physics: Conference Series.
- [3] Trosch T, Strößner J, Völkl R и Glatzel U 2016 Microstructure and mechanical properties of selective laser melted Inconel 718 compared to forging and casting Mater. Lett.
- [4] Pinz M, Weber G, Lenthe W C, Uchic M D, Pollock T M и Ghosh S 2018 Microstructure and property based statistically equivalent RVEs for intragranular γ - γ' microstructures of Ni-based superalloys Acta Mater.
- [5] Alabbad B, Li L и Tin S 2019 Controlling the grain boundary morphology and secondary γ' precipitate size distribution in Ni-base superalloys J. Alloys Compd.
- [6] Smith T M, Bonacuse P, Sosa J, Kulis M и Evans L 2018 A quantifiable and automated volume fraction characterization technique for secondary and tertiary γ' precipitates in Ni-based superalloys Mater. Charact.
- [7] Wu H, Huang Z, Zhou N, Chen J, Zhou P и Jiang L 2019 A study of solution cooling rate on γ' precipitate and hardness of a polycrystalline Ni-based superalloy using a high-throughput methodology Mater. Sci. Eng. A
- [8] Murakumo T, Kobayashi T, Koizumi Y и Harada H 2004 Creep behaviour of Ni-base single-crystal superalloys with various γ' volume fraction Acta Mater.
- [9] Papadaki C, Li W и Korsunsky A M 2018 On the dependence of γ' precipitate size in a nickel-based superalloy on the cooling rate from super-solvus temperature heat treatment Materials (Basel).
- [10] Babu S S, Miller M K, Vitek J M и David S A 2001 Characterization of the microstructure evolution in a nickel base superalloy during continuous cooling conditions Acta Mater.
- [11] Pinz M, Weber G, Lenthe W C, Uchic M D, Pollock T M и Ghosh S 2018 Microstructure and property based statistically equivalent RVEs for intragranular γ - γ' microstructures of Ni-based superalloys Acta Mater.
- [12] Moor J, Debiccari A, Lagow B, Tewari S и Kinsella M 2010 Additive manufacturing for superalloys-producibility and cost 7th International Symposium on Superalloy 718 and Derivatives 2010.
- [13] Attallah M M, Jennings R, Wang X и Carter L N 2016 Additive manufacturing of Ni-based superalloys: The outstanding issues MRS Bull.
- [14] Alekseev A, Valdaytseva E и Aleksandrov V 2019 Modeling of the Formation Process of the Coherent Intermetallics in Nickel Alloys During Laser Treatment Key Eng. Mater. 822 438–44
- [15] A.V. Alekseev, G. A. Turichin, O. G. Klimova-Korsmik et al., Simulation of the Ni₃Al intermetallic precipitate growth process during direct laser deposition using Ni-based superalloy powder, Materials Today: Proceedings, <https://doi.org/10.1016/j.matpr.2020.01.562>

11th CIRP Conference on Photonic Technologies [LANE 2020] on September 7-10, 2020

Case study on AM of an IN718 aircraft component using the LMD process

J. Kittel^{a*}, A. Gasser^a, K. Wissenbach^a, C. Zhong^a, J. H. Schleifenbaum^{a,b}, F. Palm^c

^aFraunhofer-Institut für Lasertechnik ILT, Steinbachstr. 15, 52074 Aachen, Germany

^bDigital Additive Production DAP, RWTH Aachen University, 52074 Aachen, Germany

^cAirbus Defence and Space GmbH, Willy-Messerschmitt-Str. 1, 82024 Taufkirchen, Germany

* Corresponding author. Tel.: +49-241-8906-136 ; fax: +49-241-8906-121. E-mail address: jochen.kittel@ilt.fraunhofer.de

Abstract

When manufacturing components from forged blanks of nickel-based super alloys, companies have to cope with rising prices, long delivery time as well as cost intense machining. In this case Additive Manufacturing (AM) can provide an alternative solution. To prove the feasibility of AM, an aircraft engine mounting component was successfully built up by Laser Material Deposition (LMD) from Inconel 718 powder. Due to the length of 500 mm and its complex structure, the pylon bracket component is demanding to build up by LMD. Investigations on process and build-up strategy development as well as analysis of deformation behaviour have been performed.

© 2020 The Authors. Published by Elsevier B.V.

This is an open access article under the CC BY-NC-ND license (<http://creativecommons.org/licenses/by-nc-nd/4.0/>)
Peer-review under responsibility of the Bayerisches Laserzentrum GmbH

Keywords: "Additive Manufacturing ; 3D Laser Material Deposition ; near-net-shape ; Inconel 718 ; Aviation"

1. Introduction

Laser material deposition (LMD) is a free form additive manufacturing (AM) technology that can be used to produce functional, three-dimensional components. LMD provides significant benefits over conventional manufacturing due to a low heat input, near net-shape manufacturing and a high material efficiency [1].

Investigations have been carried out on an Inconel 718 engine mount component of a civil passenger jet by applying the LMD technology. To prove the concept, a demonstrator of an aircraft pylon bracket (Fig. 1) supplied by Airbus Group was built up and machined. The investigation is focused on build-up strategies, deposition rate and deformation. One of the technological challenges is to limit the distortion of the part and substrate material during the build process in order to successfully perform final machining and thereby achieve a valid component. This aspect at the same time has a strong economic impact as this allows near-net-shape manufacturing and a high resource efficiency resulting in a low buy-to-fly ratio which represents the relation of the raw material weight to the weight of the final part. One target within the investigation is to

obtain a buy-to-fly ratio improvement of 100%. Compared to a ratio of 4 for milling from a forged blank, the goal is to achieve a buy-to-fly ratio of 2 or less.

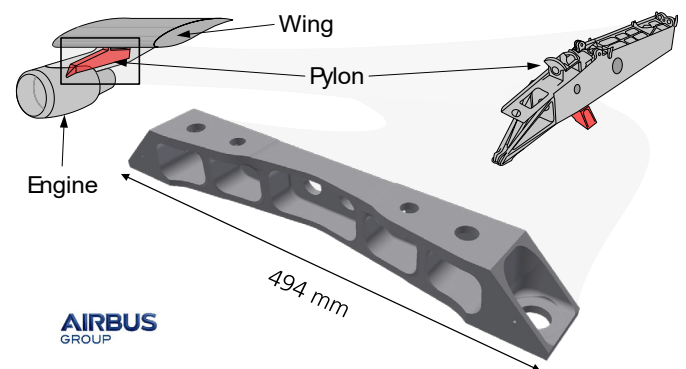


Fig. 1. Pylon bracket demonstrator component APOD11

Due to its size of 500 mm the investigated component exceeds the limits of standard powder bed machines and therefore is better suited for direct laser deposition (DED)

processes [2]. Larger AM DED components have been manufactured using wire or powder as additive material for example on rocket engine components and aircraft frames mainly applying laser radiation or electric arc as energy source [3,4,5]. Compared to a full part build, a hybrid approach can be advantageous, as demonstrated in an application of building up turbine blades on a disk [5].

2. Experimental Investigation

Within the experimental investigation, aspects related to equipment, materials, process parameter development and deformation issues are addressed in respect to the planned demonstrator.

To reach the objective of an economic and efficient production, one of the key factors of the LMD process is the deposition rate which is the mass deposited per time. As the dimensions of the individual tracks influences the build-up rate and the dimensional accuracy, this is explicitly examined in chapter 2.3. As the final geometry of the demonstrator is achieved by milling, the LMD built up volume has to be larger to supply sufficient additional material for machining. The needed amount of additional material is strongly dependent on the distortion developed during the LMD. The lower the deformation, the less additional or excess material is necessary. Due to the importance of distortion, this topic is investigated in chapter 2.4.

2.1. IN718 Additive Material

The applied additive material for the LMD process is metal powder from the alloy IN718 with a nominal powder particle size from 45 – 75 μm . IN718 is a niobium-modified nickel-based super alloy, which is widely used in the aero and space industry for critical rotating parts, airfoils and pressure vessels. It provides high tensile strength, creep-rupture strength, fatigue life and resistance to oxidation at temperatures up to 700°C. [6,7]

2.2. Experimental Setup

During LMD, a melt pool is generated on the surface of the substrate material or a previous layer by laser radiation. Simultaneously, the IN718 powder is injected into the melt pool by a powder nozzle attached to the laser processing head. By moving the laser processing head relative to the substrate material, the material solidifies and generates a clad track forming a metallurgical fused bond. By stacking tracks next to each other, deposition layers can be created and by stacking layers on top of each other, 3 dimensional structures can be produced.

The LMD setup for processing is displayed in Fig. 12. The laser radiation is emitted by a 3 kW Nd:YAG laser via a 600 μm fiber linked to a 200 mm collimation and a 200 mm focusing optic. The IN718 powder is transported to an ILT-Coax-40 powder nozzle from the powder feeder by Argon feeding gas via connected tubes and a powder splitter. The

Laser optics and the powder nozzle are adjusted to each other and mounted to a NC-controlled 5-axis handling system. During LMD processing, local shielding is applied by an argon gas flow fed through the exit of the powder nozzle to prevent oxidation.

2.3. Deposition Rate Investigation

As the LMD track dimension has a high dependency on the deposition rate, a variation of the track width has been analysed to determine the appropriate settings for the build-up of the demonstrator part. The processing velocity is a further factor with a strong influence on the deposition rate. Due to the limited LMD machine acceleration (inertia) and the demonstrator structure size, the processing velocity was fixed to 1500 mm/min to avoid inaccuracy and speed fluctuation. For deposition rate analysis, representative sections were extracted from the pylon bracket geometry as feature samples (Fig. 2). As marked in Fig. 2, a wall (1), a T-section (2) and a triangle (3) feature were designed for this purpose.

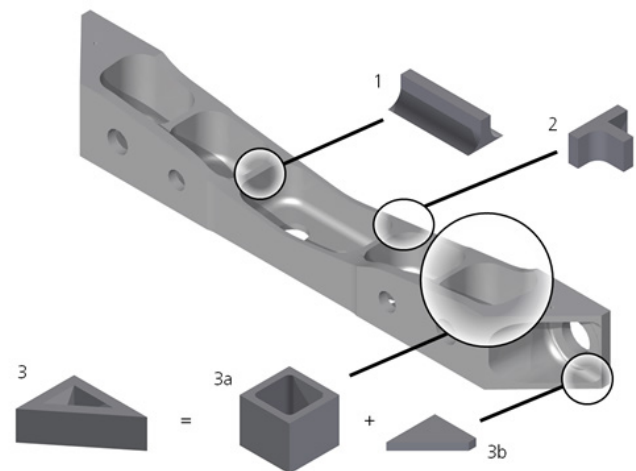


Fig. 2. Feature samples extracted from the pylon bracket geometry

Within the track size investigation, the track width was varied from 1 to 4 mm in 1 mm steps on all selected features. Exemplary the obtained samples of the triangle feature sample T1 to T4 (side length approx. 45 mm) are displayed in Fig. 3.

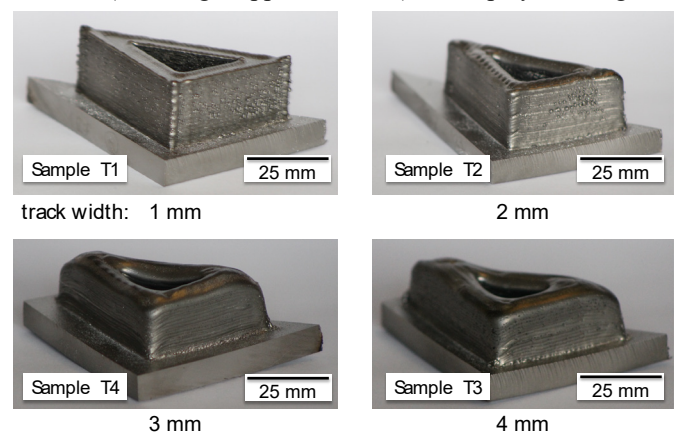


Fig. 3. Triangle feature samples T1 to T4 with track width variation (1-4 mm)

The achieved grade of resolution and accuracy distinguishes all feature samples and decreases with increasing track width. Regarding the detail resolution, the samples with 1 mm track width shows the best result.

The surface of the layers are filled up by a meander shaped pattern. The laser spot diameter has been set to the same value as the track width. The main applied process parameters used for all features are listed in table 1.

The LMD deposition rate relates to the build-up rate when processing (laser on time). As visible in table 1 the deposition rate is significantly dependent on the track size rising from 125 g/h to approx. 2 kg/h which relates to an increase by a factor of 15.

Table 1. Process parameter settings of track width variation

Track width [mm]	1	2	3	4
processing velocity [m/min]	1.5	1.5	1.5	1.5
laser power [kW]	0.5	1.2	2.6	3.3
powder feed rate [g/h]	180	600	1380	2040
track offset [mm]	0.5	1.0	1.5	2.0
layer offset [mm]	0.34	0.75	1.15	1.3
LMD deposition rate [g/h]	125	550	1270	1915

The pylon bracket as well as the features contain wall structures which heat up the part significantly during the build process. With wider tracks higher laser power settings are needed (table 1), increasing the heat input and part temperature even further. To avoid overheating and oxidation a temperature limit of 70°C before starting the next layer has been determined. The temperature on the surface of the top layer was measured by a thermocouple after each layer and if the temperature was above 70°C, a cooling break was inserted before continuing with the next layer. The duration of the build process for the feature samples was recorded and evaluated as displayed in Fig. 4 for the T-section. As the target volume is constant, the duration directly indicates the deposition rate.

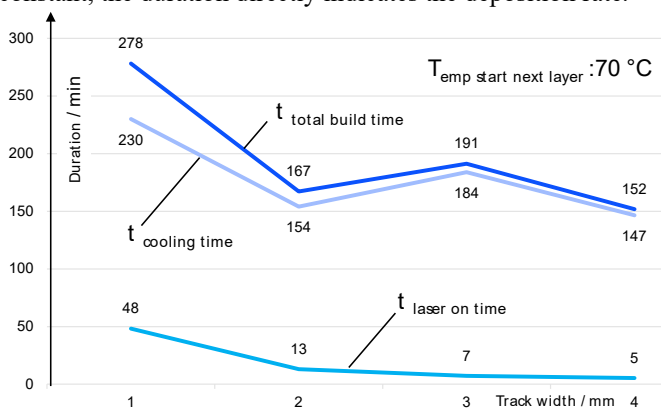


Fig. 4. Build duration of LMD feature T-section T1 – T4 with 70°C limit

The correlation of the three time curves of the T-section feature for track widths of 1 to 4 mm are presented in Fig. 4:

- Material depositing time only (laser on time)
- Time to cool down to 70°C
- Accumulated total build time

As expected, the process laser-on time decreases rapidly with larger track widths from 48 min for 1 mm to 5 min for

4 mm track width. With wider tracks, the total LMD track length is shorter, hence the laser-on time drops. Additionally the layer offset is larger too for wider tracks reducing the number of layers needed to build up the targeted height of 15 mm. Concluding the laser-on time, the deposition rate of the 4 mm tracks is 9 times higher than that of the 1mm tracks. If no cooling is considered, this would also be the total build time for the samples and an essential benefit. The situation changes dramatically if cooling of the top surface to 70°C is requested. The increased laser power (table 1) for wider tracks boosts the energy transferred to the sample, heating it up strongly and thus requiring a significant cooling time to reduce the temperature again. Due to this effect, the 3 and 4 mm wide tracks lose their advantage compared to the 2 mm tracks. The 1 mm setting offers the highest geometric resolution, but by far has the longest total build time and by this the lowest overall deposition rate and therefore is not considered for further trials.

Concluding the 2 mm track width parameter set obtains the second best deposition rate with cooling time of which is only 9% less than that of 4 mm track width. Further considering the achieved detail resolution and the wall structure of the pylon bracket the 2 mm track width is best suited compared to the 3 and 4 mm tracks. Therefore the 2 mm track width parameter set is selected for manufacturing the final demonstrator. The achieved metallographic result is documented by the displayed cross section in Fig. 5 revealing a porosity level below 100µm and no visible cracks or bonding defects.

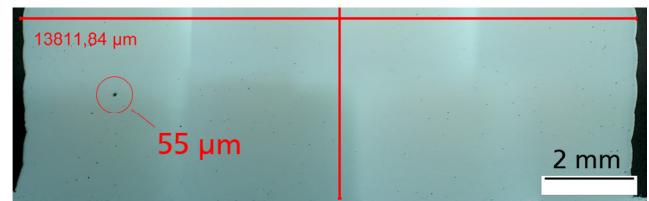


Fig. 5. Cross section analysis of the 2 mm track width parameter set

2.4. Deformation Analysis

Regarding the sleek and 500 mm long shape of the pylon bracket, deformation is a critical issue and it is a challenge to obtain a buy-to-fly ratio r_{btf} of 2 or less which can be calculated by:

$$r_{btf} = \frac{(V_{part} + V_{excess})}{V_{part} * \eta} \quad \text{with } V_{LMD} = V_{part} + V_{excess} \quad (1)$$

By applying equation 1 the deformation limit for a given buy-to-fly ratio can be determined. With a ratio r_{btf} of 2, the pylon bracket volume V_{part} of 536 cm³ and a powder efficiency η of 90% the excess volume is calculated to $V_{excess} = 429$ cm³ by equation 1. As the calculated excess volume is needed for machining and compensating deformations it is represented by an equidistant offset surface to the CAD geometry (Fig. 2). At a surface offset of 2.5 mm the offset volume matches the calculated excess volume $V_{excess} = 429$ cm³. As a consequence the offset surface also limits the distortion of the LMD part: If the distortion is larger than 2.5 mm then the CAD geometry does not fit inside the LMD part. The total LMD volume is determined to $V_{LMD} = 965$ cm³ (equation 1). The powder efficiency of 90% is calculated from table 1 for a track width

of 2 mm considering a 2% loss for process start and stop. Regarding deformation two strategies were investigated:

- Preheating to reduce the stresses induced by the LMD process and by this lower the deformation
- Increased substrate stiffness to withstand the deformation caused by the induced stresses

In an experimental study, preheating of the substrate by laser radiation was tested to reduce the induced deformation. Two identical test geometries of 150 mm x 80 mm were generated on a 15 mm thick 1.4301 substrate material (Fig. 6): Sample LH_RT starting at room temperature (25°C) and sample LH_325 with preheating to 325°C. On sample LH_325 preheating was obtained by scanning the sample surface with a defocused laser beam prior each layer.

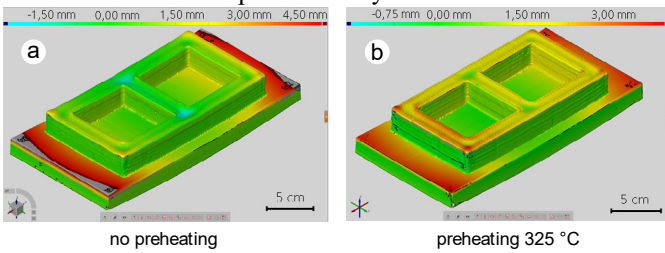


Fig. 6. Deformation analysis samples (a) LH_RT without preheating and (b) LH_325 with preheated substrate to 325°C

Due to preheating the laser power was reduced by 16%. The LMD processing of the test geometries was performed with the 2 mm track width parameter set from table 1.

A geometric analysis of the completed samples was performed with a GOM Atos Compact Scan inspection system. The deformation on the substrate surface without preheating summed up to be 4.5 mm (Fig. 6a) compared to a value of 3.4 mm (Fig. 6b) when preheated to 325°C. The deformation could be reduced by approx. 25%. Although preheating leads to a deformation reduction, this approach is not applicable for the demonstrator part due to the remaining deformation of 3.4 mm which exceeds the limit of 2.5 mm. A further disadvantage is the time consuming preheating.

Therefore an alternative strategy was studied on the APOD11-50-1 sample which is a half part of the final demonstrator. In order to reduce the deformation, a stiffer structure was added to the rear side of the 20 mm thick 1.4301 substrate by LMD (Fig. 7).

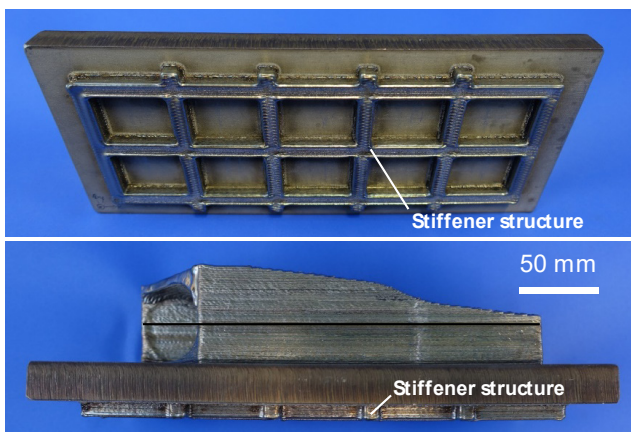


Fig. 7. Half part APOD11-50-1 with rear stiffener structure

As with the previous samples, the APOD11-50-1 sample was inspected with the GOM system, detecting a distortion of 2.75 mm along the substrate of the sample (Fig. 8).

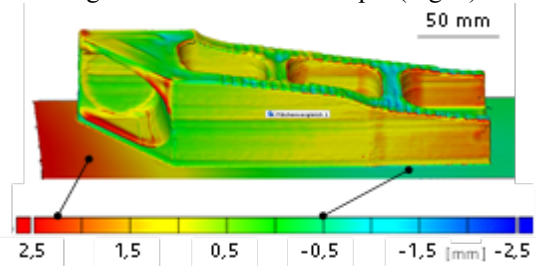


Fig. 8. Deformation analysis on the half part APOD11-50-1

In order to further improve the stiffness of the substrate and by this reduce deformation, a rigid platform was designed (Fig. 9). It is assembled as a welded construction from 20 mm thick 1.4301 sheet material (Fig. 9b) to support the demonstrator manufacturing by LMD.

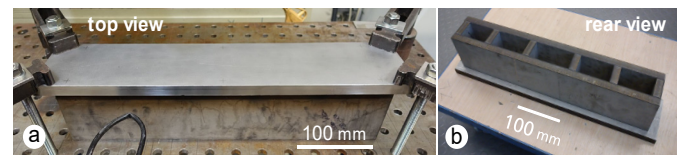


Fig. 9. LMD build platform for demonstrator

3. Manufacturing of the Demonstrator

The achieved results are taken into account when building the pylon bracket demonstrator including a geometry adaption step and a heat treatment and final machining. Due to the rigid platform a further deformation reduction is expected. To take advantage of the reduction the surface offset was lowered to further improve the buy-to-fly ratio. The planned surface offset consists of a 1 mm offset from the CAD geometry and 1 mm resulting from half of the 2 mm LMD track width. The total surface offset of 2 mm leads to a calculated LMD volume of 852 cm³ and results in a fly-to-buy ratio of 1.77 (equation 1).

3.1. LMD Related Geometry Adaption

In order to build up the demonstrator, LMD process related modifications have to be applied to the original part geometry (Fig. 10).

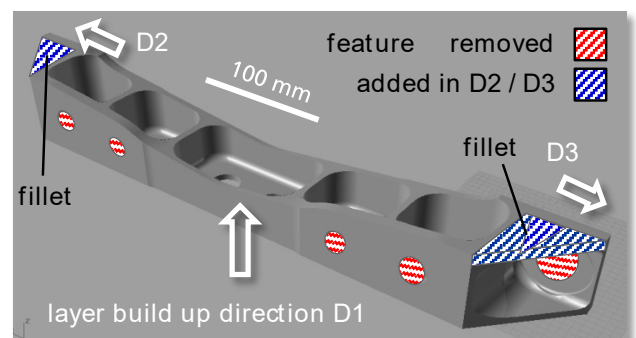


Fig. 10. Geometry adaption to achieve feasibility for LMD processing

Considering the selected main layer build-up direction, this applies to 2 types of features:

- The horizontal bore holes (marked in red in Fig. 10)
- The fillet sections on the left and right upper side of the demonstrator (marked in blue in Fig. 10)

As the horizontal bore holes cannot be generated by LMD, they are removed from the geometry and filled up. Instead, they will be manufactured in the final machining step. Due to missing support the fillet features are removed from the geometry and have to be added in a following step with a different part orientation.

3.2. LMD Build-up of Demonstrator

The demonstrator was manufactured in 2 sections consisting of the body with the build-up in direction D1 and the fillets added on the outer sides in the modified direction D2 and D3 (Fig. 10). For the demonstrator build-up, the 2 mm wide LMD tracks were applied using the settings in table 1.

The body was built on the designed platform which was clamped onto the machine table to add further stiffness to the setup (Fig. 11). The build direction is perpendicular to the platform top surface which is indicated by the white arrow.

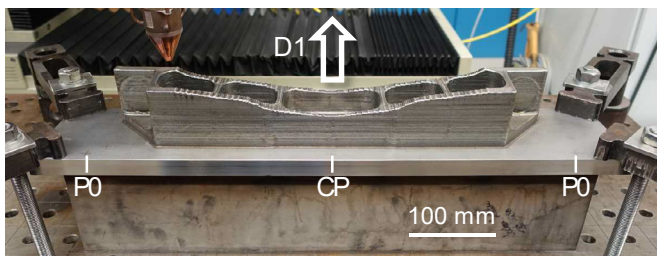


Fig. 11. LMD build-up of demonstrator body on platform

Based on the CAD-Dataset, the slicing of the LMD-layers and generating of the LMD tracks was performed with help of the ILT CAM planning tool LMDCAM. The body section was built up in 75 layers. To improve the cooling effect, water cooled copper pipes were fitted to the platform.

In the next build step, the fillets were added to the sides in the adapted build direction D2 (Fig. 10) and D3 (Fig. 12).

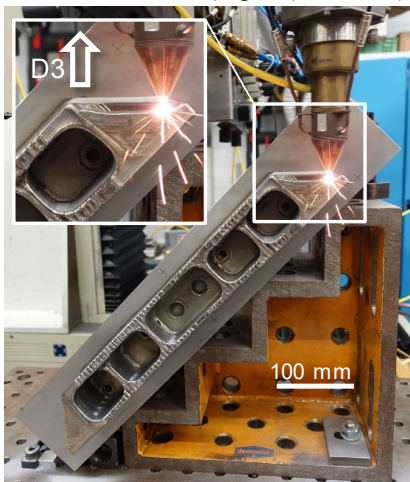


Fig. 12. LMD build-up of demonstrator of fillet 2 in direction D3

The body with the platform was aligned and clamped to a fixture to obtain the desired orientation with the Z-axis of the handling system perpendicular to the front edge of the fillet.

Fig. 13 displays the successfully completed pylon bracket on the platform after cleaning by sandblasting.

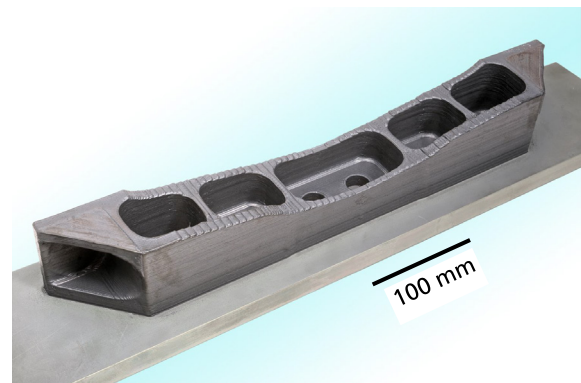


Fig. 13. LMD built pylon bracket demonstrator on the platform

The total LMD processing time for the demonstrator summed up to approx. 16.5 h. With the afforded cooling time of approx. 7.5 h, the total build time accumulated to 24 h. Before removal of the completed demonstrator from the platform a deflection of 1.25 mm was detected in the platform centre position CP (Fig. 11) in respect to the outer positions P0 which indicates a significant deformation reduction.

3.3. Post Processing and Analysis of Demonstrator

The final steps are to remove the demonstrator from the platform, to validate the build results and machine sections of the demonstrator to achieve the final part geometry.

As the LMD process induces stress in the deposited material a significant internal stress level accumulates during processing. When cutting off the LMD part from the platform, the “holding forces” of the platform are no longer present. The residual stresses present in the part can lead to a deformation. In order to eliminate or at least reduce the internal stress level, a heat treatment for stress relief has been included. The performed solution heat treatment of the LMD part and platform consisted of heating up to 980 °C at a rate of 5 K/min, holding this temperature for 1 h and cooling down to 200 °C at a rate of <2.5 K/min. Compared to an usual solution heat treatment with a harsh cooling phase, a low cooling rate was selected to avoid a new stress development. After heat treatment, the LMD demonstrator was trimmed off the platform by wire-cut electric discharge machining (EDM).

To analyse the LMD geometry, the demonstrator was scanned with the GOM Atos measurement system. The analysis of the measurement is displayed in Fig. 14. According to the colour grading, the offset from the CAD geometry ranges from 0.4 to 1.9 mm and this indicates the amount of excess material available for machining. The deformation of the LMD part causes the excess material thickness to vary.

Considering a calculated volume of 831.4 cm³ from the scan data a buy-to-fly ratio of 1.72 is obtained (equation 1). Calculating the buy-to-fly value from the parts weight of 6.9 kg

results in a ratio of 1.75 considering a density of 8.19 g/cm^3 for IN718 confirming the planned value of 1.77 (chapter 3.3).

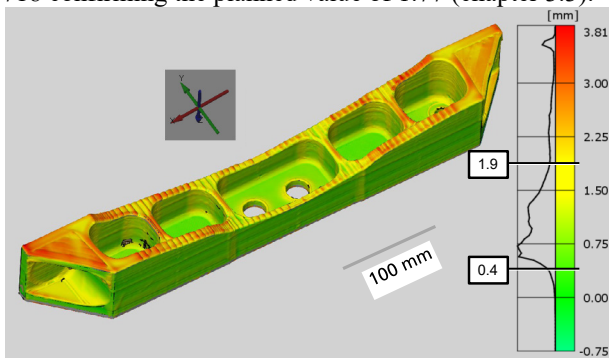


Fig. 14. Surface offset of the LMD demonstrator related to CAD-model

In order to determine the base deviation and the yield of the heat treatment the base surface was analysed. The examination reveals a low deviation of 0.4 mm as presented in Fig. 15.

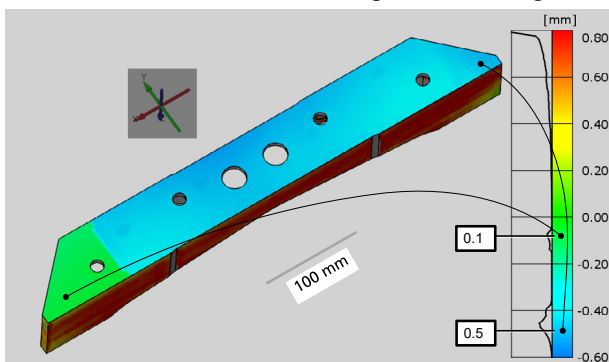


Fig. 15. Deviation of the demonstrator base surface

These results prove that the rigid platform design combined with the solution heat treatment could effectively reduce the distortion of the part to below 2 mm.

Based on the measurement data the last step of machining the pylon bracket demonstrator was planned with the CAM software Mastercam. Half of the demonstrator was milled according to the CAD-data. The remaining surface is left in the LMD processed state to allow a comparison of the processes involved. The final state of the pylon bracket demonstrator after successful machining is presented in Fig. 16.

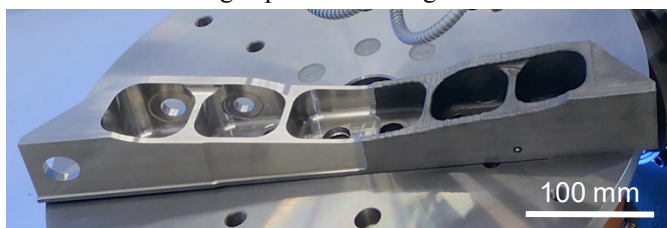


Fig. 16. Final pylon bracket demonstrator after machining

4. Conclusion

The manufacturing of a IN718 pylon bracket demonstrator by LMD served as a case study to analyse production and resource efficiency of the LMD process (chapter 2.3,2.4).

Investigations on LMD track width were performed in respect to the deposition rate and build resolution. A Temperature limit was defined to avoid overheating which afforded cooling breaks and reduced the overall deposition rate. From the track size analysis, the 2 mm wide LMD tracks were selected for all the following samples as they showed the best overall performance. The 2 mm tracks offer high detail resolution with a deposition rate only 9% below the highest score of the 4 mm tracks when considering the temperate limit.

The trials on resource efficiency focused on minimizing deformation as it has a contradictory influence and increases the buy-to-fly ratio. Two approaches, preheating and increasing stiffness of the substrate, were investigated resulting in designing a rigid platform.

The final pylon bracket demonstrator was successfully built up on the platform with a distortion below 2 mm (chapter 3.2). To avoid internal stresses deflecting, the part when cut off from the platform, a heat treatment was applied before removal. The trimmed off pylon bracket was geometrically analysed by a GOM laser scanning system. The analysis results confirm the concept and all scheduled targets are reached (chapter 3.3):

- The CAD-geometry exhibits sufficient access material (offset thickness 0.4 to 1.9 mm).
- The deflection of the base is 0.4 mm and < 2 mm.

As the final step half of the pylon bracket was machined by milling to prove that the final geometry can be obtained from the LMD raw part which successfully could be demonstrated.

Considering the goal of improving the buy-to-fly ratio, a final result of 1.75 has been achieved which is 12.5% better than the targeted ratio of 2.

5. Acknowledgements

This work has been funded through the European Commission in the AMAZE (Additive Manufacturing Aiming towards Zero Waste and Efficient Production of High-Tech Metal Products) project [Grant number 313781]. The Airbus Group contributed by providing the demonstrator geometry.

6. References

- [1] Ahn DG, Direct metal additive manufacturing processes and their sustainable applications for green technology: A review, *Int. J. of Precis. Eng. and Manuf.-Green Tech.* 3 (4), 381–395.
- [2] Bremen S, Correlation of high power SLM process with productivity efficiency and material properties for Inconel 718, Faculty of Mechanical Engineering, RWTH, Aachen, 2017.
- [3] Gradl PR, Preparation of Papers for AIAA Technical Conferences, 55th AIAA/SAE/ASEE Joint Propulsion Conference, 2019.
- [4] Gisario A, Kazarian M, Martina F, Mehrpouya M, Metal additive manufacturing in the commercial aviation industry, A review, *Journal of Manufacturing Systems*, 2019, 124-149.
- [5] Witzel J, Schrage J, Gasser A, Kelbassa I, Additive manufacturing of a blade-integrated disk by laser metal deposition, *ICALEO*. 30. *Int. Congr. on Applications of Lasers and Electro-Optics*, Paper 502, 2011.
- [6] Schirra JJ, Borg CA, Hatala RW, Mechanical property and microstructural characterization of vacuum die cast superalloy materials, in *SUPERALLOYS 2004*, Champion, Pennsylvania, 2004, 553–561.
- [7] Zhong C, Gasser A, Kittel J, Schopphoven T, Pirch N, Fu J, Poprawe R, Study of process window development for high deposition-rate laser material deposition by using mixed processing parameters, *Journal of Laser Applications*, Vol. 27, No. 3, 2015, 032008.

11th CIRP Conference on Photonic Technologies [LANE 2020] on September 7-10, 2020

Study of the reinforcement phase dilution into the metal matrix in functionally graded Stellite 6 and WC metal matrix composite by Laser Metal Deposition

Marta Ostolaza^{a,*}, Jon Iñaki Arrizubieta^a, Magdalena Cortina^a, Aitzol Lamikiz^a

^a*Department of Mechanical Engineering, University of the Basque Country UPV/EHU, Plaza Torres Quevedo 1, 48013 Bilbao, Spain*

* Corresponding author. Tel.: +34-94-601-7347. E-mail address: marta.ostolaza@ehu.eus

Abstract

Metal Matrix Composite (MMC) coatings have become increasingly important in recent years because of their high wear resistance in aggressive environments. These coatings can be efficiently manufactured by Laser Metal Deposition, as it is known to perform well in repair and coating applications due to its low substrate affection. However, there are many challenges to be faced when metallic and ceramic materials are combined. In fact, inhomogeneous material distribution and lack of metallurgical integrity are issues to be addressed. For this purpose, the use of Functionally Graded Materials is proposed. Nevertheless, there is a lack of knowledge regarding the procedure and deposition strategies to follow in order to obtain crack-free coatings.

In the present work, the main challenges for the deposition of such coatings have been experimentally identified, particularly for Stellite 6 reinforced with tungsten carbide. To that end, the quality of the deposited coatings and their composition has been assessed. Furthermore, as the dilution of the reinforcement phase has not been studied in depth in the literature when ceramic particles are used, in the present study, an analysis of the dilution of the ceramic phase in the metal matrix is performed when different WC concentrations are fed.

© 2020 The Authors. Published by Elsevier B.V.

This is an open access article under the CC BY-NC-ND license (<http://creativecommons.org/licenses/by-nc-nd/4.0/>)

Peer-review under responsibility of the Bayerisches Laserzentrum GmbH

Keywords: Metal Matrix Composite; Functionally Graded Material; Laser Metal Deposition; dilution; coating

1. Introduction

High specific surface requirements of the industry have led to the development of modern and efficient techniques for coating deposition. Thermal spraying techniques are nowadays widely used for the deposition of coatings; however, the bond achieved between the substrate and the coating is purely mechanical [1, 2]. In addition, it has been reported that coatings deposited by means of thermal spray, tend to contain cracks and pores not only at the interface between the deposited material and the substrate, but also at the coated layer itself [3]. This is one of the main limitations of such coatings, as not having a metallurgical bond increases the risk of delamination [4]. As opposed to these processes, Laser Metal Deposition (LMD) has

emerged as a reliable technology for the repair of worn or damaged components, and it has proven to be an effective process for the deposition of high-wear-resistant coatings [5]. LMD manufactured coatings have a good metallurgical bond with the substrate with a minimal heat-affected zone, which reduces the damage incurred in the coated part [6]. Furthermore, this process is unconstrained as far as geometry is concerned and it offers great control of the chemical composition of the built parts [7]. Therefore, it is suitable for multi-material processing, which has led to LMD becoming one of the main processes employed when fabricating Metal Matrix Composite (MMC) coatings (Figure 1).

A composite material is constituted by two or more integral materials, which can be macroscopically distinguished within the completed structure. The properties of composite materials are given by the characteristics of its individual constituents [8]. MMC is referred to as those that have a metallic matrix in which reinforcement phases are introduced. Hence, the metallic phase serves as a binder to the composite [9]. The development of MMCs has been driven by the need for complex materials that respond to the industry requirements in terms of, mainly, higher hardness and wear-resistant coatings manufacturing [10, 11].

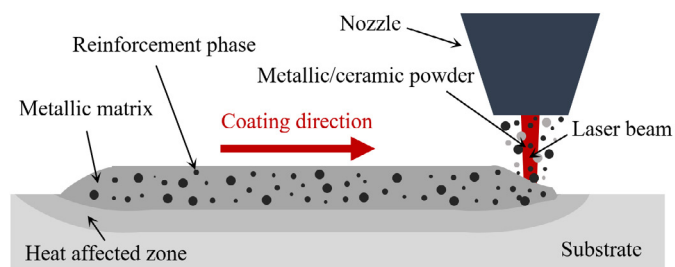


Fig. 1. MMC coating manufacturing by means of LMD.

Ceramic reinforced MMCs have been proven to offer superior properties in terms of strength, hardness, wear, and corrosion resistance, and good behavior even when exposed to high-temperature conditions [12]. Nonetheless, several issues have been also reported when manufacturing such materials by means of Additive Manufacturing. Mainly, poor bonding, severe cracking, and embrittlement of the matrix have been documented [12]. A potential solution for this lack of metallurgical integrity and delamination is the deposition of Functionally Graded Materials (FGM), in this case, Functionally Graded MMCs (FGMMC). In this manner, the sharp interface between the substrate and the coating is substituted by a gradient interface [7]. In fact, it has already been reported in the literature that such a solution can reduce cracking due to residual stress significantly, which is the main cause of failure in the manufacturing of MMCs [13, 14].

Much research has been published regarding the LMD of MMCs, with different metal matrixes and reinforcement phases [15, 16, 17, 18]. However, there is still a lack of knowledge on how to obtain good-quality MMC coatings manufactured by LMD, particularly, when multi-layer and multi-track coatings are to be deposited. This deficiency in the literature has driven the present work, in which an attempt to manufacture multi-layer MMC coatings with a compositional gradient has been performed. To that end, the main defects and difficulties when depositing such coatings have been experimentally identified. In addition, the dilution of the reinforcement phase in the resulting MMC has been experimentally measured and a relation between the fed MMC composition and the resulting reinforcement concentration has been obtained.

2. Methods

The experimental work was carried out in a 5-axis laser-processing machine, which was coupled to a Yb:YAG laser Rofin-Sinar FL010 with 1 kW maximum power and 1070 nm

wavelength. The laser beam spot had a 1.8 mm diameter at the working surface. Additionally, a Sulzer Metco Twin 10-C powder feeder was used, which allows supplying multiple materials, as two independent hoppers are available. Lastly, Argon was used as both carrier and shielding gas.

In the experimental tests, cobalt-based alloy Stellite 6 (S6) powder (45-106 μm) was used as the matrix for the MMC coating, and tungsten carbide (WC) powder (45-106 μm) was introduced as the reinforcement phase. These multi-material coatings were deposited onto a DIN C45 steel substrate. The coupons were 70 x 70 x 15 mm³ and were finished by grinding to ensure a flat and even surface, and properly cleaned with acetone to eliminate possible impurities and guarantee a proper bonding between the substrate and the deposited layers. The composition of the materials employed is detailed in Table 1.

Table 1. Material composition in wt. %.

	Co	Cr	W	Si	Fe	C
WC	0.0	0.0	Bal.	0.0	0.19	4.03
S6	Bal.	28.0	4.0	1.5	3.0	1.0
DIN C45	0.0	≤ 0.04	0.0	≤ 0.4	Bal.	0.42–0.5
	Mo	Mn	P	S	Cu	Ni
WC	0.0	0.0	0.0	0.0	0.0	0.0
S6	1.0	0.0	0.0	0.0	0.0	3.0
DIN C45	0	0.5–0.80	≤ 0.045	≤ 0.045	≤ 0.4	≤ 0.1

2.1. LMD process

The study of the FGMMC was approached in a three-step process.

1. Firstly, with the aim of characterizing the material, several initial tests were carried out, in which up to 20% wt. WC was introduced in the Co-based alloy coating. Therefore, single-track and multi-track tests were performed. Higher WC contents were not tested so as not to exponentially increase the number of initial tests.
2. Secondly, a coating constituted by 10 layers was deposited, which ranged from 0% to 40% wt. WC content, as shown in Figure 2. The process parameters employed are detailed in Table 2.
3. Thirdly, the quality of the deposited material, as well as the dilution of the reinforcement phase inside the FGMMC, was studied.

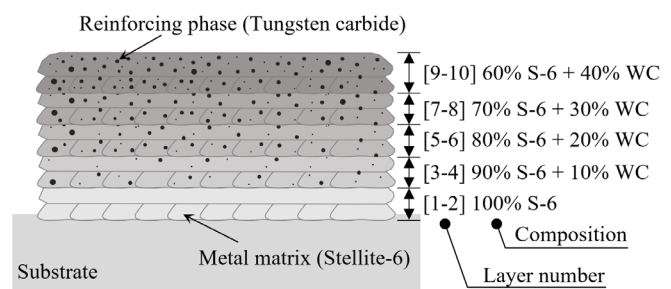


Fig. 2. FGMMC test piece.

The path strategy followed in all tests for the manufacturing of the test piece consisted in a zigzag trajectory scheme, in both X and Y directions, which were successively alternated (Figure 2).

Table 2. Process parameters for FGMMC.

Process parameter	Range
Power	800 – 980 W
Feed rate	500 mm/min
S6 powder rate	4.0 – 5.5 g/min
WC powder rate	0.0 – 2.7 g/min
Overlap	26%-50%

The powder feed rate in each layer was adjusted to keep a constant-volume clad, which ensures the stability of the process when overlapping subsequent layers. Therefore, due to the higher density of the WC (15.63 against 8.44 g/cm³) the laser power was proportionally increased with the deposited mass per unit length.

2.2. Metallographic preparation and analysis

Due to the high hardness and the need for high-precision cuts, the test pieces were cut by wire electro-discharge machining. From each test, three sections were prepared for metallographic analysis, and another three for compositional analysis in a scanning electron microscope (SEM). All samples were ground and polished following an appropriate metallographic procedure, to avoid pulling out the reinforcement particles, which may damage the sample. In addition, those prepared for metallographic analysis were etched by electrolytic etching with 10% oxalic acid solution at 20 V.

Regarding the microhardness analysis, indentations were produced every 0.2 mm along two vertical lines with the Future Tech Corp FM-800 microhardness tester. The parameters employed were 2.9 N applied load and 12 s dwell time.

Finally, a compositional analysis of the deposited layers was performed by means of scanning electron technology (Carl Zeiss EVO-40) and energy-dispersive X-ray spectroscopy (EDS) microanalysis equipment (Oxford instruments). Discrete measurements were performed at different depths of the deposited material and the chemical composition of the material was obtained. Besides, the average composition of the FGMMC was obtained at different layers.

2.3. Composition analysis

On the one hand, in order to calculate the amount of WC captured by the melt pool during the deposition of the FGMMC sample, the data from the average composition at each layer provided by the EDS analysis was employed. As this data is expressed in terms of elemental content, the WC actually absorbed by the melt pool was calculated by correlating the weight content of both chromium and tungsten measured by the EDS probe.

On the other hand, the content of unmelted WC remaining in the matrix was measured by the Image Processing Toolbox of Matlab software. In this manner, as the unmelted particles can be clearly differentiated from the matrix, the volumetric composition was calculated, and then transformed into weight composition, according to the density of each material.

3. Results

3.1. Initial tests: 0 to 10% and 0 to 20% wt. WC

In Figure 3, the mono and multi-track clads deposited for the initial tests are shown. The first tests (1.1 and 1.2) correspond to 10% wt. WC / 90% wt. S6 clads over two S6 layers. The second tests (1.3 and 1.4) correspond to 20% wt. WC / 80% wt. S6 clads over two layers of 10% wt. WC / 90% wt. WC, at the same time, deposited over two layers of S6.

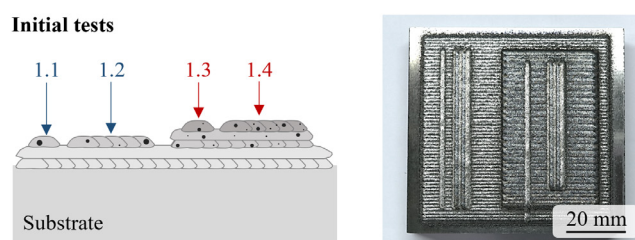


Fig. 3. Initial tests: (1.1 and 1.2) 0 to 10% wt. WC and (1.3 and 1.4) 0 to 20% wt. WC.

These samples presented good integrity based on visual observation, which was further confirmed in the metallographic analysis (Figure 4). The matrix of each layer was affected differently by the etching process, which was attributed to the enrichment of the matrix as a consequence of the dilution of the reinforcement phase. Nevertheless, no cracking nor pores were detected in the deposited material.

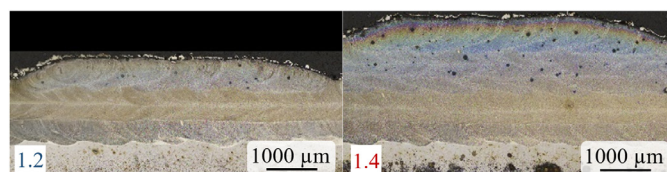


Fig. 4. Etched cross-section of the initial tests.

Based on the good results obtained in the initial tests regarding metallurgical integrity, the second set of experimental testing was carried out.

3.2. Multi-track and multilayer FGMMC: 0 to 40% wt. WC

In Figure 5, the overall aspect of the sample after the deposition process is shown. Oxidation was effectively avoided, which confirms the proper behavior of the shielding gas.

In the deposited multi-track and multilayer FGMMC, severe cracking was identified after visual inspection. This lack of metallurgical integrity was further confirmed when the cross-sections were analysed (Figure 6). The cracking was initiated in the discrete WC particles and propagated through the matrix

when high WC concentration was introduced in the multi-track and multilayer FGMMC. It was detected that concentrations higher than 30% wt. were critical in this case. As reported in the literature, the unmelted reinforcement particles are regions where stress concentration can achieve critical values. Moreover, the enrichment of the matrix by dilution of the reinforcement particles resulted in increased hardness at the expense of reduced ductility, which leads to a higher crack sensitivity.

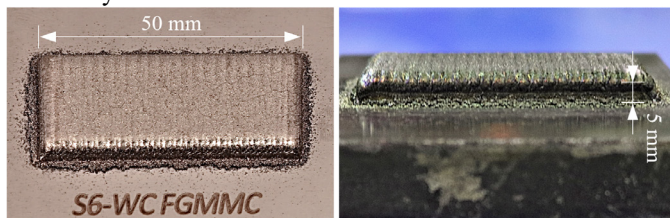


Fig. 5. 10-layer FGM coating.

In the same manner, as displayed in Figure 4 for initial tests, the dilution of the reinforcement particles resulted in a higher tungsten and carbon content as the amount of tungsten carbide fed was increased. In the cross-section shown in Figure 6, the first layers (corresponding to 0% wt. WC) were slightly etched, while the top layers (corresponding to 40% wt. WC) were strongly etched. Therefore, it can be concluded that the composition of the matrix was not constant along the coating, meaning that the upper layers have a higher concentration in both tungsten and carbon, that are either partially melted or diffused into the matrix.

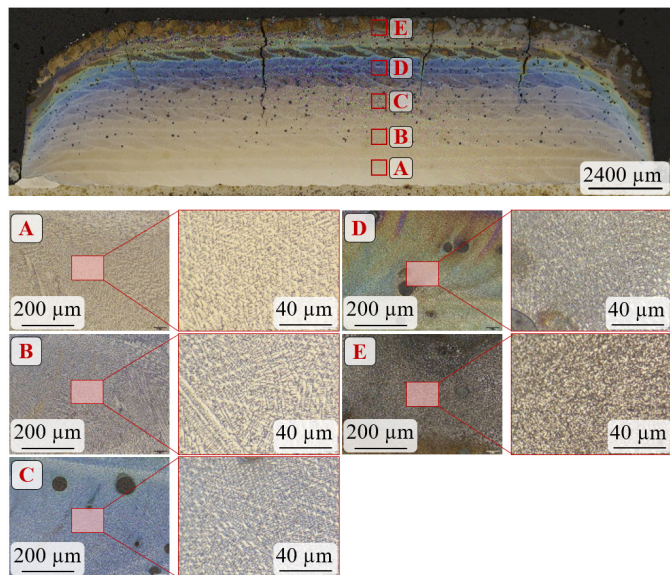


Fig. 6. Cross-section of the 10-layer FGMMC and details of the microstructure evolution of the matrix (A) 0% wt. WC, (B) 10% wt. WC, (C) 20% wt. WC, (D) 30% wt. WC and (E) 40% wt. WC.

In addition, an evolution of the microstructure of the matrix was observed along the deposited coating (Figure 6). As the concentration of WC deposited increased, the microstructure showed enrichment in intermetallic phases. In fact, the formation of carbides was clearly revealed in the obtained SEM images with backscattering diffraction (BSD) (Figure 7). This image was taken at higher WC concentration layers, i.e. upper

layers, specifically in the area adjacent to the region E shown in Figure 6.

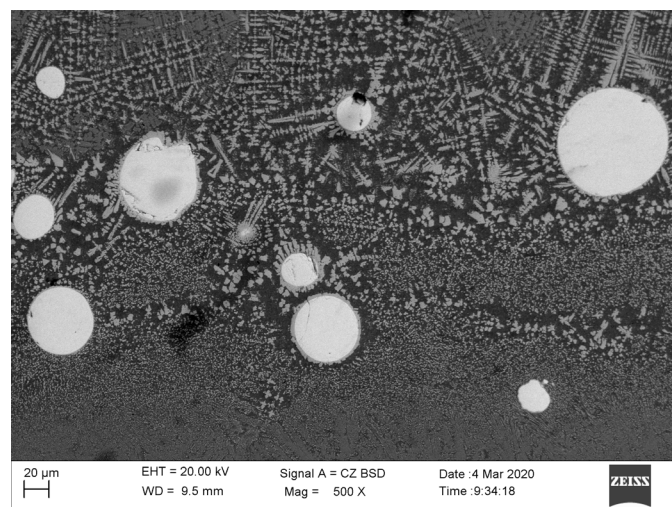


Fig. 7. SEM image of carbide formation around WC reinforcement particles.

The partial melting or dilution of WC in the Stellite 6 matrix was confirmed by both the evolution of the microstructure and the microhardness analysis performed (Figure 8). A gradual increase in the hardness of the matrix was observed. Furthermore, hardness values as high as 700 HV were measured, which are far above the values reached by Stellite 6 (390-475 HV [19]). Therefore, the presence of extra tungsten and carbon as the height of the coating was increased was confirmed. As aforementioned, this hardness rise in the matrix is the main cause of its embrittlement, which resulted in a higher crack sensibility.

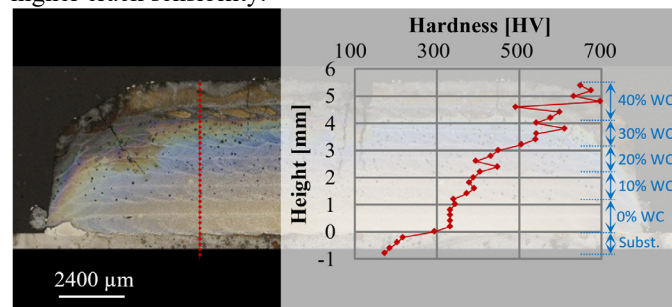


Fig. 8. Microhardness analysis of FGM sample.

In order to analyse the composition of the deposited FGMMC, the unmelted WC content was determined by image analysis at different points. Also, the actual W content of each layer of the deposited FGMMC (both at the reinforcement phase and the matrix) was measured (Figure 9B). These measurements were compared to the theoretically fed powder composition in terms of WC rather than W content, so that they were comparable (Figure 10).

As shown in Figure 10, there is a mismatch between the theoretical WC fed, the WC captured in the melt pool according to the EDS analysis, and the unmelted WC content based on Matlab image analysis. The observed differences are due to the following phenomena:

- (1) Fed WC vs. Actual WC (EDS): The mismatch between the powder composition fed and the composition of the powder captured in the melt pool.
- (2) Unmelted WC vs. Actual WC (EDS): Partial melting or dilution of the reinforcement particles in the matrix.

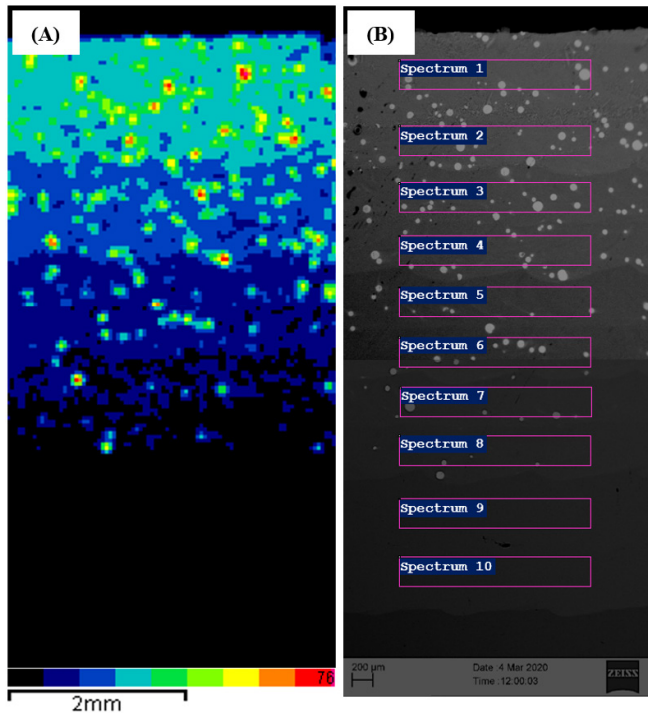


Fig. 9. (A) W content (wt. %) mapping based on EDS analysis of the FGMMC sample and (B) EDS analysis, highlighting the different regions.

The first one is caused by the higher density of the WC particles as compared to the S6. Due to differences in the particle density and inertia of the employed powders, they are not necessarily equally concentrated by the nozzle. Therefore, the composition of the powder introduced in the melt pool is not that programmed in the feeder [14]. However, the effect of this phenomenon was not as high as the dilution effect observed.

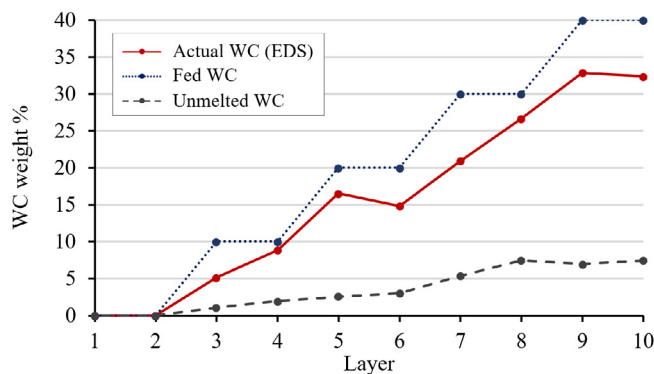


Fig. 10. Comparison of WC content of the fed powder, actual content provided by EDS analysis, and unmelted WC content

Considering the importance of the dilution phenomenon in the deposition of FGMMC, and as it directly affects the integrity of the coating, this enrichment of the matrix was further researched. In Figure 9(A), a colour map of the tungsten content of a specific region of the cross-section of the

deposited FGMMC is shown. Thus, regions with higher W concentration can be visually distinguished. In the colour map shown, the deposited layers are clearly differentiated. The lower region, coloured in black, corresponds to a small part of the substrate and the first two layers, in which the tungsten content is that of the deposited S6. In the same manner, the higher colour band (turquoise), corresponding to the last deposited layers, 9th and 10th, depicts a higher W content in the matrix, therefore showing a higher enrichment.

Moreover, to analyse the enrichment of the matrix, discrete composition measurements were performed by means of EDS at different points of the deposited FGMMC (Figure 11). In particular, the tungsten content of the matrix at different heights of the deposited coating was quantified and a clear tendency was observed. As shown in Figure 11, the W content increased as the amount of WC fed was augmented, due to the dilution of the reinforcement phase in the matrix. Note that two points of the compositional analysis were discarded: the first one, marked as (1), was not a reliable measure because it was carried out in a point in which a lack of fusion was found. The second one, marked as (2), could not be considered as a reliable measure either, because it was performed in an unmelted reinforcement particle; therefore, it was not a representative measure of the composition of the matrix.

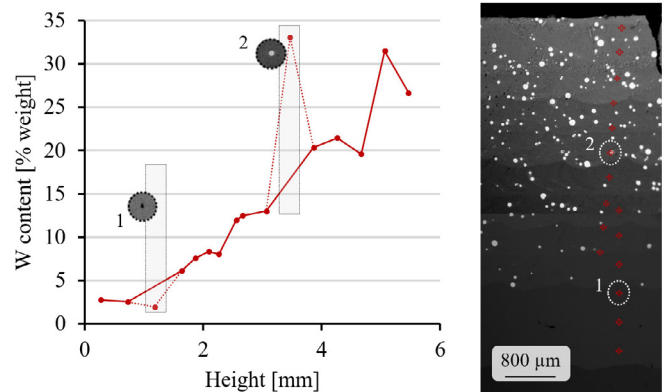


Fig. 11. Results of SEM analysis.

4. Conclusions

In this work, the capability of LMD for manufacturing FGMMC coatings with gradient hardness was demonstrated. However, some complications and challenges were identified.

Firstly, the requirement of a high number of preliminary tests for a complete characterization of every layer of the FGM was identified. Hence, an alternative based on reduced preliminary testing was proposed.

Secondly, the W content of the matrix was found to increase as the amount of WC fed increased due to the dilution of the reinforcement phase in the matrix. This enrichment of the matrix increased its hardness, which might be beneficial for industrial applications. However, this dilution led to the fragilization of the matrix, which developed a higher cracking sensitivity. This fact, together with the high-stress concentrations originated around the unmelted reinforcement particles, due to different thermal properties, led to cracking

phenomenon. Therefore, the integrity of the deposited clads was severely conditioned.

In order to face those critical issues in the LMD of FGMMC, on the one hand, parameter optimisation is required. For instance, by adjusting the laser power, the dilution of the reinforcement particles in the matrix can be reduced, therefore minimizing its fragilization and crack sensitivity. In fact, a matrix with higher ductility can effectively absorb the higher stress generated around the WC particles. On the other hand, considering that the cracks were initiated in the reinforcement particles, if all the reinforcement phase is diluted, i.e. no unmelted WC particles remain after the coating deposition, crack initiation might be mitigated. However, in this case, a coating with gradient alloying would be obtained and, therefore, the resulting mechanical and wear resistance properties should be studied.

Acknowledgements

This research has received funding from the European Union through the H2020-FoF13-2016 PARADISE project, under Grant 723440, and the Spanish Government through the AEI/FEDER ENVIDIA project, under Grant RTC-2017-6150-4. The authors also thank for technical and human support provided by the SGIker Coupled Multispectroscopy Singular Laboratory (Raman-LASPEA) (UPV/EHU/ ERDF, EU).

References

- [1] A. Rezzoug, S. Abdi, A. Kaci, M. Yandouzi, Thermal spray metallisation of carbon fibre reinforced polymer composites: Effect of top surface modification on coating adhesion and mechanical properties, *Surface and Coatings Technology*, vol. 333, 2018, pp. 13-23, <https://doi.org/10.1016/j.surfcoat.2017.10.066>
- [2] B. Huang, C. Zhang, G. Zhang, H. Liao, Wear and corrosion resistant performance of thermal-sprayed Fe-based amorphous coatings: A review, *Surface and Coatings Technology*, vol.377, 2019, pp. 124896, <https://doi.org/10.1016/j.surfcoat.2019.124896>
- [3] P. Wu, C.Z. Zhou, X.N. Tang, Microstructural characterization and wear behavior of laser clad nickel-based and tungsten carbide composite coatings, *Surface and Coatings Technology*, vol. 1661, 2003, pp. 84-88, [https://doi.org/10.1016/S0257-8972\(02\)00730-2](https://doi.org/10.1016/S0257-8972(02)00730-2)
- [4] H. Yu, W. Zhang, H. Wang, Y. Guo, M. Wei, Z. Song, Y. Wang, Bonding and sliding wear behaviors of the plasma sprayed NiCrBSi coatings, *Tribology International*, vol. 66, 2013, pp. 105-113, <https://doi.org/10.1016/j.triboint.2013.04.017>
- [5] C. Ma, D. Gu, C. Hong, B. He, K. Chang, Q. Shi, Formation mechanism and microstructural and mechanical properties of in-situ Ti-Ni-based composite coatings by laser metal deposition, *Surface and Coatings Technology*, vol. 2 In91, 2016, pp. 43-53, <https://doi.org/10.1016/j.surfcoat.2016.02.013>
- [6] L. Du, D. Gu, D. Dai, Q. Shi, C. Ma, M. Xia, Relation of thermal behavior and microstructure evolution during multi-track laser melting deposition of Ni-based material, *Optics & Laser Technology*, vol. 108, 2018, pp.207-217, <https://doi.org/10.1016/j.optlastec.2018.06.042>
- [7] L. Yan, Y. Chen, F. Liou, Additive manufacturing of functionally graded metallic materials using laser metal deposition, *Additive Manufacturing*, vol. 31, 2020, pp. 100901, <https://doi.org/10.1016/j.addma.2019.100901>
- [8] M. Hasan, J. Zhao, Z. Jiang, Micromanufacturing of composite materials: a review, *International Journal of Extreme Manufacturing*, vol. 1, 2019, pp. 012004 (26 pp), <https://doi.org/10.1088/2631-7990/ab0f74>
- [9] F. Weng, C. Chen, H. Yu, Research status of laser cladding on titanium and its alloys: A review, *Materials and Design*, vol. 58, 2014, pp. 412-425, <http://dx.doi.org/10.1016/j.matdes.2014.01.077>
- [10] F. Brueckner, M. Riede, M. Müller, F. Marquardt, R. Willner, A. Siedel, E. Lopez, C. Leyens, E. Beyer, Enhanced manufacturing possibilities using multi-materials in laser metal deposition, *Journal of Laser Applications*, vol. 30(3), 2018, <https://doi.org/10.2351/1.5040639>
- [11] D.B. Miracle, S. Donaldson, Introduction to composites, In: *ASM Handbook, Volume 21: Composites*, 2001, pp. 3-18, <https://doi.org/10.31399/asm.hb.v21.a0003350>
- [12] Y. Hu, W. Cong, A review on laser deposition-additive manufacturing of ceramics and ceramic reinforced metal matrix composites, *Ceramics International*, vol. 44, 2018, pp. 20599-20612, <https://doi.org/10.1016/j.ceramint.2018.08.083>
- [13] C. Zhang, F. Chen, Z. Hueang, M. Jia, G. Chen, Y. Ye, Y. Lin, W. Liu, B. Chen, Q. Shen, L. Zhang, E.J. Lavernia, Additive Manufacturing of functionally graded materials: a review, *Materials Science and Engineering: A*, vol. 764, 2019, pp. 138209, <https://doi.org/10.1016/j.msea.2019.138209>
- [14] Y. Chen, F. Liou, Additive Manufacturing of Metal Functionally Graded Materials: A review, In: *Solid Freeform Fabrication 2018: Proceedings of the 29th Annual International Solid Freeform Fabrication Symposium – An Additive Manufacturing Conference*.
- [15] D. Janicki, J. Gorka, A. Kotarska, Laser cladding of Inconel 625-based composite coatings, *Weld Technology Review*, vol.90(9), 2018, pp. 6-11, <http://dx.doi.org/10.26628/ps.v90i9.941>
- [16] J. Numinen, J. Näkki, P. Vuoristo, Microstructure and properties of hard and wear resistant MMC coatings deposited by laser cladding, *International Journal of Refractory Metals & Hard Materials*, vol. 27(2), 2009, pp. 4472-478, <https://doi.org/10.1016/j.ijrmhm.2008.10.008>
- [17] M.R. Fernández, A. García, J.M. Cuetos, R. González, A. Noriega, M. Cadenas, Effect of actual WC content on the reciprocating wear of laser cladding NiCrBSi alloy reinforced with WC, *Wear*, vol. 324-325, 2015, pp. 80-89, <http://dx.doi.org/10.1016/j.wear.2014.12.021>
- [18] G. Wang, J. Zhang, R. Shu, S. Yang, High temperature wear resistance and thermal fatigue behavior of Stellite-6/WC coatings produced by laser cladding with Co-coated WC powder, *International Journal of Refractory Metals & Hard Materials*, vol. 81, 2019, pp. 63-70, <https://doi.org/10.1016/j.ijrmhm.2019.02.024>
- [19] KENNAMETAL™, Stellite Hard Facing Alloys, Available online: https://s7d2.scene7.com/is/content/Kennametal/B-18-05723_KMT_Stellite_Alloys_Brochure_Direct_update_LRpdf-2 (accessed on February 24)

11th CIRP Conference on Photonic Technologies [LANE 2020] on September 7-10, 2020

Additive manufacturing of LMD nozzles for multi-material processing

R. Bernhard^{a*}, P. Neef^a, T. Eismann^b, H. Wiche^a, C. Hoff^b, J. Hermsdorf^b, S. Kaierle^b, V. Wesling^a

^a*Clausthal Centre of Materials Technology, Agricolastraße 2, 38678 Clausthal-Zellerfeld, Germany*

^b*Laser Zentrum Hannover e.V., Hollerithallee 8, 30419 Hannover, Germany*

*Corresponding author. Tel.: +49-511-2788-369; fax: +49-5323-72-3399. E-mail address: r.bernhard@lzh.de

Abstract

Additive manufacturing of metals has become a leading technology for function-integrated and individualized components. Ongoing research leverages this technology from single-material parts to gradient compositions and multi-material combinations. Powder-based laser metal deposition is the preferred process for these novel applications because of the ability to add onto freeform surfaces and flexible material use. A crucial aspect of this powder-based process is material loss due to overspray. Furthermore, the shape and size of the powder stream must be altered depending on the intended use. For example, thin walls and fine details require a narrow powder focus whereas a larger focus can accelerate the manufacturing of volumes substantially. To address this challenge, novel 3D printable and replaceable nozzles are developed. Compared to common nozzle designs, this new approach enables quick changing of different sized nozzles and incorporates additively manufactured flow paths. Finally, the stream quality is visualized by Schlieren photography.

© 2020 The Authors. Published by Elsevier B.V.

This is an open access article under the CC BY-NC-ND license (<http://creativecommons.org/licenses/by-nc-nd/4.0/>)

Peer-review under responsibility of the Bayerisches Laserzentrum GmbH

Keywords: Additive manufacturing; laser metal deposition; nozzle design

1. Introduction

Laser metal deposition (LMD) is one of the most important technologies for additive manufacturing of metals. With LMD, complex function-integrated and individualized components can be created onto free form surfaces. High deposition rates of wire-based and the high deposition quality of powder-based LMD qualify this technology for many applications in the metal industry. Repair of worn drawing dies for metal stamping [1] and reinforcement of lightweight structures are just some of the typical applications. Especially the simple setup, flexibility and wide material selection are key advantages compared to other additive manufacturing processes. A crucial aspect of powder-based LMD is powder utilization. Unlike in powder bed fusion powders are not easily recycled. The LMD powder nozzles are high-precision parts and consumables at the same time. They are exposed to heat, weld splatters and powder abrasion.

State-of-the-art are coaxial powder nozzles that feature multiple openings or annular flow gaps [2]. Commonly, they consist of two matched cones that form an annular powder outlet. With conventional machining processes, these parts are manufactured in a differential manner. That leads to higher manufacturing expenses and costly maintenance. A new approach is an integrated powder nozzle design that incorporates additive manufacturing (AM). AM opens up new opportunities and design freedom for these nozzles. In addition, by carefully deciding on the system limits, assembly and maintenance can be improved. In this paper, proofs of concept for toolless changeable nozzle designs are presented. Furthermore, possible benefits in powder gas flow and powder efficiency are highlighted.

2. Experimental setup

The used six-axis LMD machine consists of two main systems that are integrated into a process head. Starting with the optical setup, after exiting the optical fiber of the solid-state laser the beam is collimated and focused onto the substrate by a pair of lenses. The second system supplies the powder filler material alongside shielding gas through an outlet to the process zone. In combination, it results in direct metal deposition onto a substrate (see figure 1). With the help of a dichroitic mirror, a camera can observe the melt pool and the deposition during the process.

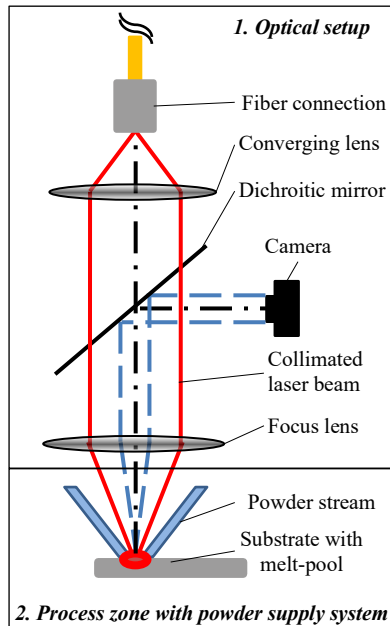


Fig. 1. Schematic drawing of the process head

In this paper, different concepts of the powder supply system are evaluated and compared to the conventional lathe-manufactured approach fitted to the machine. In order to maintain cross compatibility with the processing head and ensure comparability of the new designs, the nozzles are adapted to an existing process head (see figure 2). In consequence, the maximum radial size of the nozzle is restricted to 24 mm.

Within these constraints, the inner-structure of the nozzle can be modified freely by using the advantages of laser powder bed fusion additive manufacturing and the resulting design freedom.

The AM nozzles themselves are attached with a built-in thread to the mount on the process head. To ensure exact positioning and overcome thread tolerances, both parts are centered by two conical mating surfaces that are integrated into the assembly.

The AM nozzles are created with computer-aided design. Moreover, additive manufacturing is used to create the resulting monolithic designs. They are an evolution of conventional nozzles with annular openings. The outlet gap sizes are varied from 0.2 mm to 1.0 mm (see table 1).

Furthermore, the use of powder bed additive manufacturing allows for asymmetric designs with undercuts. Therefore, a honeycomb design with a complex inner structure and 0.4 mm wide channels is created and evaluated. The process head has

integrated cooling and powder supply connections. With help of the conical mating surfaces, the AM nozzles are centered in the thread coaxially to the laser beam. In figure 2, schematic cross sections of two additive designs are shown. A nozzle using an annular outlet is visible on the bottom left. On the bottom right, individual channels of the honeycomb design can be seen.

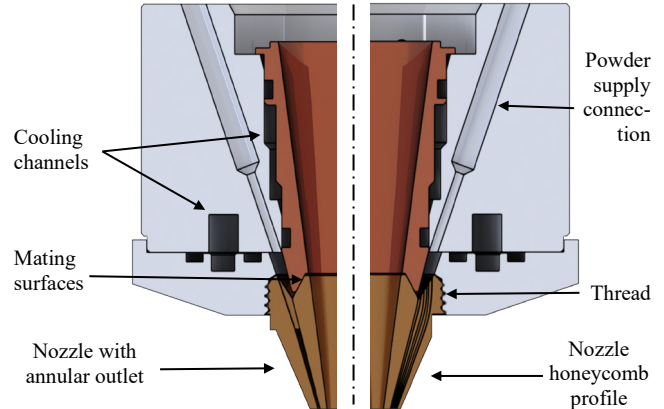


Fig. 2. Two additive nozzle designs integrated into the processing head

According to table 1, one conventional and five additively manufactured nozzles are evaluated. The AM nozzles are created by laser powder bed fusion (LPBF) using CuSn10 material. This tin bronze is used for better heat conduction compared to commonly used 316L stainless steel. The manufacturing was carried out on an Orlas Creator LPBF machine. It offers a cylindrical build volume of \varnothing 100 mm x 100 mm and a minimum beam diameter of 40 μ m. The following optimal LPBF-process parameters for this material were determined in previous work [3]:

- Laser power: 210 W
- Scanning speed: 1000 mm/s
- Hatch distance: 70 μ m

Table 1. Evaluated nozzle designs

Nozzle type	Abbreviation	Outlet	Size [mm]
Conventionally manufactured	Con-0.35	Annular	0.35
Annular LPBF	AM-xxx	Annular	0.2, 0.35, 0.55, 1.0
Honeycomb LPBF	AM-Honey	Honeycomb	0.4

After printing, the nozzle needs to go through mechanical post-processing. First, they are removed from the build plate. Secondly, the top and the bottom of the nozzle are polished to remove any excess support structures. In addition, the thread is reworked with a die. The dimensional accuracy of the inner-structures is checked by comparing the design files with x-ray tomographies.

The powder-gas streams of the printed nozzles are evaluated using a portable Schlieren-imaging setup that can be positioned in the LMD machine. This ensures a realistic process environment for the measurements. A high power LED emits light through an adjustable aperture. Two identical concave mirrors with a focal length of 500 mm project an image of the target onto a digital camera. A razor blade is placed in the focus of the beam. The sharp edge cuts all the light except the light

diffracted by density changes. It passes over the knife-edge and is picked up and visualized by the camera (see figure 3).

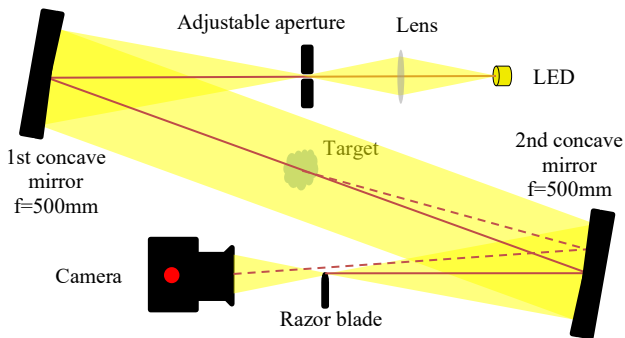


Fig. 3. Schematic Schlieren setup

The occurring density differences between the inert atmosphere and the powder gas flow are minimal. Visualizing this would require focal lengths of multiple meters to reach a higher sensitivity of the Schlieren setup [4]. Therefore, traces of tetrafluoroethane are added to the argon conveying gas. This marking agent has a density of 4.25 kg/m^3 , which is significantly higher compared to the density of argon with only 1.78 kg/m^3 . This results in clearly visible Schlieren images. The process parameters used are fixed throughout all experiments. To analyze the powder overspray, a thin wall structure and a helix were printed with each nozzle. The specimen and the oversprayed material were weighed. In consequence, the nozzle designs can be compared by calculating the powder efficiency. Additionally, the substrate was weighed before and after the LMD process. A steel container catches any excess powder for measuring.

Parameters for the Schlieren images and the laser metal deposition are shown in table 2. Stainless steel powder (1.4404) with a mean grains size of $45 \mu\text{m}$ was used for testing.

Table 2. Fixed Process Parameters

Parameter	Value	Unit
Powder gas flow	2	L/min
Shape gas flow	10	L/min
Laser Power	172	W
Powder (1.4404) grain Size	45	μm
Substrate (1.4301) thickness	6	mm

3. Results

After minor touchups, all nozzle build jobs turned out to be successful on the LPBF machine. Additional reworking of the thread allows the nozzles to be screwed into the process head smoothly. X-ray tomographies of the AM nozzles manifested a dimensional accuracy of $100 \mu\text{m}$ (see figure 4 and figure 5)

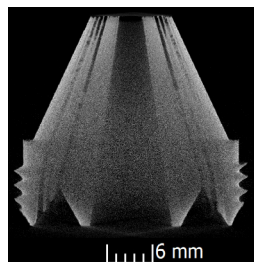


Fig. 4. X-ray tomography of the AM-Honeycomb nozzle

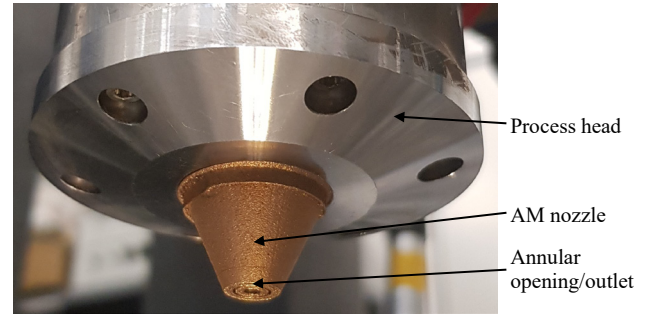


Fig. 5. AM nozzle fitted to the process head

After capturing the Schlieren images of each individual nozzle, they are scaled to size. A coordinate system with 1 mm per division is added at the focal plane of the laser at 9 mm standoff distance. The captured and edited Schlieren images are shown in figure 6. They are named according to their design concept. The conventional manufacturing nozzle design a) with an annular opening acts as a reference that the other designs b) to f) are compared with (see figure 6).

a) Conventional 0.35 mm nozzle:

The argon gas stream exiting the reference nozzle is divergent and therefore the diameter of the jet increases shortly after the outlet to 5.9 mm at the focal plane. The gas flow separates into two visible layers, which consist of small turbulences on the outside and laminar flow on the inside. Larger turbulences are only visible beyond the focal plane. The minimal diameter of the gas flow measures 4.4 mm at only 1.3 mm standoff distance.

b) AM 0.20 mm nozzle:

The first additively manufactured nozzle with a 0.20 mm annular outlet shows a convergent shape of the gas stream. The waist of the gas stream is 4.7 mm below the nozzle outlet. The diameter of the stream at this location is 3.6 mm. After this position, the stream expands to 4.3 mm at the focal plane of the laser.

c) AM 0.35 mm nozzle:

The nozzle with a 0.35 mm annular opening is comparable to its conventionally manufactured counterpart, because they share the same outlet dimensions. In comparison, the AM nozzle shows a convergent gas stream with a diameter of 4.8 mm at the focal plane. The minimal diameter of the gas flow measures 4.4 mm at 4.5 mm standoff distance. The stream on the right side seems to be deflected by environmental conditions.

d) AM 0.55 mm nozzle:

An overall increase of the outlet size to a 0.55 mm annular opening results in a wide stream diameter of 4.7 mm at the focal plane. First, the contours of the gas stream have a high contrast but after the focal plane turbulences start to occur. The minimal diameter of the stream is 4.3 mm located at 5.1 mm downstream of the nozzle.

e) AM 1.0 mm nozzle:

The AM nozzle with a 1.0 mm outlet has the largest annular gap. The gas stream breaks down into turbulences after only 3 mm. The diameter at the focal plane measures 7.1 mm. At 4.0 mm standoff distance, the minimum flow diameter is 6.2 mm.

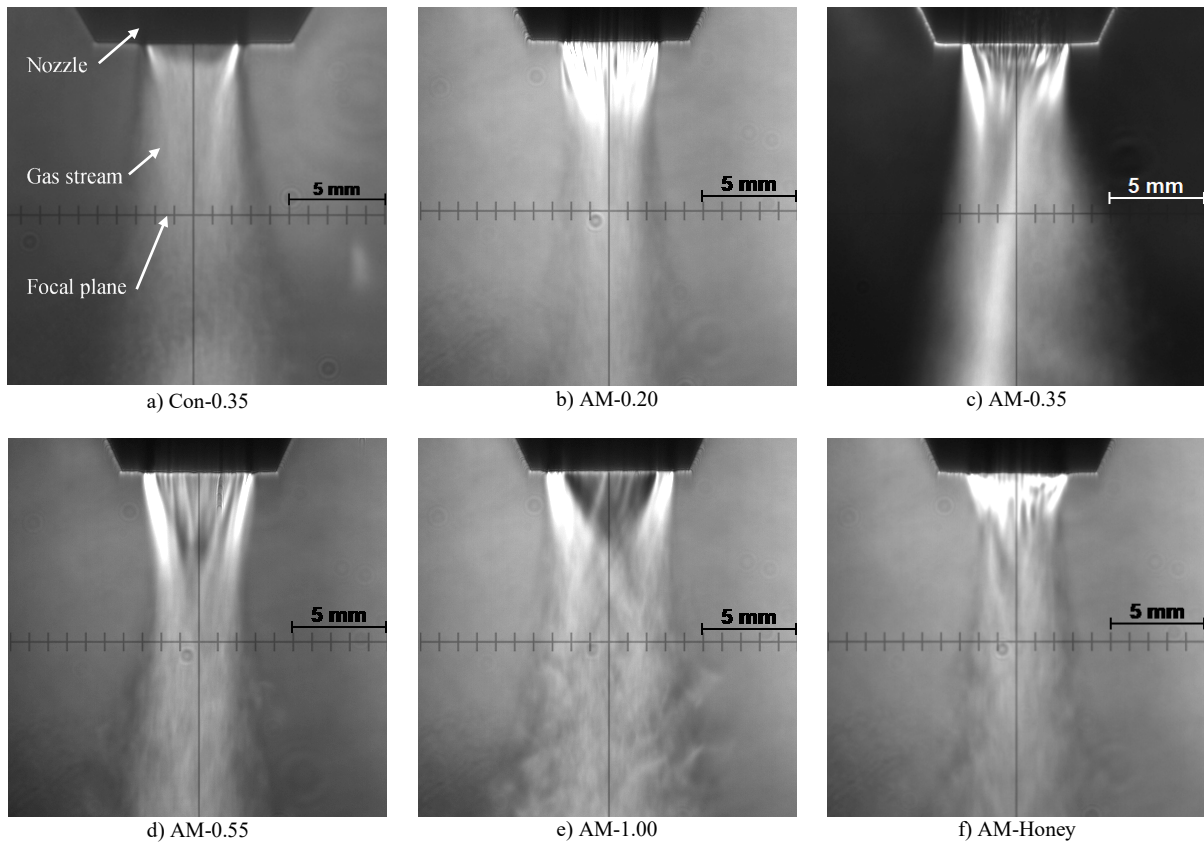


Fig. 6. Schlieren images of the nozzles with coordinates

f) AM Honeycomb:

The honeycomb design shows a convergent flow after the outlet. A strong contrast to the ambient inert atmosphere is visible. The flow starts to get turbulent before it reaches the focal plane. The minimal diameter of the stream amounts to 4.2 mm at 2.2 mm standoff distance.

Overall, the nozzles made by additive manufacturing show a characteristic tapered flow after exiting the outlet. The gas streams start to expand before reaching the focal plane of the process laser. This is contrary to the conventional manufactured nozzle, which has a divergent gas flow almost directly after the outlet. The diameter of the gas flow, the location of minimal gas flow diameter and the standoff distance measured from the nozzle are shown in table 3.

Table 3. Diameter of the gas flow at the focal plane

Nozzle design	a) Con-0.35	b) AM-0.20	c) AM-0.35	d) AM-0.55	e) AM-1.0	f) AM-Honey
Gas flow diameter at focal plane [mm]	5.9	4.3	4.8	4.7	7.1	4.8
Minimal gas flow diameter [mm]	4.4	3.6	4.5	4.3	6.1	4.2
Gas flow waist standoff distance [mm]	1.3	4.7	4.4	5.1	4.0	2.7

The results show a reduction of the gas flow diameter of up to 1.6 mm or 27% compared to the conventional nozzle.

Despite the rough surface finish of the AM nozzle due to the LPBF process, all gas streams of the additively manufactured nozzles show strong convergence behaviors. Additionally, the size of the gap influences the flow diameter significantly. The smaller the annular opening, the smaller is the gas stream diameter with an exception of the AM-0.35 nozzle. In this case, the Schlieren images only allow for qualitative assessments.

Therefore, the results of the Schlieren images were quantified by powder efficiency measurements during actual laser metal deposition. The efficiency of the deposited powder in comparison with the overspray is determined for the following three best performing AM nozzles: The powder efficiency of the AM-Honeycomb, AM-0.20 and AM-0.35 designs are compared to the conventional design. With each nozzle setup a 30 mm helical and 50 mm long straight thin wall were manufactured (see figure 7).

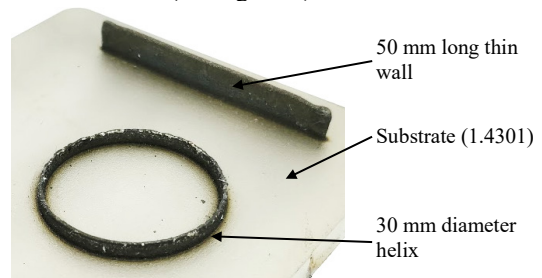


Fig. 7. AM-0.2 printed helix and thin wall specimens

The results show differences in the efficiency between the helix and the straight wall. Overall, the straight thin walls yield up to 6% higher efficiency compared to the helices. Due to the

oscillating deposition strategy of the wall, the cool down time was shorter than the helix buildup. This results in a larger melt pool and therefore more deposited powder. Despite the superior gas flow, the worst performing nozzle was the honeycomb nozzle. It only yields an efficiency of 3.3%. Disassembly of the nozzle shows agglomeration of powder inside the honeycomb channels. In consequence, the majority of the channels were congested. Therefore, the powder exited through the remaining channels with an uneven distribution. This resulted in a poor metal deposition.

The other tested AM nozzles with annular openings yield higher efficiencies compared to the conventional nozzle design. In terms of the AM-0.20 nozzle, the deposition efficiency is 20% higher. Regarding the AM-0.35 nozzle, up to 130% more deposition is reached compared to the conventional nozzle (see figure 8).

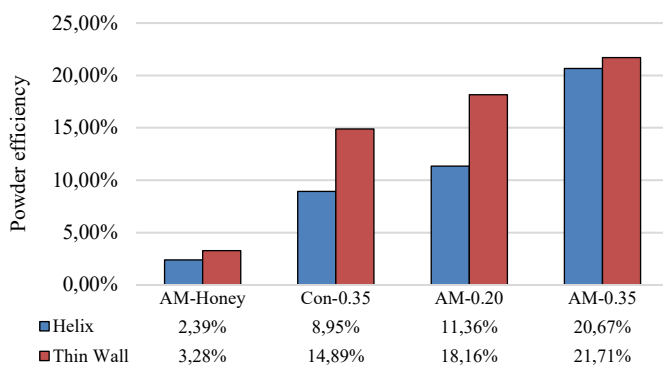


Fig. 8. Powder efficiency

Overall, the additive manufactured nozzles with annular openings show improved results compared to the conventional one. This is not only visible by the powder efficiency; it is also visible by comparing the minimal and the maximum height of the specimens. The difference in height between them is an indicator for homogeneous and direction independent buildup. Even though the conventional nozzle was able to deposit the highest thin wall, the difference between the minimal and maximum height is comparably large. Especially the helix reveals problems with the conventional and the AM-0.35 nozzles. The result show, that the best nozzle for helical buildup is the AM-0.2 nozzle. The best result for a thin wall was achieved by the AM-0.35 nozzle, almost matched by the AM-0.2 nozzle (see figure 9).

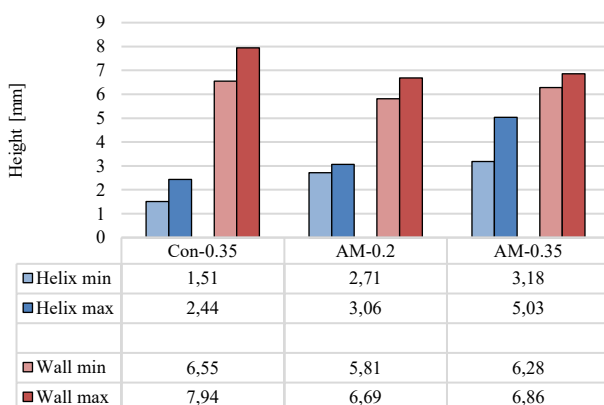


Fig. 9. AM helix and thin wall height measurements

4. Conclusion

The results conclude a great potential for the application of additively manufactured nozzles. The successful additive approach allows for innovative, complex and integrated designs while surpassing a conventional design in powder efficiency without directional dependencies. Due to the integration of mating surfaces and preformed threads, quick nozzle swaps are possible in order to react to changing conditions. This is very important for the soon intended multi-material applications that require specific free form nozzle shapes.

Eventually, by manufacturing the nozzles with the push of a button on LPBF printers, replacement parts do not need to be stocked anymore and the process can be automated. The process chain is shorter and more accessible than the conventional manufacturing route using a lathe or a milling machine.

Despite the underperforming honeycomb nozzle, integrated structures will be pursued extensively. Further improvements of the surface quality by abrasive flow machining inside the powder channels can prevent the agglomeration of powder inside the nozzle. Additionally, the focal plane of the laser will be moved closer to the nozzle.

The findings in this paper proved that additively manufactured nozzles are possible. Subsequently, the next generation of sophisticated AM nozzles will include an additional annular opening for shape gas. In consequence, the powder stream size can be adjusted by the variation of the shape gas flow.

Acknowledgements

We thank the European Regional Development Fund (ERDF) and the Ministry for Science and Culture of Lower Saxony for the funding and support.

Duration of implementation: 01.07.2018 – 30.06.2021

Project number: ZW6-8501 8048 (wGROTESK)



References

- [1] Levy, G. N.; Schindel, R.; Kruth, J.: "Rapid Manufacturing and Rapid Tooling with Layer Manufacturing (LM) Technologies"; CIRP Annals, Volume 52; 2003; Pages 589-609, [https://doi.org/10.1016/S0007-8506\(07\)60206-6](https://doi.org/10.1016/S0007-8506(07)60206-6)
- [2] A. Weisheit, G. Backes, R. Stromeyer, A. Gasser, K. Wissenbach, R. Poprawe; "Powder injection: the key to reconditioning and generating components using laser cladding"; Proceedings of International Congress on Advanced materials and Processes, Munich, Germany, 2001, ISBN: 3-88355-302-6
- [3] Emminghaus, N.; Hoff, C.; Hermsdorf, J.; Kaierle, S.; "Additive Manufacturing of CuSn10 Powder via Selective Laser Melting"; Lasers in Manufacturing Conference 2019, Munich
- [4] Settles, G. S. "Schlieren and Shadowgraph Techniques. Visualizing Phenomena in Transparent Media", Page 49; 2001; Springer-Verlag Berlin Heidelberg, ISBN 978-3-540-66155-9

11th CIRP Conference on Photonic Technologies [LANE 2020] on September 7-10, 2020

Vertical laser metal wire deposition of Al-Si alloys

Adrien Da Silva^{a*}, Sicong Wang^a, Joerg Volpp^a, Alexander F.H. Kaplan^a

^a*Department of Engineering Sciences and Mathematics. Luleå University of Technology, 971 87 Luleå, Sweden*

* Corresponding author. Tel.: +46 72 245 05 38. E-mail address: adrien.da.silva@ltu.se

Abstract

Additive Manufacturing of aluminium alloys has become crucial for lightweight applications. However, new materials and techniques need to be developed in order to achieve more advanced properties and higher efficiency. Therefore, a new energy-efficient wire deposition strategy was developed for processing aluminium-silicon alloys with Laser Metal Wire Deposition. Three alloys with different Si-contents were studied: AlSi5, AlSi10Mg and AlSi12. Different thicknesses of partially melted zones were observed and explained. The previous layer was partly remelted only by the heat conduction in the melt pool. It was found that the thickness of the partially melted zone depends on the difference of temperature between the liquidus and solidus.

© 2020 The Authors. Published by Elsevier B.V.

This is an open access article under the CC BY-NC-ND license (<http://creativecommons.org/licenses/by-nc-nd/4.0/>)

Peer-review under responsibility of the Bayerisches Laserzentrum GmbH

Keywords: Directed Energy Deposition; Direct Metal Deposition; Wire-Laser Additive Manufacturing; Laser Engineered Net Shaping; partially melted zone; mushy zone

1. Introduction

Aluminium alloys are commonly used in Additive Manufacturing (AM) due to their advantageous mechanical properties in relation to their low density, especially the Al-Si alloys that constitute the 4000 series. Silicon improves the flowability of the alloy once molten, which makes it easier to process. The main AM techniques involving aluminium today are Laser Powder Bed Fusion (LPBF), Directed Energy Deposition (DED) with powder, and Wire-Arc Additive Manufacturing (WAAM). LPBF allows high geometrical precision for small components, the other two strategies allow high deposition rates for larger components. WAAM is known as a lower cost alternative, which also present simplicity and safety advantages due to the usage of wire instead of powder. However, the arc delivers more heat input into the materials than a laser beam, which leads to a larger heat affected zone

and more distortion that requires more process monitoring [1,2,3].

Another alternative is to use a laser beam as a heat source with a wire as a feeding material. This process is commonly called Laser Metal Wire Deposition (LMWD). A wire is usually fed from the front side and a laser beam placed almost vertically melts both the wire and the substrate. The feasibility of this technique was proven with aluminium alloys such as AA5087 alloy [4,5] and AlSi5 [6]. One disadvantage is that the high reflectivity and heat conductivity of aluminium require more laser power to process these alloys. For processing AlSi5 with LMWD, the specific energy required was 102.8 kJ/g [6], whereas with WAAM the specific energy was found to be 4.0 kJ/g [3]. This is why a potentially more energy efficient alternative for LMWD was investigated in this study.

For hypoeutectic Al-Si alloys such as AlSi5, AlSi10Mg and AlSi12, the microstructure consist of two phases: the primary α -aluminium and the eutectic phase. When melting these alloys, a partially melted zone (PMZ) is created around the melt pool, where grains of solid α phases are surrounded by liquid. On the backside of the melt pool, the α phases grow from the solid α grains in the liquid, forming dendrites. This area is called the mushy zone [7]. Since there is no clear boundary between the liquid and the solid phases, aluminium alloys processing presents complex effects that are not explained yet. Therefore, in this work, the impact of the mushy zone and the PMZ on the transition between different layers was investigated.

2. Methods

The chosen setup for LMWD enables energy input only into the wire and not on the base material for potential reduction of energy need compared to conventional processes. Thus, the wire was fed vertically and the laser beam was inclined 50° from the vertical axis in front of the wire. The laser beam was focused on the wire, at a distance h above the substrate (Figure 1).

The laser was a 15 kW CW fiber laser with a beam parameter product of 10.5 mm-mrad. The optic fiber's diameter was 0.4 mm and the collimator and focus lenses had a focal length of respectively 150 mm and 250 mm resulting in a 0.67 mm laser spot size. Three different wires were investigated: AlSi5, AlSi10Mg and AlSi12, all with a diameter of 1.6 mm. The substrate was aluminium alloy 6061. The shielding gas nozzle was placed 10 mm above the substrate and the argon gas flow was 18 L/min.

High-Speed Imaging (HSI) was used to observe the process. The camera was recording from the side at 2000 fps. Two CW illumination lasers (50 W each, 810 nm wavelength) were illuminating the process. The camera was equipped with a band-pass filter of 810nm to block the process light.

HSI was used to tailor the process parameters on 10cm-long tracks, until converging to the optimized parameters for each chemical composition. The wire feeding speed was set to 4 m/min (66.7 mm/s), the scanning speed to 10 mm/s and the laser's power varied between 3500W and 7000W. With these parameters, a homogeneous track could be achieved when the height h was 4 mm, since the height of the tracks was about 3.5 mm and the wire has to melt slightly above the solidifying track (Figure 2). Walls were then built

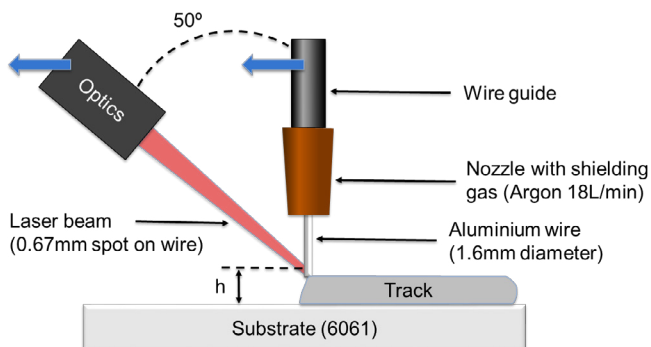


Fig. 1. Setup for vertical LMWD

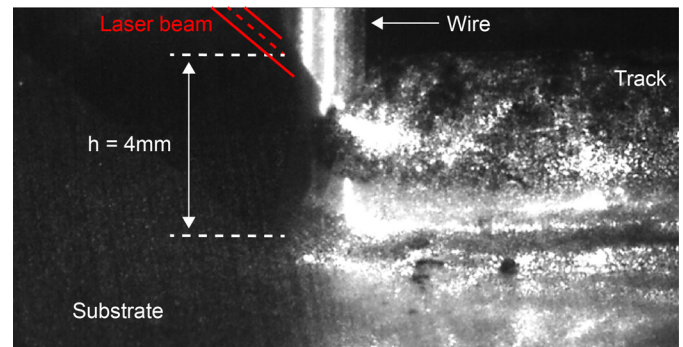


Fig. 2. High-Speed Imaging frame of the vertical LMWD process with optimised parameters

with the optimized parameters, and the power was reduced starting from the second layer in order to avoid process failure. The process failure was an interruption in the material deposition, resulting in a cut in the track. These interruptions were due to a high difference of height on the wall, thus the distance h deviated a lot from the optimal 4 mm.

One track was produced with the optimized parameters for each alloy composition. In addition, three walls were built with the same parameters and a power reduction for the upper layers until the process fails. Cross-sections of the three walls were produced, the samples were cold mounted in epoxy, grinded, polished and observed in an optical microscope.

3. Results and discussion

3.1. Process behavior

Depending on the chemical composition, different laser powers had to be chosen. Table 1 shows the optimized laser powers used for the first layer and the upper layers for each composition. It is noticeable that there is no direct relation between the silicon content in the alloy and the power needed. Especially, the alloy AlSi10Mg required considerably less power than the alloys AlSi5 and AlSi12, most probably because of the presence of magnesium. Indeed, it is well-known that magnesium increases the weldability of aluminium alloys [8].

Table 1. Optimized laser power used for building tracks and walls

	AlSi5	AlSi10Mg	AlSi12
Laser power on first layer (W)	6000	4000	7000
Laser power on upper layers (W)	5000	3500	5000
Number of layers built	4	8	5

When building walls, the first process failure happened respectively on layer 4 for AlSi5 and on layer 5 for AlSi12. With the AlSi10Mg composition, the failure came only on layer 8, which confirms the easier processability of this alloy. Figure 3 shows the resulting walls with their middle cross-section.

The specific energy E_m needed for processing the three different alloys with this present technique was calculated based on the following equation:

$$E_m = \frac{P}{\pi r^2 v \rho}, \quad (1)$$

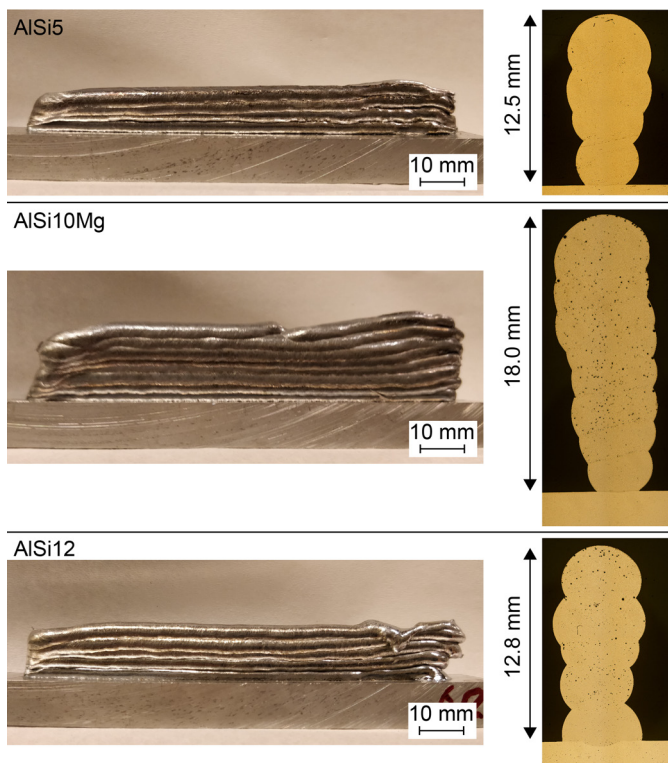


Fig. 3. Photographs of the walls with micrographs of their cross-sections

where P is the laser's power, r is the wire's radius, v is the feeding speed, and ρ is the density of the material. Thereby, even though other studies used different parameters, it is possible to compare the specific energies required to process aluminium. Manufacturing AISi5 in the present study required only 13.4 % of the energy needed for manufacturing AISi12 with a regular LMWD setup, and required 3.45 times more energy than manufacturing AISi5 with WAAM (Table 2).

Table 2. Comparison of specific energies needed for different processes and materials

Material	Process	Specific energy (kJ/g)	Reference
AA5087	LMWD	13.2	[4, 5]
AISi12	LMWD	102.8	[6]
AISi5	WAAM	4.0	[3]
AISi5	Vertical LMWD	13.8	Present study
AISi10Mg	Vertical LMWD	9.7	Present study
AISi12	Vertical LMWD	13.8	Present study

One reason for the need of lower energy compared to regular LMWD is that in [6] a smaller wire was used (0.4mm) with a laser spot that was larger than the wire (0.6mm). Another part of this difference of specific energy can be explained by the thermodynamics of the process. With regular LMWD, the laser has to melt the substrate and heat conduction occurs in three dimensions. Whereas with this setup, only the wire is melted by the laser beam and the heat conduction occurs only in one dimension, along the wire. Therefore, less energy has to be provided to counterbalance the losses in heat conduction. The higher energy required compared to WAAM is likely due to the low laser absorption in aluminium, that is

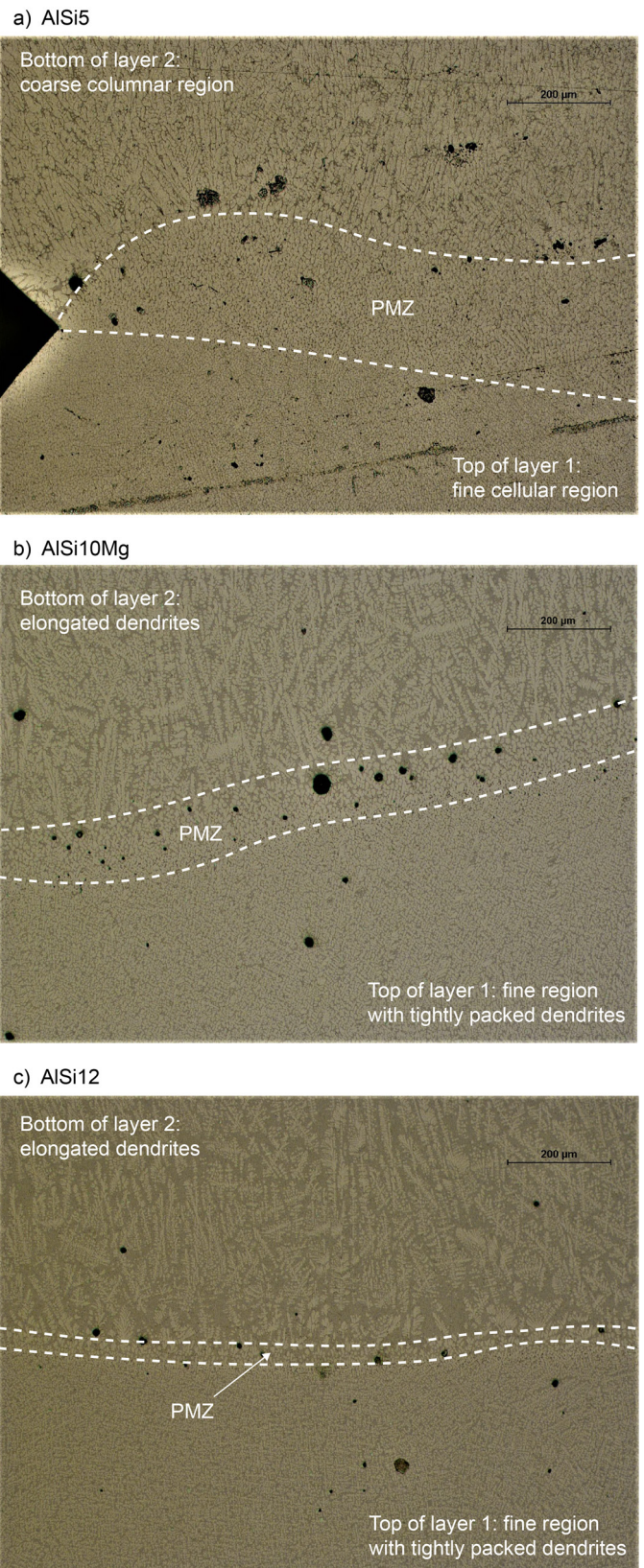


Fig. 4. Optical micrographs of the interfaces between layers 1 and 2 for each alloy investigated (magnification x10)

about 5 %. Indeed, when 13.8 kJ of laser energy are required to process one gram of wire, only 0.69 kJ are absorbed by the material, that is only 17.3 % of the energy input with WAAM.

3.2. Microstructure analysis

The microstructural study showed a difference of phases structure depending on the height in a same layer. In Figure 4, the light phase is the primary α -aluminium and the dark phase the eutectic. For each of the three alloys studied, a considerably finer microstructure was found in the upper part of a layer than in its lower part. It means that the lower part of the track should have a lower cooling rate than its upper part, which is probably due to the geometry of the track. The upper part of the track is thinner than the lower part and might cool down faster. At the interface between two layers, there is a transition between the fine microstructure in the upper part of layer 1 and the coarse microstructure in the lower part of layer 2. The PMZ forms an intermediate region between the two layers. The PMZ does not follow the convex shape of the previous track, but is more straight, or even concave. It means that the part of the previous track present above this region was remelted.

In the case of AlSi5, the upper non-melted part of layer 1 is made of a fine cellular region and the lower part of layer 2 of a coarser columnar region with few initiations of dendrites. For this alloy with low silicon content, it is likely that the primary α -aluminium phase is predominant and that the grains do not have enough space to fully extend into dendrites. At the interface between two layers, the fine cellular microstructure of the lower track became coarser. This is the mark of the PMZ when depositing layer 2, where the maximum temperature of the thermal cycle was between the eutectic temperature and the fusion temperature of the alloy, so that only the eutectic phase melted, and not the primary α -aluminium phase. In this region, due to mixing between the liquid eutectic and the liquid alloy from the second layer, the aluminium content in the liquid is increased and the solid primary α -aluminium phases grow again when the liquid solidifies.

When comparing AlSi10Mg and AlSi12, the microstructures are very similar. The upper part of the tracks are made of fine tightly packed dendrites, and the lower part is made of elongated and developed dendrites typically representative of the mushy zone occurring behind the melt pool. The main difference of microstructure between these two alloys is the thickness of their PMZ. Indeed, for AlSi12 the PMZ is approximately $40 \pm 7 \mu\text{m}$ thick, for AlSi10Mg it is about $100 \pm 10 \mu\text{m}$ thick, and for AlSi5 about $260 \pm 21 \mu\text{m}$ thick (Figure 5). This difference of thickness is most likely due to variations of liquidus and solidus temperatures for the three different alloys. In the micrographs, the boundary between the PMZ and the upper layer was at liquidus temperature during the process, and the boundary between the PMZ and the lower layer was at solidus temperature. Thus, the difference of temperature between the liquidus and solidus of the alloy [9] must be proportional to the thickness of the PMZ (dashed line in Figure 5). However, even if this proportionality is true for AlSi5 and AlSi12, it is not for AlSi10Mg that has a smaller PMZ. This difference is most probably due to the addition of magnesium in this alloy that creates other phases like Mg_2Si and make the fusion and

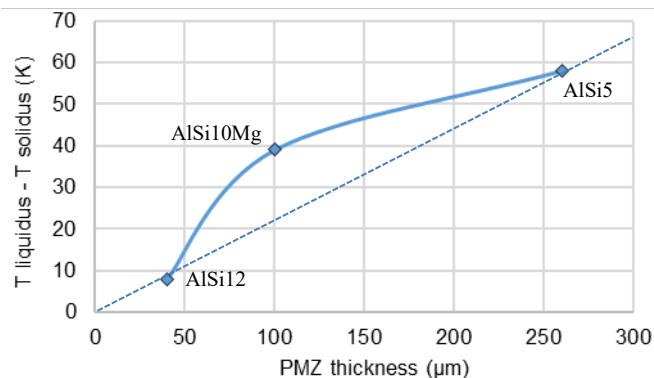


Fig. 5. Comparison between the PMZ thickness and the difference of temperature between the liquidus and the solidus of each alloy [9]

solidification patterns more complex than for AlSi5 and AlSi12 where only two main phases are present.

4. Conclusion

Base on the results obtained in this study, the following conclusions can be drawn:

- It is possible to build aluminium structures with LMWD by laser beam melting only the wire and have sufficient dilution of the previous layer.
- Using the laser beam to melt only the wire was shown to save 86.6 % of the energy compared to a regular LMWD process.
- The thickness of the PMZ increases with the increased temperature difference between the liquidus and solidus of the alloy.
- The presence of magnesium in AlSi10Mg probably reduces the thickness of the PMZ.

Acknowledgements

This work was accomplished within the European project SAMOA (no. 18079) funded by EIT Raw Materials. The authors would also like to acknowledge the division of materials science at Luleå University of Technology for their technical support.

References

- [1] Derekar KS. A review of wire arc additive manufacturing and advances in wire arc additive manufacturing of aluminium. *Mater Sci Tech-Lond*, vol. 34, no. 8. Taylor and Francis Ltd. 2018. p. 895-916.
- [2] Horgar A, Fostervoll H, Nyhus B, Ren X, Eriksson M, Akselsen OM. Additive manufacturing using WAAM with AA5183 wire. *J. Mater*, vol. 259. 2018. p. 68-74.
- [3] Nie Y, Zhang P, Wu X, Li G, Yan H, Yu Z. Rapid prototyping of 4043 Al-alloy parts by cold metal transfer. *Sci Technol Weld Joi*, vol. 23, no. 6. 2018. p. 527-535.
- [4] Froend M, Ventzke V, Riekehr S, Kashaev N, Klusemann B, Enz J. Microstructure and microhardness of wire-based laser metal deposited AA5087 using an Ytterbium fibre laser. *Mater. Charact.*, vol. 143. 2018. p. 59-67.
- [5] Froend M, Riekehr S, Kashaev N, Klusemann B, Enz J. Process development for wire-based laser metal deposition of 5087 aluminium alloy by using fibre laser. *J. Manuf. Process.*, vol. 34. 2018. p. 721-732.

- [6] Demir AG, Biffi CA. Micro laser metal wire deposition of thin-walled Al alloy components: Process and material characterization. *J. Manuf. Process.*, vol. 37. 2019. p. 362-369.
- [7] Huang C, Cao G, Kou S. Liquefaction cracking in partial penetration aluminium welds: Assessing tendencies to liquate, crack and backfill. *Sci Technol Weld Joi*, vol. 9, no. 2. 2004. p. 149-157.
- [8] Smith WF. *Structure and properties of engineering alloys*. 2nd edition. McGraw-Hill Science. 1993. p. 187-188.
- [9] <http://www.matweb.com> (10/03/2020).

11th CIRP Conference on Photonic Technologies [LANE 2020] on September 7-10, 2020

Specific aspects of the transitional layer forming in the aluminium bronze - stainless steel functionally graded structures after laser metal deposition

Konstantin Makarenko*, Oleg Dubinin, Petr Shornikov, Igor Shishkovsky

Skolkovo Institute of Science and Technology, Bolshoy boulevard 30, build. 1, Moscow 121205, Russian Federation

* Corresponding author. Tel.: +7-926-689-44-34. E-mail address: Konstantin.Makarenko@skoltech.ru

Abstract

The article describes phenomena which occur in the transitional area between stainless steel and aluminium bronze in laser deposited functionally graded structures created via direct joining method with the InssTek MX-1000 machine. The results of the research demonstrated absence of cracking achieved after changing of the synthesis scheme with the same materials and the same treatment regimes. The sources of cracking on a border between stainless steel and aluminium bronze layers were defined during the research. The results of microhardness measurement of the deposited multilayer structures demonstrated 266 HV maximum value with 43 GPa Young's modulus of elasticity in the same point of a transitional area. Intermetallics forming, dendritic growth, phase composition and microstructure specific properties of laser deposited stainless steel - aluminium bronze functionally graded materials are also observed and described in the article.

© 2020 The Authors. Published by Elsevier B.V.

This is an open access article under the CC BY-NC-ND license (<http://creativecommons.org/licenses/by-nc-nd/4.0/>)

Peer-review under responsibility of the Bayerisches Laserzentrum GmbH

Keywords: direct energy deposition; functionally graded materials; aluminium bronze; stainless steel; transitional zone; cracking; microhardness; microstructure; InssTek; aerospace applications

1. Introduction, problem statement, practical applications

Research of functionally graded materials synthesis via laser cladding [1] and rapid prototyping technologies [2] such as laser direct energy deposition (laser DED) has a high number of significant practical applications, one of which is space industry parts production (such as combustion chambers and rocket engines nozzles) created from two different kinds of material: a material with high heat conductivity and minor mechanical strength (aluminium bronze, tin bronze, chromium bronze, latten) and a material with less heat conductivity and major strength (steel, nickel superalloys). Traditional methods of manufacturing of such parts have definite disadvantages beside the methods of additive manufacturing (AM). They are:

- Minor productivity;
- Minor processibility;
- Issues with the sophisticated geometry manufacturing;

- Higher weight and non-optimized mass distribution of the manufactured object.

Development of AM leads to modernization in space industry parts producing and one of the key tasks in this field is to create 3D-printed parts with properties of same ones made via traditional methods. AM-produced parts should have the same or higher values of mechanical strength, Young's modulus, mechanical durability, high-temperature stability, heat resistance, impact toughness and microhardness. It is also necessary to mention that conversion from traditional technologies to AM methods in the field of a space industry could provide increase of a rocket engine specific impulse value. This parameter is the most important in all space engines manufacturing because it defines the highest possible payload mass of the carrier rocket. As a mathematical example (only for the visualization of the values): 8.1% increase of the specific impulse in case of the one-stage liquid engine rocket provides

4.2-fold increase of the payload mass. The main purpose of all rocket engines development is devoted, first of all, to possible growth of this extremely important parameter.

The topic of our work was research of the phenomena which appear when parts from functionally graded aluminium bronze - stainless steel materials are manufactured via laser DED technology. The main problem in this field that should be discussed and the main technical task that should be solved is clear understanding and skill of operating processes which occur in transitional areas between layers of different materials like stainless steel and aluminium bronze which have different values of physical characteristics: density, heat conductivity, temperature conductivity, melting temperature, coefficient of a temperature expansion and so on. Cracking elimination in such areas of laser deposited functionally graded samples was the most important task in our research.

There are at least three different engineering methods of functionally graded materials synthesis via direct energy deposition [3]. They are direct joining, gradient path method and intermediate section method (figure 1). Our research was devoted to the direct joining method performing in two configurations: experimental samples with two sharp transitions (a lot of layers of stainless steel, one layer of aluminium bronze, a lot of layers of stainless steel again) and multilayer samples with changing single layers of aluminium bronze and stainless steel.

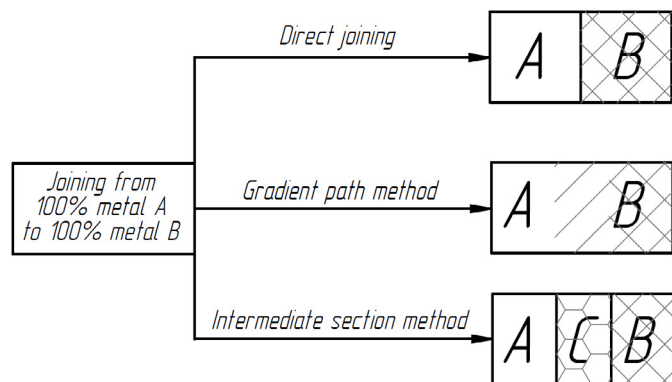


Fig. 1. Build strategies of joining a metal A and a metal B [3].

2. Materials and equipment

The materials used in experiments were stainless steel AISI 316L and aluminium bronze with 10% Al (table 1).

Table 1. Chemical elements percentage in materials under discussion.

Chemical element	AISI 316L, %	Aluminium bronze, %
C	< 0.03	-
Mn	< 2.0	-
P	< 0.045	-
S	< 0.03	-
Si	< 1.0	-
Cr	16.0...18.0	-
Ni	10.0...14.0	-

Mo	2.0...3.0	-
Ti	< 0.5	-
Fe	The rest	0.8...1
Cu	-	89.0...89.5
Al	-	9.8...10.2

All experiments were performed with the InssTek MX-1000 machine (figure 2) [4] in DMT (direct metal tooling) mode with the 308 W average output laser radiation power in case of stainless steel (450 W maximal power) and 500 W average power in case of aluminium bronze (750 W maximal). Power of laser radiation was chosen in accordance with the bronze infrared radiation absorption coefficient which is lower than the same coefficient of stainless steel. Other treatment regimes were: 0.85 m/min scanning speed, 3.5 g/min powder rate, 5 s cooling time between layers, no preliminary base surface heatup and argon usage as a feeding and shielding gas.



Fig. 2. The InssTek MX-1000 machine [4].

Configuration of single layer tracks formation is shown in the figure 3. Width of a single track was equal to 800 μm. Covering of the tracks was equal to 300 μm.

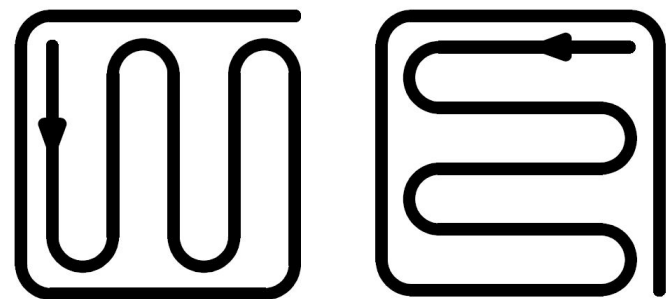


Fig. 3. Configuration of the tracks formation in a single layer of all experimental samples (left picture - layers with an odd numerical order, right picture - with an even order).

An IPG Photonics produced 1 kW ytterbium doped fiber laser was used in the experiments. Output laser wavelength was equal to a 1064 nm. Focus of a laser beam was on a 1 mm level under the surface of the piece.

Microstructure research was performed via an optical microscope Carl Zeiss and a scanning electronic microscope Quattro SEM. All samples were previously treated with the etch (the etchant - H_2SO_4 with ethanol and $CuCl_2$, the etch time - 5...7 s).

Microhardness tests and stiffness measurements were performed in automatic mode via Oerlikon microhardness measuring machine with a triangular Bercovich diamond pyramid as an indenter. An indentation force was equal to 3 N, the resulting value of microhardness was recalculated in a Vickers's scale automatically by means of Oerlikon equipment and software.

XRD (X-ray diffraction) data analysis was performed via MAUD software with usage of Crystallography Open Database.

3. Results and discussion

3.1. Microstructure analysis

As it was mentioned in the part 1 of the paper, the two series of the experimental samples were manufactured for the purposes of the research. The first one (figure 4) - the samples with one layer of aluminium bronze between two huge zones (20 layers each) of stainless steel. Thickness of each single layer was equal to 250 μm . The second series of the samples (figure 5) was created with alternation of the layers of steel and bronze (20 layers of each material) with the same as in a previous case thickness of a single layer (250 μm).

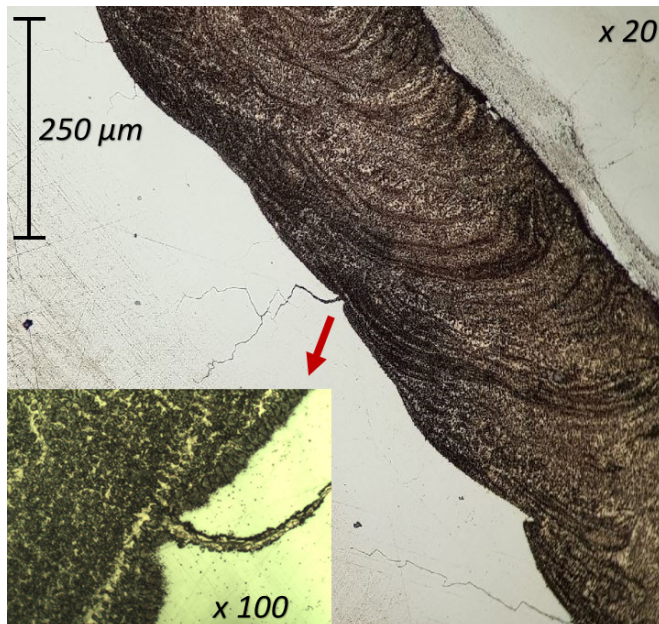


Fig. 4. Crack formation on a border of stainless steel and aluminium bronze. The dark structure - aluminium bronze, the light structure - stainless steel. The bottom part of the sample is leftward.

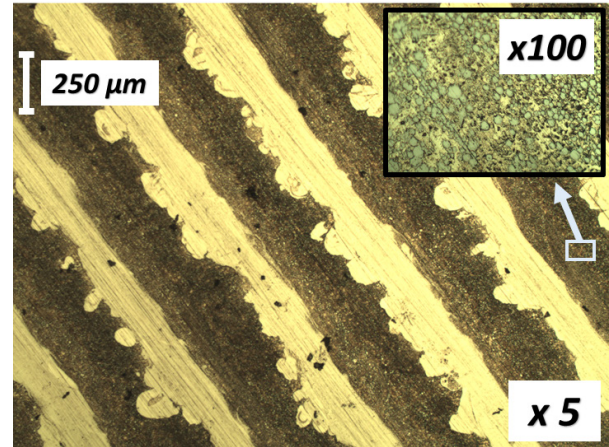


Fig. 5. A functionally graded aluminium bronze - stainless steel multilayer structure. The bottom part of the sample is leftward. The dark layers - aluminium bronze, the light layers - stainless steel.

The experimental samples series №1 (figure 4) demonstrated cracking on a border between stainless steel and aluminium bronze. We can see that the nucleus of each crack lies in the bronze part of the sample. The main task in this case is to understand what exactly was an occasion of the cracking: the powder defects (foreign deposits, defects of the shape and size), a local porosity of the part and other defects caused by issues with the treatment regimes, or the specific aspects of a structure and a chemical composition of the deposited part, local embrittlement caused by forming of brittle and hard structures like intermetallics. The experimental samples series №2 (figure 5) grown with the same materials on the same regimes had no cracks at all. One of the reasons which caused this phenomenon presumably was different thermal history in previous layers of samples series №1 and series №2, associated with differences between thermophysical characteristics of stainless steel and aluminium bronze. The huge number of layers of steel under the single layer of bronze (samples series №1) caused another sort of heat affection on the following layers comparing with structure with «sandwiched layers» (samples series №2).

3.2. Microhardness and Young's modulus of elasticity research.

The microhardness and Young's modulus of elasticity measurements were performed with a purpose to understand how does the energy deposition process exactly influence over microhardness of the part and, as it was said in a part 3.1, to identify if there was local microhardness and brittleness increase in the transitional areas of the samples caused by intermetallics growth. The first microhardness and Young's modulus of elasticity research was performed with the samples series №1 (figure 6). The measurements 1 - 3 and 10 - 21 were performed on the steel areas of the samples transitional zones, the measurements 4 - 6 - on the bronze areas and the measurements 7 - 9 and 22 - 24 - directly on a stainless steel - aluminium bronze border. The undersides of the samples under discussion are beneath in all three photos demonstrated in the figure 6.

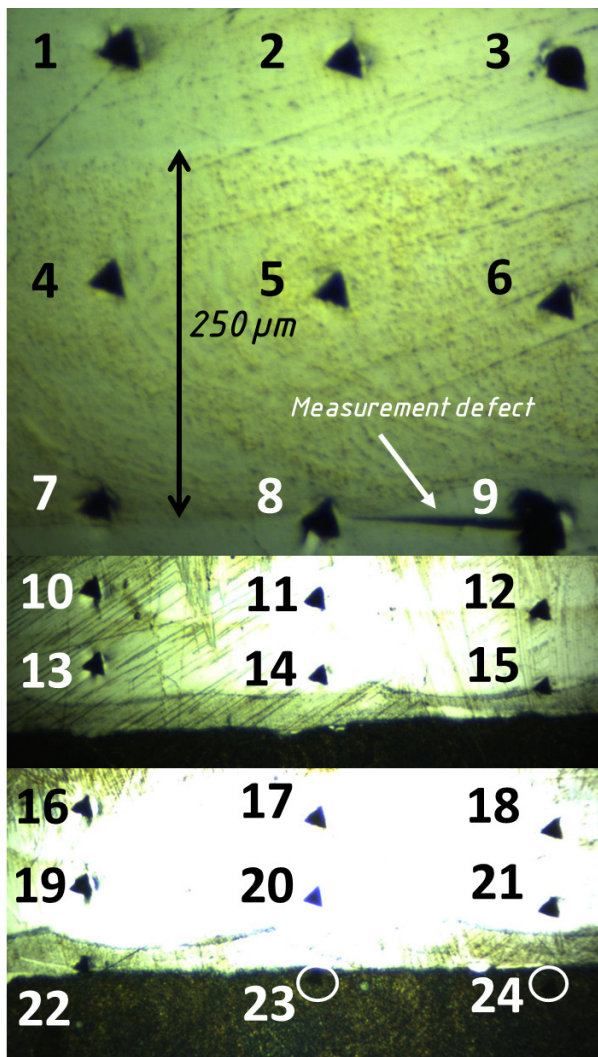


Fig. 6. A microhardness and Young's modulus of elasticity research №1 performed with the different experimental samples series №1.

The second microhardness and Young's modulus of elasticity research was performed with the samples series №2 with a multilayer structure (figure 7). The underside of the sample demonstrated in the photo is beneath.

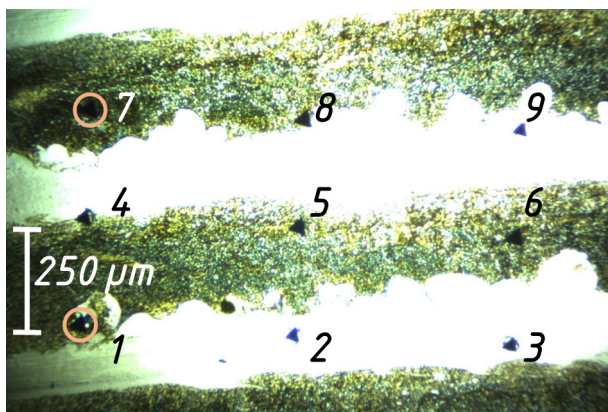


Fig. 7. A microhardness and Young's modulus of elasticity research №2 performed with the experimental samples series №2.

The results of all measurements performed with the samples series №1 and №2 are demonstrated in the table 2 and in the graphs (figure 8).

Table 2. The results of the microhardness and Young's modulus of elasticity tests performed with the experimental samples series №1 and №2.

Point №	Microhardness, [HV] (samples series №1)	Microhardness, [HV] (samples series №2)	Young's modulus of elasticity, [GPa] (samples series №1)	Young's modulus of elasticity, [GPa] (samples series №2)
1	133.1	170.1	32.6	37.8
2	171.1	266.0	34.9	43.2
3	142.5	257.3	29.8	42.1
4	178.8	241.9	34.2	40.3
5	196.1	190.7	33.8	35.6
6	194.7	198.2	33.7	36.2
7	223.0	203.0	36.7	37.1
8	177.0	188.0	33.5	36.6
9	185.8	237.9	34.4	40.6
10	135.4		19.7	
11	126.3		19.2	
12	142.7		20.2	
13	118.0		20.1	
14	140.7		21.4	
15	175.3		23.0	
16	145.2		20.1	
17	127.4		18.7	
18	145.2		19.6	
19	134.0		19.5	
20	149.9		20.6	
21	152.6		20.1	
22	217.5		24.1	
23	214.0		23.6	
24	194.4		21.7	

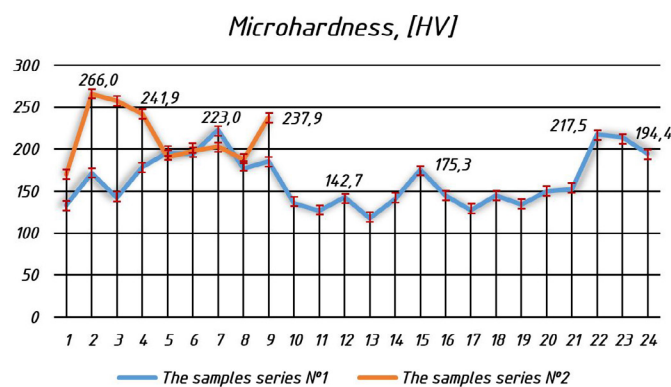


Fig. 8. The microhardness research results (comment: as it is seen, the total number of test points for the samples series №2 was less than the total number of test points for the samples series №1).

We can observe from the first research (the samples series №1) that the measurements 1 - 3 and 10 - 21 performed on the

steel zones showed the lower values of microhardness than the measurements of the bronze zone (4 - 6). The results of the border measurements (7 - 9 and 22 - 24) demonstrated the highest average value of microhardness and Young's modulus of elasticity simultaneously. The reason of microhardness increase and decrease of plasticity was growth of the brittle intermetallic structures such as $Fe - Al$. Internal stresses and deformations in the transitional zones of the samples caused by difference between the temperature expansion coefficients of materials (up to $19.6 \cdot 10^{-6} \text{ } ^\circ\text{C}^{-1}$ for AISI 316L and at the most $17.5 \text{ } ^\circ\text{C}^{-1}$ for aluminium bronze) were the reason of crack nucleus occurring on the grains of intermetallics.

The results of the second research demonstrated that the average value of microhardness of the samples series №2 is higher than microhardness of the samples series №1 and microhardness distribution within the volume of the samples is more regular for the samples series №2 than for the series №1.

3.3. Microstructure research via scanning electronic microscope

Alternation of the layers of aluminium bronze and stainless steel and higher mixing of these materials in the samples series №2 caused decrease of internal stresses and deformations in volume of the deposited parts and provided absence of cracks without changing any materials and treatment regimes. We repeatedly proved absence of cracks in the experimental samples series №2 after the detailed microstructure analysis via a scanning electronic microscope (figure 9), observed a dendritic structure (figure 10) of the material formed in nonequilibrium conditions and oversaw nanometer level porosity (figure 11) which didn't influence on the mechanical strength properties of the samples series №2.

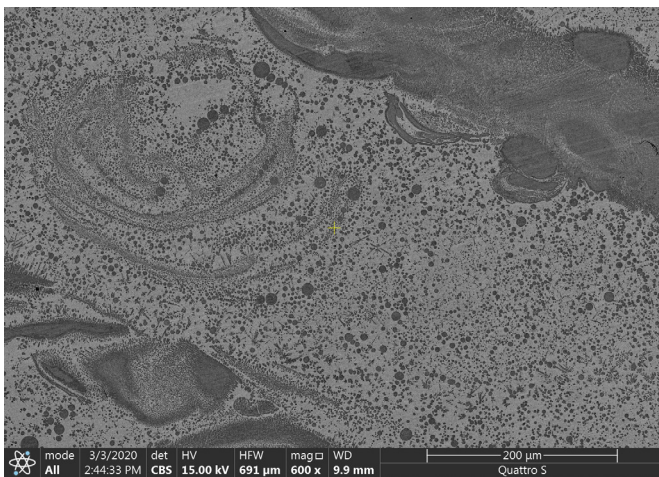


Fig. 9. Samples series №2 overall microstructure. Dark areas – stainless steel, light areas – aluminium bronze. No cracks are observed on the samples series №2 surfaces.

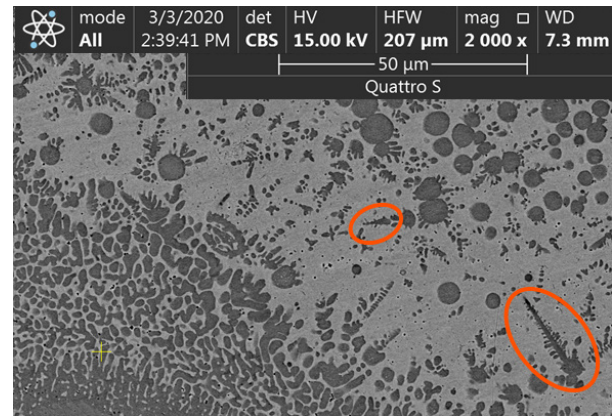


Fig. 10. Dendritic crystals observed on the samples series №2 surfaces.

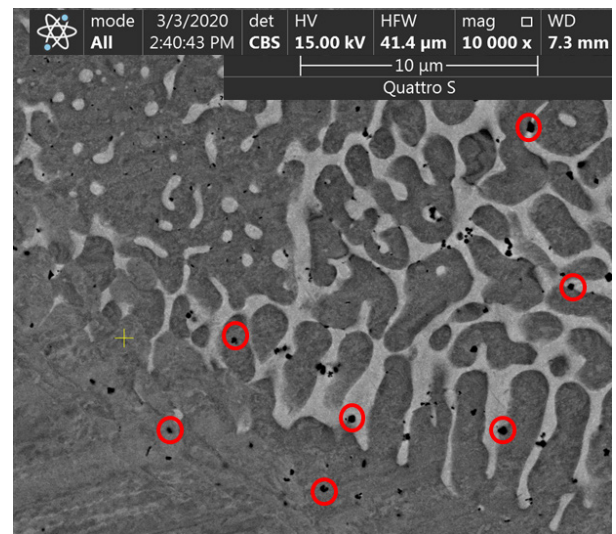


Fig. 11. Nanometer level porosity of the samples series №2.

3.4. XRD analysis

The results of XRD analysis (several of them are shown in the figure 12), performed with the experimental samples series №2, demonstrated the composition of phases, among which were:

- Cubic symmetry $AlNi$ phase (Pm-3m space group, 2.881 Å cell parameter);
- Cubic symmetry Cu phase (Fm-3m space group, 3.658 Å cell parameter);
- Cubic symmetry Cr phase (Im-3m space group, 2.884 Å cell parameter);
- Cubic symmetry $\alpha\text{-}Fe$ phase (Im-3m space group, 2.868 Å cell parameter);
- Cubic symmetry $Cr_{0.7}Fe_{0.3}$ phase (Im-3m space group, 2.872 Å cell parameter);
- Cubic symmetry $Fe_{0.95}W_{0.05}$ phase (Im-3m space group, 2.884 Å cell parameter).

Presence of W in the chemical composition of the last phase points at impurities in original powder materials or issues of diffractometry technique.

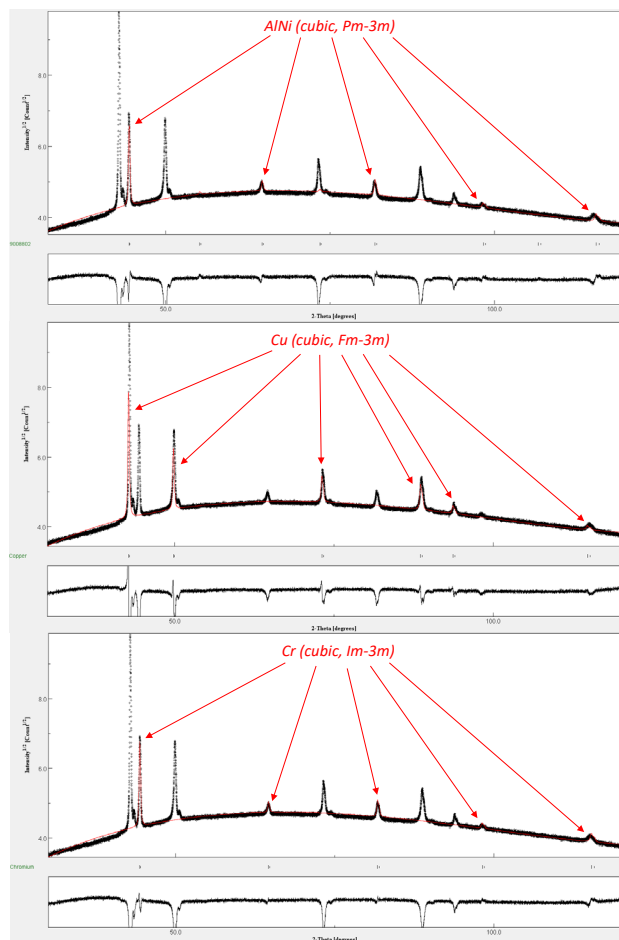


Fig. 12. XRD analysis of the experimental samples series №2 results. Black curves - XRD data distribution, red curves - crystallographic spectra.

There was no energy dispersive X-ray (EDX) research in this work, but the authors are going to perform it in future to make a microstructural analysis of the specimens. A *Cu-Fe* phase diagram (figure 13) can be used for theoretical estimation of the *Cu* and *Fe* mixture behavior in different temperature conditions.

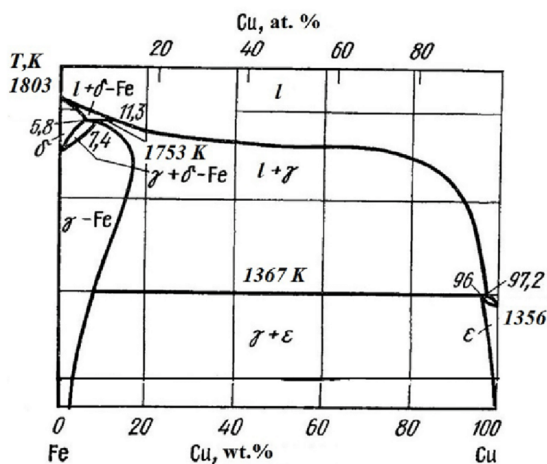


Fig. 13. A *Cu-Fe* phase diagram.

4. Conclusion

Difference between thermal expansion coefficients of materials along with rapid intermetallic growth, increase of microhardness (up to 223 *HV*), increase of Young's modulus of elasticity (up to 36.7 *GPa*) and local embrittlement of the functionally graded laser deposited parts with two sharp transitions created from stainless steel AISI 316L and aluminium bronze in a DMT mode [4] via the direct joining scheme [3] lead to cracking on a border between stainless steel and aluminium bronze. These effects can be suppressed by producing (on the same regimes) a multilayer structure with alternating of stainless steel and aluminium bronze layers, which will get comparatively more favorable thermal history during the process of laser treatment. These multilayer structures can have even a higher level of microhardness (up to 266 *HV*) and Young's modulus of elasticity (up to 43.2 *GPa*), but nevertheless, cracking of them can be entirely excluded because of reassignment of internal stresses and deformations in volume of a detail. Porosity of such multilayer structures has a nanometer level size and doesn't effect on its mechanical strength properties. The phenomena researched and the manufacturing method investigated can be used for the purposes of the space industry functionally graded parts manufacturing [5, 6, 7] from stainless steel and aluminium bronze via direct energy deposition additive technology, inter alia axial and radial deposition techniques.

Acknowledgements

We are grateful to Yulia Kuzminova, Ph.D. student of Skolkovo Institute of Science and Technology, and Stanislav Evlashin, Senior Research Scientist, for making a significant contribution in our research in the field of microstructure, microhardness and XRD analysis of the laser deposited functionally graded specimens.

References

- [1] Surinder Singh, Manoj Kumar, Gurvinder Pal Singh Sodhi, et al. Development of thick copper claddings on SS316L steel for In-vessel components of fusion reactors and copper-cast iron canisters. *Fusion Engineering and Design* 128, 2018. p. 126-137.
- [2] Igor Shishkovsky. Synthesis of functional gradient parts via RP methods. *Rapid prototyping Journal* vol. 7, № 4, 2011. p. 207-211. doi: 10.1108/13552540110402908
- [3] Lei Yan, Yitao Chen, Frank Liou. Additive manufacturing of functionally graded metallic materials using laser metal deposition. *Additive Manufacturing* 31 (2020) 100901.
- [4] InssTek MX-1000 Technical Data. An electronic source. Available at <http://www.insstek.com/content/standard/mx1000> (access date: 15 March, 2020).
- [5] Xiaodong He, Jiecai Han, Xinghong Zhang. Preparation and Ablating Behavior of FGM used in a Heat Flux Rocket Engine (2002).
- [6] D. Y. Gao, et al. (eds.). *Advances in Mechanics and Mathematics* © Kluwer Academic Publishers (2003).
- [7] Douglas C. Hofmann, Scott Roberts, Richard Otis, et al. Developing gradient metal alloys through radial deposition additive manufacturing. *Sci. Rep.* 4 (2014) 5357. doi: 2010.1038/srep05357.

11th CIRP Conference on Photonic Technologies [LANE 2020] on September 7-10, 2020

Geometrical model and strategy in single and multilayer structures deposited by powder-fed Directed Energy Deposition

Pedro Ramiro^{a,*}, Mikel Ortiz^a, Amaia Alberdi^a, Aitzol Lamikiz^b

^aTECNALIA, Basque Research and Technology Alliance (BRTA), Paseo Mikeletegi 7, 20009 Donostia-San Sebastián, Spain

^bDepartment of Mechanical engineering, Faculty of Engineering of Bilbao, University of Basque Country, Alameda de Urquijo s/n 48013 Bilbao, Spain

* Corresponding author. E-mail address: pedro.ramiro@tecnalia.com

Abstract

This work presents a geometrical model of coatings fabricated by powder-fed Directed Energy Deposition (DED) and defines guidelines and manufacturing strategies for multilayered structures based on the geometrical model results. This model obtains as output both the overlapped clad geometry and the dilution area of the coating at different input parameters and defines the strategy of multi-layer structures.

The results of this work validate the model that comes in handy: a) To understand the influence of each parameter and the single clad geometry when fabricating coatings and structures; b) To select the parameters depending on the requirements of the coating like effective thickness and dilution; c) To detect lack of fusion with the substrate due to an excessive overlap percentage; d) To select the deposition strategy and the tool path for additive manufacturing; e) To select the subsequent machining strategy based on the predicted geometry of the model.

© 2020 The Authors. Published by Elsevier B.V.

This is an open access article under the CC BY-NC-ND license (<http://creativecommons.org/licenses/by-nc-nd/4.0/>)

Peer-review under responsibility of the Bayerisches Laserzentrum GmbH

Keywords: Directed Energy Deposition; Powder-fed; Coatings; Multilayer Structure; Geometrical model; Deposition Strategy; Ni-based; Alloy 718.

1. Introduction

The powder-fed Directed Energy Deposition (DED) technology is an Additive Manufacturing process that employs a laser beam to create a melt pool in a metallic substrate where the material is injected in powder form. The added material is fused and solidified by creating a high-quality metallurgical union between the substrate and the added material. The desired part is created layer by layer, thus allowing to manufacture near-net-shape parts with complex geometries that must be finished by a machining process.

Currently, there are different powder injection techniques depending on the application and the kinematic configuration of the DED system: the off-axis powder injection when the deposition strategy is unidirectional [1], the continuous coaxial powder injection for vertical configurations [2], the discrete coaxial powder injection when it is necessary to tilt the nozzle in a multidirectional deposition strategy [3] and the inside beam

powder injection with an annular laser beam when it is necessary to achieve a wider tilt range comparing to the commercially available nozzles [4].

One of the most relevant challenges of the DED is the geometric uncertainty of the additive process that must deal with the tool in the subsequent machining operation [5]. Although recently, it has been made great progress in the numerical simulation [6-8], a complete model considering all stages and process parameters is still a complex procedure and far from the real status [9] with a high computational cost and time consuming of the simulation [10].

As an alternative, many authors developed empirical geometrical models [11-14] that cannot predict characteristics as the grain size, hardness, and porosity but that are useful for answer pure geometrical requirements as height, width, waviness or thickness of the deposited material trying to reduce significantly the time rely on expensive and time-consuming techniques, such as multiple experimental runs [15].

On the basis of the single clad characteristics (height, width, area and penetration) and based on both the model developed by Ocelík et al. [16] and an own-developed model of the dilution zone, this work validates a geometrical model of coatings fabricated by powder-fed Directed Energy Deposition (DED) and defines guidelines and manufacturing strategies for multilayered structures based on the experimental results.

Nomenclature

A	Area
d_o	Overlap percentage
h	Height
i	Overlapped clad number
O_i	Origin of the overlapped clad i
O_{i+1}	Origin of the overlapped clad i+1
p	Penetration
w	Width
Y_i	Height in the point P of the clad i

2. Materials and methods

2.1. Materials

The material used in the experimental tests as filler and substrate material was the Nickel-based Alloy 718. The filler material consisted of powder with a granulometry between 45 and 150 μm , from Flame Spray Technologies (FST), and the substrate material was in an annealed state. Table 1 presents the chemical composition of the powder and the substrate materials. This Nickel-based alloy presents excellent properties at high-temperature applications (useful up to 980°C), oxidation, and corrosion-resistant properties, and it is widely used in the aeronautical sector.

Table 1. Chemical composition (Wt. %) of Alloy 718 powder and substrate.

	Ni	Cr	Fe	Nb+Ta	Mo	Ti	Al
Powder	52.8	18.5	18	4.8	3.5	0.75	0.3
Substrate	53.5	18.7	17.7	5	2.9	0.94	0.58

2.2. Machine

All tests were performed in an IBARMIA ZVH45/1600 Add+Process hybrid machine (Fig. 1). This multiprocess machine combines the DED technology with 5-axis milling and turning (horizontal and vertical) capability. This machine is equipped with a Precitec YC52 cladding head with a collimating and focusing optics of 125 mm and 250 mm respectively, a Sulzer Metco TWIN-10-C Powder Feeder, and an Yb-Fiber Rofin FL030 Laser generator of 3 kW with a continuous wavelength of 1.07 μm . For nozzle, a 4-stream coaxial discrete nozzle from Precitec was used.



Fig. 1. IBARMIA ZVH45/1600 Add+Process hybrid machine.

2.3. Geometrical model of single layer coatings

This work proposes a model for the overlapped clad based on the model developed by Ocelík et al. [16], supposing that each new clad of the coating has a second-degree parabolic shape. This model achieved a high level of accuracy by taking into account purely geometrical parameters such as the characteristics of the single clad (Fig. 2) and the overlap percentage (d_o) of the coating.

The model supposes that each new clad is deposited with the same characteristics than the single clad (Fig.3.a) forming a new clad i+1 with the overlapped area of the previous clad i (Fig. 3.b). This clad i+1 is calculated by assuming the height Y_i in the overlapped point P is the same as in the previous (clad i) and it has a second-degree parabola shape with a higher width (w_{i+1}). The area from the origin O_{i+1} to P is the sum of the single clad area and the overlapped area of the previous clad i. The distance from the from the origin O_{i+1} to P is the same than the single clad width (w). In the first iteration, the clad i is the single clad.

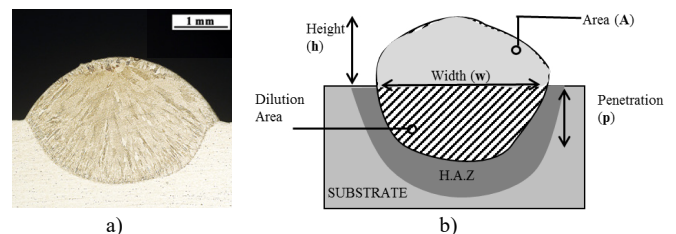


Fig. 2. Single clad: a) Macro photograph of a cross-section of a single clad; b) Single clad characteristics.

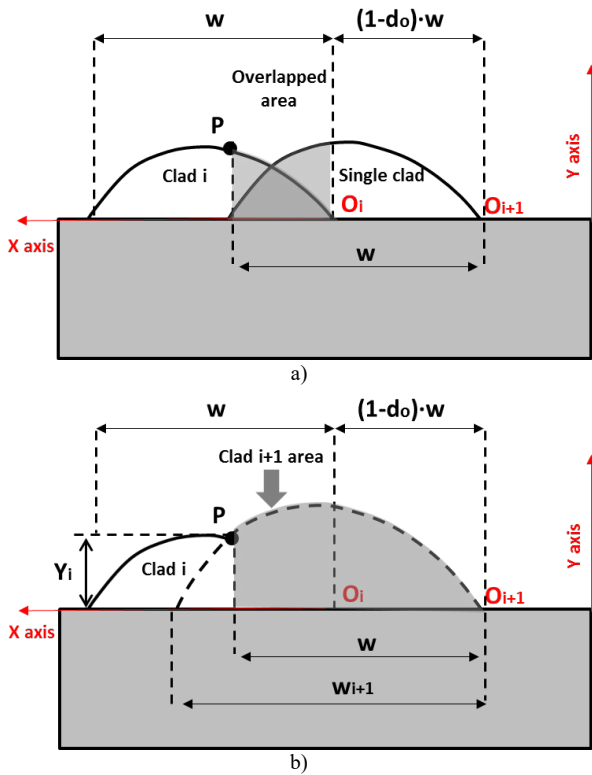


Fig. 3. Geometrical model of the deposited material. a) Clad deposited overlapping the previous clad; b) Clad i+1 of the model.

Furthermore, to complete the model, it is proposed a simple model of the dilution zone of the overlapped clad based on experimental results of previous works [17-19].

This model simplifies the real dilution of the clad (Fig. 4.a) to a second-degree parabola in the substrate (Fig. 4.b) and supposes that the sum of the height and penetration remain constant in all the clads that belong to the coating (eq.1). This assumption is a simplified form of energy balance between the deposited material and the melted substrate and it was obtained by analysing all the fabricated coatings in previous works with different nozzles, metallic powders and substrates.

$$h_i + p_i = h_{i+1} + p_{i+1} \tag{1}$$

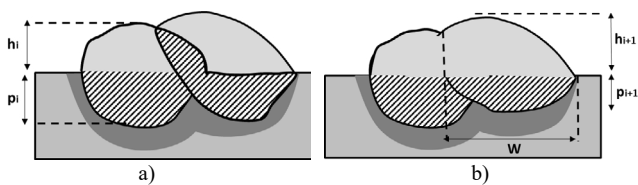


Fig. 4. Dilution of the adjacent clad i+1. a) Real; b) Model.

The model serves to calculate and simulate the geometry of the coatings and the dilution area, including the prediction of lack of fusion with the substrate due to a high overlap percentage, by knowing the height, area, width and penetration of the single clad. In addition, the characteristics of the single

clad can be estimated using empirical models obtained in previous works [17-18].

2.4. Strategy for multilayer coatings

When fabricating a multilayer structure with more than two clads per layer, the coating thickness increases from the first clad until it reaches to constant thickness. In addition, the last clad presents a sharp curve from the top to the substrate. Both situations generate a lack of material on the edges (Fig. 5.a), generating a distortion on the edges that increases at a higher number of layers.

This work proposes to deposit one extra clad on the edge of the layer to compensate this phenomenon of lack of material. The model can be used to predict the area needed on the edges of the layer to obtain a constant growth without distortions. The growth per layer it is the constant thickness obtained supposing a coating formed by rectangular blocks at the same area than the area within the overlapped parts of the model (Fig. 5.b). The extra clad area is the needed area to obtain a constant thickness in each edge.

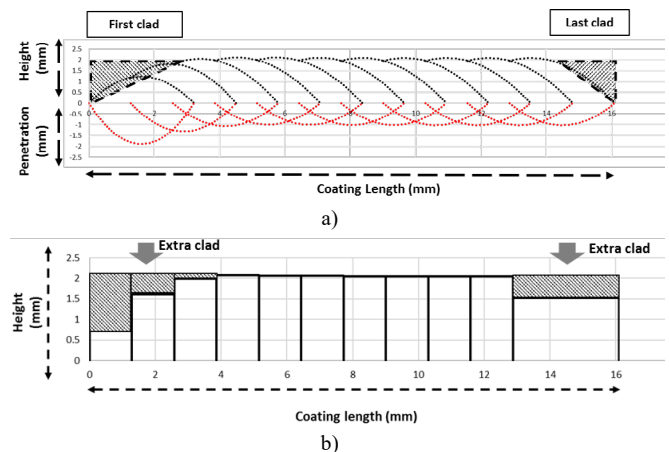


Fig. 5. Lack of material predicted by the model in the edges of the layer. a) Second degree parabola shape; b) Supposing rectangular blocks.

The extra clad parameters must be calculated depending on the area needed for a straight growth. The simplest way to obtain them is to adapt the feed rate maintaining the same laser power and powder mass flow rate. This occurs because the area of the single clad presents a linear trend with the inverse of the feed rate [17-18]. The area of the extra clad needed per layer is significantly lower than the area of the clad used for coating. Thus, the extra clad must be deposited at higher feed rates. As the powder efficiency is lower at higher feed rate, it was determined to deposit one extra clad every two layers with twice the calculated area to obtain an extra clad with similar feed rate (thus, similar efficiency) to the coating clads. The accuracy of the model depends on the accuracy of the single clads characteristics.

2.5. Experimental validation

To validate the model when employing Alloy 718 with the 4-stream nozzle three coatings of Alloy 718 were deposited for

validating the model. Each coating was done overlapping 8 clads employing different single clads characteristics (Table 2). The cross-sections of the coatings were compared with the model, and the error was calculated.

Table 2. Single clad characteristics of each coating.

Single clad Characteristics	Coating 1	Coating 2	Coating 3
h (mm)	1.22	0.63	0.88
w (mm)	3.22	2.72	2.90
A (mm²)	2.63	1.15	1.68
p (mm)	1.88	1.25	1.61
d₀ (%)	40	50	60

The distance from the 4-stream coaxial discrete nozzle to the substrate was 14.5 mm. As a carrier and protective gas, 4.5 and 18 l·min⁻¹ of argon flow were used respectively. Finally, a spot size of 2.6 mm was employed.

After the validation of the geometrical model, two walls were fabricated at the same conditions (Table 3) with and without extra clads to compare the results and thus, for validating the proposed strategy for multilayer coatings. The extra clads were added in the edges of the wall every two layers at the same parameters than the rest of the clads excepting a feed rate of 600 mm·min⁻¹ to obtain the calculated area by the model for correct growth. The wall was fabricated with 12 layers, the growth per layer was 1.3 and the number of clads per layer was 6.

Table 3. Straight wall parameters.

Laser Power (W)	Feed rate (mm·min ⁻¹)	Powder mass flow (g·min ⁻¹)	d ₀ (%)
2500	500	18	40

3. Results and discussion

3.1. Validation of the geometrical model

The obtained results were close to the real cross-section in all coatings (Fig. 6). The maximum deviation of the real coating thickness and the model was 0.14 mm. In the case of the penetration, although most of the overlapped clads are close to the model, the deviation reaches 0.3 mm in one of them, due to the process variability. The maximum deviation of the real value of the coating thickness and penetration are calculated, and it is shown in Table 4.

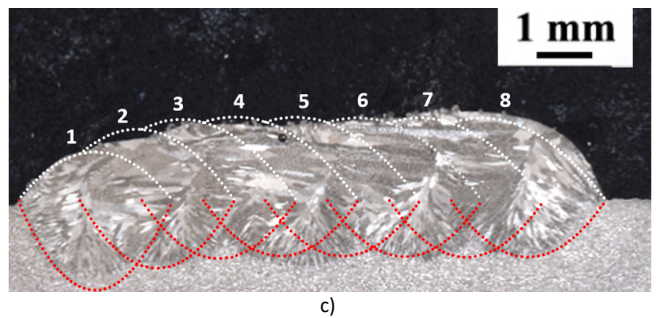


Fig. 6. Real Coatings macrographs compared with the model: a) Coating 1; b) Coating 2; c) Coating 3.

Table 4. Coatings thickness and penetration: maximum and minimum deviation of the real section regarding the model.

Coating Characteristic	Error (mm)	Coating 1	Coating 2	Coating 3
Thickness	Maximum deviation	0.14	0.1	0.13
Penetration		0.3	0.25	0.19

3.2. Validation of the strategy for multilayer coating

In the case of the multilayer structures (Fig. 7), the wall deposited with the extra clad strategy presents a rectangular shape without distortions in the edge and a total wall height close to expected with low variability. The obtained structure allows to deposit accurately more layers.

On the contrary, the wall deposited without the extra clad presents a high distortion with a bullet shape. The distortion increases sharply at a higher number of layers.

In addition to the loose of the geometrical accuracy, this distortion has one additional effect over the material deposition: the decrease on the powder efficiency. In fact, the powder efficiency of the first structure was 52.4%, while it increased to a 60.1% in the structure with extra clads.

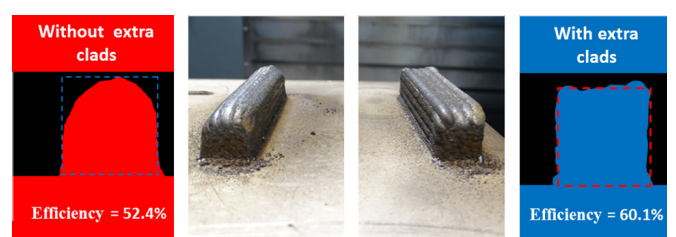


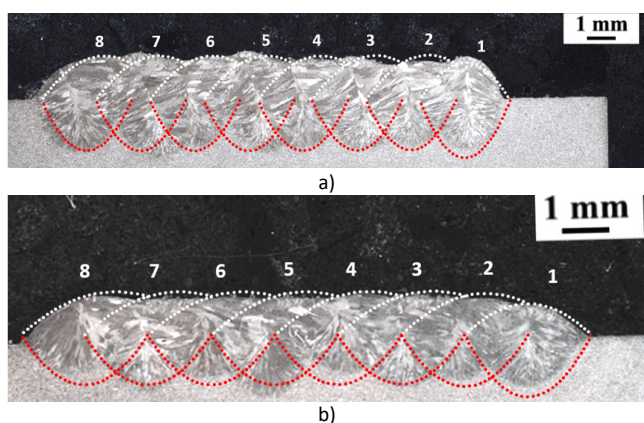
Fig. 7. Straight wall results. In red, cross-section without extra clad strategy; In blue, cross-section with extra clad strategy.

4. Conclusions and future work

The model allows to select the single clad geometry and the overlapped percentage for a determinate thickness or dilution of the coating based on pure geometrical characteristics of the single clad. At higher accuracy of the single clad characteristics, higher accuracy of the model can be obtained.

The model could also determine the possible maximum thickness without a lack of fusion due to an excess of overlap.

The accuracy of the model allows to select the tool path of the machining process and predicts the material that is necessary to remove until it reaches to a constant thickness,



In addition, thanks to the extra clad strategy, it has been demonstrated that it is possible to obtain constant growth when fabricating a multilayer structure, which increases also the powder efficiency of the process.

In future works, it would be advisable to address the following aspects:

- To develop geometric models for coatings and walls using the equations for the single clad characteristics and the evolution of the characteristics linked to head tilting and non-perpendicularity.
- To use the models that are developed to manufacture walls of variable thickness.
- To include the models developed in Computer-Aided Manufacturing software, in order to calculate the DED process toolpath, the Computer Assisted Design expected from the DED process and the subsequent machining toolpath.

Acknowledgments

The authors acknowledge support from the European Commission through the project "PARADISE: a Productive, Affordable and Reliable solution for large scale manufacturing of metallic components by combining laser-based Additive and Subtractive processes with high Efficiency" (Grant Agreement 723440), an initiative of the Public-Private Partnership "Photonics and Factories of the Future".

The authors also acknowledge support from the European Institute of Innovation & Technology (EIT) through the project "DEDALUS: Directed Energy Deposition machines with integrated process ALgorithms Under dedicated monitoring and control System" (ID 20094), an initiative of the EIT Manufacturing.

Finally, the authors acknowledge the vice-counseling of technology, innovation and competitiveness of the Basque Country for support of the project "PROCODA: Procesos de alto valor basados en el conocimiento y los datos" (KK-2019/00004) within Elkartek 2019 and the project "ADDISEND: cooperación científica en fabricación aditiva para un control robusto de la cadena de valor" (kk-2018/00115).

References

- [1] Ur Rahman, N.; Capuano, L.; Van der Meer, A. et al. (2018). Development and characterization of multilayer laser clad high speed steels. *Additive Manufacturing*, 24, 76-85. DOI: <http://doi.org/10.1016/j.addma.2018.09.009>
- [2] Zhong, C.; Pirch, N.; Gasser, A. et al. (2017). The Influence of the Powder Stream on High-Deposition-Rate Laser Metal Deposition with Inconel 718. *Metals*, 7 (10), 443. DOI: <http://doi.org/10.3390/met7100443>
- [3] Ramiro-Castro, P.; Ortiz, M.; Alberdi, A. et al. (2020). Effects of Gravity and Non-Perpendicularity during Powder-Fed Directed Energy Deposition of Ni-Based Alloy 718 through Two Types of Coaxial Nozzle. *Metals*, 10, 560. DOI: <https://doi.org/10.3390/met10050560>
- [4] Zhu, G.; Shi, S.; Fu, G. et al. (2017). The influence of the substrate-inclined angle on the section size of laser cladding layers based on robot with the inside-beam powder feeding. *Int J Adv Manuf Technol*, 88 (5-8), 2163-2168. DOI: <https://doi.org/10.1007/s00170-016-8950-4>
- [5] Cortina, M.; Arrizubieta, J.I.; Ruiz, J.E. et al. (2018). Latest Developments in Industrial Hybrid Machine Tools that Combine Additive and Subtractive Operations. *Materials*, 11, 2583. DOI: <https://doi.org/10.3390/ma1122583>
- [6] Arrizubieta, J.I.; Lamikiz, A.; Cortina, M. et al. (2018). Hardness, grainsize and porosity formation prediction on the Laser Metal Deposition of AISI 304 stainless steel. *Int. J. Mach. Tool Manufact.*, 135, 53-64. DOI: <https://doi.org/10.1016/j.ijmachtools.2018.08.004>
- [7] Wei, H.L.; Knapp, G.L.; Mukherjee, T. et al. (2019). Three-dimensional grain growth during multi-layer printing of a nickel-based alloy Inconel 718. *Additive Manufacturing*, 25, 448-459. DOI: <https://doi.org/10.1016/j.addma.2018.11.028>
- [8] Lu, X.; Lin, X.; Chiumenti, M. et al. (2019). Residual stress and distortion of rectangular and S-shaped Ti-6Al-4V parts by Directed Energy Deposition: Modelling and experimental calibration. *Additive Manufacturing*, 26, 166-179. DOI: <https://doi.org/10.1016/j.addma.2019.02.001>
- [9] Tamanna, N.; Crouch, R. and Naher, S. (2019). Progress in numerical simulation of the laser cladding process. *Optics and Lasers in Engineering*, 122, 151-163. DOI: <https://doi.org/10.1016/j.optlaseng.2019.05.026>
- [10] Salonitis, K.; D'Alvise, L.; Schoinochoritis, B. et al. (2016). Additive manufacturing and post-processing simulation: laser cladding followed by high speed machining. *Int. J. Adv. Manuf. Technol.*, 85 (9-12), 2401. DOI: <https://doi.org/10.1007/s00170-015-7989-y>
- [11] Bax, B.; Rajput, R.; Kellet, R. et al. (2018). Systematic evaluation of process parameter maps for laser cladding and directed energy deposition. *Additive Manufacturing*, 21, 487-494. DOI: <https://doi.org/10.1016/j.addma.2018.04.002>
- [12] El Cheikh, H., Courant, B., Branchu, S. et al. (2012). Analysis and prediction of single laser tracks geometrical characteristics in coaxial laser cladding process. *Optics and Lasers in Engineering*, 50 (3), 413-422. DOI: <https://doi.org/10.1016/j.optlaseng.2011.10.014>
- [13] Chen, T.; Wu, W.; Li, W. et al. (2019). Laser cladding of nanoparticle TiC ceramic powder: Effects of process parameters on the quality characteristics of the coatings and its prediction model. *Optics & Laser Technology*, 116, 345-355. DOI: <https://doi.org/10.1016/j.optlastec.2019.03.048>
- [14] Zhang, K.; Wang, S.; Liu, W. et al. (2014). Characterization of stainless steel parts by Laser Metal Deposition Shaping. *Materials & Design*, 55, 104-119. DOI: <https://doi.org/10.1016/j.matdes.2013.09.006>
- [15] Dass, A.; Moridi, A. (2019). State of the Art in Directed Energy Deposition: From Additive Manufacturing to Materials Design. *Coatings*, 9, 418. DOI: <https://doi.org/10.3390/coatings9070418>
- [16] Ocelik, V.; Nenadl, O.; Palavra, A. et al. (2014). On the geometry of coating layers formed by overlap. *Surface and Coatings Technology*, 242, 54-61. DOI: <https://doi.org/10.1016/j.surfcoat.2014.01.018>
- [17] Ramiro, P., Ortiz, M., Alberdi, A. et al. (2018). Characteristics of Fe-based powder coatings fabricated by laser metal deposition with annular and four stream nozzles. *Procedia CIRP*, 74, 201-205. DOI: <https://doi.org/10.1016/j.procir.2018.08.094>
- [18] Ramiro, P., Alberdi, A., Ortiz, M. et al. (2018). Characteristics of Fe-, Ni- and Co-based powder coatings fabricated by laser metal deposition without preheating the base material. *Procedia CIRP*, 68, 381-386. DOI: <https://doi.org/10.1016/j.procir.2017.12.099>
- [19] Ramiro, P., Ortiz, M., Alberdi, A. et al (2018). Optimization of the efficiency of the laser metal deposition process applied to high hardness coatings by the analysis of different types of coaxial nozzles. *DYNA*, 93(6). 613-619. DOI: <http://dx.doi.org/10.6036/8836>

11th CIRP Conference on Photonic Technologies [LANE 2020] on September 7-10, 2020

Distortion prediction and compensation in direct laser deposition of large axisymmetric Ti-6Al-4V part

Konstantin Babkin^a, Evgeniy Zemlyakov^{a, b}, Sergei Ivanov^{a, b, *},
Artur Vildanov^a, Ilya Topalov^a, Gleb Turichin^a

^a*Saint Petersburg State Marine Technical University, St.Petersburg, 190121, Russia*

^b*Peter the Great St.Petersburg Polytechnic University, St.Petersburg, 195251, Russia*

* Corresponding author. Tel.: +7-812-552-9843; fax: +7-812-552-9843. E-mail address: sergei.yu.ivanov@gmail.com

Abstract

A Ti-6Al-4V alloy aircraft engine part consisting of a cylinder (inner radius 977 mm, height 250 mm and 7.5 mm wall thickness) and two flanges (10.5 and 13.5 mm thick) was manufactured by direct laser deposition technology. A two-dimensional thermomechanical model was developed to simulate distortion of large axisymmetric parts during direct laser deposition. As it was established the shape and dimensions of the finished part, simulated using the original CAD model, have unacceptable deviations from the required parameters. A significant correction of the model is necessary to ensure the required accuracy. It was found that for complete compensation of deformations, an initial geometry should be pre-distorted according to the inverted distortions predicted by the FE simulation. To prevent fracture of the build-up, an 8 mm thick flexible substrate was used. The DLD process stability was ensured by taking into account spatial position of the deposited part in the motion path of the processing head. The simulated shape and size of the finished part satisfactory agrees with the experimentally obtained.

© 2020 The Authors. Published by Elsevier B.V.

This is an open access article under the CC BY-NC-ND license (<http://creativecommons.org/licenses/by-nc-nd/4.0/>)

Peer-review under responsibility of the Bayerisches Laserzentrum GmbH

Keywords: Direct Laser Deposition; Titanium Alloy; Simulation; Distortion Compensation.

1. Introduction

In the last decade, additive technologies have found increasing applications in industry, especially in aerospace due to its numerous advantages, such as high efficiency and flexibility [1-3]. There are two of the most critical challenges that impede the advancement of additive technologies for manufacturing large parts are residual stresses and part distortion [4-6]. At present, there are a lack of publications raise and solve problems of microstructure, mechanical properties, residual stresses and deformations in rather bulky parts required hundreds of hours for build-up [7-11]. As a rule, small academic samples in which thermal history essentially differs from one's real parts are studied. As it was noted in [7, 12], the

level of stresses in some areas of manufactured part can significantly exceed the yield strength. Prolonged build-up time requires minimization of costly experimental trials by using numerical simulation. Different approaches have been proposed to mitigate distortion in additive manufacturing. The most common approaches are the development of optimal process parameters and the use of different toolpath planning strategies [13-15]. Unfortunately, it can be only successful in reducing the level of distortion but cannot eliminate them. Another approach is to compensate distortion using pre-distorted initial CAD model [16]. Results of the FE-simulation or experimentally obtained data can be used for the pre-distortion.

The motivation of this paper arises from the need to develop time-efficient and reliable simulation methods for the fabrication of parts by direct laser deposition (DLD) technology with a high level of precision. Its contribution is a distortion compensation approach, which demonstrates the potential of simulation in predicting the shape distortion and developing the process chain of fabrication of large axisymmetric parts.

2. Materials and methods

2.1. Experimental procedure

A Ti-6Al-4V alloy aircraft engine part consisting of a cylinder (inner radius 977 mm, height 250 mm and 7.5 mm wall thickness) and two flanges (10.5 and 13.5 mm thick) (Fig.1) was manufactured by direct laser deposition technology. The part build-up sequence was as follows: (1) the cylinder, (2) the bottom flange, (3) the top flange. Considering part dimensions an extensive length of a pass leads to a low inter-pass temperature and high cooling rates. Therefore, the microstructure of the buildup completely consists of a brittle martensite [1, 17]. Based on this and previous studies [5, 7, 12], it was concluded that a rigid substrate will cause the fracture of the build-up near the substrate. Since the hot spot stress level can be reduced by using a flexible substrate, the part was build-up onto an 8 mm thick sheet of annealed Ti-6Al-4V alloy. In this case, a significant residual distortion of the substrate makes it extremely difficult to unmount it from the rotary table after the build-up. This problem was overcome by application of the following solution: the flexible titanium substrate was fixed on a 20 mm thick steel plate, which in its turn was attached directly to the rotary table (Fig. 1).

Bending of the free edge of the titanium substrate during the build-up leads to the gradual displacement of the manufactured part along the vertical and horizontal axis. Irregular variations in the distance between the build-up and processing head cause the disturbance of the process stability. Therefore, the spatial position of the part during manufacturing must be taken into account in the motion path of the processing head. The control program for the robot controller was generated based on the results of the distortion kinetics predicted by the FE simulation.

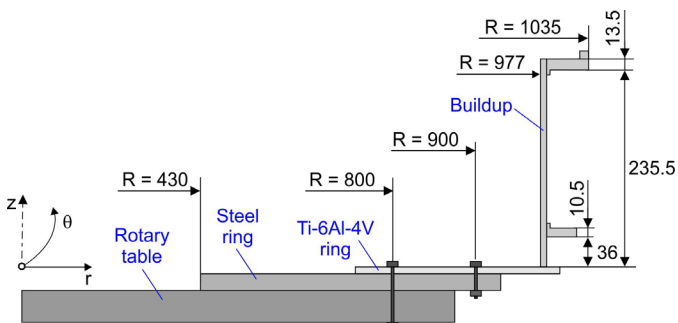


Fig. 1. Schematic of the build part and substrate clamping.

The in-house developed large-format robotic direct laser deposition machine (Fig. 2) consisting of a Fanuc robot equipped with a 5 kW fiber laser and a discrete coaxial powder nozzle was used. The powder, carried by the inert gas through four radially symmetrical nozzles, is injected into the molten

pool. The process parameters were as follow: a beam power of 3.0 kW, a beam radius of 2.5 mm and a forward speed of 15 mm s⁻¹. The cross-section size of unit pass was 3.75 × 1.0 mm (width × height). Each deposited layer was formed by two passes for the cylinder, three passes for the bottom flange and four passes for the top flange. Total build time was 120 hours. The shape of the finished part was measured by the Shining 3D EinScan-Pro laser scanner.

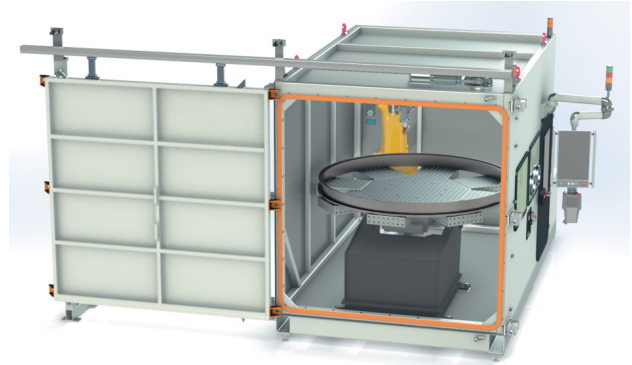


Fig. 2. The in-house developed large-format robotic direct laser deposition machine.

2.2. Simulation model

Due to the complexity of the distortion simulation problem, some simplifications need to be made in order to obtain reasonable CPU-time. It was adopted an assumption of rotational symmetry common for most analyses of multipass circumferential butt welds of pipes [18, 19], i.e. heat is assumed to be deposited at the same time around the circumference. The sequentially-coupled heat conduction analysis in transient mode followed by elastic-plastic large displacement analysis has been performed using the finite element method.

Deposition of material during DLD was simulated using the so-called element birth technique. In this method, elements to be deposited are deactivated at the beginning and then gradually activated or “born” into the solution domain. The pass shape was not accurately modeled. A 4-node axisymmetric elements were employed in 2D model. A laser beam thermal efficiency was assigned a value of 0.45 based on [20]. An internal volumetric heat source with uniform density was applied to model heat input for each pass. To account for heat losses, convective heat transfer on the all surfaces exposed to air was modeled. The convective heat transfer coefficient is taken as 18 W m⁻² K⁻¹ [21]. The ideal thermal contact between the Ti-6Al-4V and steel substrate is suggested. The temperature-dependent thermophysical properties for Ti-6Al-4V including the enthalpy, thermal conductivity, density were taken from [22]. Solid-to-liquid phase transformation releases the latent heat of fusion, resulting in an increase in the enthalpy.

A multi-linear isotropic hardening model has been used in the analysis. Creep was not included in the model. The temperature-dependent mechanical properties for Ti-6Al-4V including the yield strength, elastic modulus, Poisson’s ratio and thermal expansion coefficient were taken from [23]. Strain hardening behavior at different temperatures was adopted from [24]. Since the FE mesh is gradually distorted and displaced

during the simulation, the position of deactivated elements shall be corrected according to the initial CAD model right before the deposition of each part component. For example, the distortion of the cylinder wall causes the bottom flange axis to slope against the horizontal axis (Fig. 3a). Therefore, the deactivated elements of the bottom flange should be aligned according to the original model before its activation (Fig. 3b).

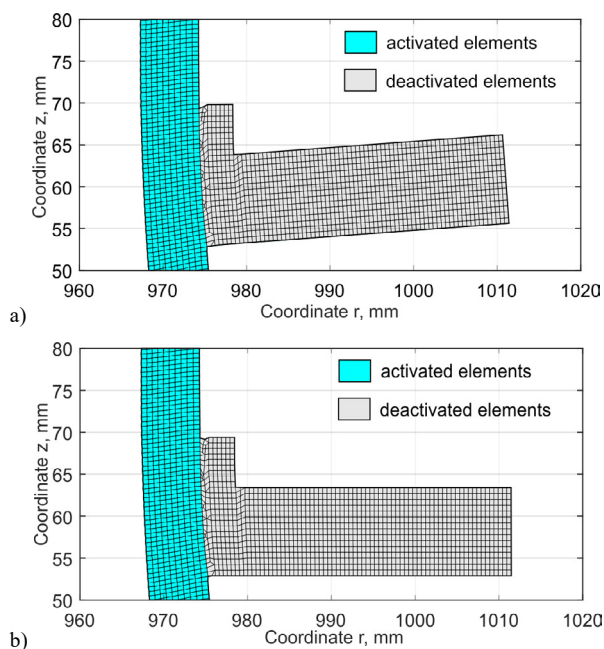


Fig. 3. Position of the deactivated elements of the bottom flange before (a) and after (b) correction.

2.3. Distortion compensation approach

Due to the shrinkage and deformation, the shape and size of the finished part will differ from those required. The initial geometry should be pre-distorted in such a way as to result in the desired shape after the buildup. The distortion compensation includes inverting the distortions predicted by the FE simulation followed by modifying the original model. Calculated distortions are inverted so that all positive distortions are turned into negatives of the same magnitude and vice versa. As it was established, additional distortion-compensation iterations are not required because there is no local bulging.

3. Results and discussion

3.1. Simulation of the part build-up using the original CAD model

Simulation of the manufacturing of the cylinder, according to the original CAD model, revealed significant distortion of the cylinder wall (Fig. 4a). The peak radial displacement $U_r = -10.8$ mm is achieved at the distance of 150 mm from the substrate. The wall curvature significantly changes over approximately 40 and 50 mm near the substrate and top of the cylinder, respectively. Between these areas, the wall is almost straight (radial displacement varies within ± 1.5 mm). The deposition of the bottom flange causes it to deviate significantly

from the horizontal axis (Fig. 4b). The angle between the flange axis and the horizontal axis is minus 5.8° , which corresponds to a vertical displacement of the flange end by 2.9 mm. Such an effect is not observed during deposition of the top flange (Fig. 4c). In this case, a significant shrinkage force causes bending of the upper part of the cylinder wall. Thus, the value of the peak radial displacement increases to minus 15.6 mm, and its location shifts to the top of the build-up by 45 mm. The shape and dimensions of the finished part, simulated using the original CAD model, have unacceptable deviations from the required parameters. A significant correction of the model is necessary to ensure the required accuracy.

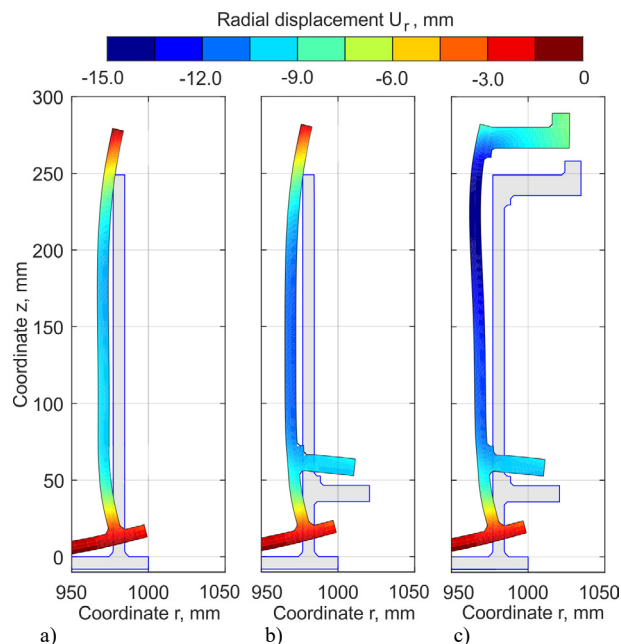


Fig. 4. Evolution of the build-up shape and radial displacement field during the manufacturing of the part using the original CAD model.

Bending of the titanium substrate causes a significant displacement of the build-up. During the deposition of the cylinder, the axial displacement of the free edge (point A) reaches a peak when a half of its height is deposited (Fig. 5). The peak increment per unit pass of axial displacement is achieved at the 32 mm of the cylinder height, and then it decreases sharply. During the buildup of the bottom flange, the displacement at the point A increases linearly. The force generated during the processing of the top flange has little effect on the displacement at the point A. It should be noted that the bulky steel ring also undergoes elastic deformation. The peak axial displacement at the point B reaches only 6 mm. If the increment of an axial and radial displacement of the deposited part does not account in the motion path of the processing head, it will cause an emergency stop of the process. In the case of the cylinder wall processing, the significant axial displacement of the substrate causes a quick reduction of the distance between the head and the build-up. Conversely, during the deposition of the flanges due to the distortion of the cylinder wall, the distance gradually increases, resulting in a lack of fusion.

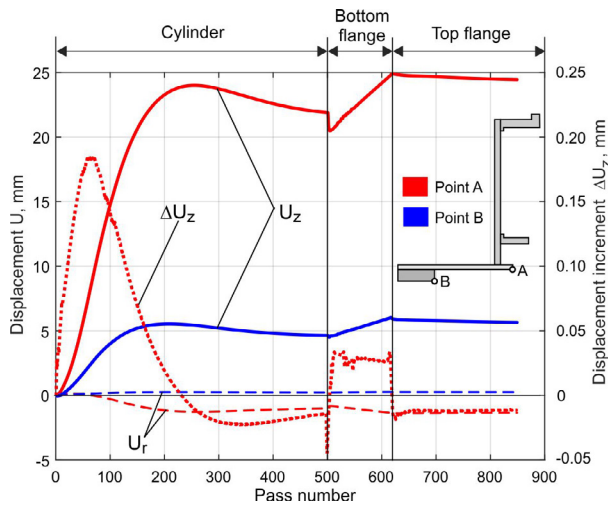


Fig. 5. Simulated radial (U_r) and axial (U_z) displacement at the point A and B, increment of radial displacement (ΔU_r) at the point A.

3.2. Simulation of the part build-up using the pre-distorted CAD model

The correction of the original CAD model was made according to the procedure described in 2.3. The pre-distorted shape of the cylinder wall (Fig. 6a) takes into account both shrinkage and deformation associated with the build-up of the flanges. The values of the peak radial displacement during the manufacturing of the part was as follows: the cylinder $U_r = -11.5$ mm (Fig. 6a); the bottom flange $U_r = -12.4$ mm (Fig. 6b); the top flange $U_r = -15.4$ mm (Fig. 6c). A circular segment of the experimentally obtained part (Fig. 7a) was measured by the laser scanner. The averaged points which represent the cross-section of the part are shown in Fig. 7b. As a result, the simulated shape of the part satisfactory agrees with the experimentally obtained (Fig. 7b). The average deviation of the radial displacement is ± 1.5 mm, and the peak deviation observed near the substrate is 3.5 mm.

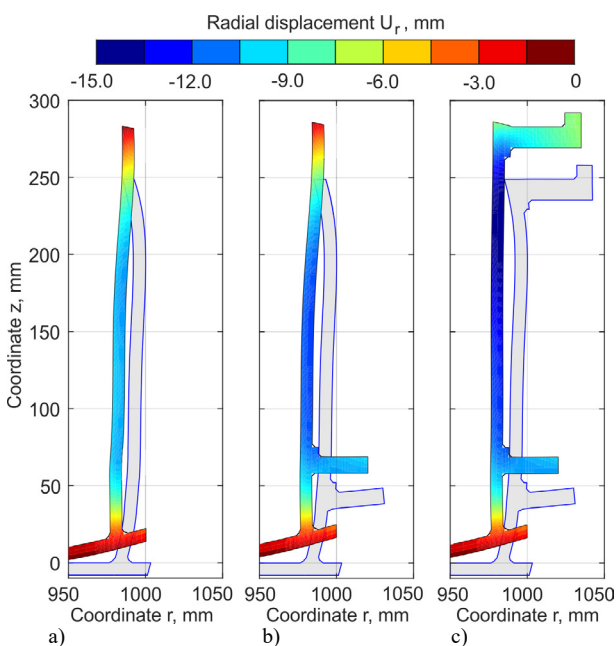


Fig. 6. Evolution of the build-up shape and the radial displacement field during the manufacturing of the part using the pre-distorted CAD model.

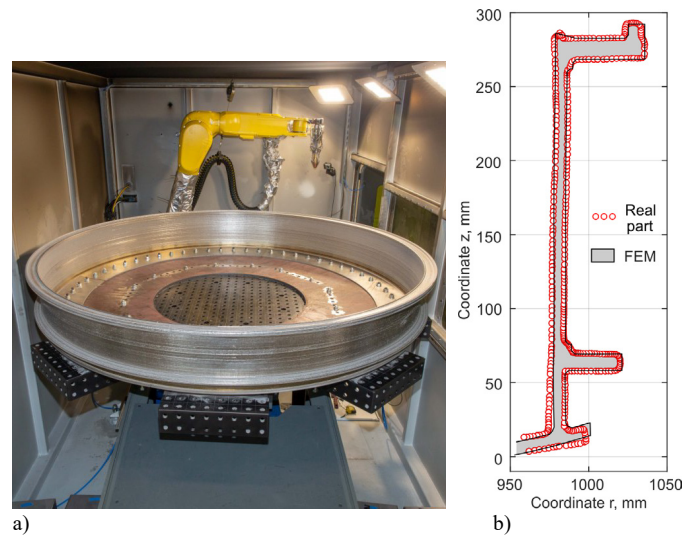


Fig. 7. The finished part after buildup (a) and comparison between the simulated and the experimentally obtained part (b).

4. Conclusions

In this study, a two-dimensional thermomechanical model was developed to simulate the distortion of the large axisymmetric parts during direct laser deposition. The shape and dimensions of the finished part, simulated using the original CAD model, have unacceptable deviations from the required parameters. A significant correction of the model is necessary to ensure the required accuracy. It was found that for complete compensation of deformations, an initial geometry should be pre-distorted according to the inverted distortions predicted by the FE simulation. To prevent fracture of the build-up, an 8 mm thick flexible substrate was used. The DLD process stability was ensured by taking into account spatial position of the deposited part in the motion path of the processing head. The simulated shape and size of the finished part satisfactory agrees with the experimentally obtained.

References

- [1] DebRoy T, Wei HL, Zuback JS, Mukherjee T, Elmer JW, Milewski JO. Additive manufacturing of metallic components-process, structure and properties. *Progress in Materials Science* 2018; 92:112-224.
- [2] Froes F, Boyer R, editors. *Additive manufacturing for the aerospace industry*. Elsevier; 2019. 465 p.
- [3] Tepylo N, Huang X, Patnaik PC. Laser - based additive manufacturing technologies for aerospace applications. *Adv. Eng. Mater* 2019; 21:1900617.
- [4] Biegler M, Marko A, Graf B, Rethmeier M. Finite element analysis of in-situ distortion and bulging for an arbitrarily curved additive manufacturing directed energy deposition geometry. *Additive Manufacturing* 2018; 24:264-272.
- [5] Em VT, Ivanov SY, Karpov ID, Rylov SA, Zemlyakov EV, Babkin KD. Residual stress measurements of laser metal deposited Ti-6Al-4V parts using neutron diffraction. *Journal of Physics: Conference Series* 2018; 1109:1:012049.
- [6] Gouge M, Michaleris P. *Thermo-mechanical modeling of additive manufacturing*. Butterworth-Heinemann; 2017.
- [7] Turichin G, Zemlyakov E, Babkin K, Ivanov S, Vildanov A. Analysis of distortion during laser metal deposition of large parts. *Procedia CIRP* 2018; 74:154-157.

- [8] Papadakis L. Experimental and computational appraisal of the shape accuracy of a thin-walled vireole aero-engine casing manufactured by means of laser metal deposition. *Prod. Eng. Res. Devel.* 2017; 11:389–399.
- [9] Hu X, Nycz A, Lee Y, Shassere B, Simunovic S, Noakes M, Ren Y, Sun X. Towards an integrated experimental and computational framework for large-scale metal additive manufacturing. *Materials Science and Engineering: A* 2019; 761:138057.
- [10] Greer C, Nycz A, Noakes M, Richardson B, Post B, Kurfess T, Love L. Introduction to the design rules for Metal Big Area Additive Manufacturing. *Additive Manufacturing* 2019; 27:159-166.
- [11] Shassere B, Nycz A, Noakes MW, Masuo C, Sridharan N. Correlation of microstructure and mechanical properties of metal big area additive manufacturing. *Appl. Sci.* 2019; 9:787.
- [12] Ivanov S, Zemlyakov E, Babkin K, Turichin G, Karpov I, Em V, Rylov S. Stress distribution in laser metal deposited multi-layer thick-walled parts of Ti-6Al-4V. *Procedia Manufacturing* 2019; 36:240-248.
- [13] Wu Q, Mukherjee T, Liu C, Lu J, DebRoy T. Residual stresses and distortion in the patterned printing of titanium and nickel alloys. *Additive Manufacturing* 2019; 29:100808.
- [14] Nickel AH, Barnett DM, Prinz FB. Thermal stresses and deposition patterns in layered manufacturing. *Materials Science and Engineering: A* 2001; 317:59-64.
- [15] Ren K, Chew Y, Fuh J, Zhang Y, Bi G. Thermo-mechanical analyses for optimized path planning in laser aided additive manufacturing processes. *Materials & Design* 2019; 162:80-93.
- [16] Afazov S, Okioga A, Holloway A, Denmark W, Triantaphyllou. A methodology for precision additive manufacturing through compensation. *Precision Engineering* 2017; 50:269-274.
- [17] Liu S, Shin YS. Additive manufacturing of Ti6Al4V alloy: A review. *Materials & Design* 2019; 164:107552.
- [18] Deng D, Murakawa H. Numerical simulation of temperature field and residual stress in multi-pass welds in stainless steel pipe and comparison with experimental measurements. *Computational Materials Science* 2006; 37:269–277.
- [19] Yaghi AH, Hyde TH, Becker AA, Sun W. Finite element simulation of welding residual stresses in martensitic steel pipes. *Materials Research Innovations* 2013; 17(5):306-311.
- [20] Kwon H, Baek WK, Kim MS, Shin WS, Yoh JJ. Temperature-dependent absorptance of painted aluminum, stainless steel 304, and titanium for 1.07 μm and 10.6 μm laser beams. *Opt. Lasers Eng.* 2012; 50:114–121.
- [21] Thermo-Mechanical Modeling of Additive Manufacturing 1st Edition. Gouge M, Michaleris P, editors. Butterworth-Heinemann; 2017. p. 294.
- [22] Mills KC. Recommended values of thermophysical properties for selected commercial alloys, Cambridge: Woodhead Publishing; 2002.
- [23] Cao J, Gharghoury M, Nash P. Finite-element analysis and experimental validation of thermal residual stress and distortion in electron beam additive manufactured Ti-6Al-4V build plates. *Journal of Materials Processing Technology* 2016; 237:409-419.
- [24] MSC Software, Simufact Additive 1.0, Material Database. 2016.

11th CIRP Conference on Photonic Technologies [LANE 2020] on September 7-10, 2020

Distortion-based validation of the heat treatment simulation of Directed Energy Deposition additive manufactured parts

Bassel El-Sari^{a,*}, Max Biegler^a, Benjamin Graf^a, Michael Rethmeier^{b,a,c}

^a Fraunhofer IPK, Pascalstr. 8-9, 10587 Berlin, Germany

^b Technische Universität Berlin, Chair of Joining, Straße des 17. Juni 135, 10623 Berlin, Germany

^c Bundesanstalt für Materialforschung (BAM, Unter den Eichen 87, 12205 Berlin, Germany)

* Corresponding author. Tel.: +49-30-39006-295; fax: +49-30-3911-037. E-mail address: bassel.el-sari@ipk.fraunhofer.de

Abstract

Directed energy deposition additive manufactured parts have steep stress gradients and an anisotropic microstructure caused by the rapid thermo-cycles and the layer-upon-layer manufacturing, hence heat treatment can be used to reduce the residual stresses and to restore the microstructure. The numerical simulation is a suitable tool to determine the parameters of the heat treatment process and to reduce the necessary application efforts. The heat treatment simulation calculates the distortion and residual stresses during the process. Validation experiments are necessary to verify the simulation results. This paper presents a 3D coupled thermo-mechanical model of the heat treatment of additive components. A distortion-based validation is conducted to verify the simulation results, using a C-ring shaped specimen geometry. Therefore, the C-ring samples were 3D scanned using a structured light 3D scanner to compare the distortion of the samples with different post-processing histories.

© 2020 The Authors. Published by Elsevier B.V.

This is an open access article under the CC BY-NC-ND license (<http://creativecommons.org/licenses/by-nc-nd/4.0/>)

Peer-review under responsibility of the Bayerisches Laserzentrum GmbH

Keywords: Directed Energy Deposition; Additive Manufacturing; Heat Treatment; Numerical Simulation; Finite Element Method

1. Introduction

Parts manufactured by directed energy deposition (DED) additive manufacturing (AM) require specific post-processing depending on their application. They are exposed to rapid localized heating during the welding and rapid cooling during the solidification, hence steep residual stress gradients appear in the part. The layer-upon-layer manufacturing causes anisotropic mechanical and structural properties. Heat treatment can be used to reduce the residual stress level of the AM part through plastic deformation [1] and to minimize the anisotropy of the microstructure through recrystallization [2]. After the heat treatment, electrical discharge machining (EDM) can be used to remove the built part from the substrate. The numerical simulation is a powerful method to reproduce these

process steps to avoid expensive experiments by conducting digital tests to determine suitable process parameters.

Nomenclature

AM	additive manufacturing
DED	directed energy deposition
OD	outside diameter
ID	inside diameter
GW	gap width

The DED AM and the heat treatment are both characterized as complex metallo-thermo-mechanical processes where the thermal state, the microstructure and the mechanical state influence each other. The structural FEM welding simulation is capable of simulating such processes.

FEM welding models predict the temperature distribution, the residual stress and the distortion. The latter was chosen to validate the simulated process steps because it can be measured easily with a 3D scanning system before and after each process step. To simplify the comparison between the simulated distortion and the measurements, a suitable specimen geometry is required.

In the field of DED AM, thin-walled samples are used to validate simulations [3, 4], whereas, in the field of heat treatment, C-rings are common specimens. They have three metrics to evaluate the deformation: the outside diameter (OD), the inside diameter (ID) and the gap width (GW) [5], as displayed in Fig. 1 (c). Those dimensions can be measured using a coordinate measuring machine or a 3D scanning system. Hardin and Beckermann [6] used C-rings as specimen to compare their heat treatment simulation results with measured distortions. This work will mainly focus on the heat treatment simulation, therefore a DED AM adapted C-ring will be used as a specimen geometry.

2. Materials and Methods

A total of six specimens were built by DED AM using the austenitic stainless steel AISI 316L as powder feedstock (Metco 41C) from Oerlikon with a grain size of 45 μm - 90 μm . The manufacturing was conducted on a “Trumpf TruLaser Cell 7020” equipped with a 2 kW disc laser and a “Trumpf” coaxial powder nozzle. The laser power was set to 600 W, the laser spot diameter was set to 0.6 mm and the forward speed was set to 600 mm/min. Between each layer, the process was paused for 30 s for cooling. 12 Layers were built with a layer height of 0.65 mm, a track width of 1.2 mm and an overlap of 30%. The parameters are summarized in Table 1. To promote an isotropic infill structure, two zigzag path strategies with different inclination angles were used alternately during the buildup. An as-built C-ring is depicted in Fig. 1 (a) and a sample after EDM is shown in Fig. 1 (b).

Table 1. Parameters of the DED AM process

Parameters	
laser power in W	600
laser spot diameter in mm	0.6
forward speed in mm/min	600
track width in mm	1.2
overlap in %	30
layer height in mm	0.65
number of layers	12
pause in s	30

Fig. 1 (c) shows a schematic of the C-rings of this work and its characteristic dimensions.

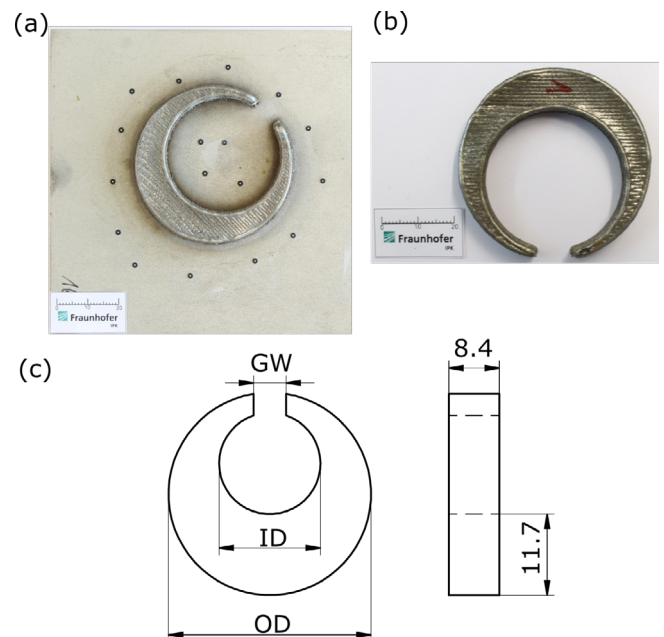


Fig. 1. (a) an as-built C-ring after 3D scanning. The dark spots are markers which were used to fit the different pictures of the 3D scanner to a 3D model; (b) a C-ring after the removal from the substrate via EDM; (c) a schematic of the C-ring and its dimensions (OD=50.9 mm, ID=31. Mm, GW = 9.3).

Table 2 shows the post-processing steps which were conducted after the buildup of the C-rings. The as-built samples were only removed from their substrates directly after the buildup, this was meant to quantify the distortion which are caused by EDM of an as-built sample without prior heat treatment. Cross-sections from an as-built C-ring and a preheated one were made to investigate the effects of the heat treatment on the microstructure.

Table 2. Post-processing history of the C-ring samples

C-ring	quantity	post process no.1	post process no.2
as-built	2	EDM	-
preheated	4	Heat treatment	EDM

The four preheated C-rings were heat-treated under an argon atmosphere using a Nabertherm LH60/13 industrial furnace at a holding temperature of 1050°C. The furnace Chamber was heated from room temperature to the holding temperature within 210 min and held for 140 min. Subsequently, the furnace was shut down and the specimens were kept in the furnace until they cooled down to room temperature within 500 min. The holding time and temperature of the heat treatment were determined in accordance with the assumptions and recommendations of the “ASM metals reference book” [7].

A structured light 3D scanner “GOM ATOS TripleScan” with a measuring volume of 100 mm x 75 mm x 70 mm, a measuring point distance of 30.6 μm and an accuracy of 2 μm to 5 μm was used to investigate the distortion after each process step. Then the dimensional changes of the specimens were determined using the software Tool “GOM Inspect” through measuring the OD, the ID and the GW at different scanned states to provide a validation dataset for the simulation.

The simulation model was discretized with 26,228 elements of hexahedral and pentahedral shape with a characteristic element length of nearly 0.7 mm. Fig. 2 shows the full finite element model during the DED AM simulation at three different stages.

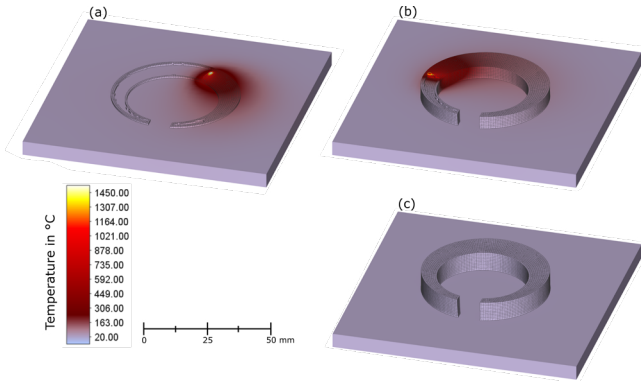


Fig. 2. DED AM simulation during the buildup; (a) simulation is building the first layer; (b) simulation is building the 8th layer; (c) simulated as-built C-ring.

The simulation of the buildup via DED is based on the papers from Biegler et al. [4, 8, 9]. They introduced a 3D coupled thermo-mechanical structural welding simulation model with a moving heat source that activates the elements of the deposition gradually. These elements represent the deposited powder feedstock, they are already in their final position before the simulation is started, but their material properties are scaled down with a factor of 10^{-5} by default. This factor is suspended when the moving heat source activates the elements by heating them above the melting temperature. Besides, the weld pool was considered as a low stiffness solid without any flow dynamics, the vaporization of alloying elements was neglected and the change in microstructure due to multiple heating cycles as well as the influence of mechanical deformations on the temperature field was neglected.

The AISI 316L powder feedstock remains austenitic at all temperatures, therefore phase transformations were not considered. The temperature-dependent material properties of standard AISI 316L were taken from [10] and applied to the simulation model. The density was fixed to 8000 kg/m^3 , the Poisson's ratio was set to 0.3, the enthalpy of melting was assumed as 256.4 J/g and an isotropic work hardening model with von Mises yield criterion was applied.

The heat treatment simulation was also done with the same thermo-mechanical coupled model as it was used in the simulation of the DED process with some differences. Flow dynamics in the furnace chamber and the contact heat transfer were neglected. Only the convective and radiative heat transfer was considered. A heat transfer coefficient to the furnace chamber was set for each process step of the heat treatment (during heating and holding: $35 \text{ W/(m}^2\text{K)}$; during cooling: $2.3 \text{ W/(m}^2\text{K)}$). Fig. 3 shows the time-temperature cycles of the simulation and the conducted heat treatment. The measured

temperature was obtained from thermocouples of the furnace chamber during the heat treatment process and it was assumed that the temperature of the furnace is approximately similar to the temperature of the samples. The temperature of the simulation was obtained from the marked reference point as labeled in Figure 3. It can be seen that the measured temperature curve during the heating and the holding stage is well represented by the simulation. The cooling of the simulation is slightly slower than the experiment. Nevertheless, both have approximately the same cooling time.

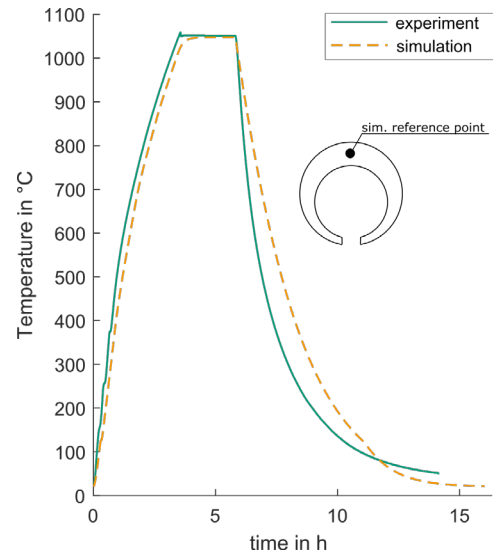


Fig. 3. Simulated and experimental time-temperature cycle of the heat treatment process.

Fig. 4 shows the heat treatment simulation during the heating, the holding and after the cooling. The DED AM simulation results, consisting of a 3D mesh, the temperature history and the residual stress distribution, were used as a starting point in the heat treatment simulation.

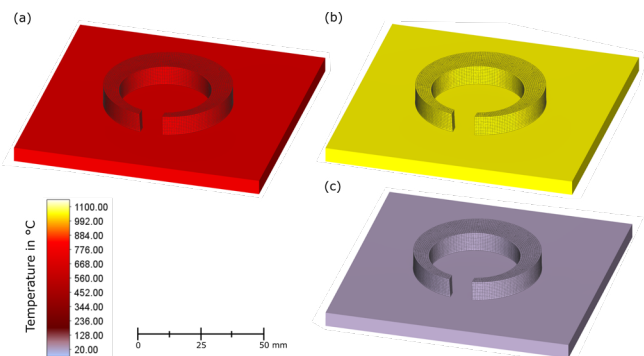


Fig. 4. Heat treatment simulation: (a) during the heating stage; (b) during the holding stage; (c) after the cooling.

During the heat treatment, the parts are held at an elevated temperature for a certain time and the residual stresses are transformed into plastic deformation, therefore it is necessary to consider creep, which commonly occurs at temperatures above 40% of the material melting temperature in Kelvin under a certain load (here the residual stresses). To simulate the heat

treatment process with the prescribed models of the DED AM process, it was necessary to expand the material model and to include a creep model. The creep power-law is a suitable constitutive equation to model the creep of austenitic stainless steel [11,12] and it is commonly used to simulate the heat treatment process. The creep power-law can be written as:

$$\epsilon = A\sigma^n \quad (1)$$

Where A is a constant related to the microstructure of the material, n is the exponent of stress and the applied stress is denoted as σ . To minimize the experimental complexity, it will be assumed that the creep behavior of additive manufactured AISI 316L is similar to conventional machined material. Therefore, the power-law parameters from the literature will be applied for the simulation of the current work. The creep parameters A and n were calculated using a linear regression model from creep parameter data obtained by [11] ($A = 1.33 \times 10^{-1}$ and $n = 4.84$).

The process of EDM is represented by deactivating the elements at the level of the EDM cutting path while the simulation calculates a new mechanical equilibrium considering the changed mechanical conditions to simulate the stress relaxation and the distortion after the removal of the substrate. This method was already used by [3] and by [4] to simulate the removal of a DED part from a substrate.

3. Results and Discussion

To investigate the distortion of the C-rings, the differences between the C-ring dimensions (OD, ID and GW) at different scanned states were calculated as follows:

$$\Delta D = D_{m-1} - D_m \quad (2)$$

Where D stands for OD, ID or GW of the C-ring and m represents the last post-processing step. For example, the characteristic dimensions which were measured after post-process no. 2 ($m=2$) are subtracted from the characteristic dimensions which were measured after post-process no. 1 ($m=1$) and the dimensional change is denoted to ΔD .

Fig. 5 shows the dimensional changes of the OD, the ID and the GW of the samples with different post-processing histories extracted from the experiments and from the simulation. The as-built samples were removed from their substrates directly after the buildup, whereas the preheated C-rings were heat-treated before the EDM. The first row of Fig. 5 shows the dimensional changes and the second row shows the absolute values of the deviations, to compare the absolute distortion between the samples with different post-processing histories. From the experimental data in the first row it can be seen, that the OD, the ID and the GW of the as-built C-rings increased after the EDM, hence the samples have widened. The dimensions of the preheated samples decreased, hence the preheated C-rings have contracted. Considering the absolute values of the dimensional changes of the samples, which are plotted in the second row of Fig. 5, it can be seen that the removal of an as-built C-ring from the substrate evokes the

largest deformations in OD, ID and GW. This is mainly caused by the relaxation of the steep residual stress gradients which are induced during the rapid thermo cycles of the DED process. The dimensional changes after the removal of the preheated C-rings from the substrate are in general smaller than the prior described ones, which is plausible, because of the stress-relieving effects of the heat treatment.

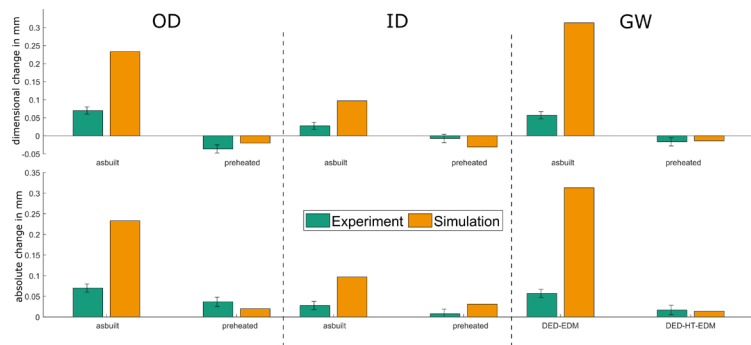


Fig. 5. Comparison of the simulated and measured dimensional changes of the C-rings. The first row shows the real dimensional changes, calculated in accordance to Equation 2. The second row shows the absolute dimensional changes.

The simulation overrated the distortion of the as-built C-rings after the EDM, because the residual stress level of the as-built part was overestimated by the DED AM simulation, therefore it would have been necessary to measure the residual stresses after the buildup to ensure a quantitative validation of the simulation model.

The disagreement between the dimensional changes of the preheated simulation and the measurements can be related to the made simplifications, e.g. the model assumed a homogeneous heat distribution in the whole part during the heat treatment process, as can be seen in Fig. 4, neglecting that the temperature history on the surface of the part can differ from the temperature history inside the part, which can have an influence on the resulting residual stress distribution. Further, the Simulation model only considered the stress relaxation through creep. Therefore, creep can be assumed as a major driver of the simulation in this paper, hence the creep parameters, from Equation 1, have a significant influence on the stress relaxation during the heat treatment. Therefore, it can be assumed, that the application of creep parameters obtained from standard material instead of additive manufactured material cannot represent the processes in the microstructure of an AM part during the heat treatment. Fig. 6 shows close-ups of the made cross-sections from an as-built sample and a heat-treated one. It can be seen that the heat treatment dissolved the weld bead boundaries and certain grain growth occurred, similar observations were made by Montero-Sistiaga et al. [1]. Hence, it is necessary to obtain creep parameters from additive manufactured AISI 316L in order to represent the prescribed microstructural processes during the stress relaxation to enhance the predictive capabilities of the simulation model.

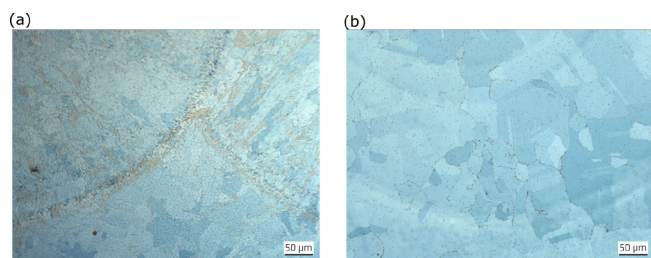


Fig. 6. close-ups of the made cross-sections; (a) Cross section of an as built sample; (b) Cross-sections of a heat-treated sample.

4. Conclusion

In summary, the simulation was able to predict the experiments qualitatively and to reproduce the observations from the experiment. The model was able to calculate the widening of the as-built C-rings after EDM as well as the contracting of the preheated C-rings after their removal from the substrates. The model was able to represent the significant distortions which were evoked by removing the as-built samples from the substrate via EDM, due to the pre-stressed state of the sample and the model showed that the heat treatment prior the removal of the substrate via EDM reduces the distortion through the stress-relieving effects of the heat treatment.

It was showed that the distortion-based validation approach can validate a simulation, consisting of DED AM buildup, heat treatment and EDM, qualitatively. A further quantitative enhancement of the predictive capabilities of the simulation model can be achieved through a validation of the residual stresses and trough the application of creep parameters obtained from AM material.

References

- [1] Montero Sistiaga ML, Nardone S, Hautfenne C, Van Humbeeck J. Effect of Heat Treatment Of 316L Stainless Steel Produced by Selective Laser Melting (SLM). Proceedings of the 27th Annual International Solid Freeform Fabrication Symposium – An Additive Manufacturing Conference 2016; 558-565.
- [2] Kawasaki S, Hishinuma A. Effect of Condition of Recrystallization Heat Treatment on High-Temperature Mechanical Properties of an Irradiated AISI 316 Austenitic Steel. Journal of Nuclear Science and Technology 1974; 11:505-509.
- [3] Papadakis L, Hauser C. Experimental and computational appraisal of the shape accuracy of a thin-walled virole aero engine casing manufactured by means of laser metal deposition. Production Engineering Research and Development 2017; 11:389-399.
- [4] Biegler M, Graf B, Rethmeier M. Assessing the predictive capability of numerical additive manufacturing simulations via in-situ distortion measurements on a LMD component during build up. Procedia CIRP 2018; 74:158-162.
- [5] Manivannan M, Northwood DO, Stoilov V. Use of Navy C-rings to study and predict distortion in heat-treated components: experimental measurements and computer modelling. International Heat Treatment and Surface Engineering 2014; 8:168-175.
- [6] Hardin RA, Beckermann C. Simulation of Heat Treatment Distortion. 59th Technical and Operating Conference 2005; 3:1-32
- [7] Baucio M. ASM metals reference book. 3rd ed. Ohio: ASM International; 1994.
- [8] Biegler M, Graf B, Rethmeier M. In-situ distortions in LMD additive manufacturing walls can be measured with digital image correlation and predicted using numerical simulations. Additive Manufacturing; 24:101-110.
- [9] Biegler M, Graf B, Rethmeier M. Finite element analysis of in-situ distortion and bulging for an arbitrarily curved additive manufacturing directed energy deposition geometry. Additive Manufacturing 2018; 24:264-272.
- [10] Janosch JJ. IIW round robin protocol for residual stress and distortion prediction: phase II (proposal rev. 1). IIW-Document IIW-X/XV-RSDP-59-0.1; 2000.
- [11] Nassour A, Bose WW, Spinelli D. Creep properties of Austenitic Stainless-Steel Weld Metals. Journal of materials engineering and performance 2001; 10:693-698.

11th CIRP Conference on Photonic Technologies [LANE 2020] on September 7-10, 2020

Multivariate prediction of laser deposited geometry based on machine vision

Piotr Jurewicz^{a,*}, Piotr Koruba^a, Jacek Reiner^a

^a*Wrocław University of Science and Technology, Wybrzeże Wyspiańskiego st., Wrocław 50-370, Poland*

* Corresponding author. Tel.: +48-71-320-4635. E-mail address: piotr.jurewicz@pwr.edu.pl

Abstract

Laser Metal Deposition is a widely used technology allowing metal component regeneration, rapid prototyping and functional coating deposition. Its main limitations are low stability and repeatability making it necessary to monitor and often control the process in real time. This paper presents a study on modelling the influence of process parameters on clad geometry and assessment if including sensor data can help model the outcome properly. For this purpose 9 sets of parameters were used with multiple repetitions. During the process a profile of deposited geometry, temperature and images in visible range were acquired. Multivariate analysis was performed to investigate correlations. Multiple prediction models were constructed including signals' non-linearity correction. The results prove that process parameters have main influence on process outcome but cannot explain natural process variation whereas models including sensor data allow prediction of those deviations.

© 2020 The Authors. Published by Elsevier B.V.

This is an open access article under the CC BY-NC-ND license (<http://creativecommons.org/licenses/by-nc-nd/4.0/>)

Peer-review under responsibility of the Bayerisches Laserzentrum GmbH

Keywords: Laser Metal Deposition; Multivariate Modeling; Process Monitoring; Geometry Prediction

1. Introduction

Laser Metal Deposition (LMD) is an additive manufacturing technology [1,2], applicable for remanufacturing of machine parts [3], rapid prototyping [4] and deposition of functional coatings [5].

The main limitations of LMD process are its low stability and repeatability [6]. Even with a given set of process parameters the outcome of the process (clad height or width) may vary significantly with each repetition. Therefore, the LMD closed loop process control is necessary, but this issue is still not sufficiently solved in spite of being discussed in many recent studies [2,6,7].

The LMD process monitoring is based on phenomena such as optical or acoustic emission, while most popular measuring systems use pyrometers or cameras [6]. For predictive control the nonlinear process modelling, taking into account laser power, powder feed rate and scanning speed [8,9] is additionally required.

The LDM process output modelling taking into consideration both process parameters and sensor data has not yet been reported. In order to investigate this approach, a technological experiment was planned and repeated multiple times to obtain representative data set. For each experimental case a clad geometry was measured, camera and pyrometer data was registered. The acquired data were used for multivariate regression modelling. The deeper insight was related to PLS (Projection to Latent Structures) model, investigating variable selection. Additionally, other multivariate regression models PCR ((Principal Component Regression) and MLR (Multiple Linear Regression) were compared.

2. Materials, methods and results

2.1. Research plan

The presented study was divided into three stages as presented in the Fig. 1. Firstly, the designed experiment was developed, performed and process data was registered.

Subsequently, the obtained raw data (temperature signal and images) was processed as well as the calibration and testing data sets were constructed. During the modelling, the PLS calibrations were investigated in respect to different signal sources. Because of observed nonlinearity a data pre-processing was introduced. Finally, other multivariate regression models as PCR and MLR were compared. The modelling was performed within PLS_Toolbox for Matlab® [10].

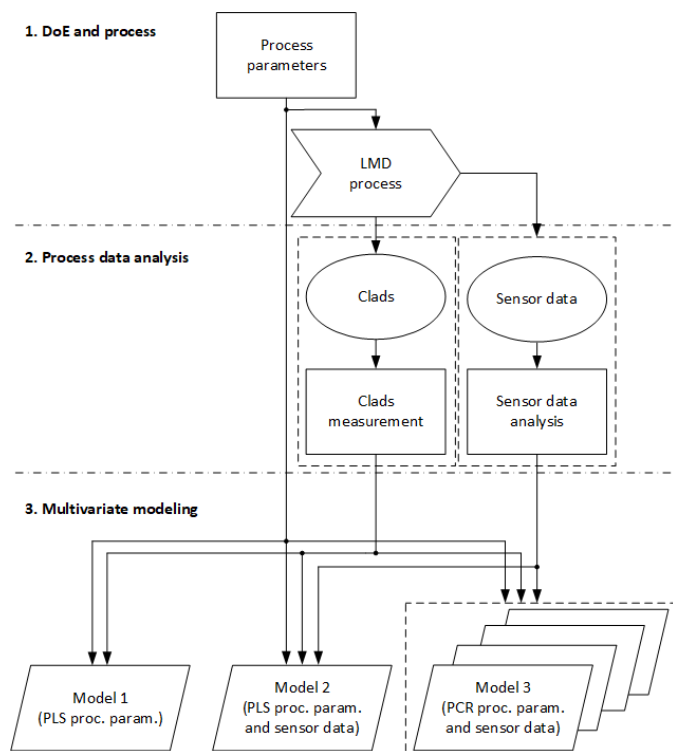


Fig. 1. Workflow chart

2.2. Experimental design and performance

The technological experiment was carried out with the High Power Diode Laser (laserline LDF 4000-30) and LMD head (COAX 8) installed on 3-axis CNC machine. The high dynamic range Camera (Photonfocus) and pyrometer (Lascon) optics were integrated with the laser head by standard monitoring port using dichroic mirror. Additionally, a 2D laser profilometer (Keyence) was installed at the bottom part of the head, near the processing point (Fig. 2).

As the main LMD process control variables, which are varying in the experiment, laser power, powder feed rate and laser scanning speed were selected [1] (Table 1). Remaining ones like carrier gas flow rate, shielding gas flow rate, additional material and laser beam focus were kept constant.

Table 1. Experiment parameters set

Process parameter [unit]	Min value	Max value
Laser power [W]	500	1000
Powder feed rate [g/min]	1,7	5,1
Laser scanning speed	5	15

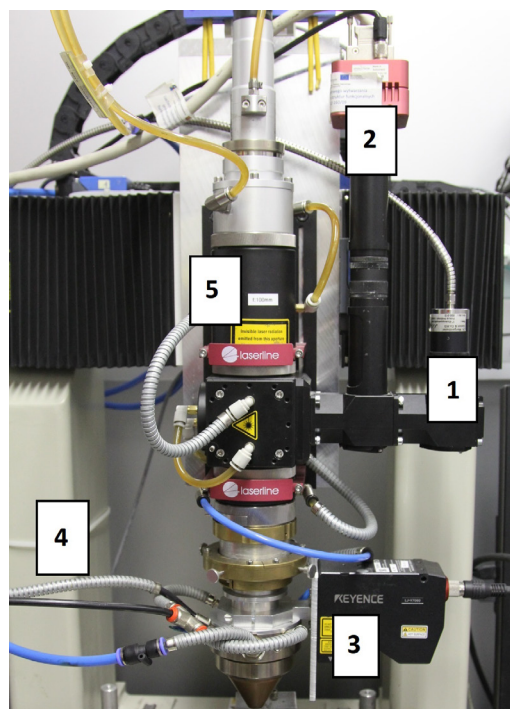


Fig. 2. Workstation for LMD process: 1 – pyrometer, 2 – camera, 3 – profilometer, 4 – CNC station, 5 – laser head.

For each of the selected variables, two levels were chosen resulting in 8 experiment cases. This 8 cases were then expanded with middle point for building a central plan and repeated 3 times in random order. Each experiment consisted of depositing single clad with 40 mm length with one parameter set. That experiment was then repeated 3 times in 3 different attempts (days) resulting in 81 data observations

2.3. Geometry measurement and sensors data analysis

Every deposited clad was scanned and measured with laser in-line 2D profilometer after the process. The profilometer was connected to laser head and synchronized with its movement to obtain multiple scans of deposited clad. Each profile scan consisting of the 3D points cloud was then fitted with 2nd order polynomial to determine get its height and width.

For process monitoring the pyrometer and camera were coaxially integrated with the laser head. The acquisition module was synchronized with CNC movement. For each deposition process the temperature was measured and a series of images were acquired. The temperature signals were processed with averaging filter while from images the following features of melt pool were calculated: brightness [11], second orders of bright area [12] and width and length of melt pool area [13].

2.4. Data set organization

Data processing presented in chapter 2.3 resulted in 11 variables for each observation (sample) as it is presented in Table 2. Those variables were divided in 3 groups being: process parameters (3 variables), sensor data (6 variables) and measured geometry (2 variables).

Table 2. Data set organization

Experiment no.	Parameters			Sensor data					Geometry		
	Laser power	Powder feed	Velocity	Brightness	Moment X	Moment Y	Pool width	Pool length	Temperature	Height	Width
1											
2											
3											
...											

The whole data set containing 81 experiments was divided into calibration and testing sets according to Kernard-Stone 66% algorithm. It resulted in 54 experiments in calibration set and 27 experiments in testing set. The test set was used to computer RMSEP (Root Mean Square Error of Prediction). This approach allowed to detect potential overfitting of models. Each model type was tested for two features: height and width.

2.5. Multivariate modeling

Multivariate modelling is branch of statistics looking for correlation between two data sets. It is used when some information about process (variables) are easy to obtain while not directly correlated with the process outcome. If the process outcome is available to obtain but at a high cost, the question emerge, if it is possible to predict this outcome cheaper with investigation of cheaper variables. It is common tool used in spectroscopy where intensities of multitude wavelengths are used to evaluate food quality [14].

PLS is tool using Latent Variables (LVs) for a multivariate modelling. The LVs are linear combinations of independent variables (inputs), chosen so first LV corresponds to the largest change in variation of input data. Each another LV is perpendicular to the previous one in independent variable space and chosen so it represents another largest variation in input data. Due to projection to LVs the PLS method can successfully model based on data with correlations between inputs and avoid model overfitting. After selection of optimal LVs number, the linear correlation between LVs and dependent variables (output) is built [15].

2.6. PLS 1 – process parameters model

The first tested model was based only on process parameters. This approach is similar to the one presented in previous studies [9]. The received model was evaluated based on prediction against measurement plot, residuals plot and RMSEP value.

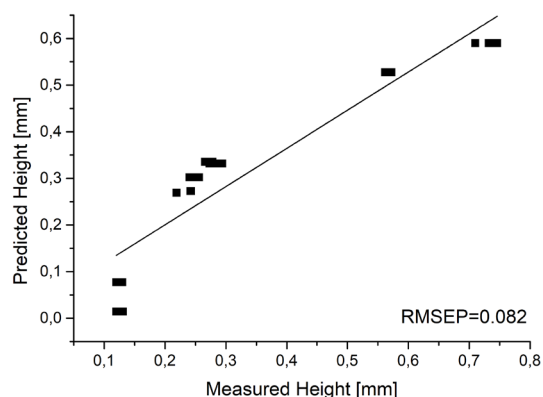


Fig. 3. PLS 1 (Height) - prediction against measurement

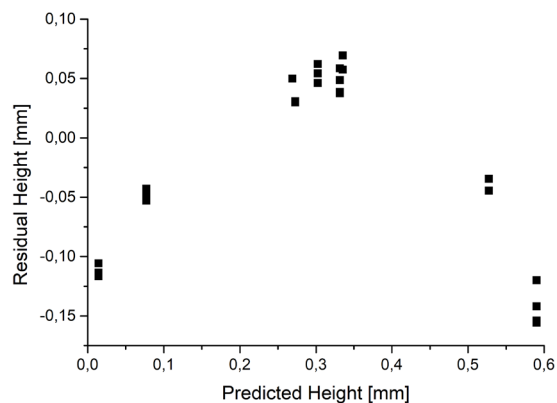


Fig. 4. PLS 1 (Height) - model residuals

As can be seen on graphs (Fig. 3 to Fig. 6) this method offers moderately good models (RMSEP=0.082 for height and RMSEP=0.096 for width). Moreover, for height dependency between measured and predicted value the explicit nonlinearity can be observed. This is also visible on residual plot. On the contrary, the nonlinearity problem was not observed within the width model.

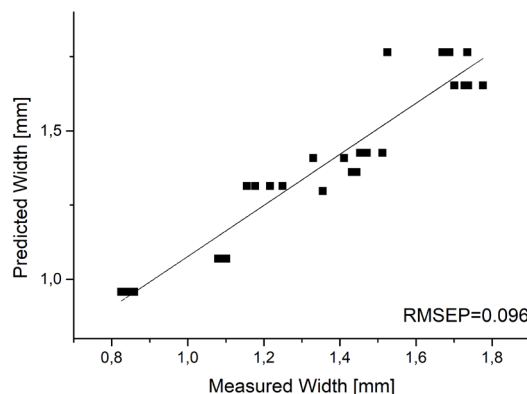


Fig. 5. PLS 1 (Width) - prediction against measurement

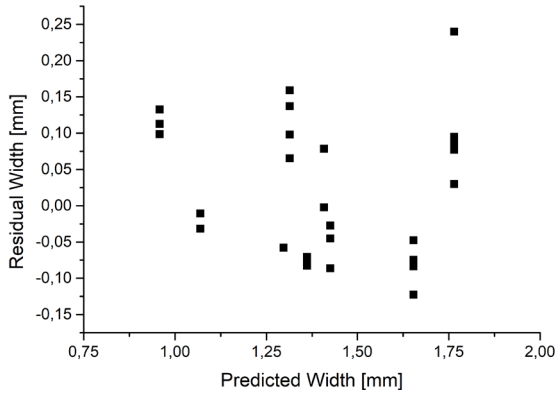


Fig. 6. PLS 1 (Width) - model residuals

nonlinearities for height are still present. On the contrary width modelling offers pretty much the same quality of the model.

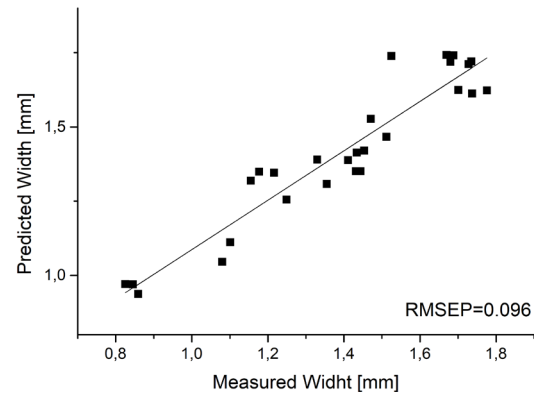


Fig. 9. PLS 2 (Width) - prediction against measurement

2.7. PLS 2 – process parameters and sensors data model

The second model was calibrated with both process parameters and sensor data (temperature and image features). It is important to outline that not all available LVs were used for calibration. As using more variables would obviously result in a better fitted model. To allow comparison with PLS 1 model the number of LVs number was limited to 3. As in PLS 1, this model was also evaluated based on prediction against measurement plot, residuals plot and RMSEP value.

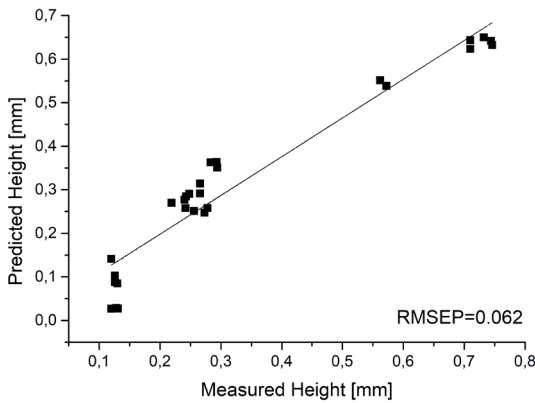


Fig. 7. PLS 2 (Height) – prediction against measurement

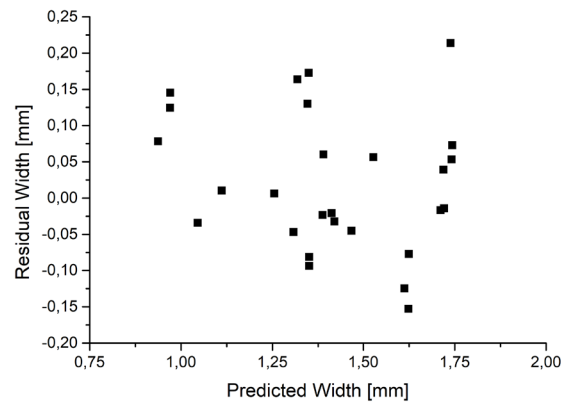


Fig. 10. PLS 2 (Width) - model residuals

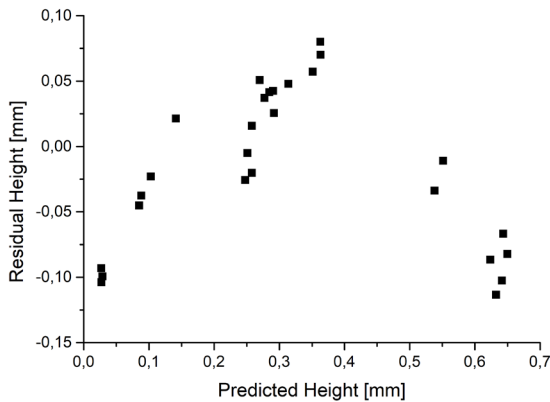


Fig. 8. PLS 2 (Height) - model residuals

As can be seen on graphs (Fig. 7 to Fig. 10) PLS 2 method offers slightly better model for height (RMSEP=0.062 against RMSEP=0.082 in first model). The plots analysis suggests that

2.8. PLS 3 – nonlinearity

In case of height modelling nonlinearities seem to have high impact on results. As presented in [9] there are many approaches to use nonlinear transformations of process parameters in aspect of modelling.

Since it is hard to propose a methodical approach to look for nonlinearities in process parameters, we propose a different solution based on looking for nonlinear transformation of measured geometry features. In other words, the nonlinear transformation of values of model outputs is performed rather than application of such transformations of model inputs. Moreover, instead of building nonlinear model of clad height a linear model of root of its value was built. Presented solution is simple and results in improving height model correctness as presented in Table 3.

Table 3. Nonlinear model of height

Root order	1 st (linear)	2 nd	3 rd	4 th	5 th
RMSEP	0,082	0,070	0,066	0,064	0,063

2.9. A matter of sensors

While using both camera and pyrometer is common industrial solution it is worth asking if it both are necessary.

Considered PLS models allow fast calibration and testing of models based on different variables. We use that to investigate which variables group offers highest model quality.

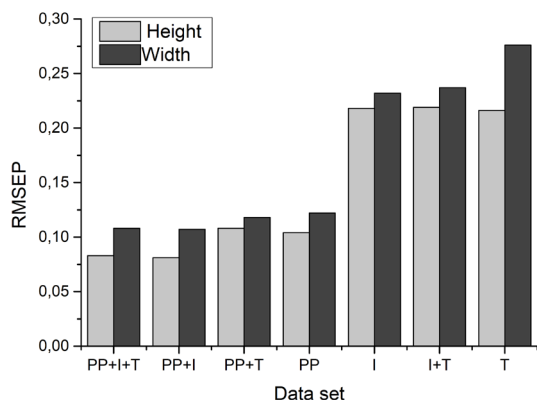


Fig. 11. Different data set comparison for PLS model (PP - process parameters, I - image features, T - temperature signal)

Results are presents on Fig. 11. It is clear that process parameters are necessary to properly model the outcome. It is also worth noticing that image features (camera data) slightly improve model quality, while temperature (pyrometer data) does not influence model quality in significant way. One can conclude from that VIS camera gives more information about geometry than pyrometer.

2.10. Different multivariate models

The same approach as presented above was applied for different modelling techniques such as PCR and MLR. As a result the RMSEP values for all the models are presented in Fig. 12. Comparing RMSEP value of the models, one may state that in case of height the PLS2 model is the most accurate, whereas for width model the MLR gives the best results. In overall, the PLS models can be considered as competitive to MLR and PCR models.

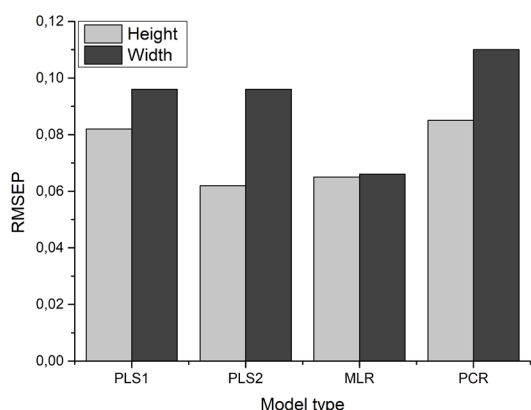


Fig. 12. Different models comparison

3. Conclusion

In the study presented in this paper the LMD process experiments were performed with multiple repetitions and both the geometry features (clad height and width) and sensor data (temperature signal and VIS images) were obtained. With this

data variety the multivariate models were tested including variable selection and nonlinearity consideration.

It has been shown that for modelling height of deposited clad the use of sensor data can improve model quality by decreasing RMSEP from 0.082 to 0.062. In similar manner simple nonlinear transformation in form of root function can help reduce the model error. On the other hand, in case of width model inclusion of sensor data does not influence the model quality. For both presented models the RMSEP value is 0.096.

Further it has also been shown that process parameters are essential for properly model height and image features from camera help improving model quality while the temperature signal from pyrometer hardly affects the model.

It is worth noting that the focus of this paper was on preparing proper learning dataset and on comparing process parameter based models with models including sensors data. Due to that chosen modeling technics were limited to linear models. Nonlinear modeling and artificial intelligence technics will be investigated in further studies.

References

- [1] Toyserkani E, Khajepour A, Corbin S. Laser cladding. Boca Raton, FL: CRC press; 2005
- [2] Lavrens JR. Advances in laser materials processing. 2nd ed. Duxford, UK: Woodhead Publishing, an imprint of Elsevier; 2018
- [3] Kaierle S, Overmeyer L, Alfred I, Rottwinkel B, Hermsdorf J, Wesling V, Weidlich N. Single-crystal turbine blade tip repair by laser cladding and remelting. CIRP Journal of Manufacturing Science and Technology 2017
- [4] Abdulrahman KO, Akinlabi ET, Mahomood RM, Pityana S, Tlotleng M. Laser Metal Deposition of Titanium Aluminide Composites: A Review. Materials Today: Proceedings 2018
- [5] Lampa C, Smirnov I. High speed laser cladding of an iron based alloy developed for hard chrome replacement. Journal of Laser Applications 2019
- [6] Liu W-W, Tang Z-J, Liu X-Y, Wang H-J, Zhang H-C. A Review on In-situ Monitoring and Adaptive Control Technology for Laser Cladding Remanufacturing. Procedia CIRP 2017
- [7] Rafajłowicz W, Jurewicz P, Reiner J, Rafajłowicz E. Iterative learning of optimal control for nonlinear processes with applications to laser additive manufacturing. IEEE Transactions on Control Systems Technology 2019
- [8] Nabahani M, Razavi RS, Barekat M. An empirical-statistical model for laser cladding of ti-6Al-4V powder on ti-6Al-4V substrate. Optics and Laser Technology 2017
- [9] Bax B, Rajput R, Kellet R, Reisacher M. Systematic evaluation of process parameter maps for laser cladding and directed energy deposition. Additive Manufacturing 2018
- [10] <https://eigenvektor.com/software/pls-toolbox/> [access 09.03.2020]
- [11] Jurewicz P, Rafajłowicz W, Reiner J, Rafajłowicz E. Sterowanie procesem napawania laserowego bazujące na przetwarzaniu obrazu. Warszawa: Akademicka Oficyna Wydawnicza EXIT; 2017
- [12] Hofman JT, Pathiraj B, van Dijk J, de Lange DF, Meijer J. A camera based feedback control strategy for the laser cladding process. Journal of Materials Processing Technology 2012
- [13] Ocylok S, Alexeev E, Mann S, Weisheit S, Wissenbach K, Kelbassa I. Correlations of melt pool geometry and process parameters during laser metal deposition by coaxial process monitoring. Physics Procedia 2014
- [14] Markiewicz-Keszycka M, Cama-Moncuñil R, Casado-Gavaldá MP, Sullivan C., Cullen PJ. Laser-induced breakdown spectroscopy for food authentication. Current Opinion in Food Science 2019
- [15] Escensen KH, Multivariate Data Analysis – in practice. 5th edition. Aalborg University, Esbjerg

11th CIRP Conference on Photonic Technologies [LANE 2020] on September 7-10, 2020

Experimental study and modeling of melt pool in laser powder-bed fusion of thin walls

S.A. Egorov, R.S. Khmyrov, A.D. Korotkov, A.V. Gusarov*

Laboratory of 3D Structural and Functional Engineering, Moscow State University of Technology STANKIN, Vadkovsky per. 3a, 127055 Moscow, Russia

* Corresponding author. Tel.: +7-499-973-3961. E-mail address: av.goussarov@gmail.com

Abstract

Laser powder-bed fusion (L-PBF) is promising for manufacturing of lightweight cellular structures. A thin wall is the key element of such structures. Heat and mass transfer in the melt pool formed on the top of a thin wall is essentially two-dimensional. That is why L-PBF process parameters adapted for thin walls strongly differ from those necessary for bulk material. In the present work, a high speed camera records a side view of the melt pool formed on the top of a thin metallic wall due to a laser beam scanning along the wall edge. The melt pool profile and the position of the keyhole are observed. The results are compared with a two-dimensional model of coupled heat conduction and Marangoni convection in the laser-interaction zone. In the studied conditions, the best agreement between the experiment and the modeling implies that a keyhole is formed with the depth comparable with that of the melt pool.

© 2020 The Authors. Published by Elsevier B.V.

This is an open access article under the CC BY-NC-ND license (<http://creativecommons.org/licenses/by-nc-nd/4.0/>)

Peer-review under responsibility of the Bayerisches Laserzentrum GmbH

Keywords: additive manufacturing; cellular structures; melt pool; keyhole; heat and mass transfer; laser powder-bed fusion; selective laser melting

1. Introduction

Laser powder-bed fusion (L-PBF) is a key additive technology applicable to a wide range of structural and functional materials. The scanning laser beam used can melt even refractory materials. In view of the high scanning speed attaining few meters per second and the small beam diameter around 100 microns, the duration of laser action on a given portion of material is measured in fractions of a millisecond. It can be not sufficient for complete material consolidation. Besides, the distribution of temperature in the laser-interaction zone is highly non-uniform [1]. The material formed in these conditions can contain non-satisfactory concentration of such defects as pores, micro-cracks, and extended defects of metallurgical bond [2]. The L-PBF process essentially depends on both the numerous processing parameters as the laser power and scanning speed and the properties of initial powder material. That is why the most labor-consuming task remains optimizing the process parameters for attaining stable regimes and reducing the number of defects [3]. Often one looks for a

compromise between the productivity of the process and the quality of the obtained material [4]. The optimizing of L-PBF requires clear understanding of the basic physical processes in the laser-interaction zone.

Additive manufacturing offers wide possibilities for topology optimization. For example, lightweight periodic metallic cellular structures with excellent mechanical properties were obtained by L-PBF [5]. Stochastic cellular structures [6] and gradient ones [7] were manufactured too. The mentioned works show that such structures are promising for industry and other domains. Panesar *et al.* [8] proposed strategies for designing the cellular structures for additive manufacturing. Souza *et al.* [9] described new approaches to topology optimization adapted for manufacturing by L-PBF. Despite different design, all the cellular structures consist of thin shells. The shell thickness is comparable with the size of the laser-interaction zone at L-PBF [5-7]. Therefore, the conditions of heat and mass transfer in this zone considerably differ from the conditions occurred at manufacturing of bulk material. The present work aims to visualize the melt pool at laser treatment

of a thin wall and to model heat and mass transfer in the conditions similar to those occurred at L-PBF of cellular structures. This will clarify the basic physical processes in the laser-interaction zone and may help to optimize L-PBF manufacturing of cellular lightweight structures.

2. Experiment

Figure 1 shows the sketch of the experimental setup. The working laser beam scans a vertical metal blade along its top edge. Table 1 lists the laser parameters. Pulsed laser lighting CAVILUX illuminates the laser-interaction zone at 810 nm wavelength. High-speed CCD camera Photron SA5 records the profile of the laser-interaction zone at the frame rate of $2 \cdot 10^4 \text{ s}^{-1}$ through a 1064 nm bandstop filter used to exclude reflected radiation of the working laser. The blade has the thickness of 250 μm and consists of stainless steel EOS PH1 with the composition listed in Table 2 [10]. It corresponds to standard 15-5 precipitation hardening steel.

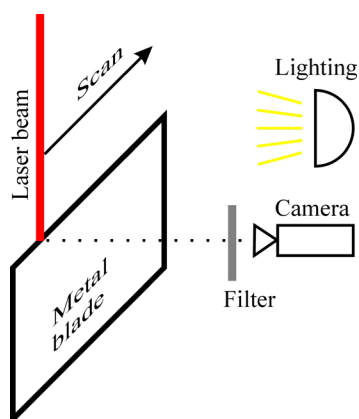


Fig. 1. Experimental setup to visualize the interaction zone of a laser beam with a thin metal blade.

Table 1. Laser processing parameters.

Wavelength	Spot diameter	Beam power	Scanning speed
1064 nm	100 μm	110 W	25 mm/s

Table 2. Chemical composition of steel EOS PH1 [10].

Element	Fe	Cr	Ni	Cu	Mn	Si
Weight %	Balance	14-15.5	3.5-5.5	2.5-4.5	<1	<1

Figure 2 shows several frames of the same record taken with the interval of 15 ms. Reflection of laser lighting from crystallites forms a speckled pattern of the solid phase. The liquid phase in the melt pool can be clearly distinguished by a uniform brightness. The contours of the melt pool are steady. The melt pool moves uniformly from left to right with the scanning laser beam. The dimensions of the melt pool measured on the 30-ms frame in Fig. 2 are around $950 \pm 50 \mu\text{m}$ in length and $300 \pm 50 \mu\text{m}$ in depth. One can observe a large contrast spot in the middle of the melt pool. The size of this spot and its position relative the melt pool boundaries are the same on each frame: the size is around 200-300 μm and the position is shifted to the top and front boundaries. The recorded films show considerable fluctuations inside the spot. When comparing two

consecutive frames with the time interval of 50 μs between them, one can clearly distinguish differences in the internal structure of the spot. This gives an estimate of the time scale of the fluctuations. The spot contrast can be due to distortions of the melt surface. One can not determine from the images if the spot surface is convex or concave. Probably, it is a keyhole cavity or a distortion of a lateral free surface of melt due to a keyhole.

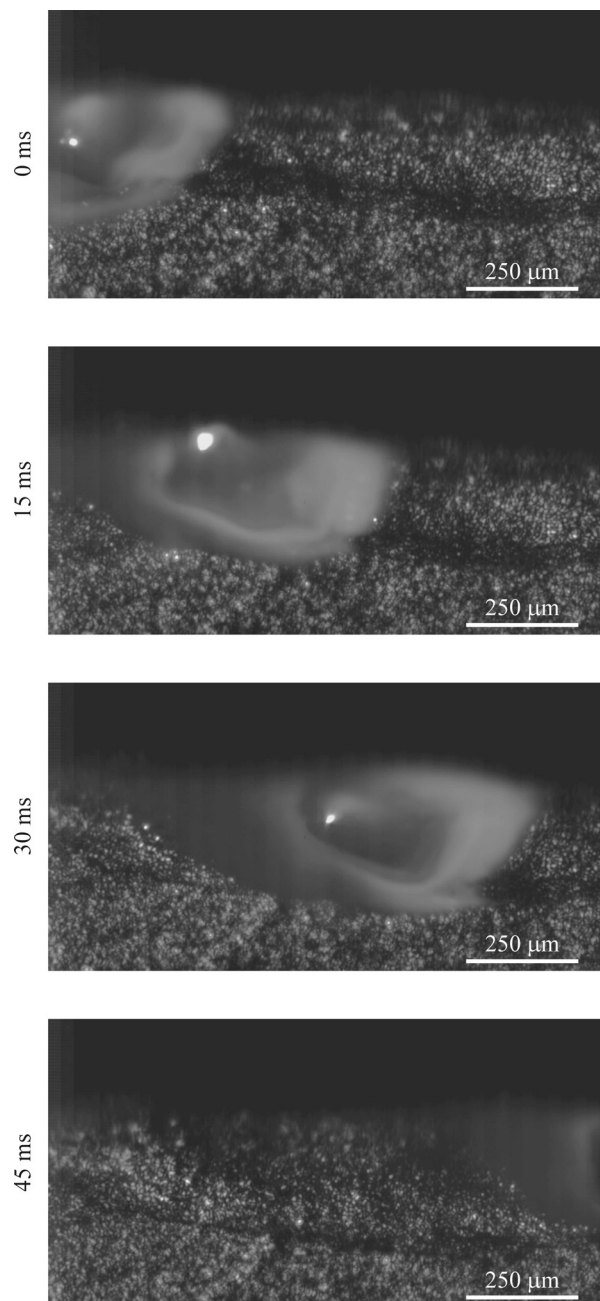


Fig. 2. Profile views of the laser-interaction zone at the time instances indicated on the left.

3. Mathematical model

The above experiments on laser processing of a thin wall indicate that the melt pool occupies the entire thickness of the wall. Thus, a two-dimensional (2D) profile can essentially specify the melt pool shape. The normal component of melt

flow velocity equals zero on the lateral sides of the wall. The heat flux through the wall sides is controlled by the adjacent gas or powder bed in the conditions of L-PBF. In any case, the thermal conductivity of the media adjacent to the sides is much less than that in the bulk of the wall. Therefore, the heat flow in the direction normal to the wall plane is much less than the heat flow components in the directions parallel to the wall plane. That is why the mathematical model neglects the variation of physical fields in the direction normal to the wall plane. We model the coupled thermocapillary flow and thermal conduction in 2D Cartesian coordinates. The following equations of continuity, momentum, and energy describe melt dynamics:

$$\begin{aligned} \rho_t + \nabla \cdot (\rho \mathbf{u}) &= 0, & (\rho \mathbf{u})_t + \nabla \cdot \mathbf{\Pi} &= 0, \\ E_t + \nabla \cdot \mathbf{Q} &= 0, \end{aligned} \quad (1)$$

where ρ is the density, \mathbf{u} the flow velocity, E the energy per unit volume, and index t designates the time derivative. In a viscous conductive medium, the flows of momentum $\mathbf{\Pi}$ and energy \mathbf{Q} are

$$\mathbf{\Pi} = p\mathbf{I} + \rho \mathbf{u} \otimes \mathbf{u} - \boldsymbol{\sigma}, \quad \mathbf{Q} = E\mathbf{u} + \mathbf{\Pi} \cdot \mathbf{u} + \mathbf{q}, \quad (2)$$

where p is the pressure, \mathbf{I} the identity tensor, and $\boldsymbol{\sigma}$ the viscous stress tensor,

$$\boldsymbol{\sigma} = 2\eta \left[\mathbf{e} - \frac{1}{3} \text{Itr}(\mathbf{e}) \right], \quad (3)$$

depending on the dynamic viscosity η and the strain rate tensor \mathbf{e} defined as the symmetric component of tensor $\nabla \mathbf{u}$. The Fourier law gives the conductive heat flow,

$$\mathbf{q} = -\lambda \nabla T, \quad (4)$$

where λ is the thermal conductivity and T the temperature. The equation of state $p(\rho, T)$ and the thermal equation of state $U(\rho, T)$ close the system of Eqs. (1)-(4), where $U = E - \rho u^2/2$ is the internal energy per unit volume.

The model equations of state applied in the present work take into account absorption/release of the latent heat at melting/solidification, which is important in laser processing. The model neglects the thermal expansion of the medium and assumes that its compressibility is small. The equation of state is

$$p = B \left(\frac{\rho}{\rho_0} - 1 \right), \quad (5)$$

where B is the bulk modulus and ρ_0 the density at zero pressure. The thermal equation of state neglects the energy of elastic deformation and assumes a constant specific heat C per unit volume,

$$T = \begin{cases} U/C, & U < CT_m \\ T_m + \frac{(T_l - T_m)(U - CT_m)}{C(T_l - T_m) - L_m}, & CT_m \leq U \leq CT_l + L_m \\ (U - L_m)/C, & U > CT_l + L_m \end{cases} \quad (6)$$

where T_m is the solidus and T_l the liquidus temperatures and L_m the latent heat of melting per unit volume. The no-slip condition is applied on the melt/solid boundary. On the free surface of the melt, the Marangoni condition for the shear stress is imposed,

$$\sigma_{nr} = \beta \boldsymbol{\tau} \cdot \nabla T, \quad (7)$$

where $\beta = d\alpha/dT$ is the derivative of the surface tension coefficient with respect to temperature and $\boldsymbol{\tau}$ is the unit vector tangent to the surface. The incident laser beam has a Gaussian profile with the nominal radius r_0 . The interaction of the beam with the melt gives rise to the heat flux through the melt surface

$$q_z = \frac{P}{r_0 \sqrt{\pi}} \exp\left(-\frac{x^2}{r_0^2}\right), \quad (8)$$

where P is the absorbed laser beam power per unit width of the wall, z the coordinate along the beam, and x the transversal coordinate. Note that P is the net thermal impact of the laser beam. It equals the incident power of the laser beam minus the power of reflected radiation minus the heat loss to evaporation.

The conservation laws, Eq. (1), are numerically solved in a rectangular domain (see Fig. 3) by the finite volume method using an explicit second-order Kurganov-Tadmor scheme [11] on a uniform rectangular grid. A steady-state solution is looked for. The coordinate system used for numerical calculation moves with the scanning laser beam. The beam axis intersects the plane extension of the solid-phase surface in the origin, $x = 0$, $z = 0$ (see Fig. 3). In this coordinate system, the solid phase moves from left to right with the flow velocity equal to the scanning speed u_s . A Gaussian shape of the keyhole is imposed. The level function

$$s(x, z) = z + D_k \exp\left(-\frac{(x - x_k)^2}{r_k^2}\right), \quad (9)$$

specifies the condensed-phase surface as curve $s = 0$, where D_k is the keyhole depth, r_k its effective radius and x_k the shift of the keyhole axis relative the beam axis. Figure 3 shows the level function. The level function defines the external normal to the surface \mathbf{n} and the unit tangent vector $\boldsymbol{\tau}$ as follows:

$$\mathbf{n} = -\frac{\nabla s}{|\nabla s|}, \quad \boldsymbol{\tau} = \begin{pmatrix} \tau_x \\ \tau_z \end{pmatrix} = \begin{pmatrix} -n_z \\ n_x \end{pmatrix}. \quad (10)$$

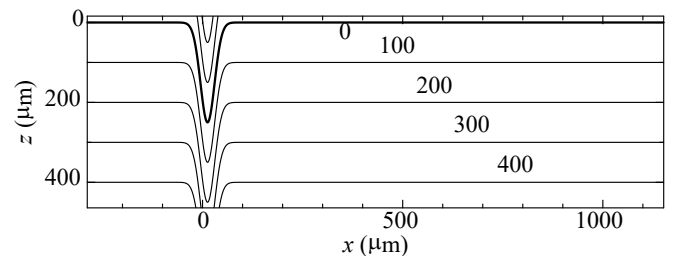


Fig. 3. Computation domain and contours of the level function s (μm). Level $s = 0$ (bold line) is the top surface of the condensed phase.

The solid/liquid boundary is not tracked. It is explicitly defined as the temperature level $T = T_m$. To model the solid state, a ghost external force field is applied at $T < T_m$ at every time step, which stops convection. This assures the right flow

field in the solid phase and the no-slip condition on the solid/melt boundary. To reduce the influence of the external boundaries of the calculation domain, we apply the non-disturbing boundary conditions derived from the asymptotic temperature field in a half space [12] as follows:

$$-\frac{1}{T-T_a} \frac{\partial T}{\partial x} = \frac{u_s}{2a} \left(x \frac{K_1\left(\frac{u_s r}{2a}\right)}{r K_0\left(\frac{u_s r}{2a}\right)} - 1 \right), \quad (11)$$

on the left and right boundaries $x = \text{const}$ (see Fig. 3) and

$$-\frac{1}{T-T_a} \frac{\partial T}{\partial z} = \frac{u_s z}{2a r} \frac{K_1\left(\frac{u_s r}{2a}\right)}{K_0\left(\frac{u_s r}{2a}\right)}, \quad (12)$$

on the bottom boundary $z = \text{const}$, where T_a is the ambient temperature, u_s the scanning speed, $a = \lambda/C$ the thermal diffusivity, $r^2 = x^2 + z^2$, and K_0 and K_1 are the modified Bessel functions of the second kind.

4. Modeling results

Modeling conditions are similar to the experimental ones. Table 3 shows the following thermophysical properties of steel EOS PH1 accepted for calculations. Density ρ_0 is taken at the room temperature [13]. Solidus T_m and liquidus T_l temperatures are estimated by the Thermo-Calc software and thermodynamic databases [14] for ternary alloy 80 wt.% Fe 15 wt.% 5 wt.% Ni. Latent heat of melting L_m and boiling point T_b are taken for pure iron [13]. Specific heat C of a steel considerably growth with temperature while it is less sensitive to the composition. Thus, C/ρ_0 varies from 500 ± 50 J/(kg K) at the room temperature to 700 J/(kg K) at the melting point for AISI 304 [8]. In the same temperature interval, it varies from 450 to 700 J/(kg K) for pure iron [13]. For steels AISI 631 (17-7 PH) and AISI 410 with similar chemical and phase composition, thermal conductivity λ varies from 15 to 27 and from 23 ± 5 to 33 W/(m K), respectively [15]. Table 2 shows the values of C and λ around the melting point. Dynamic viscosity η is taken for iron at the melting point [16]. Surface tension α of a molten steel is known to be extremely sensitive to the content of sulfur and oxygen. Table 3 lists the values of α and its temperature coefficient $\beta = d\alpha/dT$ measured around the melting point in the ideal conditions of pure iron in reducing atmosphere [17].

Table 4 lists the parameters of the model. The wall thickness w is the same as in experiment. The absorbed laser power wP is considerably less than the incident laser power in experiment (see Table 1). It is reasonable because a considerable fraction of the incident laser radiation is reflected and a certain portion of the absorbed energy is lost to evaporation. The beam radius r_0 corresponds to the experimental laser spot size of 100 μm because according to Eq. (8), around 90% of beam power is within a 100 μm -diameter circle. The scanning speed u_s corresponds to the experimental one. The keyhole depth D_k is fitted to obtain a satisfactory agreement with the experimentally observed shape of the melt pool. The effective

keyhole radius r_k is chosen equal to the beam radius because the keyhole is due to evaporation within a laser spot. A small keyhole shift x_k is chosen to approach the maximum of the calculated temperature field to the keyhole center. The model value of the bulk modulus B is taken much less than a realistic value for a steel because numerical errors strongly increase with B . However, this value of B is still considerably greater than the calculated variation of pressure. Therefore, the calculated flow is essentially incompressible. The calculation domain is $1440 \times 480 \mu\text{m}^2$. Calculations are accomplished on the grids of various size to verify convergence. A grid of 1440×480 cells is found to be satisfactory. The calculation time from the laser onset to obtaining steady state temperature, pressure, and flow velocity distributions in the calculation domain is $t = 150$ ms.

Table 3. Properties of steel EOS PH1.

Property	Value	Unit	Reference
Density, ρ_0	7800	kg/m ³	[13]
Solidus temperature, T_m	1762	K	Calculated
Liquidus temperature, T_l	1769	K	Calculated
Boiling point, T_b	3135	K	[13]
Latent heat of melting, L_m/ρ_0	247	kJ/kg	[13]
Specific heat, C/ρ_0	700	J/(kg K)	[13,15]
Thermal conductivity, λ	30±3	W/(m K)	[15]
Dynamic viscosity, η	6·10 ⁻³	Pa s	[16]
Surface tension, α	1.9	N/m	[17]
Temperature coefficient of surface tension, β	-7.5·10 ⁻⁴	N/(m K)	[17]

Table 4. Parameters of the model.

Parameter	Value	Parameter	Value
Wall thickness, w	250 μm	Keyhole radius, r_k	25 μm
Absorbed power, wP	37.5 W	Keyhole shift, x_k	12.5 μm
Beam radius, r_0	25 μm	Bulk modulus, B	100 kPa
Scanning speed, u_s	25 mm/s	Domain size (μm)	1440×480
Keyhole depth, D_k	250 μm	Grid size	1440×480

Figure 4 shows the calculated temperature field. The temperature attains its maximum near the bottom of the keyhole. The solidus isotherm $T = T_m$ (bold line in Fig. 4) is the boundary of the melt pool. The calculated dimensions of the melt pool estimated by this isotherm are $900 \pm 20 \mu\text{m}$ length and $320 \pm 20 \mu\text{m}$ depth. Considerable temperature variation over the surface induces a Marangoni thermocapillary convection in the melt pool. Figure 5 shows the calculated fluid-dynamic fields in the melt pool. Streamlines (top diagram) enter from the left and exit to the right through the solid phase, which moves uniformly from left to right. They form four vortices in the melt pool. Two vortices are upstream of the keyhole and two of them are downstream of the keyhole. Two vortices are on the top of the melt pool and two of them are near the bottom of the keyhole. One can distinguish two shear flow domains between the front-bottom boundaries of the melt pool and the keyhole. The first shear flow domain is between the top-upstream and bottom-upstream vortices and the second one is

between the bottom-upstream and bottom-downstream vortices. The top-upstream vortex is very small. Figure 6 zooms the region of this vortex.

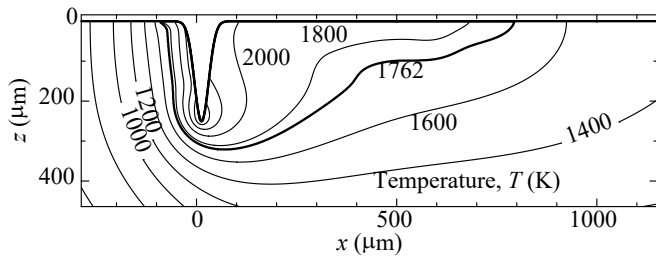


Fig. 4. Temperature distribution in the laser-interaction zone. The solidus isotherm $T = 1762$ K (bold line) bounds the melt pool.

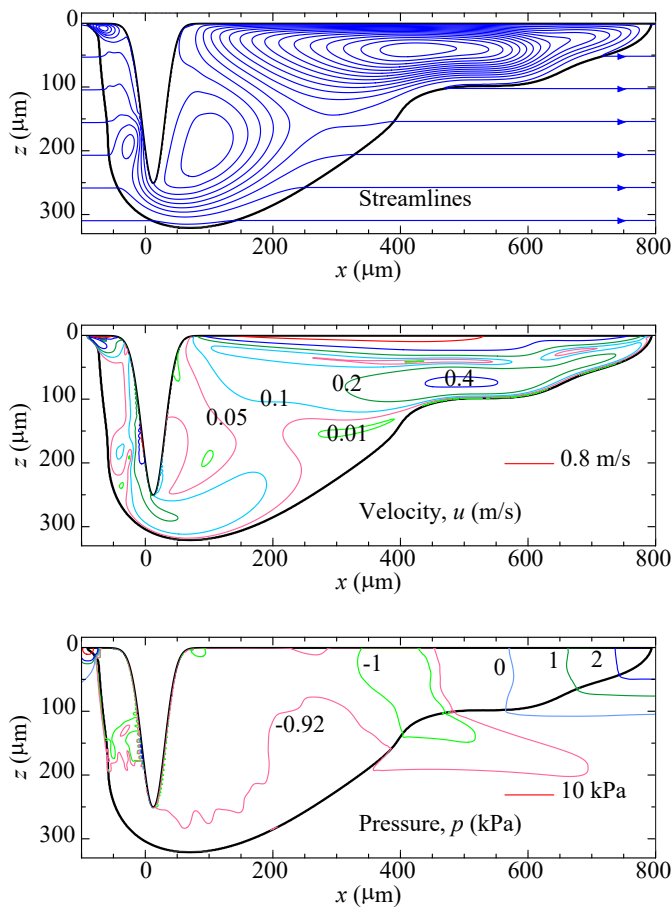


Fig. 5. Fluid-dynamic fields in the melt pool: streamlines (top), absolute value of flow velocity (middle), and pressure (bottom).

While the top diagrams in Figs. 5-6 show the direction of flow velocity, the middle diagrams indicate the velocity absolute value. Note that the smallest top-upstream vortex is the strongest one because the flow velocity attains its absolute maximum around 2 m/s on the free surface adjacent to this vortex (see the middle diagram in Fig. 6). The maximum flow velocity in the top-downstream vortex is around 1 m/s (see the middle diagram in Fig. 5). The bottom-upstream and bottom-downstream vortices are considerably weaker. The melt pressure (bottom diagrams in Figs. 5-6) considerably increases when approaching to the top-left and top-right corners of the melt pool. The top-left pressure peak attains ≈ 40 kPa and the

top-right one attains ≈ 3 kPa. The sharp pressure peaks near the corners are consistent with the drastic changing the flow direction occurred in these regions (see the streamlines).

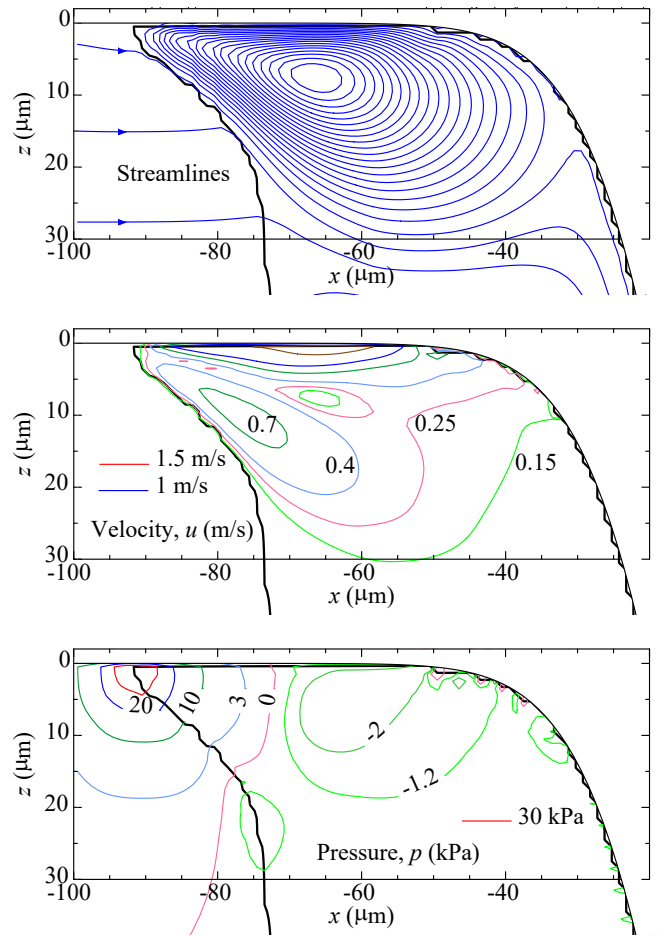


Fig. 6. Fluid-dynamic fields in the top-left region of the melt pool: streamlines (top), absolute value of flow velocity (middle), and pressure (bottom).

5. Discussion

The calculated profile of the melt pool (see the solidus isotherm in Figs. 4-6) is mirror similar to the experimental images of Fig. 2. It is reasonable because the laser scanning direction is from left to right in the experiment and from right to left in the modeling. Table 5 summarizes the experimentally measured and calculated dimensions of the melt pool.

Table 5. Dimensions of the melt pool (μm).

	Experiment	Modeling
Length	950 ± 50	900 ± 20
Depth	300 ± 50	320 ± 20

The good quantitative agreement observed indicates that the model parameters chosen are realistic. This primarily concerns the keyhole depth set to $D_k = 250 \mu\text{m}$ in the calculations. In other words, the modeling shows that the keyhole formation can explain such a large melt depth experimentally observed. Besides, a large spot of non-steady contrast visible in the middle of the melt pool may indicate a keyhole. The keyhole depth is

comparable with the melt pool depth. A considerable keyhole depth was observed in L-PBF of slabs [18]. The present work demonstrates the similar regime for thin walls.

The present modeling of a 2D melt pool in a thin wall reveals formation of four vortices. The same number of vortices was reported for a 3D pool [19]. The number of vortices depends probably on the Reynolds number of the flow. In the considered conditions, one can estimate it from the melt depth $D = 300 \mu\text{m}$ and the maximum velocity $u_{\text{max}} = 2 \text{ m/s}$ as

$$\text{Re} = \frac{\rho_0 D u_{\text{max}}}{\eta} = 780. \quad (13)$$

The thermal Peclet number

$$\text{Pe} = \frac{C D u_{\text{max}}}{\lambda} = 110, \quad (14)$$

gives the ratio of the convective heat transfer to the conductive one. The obtained value indicates that the convective heat transfer is much more important than the conductive one even in such a small melt pool typical for L-PBF.

6. Conclusions

In the developed experimental setup, a high-speed CCD camera records the dynamics of the melt pool profile on the top of a thin wall during laser beam scanning along the wall edge. The melt pool is observed in the conditions similar to those at L-PBF manufacturing of shell elements of lightweight cellular structures. The clearly distinguished melt pool boundary is steady and moves uniformly with the laser beam. A large spot of non-steady contrast in the middle of the pool may indicate formation of a keyhole.

The proposed mathematical model numerically solves the system of conservation laws for a viscous conductive medium in 2D geometry. It simulates the solid state by a ghost field of external force. The length and depth of the calculated melt pool agree with the corresponding experimental parameters in assumption of formation of a deep keyhole. The modeling reveals a developed Marangoni convection with the Reynolds number around 780. One can distinguish four vortices and two domains of shear flow. The thermal Peclet number is around 110 indicating that the convective heat transfer is much greater than the conductive one in the melt pool in the considered L-PBF conditions.

Acknowledgements

This work was supported by the Ministry of Science and Higher Education of the Russian Federation under project 0707-2020-0034.

References

- [1] Meier C, Penny R, Zou Y, Gibbs J, John Hart A. Thermophysical phenomena in metal additive manufacturing by selective laser melting: fundamentals, modeling, simulation and experimentation. *Annu. Rev. Heat Transf.* 2018; 20:241-316.
- [2] Yap CY, Chua CK, Dong ZL, Liu ZH, Zhang DQ, Loh LE, Sing SL. Review of selective laser melting: Materials and applications. *Appl. Phys. Rev.* 2015; 2:041101.
- [3] Yadroitsev I, Gusarov A, Yadroitsava I, Smurov I. Single track formation in selective laser melting of metal powders. *J. Mater. Process. Technol.* 2010; 210:1624-31.
- [4] Gusarov AV, Grigoriev SN, Volosova MA, Melnik YA, Laskin A, Kotoban DV, Okunkova AA. On productivity of laser additive manufacturing. *J. Mater. Process. Technol.* 2018; 261:213-232.
- [5] Al-Ketan O, Rowshan R, Abu Al-Rub RK. Topology-mechanical property relationship of 3D printed strut, skeletal, and sheet based periodic metallic cellular materials. *Additive Manufacturing* 2018; 19:167-183.
- [6] Evans S, Jones E, Foxand P, Sutcliffe C. Photogrammetric analysis of additive manufactured metallic open cell porous structures. *Rapid Prototyping J.* 2018; 24:1380-91.
- [7] Favre J, Lohmuller P, Piotrowski B, Kenzari S, Laheurte P, Meraghni F. A continuous crystallographic approach to generate cubic lattices and its effect on relative stiffness of architected materials. *Additive Manufacturing* 2018; 21:359-368.
- [8] Panesar A, Abdi M, Hickman D, Ashcroft I. Strategies for functionally graded lattice structures derived using topology optimisation for Additive Manufacturing. *Additive Manufacturing* 2018; 19:81-94.
- [9] Souza J, Großmann A, Mittelstedt C. Micromechanical analysis of the effective properties of lattice structures in additive manufacturing. *Additive Manufacturing* 2018; 23:53-69.
- [10] EOS, 2019. <https://www.eos.info/material-m>
- [11] Kurganov A, Tadmor E. New high-resolution central schemes for nonlinear conservation laws and convection-diffusion equations. *J. Computat. Phys.* 2000; 160:241-282.
- [12] Kovaleva IO, Grigoriev SN, Gusarov AV. Non-disturbing boundary conditions for modeling of laser material processing. *Phys. Procedia* 2014; 56:421-428.
- [13] Gray DE. *American Institute of Physics Handbook*. New York: McGrawHill; 1972.
- [14] Thermo-Calc Software, 2019. <https://www.thermocalc.com>
- [15] Bogaard RH, Desai PD, Li HH, Ho CY. Thermophysical properties of stainless steel. *Thermochemica Acta* 1993; 218:373-393.
- [16] Assael MJ, Kakosimos K, Banish RM, Brillo J, Egry I, Brooks R, Quedest PN, Mills KC, Nagashima A, Sato Y, Wakeham WA. Reference data for the density and viscosity of liquid aluminum and liquid iron. *J. Phys. Chem. Ref. Data* 2006; 35:285-300.
- [17] Morohoshi K, Uchikoshi M, Isshiki M, Fukuyama H. Surface tension of liquid iron as functions of oxygen activity and temperature. *ISIJ International* 2011; 51:1580-86.
- [18] King WE, Barth HD, Castillo VM, Gallegos GF, Gibbs JW, Hahn DE, Kamath C, Rubenchik AM. Observation of keyhole-mode laser melting in laser powder-bed fusion additive manufacturing. *J. Mater. Process. Technol.* 2014; 214:2915-25.
- [19] Kovalev OB, Gurin AM. Multivortex convection of metal in molten pool with dispersed impurity induced by laser radiation. *Int. J. Heat Mass Transfer* 2014; 68:269-277.

11th CIRP Conference on Photonic Technologies [LANE 2020] on September 7-10, 2020

FE-Simulation of the influence by material defects on the endurance of additive built metal parts

Patrick Alexander Ralf^a, Jan-Philip Wenzl^a, Peter Lindecke^{a,*}, Claus Emmelmann^a

^aFraunhofer IAPT, Am Schleusengraben 14, Hamburg-Bergedorf 21029, Germany

* Corresponding author. Tel.: +49-40-484010-730 ; E-mail address: peter.lindecke@iapt.fraunhofer.de

Abstract

The interaction between the process parameters in powder bed based additive manufacturing complicates the fatigue life prediction of the manufactured parts by a magnitude. A slight shift in a single parameter during a print job can lead to a highly divergent process result. The consequences can be observed in manufacturing defects inside the printed structure like pores and bonding defects which lead to locally inhomogeneous material properties. In this paper a method for predicting the fatigue life of additively manufactured structures based on the classical Stress-Life model is being developed. In a first step an experimental S-N curve for fatigue specimens is calculated by analyzing experimental data from literature. A Finite Element simulation of fatigue specimens with different internal defects is conducted and the life expectancy is determined. The specimens are built and inspected by means of destructive testing. The simulation is being validated and modified according to these results.

© 2020 The Authors. Published by Elsevier B.V.

This is an open access article under the CC BY-NC-ND license (<http://creativecommons.org/licenses/by-nc-nd/4.0/>)

Peer-review under responsibility of the Bayerisches Laserzentrum GmbH

Keywords: Laser additive manufacturing, titanium alloy TiAl6V4, FE-Simulation, effect of imperfections, Wöhler curve, fatigue behaviour

1. Introduction

The definition Additive Manufacturing (AM) describes today all processes including the producing of components from electronic data without any forming tools [1]. Further the process of the Selective Laser Melting (SLM) should be explained more detailed. In this process the component will be put together by several layers. During this, a thin layer made of base metal powder is melted on in closed lines by a laser beam. After a layer is finished, the component will be sank down to one layer thickness and a new layer of base metal powder will be filled up by a roller. Following the new powder layer will be melted on together with the subjacent layer whereby the component is generated. All subsequent analyses are based on the SLM process using the titanium alloy TiAl6V4. The results, which are presented in this paper,

are developed during the research project futureAM at Fraunhofer IAPT. Background is the increase of scalability, productivity and quality of Additive Manufacturing processes in a way relevant to praxis for the production of tailor-made metal components [2]. In one of this project domains the influence of manufacturing defects to the endurance of these metal components is simulated. Thereby it should be enabled, making statements about the fatigue behavior of produced components. After a technical measurement identification of existing manufacturing defects, it will be possible with help of a simulation, to decide whether the component is useable or not. In addition to the development of a simulation the influence of different defect parameters should be analyzed. It concerns the defect count, the distance to the surface and the defect size. Therefore models with different defect are designed and built by a SLM machine 250HL from Co. SLM

Solutions. All specimen are built in longitudinal direction and machine finished. For the FE-Simulation a S-N curve must be determined. For that many literature sources are used to generate a universal curve. After the simulation is finished, the specimen will be destroyed by fatigue tests made with a hydraulic ram. Afterwards the results of the simulation and the experiments can be matched und adjustments can be made.

2. Defect model types and making of specimen

During the manufacturing process defects are regularly occurring. To compare particular defects among each other, some parameters have to be constant. Therefore defects are placed in the specimen on purpose. To create pores and bonding defects, defined areas during the manufacturing process are left unexposed to the laser beam. Thereby a predefined space filled up with powder is generated. These spaces have spherical and flat square geometries. To ensure that the specimen will fail by the designedly defects, these are at least twice as big as the usual defects. To research the influence of the defect count, surface distance and defect size separately, individual models have been developed. The basic model was designed after a classic tensile specimen. For the geometric dimensions see figure 1.

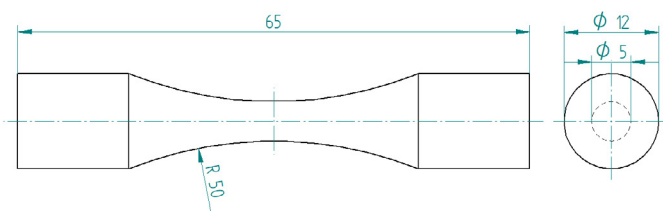


Fig. 1. Geometric dimensions of the specimen

To analyze the effect of the defect count, the effect of the surface distance und the defect size should be constant as possible. Therefore defects with 600 μm are placed in three different configurations. These configurations are shown in figure 2.

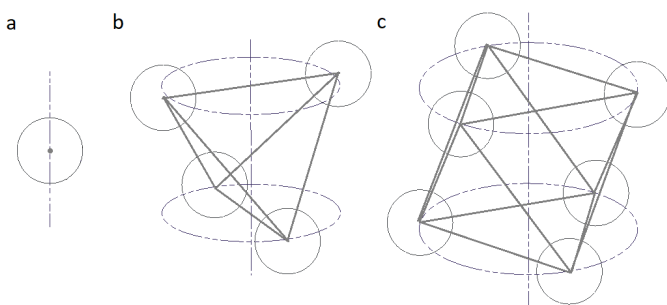


Fig. 2. (a) single config.; (b) quad config.; (c) sixfold config.

For the analysis of the effect of the surface distance the defects are placed central with particular distances of 0.5, 1.5 and 2.5 mm. To analyze the size effect the defects are placed in the center with different magnitudes of 0.3, 0.6 und 0.9 mm.

According to the manufacturing process all specimen are heat-treated to reduce residual stresses. Some specimen are

scanned by a Computed Tomography (CT) to test for unwanted manufacturing defects. Figure 3a shows many problematic pores under the surface. These pores will be eliminated by spherical turning of the surface. Thereby the diameter of the specimen become 0.4 mm less. Because of this mechanical machining some surface defects are occurred by specimen with defects near to the surface. These specimen can't be used anymore for the study.

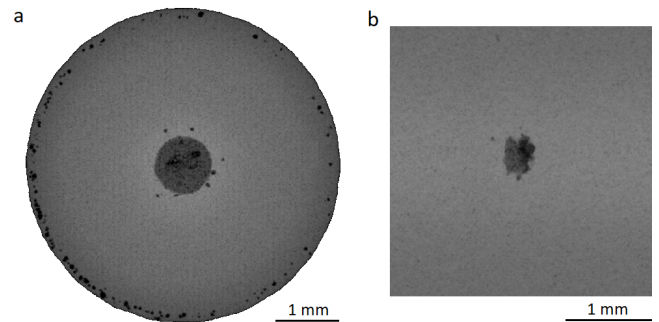


Fig. 3. (a) cross section at a 0.9 mm spherical defect; (b) anomalous profile of a 0.3 mm square defect

As figure 3b exemplifies the geometry of the bonding defects deviates distinctly from the ideal geometry. Further the specimen with spherical defects will be considered only. Subsequently the specimens are stabilized-blasted to strengthen the surface. The machined surfaces are shown in figure 4.



Fig. 4. (a) machine finished; (b) blasted finished

3. Modeling the S-N-curve

S-N curves can be always separated in component S-N curves und material S-N curves. Because local stress concepts will be used further, a material S-N curve has to be determined. These curves are characterized by not having influence parameters except the material influence. For that literature sources will be consulted. The specimen, which are used in these tests, should be round specimen with a similar geometry and size. Furthermore these specimen should be heat-treated und the surface should be at least machined. The tests are conducted at the frequency of about 50 Hz. Following these measurement data are used to generate a material S-N curve. Therefore a best-fit curve is placed through the measurement points. This curve represents the conditional probability of failure of 50%. For the fitted curve a double exponential approach is used. The result is an analytic S-N-curve shown in equation 1.

$$f_{SN}(x) = a \cdot e^{b \cdot x} + c \cdot e^{d \cdot x} \quad (1)$$

The measurement data from the literature shows differences in the load ratio R . As the later performed fatigue tests will be made with alternating loads, the fitted curve will only be placed through the blue data points. The parameters used in equation 1 are specified in table 1.

Table 1. Parameter values for the fitted S-N curve for $R = -1$.

Parameter	Value
a	2.051e4
b	-0.9863
c	308.5
d	0.006978

The measurement data collected from the literature and the fitted curve are shown in figure 5. Because the high influence of the load ratio the measure points are separated in terms of color.

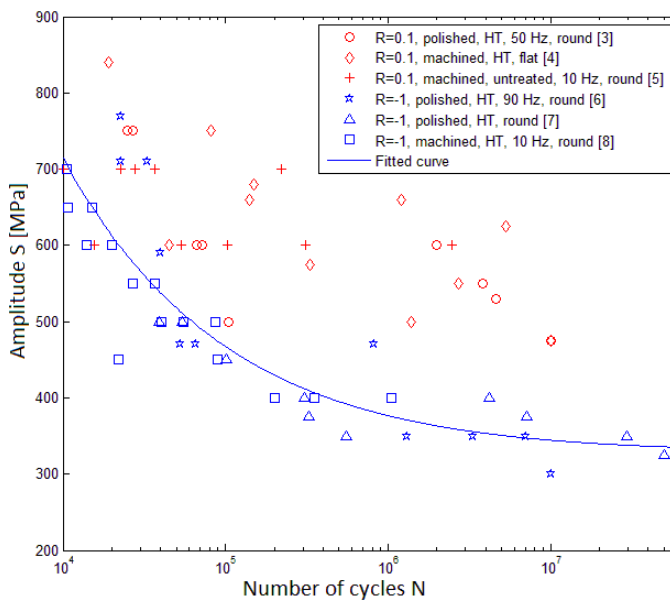


Fig. 5. Measurement points from literature and the fitted curve which represents the material S-N curve.

4. FE-Simulation

The FE-Simulation will be performed using the computer program COMSOL Multiphysics (CM). The basic concept of this FE-simulation is a stress-life-model. This model includes a local stress analysis of a load cycle and a following comparison with a S-N curve. In this case it is valid to use the stress-life-model because on the one hand at high cycle fatigue (HCF) the elastic strains are dominant [9] and on the other hand there are sinusoidal proportional loads. To eliminate some specific modeling issues and to generate the best possible model, some of these modeling issues are analyzed by a mesh converged model. As a result of these tests it is possible to put on the load by the face surface of the model. Furthermore the load cycle can be represented by at least five stationary load cases. Modeling the influence of frequency by a time dependent study for example is not possible in CM. Symmetric models are used because of the

very fine meshing of the defect geometries. By these models some of the simulations will even be disabled because of the limited computer performance. Therefore the amount of the degrees of freedom (DOF) decreases hence the time of calculation falls off. All of the models have at least two symmetric planes. During the simulation the load will be customized to generate local stresses of a magnitude of approximately 600 MPa. Therefore a good compromise between the tolerance, caused by the logarithmic diagram of the number of cycles, and the duration of the single fatigue test should be targeted. In figure 6 some symmetric models are shown for example.

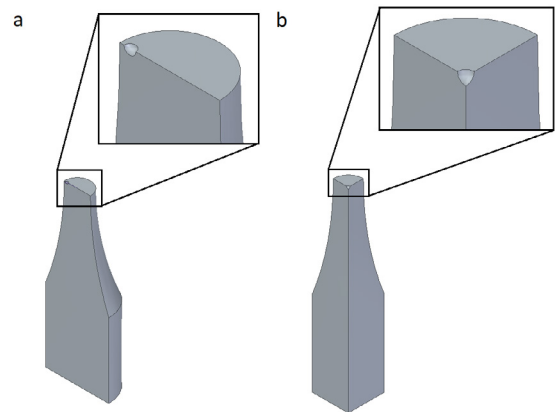


Fig. 6. (a) model with two symmetric planes; (b) model with three symmetric planes

To differentiate between the types of used models in the following context, they are marked with a code. This code consists of a letter and three numerals. The letter describes the kind of defect type (in this case S for spherical). The first numeral describes the size of the defect (in 100 μm), the second the number of defects and the third the distance from the surface (7: 0.5 mm; 8: 1.5 mm; 9: 2.5 mm). The computational output shows a unique stress respectively fatigue distribution for each model as shown in figure 7.

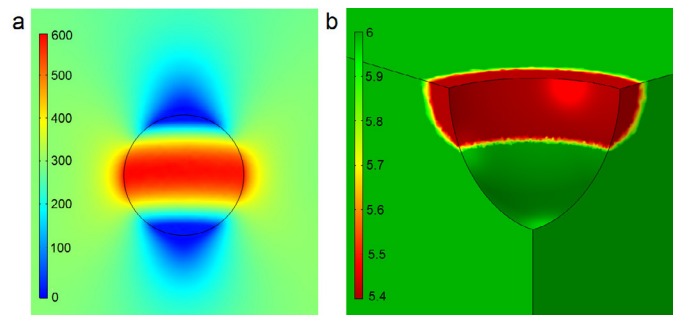


Fig. 7. (a) stress distribution at model S669; (b) fatigue distribution at model S319

From the results of the simulation, which are shown in table 2, it is obvious, that if the defect size increases the stress increases as well and the number of cycles declines. Therefore the defect size has a negative effect on the endurance limit. A direct negative effect of the defect count could not be confirmed. It should be noted that statistical effects in this simulation are not included. In contrast the distance to the

surface affects the result strongly. The closer the defect is located to the surface the worse is the endurance limit because of the greater local stress.

Table 2. The solution data from the simulation

Model type	Load [N]	Stress [MPa]	No. of Cycles
S669	5681	597.6	24204
S649	5660	600.3	25598
S619	5800	600.8	23309
S618	5725	598.9	24054
S617	4930	600.3	25821
S919	5790	600.4	23939
S319	5820	600.4	23725

5. Alternating stress fatigue tests

For the fatigue tests a hydraulic ram model 810 made by Co. MTS Systems Corporation is used. Tests conducted before have shown that the specimen are passing 1 million cycles before they fail under similar circumstances. Because of this the test load will be increased up to 8500 N. Afterwards the specimen will be stressed till they break. To determine statistical deviation every kind of specimen will be manufactured and tested five times. Then the arithmetic average will be taken from those measurement data. The specimen are tested at approximately 20°C room temperature, a frequency of 50 Hz and a stress ratio of $R = -1$. The results are shown in table 3.

Table 3. Results of the fatigue tests

Specimen type	Number of cycles (arithmetic average)
S669	53247
S649	57881
S619	66939
S618	52779
S617	(14336)
S919	44678
S319	154176

By looking at the measurement data from table 3 it is clear that the number of cycles is much bigger than the simulated values. However it is confirmed, that the increasing defect size as well as the decreasing distance to the surface both have a negative effect on the endurance limit. During the measurement of specimen S617 the surface defect may have caused the low number of cycles. Because of that these measurement data have to be examined skeptical. In contrast to the simulation the number or rather the placement of several defects have a negative effect. On the fracture plane (see figure 8) it is visible, that the fatigue crack formation exactly started at the critical failure domain which is a result of the simulation. Anyhow the metal powder inside the defect is no more powdery. Because of heat input a hard sinter like structure has formed out. This structure is at least hardened

that it holds its shape after the overload breakage has destroyed the specimen.

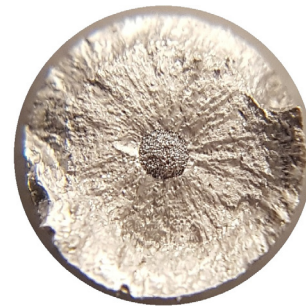


Fig. 8. Fracture plane of a specimen type S619

6. Modification of the simulation

To modify the simulation, the used S-N curve will be matched with some measurement data, which belong to specimen who doesn't failed in the center. Thereby the curve will be shifted above by a correction factor of 1.09 in CM. Subsequently the simulation is made with the von Mises stress in place of the first principal stress. Additionally a substitute model is placed in the defects, which should represent the load or rather the stress caused by a reduced Young's modulus (see figure 9).

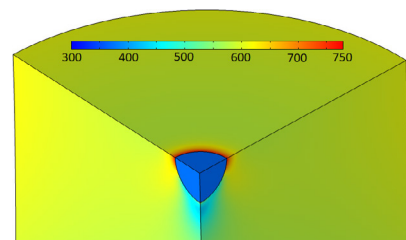


Fig. 9. Adapted model S619 for example with new distribution of stress.

It becomes apparent that, if the S-N curve fits to the material with the right correction factor and the right comparison stress hypothesis is used, the Young's modulus became about 80% of the basic modulus.

Acknowledgements

Founding by Fraunhofer by the project 809306 futureAM is gratefully acknowledged.

References

- [1] Schmid, Additive Fertigung mit selektivem Lasersintern (SLS), Wiesbaden: Springer, 2015.
- [2] [Online]. Available: <https://www.fraunhofer.de/de/ueber-fraunhofer.html>. [Access at June 05 2019].
- [3] Wycisk, Ermüdungseigenschaften der laseradditiv gefertigten Titanlegierung TiAl6V4, Deutschland: Springer, 2017.
- [4] Greitemeier, Untersuchung der Einflussparameter auf die mechanischen Eigenschaften von additiv gefertigtem TiAl6V4, Wiesb.: Springer, 2016.
- [5] Walker, Liu and Brandt, „Evaluation of fatigue crack propagation behaviour in Ti-6Al-4V manufactured by selective laser melting,” International Journal of Fatigue, pp. 302-308, February 2 2017.

- [6] Chastand, Tezenas, Cadoret, Quaegebeur, Maia and Charkaluk, „Fatigue characterization of Titanium Ti-6Al-4V samples produced by Additive Manufacturing,” *Procedia Structural Integrity* 2, pp. 3168-3176, June 20-24 2016.
- [7] Benedetti, Cazzoli, Fontanari and Leoni, „Fatigue limit of Ti6Al4V alloy produced by Selective Laser Sintering,” *Procedia Structural Integrity* 2, pp. 3158-3167, June 20-24 2016.
- [8] Günther, Krewerth, Lippmann, Leuders, Tröster, Weidner, Biermann and Niendorf, „Fatigue life of additively manufactured Ti-6AL-4V in the very high cycle fatigue regime,” *International Journal of Fatigue*, pp. 236-245, May 18 2016.
- [9] Einbock and Mailänder, *Betriebsfestigkeit mit FEM*, Norderstedt: Books on Demand, 2018

11th CIRP Conference on Photonic Technologies [LANE 2020] on September 7-10, 2020

Design of electrode for electrochemical gold separation process manufactured via laser-based powder bed fusion

Atte Heiskanen^{a*}, Eveliina Repo^b, Heidi Piili^a

^aLUT University, LUT School of Energy Systems, Department of Mechanical Engineering, Research Group of Laser Materials Processing and Additive Manufacturing, Yliopistonkatu 34, 53850 Lappeenranta, Finland

^bLUT University, LUT School of Engineering Sciences, Department of Separation Science, Research Group of Hydrometallurgy for Urban Mining, Yliopistonkatu 34, 53850 Lappeenranta, Finland

* Corresponding author. Tel.: +358 50 477 9592; E-mail address: atte.heiskanen@lut.fi

Abstract

A possible field benefitting from this geometrical freedom offered by L-PBF is electrochemistry, as electrodes can be designed with unprecedented freedom to increase the efficiency of electrochemical processes. In this study an optimized electrode to be manufactured with L-PBF designed. Literature was used to determine critical factors affecting the electrode performance. Finally, manufacturability of the electrode via L-PBF was assessed by conducting build process simulations. It was concluded that the high surface area and uniform porosity, which can be achieved by using lattice structures, are the most important factors affecting electrode performance. The designed electrode structure was also deemed to be manufacturable via L-PBF based on simulation results.

© 2020 The Authors. Published by Elsevier B.V.

This is an open access article under the CC BY-NC-ND license (<http://creativecommons.org/licenses/by-nc-nd/4.0/>)

Peer-review under responsibility of the Bayerisches Laserzentrum GmbH

Keywords: Design for additive manufacturing; powder bed fusion; electrode; electrochemistry; process simulation

1. Introduction

Laser-based powder bed fusion (L-PBF) is the most widely adopted metal additive manufacturing (AM) method, of which use has increased considerably in recent years [1–3]. It can be used to manufacture geometries with increased complexity and fine details [1].

A possible field benefitting from this newfound geometrical freedom is electrochemistry, as electrodes can be designed with much more freedom to increase the efficiency of electrochemical processes [4]. An example of such electrochemical process is the process for gold recovery from electronic waste. As the economic growth and technological advances have resulted in the increase of obsolete electronics, this process has generated interest. The waste contains high quantities of gold, with concentrations up to 100 times higher than generally found in gold ore. [5]

The process utilizes electrogenerated chlorine (Cl_2), which is used to dissolve precious metals from electronic waste, making it possible to be recovered [5–6]. Cl_2 is generated on the anode side during the process [5]. Schematic of the process is presented in Fig. 1a.

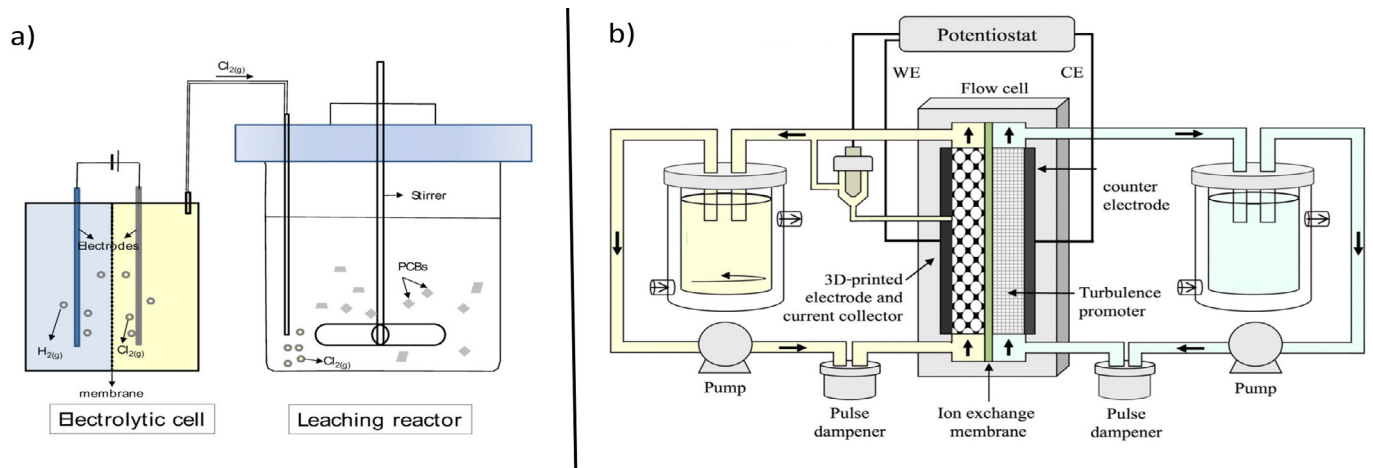


Fig. 1. (a) process schematic of electrochemical gold separation process [5]; (b) schematic of flow reactor [4]

Release of gaseous products can be further increased by utilizing porous, three dimensional electrodes and flow type reactor. Schematic for flow reactor is presented in Fig. 1b. The problem with traditionally used porous electrodes, such as metal foams, is their non-uniform structure [7]. This non-uniformity can lead to un-optimal current distribution throughout the electrode, which lead to several undesired effects, such as reduced current efficiency and reaction variance over the surface area of the electrode [7–8]. Additionally, gas bubbles can get trapped within the unregular structure, unbalancing the current distribution even further [8]. Metal foams do not have features for securing the necessary current feeder connection, and will need additional adhesives to facilitate this, which can also negatively affect the current distribution [4, 7].

These electrode features could be enhanced by utilizing possibilities offered by L-PBF [4]. Electrodes manufactured with this method have been studied in numerous studies, for example Refs. [4, 8–9].

In this work, anode electrode manufactured via L-PBF is designed to be used in flow reactor for the aforementioned gold separation process to enhance the release of Cl₂ and thus improve the gold dissolving. Electrode is designed based on critical performance factors found from literature and its manufacturability is assessed by utilizing build process simulation.

2. Electrode performance factors

The effectiveness of electrochemical processes highly depends on the surface area of the electrode, as the reaction rate of the process at fixed current density is directly proportional to the electroactive area. Therefore, maximizing the surface area of the electrode while minimizing its occupied volume will increase the efficiency of the reactor. This is demonstrated by the volumetric mass transport coefficient, which is a useful figure to assess the reactor performance [7]:

$$k_m A_e = \frac{k_m A}{V_e} \quad (1)$$

Where $k_m A_e$ is the volumetric mass transport coefficient, k_m is the mass transport coefficient, A_e is the electroactive area of the

electrode per unit volume, A is the electroactive area and V_e is the electrode volume [7]. In addition, the value for k_m depends on the electrode geometry, orientation, volumetric porosity and surface roughness, which can be controlled through design when electrode is additively manufactured [4].

Fractional conversion, which is the ratio of reactant amount reacted to the reactant amount fed, of the reactor can be described by following equation [10].

$$X_A = 1 - \exp\left(-\frac{k_m A_e L}{v}\right) \quad (2)$$

Where X_A is the fractional conversion, L is the electrode length and v is the mean linear velocity of the flow. In addition, k_m is as follows [4]:

$$k_m = \alpha v^\beta \quad (3)$$

Where α and β are empirical constants and increasing with the flow turbulence. When this is substituted into equation 2, following equation is achieved [10]:

$$X_A = 1 - \exp(-\alpha A_e L v^{\beta-1}) \quad (4)$$

The equation 4 shows that the electrode length and electroactive surface area are the most important factors affecting the fractional conversion of the reactor, with flow velocity and turbulence also affecting. [10]

In equations 8-10, it has been assumed that the electrode operates at optimal current [10]. However, in practice the current distribution of three-dimensional electrode always has some non-uniformity [7]. Three-dimensional electrodes should have as isotropic porosity, electrical conductivity, and flow characteristics as possible to promote uniformity [7]. Non-uniformity through the electrode can lead to some of its area to have negligible current and will not participate in the electron transfer, effectively reducing A_e [7]. Non-uniform current distribution will cause reaction rate to vary throughout the electrode, thus the uniformity should be maximized to achieve highest possible A_e [7–8].

3. Electrode design process

3.1. Electrode structure modeling

To achieve as high surface area as possible, while retaining isotropic porosity, flow characteristics and electrical conductivity, lattice structures manufacturable with L-PBF [11–12] were utilized. Lattice strut thickness and cell size of 0.3 mm and 1.2 mm respectively were used to achieve maximal surface area, corresponding to minimum feature size achievable with L-PBF [11, 13]

For lattice design, so-called design space for the electrode structure was first modelled by utilizing CATIA apps within Dassault Systemés' 3DEXPERIENCE platform. Electrode dimensions were set to fit within the flow reactor designed at LUT University and are presented in Fig 2.

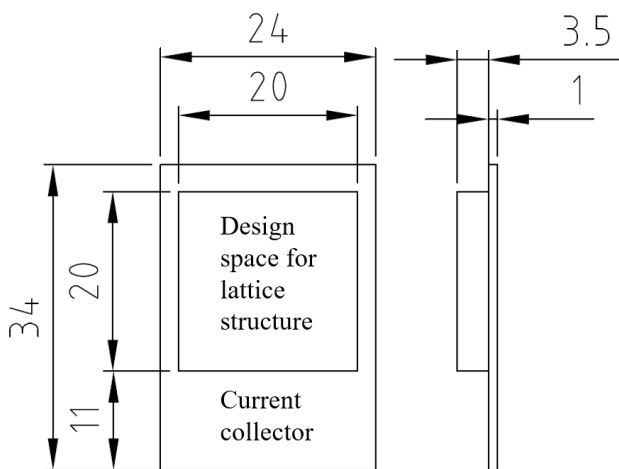


Fig 2. Electrode design space dimensions

The designed geometry was imported into ANSYS SpaceClaim R2 software for lattice creation. Different symmetrical lattice cell types were compared to determine one with highest surface area, while fulfilling the requirement for isotropic properties. Cell comparison is presented in Table 1.

Table 1. Lattice cell comparison.

Lattice cell geometry	1	2	3	4
Surface Area [mm ²]	5.99	5.76	9.4	10.39

As the lattice cell geometry 4 possesses highest surface area, it was used to fill the design space with lattice structure.

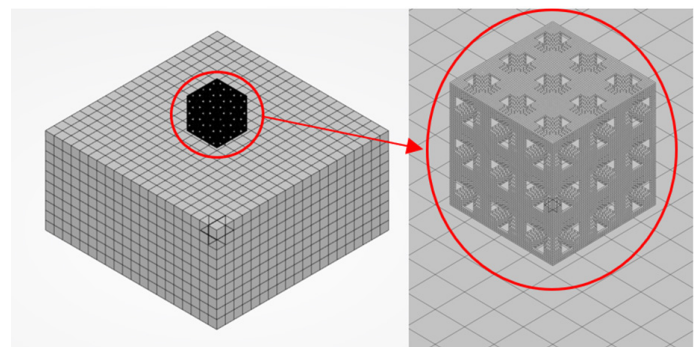
3.2. Build process simulation

Build process simulation was carried out to verify the manufacturability of designed lattice structure with L-PBF. The simulation was done on Dassault Systemés' 3DEXPERIENCE Platform Apps. The software utilizes Abaqus finite element solver and has an option to use inherent

strain or thermo-mechanical based process simulation. For this work, loosely coupled thermo-mechanical simulation was applied.

The electrode model was imported into the software in STL-format. As the electrode is composed of dense lattice structure, very fine FE-mesh is required to accurately represent the geometry. Simulating the whole lattice structure with very small elements would be unfeasible due to large nodal count in the simulation. Therefore, the lattice size was reduced to 3.5 mm x 3.5 mm x 3.5 mm block for the simulation. The current collector was excluded from the simulation due to its very simple geometry. This was deemed to be reasonable compromise to assess the manufacturability of the designed lattice structure in reasonable time. Another part representing the build plate was created and included in the simulation. This is important, as build plate considerably affects the thermal history prediction [14]. However, the build plate size can be reduced compared to the real one and still sufficiently account for the heat sink effect [14]. Modeled build plate dimensions were 20 mm x 20 mm x 10 mm.

Finite element mesh for the simulation was created on SIMULIA Additive Manufacturing Scenarios App. Lattice geometry and build plate were meshed using linear hexahedron DC3D8 elements. Element sizes used for build plate and lattice geometry were 1 mm and 0.05 mm, respectively. The two meshes were connected by applying tie contact. The FE-mesh is presented in Fig 3.



Progressive element activation feature available in Abaqus

Fig 3. FE-mesh used for the simulation

was utilized to mitigate the difference between used element size and actual powder layer thickness [14–15].

DELMIA Powder Bed Fabrication App within the platform was used to create slicing, recoating and laser beam information for the part. The process parameters used for the simulation are actual build parameters recommended by EOS and are presented in Table 2. The process parameters were input into the software and toolpath data (laser and recoating paths) was created accordingly. Abaqus allows the heating to be computed during each time increment by considering these actual process parameters, by utilizing path intersection module, which recognizes all the elements that the heat source passes through during each time increment [14–15].

Table 2. Process parameters used in the simulation.

Layer thickness [mm]	0.02	-
Spot size [mm]	0.07	-
Recoating time [s]	10	-
	Infill	Contour
Laser Power [W]	195	110
Scan speed [mm/s]	1083	800
Hatch spacing [mm]	0.09	0.09
Scanning strategy	Stripes	Two contours
Stripe width [mm]	5	-
Stripe overlap [mm]	0.12	-
Scan rotation [°]	67	-
Build plate preheating [°C]	80	-

Material used for the build simulation was 316L stainless steel. Due to thermal simulation step, some temperature-dependent material properties are required as an input for the simulation. Material density, solidus and liquidus temperatures, latent heat of fusion, absorption coefficient and Poisson's ratio were set as temperature independent. Thermal conductivity, specific heat capacity, Young's modulus, and coefficient of thermal expansion are set as temperature dependent. Additionally, the plasticity of the material is set as temperature independent, as the plastic behavior shows only a small dependency on temperature due to the range of temperatures experienced during single time increment [14]. The material properties were extracted from literature [17–18].

For the simulation, thermal analysis was first conducted to predict the thermal history of the part due to the build process. For this analysis, a single transient heat transfer analysis step, with duration slightly longer than total build of the part is conducted. The added time allows the part to cool down to room temperature after the build is complete. Time increments during the step were set to include spreading and heating of one layer during each time increment. The laser beam is modeled as a moving concentrated point heat source. As the parameters and scan paths are considered through the features available in Abaqus, the energy input is distributed accordingly in each time increment. Initial temperatures for the part and build plate were set to 26°C. Heat loss was considered through convection and radiation. Heat transfer coefficient, h , was set to 18 W/m²K and emissivity, ϵ , to 0.25, as deemed suitable for same material in [17]. The preheating of the build platform was modeled by applying thermal boundary condition of 80 °C on the bottom of the build plate.

Modeling of material deposition during the simulation is important, as it has large effect on the thermal behavior of the system [14]. The material deposition was modeled by applying element birth method available in Abaqus, allowing elements to be added to the model at each time increment.

For mechanical analysis, static mechanical step was used, with time step corresponding to the thermal analysis. Fixed boundary condition was set on the bottom of the build plate geometry. The thermal history was imported into the

mechanical analysis and developing stresses and deformations were calculated through thermal expansion.

4. Results

4.1. Electrode design

An optimized electrode was designed by utilizing lattice structure. The electrode geometry follows the requirement specifying it needs to fit in the flow reactor designed at LUT University. Therefore, only the area of the lattice was possible to be subjected for further optimization. Designed electrode geometry is presented in Fig. 4.

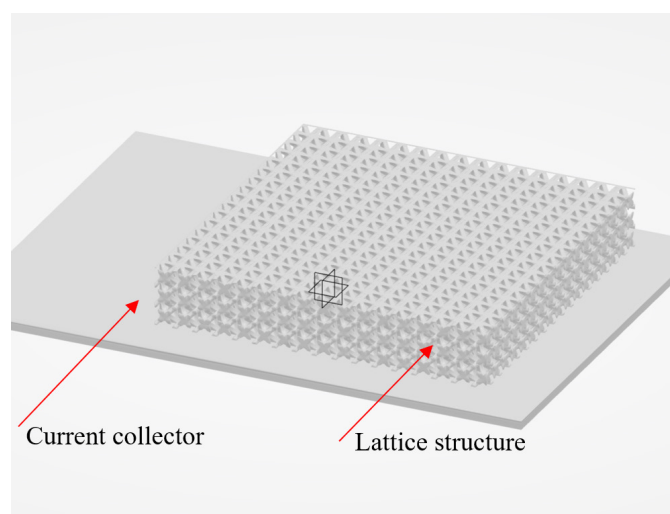


Fig. 4. Designed electrode structure

The electrode is composed of very dense lattice structure. The most important factor affecting three-dimensional electrodes performance in flow reactor was determined to be its surface area. Large surface area was achieved by using lattice strut and cell sizes corresponding to smallest feature sizes manufacturable with L-PBF. Lattice geometry was also modeled to have cell geometry with maximized surface area. The surface area of the lattice part is approximately 5800 mm².

Additionally, the electrode lattice is designed to be symmetrical in every direction. This ensures isotropic porosity across the electrode structure, enhancing the isotropy of its flow and electrical conductivity properties. This promotes the uniformity of current distribution within the electrode, which is critical to achieve optimal performance during the electrochemical process.

The current collector and lattice structure are manufactured from same material as a single part. This ensures uniform connection between the two, as no additional adhesives or welds are required. This feature also promotes the uniformity of the current distribution [4].

4.2. Build process simulation

To assess the manufacturability and usability of the lattice structure, displacement values were plotted from the simulation results. Displacement contour plot predicted by thermo-mechanical analysis is presented in Fig. 5.

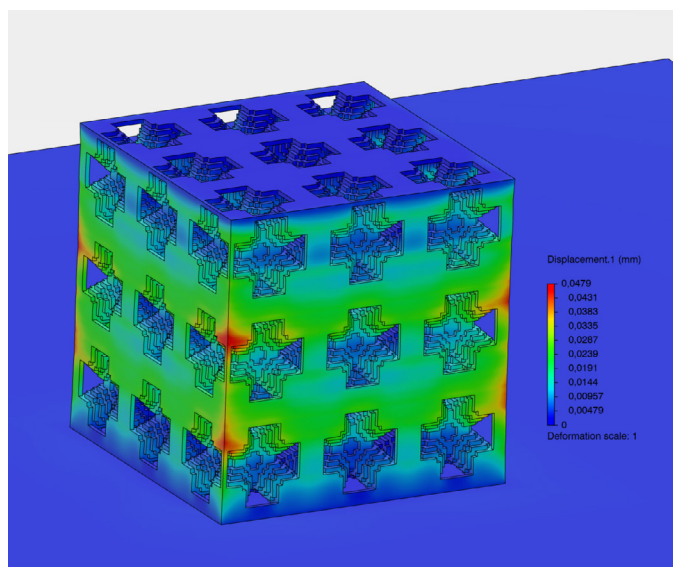


Fig. 5. Displacement contour plot predicted by thermo-mechanical analysis.

Fig. 5. shows that maximum displacements are circa 0.048 mm. Maximum displacements are located in relatively small areas in the outer corners of the simulated lattice structure. Smaller deformations can be observed around the lattice structure, especially on its outer facets, with values less than 0.010 mm. Inside the lattice structure, displacements are even smaller.

The possibility of recoater collision was also assessed from the simulation results. As the displacements were small, no potential areas for recoater collision were identified.

5. Discussion and conclusions

Three-dimensional electrodes used in flow reactors benefit from increased surface area and uniform, well controlled porosity. These features can be achieved through use of lattice structures, which can be generated through specific design tools and manufactured with L-PBF. The structure of the lattice can be optimized by considering the limitations of L-PBF together with the requirements to achieve highest possible surface area and uniform flow properties.

In this paper, optimized electrode structure to be used for electrochemical gold separation process was designed. Large surface area was achieved by utilizing lattice structure.

The manufacturability of the lattice was assessed by applying build process simulation, utilizing thermo-mechanical method. The deformations of the lattice predicted by the analysis is minimal. This indicates that the lattice should be close to the intended shape after manufacturing. Therefore, its structure should still be reasonably uniform and thus fill the requirement for uniform structure and porosity.

In this study, the performance of the electrode or its manufacturability were not validated experimentally. Therefore, these validations could be a subject for later studies.

Acknowledgements

The work was carried out in the research group of Laser Material Processing and Additive Manufacturing of LUT University as a part of ReGold-AM project funded by Academy of Finland. The project is done in co-operation with research group of Hydrometallurgy for Urban Mining. The aim of the project is to construct novel electrochemical reactors for gold recovery purposes by leveraging possibilities offered by AM. The project lasts from 01.09.2019 to 31.08.2023.

References

- [1] Wohlers, T., Campbell, I., Diegel, O., Hugg, R., Kowen, J., Bourell, D.L. & Ismail, F. 2019. Wohlers report 2019. 3D printing and additive manufacturing state of the industry. 369 p.
- [2] Milewski, J.O. 2017. Additive Manufacturing of Metals. From Fundamental Technology to Rocket Nozzles, Medical Implants, and Custom Jewelry. Cham: Springer. 343 p.
- [3] Yang, L., Hsu, K., Baughman, B., Godfrey, F., Medina, F., Menon, M. & Wiener, S. 2017. Additive Manufacturing of Metals: The Technology, Materials, Design and Production. Cham: Springer. 168 p.
- [4] Arenas, L.F., Ponce de León, C. & Wals, F.C. 2017. 3D-printed porous electrodes for advanced electrochemical flow reactors: A Ni/stainless steel electrode and its mass transport characteristics. *Electrochemistry Communications* 77. Pp. 133-137.
- [5] Kim, E., Kim, M., Lee, J. & Pandey, B.D. 2011. Selective recovery of gold from waste mobile phone PCBs by hydrometallurgical process. *Journal of Hazardous Materials* 198. Pp. 206-215.
- [6] Kim, E., Kim, M., Lee, J., Yoo, K. & Jeong, J. 2010. Leaching behavior of copper using electro-generated chlorine in hydrochloric acid. *Hydrometallurgy* 100. Pp. 95-102.
- [7] Pletcher, D & Walsh, F.C. 1990. *Industrial Electrochemistry*. Second Edition. New York: Chapman and Hall. 661 p.
- [8] Sun, X., Lin, H., Zhang, C., Huang, X., Jin, J. & Di, S. 2019. Electrosynthesized nanostructured polypyrrole on selective laser melted titanium scaffold. *Surface & Coatings Technology* 370. Pp. 11-17.
- [9] Huang, X., Chang, S., Siang, W., Lee, W., Ding, J & Xue, J.M. 2017. Three-dimensional printed cellular stainless steel as high-activity electrode for oxygen evolution. *Journal of Materials Chemistry A* 5. Pp. 18176-18182.
- [10] Pletcher, D & Walsh, F.C. 1991. Chapter 3: Three-dimensional electrodes. *Electrochemistry for a cleaner environment*. Pp. 51-100.
- [11] Diegel, O., Nordin, A. & Motte, D. 2019. *A Practical Guide to Design for Additive Manufacturing*. Singapore: Springer. 226 p.
- [12] Gibson, I., Rosen, D. & Stucker, B. 2015. *Additive Manufacturing Technologies. 3D Printing, Rapid Prototyping, and Direct Digital Manufacturing*. Second Edition. New York: Springer. 498 p.
- [13] EOS. 2019. *Materials for Metal Additive Manufacturing*. [EOS webpage]. [Referred 17.10.2019]. Available: <https://www.eos.info/material-m>
- [14] Yang, Y., Allen, M., London, T. & Oancea, V. 2019. Residual Strain Predictions for a Powder Bed Fusion Inconel 625 Single Cantilever Part. *Integrating Materials and Manufacturing Innovation*. Pp. 1-11.
- [15] Zhang, Q., Xie, J., Gao, Z., London, T., Griffiths, D. & Oancea, V. 2019. A metallurgical phase transformation framework applied to SLM additive manufacturing process. *Materials and Design* 166. Pp. 1-18.
- [16] Deering, R.A. 2018. Additive Manufacturing Part Level Distortion Sensitivity Analysis within Abaqus on a Thin-walled, Tubular Structure. *Science in the Age of Experience 2018 Proceedings*. Pp. 1-14
- [17] Valencia, J.J & Quedsted, P.N. 2008. *Thermophysical Properties*. ASM Handbook, Volume 15: Casting. Pp. 468-481

11th CIRP Conference on Photonic Technologies [LANE 2020] on September 7-10, 2020

In-situ monitoring in L-PBF: opportunities and challenges

Bianca Maria Colosimo^a, Marco Grasso^{a,*}

^a*Politecnico di Milano, Department of Mechanical Engineering, Via La Masa 1, 20156, Milan, Italy*

* Corresponding author. Tel.: +39-02-23998560. E-mail address: marcoluigi.grasso@polimi.it

- Invited Paper -

Abstract

In the recent years, several studies and industrial developments have been devoted to the improvement of process repeatability, stability and robustness to enhance the industrial breakthrough of Additive Manufacturing (AM) technologies. Indeed, highly regulated sectors like aerospace and healthcare have been pulling the industrial innovation in metal AM, and this makes defect avoidance and qualification issues of fundamental importance. This imposes an urgent need for novel in-line and in-situ qualification and control tools able to guarantee a stable process and defect-free products. On the one hand, the layerwise paradigm of AM processes enables the capability of acquiring a large amount of data during the process to measure quality characteristics of the part and measure process signatures that are proxies of the process stability over time. On the other hand, data mining and statistical methods are needed to make sense of big data streams gathered in-line and in-situ, to design automated and robust defect detection tools. This paper reviews the opportunities and challenges related to in-situ sensing and monitoring solutions for zero-defect and first-time-right AM processes, with a special focus on metal Powder Bed Fusion (PBF) processes.

© 2020 The Authors. Published by Elsevier B.V.

This is an open access article under the CC BY-NC-ND license (<http://creativecommons.org/licenses/by-nc-nd/4.0/>)

Peer-review under responsibility of the Bayerisches Laserzentrum GmbH

Keywords: Additive Manufacturing; in-situ monitoring; in-situ sensing; defects; quality control.

1. Introduction

Considerable effort has been devoted so far in the scientific and industrial communities to understand the nature and the source of defects in additive manufacturing (AM) processes, their effects on product quality, and how they can be mitigated or avoided by acting on controllable parameters. In the framework of metal Powder bed Fusion (PBF) processes, their lack of repeatability and stability, together with several possible sources of defects, have been widely pointed out as major issues that deserve further technological advances to meet challenging industrial requirements [1-4]. The development and implementation of in-situ sensing and monitoring solutions represents a priority to push forward the industrial breakthrough of metal AM systems.

The research in this field is growing and evolving very fast. First seminal studies were mainly aimed at demonstrating the feasibility of in-situ sensing methods and characterizing specific process phenomena with the support of in-situ gathered data. More recent studies have been proposing, testing and demonstrating in-situ measurement and monitoring methodologies. An increasing interest has also been devoted to the use of machine learning and artificial neural network techniques to make sense of large in-situ data streams for robust and reliable identification of defects and process errors [5-9]. Recent studies also proposed novel in-situ sensing solutions or the combination of multiple sensors to achieve better in-situ measurement and monitoring performance [10-11].

As far as the industrial implementation of these methods is concerned, it is worth noting that most PBF system developers

have equipped their systems with in-situ sensing and monitoring modules and toolkits. Most of these tools are mainly used to collect data during the process and provide the user with some post-process data reporting and/or datasets to support the investigation of specific problems and defects. Further development efforts are still needed to implement analytical tools that are able to quickly make sense of gathered data during the process and automatically signal the onset of defects and process instabilities.

An exhaustive review of the rapidly evolving literature devoted to in-situ sensing, metrology and monitoring would require a much more extended paper. Nevertheless, this study aims to contribute to the AM community in two ways. On the one hand, it presents a framework to classify different methods and solutions presented in the literature into distinct categories in terms of monitoring levels and process signatures of interest. The increasing number of studies also caused an increasing variety of terminology and an increasing fragmentation of application fields. The proposed framework aims to simplify

the mapping of the wide literature, aiding the identification of competitor methods belonging to the same family. On the other hand, it presents a summary of issues and challenges that still need to be tackled which may drive future research developments.

Starting from the classification of in-situ sensing and monitoring methods into different levels (Section 2), Section 3 includes a brief review of the mapping between measurable signatures of the process, categories of defects and sensing solutions. Section 4 finally reviews the major challenges and open issues in this field.

2. Classification of in-situ sensing and monitoring methods

Fig. 1 shows a classification of in-situ sensing and monitoring methods into four different categories of measurable process signatures.

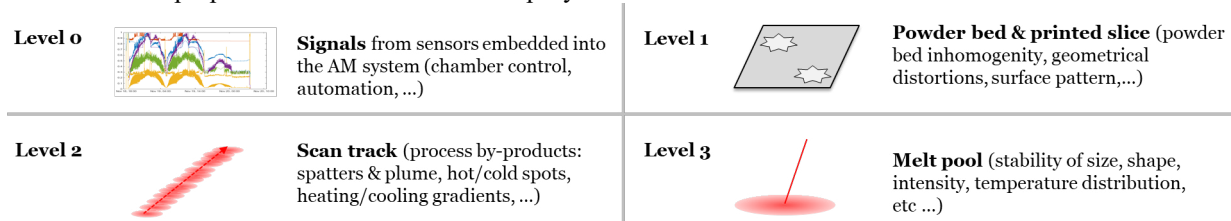


Fig. 1 – Classification of in-situ sensing and monitoring methods in PBF processes

Table 1 – Mapping between in-situ measurable signatures, sensing methods and process defects in PBF. An “X” is shown in correspondence of known relationship demonstrated in the literature, while (X) is used to represent links still not deepened in the literature or other indirect links of potential interest

Level	Process signature	In-situ sensing method	Defects					
			Porosity	Residual stresses, cracks, delaminations	Microstructural inhomogeneity	Balling	Geometrical distortions	Surface defects
1 (powder bed)	Powder bed homogeneity	Off-axis imaging, visible range	(X)	X			X	
	Slice geometry	Off-axis imaging, visible range					X	
	Slice surface pattern	Off-axis imaging, visible range, fringe projection	(X)	X		X	(X)	X
2 (track)	Hot and cold spots	Off-axis video imaging, visible or infrared range	X	X		X	X	
	Temperature profile / cooling history	Off-axis thermal imaging		X	X			
	Process by-products	Off-axis video imaging, visible or infrared range	X		(X)			
3 (melt pool)	Size	Co-axial video imaging, visible or infrared range	X	X		X		X
	Shape	Co-axial video imaging, visible or infrared range	X	X		X		X
	Average intensity	Co-axial pyrometry	X	X	(X)	X		X
	Intensity profile	Co-axial video imaging, visible or infrared range	X	X	(X)	X		X

Level 0 involves the use of signals from sensors that are already embedded into the AM system. This includes chamber pressure, temperature and oxygen content, current and torque signals from linear axis motors, etc. This type of signals potentially enables a process monitoring architecture that avoids the need for external or additional sensors. This is particularly attractive in electron beam PBF (EB-PBF), where hundreds of so-called “log signals” are freely available from embedded sensors and potentially usable in-process [12].

Level 1 consists of measurements gathered once (or more than once) per layer, with a field-of-view that covers the entire build area. This level includes quantities that are representative of the homogeneity of the powder bed, together with geometrical and dimensional features of the printed slice or its surface pattern and topography. Level 2 involves process signatures that can be measured while the laser or the electron beam is displaced within the build area to produce the current layer. This entails the capability to observe the interaction

between the beam and the material, the very fast cooling history of the solidified area after the beam has moved to another location and, in the laser PBF (L-PBF) process, the by-products of the process, i.e., spatters and plume emissions. Level 3 finally consists of process signatures that are representative of the highest level of detail at which the PBF process can be observed, i.e., the melt pool. Further classifications of in-situ sensing and monitoring methods can be considered, in terms of sensing architectures (e.g., co-axial vs off-axis monitoring), sensing technologies (spatially integrated vs spatially resolved sensors), wavelength of the measured quantities (visible range, near infrared, middle and long infrared), etc. The reader is referred to [1-4] for an exhaustive classification of in-situ sensing and monitoring approaches.

3. Mapping between in-situ sensing, process signatures and process defects

Table 1 presents a mapping between the process signatures that can be measured in-situ, the corresponding defects that can be detected and the most suitable sensing methods. The relationships indicated with “X” have been already discussed and demonstrated in the literature through experimental studies. Some relationships, indicated with “(X)”, represent links between defects and process signatures that have not been yet demonstrated in the literature. Despite being of potential interest, they still need to be confirmed through further research.

Embedded sensor signals (level 0) have been pointed out as possible sources of information in EB-PBF to gather information about the powder spreadability [13] and the occurrence of geometrical distortions caused by powder recoating errors [14], but various other potential uses have been pointed out in the literature and they can be explored in future studies [12]. Analogous solutions in L-PBF have been not explored so far.

A lack of powder bed homogeneity (level 1) may change the local layer thickness leading to possible volumetric and geometrical defects because of improper energy density variations. Errors in the powder recoating of the slice can also lead to poor welding between one layer and the following layer, with consequent risk of delamination, together with possible geometrical distortion in the presence of severe recoating errors and contamination. Different authors have investigated in-situ sensing and monitoring methods suitable to characterize the surface pattern and surface topography of the printed slice and the entire powder bed as a possible source of information about process stability and surface and volumetric defects [10, 15-16]. The in-situ reconstruction of the layerwise geometry of the part has attracted an increasing attention in the literature too, to quickly detect geometrical distortions [17-18]. Regarding level 2 process signatures, the detection of hot and cold spots may be suitable to identify either geometrical distortions (in case of excessive heat accumulations) or lack-of-fusion conditions [19-20]. Static and dynamic thermal mapping through in-situ thermography can provide information about geometrical distortions, variations in the microstructure of the part and thermal stress accumulation related to improper heat exchanges [21]. An increasing attention in the literature has been devoted

to the use of process by-products, such as spatter and plume emissions in L-PBF, as potential proxies of volumetric defects [11, 22 – 27]. Spatters are caused by an ejection of material from the melt pool and the surrounding powder bed, leading to the formation of denudation zones around the melt pool and a possible lack of material in the solidified track, which may influence the formation of pores. Large and intense plume emissions may partially absorb and deflect the laser beam reducing the energy input provided to the part, with consequent lack-of-fusion porosity.

Several information about the process stability and the part quality can be gathered by monitoring the melt pool signatures (level 3) and their evolution over time. Indeed, the melt pool properties are relevant to determine the possible formation of volumetric defects (both key-hole and lack-of-fusion porosity), thermal stress accumulation because of insufficient heat dissipation and surface defects related to the solidification properties of scanned tracks [5, 28].

4. Open issues and future challenges

Despite continuous and fast technological developments related to in-situ sensing and monitoring methods, several challenges and open issues must be faced to develop new generations of smart PBF machines able to achieve first-time-right and zero-defect production capabilities [1, 29].

One challenge regards the limitation of the layerwise monitoring paradigm. Indeed, looking at the current layer prevents the gathering of information about physical phenomena that are occurring below the layer, involving partial re-melting, heat accumulation and dissipation, and consequent effects on volumetric, microstructural and thermal stress properties of the material. Another challenge regards the lack of robust in-situ porosity detection methods. Volumetric defects are particularly critical in many industrial applications, but accurate methods – so called “optical tomography” – for their robust identification by means of in-situ sensors are still missing. Several process signatures can be used as proxies of either lack-of-fusion or key-hole porosity, but further research efforts are needed to achieve robust in-situ porosity detection capabilities. One additional challenge regards the management of big data streams gathered with in-situ sensing methods. Several gigabytes of data may be generated during the production of a part, and this pushes the need for computationally efficient methodologies for in-situ and in-process data processing. There is also the need for transfer learning solutions, suitable to transfer knowledge and empirical models gathered on one part by using one AM system to other parts produced with the same machine or with different machines. As an example, it would be relatively convenient to carry out experimental conditions in a limited and controlled set of process conditions, and to transfer the acquired knowledge to other conditions, reducing experimental costs and time-to-market. However, this is still an open issue, inflated by the large system-to-system and lab-to-lab variability that characterizes metal AM applications. Only a small number of seminal studies have investigated the application of transfer learning methods to AM [30]. One interesting opportunity for future research regards the development and implementation of cyber-physical

approaches. Process simulations have a great potential as technological enablers of novel enhanced AM performance and zero-defect production capabilities. As an example, simulations enable feedforward control strategies for local process parameter adjustment, but they also allow the development of in-situ monitoring methods augmented by process simulations, and vice versa. The combination of real data with process simulation is a field that deserves novel and additional research effort. Eventually, the achievement of zero-defect and first-time-right production capabilities relies not only on in-situ sensing and monitoring technologies, but also on effective and robust process control strategies. Despite seminal studies on closed-loop control in L-PBF and a few recent developments [31], a wide gap still needs to be filled in order to make intelligent control solutions industrially available. Rather than adapting the process parameters based on model outputs or real-time sensor signals, other in-situ defect mitigation or defect correction solutions have been proposed in the literature [32–35]. In-situ defect correction represents a further research field that may contribute to the development of novel generations of smart AM systems, passing from highly sensorised machines to intelligent machines that are able to autonomously identify and remove the defect.

References

- [1] Colosimo, B. M., Huang, Q., Dasgupta, T., and Tsung, F. 2018. Opportunities and challenges of quality engineering for additive manufacturing. *J. Qual. Technol.*, 50: 233–252.
- [2] Grasso M., Colosimo B.M., 2017, Process defects and in-situ monitoring methods in metal powder bed fusion: a review, *Meas. Sci. Technol.*, 28: 1–25.
- [3] Mani, M., Lane, B. M., Donmez, M. A., Feng, S. C., and Moylan, S. P. 2017. A review on measurement science needs for real-time control of additive manufacturing metal powder bed fusion processes. *Int. J. Prod. Res.*, 55: 1400–1418.
- [4] Everton, S. K., Hirsch, M., Stravroulakis, P., Leach, R. K., and Clare, A. T. 2016. Review of in-situ process monitoring and in-situ metrology for metal additive manufacturing. *Mater. Des.*, 95: 431–445.
- [5] Kwon, O., Kim, H. G., Ham, M. J., Kim, W., Kim, G. H., Cho, J. H., ... and Kim, K. 2018. A deep neural network for classification of melt-pool images in metal additive manufacturing. *J. Intell. Manuf.*, 1–12.
- [6] Gobert, C., Reutzel, E.W., Petrich, J., Nassar, A.R., Phoha, S., 2018. Application of supervised machine learning for defect detection during metallic powder bed fusion additive manufacturing using high resolution imaging. *Addit. Manuf.* 21: 517–528.
- [7] Okaro, I. A., Jayasinghe, S., Sutcliffe, C., Black, K., Paoletti, P., and Green, P. L. 2019. Automatic fault detection for laser powder-bed fusion using semi-supervised machine learning. *Addit. Manuf.*, 27: 42–53.
- [8] Wasmer, K., Le-Quang, T., Meylan, B., and Shevchik, S. A. 2019. In situ quality monitoring in am
- [9] Scime, L., Beuth, J., 2018. Anomaly detection and classification in a laser powder bed additive manufacturing process using a trained computer vision algorithm. *Addit. Manuf.* 19: 114–126.
- [10] Tan Phuc, L., Seita, M. 2019. A high-resolution and large field-of-view scanner for in-process characterization of powder bed defects during additive manufacturing. *Mater. Des.*, 164: 107562.
- [11] Barrett, C., Carradero, C., Harris, E., McKnight, J., Walker, J., MacDonald, E., and Conner, B. 2018. Low cost, high speed stereovision for spatter tracking in laser powder bed fusion, Proc. 29th Annual International Solid Freeform Fabrication Symposium, Austin, Texas, USA, August.
- [12] Steed, C. A., Halsey, W., Dehoff, R., Yoder, S. L., Paquit, V., & Powers, S. 2017. Falcon: Visual analysis of large, irregularly sampled, and multivariate time series data in additive manufacturing. *Computers & Graphics*, 63, 50–64.
- [13] Chandrasekar, S., Coble, J. B., Yoder, S., Nandwana, P., Dehoff, R. R., Paquit, V. C., & Babu, S. S. 2020. Investigating the effect of metal powder recycling in Electron beam Powder Bed Fusion using process log data. *Additive Manufacturing*, 32, 100994.
- [14] Grasso M., Gallina F., Colosimo B.M. 2018b, Data fusion methods for statistical process monitoring and quality characterization in metal additive manufacturing, 15th CIRP Conference on Computer Aided Tolerancing, Milan, Italy.
- [15] Foster, B. K., Reutzel, E. W., Nassar, A. R., Hall, B. T., Brown, S. W., and Dickman, C. J. 2015. Optical, layerwise monitoring of powder bed fusion. Proc. 26th Annual International Solid Freeform Fabrication Symposium, Austin, Texas, USA, August.
- [16] Zhang, B., Ziegert, J., Farahi, F., and Davies, A. 2016. In situ surface topography of laser powder bed fusion using fringe projection. *Addit. Manuf.*, 12: 100–107.
- [17] Aminzadeh, M. 2016. A machine vision system for in-situ quality inspection in metal powder-bed additive manufacturing, Doctoral dissertation, Georgia Institute of Technology.
- [18] Caltanissetta, F., Grasso, M., Petró, S., Colosimo, B. M. 2018. Characterization of in-situ measurements based on layerwise imaging in laser powder bed fusion, *Addit. Manuf.*, 24: 183–199
- [19] Grasso, M., Laguzza, V., Semeraro, Q., and Colosimo, B. M. 2016. In-process monitoring of selective laser melting: spatial detection of defects via image data analysis. *J. Manuf. Sci. Eng.*, 139: 051001-1 –051001-16.
- [20] Colosimo, B.M., Grasso, M. 2018, Spatially weighted PCA for monitoring video image data with application to additive manufacturing, *J. Qual. Technol.*, 50: 391–417
- [21] Raplee, J., Plotkowski, A., Kirka, M.M., Dinwiddie, R., Okello, A., Dehoff, R.R., Babu, S.S. 2017, Thermographic microstructure monitoring in electron beam additive manufacturing, *Nature Sci. Rep.*, 7:43554.
- [22] Repossini G., Laguzza V., Grasso M., Colosimo B.M., 2018, On the use of spatter signature for in-situ monitoring of laser powder bed fusion, *Addit. Manuf.*, 16: 35–48.
- [23] Grasso, M., Demir, A.G., Previtali, B., Colosimo, B.M. 2018a, In-situ monitoring of selective laser melting of zinc powder via infrared imaging of the process plume, *Rob. Comput. Integr. Manuf.*, 49: 229–239
- [24] Grasso, M., Colosimo, B.M. 2019, A statistical learning method for image-based monitoring of the plume signature in laser powder bed fusion, *Rob. Comput. Integr. Manuf.*, 57: 103–115
- [25] Eschner, E., Staudt, T., & Schmidt, M. 2019. 3D particle tracking velocimetry for the determination of temporally resolved particle trajectories within laser powder bed fusion of metals. *Int. J. of Extr. Manuf.*, 1: 035002.
- [26] Nassar, A. R., Gundermann, M. A., Reutzel, E. W., Guerrier, P., Krane, M. H., and Weldon, M. J. 2019. Formation processes for large ejecta and interactions with melt pool formation in powder bed fusion additive manufacturing. *Sci. Rep.*, 9: 1–11.
- [27] Zhang, Y., Fuh, J. Y., Ye, D., & Hong, G. S. 2019. In-situ monitoring of laser-based PBF via off-axis vision and image processing approaches. *Addit. Manuf.*, 25: 263–274
- [28] Kolb, T., Mahr, A., Huber, F., Tremel, J., and Schmidt, M. 2019. Qualification of channels produced by laser powder bed fusion: Analysis of cleaning methods, flow rate and melt pool monitoring data. *Addit. Manuf.*, 25: 430–436.
- [29] Colosimo, B. M. 2018. Modeling and monitoring methods for spatial and image data. *Qual. Eng.*, 30: 94–111.
- [30] Sabbaghi, A., and Huang, Q. 2018. Model transfer across additive manufacturing processes via mean effect equivalence of lurking variables. *Ann. Appl. Stat.*, 12: 2409–2429.
- [31] Renken, V., von Freyberg, A., Schünemann, K., Pastors, F., and Fischer, A., 2019. In-process closed-loop control for stabilising the melt pool temperature in selective laser melting. *Progr. Addit. Manuf.*, 1–11.
- [32] Colosimo, B.M., Grossi, E., Caltanissetta, F., Grasso, M. 2019. PENELOPE: a new solution for in-situ monitoring and defect removal in L-PBF. Proc. 30th Annual International Solid Freeform Fabrication Symposium, Austin, Texas, USA, August.
- [33] Grasso, M., Caltanissetta, F., Colosimo, B.M., 2019. A novel self-repairing additive manufacturing system for in-situ defects detection and correction, Proc. Euspen, Bilbao, Spain, June.
- [34] Heeling, T., and Wegener, K. 2018. The effect of multi-beam strategies on selective laser melting of stainless steel 316L. *Addit. Manuf.*, 22: 334–342.
- [35] Mireles, J., Ridwan, S., Morton, P. A., Hinojos, A., and Wicker, R. B. 2015a. Analysis and correction of defects within parts fabricated using powder bed fusion technology. *Surf. Topogr. Metrol. Prop.*, 3: 034002

11th CIRP Conference on Photonic Technologies [LANE 2020] on September 7-10, 2020

Analysis of time, frequency and time-frequency domain features from acoustic emissions during Laser Powder-Bed fusion process

Vigneashwara Pandiyan^a, Rita Drissi-Daoudi^b, Sergey Shevchik^a, Giulio Masinelli^a, Roland Logé^b, Kilian Wasmer^{a,*}

^a *Laboratory for Advanced Materials Processing (LAMP), Swiss Federal Laboratories For Materials Science and Technology (Empa), CH-3602 Thun, Switzerland*

^b *Thermomechanical Metallurgy Laboratory – PX Group Chair, Ecole Polytechnique Fédérale de Lausanne (EPFL), CH-2002 Neuchâtel, Switzerland*

* Corresponding author. Tel.: +41-58-762-62-71; fax: +41-58-762-69-90. E-mail address: kilian.wasmer@empa.ch

Abstract

Sensor integration for in situ monitoring during additive manufacturing promises to enhance control over the process and assures quality in the fabricated workpieces. Acoustic emissions from the process zone of the laser powder-bed fusion process carry information about the events and failure modes of the printed workpiece. Analysis of acoustic signals emitted during different laser regimes, such as conduction, keyhole, etc. in time, frequency and time-frequency domains could provide quantitative information about the underlying physical mechanisms. This article reports a statistical analysis of the features in acoustic signals to perceive the characteristics of failure modes occurring during layering of stainless steel 316L. The visualization of the feature space distribution that corresponds to different failure modes shows the potentials of applying machine learning for in situ classification. The paper also proposes strategies in terms of data acquisition and preprocessing for building a comprehensive monitoring system.

© 2020 The Authors. Published by Elsevier B.V.

This is an open access article under the CC BY-NC-ND license (<http://creativecommons.org/licenses/by-nc-nd/4.0/>)

Peer-review under responsibility of the Bayerisches Laserzentrum GmbH

Keywords: Laser material processing; In-situ monitoring; Signal processing; Sensing; Additive manufacturing;

1. Introduction

Laser Powder-Bed Fusion (LPBF) is an additive manufacturing technique where the laser source melts the particles in the powder pool to fuse together. The laser beam selectively melts the powder-bed that is previously overlaid on the substrate through an arrangement of mirrors based on pre-programmed scan paths. During manufacturing, the powder is added layer by layer and each layer is exposed to irradiation of the laser source, resulting in the workpiece built one layer upon another [1]. In LPBF, process interaction of laser with powder particles results in complex physics such as radiation absorption [2], rapid melting, solidification of material, microstructure evolution [3], flow in a molten pool [4] and materials evaporation. The choice of parameters such as laser

power, powder composition, scan speed and strategy, layer thickness, environment, etc. affects the physics involved, thus affecting the quality of the fabricated workpieces [5–7].

To ensure the quality of printing in each layer, the starting powder and the process parameters are overseen. Not adhering to the optimum parameter levels and abrupt change in environmental conditions will result in the occurrence of undesired mechanisms such as balling, Lack of Fusion (LoF) crack propagation, delamination and formation of pores. Balling and LoF mainly occur due to the shortage of energy input during the LPBF process [8], while the formation of pores is the result of entrapped gases in the molten pool due to the excessive pumping of energy input [9]. Since defect formation is a critical issue in an LPBF process, researches have been directed towards understanding and suppression of defect

formation. To describe and to understand these mechanisms of the LPBF process, more accurate monitoring and overlooking of the process using sensors have been proposed as a strategy [10,11]. Regardless of the type of sensor used in LPBF, owing to the process nature, one primary characteristic feature that these sensors should possess is that they should have a fast response time and a high spatial resolution.

Furomoto *et al.* [12] have correlated the solidification phenomena with the surface temperature using a pyrometer to understand the solidification mechanism of the molten pool. In-situ monitoring method based on infrared imaging of the melt pool has been demonstrated for detecting unstable behaviors in the process [13]. Semiconductor (CMOS) cameras and photodiodes have been used to understand the melt pool dynamics and to detect process failures [14–17]. Acoustic emission (AE) has also been combined with machine learning (ML) algorithms for defect detection, such as pores [18,19]. AE and high speed X-ray radiography allowed to classify accurately categories such as conduction, stable and unstable keyhole, blowout and even pore formation and removal [20,21]. A defect detection system using a deep belief network (DBN) has also been reported to classify balling and other mechanisms based on microphone data [22].

With melt pools dimensions ranging from 50 to 250 μm wide appearing in a few microseconds, monitoring LPBF using visual and optical sensors that lack in spatial and temporal resolution is difficult. Processing of the data from these sensors also require heavy computational resource. AE sensors are a suitable alternative as they have reliable temporal resolution [23] and are also an economical solution for monitoring the additive manufacturing process [24]. Also, installation of AE monitoring system requires minimum alteration to the existing commercial machines available in the market [18,19].

Stainless steel alloys have low thermal conductivity and high thermal expansion coefficient, making them prone to mechanisms such as cracks, porosity, balling, etc. The work presented in this paper analyses characteristics of acoustic signals in three domains, namely time, frequency and time-frequency for four mechanisms or laser regimes. They are *balling*, *LoF*, *no pores* and *keyhole* during the processing of stainless steel 316L. Thus, *t*-Distributed Stochastic Neighbor Embedding (*t*-SNE) based feature reduction technique is applied to the features extracted from three domains to visualize the low dimensional feature space. Understanding the information embedded in the sensor signals and resolving them will help to identify the physics and so rises the building of in situ monitoring and virtual verification systems.

2. Experimental conditions and setup

The quality of the workpieces fabricated during the LPBF depends on the characteristics of the melted process zone in each layer. In this study, gas atomized austenitic steel 316L powder was used for building line tracks during the experiments. Most particles in the powder-bed had a diameter no larger than 45 μm . The stainless steel powder composition used in this study is listed in Table 1. The line track experiments were carried out by spreading stainless steel 316L metal powder with a thickness of 40 μm over a defect-free 3D

printed cube using a re-coater blade in a customized setup shown schematically in Fig. 1. A continuous-wave laser of 1070 \pm 10nm wavelength with a spot size of 72 μm is used to irradiate the powder to create overlapping line tracks. The physical mechanisms resulting from different laser interaction regimes are known to depend on the energy density. The energy density E is defined from parameters such as laser power P , hatch distance h , and powder layer thickness t . The energy density is the average applied energy per volume of material during a powder-bed fusion process according to Eq. (1).

Table 1. Composition of austenitic steel 316L powder

Weight Percent (nominal)					
Fe	Cr	Ni	Mo	C	Other
Balance	18	122	2	< 0.03	< 1.00

$$E = \frac{P}{V \cdot h \cdot t} \quad (1)$$

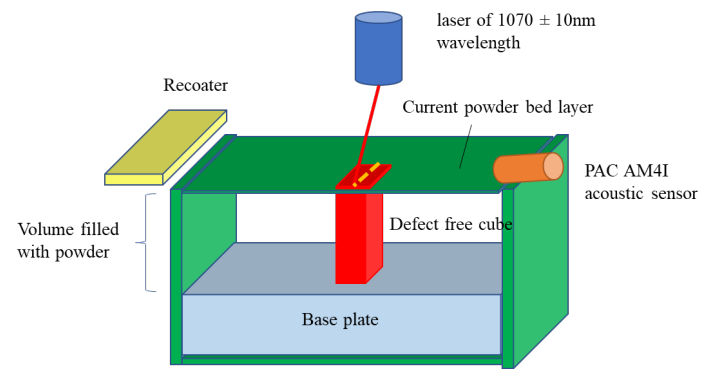


Fig. 1. Schematic of the experimental setup.

In this contribution, the phenomena occurring during the LPBF process, in particular *balling*, *LoF*, *no pores* and *keyhole* were voluntarily induced by varying the scan speed and the laser power and so the energy density (E) according to Fig. 2.

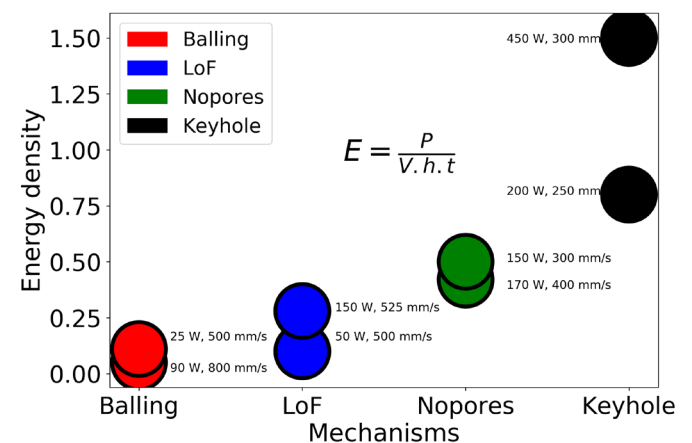


Fig. 2. The laser regimes used in this work with their corresponding energy density for *balling*, *LoF*, *no pores* and *keyhole*

The four mechanisms (*balling*, *LoF*, *no pore* and *keyhole*) or their respective laser regimes were confirmed by visual inspection of optical images of cross-sections of the line tracks built on a defect-free surface. Typical light microscopy images corresponding to the laser regimes are presented in Fig. 3.

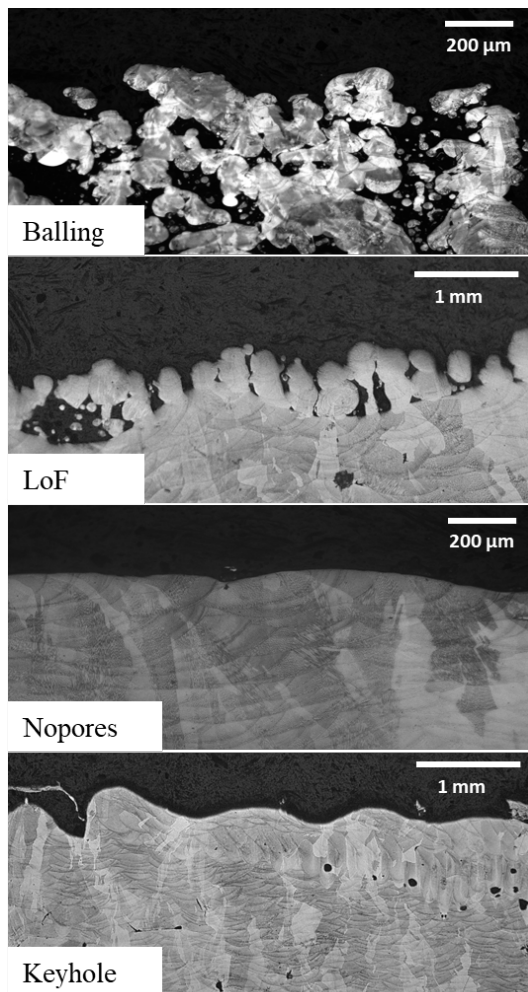


Fig. 3. Light microscopy images for *balling*, *LoF*, *no pores* and *keyhole*

The acoustic waves created during the different laser regimes were captured using a PAC AM4I acoustic sensor with a frequency range of 0-100 kHz. The acoustic sensor was placed at the proximity of the build platform, and the sampling rate was 1 MHz using an Advantech DAQ board. A low pass Butter-worth filter of 100 kHz was applied to the raw signal to eliminate noises with frequencies higher than 100 kHz. The analysis of the acoustic signatures is discussed in Section 3.

3. Analysis of the acoustic features in time, frequency and time-frequency domains

Typical acoustic signals corresponding to the four mechanisms with a window size of 5000 μ s are presented in Fig. 4. As can be noted, signal amplitude increases from *balling* to *keyhole* and the amplitude values are directly proportional to energy density imparted on the melt zone.

3.1. Time-domain

Descriptive statistics features from time waveform signals such as Root Mean Square (RMS), mean, skewness, kurtosis crest-power, etc. were also analyzed and visualized to understand their distribution with respect to the four different mechanisms. The time-domain features were calculated for a window size of 5000 μ s.

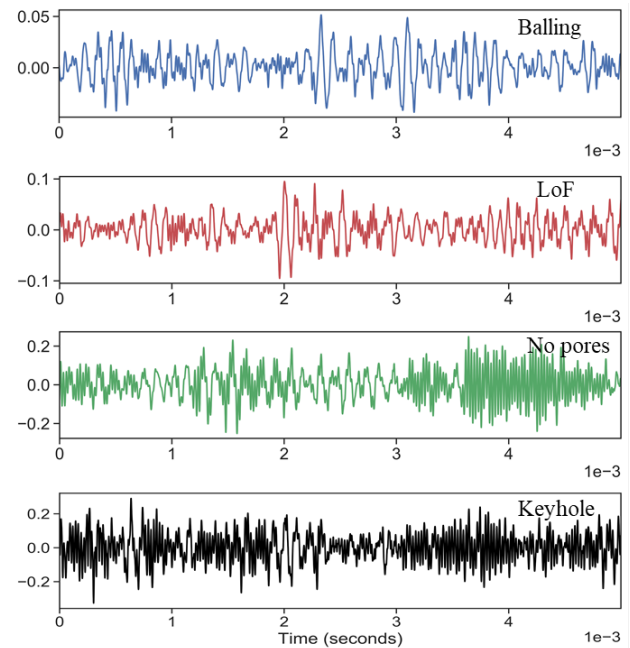


Fig. 4. Raw acoustic signals acquired for four different mechanisms: *balling*, *LoF*, *no pores* and *keyhole*

Fig. 5 and Fig. 6 show the distribution of the skewness and RMS feature for the laser regimes studied. The skewness distribution shows that skewness statistics are not identical for these mechanisms. However, the RMS feature distribution of *balling* and *LoF* had a good similarity index. Close similarity was also found between *no pores* and *keyhole*. From Fig. 6, we can infer that RMS feature distribution is a function of scanning speed and laser power. Analysis of other time features such as crest-power, kurtosis, etc. also showed dissimilar distribution between the mechanisms.

3.2. Frequency domain

The analysis of the acoustic signature in the frequency domain provided intriguing insights. The frequency range (0-100 kHz) of the acoustic sensor was divided equally into five energy bands, namely 0-20 kHz, 20-40 kHz, 40-60 kHz, 60-80 kHz, and 80-100 kHz as shown in Fig. 7. Most of the energy was concentrated around 60 kHz. For *balling* and *LoF*, the energy level concentration was predominant in the frequency range of 0-20 kHz. However, for *no pores* and *keyhole*, the energy level concentration was spread between three energy bands; they are 0-20 kHz, 20-40 kHz and 40-60 kHz. From the energy distribution, it is evident that the laser interaction with the molten pool results in higher frequency events. Fig. 8 shows a comparison of Fast Fourier Transforms (FFT) for the four mechanisms. Irrespectively of the mechanisms or laser regimes, distinct peaks were found around 10 kHz and 40 kHz for the acoustic signals acquired during the laser interaction with the stainless steel powder. From the FFT, it can be inferred that during *balling* and *LoF*, the energy content in the range of 10 kHz are higher than the one around 40 kHz and vice-versa as we move to mechanisms such as *no pores* and *keyhole*. The high frequency components visible in the AE signatures during *no pores* and *keyhole* regimes may be the result of recoil pressure and vapor interaction with the molten material.

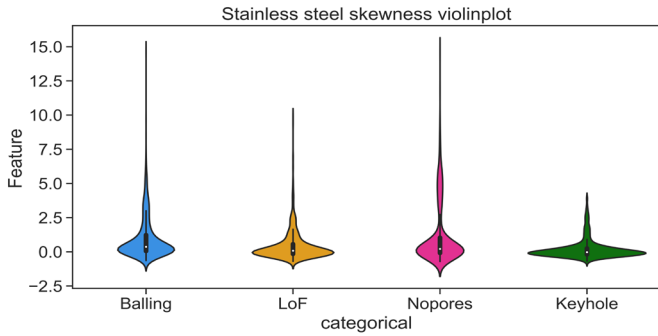


Fig. 5. Skewness distributions of the four different mechanisms

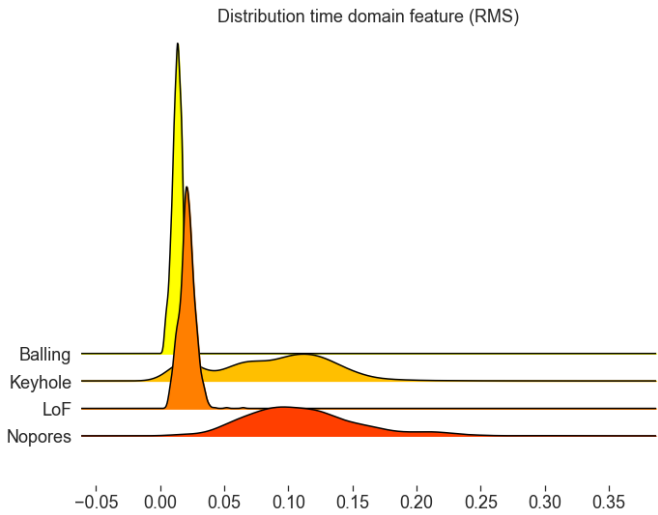


Fig. 6. Distributions of RMS feature for four different mechanisms

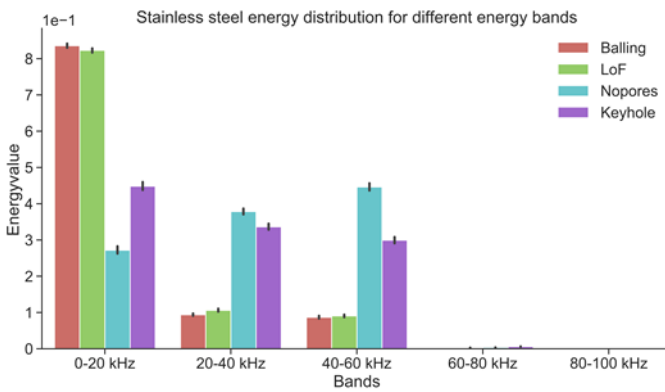


Fig. 7. Comparison of energy density between five different energy bands for the four mechanisms: *balling*, *LoF*, *no pores* and *keyhole*.

3.3. Time-Frequency domain

The acoustic signals were resolved using wavelet transformation to visualize their representation in both the time and frequency domains. The wavelet transformation was also performed on the filtered acoustic signals for a window size of 5000 μ s. Continuous Wavelet Transformation (CWT) was performed on the acoustic signals using Morlet as mother wavelet with 500 scales. The 3D representation of the wavelet transforms is shown in Fig. 9. The time-frequency representation of the acoustic signals also confirmed with the outcomes of the study performed with the frequency domain analysis in Section 3.3.

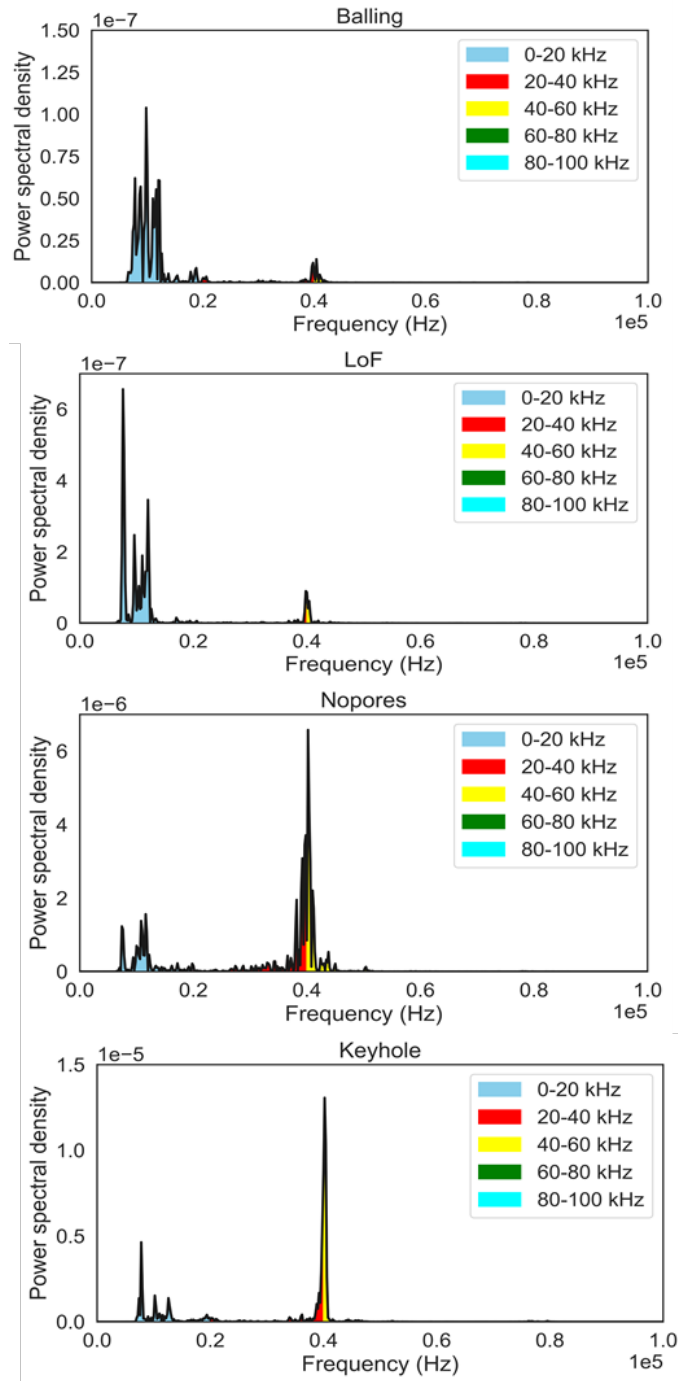


Fig. 8. Fast Fourier Transform (FFT) plots for the four mechanisms: *balling*, *LoF*, *no pores* and *keyhole*.

Wavelet coefficient values were found to be higher at more or less 10 kHz and 40 kHz for the acoustic signals irrespective of the processing mechanism when the laser interacted with the stainless steel powder. In addition, wavelet coefficient values were also found to be directly proportional to the energy density imparted on the process zone, and evidence of this is in Fig. 9. Resolving the signal time-frequency domain also showed that though the mechanisms concentrated in frequencies around 10 kHz and 40 kHz, they appeared discontinuous in the form of distinct peaks. The discontinuity emphasizes on the choice of the window size to localize the defect during the part printing as well the resolution of the predictability of ML algorithms.

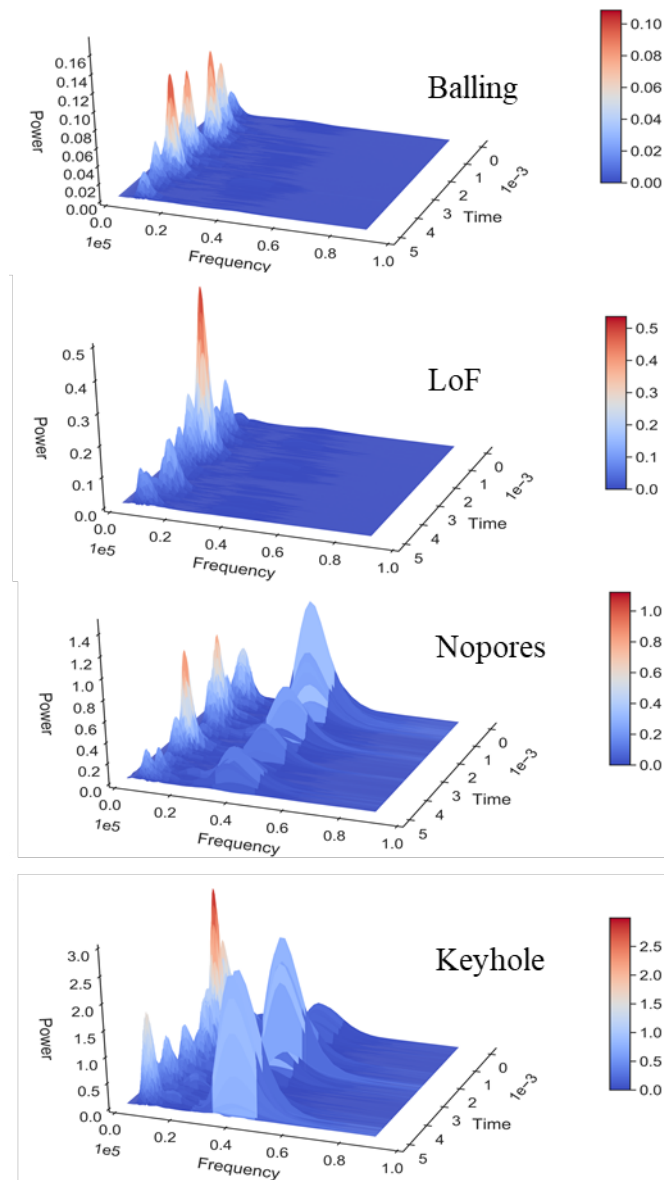


Fig. 9. 3D wavelet representation of the acoustic signals for the four mechanisms (*balling*, *LoF*, *no pores* and *keyhole*).

4. Visualization of the feature space

t-Distributed Stochastic Neighbor Embedding (*t*-SNE) is a non-linear dimensionality reduction technique that is employed for identifying relevant patterns and visualization of high-dimensional feature space [25]. The *t*-SNE technique maps the multi-dimensional data to a lower-dimensional space by modeling the probability distribution of neighbors around each point and provides some insights into the data space by identifying the clusters. In other words, *t*-SNE is mainly a data exploration, and a visualization technique as the input features become no longer identifiable, and one cannot make any inference. However, *t*-SNE is better than Principle Component Analysis (PCA) since *t*-SNE preserves the local similarities, whereas PCA is concerned with preserving large pairwise and fails to represent a non-linear data space [25].

The time, frequency and time-frequency features listed in Table 2 were used as inputs to the *t*-SNE algorithm. A perplexity value of 10 was used to understand the feature space

distribution on the sensor data captured during the four mechanisms (*balling*, *LoF*, *no pores* and *keyhole*) during the line track experimental trials. Fig. 10 shows the 3-dimensional representation of the feature space. From Fig. 10, it can be inferred that *no pores* and *keyhole* are clustered together from *balling* and *LoF*, i.e., the clusters visualized in the feature space were proportional to the energy density imparted in the melt zone.

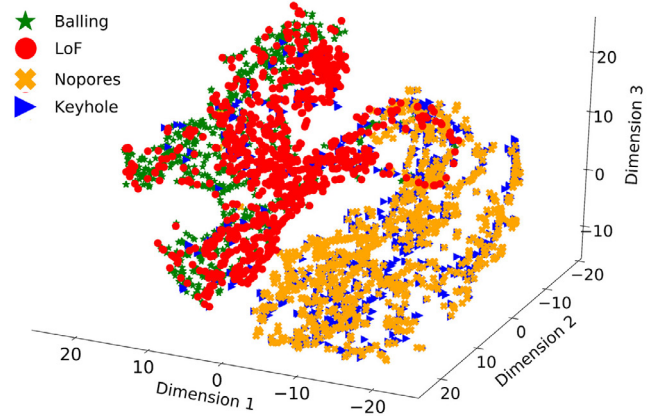


Fig. 10. Low dimension representation of the feature space using *t*-SNE with perplexity = 10 for the four mechanisms (*balling*, *LoF*, *no pores* and *keyhole*) in the LPBF process.

Table 2. Features for input to *t*-SNE with perplexity = 10.

Domain	Feature
Time	Mean, RMS, Kurtosis, Skewness, Crest factor, Standard deviation, Minimum, Maximum, etc
Frequency	Position of peaks with high intensity, Energy distribution in respective energy bands
Time-Frequency (Wavelet)	Enthalpy, RMS, Kurtosis, Skewness, Standard deviation in respective decomposition levels, etc.

5. Conclusions

The proposed work aims to quantify and characterize the acoustic sensor signatures in three domains (time, frequency and time-frequency domains) for four laser regimes which are *balling*, *LoF*, *no pores* and *keyhole* that commonly occur in the LPBF process. The experimental work was performed on the stainless steel powder 316L in a customized setup. The four different mechanisms/laser regimes were simulated by varying the scanning speed and laser power. Based on the experimental results, the following generalized conclusions are drawn for a window size of 5000 μ s for acoustic signals captured with an acquisition rate of 1 MHz. The main results of this study can be summarized in four aspects.

- As all the four mechanisms are functions of the energy density, the sensor features in the time domain, such as skewness and RMS, had different distributions. From the distribution of the time domain features, we can confirm that the mechanisms have a direct relationship with the energy density, emphasizing on the optimum choice of the laser power and scanning speed for a good build.

- Comparing the energy concentration between five different bands equally divided within the range 0-100 kHz, it was evident that these four mechanisms (*balling*, *LoF*, *no pores* and *keyhole*) exhibit discrete energy levels. It is important to note that the frequency bands between 1 kHz and 60 kHz carried most of the energy. The FFT plots pointed out that as the laser interacted with the stainless steel powder, the acoustic signal showed a higher energy concentration around 10 kHz and 40 kHz.
- Peaks from the wavelet plot indicated that the event is discontinuous, and an appropriate choice of the window size is required to localize the defects in real-time.
- *t*-SNE feature reduction technique suggested that these mechanisms are clustered in the feature space and appropriated classification algorithm can be used to individualize them. The visualization also endorses the fact that clustering is based on energy density.

In general, the outcomes of this research confirm that the features in time, frequency and time-frequency domains can characterize the four defined mechanisms that commonly occur during the LPBF process. Out of all the events happening in the process zone, only four mechanisms (*balling*, *LoF*, *no pores* and *keyhole*) are discussed in this research work. The window size used in this study is of 5000 μ s in time scale, however for finer resolution and location of the defects a smaller time scales have to be explored which is a work in progress. It must also be mentioned that the acoustic sensor used in this work had a working range of 0-100 kHz and the understanding of the phenomenon at frequencies higher than 100 kHz is a work under investigation. The exploration of frequencies associated with other events such as delamination, crack propagation and microstructure evolution is also part of our future work.

References

- [1] W.E. King, A.T. Anderson, R.M. Ferencz, N.E. Hodge, C. Kamath, S.A. Khairallah, A.M. Rubenchik, Appl. Phys. Rev. 2 (2015) 41304, DOI:10.1063/1.4937809.
- [2] J. Trapp, A.M. Rubenchik, G. Guss, M.J. Matthews, Appl. Mater. Today. 9 (2017) 341–349, DOI:10.1016/j.apmt.2017.08.006.
- [3] R. Acharya, J.A. Sharon, A. Staroselsky, Acta Mater. 124 (2017) 360–371, DOI:10.1016/j.actamat.2016.11.018.
- [4] W.E. King, H.D. Barth, V.M. Castillo, G.F. Gallegos, J.W. Gibbs, D.E. Hahn, C. Kamath, A.M. Rubenchik, J. Mater. Process. Technol. 214 (2014) 2915–2925. DOI:10.1016/j.jmatprotec.2014.06.005.
- [5] Z.Y. Chua, I.H. Ahn, S.K. Moon, Int. J. Precis. Eng. Manuf. Technol. 4 (2017) 235–245, DOI:10.1007/s40684-017-0029-7.
- [6] M. Van Elsen, Complexity of selective laser melting : a new optimization approach, 2007.
- [7] T.G. Spears, S.A. Gold, Integr. Mater. Manuf. Innov. (2016), DOI:10.1186/s40192-016-0045-4.
- [8] H. Gong, K. Rafi, H. Gu, T. Starr, B. Stucker, Addit. Manuf. 1–4 (2014) 87–98, DOI:10.1016/j.addma.2014.08.002.
- [9] N.T. Aboulkhair, N.M. Everitt, I. Ashcroft, C. Tuck, Addit. Manuf. 1–4 (2014) 77–86, DOI:10.1016/j.addma.2014.08.001.
- [10] S.A. Shevchik, C. Kenel, C. Leinenbach, K. Wasmer, Addit. Manuf. (2017), DOI:10.1016/j.addma.2017.11.012.
- [11] S.K. Everton, M. Hirsch, P. Stravroulakis, R.K. Leach, A.T. Clare, Mater. Des. 95 (2016) 431–445, DOI:10.1016/j.matdes.2016.01.099.
- [12] T. Furumoto, T. Ueda, M.R. Alkahari, A. Hosokawa, CIRP Ann. - Manuf. Technol. 62 (2013) 223–226, DOI:10.1016/j.cirp.2013.03.032.
- [13] M. Grasso, A.G. Demir, B. Previtali, B.M. Colosimo, Robot. Comput. Integr. Manuf. 49 (2018) 229–239, DOI:10.1016/j.rcim.2017.07.001.
- [14] J.-P. Kruth, P. Mercelis, J. Van Vaerenbergh, T. Craeghs, Proc. 3rd Int. Conf. Adv. Res. Virtual Rapid Prototyp. (2007) 521–527.
- [15] T. Craeghs, S. Clijsters, E. Yasa, F. Bechmann, S. Berumen, J.-P. Kruth, Opt. Lasers Eng. 49 (2011) 1440–1446, DOI:10.1016/j.optlaseng.2011.06.016.
- [16] S. Clijsters, T. Craeghs, S. Buls, K. Kempen, J.-P. Kruth, Int. J. Adv. Manuf. Technol. 75 (2014) 1089–1101, DOI:10.1007/s00170-014-6214-8.
- [17] F. Vakili-Farahani, J. Lungershausen, K. Wasmer, J. Laser Appl. 29 (2017) 22424, DOI:10.2351/1.4983507.
- [18] S.A. Shevchik, G. Masinelli, C. Kenel, C. Leinenbach, K. Wasmer, IEEE Trans. Ind. Informatics. 15 (2019) 5194–5203, DOI:10.1109/TII.2019.2910524.
- [19] K. Wasmer, T. Le-Quang, B. Meylan, S.A. Shevchik, J. Mater. Eng. Perform. 28 (2019) 666–672, DOI:10.1007/s11665-018-3690-2.
- [20] K. Wasmer, T. Le-Quang, B. Meylan, M. Olbinado, A. Rack, S.A. Shevchik, Procedia CIRP. (2018), DOI:10.1016/j.procir.2018.08.054.
- [21] S. Shevchik, T. Le-Quang, B. Meylan, F.V. Farahani, M.P. Olbinado, A. Rack, G. Masinelli, C. Leinenbach, K. Wasmer, Sci. Rep. 10 (2020) 3389, DOI:10.1038/s41598-020-60294-x.
- [22] D. Ye, G.S. Hong, Y. Zhang, K. Zhu, J.Y.H. Fuh, Int. J. Adv. Manuf. Technol. 96 (2018) 2791–2801, DOI:10.1007/s00170-018-1728-0.
- [23] V. Pandiyan, T. Tjahjowidodo, Wear. 436–437 (2019) 203047, DOI:10.1016/j.wear.2019.203047.
- [24] T. Purtonen, A. Kalliosaari, A. Salminen, Phys. Procedia. 56 (2014) 1218–1231, DOI:10.1016/j.phpro.2014.08.038.
- [25] L. van der Maaten, G. Hinton, J. Mach. Learn. Res. 9 (2008) 2579–2605.

11th CIRP Conference on Photonic Technologies [LANE 2020] on September 7-10, 2020

Detecting spattering phenomena by using high speed imaging in L-PBD of 316 L

Eetu Kivirasi^{a,*}, Heidi Piili^b, Kevin Minet-Lallemand^c, Juha Kotila^c

^a HAMK Tech, Häme University of Applied Sciences, PL 230, Hämeenlinna 13101, Finland

^b LUT University, School of Energy Systems, Department of Mechanical Engineering, Research Group of Laser Material Processing and Additive Manufacturing, Yliopistonkatu 34, Lappeenranta 53850, Finland

^c EOS Finland, Lemminkäisenkatu 36, Turku 20520, Finland

* Corresponding author. Tel.: +358 442626808 ; E-mail address: eetu.kivirasi@hamk.fi

Abstract

High-speed imaging is nowadays a widely used monitoring system in laser based powder bed fusion (L-PBF), because it enables observation of the occurring process phenomena. The quality-price ratio of the high-speed cameras has significantly increased over the last few years, and therefore it is a more suitable method for monitoring. This study concentrates on preliminary understanding of the spattering phenomena based on theoretical background and experimental findings. A better understanding of the spattering phenomena provides a possibility to achieve better part quality more cost-efficiently and to optimize the quality control during the process. According to the results of this high-speed imaging study, spattering is in the key role of the build part quality in L-PBF. The spattering phenomena can be categorized into three different types: entrainment driven spattering, recoil pressure driven spattering and Marangoni effect. These types are linked to the melt pool modes and can be detected from different amounts and sizes of the spatters.

© 2020 The Authors. Published by Elsevier B.V.

This is an open access article under the CC BY-NC-ND license (<http://creativecommons.org/licenses/by-nc-nd/4.0/>)

Peer-review under responsibility of the Bayerisches Laserzentrum GmbH

Keywords: Additive Manufacturing; AM; Laser based Powder Bed Fusion; L-PBF; 316L; Monitoring; High-speed imaging; Spattering

1. Introduction

According to Wohlers et al. [1] the increase of using additive manufacturing technology has been much more rapid as any prediction could have shown. Growth from the year 2016 to 2017 was as high as 80 %. Laser powder bed fusion (L-PBF) of metallic materials is one of the most promising one of the additive manufacturing technologies because of the high quality of build parts, and the availability of several different materials from aluminum, titanium, steels to nickels. [1]

The monitoring and controlling of the powder bed fusion processes are nowadays much more used than before, because the system manufacturers have increased the availability of monitoring systems on their product portfolio. A demand for better understanding of the process modes and melt pool dynamics has also increased in R&D sector, because the demand for better quality of the manufactured parts has increased rapidly. A real time quality control system can

monitor the part quality during the build process, and necessarily expensive computed tomography measurements after the build are no longer needed. Most of the defects in powder bed fusion are caused by the unstable process, hobbling between process modes and spattering. [2]

The main goal in AM process monitoring is to observe the quality of the process, and in the future to develop a real-time closed-loop feedback control. [3, 4] In order to build the closed-loop feedback control system, a deeper understanding on how the process parameters effect to the melt pool behavior and spattering phenomena is required. [4] It is quite time-consuming to study and understand the number of variables that simultaneously affect the same process. [5] Rehme and Emmelmann [6] have evaluated that there are over 100 parameters that are affecting the powder bed fusion process, and ten of those parameters are crucial.

1.1. In-situ monitoring of spatters

The challenging quality and certification requirements of aerospace and medical sectors have attached the interest of researchers and AM system developers to develop the in-situ process monitoring to reduce the cost of quality testing for AM parts. The researchers have studied in-situ monitoring of the spatters in several articles over the past few years. [7, 8, 9, 10, 11]

There are currently no commercially available in-situ monitoring systems for analyzing the spattering in L-PBF. However the AM machine manufacturers offer in-situ process monitoring systems for their machines. Photodiode based melt pool monitoring systems have been available commercially for a few years now by EOS, Renishaw, SLM and Trumpf. EOS has developed a camera based optical tomography monitoring system for their machines. [12, 13]

1.2. Spattering mechanism

The spattering mechanisms and melt pool dynamics in PBF are generally explained by formation of a phenomenon known as recoil pressure [14]. The recoil pressure is a strong metal evaporation created by the laser beam as it can be seen in Fig. 1.

The vapor vortex is formed when the powder bed is rapidly heated by the laser beam. That increases the recoil pressure which causes the melt to eject from the melt pool. [15]

As the laser beam interacts with the powder bed the surface temperature increases, and the melt pool is formed. Eventually the temperature reaches vaporization point and a metallic vapor jet is formed up towards the laser beam. The motion of the melt pool ejects molten metal spatters from the melt pool. [16, 17] Fig. 1. shows three different types of spatters. Fig. 2. shows spatter morphology.

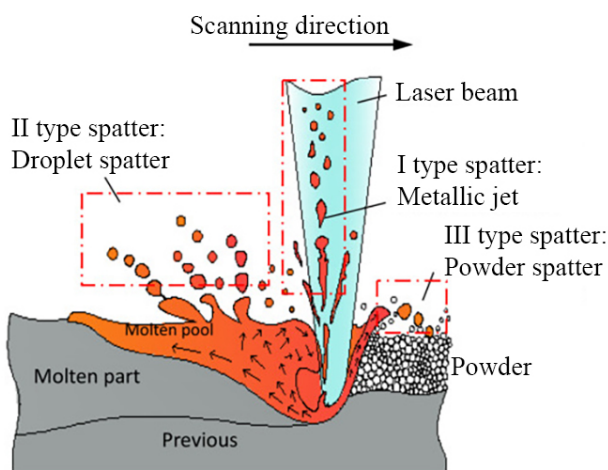


Fig. 1. Three different spatter types in powder bed fusion processes [18].

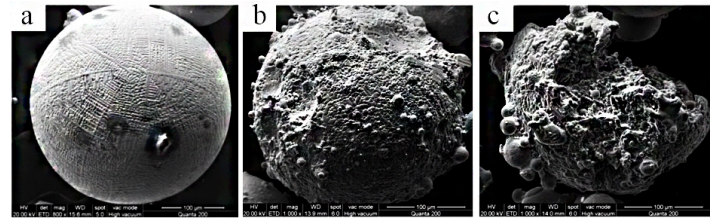


Fig. 2. Scanning electron microscope (SEM) morphology Figs of different type of spatters. [18].

As Fig. 1. illustrates, Wang et al. [18] presented three different types of spatters. The first type of spatter is created by the shield gas that is rapidly heated which creates a metallic jet up towards the laser beam (I type spatter that is seen in Fig. 1.). It can be noticed from the scanning electron microscope (SEM) image (seen in Fig. 2a.) that the powder particle has not been in contact with the laser beam. The second type of spatter is a recoil pressure and Marangoni effect created droplet spatter (II type spatter that is seen in Fig. 1.). The II type spatter powder particle has been in contact with the laser beam (seen in Fig. 2b.). [18]

The Marangoni effect is fluid convection that is pulling the hot fluid from the surface towards the cold spot inside of the melt pool, therefore decreasing dimension of the melt pool. [19] The third type of spatter is the recoil pressure and snowplow effect created powder spatter from the front line (III type spatter seen that is in Fig. 1.). SEM image of III type powder particle (seen in Fig. 2c.) indicates that the laser beam has melted the particle and it has an irregular shaped ejection on it. [18]

Liu et al. [20] have classified the droplet and powder-based spatters. Both spatters are generated by the recoil pressure and metallic vapor jet. The metallic vapor crushes the metallic jet into droplets during the laser irradiation field, forming the droplet spatter. Powder-based particles are sucked from the powder bed to the vapor jet. Interaction with the metal vapor and the laser beam creates the spattering. [29]

1.3. Entrainment driven spattering

According to Ly et al. [26], the metallic vapor vortex created by the laser beam and shield gas raise up cold powder particles and incandescent liquid droplets from the powder bed. 60 % of the spatters in PBF are hot ejections and 25 % are cold ejections [26, 29, 30]. Different types of entrainment driven spatters are shown in Fig. 3.

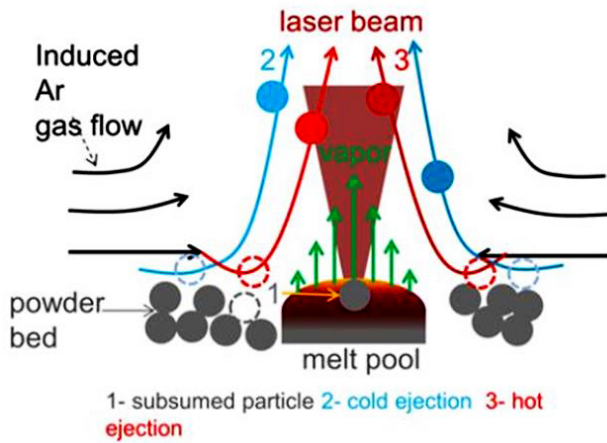


Fig. 3. Schematic of the three different types of entrainment driven spatters created by vapor jet. [26].

As Fig. 3. illustrates, Ly et al. [15] have recognized three different types of entrainment driven spatters: (1) the subsumed particles, which are pulled from the powder bed near the melt pool into the melt pool, (2) the cold powder particles that vapor vortex pulls towards to the jet but miss the laser beam or (3) the powder particles which hit to the laser beam and become droplet spatters. [15, 21, 22]

1.4. Recoil pressure driven spattering

The laser beam creates a strong metal evaporation around itself and the rapidly heating metal vapor vortex generates the recoil pressure gradients causing the molten metal ejections from the melt pool. The recoil pressure results a downward force on the melt pool causing a rapid fluid convection in the melt pool. [15, 23] Ly et al. [26] have studied the spatter formation with powder layer and solid plate situation seen in Fig. 4. using a particle image velocimetry (PIV). PIV is a nonintrusive laser optical measurement system for the flow diagnostic. The system consists of laser illumination, camera and software. [24]

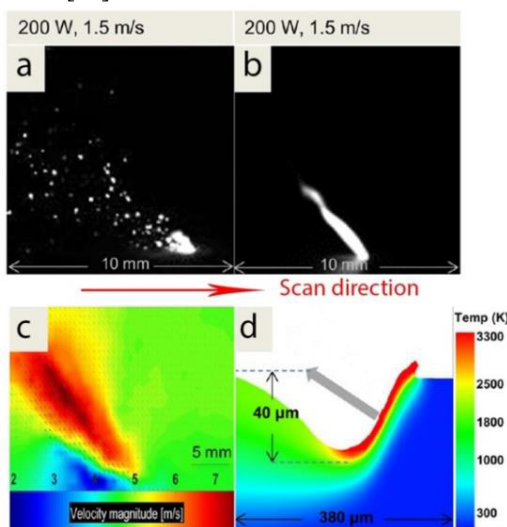


Fig. 4. a) Recoil pressure driven spattering from powder bed and b) from platform. c) Recoil pressure driven material jet simulation from powder bed. d) Grey arrow showing expected direction of the vapor plume in simulation model from platform. [15].

The recoil momentum, as Fig. 4d. shows as an grey arrow, ejects droplet spatters backwards of the scanning direction from the melt pool. The high temperature region spreads ahead of the melt pool as the laser beam energy decreases forming a vapor plume backwards of the scanning direction (seen in Fig. 4a, c). If the kinetic energy is greater than the surface tension of the molten material, the melt pool can eject spatters in the opposite direction of the scanning direction. [15]

1.5. Marangoni effect driven spattering

The Marangoni effect is a strong flow inside the melt pool. Its purpose is to transfer the heat inside the melt pool flow to maintain a minimum surface tension. The Marangoni convections increase as the laser beam energy density increases, causing instability to the melt pool which creates the pores. [23, 25]

A high scanning speed causes Plateau-Rayleigh instability to the melt pool, which increases the surface tension and Marangoni convection in the melt pool. Plateau-Rayleigh instability is a force that tries to minimize the surface area of the molten stripe breaking track to smaller surface area balls. This phenomenon is behind the often-seen balling effect. When the melt pool is stable, the temperature field is circle-shaped and therefore the melt track is uniform. The melt pool temperature field is decreasing as the scanning speed is increasing. Small temperature field of the melt pool and low temperature in the melt pool causes an unstable melt pool flow. [26, 27]

The unstable melt pool flow increases the surface tension and therefore more Marangoni convection, which increases the porosity. [23, 25, 28, 29]

2. Aim and purpose of this study

The aim of this study was to detect the spattering phenomena using a high-speed imaging with laser illumination in L-PBF process of stainless steel 316L. The purpose was also to find a correlation between the process modes and spattering mechanism.

The industrial relevance of this article is to provide a better and deeper understanding of the process phenomena and thereby to enable the development of more accurate, faster and cost-effective process monitoring systems for L-PBF.

This study was carried out at LUT University as a part of Manufacturing 4.0 (MFG4.0) project funded by the Strategic Research Council of Finland. All experiments done in this study were done at EOS Finland (Turku, Finland).

3. Material

The material used in this study was EOS StainlessSteel 316L gas atomized powder. The powder meets the requirements of the ASTM F138 (UNS S31673). [23] The chemical composition of the powder is shown in table 1.

Table 1. Material composition of EOS StainlessSteel 316L [23].

Element	Min [wt.-%]	Max [wt.-%]
Fe	Balance	N/A
Cr	17.00	19.00
Ni	13.00	15.00
Mo	2.25	3.00
C	N/A	0.030
Mn	N/A	2.00
Cu	N/A	0.50
P	N/A	0.025
S	N/A	0.010
Si	N/A	0.75
N	N/A	0.10

4. Experimental set-up

This study was done at EOS Finland (Turku, Finland) using industrial metal 3D printer EOS M280. This system has a building volume of 250 x 250 x 325 mm. It has 400 W ytterbium-fiber laser at 1064 nm wavelength with 80 μm focused laser beam diameter.

The high-speed imaging system consists of Optronis CR3000x2 high-speed camera and Cavitar Cavilux HF active illumination system. The system is designed for imaging bright and fast objects in the following applications: welding, shockwaves and thermal spraying.

The high-speed camera captures 1140 frames per second (fps) with a resolution of 1280 x 1024 pixels. The camera uses CMOS imaging sensor providing 8-bit dynamics with pixel size of 8 μm . The camera is equipped with bandpass filter equivalent to the light source wavelength preventing overexposure of the imaging sensor. The illumination system is fiber coupled high-speed pulsed diode laser providing power up to 500 W at 810 nm wavelength. The experimental set-up is shown in Fig. 5.

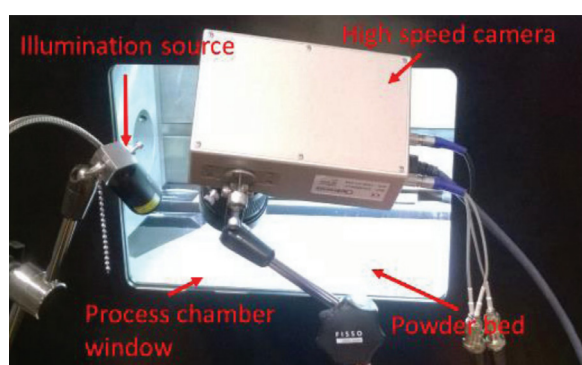


Fig. 5. Experimental set-up with high-speed camera and active illumination.

The camera and the illumination system were placed outside of the building chamber. Monitoring the build process is done through the window of the process chamber door.

5. Experimental procedure

The test pieces were built on top of each other using different process parameters (shown in Table 2.).

The size of the test piece was selected to be 20 x 40 x 15 mm due to the restrictions of the image area of the camera. All tests were done using a constant laser power of 195 W, when the scanning speed was varied. Each of the test points in table 2 were monitored separately to ensure the quality of the monitored data.

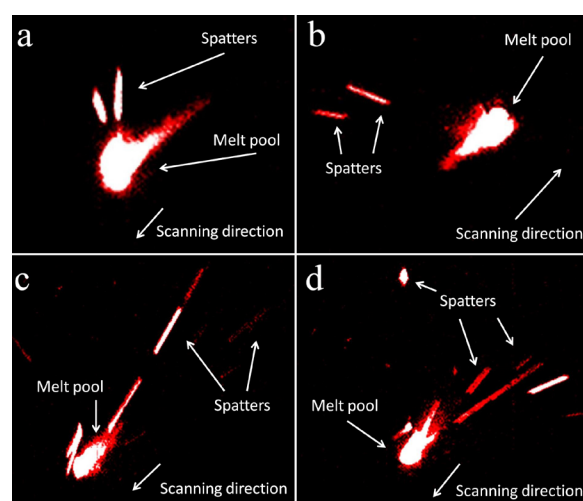
Table 2. Process parameters used in L-PBF when laser power was constant and scanning speed varied.

Parameter	Ss ₋₂	Ss ₋₁	Ss ₊₁	Ss ₊₂
Scanning speed [mm/s]	400	800	1200	1600
Hatch distance [mm]	0.09	0.09	0.09	0.09
Laser power [W]	195	195	195	195
Laser spot diameter [mm]	0.08	0.08	0.08	0.08
Layer thickness [mm]	0.02	0.02	0.02	0.02

Images taken from the experiment were edited in Camtasia and Adobe Photoshop Lightroom. The powder bed was blotted out from the background and then the colors were edited in a way that the melt pool and spatters were clearly distinguished from the background for easier analysis.

6. Results and discussion

The shape of the melt pool changes from round to drawn droplet through a drop when the scanning speed is increased. Fig. 6. shows different types of spattering mechanisms.

Fig. 6. (a) Melt pool and spatters in Ss₋₂; (b) melt pool and spatters in Ss₋₁; (c) melt pool and spatters in Ss₊₁; (d) melt pool and spatters in Ss₊₂.

As Fig. 6a. illustrates, the melt pool is large and round shaped and only a few large spatters can be detected flying rearwards from the scanning direction. The laser beam heats the melt pool to the boiling point and the recoil pressure driven spattering is increased. The illumination and the focus plane of the camera prevents the imaging system of detecting entrainment driven spatters created by the vapor vortex, that are flying straight up towards the camera and therefore out of the illuminated focus plane.

Fig. 6b. shows that the increase in scanning speed changes the melt pool shape from round to droplet-shaped, because the

volumetric energy density of the melt pool decreases. The spatters flying rearwards of the scanning direction are smaller and faster. The laser beam does not have enough energy to boil the melt pool, therefore the process becomes more stable. The amount of entrainment driven spatters reduces as the vapor vortex around the laser beam is decreased. This can be verified by reduced amount of spatters seen in Fig. 6b.

The faster scanning speed changes the shape of the melt pool to be similar as elongated drop can be seen in Fig. 6c. Longer and narrower melt pool increases the recoil pressure and Marangoni effect driven spattering. This can be detected from the small and hot spatters flying backwards from the scanning direction in high speed. As it can be seen in Fig. 6c. a swirl is formed at the borderline of the melt pool front and powder bed, which creates a protuberance, which causes the ejected droplet spattering.

The high scanning speed causes Plateau-Rayleigh instability to the melt pool, which increases the surface tension and Marangoni convection in the melt pool. An unstable melt pool produces more molten droplet spatters that fly backwards from the scanning direction, which can be seen in Fig. 6d.

7. Conclusions

The experiments were done with constant laser power of 195 W, the scanning speed was varied. The L-PBF system used in this experiment was EOS M280 located in EOS Finland (Turku, EOS). This study was carried out at LUT University as a part of Manufacturing 4.0 (MFG4.0) project funded by Strategic Research Council of Finland.

The spattering was monitored with active illuminated high-speed imaging system of a company named Optronis, and by utilizing active illumination system of a company named Cavitator.

It was concluded that the scanning speed has more impact to the number of detected spatters than the laser power, hatch distance and volumetric energy density when using a gas atomized 316L powder.

According to the results of this study, the spatters are ejected from the melt pool and vapor vortex created by the process laser and powder bed interaction. The process modes are directly linked to the different spattering mechanisms. The size and flying direction of the spatters change when the process mode changes. For example, in Fig. 5a the process is in the deep keyhole mode because the detected spatters are large and flying forwards from the scanning direction. In Fig. 5c the process is in the keyhole mode because the spatters are smaller, faster and are flying backwards from the scanning direction. Each process mode has their prevalent spattering mechanism which can be monitored during the build process.

Most of the large spatters are generated in the melt pool by recoil pressure and Marangoni effect. The smaller hot and cold spatters are born from the powder bed by entrainment driven spattering. This information enables the development of a monitoring system that allows a better and faster quality assurance during the build process.

Acknowledgements

This study was carried out at LUT University as a part of Manufacturing 4.0 (MFG4.0) project funded by the Strategic Research Council of Finland. All experiments done in this study were done at EOS Finland (Turku, Finland).

MFG4.0 project is carried out by University of Turku, University of Jyväskylä, University of Helsinki and LUT University. The project aims to investigate on how the digital manufacturing will change fabrication in Finland. The project started 1.1.2018 and ends 31.12.2023.

The authors would like to acknowledge all relevant personnel in EOS Finland for enabling the experiments carried out for this study and thank for their assistance and knowledge. Authors would also like to gratitude LUT University and HAMK Tech for their assistance and knowledge.

References

- [1] Wohlers, T., Campbell, I., Diegel, O., Kowen, J. 2018. Wohlers Report 2018: 3D Printing and Additive Manufacturing State of the Industry Annual Worldwide Progress Report. Colorado, USA: Wohlers Associates. 343 p.
- [2] Clijsters, S., Craeghs, T., Buls, S., Kempen, K., Kruth, J-P. 2014. In situ quality control of the selective laser melting process using a high-speed, real-time melt pool monitoring system. *The International Journal of Advanced Manufacturing Technology*. Vol. 75, pp. 1089-1101.
- [3] Bi, G., Sun, C.N. & Gasser, A. 2013. Study on influential factors for process monitoring and control in laser aided additive manufacturing. *Journal of Materials Processing Technology*. Vol 213(3), pp. 463–468.
- [4] Pavlov, M., Doubenskaia, M. & Smurov, I. 2010. Pyrometric analysis of thermal processes in SLM technology. *Physics Procedia*. Vol 5, pp. 523–531.
- [5] Everton, S., Hirsch, M., Stravroulakis, P., Leach, R., Clare, A. 2016. Review of in-situ process monitoring and in-situ metrology for metal additive manufacturing. *Materials and Design*. Vol. 95, pp. 431-445.
- [6] Rehme, O., Emmelmann, C. 2005. Reproducibility for properties of selective lasermelting products. *Proceedings of the Third International WLT-Conference on Lasers in Manufacturing*, pp. 227–232.
- [7] M. Mani, B. Lane, A. Donmez, S. Feng, S. Moylan, R. Fesperman, Measurement science needs for real-time control of additive manufacturing powder bed fusion processes, National Institute of Standards and Technology, Gaithersburg, MD, 20158036, NIST Interagency/Internal Report (NISTIR).
- [8] G. Tapia, A. Elwany, A review on process monitoring and control in metal-based additive manufacturing, *J. Manuf. Sci. Eng.* 136 (6) (2014) 060801.
- [9] S.K. Everton, M. Hirsch, P. Stravroulakis, R.K. Leach, A.T. Clare, Review of in-situ process monitoring and in-situ metrology for metal additive manufacturing, *Mater. Des.* 95 (2016) 431–445.
- [10] T.G. Spears, S.A. Gold, In-process sensing in selective laser melting (LPBF) additive manufacturing, *Integr. Mater. Manuf. Innov.* 5 (1) (2016) 1.
- [11] B.M. Sharratt, Non-Destructive Techniques and Technologies for Qualification of Additive Manufactured Parts and Processes. A literature Review. Contract Report DRDC-RDDC-2015-035, 2015, Victoria, BC.
- [12] Repposini, G., Laguzza, V., Grasso, M., Colosimo, A. 2016. On the use of spatter signature for in-situ monitoring of Laser Powder Bed Fusion. *Additive Manufacturing* 16, pp. 35-48.
- [13] Everton, S., Hirsch, M., Stravroulakis, P., Leach, R., Clare, A. 2016. Review of in-situ process monitoring and in-situ metrology for metal additive manufacturing. *Materials and Design* 95, pp.431-445.
- [14] Anwar, A., Ibrahim, I. & Pham, Q-C. 2019. Spatter transport by inert gas flow in selective laser melting: A simulation study. *Powder Technology* 352., pp. 103-116.
- [15] Wang, D., Wu, S., Fu, F., Mai, S., Yang, Y., Liu Y., Song, C. 2017. Mechanisms and characteristics of spatter generation in SLM processing

- and its effect on the properties. *Materials and Design*. Vol. 117, pp. 121-130.
- [16] Sun, S., Brandt, M. & Easton, M. 2017. 2 - Powder bed fusion processes: An overview. *Laser Additive Manufacturing*, pp. 55-77.
- [17] Gibson, I., Rosen, W. & Stucker, B. 2010. *Additive Manufacturing Technologies: Rapid Prototyping to Direct Digital Manufacturing*. New York: Springer Science + Business Media. 459 p.
- [18] Lee, Y.S. & Zhang W. 2015 *Mesosopic Simulation of Heat Transfer and Fluid Flow in Laser Powder Bed Additive Manufacturing*.
- [19] Simonelli, M., Tuck, C., Aboulkhair, N.T., Maskey, I., Ashcroft, I., Wildman, R.D. & Hague, R. 2015. A Study on the Laser Spatter and the Oxidation Reactions During Selective Laser Melting of 316L Stainless Steel, Al-Si10-Mg, and Ti-6Al-4V. *Metallurgical and Materials Transactions A*. Vol. 46(9), pp. 3842-3851.
- [20] Liu, Y., Yang, Y., Mai, S., Wang, D. & Song, C. 2015. Investigation into spatter behavior during selective laser melting of AISI 316L stainless steel powder. *Materials & Design*. Vol. 87, pp. 797-806.
- [21] Guo, Q., Zhao, C., Escano, L., Young, Zachary., Xiong, L., Fezzaa, K., Everhart, W., Brown, B., Sun, T. & Cheng, L. 2018. Transient dynamics of powder spattering in laser powder bed fusion additive manufacturing process revealed by in-situ high-speed high-energy x-ray imaging. *Acta Materialia*. Vol. 151, pp. 169-180.
- [22] Guo, Q., Zhao, C., Escano, L., Young, Zachary., Xiong, L., Fezzaa, K., Everhart, W., Brown, B., Sun, T. & Cheng, L. 2018. Transient dynamics of powder spattering in laser powder bed fusion additive manufacturing process revealed by in-situ high-speed high-energy x-ray imaging. *Acta Materialia*. Vol. 151, pp. 169-180.
- [23] Lavery, N.P, Brown, S.G.R., Sienz, J., Cherry, J. & Belblidia, F. 2014. A Review of Computational Modelling of Additive Layer, Manufacturing - Multi-Scale and Multi-Physics. *Sustainable Design and Manufacturing*. Pp. 668-690.
- [24] Dantec Dynamics. Products & Services. Fluid Mechanics. Particle Image Velocimetry (PIV). 2018. Internet source. [Available: <https://www.dantecdynamics.com/particle-image-velocimetry>] [Accessed 11.3.2019].
- [25] Pei, W., Zhengying, W., Zhen, C., Junfeng, L., Shuzhe, Z. & Jun, D. 2017. Numerical simulation and parametric analysis of selective laser melting process of AlSi10Mg powder. *Applied Physics A*. Vol. 123(8), pp. 1-15.
- [26] Malekipour, E. & El-Mounayri, H. 2018. Common defects and contributing parameters in powder bed fusion AM process and their classification for online monitoring and control: a review. *The International Journal of Advanced Manufacturing Technology*. Vol. 95, pp. 527-550.
- [27] Leung, C., Marussi, S., Atwood, R., Towrie, M., Withers, P & Lee, P. 2018. In situ X-ray imaging of defect and molten pool dynamics in laser additive manufacturing. *Nature* referred: 02.03.2019, available: <https://www.nature.com/articles/s41467-018-03734-7.pdf>.
- [28] Khairallah, S.A., Anderson, A.T., Rubenchik, A. & King, W.E. 2016. Laser powder-bed fusion additive manufacturing: Physics of complex melt flow and formation mechanisms of pores, spatter, and denudation zones. *Acta Materialia*. Vol 108, pp. 36-45.
- [29] Qiu, C., Panwisawas, C., Ward, M., Basoalto, H.C., Brooks, J.W. & Attallah, M.Z. 2015. On the role of melt flow into the surface structure and porosity development during selective laser melting. *Acta Materialia*. Vol. 96, pp. 72-79. P.J. & King, W.E. 2016. Denudation of metal powder layers in laser powder bed fusion processes. *Acta Materialia*. Vol. 114, p. 33-42.
- [30] EOS. System & Solutions. Metal. Materials. 2020. Internet source. [Available: <https://cdn0.scrvt.com/eos/77d285f20ed6ae89/dd6850c010d3/EOSStainlessSteel316L.pdf>] [Accessed 22.3.2020].

11th CIRP Conference on Photonic Technologies [LANE 2020] on September 7-10, 2020

A proof-of-concept analysis relating dimensions of a melt pool to its vibrational behavior to control a laser-based additive manufacturing process

Galid Arroud^{a*}, Julien Ertveldt^a, Patrick Guillaume^a

^a Department of Mechanical Engineering, AVRG, Vrije Universiteit Brussel, Pleinlaan 2, 1050 Brussels, Belgium

* Corresponding author. E-mail address: galid.arroud@vub.be

Abstract

The formation of a melt pool, during an additive manufacturing process, is a complex multi-physical process. Apparent factors, contributing to its complexity, are among others: the high temperatures, the existence of the material in multiple physical states and the involved high dynamics. However, it is a challenge to have full real-time control over all these factors. In this contribution, we will present our results and shed light, on the basis of measurements with a scanning laser doppler vibrometer, on how the vibrational behavior of the melt pool relates to its penetration depth into the substrate.

© 2020 The Authors. Published by Elsevier B.V.

This is an open access article under the CC BY-NC-ND license (<http://creativecommons.org/licenses/by-nc-nd/4.0/>)

Peer-review under responsibility of the Bayerisches Laserzentrum GmbH

Keywords: "laser Doppler vibrometry; melt pool; additive manufacturing; vibration; process monitoring; operational deflection shape, liquid metal"

1. Introduction

Additive Manufacturing (AM), also more known as 3D printing, is a disruptive manufacturing technology. It is leading to a paradigm shift in the manufacturing industries across multiple industrial sectors [1,2]. AM parts can be manufactured to reach a certain level of desired material properties and geometry by optimizing the processing parameters (e.g. laser power, powder flow rate, scanning speed, etc.). Although, this typically leads to the use of one of the two following approaches. Either a cumbersome trial-and-error campaign to fine-tune the parameters or to use a non-sophisticated feedback/feedforward controller that, for example, adapts the laser power on a priori information of the melt pool. More specifically, on the basis of available thermal data that stems from numerical simulations and/or data measured with an optical system (photodiode, pyrometer or a camera) [3,4]. However, one of the crucial aspects that is currently limiting the widespread acceptance of this manufacturing technology, is the lack of uniformity and consistency across multiple dimensions

(e.g. material properties on a macroscopic level, the material structure on a microscopic level, the geometrical features, etc.) [5,6]. Therefore, there is a need to monitor the process and to adequately adjust the relevant process parameters to safeguard the quality of the printed part.

The available literature majorly reports on the investigation and the development of monitoring solutions or feedback control systems that either monitor the temperature within the melt pool, as a controllable variable, or the geometry of the molten pool [5,7,8]. In this contribution, we divert our attention to measure the vibrational behavior of the melt pool. Apart from being inspired by the work presented by Han et al. in [9], we also firmly believe that tackling the melt pool process from alternative physical perspectives will allow us to understand and unravel its complex nature.

Measuring the vibrations in structures is usually done by means of an accelerometer. These type of sensors do require to be physically in contact with the structure. However, multiple

factors that are involved during the formation of a melt pool (e.g. among others the high temperatures) make it unfeasible to use them as a measurement tool during an additive manufacturing process. Moreover, within the scope of this paper, our aim is to measure the vibrations in the vicinity of the melt pool and in its immediate surrounding. This implies a high-spatial resolution is required and adds another practical constraints. Therefore, alternative solutions to measure the vibrations while meeting these requirements need to be sought. Hence, the use of laser Doppler vibrometry (LDV) as a non-intrusive optical measurement technique answers the set criteria to overcome the constraints and allows us to use the technique to measure at the level of the melt pool. Indeed, LDV allows us to perform a measurement on a single point as well as on multiple points in a sequential way.

The measurement principle underlying the LDV technique is actually based on a two-beam interferometric approach. More specifically, a modified Mach-Zehnder interferometer as described in [10,11]. The schematics depicted in Figure 1, shows that a laser source, emitting light with wavelength λ , is split by means of a beam splitter into a reference beam and a measurement beam. The measurement beam follows an optical path to illuminate a moving target.

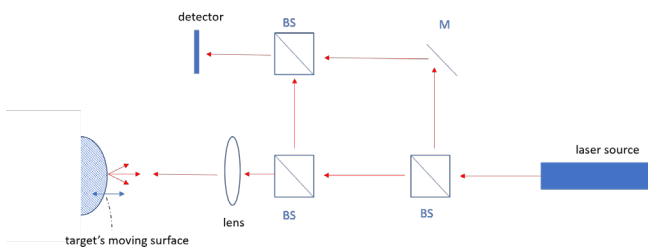


Fig. 1. Schematic of the two beam interferometer principle used in a LDV system; BS = beam splitter/combiner and M = mirror

The vibrating surface, with velocity v , moves in the direction of the incident laser beam and it reflects the laser light partially back to the LDV system causing a Doppler shift. More specifically, the reflected beam is brought into interference with a reference beam causing a phase modulation $\varphi_m(t)$ and simultaneously a frequency shift Δf . Thus, the signal that arrives at the detector contains information about the displacement and the velocity quantity of the measured point on the vibrating surface. This entails, according to equation (1), that a displacement $s(t)$ leads to a phase modulation:

$$\varphi_m(t) = \frac{4\pi s(t)}{\lambda} \quad (1)$$

After differentiating equation (1) with respect to dt and knowing that $d\varphi/dt = 2\pi f$ and $ds/dt = v$ this results in:

$$f_d(t) = \frac{2v(t) \cos \theta}{\lambda} \quad (2)$$

In equation (2) is $f_d(t)$ known as the Doppler frequency. In addition the term $v(t) \cos \theta$ indicates the velocity component

along the line-of-sight axis of the laser. This entails that from equation (1) we can deduce the displacement information from the moving object and from equation (2) its velocity. This is done by demodulating the signal that is received at the detector into an analogue voltage signal that is in proportion with the velocity of the vibration. [10]

This paper presents a proof-of-concept analysis to evaluate the applicability of a scanning LDV system as a measurement system to measure the vibrations in a liquid melt pool. Furthermore, we also present our experimental results that we obtained to show that, on the basis of the measured data, a change in the depth of the melt pool affects the measured data in the frequency spectrum. The continuation of this paper is as follows: section 2 discusses the experimental setup, while the results are reported in section 3. Finally, we draw some conclusions from this work and summarize them in Section 4.

2. Experimental setup

As aforementioned, this paper presents a proof-of-concept investigation to assess the feasibility of LDV measurements as an in-situ measurement approach for an additive manufacturing process. Therefore, we have designed an experimental setup as it is depicted in Figure 2. The used LDV system is a Polytec PSV-400 with an added objective to increase the spatial resolution. The digital camera built in the measurement head streams a live image spanning a field-of-view that measures 1.8mm x 1.3mm.

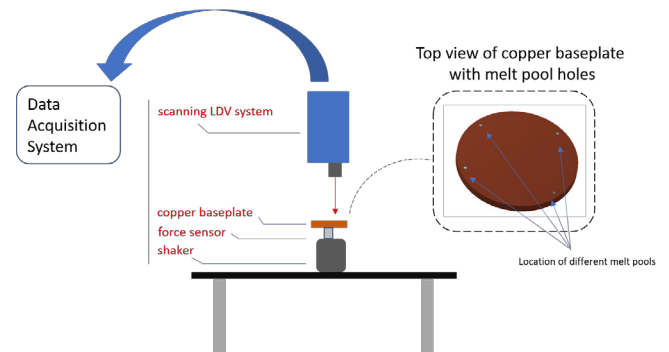


Fig. 2. Schematic of the experimental setup

The copper baseplate is 3.6mm thick and has an outer diameter of 52 mm. As illustrated in Figure 2, the copper plate contains 7 flat-bottom holes. Here, we have chosen to keep the diameter of these holes, mimicking a melt pool, fixed to a value of 1.6 mm. On the other hand, we varied the depth of the holes. For an overview of the depth values, we refer to Table 1. The flat-bottom holes were filled to the best of our ability with 99.99% pure Gallium, since this type of material is in a liquid state under ambient conditions. Figure 3 gives the reader an impression and shows how it looks like when we have filled one of the flat-bottom holes with the liquid metal. In this work, we used a B&K mini-shaker type 4810 to excite the different melt pools. As it can be noticed from Figure 2, there is also an ICP force sensor (from PCB Piezotronics model no. 208B02) attached between the plate and the shaker to record the force

signal that is transmitted to the base plate. Here, we consider the measured force signal, transmitted from the shaker into the copper plate, as an input for the calculation of the frequency response functions.

Table 1. Depth values of the pseudo melt pool in the copper plate

flat-bottom hole identification tag	depth (mm)
#1	1
#2	0.9
#3	0.8
#4	0.7

The data management system of the scanning LDV generates an electrical signal that drives the shaker and also acquired at the same time the measured velocities at each point. After a measurement is finished we manually rotated the copper disk and redid the necessary alignment, as a part of the standard procedure, before launching a new scan with the LDV system.

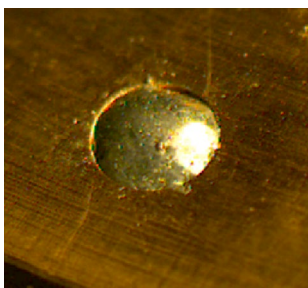


Fig. 3. A close-up view of one of the flat-bottom holes, in the copper disk, filled with liquid

Figure 4 shows an overlay of the chosen scanning grid on the digital image acquired by the LDV system. Here, 21 scanning points are within the area of the liquid metal and 8 scanning points outside on the copper disk. Notice that it was possible to increase the amount of scanning points, however, the cost is an increase in measurement time. Therefore, we have limited the amount to a total of 29 of scanning points. In addition, we have used the same grid for all the different cases (i.e. melt pool depths)

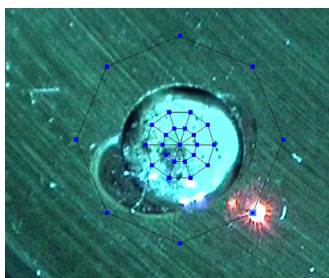


Fig. 4. An overlay of the defined scanning grid as acquired by the LDV system

3. Experimental results

The measurement principle that underpins the LDV system only allows to measure dynamic responses. Therefore, we used

the shaker, an electrodynamic type, to induce a forced vibration so that we were able to measure the dynamic response. However, an excitation signal needs to be sent to the shaker. Hence, for the presented analysis and also consistent over all the cases, we used a swept sine signal that starts from 80 Hz and goes up to 800 Hz in 8 seconds. The frequency spectrum of the used signal is shown in the top graph in Figure 5.

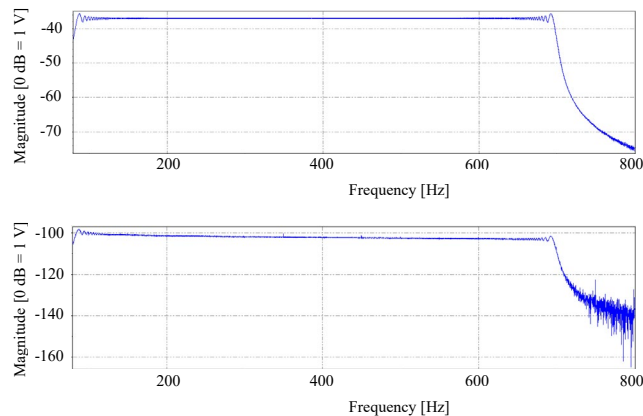


Fig. 5. (Top graph) Frequency spectrum of the electrical signal, used as an excitation signal, sent to the shaker; (bottom graph) Frequency spectrum of the measured force.

The signal's bandwidth was set to these values after a couple of initial trial measurements in order to maximize the transmitted vibration energy and excite the liquid metal for the different cases. Here, we noticed that starting below the lower limit of 80 Hz was not necessary, since we only observed strong rigid body motions below this limit. As for the upper limit of 800 Hz, it was not needed to go beyond this limit either, since lower order operational deflection shapes were measured below this limit. As one can notice from the bottom graph in Figure 5, the measured force signal follows the sent electrical signal.

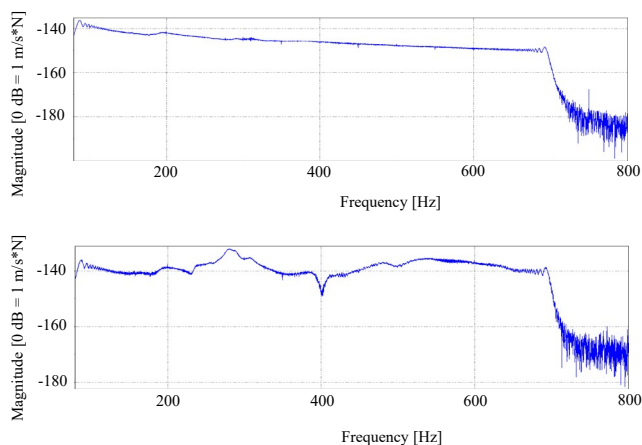


Fig. 6. Comparison between obtained frequency response function on copper plate (top graph) and within the liquid metal (bottom graph)

When looked to the calculated frequency response functions (FRF), i.e. measured velocity over the measured force, we noticed a clear difference as one can see in Figure 6. The top graph represents the calculated FRF on a solid (i.e. copper disk), as the bottom graph in Figure 6 is the calculated FRF in a point that is measured within the liquid metal. On the basis of this comparison, one can see that the obtained FRF in the liquid metal has a different shape and that it also contains several flattened peaks.

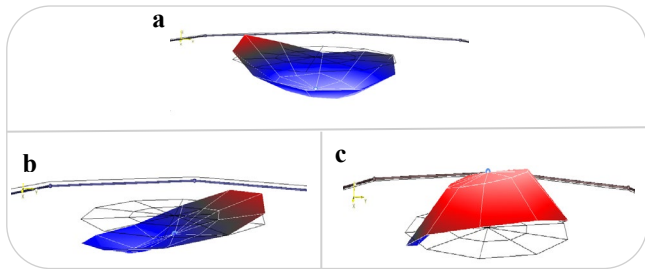


Fig. 7. The obtained ODS at resonance peak for case #1. Here, referring to the highlighted peak from Figure 9 (top graph)

If we focus our attention on the calculated FRFs, obtained from data measured within the liquid metal, then we noticed that with each flattened peak there is a corresponding operational deflection shape (ODS). The theoretical fundamentals behind the topic of ODS, mode shapes and their association with resonance frequencies are extensively covered within many references that can be found in the literature, e.g. in [12-14]. From the latter references we know that a resonant vibration originates from an interaction between the inertial and the elastic material properties of the vibrating test object. Moreover, the ODS at the resonance frequency is heavily dominated by the contribution of one specific mode shape. Figure 7 shows the ODS for a melt pool depth of 1 mm (case #1 from Table 1). The shown ODS is taken at the resonant peak with the highest amplitude (highlighted peak in the top graph that is shown in Figure 9). As one can see from Figure 7, this ODS corresponds to an up-and-down movement of the liquid metal while the solid structure doesn't move and stays at the level of the reference plane.

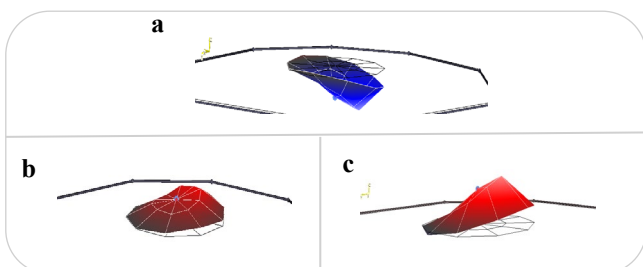


Fig. 8. The obtained ODS at resonance peak for case #4. Here, we refer to the highlighted peak from Figure 9 (bottom graph)

Hence, we identify the ODS shown in Figure 7 as a first mode of the melt pool that is uncoupled from the surrounding solid structure. Furthermore, if we repeat the same procedure for the different cases listed in Table 1, then we obtain consistent

results. This entails we identify the same mode shape at the frequency with the highest amplitude. Figure 8 shows the same mode, as identified in Figure 7, but for case #4. Thus, for a different melt pool depth. On the other hand, while there is a consistency in the identified ODS, as the mode shape of the melt pool, the corresponding frequency undergoes a shift. More specifically, as depicted in Figure 9, we clearly see that the resonance frequency of the melt pool shifts depending on the depth of the melt pool.

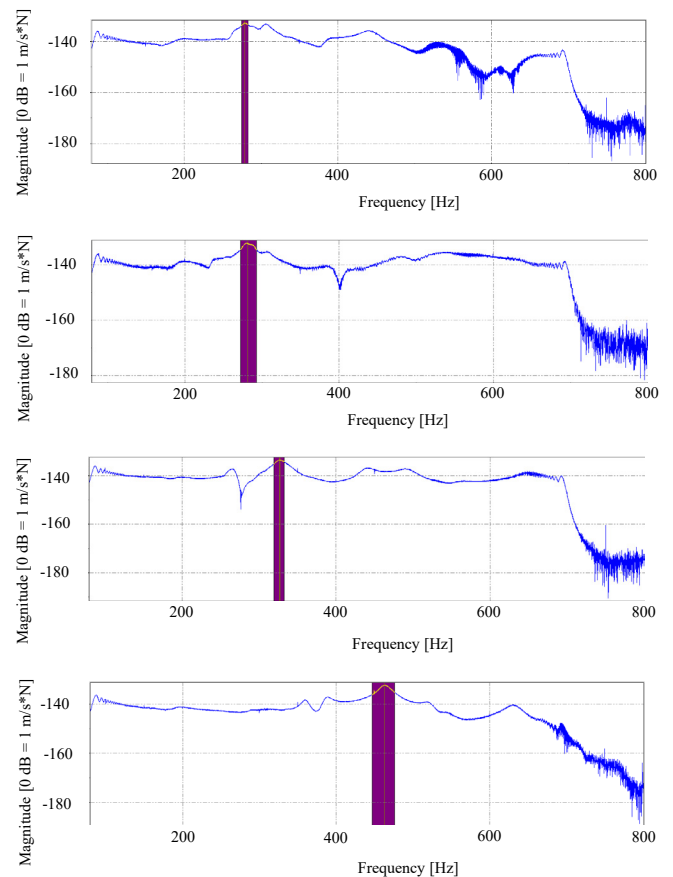


Fig. 9. Calculated FRFs for all the different melt pool depths that are given in Table 1. The top graph corresponds to case #1 and bottom graph case #4.

In Figure 10 we show the variation of the frequency corresponding to the identified first mode (shown in Figure 7 and 8) as a function of the melt pool's depth.

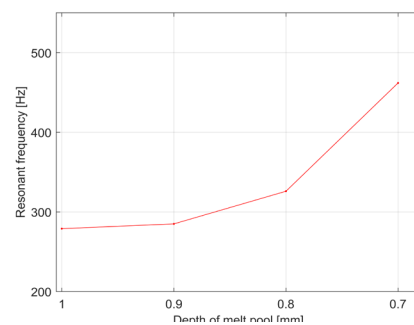


Fig. 10. Obtained variation in resonance frequency in function of melt pool depth

4. Conclusions

This paper presents a proof-of-concept analysis that confirms the applicability of a scanning LDV system as a measurement system to identify the vibrations in a liquid melt pool. Furthermore, we have shown in this contribution, on the basis of experimental data, that a change in the depth of the melt pool can be tracked via the resonance frequency that corresponds to the operational deflection shape of the melt pool. We believe that the presented proof-of-concept shows potential for further investigation in order to better understand the complex nature of a formed melt pool during an additive manufacturing process.

Acknowledgements

The authors acknowledge financial support from the Flemish government and the research council of the Vrije Universiteit Brussel (OZR) for their funding (grants IOF3002 and SRP46).

References

- [1] D.L. Bourell, M.C. Leu and D.W. Rosen. Roadmap for Additive Manufacturing: Identifying the Future of Freeform Processing, The University of Texas at Austin, Austin, TX (2009).
- [2] M. Mani, K.W. Lyons and S.K. Gupta. Sustainability characterization for additive manufacturing. *J. Res. NIST* 119, 419-428 (2014).
- [3] T. Purtonen, A. Kalliosaari, A. Salminen, *Phys. Procedia* 56 (2014) 1218–1231.
- [4] J.T. Hofman, B. Pathiraj, J. van Dijk, D.F. de Lange and J. Meijer. A camera based feedback control strategy for the laser cladding process. *J. Mater. Proc. Technol.* 212(11), 2455-2462 (2012).
- [5] M. Mani, B. Lane, A. Donmez, S. Feng, S. Moylan and R. Fesperman. Measurement science needs for real-time control of additive manufacturing powder bed fusion processes. Technical Report NISTIR 8036, NIST (2015).
- [6] T. Craeghs, S. Clijsters, E. Yasa, F. Bechmann, S. Brumen, J.P. Kruth Determination of geometrical factors in Layerwise Laser Melting using optical process monitoring. *Optics and Lasers in Engineering*. Vol. 49, Iss. 12, December 2011, p. 1440-1446, ISSN 0143-8166
- [7] S. K. Everton, M. Hirsch, P. Stravroulakis, R. K. Leach, and A. T. Clare, Review of in-situ process monitoring and in-situ metrology for metal additive manufacturing *JMADE*, vol. 95, pp. 431–445, 2016.
- [8] J. Mazumder, D. Dutta, N. Kikuchi and A. Ghosh. Closed loop direct metal deposition: Art to part. *Opt. Lasers Eng.* 34(4-6), 397-414 (2000)
- [9] D.H. Han, E.B. Flynn, C.R. Farrar, L.K. Kang, A Study on the In-Situ Melt Pool Size Estimation Method for Directed-Energy Additive Manufacturing Based on Modal Parameters, *3D Printing And Additive Manufacturing*, Volume00, Issue 00 (2018), doi: 10.1089/3dp.2017.0058
- [10] E. Lawrence, Optical Measurement Techniques for Dynamic Characterization of MEMS Devices, Polytec, Technical Paper (2012)
- [11] J. Vanherzeele, S. Vanlanduit, P. Guillaume, Acoustic source identification using a scanning laser Doppler Vibrometer, *Optics and Lasers in Engineering*, Volume 45, (2007), pp 742-749
- [12] D. Ewins, *Modal Testing: Theory and Practice*. Research Studies Press (1986)
- [13] L. Hermans, H. Van der Auweraer, *Modal Testing and analysis of structures under operational conditions: Industrial Applications, Mechanical Systems and Signal Processing* (1999)
- [14] N. Maia and J. Silva, *Theoretical and experimental Modal Analysis*. Research Studies Press (1997)

11th CIRP Conference on Photonic Technologies [LANE 2020] on September 7-10, 2020

Calibration approach for reliable in-situ process monitoring of multi-optic selective laser melting

Daniel Alberts^{a,*}, Marco Standfuß^a, Dieter Schwarze^a, Gerd Witt^b

^aSLM Solutions Group AG, Estlandring 4, 23560 Lübeck, Germany

^bUniversity of Duisburg-Essen, Institute for Product Engineering, Lotharstr. 1, 47057 Duisburg, Germany

* Corresponding author. Tel.: +49-451-4060-3186; fax: +0-000-000-0000. E-mail address: daniel.alberts@slm-solutions.com

Abstract

Additive Manufacturing is on the threshold of full industrial use in various leading industries. This is due to the continuous development of machine systems regarding availability, stability, reproducibility and repeatability alongside their ever-increasing productivity. To achieve high quality parts, process variables must be monitored during production, for example with a Melt Pool Monitoring (MPM) system to measure their characteristics. Initial and long-term stable calibration of the monitoring system must be ensured with proper alignment, positioning and the size of the measuring surface itself. To secure direct comparison of multi-optics within a machine as well as transferability from machine to machine, a quantitative intensity calibration must also be carried out. This paper provides a new calibration approach with measuring equipment and tools including a Measurement System Analysis (MSA), exploring possibilities and limitations in terms of absolute accuracy, repeatability and reproducibility as well as workflows for the measurement equipment and machine calibration.

© 2020 The Authors. Published by Elsevier B.V.

This is an open access article under the CC BY-NC-ND license (<http://creativecommons.org/licenses/by-nc-nd/4.0/>)

Peer-review under responsibility of the Bayerisches Laserzentrum GmbH

Keywords: Calibration, MSA, In-Situ, Process Monitoring, Melt Pool Monitoring, Multi-Optics, Selective Laser Melting

1. Introduction

The industrialization of metal Additive Manufacturing (AM) by means of laser powder bed fusion (LPBF), in particular also known as Selective Laser Melting, focuses on aspects such as process safety and the basic requirements of a necessarily economical operation, quality assurance and certification. The latter is currently one of the highest priorities of machine manufacturers, end users as well as national and international platforms for standardization such as DIN, ISO or ASTM [1,2,3]. In the course of machine, process and part

qualification, all the parameters used for the validation of qualification manufacturing processes are recorded as basic parameters for part qualification and defined for the subsequent manufacturing processes. In order to ensure the required quality criteria of the product, regular maintenance is defined at fixed time intervals or after a predetermined number of production hours, documenting the proper functioning of all important machine action and machine components within a defined maintenance procedure.

Throughout the course of these qualification phases, the implementation of process monitoring systems increases in

* Corresponding author. Tel.: +49-451-4060-3186

E-mail address: daniel.alberts@slm-solutions.com

order to record not only machine condition but also process stability and/or the detection of any process anomalies, which in turn can lead to defects in part structures [4,5]. The real-time monitoring of the melt pool is used to detect thermal process emissions and is of main focus to assure in-process quality in both the scientific and industrial environment [6]. This type of process monitoring is used, as an example, to gain knowledge of sophisticated interaction between mechanisms or for process parameter studies (as noted above) within research and development or during the part qualification phase. With this process monitoring used in the field of applications during industrial production, the corresponding quality requirements for functionally correct operations apply here, as well as, for all other machines and machine components. For coaxial melt pool monitoring (MPM), similar optical reference values and parameters for the actual optics of the machine are relevant. The quality of the measured data recorded during operation is defined by the quality of the initial alignment and positioning of the detection area, in relation to the beam position, as well as, the size of the actual detection area of an imaging optics at the location of the laser-powder interaction. During maintenance, it must be ensured that the detection position specified by the software and the actual beam position and the detection area are within the tolerances recommended by the machine manufacturer.

To significantly increase productivity, machine manufacturers are intensifying the development of multi-optic systems. Since spatially resolved, MPM also requires a corresponding monitoring system for each laser system (complete recording of the entire layer information), and as such, the alignment of the optics to each other is also required. Most applications of such a coaxial process monitoring are currently dedicated to relative, i.e. qualitative analysis approaches, because due to the arrangement and the number of complex, optical systems and interfaces of a machine optic (i.e. the laser beam entry window, scanner etc.) require extensive spectral properties to be taken into account in order to calibrate them to an absolute value. In order to be able to extend the current qualitative analyses to quantitative analyses on one hand, versus the ability to use the application on multi-optic systems on the other, a sufficient transferability between the optics within a multi-optic system along with the transferability from single optic machines to multi-optic machines and their spectral sensitivity to its detection position and area must be guaranteed.

2. Experimental setup

The utilized melt pool monitoring (MPM) system is based on two photodiodes with distinct wavelength ranges up to 2500nm in the near infrared region (NIR) of spectral emission [6]. Therefore, the system approach for calibration must operate and detect emission within the same range of wavelengths.

The NIRQuest512 from OceanInsight is the utilized spectrometer and serves as reference for the calibration of the MPM system [7]. One key factor of the spectrometer is the ability for an external calibration according to international standards. The calibration of the spectrometer includes an

integrating sphere and an optical fiber. The integrating sphere homogenizes the light emitted by the transfer medium to secure a higher accuracy and repeatable measurement.

The light source HL-2000LL from OceanInsight served as the transfer medium [8]. Key factors are a lifetime of approximately 10,000h and a stabilizing power supply for constant emission from the halogen tungsten lamp.

The calibration presented here of the melt pool monitoring systems are conducted on multi-optic machine systems with two parallel lasers, so that one MPM system is mounted on each optical bench. Both the machine, SLM280^{HL}-Twin system, and the MPM systems are from SLM Solutions [9]. The optical components have an influence on the calibration due to quantitatively different spectral properties. Prior to the calibration of the MPM system the position and size of the detection area is adjusted with a patented calibration plate [10].

3. Method - Adjustment and calibration routine

The spectrometer serves as reference for calibration of the MPM system. The selection of a specific MPM system representing the “golden-unit” is not suitable because of the unknown long time behavior and possibly occurring changes in the set-up of the series system.

The spectrometer has been calibrated according to DIN/ISO 17025 with a precision light source according to the following scheme; see Figure 1 [11].

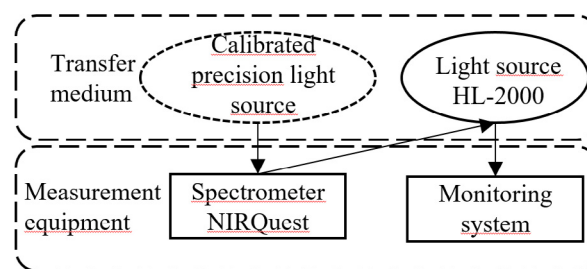


Figure. 1. Calibration scheme of transfer medium and measurement equipment

The check of the calibration is carried out at regular intervals set by the measurement equipment guidelines for the relevant measurement range between 900nm to 2500nm.

The spectrometer serves as the measurement device to measure the emission from the light source as a transfer medium. A schematic representation of an experimental setup for determining calibration factors of a transfer medium is shown in Figure 2.

Additionally, the light source can be utilized to illuminate the calibration plate for positioning and focusing of the measurement spot resp. the detection area. Significant basic conditions for the choice of the light source are:

- Safe handling in terms of heat radiation
- Compact design to fit in all types of machines
- Suitable intensity to meet the intensity levels of the process and get a sufficient signal level

- Repeatable emission for plenty of measurement cycles

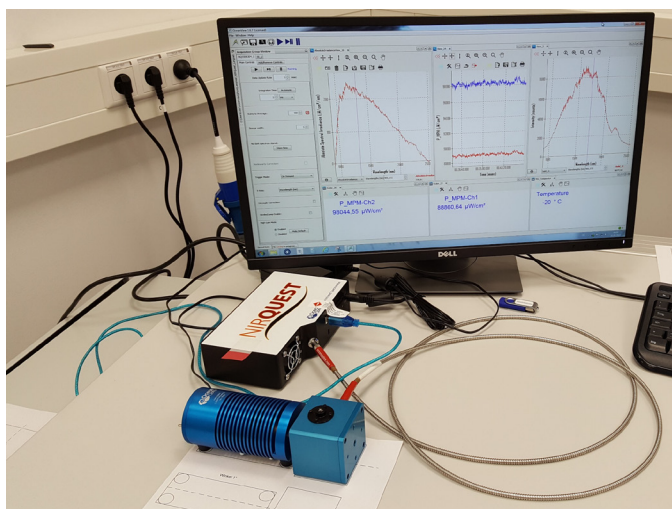


Figure 2. Experimental calibration setup with spectrometer, optical fiber, integrating sphere and light source

Channel specific calibration factors for both photodiodes are calculated with an analysis from the measurement of spectrometer and light source. The calibration factors resulting from this light source measurement are considered for the further adjustment of the MPM systems.

Subsequently, each MPM system has to be adjusted to meet the specifications set by the manufacturer with the calibration plate. A coaxial alignment of laser spot with measurement spot resp. detection area is adjusted to avoid various influencing factors on process monitoring data. The measurement spot size resp. detection area is set by focusing of the system in order to have a comparable measurement spot across all machines and optical benches. The aim is to avoid different influence of surrounding area on process monitoring data [4].

The light source is aligned exactly vertically below the optic and in the later working plane to measure its emission with the MPM system for the absolute intensity calibration, see Figure 3.

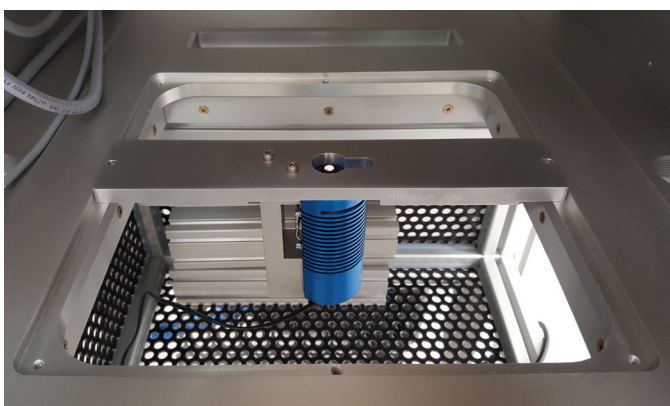


Figure 3. Representation of the aligned transfer medium inside the build chamber of a machine system/ test bench

A comparison of the captured data under consideration of the light source calibration factors to a set reference. The

calibration factors for both channels have to be calculated separately, see Formula 1.

$$Cal = \frac{MPM_{Ref}}{MPM * Cal_{Light}} \quad (1)$$

4. Measurement System Analysis

Procedure

The standard approach of measurement system analysis (MSA) is adapted to meet the needs of the current process [12]. The two-stage calibration approach is analyzed separately for this chapter. The combination of both is evaluated in chapter 5 in respect to calibration accuracy. Three light sources represent the reference parts. The measurements with the light sources are repeated several times with the spectrometer and the MPM system. Three different operators measure every light source five times with the same measurement equipment. The measurements with the different systems are spatial and temporal, separated to simulate application of a field operation. The light sources are changed and the measurement systems are set to their original state after each repeated measurement to eliminate further influencing factors regarding the warming-up phase. A certain warm-up time is defined and applied for each measurement and reference part.

The light sources are as standard regarding their emission intensity not calibrated. The halogen tungsten lamp reduces its emission due to aging for longer power-on times. For the first ten hours, power-on time leads to an aging of one percent when measuring it with the spectrometer. After a power-on time of 60 hours, the power loss of all further 10 hours intervals is now reduced to 0.25%. The aging of the lamp resp. the light source is one influencing factor for the following results and will be indicated when needed.

Spectrometer measurement

Firstly, the light sources are measured with the spectrometer. After 10 minutes of warm up time for the spectrometer, the light sources are switched on. The data is captured for 10 minutes and the last 3 minutes are used for further calculation. This results in 7 minutes warming-up time for the light sources. The spread of the data acquisition is calculated with data from 25 repeated measurements conducted by one operator and one light source. The standard derivation is 0.6% of the measurement value including 0.1% aging over a power-on time of 250 minutes. Three operators measured the three light sources in five repeated measurements to determine the repeatability and reproducibility (GageR&R) of the measurement process. The aging of every light sources amounts to 0.06% for the 15 measurements and 150 minutes power-on time. To determine the variance, ANOVA (analysis of variance) method is used to analyze the results of the measurements [12]. For new measurement systems, a GageR&R with a maximum of 20% is recommended.

The GageR&R for both measurement channels averaged is 5,89% and proves a suitability of the measurement equipment.

MPM measurement

The MPM system measures in the second stage the light source to determine the suitability of the measurement system. The test is similar to the approach taken with the spectrometer. First, 25 measurements with one light source resulted in a standard deviation of 0,5% with a negligible aging of 0,01% due to shorter power-on times. For the R&R-Gage is again conducted by three operators with three light sources with five measurement repetitions. Additionally, two MPM systems of the SLM280^{HL}-Twin system are used to get more data and hence, a more reliable result. The light source is removed from the machine and disassembled between each measurement to ensure constant boundary conditions. The aging of the light source can again be neglected (45 minutes results in 0.02% aging). The results for both MPM systems are shown in Table 1.

Table 1. GageR&R for MPM-system calibration

	Channel 1	Channel 2
MPM system 1	2.35%	3.16%
MPM system 2	3.31%	3.69%

The GageR&R averaged for all combinations is 3.13% and proves the suitability of the MPM system as a viable measurement method to capture the emission of the light source.

5. Transferability between optical benches and machines

Using the data from the calibration of the light sources determined in chapter 4, their calibration factors “ Cal_{Light} ” are calculated and later taken into account in the calibration of the individual optics.

The calibration of two optics with all three light sources in comparison to each other show a scatter of 0.98% for channel 1 and 0.72% for channel 2 during this relative adjustment. When assessing an absolute adjustment, the absolute signal level of the individual transfer media (light source), in this case light sources, is decisive, since in practice different light sources or lamps of light sources would be used to calibrate one and the same machine over several preventive maintenance intervals, regardless of the fact that this will generally not be the case within one maintenance assignment. The accuracies or differences to be determined here show the absolute, quantifiable difference between the light sources after application of the light source specific calibration factor (Cal_{Light}). In this procedure, individual measurements of different light sources are compared to each other on both optical benches (MPM01, MPM02). For each MPM system, 45 individual measurements are made, which result in a maximum absolute deviation of approx. 7%, see Table 2.

Table 2. Maximum absolute deviation in respect of of two MPM systems, two optics as well as different light sources

	Channel 1	Channel 2
MPM01	7.02%	4.49%
MPM02	5.67%	3.09%

This is a worst-case scenario, which does not correspond to reality as it does not provide a conclusive statement on the transferability of the entire approach. For a better approximation, individual measurements of each light source are averaged. The comparison of the light sources results in a maximum deviation, see Table 3.

Table 3. Maximum absolute deviation of the approach in respect of transferability between optical benches and machines

	Channel 1	Channel 2
Δ Lamp	5,4%	2,8%

6. Summary and outlook

The study shows a procedure for the reliable and statistically validated calibration of a coaxial melt pool monitoring (MPM) system operating in real time over its entire spectral sensitivity range including the transferability to different optical systems and machines for the application of multi-optic Selective Laser Melting. This was preceded by a necessary procedure to ensure the positioning accuracy between the detection area and the actual laser position as well as a stable and comparable detection area itself.

The method comprises two transfer media with a high-precision, initially absolutely calibrated light source (transfer medium 1) and an additionally used light source (transfer medium 2), whose emission is absolutely measured in the course of the method. One of the two measuring devices is a calibrated spectrometer, which is calibrated by transfer medium 1 and measures transfer medium 2. This forms the first part of the two-step calibration procedure. In the course of a measurement system analysis (MSA), performed according to the ANOVA (analysis of variance) method, it could be proven that the Gage Repeatability and Reproducibility (GageR&R) for both photodiode-based measuring channels of the MPM is only 5.89% on average and thus suitable as measuring equipment with a safety factor >3 .

The use, and in particular the accuracy of transfer medium 2, was determined within the second calibration process, during which the suitability of the MPM systems used was determined in the course of a further MSA. Fortunately, the GageR&R averaged for all combinations is 3.13% and, with a safety factor of >6 , also proves the suitability of the MPM system as a practicable measuring method for detecting thermal emission from the light source used (transfer medium 2).

Finally, with the help of the calibration routine presented, an absolute accuracy of 5.4% could be determined for the initial application as well as its transferability from optics to optics and from machine to machine when using MPM.

With this procedure, in addition to the identification of limits and possibilities, a first initial tolerance to be specified could be worked out, which in the holistic approach, meets the standardization requirements according to DIN, ISO and ASTM [1,2,3]. In addition, a more precise comparability of such a process monitoring system by factors was given and the basis for further quantitative analyses was laid.

References

- [1] N., N.. ISO/ASTM PWI 52920, additive manufacturing - qualification principles - quality-assured processes for industrial AM centres. ASTM; 2020.
- [2] N., N.. DIN EN ISO/ASTM 52942:2019-06 - Draft, Additive manufacturing - Qualification principles - Qualifying machine operators of metal powder bed fusion machines and equipment used in aerospace applications (ISO/ASTM DIS 52942:2019). EN ISO/ASTM; 2019.
- [3] N., N.. ISO/ASTM 52904:2019, Additive manufacturing - Process characteristics and performance - Practice for metal powder bed fusion process to meet critical applications. ISO/ASTM; 2019.
- [4] Alberts D, Schwarze D, Witt G. In situ melt pool monitoring and the correlation to part density of Inconel[®]718 for quality assurance in selective laser melting. Solid Freeform Fabrication: Proceedings of the 28th Annual International 2017; pp. 1481–1495.
- [5] Alberts D, Schwarze D, Witt G. Neural Networks for Modeling an In-Situ Melt Pool Monitoring System for Selective Laser Melting. Fraunhofer Direct Digital Manufacturing Conference DDMC 2020: Conference Proceedings
- [6] Alberts D, Schwarze D, Witt G. High speed melt pool and laser power monitoring for selective laser melting (SLM[®]). 9th International Conference on Photonic Technologies, LANE, 2016. [Online]. Available at: https://www.lane-conference.org/app/download/11537198949/LANE2016_1219_Alberts_IC_endformat.pdf?t=1534490222
- [7] Ocean Optics Inc. 2020. [online]. Available at: <https://www.oceaninsight.com/products/spectrometers/near-infrared/nirquest-series/>
- [8] Ocean Optics Inc. 2020. [online]. Available at: <https://www.oceaninsight.com/products/light-sources/vis-and-nir-light-sources/tungsten-halogen/>
- [9] SLM Solutions Group AG. 2020. [online]. Available at: https://www.slm-solutions.com/fileadmin/user_upload/SLM_R_280-DE200122-02_WEB.pdf
- [10] Alberts D, Schwarze D. Pyrometric detection device, method for calibrating the same, and apparatus for producing three-dimensional work pieces, EP3023757A1; 2018.
- [11] N., N.. DIN EN ISO/IEC 17025:2018-03, General requirements for the competence of testing and calibration laboratories (ISO/IEC 17025:2017). DIN EN ISO/IEC: 2018.
- [12] Dietrich E, Conrad S. Eignungsnachweis von Messsystemen. 4rd. ed. Munich: Carl Hanser Verlag; 2015.

11th CIRP Conference on Photonic Technologies [LANE 2020] on September 7-10, 2020

Assessment and verification of mean effective diameter of internal channels fabricated by laser powder bed fusion

Lokesh Chandrabalan^{a,b,*}, Markus Baier^b, Roberto Meloni^a, Luca Ammannato^a,
Eugenio Del Puglia^a, Simone Carmignato^b

^a*Baker Hughes, Via Felice Matteucci 2, 50127 Florence, Italy*

^b*University of Padova, Department of Management and Engineering, Stradella S. Nicola 3, 36100 Vicenza, Italy*

* Corresponding author. Tel.: +39-351-053-5522 ; E-mail address: Lokesh.Chandrabalan@bakerhughes.com

Abstract

Channels with small diameters, used for example in conformal cooling, can nowadays be fabricated by laser powder bed fusion. Measurements of the mean effective diameter and surface topography are important to quantify the flow capabilities through the channel. In this paper, a new method using X-ray computed tomography is developed to obtain the mean effective diameter and mean surface topography height. The developed method is verified by determining the mean effective diameter using incompressible turbulent fluid flow simulations, whereupon the determined mean surface topography height is fed as an input to the simulation. The method is proved to offer a non-destructive and relatively fast approach to measure the mean effective diameter and mean surface topography height in circular channels.

© 2020 The Authors. Published by Elsevier B.V.

This is an open access article under the CC BY-NC-ND license (<http://creativecommons.org/licenses/by-nc-nd/4.0/>)

Peer-review under responsibility of the Bayerisches Laserzentrum GmbH

Keywords: Industrial X-ray computed tomography; laser powder bed fusion; mean effective diameter; mean surface topography height; incompressible turbulent fluid flow

1. Introduction

The process capabilities of metal additive manufacturing are improving drastically, now allowing the fabrication of intricate structures with reduced deviations and errors [1]. The production of channels with small diameters and different inclinations has always been of significant interest in manufacturing advanced industrial components, such as gas turbine parts. With the aid of laser powder bed fusion (L-PBF) process, the fabrication of internal channels in metallic parts has been made easier and rapid. However, a major challenge lies in the dimensional and quality assessment of the produced part. Furthermore, the surface of additively manufactured channels

is subject to high surface irregularities, which could potentially affect the channels' functionality, for example causing pressure drop and heat transfer reduction [1,2]. Therefore, the mean effective diameter affected by the microscale surface irregularities must be carefully analyzed in a non-destructive manner to understand the effects on the functionality of the channel [1].

X-ray computed tomography (CT) offers the advantage of non-destructively assessing the fabricated parts both internally and externally over a wide variety of components [3,4]. There are different approaches to perform dimensional and geometrical analyses, such as the nominal to actual comparison analysis on the CT scanned part using different post-processing

software [5]. However, for parts with high surface irregularities and deformations, the alignment between the nominal (CAD model) and the actual (CT) geometry of the scanned part is prone to bias and errors, which can impair the accuracy of the dimensional assessment [5]. Especially, in the case of channels fabricated by laser powder bed fusion process (L-PBF) deviating from the build platform, poor surface quality can be witnessed predominantly due to several causes such as staircase effect or sag and dross formations.

To overcome these hurdles, a new method is proposed in this paper to assess the mean diameter and internal surface topography of cylindrical channels fabricated by L-PBF with respect to the functionality of the part. Using algorithms for ‘wall thickness analysis’ in VGStudio MAX 3.3 (Volume Graphics GmbH, Germany) which are based on the voxel grey values of the scanned volume [6], it is possible to analyse the part geometrical deviations without the necessity of an alignment with the nominal object. In particular, in this work wall thickness analysis is performed on the CT reconstructed volume inside a specific region of interest, including only the internal channel to avoid contributions from the external deviations. The method is applied once operating in background (i.e. the volume inside the channel) and once in material mode. The resulting thickness histograms are used to obtain the mean diameter (background mode) and microscale surface features (material mode).

In fluid mechanics, the microscale surface features in the channel are evaluated through functional-related parameters, particularly the so called ‘sand grain roughness’ (k_s) or ‘mean roughness height’ (ε), which is defined as the mean height of tightly packed protruding sand grain like features that are uniformly distributed inside the channel [7]. Further work is needed to correlate the functional-related parameters with standard surface texture parameters. Since metal additive manufacturing technologies have been in use over a short period of time, the research studies on influence of k_s over the functionality in additively manufactured parts are limited [8,11]. Increasing dimensions of microscale surface features in the channel (and corresponding k_s values) lead to increase in friction during fluid flows and affect the mass flow rate due to the resulting pressure drop [2]. As part of this work, the obtained values from wall thickness analysis were compared to flow simulations using ANSYS Fluent 19.2 (ANSYS, Inc., United States of America) to evaluate the corresponding pressure drop throughout the length of the channel and thereby the resulting hydraulic diameter (d_h) were calculated.

The specimen investigated in this study is a cylinder, which is a part of the benchmark artefact proposed in [9], with a nominal internal hole diameter of 1 mm and a wall thickness of 0.8 mm with an overall cylinder length of 19.2 mm. The material used for fabrication was INCONEL 718, which is an austenitic nickel-chromium-based superalloy, commonly used for high temperature applications in gas turbines. The specimen was fabricated vertically with an orientation perpendicular to the build platform. Upon fabrication, the specimen was cut from the build platform by electrical discharge machining (EDM).

Nomenclature

CT	X-ray computed tomography
L-PBF	Laser Powder Bed Fusion
ROI	region of interest
$msth$	mean surface topography height
k_s	sand grain roughness
ε	mean roughness height
d_h	hydraulic diameter
ΔP	pressure drop
\dot{m}	mass flow rate
d_{mean}	mean diameter

2. Methodology

2.1. X-ray Computed Tomography measurements

The component was scanned using a metrological CT system (Nikon MCT 225, Nikon Metrology X-Tek, UK). To be able to resolve the microscale surface features inside the channel, the part was positioned as close as possible to the X-ray source to achieve the highest resolution, resulting in a voxel size of 4 μm . Table 1 represents the optimised scan parameters that were applied to scan the part. Due to the density of the material, a filter of 0.5 mm thickness made of tin was used to reduce beam hardening artefacts. The specimen was CT scanned at its centre, for a total length of the reconstructed channel of around 7 mm. Subsequently, the acquired images were reconstructed with the reconstruction software provided by the CT system manufacturer, without any additional mathematical filtering or artefact reduction. Upon reconstruction, the volume was imported in VGStudio MAX 3.3 for further analysis.

Table 1. Optimized scan parameters used for CT measurements

Parameter	Value
Power	6.8 W
Voltage	170 kV
Exposure time	2 seconds
Number of projections	2000

After surface determination, a region of interest (ROI) comprising only the internal channel was created to perform the wall thickness analysis, in two different modes (background and material). Figure 1 shows the cross-section of the analyzed channel. The section marked in red is the ROI comprising the internal channel. As denoted in the legend of the figure, the direction of the blue and yellow arrows represents the operational direction of the background and material modes. The background mode operates on the internal volume of the channels (i.e. non-material voxels) using the determined surface as the starting point to find the opposite surface under a certain opening angle [10]. On the other hand, the material mode functions in the same manner with the difference that it determines the thickness distribution of the material voxel contained in the ROI. In both the cases, the Ray method was chosen with a search angle of 15° [10]. The resulting wall

thickness histograms were exported and further processed with the aid of an in-house developed MATLAB script to obtain the mean diameter and the mean surface topography height (*msth*).

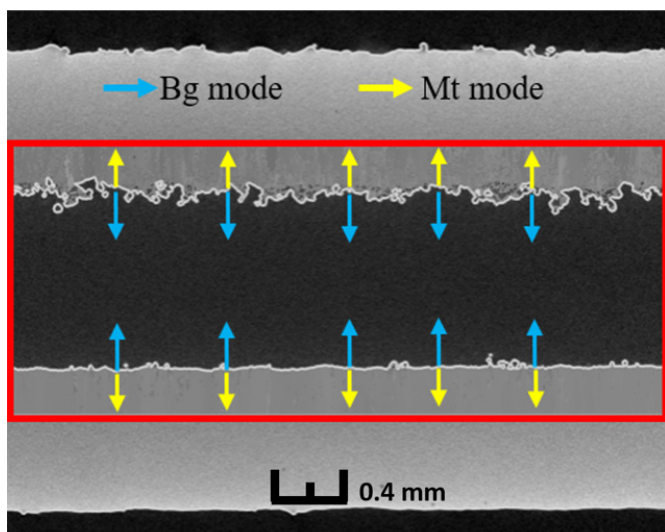


Fig. 1. Cross-section of the analysed channel with the ROI denoted in red. The blue and yellow arrows represent the analysis direction for background and material mode of the wall thickness analysis.

2.2. Application of Computational Fluid Mechanics

Incompressible Reynolds-averaged Navier-Stokes (RANS) turbulent fluid flow simulations were performed with $k-\epsilon$ turbulence model at four different mass flow rates (\dot{m}) using ANSYS Fluent. The nominal diameter is used as the channel diameter in the Computational Fluid Mechanics model and the aforementioned *msth* is used as the k_s inside the channel, which is a necessary input to determine the associated pressure drop (ΔP) and the exit fluid flow velocity over a certain channel length [11]. To achieve comparability, the channel length in the CFD model was the same as analyzed by CT. Subsequently, the general mass flow rate (\dot{m}) equation was used to calculate the corresponding d_h . To perform high fidelity simulations, polyhedral mesh was used, thereby increasing the accuracy. Furthermore, to achieve fully developed turbulent flow at the inlet of the channel, the length of the channel was extruded 10 times more before the actual inlet. In addition, the theoretical pressure-drop and the friction factor for the mean diameter and *msth* were calculated using the Colebrook-White and Darcy-Weisbach equations, as a theoretical reference case [12].

3. Results and discussion

The results discussed in this paper do not reflect the actual additive manufacturing capabilities of Baker Hughes. Figure 2 shows a cross-sectional view of the analyzed channel perpendicular to channel direction, whereas Figure 3 displays a 3D rendering of the wall thickness analysis performed in material mode inside the ROI. The microscale surface features show sizes up to 120 μm (shown in red in Figures 2 and 3). Analyzing the 3D rendering, there is a trend in the distribution of the surface features leading to an increased number of particles on one side of the channel, which is caused by the

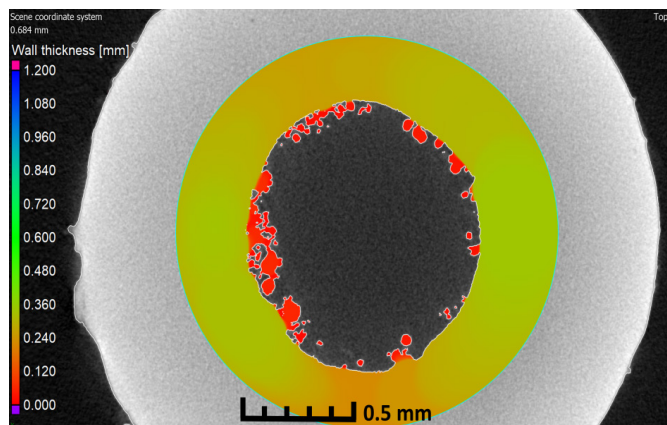


Fig. 2. Cross-sectional view of the wall thickness analysis performed in material mode on the channel, revealing the microscale surface features in red.

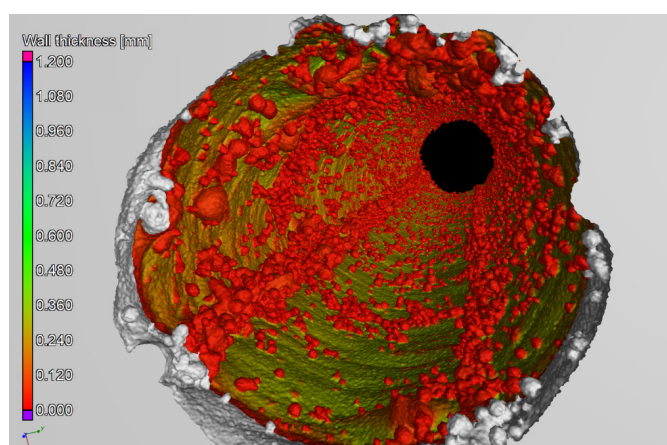


Fig. 3. 3D rendering view of the wall thickness analysis performed in material mode on the 1 mm channel over a total length of 6.8 mm, revealing the microscale surface features in red.

interaction between the previously printed layer and the recoater, while spreading a new powder layer. Furthermore, from Figure 3, it is evident that the microscale surface features have an anisotropic distribution.

The cropped wall thickness histograms and the corresponding Gaussian fits of the CT analysis are shown in Figure 4 and 5. The fits are performed in a selected region around the main peak avoiding the tails where it includes features that do not correspond either to the microscale surface features or to the channel diameter, but are rather intermediate distances caused by the methodology involved in the wall thickness analysis. Figure 4 shows the obtained *msth* with the centre of the fitted Gaussian at 25 μm . In this case, the fitting was performed between 0 to 50 μm . On the other hand, Figure 5 displays the histogram data and the Gaussian fit for the mean internal channel diameter, resulting in a mean diameter of 0.93 mm, which is a reduction of 70 μm with respect to the design value. In this case, the range for the Gaussian was chosen again around the centre of the main peak considering the histogram data between 880 μm and 1100 μm . As mentioned above, the determined *msth* is used in the flow simulations to verify the mean channel diameter obtained by CT.

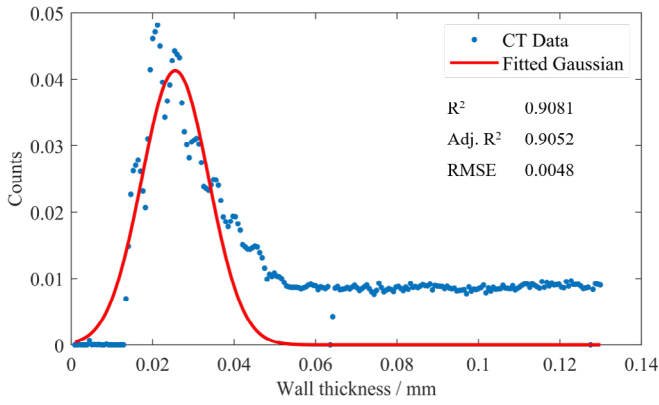


Fig. 4. Wall thickness histogram with fitted Gaussian for *msth*.

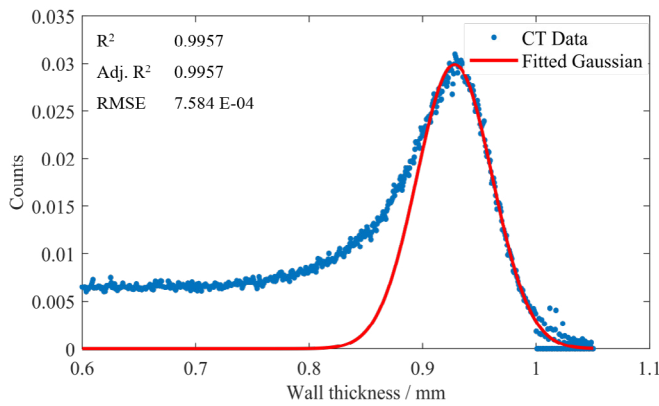


Fig. 5. Wall thickness histogram with fitted Gaussian for mean internal channel diameter.

The developed CFD model and the axial velocity contour plot of an incompressible turbulent fluid flow simulation are shown in Figure 4 and Figure 5 respectively. The *msth* of 25 μm from the wall thickness analysis in the material mode was given as an input for ε in ANSYS Fluent, only in the domain consisting the actual length of the channel excluding the additional extruded length before the inlet [11].

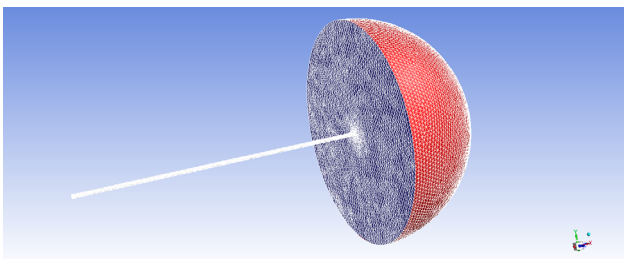


Fig. 6. Developed CFD model for incompressible turbulent fluid flow simulations.

The results of the incompressible turbulent fluid flow simulations at different \dot{m} and the corresponding theoretical values are summarized in Table 2. The theoretical and the calculated pressure drop (ΔP) values from the CFD simulations are in line, with an error less than 1%. This indicates that the obtained *msth* from CT is equivalent to k_s or ε in circular pipe

flows. Since the channel has a cylindrical geometry, the mean diameter from the wall thickness method is equivalent to the calculated hydraulic diameter from the incompressible turbulent fluid flow simulations. The calculated d_h , at all mass flow rates, has a deviation of less than 1.5% from the mean internal channel diameter obtained from CT. This additionally confirms the hypothesis of *msth* corresponding to ε or k_s and verifies that the mean channel diameter is equivalent to the hydraulic diameter.

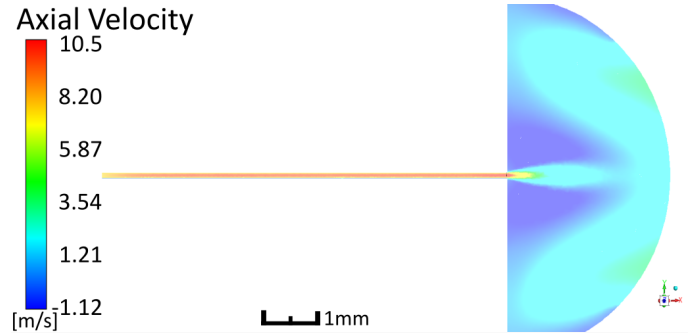


Fig. 7. Exemplary axial velocity contour plot.

Table 2. Comparison of theoretical and simulated results, d_h based on CFD simulations

\dot{m} (kg/s)	ΔP (Pa) (Theoretical)	ΔP (Pa) (Simulation)	d_h (mm)	$\Delta P_{the.}$ vs $\Delta P_{sim.}$ (% Error)	d_{mean} vs d_h (% Error)
0.004	7522	7455	0.916	0.89	1.26
0.0055	13925	13963	0.915	0.27	1.40
0.007	22272	22305	0.914	0.14	1.47
0.0085	32565	32376	0.914	0.58	1.47

4. Conclusions

The study focused on developing a new approach using CT to determine the mean effective diameter and internal microscale surface features of cylindrical channels fabricated by L-PBF, taking strongly into consideration the flow functionality of the component. The mean channel diameter obtained from CT was verified by comparison with the calculated hydraulic diameter from CFD simulations, showing deviations less than 1.5%.

The obtained pressure-drops for different mass flow rates from the CFD simulations were compared to the reference case. The comparison studies showed error less than 1%, confirming the hypothesis that the mean surface topography height corresponds to k_s or ε in circular channel.

The results presented in this work are the first proof of concept of the proposed method. Future work will include analyzing inclined channels with high surface irregularities due to stair-case effects and dross formations and thereby verify and correlate the concept of k_s . Furthermore, the methodology will be validated with experimental flow tests on different internal channel geometries, with respect to actual applications.

Acknowledgements

This work was made within PAM², ‘Precision Additive Metal Manufacturing’, a research project funded by The EU Framework Programme for Research and Innovation - Horizon 2020 - Grant Agreement No 721383.

References

- [1] Stimpson CK, Snyder JC, Thole KA, Mongillo D. Scaling roughness effects on pressure loss and heat transfer of additively manufactured channels. *J. Turbomachinery* 2017; 139, 021003.
- [2] Klingaa, CG, Bjeree MK, Baier S, De Chiffre L, Mohanty S, Hattel JH. Roughness Investigation of SLM Manufactured Conformal Cooling Channels Using X-Ray Computed Tomography. 9th Conference on Industrial Computed Tomography 2019, Padova, Italy.
- [3] Kraemer A, Lanza G. Assessment of the measurement procedure for dimensional metrology with X-ray computed tomography. 14th CIRP Conference on Computer Aided Tolerancing (CAT) 2016; *Procedia CIRP* 43. p.362 – 367.
- [4] Aloisi V, Carmignato S. Influence of surface roughness on X-Ray computed tomography dimensional measurements of additive manufactured parts. *Case Studies in Nondestructive Testing and Evaluation* 2016; 6. p.104-110.
- [5] Kruth JP, Bartscher M, Carmignato S, Schmitt R, De Chiffre L, Weckenmenn A. Computed Tomography for Dimensional Metrology. *CIRP Annals - Manufacturing Technology* 2011; 60(2). p.821-842.
- [6] du Plessis A, Rossouw P. X-ray computed tomography of a titanium aerospace investment casting. *Case Studies in Nondestructive Testing and Evaluation* 2015; 3. p. 21-26
- [7] Arshad FF, Rieke HH. Surface-Roughness Design Values for Modern Pipes. *SPE Drilling & Completion* 2006.
- [8] Stimpson CK, Snyder JC, Thole KA, Mongillo D. Roughness Effects on Flow and Heat Transfer for Additively Manufactured Channels. *J.Turbomachinery* 2016; 138, 051008.
- [9] Chandrabalan L, Matoni E, Malarco M, Del Puglia E, Ammannato L, Carmignato S. Investigation on precision of laser powder bed fusion process using statistical process control. Joint Special Interest Group meeting between euspens and ASPE. *Advancing precision in Additive Manufacturing* 2019. Nantes, France.
- [10] Sbettega E, Zanini F, Benedetti M, Savio E, Carmignato S. X-ray computed tomography dimensional measurements of powder fusion cellular structures. euspens's 18th International Conference & Exhibition 2018. Venice, Italy.
- [11] Kilpatrick E, Sung K. Roughness effects on flow and heat transfer in a ribbed duct considering additive manufacturing. *Global Power and Propulsion Society Forum* 2018. Zurich, Switzerland.
- [12] Nikuradse J. *Laws of Flow in Rough Pipes*. 1933; NACA Technical Memorandum 1292.

11th CIRP Conference on Photonic Technologies [LANE 2020] on September 7-10, 2020

Simultaneous *in operando* monitoring of keyhole depth and absorptance in laser processing of AISI 316 stainless steel at 200 kHz

Troy R. Allen^{a*}, Brian J. Simonds^b, Jack R. Tanner^b, and James M. Fraser^a

^aQueen's University, 64 Bader Lane, Kingston, Ontario K7L 3N6, Canada

^bNational Institute of Standards and Technology, 325 Broadway, Boulder, Colorado 80305, USA

* Corresponding author. E-mail address: troy.allen@queensu.ca

Abstract

The formation of keyholes during high-irradiance laser-metal interaction is the complex, multiphysics phenomenon that underpins industrial processes such as laser-based additive manufacturing, laser welding, and laser cutting. The complex dynamics of energy coupling in keyhole formation are not well understood, and the energy absorptance in these processes are often assumed to be constant. Therefore, we implement two state-of-the-art measurement techniques *in operando* to simultaneously measure keyhole depth using inline coherent imaging and laser energy absorptance using integrating sphere radiometry at imaging rates of 200 kHz. Results directly reveal the time evolution of cavity-enhanced absorptance in these keyholes generated by the laser-metal interaction. For stationary irradiance on AISI 316 stainless steel, we find that processing in an argon-rich environment compared to air reduces coupling efficiency by $50\% \pm 11\%$ in conduction, $27\% \pm 2\%$ in transition, and $8\% \pm 3\%$ in keyhole mode. High imaging rates allow clear observation of liquid surface oscillations and corresponding changes to absorptance, declining from 15 kHz to 10 kHz over the first 10 ms of the spot weld.

© 2020 The Authors. Published by Elsevier B.V.

This is an open access article under the CC BY-NC-ND license (<http://creativecommons.org/licenses/by-nc-nd/4.0/>)

Peer-review under responsibility of the Bayerisches Laserzentrum GmbH

Keywords: laser welding; absorption; additive manufacturing; keyhole depth; *in operando* monitoring

1. Introduction

Laser welding, cutting, and additive manufacturing suffer from a lack of *in situ* monitoring tools and real-time control methods, leading to long development cycles for new processes, high rates of defects, and difficulty in setting industry standards [1, 2, 3, 4]. A crucial element of the laser-metal interaction that is often simulated but lacks experimental validation is the relationship between melt pool shape (including keyholes) and energy absorption [5, 6, 7, 8]. Recent efforts have made great progress on this problem through specialized research monitoring tools that directly image the melt pool and keyhole shapes (*i.e.*, high-speed x-ray imaging [9, 10]) and measure dynamic absorptance change (integrating sphere radiometry [11, 12]). Nevertheless, for purposes of modelling and predicting final part properties, absorptance is

often measured pre-processing and treated as a static constant and melt pool/keyhole shape is simulated dynamically but only compared to post-mortem analysis. In this work, we combine inline coherent imaging (ICI), a tool designed to measure melt pool surface height/depth with micrometer precision at 200 kHz in industrial settings [13, 14, 15, 16], and integrating sphere radiometry (ISR), a tool able to measure absolute absorptance of laser power during the process at speeds up to 1 MHz [11, 17]. By observing both depth and absorptance at speeds faster than the system is changing, we can provide a clearer picture of how these intrinsically linked physical phenomena affect each other; thus, enabling the development of high-fidelity, deterministic models of the laser-metal processing system.

In this work, we apply this combined method to explore the effects of inert environments on the relationship between melt pool and keyhole depth and absorptance *in operando*. Argon

cover-gas is regularly used in laser-metal processing applications to reduce oxidation induced defects at the liquid metal surface [18, 19]. We directly compare time-resolved melt pool and keyhole depth with absorptance data for spot welds performed in argon-rich atmosphere and air environments. Also presented is a comparison of the time-averaged data and a frequency analysis of the observed liquid surface oscillations.

2. Methods

2.1. Processing laser

High-irradiance stationary laser illumination is performed using a 1 kW Yb-doped fiber laser with a 100 μm core delivery fiber. A 150 mm focusing optic is used to focus the processing laser beam to a $1/e^2$ spot size of 238 μm . The focused beam has an M^2 value of 9.8 and a Rayleigh length of 4.23 mm. In this experiment, the laser is operated with powers ranging from 100 W to 410 W, confirmed to within 3 % with a commercial power meter. Pulse irradiance is calculated from the average power and the area of the beam incidence using the $1/e^2$ diameter. The laser is fired in pulsed mode to produce single pulses of 10 ms nominal duration. The actual pulse durations range from 9.896 ms to 9.972 ms depending on the laser power setting. The temporal distributions of the laser pulses are top hat in nature with rise times shorter than 75 μs .

2.2. Simultaneous inline coherent imaging and integrating sphere radiometry

ICI is low coherence interferometry implemented collinearly with the high-power processing beam [13, 14, 15, 16, 20]. The ICI system used in this work can extract sample height at a rate of 200 kHz, with an axial resolution of 15 μm (minimum axial distance between two interfaces that can be distinguished) and a single-point measurement repeatability of 0.6 μm . ISR is a technique that uses an integrating sphere to measure off-axis scattered light from laser illumination in order to calculate absolute absorptance [11, 17, 12]. The ISR system used in the present work measures scattered light in the sphere with a photodiode with a rise time of 4.4 μs . This system does not include a photodiode in the weld head, so absorptance from early in the welds, when reflections are primarily specular, are not reported in the figures (for durations after laser turn-on of up to 385 μs in air and 645 μs in argon). The influence of the vapor plume on integrating sphere-based absorptance measurements has been discussed in a previous work [12]. For the relatively short pulse durations and low irradiance values used in this work, the effect is expected to be negligible. ICI and ISR have previously been combined for simultaneous monitoring. Further description of the individual systems and the method for combining them can be found in Ref. [21].

2.3. Sample preparation

Samples of NIST SRM 1155a (AISI 316 stainless steel) [22] are prepared as described in Ref. [11]. Each SRM puck is polished to a consistent mirror-like finish and washed with methanol. NIST SRM 1155a was chosen for this experiment as

there have been recent high-fidelity thermophysical property measurements into this system [23]. These improved measurements increase the accuracy of existing models, which when coupled with the proposed measurements allow for a more robust understanding of the keyhole dynamics during laser processing.

2.4. Processing in argon environment

For experiments involving an inert processing environment, modular gas flow ports on the integrating sphere are switched to allow it to be filled with argon. This experiment used 99.995 % industrial grade argon. Before each trial, the argon tank is opened and the flow rate into the sphere is monitored and kept low enough to ensure the position of the sphere is not disturbed. The gas flow is left on long enough to be confident that the full volume of the sphere has been recycled multiple times with argon gas. To remove any effect of the flow on melt pool behavior, it is shut off just before firing the laser pulse.

3. Results and Discussion

Single, stationary laser pulses of 10 ms each are applied to the NIST SRM samples, with a range of irradiance values encompassing conduction through keyhole mode (0.23 MW/cm² to 0.92 MW/cm²). The ICI system performs one-dimensional depth measurements at a rate of 200 kHz with an axial resolution of 15 μm . ICI monitors the axial position of the metal surface at the center of the melt pool, which may be either a keyhole depth (positive value) or melt bead height (defined here as negative depth). This versatility which comes from its large depth of field and dynamic range, serves well for monitoring transition mode processing where it may need to track both behaviors at different times. Absolute absorptance of the processing laser energy by the metal sample is measured using ISR with a time resolution of 4.4 μs .

3.1. Dynamic depth and absorptance measurements in argon and in air

Figure 1 shows select time-resolved measurements of depth and absorptance from each processing regime (conduction, transition, and keyhole) and for processing in argon and in air. The zero point on the depth scale represents the position of the metal surface measured by ICI before the laser is turned on. Negative values for depth correspond to above the initial sample surface. Laser turn-on occurs at 0 ms.

First, considering conduction mode (Fig. 1 a-b), at 0.35 MW/cm², the most noticeable difference is the reduced absorptance under inert conditions. In both cases, the absorptance slowly rises with some rapid fluctuations, but in argon it plateaus to an average value of 0.21 and in air it rises to a maximum of 0.51. This difference is explained by reduced oxidation under inert conditions. This is consistent with the difference in appearance in the weld beads after processing. The welds performed in air were dark brown while in argon they were bright and shiny. Considerable difference is also seen in the depth measurements. In air, the center of the melt pool rises over time to a maximum height of 83 μm , with slight

fluctuations throughout. In argon, the melt bead rises briefly before showing oscillatory behavior. In the figure, this appears as two distinct bands of data points around $-25\ \mu\text{m}$ and $20\ \mu\text{m}$.

In transition mode (Fig. 1 c-d), at $0.46\ \text{MW}/\text{cm}^2$, the behaviors in the two environments become more distinct. In air, we regularly observe the formation of temporary, highly volatile keyholes. These appear in the ICI data as sudden increases in depth, followed by rapid fluctuations, and eventually a sudden return to the pre-keyhole depth. Depth fluctuations are likely caused by sidewall protrusions or partial keyhole collapse, as both have the potential to limit the penetration of the ICI beam. The absorptance increases during these temporary keyholes to a maximum of 0.56, due to the temporary cavity formation. These shallow keyholes allow most of the processing light to interact with the workpiece multiple times due to reflections. It is interesting that even with the increased absorptance, the incident beam has sufficient energy to form a keyhole but not to sustain it. Surface tension pressure has been proposed as the likely cause for this behavior [24]. As irradiance increases through the transition mode in air ($0.44\ \text{MW}/\text{cm}^2$ to $0.49\ \text{MW}/\text{cm}^2$), the frequency and duration of temporary keyholes increases until a consistent keyhole can be maintained [21]. In argon, it was possible to observe this behavior, albeit less frequently. More often, a keyhole would not form at all and instead the depth and absorptance would oscillate, similar to what was seen in

conduction mode. This seemingly high variability between forming temporary keyholes or strong surface oscillations occurs over the narrow processing window from $0.45\ \text{MW}/\text{cm}^2$ to $0.52\ \text{MW}/\text{cm}^2$. The oscillating behavior is analyzed in greater detail in Section 3.3.

In keyhole mode (Fig. 1 e-f), at $0.58\ \text{MW}/\text{cm}^2$, the differences between air and argon conditions are reduced. For both environments, this irradiance is sufficient to quickly initiate keyhole formation and keep it open for the full 10 ms pulse. In argon, the keyhole growth rate is lower and does not reach the same maximum depth as in air for identical irradiances. The measured maximum absorptance is similarly reduced. These differences are expected, as oxygen content in assist gas has been shown to increase laser cutting speed [25] and improve the weldability of copper [26]. In both cases, an increase in initial absorptance due to oxidation was cited as the reason for these benefits. This claim seems to be confirmed by our data, as the weld in air has increased initial absorptance and greater achieved depths for the same laser exposure. Another effect that may play a part is the change in convective melt pool dynamics in inert environments. Specifically, the Marangoni flow is inward towards the center of the melt pool in the presence of high concentrations of oxygen and generally switches to outward flow when oxygen concentration is significantly reduced [27].

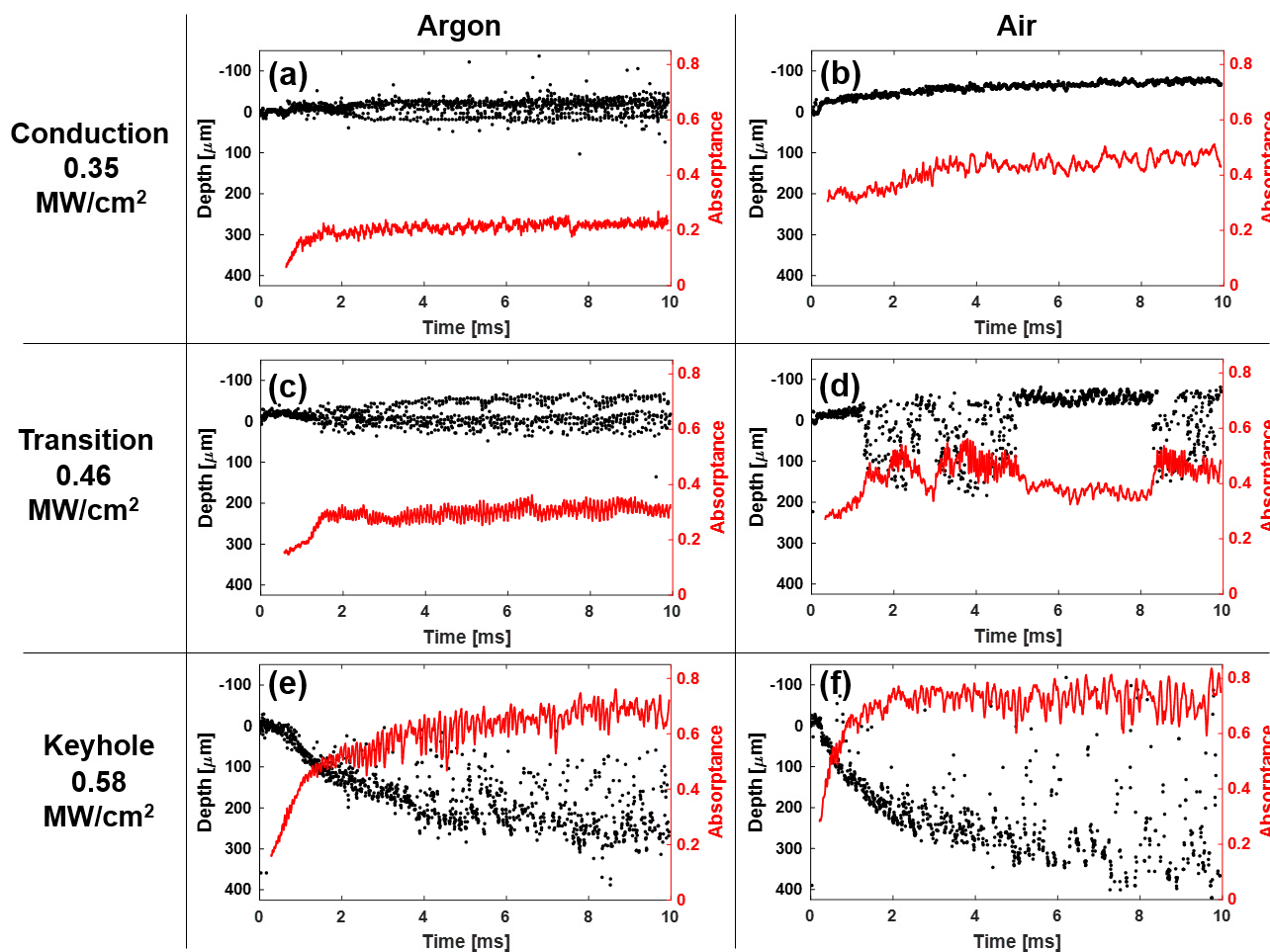


Fig. 1. Time-resolved depth and absorptance data from spot welds: (a) in argon at $0.35\ \text{MW}/\text{cm}^2$, (b) in air at $0.35\ \text{MW}/\text{cm}^2$, (c) in argon at $0.46\ \text{MW}/\text{cm}^2$, (d) in air at $0.46\ \text{MW}/\text{cm}^2$, (e) in argon at $0.58\ \text{MW}/\text{cm}^2$, (f) in air at $0.58\ \text{MW}/\text{cm}^2$.

3.2. Average depth and coupling efficiency in argon and in air

Time-averaged data, while only giving limited information about the dynamics of the process, are still useful for distinguishing thresholds between conduction and keyhole mode and for comparing general trends between processing parameters. From the time-resolved data shown in Section 3.1, it is straightforward to calculate the average absorptance (coupling efficiency) and average depth for each irradiance, as shown in Fig. 2.

For coupling efficiency, there is a striking gap at low irradiance due to lack of oxidation in inert environments. The largest difference is observed at an irradiance of 0.23 MW/cm², with argon and air environments giving coupling efficiencies of 0.08 and 0.42, respectively. As irradiance increases the argon coupling efficiency rises until the point where we start to observe temporary keyholes (the end of the conduction mode). In the absence of oxide formation this can be explained by the temperature dependence of absorptance [28, 29]. Over the same range in air, the measured coupling efficiency is relatively stable and even drops slightly before the transition mode starts, suggesting that oxide formation has a stronger influence than temperature on absorptance under these conditions. The slight drop may be caused by irradiance becoming high enough for oxide vaporization, but not yet high enough to generate sufficient recoil pressure to open a keyhole. Overall, conduction mode in argon compared to air has a 50 % ± 11 % reduction in coupling efficiency.

The main differences that occur in the transition regime between argon and air were described above alongside the time-resolved data, but here the difference in keyhole threshold

is better displayed. At 0.45 MW/cm², both environments start to allow temporary keyholes to form. By 0.52 MW/cm², spot welds in air consistently form sustained keyholes. In argon, we do not observe this until 0.58 MW/cm². The coupling efficiencies measured at these thresholds are 0.58 for air and 0.59 for argon. These values are obviously similar, but also close to the expected Fresnel absorption value that one would obtain from two reflections off a liquid steel surface [30, 31, 8]. This may imply that regardless of processing conditions the start of keyhole mode is the formation of a shallow cavity that supports two reflections (e.g., a cone with an aspect ratio of 1). This condition has been predicted in models for moving welds [32, 24].

In keyhole mode, the coupling efficiencies in both environments start to approach similar behavior. In this regime, factors that dominate absorptance in conduction and transition mode are now dwarfed by the geometric effects of keyholes and the multiple reflections they facilitate. Interestingly, the coupling efficiencies are closer than one would expect when considering that the argon spot welds have disproportionately lower average depth in this regime. Firstly, this may simply be because absorptance has a reduced sensitivity to depth as depth increases [6]. At a certain point, more reflections will have a negligible effect on the absorptance, so keyholes over a range of depths can all give similar absorptance. Another possibility is that the shape of the keyhole is generally different between the two environments, allowing the shallower keyholes in argon to give similar absorptance as those deeper ones in air. Regardless of the exact mechanisms, the coupling efficiency in keyhole mode in argon compared to air is reduced by only 8 % ± 3 %.

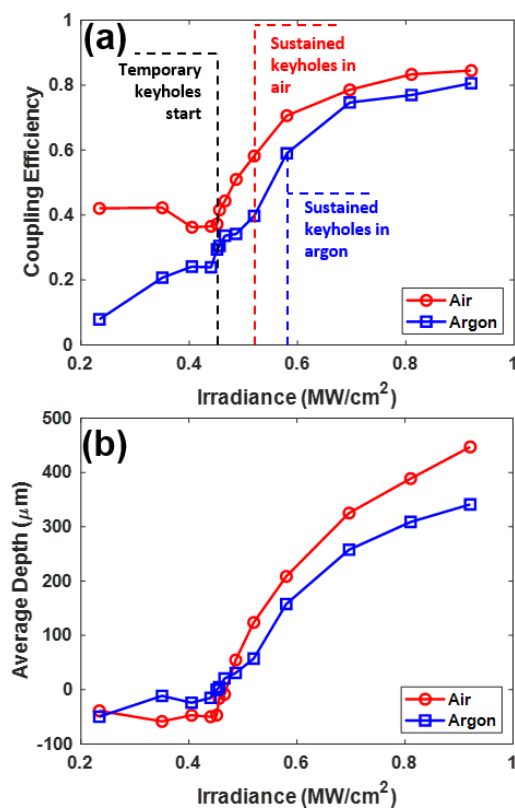


Fig. 2. Time-averaged data for (a) coupling efficiency and (b) average depth, for both argon and air environments.

3.3. Time-frequency data from transition mode in argon

Time-resolved data from the transition mode in argon suggests oscillatory behavior, but the relationship between frequency of depth and absorptance fluctuations is not obvious from simple inspection of Fig 1 c. We use a short-time Fourier transform (STFT) to quantify oscillation frequencies of the time-resolved depth and absorptance data and see how they evolve in time. STFTs cannot be performed on sparse data sets, and since ICI experiences occasional signal loss in this regime due to off-axis specular reflections, gaps in the depth measurements are linearly interpolated before frequency analysis. STFTs were performed on depth and absorptance data independently, using a Hann window with a length of 1 ms and 50 % overlap (to ensure equal sampling of all data points). Since absorptance data only starts at 0.57 ms (see Section 2.3) and because the pulse durations are not a full 10 ms, the STFTs exclude data from the first 1.07 ms and last 0.93 ms of the spot weld.

Figure 3 a-b show the results of STFTs performed on the time-resolved data in Fig. 1 c. In both the absorptance and depth spectrograms there is a distinct curve that starts near 15 kHz and decreases to 10 kHz over the weld duration. There are also fainter curves at multiples of these frequency values. These higher harmonics suggest that the oscillations are not perfectly sinusoidal. Also notable from the spectrograms is the width of the fundamental frequency peaks. These peaks are modeled well by Gaussian functions and all have full width at half

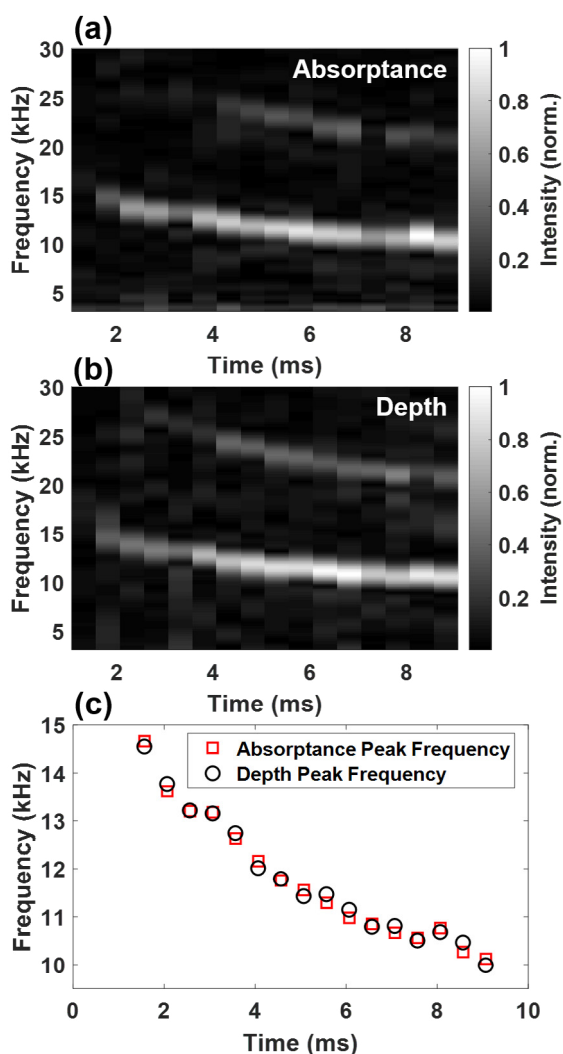


Fig. 3. Time-frequency data from a spot weld performed in argon environment at irradiance of 0.46 MW/cm^2 . (a) and (b) show spectrograms generated by STFT for absorptance and depth, respectively. A Hann window was used with 1 ms length and 50 % overlap. Low frequencies ($< 3 \text{ kHz}$) are excluded from the plot as they are not in a region of interest and contain DC noise. (c) Plot of the peak frequencies from each window of the STFTs found using Gaussian fits.

maximum close to 2 kHz. This gives a good estimate on the frequency resolution of this method, although the fit uncertainties on the center frequency positions are much lower (less than 10 Hz).

Figure 3 c plots the peak frequency (found by Gaussian fitting) as a function of time for both depth and absorptance. This shows more clearly how the fundamental frequency decreases over time, which is expected to occur as the melt pool volume grows [33]. The analogy of a vibrating drumhead is useful: a larger surface area drum has a lower resonance frequency. The second point is that the frequency of oscillations in depth and absorptance, which are measured independently, evolve together with similar values. This suggests that these non-keyhole surface oscillations are directly responsible for the oscillations in absorptance.

As mentioned in Section 3.1, we observe these strong surface oscillations throughout the transition mode in argon, but sometimes a repeated trial at the same irradiance will show temporary keyhole formation. Being so close to the threshold of keyhole formation, it is possible that the amplitude of the

absorptance oscillations may dictate when these temporary keyholes form. As other work has shown, the fundamental frequency of the melt pool can be driven by modulating the laser beam at the same frequency to assist in laser drilling [34]. Here we show that driving these surface oscillations may not work only by mechanical resonance, but also by dynamic increases in energy coupling. This may open the possibility of fine control over keyhole formation (or suppression) by monitoring and exploiting surface mode oscillations.

4. Conclusion

By implementing ICI and ISR simultaneously to monitor laser spot welding of AISI 316 stainless steel, we have revealed unique insights into the underlying physics of laser-metal interaction. We showed that processing in argon compared to air significantly reduces coupling efficiency in conduction mode due to the lack of oxide formation. We observed that transition mode melt pools in argon undergo well-defined surface oscillations, decrease in frequency from 15 kHz to 10 kHz over time, and sometimes form temporary keyholes. These surface oscillations also produced highly correlated oscillations in absorptance. In a range of irradiance where sustainable keyholes could be formed, time-resolved and time-averaged data for spot welds in argon and in air become more similar, providing further evidence that multiple reflections is the dominant factor that influences absorptance in keyhole mode. These observations will be valuable for development of models and active control schemes, highlighting the importance of hybrid monitoring tools that measure multiple aspects of the process simultaneously.

Acknowledgements

The authors thank Chris Yung (NIST, Boulder), Nicholas Derimow (NIST, Boulder), and Norman Sanford (NIST, Boulder) for their careful reading of the manuscript and insightful comments. T.R.A. and J.M.F. acknowledge funding received from the Natural Sciences and Engineering Research Council of Canada, the Canadian Foundation for Innovation, and the Ontario Centres of Excellence.

References

- [1] J. Svenungsson, I. Choquet and A. F. Kaplan, "Laser welding process – a review of keyhole welding modelling," *Physics Procedia*, vol. 78, pp. 182-191, 2015.
- [2] B. Zhang, Y. Li and Q. Bai, "Defect formation mechanisms in selective laser melting: a review," *Chinese Journal of Mechanical Engineering*, vol. 30, no. 3, pp. 515-527, 2017.
- [3] H. Bikas, P. Stavropoulos and G. Chryssolouris, "Additive manufacturing methods and modelling approaches: a critical review," *The International Journal of Advanced Manufacturing Technology*, vol. 83, pp. 389-405, 2016.
- [4] M. Francois, A. Sun, W. King, N. Henson, D. Turrett, C. Bronkhorst, N. Carlson, C. Newman, T. Haut, J. Bakosi, J. Gibbs, V. Livescu, S. Vander Wiel, A. Clarke, M. Schraadt, T. Blacker, H. Lim, T. Rodgers, S. Owen, F. Abdeljawad, J. Madison, A. Anderson, J.-L. Fattebert, R. Ferencz, N. Hodge, S. Khairallah and O. Walton, "Modeling of additive manufacturing processes for metals: Challenges and opportunities," *Current Opinion in Solid State and Materials Science*, vol. 21, no. 4, pp. 198-206, 2017.
- [5] A. Kaplan, "A model of deep penetration laser welding based on calculation of the keyhole profile," *Journal of Physics D: Applied*

- Physics*, vol. 27, pp. 1805-1814, 1994.
- [6] S. C. Wang and P. S. Wei, "Energy-Beam redistribution and absorption in a drilling or welding cavity," *Metallurgical Transactions B*, vol. 23, no. 4, pp. 505-511, 1992.
- [7] C. Y. Ho and P. S. Wei, "Energy absorption in a conical cavity truncated by spherical cap subject to a focused high-intensity beam," *International Journal of Heat and Mass Transfer*, vol. 40, no. 8, pp. 1895-1905, 1997.
- [8] W. Tan, N. S. Bailey and Y. C. Shin, "Investigation of keyhole plume and molten pool based on a three-dimensional dynamic model with sharp interface formulation," *Journal of Physics D: Applied Physics*, vol. 46, no. 5, p. 055501, 2013.
- [9] R. Cunningham, C. Zhao, N. Parab, C. Kantzos, J. Pauza, K. Fezzaa, T. Sun and A. D. Rollett, "Keyhole threshold and morphology in laser melting revealed by ultrahigh-speed x-ray imaging," *Science*, vol. 363, no. 6429, pp. 849-852, 2019.
- [10] A. A. Martin, N. P. Calta, J. A. Hammons, S. A. Khairallah, M. H. Nielsen, R. M. Shuttlesworth, N. Sinclair, M. J. Matthews, J. R. Jeffries, T. M. Willey and J. R. Lee, "Ultrafast dynamics of laser-metal interactions in additive manufacturing alloys captured by in situ X-ray imaging," *Materials Today Advances*, vol. 1, p. 100002, 2019.
- [11] B. J. Simonds, J. Sowards, J. Hadler, E. Pfeif, B. Wilthan, J. Tanner, C. Harris, P. Williams and J. Lehman, "Time-resolved absorptance and melt pool dynamics during intense laser irradiation of a metal," *Physical Review Applied*, vol. 10, p. 044061, 2018.
- [12] B. J. Simonds, E. J. Garboczi, T. A. Palmer and P. A. Williams, "Dynamic Laser Absorptance Measured in a Geometrically Characterized Stainless-Steel Powder Layer," *Physical Review Applied*, vol. 13, no. 2, pp. 024057, 2020.
- [13] P. J. L. Webster, L. G. Wright, Y. Ji, C. M. Galbraith, A. W. Kinross, C. Van Vlack and J. M. Fraser, "Automatic laser welding and milling with in situ inline coherent imaging," *Optics Letters*, vol. 39, no. 21, pp. 6217-6220, 2014.
- [14] J. J. Blecher, C. M. Galbraith, C. Van Vlack, T. A. Palmer, J. M. Fraser, P. J. L. Webster and T. DebRoy, "Real time monitoring of laser beam welding keyhole depth by laser interferometry," *Science and Technology of Welding and Joining*, vol. 19, no. 7, pp. 560-564, 2014.
- [15] J. A. Kanko, A. P. Sibley and J. M. Fraser, "In situ morphology-based defect detection of selective laser melting through inline coherent imaging," *Journal of Materials Processing Technology*, vol. 231, pp. 488-500, 2016.
- [16] T. G. Fleming, S. G. Nestor, T. R. Allen, M. A. Boukhaled, N. J. Smith and J. M. Fraser, "Tracking and controlling the morphology evolution of 3D powder-bed fusion in situ using inline coherent imaging," *Additive Manufacturing*, vol. 32, p. 100978, 2020.
- [17] J. T. Norris, C. V. Robino, M. J. Perricone and D. A. Hirschfeld, "Development of a time-resolved energy absorption measurement technique for laser beam spot welds," *Welding Journal*, vol. 89, pp. 75-81, 2010.
- [18] J. Xie and A. Kar, "Laser welding of thin sheet steel with surface oxidation," *Welding Journal*, vol. 78, pp. 343s-348s, 1999.
- [19] C. L. A. Leung, S. Marussi, M. Towrie, R. C. Atwood, P. J. Withers and P. D. Lee, "The effect of powder oxidation on defect formation in laser additive manufacturing," *Acta Materialia*, vol. 166, 2019.
- [20] P. J. DePond, G. Guss, S. Ly, N. P. Calta, D. Deane, S. Khairallah and M. J. Matthews, "In situ measurements of layer roughness during laser powder bed fusion additive manufacturing using low coherence scanning interferometry," *Materials & Design*, vol. 154, pp. 347-359, 2018.
- [21] T. R. Allen, W. Huang, J. R. Tanner, W. Tan, J. M. Fraser and B. J. Simonds, "Energy coupling mechanisms revealed through simultaneous keyhole depth and absorptance measurements during laser-metal processing," *Physical Review Applied*, to be published.
- [22] SRM 1155a., *AISI 316 Stainless Steel*, (National Institute of Standards and Technology; U.S. Department of Commerce, Gaithersburg, MD, 2013).
- [23] P. Pichler, B. J. Simonds, J. W. Sowards and G. Pottlacher, "Measurements of thermophysical properties of solid and liquid NIST SRM 316L stainless steel," *Journal of Materials Science*, vol. 55, no. 9, pp. 4081-4093, 2019.
- [24] R. Fabbro, "Depth dependence and keyhole stability at threshold, for different laser welding regimes," *Applied Sciences*, vol. 10, no. 4, p. 1487, 2020.
- [25] H. Golnabi and M. Bahar, "Investigation of optimum condition in oxygen gas-assisted laser cutting," *Optics and Laser Technology*, vol. 41, no. 4, pp. 454-460, 2009.
- [26] E. Biro, D. C. Weckman and Y. Zhou, "Pulsed Nd:YAG laser welding of copper using oxygenated assist gases," *Metallurgical and Materials Transactions A: Physical Metallurgy and Materials Science*, vol. 33, no. 7, pp. 2019-2030, 2002.
- [27] C. Zhao, C. Kwakernaak, Y. Pan, I. Richardson, Z. Saldi, S. Kenjeres and C. Kleijn, "The effect of oxygen on transitional Marangoni flow in laser spot welding," *Acta Materialia*, vol. 58, no. 19, pp. 6345-6357, 2010.
- [28] S. Boyden and Y. Zhang, "Temperature and wavelength-dependent spectral absorptivities of metallic materials in the infrared," *Journal of Thermophysics and Heat Transfer*, vol. 20, no. 1, pp. 9-15, 2006.
- [29] T. J. Wieting and J. L. Derosa, "Effects of surface condition on the infrared absorptivity of 304 stainless steel," *Journal of Applied Physics*, vol. 50, no. 2, pp. 1071-1078, 1979.
- [30] W. Schulz, G. Simon, H. M. Urbassek and I. Decker, "On laser fusion cutting of metals," *Journal of Physics D: Applied Physics*, vol. 20, no. 4, pp. 481-488, 1987.
- [31] R. Ducharme, K. Williams, P. Kapadia, J. Dowden, B. Steen and M. Glowacki, "The laser welding of thin metal sheets: an integrated keyhole and weld pool model with supporting experiments," *Journal of Physics D: Applied Physics*, vol. 27, pp. 1619-1627, 1994.
- [32] V. Semak and A. Matsunawa, "The role of recoil pressure in energy balance during laser materials processing," *Journal of Physics D: Applied Physics*, vol. 30, no. 18, pp. 2541-2552, 1997.
- [33] Y. H. Xiao and G. Den Ouden, "A study of GTA weld pool oscillation," *Welding Journal*, vol. 69, pp. 289s-293s, 1990.
- [34] S. Ly, G. Guss, A. M. Rubenchik, W. J. Keller, N. Shen, R. A. Negres and J. Bude, "Resonance excitation of surface capillary waves to enhance material removal for laser material processing," *Scientific Reports*, vol. 9, no. 1, pp. 1-9, 2019.

11th CIRP Conference on Photonic Technologies [LANE 2020] on September 7-10, 2020

Geometrical control of DED processes based on 3D scanning applied to the manufacture of complex parts

Iker Garmendia^{a*}, Jon Flores^a, Mikel Madarieta^a, Aitzol Lamikiz^b, Luis Gerardo Uriarte^a,

Carlos Soriano^a

^aTEKNIKER, Iñaki Goenaga 5, Eibar 20600, Spain

^bUniversity of the Basque Country, ETSII, Alameda de Urquijo s/n, Bilbao 48013, Spain

* Corresponding author. Tel.: +34-943-206-744 ; fax: +34-943-202-744. E-mail address: iker.garmendia@tekniker.es

Abstract

Directed Energy Deposition (DED) processes are known for producing parts close to their final shape where only a post-process finish machining is required. However, geometrical deviations due to thermal effects may occur during the process, which results in the final geometry not being achieved or in the necessity of oversizing the part in order to compensate the distortion in the subsequent machining. In this article, a 3D scanning methodology of the manufactured part will be used to measure the geometry at different stages of the Laser Metal Deposition (LMD) process. In this way it is possible to assist the manufacturing as well as to make a comparison with the theoretical geometry during the process. This results in a higher probability of manufacturing the part without process failures and obtaining a precise reproduction of the geometry to be manufactured, reducing the subsequent post-processing operations and saving manufacturing time and cost.

© 2020 The Authors. Published by Elsevier B.V.

This is an open access article under the CC BY-NC-ND license (<http://creativecommons.org/licenses/by-nc-nd/4.0/>)

Peer-review under responsibility of the Bayerisches Laserzentrum GmbH

Keywords: Laser Metal Deposition; Additive Manufacturing, Directed Energy Deposition, control, 3D scanner

1. Introduction

Additive Manufacturing (AM) methods based on Directed Energy Deposition (DED) offer the opportunity to generate medium to large sized and moderately complex parts in a near net shape way, i.e. close to the geometry of the final part. This makes them an alternative to conventional manufacturing methods with great flexibility and high savings in waste material [1,2].

However, the precision with which the parts are achieved together with the surface finish obtained after the process means that in most cases a subsequent machining finishing operation is required. In addition, due to the high heat input on the part, it is usual to have geometrical deviations on the component due to the induced residual stresses that may require rejects in manufacturing or an oversizing of the part. On the

other hand, there is often irregular growth in the different areas of the part due to thermal effects, part geometry or deposition patterns. For this reason there is an increasing interest in dimensionally controlling the part while it is being manufactured [3].

In [4] Stravroulakis et al. reviewed current metrological methods and studied their possible incorporation into AM processes. From their point of view, new sensors with software and hardware improvements could appear in the future, with a higher precision and measurement range than the current ones and that would allow working under process conditions.

In some cases, geometrical analyses have been carried out by digitizing the parts after their manufacture. In [5] Möller and Emmelmann conducted a study of the deviations of the manufactured part from the original CAD by relating them to the residual stresses resulting from the process. Turichin et al.

employed a similar procedure in the manufacture of a large cylinder, again analysing distortions due to residual stresses [6]. In these cases, the distortions were measured after the process once the part had cooled down. Nevertheless, it is possible that under certain conditions the geometrical deviations are such that a process failure occurs, so a measurement would be necessary during the manufacturing process.

Some works have aimed at making measurements during the deposition process by projecting laser light on the beads already deposited and processing the image obtained by a vision camera [7,8]. These systems are focused on providing closed-loop control over the process, although they present challenges such as the directionality of the measurement and the difficulty of making precise measurements on the area close to the melt pool. On the other hand, there are some works in which measurements of the part were made in intermediate stages of manufacture, either with the use of line scanners [9] or scanners based on structured light projection [10–12].

Moreover, the exposed works perform measurements only on the last deposited layer or on the complete part once manufacturing has been completed and the component moved from the manufacturing system to the measurement environment, so developments are still needed to incorporate these dimensional measurements in-process.

This work presents a methodology that allows the incorporation of the digitalization of the piece in the DED AM system, establishing a quality control as an intermediate stage of the manufacture, and can provide an auxiliary tool for the process trajectory generation.

2. Experimental set-up

The LMD cell in Fig. 1 was used for the development of this work. A 4kW IPG YLS4000 processing laser an ABB IRB4400 robot with an IRBP 250A positioner were used. Ti6Al4V wire of 0.8 mm diameter was deposited by means of a DINSE wire feeder and the COAXwire deposition head developed by Fraunhofer IWS [13].

The structured light based GOCATOR 3109 3D scanner was used to scan the manufactured part. The scanner has a near field of view of 67x86 mm and a far field of view of 93x88 mm, with a measurement range of 70 mm. As the part to be scanned was larger than the scanning volume, multiple scans from different robot poses were necessary to acquire the complete surface. The source of the projected light consists of blue LED emitted at a wavelength around 460 nm. The measurement accuracy is of +/- 50µm.

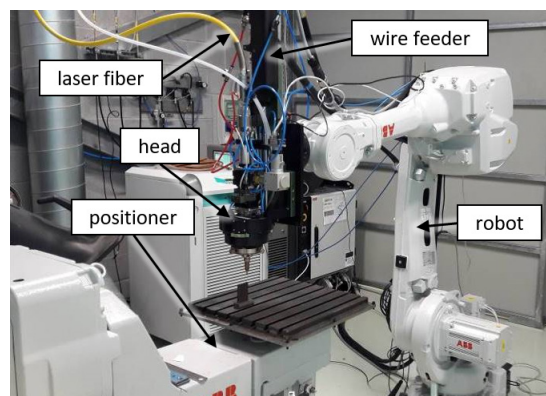


Fig. 1. Laser Metal Deposition robotic cell consisting of an industrial robot and a two-axis positioner.

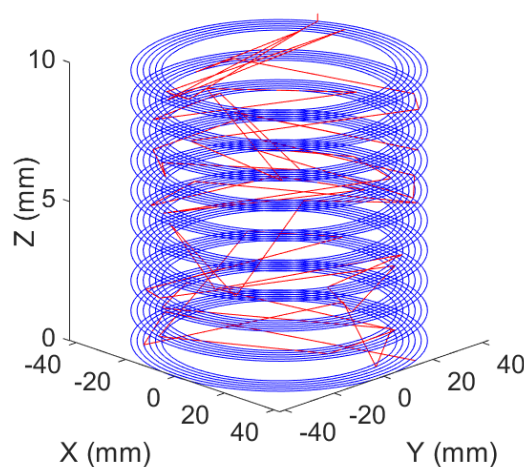


Fig. 2. Robotic trajectories with deposition (blue) and air (red) movements.

3. Methodology

3.1. DED robotic trajectory generation

The manufactured part consisted of a solid cylinder composed of coaxial circles with a distance between layers of 1.08 mm (Fig. 2). The separation between the cylinders was set at 1.76 mm corresponding to a 40% overlap. In order to avoid the possible appearance of defects at the union between the end and the beginning of each circle, both the starting point and the direction of rotation were set randomly. Also, the direction in which the cylinders were deposited was alternated from inside to outside and from outside to inside.

In this case, the rotation of the vertical axis of the positioner was used to reproduce the circular movements. Since the robot's working coordinate system, referred to as Work Object Coordinate System (CS_{WO}) moves together with the positioner, it is necessary to introduce a rotation in the head opposite to the rotation of the positioner. In this way, the head is kept with a constant orientation while the positioner rotates. On the other hand, the rotation of the positioner has angular limits ranging from -720° to 720° , which makes it impossible to deposit all the cylinders continuously. For this reason, after each cylinder has been deposited, the rotation of the positioner is restored.

3.2. Hand-eye calibration

The purpose of a hand-eye calibration is to obtain the coordinates of a scan, which by default are referenced to a scanner's coordinate system, CS_{scan} , referenced to the robot's CS_{WO} ,

$$\{p\}^{WO} = [T]_{scan}^{WO} \{p\}^{scan} \quad (1)$$

where:

- $\{p\}^{WO}$ are the coordinates of a scanned point referenced in the CS_{WO} .
- $\{p\}^{scan}$ are the coordinates of a scanned point referenced in the CS_{scan} .
- $[T]_{scan}^{WO}$ is the transformation matrix from CS_{scan} to CS_{WO} .

In order to obtain $[T]_{scan}^{WO}$ a new coordinate system is introduced, the Tool Center Point, TCP, of the robot, CS_{TCP} . Typically, this coordinate system refers to the tool tip or laser spot during AM, but in the case of the calibration, any coordinate system fixed in the deposition head can be used. Thus, $[T]_{scan}^{WO}$ is divided into two new transformation matrices,

$$\{p\}^{WO} = [T]_{TCP}^{WO} [T]_{scan}^{TCP} \{p\}^{scan} \quad (2)$$

where:

- $[T]_{TCP}^{WO}$ is the transformation matrix from CS_{TCP} to CS_{WO} , which is obtained as the pose of the robot on each scan.
- $[T]_{scan}^{TCP}$ is the transformation matrix from CS_{scan} to CS_{TCP} , and corresponds to the fixed relation between the scanner and the TCP of the robot, which is obtained by the hand-eye calibration.

To solve the calibration, a variant of equation (2) is used, which instead of working with the coordinates of a scanned point, $\{p\}^{scan}$, takes the position and orientation of the coordinate system of a calibration object, $[T]_{obj}^{scan}$:

$$[T]_{scan}^{TCP} = [T]_{TCP}^{WO} [T]_{obj}^{WO} [T]_{scan}^{obj} \quad (3)$$

An illustration of the coordinate systems involved in the calibration is shown in Fig. 3a. In this case, the Tsai-Lenz hand-eye calibration method was chosen to solve the calibration [14]. The procedure was set up by fixing the scanner on the deposition head. This method solves two transformation matrices at the same time, $[T]_{obj}^{WO}$ and $[T]_{scan}^{TCP}$, so as $[T]_{scan}^{TCP}$ is known for each robot pose, it is only necessary to solve $[T]_{scan}^{obj}$. Scans from various positions are necessary to resolve the system and reduce the calibration error, while the placement of the calibration object is indifferent. In this case, 10 different robot poses were used for the calibration.

$[T]_{scan}^{obj}$ was obtained in this case by scanning a four-sphere pattern made of plastic using Fused Deposition Modeling (FDM) AM technology. The spheres were detected by means of sphere fitting, and knowing the coordinates of their centres with respect to the scanner and to the coordinate system of the object, the transformation was obtained (Fig. 3b).

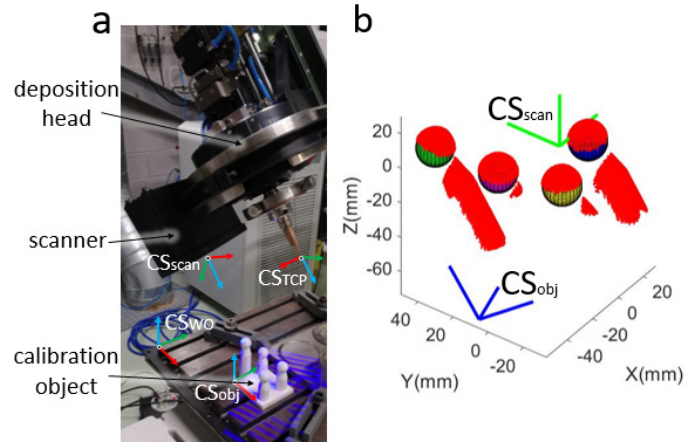


Fig. 3. (a) Representation of the coordinate systems involved in the hand-eye calibration; (b) Sphere fitting performed to obtain the calibration object to scanner transformation.

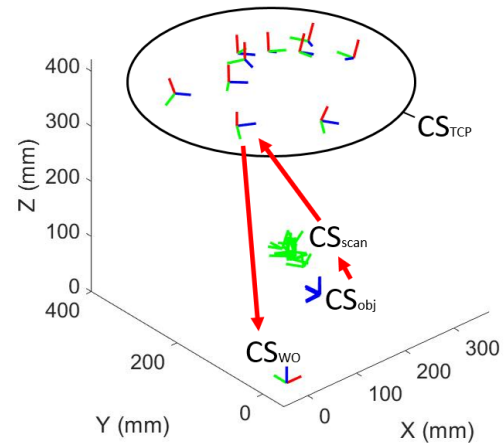


Fig. 4. Validation of the calibration output, showing the coordinate systems obtained from the different robot poses. As a result of the hand-eye calibration, CS_{obj} matches for all scanning poses.

Finally, equation (3) is computed and $[T]_{scan}^{TCP}$ is obtained, i.e. the position and orientation of the scanner relative the TCP of the robot. Fig. 4 shows the validation of the calibration where CS_{obj} is overlaid for the different robot poses used in the calibration. Red arrows indicate the transformations needed to obtain the transformation from CS_{obj} to CS_{WO} , or in other words, the path used to reference a acquired point in the scanner's coordinate system, $\{p\}^{scan}$, to the robot's coordinate system, $\{p\}^{WO}$.

3.3. Laser Metal Deposition

The part in Fig. 5 was manufactured with a laser power of 1800 W, a robot speed of 25 mm/s and a wire insertion speed of 5 m/min resulting in a feed rate of 0.667 kg/h. Argon was used as protective gas through the deposition nozzle. In this case work was done with the laser defocused at 0.5 mm above the focus.

The result was a part with an outer diameter of 85 mm and an inner diameter of 63.5 mm with a height of 49.6 mm.

To avoid surface oxidation of the part in the future, a robotic bag with a protective atmosphere should be integrated, capable

of working with the coordinated movement between the robot and the positioner.

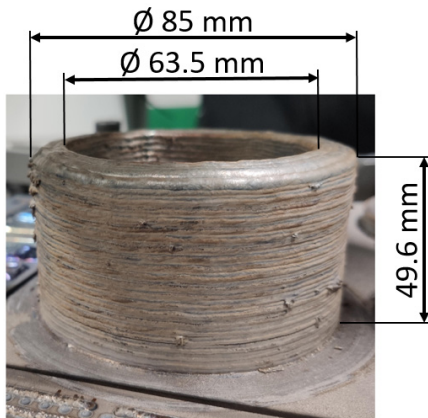


Fig. 5. Cylindrical Ti6Al4V part manufactured by wire Laser Metal Deposition.

4. Results

After the hand-eye calibration and manufacturing of the part, a scanning from different locations was conducted. Fig. 6 shows one of the positions in which the side wall of the manufactured cylinder was scanned. The positioner was again employed to rotate the part and achieve relative positioning between scanner and part. As a result of the calibration, the coordinates obtained from the different points of view were referenced to the coordinate system of the manufacturing system, so no further translation or orientation transformations were required.

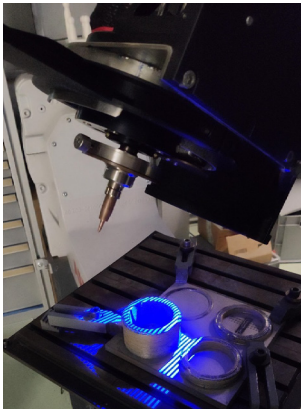


Fig. 6. Scanning of the manufactured cylinder from one of the robot poses.

However, the point clouds obtained were filtered and downsampled to reduce their size and facilitate their handling. Fig. 7 shows the result after the stitching of the different point clouds acquired. The colour scales represent the height reached in the piece with respect to the base of the manufacture (top) and to the mean height of the last deposited layer (bottom). This information can be especially useful to determine if the growth of the part is being adequate, allowing to implement corrections on the robot position in order to maintain an optimal distance between deposition nozzle and part.

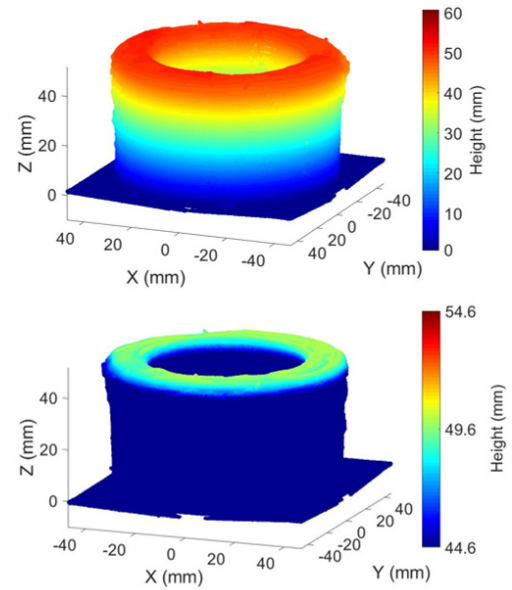


Fig. 7. Point cloud obtained after stitching the scans obtained from different positions, indicating the height obtained in the deposition.

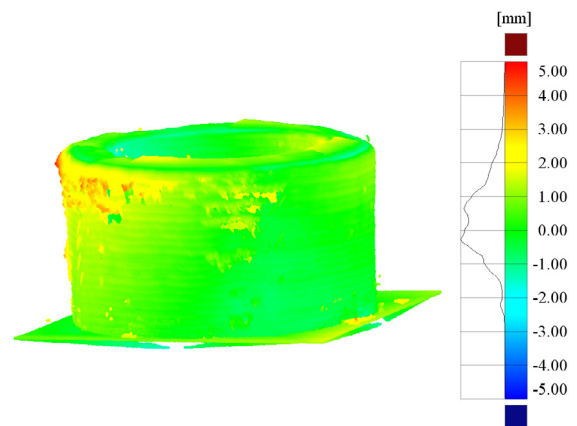


Fig. 8. Comparison of the scan of the manufactured part against the CAD model showing the geometrical differences.

Finally, in Fig. 8 a comparison against the CAD model of the manufactured part is presented. The geometrical deviations due to the process can therefore be examined.

5. Conclusion

This study has introduced a methodology for the integration of a three-dimensional measurement system into an AM system based on DED technologies. Compared to other part digitizing methods, which only obtain information from the last layer or bead deposited, the developed approach allows to obtain a complete reconstruction of the manufactured geometry in the coordinates of the manufacturing machine or robot and in an efficient and automatable way.

As a result, in-process dimensional quality control of the part can be performed, without the need to conclude production and dismount the part to an external 3D measurement environment. This allows an early control of geometric distortions through comparison against the CAD of the component to be manufactured. On the other hand, the

development can be employed to digitalize component surfaces and generate robot or machine trajectories without the need of a CAD model, enabling its implementation in cutting, deburring, cladding or AM applications.

Future challenges include the construction of a more accurate calibration object and the verification of the uncertainty of the calibration method as a result of errors induced by the scanning, calibration methodology and robot movement.

In addition, their suitability for DED processes, and in particular the LMD, will be investigated by incorporating intermediate scans in the manufacture of geometrically complex components. The effect of the part shrinkage due to cooling and geometrical distortion due to thermal stresses will be further studied.

Acknowledgements

The authors wish to acknowledge the financial support given by ASSALA project under H2020-EU.3.4.5 CLEANSKY2 programme (Grant agreement ID: 831857), and by the Basque Government through the ADDISEND and LASPRINT projects part of the Elkartek 2018 and Hazitek 2018 programmes.

References

- [1] Thomas, D.; Gilbert, S. Costs and Cost Effectiveness of Additive Manufacturing. In Proceedings of the NIST Special Publication; 2014; Vol. 1176, pp. 1–77.
- [2] Allen, J. An Investigation into the Comparative Costs of Additive Manufacture vs. Machine from Solid for Aero Engine Parts. In Proceedings of the Cost Effective Manufacture via Net Shape Processing.; 2006; pp. 17-1-17–10.
- [3] Mani, M.; Lane, B.M.; Donmez, M.A.; Feng, S.C.; Moylan, S.P. Measurement science needs for real-time control of additive manufacturing metal powder bed fusion processes; 2016.
- [4] Stavroulakis, P.I.; Leach, R.K. Stavroulakis, P. I. and Leach, Richard K. (2016) Review of post-process optical form metrology for industrial-grade metal additive manufactured parts. Review of. 2016, 87, <https://doi.org/10.1063/1.4944983>.
- [5] Möller, M.; Emmelmann, C. Quality target-based control of geometrical accuracy and residual stresses in laser metal deposition. J. Laser Appl. 2018, 30, 32303, <https://doi.org/10.2351/1.5040623>.
- [6] Turichin, G.; Zemlyakov, E.; Babkin, K.; Ivanov, S.; Vildanov, A. Analysis of distortion during laser metal deposition of large parts. Procedia CIRP 2018, 74, 154–157, <https://doi.org/10.1016/j.procir.2018.08.068>.
- [7] Davis, T.A.; Shin, Y.C. Vision-based clad height measurement. Mach. Vis. Appl. 2011, 22, 129–136, <https://doi.org/10.1007/s00138-009-0240-9>.
- [8] Heralić, A.; Christiansson, A.K.; Ottosson, M.; Lennartson, B. Increased stability in laser metal wire deposition through feedback from optical measurements. Opt. Lasers Eng. 2010, 48, 478–485, <https://doi.org/10.1016/j.optlaseng.2009.08.012>.
- [9] Heralić, A.; Christiansson, A.-K.; Lennartson, B. Height control of laser metal-wire deposition based on iterative learning control and 3D scanning. Opt. Lasers Eng. 2012, 50, 1230–1241, <https://doi.org/http://dx.doi.org/10.1016/j.optlaseng.2012.03.016>.
- [10] Buhr, M.; Weber, J.; Wenzl, J.-P.; Möller, M.; Emmelmann, C. Influences of process conditions on stability of sensor controlled robot-based laser metal deposition. Procedia CIRP 2018, 74, 149–153, <https://doi.org/10.1016/j.procir.2018.08.067>.
- [11] Garmendia, I.; Pujana, J.; Lamikiz, A.; Flores, J.; Madarieta, M. Development of an Intra-Layer Adaptive Toolpath Generation Control Procedure in the Laser Metal Wire Deposition Process. Materials (Basel). 2019, 12, 352, <https://doi.org/10.3390/ma12030352>.
- [12] Garmendia, I.; Pujana, J.; Lamikiz, A.; Madarieta, M.; Leunda, J. Structured light-based height control for laser metal deposition. J. Manuf. Process. 2019, 42, 20–27, <https://doi.org/10.1016/j.jmapro.2019.04.018>.
- [13] Ocylok, S.; Lechnitz, M.; Thieme, S.; Ocylok, S. Investigations on laser metal deposition of stainless steel 316L with coaxial wire feeding. In Proceedings of the 9th International Conference on Photonic Technologies LANE 2016; 2016; pp. 1–4.
- [14] Tsai, R.Y. An Efficient and Accurate Camera Calibration Technique for 3D Machine Vision. In Proceedings of IEEE Conference on Computer Vision and Pattern Recognition; 1986; pp. 364–374.

11th CIRP Conference on Photonic Technologies [LANE 2020] on September 7-10, 2020

A multi-parameter control of track geometry and melt pool size for laser metal deposition

Dieter Tyralla^a *, Henry Köhler^a, Thomas Seefeld^a, Claus Thomy^a, Ryuichi Narita^b

^aBIAS – Bremer Institut für angewandte Strahltechnik GmbH, Klagenfurter Str. 5, 28359 Bremen, Germany

^bMitsubishi Heavy Industries, Ltd., 2 Chome-1-1 Araicho Shinjima, Takasago, Hyogo 676-8686, Japan

* Corresponding author. Tel.: +49-421-218-58113; fax: +49-421-218-58063. E-mail address: tyralla@bias.de

Abstract

The present work demonstrates a multi-parameter control for constant track geometry and consistent layer height in laser metal deposition process. A two-channel pyrometric camera is used to maintain a constant melt pool size by a laser power control, whereby a constant bead geometry can be provided. In addition, laser triangulation sensors are used to observe the layer shape and maintain an optimum overlap by the lateral movement of the processing head. Without prior parameter studies a net shape geometry with a machining allowance of only 2% can be achieved.

© 2020 The Authors. Published by Elsevier B.V.

This is an open access article under the CC BY-NC-ND license (<http://creativecommons.org/licenses/by-nc-nd/4.0/>)

Peer-review under responsibility of the Bayerisches Laserzentrum GmbH

Keywords: Laser metal deposition; process monitoring & control; temperature field measurement; melt pool geometry; heat input; laser power control; seam tracking; laser triangulation; overflow control

1. Introduction

Laser metal deposition (LMD) is widely used as a reconditioning process for machine parts or as cladding process for the functionalization of part surfaces. After the cladding process, machining is mandatory in many cases. The post processing effort can be reduced by near net shape production. The layer geometry is especially influenced by the geometry of the single tracks and the overlap between neighboring beads. Therefore, the laser metal deposition process is usually validated by the dilution and the height of the resulting layer. Different approaches are known from literature to provide optimal overlap and dilution, but up to today extensive parameter studies are done in most cases.

1.1. Dilution and thermal process monitoring

The dilution influences the purity of the clad material and thus the resulting properties. The dilution is commonly

validated by the help of a cross-section. The melted area under the substrate surface is related to the total melted area [1]. The dilution is primarily influenced by the relation of energy per unit length and powder mass per unit length. For a constant layer quality, the thermal conditions have to be controlled. Hence, the temperature field of the process zone is a suitable indicator for the current state of the process [2].

Temperature measurement in LMD process is demanding because of high temperature ranges and the high welding speeds [3]. Optical measurement methods with high frame rates are necessary. The most common method for the temperature measurement in LMD is a lateral or coaxial pyrometer measurement [4]. Sometimes a camera is used for a correlation of grayscale and temperature [5] or IR-cameras are used to determine the temperature laterally [6]. There are experiments that combine the temperature measurement of a pyrometer and the images of a camera to determine the temperatures field [7]. In other cases, pyrometers in the near infrared range are integrated coaxially into the beam path to

overcome the direction dependency of lateral observation [8]. The coaxial integration of IR-cameras is limited however, because of the optical properties of common lenses. Pyrometers and two-channel-pyrometers enable the measurement of an average temperature or a maximum temperature value within the process zone. The coaxial observation with a pyrometer can be disturbed because of spatter and powder that attenuates the process zone [9]. In addition, the averaging measurement may lead to misinterpretation of different shaped melt pool geometries. Two-channel pyrometers are preferred for the measurement, but only allow the measurement of maximum temperature values [10].

A novel two-channel-pyrometer camera is known from other cladding processes which enables the emissivity corrected temperature field measurement [11]. Different temperature field related values become available for evaluation like melt pool geometry [12] or temperature gradients [13] and have been used for close loop control in wire-based cladding process [14].

1.2. Near net-shape production and geometrical monitoring

The geometry of a single bead is determined by the thermal conditions during process. Constant energy balance is necessary for a consistent width and height of the bead which is mandatory for a uniform layer geometry like was mentioned in the previous section.

Several welding beads have to be deposited side-by-side to generate a consistent layer. The distance between single beads usually is related to the width of a single bead and specified as overlap parameter. It determines the depth of the valleys between the beads and the height of the layer in a cross-section view.

The difference of peak height and target height determines the effort of post processing, like milling. A reduction of post-processing can be achieved by a near net-shape production due to the minimization of the difference between peak height h_{max} and target height h_{target} . A novel parameter is defined to describe the relation between target height and peak height and thus to validate the degree of net-shape. The overfill η_{shape} is calculated by:

$$\eta_{shape} = \frac{h_{max} - h_{target}}{h_{target}}$$

In the present work the minimum height of the layer h_2 defines the target value as effective height, whereas h_1 is the maximum height.

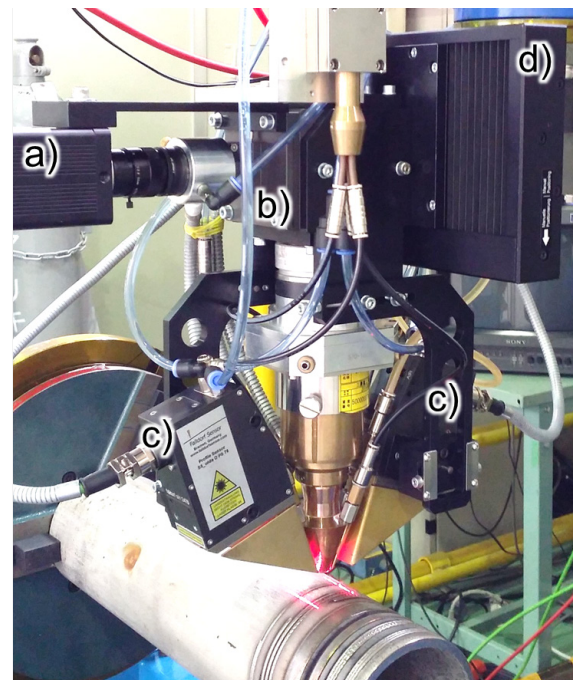
Different approaches for bead geometry and overlap prediction are known from literature. In most case simulations are used to predict the single bead geometry [15] or to optimize the overlap in laser cladding processes [16]. Different approaches rely on more or less complex models of welding bead and layer formation [17] by the help of thermal based [18] or geometrical based models [19]. However, usually extensive parameter studies are necessary for reference values beforehand.

The required geometrical indicators are often determined in metallographic cross-section [20]. Sometimes optical measurement methods are used to determine the bead

geometry after welding [21] whereas a known in-process measurement is rather popular in laser welding as seam tracking [22]. Usually laser triangulation [23] or recently OCT systems are used for geometry monitoring & control [24].

2. Experimental & methodology

Figure 1 shows the experimental set-up. A fiber laser (YLS-8000, IPG) and a beam guidance with beam splitter (BEO70, TRUMPF) are used for the investigation applying a maximum laser power of 8 kW and a laser spot diameter of 2.5 mm.



Tyralla 2019

BIAS ID 200269

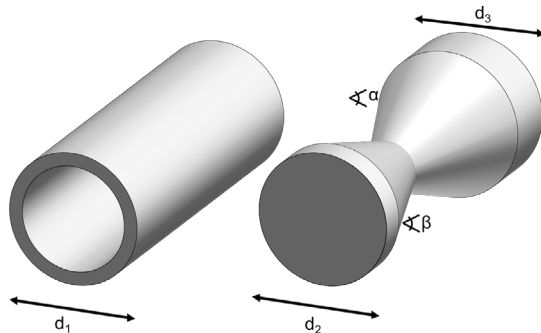
Fig. 1. Experimental setup with a) PyroCam, b) beam splitter, c) laser-line triangulation sensors and d) linear stage.

Different thermal and geometrical sensors are used in the investigation. The PyroCam is a novel two-channel-pyrometer camera which was applied for emissivity corrected temperature field measurement in a range of 600 °C up to 1900 °C. The camera is coaxially integrated into the beam path of the processing head by the help of a beam splitter to observe the whole process zone with a frequency of 100 Hz.

A pair of laser-line-triangulation-sensors (S5 Wide 78, Falldorf Sensor) is assembled next to the process zone to observe the deposited welding beads in leading and trailing position with a frequency of 330 Hz. The high laser power at ca. 660 nm enables accuracy in height of 35 μm and a lateral resolution of 25 μm. A dust protected high accuracy linear stage (PMT160-DC, Steinmeyer) enables movements of the processing head with a speed of up to 30 mm/s which is independent from the taught path of CNC-control.

Figure 2 shows the investigated geometries. Tubes of carbon steel JIS G3101 with an outer diameter d_1 of 115 mm and a wall thickness of 6 mm are cladded with a nickel-based alloy (2.4668, LPW718). The particle size is specified from 44 μm up to 88 μm. The powder is fed by a 3-jet coaxial

nozzle. In a further experiment a geometry is cladded which is consisting of two truncated cones with a slope α of 30° and β of 20° . The transition is performed as a radius of 100 mm and thus a minimum diameter of 50 mm is generated in the middle. The diameter d_2 is 110 mm and d_3 is 130 mm



Tyralla 2019

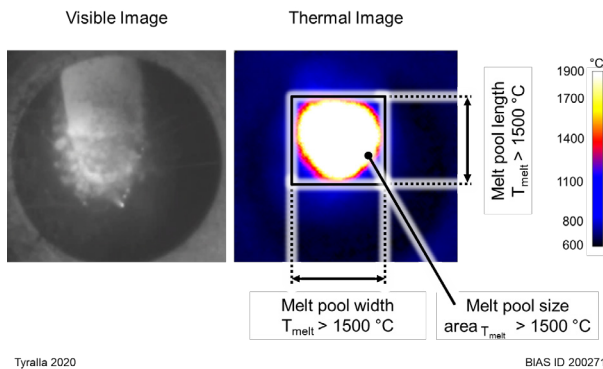
BIAS ID 200270

Fig. 2. Schematic of investigated geometries. A tube is used as simple geometry to develop the control approaches, shown on the left side. A complex geometry with different angles and diameters is used to evaluate limitations of the measurement system.

The experiments on tube applies a laser power of 3000 W, a powder feed rate of 20 g/min and a fixed rotation speed of 5.8 U/min which leads to a welding speed of 2.1 m/min. A fixed lateral speed of 0.1 mm/min is used for thermal control approach whereas 0.3 mm/min is used for the geometrical control approach.

The experiments on complex shaped geometry applies a laser power of 2500 W, feed rate of 18 g/min, a fixed lateral speed of 0.2 mm/min and a fixed rotation speed of 5.8 U/min which leads to variations of welding speed between 0.9 m/min up to 2.1 m/min. Several layers are cladded and observed by the sensor system. The raw signals are evaluated by a LabView based algorithm.

The thermal images are used to determine the melt pool area by summarizing the total number of pixels with melt temperature or above. The recognized melt pool has to be assembled by more than 10 pixels to avoid an incorrect detection. The melt pool width, length and area are determined, like shown in figure 3. The control approach requires the input of a melt pool area and the melt temperature as set-value. A PID control maintains the melt pool area by a variation of laser power.



Tyralla 2020

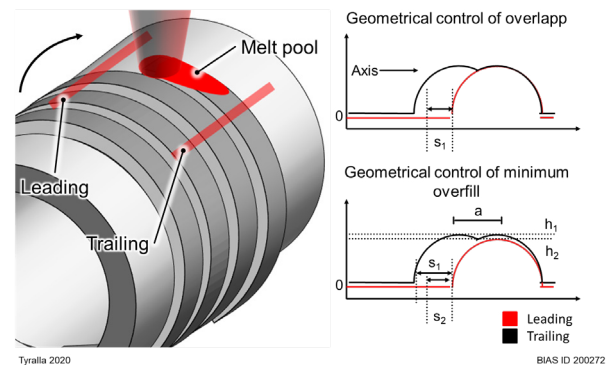
BIAS ID 200271

Fig. 3. In-situ process images of the emissivity corrected PyroCam and schematic evaluation method for the thermal control approach.

The height signals of the triangulation sensors have to be extensively filtered in temporal and lateral dimension for further evaluation. Two different approaches are developed for the geometrical control.

The first control approach measures the height and the width of the initial welding bead during the first rotation of the cylindrical substrate. The information is used to determine the positions of the layer in leading and trailing signal in further rotations and calculate the actual overlap. A PID control algorithm moves the linear stage to reach and to maintain the set overlap like shown in figure 4. The control only requires the input of the relative overlap s_1 as set-value.

The second control approach is composed of inner and outer control loop. The inner control loop is the mentioned first control approach which maintains a given set overlap s_1 . The outer control loop starts after the first rotation of the cylindrical substrate and measures the height of the existing layer over the length a of one bead width. The lowest height h_2 value in this interval is compared with the peak height h_1 , like shown in figure 4. There is no control action for a difference of less than 2 % whereas a difference of more than 2 % leads to an adjustment of the set overlap. The adjustment depends on the magnitude of the difference. The inner control loop is processed 100 times faster than the outer loop. The second approach requires no set-values for laser cladding but a suitable start value for overlap assists a fast adjustment of the process.



Tyralla 2020

BIAS ID 200272

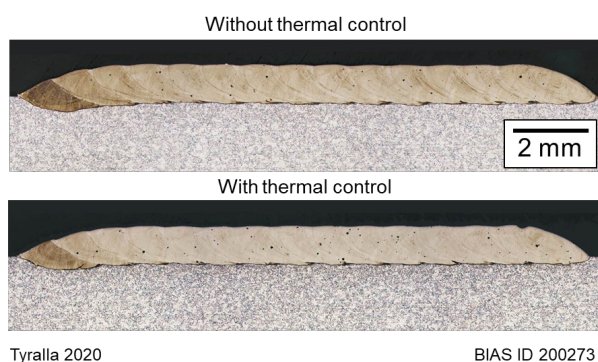
Fig. 4. Schematic of geometrical measurement and evaluation methods of set overlap and set overfill control approach.

3. Results

3.1. Thermal control experiments on cylindrical geometry

Figure 5 shows a result of the thermal control experiments. Both layers are deposited with the same parameters except of the laser power. The first layer applies a suitable parameter for laser cladding process. A higher penetration depth at the beginning of the layer can be identified like expected and already known from literature. The penetration depth of the first bead is ca. 2.5 times deeper than of the remaining layers. The total dilution is 17.2 %. The dilution varies with a coefficient of variation of 4.4 %. The melt pool size is measured during the process by the help of the PyroCam. The mean value after the first revolutions is selected as set-value for the following thermal control experiment.

The second layer in figure 5 shows the cross-section of the thermal controlled laser cladding process. The closed loop control starts at the beginning of cladding and attempts to obtain the given melt pool area by a reduction of laser power. A lower penetration depth is generated compared to the uncontrolled case. The required melt pool area is faster reached and constantly maintained. The penetration depth of the first bead is ca. 1.5 times deeper than the remaining layer and thus it is nearly halved compared to the uncontrolled case. The absolute penetration depth is reduced by 28 % compared to the uncontrolled case. The total dilution is 16.0 % and thus, it is slightly lower. The coefficient of variation is 2.1 % and thus it is also more than halved. It is suggested that the thermal control maintains the heat input by an adjustment of laser power and thus stabilizes bead geometry and dilution. In addition, bead geometry is adapted even in first rotation.



Tyralla 2020

BIAS ID 200273

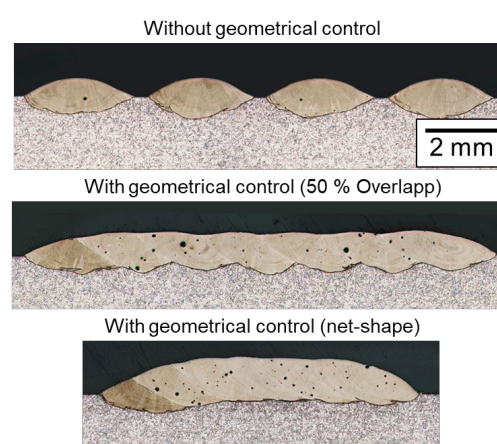
Fig. 5. Cross-sections of the thermal control experiments on tubes. First section shows a layer without control and the second layer applies thermal control on basis of in-process evaluated and controlled melt pool area.

3.2. Geometrical control experiments on cylindrical geometry

Figure 6 shows the results of geometrical control experiments. The both control approaches are compared to the case without control. All layers are deposited with the same parameter, including the lateral speed. The beads are deposited with a high offset side-by-side in the uncontrolled case to demonstrate the potential of the geometrical control approach. The beads have a width of (2.07 ± 0.07) mm and a height of (0.51 ± 0.04) mm. The overlap is measured from cross-section. The fixed rotation speed and lateral speed causes an overlap of (-13.0 ± 1.3) % and leads to an effective height of 0 mm. The coefficient of variation is 1.2 % and can be used as reference for positioning accuracy.

The first control approach is used for the second layer, shown in figure 6. The control applies a set overlap of 50 %. The resulting overlap is measured in the cross-section and is (41.8 ± 3.1) %. The overlap is smaller than the set-value but almost constant which is demonstrated by a low coefficient of variation of overlap of 5.3 %. It is suggested that the comparison of leading and trailing signal results in a constant overlap of nearly 50 % for the control algorithm. However, the distance of the measurement lines and the lateral speed causes a constant offset between measured signal and factual deposited track. Higher distances between the measurement lines and lateral speed increase the offset. A constant overfill of 14.9 % is achieved.

The second control approach is composed by inner and outer control loop and is used for the third layer which is shown in figure 6. In this case, the algorithm maintains an optimal overfill by the continuous adjustment of overlap. The resulting overlap is measured in the cross-section and it is (61.1 ± 1.4) %. The coefficient of variation of overlap is 3.6 %. The low value indicates a fast adjustment of an optimal overlap which is subsequently maintained over the whole layer. The overfill of the layer equals less than 2 %. This value was expected because of the condition to stop overlap adjustment for a difference lower than 2 %. It is suggested that the overfill can further be decreased with an adjustment of the outer control loop parameter. The coefficient of variation of overlap is low for both control approaches and thus, the control approaches demonstrate constant, uniform layer quality.



Tyralla 2020

BIAS ID 200274

Fig. 6. Cross-sections of the geometrical control experiments on tubes. First section shows a layer without control, second layer is geometrical controlled with set the overlap of 50 % and the third layer applies geometrical control with the set of minimum overfill.

3.3. Multi-parameter control on complex shaped geometry

Figure 7 shows a result of laser cladding with thermal and geometrical control for a rotational symmetrical geometry with double truncated cone. The shape results in a continuous variation of diameter and thus causes variations of heat sink volume. Nevertheless, a fixed rotation speed and a fixed lateral speed are used for a worst-case scenario. The thermal control adjusts the laser power to maintain the heat input for a constant bead geometry to compensate the changes of substrate diameter whereas the geometrical control is used to maintain a set overlap of 50 % and to generate a consistent layer with homogeneous overfill.

The dilution measured at different positions of the cross-section is 15.4 % at the beginning, 15.3 % in the center and 15.0 % at the end of the layer. The coefficient of variation is 10 % which indicates a significant higher value than in experiment on tube. It is suggested that the slope of the substrate influences the thermal measurement. The melt pool area changes during downhill and uphill movement because of the different perspectives onto the melt pool. However, the increasing dilution which commonly results from a reduction

of diameter can be avoided by the laser power control. The heat accumulation can be compensated.

The geometrical control achieves a resulting overlap of 47.1 % at the beginning, 46.5 % in the middle and 44.2 % at the end of the layer. The total overlap is (45.8 ± 4.2) %. The overlap is smaller than the set-value like already expected from previous experiments. A similar overfill of 17.6 % can be achieved for the whole layer. It is a slightly smaller value than in experiment on tube. However, the coefficient of variation is 7.6 % and indicates a strong activity of control.

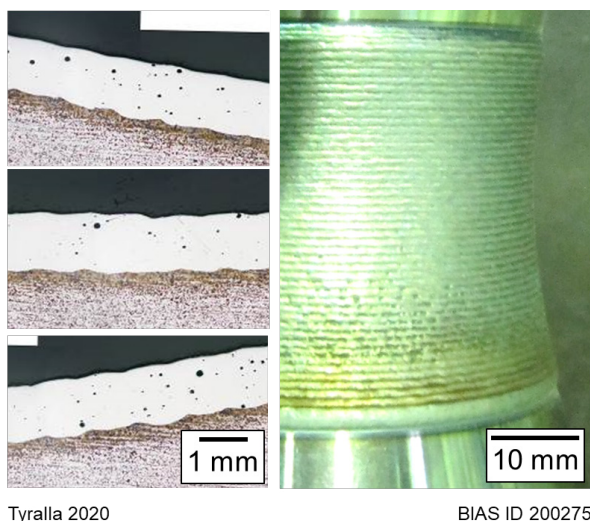


Fig. 7. Result of a layer on double-truncated-cone-shaped geometry with geometrical and thermal control.

3.4. Limitations of present system

Figure 8 demonstrates the limitations of the presented multi-parameter control. Both layers are cladded under the same parameter on a 20° angled truncated cone shaped geometry. The first layer is cladded uphill without control. The bead height, width and the dilution decrease by ca. 10 % because of the higher heat sink volume and the higher welding speed, like already expected. The averaged melt pool area after the first revolutions was used as set-value for thermal control. The overlap is 37 % which lead to a overfill of 159.7 %.

The second layer in figure 8 shows a thermal and geometrical controlled cladding process on truncated cone geometry in uphill direction. The dilution increases from 31 % for the first three beads to a dilution of more than 70 % for the last three beads. The geometrical control uses a set overlap of 50 %. The resulting overlap from cross-section is 44 % at the beginning of the layer but decreases to a value of 38 %.

The cross-section indicates that both controls work as expected at the beginning of the experiment. A homogeneous dilution including first bead demonstrates the capability of thermal control whereas a constant overlap is generated by geometrical control, like also demonstrated in experiment on tubes. However, pores appear at the interface and the control fails after a while. It is suggested that the taught path of handling system moves the processing head with a continuous speed along the truncated cone uphill with a constant distance

to the surface. The linear stage is assembled parallel to the rotation axis and moves the processing head horizontal against the direction of the handling system to maintain the set overlap. Thus, the nozzle-to-workpiece-distance increases during process and causes a mismatch of laser and powder spot diameter. A thinner bead shape with higher dilution and pores is generated and complicates the accurate recognition of the beads position. In addition, the factual deposited overlap is influenced by the modification of bead geometry and the shifted distance of the measurement lines of triangulation system.

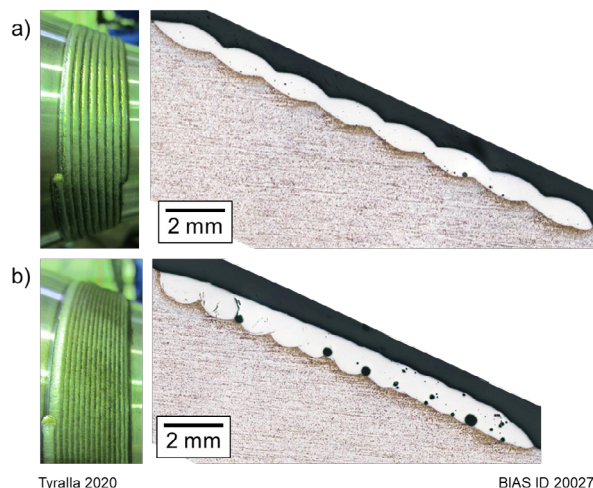


Fig. 8. Result of the layers which are cladded uphill on truncated-cone-shaped geometry. a) Without and b) with geometrical and thermal control.

4. Discussion

An offset is determined between set-value and resulting overlap. The measured deviation of ca. 8 % is composed by the given accuracy of handling system, the accuracy of the additional linear stage and the quality of the geometrical control algorithm. It is suggested that a deviation occurs between measured triangulation signal and factual deposited track which is caused by the distance between triangulation measurement lines as well as the lateral speed. Thus, a constant offset is generated between the set-value and resulting overlap.

Nevertheless, for the first time a multi-parameter control is demonstrated which controls the bead geometry by the help of a laser power adjustment and controls the layer geometry by the positing of processing head. A constant bead geometry and a high accordance in set overlap can be achieved and thus, a overfill of less than 2 % can be reached in experiment on cylindrical geometry. The capability of the control is even demonstrated in worst-case scenario on double truncated cone geometry. In the present case, the functionality was only limited by to the arrangement of parallel linear stage which causes an impermissible increase of the nozzle-to-workpiece distance. An additional vertical linear stage or the direct intervene in taught path planning can overcome this limitation.

5. Conclusion

A pair of triangulation sensors and a temperature field measurement system were integrated into a common laser powder cladding head and enables the determination of melt pool area and layer geometry in laser powder cladding process.

The PyroCam is used to obtain a set melt pool area by a laser power adjustment and thus, control the heat input for a constant bead geometry during cladding.

A novel characteristic value is defined to describe the relation of maximum height and target height of a clad layer. The parameter is called overfill

The triangulation sensor signal is used to obtain a constant overlap by the position of the process head or to achieve low overfill less than 2 %.

Both controls obtain applicable results regarding dilution, overlap and overfill on cylindrical geometry and even on lightly curved geometry like a truncated cone.

Acknowledgements

The authors gratefully acknowledge the collaboration with the members of Mitsubishi Heavy Industries, Ltd. regarding the support of knowledge, material and equipment over the course of the research.



References

- [1] Steen, W. M.; Mazumder, J.: Laser Material Processing, 4. Aufl., Springer-Verlag London 2010.
- [2] Islam, M., Purtonen, T., Piili, H., Salminen, A., Nyrhila, O.: Temperature profile and imaging analysis of laser additive manufacturing of stainless steel, *Physics Procedia* 41, 2013, 835–842
- [3] Purtonen, T.; Kalliosaari, A.; Salminen, A.: Monitoring and adaptive control of laser processes, *Physics Procedia* 56, 2014, 1218–1231.
- [4] Bi, G., Gasser, A., Wissenbach, K., Drenker, A., Poprawe, R.: Identification and qualification of temperature signal for monitoring and control in laser cladding, *Optics and Lasers in Engineering* 44, 2006, 1348–1359
- [5] Bonß, S.: Laser transformation hardening of steel, *Advances in laser materials processing*, 2010, 291–326.
- [6] Doubenskaia, M.; Pavlov, M.; Grigoriev, S.; Smurov, I.: Definition of brightness temperature and restoration of true temperature in laser cladding using infrared camera, *Surface and Coatings Technology* 220, 2013, 244–247. DOI: 10.1016/j.surfcoat.2012.10.044.
- [7] Bi, G.; Gasser, A.; Wissenbach, K.; Drenker, A.; Poprawe, R.: Identification and qualification of temperature signal for monitoring and control in laser cladding, *Optics and Lasers in Engineering* 44, 2006, 1348–1359. DOI: 10.1016/j.optlaseng.2006.01.009.
- [8] Bi, G.; Gasser, A.; Wissenbach, K.; Drenker, A.; Poprawe, R.: Investigation on the direct laser metallic powder deposition process via temperature measurement. In: *Applied Surface Science* 253, 2006, 1411–1416. DOI: 10.1016/j.apsusc.2006.02.025.
- [9] Bi, G.; Sun, C.N.; Gasser, A.: Study on influential factors for process monitoring and control in laser aided additive manufacturing, *Journal of Mat. Processing Techn.* 213, 2013, 463–468.
- [10] Bernhard, F.: *Handbuch der Technischen Temperaturmessung*, 2. Aufl., Springer-Verlag Berlin Heidelberg 2014.
- [11] Köhler, H.; Jayaraman, V.; Brosch, D.; Hutter, F.X.; Seefeld, T.: A novel thermal sensor applied for laser materials processing, *Lasers in Manufacturing (LIM13)*, *Phys. Proc.* 41, 2013, 495-501.
- [12] Volpp, J.; Hohenäcker, V.; Tyralla, D.; Freiß, H.; Brocke, N.; Silze, F.; Schnick, M.; Thomy, C.: Observing melt pool temperature fields for process characterization, *Lasers in Manufacturing (LIM17)*, 2017, 1-10
- [13] Goecke, S.-F., Seefeld, Th., Tyralla, D., Krug, A.: Monitoring and Control of the Heat Input in MAG-Laser-Hybrid Welding of High Strength Steel in Telescopic Crane Booms, *Proc. Of 15th International Conf. on Automation and engineering*, 2019, 1744-1747, doi:10.1109/COASE.2019.8843219
- [14] Tyralla, D.; Seefeld, T.: Higher deposition rates in laser hot wire cladding (LHWC) by beam oscillation and thermal control, *Production at the leading edge of technology*, Springer Vieweg, 2019, 401-409
- [15] Hofman, J. T.; Lange, D. F. de; Pathiraj, B.; Meijer, J.: FEM modeling and experimental verification for dilution control in laser cladding. In: *Journal of Materials Processing Technology* 211, 2011, 187–196. DOI: 10.1016/j.jmatprotec.2010.09.007.
- [16] Ding, D.; Pan, Z.; Cuiuri, D.; Li, H.: A multi-bead overlapping model for robotic wire and arc additive manufacturing (WAAM), *Robotics and Computer-Integrated Manufacturing* 31, 2015, 101–110. DOI: 10.1016/j.rcim.2014.08.008.
- [17] Chew, Y.; Pang, J. H. L.; Bi, G.; Song, B.: Thermo-mechanical model for simulating laser cladding induced residual stresses with single and multiple clad beads, *Journal of Materials Processing Technology* 224, 2015, 89–101. DOI: 10.1016/j.jmatprotec.2015.04.031.
- [18] Arrizubieta, J. I.; Lamikiz, A.; Klocke, F.; Martínez, S.; Arntz, K.; Ukar, E.: Evaluation of the relevance of melt pool dynamics in Laser Material Deposition process modeling, *International Journal of Heat and Mass Transfer* 115, 2017, 80–91. DOI: 10.1016/j.ijheatmasstransfer.2017.07.011.
- [19] Farahmand, P.; Kovacevic, R.: An experimental–numerical investigation of heat distribution and stress field in single- and multi-track laser cladding by a high-power direct diode laser, *Optics & Laser Technology* 63, 2014, 154–168. DOI: 10.1016/j.optlastec.2014.04.016.
- [20] Ya, W.; Pathiraj, B.; Liu, S.: 2D modelling of clad geometry and resulting thermal cycles during laser cladding. In: *Journal of Materials Processing Technology* 230, 2016, 217–232. DOI: 10.1016/j.jmatprotec.2015.11.012.
- [21] Ding, D.; Pan, Z.; Cuiuri, D.; Li, H.: A multi-bead overlapping model for robotic wire and arc additive manufacturing (WAAM). In: *Robotics and Computer-Integrated Manufacturing* 31, 2015, 101–110. DOI: 10.1016/j.rcim.2014.08.008.
- [22] Kos, M.; Arko, E.; Kosler, H.; Jezeršek, M.: Remote-laser welding system with in-line adaptive 3D seam tracking and power control, *Procedia CIRP* 81, 2019, 1189–1194. DOI: 10.1016/j.procir.2019.03.290.
- [23] Donadello, S.; Motta, M.; Demir, A. G.; Previtali, B.: Monitoring of laser metal deposition height by means of coaxial laser triangulation. In: *Optics and Lasers in Engineering* 112, 2019, 136–144. DOI: 10.1016/j.optlaseng.2018.09.012.
- [24] Mittelstädt, M.; Mattulat, T.; Seefeld, T.; Kogel-Hollacher, M.: Novel approach for weld depth determination using optical coherence tomography measurement in laser deep penetration welding of aluminum and steel, *Journal of Laser Applications* 31 (2), 2019, <https://doi.org/10.2351/1.5082263>

11th CIRP Conference on Photonic Technologies [LANE 2020] on September 7-10, 2020

Model-based pyrometer alignment method for additive manufacturing by laser metal deposition

David Dillkötter*, Magnus Thiele, Johann Stoppok, Henrik Dobbelstein, Cemal Esen, Martin Mönnigmann

Department of Mechanical Engineering, Ruhr University Bochum, Universitätsstraße 150, 44801 Bochum, Germany

* Corresponding author. Tel.: +49 234 3224035. E-mail address: david.dillkoetter@rub.de

Abstract

The melt pool temperature is a key parameter in laser metal deposition (LMD) processes. Reliable temperature measurements are of obvious interest and essential for supervising and controlling the process. However, pyrometers tend to show a non-negligible directional dependency, due to the direction-dependent temperature distribution in the melt pool. We propose a model-based method for determining and physically compensating the misalignment of a pyrometer in an LMD process. The approach is based on a brief calibration run based on which the focus offset can be determined. The resulting offset is used to physically adjust the pyrometer.

© 2020 The Authors. Published by Elsevier B.V.

This is an open access article under the CC BY-NC-ND license (<http://creativecommons.org/licenses/by-nc-nd/4.0/>)

Peer-review under responsibility of the Bayerisches Laserzentrum GmbH

Keywords: additive manufacturing; laser metal deposition; pyrometer; control

1. Introduction

Laser metal deposition (LMD) is a well-known additive manufacturing process, characterized by a laser source and a powder feeding system. The powder feeding system is used to add material through a nozzle to the melt pool. The melt pool is created by the process laser focused on the substrate.

For supervising and controlling the process, reliable measurements of key process parameters are required. However, challenging process conditions (e.g. high process temperatures of more than 2000K) make reliable measurements difficult. Nevertheless, the melt pool temperature and geometry are accessible to measurements. For example, Song and Mazumder [1] use a pyrometer to monitor and control the melt pool temperature. Based on their measurements, they identify a state-space model and design a controller. Petrat et al. [2] measure and compare the temperature of the substrate near the melt pool for different scanning strategies. Bi et al. [3] compare a photodiode, pyrometer and a CCD-camera for the

measurement of the melt pool temperature. They conclude the measurement of a laterally mounted pyrometer to depend significantly on the scanning direction. This implies a coaxially mounted pyrometer is preferable for achieving reliable measurements.

Devesse et al. [4] show the melt pool temperature can be characterized by elliptical isotherms. These isotherms have a steeper temperature gradient in the direction of motion. Therefore, a pyrometer that is not perfectly aligned with the heat source measures a temperature depending on the direction of motion (see Fig. 2).

Recently, a model-based method for the calculation of the misalignment of the pyrometer was derived [5]. The model is based on a solution of the heat conduction equation that describes the elliptically shaped temperature distribution in the substrate. The method allows to calculate the offset of the pyrometer from the center of the melt pool based on a simple measurement routine, which takes the pyrometer measurements and the direction of motion of the process head into account.

We propose a model-based method for calculating and physically correcting the offset of a pyrometer measuring a point heat source and apply the method to the LMD process. While the proposed approach is still applied in a manual way here, its automation is straight-forward. In contrast to the related work [5], we here physically correct the pyrometer alignment, while a software-based correction was proposed in [5].

In Section 2 we briefly summarize the model on which the pyrometer measurement is based, which was already presented in [5] in greater detail. We show the model predicts the directional dependency of a misaligned pyrometer. In Section 3 we identify the offset of a pyrometer in a laboratory LMD process. The results are used to physically align the pyrometer in Section 4.

2. Physical model

Two Cartesian coordinate systems are required for the model. The machine coordinate system (x, y, z) describes the position of the process head. The origin is an arbitrarily chosen but fixed point in the workspace. The second system (ξ, η) is fixed on the substrate in the center of the point heat source with the ξ -axis pointing in the opposite direction of the movement. The coordinate systems are coplanar. Furthermore, the angle ϕ refers to the angle between the x - and ξ -axis and describes the direction of the movement of the nozzle. Note that the nozzle (to which the pyrometer is attached) does not rotate and only moves linearly along the x -, y - and z -axis. The coordinate systems are illustrated in Fig. 1.

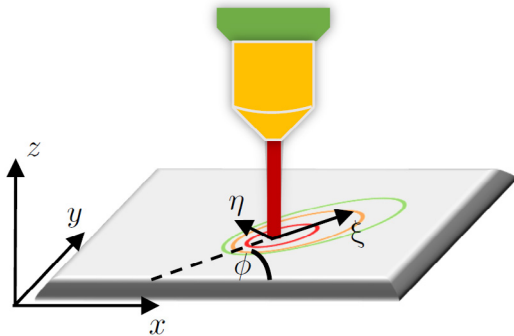


Fig. 1. Directional dependence of the measurement of the melt pool temperature [4]

2.1. Directional dependency of temperature measurements

The heat distribution in the substrate can be described by isotherms, which depend on the direction of motion of the process head. The mathematical description for a point heat source moving with constant velocity $\|U\|_2$, assuming a semi-infinite work piece, is given by the Rosenthal equation [6]

$$T(\xi, \eta, U, P) = T_0 + \frac{A_b P}{2\pi k r} \exp\left(\frac{(\xi - r)\|U\|_2}{2\alpha}\right), \quad (1)$$

where $r = \sqrt{\xi^2 + \eta^2}$, A_b is the absorption coefficient, P is the laser power, $\|U\|_2$ is the relative velocity and α is the thermal diffusivity. All parameters are assumed to be independent of the temperature and the material is assumed to be isotropic and homogeneous. Fig. 2 sketches the resulting elliptical isotherms.

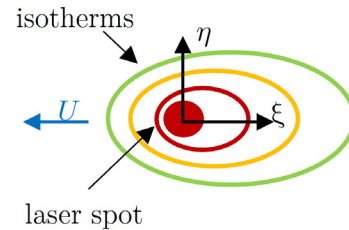


Fig. 2. Isotherms as derived with (1). The elliptical shape and the steeper gradient in the movement direction result from the directional dependence [5].

The melt pool temperature in the LMD process is typically measured with IR-cameras and pyrometers [7]. While IR-cameras have the advantage of measuring the heat distribution in the melt pool, their high spatial resolutions usually imply low framerates. In contrast, pyrometers measure the temperature in a small, point-like area, but do so with high sampling rates.

More precisely, a pyrometer measures the radiation emitted by an area A_p , which is projected onto the detector by an optical system. The alignment of the pyrometer is critical, because small deviations of the pyrometer measurement area (A_p) from the center of the heat source result in a notable directional dependency (see Fig. 3).

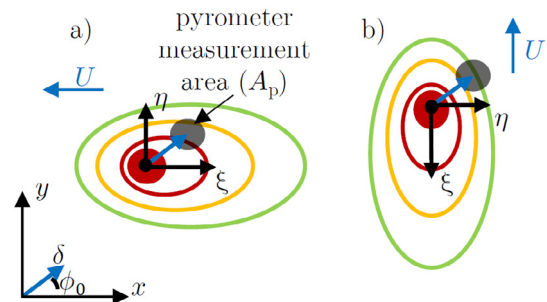


Fig. 3. The area (A_p) is offset by δ at an angle ϕ_0 in the machine coordinate system. While δ and ϕ_0 are constant, the orientation of the elliptical isotherms depends on the vector of the velocity U , which is a function of time. As a result, the measurement error induced by the misplacement depends on U and is a function of time [5].

2.2. Model of the pyrometer with offset

A detector of a pyrometer integrates the radiation of the melt pool projected on the detector. The corresponding black body temperature is determined by the Stefan-Boltzmann law, given by

$$P_{rad} = \sigma \int_{A_p} \bar{T}^4(\xi, \eta; U, P) dA \quad (2)$$

$$= \sigma T_p^4 \int_{A_p} dA = \sigma T_p^4 A_p.$$

The temperature \bar{T} describes the temperature given by the Rosenthal equation (1) up to a saturation temperature depending on the pyrometer. T_p is the temperature value measured by the pyrometer. Assuming a circular aperture, the area A_p is given by

$$A_p = \pi r_{pyro}^2. \quad (3)$$

By applying the coordinate transformation shown in Fig. 3 and integrating the temperature over the offset area A_p , a prediction of the temperature measured by a pyrometer with offset can be determined. The dependencies of the measured temperature T_p on the discussed quantities can be summarized by

$$T_p(\bar{T}(\xi, \eta; U, P), \phi_0, \|\delta\|_2, r_{pyro}) \quad (4)$$

These quantities are the velocity of the process head U , the laser power P , the offset angle ϕ_0 and offset radius $\|\delta\|_2$, and the radius of the pyrometer measurement area r_{pyro} .

We illustrate the directional dependency (4) with Fig. 4. Fig. 4 shows the relative error of T_p for a list of offsets $\|\delta\|_2$ as a function of the velocity $\|U\|_2$. If there is no offset, the relative error equals zero. Both an increasing offset and an increasing velocity result in a higher absolute minimum relative error. Note that the minimum relative error is given for $\phi - \phi_0 = \pi$. This corresponds to A_p located in front of the moving heat source. Correspondingly, the maximum relative error occurs if A_p is located behind the moving heat source.

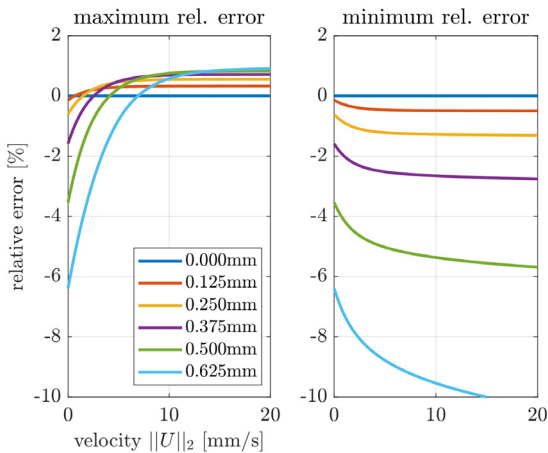


Fig. 4. Maximum and minimum relative error of the temperature measurement of a pyrometer offset by $\|\delta\|_2$ as a function of the velocity $\|U\|_2$ for $P = 250\text{W}$ and $r_{pyro} = 1\text{mm}$.

3. Physical correction

In this section, we present techniques for determining the offset of the pyrometer and for correcting the misalignment.

3.1. Pyrometer offset estimation

Essentially, the offset of the pyrometer is determined by fitting measurements to the model (4). A best fit for the unknown parameters r_{pyro} , ϕ_0 and $\|\delta\|_2$ can be determined by solving the nonlinear least-squares optimization problem

$$\min_{\|\delta\|_2, \phi_0, r_{pyro}} \sum_{k=1}^K \left(T_{exp}^{(k)} - T_p(\bar{T}(\xi, \eta; U^{(k)}, P), U^{(k)}; \phi_0, \|\delta\|_2, r_{pyro}) \right), \quad (5)$$

where $T_{exp}^{(k)}$, $k = 1, \dots, K$, refers to K measured temperatures.

We propose a simple routine for determining $T_{exp}^{(k)}$. It is based on a continuous movement of the process head along a circular path with a constant laser power and the powder feeder disabled. Due to the circular path, temperature measurements of every direction of the processing head are recorded. Note that no measurement is conducted for the first rotations to ensure transients have decayed. We propose to use the maximum temperature deviation along the circular path for benchmarking. A higher temperature deviation corresponds to a higher offset $\|\delta\|_2$ of the pyrometer.

3.2. Physical offset correction

We mounted the pyrometer to a kinematic mirror mount, usually used to fix optical devices, to allow for adjustments of the offset of the pyrometer.

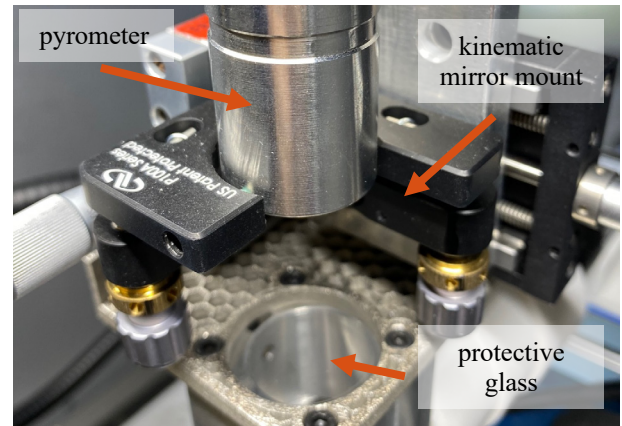


Fig. 5. Setup of the angular adjustment device of the pyrometer. The two knurled wheels are used to adjust the angle of the pyrometer. The left wheel is used to adjust the y -offset, the right wheel adjusts the x -offset. The beam path is secured by a protective glass.

Specifically, the mount allows to adjust the angle of the pyrometer and thus the position of A_p . The setup, including the mirror mount and coaxial input to the process head, is shown in Fig. 5.

4. Results

To obtain reliable temperature data for supervising and controlling the LMD process, the pyrometer must be adjusted to measure the temperature at $(\xi, \eta) = (0, 0)$. We combine the offset estimation with the physical correction in an iterative manner. The laboratory machine is an OR-Laser Evo Cube.

The pyrometer is a Metis M3 H322. The process was carried out as follows, starting with a pyrometer that was carefully aligned according to the vendor instructions:

- At first, the initial offset of the pyrometer is determined.
- Based on the offset, the most misaligned axis (x, y) is corrected by one tick of the corresponding adjustment screw and the resulting offset is determined again. Using the resulting offset and the initial offset, the gradient is determined.
- The remaining offset is iteratively compensated by adjusting the pyrometer by $2/3$ of the theoretically necessary value.

We performed the adjustment of the pyrometer with the proposed procedure and achieved a sufficient result after two iterations. Fig. 6 shows the result of the alignment process. The offset estimation of the initial measurement resulted in $\|\delta\|_2 \approx 0.4$ mm. Based on the gradient derived with the second measurement, the pyrometer was adjusted close to the origin to yield $\|\delta\|_2 \approx 0.06$ mm. A final iteration resulted in an unmeasurable offset. Note that the first iteration resulted in an offset compensation of more than $2/3$ of the distance, possibly due to a slight model mismatch or measurement noise.

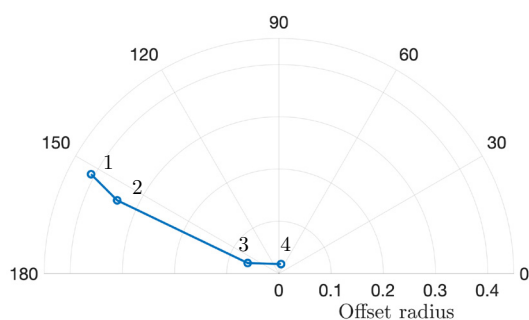


Fig. 6. Process of the iterative correction of the pyrometer. The leftmost circle shows the start of the 4 steps. The final offset (4) is close to the origin.

The decreasing offset of the pyrometer leads to a decreased variation of the temperature on the circular path. The correlation is shown in Fig. 7. The initially aligned pyrometer shows a significant directional dependency of 147.9K at an offset of 0.41mm. After the first gradient based alignment (cycle 3) the variation could be reduced to 13.45K and 0.06mm offset, respectively. The final adjustment lead to a variation of 4.75K and an unmeasurable offset.

While the correction has been implemented in a manual way, the method can obviously be automated with a motorized kinematic mirror mount.

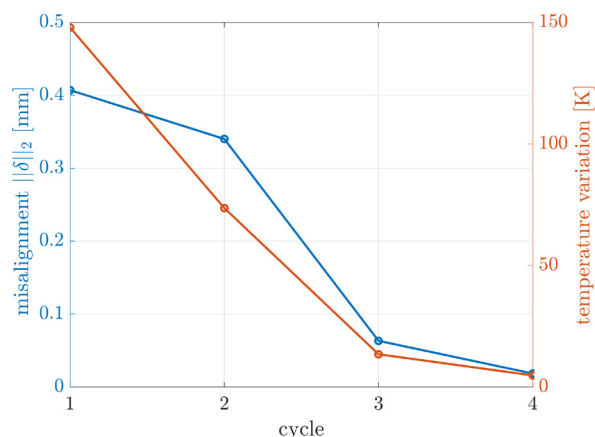


Fig. 7. The blue circles show the determined offset of the pyrometer. After the initial measurement (cycle 1) and the adjustment of a single tick (cycle 2), the pyrometer was adjusted by $2/3$ of the derived ticks. The red line shows the measured temperature variation within a circular move.

5. Conclusion

We developed a model-based method for aligning a pyrometer in an LMD process. With the proposed method, a pyrometer can be used as a reliable measurement device to control or supervise the LMD process.

The paper presented a method for the physical alignment of a pyrometer. A simple iterative calibration run was presented that simplifies the manual process considerably. Due to the gradient-based approach, no information on the optical system is necessary. The results underline the importance of a carefully executed alignment process. Furthermore, the procedure can easily be extended to an automatic calibration. Future work will focus on this automation and on techniques for adjusting the pyrometer without requiring a calibration run but using production run data instead.

Acknowledgements

We gratefully acknowledge funding by the German Federal Ministry of Education and Research under grant 13N14305.

Parameters

A.1. Table of physical parameters

Parameter	Symbol	Value
Thermal diffusivity	α	$5.006 \cdot 10^{-6} \text{m}^2/\text{s}$
Specific heat	C_p	$500 \text{J}/(\text{kgK})$
Thermal conductivity	k	$20 \text{W}/(\text{Km})$
Density	ρ	$7990 \text{kg}/\text{m}^3$
Melting temperature	T_m	1713.15K

A.2. Table of other parameters

Parameter	Symbol	Value
Maximum measurable temperature	T_{max}	2573K
Maximum motion speed	U	20mm/s
Maximum laser power	P_{max}	450W
Laser power (calibration)	P	250W
Absorption coefficient	A_p	0.625
Process laser wavelength	λ	1070nm
Pyrometer wavelength	λ_p	1450-1800nm

References

- [1] Song, L., and Mazumder J.. "Feedback control of melt pool temperature during laser cladding process." IEEE Transactions on Control Systems Technology 19.6 (2010): 1349-1356.
- [2] Petrat, T., et al. "Build-up strategies for temperature control using laser metal deposition for additive manufacturing." Welding in the World 62.5 (2018): 1073-1081.
- [3] Bi, G., et al. "Identification and qualification of temperature signal for monitoring and control in laser cladding." Optics and lasers in engineering 44.12 (2006): 1348-1359.
- [4] Devesse, W., De Baere D. and Guillaume P. "The isotherm migration method in spherical coordinates with a moving heat source." International Journal of Heat and Mass Transfer 75 (2014): 726-735.
- [5] Dillkötter, D., Stoppok J., Thiele M, Esen C., and Mönningmann M. "Model-based temperature offset compensation for additive manufacturing by directed energy deposition." 21st IFAC World Congress, Berlin (accepted), 2020.
- [6] Rosenthal, D. "The theory of moving sources of heat and its application of metal treatments." Transactions of ASME 68 (1946): 849-866.
- [7] Liu, W., et al. "A review on in-situ monitoring and adaptive control technology for laser cladding remanufacturing." Procedia CIRP 61 (2017): 235-240.

11th CIRP Conference on Photonic Technologies [LANE 2020] on September 7-10, 2020

Laser metal deposition controlling: melt pool temperature and target / actual height difference monitoring

Magnus Thiele^{1,*}, David Dillkötter², Johann Stoppok², Martin Mönnigmann², Cemal Esen¹

¹*Applied Laser Technologies, Ruhr-Universität Bochum, Germany*

²*Automatic Control and Systems Theory, Ruhr-Universität Bochum, Germany*

* Corresponding author. Tel.: +49 234 32 25698; fax: +49 234 32 14259. E-mail address: thiele@lat.rub.de

Abstract

Over the last decade, additive manufacturing has become increasingly popular and is used in many industries. Laser metal deposition is used for repairing large or expensive tools and for application of coatings. The technique is also increasingly used for the production of three-dimensional parts. However, process control is not fully developed, so that errors in terms of the height of the part occur, especially on complex geometries, due to an inhomogeneous melt pool temperature.

In this paper, the melt pool temperature as well as the component height deviation is recorded simultaneously during the process with only one thermal-optical camera.

© 2020 The Authors. Published by Elsevier B.V.

This is an open access article under the CC BY-NC-ND license (<http://creativecommons.org/licenses/by-nc-nd/4.0/>)

Peer-review under responsibility of the Bayerisches Laserzentrum GmbH

Keywords: additive manufacturing; laser metal deposition; 3D printing; temperature control

1. Introduction

The past decade has been strongly influenced by additive manufacturing in the industry and continues to this day. The manufacturing possibilities in the area of polymers by means of Fused Deposition Modeling (FDM), Selective Laser Sintering (SLS) and Stereolithography, and also in the area of metals by means of Selective Laser Melting (SLM) or Laser Metal deposition (LMD), are increasing significantly and first conquered the prototype scene and now also the aerospace sector with focus on special material [1] as well as combination of multiple parts into one or design of lightweight parts [2]. Due to the high safety requirements in the aerospace sector, only limited components have been

manufactured so far [3]. Highly safety-relevant components are still subject to individual testing, which makes it difficult for them to reach the break-even point with respect to costs despite possible series production. Due to insufficient process monitoring and control, it cannot be ensured that the component is free of defects, so that individual testing is still necessary [4].

In contrast to the well-known SLM technology for filigree components, the LMD process is suitable for larger components. Due to the higher deposition rate, these 3D parts can be built up faster compared to the SLM process. However, process monitoring and control are not yet fully developed for either technique but are currently subject to research.

Tang et al [5] and Arrizubieta et al [6] determined the temperature during the process as well as the weld height of each individual layer after deposition. A laser triangulation sensor was used for the height determination and a pyrometer for the temperature. For the height measurement a separate drive over and scan of the produced part was required. Similarly, Gegel et al. [7] measured the height of the component. They used a laser line triangulation sensor so that larger areas of the component could be measured. It resulted that component slopes or welding seam ends can cause faulty measurements due to the tilted surface. To avoid the measurement error and the second drive over, Donadello et al. [8] [9] designed an almost coaxial laser triangulation sensor so that the height of the component could be determined during the process through the powder nozzle and in a sharp angle to the component surface. Altenburg et al. [10] and Wargulski et al. [11] investigated temperature monitoring by means of CMOS cameras, whereby a thermographic image could be recorded.

In this paper the building process of a component is monitored by means of a thermographic camera. In addition, the height of the component during the process is monitored by image evaluation and the offset to the target value is determined. The advantage is that a single sensor can be used for monitoring the temperature and component height.

2. Experimental Setup

The experiments are carried out in a 3-axis laser cladding system OR-Cube of the company Coherent OR-Laser. A coaxial powder nozzle Coax-36 of the Fraunhofer ILT Aachen and a fiber laser of the company IPG with a wavelength of 1070nm is used for the deposition process. A thermographic camera PI05, with a temperature range between 900 and 2000 °C, of the company Optris GmbH is integrated at a 45° angle, which is aligned to the molten bath zone, as shown in Fig. 1. The working distance between the nozzle tip and the deposition

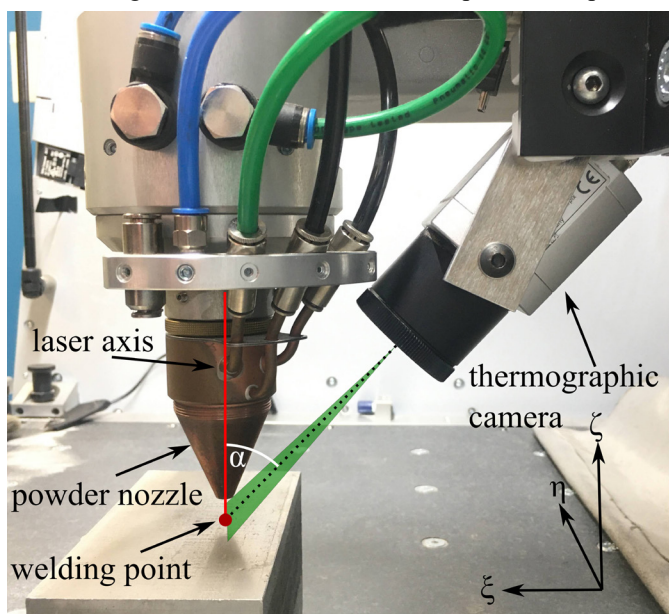


Fig. 1. Experimental setup. The IR camera is mounted in a 45° angle to the z-axis. The nozzle distance to the processing point is 8mm.

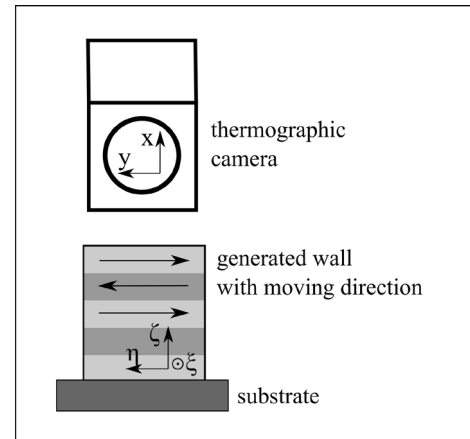


Fig. 2. Schematic drawing of the coordinate systems and the moving strategy

area should be 8mm. It is adjusted with a calibration tool before the process is started. The IR-camera is carried along with the axes without any relative movement to the powder nozzle.

The temperature data as well as the position of the hottest point (hot spot) in the captured image from the camera are recorded by a PC and processed in real time. The temperature is averaged from an array of 5x5 pixels around the hot spot. The position of the hot spot is determined by the camera and given as a coordinate in x and y direction from the image, where the x-axis of the IR-Camera $x_{camera}(\xi, \eta)$ represents the height axis ζ of the machine $\zeta_{machine}(\xi, \eta)$. Since the IR camera is carried along, the change on the x-axis plus the ζ -axis of the machine is the total real wall height h_{total} as described in equation (1).

In order to assign the x-axis values of the camera to the corresponding z-axis difference, a calibration run has been performed beforehand. For this purpose, the powder nozzle was moved to the starting height of 8mm. Then the laser was switched on, so that a melt pool was formed on the substrate. While the working distance between the powder nozzle and the substrate was on the one hand reduced and on the other hand increased, the data of the ζ -axis of the machine and the x-values of the IR camera were recorded. Thus, a calibration curve could be created to convert from the x-values of the IR camera to the height change in ζ -direction. If the actual height corresponds to the target height, $\Delta_{target-actual}$ is zero.

$$\begin{aligned} \zeta_{machine}(\xi, \eta) + x_{camera}(\xi, \eta) &= \\ \zeta_{machine}(\xi, \eta) + \Delta_{target-actual}(\xi, \eta) &= h_{total} \end{aligned} \quad (1)$$

For this paper, walls with the parameters from Table 1 are made of the metal 316L.

Table 1. Parameter to generate different walls

Wall ID	W1	W2	W3
Laser power	225 Watt	315 Watt	405 Watt

Layers are welded in η direction of the system which the IR camera records from the side, see Fig. 2. The axis movements and the data from the thermal camera are recorded. The temperature and the target/actual deviations are graphically displayed for each positions of the wall.

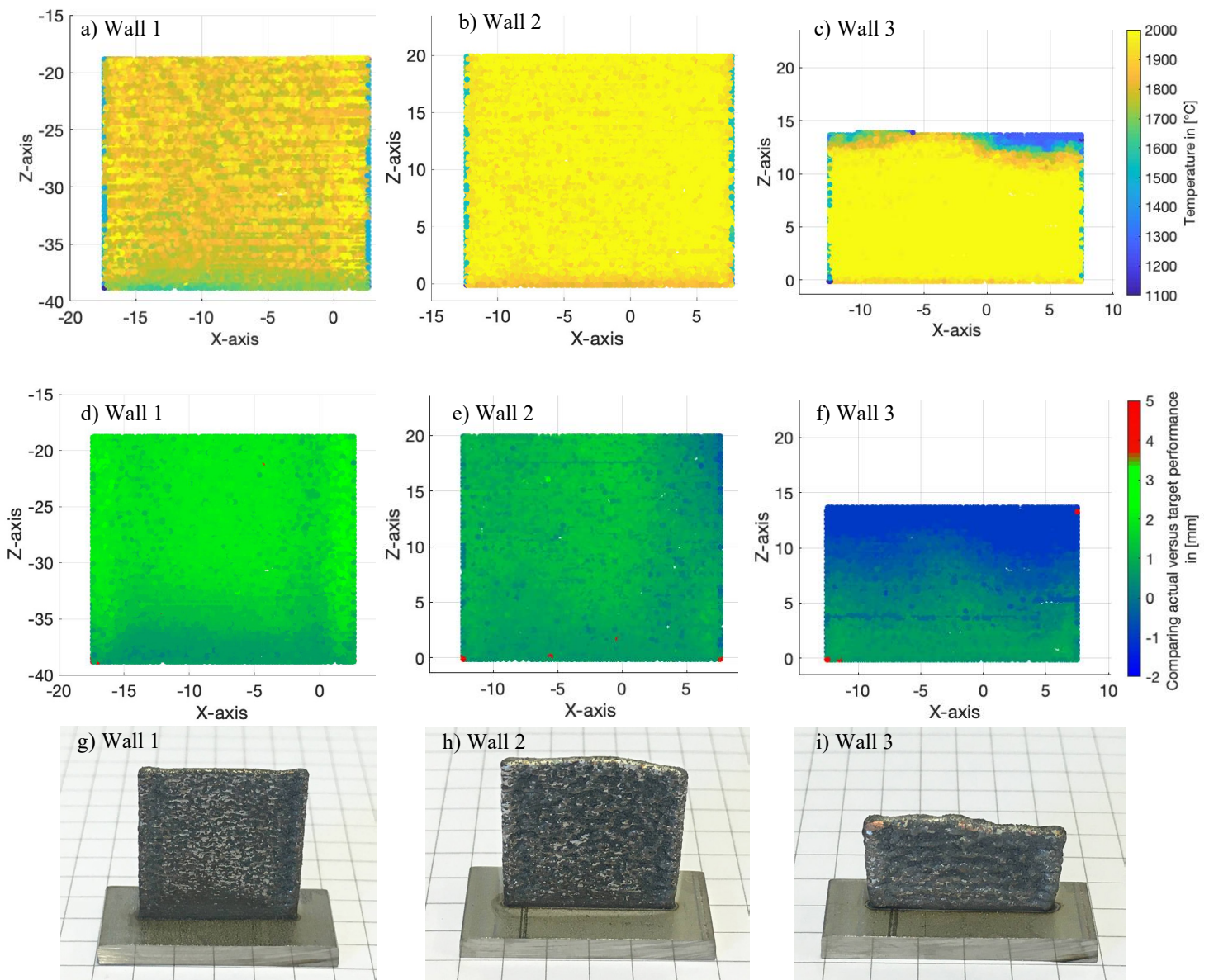


Fig. 3. a), b), c) thermographic images of the melt pool temperature. d), e), f) are target / actual differences for each wall position at the time of manufacturing. g), h), i) are photos of the prepared samples. The results for a), d), and g) are from wall W1. The results for b), e), and h) are from wall W2. The results for c), f), and i) are from wall W3.

3. Results

Fig. 3a (wall 1) shows that the temperature is low in the first layers and increases in the Z direction. After the first third of the finished wall the temperature remains constant. The temperature only drops at the ends of the generated layers. This is due to the build-up strategy. At these points the laser is switched off and the process head is moved in Z direction by a predefined layer height.

Fig. 3d shows the target/actual difference at each position of the wall at the time of production. At the beginning of build-up welding, the actual height is equal to the target height, which is specified by a difference of zero. Subsequently, the difference changes to positive values which are in the range of 2mm. This indicates a higher rate of build-up than expected. As a result, the wall is above the target height. After the first third of the

wall the difference remains constant. In this area, the process stabilizes itself, as Haley et al. [12] described. In the figure a height difference along the X axis can be observed. The variance is in the range between 1.5 and 2.1mm, corresponding to the manufactured wall in Fig. 3g and validation measurements with a triangulation line sensor with positive values between 1.2 and 1.8mm.

Fig. 3b (wall 2) shows a similar behavior to Fig. 3a. However, the static temperature range is already reached after the sixth layer and the temperature is higher overall. As described above, a lower temperature is measured at the ends of the individual layer, due to the process strategy.

In Fig. 3e, the target/actual differences are minor and in the range of 0.7 to 1.3mm. However, the upper right area of the figure constitutes an exception. From half the height of the wall to the upper end, the difference from the target/actual value becomes negative (-0.3mm) and means that the target height is

not reached. This can also be seen in Fig. 3h. In comparison to this, the measured values from the triangulation line sensor are between 0.8 and 1.1mm. The upper right corner is 0.5mm under the expected height.

The construction process of the wall 3 was stopped early, because the wall did not built up further shortly after the start of the process. In Fig. 3c, a very rapid temperature increase can be seen within the first three layers. Subsequently, the temperature rises to exceed the measuring range of the IR camera. From a height of about 10mm the temperature drops again. This is due to the fact that the molten pool is outside the field of view of the camera.

Looking more closely at the height difference in Fig. 3f, it can be observed that after 15 layers the difference quickly falls into the negative range. Beyond this time and height, the process was no longer stable. The defined layer height was higher than the real deposited layer height. Fig. 3i shows the generated part, which corresponds to the results from height measurement.

4. Conclusion

This paper successfully demonstrates how a thermal camera can be used to monitor the melt pool temperature as well as the height of the component during the process. For this purpose, the IR camera is directed at the area of the melt pool and is moved with the axes without relative movement to the powder nozzle.

This offers the advantage that, on the one hand, only one sensor has to be used to determine two measured variables and thus costs can be reduced. On the other hand, space and, if necessary, also the movement space around the powder nozzle can be saved.

The position of the hot spot in the melt pool is determined by image processing. The fixed position to the powder nozzle allows to calculate the target/actual difference from the change in position of the hot spot. The graphical images of the target/actual comparison and the images of the generated samples show a good agreement.

The accuracy of the height measurement is verified with a triangulation sensor, which shows excellent agreement and is in the range of the melt pool height. The hot spot is located in the molten bath, but it can move within the bath due to dynamic processes which may create measurement inaccuracies.

By measuring the height of the wall or the current error, the cause of the construction error can be found or compensated in the process itself by control of the generation process.

5. Acknowledgements

We gratefully acknowledge funding by the German Federal Ministry of Education and Research under grant 13N14307.

References

- [1] F. Froes, R. Boyer und B. Dutta, „1 - Introduction to aerospace materials requirements and the role of additive manufacturing,“ *Additive Manufacturing for the Aerospace Industry*, pp. 1-6, 2019.
- [2] J. Kranz, D. Herzog und C. Emmelmann, „Design guidelines for laser additive manufacturing of lightweight structures in TiAl6V4,“ *Journal of Laser Applications*, Bd. 27, p. 14001, 2015.
- [3] R. Russell, D. Wells, J. Waller, B. Poorganji, E. Ott, T. Nakagawa, H. Sandoval, N. Shamsaei und M. Seifi, „Qualification and certification of metal additive manufactured hardware for aerospace applications,“ *Additive Manufacturing for the Aerospace Industry*, pp. 33-66, 2019.
- [4] R. Liu, Z. Wang, T. Sparks, F. Liou und J. Newkirk, „Aerospace applications of laser additive manufacturing,“ *Additive Manufacturing*, pp. 351-371, 2017.
- [5] L. Tang, J. Ruan, T. E. Sparks, R. G. Landers und F. Liou, „Layer-to-layer height control of Laser Metal Deposition processes,“ in *American Control Conference*, 2009.
- [6] J. Arrizubieta, J. Ruiz, S. Martinez, E. Ukar und A. Lamikiz, „Intelligent nozzle design for the Laser Metal Deposition process in the Industry 4.0,“ *Procedia Manufacturing*, Nr. 14, pp. 1237-1244, 2017.
- [7] M. Gegel, A. Nisbett, D. Bristow und R. G. Landers, „Laser line scan characterization of geometric profiles in laser metal deposition,“ in *Solid Freeform Fabrication*, 2016.
- [8] S. Donadello, M. Motta, A. G. Demir und B. Previtali, „Coaxial laser triangulation for height monitoring in laser metal deposition,“ *Procedia CIRP*, pp. 144-148, 2018.
- [9] S. Donadello, M. Motta, A. G. Demir und B. Previtali, „Monitoring of laser metal deposition height by means of coaxial laser triangulation,“ *Optics and Lasers in Engineering*, Nr. 112, pp. 139-144, 2019.
- [10] S. Altenburg, C. Maierhofer, A. Straße und A. Gumenyuk, „Comparison of MWIR thermography and high-speed NIR thermography in a laser metal deposition (LMD) process,“ in *Quantitative InfraRed Thermography Conference*, Berlin, 2018.
- [11] D. R. Wargulski, T. Nowak, M. Thiele, H. Dobbstein, R. Schacht und M. A. Ras, „Quality Management of Laser Cladding Processes for Additive Manufacturing by New Methods of Visualization and Evaluation of Thermographic Data,“ in *Quantitative InfraRed Thermography Conference*, Berlin, 2018.
- [12] J. C. Haley, B. Zheng, U. S. Bertoli, A. D. Dupuy, J. M. Schoenung und E. J. Lavernia, „Working distance passive stability in laser directed energy deposition additive manufacturing,“ *Materials and Design*, Bd. 161, pp. 86-94, 2019.

11th CIRP Conference on Photonic Technologies [LANE 2020] on September 7-10, 2020

Spatial distributed spectroscopic monitoring of melt pool and vapor plume during the laser metal deposition process

Dieter De Baere^{a,*}, Wim Devesse^a, Jan Helsen^a, Patrick Guillaume^a

^a*Vrije Universiteit Brussel, Acoustics and Vibration Research Group, Pleinlaan 2, Brussels B-1050, Belgium*

* Corresponding author. Tel.: +32-2-629-2807 ; fax: +32-2-629-0000. E-mail address: dieter.de.baere@vub.be

Abstract

Laser metal deposition is an additive manufacturing process that allows the production of near net shape structures. In order to obtain structures with reproducible and excellent material properties, it is necessary to understand the behaviour of the process better. Also the monitoring and the development of useful control approaches require a better physical understanding of the process. In this paper we present calibrated spectral measurement results from 400 nm up to 850 nm at different locations in the melt pool region of stainless steel (316L). The spectral information can be used for temperature estimation and the extraction of spectral characteristics. The collected spectra contain specific discrete spectral absorption and emission lines. These lines indicate the onset of the formation of a plasma for the vapor plume and shield gas. The onset takes place even at the applied laser power density level. The presented results can contribute to a better understanding of the process.

© 2020 The Authors. Published by Elsevier B.V.

This is an open access article under the CC BY-NC-ND license (<http://creativecommons.org/licenses/by-nc-nd/4.0/>)

Peer-review under responsibility of the Bayerisches Laserzentrum GmbH

Keywords: spectroscopy; laser metal deposition; temperature estimation; ionization; spectral lines; 316L

1. Introduction

Additive manufacturing (AM) is a group of technologies used for manufacturing of (near)-net shape products starting from 3D computer-aided design (CAD) data or other geometry representations.

Nowadays numerous types of metal alloys, polymers and ceramics can be processed with these new technologies. In this paper, the focus will be on the metallic laser metal deposition (LMD) technology. The additive processes were originally developed for the production of prototypes and work typically in an open loop configuration without feedback controller. For high-end applications a robust and controllable manufacturing process is mandatory for a general introduction of these techniques. There is a clear interest from the AM community to determine and control the temperature online. In the future, temperature measurements should prevent the introduction of excessive laser power and minimize in this manner the residual

stress build-up, distortions, the dilution and prevent cracking of the components during the production.

The temperature measurement of the AM process requires a non-invasive method in order to avoid inter alia altering the flow velocity fields within the melt pool and the region above the melt pool. As such, contact measurements would alter the temperature distribution too drastically. Also the large temperature gradients that appear would be averaged due to the large contact surface of the sensors.

The temperature distribution of the melt pool can be measured in contactless manner by measuring the radiation emission field of the melt pool and its direct surroundings using a thermographic camera without any influence on the process itself if the emissivity would be a constant for the melt pool and its direct surroundings. However, the emissivity varies with composition, observation angle, crystal structure, surface morphology, oxide layers, phase, liquid flow turbulence, temperature and wavelength. [1-2] The unknown emissivity

leads to a mathematical underdetermined system which cannot be directly resolved and which forms a fundamental physical problem. In literature different approaches can be retrieved to circumvent this problem. Two main relevant categories can be distinguished for the non-invasive temperature measurement for melt pool monitoring. Each category addresses the varying emissivity in a different manner. In the first category, the varying emissivity is tackled by measuring the reflected energy from a monochromatic additional source in order to estimate the emissivity [3]. In the second category, only the emitted radiation is measured and is used in combination with prior knowledge of the behaviour of the emissivity. The well-known ratio two-colour pyrometry belongs to this last category due to the fact that these systems assume a grey body behaviour. In literature different points of view and controversy regarding the different methods can be retrieved with respect to the accuracy obtained for the true temperature measurements [4].

Besides a varying emissivity the formation of a plasma could also provide an extra challenge. Two types of plasmas have been observed during laser welding operations. The first kind of plasma is related to the material that is being processed, the second is related to the applied shielding gas. It has been concluded that the plasma induced by laser welding have a low temperature and are weakly ionised plumes [5]. The first type of plasma has also been reported by different authors [6, 7], which applied optical emission spectroscopy during LMD in order to evaluate the vapour plumes.

In this paper, our measurement setup will be described together with the obtained spectral measurement results. In the second section the temperature results for seven different locations along the longitudinal axis of the melt pool are presented. Finally also the appearing spectral peaks are examined.

2. Experimental setup

A schematic overview of the experimental measurement setup is depicted in Fig. 1. A fibre laser operating at a wavelength of 1070 nm generates a melt pool with a diameter of approximately 1200 μm during the LMD process. The radiation emitted by a partial volume of the area of interest is captured by the focussing head. The focus plane, that stands perpendicular to the optical axis of the focussing head, has a diameter of 200 μm . A notch filter with a peak optical density (OD) larger than 6 at 1064 nm is integrated within the focussing head in order to exclude the collection of reflected high power laser light of 1070 nm. The average transmission of the notch filter is above 90% in a band from 375 nm to 1027 nm. One neutral density filter with an OD of 0,3 is incorporated for the presented data. The focussing head collects the emitted light and further focuses it on the end facet of an optical fibre. This optical fibre transmits the captured light further to the Avantes spectrometer (Avaspec-3648-USB2 with grating: UA, from 200 nm to 1100 nm providing a spectral resolution of 2,2-2,4 nm). The workpiece is mounted on a linear translation stage. This stage enables a motion out of the figure plane as indicated in Fig. 1. This configuration prevents relative displacements between the

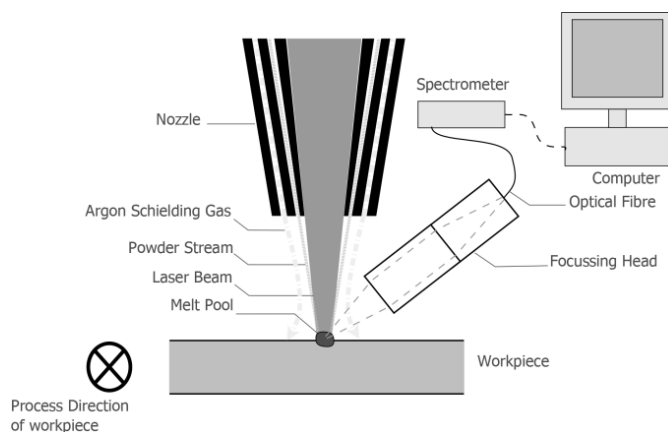


Fig. 1. Schematic overview experimental setup

focussing head and the laser beam during the deposition of a single track. As such the same location is monitored. The optical axis of the focussing head forms an angle of 60° with respect to the centre line of the laser beam.

3. Spectral Measurements

A number of experiments were conducted with the experimental setup described above. The spectral radiant energy is captured while the LMD machine deposits straight tracks of AISI 316L on a flat substrate of the same material. The melted powder particles have a size range of 44-106 μm . The tracks are only supported by the substrate and have no contact with neighbouring tracks. In order to prevent oxidation argon shielding gas is provided. The principal LMD production parameters of the experiments are depicted in Table 1.

The spectral measurement results of 7 different deposited tracks are presented; for each track a different location of the melt pool is monitored. The focus zone of the monitored locations are positioned along the longitudinal centre line of the laser spot of 1200 μm . The alignment is accomplished by using the pilot laser of the main laser system. A graphical representation of the different locations, with the focus planes

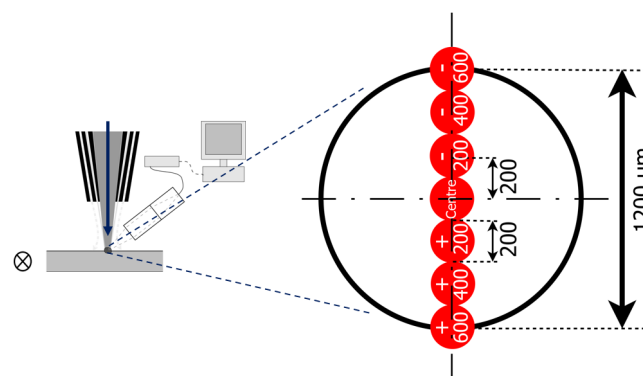


Fig. 2. Measurement locations

Table 1. Production parameters.

Laser power	Speed	Powder Mass Rate
450 W	1 m/min	2 g/min

is depicted in Fig. 2. Three locations are selected up front the centre of the laser beam. The locations will be referred to further in the paper with the number and sign specified in the red dots. This number represents the centre distance from the centre of the location to the centre of the laser beam (reference point). All measurements have an exposure time of 300 μ s and are captured at the maximum sampling frequency of the spectrometer 258,4 Hz. The collected radiant energy of each location is captured for a number of time points. The number of captured time points varies between 58-80 depending on the location. In Fig. 3 the relative average spectra are represented without taking any calibration factor into account for the 7 locations. These spectra were obtained directly from the raw data of the spectrometer with following formula:

$$\bar{E}(\lambda) = \frac{\sum_i^n E(\lambda, i)}{n}$$

In this equation n stands for the total number of time points. For each time point a spectrum is obtained.

The red curve from Fig. 3 is directly observed due to the large amount of energy radiated from the location at -200 μ m (towards the tail of the melt pool). Also the large difference between -200 μ m and +200 μ m is a quite remarkable result. For the other symmetric locations -400 μ m and +400 μ m almost the same spectra are obtained. For the locations -600 μ m and +600 μ m the averaged values are different but this was expected.

In a second step the obtained spectra represented in Figure 3 are multiplied with the calibration factor of the complete optical setup. In the next step the obtained spectra are normalised with the measurement value with a wavelength of 850 nm for each spectrum. In this manner normalised calibrated spectra are obtained which all cross 1 at a wavelength of 850 nm. These spectra are depicted in Fig. 4.

The following observations can be made after examining Fig. 4. The three curves at the -200 μ m, +200 μ m and centre location have a similar qualitative behaviour: a continuously increasing linear graph. The other 4 graphs have also a similar

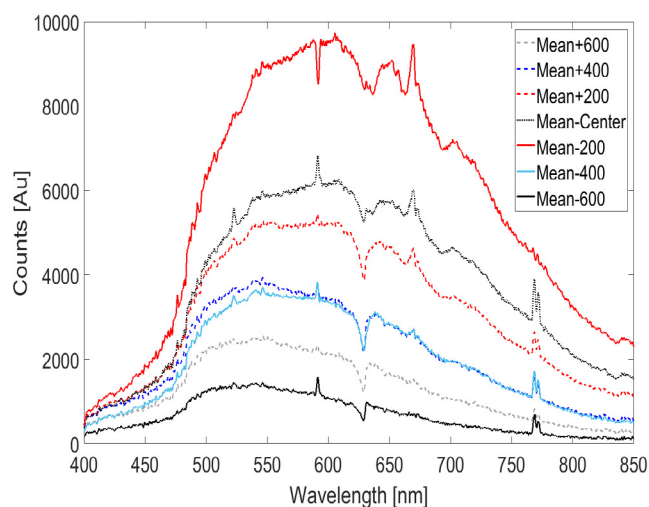


Fig. 3. Spectral radiant energy at 7 locations

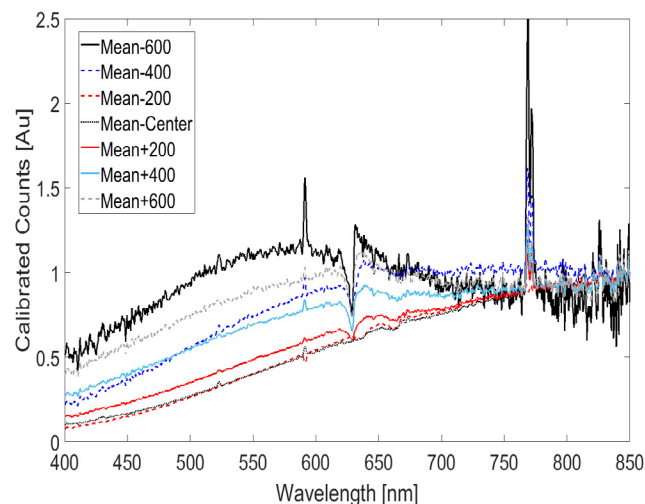


Fig. 4. Normalized calibrated radiant energy at 7 locations

behaviour but instead of continuously increasing graph up to 850 nm a clear turning point can be detected in a wavelength range from 550 nm – 650 nm. After this turning point the curves can be approximated by a constant value. The noise level for the location -600 μ m is a lot higher compared to the other locations, this is of course linked with low signal strength at this location, see Fig. 3. A final observation, if all curves in Fig. 4 would be approximated by a linear equation taking only the values into account obtained at 400 nm and at 850 nm, the gradients would be ranked from high to low in the following order: -200 μ m, centre, +200 μ m, -400 μ m, +400 μ m, +600 μ m, -600 μ m.

The signal strength variation of the average values can appear high for the different measurement points but the variation between the different time points of each location can also be very high without a clear transition between them. The reason for this behaviour could be linked with the fact that the sampling frequency of the spectrometer is not high enough compared to the dynamics of the melt pool.

The reason for the appearance of this turning point and relative building up of spectral energy between 400 nm and 650 nm will further be discussed in the next sections.

4. Temperature estimation results

The temperature estimation based on ratio pyrometry is a classical approach. According to Kahn, ratio pyrometry methods are shown to be very sensitive to measurement noise. This sensitivity grows quickly with respect to the number of terms in the ratio. Therefore the recommendation was made to use only the two colour method and avoid employing any higher number of colour/wavelengths [8].

In order to evaluate the impact of the wavelength selection, twelve different wavelengths were selected across wavelength range with a constant spacing of 40 nm between each other.

Besides the normalized radiant energy signals, that are depicted in Fig. 4 for the different locations, also two post processing methods were applied in order to generate two extra types of input data. The first type is a moving average with a subset size of 15 points, the second procedure applies a least

squares spline modelling using a piecewise cubic Hermite function with 4 knots. The objective of these post processing procedures is to evaluate the impact of measurement noise and superimposed spectral lines.

The two-colour temperature estimates are represented in the graphs of Fig. 5-10. If the first temperature estimates at 400 nm are ignored for the different graphs. It can be noticed, that for the location centres, 200 μm and -200 μm, the temperature estimates are clustered around a constant value for the different wavelengths. These were also the locations with a monotonic increasing radiant energy average value as function of the wavelength, see Fig. 4.

The variation of the estimated two-colour temperatures is the smallest for the input data of the piecewise cubic Hermite functions for the locations centre, 200 μm and -200 μm. This is driven by the fact that this post processing procedure is able to remove the spectral emission and absorption peaks and reduces the impact of other higher frequency variations. This kind of input data fits better with one theoretical blackbody curve and the grey body assumption.

The average results (excluding 400 nm values) for this type of input data is represented in table 2 for the three locations with monotonic increasing radiant energy behaviour. The estimated temperature values are higher than expected if they would only represent the melt pool temperatures at the different locations. Certainly if you take into account that the boiling point of the metal is at 3153 K [9]. Besides the temperature values also the spatial temperature gradients have an opposite sign compared to what is expected. The root cause is probably that other phenomena such as an onset of the formation of a plasma are also emitting light. These effects are of course relatively weaker/stronger depending on the zone where the measurement is performed. Also the melt pool locations with the highest temperatures will be less influenced due to the fact that these points are emitting more light with a specific spectrum signature linked to the melt pool temperature. This hypothesis could also explain the appearance of the turning point as already mentioned in the previous section of spectral measurements for the lower signal strengths. Other potential important parameters influencing the accuracy of the temperature measurement:

- The influence of reflected background radiation by the melt pool or other reflectors. The specular character of the melt pool surface has been indicated [10].
- The variability of the melt pool surface shape could provide an extra challenge. The captured emitted radiance and reflected radiance will vary depending on the orientation of melt pool surface with respect to the optical axis of the focusing head. The variation of the melt pool shape can provide an impact of the relative strength ratio between phenomena driven by the melt pool surface and other sources such as a plasma.

Table 2. Average two-colour temperature results.

Location	Temperature [K]
+200 μm	3234
Centre	3024
-200 μm	2981

- Calibration errors

- Non-grey body behaviour of the melt pool.
- The selection of the two spectral bands or wavelength values (spectral width and spectral separation between the bands/values). This parameter has partly been evaluated in this paper by the evaluation of different wavelengths and the results indicate the validity for some measurement locations.
- Validity of Wien approximation.

The locations -400 and 400 μm show rather constant ratio two-colour temperature estimates at least in the wavelength region from 450 nm up to 550 nm. From 600 nm up to 680 nm, the input data deviates from a monotonic increasing function, see Fig. 4. These deviations are causing fluctuations

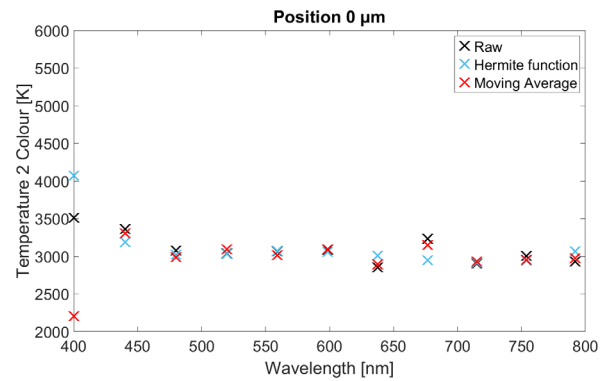


Fig. 5. Ratio two-colour temperature estimation centre position

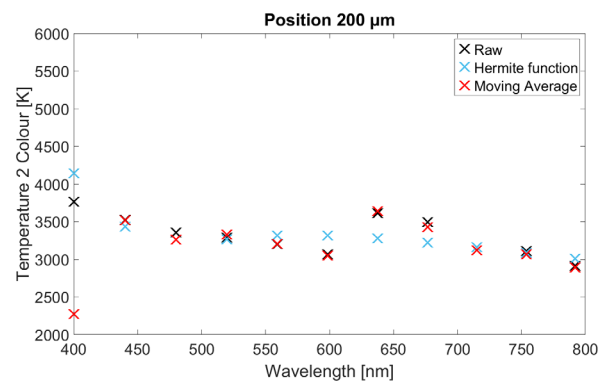


Fig. 6. Ratio two-colour temperature estimation 200 μm position

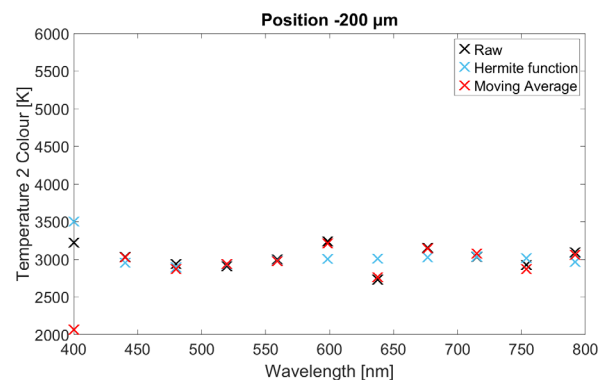


Fig. 7. Ratio two-colour temperature estimation -200 μm position

of the calculated temperatures for the different input data types. These temperature fluctuations at 600, 640 and 680 nm are

relatively stronger between the different input data types for 400 and -400 μm compared to the locations -200 μm and 200 μm (see Fig. 6-9). The input data of the piecewise cubic Hermite functions is able to cope better with these deviations. This results in temperature values for this input data type that are better in accordance with the obtained values for the lower wavelengths.

The locations -600 and 600 μm have the lowest absolute values which results in the worst signal to noise ratio. The absolute values for the -600 μm location were even so low that the different post processing methods were not able to stabilize the estimated ratio two-colour temperatures in any specific wavelength region. Therefore, these results were not included in this paper.

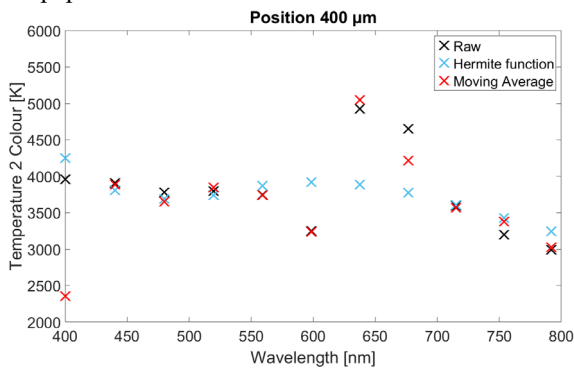


Fig. 8. Ratio two-colour temperature estimation 400 μm position

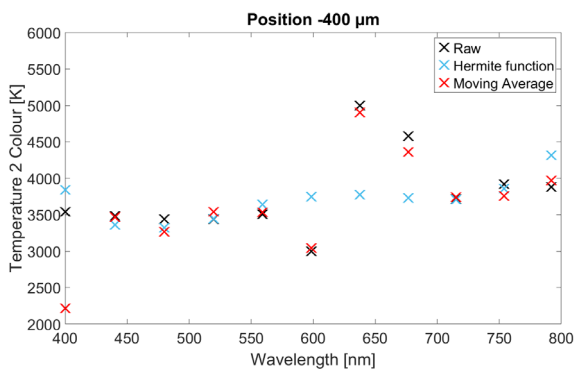


Fig. 9. Ratio two-colour temperature estimation -400 μm position

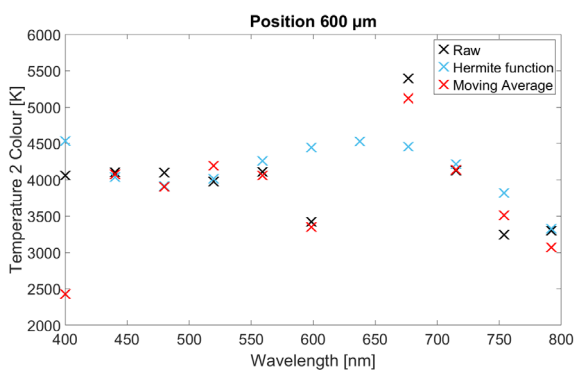


Fig. 10. Ratio two-colour temperature estimation 600 μm position

Another approach is the usage of an emissivity model. The best fit between the experimental normalized data (depicted in

Fig. 4) and theoretical curves of Planck’s law in combination with the assumed emissivity model allows the determination of the temperature and the parameters of the emissivity model.

The fitting operation was conducted by using the Levenberg-Marquardt algorithm, which is suited to solve non-linear problems. This method is implemented, in order to determine the parameters of a polynomial emissivity model of degree 0, 1 and 2 and the temperature. The implementation of the Levenberg-Marquardt algorithm was also recommended by Gathers for the analysis of multi-wavelength pyrometry data [11]. The temperature estimation results of the non-linear least-square minimization (Levenberg-Marquardt) technique are depicted in Fig. 11.

The ratio two colour estimation results of table 2 correspond well with the obtained estimated temperatures of the emissivity model for the zero-order emissivity model (constant). Similarly as for the two colour estimation approach an opposite spatial temperature distribution is obtained compared to the expected distribution on the basis of the overall strength of the non-normalised values shown in Fig. 3. For the second order the opposite behavior is less pronounced but still present but to a smaller extent. The reason for this behaviour has been discussed in the paragraph about the results of the ratio two-colour temperature estimation.

5. Vapour plume & shield gas

Discrete lines were observed in the spectrum. These lines are generated by bound-bound transitions of electrons. Characteristic absorption lines occur whenever an electron is excited from a specific lower energy level to a specific upper level. Characteristic radiation is emitted whenever an electron drops from a specific upper level to a specific lower level.

The onset of the formation of a plasma was detected by observing spectral lines at the following wavelength values, 772 nm, 769 nm, 629 nm, 591 nm and 523 nm. The wavelength 772 nm can be linked to the shield gas, namely Argon, from the Atomic Spectra Database of NIST. For example, the spectral line at 772 nm can be identified in the NIST database as 772,4207 nm (with a relative intensity of 10000 and a transition probability of $1,17 \cdot 10^7$). The

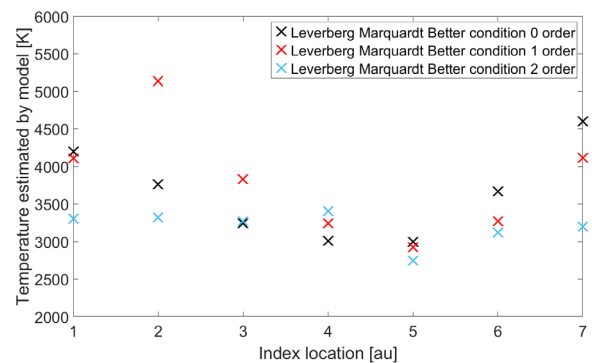


Fig. 11. Estimated temperatures with emissivity model (index 1= 600 μm, 2=400 μm, 3=200 μm, 4=centre, 5=-200 μm, 6=-400 μm, 7=-600 μm)

wavelength 523 nm can be linked to the vapour plume and more specifically to Fe I. (NIST database 523,2940 nm, relative intensity 123000 and transition probability of $1,94 \cdot 10^7$). The

detection frequency of these spectral lines was location dependent, the relative strength in Fig. 3 provides an indication of the strength and occurrence frequency. The impact of these spectral lines on the temperature estimation can be minimized with proper filtering.

Besides the bound-bound transition of electrons also free-bound and free-free transitions of electrons exist. The transitions emit continuum radiation as a result of deexcitation and inelastic collisions of high energy free electrons with ions (free-free bremsstrahlung and free-bound recombination) or neutral atoms (free-free bremsstrahlung). This continuum radiation can be superimposed on the thermal radiation of the melt pool as consequence of the inherent drawback of all spectroscopic measurement systems that the information is captured along the line of sight. It has been demonstrated in literature that for weakly ionized argon plasma, the continuum radiation emitted via interactions of free electrons with neutral atoms is significant and has a wavelength distribution that could declare the occurrence of the turning point in Fig. 4 [12].

6. Conclusions

In this paper the developed spectral measurement setup was presented to perform localized spectroscopic measurements, nevertheless the optical emission spectroscopy captures the information along the line of sight.

The obtained spectral radiant energies (see Fig. 3) had an expected ranking, in correspondence with the expected temperature distribution.

The estimated temperature values obtained with the current setup for the emissivity model approach and for the two-colour pyrometry method corresponded acceptably. Both approaches also obtained a similar temperature distribution. However this distribution is opposed to the expected distribution. Namely the location where the highest temperature was expected obtained the lowest temperature values for both approaches. The temperature values obtained at the other locations were almost everywhere above the boiling point of the metal. A number of potential root causes for this strange behavior have been discussed in the paper. The onset of the plasma formation with continuum radiation not directly linked with the thermal radiation of the melt pool, has for the current setup probably the highest potential impact. The impact of the plasma is higher for the locations where a lower melt pool temperature is expected. This can explain the too high temperature values and the opposed temperature distribution. Further research regarding the identification of the disturbing parameters/causes is highly recommended.

For the presented measurement setup the best location to monitor the temperature was $-200\ \mu\text{m}$ behind the centre point of the laser of the LMD machine.

In order to improve the measurement accuracy in future test campaigns it is recommended to apply a spectrometer with a higher quantum efficiency in the 700 – 1000 nm range. Also the sampling frequency of the spectrometer should be increased in order capture the quickly varying phenomena.

The clear conclusion regarding the vapor plume and shield gas is that the occurrence of the spectral lines indicate the onset of plasma formation for both the vapour plume and shield gas

for the LMD process. According to the knowledge of the authors the spectral line of 772 nm have not been mentioned in literature for the LMD process.

Acknowledgements

This work was supported by the Research Foundation - Flanders (FWO) within the SBO project: Hi-PAS.

References

- [1] Felice RA, Nash D. Pyrometry of materials with changing, spectrally-dependant emissivity- Solid and liquid metals, AIP Conference Proceedings, Vol. 1552 Issue 1, 2013. p.734.
- [2] Doubenskaia M, Pavlov M, Grigoriev S, Smurov I. Definition of brightness temperature and restoration of true temperature in laser cladding using infrared camera, Surface Coating Technology 220, 2013. p.244-247.
- [3] Gardner JL, Jones TP. Multi-wavelength radiation pyrometry where reflectance is measured to estimate emissivity, J. Phys. E: Sci. Instrum., Vol 13, 1980. p.306-310.
- [4] Duvaut Th. Comparison between multiwavelength infrared and visible pyrometry: Applications to metals, Infrared Physics & Technology 51, 2008. p.292-299.
- [5] Matsunawa A, Kim JD. Basic understanding on beam – Plasma interaction in laser welding. Pacific International Conference on Applications of Lasers and Optics; 2006. P. 128-133
- [6] Song L, Wang C, Mazumder J. Identification of phase transformation using optical emission spectroscopy for direct metal deposition process. High Power Laser Materials Processing: Lasers, Beam Delivery, Diagnostics, and Applications. SPIE, 2012 p. 120-130
- [7] Ya W, Konuk AR, Aarts R, Pathiraj B, Huis in 't Veld B.. Spectroscopic monitoring of metallic bonding in laser metal deposition. Journal of Materials Processing Technology, Volume 220, 2015. p. 276-284,
- [8] Kahn MA, Allemand C, Eager T. Noncontact temperature measurement. I. Interpolation based techniques, Review of Scientific Instruments 62, 1991. p.392-402
- [9] Kraus HG. Experimental Measurement of Stationary SS 304, SS 316 L and 8630 GTA Weld Pool Surface Temperatures. Weld. J., 68(7), 1989. p.269-279.
- [10] De Baere D, Devesse W, De Pauw B, Hinderdael M, Guillaume P. Evaluation of the Diffuse Reflectivity Behaviour of the Melt Pool During the Laser Metal Deposition Process. In 35th international congress on applications of lasers & electro-optics. 2016. 506
- [11] Gathers GR. Analysis of multi-wavelength pyrometry using non-linear chi-square fits, Int. J. Thermophys. 13 (2), 1992. p.539-554
- [12] Park S, Choe W, Youn Moon S and Park J. Electron density and temperature measurement by continuum radiation emitted from weakly ionized atmospheric pressure plasmas Appl. Phys. Lett.104084103 2014

11th CIRP Conference on Photonic Technologies [LANE 2020] on September 7-10, 2020

Temperature field based closed-loop control of laser hot wire cladding for low dilution

Dieter Tyralla^{a,*}, Thomas Seefeld^a

^a *BLAS – Bremer Institut für angewandte Strahltechnik GmbH, Klagenfurter Str. 5, 28359 Bremen, Germany*

* Corresponding author. Tel.: +49-421-218-58113; fax: +49-421-218-58063. E-mail address: tyralla@bias.de

Abstract

A modified laser hot wire cladding process is demonstrated with beam oscillation for high productivity and low dilution. A 2-channel pyrometer camera is used to observe the melt pool geometry during process to evaluate the current status of the process. Deviations from a set optimum are recognized and automatically compensated by a laser power control. A comparison of uncontrolled and controlled cladding process shows a significantly lower standard deviation of the dilution compared to the uncontrolled cladding process. The experiment verifies a relation of penetration depth and melt pool length.

© 2020 The Authors. Published by Elsevier B.V.

This is an open access article under the CC BY-NC-ND license (<http://creativecommons.org/licenses/by-nc-nd/4.0/>)

Peer-review under responsibility of the Bayerisches Laserzentrum GmbH

Keywords: Laser hot-wire cladding, beam oscillation, process monitoring and control, temperature measurement

1. Introduction

Laser cladding is a well-established production technique for the protection of a substrate material against high corrosive or high abrasive environment by the help of a filler material [1]. Also worn parts can be repaired with clads of the same material [2].

In a conventional (hot) wire-based cladding process (LHWC) a melt pool is generated by a large defocused laser beam. The wire is plunged into the melt pool and is melted from the energy inside the melt pool [3]. As less substrate material as possible should be melted to obtain a pure functional layer which shows the properties of the filler material. However, enough material must be melted to ensure a strong bond. The relation between substrate material and filler material within the weld bead is an important criterion of quality and is called dilution. A higher deposition rate requires a larger melt pool to increase the provided energy, but causes higher dilution which indisposes the process for applications which demand high

quality. Typical wire-based laser processes provide a high deposition rate of 2 kg/h with a dilution of 6.5 % [4]. In single cases the deposition rate reaches values of up to 7 kg/h by the utilization of three wires [5] or by the help of strips instead of wire material but here, with particularly higher dilution [6]. The provision of highest possible deposition rates requires more than the accurate adjustment of parameters. Here, closed-loop control is necessary to provide uniform dilution and a constant layer geometry.

Dilution strongly depends on the energy per unit length and the molten mass per unit length which are mostly influenced by the laser power, the welding speed and the wire feed rate [7]. Variations modify the temperature field in the process zone [8] and thus can be recognized by a temperature measurement. Thermal process monitoring enables the determination of the current process state and the recognition of heat condition changes.

In most cases pyrometers are used for process monitoring [9]. Here, the signal correlates with the temperature in the

process zone and enables the closed-loop control of the process [10]. Welding fumes attenuate the process radiation and modify the spectral emissions selectively [11]. Sometimes two-channel-pyrometers are used to overcome this problem [12]. However, pyrometers and two-channel-pyrometers only provide low information density because the whole temperature field is integrated to one value [13].

Cameras ensure spatially resolved information and enable the evaluation of geometrical information. Often cameras are used to correlate greyscale with temperature, e.g. in laser hardening [14]. A novel two-channel-pyrometer camera enables the evaluation of melt pool width, length and area in laser metal deposition [15] and selective laser melting [16]. In addition, temperature gradients can be determined in hybrid welding [17].

2. Experimental set-up

A laser processing head with a 2-dimensional beam oscillator (modified ALO-3, Scansonic) is used for the investigation. A disc laser (TruDisk 12002, TRUMPF) provides a laser power of up to 4 kW which is limited by the oscillator. The laser spot diameter can be varied between 200 μm and 2 mm by defocusing. The filler material is fed in leading position at 45° to the work piece. The wire feeder (Masterliner MF1, Abicor Binzel) enables wire feed rates of up to 10 m/min. The power source delivers a maximum current of 170 A. A real-time LabView controller operates the different devices. Figure 1 shows the experimental set-up.

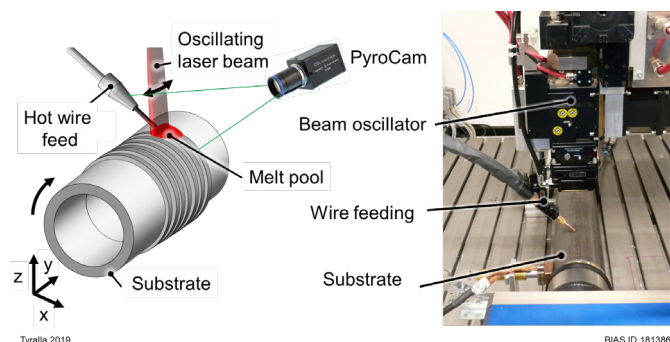


Fig. 1. Schematic of thermal process monitoring and experimental set-up for laser hot wire cladding [18].

Different experiments are carried out:

- Investigation of a thermal-based laser power control approach for laser hot wire cladding
- Development of hot wire process with both, high deposition rate and low dilution

The thermal control approach is processed on tubes with a diameter of 50 mm and a wall thickness of 5 mm. The tubes of 1.5415 (16Mo3) are cladded with a stainless-steel filler 1.4430 (316L) of 1.2 mm, a wire feed rate of 5 m/min, a welding speed of 4 m/min, a laser power of 3.5 kW, a laser spot diameter of 1 mm and a preheating current of 170 A. A triangle oscillation with a frequency of 200 Hz and an oscillation width of 3.6 mm is applied.

Current and voltage are monitored by a high frequency of at least 100 kHz (P1000-S3 process sensor, HKS). The laser power distribution is measured by a beam profile analyzer (SP300+LBS300, Ophir Spiricon). The temperature field is observed spatially resolved by a two-channel pyrometer camera (PyroCam, IMS CHIPS) that enables emissivity corrected temperature measurement between 600 °C and 1900 °C [19]. Optical filters are used to avoid issues with stray light and non-thermal radiation.

A fast FPGA algorithm is developed to determine thermal indicator values in the images of the PyroCam. The method enables the evaluation of different values like melt pool geometry, wire temperature or temperature gradients. The evaluation procedure starts with the determination of the brightest area within the images which correlates with the laser irradiation position. The algorithm starts at this location with the identification of the melt pool by the help of the melt temperature which is taken from literature. Areas of connected pixels of melt temperature or above are recognized as melt pool. If there is more than one area detected, the one with the highest number of pixels is chosen for further evaluation. The expansion in x-direction and in y-direction equals melt pool width and length, respectively. The melt pool area is determined by summarizing the number of pixels with melt temperature or above. The melt pool length is used for the close loop control. Figure 2 shows a process image of the PyroCam and a schematic with the identified values.

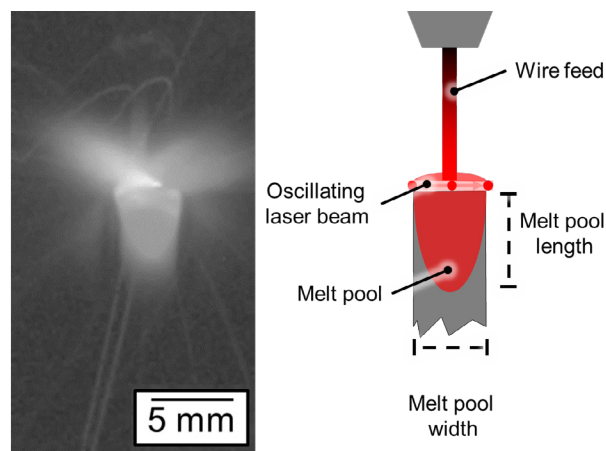


Fig. 2. PyroCam process image and schematic of melt pool geometry determination [18].

The thermal control approach uses the melt pool length to validate the energy which is introduced into the process and adjusts the laser power to maintain a given set melt pool length value. This value is adjustable during process duration for step function response experiment. Figure 3 shows the schematic of the thermal control approach.

In step function response experiment, the set melt pool length value is modified during the cladding process. After an initial phase, the set value is manually adjusted every approx. 10 seconds. The set value is alternately adjusted to different values with different ranges of value to investigate the response behavior of the thermal control and the corresponding influences on penetration depth. The adjustments of the laser

power by the control and the resulting melt pool length response is measured. Further the corresponding penetration depth is determined after the process by the evaluation of the cross-section.

The control experiment compares an uncontrolled process with a controlled process. Here, a reference process without control is used to identify a suitable set value for the melt pool length in the controlled case. Further the penetration depths are determined after the process by the evaluation of the corresponding cross-sections.

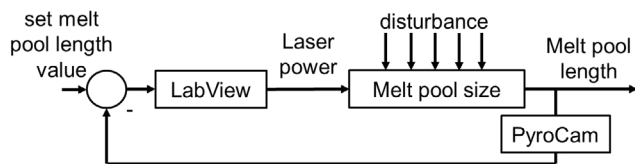


Fig. 3. Schematic of thermal control approach.

The experiments of high deposition rate are processed on mild steel tubes of 1.0038 (S235) with an outer diameter of 100 mm and a wall thickness of 8 mm. The tubes are clad with a stainless-steel filler 1.4430 (316L) and a nickel-based alloy 2.4856 (Inconel718) of 1.2 mm diameter, a feed rate of 10 m/min, a welding speed of 2 m/min, a laser power between 3.5 kW and 4 kW and an electrical preheating current of 170 A. The laser spot diameter is 2.8 mm. A triangle oscillation with a frequency of 200 Hz and an oscillation width of 3.6 mm is applied. The tracks are evaluated regarding height, width, dilution and deposition rate by metallographic cross-section.

3. Results

3.1. Thermal control approach

Figure 4 shows a step function experiment of a thermal based laser power control.

The graph is divided into four sections which correspond with the variation of melt pool length set value. The first section expires after 20 s. The second section contains the interval between 20 s and 30 s. The third section follows up to a process time of 42 s. Afterwards the fourth section starts and runs until the end of the process.

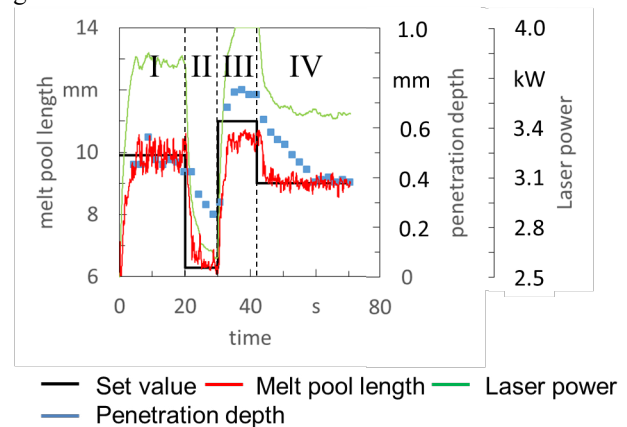
In section one the set melt pool length value is adjusted to 9.90 mm. The measured melt pool length reaches the set-value after a delay of 5 s and stays at 9.92 mm on average. In the second section the set melt pool length value is adjusted to 6.30 mm. The melt pool length is measured after 5 s and is 6.38 mm on average. In the third section the set value is adjusted to 10.80 mm. In this section the measured melt pool length receives an average value of 10.44 mm after 5 s. In the last section the set value is adjusted to 9.00 mm. After 5 s an average melt pool length of 9.02 mm is measured.

The coefficient of variation is less than 2 % except for the first section where it is 3.8 %. It is suggested that a strong control activity causes the higher value in this section.

The deviation between set-value and measured value is at most 1.6 % excepting the third section where it is 3.7 %. It is suggested that the laser power limit of 4 kW inhibits the

obtainment of the set value in this section. Here, the laser power is almost always at the maximum value.

The penetration depth is also shown in figure 4. It can be noticed that the values certainly follow the melt pool length but with a much larger delay compared to measured melt pool length.



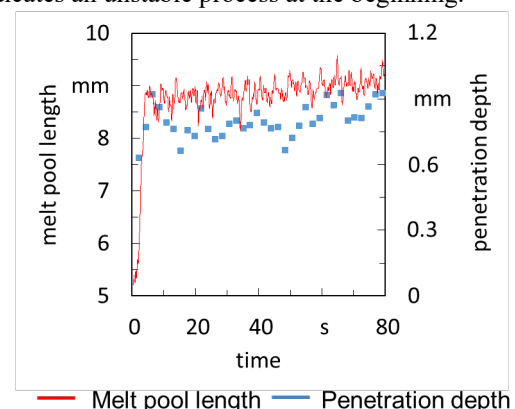
Tyralla 2020

BIAS ID 200277

Fig. 4. Step-function experiment: The measured melt pool length as indicator for penetration depth is controlled by an adjustment of laser power under variation of set melt pool length.

Figure 5 shows a result of cladding without thermal based laser power control. A constant laser power of 3.5 kW is applied. The melt pool length increases during process by 11.0 % from 8.2 mm to 9.1 mm. It is suggested that the tube accumulates heat because of the small heat sink volume. The coefficient of variation is 3.1 % after compensation of the slope.

The penetration depth increases after several revolutions by 11.7 % from ca. 0.77 mm to 0.86 mm. Here, a proportional dependency is demonstrated between melt pool length and penetration depth by the comparable slope. The penetration depth strongly fluctuates during the first revolutions in a range of 0.63 mm to 0.92 mm. Here, the corresponding image indicates an unstable process at the beginning.



Tyralla 2020

BIAS ID 200278

Fig. 5. Measured melt pool length and corresponding penetration depth for laser cladding without thermal control.

Figure 6 shows a result with thermal closed-loop control. A set melt pool length of 9.0 mm is applied. The measured melt pool length reaches the set-value the first time after a delay of 5 s and stays at 9.0 mm on average. The closed-loop control compensates the thermal drift which was observed in uncontrolled case and maintains the melt pool length to the set value. For this purpose, the laser power is reduced during process duration from 3675 W to 3475 W.

The coefficient of variation of melt pool length of 1.9 % is significantly lower compared to uncontrolled case and indicates a stabilization of melt process which is also demonstrated by the work piece due to a stable starting behavior.

The fluctuation of penetration depth at the beginning of the process is reduced to a range of 0.67 mm to 0.81 mm. After a few revolutions the depth passes to a constant value of 0.66 mm with a coefficient of variation of 3.2 %

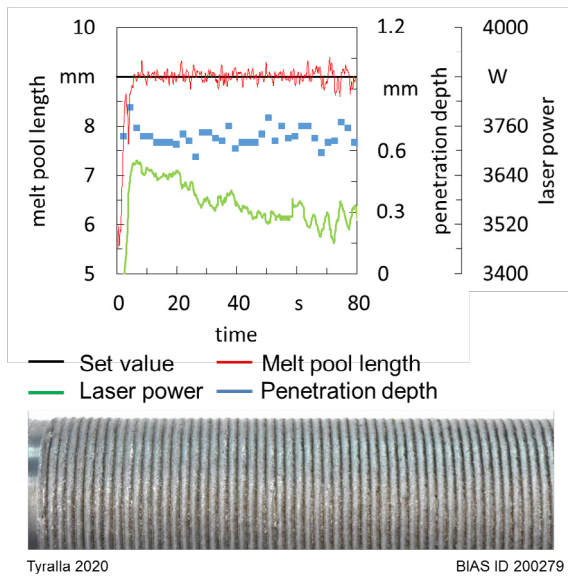
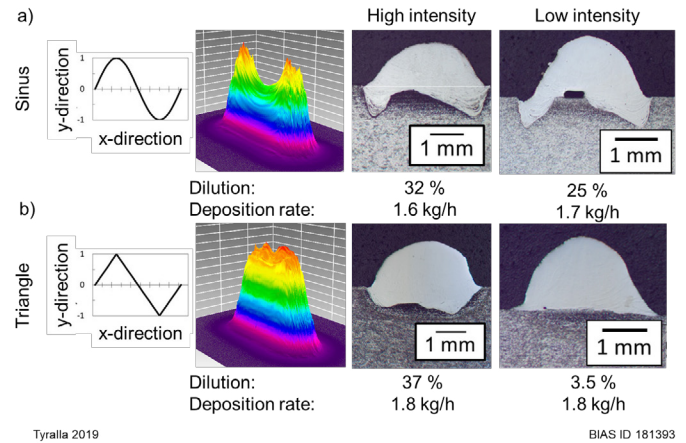


Fig. 6. Measured melt pool length and corresponding penetration depth for laser cladding with thermal control.

3.2. Higher deposition rate cladding

Figure 7 shows the adaption of oscillation parameter for a suitable energy deposition in LHWC. The energy is distributed perpendicular to the welding direction by the help of a beam oscillator. Figure 7a shows the common sinusoidal oscillation which induces high energy at the turning points of oscillation and thus, generates high penetration at the borders. Less laser intensity leads to lack of fusion while dilution is still high.

The triangle oscillation ensures a sufficiently deposition of energy in the process zone and thus, a uniform penetration depth is generated like shown in figure 7b. Here, the decrease of intensity leads to uniform reduction of penetration depth and enables low dilution without lack of fusion.



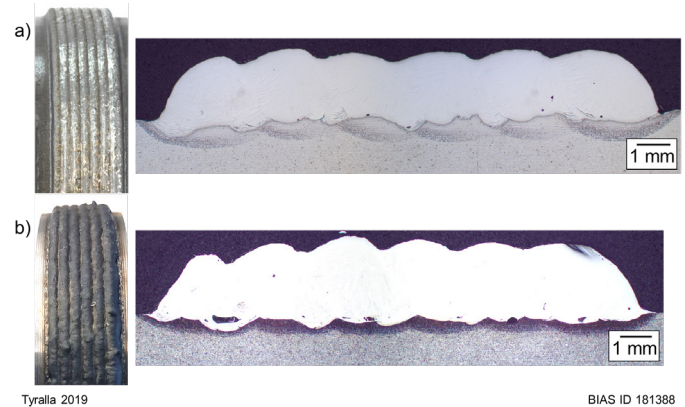
Tyralla 2019

BIAS ID 181393

Fig. 7. Oscillation strategy, intensity distribution and cross-section for a) sinus and b) triangle oscillation.

Figure 8a shows a cross-section of a layer with stainless steel wire. A deposition rate of 5.1 kg/h and a dilution of 8.3 % are achieved. Here, a laser power of 3.5 kW leads to a relative deposition rate of 1.4 kg/h per kilowatt of laser power.

The nickel-based alloy is shown in figure 8b. In this case, a deposition rate of 5.3 kg/h and a dilution of 8.6 % are achieved. The thermo physical properties of the nickel alloy increase the necessary amount of energy. The laser power has to be adjusted to 4 kW to provide a comparable result.



Tyralla 2019

BIAS ID 181388

Fig. 8. Cross-section of hot wire cladding experiment high deposition rate and low dilution for a) stainless steel and b) nickel-based alloy

4. Discussion

In the present work beam oscillation is used to distribute the energy in the process zone and to generate a uniform penetration depth. A triangle oscillation ensures low dilution and high deposition rate for a wire diameter of 1.2 mm and a laser power of up to 4 kW.

Furthermore, a laser power control is demonstrated which improves the process start behavior and reduces dilution variations during process. The control uses spatially resolved thermal indicators which are provided by a two-channel pyrometer camera. A relation between lateral melt pool dimension and penetration depth is already known from 3-dimensional heat conduction by e.g. Rosenthal [20]. Here, the melt pool size is linked to the corresponding melt pool

width, length and melt pool depth for a given set-up of energy source, welding speed and material. Therefore, the melt pool width or the melt pool length can be used for process characterization in laser welding and for melt pool depth estimation. In the present case, the melt pool width is mainly determined by the laser beam deflection amplitude and thus it is unsuitable for the mentioned process characterization. Therefore, the melt pool length is used as thermal indicator value. However, changes of the length are detectable at the end of molten pool at most and thus the length responds slower to variations of process conditions and leads to a time lag of the closed-loop control.

The experiments demonstrate a dependency between measured melt pool length and penetration depth. However, compared to melt pool length, the penetration depth responds even slower to laser power variations and ensures a constant penetration depth even for temporal fluctuations of the melt pool length. It is suggested that the selective evaluation of the penetration depth at one cross-section influences the accuracy of penetration depth value and complicates a correlation. Here, a longitudinal section would give more detailed values.

5. Conclusions

- A novel process method is used to provide high deposition rate and low dilution in laser hot wire cladding. The wire is melted directly and beam oscillation ensures sufficient distribution of energy. Thus, a high deposition rate of 5.3 kg/h with a dilution of 8.6 % is achieved for different materials.
- A two-channel-pyrometer camera is used for temperature field observation and provides thermal based information of the current process state. The information is used to compensate variations of thermal conditions during the process and maintain a constant melt pool length.
- The experiments verify a relation of penetration depth and melt pool length. Thus, the adjustment of melt pool length ensures the online monitoring and control of dilution by the help of the laser power.

Acknowledgements

The IGF-Project-No.: 19.674N / DVS-No.: 06.100 “Kontrolliertes Laser-Heißdrahtbeschichten” of the “Forschungsvereinigung Schweißen und verwandte Verfahren e.V.” of the German Welding Society (DVS), Aachener Str. 172, 40223 Düsseldorf was funded by the Federal Ministry for Economic Affairs and Energy (BMWi) via the German Federation of Industrial Research Associations (AiF) in accordance with the policy to support the Industrial Collective Research (IGF) on the basis of a decision by the German Bundestag. Furthermore, the authors gratefully acknowledge the collaboration with the members of the project affiliated committee regarding the support of knowledge, material and equipment over the course of the research.

Gefördert durch:



References

- [1] Atamert, S.; Bhadeshia, H.K.D.H: Comparison of the microstructures and abrasive wear properties of stellite hardfacing alloys deposited by arc welding and laser cladding, Metallurgical Transactions A 20A, 1989, 1037-1054
- [2] Kattire, P.; Paul, S.; Singh, R.; Yan, W.: Experimental characterization of laser cladding of CPM 9V on H13 tool steel for die repair applications, Journal of Manufacturing Processes 20, 2015, 492-499
- [3] Xu, X.; Mi, G.; Chen, L.; Xiong, L.; Jiang, P.; Shao, X.; Wang, C.: Research on microstructures and properties of Inconel 625 coatings obtained by laser cladding with wire, Journal of alloy and compounds 715, 2017, 362-373
- [4] Pajukoski, H.; Näkki, J.; Thieme, S.; Tuominen, J.; Nowotny, S.; Petri, V.: Laser cladding with coaxial wire feeding, 31st International Congress on Applications of Lasers & Electro-Optics (ICALEO2012), 2012, 1196-1206
- [5] Freiße, H.; Thomy, C.; Vollertsen, F.; Narita, R.: Process for Laser Cladding Features Three Hot Wires, Welding Journal 52, 2018
- [6] Tuominen, J.; Kaubisch, M.; Thieme, S.; Näkki, J.; Nowotny, S.; Petri, V.: Laser strip cladding for large area metal deposition, Additive Manufacturing 27, 2019, 208-216
- [7] Steen, W. M.; Mazumder, J.: Laser Material Processing, 4. Aufl., Springer-Verlag London 2010.
- [8] Islam, M.; Purtonen, T.; Piili, H.; Salminen, A.; Nyrhila, O.: Temperature profile and imaging analysis of laser additive manufacturing of stainless steel, Physics Procedia 41, 2013, 835-842
- [9] Muvvala, G.; Karmakar, D. P.; Nath, A. K.: Monitoring and assessment of tungsten carbide wettability in laser clad metal matrix composite coating using an IR pyrometer. In: J. of Al. & Comp. 714, 2017, 514-521. [10] Bi, G., Gasser, A., Wissenbach, K., Drenker, A., Poprawe, R.: Identification and qualification of temperature signal for monitoring and control in laser cladding, Opt. & Lasers in Eng. 44, 2006, 1348-1359
- [11] Bi, G.; Sun, C.N.; Gasser, A.: Study on influential factors for process monitoring and control in laser aided additive manufacturing, Journal of Mat. Processing Techn. 213, 2013, 463-468
- [12] 8. Doubenskaia, M., Bertand, P., Smurov, I.: Pyrometry in laser surface treatment. Surface and coating technology 201 (5), 1955-1961 (2006).
- [13] Bernhard, F.: Handbuch der Technischen Temperaturmessung, 2. Aufl., Springer-Verlag Berlin Heidelberg 2014.
- [14] Bonß, S.: Laser transformation hardening of steel, Advances in laser materials processing, 2010, 291-326.
- [15] Köhler, H.; Jayaraman, V.; Brosch, D.; Hutter, F.X.; Seefeld, T.: A novel thermal sensor applied for laser materials processing, Lasers in Manufacturing (LIM13), Phys. Proc. 41, 2013, 495-501.
- [16] Dörfert, R.; Tyralla, D.; Freiße, H.; Vollertsen, F.: Coaxial implementation of a temperature field monitoring device for in-situ melt pool measurements in additive manufacturing, Procédés Laser Pour L'Industrie Conférences (PLI), Colmar, 2019, 166-169
- [17] Goecke, S.-F.; Seefeld, Th.; Tyralla, D.; Krug, A.: Monitoring and Control of the Heat Input in MAG-Laser-Hybrid Welding of High Strength Steel in Telescopic Crane Booms, Proc. Of 15th International Conf. on Automation and engineering, 2019, 1744-1747, doi:10.1109/COASE.2019.8843219
- [18] Tyralla, D., Seefeld, T.: Higher deposition rates in laser hot wire cladding (LHWC) by beam oscillation and thermal control. In: Wulfsberg J., Hintze W., Behrens BA. (eds) Production at the leading edge of technology, Springer Vieweg, 2019, 401-409
- [19] Hutter, F. X., Brosch, B., Graf, H.-G., Klingler, W., Strobel, M., Burghartz, J. N.: A 0.25µm logarithmic CMOS imager for emissivity-compensated thermography, 2009 IEEE, 20/8, 2019
- [20] Rosenthal, D.: The theory of moving sources of heat and its application to metal treatments. Transactions of ASME 43(11), 1946, 849-866

11th CIRP Conference on Photonic Technologies [LANE 2020] on September 7-10, 2020

MiCLAD as a platform for real-time monitoring and machine learning in laser metal deposition

Julien Ertveldt^{a,*}, Patrick Guillaume^a, Jan Helsen^b

^aVrije Universiteit Brussel, Dept. MECH, Pleinlaan 2, B-1050 Brussels, Belgium

^bVrije Universiteit Brussel, Dept. INDI, Pleinlaan 2, B-1050 Brussels, Belgium

* Corresponding author. Tel.: +32-2-6292324. E-mail address: julien.ertveldt@vub.be

Abstract

The MiCLAD machine designed at the VUB, Belgium, allows for closed-loop controlled laser metal deposition including various in-situ optical based measurement systems. These integrated sensors collect information on deposition geometry and temperature during the building process. Hence, each cubic millimeter of material that is either added or removed is mapped to its digital twin with a millisecond temporal resolution in the machines database. This paper introduces the platform and its capabilities by focusing on the procedure of obtaining the necessary training data for the future application of machine learning algorithms, with the goal of controlling the geometry and temperature history during additive manufacturing.

© 2020 The Authors. Published by Elsevier B.V.

This is an open access article under the CC BY-NC-ND license (<http://creativecommons.org/licenses/by-nc-nd/4.0/>)

Peer-review under responsibility of the Bayerisches Laserzentrum GmbH

Keywords: Laser Metal Deposition (LMD); Machine learning; Real-time monitoring; Feed-back control

1. Introduction

It is generally known that the result of the material deposition in a Laser Metal Deposition (LMD) additive manufacturing process is subject to many parameters. The following parameters are considered amongst the most influential for the LMD process [1,2,3]: deposition geometry, laser power, scanning speed, material mass flow rate. These are all instantaneous. However, also the temporal history in terms of heating and cooling rates, related to laser power and scanning speed, has a significant influence on the obtained material properties in terms of strength and residing residual stresses [4,5]. Hence, not only the deposited geometry is important, but also the instantaneous and history of temperature gradients in the part during the building process are. If the process parameters such as laser power and material deposition rate are not kept in the correct range during the building process this will result in both geometrical as well as material defects such as porosities and an altered microstructure will result. Hence, a

continuous control of both temperature as well as deposition geometry is required for qualitative laser metal deposition. However, due to the strong correlation between all the process parameters often the control of the deposition is based on only geometrical [6,7] or metallurgical (through temperature) control [8,9,10,11]. In this paper a framework is presented that makes control based on multiple sensor modalities (i.e. geometry and temperature) in a machine learning framework possible.

It is therefore that many current research is aimed at on-line measurement, monitoring and control solutions for the LMD process [3]. Most of these control systems are point based systems [10,11,12,13], using either pyrometers for temperature measurement, or optical coherence tomography sensors for height measurement. The advantage of these point based, or scalar, systems is the fast processing and thus real-time implementation possibilities. However, because only one coordinate in space can be monitored at a time, no time series history for these points is available or only an average value

over a larger area can be obtained. Therefore, a first extension to these scalar systems was found in the usage of matrix or line based imaging sensors as demonstrated by [2,14,15]. In these papers it was shown that the extension of scalar measurements to multi-dimensional measurements strongly improves the actual deposition geometry and metal components [7]. However, the drawback of these multi-dimensional sensors such as 2D camera's or 3D scanning systems, is the fact that they become relatively slow and the processing of the data within the required typical cycle time for real-time control of the melt pool of the order of magnitude of 1 ms [16], is very difficult.

The current paper introduces a machine and its data acquisition framework that allows to obtain for each spatial coordinate within the 3D printed part both the geometry and temperatures at different time steps during the building process. Hence, allowing to study not only the effect of the addition of material for that given point in space, but also the deformation of the part due to the additional heat input from the build process of the next layers. Additionally, a temperature history in the part over time for all positions is becoming available too. Hence, a data driven digital twin of the part during the manufacturing process can be reconstructed based on the collected process data. Although the processing of such amount of data can typically not occur fast enough to do it in real-time, nonetheless, the processing can run in parallel to the part building process and corrections or changes in the part geometry can still be performed over multiple layers, rather than only instantaneously. A second advantage is that such off-line methods can consider the full history, not only of the part, but of also of the machine and all the input parameters (i.e.: geometry, deposition strategy and trajectory, material & powder characteristics, process parameters, etc.)

In order to take full advantage of this benefit the Micron precision Milling Closed-Loop Additive (MiCLAD) research platform was built at the Vrije Universiteit Brussels, Belgium. Figure 1 shows a CAD render of the inside of the MiCLAD machine designed by the author at the VUB. The machine combines a powder blown laser metal deposition head with a high-speed mechanical milling tool. Hence, both addition and removal of material is capable and corrections to the part can

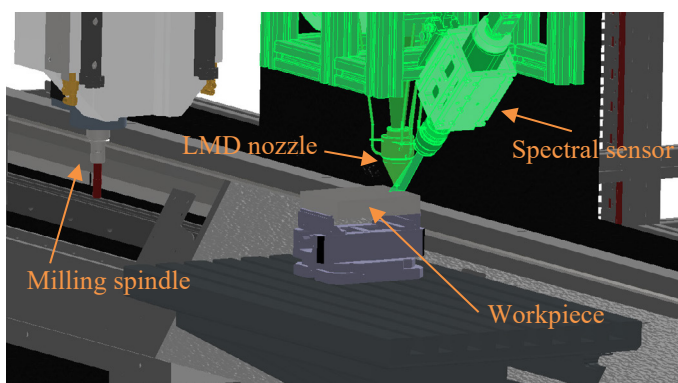


Fig. 1. MiCLAD machine with LMD station (green) and milling spindle.

be either additive or subtractive. It was illustrated by [7] that the correction of a local excess deposition in a particular layer typically takes up to tens of layers to compensate for the error. Hence, having the opportunity to also decide for removal of

excess material can significantly decrease the additional number of layers required to compensate for the excess. A more in-depth look to the MiCLAD machine is given in the next section.

2. MiCLAD hybrid LMD machine

2.1. Machine concept

MiCLAD (Figure 1) is the in-house developed hybrid laser metal deposition and high-speed milling machine of the Vrije Universiteit Brussel. By opting for a hybrid machine with both additive and subtractive capabilities, the machine allows to correct the part geometry over multiple layers. With only an additive possibility, once too much material is deposited, no correction in the machine is possible anymore. A separate milling spindle and laser deposition head were chosen to allow for a fast transition from additive to removal capability. Within a time of less than 1 second a milling operation can be started after finalizing a deposition process. Hence, due to the relative slow rate of material addition in the range of 2 to 10g/min, the cost of a finish milling operation is small. Because the more challenging and relevant aspect of the correct addition of material than the removal, to the current paper, the sequel of this paper only focusses on the laser additive features of the machine. The most relevant machine properties for this paper are summarized in Table 1.

Table 1. MiCLAD machine specifications.

Machine travel	450 mm x 300 mm x 300 mm
Speed & Acceleration	Up to 50 000 mm/min and 1.5 G
Encoder accuracy	6 μ + 3 μ /m
Table load	300 kg
Machine weight	6000 kg granite machine base
Milling spindle	HSK-E32 30 000 rpm, 4kW
Laser	SPI redPOWER® QUBE 2kW 1064 nm fiber laser
Laser spot	1 mm flat-top
Laser processing head focusing & collimation	II-VI HIGHYAG BIMO 2W 1.25 @ 250 mm & 1.33 @ 150 mm
Powder nozzle	Fraunhofer ILT COAX-S40
Carrier gas	Argon 3 – 10 l/min
Central shielding gas	Argon 2.5 – 8 l/min
CNC Control	Bosch Rexroth MTX 5 axis control

Important within this study is also to notice the acceleration rates that can be obtained with the MiCLAD machine. Besides being interesting for modern metal milling strategies, this is also a very useful feature for laser metal deposition as a constant velocity can be obtained with very small delay after initiating the motion. Therefore, typical edge buildup as seen in many LMD parts with sharp corners such as cubes can be minimized by ensuring constant velocity throughout a deposition contour.

2.2. Data platform

Figure 2 illustrates the data platform that is constructed to join the hardware of the machine. Including from left to right, 1) the pre-processing data that is a user input to the system (CAD/CAM software based deposition trajectory definition, powder properties and process settings) step, 2) the Bosch Rexroth MTX industrial CNC controller doing the actual path planning and laser setpoint generation from the trajectory & process data. The benefit of this commercial CNC system in the proposed application is that it is both offering the industrial robustness and practicalities for 5-axis CNC control, whereas it also offers hardware based real-time communication between the CNC control and the dedicated laser controller over the ethernet based SERCOS communication bus. As such, cycle times of down to 1 ms are achieved with a 100% guarantee that on both master (CNC controller) and slave devices (laser controller and motors) all tasks are accomplished within this periodic cycle. This CNC system and laser controller are appended with different real-time process control and measurement systems with different resolution, temperature measurement possibility as well as processing time. From the fastest to the slower are implemented: 3a) an in-house developed hyperspectral line camera based system for melt pool width & temperature control [9,16,17].

The image frames of the hyperspectral line camera are transferred to an FPGA based dedicated controller that extracts a temperature profile and laser setpoint commands in real-time with a cycle time of 1 ms. Due to the deterministic behavior of the SERCOS ethernet bus with a 1 ms cycle time and a software implementation in the dedicated laser controller to assure processing time below this 1 ms, this becomes the limiting update rate for the closed-loop feedback control. It was previously proven in [16] that this 1 ms is sufficient for real-time control of the melt pool temperature in the MiCLAD machine. The next monitoring system 3b) is a visual coaxial high-speed machine vision camera (Basler aca720-520um) with KG-3 heat absorbing IR filter installed on the coaxial

optical port of the II-VI HIGHYAG BIMO laser processing head mounted in the MiCLAD. This camera is used mainly for the visual inspection of melt pool size and to a less extent its intensity. Finally, 3c) is a Micro-Epsilon 3060-25/bl laser triangulation scanner with a Z resolution of 1.5 μm and lateral resolution of 12,5 μm . Based on the scanning speed of 120mm/min and a chosen acquisition rate of 160 lines/second the longitudinal resolution is also 12,5 μm . Finally, illustrated in 4) is the user input of post-processing data such as tensile test data and micro structure images to the central database.

3. Machine learning concept in additive manufacturing

3.1. Machine learning for laser metal deposition process optimization

The idea of applying machine learning or artificial intelligence to the problem of laser metal deposition control is not new. Indeed, because the possibly large influence of many parameters, such methods covering multi-dimensional sensor observations are ideal for the control of the LMD process. Amongst the most important references is [18], in which the authors use an Artificial Neural Network approach to find the ‘best’ laser power setting in the deposition of single melt pool beads with Al 2024 powder based filler metal on a solid plate substrate of the same base material. In order to extract the necessary features for a correct qualification of the melt pool, cross sections are polished and analyzed such that track width, dilution depth and deposited height can be measured manually. Similar research was earlier performed by [19], where a two stage machine learning approach is proposed. In first instance the usage of particle swarm optimization allows them to model the 2D geometrical shape of the melt pool based on the set laser power (P), powder mass flow (m) and scanning speed (s). In a second step the real-time melt pool geometry prediction model is used in a Self-organizing Pareto based Evolutionary Algorithm (SOPEA) in order to obtain an optimal setpoint for the LMD process, optimizing two objective functions: correct

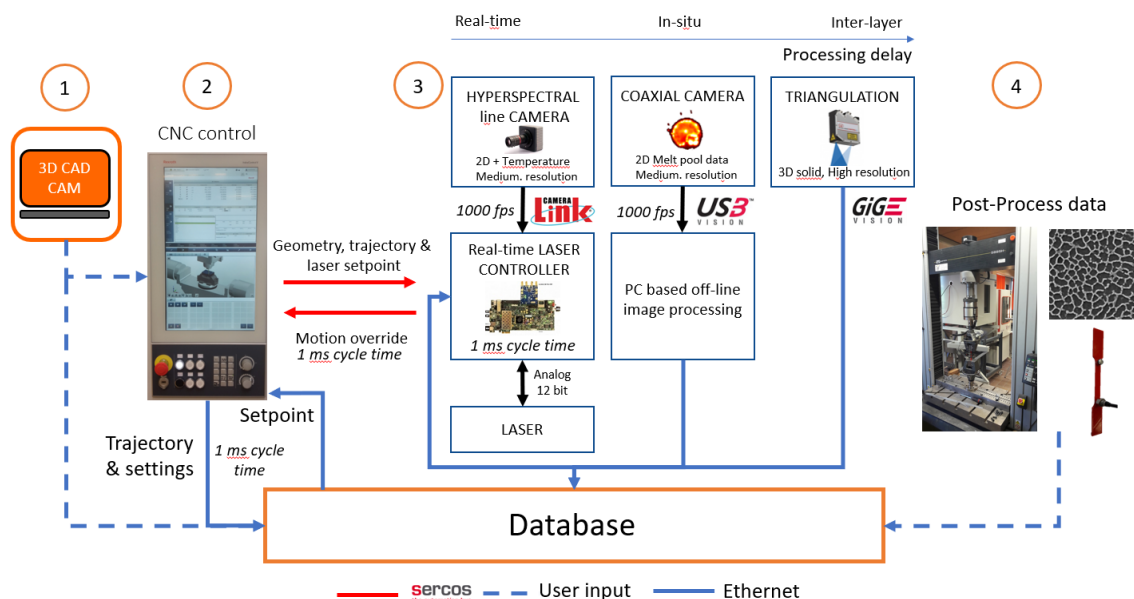


Fig. 2. MiCLAD data acquisition framework.

deposited track height and dilution depth. Due to the strong correlation but nonlinear relation between the process parameters and the desired objective functions a Pareto based Evolutionary Algorithm was found as the most efficient in their comparison.

The previously mentioned work focusses on applying machine learning algorithms to the obtained metrics (e.g. laser power, deposition height & width, ...), however, it was observed that also the extraction of these metrics from the raw sensor data or images is not so straightforward. Therefore, a second opportunity for improving data processing using machine learning algorithms during LMD arises from the processing of the raw images and sensor data to extract the desired metrics [5,20,21].

3.2. Training data collection

For the collection of training data, the MiCLAD machine was operated in open loop, without any laser feedback control. Different square cubes with a width and length of 9mm and height of 8mm (Figure 3) were built with different setpoints. The setpoints for these experiments are listed in Table 2. The toolpath used to build the cubes firstly deposits the contour, followed by a line hatch infill where parallel lines are formed and change every layer from 90° (Y axis) to 0° direction. This toolpath is illustrated by the dots in Figure 4. Transition of the dots from black to bright green illustrate the trajectory from start to finish.

Table 2. Cube printing parameters.

Powder	Carpenter Additive Gas Atomised 316L Stainless Steel LPBF
Powder size distribution	15 – 45 μm
Shielding gas	3,5 l/min Argon
Carrier gas	8 l/min Argon
Powder mass flow	4 g/min
Laser power	270 - 350 W
Scan velocity	700 - 1200 mm/min
Theoretical layer thickness	0.25 mm
Scan strategy	0° & 90° alternating every layer
Track overlap (infill & contour)	50 %

The deposition time history is visualized in Figure by the color in the square deposited area of 9 x 9 mm with the blue to red fading color scale indicating the measured height of the deposition. The additional markers with varying color from black to green visualize the toolpath used for building this particular layer in the part. During the build each layer is rotated by 90°. The intensity of these markers therefore shows the toolpath over time. From this we can see that the contour that was deposited first as the markers are all near black. Only one out of each 10 data points that were collected at a rate of 500 Hz or are shown. Notice the increased density in data points at the corners and ends of the lines due to the reduced velocity in these locations. The contour started in the left bottom corner and the infill pattern ends in the top right corner. Furthermore, Figure shows also a colormap in the background from blue to red indicating the measured deposition height obtained from a scan with the Micro-epsilon scancontrol laser

triangulation sensor after the deposition of this first layer. It becomes clearly visible from the red color that at the points of zero velocity the buildup is the highest ranging around 0.3 mm per layer, in contrast to the infill area only showing values close to 0.15 mm.

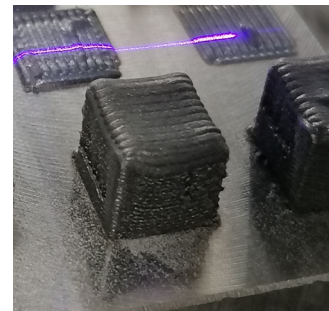


Fig. 3. Scan of the height (purple laser line) after deposition of each layer of square cubes of 9 x 9 mm deposited on the MiCLAD machine.

As both the geometry scan with the laser triangulation sensor and the deposition process use the same reference point, a trace of the deposited material height in function of time can be generated. The resulting trace of layer thickness (left axis) and path velocity (right axis) in function of the time for this

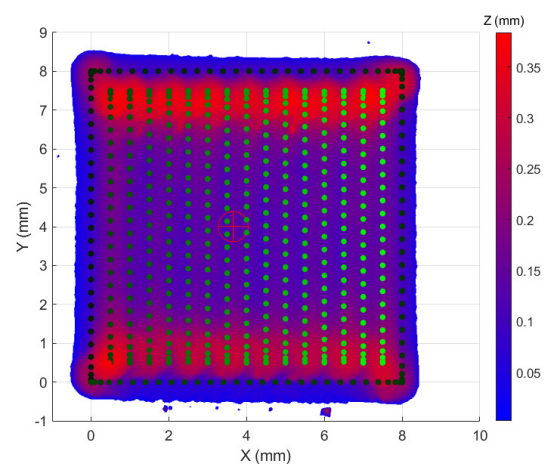


Fig. 4. Edge buildup after deposition of a first layer on a flat substrate due to start and stop of trajectory at endpoints. Colors indicate deposited material height. Dots indicate the toolpath illustrated by increasing intensity with time.

first layer deposition is shown in Figure 5. The first three seconds are recorded during deposition of the contour of the cube, the sequel during the infill of this contour. From the blue line, representing the deposition height, one can notice that the overall deposition height is lower than for the points in the infill region. This is because the infill region is deposited after the contour is deposited, hence overlap of the infill tracks with the contour exists (see Figure). Therefore, the measured deposition height at start and stop of the infill lines of the hatch is found as almost double the contour height. Secondly, it is important to notice that the layer thickness is related to the deposition velocity, as expected. Indeed, when the machine slows down and comes to a stop, the melt pool grows due to increased heat input to the part. The activation of the closed-loop control system typically has the goal to counteracts this effect of heat buildup towards an edge or a change in velocity [9]. However,

operating in open loop with a constant 300 W laser, started and stopped at the end of each track, delivers good training data for an iterative learning control approach.

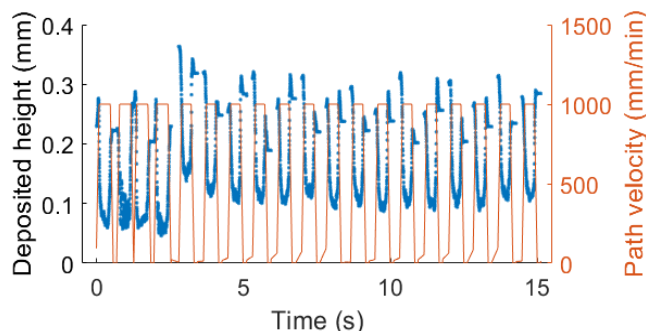


Fig. 5. Layer height (blue) and path velocity (orange) in function of time for the first layer.

One should also notice that the deposited height at the start and the end of each line trajectory is not equal. However, in terms of motion profile the acceleration and deceleration rate are the same. This behavior can be explained due to the fact that the time history of the temperature, and thus the presence of a melt pool is also an important factor. Therefore, the MiCLAD platform is built to take advantage of both real-time control, where time history is commonly not taken into account, and machine learning, where the underlying geometry (i.e. thin wall or solid block) can be taken into account for correction of the deposited geometry. A clear illustration of this time history effect during real 3D printing where motions have no infinite acceleration, is observed in the analysis of the coaxial images recorded during deposition.

Recent publications in the field of geometry control during laser metal deposition have shown that the geometrical accuracy can be greatly improved by either real-time feedback control [2,22] or inter-layer control approach [7,23]. However, those papers only discuss the layerwise height control of the geometry. No link with the actual melt-pool size and temperature can be created in the referred papers. Therefore, besides a 3D line scanner for scanning of the deposited geometry, the MiCLAD platform also captures coaxial images through the same optics as the delivery of the laser beam. These images are particularly interesting to monitor the behavior of the liquid metal in the melt pool, in comparison with the 3D scanner, that is measuring solidified geometry. In Figure four melt pool images are shown. These are average images recorded with the coaxial camera using a shutter time of 50 μ s. The color of the images was arbitrarily scaled to obtain a full 8 bit dynamic range for visualization from the original grayscale images obtained with the a-priori mentioned machine vision camera. One can clearly see the tail of the melt pool that is being generated based on the direction of the path (right-down-left-up). These images were recorded during the deposition of the second layer, being the one deposited on top of the results discussed in Figure 4 and Figure 5.

In Figure 7 some instantaneous coaxial images for the theoretical 1mm melt pool during an infill of the second layer of the cube discuss in the previous part of this paper. The first image was recorded 15 ms after the start of the laser and simultaneous start of the acceleration.

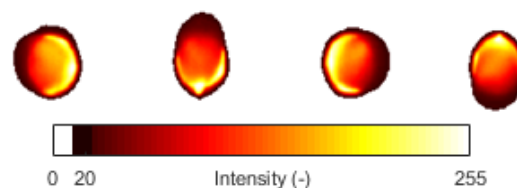


Fig. 6. Average images of coaxial observed melt pool during the four phases of scanning a rectangular contour. The colorbar indicates light intensity on the camera with an arbitrary scaling for maximum dynamic range.

Due to the zero velocity at $t = 0$ ms, and the rapid settling time of the laser power source an overheated melt pool is created, which results in a long tail that is created behind the melt pool once motion is picking up speed, as illustrated at a time step of 200 ms. The tail is clipped by the region of interest of the camera on the left side. This tail slowly decreases in length and the image at a time of 350 ms shows the typical melt pool shape at constant velocity of 1000 mm/min and laser power of 300 W. At a time of 670 ms the machine already approaches the opposite edge of the 9 mm cube and the velocity decreases while the laser is shut down in the approach of the commanded position. Therefore, one notices that the intensity of the melt pool raises slightly and becomes more uniform compared to the view at 350 ms. However, one can also notice that only 10 ms later the intensity starts to decrease and the edge around the liquid region that is the melt pool grows and dies out less than 20 ms later. In conclusion, whereas during the start of the motion an overheated melt pool is generated, which is clearly visible at a time 200 ms after the start of the motion and the laser, the dying-out of the melt pool at switch-off of the laser is almost instantaneous.

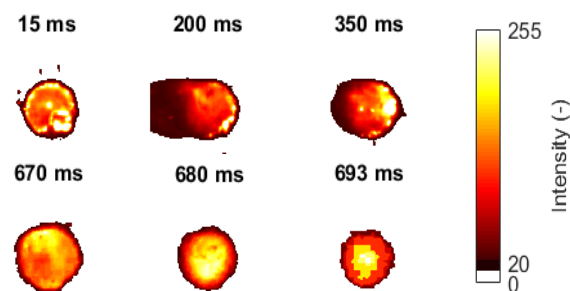


Fig. 7. Coaxial melt-pool images recorded at different time steps during a horizontal infill pattern. Theoretical melt-pool size is 1 mm.

The data collected of only one shape is insufficient to obtain enough training data for applying machine learning algorithms to be usable in practice. Therefore, now the usability of the proposed data acquisition framework is validated, the collection of training data during the deposition of all kind of geometrical shapes will continue as further work. An example of a test plate that was built using optimized printing parameters is shown in Figure 8. The total size of this test plate is 10 x 10 cm.

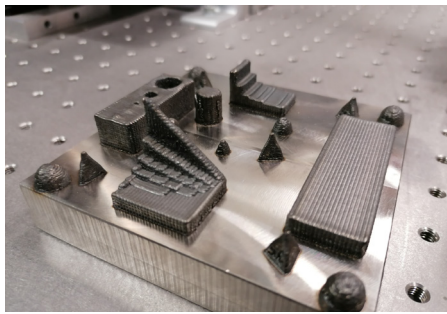


Fig. 8. Test plate built for training the machine printing parameters based on primitive geometrical shapes. Built plate measures 10 x 10 cm.

5. Conclusion

In this paper a newly build hybrid laser metal deposition & milling machine from the VUB, Brussels, Belgium was described. Not only as a machine, but also as a data platform for development of real-time monitoring and machine learning algorithms for the laser metal deposition process. For LMD in repair or additive manufacturing of 3D components both material properties as well as deposited geometry are essential. However, as many process parameters have an influence on both the deposited geometry as well as the material properties, an independent tuning of these through independent multi-input, multi-output controllers is not straightforward. Hence, a complex optimization and control problem arises when considering the correlation between the parameters. These kind of strongly problems are lending themselves ideally to machine learning based optimization.

Acknowledgements

The authors would like to acknowledge Mr. Wim Devesse and Mr. Jorge Sanchez Medina for their contributions in setting up the camera integration in the machine. As well as Mr. Jona Gladines from the University of Antwerp for delivery of the CAD geometry of the test plate. This work was financed by the Research Foundation Flanders (FWO) through project HiPAS and the Department of Economics, Innovation and Science (EWI) of the Flanders government, Belgium, through the project HyLaFORM.

References

- [1] U. de Oliveira, V. Ocelik, and J. Th. M. De Hosson, "Analysis of coaxial laser cladding processing conditions," *Surf. Coat. Technol.*, vol. 197, no. 2, pp. 127–136, Jul. 2005.
- [2] M. Asselin, E. Toyserkani, M. Irvani-Tabrizipour, and A. Khajepour, "Development of trinocular CCD-based optical detector for real-time monitoring of laser cladding," in *IEEE International Conference Mechatronics and Automation, 2005*, Jul. 2005, vol. 3, pp. 1190–1196 Vol. 3.
- [3] M. Schmidt et al., "Laser based additive manufacturing in industry and academia," *CIRP Ann.*, vol. 66, no. 2, pp. 561–583, Jan. 2017.
- [4] N. Shamsaei, A. Yadollahi, L. Bian, and S. M. Thompson, "An overview of Direct Laser Deposition for additive manufacturing; Part II: Mechanical behavior, process parameter optimization and control," *Addit. Manuf.*, vol. 8, pp. 12–35, 2015.
- [5] A. Staub, A. B. Spierings, and K. Wegener, "Correlation of melt pool characteristics and residual stresses at high laser intensity for metal lpb process," *Adv. Mater. Process. Technol.*, vol. 5, no. 1, pp. 153–161, Jan. 2019.
- [6] A. Heralić, A.-K. Christiansson, and B. Lennartson, "Height control of laser metal-wire deposition based on iterative learning control and 3D scanning," *Opt. Lasers Eng.*, vol. 50, no. 9, pp. 1230–1241, Sep. 2012.
- [7] I. Garmendia, J. Leunda, J. Pujana, and A. Lamikiz, "In-process height control during laser metal deposition based on structured light 3D scanning," *Procedia CIRP*, vol. 68, pp. 375–380, Jan. 2018.
- [8] M. Lison, W. Devesse, D. de Baere, M. Hinderdael, and P. Guillaume, "Hyperspectral and thermal temperature estimation during laser cladding," *J. Laser Appl.*, vol. 31, no. 2, p. 022313, Apr. 2019.
- [9] W. Devesse, D. De Baere, M. Hinderdael, and P. Guillaume, "Model-based temperature feedback control of laser cladding using high-resolution hyperspectral imaging," *IEEEASME Trans. Mechatron.*, vol. 22, no. 6, pp. 2714–2722, 2017.
- [10] L. Song and J. Mazumder, "Feedback Control of Melt Pool Temperature During Laser Cladding Process," *IEEE Trans. Control Syst. Technol.*, vol. 19, no. 6, pp. 1349–1356, Nov. 2011.
- [11] C. Kledwig, H. Perfahl, M. Reisacher, F. Brückner, J. Bliedtner, and C. Leyens, "Analysis of Melt Pool Characteristics and Process Parameters Using a Coaxial Monitoring System during Directed Energy Deposition in Additive Manufacturing," *Materials*, vol. 12, no. 2, p. 308, Jan. 2019.
- [12] T. Craeghs, "A Monitoring System for On-line Control of Selective Laser Melting A Monitoring System for On-line Control of Selective Laser Melting (Een monitoring systeem voor on-line controle van Selectief Laser Smelten)," PhD thesis, KULeuven - PMA, Leuven, Belgium, 2012.
- [13] E. Toyserkani, A. Khajepour, and S. Corbin, "Closed-loop control of laser cladding process by powder injection," *Int. Congr. Appl. Lasers Electro-Opt.*, vol. 2003, no. 1, p. 1310, Oct. 2003.
- [14] J. T. Hofman, B. Pathiraj, J. van Dijk, D. F. de Lange, and J. Meijer, "A camera based feedback control strategy for the laser cladding process," *J. Mater. Process. Technol.*, vol. 212, no. 11, pp. 2455–2462, Nov. 2012.
- [15] M. Irvani-Tabrizipour, M. Asselin, and E. Toyserkani, "Development of an image-based feature tracking algorithm for real-time clad height detection," *IFAC Proc. Vol.*, vol. 39, no. 16, pp. 914–920, Jan. 2006.
- [16] W. Devesse, *Development and Validation of Innovative Modeling, Monitoring and Control Strategies for 3D Metal Printing*, PhD Thesis., vol. VUB-Dept. of Mechanical Engineering. Brussels, Belgium: VUBPRESS, 2017.
- [17] W. Devesse, D. De Baere, M. Hinderdael, and P. Guillaume, "High resolution temperature estimation during laser cladding of stainless steel," *Phys. Procedia*, vol. 83, pp. 1253–1260, 2016.
- [18] F. Caiazzo and A. Caggiano, "Laser Direct Metal Deposition of 2024 Al Alloy: Trace Geometry Prediction via Machine Learning," *Materials*, vol. 11, no. 3, Mar. 2018.
- [19] A. Mozaffari, A. Fathi, A. Khajepour, and E. Toyserkani, "Optimal design of laser solid freeform fabrication system and real-time prediction of melt pool geometry using intelligent evolutionary algorithms," *Appl. Soft Comput.*, vol. 13, no. 3, pp. 1505–1519, Mar. 2013.
- [20] A. Caggiano, J. Zhang, V. Alfieri, F. Caiazzo, R. Gao, and R. Teti, "Machine learning-based image processing for on-line defect recognition in additive manufacturing," *CIRP Ann.*, vol. 68, no. 1, pp. 451–454, 2019.
- [21] M. Khanzadeh, S. Chowdhury, M. Marufuzzaman, M. A. Tschoop, and L. Bian, "Porosity prediction: Supervised-learning of the thermal history for direct laser deposition," *J. Manuf. Syst.*, vol. 47, pp. 69–82, 2018.
- [22] S. Donadello, M. Motta, A. G. Demir, and B. Previtali, "Monitoring of laser metal deposition height by means of coaxial laser triangulation," *Opt. Lasers Eng.*, vol. 112, pp. 136–144, Jan. 2019.
- [23] I. Garmendia, J. Pujana, A. Lamikiz, M. Madarieta, and J. Leunda, "Structured light-based height control for laser metal deposition," *J. Manuf. Process.*, vol. 42, pp. 20–27, Jun. 2019.

11th CIRP Conference on Photonic Technologies [LANE 2020] on September 7-10, 2020

Comparison of visual and hyperspectral monitoring of the melt pool during Laser Metal Deposition

Jorge Sanchez Medina^{a,*}, Wim Devesse^a, Julien Ertveldt^a, Patrick Guillaume^a

^aVrije Universiteit Brussel, Acoustics and Vibration Research Group, Pleinlaan 2, Brussels-1050 Brussels, Belgium

* Corresponding author. Tel.: +32-(0)26-292-324. E-mail address: jorge.sanchez.medina@vub.be

Abstract

In the field of additive manufacturing the implementation of real time process monitoring is required to enhance the quality and repeatability of the printed parts. Laser metal deposition (LMD) is a technique where the deposition of material is done in a melt pool created by a high-power laser beam. This paper presents the geometrical properties of such melt pool obtained during blown powder LMD. For achieving these results, the visual and hyperspectral information of the melt pool is used. An analytical model of the melt pool boundary is fitted to high-speed visual images recorded during 3D deposition. At the same time the hyperspectral information provides a way to estimate the temperature and emissivity profiles within the melt pool. The proposed paper discusses the correlation of the hyperspectral and visual high-speed camera results.

© 2020 The Authors. Published by Elsevier B.V.

This is an open access article under the CC BY-NC-ND license (<http://creativecommons.org/licenses/by-nc-nd/4.0/>)

Peer-review under responsibility of the Bayerisches Laserzentrum GmbH

Keywords: “Image processing; Metal Deposition; Melt pool; 3D printing; Hyperspectral imaging”

1. Introduction

1.1. LMD and melt pool geometry

Laser Metal Deposition (LMD) is a technology that has several diverse applications such as coating metallic surfaces principally for erosion or corrosion mitigation, part repair or rapid prototyping [1]. LMD is an additive production process in which a laser beam forms a melt pool on the surface of a metallic substrate, into which metal powder is injected.

The result of the building process in terms of material and geometrical properties of the part are strongly dependent of many of the process parameters. Therefore, the use of a closed-loop control system is strongly suggested to improve the part quality [2].

In this paper two methods for the measurement of the melt pool as an essential step in the closed-loop control of the melt pool are compared and discussed. The aim of both methods is

to collect information about the geometrical characteristics and estimate the size of the melt pool.

The first method uses visual 2D images to fit an analytical model able to define the geometric parameters that represent the melt pool perimeter.

The second method uses hyperspectral measurements to estimate the temperature and emissivity inside the melt pool. Through the temperature and emissivity profiles information about the melt pool boundaries can be obtained and three regions can be identified: liquid, mushy and solid region [3].

Both methods provide absolute values of the melt pool size, but the goal of this paper is the comparison between these methods and observe possible relations with each other.

1.2. Visual method

The visual method is based on image segmentation or region extraction. Image segmentation is an operation that gives

information about the objects in an image. By using a visual high-speed camera, the result of segmentation on an acquired visual image is a contour with the points of the boundary of the melt pool. After segmentation geometric primitives can be fit to the obtained contour data from the first step, defining consequently the geometric parameters of the melt pool.

1.3. Hyperspectral method

Traditional contactless temperature monitoring uses multi-wavelength pyrometers and infrared thermographic cameras [4] where the temperature is estimated from the object's emitted light, assuming it is a gray body object. This assumption can result in a source of errors because the emissivity is an unknown function of wavelength, temperature, material composition and different material properties [5].

An alternative to the conventional devices is the use of a hyperspectral camera for monitoring the temperature. Measurements at many wavelengths are taken from the emitted spectral radiance of several closely spaced points, thereby increasing the signal-to-noise ratio compared to pyrometry methods that use only a small number of wavelengths. An absolute temperature is deduced from these spectral radiance measurements using a least squares curve fitting procedure. The hyperspectral method is still approximative, but by using more wavelengths a better result can be obtained. This method allows the calculation of an upper and lower temperature bound without knowing the exact emissivity values or their variation with wavelength, being able to consistently determine the absolute temperature in the liquid region of a melt pool with an uncertainty of about 10% [3].

2. Experimental environment

2.1. Experimental setup

On the surface of a 20 mm thick substrate of AISI 316L stainless steel is focused a SPI redPOWER® QUBE 2kW fiber laser with a center wavelength of 1064 nm, a focus spot diameter of 1000 μm and a flat-top beam profile. The incident laser beam heats the surface and creates a melt pool whose size depends on the laser power.

During the experiments a coaxial flow of argon is directed towards the substrate with the addition of metal powder. The powder that is used is of the type LPW 316L 44-106 μm and it is delivered to a Fraunhofer ILT COAX-40-S nozzle by a Medicoat CH-5506 powder feeder.

The melt pool is monitored with two different devices. The first one is a hyperspectral line camera with a pixel pitch of 5.5 μm resulting in a spatial resolution of 17.4 $\mu\text{m}/\text{pixel}$ in the object plane and high quantum efficiency in the visible and near-infrared (VNIR) spectrum from 400 nm to 1000 nm. An absolute calibration of the camera was performed by measuring the spectrum of an Optronic Laboratories OL455 integrating sphere calibration source with a halogen lamp. The same spectrum was then measured with a NIST traceable JETI Specbos 1211 spectroradiometer. The ratio between these two spectra provides the optical sensitivity of the hyperspectral camera.

The second monitoring device is a monochrome visual camera with a Sony IMX287 CMOS sensor, a pixel pitch of 6.9 μm resulting in a spatial resolution of 14 $\mu\text{m}/\text{pixel}$ in the object plane and high spectral sensitivity in the VNIR region from 400 nm to 1000 nm.

Optical filters were added on both cameras. A notch filter with center wavelength of 1064 nm for the hyperspectral camera and a KG-3 heat absorbing IR glass for the visual camera.

The mounting of both devices in the system entailed the coaxial positioning of the visual camera, while the hyperspectral camera was inclined at an angle of 38 degrees relative to the surface normal.

Both cameras were connected to respective frame grabbers, via USB 3.0 in case of the visual camera and via a CameraLink interface for the hyperspectral camera.

2.2. Experimental conditions

Tracks of length 30 mm were printed at a constant speed of 1200 mm/min using four different power values: 280W, 320W, 360W and 400W.

The injected metal power was fed to the melt pool at a mass flow rate of 3 g/min.

Regarding camera settings, the images were acquired with an exposure time of 100 μs and a window size of 260x260 pixels for the visual camera and 78 μs and 512x256 pixels for the hyperspectral camera.

The frame acquisition in both cameras was hardware synchronized. The frames were taken at a frame rate of 1000 fps and triggered by a pulse wave with the help of a signal generator. The used pulse width was 200 μs .

3. Segmentation and geometric fitting of visual images

The processing of the coaxial images collected with the visual camera consists of three steps. Firstly, segmentation of the images is carried out as a pre-processing step by converting the grayscale image into a binary image. The application of a binary threshold segments the image into the desired melt pool and the background. Due to the images presenting different gray value distributions, the use of a constant threshold is not possible, and a method is required that is able to determine the threshold level automatically. The statistical-based Otsu thresholding algorithm [6] showed good results in this regard and it was selected as a first step for segmenting the images.

The previously described image binarization step returns roughly the melt pool domain in the image, but the focus of interest is the border of the melt pool since it provides information of the geometrical properties of the clad. Therefore, in a second step, the Suzuki's contour tracing algorithm is employed [7] to find and extract the boundary points of the perimeter of the melt pool. Using this contour data, in a third step, an ellipse geometric primitive is fitted, defining therefore the size of the melt pool in terms of length and width or the major and minor axis of the fitted ellipse respectively.

The ellipse fitting principle consists of representing a general conic by an implicit second order polynomial equation:

$$F(\mathbf{a}; \mathbf{x}) = \mathbf{a} \cdot \mathbf{x} = ax^2 + bxy + cy^2 + dx + ey + f = 0 \quad (1)$$

where $\mathbf{a} = [a \ b \ c \ d \ e \ f]^T$ and $\mathbf{x} = [x^2 \ xy \ y^2 \ x \ y \ 1]^T$, and provided $b^2 - 4ac < 0$ to represent an ellipse, because the equation can also describe hyperbolas and parabolas. The point coordinates are substituted in the previous implicit equation to get a distance measure for the points $\mathbf{x}_i = (x_i, y_i)$ to the ellipse $F(\mathbf{a}; \mathbf{x}) = 0$. This distance is called the algebraic distance $F(\mathbf{a}; \mathbf{x}_i)$.

The ellipse is fitted using the method proposed by Fitzgibbon [8], where the fitting is approached as a least squares problem, by minimizing with a linear method the algebraic error or sum of squared algebraic distances:

$$D_A(\mathbf{a}) = \sum_{i=1}^N F(\mathbf{x}_i)^2 \quad (2)$$

4. Temperature and emissivity from hyperspectral images

According to Planck's law, the spectral radiance B ($W \cdot sr^{-1} \cdot m^{-3}$) emitted by a black body is a function of the wavelength λ and temperature T , but ideal black bodies do not exist. The emitted spectral radiance E_i of a real body measured at wavelength λ_i ($i = 1, \dots, N_\lambda$) is the result of modifying the black body equation B by a spectral emissivity parameter ε_λ that takes values between 0 and 1 and includes some measurement noise n_i :

$$E_i = \varepsilon_\lambda(\lambda_i)B(\lambda_i, T) + n_i \quad (3)$$

For metals the spectral emissivity ε_λ is a linearly decreasing function of wavelength in the VNIR range [9]:

$$\varepsilon_\lambda(\lambda) = B_\varepsilon - A_\varepsilon \frac{\lambda - \lambda_1}{\lambda_{N_\lambda} - \lambda_1} \quad (4)$$

where the constants A_ε and B_ε are constrained by $0 \leq A < B \leq 1$ to have a negative slope and $0 < \varepsilon_\lambda \leq 1$.

Assuming that the noise n_i is zero-mean and Gaussian with known variance $\sigma_{E_i}^2$, fitting the measured spectrum $E_i(\lambda_i, T)$ to a black body model $B(\lambda_i, T)$ with a linearly decreasing spectral emissivity ε_λ is a matter of solving the following least squares problem:

$$(\hat{\mathbf{A}}_\varepsilon, \hat{\mathbf{B}}_\varepsilon, \hat{\mathbf{T}}) = \arg \min \sum_{i=1}^{N_\lambda} \frac{\left| E_i - \left(B_\varepsilon - A_\varepsilon \frac{\lambda_i - \lambda_1}{\lambda_{N_\lambda} - \lambda_1} \right) B(\lambda_i, T) \right|^2}{\sigma_{E_i}^2} \quad (5)$$

The minimizing solution to this problem is obtained by either setting the value of the slope A_ε to zero, i.e. using a gray body assumption, or leaving the slope A_ε free and setting the offset B_ε to 1. This allows us to calculate the upper and lower bounds of the melt pool temperature and emissivity.

5. Results and discussion

The estimated temperature and emissivity profiles from the

hyperspectral measurements provide information of the melt pool boundary because three regions can be identified: liquid, mushy and solid region.

The hyperspectral measurements were made perpendicular to and along the direction of movement of the workpiece during a laser cladding process in order to study the width and the length of the melt pool. These geometrical dimensions are correlated with the visual measurements.

During the fitting of ellipses the image binarization becomes a very important step, the selected Otsu's threshold [6] is based on intensity information captured by the visual camera and is calculated to minimize the spread of the pixels that fall in the foreground or background or in other words it minimizes the within-class variance σ_W^2 :

$$\sigma_W^2 = W_b \sigma_b^2 + W_f \sigma_f^2 \quad (6)$$

with σ_b^2 and σ_f^2 the background and foreground variance multiplied by their associated weights W_b and W_f .

The distinction of the mushy region of the melt pool with this intensity variance based method is complicated, because for example low level intensity pixels could be considered as background and not taken into account in the ellipse fitting.

The binarization topic will be explored by using different threshold levels that are multiples of Otsu's threshold. The multiplication factors are: 2, 1.5, 1, 0.5, 0.25 and 0.125. This set of thresholds will be compared with the temperature and emissivity profiles to find possible relationships in the observed melt pool sizes.

The measurements that will be presented in the following subsections are time averaged profiles of the middle part of the printing process of the tracks corresponding to a period of approximately 1.1 seconds. Each time averaged profile represents the result of a specific power setting as explained in subsection 2.2.

5.1. Melt pool width

The analysis of the melt pool width involves the examination of the hyperspectral measurements that were made perpendicular to the Y direction movement of the workpiece according to Figure 1.

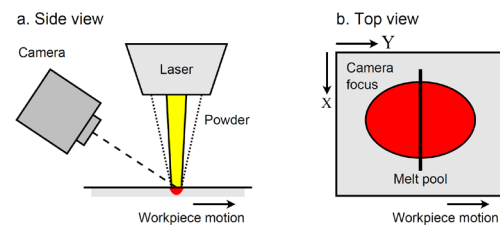


Fig. 1. Side view (a) and top view (b) of the transverse laser cladding

Figure 2 shows the time averaged temperature profile during irradiation with a constant laser power of 320W and Figure 3 shows the standard deviation of the temperature during this time average. It is visible in the temperature figure that the liquid region extends from $x = -200 \mu\text{m}$ to $x = 300 \mu\text{m}$ and that the temperature deviation in Figure 3 in this range is relatively low, about 50 K. In the liquid region can be observed that the temperature is relatively flat, this is due to the powder flow mixing with the molten metal in the pool. Despite this

observation, the temperature is highest at the center of the melt pool and gradually decreases towards the edges, as expected. In Figure 2, to the left and right of the liquid region two peaks can be observed at $x = -325 \mu\text{m}$ and $x = 400 \mu\text{m}$: the temperature is expected to decrease but instead a rise is observed. This is due the spectra in this region that can not be fitted to the model of Equation 3. Even though the temperature value can not be determined, the provided information is useful to identify the spatial boundaries of the mushy region [10].

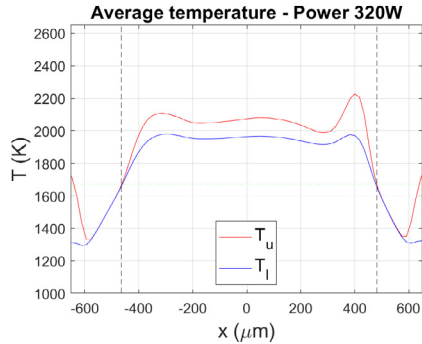


Fig. 2. Transverse temperature profile for 320W. The red and blue curves correspond to the upper and lower temperature bounds. The dashed vertical lines indicate the melt pool width. The dashed horizontal line indicates the melting point of AISI 316 stainless steel at 1670K [11].

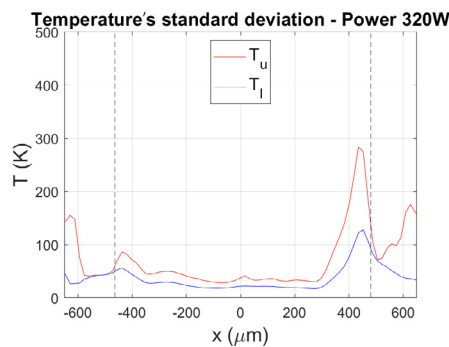


Fig. 3. Standard deviation of the transverse temperature profile for 320W. The red curve corresponds to the upper temperature bound and the blue curve to the lower bound. The dashed vertical lines indicate the melt pool width.

Looking at the emissivity profile of Figure 4 two large emissivity peaks are visible near $|x| = 525 \mu\text{m}$. These high values can be attributed to the large amount of oxidation that is present in the solid region and is visible on the surface of the building plate surrounding the track [3]. Inspecting again Figure 2 there are two positions marked with dashed vertical lines: at these points the upper temperature bound T_u crosses the dashed horizontal line that indicates the melting point of AISI 316 stainless steel, which is approximately 1670K [11].

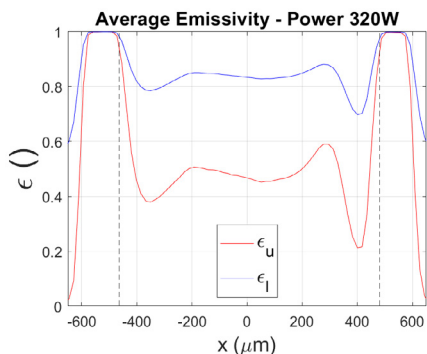


Fig. 4. Transverse emissivity profile for 320W. The red and blue curves correspond to the upper and lower temperature bounds. The dashed vertical lines indicate the melt pool width.

Summarizing the information from Figures 2, 3 and 4, it can be estimated that the liquid region of the melt pool comprises approximately $|x| = 250 \mu\text{m}$, and from $|x| = 250 \mu\text{m}$ to the dashed vertical lines the mushy region and the start of oxidation in the solid region. The estimated temperature values are only reliable in the liquid region and present also small temperature deviations. The distance between the dashed vertical lines will be called the hyperspectral width in our comparisons later in Table 1.

Figure 5 shows the temperature estimation for a laser power of 400W. The difference between this temperature profile and the 320W profile is a slight increase of the temperature of about 50K. Like the previous case, the same conclusions can be drawn regarding the boundary limits for the liquid region and the mushy and oxidized solid regions.

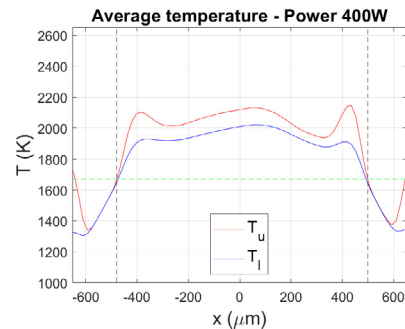


Fig. 5. Transverse temperature profile for 400W. The red and blue curves correspond to the upper and lower temperature bounds. The dashed vertical lines indicate the melt pool width. The dashed horizontal line indicates the melting point of AISI 316 stainless steel at 1670K [11].

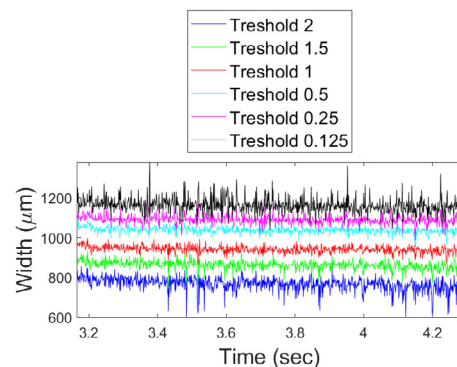


Fig. 6. Different binarization levels for the 320W experiment

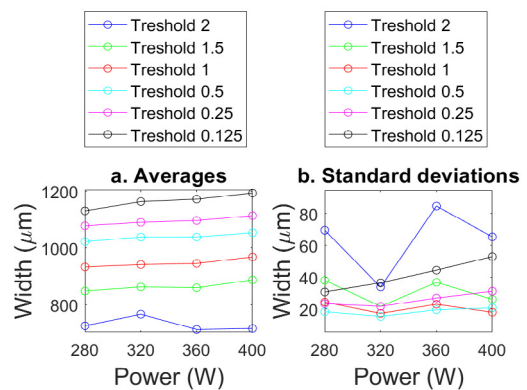


Fig. 7. Averages (a) and standard deviations (b) of the calculated widths by ellipse fitting for each laser power setting

Unlike the results obtained with the hyperspectral camera, the visual measurements get an absolute value of the size of the melt pool without distinction between the liquid, the mushy and the solid regions. Performing a study with different binarization levels that are multiples of Otsu's threshold, the outcome for the 320W experiment is presented in Figure 6. Each binarization threshold shows a constant average value with higher deviations for factors 2 and 0.125. The lower the factor is, the higher is the calculated width.

A thorough investigation by calculating the average and standard deviation for each threshold level for all the different laser power cases results in Figure 7.

Comparing the average width curves with the hyperspectral results:

Table 1. Comparison of the calculated width between the hyperspectral and the visual method

Power (W)	Hyperspectral Width (μm)	Visual Width for Threshold 1 (μm)	Visual Width for Threshold 0.5 (μm)
280	901.97	933.2	1023
320	945.11	941.5	1038
360	958.11	945.5	1038
400	972.27	968.18	1054

where according to Figure 8.b and taking into account the worst case deviation, the width values for the factors 1 and 0.5 are $\pm 20 \mu\text{m}$.

The results from Table 1 show that changes in the average laser power yield small changes of the melt pool width. An increase of the laser power from 280W to 400W produces an enlargement of about $70 \mu\text{m}$. This can be explained by the fact that most of the additional heat goes down into the work piece vertically [12].

Focusing on the results of the visual method, from Table 1 it can be noticed that the best threshold factor is 1, but calculating the exact threshold required to obtain the best correspondance, it turns out that the average threshold factor is 1.0313 with a standard deviation of 0.1083. It's observed then that the width of a fitted ellipse with a binarization level factor 1.0313 of Otsu's threshold matches with the hyperspectral width, which covers the liquid and mushy regions and oxidation start of the melt pool.

5.2. Melt pool length

The analysis of the melt pool length involves the examination of the hyperspectral measurements that were made along the X direction movement of the workpiece according to figure 8.

The longitudinal average temperature and emissivity measurements for the 320W experiment are presented in Figures 9 and 10. The front of the melt pool is situated on the negative x axis and the tail on the positive x axis. As previously during the analysis of the width of the melt pool the following key points are identified: high emissivity peaks due to oxidation and the upper temperature bound crossing the melting point line around $x = -400 \mu\text{m}$ and $x = 730 \mu\text{m}$, and a small peak or bump in the temperature at $x = 350 \mu\text{m}$ indicating the mushy region. The distance between the dashed vertical

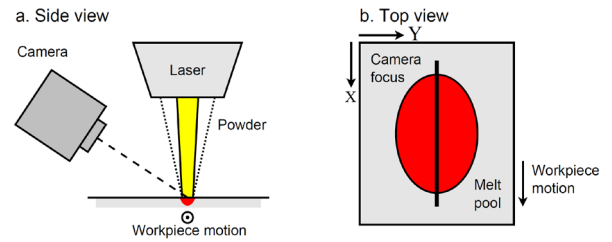


Fig. 8. Side view (a) and top view (b) of the longitudinal laser cladding

lines will be called the hyperspectral length in our comparisons later in Table 2.

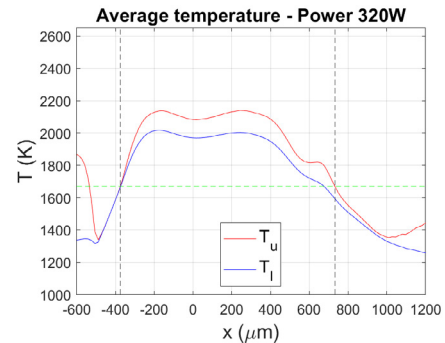


Fig. 9. Longitudinal temperature profile for 320W. The red and blue curves correspond to the upper and lower temperature bounds. The dashed vertical lines indicate the melt pool length. The dashed horizontal line indicates the melting point of AISI 316 stainless steel at 1670K [11].

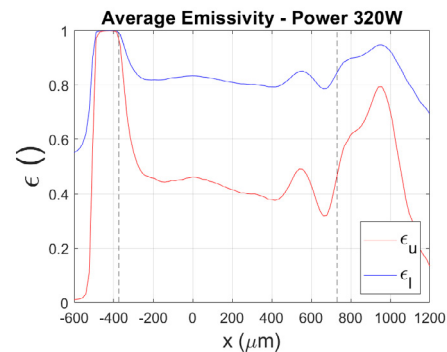


Fig. 10. Longitudinal emissivity profile for 320W. The red and blue curves correspond to the upper and lower temperature bounds. The dashed vertical lines indicate the melt pool length.

Examining all the remaining laser power cases the difference between them is the obtained length and the temperature peak value at $x = 350 \mu\text{m}$, see Figure 11 for the 400W case.

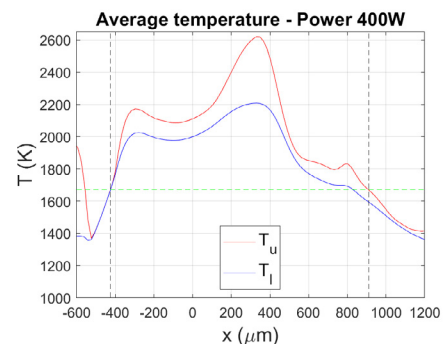


Fig. 11. Longitudinal temperature profile for 400W. The red and blue curves correspond to the upper and lower temperature bounds. The dashed vertical lines indicate the melt pool length.

The dashed horizontal line indicates the melting point of AISI 316 stainless steel at 1670K [11].

Regarding the visual method, like the width analysis the same set of different Otsu’s threshold factors was applied. The obtained average lengths and deviations for the different laser powers can be seen in Figure 12.

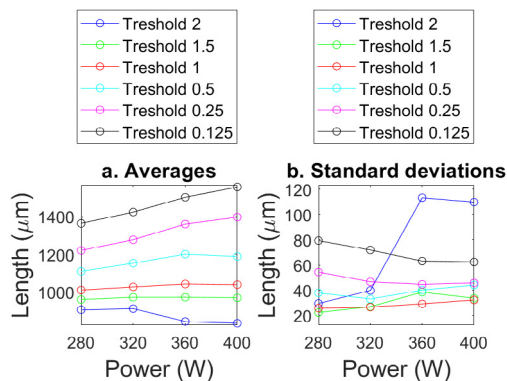


Fig. 12. Averages (a) and standard deviations (b) of the calculated lengths by ellipse fitting for each laser power setting

Comparing these results with the hyperspectral lengths:

Table 2. Comparison of the calculated length between the hyperspectral and the visual method

Power (W)	Hyperspectral Length (μm)	Visual Length for Threshold 0.5 (μm)	Visual Length for Threshold 0.25 (μm)
280	944.37	1110	1221
320	1106.79	1153	1277
360	1228.35	1201	1360
400	1334.34	1188	1396

From Table 2 the following interesting observation can be made: for the higher laser power conditions, 360W and 400W, a threshold factor between 0.5 and 0.25 seems a good fit, whereas for the lower laser power settings, 280W and 320W, a threshold factor higher than 0.5 is required. After this first observation the correct thresholds values were calculated for each laser power. The outcome of this closer examination is presented in Table 3.

Table 3. Correct threshold factor for each laser power

Power (W)	Hyperspectral Length (μm)	Threshold Factor	Visual Length (μm)
280	944.37	1.6875	941.33
320	1106.79	0.6875	1109.6
360	1228.35	0.4375	1238.7
400	1334.34	0.3125	1343.8

The results in Table 3 show that the threshold factor for the calculation of the length is laser power dependent.

6. Conclusions

This paper presented the comparison between two camera-based methods, one of them visual, and the other one hyperspectral, in order to get the geometrical information of the melt pool. The visual method is based on the intensity values

captured by the camera and fits an ellipse as an approach to measure the width and length of the melt pool. The hyperspectral method uses a VNIR line camera for measuring the spectrum from which temperature and emissivity information can be obtained and used for getting a size estimate of the different regions the melt pool is composed of: liquid, mushy and solid. Each of the methods alone provides an absolute value, but through their comparison interesting results can be observed.

One of the steps of the visual method is the image binarization, which plays an important role on what information the ellipse will be fitted to. For the binarization different levels that are multiples of the Otsu’s threshold are used with the goal to understand the relationship between the visual intensity values and the hyperspectral values.

The comparison between these methods leads to that there is not a single threshold value that can be used to identify the melt pool size at different laser power levels. The calculation of the width and length require different thresholds, but regarding only the width a single threshold value is enough unlike the length, where the threshold is laser power dependent. A possible solution in determining the size of the melt pool from visual images would be in fitting two ellipses, the first one with a fixed factor of Otsu’s threshold for calculating the width, and the second ellipse with a variable factor that depends on the used laser power for calculating the length.

Further work should explore the metallographic properties. Cuts are to be performed in order to validate the presented results and investigate the microstructure and material properties.

This paper shows a better understanding of the geometry of the melt pool and the relation between the visual intensity and the temperature and emissivity.

References

- [1] Toyserkani E, Khajepour A, Corbin S. Laser Cladding, Boca Ratin, USA, CRC Press; 2005, pp. 1-10.
- [2] Vidal F, Mato JL, Montealegre MÁ, Colodrón P, Fariña J, Rodriguez-Andina JJ. Improvements in laser cladding process through an FPGA-based control system. 30th International Congress on Applications of Lasers and Electro-Optics, ICALEO 2011; April 2017, 205–210.
- [3] Devesse W, De Baere D, Guillaume P. High resolution temperature measurement of liquid stainless steel using hyperspectral imaging, Sensors 17(1), 91; 2017
- [4] Duvaut Th. Comparison between multiwavelength infrared and visible pyrometry: Applications to metals, Infrared Physics & Technology 51, 292-299; 2008
- [5] Doubenskaia M, Pavlov M, Grigoriev S, Smurov I. Definition of brightness temperature and restoration of true temperature in laser cladding using infrared camera, Surface Coating Technology 220, 244-247; 2013.
- [6] Otsu N, "Threshold selection method from gray-level histograms," IEEE Transactions on Systems, Man and Cybernetics, vol. 9, pp. 62-66; 1979.
- [7] Suzuki S, Abe K, Topological Structural Analysis of Digitized Binary Images by Border Following. CVGIP 30 1, pp 32-46; 1985
- [8] Fitzgibbon A, Pilu M, Fisher RB. "Direct least square fitting of ellipses". IEEE Transactions on Pattern Analysis and Machine Intelligence: 1999; 21(5):476-480
- [9] Hagen E, Rubens H. Über Beziehungen des Reflexions - und Emissionsvermögens der Metalle zu ihrem elektrischen Leitvermögen. Annalen der Physik 316(8), 873-901; 1903.
- [10] Devesse W, De Baere D, Hinderdael M, Guillaume P. High resolution temperature estimation during laser cladding of stainless steel. Physics Procedia, 83, 1253–1260; 2016.
- [11] Davis JR. Metals Handbook Desk Edition, 2nd ed.; ASM International: Materials Park, OH, USA; 1998

- [12] Han L, Liou FW, Musti S. Thermal behavior and Geometry model of melt pool in laser material process. *Journal of Heat Transfer*, 127(9); 2005

11th CIRP Conference on Photonic Technologies [LANE 2020] on September 7-10, 2020

Image-based roughness estimation of laser cut edges with a convolutional neural network

Leonie Tatzel^{a,b,*}, Fernando Puente León^a

^aKarlsruhe Institute of Technology: Institute of Industrial Information Technology, Hertzstr. 16, Bldg. 06.35, 76187 Karlsruhe, Germany

^bTRUMPF Werkzeugmaschinen GmbH + Co. KG, Johann-Maus-Str. 2, 71254 Ditzingen, Germany

* Corresponding author. Tel.: +49 7156 303-33775. E-mail address: Leonie.Tatzel@kit.edu

Abstract

Laser cutting of metals is a complex process with many influencing factors. As some of them are subject to change, the cut quality needs to be checked regularly. This paper aims to estimate the roughness of cut edges based on RGB images instead of surface topography measurements.

We trained a convolutional neural network (CNN) on a broad database of images and corresponding roughness values. The CNN estimates the roughness well with a mean error of 3.6 μm . Sometimes it is more reliable than the surface measuring device because the RGB images are less prone to reflectivity problems than the measurements.

© 2020 The Authors. Published by Elsevier B.V.

This is an open access article under the CC BY-NC-ND license (<http://creativecommons.org/licenses/by-nc-nd/4.0/>)

Peer-review under responsibility of the Bayerisches Laserzentrum GmbH

Keywords: laser cutting; cut edge quality; roughness, convolutional neural network

1. Introduction

Laser cutting is a complex process that depends on numerous parameters: properties of the laser beam (e.g. focus position), transport properties (e.g. feed rate), properties of the assist gas (e.g. gas pressure) and material properties (e.g. quality of the sheet) [1]. Even the change of a single parameter can cause a deterioration of the process quality, which therefore needs to be closely monitored. Despite decades of industrial application laser cutting is still the subject of current research. Arntz-Schroeder and Petring [2] and Pocorni et al. [3] recently presented analyses of the melt flow dynamics at the cut front. These dynamics influence the roughness of the resulting cut edge.

According to the ISO standard 9013 [4] roughness (R_z) and perpendicularity tolerance (u) define the quality of a thermal cut. Both are derived from the height profile of the cut edge. Consequently, a surface measuring device is required to determine them. This is usually not available in production.

Instead, the machine operator carries out the quality inspection manually by simply looking at the edge. This method is subjective and difficult to automate. It would be better to complement or replace this procedure with an objective quality assessment.

This paper presents a contact-less approach to deduce the roughness of a cut edge from an RGB image (image with three additive colour channels, R: red, G: green, B: blue) without a measuring device. For this purpose, we generated a broad database containing cut edges of very different qualities: for each edge an RGB image was taken and R_z was determined. This data was used to train a convolutional neural network (CNN). In section 4 we evaluate the performance of the model in detail. The CNN sometimes estimates the roughness better than the actual measurement because the RGB images are less prone to reflectivity problems than the surface topographies.

Sun et al. [5] describe a CNN-based approach to evaluate the surface of milled metals. On milled surfaces grooves are clearly visible and can be easily identified. This is not the case

for parts produced with a laser. Stahl and Jauch [6] present a CNN to estimate the roughness of a cut edge. They used R_a instead of R_z to describe the roughness and they labelled each edge with the mean value of all measuring lines. The average roughness, however, says little about the maximum roughness, which can occur very locally. Since they did not ensure that the images of one edge (that look very similar and have the same label) are either in the training or in the test split, they might overestimate the performance of the model.

2. Database

2.1. Generating edges of very different qualities

The database consists of 3336 stainless steel (1.4301) cut edges. All of them are 3 mm thick and were cut on a state-of-the-art laser cutting machine (TruLaser 5030 fiber with TruDisk 12001). To generate different cut edges four dominant process parameters were varied: the distance between the nozzle and the focus of the laser beam (-3.5 to -0.5 mm), the distance between the nozzle and the sheet metal (0.5 to 3 mm), the feed rate (13 to 29 m/min) and the pressure of the assist gas (9 to 21 bar). The fully factorial combination resulted in 1050 different parameter combinations and (less the miscuts) in 834 unique samples. Each sample is a square with a side length of 10 cm. In the following only the middle 5 cm of each edge were considered as the process parameters are constant only there.

2.2. Roughness measurement

The roughness was determined with an optical measurement system (3D profilometer VR-3200, Keyence Corporation) using light section. Light section is based on triangulation [7]. A thin line is projected onto the object to be measured and the projection is observed by a camera. Displacements of the line can be converted into 3D point clouds. The accuracy of the height measurement is ± 3 μm .

The mean height of the profile R_z (here: roughness) indicates the absolute vertical distance between the highest profile peak and the deepest profile valley along the sampling length. Due to the dependency on the extreme values of the profile R_z is strongly influenced by local outliers.

The roughness values were calculated as follows: the 5 cm of the edge were divided into five areas of 10 mm length. In each area nine measurement lines were placed at different depths of the sheet with 0.3 mm spacing. This is shown in Fig. 1.

The lines are named after their distance (in mm) from the upper edge. For each of the measurement lines, the roughness was determined following the ISO standard [4] (with one minor change: we applied a fixed cut-off wavelength of 2.5 mm).

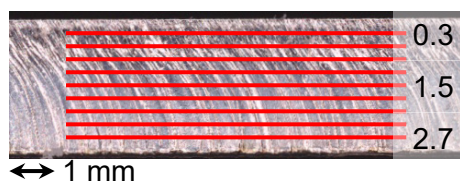


Fig. 1. RGB image of 10 mm (one area) of a laser cut edge with roughness measurement lines at different depths of the sheet.

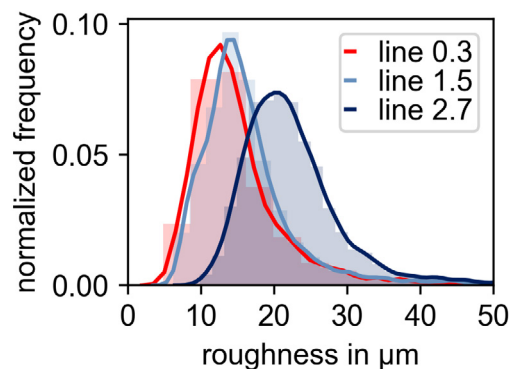


Fig. 2. Distribution of the roughness values for the lines 0.3, 1.5 and 2.7. The x-axis was limited to 50 μm . Less than 2% of the edges have higher roughness values.

The R_z values of the five areas were then averaged. This resulted in nine regression targets (labels) for each edge: one value for line 0.3, one value for line 0.6, etc.

In Fig. 2 the roughness histograms of line 0.3, 1.5 and 2.7 are shown. The corresponding expected values are 15.8 , 17.0 and 22.6 μm and the standard deviations are 10.4 , 9.1 and 7.3 μm respectively.

According to the ISO standard [4] roughness and perpendicularity tolerance define the quality of a laser cut edge. The perpendicularity could probably be estimated analogously to the presented approach, though images taken from a different perspective would be needed.

2.3. RGB images of the cut edges

The measurement device was also used to take the RGB images. It is equipped with a double telecentric lens, a monochromatic CMOS Sensor and red, green and blue LEDs. The raw images have a size of about 3400×530 pixels and a resolution of 15 $\mu\text{m} \times 15$ μm per pixel.

3. Model and methods

3.1. Convolutional neural networks

Convolutional neural networks (CNNs) are artificial neural networks that are mainly used in the field of computer vision. They are designed to extract local (image) features invariant to their location by using shared parameters and local receptive fields. Shared parameters lead to a reduced total number of parameters, which allows to increase the number of layers compared to a neural network with full connectivity [8].

The core building block of a CNN is the convolutional layer. Each of these layers applies $K \in \mathbb{N}$ different filter kernels resulting in K feature maps. Most modern CNNs (e.g. ResNet [9]) reduce the spatial size of the layers and increase the depth dimension (number of kernels) of the feature maps.

The architecture of the CNN used in this paper is shown in Fig. 3 and explained in more detail in Table 1. It was inspired by the VGG16 network [10], but with only $1,974,441$ trainable parameters it is significantly smaller.

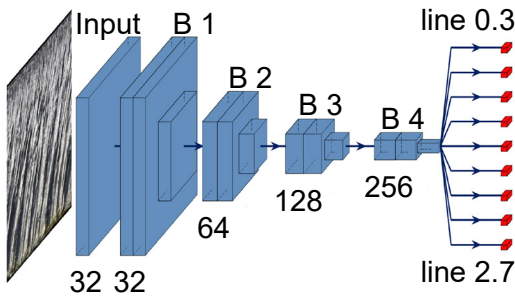


Fig. 3. CNN architecture: one input layer and four blocks (B 1, B 2, B 3 and B 4) each containing three convolutional layers. Input: square image of the cut edge. Output: nine Rz values, one for each measurement line.

The CNN consists of 13 convolutional layers, which are organized in blocks. The input block contains one convolutional layer, the subsequent four blocks contain three convolutional layers each, where the last layer of the block serves as spatial downsampling operation (convolution with stride 2, [11]). The number of filters increases from 32 to 256 while the dimension decreases from 112 x 112 to 7 x 7 pixels. Each convolutional layer uses a kernel size of 3 x 3 pixels (except for the input block which applies 7 x 7 kernels). After each convolutional layer batch normalization is performed [12] and the ReLu activation function [13] is applied. To connect the last block with the nine regression targets, we use global average pooling (GAP) [14] in combination with one dense layer.

Table 1. CNN architecture: The model consists of an input block and four subsequent blocks each containing three convolutional layers; the regression targets are connected with global average pooling and one dense layer.

layer	number of kernels	output spatial resolution
input block, conv 1	32	112 x 112
block 1, conv 1	32	112 x 112
block 1, conv 2	32	112 x 112
block 1, conv 3	32	56 x 56
block 2, conv 1	64	56 x 56
block 2, conv 2	64	56 x 56
block 2, conv 3	64	28 x 28
block 3, conv 1	128	28 x 28
block 3, conv 2	128	28 x 28
block 3, conv 3	128	14 x 14
block 4, conv 1	256	14 x 14
block 4, conv 2	256	14 x 14
block 4, conv 3	256	7 x 7
GAP	-	256 x 1
dropout	-	256 x 1
dense	-	9 x 1

3.2. Image preprocessing

The preprocessing of the raw images is displayed in Fig. 4. Since they contain a lot of black background, they were first cropped. This resulted in an image of approximately 215 pixels height (~3 mm) and 3,400 pixels length (~50 mm), which was

then cut into 15 square images. Each of them was slightly rescaled to 224 x 224 pixels. The 15 images of one edge were labeled with the same roughness values.

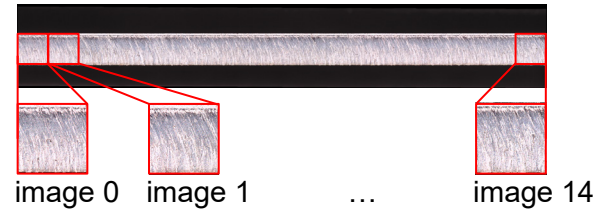


Fig. 4. The raw image was cropped and cut into 15 square images.

3.3. Train, validation and test split

The database consists of 834 samples, which correspond to 3,336 edges and 50,040 images. It was split into three parts: training set (72 %), validation set (13 %) and test set (15 %). The training set was used to learn the model parameters, the validation set was necessary for the hyperparameter optimization and with the test set the performance of the model is evaluated on unseen data.

When splitting the data, it must be guaranteed that a particular parameter combination (all images of one sample) is only contained in one of the three sets instead of splitting the images randomly. Otherwise we might overestimate the performance of the CNN: instead of generalizing well, it might only memorize the images.

3.4. Training

Since pre-trained architectures (e.g. ResNet [9] and VGG16 [10], pretrained on the ImageNet database) did not extract relevant features, we trained the CNN from scratch. The weights of the network were initialized with the Xavier uniform initializer [15] and updated with the Adam algorithm ($\beta_1=0.9$, $\beta_2=0.999$) [16]. The learning rate was set to 0.001. The batch size was 60.

To prevent overfitting during training we used 50 % dropout, data augmentation (vertically and horizontally flipping and rotating the images) and validation-based early stopping: when the validation loss does not improve for 20 epochs the training is aborted.

3.5. Evaluation

The mean absolute error (MAE) was used as loss function during training and to evaluate the quality of the regression on the test set. It was calculated for each of the nine targets separately:

$$MAE = \frac{1}{N} \sum_{i=1}^N |\hat{Y}_i - Y_i|$$

with N : number of test images, \hat{Y}_i : predicted value, Y_i : true value (label) for the image i .

In order to obtain a more stable statement about the model performance, the data was divided into training, validation and test set three times with a random permutation cross-validator

(in compliance with the boundary conditions described in 3.3). These splits are referred to as run 1, 2 and 3.

To the best of our knowledge there is no analytical method (for the calculation of Rz based on RGB images) to which the CNN could be compared.

3.5.1. Python libraries and hardware

The CNN was implemented in Python using the libraries TensorFlow 1.13.1 [17] and Keras 2.2.4 [18]. It was trained on the GPU GeForce RTX 2080 Ti graphical processing unit (NVIDIA corporation). The training time was below eight hours and is not considered further.

4. Results and discussion

In Table 2 the MAEs for the different measurement lines are shown. They range between 2.7 μm and 5.7 μm . For the same line they vary by up to 1.4 μm for different runs. The fact that the performance depends on the partitioning of the data is probably caused by the small database. The MAEs vary for different measurement lines. The prediction is generally better for lines in the lower region of the cut edge. The MAEs of line 0.3 are by far the worst for all three runs.

Table 2. Mean absolute errors (rounded) of the nine regression targets (line 0.3 to line 2.7) on the respective test set for three random splits of the data.

line		0.3	0.6	0.9	1.2	1.5
MAE in μm	run 1	5.7	3.7	3.8	2.9	2.9
	run 2	4.5	4.2	4.3	4.0	3.2
	run 3	4.3	3.6	4.2	3.5	3.4
	\emptyset	4.8	3.9	4.1	3.4	3.2
line		1.8	2.1	2.4	2.7	\emptyset
MAE in μm	run 1	3.4	3.0	2.9	2.9	3.5
	run 2	2.7	2.8	2.8	3.4	3.5
	run 3	3.5	3.4	3.6	3.6	3.7
	\emptyset	3.2	3.1	3.1	3.3	3.6

In Fig. 5 the roughness values predicted by the CNN on the test set of run 1 are compared with the labels (measurement results) for the lines 0.3, 1.5 and 2.7. Prediction and label are mostly similar at the middle and bottom line. The model is slightly biased: for low roughness values the predicted value is generally a little too high, for high roughness values it is too low. This is probably caused by the distribution of the data (see Fig. 2).

Line 0.3 stands out negatively again in Fig. 5. For some samples the prediction of the CNN seems to be completely wrong. It estimates roughness values of less than 25 μm for samples with labels of more than 50 μm . In truth, the higher MAEs in Table 2 and the huge differences between prediction and label are due to the quality of the data. In rare cases, the optical measurement device cannot cope with the high reflectivity of the stainless steel surfaces. This results in faulty surface topography measurements with outliers (deep holes) and causes very large roughness values. The uppermost part of

the cut edge (line 0.3 to 0.9) is most affected because the reflectivity is particularly high there.

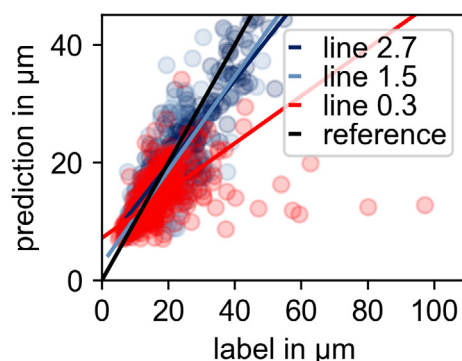


Fig. 5. Comparison of predicted value and label for the lines 0.3, 1.5 and 2.7, exemplarily for run 1.

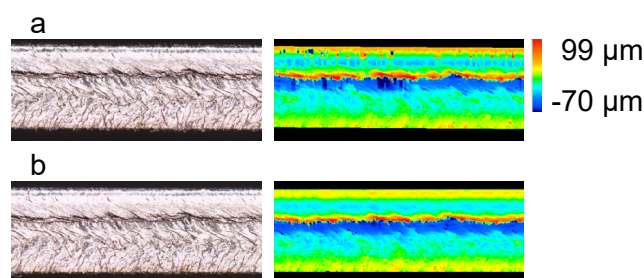


Fig. 6. RGB image and height topography of two measurements of edge 0700-4, a: with measurement errors (deep holes) caused by reflections, b: without errors.

For example, edge 0700-4 (see Fig. 5, rightmost red dot) is labelled with a value of 97 μm . The high Rz value is mainly caused by small, but very deep holes (see Fig. 6, a). The repetition of the measurement with a slightly deviating positioning of the edge in the sample holder, produces a surface topography without any holes (see Fig. 6, b). In this case Rz is 12 μm instead of 97 μm . The CNN estimates a value of 13 μm . It follows that the label is wrong. The CNN estimates the roughness better than the measurement system. The same applies to the other outliers in Fig. 5.

The neural network correctly maps the relationship between RGB image and roughness. Prediction and label only differ greatly, if the label is wrong. Although the outliers only affect few edges, they are not negligible due to their magnitude. They do not only increase the test error, but also the training error and influence the training process negatively. As the loss is averaged over the nine regression targets during training, the outliers affect the quality of the overall regression. A reliable detection and elimination of the outliers would surely improve the model, but not all outliers are as easy to detect as the one in the example above and repeating the measurement of each edge several times is too time-consuming.

5. Conclusion and outlook

We have shown that it is possible to estimate the roughness Rz of a laser cut edge with a CNN based on an RGB image. The roughness at different depths of the sheet could be determined with a mean error between 4.8 (for line 0.3) and 3.2 μm (for line 1.5). Consequently, a 3D measurement device is only

needed to generate training data for the model and obsolete in practice. Systems that automatically sort laser cut parts could for example be supplemented with cameras that take images of the cut edges or separate photo stations could be used by the machine operators when necessary.

The CNN performs only apparently worse for the uppermost measurement line. In truth, some labels are wrong due to measurement errors and in these cases the prediction of the CNN is better than the actual measurement. By comparing the errors of the different runs, it becomes clear that improvements could be made, if more or better data was available. Then the performance would be less dependent on the split of the data and the outliers would have less impact on the overall performance. The data quality could be improved by using a mechanical instead of an optical measuring method (e.g. stylus tip measuring device). However, this would make data collection even more time consuming.

Further interesting steps include the application of the network to other sheet thicknesses and materials. In addition, it would be desirable to estimate the roughness based on RGB images with a poorer resolution that are taken by simpler cameras without double telecentric lenses.

Acknowledgements

Part of the work has been performed within the SeHer research project, which is funded by the German Federal Ministry of Education and Research. The authors wish to express their sincere gratitude for the support.

References

- [1] Steen WM, Mazumder J. Laser Material Processing, 4. ed. London: Springer, 2010.
- [2] Arntz-Schroeder D, Petring D. Analyzing the Dynamics of the Laser Beam Cutting Process: An explanation of characteristic frequencies of melt film dynamics. *PhotonicsViews* 2020; 17: 43–7.
- [3] Pocorni J, Powell J, Deichsel E, Frostevarg J, Kaplan AFH. Fibre laser cutting stainless steel: Fluid dynamics and cut front morphology. *Optics & Laser Technology* 2017; 87: 87–93.
- [4] DIN ISO 9013. Thermal cutting - Classification of thermal cuts - Geometrical product specification and quality tolerances. 2017.
- [5] Sun W, Yao B, Chen B et al. Noncontact Surface Roughness Estimation Using 2D Complex Wavelet Enhanced ResNet for Intelligent Evaluation of Milled Metal Surface Quality. *Applied Sciences* 2018; 8: 381.
- [6] Stahl J, Jauch C. Quick roughness evaluation of cut edges using a convolutional neural network. In: Fourteenth International Conference on Quality Control by Artificial Vision. Munich, Germany, 2019.
- [7] Leach R, ed. Optical Measurement of Surface Topography. Berlin: Springer, 2011.
- [8] LeCun Y, Bengio Y, Hinton G. Deep learning. *Nature* 2015; 521: 436–44.
- [9] He K, Zhang X, Ren S, Sun J. Deep Residual Learning for Image Recognition. In: 2016 IEEE Conference on Computer Vision and Pattern Recognition. Las Vegas, USA, 2016.
- [10] Simonyan K, Zisserman A. Very Deep Convolutional Networks for Large-Scale Image Recognition. In: 3rd International Conference on Learning Representations. San Diego, USA, 2015.
- [11] Springenberg JT, Dosovitskiy A, Brox T, Riedmiller M. Striving for Simplicity: The All Convolutional Net. In: 3rd International Conference on Learning Representations. San Diego, USA, 2015.
- [12] Ioffe S, Szegedy C. Batch Normalization: Accelerating Deep Network Training by Reducing Internal Covariate Shift. In: Proceedings of the 32Nd International Conference on Machine Learning. Lille, France, 2015.
- [13] Nair V, Hinton GE. Rectified Linear Units Improve Restricted Boltzmann Machines. In: Proceedings of the 27th International Conference on International Conference on Machine Learning. Madison, USA, 2010: 807–814.
- [14] Lin M, Chen Q, Yan S. Network In Network. In: 2nd International Conference on Learning Representations. Banff, Canada, 2014.
- [15] Glorot X, Bengio Y. Understanding the difficulty of training deep feedforward neural networks. In: Proceedings of the Thirteenth International Conference on Artificial Intelligence and Statistics. Sardinia, Italy, 2010.
- [16] Ba J, Kingma D. Adam: A Method for Stochastic Optimization. In: 3rd International Conference for Learning Representations. San Diego, USA, 2015.
- [17] Abadi M, Agarwal A, Barham P et al. TensorFlow: Large-Scale Machine Learning on Heterogeneous Distributed Systems. arXiv preprint, 2016.
- [18] Chollet F. Keras. Keras Documentation, 2015. <https://keras.io> (accessed February 26, 2020).

11th CIRP Conference on Photonic Technologies [LANE 2020] on September 7-10, 2020

Application of machine learning to predict the product quality and geometry in circular laser grooving process

Esmail Ghadiri Zahrani^{a,b*}, Faramarz Hojati^a, Amir Daneshi^a, Bahman Azarhoushang^a, Jürgen Wilde^b

^a*Institute of Precision Machining (KSF), Hochschule Furtwangen University, Tuttlingen 78532, Germany*

^b*Department of Microsystems Engineering (IMTEK), University of Freiburg, Freiburg 79110, Germany*

* Corresponding author. Tel.: +49-74-611-502-6725; fax: + 49-74-611-502-6201 E-mail address: gze@hs-furtwangen.de

Abstract

Micro-grooves have various applications in different industries. Circular laser grooving is a new method for manufacturing micro-grooves on the circumference of cylindrical parts. In this process, the selection of appropriate parameters to reach experimentally the desired groove aspect ratio along with minimum dross formation requires tremendous efforts. Here, the role of a decision-making technique, similarly machine learning is highlighted to evaluate the significance of process inputs and provide the appropriate model for prediction concerning the input parameters. The experiments were conducted with the various inputs such as workpiece rotational speed, laser beam position, duty cycle, power and frequency. The outputs are the groove geometry in terms of width and depth of the circular groove as well as the groove quality considering the dross formation. Then, Random Forest (RF) technique was utilized to derive the most influential inputs on the outputs. The RF analysis revealed that the rotational speed, laser position and duty cycle are the most decisive process parameters in the groove geometry and groove quality. Also, the enhancement of the assist gas pressure does not improve the process outputs according to the results of RF analysis.

© 2020 The Authors. Published by Elsevier B.V.

This is an open access article under the CC BY-NC-ND license (<http://creativecommons.org/licenses/by-nc-nd/4.0/>)

Peer-review under responsibility of the Bayerisches Laserzentrum GmbH

Keywords: laser; circular groove; width; depth; dross; machine learning

1. Introduction

With the advancement of micro-technology in different industries, the need to create features with micro-geometries rises. One example is micro-grooves with a high dimensional aspect ratio used in hydraulic applications where sudden loads should be damped gently via leading the lubricant through these grooves [1]. There, for optimal performance, it is desirable to access maximum groove depth and minimum width. In such cases, traditional methods like turning and milling are inefficient. Generally, in conventional turning, the minimum grooves width is approximately limited to 0.5 mm. When the conventional turning is combined with ultrasound technique [2], it is able to produce micro-grooves but the achieved depth is not deep enough and the process is hard to implement. Other

non-conventional methods like laminated disk EDM [3] are mostly sequential, time-consuming and limited to specific dimensions.

The laser beam as a potent alternative in combination with a multi-axis workpiece positioning system [4], which synchronizes the workpiece and laser beam, allows creating high-aspect ratio grooves. Depending on beam specifications such as power, frequency, etc, it is possible to obtain higher depth and smaller kerf widths in laser machining compared to mechanical techniques.

Despite all the laser machining capabilities, the choice of appropriate laser parameters is a challenging task as the interaction of the process inputs and their influence on the output results are not fully understood [5]. As such, the role of

decision-making techniques, like machine learning is highlighted to make a reliable prediction. Among different methods of machine learning, such as logistic regression, Support Vector Machine (SVM), and decision tree, the latter is easy to use in practice and can graphically be interpretable [6]. The decision tree includes several nodes, edges and leaves which predicts the output in a top-down manner. The classification tree starts at the root node. At each node, the training data set is divided into the subsets. The edge starting from each node is linked to the child node or a leaf node. Each leaf indicates a class label. Tercan et al. [7] applied the decision tree method for improvement of laser cutting process. Beam quality, astigmatism, focal position, beam radius in x and y directions were considered as input parameters, while eight different surface roughness values were considered as output parameters. Through clustering of 22468 datasets, one class label (good and bad) is determined. Several experiments with different tree sizes were carried out. They found that the change in the number of nodes has no effect on the model accuracy. With respect to the decision tree, it was also concluded that the astigmatism and beam radius in y direction had the most and least effects on the roughness parameters.

Despite the advantages of the decision tree, this method has a risk of overfitting [6]. Also, it demonstrates poor accuracy in the case of large datasets or datasets with complex variable interactions. Alternatively, Breiman [8] introduced the Random Forest (RF) method which is currently one of the popular machine learning techniques. In RF, a group of trees is used for data classification. Each tree is constructed using a random selection of training datasets and a random subsets of predictor variables. For each observation, the results of all trees are collected to give a prediction based on the majority vote. Thus, RF provides high accuracy compared to the single decision tree while maintaining the properties of the decision tree.

In the current study, it is aimed to predict the outputs of the circular laser grooving process using the RF approach. As input parameters, X and Y position of the laser with respect to the workpiece center, rotational speed of the workpiece, laser power, laser frequency, gas pressure and duty cycle are considered. The output parameters are: (1) the groove depth, (2) groove width as well as (3) the state of the laser cut in terms of presence or absence of formed dross at the groove edge.

2. Experimental details

The experiments were conducted by a fiber laser system (Fanuc FF3000i-A), which is integrated into a CNC swiss type turning machine (Maier MK36LASER) [4]. Figure 1 illustrates the location of the laser head positioned above the workpiece surface which should be necessarily off-centered in different values of X and Y directions. During the laser radiation on the rotating workpiece, a coaxial pressurized assist gas (N₂) blows through the nozzle. This pressure helps to expel the melts from the groove and produce a circular groove that is free of melt.

Table 1 provides the experimental results for different combinations of input parameters. The X and Y position of the laser beam with respect to the workpiece center, rotational speed of the workpiece, laser power, laser frequency, gas pressure and duty cycle are the input parameters. The width and depth of the grooves are the process outputs. All the

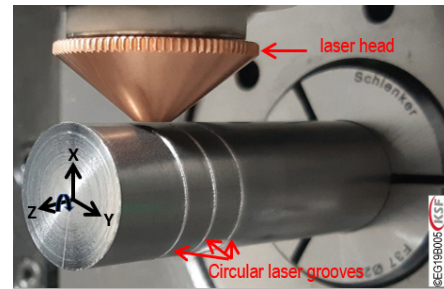


Fig. 1. Experimental setup of circular laser grooving.

experimental tests were conducted on a steel bar (DIN 1.7139) with a diameter of 12 mm and repeated two times. The nominal beam spot size and the nozzle diameter were respectively 140 μm and 2 mm.

Figure 2 shows an example of the groove geometry generated by laser processing. Here, the quality of the outer surface is assessed concerning the presence of dross. In laser cutting, the dross formation as an incomplete melt expulsion from the kerf [5] clinging on the backside surface is considered as an undesirable phenomenon. In the circular laser

grooving unlike the conventional laser cutting, due to the dynamic force exerted by the gas jet on the cutting front (Fig. 3), the dross forms on the top surface because the cutting does

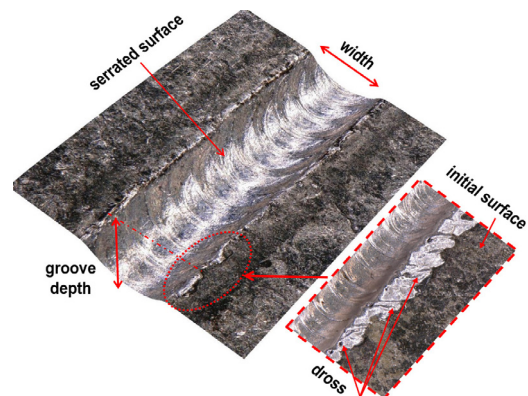


Fig. 2. Illustration of a laser groove- top view.

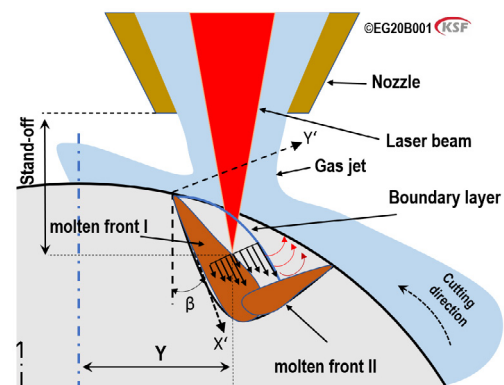


Fig. 3. Scheme of the assist gas acting on the molten pool during circular laser grooving

not happen through the whole thickness and the melt tends to flow at the groove edges.

For each experiment, the dross formation was visually evaluated which is considered as either acceptable (in table 1 with the notation of 'G') or unacceptable amount (in table 1 with the notation of 'B'). Also, the groove geometries (width

and depth) were measured from the captured images for each experiment.

3. Methodology

In this study, the Random Forest (RF) classification method is used for the prediction of the groove geometry and groove quality (dross formation) as two outputs. Prior to training the RF model, the outputs need to have labels. Section 3.1 is allocated to clustering and labeling of dataset concerning groove geometry and dross formation. Afterwards, the training

cluster. For the reproducibility of clustering, it is highly necessary to select other points (as means of two other clusters) with the highest distance from each other. Then, the nearest points of the observations from each of these three means are found based on Euclidean distance. Further, the mean of each cluster is calculated based on its corresponding points. In the next step, the nearest points from each new cluster mean are again found to generate new clusters. This procedure is repeated until no change in cluster means is detected. Eventually, the points in each cluster are reported and labeled with the notation of ‘I’, ‘II’ or ‘III’ as shown in Fig. 5-a. Accordingly, the

Table 1. Experimental parameters and results

Ex. No	X (mm)	Y (mm)	Rotation (deg/min)	Power (W)	Frequency (Hz)	Assist Gas Pressure	Duty cycle (%)	Width (µm)	Depth (µm)	Dross	Ex. No	X (mm)	Y (mm)	Rotation (deg/min)	Power (W)	Frequency (Hz)	Assist Gas Pressure	Duty cycle (%)	Width (µm)	Depth (µm)	Dross
1	8	6	50000	500	1000	20	50	85	325	G	21	7.75	4.5	30000	500	1000	20	50	574	206	G
2	8	7	50000	500	1000	20	50	74	261	G	22	7.75	4.5	20000	500	1000	20	50	706	214	G
3	8	6.5	50000	500	1000	20	50	74	365	G	23	7.75	4.5	10000	500	1000	20	50	1093	231	B
4	8	5.5	50000	500	1000	20	50	243	276	G	24	7.75	4.5	10000	500	1000	20	50	940	225	B
5	8	5	50000	500	1000	20	50	339	223	B	25	7.75	4.5	15000	500	1000	20	50	750	220	B
6	8	4.5	50000	500	1000	20	50	390	216	G	26	7.75	4.5	15000	500	1000	10	50	665	216	B
7	7.75	4.5	50000	500	1000	20	50	400	194	G	27	7.75	4.5	15000	500	1000	5	50	801	226	G
8	7.75	5	50000	500	1000	20	50	360	216	G	28	7.75	4.5	10000	500	1000	5	50	710	256	B
9	7.75	5.5	50000	500	1000	20	50	233	267	B	29	7.75	4.5	12500	500	1000	5	50	915	243	B
10	7.75	6	50000	500	1000	20	50	169	311	B	30	7.75	4.5	15000	500	2000	5	50	766	222	B
11	7.75	7	50000	500	1000	20	50	77	250	G	31	7.75	4.5	15000	500	3000	5	50	804	225	G
12	7.5	4.5	50000	500	1000	20	50	398	185	G	32	7.75	4.5	15000	500	4000	5	50	799	224	G
13	7.5	5	50000	500	1000	20	50	362	208	G	33	7.75	4.5	15000	500	3500	5	50	797	220	G
14	7.5	5.5	50000	500	1000	20	50	311	239	B	34	7.75	4.5	15000	500	3000	5	75	888	258	B
15	7.5	6	50000	500	1000	20	50	154	308	B	35	7.75	4.5	15000	500	3000	5	25	376	197	G
16	7.5	6.5	50000	500	1000	20	50	87	308	G	36	7.75	4.5	15000	500	3000	5	38	645	205	G
17	7.5	7	50000	500	1000	20	50	10	322	G	37	7.75	4.5	15000	500	3000	5	63	820	248	B
18	8	4	50000	500	1000	20	50	407	193	G	38	7.75	4.5	15000	700	3000	5	50	885	249	B
19	8	3.5	50000	500	1000	20	50	387	183	B	39	7.75	4.5	15000	600	3000	5	50	848	247	B
20	7.75	4.5	40000	500	1000	20	50	483	197	G	40	7.75	4.5	12500	500	3000	5	50	850	227	B

of the RF model is explained in section 3.2.

3.1. Clustering

As mentioned in Section 2, the dross formation was considered as a parameter for the evaluation of the groove quality. In this regard, two labels ‘G’ and ‘B’ were defined to indicate respectively acceptable and unacceptable amount of dross formation. The geometries of the grooves were characterized by their width and depth.

For labelling the geometries of the grooves, they should firstly be clustered based on their width and depth. Eventually, the geometries in the same cluster are more similar to each other regarding their width and depth than to those in other clusters. The scatter plot shown in figure 4 illustrates the width versus depth of each groove as listed in table 1. To cluster the geometry of the grooves, a k-means approach [6] was applied. In this approach, the observations (here e.g. width and depth of the grooves) are divided into k-clusters in which each observation is considered as a subset of the cluster whose mean has minimum distance from that observation [6]. For the implementation of the k-means method in this study, the number of clusters, k, is set to 3. Further, one point from the observations is randomly selected as the primary mean of one

clustering for the groove depth has been performed very well through the k-means method. By increasing the number of clusters, the observations were again distinctly clustered regarding the groove depth. Using the k-means approach, the clustering for the groove width (with three clusters) was not as satisfactory as that of the groove depth. In order to have better clustering, the observations were again clustered into four and five groups without using the k-means method and labelled as shown in the figures 5-b and 5-c. Considering the dross formation, figure 6 represents the clustered observations by red and blue colors. They refer to the unacceptable and acceptable

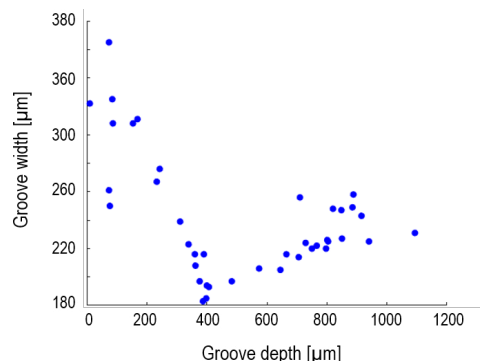


Fig. 4. Groove width versus groove depth

amount of dross formation, respectively. In summary, two types of label for the outputs were provided through clustering. One label type (with the notation of ‘G’ and ‘B’) is associated with the dross formation, and another one (with the notation of Roman numerals) deals with the groove geometries.

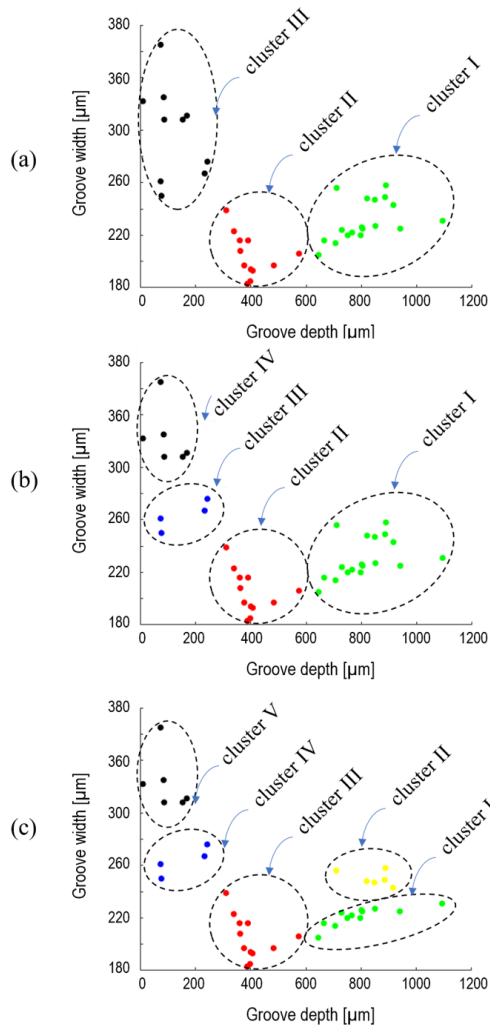


Fig. 5. Clustering of data with respect to the groove geometries. a) three clusters, b) four clusters, c) five clusters

3.2. Classification

In the RF classification method, the laser position, rotational speed, power, frequency, assist gas pressure and duty cycle are considered as input parameters. The outputs (groove geometry and dross formation) were summarized in two types of labels as derived in section 3.1. Therefore, RF model is individually trained for each label type. For the groove quality, the prediction means whether the amount of dross formation is acceptable (‘G’) or unacceptable (‘B’). Concerning the groove geometry, the predicted label associated with one cluster provides the range of width and depth. It means that the generated geometry with the given input parameters should be in this range.

For training of the RF model, TreeBagger class in MATLAB software has been applied. The number of trees, minimum leaf size, maximum number of split and the number of randomly selected variables at each node (N.R.S.V) are important

hyperparameters in the RF model. To find the optimum combination of hyperparameters, the grid search optimization algorithm [6] was implemented to evaluate the different combinations of hyperparameters. The range of hyperparameters is summarized in table 2.

Table 2. Ranges of Hyperparameters

Hyperparameters	Range
Number of tree	10-100
Minimum leaf size	2-10
Maximum number of split	1-39
Number of randomly selected variables at each node (N.R.S.V)	2-7

To evaluate the developed RF model with each combination of hyperparameters, k-fold cross-validation with k=5 has been applied. In detail, the dataset is divided into five groups. Four groups are used to train the RF model and the remaining one is for testing. To evaluate the model performance, a new combination of laser input parameters is imported into the trained RF model in order to predict a label that would be ‘G’ or ‘B’ for the dross formation and Roman numerals for the groove geometry. If the predicted label is matched with that in the dataset, the correct prediction is made by the trained model. The total number of datasets in this study is 40. Therefore, 32 data points are used for training and 8 points for testing the model. This procedure is repeated five times (corresponding to k=5) by resampling the testing group and the rest is used to train the RF model. Eventually, the average calculation of accuracy obtained from different test groups is considered as the prediction accuracy of the RF model with the given combination of hyperparameters. Then, the optimization loop starts again with another combination of hyperparameters and finally, optimum hyperparameters are found through comparing the prediction accuracy of the RF model. If the same accuracy is obtained from two different combinations of hyperparameters, the one is selected as an optimum value with less forest size and tree depth that results in a RF model with less computation time.

4. Results and discussion

4.1. Hyperparameters of RF model

To study the effect of the number of clusters on accuracy in prediction of the groove geometry, the RF model is individually trained for the scatter plot shown already in figure 5. According to table 3, it can be concluded that the accuracy of RF model is influenced by the number of clusters. The increase in number of clusters from 3 to 5 led to the reduction of model accuracy from 95% to 80%. Although the model accuracy in the case of 3 clusters (Fig. 5a) is higher than other cases, the five clusters (Fig. 5c) is able to predict the groove width in narrower ranges. By increasing the number of the clusters, the number of data points in some clusters is considerably lower than others. This has led to a reduction of prediction accuracy.

Table 3. Prediction accuracy for clustered data shown in Fig. 5 and their corresponding optimum hyperparameters

No. clusters	Prediction accuracy (%)	No. of trees	N.R.S.V	Max. no. split	Min. leaf size
3	95	10	3	3	3
4	87.5	10	4	5	3
5	80	10	7	13	1

Regarding the dross formation, the model prediction accuracy is 80%. In this case, the optimum hyperparameters are 30 for the number of trees, 3 for the N.R.S.V, 13 for the maximum number of split and 1 for the minimum leaf size.

As explained before, the series of optimum combination of hyperparameters resulting in the maximum accuracy can be obtained after optimization. For each hyperparameter, the collected data have been normalized and then, the variance was calculated which can be used as a factor for evaluation of the model sensitivity for a given hyperparameter. The higher variance of one hyperparameter compared to others indicates that the wider range of this hyperparameter results in the maximum accuracy and the model has minimum sensitivity to this hyperparameter in the given range. In contrast, in the case of the lowest variance, the model has the maximum sensitivity to the corresponding hyperparameter. The zero variance indicates that for this hyperparameter, only one value resulted in the maximum accuracy. As a result, the model is considerably sensitive to that hyperparameter. Figure 7-a illustrates the model sensitivity for the groove geometry with 5 clusters. Accordingly, the RF model has the maximum sensitivity to the minimum leaf size. Afterwards, the model is in particular order sensitive to the N.R.S.V, maximum number of split and number of trees. As shown in figure 7-b, for the RF model trained for the dross formation, the sensitivity of the model is considerable for the N.R.S.V and minimum leaf size. Following, the number of trees and the maximum number of splits come in sequence.

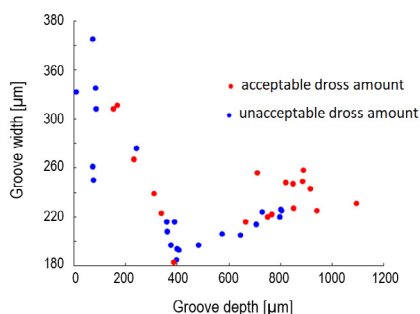


Fig. 6. Data clustering for the groove quality considering acceptable and unacceptable amount of dross formation

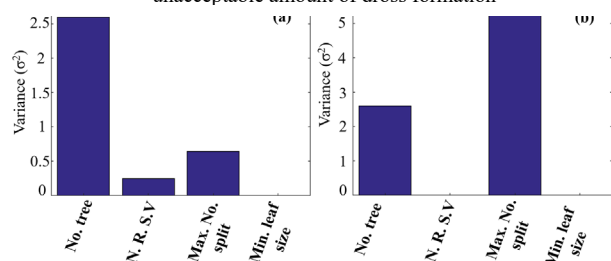


Fig. 7. Model sensitivity for hyperparameters: a) groove geometry with 5 clusters, b) dross formation with 2 clusters

4.2. Laser input parameters importance

In this section, the importance of the laser input parameters

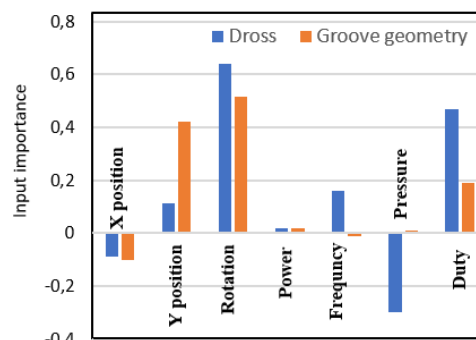


Fig. 8. Input importance for the groove geometries and dross formation

in the circular laser grooving process is studied. As discussed, seven input parameters were used for training the RF model. For evaluating their importance, the Out-Of-Bag (OOB) Predictor Importance method in the library of TreeBagger class was called. In this regard, the prediction accuracy of the trained model for each tree was calculated using the OOB data. The OOB data for each tree are those which were not engaged for the training of that tree. Further, i -th input of OOB data is permuted while other inputs remain the same because the importance of i -th input will be evaluated. This contributes to the destruction of association between permuted i -th input and the output. Finally, the accuracy of the model is calculated with respect to the permuted OOB data. Since the RF model used permuted i -th input for prediction, the reduction in the prediction accuracy is expected. The difference between the accuracy of the model using OOB data and the permuted OOB data was calculated for each tree and averaged over all trees. As expected, the obtained average value would be positive which confirms the role of the i -th input in the classification. The zero or negative values indicate that the permutation of the i -th input had respectively no influence on the classification or worked better. For both cases, it can be concluded that the i -th input is not predictive enough and has no significance. Figure 8 shows the normalized input importance of the RF model for the dross formation and the groove geometry (with five clusters). For the groove geometry, the rotational speed of the workpiece is the most influential input that is followed by Y position of the laser and duty cycle. The laser power and gas pressure have the least effect. Moreover, the X position of the laser and laser frequency have no influence on the groove geometry. Regarding the dross formation, the rotational speed of the workpiece is still the most effective input. Duty cycle, frequency and Y position of the laser stand in the next levels of importance. The laser power has the least influence. Additionally, the X position of the laser and the gas pressure are considered as the neutral inputs. The insignificance of the assist gas pressure in the RF model complies with the experimental results in table 1, where increasing the assist gas pressure from 5 bar to 20 bar does not effectively increase the groove depth.

The idea behind the shifting the laser beam position in the X and Y directions is to dislocate the melting pool to a place where the produced melt is practically being able to be blown out from the bottom of the groove by the pressurized gas. As the workpiece has a circular cross-section, this inevitable off-

center positioning should dependently be adjusted in both x and y directions to keep the maximum irradiation intensity on the laser spot.

When the assist gas is flowing into the kerf, the momentum necessary for melt expulsion, which is exerted from the gas, is transferred through a boundary layer (depicted in Fig. 3). To maximize this transference to the molten material, which is practically equal to more effective melt expulsion, the boundary layer must be maintained into the laminar regime which literally means much lower Reynolds numbers (Re_g) than the critical value (3.2×10^5) [9,10]. When $Re_g > Re_{g,critical}$ the flow turns from laminar to turbulent. This condition happens when a very high-pressure gas enters into the cutting kerf and as a consequence; the melt expulsion continuous in a turbulent manner compared to the case where low pressure is applied to the melt. This consequence was already observed in the current experiments when the gas pressure increased from 5 to 20 bar which practically led to no growing increase in the groove depths. The results of the RF model confirm the insignificance of the pressure increase. During the initial parameter screening whose results are not provided here, the influence of the gas pressure in the range of 0 to 5 bar was approved.

Shifting the laser beam down in x-direction can change the melting pool dimension by varying the spot size and power density [11] in such a way, a decrease in the melting pool depth and an increase in the width is expected which are not desirable in this process. The reducing effect of the x-shifting was previously seen in the experimental results (Exp. no. 6 & 7 in table 1). Due to the high volume of melt produced in this process at the kerf bottom (molten front II in Fig. 3), other reasons may contribute to the depth reduction as well. As discussed before, one reason can be originated from the assist gas pressure which is not productive enough in the range of 5 to 20 bar to expel the melt out of the groove properly, causing the ineffectiveness of the x-shifting. The other reason arises from the kinematics of the circular laser grooving process. In this process, the workpiece rotates during the laser irradiance so that the melt intends to rotate at the groove bottom as well. This rotation especially in high speeds imposes a temperature gradient to melt which results in a temporally repeatable melting and solidification cycle, which eventually results in less material removal. This behaviour of melt can be seen at the bottom of the groove as a frequent serrated surface (Fig. 2). In compliance with the RF results, the experimental results confirm the ineffectiveness of the beam shifting in the x-direction.

Even though the laser power considerably affects the laser process performance, the RF Model here has considered it as a neglectable variable. Since almost in all the experiments (table 1), the laser power was set to 500W and only in two tests, it was changed to 600W and 700W, the corresponding variance is substantially small. Consequently, it affects the determination of input importance so that the RF model has not taken into account the laser power.

The duty cycle defines the on/off ratio of the laser power. A higher value of the duty gives more output energy to the surface [5] which here correspondingly, it is led to larger groove depth and width (Exp. no. 34-37 in table 1). Concurrently, increasing the duty results in much melt and consequently much dross.

This is noted in table 1 with the notation of 'B' for the relevant tests. These experimental results support the findings of the RF model about the duty cycle.

Increasing frequency corresponds to a higher number of pulses and peak irradiance to the molten material which causes an overheat of the melt [5]. The enhance of the temperature provides a considerable reduction of the viscosity and surface tension of melt [12]. In this situation, applying the pressurized gas expulses the melt out of the groove more undisturbed and practically results in less dross. The experimental results (i.e., tests 30 & 31), as well as the RF model results (Fig. 8), confirm the effect of the frequency increment on the dross formation.

5. Conclusion

Due to the complexities in the parameter selection for the circular laser grooving process, the Random Forest method (RF), as one of the machine learning techniques, has been applied in this study to evaluate the significance of input parameters and predict the outputs. The X and Y position of the laser, power, frequency, duty cycle, assist gas pressure and workpiece rotational speed were selected as input parameters. The process outputs are groove geometry and groove quality (dross formation). For the groove geometries, the prediction accuracies of 95%, 87.5% and 80% by the RF models were obtained for datasets with three, four, and five clusters, respectively. Regarding the dross formation, the prediction accuracy of 80% was achieved with two clusters. Based on the given dataset, the Y-position of the laser and workpiece rotational speed have the maximum influence on the geometries of the groove. Also, the duty cycle is the next influential parameter. The rotational speed and duty cycle are the most effective parameters in the dross formation. Considering the fact that the laser power was constant in almost all experiments (except two), its importance was overlooked by the applied RF model.

Based on the obtained accuracy in the prediction of the groove geometry and groove quality in this process, it can be concluded that the RF method is a reliable machine learning technique. Notably, it has the potential to be utilized for industrial applications with the random dataset.

Acknowledgment

The authors would like to acknowledge the financial support from the Federal Ministry for Economic Affairs and Energy (based on a decision of the German Parliament). The project was carried out with support of the German Federation of Industrial Research Associations (AiF) for ZIM-project No ZF4575002SY8. Also, many thanks from Maier Machine Tools Co., Wehingen, Germany, for all their sincere supports.

References

- [1] Winoto SH, Hou ZQ, Ong SK, Rondonuwu CC, Zhang QD. Effects of Herringbone Groove Patterns on Performance of Vertical Hydrodynamic Journal Bearings. *Tribology Transactions* 2002; 45:318-23.
- [2] Zhang C, Guo P, Ehmann KF, Li Y. Effects of ultrasonic vibrations in micro-groove turning. *Ultrasonics* 2016; 67:30-40.
- [3] Lei J, Wu X, Wang Z, Xu B, Zhu L, Wu W. Electrical discharge machining of micro grooves using laminated disc electrodes made of Cu and Sn foils. *Journal of Materials Processing Technology* 2019; 271:455-

- 62.
- [4] Azarhoushang B, Ghadiri Zahrani E, Kitzig-Frank H. Hybridbearbeitungsprozesse – Hybride Laser- und Drehbearbeitung. Teil 2. DIAMOND BUSINESS 2019; 2C:1-14.
 - [5] 2008 Laser Fabrication and Machining of Materials. Springer US, Boston, MA.
 - [6] Sheppard C 2019 Tree-based machine learning algorithms: *Decision trees, random forests, and boosting*. Clinton Sheppard, Austin, Texas.
 - [7] Tercan H, Khawli TA, Eppelt U, Büscher C, Meisen T, Jeschke S. Improving the laser cutting process design by machine learning techniques. *Prod. Eng. Res. Devel.* 2017; 11:195-203.
 - [8] Breiman L. Random Forests. *Machine Learning* 2001; 45:5-32.
 - [9] Vicanek M, Simon G. Momentum and heat transfer of an inert gas jet to the melt in laser cutting. *J. Phys. D: Appl. Phys.* 1987; 20:1191-6.
 - [10] Rao BT, Nath AK. Melt flow characteristics in gas-assisted laser cutting. *Sadhana* 2002; 27:569-75.
 - [11] Shan J 2011. Laser welding of magnesium alloys. in Liu L, (Ed.). *Welding and joining of magnesium alloys*. Woodhead. Oxford, pp. 306–350.
 - [12] Rywotycki M, Malinowski Z, Gielzecki J, Gołdasz A. Modelling Liquid Steel Motion Caused by Electromagnetic Stirring in Continuous Casting Steel Process. *Archives of Metallurgy and Materials* 2014; 59:487-92.

11th CIRP Conference on Photonic Technologies [LANE 2020] on September 7-10, 2020

Laser Cutting with annular intensity distribution

Hao Pang^{a,b,*}, Tobias Haecker^a

^aTRUMPF Werkzeugmaschinen GmbH +Co. KG, Johann-Maus-Strasse 2, 71254 Ditzingen, Germany

^bInstitute of Applied Optics, University of Stuttgart, Pfaffenwaldring 9, 70569 Stuttgart, Germany

* Corresponding author. Tel.: +49-7156-303-36072; E-mail address: hao.pang@trumpf.com

Abstract

An annular intensity distribution has been assumed theoretically with great potential to provide high quality improvements to the cut flank during laser cutting process. We introduce several optical concepts to realize an annular intensity distribution with a high-power laser beam, such as an optical fiber with an annularly formed fiber core, a diffractive optical element, and axicons. Furthermore, cutting experiments for an axicon telescope with stainless steel are presented. With a specific optical setup and appropriate cutting parameters, a burr free cut flank with a surface roughness comparable to the state of art could be achieved. By means of cut front analysis, we assume that the burr free cut flank is a result of an improved gas coupling and the change of cut front geometry at the bottom side of the sheet.

© 2020 The Authors. Published by Elsevier B.V.

This is an open access article under the CC BY-NC-ND license (<http://creativecommons.org/licenses/by-nc-nd/4.0/>)

Peer-review under responsibility of the Bayerisches Laserzentrum GmbH

Keywords: laser cutting; beam shaping; annular intensity distribution; axicon telescope

1. Introduction

The high-power solid-state laser is a widely spread solution for industrial material processing. The global market for laser material processing systems reached \$19.8 Billion in 2018 [1]. Regarding process optimization approaches in the recent years, a shift from directly increasing laser power to smartly and efficiently exploiting the available power to the workpiece has been observed. Here, remarkable examples can be found in the multi-spot technology for high-quality welding of zinc-coated steel [2] or the use of Bessel-like beams for efficient cutting of transparent materials [3].

In case of sheet metal laser cutting, it has been recognized that a much better cut flank quality in terms of flank roughness and remained burr can be achieved with CO₂ lasers (wavelength 10.6 μm) instead of solid-state lasers (wavelength 1.03/1.06 μm) [4]. However, due to the higher productivity as well as the lower maintenance and operating costs, CO₂ lasers are gradually being replaced by solid-state lasers for industrial applications [5]. To improve the solid-state laser cutting

process, beam shaping has been considered as one of the key solutions.

The optimal intensity distribution for laser cutting processes is still unknown. Different kinds of models and suggestions of intensity distributions have been declared with potential to improve the cutting process, for instance multi spots in [6] and an annular profile in [7]. The main theoretical argument for an annular intensity distribution is that to cut thick-sheet stainless steel ($h_{\text{sheet}} > 6$ mm), a wider cut kerf is expected to improve the working efficiency of the gas flow. This enhances the melt ejection from the cut kerf and therefore raises both the cut flank quality and the feed rate. One obvious method to widen the cut kerf is to enlarge the laser spot size. This is usually achieved by a larger image scale of the optical system or a deteriorated beam quality. However, the enlarged spot size leads to a reduced intensity, especially at the spot edge. The annular intensity distribution mitigates this effect because the energy is concentrated at the edge of the spot. Therefore, the energy can be used more efficiently to melt the material and the cutting process is optimized.

In this paper, we firstly introduce several optical concepts to generate an annular intensity distribution in or close to the focal plane appropriate to high-power multi-mode laser beams. Then, we focus on cutting experiments with an axicon telescope. Finally, the results and a cut front analysis are presented in order to understand the optimization achieved by the corresponding processes.

2. Beam shaping concepts

For a beam shaping concept applied to industrial high-power laser applications, several aspects must be considered:

- It is supposed to form the desired beam accurately.
- The efficiency must be high enough, therefore only phase modulation is suggested. Scattered and unwanted diffracted light must be controlled.
- It must be insensitive to misalignment and change of the input beam.
- It must be adaptive to different processes, materials, and material thicknesses.
- The deterioration of beam quality must be controlled.

Considering these conditions, several optical concepts to create an annularly distributed laser beam are introduced and discussed in the following.

2.1. Optical fiber with annularly formed core

Since an optical imaging system is applied to transmit the laser beam from the fiber end to the workpiece, the most obvious approach for beam shaping is to modify the light source, in this case by using a fiber with an annular core, see Fig. 1. This kind of optical fiber has been frequently implemented in many industrial applications, such as [8]. When the ring core is illuminated by laser light, an exact annular intensity distribution is achieved at the near field. However, the near field annular intensity profile disappears after a few millimeters' propagation.

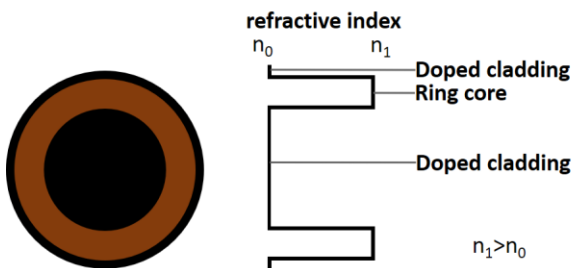


Fig. 1. Left: Optical fiber with annularly formed core (red). Right: The corresponding refractive index distribution.

2.2. Optical vortex

An optical vortex is a phase singularity nested in electromagnetic waves [9]. At the phase singularity, the phase of the wave is undefined, and the wave intensity vanishes. This physical phenomenon can be used to create a propagating annular intensity distribution. A vortex phase mask is defined by

$$u(\theta) = \exp(il\theta), \quad (1)$$

with θ the azimuthal angle of the polar coordinate system and l the topologic charge. The graphical representation of such a phase distribution with topologic charge 1 and the corresponding simulated near field intensity distribution for a single mode laser are depicted in Fig. 2.

Generally, the whole system is very sensitive to aberrations and misalignment. The homogeneity of the near field is strongly influenced by the wave front of the input beam. Furthermore, the intensity vanishes at the phase singularity only in a coherent system. On the contrary, in a completely incoherent system, neither the helical phase nor the characteristic zero intensity at the vortex centre is observable.

Recently, several investigations have shown possibilities to generate a partially coherent vortex beam [10] [11]. However, a system suitable for high-power multi-mode lasers remains to be developed.

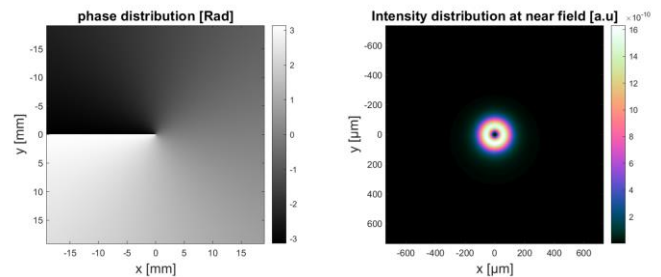


Fig. 2. Left: phase distribution of an optical vortex with topologic charge = 1. A phase singularity at the centre of phase distribution is observable. Right: resulting intensity distribution at the near field. The simulation is based on a single mode laser with 2 mm diameter at the far field.

2.3. Diffractive optical element

With the development of optical manufacturing technology, diffractive optical elements (DOE), especially diffractive diffusers and diffractive micro-lens arrays, offer new possibilities for laser beam shaping.

A general numerical design process for diffractive diffusers is known as Gerchberg-Saxton algorithm [12], which was originally developed for recovering the phase of an electromagnetic wave from its intensity distributions in two transverse planes. Fig. 3 presents a typical phase distribution calculated with the Gerchberg-Saxton algorithm to form an annular intensity distribution and the corresponding intensity distribution at the near field.

Due to the design and manufacturing errors, there is always a few percent of light being diffracted or scattered to an unwanted direction by applying DOEs. This causes local heating of the mechanical components and might result in problems for high-power applications, such as damage of the processing unit or a large focal shift. There are still many problems to be solved to integrate such an optical element into the processing unit.

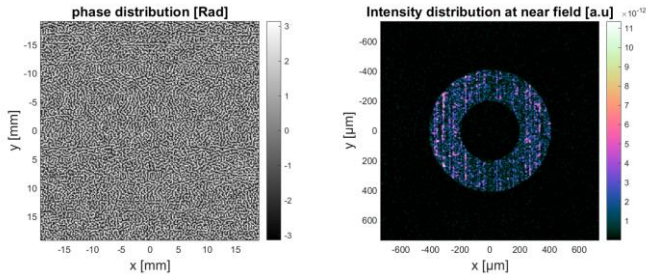


Fig. 3. Left: Phase mask of a diffractive diffuser designed for an annular intensity distribution at the near field. Right: The corresponding near field intensity distribution with far field beam diameter 10 mm. The simulation is based on a single mode laser.

2.4. Axicon

An axicon is known as a conical lens [13], which is commonly used to create a Bessel-like beam profile [14]. The phase function of an axicon can be written as

$$u(r) = \exp(-i\gamma r), \tag{2}$$

with r the radius in polar coordinates and γ the scale factor.

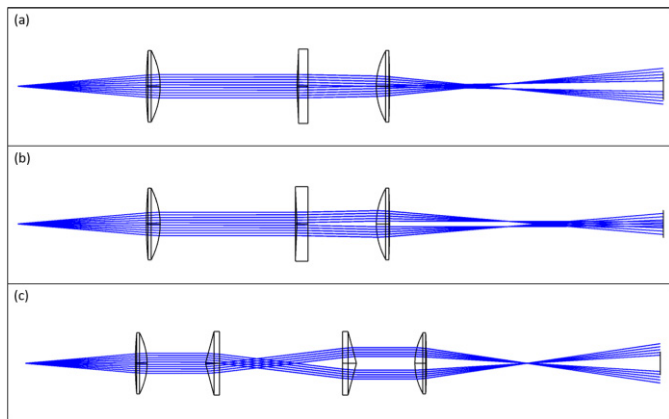


Fig. 4. Typical ray path of a positive axicon, a negative axicon and an axicon telescope. (a) Positive axicon: divergent ring behind the focal plane. (b) Negative axicon: convergent ring in front of the focal plane. (c) Axicon telescope: annular distribution in front of and behind the focal plane.

With a single positive or negative axicon, we achieve a divergent or a convergent profile with an annular intensity distribution behind or in front of the focal plane, respectively. To realize extra flexibility and a symmetric caustic, a zoom system based on two axicons sharing the same basic angle is preferred, see Fig. 4 [7]. With such an axicon telescope, we

achieve an annular intensity distribution along the propagation direction except for the focal plane.

In this paper, we concentrate on the optical design of an axicon telescope and present the cutting result with it.

3. Optical design of the axicon telescope

The design of an axicon telescope system shown in Fig. 4(c) has a large degree of flexibility, such as the image scale based on two lenses, the base angle of the axicons and the distance between the axicons. We presume that the input beam is a collimated flat-top beam and consider the axicon to be very thin. The diameter D_2 in Fig. 5 is calculated by

$$D_2 \approx 2z_0 \tan[\beta(n - 1)], \tag{3}$$

with z_0 the distance between the two axicons, β the axicon base angle and n the refractive index. The breadth d of the ring

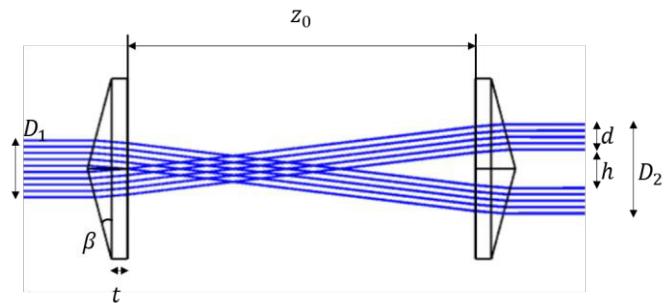


Fig. 5. Ray optical demonstration of the axicon telescope.

at the far field is half of the input beam diameter D_1 . The diameter of the cavity can be calculated as $h = D_2 - D_1$. There is a minimum distance of the two axicons given by

$$z_{\min} \approx \frac{D_1}{2 \tan[\beta(n-1)]} \tag{4}$$

In this case, D_2 is identical to D_1 and the laser beam is simply mirrored at the optical axis. Additionally, different distances z_0 can be used to adjust h .

For the experiments, a disk laser with 100 μm fiber core (TruDisk 8001, $\lambda = 1030$ nm, $M^2 \approx 12$) was applied. As already explicated in Fig. 4(c), two axicons ($\beta = 15^\circ$) were integrated between the collimator and the focal lens with the distance $z_0 = 101$ mm. The image scale of the system was two. In the second line of Fig. 6, the corresponding simulated intensity profiles at the near field with ideal lenses are presented.

In the experimental setup, the main difficulty is to align the whole optical system inside the cutting unit with high laser power. Because of the completely closed environment, the flexibility to align the optics is extremely narrowed. In Fig. 6, simulated intensity distributions along the caustic with corresponding misalignments are presented. If the input beam is tilted with respect to the axicon telescope, the asymmetrical deformation of the beam remains the same direction during propagation. When the axicon telescope is decentered to the

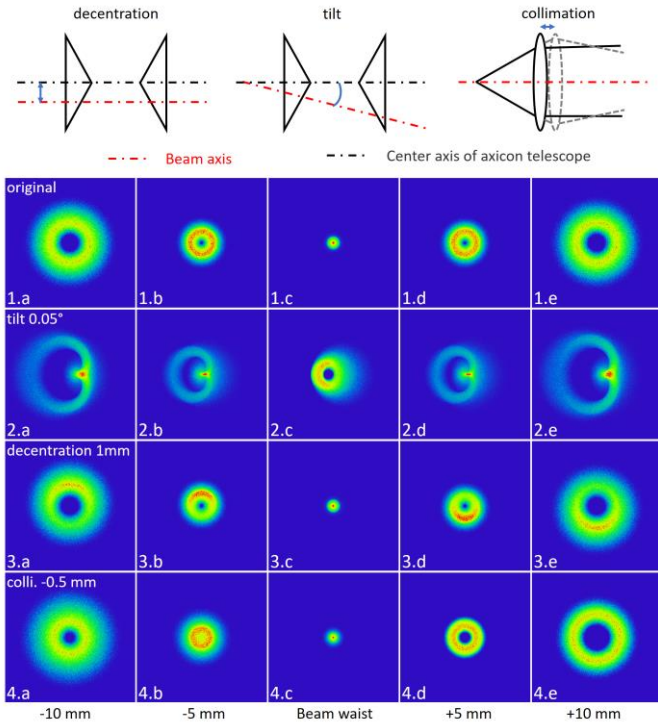


Fig. 6. Intensity distributions simulated by the ray tracing with different Misalignments. Light source: flat top with 100 μm diameter. Corresponding representative sketches are attached for each misalignment.

laser beam, the asymmetrical deformation changes its direction in front of and behind the beam waist. With a not well collimated laser beam, we observe an asymmetrical distribution of the ring breadth along the propagation, which is a good input for collimation check.

In order to align the axicon telescope in the experimental setup, the intensity distribution around the focal area was measured with a PRIMES FocusMonitor. By comparing the result with the simulations of misaligned optical systems, we were able to properly align the axicon telescope. In Fig. 7, measurements of the aligned system with 500 W laser power are explicated. An annularly distributed intensity is observed in front of and behind the beam waist. At the beam waist, the cavity vanishes, and a centered intensity peak appears as expected.

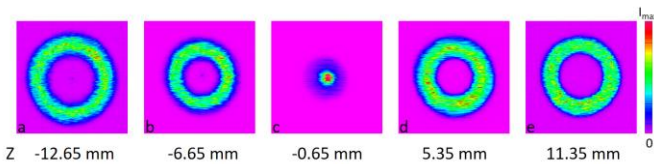


Fig. 7. Caustic measurements. Z: relative z-position with respect to the beam waist. Device: Primes FocusMonitor. Laser: TruDisk8001. Power: 500 W. Diameter of optical fiber core: 100 μm.

4. Cutting experiment

There are plenty of parameters to vary for laser cutting, which makes the design of experiments complicated. We varied

primarily the feed rate and the beam waist position with respect to the upper surface of the sheet, because these parameters have the largest impact on the cut flank quality.

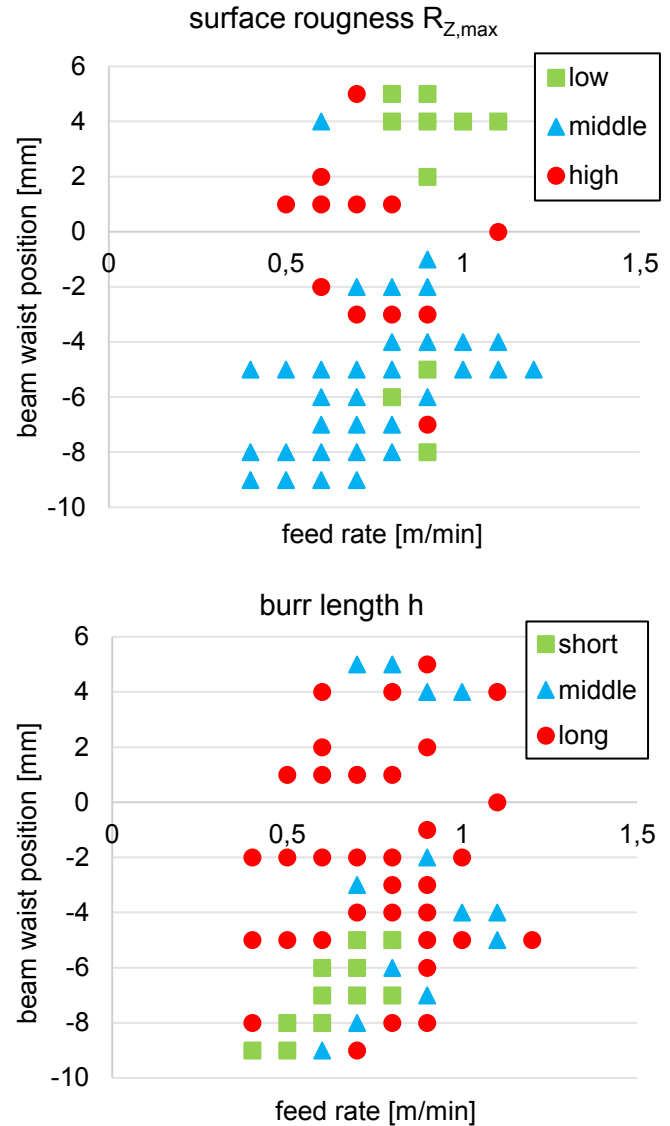


Fig. 8. Diagram to present the flank quality in respect to the feed rate and the beam waist position. Surface roughness low: $R_{z,max} < 50 \mu\text{m}$, middle: $50 \mu\text{m} \leq R_{z,max} < 70 \mu\text{m}$, high: $R_{z,max} \geq 70 \mu\text{m}$; Burr length short: $h < 50 \mu\text{m}$, middle: $50 \mu\text{m} \leq h < 200 \mu\text{m}$, long: $h \geq 200 \mu\text{m}$.

Table 1. Basic parameters for laser cutting experiments.

laser power	6000 W (TruDisk 8001)
fiber core diameter	100 μm
beam parameter product (without axicon telescope)	4 mm×mrad
gas pressure	22 bar
cutting gas	nitrogen
nozzle distance	0.3 mm
material	1.4301 (10 mm)

To evaluate the burr length, an outside micrometer was used. We firstly measured the thickness of the blank sheet h_{sheet} and then determined the thickness of the sheet including burr h_i at three representative points. The regarding burr length \bar{h} is defined as $\bar{h} = (h_1 + h_2 + h_3)/3 - h_{\text{sheet}}$. To evaluate the surface roughness Rz_{max} , we followed DIN EN ISO 4288: 1998-04, where the topographical information of the cut flank was measured with a chromatic confocal scanner.

For the optical setup with $z_0 = 101$ mm, for which a BPP (beam parameter product) of $10.5 \text{ mm} \times \text{mrad}$ and a Rayleigh length of 3.15 mm were measured, the resulting surface roughness and burr length are presented in Fig. 8.

For both evaluation criteria \bar{h} and Rz_{max} , three quality levels are defined. In general, we observed that with a positive beam waist position, which means that the beam waist is above the sheet, the cut flank roughness tends to decrease. On the contrary, with a negative beam waist position, especially when the beam waist is located at the bottom of the sheet, the burr length tends to get shorter. With a feed rate in the range of 0.6 m/min, we achieved a burr free cut flank where the surface roughness $Rz_{\text{max}} = 50 \mu\text{m}$ and is comparable to the standard process with 6 kW. Microscopic images of two representative cuts with low surface roughness and zero burr are shown in Fig. 9, respectively.

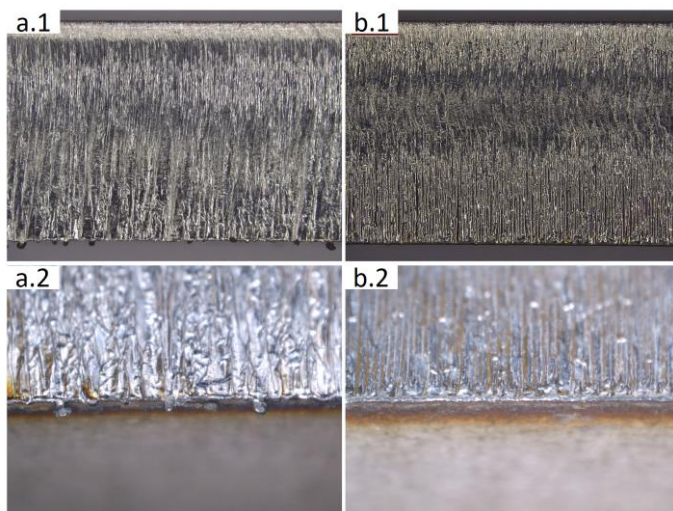


Fig. 9. Microscopic image of cut flank. (a): Beam waist position: $+4$ mm, feed rate: 1 m/min, burr length: $100 \mu\text{m}$; (b): Beam waist position: -8 mm, feed rate: 0.6 m/min, burr length: $0 \mu\text{m}$. The view in a.2 and b.2 is inclined by 20° to offer a better observation of burr.

5. Process model for burr free cutting

Generally, the intensity distribution is not the only factor affecting burr formation. From the cutting experiments we experienced that the burr formation was influenced by gas dynamics and feed rate as well. These three factors are often coupled to each other. In this subsection, we postulate an assumption to explain why the burr free cut flank was achieved with the axicon telescope.

Our process model for explaining the burr reduction is based on the analysis of the cut front geometry. For this purpose, we

generated so-called “frozen cuts”, i.e. we abruptly switched off laser power during the cutting process while maintaining all other process parameters to enforce the cut front to solidify in its original form. This technique is sketched in Fig. 10 and explained in detail in [15], for instance.

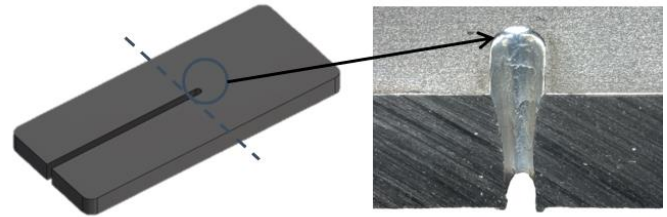


Fig. 10. Generation of a “frozen cut”. By abruptly switching off laser power, the cut kerf solidifies close to its original form and can be analysed by a microscope or topology scanner.

Our process model is now based on two aspects. Firstly, due to the annular intensity distribution and the deep beam waist position, the cut kerf is opened widely, see Fig. 11(a). This leads to an improved gas coupling and the melt might be ejected more efficiently.

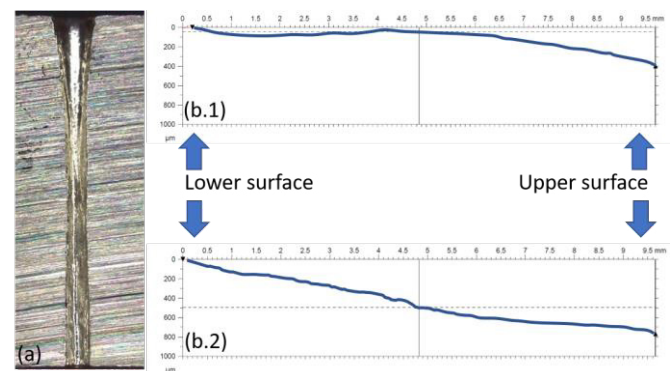


Fig. 11. (a): The cross section of a frozen cut with beam waist position -9 mm and feed rate 0.4 m/min, leading to zero burr. A wide cut kerf is observable. (b): Cut front profiles for two different beam waist positions at identical feed rate 0.7 m/min. (b.1): Beam waist position $+5$ mm, leading to middle-sized burr. (b.2): Beam waist position -6 mm, leading to zero burr.

Secondly, since the annular laser beam has a significantly higher intensity at the edge of the spot, the cut kerf is expected to open earlier compared to a Gaussian-like laser beam, and the beam axis is set back relative to the cut front, see Fig. 12.

As a result, laser power at the rear part of the beam (in front of the beam waist) can propagate through the cut kerf and reaches the bottom part of the cut front. With beam waist close to the bottom of the kerf, the laser intensity is rather high and therefore more material is molten than in case of a positive beam waist position. This conclusion is supported by an analysis of the cut front profile along the sheet thickness. As shown in Fig. 11(b), the cut front evolves much steeper in case of a deep beam waist position. The resulting elevated melt film temperature is expected to reduce the viscosity of the melt film as well as to prevent melt from solidification as burr before being ejected from the kerf as liquid [16].

Our next focus will be to find a method to determine the beam position relating to the cut kerf, which is the prerequisite to calculate the absorption inside the cut kerf. Furthermore, we will study melt dynamics with a highspeed-camera for a deeper understanding of the burr formation process.

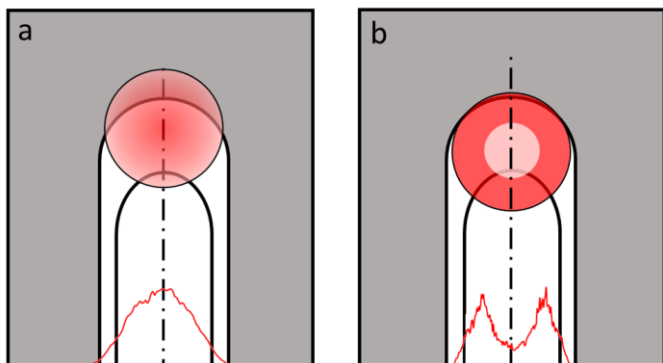


Fig. 12. Position of the laser beam relative to the cut front. (a): A Gaussian-like laser beam. (b): An annular laser beam. Due to the high intensity at the edge of the laser beam, the cut kerf is opened earlier with the annular intensity distribution, i.e. the beam axis is set back compared to the Gaussian-like beam.

6. Conclusion

The presented cutting experiments prove that burr free cuts in 10 mm stainless steel can be achieved with a solid-state laser if an annular intensity profile created by the axicon telescope is used. However, the optimal process parameters for burr free cuts differ from those for minimal surface roughness. Generally, burr is minimized with beam waist positions close to the bottom of the sheet, while the roughness is minimal if the beam waist lies at the upper surface or even above.

An analysis of the cut kerf geometry indicates that the burr reduction is probably indirectly achieved by a wider kerf and a steeper cut front rather than a direct result of the annular intensity profile. Due to the wider cut kerf, gas inflow and thus melt ejection are supposed to be improved. The steeper cut front implicates that more laser power reaches the lower part of the cut front, which prevents the melt from solidification before being released from the cut flank.

To prove these assumptions, further research including simulations of the absorbed intensity as well as in-situ studies of the melt flow dynamics and the burr formation process with a high-speed camera will be necessary.

References

- [1] OPTECH CONSULTING, "2018_laser_market_data," 11 April 2019. [Online]. Available: http://www.optech-consulting.com/html/2018_laser_market_data.html.
- [2] R. Wilfried, D. Michael, M. Goede, S. Michael und K. Dilger, „Three-beam laser brazing of zinc-coated steel,“ *he International Journal of Advanced Manufacturing Technology*, Nr. 90, pp. 317-328, 2017.
- [3] M. Jenne, D. Flamm, O. Taoufiq, J. Hellstern, J. kleiner, D. Grossmann, M. Koschig, M. Kumkar and S. Nolte, "High-quality tailored-edge cleaving using aberration-corrected Bessel-like beams," *Optics letters*, vol. 13, no. 43, pp. 3164-3167, 2018.
- [4] L. D. Scintilla, L. Tricarico, A. Mahrle, W. Andreas, T. Himmer und E. Beyer, „A comparative study on fusion cutting with disk and CO2 lasers,“ *International Congress on Applications of Lasers & Electrooptics Vol.2010.No.1*, pp. 249-258, 2010.
- [5] J. Powell, D. Petring, J. Pocorni und A. Kaplan, LIA Guide to high power laser cutting, Laser Institute of America, 2017.
- [6] F. Olsen, „An evaluation of the cutting potential of different types of high power lasers,“ *International Congress on Applications of Lasers & Electro-Optics. Vol.2006. No. 1.*, p. 401, Oct 2006.
- [7] W. Schulz, D. Petring, F. Schneider und M. Niessen, „Method for material removal and device for carrying out said method“. WO Patent WO2008145311A1, 04 Dec 2008.
- [8] M. R. Maina, Y. Okamoto, A. Okada, M. Narhi, J. Kangastupa und J. Vihinen, „High surface quality welding of aluminum using adjustable ring-mode fiber laser,“ *Journal of Materials Processing Technology*, pp. 180-188, 2018.
- [9] A. S. Desyatnikov, L. Torner and Y. S. Kivshar, Optical vortices and vortex solitons, arXiv preprint nlin/0501026, 2005.
- [10] B. Peres-Garcia, A. Yepiz, R. I. Hernandez-Aranda, A. Forbes und G. A. Swartzlander, „Digital generation of partially coherent vortex beams,“ *Optics Letter*, pp. Vol. 41, No. 15, 1 August 2016.
- [11] Y. Chen, F. Wang, C. Zhao und Y. Cai, „Experimental demonstration of a Laguerre-Gaussian correlated Schell-model vortex beam,“ *Optics express*, pp. 5826-5838, 10 March 2014.
- [12] R. W. Gerchberg und W. O. Saxton, „A practical algorithm for the determination of phase from image and diffraction plane pictures,“ *Optik 35*, pp. 237-246, 1972.
- [13] J. H. McLeod, „The axicon: a new type of optical element,“ *JOSA 44, no 8*, pp. 598-597, 1954.
- [14] B. Vladimir, A. Forbes, N. Kazak, N. Khilo und P. Ropot, „Bessel-like beams with z-dependent cone angles,“ *Optics express 18(3)*, pp. 1966-1973, 2010.
- [15] O. Bocksrocker, P. Berger, B. Begaard, V. Rominger und T. Graf, „Characterization of the melt flow direction and cut front geometry in oxygen cutting with a solid state laser,“ *Journal of Laser Applications*, p. 022202, 15 May 2017.
- [16] E. A. Brabdes und G. B. Brook, Smithells Metals Reference Book 7th Edition, London, UK: Butterworth-Heinemann, 2013.

11th CIRP Conference on Photonic Technologies [LANE 2020] on September 7-10, 2020

Effect of reduced ambient pressure and atmospheric composition on material removal mechanisms of steel and aluminum by means of high-speed laser processing

Peter Hellwig^{a*}, Klaus Schrickler^a, Jean Pierre Bergmann^a

^aTechnische Universität Ilmenau, Department of Production Technology, Gustav-Kirchhoff-Platz 2, 98693 Ilmenau

* Corresponding author. Tel.: +49-3677-69-3866; fax: +49-3677-69-1660. E-mail address: info.fertigungstechnik@tu-ilmenau.de

Abstract

Balancing processes require highly precise mass corrections especially in case of high-speed turning rotors. Material removal by means of cw-mode laser radiation represents a novel approach for industrial balancing applications in order to achieve sufficient removal rates. Thereby, spatter formation was identified as primary removal mechanism. In this study, the effect of reduced ambient pressures and atmospheres with varying concentrations of argon, nitrogen and oxygen on spatter formation and loss of mass were investigated for AISI304 (1.4301, X5CrNi18-10) and EN AW-2618 (DIN 3.1924) under the use of a 400W single mode-fiber laser.

© 2020 The Authors. Published by Elsevier B.V.

This is an open access article under the CC BY-NC-ND license (<http://creativecommons.org/licenses/by-nc-nd/4.0/>)

Peer-review under responsibility of the Bayerisches Laserzentrum GmbH

Keywords: material removal; reduced ambient pressure; atmospheric composition; spatter formation;

1. Introduction

High-speed rotating rotors require unbalances approaching zero. Due to that, mass corrections have to be set very precisely. The application of laser based material removal instead of conventional chipping methods represents an innovative approach in this context. Compared to ablation methods, the cycle time can be shortened by means of cw-mode laser radiation due to higher removal rates. Responsible for this advantage is the difference in the removal mechanism, which is primarily based on ejections of the melt pool (spatters) when cw-mode laser radiation in combination with high processing speeds is applied. This is already well known in remote welding applications, e. g. for cutting thin electrical sheets, relying on this removal mechanism [1-3].

In general, spatter formation occurs if a local volume of melt is exposed to a certain amount of momentum perpendicular to the melt surface to leave the melt pool [4]. The extraction of a

single spatter requires the kinetic energy of the fluid element in the melt to be greater than the sum of the kinetic energy of the droplet and the surface energy of the melt (see Eq. 1) [5]. This is represented by the density of the melt ρ , droplet volume V_{dr} , velocity of the fluid element v_{fl} , velocity of the droplet v_{dr} , surface tension σ and droplet surface area O_{dr} . The parameters are determined by the characteristics of the material and the process, whereby some factors can be significantly influenced.

$$\rho V_{dr} |\vec{v}_{fl}|^2 > \rho V_{dr} |\vec{v}_{dr}|^2 + 2\sigma O_{dr} \quad (1)$$

The velocity of the melt flow strongly depends on the welding speed as shown in [6]. It should be noted that the velocity of the melt flow is significantly higher than the welding speed due to the pressure exerted on the melt by the vaporized material of the keyhole front wall [4, 7]. Therefore, increasing processing speeds lead to high flow velocities in the melt pool and support the formation of melt ejections. By striving to

achieve maximum processing speeds at several hundred meters per minute, the formation of melt ejections can be increased strongly.

In addition, such high welding speeds lead to changes of the keyhole wherefore the characteristic cylindrical model of a vertical keyhole is no longer valid [4, 8, 9]. Already at welding speeds of 20 m/min, a huge enlargement of the keyhole in feed direction occurs due to the increased inclination of the keyhole front wall [9-11]. Thereby, the changed reflection conditions of the laser beam at the front wall leads to a significant reduction of the penetration depth. When it comes to processing speeds up to a several hundred meters per minute, there is a change in the welding regime. Up to welding speeds of 200 m/min, deep penetration welds with an unintentionally blow out of the melt are produced, while further increased welding speeds lead to decreased penetration depth and the generation of cut kerfs starts [3]. *MUSIOL, 2015* attempted to create a model of the fusion zone at these high processing velocities. It was assumed that the recoil pressure, resulting from the vaporized material at the front wall, accelerates the melt upwards the side walls and along the bottom of the resulting kerf. According to Equation 1, these high velocities cause a high amount of spatter to be released from the melt pool.

Besides the velocity of the fluid element, surface tension of the melt has a decisive impact on spatter formation (see Equation 1). It is well known that the appearance of oxygen as well as an increased temperature leads to a reduction of surface tension, which in turn causes a change of fluid flow pattern, e. g. Marangoni convection [12]. This affects the heat transport of the laser energy in the weld pool, which is responsible for the formation of the resulting fusion zone [13]. In the context of the high processing speeds and the aim of primarily generating melt pool ejection, this aspect is regarded as subordinate. Studies, which investigated the influence of argon atmospheres compared to atmospheric conditions in fiber laser welding focused on penetration and surface appearance [13-15]. Therefore, no information on spatter formation is provided for sheet welding.

Furthermore, it can be assumed that a reduction of the atmospheric pressure can affect surface tension as well, due to the presence of less oxygen particles in the atmosphere. At the same time, numerous properties of the material are affected, too. On the one hand, the evaporation temperature is significantly reduced. This exemplarily shown for pure iron, whereby the evaporation temperature drops by more than 1,000 K between ambient pressure (approx. 1,000 mbar) and 0.1 mbar [16]. This also leads to a lowering of the critical intensity threshold, which is required for creating the keyhole [17]. Additionally, the density of metal vapor and atmosphere in the beam path is reduced due to the lowered ambient pressures. This leads to less absorption and scattering of the laser beam directly above the keyhole compared to atmospheric conditions [7, 18]. Besides these effects, a reduction of spatter formation is a well-known effect in this context, as shown in several studies [7, 17, 19]. This is attributed to the interaction of reduced melting and evaporation temperature, preceding melt pool size as well as changed pressure conditions of the keyhole [17].

At this point, it can be stated that the fundamental effects on spatter formation during laser beam welding are sufficiently known, whereby no sufficient knowledge for processing at high welding speeds under varied ambient conditions is provided. However, these parameters would allow the specific adjustment of spatter detachment in order to increase the economic efficiency of balancing processes.

In this paper, investigations regarding the influence of reduced ambient pressure and varied atmospheric composition on the resulting loss of mass while processing AISI 304 and EN AW-2618 with welding speeds of 600 m/min are carried out. Besides the determination of loss of mass, investigations on micro-sections and scanning electron microscope (SEM) images of the resulting surfaces, high-speed recordings give a further characterization of the resulting spatter formation.

2. Experimental design

The experiments were carried out with stainless austenitic steel sheets of AISI 304 (1.4301, X5CrNi18-10) and EN AW-2618, each with a thickness of 3 mm. In order to realize the relative motion between the laser beam and the work piece of up to 600 m/min, a 400 W single mode fiber laser (TruFiber 400, Trumpf, $\lambda = 1070$ nm) in combination with a galvanometric scanner (PFO20, Trumpf) was used. The technical data of the laser and scanning system are summarized in Table 1. The laser power was set to 320 W for all experiments, so that a laser beam intensity of approximately $1.5 \cdot 10^8$ W/cm² resulted.

Table 1. Technical data of the laser and scanning system.

technical data of laser and scanning system	values
wavelength [nm]	1070
operation mode of the laser beam	cw
focal diameter - calculated [μ m]	16,5
max. laser power on work piece [W]	320
max. scan speed [m/min]	600

For the determination of the resulting loss of mass, the weighing of the specimens was carried out using a precision balance (Sartorius ME 235S). The samples were weighed before and after the laser process. In each case, this is preceded by a two-stage cleaning procedure in an ultra-sonic bath with acetone and isopropyl alcohol. This cleaning procedure was applied due to the high resolution of 0.01 mg of the balance. For the observation of the melt pool ejections, high-speed recordings were carried out using a Photron Fastcam SA-X2 with Navitar 12x ZoomLens objective was used. The process was then illuminated by the Cavilux HF system with pulsed laser energy ($\lambda = 808$ nm). A matching band-pass filter was implemented into the optical path of the camera. The high-speed recordings were carried out at a recording rate of 90 kHz. A schematically view of the experimental setup is given in Figure 1. In order to adjust the different atmospheric conditions, the experiments took place inside a vacuum chamber. For applying the reduced ambient pressures, the chamber was vacuumed until the desired value is reached. To achieve the different atmospheric compositions, the chamber

was vacuumed until a minimum ambient pressure of approx. 5 mbar. Subsequently it was flooded with the adjusted gas mixture, which was generated by means of a gas mixing system (Witt-Gasetechnik Ltd.). In order to determine the actual oxygen concentration in the working area, a Zirox oxygen measurement device was used, after the vacuum chamber was flooded with the gas mixture until an atmospheric pressure of approx. 960 mbar was reached.

The sample size n of the respective trial was 3 and is shown in each diagram. The error bars of the diagrams show the corresponding standard deviation of the sample.

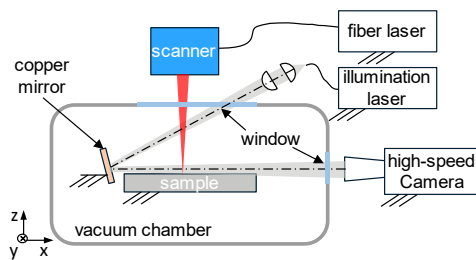


Fig. 1. Schematic depiction of the experimental setup, feed direction of laser beam into the image plane (y -direction).

3. Results and Discussion

3.1. Effect of reduced ambient pressures

In order to determine the effect of reduced ambient pressure on the loss of mass, six different pressures were applied by means of the vacuum chamber (5, 50, 200, 500 mbar). The atmospheric pressure of approx. 960 mbar is used as reference parameter when the vacuum chamber was kept open during the experiments. The specimens of the two test materials were processed within a constant area (16.30 mm^2) to realize the material removal. In this area, 300 single lines with a line spacing of $100 \mu\text{m}$ were performed. Thereby each line was passed by four scans to increase the loss of mass. This approach clarifies the difference in loss of mass between the applied ambient pressures and at the same time reduces the effect of measurement errors due to the weighing. The scanning speed for all trials in the range of this work was set to 600 m/min . This scanning speed in combination with the applied laser beam energy of 320 W is the result of previous studies in which it led to the maximization of the removal rate [20].

The results are depicted in Figure 2a. First, it should be noted that the enormous difference in the achieved loss of mass between the two test materials depends primarily on their density, which differs by a factor of approx. 2.8 [21, 22]. When processing AISI 304, the application of an ambient pressure of 200 mbar leads to the highest reduction of the loss of mass by 27 % compared to the reference process. A further reduction of the ambient pressure leads to no significant change in the loss of mass. This effect is recognizable in the spatter formation, which is depicted in Figure 2b. It can be seen that the number of spatters decrease significantly by reducing the ambient pressure. It should be noted that the footage allows no clear conclusion about a change of the size of the resulting spatters for AISI 304 at this point due to the low depth of focus and the

limited resolution at these high process speeds. However, the process shows a contrary behavior while processing EN AW-2618 by applying reduced ambient pressures. Compared to the reference process, the loss of mass at an ambient pressure of 5 mbar increased by approx. 130 % from 3.52 to 8.25 mg. There seems to be a rising trend of the loss of mass, although the results are widely scattered, e. g. the mean value at 500 mbar deviates from the trend, even though the standard deviation is very high. The pictures from the high-speed recordings also illustrate the trend of a raise in loss of mass (Fig. 2.b). The number of spatters occurring at 5 mbar seems to be increased compared to the reference process at 960 mbar. Further it can be seen that the spatters change from a disorderly and edged shape to a more spherical shape at reduced pressure, like it can be seen in Figure 2b (right). This effect probably can be attributed to a higher surface tension of the melt. At reduced ambient pressures there is correspondingly less oxygen, which has a significant increasing influence on the surface tension. The higher the surface tension, the greater the internal forces of attraction of a fluid element, which basically aims to form the smallest possible surface. This could be taken as an explanation for the more spherical shape of the spatters. In addition, the resulting burr, which consists of re-solidifications of the out blowing melt, seems to be smoother compared to the reference process, which is clearly visible for the aluminum. The higher surface tension also could explain the decrease in loss of mass at AISI 304, regarding Equation 1.

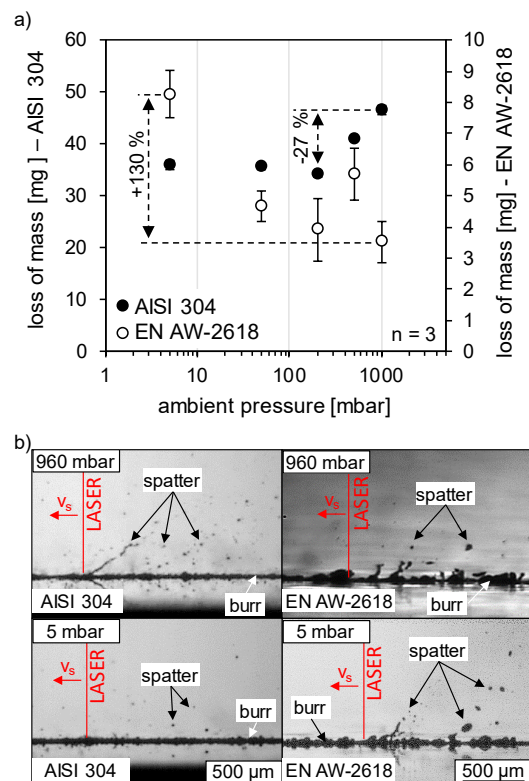


Fig. 2. (a) Effect of ambient pressure on loss of mass; (b) Footage of spatter formation during fourth pass for atmospheric condition (top) and 5 mbar (bottom) for AISI 304 and EN AW-2618.

Micro sections enable a more detailed examination of the resulting fusion zone and can assist in understanding the

removal mechanism. Because of its characteristic formation, the fusion zone from here will be referred to as a kerf in the further context of this work. Figure 3a depicts the resulting kerfs in cross sections for the reference process and the lowest applied ambient pressure of 5 mbar for both test materials. The micro sections and the corresponding analyses (see Fig. 3b) show that the resulting kerf depth at reduced ambient pressures only for the used aluminum alloy follows a similar trend to that already seen in loss of mass (Fig. 2a). There is an increase in kerf depth from 103 μm , at atmospheric pressure, to 143 μm at 200 mbar. No significant change in the resulting kerf depths can be seen for AISI 304. Although, on the base of Figure 2a a decreasing trend with reduced ambient pressures would be expected. The results leads to the assumption that there is a much smaller influence of the reduced ambient pressures regarding the achieved penetration depth like it is shown in the literature [17]. This may due to the much higher welding speeds in this work, which means that the metal vapor produced, could have less impact on the process regarding the beam absorption and scattering. The solidification at the sidewall of each kerf leads to a widely varying width, which is why a clear statement about the kerf width and its correlation to the loss of mass cannot be given reliably.

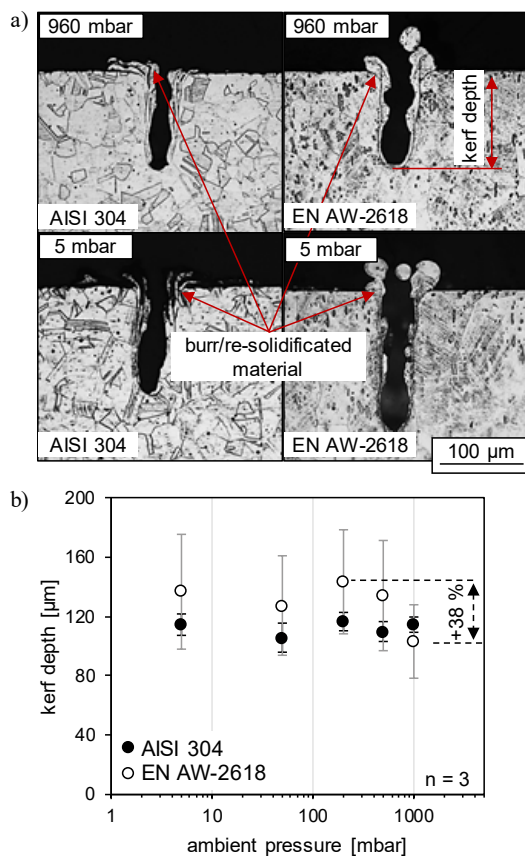


Fig. 3. (a) Effect of reduced ambient pressure on resulting kerf depth after four scans, (b) Comparison of cross sections for atmospheric conditions (top) and 5 mbar (bottom) after four scans

3.2. Effect of different atmospheric composition

In order to examine the difference between the influence of reduced ambient pressures on the one hand and changed

oxygen concentrations on the other hand, the vacuum chamber was filled with specifically adjusted gas mixtures in further investigations. The central issue of that approach was the reduction of the oxygen content in the process surrounding atmosphere to affect the surface tension. By means of a gas mixing system the adjustment of the different oxygen concentrations was done in five steps (0.5, 5, 10, 15, 20 vol.-%). At this point, it should be noted that these values are only target quantities, which cannot be set or reached exactly, respectively. This behavior is caused by the certain deviation of the gas mixing system. For this reason, the respective oxygen contents were measured in every experiment. Therefore, the standard deviation of the oxygen concentration, which can be seen in Figure 4a and Figure 5a, is also provided. For the determination of the loss of mass, the same procedure was used as already described in chapter 3.1.

The results for the loss of mass after the processing of AISI 304 in argon and nitrogen atmosphere with different oxygen concentrations are shown in Figure 4a. An approximately linear connection can be recognized for the argon and the nitrogen atmosphere. The loss of mass decreases with reducing oxygen concentration, whereby the values for the nitrogen atmosphere are consistently higher than the ones for the argon atmospheres. The maximum reduction in loss of mass of 21 % compared to the reference process occurs at an oxygen concentration of 0.4 vol.-% in argon atmosphere.

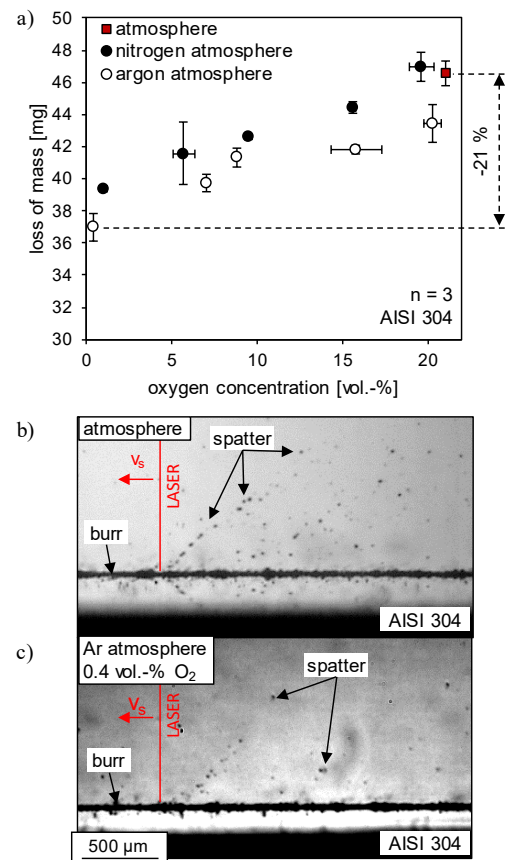


Fig. 4. (a) Effect of reduced oxygen concentrations in argon and nitrogen atmosphere on the loss of mass for AISI 304, (b) high-speed record for normal atmosphere, 4th scan and (c) high-speed record for 0.4 vol.-% O₂ in argon, 4th scan

The snapshots, which are depicted in Figure 4b and Figure 4c confirm this effect. The number of spatters is visibly reduced compared to that which occurs at normal atmosphere. Further, there is a noticeable difference between the loss of mass at normal atmosphere compared to the loss of mass at approx. 20 vol.-% oxygen in argon atmosphere. This leads to the assumption that also the accompanying elements in the atmosphere play a decisive role in spatter formation because the oxygen concentrations differ only very slightly. The negligible difference between the values for the normal atmosphere and the nitrogen atmosphere with approx. 20 vol.-% oxygen confirms this assumption, because of the nitrogen content of about 78 vol.-% in air. An increasing nitrogen content results in a reduction of the surface tension of liquid iron, similar to oxygen but less pronounced [23].

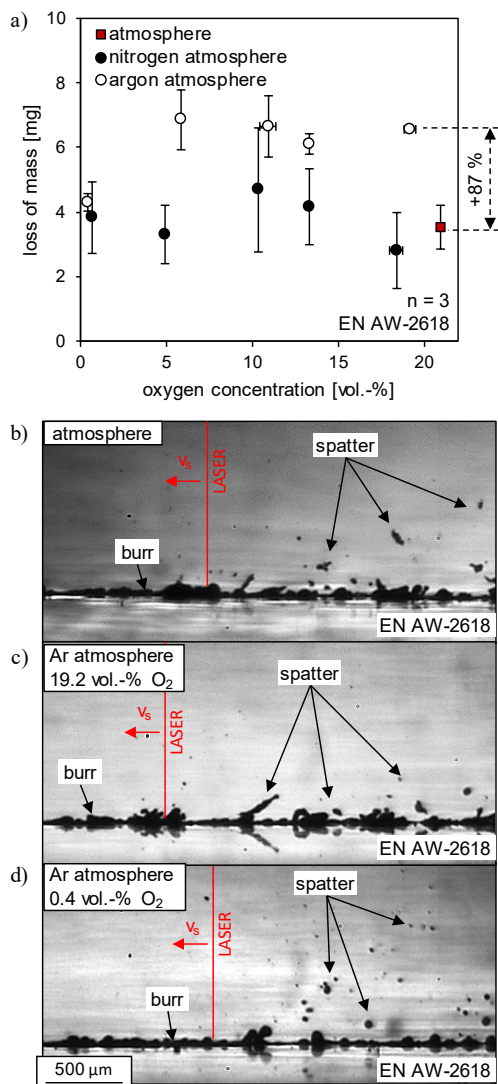


Fig. 5 (a) Effect of reduced oxygen concentrations in argon and nitrogen atmosphere on the loss of mass for EN AW-2618, (b) high-speed record for normal atmosphere, 4th scan, (c) high-speed record for 19.2 vol.-% O₂ in argon, 4th scan and (d) high-speed record for 0.4 vol.-% O₂ in argon, 4th scan

The effect of the different atmospheric compositions on the loss of mass for EN AW-2618 are depicted in Figure 5a. Again, the aluminum shows a contrary behavior regarding the influence of argon and nitrogen atmosphere. The values of the

loss of mass for the argon atmosphere are constantly higher than those generated in nitrogen atmosphere. This trend may be due to the formation of AlN-layers on the melt surface, which have already been observed in [24]. These layers lead to a suppression of the melt flow and thus to a reduction of spatter formation. This may explain the remarkable increase of 87 % in loss of mass, which can be seen at 19.2 vol.-% of oxygen in argon compared to the reference process at a very comparable oxygen content. A further reduction of the oxygen content to 0.4 vol.-% in turn results in a reduction of the loss of mass, which is close to the reference process.

Furthermore, the footages depicted in Figure 5b - Figure 5d shows the effect of the reduced oxygen concentration on the shape of the escaping spatters during the fourth pass. While the spatters in Figure 5b and Figure 5c show a rather disordered and edged shape, in Figure 5d the spatters have a more spherical shape. The same has been observed for the resulting spatters in nitrogen atmosphere. The less oxygen there was in the surrounding atmosphere, the more spherical the spatters were. A similar observation can be made for the formation of the remaining burr. This effect can be attributed to the increasing surface tension with decreasing oxygen content, as already shown in chapter 3.1. The resulting burr, which is visible in the high-speed recordings, leads to the assumption, that the amount of these re-solidifications at the sheet surface could be affected by the different atmospheric conditions. This could be another explanation for the differences in loss of mass beside the amount of spatters, which are leaving the processing zone. A surface characterization of the processed areas by means of SEM-images is given in Figure 6.

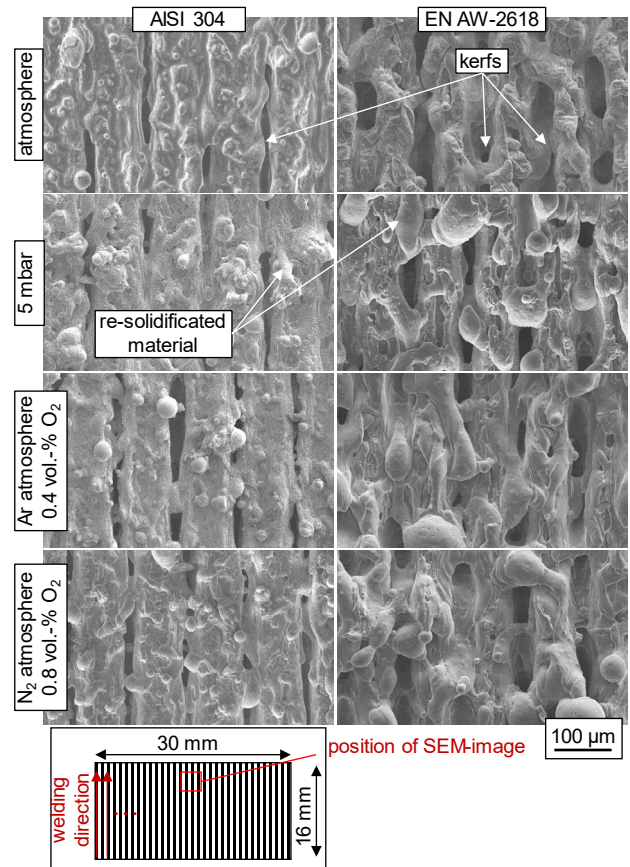


Fig. 6 SEM-images of resulting surface structure of the areal processed specimens for AISI 304 (left) and EN AW-2618 (right) after four scans

However, it is not possible to state differences for the amount of re-solidifications on the surface on the basis of the SEM-images. Merely, it can be seen, that the size of the melt accumulations are significantly bigger for EN AW-2618 compared to AISI 304, which also corresponds to the observations of spatter formation in the high-speed recordings. Particularly in the case of aluminum, it can also be seen that a more rough surface on the re-solidifications results in the reference process, compared to the surfaces generated under the adjusted environmental conditions (see Fig. 6, right). Further investigations on the surface appearance might give a deeper understanding regarding the effects on surface tension of the melt.

4. Conclusion

In this paper, the effect of reduced ambient pressures and different atmospheric composition on the loss of mass while remote laser welding with scanning speeds of 600 m/min was examined. For both processed materials in the present study, the following conclusions can be drawn for the applied conditions:

1. The loss of mass while processing EN AW-2618 can be increased of up to 230 % in a reduced ambient pressure of 5 mbar. For AISI 304 a decrease of about 27 % was observed. This contrary behavior could be due to the different material properties such as viscosity of the melt and the formation of an oxide layer in aluminum, which leads to changed fluid dynamics and affect the droplet escape conditions.
2. Regarding the different atmospheric compositions, it can be stated that the loss of mass and respectively the spatter formation while processing AISI 304 in argon atmospheres is consistently lower than in nitrogen atmospheres. EN AW-2618 also shows a contrary behavior at this point. The processing in argon atmosphere results in a higher loss of mass (about 87 %) than in nitrogen atmosphere. Further, it seems that the reduced oxygen concentration has more impact on the surface tension than the applied reduced ambient pressures, regarding the shape of the occurring spatters in case of aluminum.

In further investigations, high-speed recordings will be improved regarding the frame rate and the angle of view. E.g. coaxial recordings could be carried out to determine the geometry of the processing zone to provide more information of the removal mechanism. In addition, the application of image processing will be carried out for a deeper understanding of the process. A further separation of the effects of surface tension and reduced ambient pressures on spatter formation will be gained by experiments, considering different alloys and atmospheric compositions.

Acknowledgements

The project on which these results are based was supported by the Free State of Thuringia under the number 2017 FE 9091

and co-financed by European Union funds under the European Regional Development Fund (ERDF).

Furthermore, the authors would like to thank Prof. U. Füssel and Dr. M. Hertel from the Chair of Joining Technology and Assembly at Technische Universität Dresden for supporting the investigations by lending the Zirox oxygen measurement device. We also would like to thank Michael Grätzel for supporting the SEM-measurements.

References

- [1] Wetzig A, et al. Laser remote cutting of metallic materials: opportunities and limitations. in *Industrial Laser Applications Symposium (ILAS 2015)*. 2015. International Society for Optics and Photonics.
- [2] Musiol JD, Remote-Laserstrahl-Abtragschneiden. Vol. 307. 2015: Herbert Utz Verlag.
- [3] Mahrle A, Lütke M, Beyer E. *Journal of Mechanical Engineering Science*, Fibre laser cutting: beam absorption characteristics and gas-free remote cutting. 2010. 224(5): p. 1007-1018.
- [4] Kaplan AFH, Powell J, Spatter in laser welding. 2011. 23(3): p. 032005.
- [5] Hügel H, Graf T. *Laser in der Fertigung: Grundlagen der Strahlquellen, Systeme, Fertigungsverfahren*. Vol. 3. 2014: Vieweg+Teubner, Wiesbaden
- [6] Beck M. *Modellierung des Lasertiefschweißens*. 1996: Teubner.
- [7] Rominger V, Berger P, Hügel H. Effects of reduced ambient pressure on spattering during the laser beam welding of mild steel. 2019. 31(4): p. 042016.
- [8] Kaplan AFH. A model of deep penetration laser welding based on calculation of the keyhole profile. 1994. 27(9): p. 1805.
- [9] Fabbro R. Depth Dependence and Keyhole Stability at Threshold, for Different Laser Welding Regimes. 2020. 10(4): p. 1487.
- [10] Fabbro R. Melt pool and keyhole behaviour analysis for deep penetration laser welding. 2010. 43(44): p. 445501.
- [11] Heß A. Vorteile und Herausforderungen beim Laserstrahlschweißen mit Strahlquellen höchster Fokussierbarkeit. Vol. 71. 2012: Herbert Utz Verlag.
- [12] Wang Y, et al. Modeling of the effects of surface-active elements on flow patterns and weld penetration. 2001. 32(1): p. 145-161.
- [13] Hu Y, et al., Experimental and numerical study on laser keyhole welding of 42CrMo under air and argon atmosphere. 2017. 90(9-12): p. 3555-3565.
- [14] Chowdhury S, Nirsanametla Y, Manapuram M.: *Journal of Mechanical Engineering Science*, Investigation on keyhole mode fiber laser welding of SS 316 in a self-protected atmosphere. 2019. 233(18): p. 6602-6615.
- [15] Yadaiah N, et al. Influence of self-protective atmosphere in fiber laser welding of austenitic stainless steel. 2016. 86(1-4): p. 853-870.
- [16] Honig RE.R. Vapor pressure data for the solid and liquid elements. 1969. 30: p. 285-305.
- [17] Reisinger U, et al. Laser beam welding under vacuum of high grade materials. 2016. 60(3): p. 403-413.
- [18] Shcheglov P. Study of Vapour-plasma plume during high power fiber laser beam influence on metals. 2012.
- [19] Reisinger U, et al. Laser beam welding in mobile vacuum. in *Lasers in Manufacturing*. 2017. Munich.
- [20] Hellwig P, Schrickler K, Bergmann JP. Investigations on material removal mechanisms of steel by means of laser processing for balancing processes. in *Lasers in Manufacturing*. 2019. Munich.
- [21] <http://woite-edelstahl.info/aisi304de.html>.
- [22] <https://www.otto-fuchs.com/werkstoffinformationen/Al-Datenblaetter/>.
- [23] Hirashima N, et al., The effect of surface movements on nitrogen mass transfer in liquid iron. 1995. 26(5): p. 971-980.
- [24] Kawahito Y, et al., High quality welding of stainless steel with 10 kW high power fibre laser. 2009. 14(4): p. 288-294.

11th CIRP Conference on Photonic Technologies [LANE 2020] on September 7-10, 2020

Controlling the kerf properties of underwater laser cutting of stainless steel with 3 mm thickness using an Yb:YAG laser source in nuclear decommissioning processes

Jan Leschke^{a,*}, Benjamin Emde^a, Jörg Hermsdorf^a, Stefan Kaieler^a, Ludger Overmeyer^a

^aLaser Zentrum Hannover e.V., Hollerithallee 8, 30419 Hannover, Germany

* Corresponding author. Tel.: +49-511-2788-279; fax: +49-511-2788-0. E-mail address: j.leschke@lzh.de

Abstract

For nuclear decommissioning, the formation of secondary wastes has to be avoided to minimize the need for water and air filtering. Aiming at the minimization of material loss at cutting assignments, this study deploys an Yb:YAG laser for the underwater laser cutting of AISI304 (SS304) stainless steel samples with a thickness of 3 mm used in a range from 2 to 4 kW. Compressed air and nitrogen are applied as the cutting gases with a maximum of 6 bar. For studying the generation of waste material in the surrounding water, the influence of the process parameters on the kerf properties has been studied. Therefore, the characteristics of the resulting kerfs, particularly the weight loss and the occurring dross, were categorized and classified with respect to the weight loss of the samples. Regarding the application of nuclear decommissioning, a weight loss of more than 95 % compared to conventional saw cutting was obtained due to the formation of adhering dross.

© 2020 The Authors. Published by Elsevier B.V.

This is an open access article under the CC BY-NC-ND license (<http://creativecommons.org/licenses/by-nc-nd/4.0/>)

Peer-review under responsibility of the Bayerisches Laserzentrum GmbH

Keywords: underwater, laser cutting, weight loss, adhering dross, nuclear decommissioning

1. Introduction

Until 2017, more than 600 nuclear reactors were shut down worldwide; in 2018, another six nuclear power plants were closed worldwide. In Germany alone, 21 nuclear power plants are under decommissioning due to Germany's nuclear phase-out till 2020. Regarding decommissioning durations of about 10 to 20 years and over 50 nuclear reactors which are under construction worldwide (plus more than 100 planned), nuclear decommissioning will remain an important task in the coming decades [1, 2].

In Germany, the facilities will be decommissioned by immediate dismantling, i.e. the reactor pressure vessel and its associated components are disassembled in the existing cooling water for radiation protection [1]. For this purpose, processes which are suitable for underwater operation are needed. Since

filtering of the surrounding air and water and especially the storage space in nuclear waste containers are huge cost factors, there is a need for dismantling processes which generate low emissions in terms of particles and aerosols, commonly known as secondary wastes. Additionally, the feasibility of cutting complex geometries is preferable, as it allows an optimized waste storing. Besides conventional cutting techniques like sawing, plasma cutting or water jet cutting, underwater laser cutting has become a tool for nuclear decommissioning, as it offers the possibility of cutting nearly every material with cutting depths depending on the deployed laser power [3].

First studies about underwater laser cutting were carried out in the late 1980s and 1990s using CO, CO₂ and also pulsed YAG lasers [4, 5, 6]. Since the 2000s, fiber guided high power lasers were considered for scientific investigations, allowing for higher flexibility [7, 8]. Studies carried out were focused

towards decommissioning in the field of maritime usage [9, 10] or nuclear applications [11, 12, 13]. In nuclear based studies, where the cutting of stainless steels and zirconium alloys is of primary interest, the focus was on the cutting of high material thicknesses, as well as on the reduction of secondary wastes. Alfillé et al. and Chida et al. used fixed parameters for laser power and gas pressure for their tests with material thicknesses up to 30 mm [6, 8]. The results presented by Chida et al. revealed a slightly lower total weight loss of 93 g/m cutting 14 mm thick SS316L. Though, besides the generation of smaller cutting kerfs resulting from the use of the YAG laser instead of the CO₂, the influences of the process parameters on the resulting kerfs were not discussed [6].

Khan and Hilton compared underwater laser cutting with laser cutting in atmospheric conditions for S275JR C-Mn and SS304 in 6, 12 and 32 mm thickness. The examined average dross height and mass reduction regarding cutting speed and gas pressure, using compressed air as cutting gas. Large dross formations were primarily noticed for S275JR, especially with material thicknesses from 12 mm upwards. The relationship between dross height, mass reduction and the process parameters was no object of research. However, it was pointed out that underwater laser cutting leads to significant benefits regarding mass reduction in contrast to cutting in air [11].

Jain et al. realized nearly no dross adhesion by using oxygen as cutting gas when cutting SS304 in 6 mm thickness. The dross formation is lower when cutting underwater instead in air [13].

Regarding the generation of aerosols by underwater laser cutting, Peillon et al. discovered a reduction by a factor of 10 compared to laser cutting processes in air. Furthermore, the investigations revealed that limiting the size of the heat affected zone (HAZ) is beneficial for a further reduction of aerosol emissions. This is realized by using high laser powers combined with high cutting speeds. An additional reduction of the aerosol generation can be achieved by raising the water depth [14].

There have been investigations in atmosphere using DOE methods using similar factors and responses, but due to the different process conditions comparisons to underwater cutting are not feasible [15].

Even though extensive research has been carried out concerning underwater laser cutting throughout the last 30 to 40 years, the mechanisms and relationships between kerf characteristics and process parameters, especially for thin plates which offer potential for low material loss due to adhering dross, have not been fundamentally determined yet. In this paper, an extensive investigation on the kerf characteristics and their formation is carried out with the goal of a better understanding and the ability to control the cutting results to the needs of the respective application. Regarding nuclear applications considering a low weight loss, it needs to be clarified if the focus should lie on the maximization of adhering dross or on the generation of preferably thin cutting kerfs. The study is carried out with SS304 samples of 3 mm thickness, since it allows to spread the parameter range resulting in successful cuts to obtain a variety of kerf characteristics as well as it is a common subject in nuclear decommissioning.

2. Experimental setup

The investigations were accomplished in a water tank with a volume of 1 m³, where SS304 samples are positioned in a clamping system in approx. 0.7 m water depth. The samples have a size of 200 mm x 20 mm x 3 mm. An Yb:YAG laser with a wavelength of 1030 nm and a beam parameter product of 8 mm·mrad is used in a power range from 2 up to 4 kW. The optical system consists of a 200 mm collimation, a 200 mm focusing lens and a fiber with a diameter of 200 μm, which results in a calculated Rayleigh length of 1.25 mm. For more information about the optical system refer to [9]. The focus is positioned on the top surface of the samples. A gantry axis system is utilized to move the optics. The gas nozzle is positioned coaxially to the laser beam and the laser beam is set perpendicularly to the sample surface. Conical nozzles with different outlet diameters were applied.

3. Methodology

The measured amount of lost material m_r , which went into the surrounding water or turned gaseous, is defined as the main target response in this study. It is obtained by weighing the samples before and after applying the cutting tests. The characteristics that define the final weight of the sample are the size of the kerf, the kerf geometry, the amount of adhering dross and the type of dross. As the size of the kerf is difficult to measure, the cut area A is used to determine the kerf size in this study. A is measured by filling the kerfs with acrylic to maximize contrast and then scanning the samples with a flatbed scanner unit. Afterwards, the cut area A is quantified using digital image processing via OpenCV. The amount of adhering dross is calculated taking account of the definitions depicted in Fig. 1.

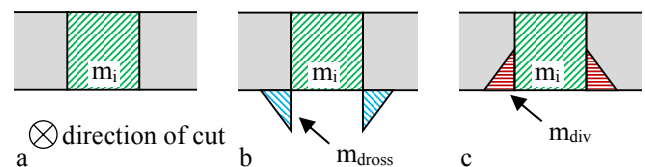


Fig. 1. Schematic transverse cross section of cut samples showing the theoretic cut types supposed in this study (a) 1. ideal cutting result: kerf is orthogonal to the sample surface (m_i , green profile); (b) 2. orthogonal kerf with additional dross on the backside of the sample (m_{dross} , blue profile); (c) 3. orthogonal kerf with missing material on the backside of the sample (m_{div} , red profile)

Fig. 1 points out schematic transverse cross sections of hypothetical cuts showing three different cut types supposed in this study. Fig. 1a shows a theoretic ideal cut: The area of the cut on the top of the sample is the same as the area on the bottom. The weight of the material removed from the sample by the ideal cut is defined as m_i (marked green). Fig. 1b shows an ideal cut with adhering dross (weight m_{dross}) formed on the backside of the sample, leading to a weight difference between m_r and m_i . Fig. 1c shows a diverging kerf or a kerf with missing material on the backside of the sample. The weight of the missing material is defined as m_{div} .

The weight loss of the ideal cut m_i is calculated by

$$m_i = \rho_{SS304} \cdot A \cdot d, \quad (1)$$

with the density of stainless steel ρ_{SS304} ($= 7.9 \text{ g/cm}^3$) and the

material thickness d . Regarding the characteristics in Fig. 1, m_r can be described as

$$m_r = m_i - m_{dross} + m_{div} = m_i - \Delta m, \quad (2)$$

with Δm as the general variation between the measured and the ideal weight loss:

$$\Delta m = m_i - m_r. \quad (3)$$

Regarding formula 3, a positive value of Δm indicates the formation of dross, while a negative value indicates a diverging kerf. As real cutting results are always a combination of both characteristics, Δm shows a tendency towards one or the other. The kerfs are inspected visually for validation and for the classification of the dross type DT. Analyzing the backsides of the kerfs shows three characteristic dross types as well as mixtures of the three of them. The occurring DTs are listed in Fig. 3, including the ball type (Fig. 3c), the line type (Fig. 3b) and inhomogeneous results (Fig. 3a, Fig. 3d).

The classification in the following section combines the kerf characteristics listed in Table 1.

Table 1. Kerf characteristics considered in the study

characteristic	symbol
measured amount of material loss per meter	m_r
amount of adhering dross per meter	Δm
cut area for 140 mm cutting length	A
dross type	DT

For gaining process understanding and qualitative knowledge, including possible two-factor interactions as well as quadratic terms, a definitive screening design (DSD) approach was used via the statistical software jmp® [16]. The benefit of DSD is that the main effects are completely independent from two-factor interactions. Additionally, the quadratic terms are not completely confounded with the two-factor interactions, giving the design a high statistical efficiency.

4. Results and discussions

For the investigations, a close nozzle distance of $d_n = 2$ mm was chosen to allow the implementation of low-level parameter sets. A DSD consisting of 18 runs, covering the factors laser power P_L , cutting gas pressure p , speed v and nozzle diameter \varnothing_n with factor ranges as listed in Table 2 was carried out to identify the fundamental relations between factors and responses.

Table 2. Factor ranges used for the DSD test at a nozzle distance of $d_n = 2$ mm

factor	range of tested values
P_L	2 – 4 kW
p	0.25 – 3.75 bar
v	5 – 15 mm/s (0.3 – 0.9 m/min)
\varnothing_n	1.4 & 2.7 mm

The distance of travel is 140 mm, and air is used as cutting gas. The ranges for the factors were chosen to ensure proper cutting results, since uncut samples cannot be used for the analysis. The resulting active effects determined to be significant at the 0.05 significance level were the cutting gas pressure and the laser power as well as the interaction between the two of them and the cutting gas pressure as a quadratic

effect. All higher-order effects obey strong effect heredity. The residuals do not show significant deviation from the normal distribution. Fig. 2 shows the prediction results for the low and high levels of the active effects and the three responses of interest: the measured weight loss m_r , the adhering dross Δm and the cut area A.

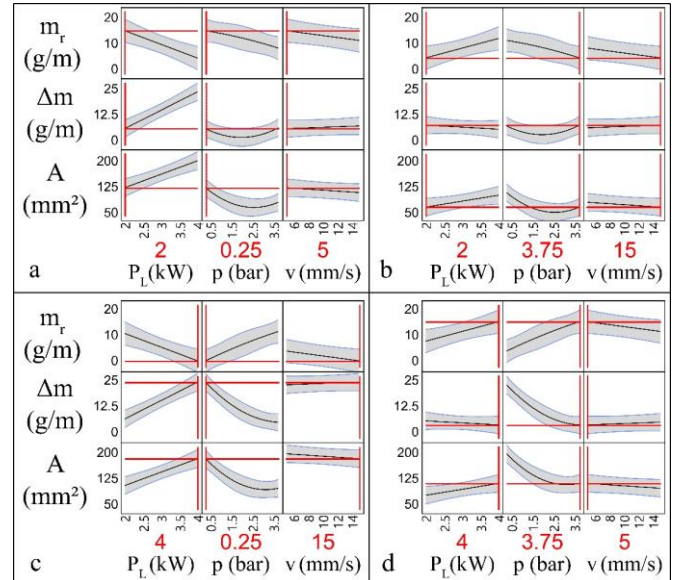


Fig. 2. Prediction results of the fitted model of the DSD at a nozzle distance of $d_n = 2$ mm, (a), (b), (c), (d) effects of the low and high value combinations of the significant factors laser power, gas pressure and speed on the responses. Considered parameter combinations are marked with red lines

Because the cutting speed has a noticeable impact on the cutting result, the effect has also been added to the plots, as its p-value only slightly exceeds the 0.05 significance level with a p-value of 0.062. The red numbers and lines mark the specific parameter set for the factors (x-axis) and the responses (y-axis). The sets are named (a) – (d) in the following, corresponding to the figure. The two-factor interaction between the laser power and the cutting gas pressure gets visible, for example in Fig. 2a and Fig. 2b, where the slope of the relationship between weight loss m_r and laser power P_L changes due to raising the gas pressure value.

Fig. 3 shows the adhering dross and the kerfs in top view as well as response values of corresponding example cuts processed with the parameter sets marked in Fig. 2. The red markers in Fig. 2 show the high and low levels of the factors laser power and cutting gas pressure and the prediction for the three responses. The cutting speed is adjusted to maximize the effect on the weight loss, resulting in four different sets of kerf characteristics.

The parameter set in Fig. 2a includes the high levels of all three factors, where the predicted result is a large weight loss, based on a mid-sized cut area and a low amount of dross. The example kerf in Fig. 3a depicts this scenario showing an inhomogeneous distribution of adhering dross that makes up only about 1.2 g/m and a cut area of over 130 mm². The top surface of the sample shows distinct markings of the exothermic reaction with the oxygen portion contained in the compressed air. The low gas pressure and flow allow the exothermic reaction take place right at the sample. The low

laser power in combination with the burning marks on the top of the sample lead to the conclusion that the cut process mainly works through exothermic energy, causing a relatively large cut area. The high impact of the exothermic reaction in combination with a low cutting speed seems to eject the oxidized and brittle dross directly into the surrounding water.

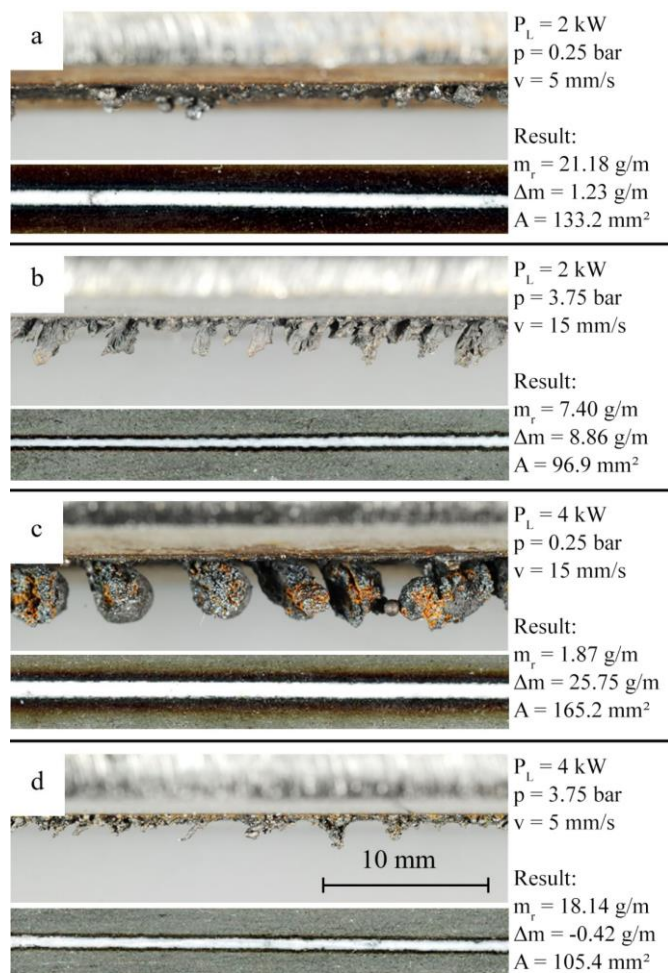


Fig. 3. Occurring dross types (DT), side view and top surface of the kerfs of samples corresponding to the parameter sets of Fig. 2 with responses (a) none/inhomogeneous; (b) line type; (c) ball type and (d) none/inhomogeneous

Parameter set (b) in Fig. 2b consists of the low-level value of the laser power and the high levels of the cutting gas pressure and the cutting speed. The outcome is a moderate amount of adhering dross and a small kerf, which adds up to a relatively low weight loss of around 7 g/m (Fig. 3b). The type of generated dross is homogeneously distributed and line-shaped. Due to the low laser power, a small cut area is generated. The high cutting gas pressure and flow bends the molten material into the line-shaped geometry and also reduces the impact of the exothermic reaction. Marks from the burning gas are barely visible. The high cutting speed supports the formation of dross, as the short impact of the flow allows the melt to solidify at the sample.

Fig. 2c shows the prediction for the high level of the laser power and the cutting speed and the low level of the cutting gas pressure. It results in the highest formation of dross, as it can be seen in Fig. 3c, which is defined as ball type. The amount of

dross sums up to around 25 g/m, leading to lowest weight loss in the investigation, even though the cut area is the largest. Markings of the exothermic reaction are visible, but less pronounced than in Fig. 2a. Similar to parameter set (a), a large cut area is generated, but as the laser power and the cutting speed are high, the impact of the exothermic reaction is reduced and seems to be sufficient to open up the kerf. The ratio between laser and exothermic energy is shifted towards the laser resulting in a more controlled cut. Due to the low gas flow and the high cutting speed, the dross balls are not further affected which allows them to solidify at the backside of the sample.

Parameter set (d), shown in Fig. 2d, utilizes a high laser power and cutting gas pressure, but a low cutting speed. Caused by the combination of high gas pressure and low cutting speed, a huge amount of the melt is ejected into the water, as the slow-moving nozzle and the gas flow do not allow the melt to solidify at the sample. The small amount of dross has line type characteristics, but a sparse and inhomogeneous distribution (Fig. 3d).

The cutting speed v has a linear effect on all parameter combinations, where low speed values result in larger kerf areas and less dross, leading to a higher weight loss. Higher speed values, on the other hand, cause smaller kerfs and larger amounts of dross and consequently less weight loss. This result stands in contrast to the results of Khan and Hilton, who stated that a decrease in speed leads to an increase in adhering dross or dross height, respectively [11]. Possibly, the behavior of the dross changes with higher material thicknesses as in the named study, even though this effect was described as comparatively low and only noticeable with thicknesses above 30 mm for SS304, working in focus.

The nozzle diameter \varnothing_n was not determined as significant effect in this test, even though its impact on the cutting gas pressure, which instead was identified to be significant, and the gas flow is obvious.

The effects of the laser power and the cutting gas pressure are connected via the two-factor interaction caused by the ratio of the exothermic and the laser energy. While a controlled portion of exothermic energy helps the generation of a large amount of dross, too much of it leads to a dross reduction, due to the huge impact of the reaction. This ratio can be controlled by the laser energy, but also by the cutting speed as the duration of the exothermic impact affects the dross formation.

A subsequent investigation shows another factor besides the effects regarding the exothermic reaction: the nozzle distance d_n , which affects the gas flow due to the water density. The test was carried out using a low cutting gas pressure of 0.25 bar, adapting the parameter sets (c) and (a) from Fig. 2, but with an increased nozzle distance of $d_n = 5$ mm. Set (c) shows the same characteristics as in the former study at 2 mm distance and forms out solid ball type dross (Fig. 4a). Fig. 4b shows the result of an example cut with parameter set (a), which completely differs from the result with the lower d_n , since large amounts of ball type dross can be found on the backside of the sample. The lowered amount of air that reaches the sample seems to lower the exothermic reaction affecting the dross. Even though, there is an effect that can be noticed by the brittle formation of the dross, comparable to cuts with oxygen [9]. The

cut in Fig. 4c shows parameter set (c) with nitrogen as cutting gas. As it can be seen, ball type dross is produced, but the kerf is closed again by solidified melt. This shows another mechanism of the exothermic reaction, as it causes the solidifying melt to open up the kerf.

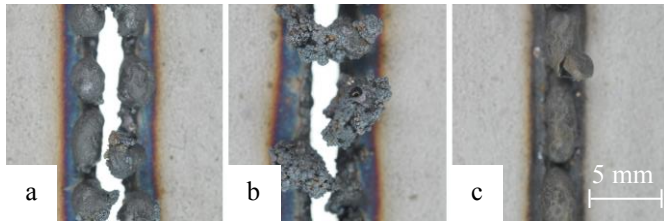


Fig. 4. Different dross examples at a cutting gas pressure of $p = 0.25$ bar and a nozzle distance of $d_n = 5$ mm (a) $P_L = 4$ kW, $v = 15$ mm/s, gas = air: large and solid dross balls; (b) $P_L = 2$ kW, $v = 5$ mm/s, gas = air: large and brittle dross balls; (c) $P_L = 4$ kW, $v = 15$ mm/s, gas = nitrogen: kerf filled with solidified melt, large and solid dross balls

Based on parameter set (c), a study examining the influence of the cutting gas pressure was carried out, keeping the d_n of 5 mm, a laser power of 4 kW and a cutting speed of 15 mm/s. Both air and nitrogen were tested as cutting gases (Fig. 5).

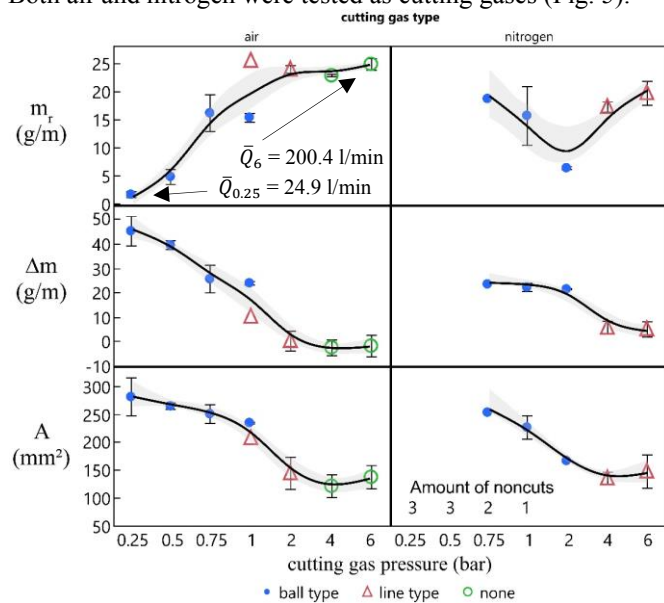


Fig. 5. Influence of the cutting gas pressure on the kerf characteristics, comparing air and nitrogen as cutting gas, with cutting gas flow Q . Parameters: $P_L = 4$ kW, $\varnothing_n = 1.7$ mm, $d_n = 5$ mm, $v = 15$ mm/s, SS304, $d = 3$ mm. Three measurements for each point.

Corresponding to the diagrams in Fig. 2, the figure shows the influence of the cutting gas pressure on the kerf characteristics. The markers in the diagram indicate the dross type as defined in Fig. 3. The resulting cutting gas flow Q lies in a range of around 25 l/min at $p = 0.25$ bar and 200 l/min at $p = 6$ bar.

As expected, using air as cutting gas leads to a low amount of weight loss in the low-pressure range, increasing with the pressure value. The amount of dross and the size of the cut area show the contrary behavior, following the mechanics described above. Table 3 shows the means and standard deviations of eight replications of the best parameter set in terms of low material loss ($p = 0.25$ bar) with air for statistical purposes.

Table 3: Mean and standard deviation with $p = 0.25$ bar and air as cutting gas, eight measurements. Same parameters as used for Fig. 5.

Response	m_r (g/m)	Δm (g/m)	A (mm ²)
Mean	2.33	46.86	294.98
Standard dev.	0.85	3.77	22.89

At a cutting gas pressure of about 0.75 – 1 bar, the process shows some instabilities regarding the weight loss and the resulting dross type. The standard deviation raises and the dross type is at the transition from ball type to line type. At $p = 1$ bar, one of the samples shows line type characteristics, leading to a larger weight loss due to a smaller amount of adhering dross. Further raising the cutting gas pressure leads to smaller kerfs, but also to smaller amounts of adhering dross. This results in a cleaner kerf, but also in a larger amount of material loss. In contrast to the results of the DSD at a nozzle distance of $d_n = 2$ mm, the kerf characteristics for the line dross and the cuts with none or inhomogeneous dross are very similar.

The tests with nitrogen as cutting gas show a substantially different behavior, as there is no exothermic reaction in the process. An obvious difference compared to the tests with air is that low cutting gas pressures lead to unsuccessful cuts, as the solidified dross fills up the kerf again after cutting, as already shown in Fig. 4c. In contrast to the cuts with air, the lack of exothermic energy causes the closure of the kerfs. At $p = 2$ bar, a stable process can be established with comparably low weight loss due to the formation of ball type dross and a relatively small cut area. Further raising p leads to the formation of line dross, even at $p = 6$ bar.

By producing ball type dross even at the larger nozzle distance of $d_n = 5$ mm, parameter set (c) used with air as cutting gas indicates robustness against varying work distances. It also allows for a reduced risk of collisions with the material to be cut as well as of contaminations on the safety glass.

Additionally, focus position variation has been tested at the $p = 0.25$ bar setting with air since it allows for the lowest weight reduction in the presented investigations. The focus positions -1.5 mm (below plate surface), 0 mm (plate surface) and 1.5 mm (above plate surface) have been tested 5 times each with no significant changes in the response means. However, the standard variation increases at all three responses when the focus is positioned above the surface.

It becomes apparent that kerfs displaying ball type dross feature a considerably low weight loss for the given sample thickness, even if the cut area is comparatively large. The generation of a thin kerf by high gas pressure, producing line type dross, interestingly leads to a higher weight loss and spread of potential secondary wastes. This is of high interest for the application in the nuclear decommissioning sector. Since this DT requires only a low cutting gas flow of around 25 l/min, it adds to the profitability of the process by saving gas, but also by lowering the filtering effort for water and air, since the spread of the secondary wastes is reduced. The high cutting speed offers time advantages and possibly positive effects regarding the production of aerosols, as stated by Peillon et al., to a reduced HAZ in combination with high laser powers [14].

For a comparison between the result of the test shown in Fig. 5 and a conventional cutting technique in nuclear

decommissioning, saw cutting allows straightforward calculations assuming ideal cuts as defined in Fig. 1a. The average minimal weight loss reached in the cutting gas test in Fig. 5 at $p = 0.25$ bar with air as cutting gas is 1.6 g/m. Typical saw bands used for decommissioning purposes have a thickness of 1.5 mm, common saw blades typically have a thickness of 4.5 mm. Considering a saw band, at least a volume of 4.5 cm³ is removed from a component with a thickness of 3 mm and a length of 1 m (1.5 mm x 3 mm x 1 m). Assuming SS304 as material with $\rho_{SS304} = 7.9$ g/cm³, the weight loss will be $m_{r, bandsaw} \geq 35.55$ g/m. Considering this value, the weight loss achieved with the laser process is about 95 % lower. Additionally, the laser process offers the opportunity for improved cutting strategies, as the cuts do not have to be linear.

5. Conclusion and outlook

In this study, the relationships between the kerf characteristics, namely the weight loss, the cut area, the amount of adhering dross and the dross type, and the process parameters of the underwater laser cutting process were determined for 3 mm thick SS304 samples. It could be shown that with respect to weight loss reduction, the formation of large, ball type dross is advantageous, as it allows for a weight loss of less than 2 g/m. Its formation is supported by a low cutting gas pressure, high laser power and high cutting speed. This parameter set is also beneficial for nuclear purposes, as the amount of compressed air as cutting gas with 25 l/min is very low. Compared to conventional bandsaw cutting, the laser process offers weight loss advantages of about 95%. If cleaner edges are needed, for example, in repair applications, lower cutting speeds and especially higher cutting gas pressures should be utilized for less dross adhesion and smaller kerfs.

The use of air as cutting gas provides more opportunities for controlling the generated kerfs in terms of the characteristics listed in Table 1. Nitrogen can be useful, if exothermic reactions need to be avoided, even though it needs to be used at higher pressures and flow rates.

Since the underwater process inherits more losses than processes in air, it is necessary to gain knowledge about the process zone for a more exact control of the cutting results. For a better understanding of the losses in laser power and cutting gas pressure/flow due to the surrounding water, further studies on their impact at the sample surface as well as the reached laser intensity are in progress at the LZH. It includes the verification of a transfer of the results of Peillon et al. regarding a decreased production of aerosols, when working with high cutting speeds and laser powers [14].

Acknowledgements

The investigations were carried out in the project "AZULa – Automatisierte Zerlegung von Reaktordruckbehältereinbauten mit Hilfe von Unterwasser-Lasertechnik" (01.09.2018 – 31.08.2020). The research project (FKZ 15S9408) was supported from the budget of the Federal Ministry of Education and Research through the Gesellschaft für Anlagen- und Reaktorsicherheit (GRS) gGmbH. We would like to thank all funding organizations.

Supported by



Federal Ministry
of Education
and Research

References

- [1] B. Brendebach, G. Bruhn, M. Dewald, H. May, S. Schneider and T. Stahl, "Stilllegung kerntechnischer Anlagen," Gesellschaft für Anlagen- und Reaktorsicherheit (GRS) gGmbH, 2017.
- [2] Nuklearforum Schweiz, "nuklearforum.ch," 2019. [Online]. Available: https://www.nuklearforum.ch/sites/default/files/page/Kernkraftwerke_der_Welt_2019.pdf. [Accessed 15 03 2020].
- [3] J. Kaulard, B. Brendebach and E. Strub, "Strahlenschutzaspekte gängiger Abbau- und Dekontaminationstechniken," Gesellschaft für Anlagen- und Reaktorsicherheit (GRS) gGmbH, 2010.
- [4] F.-W. Bach, H. Haferkamp, T. Vinke and H.-P. Wendorff, "Laser beam cutting under water - procedure, use, development," in *2nd European Conference on Laser Treatment of Materials*, Bad Nauheim, 1988.
- [5] G. Takano, S. Beppu, O. Matsumoto, N. Sakamoto, T. Onozawa, M. Sugihara and K. Miya, "Development of Cutting Technique of Reactor Core Internals by CO Laser," in *ICONE JSME/ASME Joint International Conference on Nuclear Engineering*, Kyoto, 1995.
- [6] J. P. Alfillé, G. Pilot and D. de Prunelé, "New pulsed YAG laser performance in cutting thick metallic materials for nuclear applications," *Proc. SPIE 2789, High-Power Lasers: Applications and Emerging Applications*, pp. 134-144, 1996.
- [7] H. Okado, T. Sakurai, J. Adachi, H. Miyao and K. Hara, "Underwater cutting of stainless steel with the laser transmitted through optical fiber," *Proc. SPIE 3887, High-Power Lasers in Civil Engineering and Architecture*, pp. 152-160, 2000.
- [8] I. Chida, K. Okazaki, S. Shima, K. Kurihara, Y. Yuguchi and I. Sato, "Underwater cutting technology of thick stainless steel with YAG laser," *Proceedings of SPIE, First International Symposium on High-Power Laser Macroprocessing*, no. 4831, pp. 453-458, 2003.
- [9] J. Leschke, A. Barroi, S. Kaielerle, J. Hermsdorf and L. Overmeyer, "Studies on the robustness of underwater laser cutting of S355J2+N using a Yb:YAG disk laser source," *Physics Procedia*, no. 83, pp. 310-316, 2016.
- [10] J. Leschke, A. Barroi, B. Emde, S. Kaielerle and J. Hermsdorf, "Investigations on underwater laser cutting for decommissioning of marine constructions," in *Conference on Maritime Energy (COME)*, Hamburg, 2017.
- [11] A. Khan and P. Hilton, "Optimisation of Underwater Laser Cutting for Decommissioning Purposes," in *ICALEO 2014 Congress Proceedings*, San Diego, 2014.
- [12] P. D. Gupta, "Laser Applications in Indian Nuclear Power Programme," *Energy Procedia*, no. 7, pp. 560-576, 2011.
- [13] R. K. Jain, D. K. Agrawal, S. C. Vishwakarma, A. K. Choubey, B. N. Upadhyaya and S. M. Oak, "Development of underwater laser cutting technique for steel and zircaloy for nuclear applications," *Pramana - journal of physics*, vol. 75, no. 6, pp. 1253-1258, 2010.
- [14] S. Peillon, S. Fauvel, C. Chagnot and F. Gensdarmes, "Aerosol Characterization and Particle Scrubbing Efficiency of Underwater Operations during Laser Cutting of Steel Components for Dismantling of Nuclear Facilities," *Aerosol and Air Quality Research*, vol. 17, pp. 1463-1473, 2017.
- [15] H. Wahab and J. Gröninger, "Optimization of Laser Cutting Quality with Design of Experiments," *Laser Technik Journal*, vol. 11, no. 5, pp. 27-31, 2014.
- [16] B. Jones and C. J. Nachtsheim, "A Class of Three-Level Designs for Definitive Screening in the Presence of Second-Order Effects," *Journal of Quality Technology*, pp. 1-15, 2011.

11th CIRP Conference on Photonic Technologies [LANE 2020] on September 7-10, 2020

Real-time monitoring of fiber laser cutting of thick plates by means of photodiodes

Nikita Levichev*, Gonçalo Costa Rodrigues, Joost R. Duflou

Department of Mechanical Engineering, KU Leuven, Celestijnenlaan 300B, Heverlee 3001, Belgium, Member of Flanders Make

* Corresponding author. Tel.: +3216377434. E-mail address: nikita.levichev@kuleuven.be

Abstract

Adaptive real-time monitoring and control is a natural solution for automated unmanned laser cutting that has been intensively studied for the last decades. However, sensor solutions for laser cutting are rarely used in practice. In this paper, a coaxial photodiode-based monitoring system has been developed and investigated for 4 kW fiber laser cutting of mild and stainless steel thick plates. Based on the obtained results, the feasibility of industrial application of the implemented setup is discussed.

© 2020 The Authors. Published by Elsevier B.V.

This is an open access article under the CC BY-NC-ND license (<http://creativecommons.org/licenses/by-nc-nd/4.0/>)

Peer-review under responsibility of the Bayerisches Laserzentrum GmbH

Keywords: Laser cutting; Fiber laser; Sheet metal; Process monitoring; Optical sensor

1. Introduction

Laser cutting is a well-established industrial process for sheet metal applications. However, cutting of thick plates is still a problem because of the characteristic limited process parameter window. Adaptive real-time monitoring and control is a natural solution but the majority of previous studies were focused on the design of monitoring systems for CO₂ laser cutting using acoustic sensors [1], photodiodes [2] or camera systems [3]. Nowadays, cutting by means of fiber lasers has become dominant and, therefore, tailored solutions are required in such systems for industrial applications.

Real-time monitoring systems have been widely investigated for a variety of laser processes [4], such as laser welding [5], additive manufacturing [6] and laser cladding [7]. In contrast to other processes, monitoring solutions for laser cutting are scantily presented in the literature, especially for near-infrared lasers. A photodiode-based cutting interruption sensor has been introduced [8] and evaluated for burr formation detection for cutting steels in the thickness range of up to 3 mm [9]. Furthermore, a cross-correlation algorithm for an InGaAs and Si photodiode-based sensor system that allows detection of

cut interruption has been reported in [10]. A coaxial photodiode-based monitoring system has been implemented for piercing optimization [11]. Optical pyrometry has been used in order to detect the fluctuations of the brightness temperature of the cutting front [12]. An optical setup, based on two Si photodiodes collecting radiation from both sides of the plate, has been presented for in-situ quality assurance [13].

The development of a robust real-time monitoring system could become an important step forward towards fully automated laser cutting. The information obtained from this monitoring system could be used as input for a control system that adapts the cutting parameters during the process [14].

As already mentioned, the laser cutting of thick plates (≥ 10 mm) differs from the processing of thin sheets. The dimensions and dynamics of the cutting front are significantly different. At the same time, the cut quality by way of the equilibrium between process parameters is highly sensitive to the process fluctuations, e.g. thermal focus shift, deviations in thickness, material microstructure and chemical composition.

Within this paper, a developed coaxial photodiode-based monitoring system is investigated in depth for fiber laser cutting of 15 mm mild steel plates. Quality deteriorations

caused by speed changes as well as by the heat accumulation effects are examined. Moreover, experiments with both stainless steel and mild steel for different plate thicknesses have been performed. Eventually, the feasibility of industrial application of the implemented monitoring setup is discussed.

2. Experimental setup

2.1. Laser cutting

The experiments were performed on a commercial 2D flat-bed laser cutting machine with a 4 kW IPG Ytterbium multimode fiber laser source emitting at 1.07 μm wavelength. The laser beam is delivered from a 100 μm core optical fiber into a Precitec ProCutter laser head equipped with a 200 mm focusing lens and a 100 mm collimation lens. The beam parameter product and the beam waist diameter were measured by means of an Ophir BeamWatch device as 2.84 mm mrad and 224 μm , respectively.

Table 1 provides the chemical composition of the hot rolled 15 mm mild steel plates used during the experiments according to the Certificate 3.1 (DIN-EN-10204). Three grades with different characteristics were selected, such as S355MC, both standard as well as pickled and oiled, which have the same chemical composition, and Ympress 250C laser quality. In order to test the monitoring system, thinner S355MC mild steel and 304L stainless steel plates were used as well.

Table 1. Chemical composition (wt. %) of the 15 mm plates being used.

Grade	C	Mn	Cu	Cr	Ni	Al	Si	Fe
S355MC	0.057	1.31	0.036	0.021	0.017	0.040	0.012	rest
Ympress 250C	0.148	0.90	0.016	0.025	0.017	0.043	0.004	rest

Table 2 lists process parameters obtained from the machine supplier that were used for cutting experiments. As an assist gas, oxygen of 99.95 % and nitrogen of 99.999 % purity were used for cutting of mild and stainless steel, respectively. The cutting was performed with a laser power of 4 kW and a duty cycle of 100 %.

Table 2. Process parameters for material-thickness combinations being used.

Parameter	Mild steel 8 mm	Mild steel 10 mm	Mild steel 15 mm	Stainless steel 10 mm
Speed [mm/min]	2000	1700	1100	1000
Focus position [mm] (positive is above the plate)	+4.5	+4.5	+5.5	-9.3
Nozzle diameter [mm]	1.2	1.2	1.5	3.5
Assist gas pressure [bar]	0.5	0.5	0.6	16
Stand-off distance [mm]	1.2	1.2	1.2	0.4

2.2. Monitoring system

A coaxial monitoring setup, schematically represented in Fig. 1, was built by replacing a conventional laser head mirror by a dichroic one that transmits towards the sensor the radiation with a wavelength shorter than 800 nm and longer than 1200 nm as schematically shown in Fig. 2. Then, a diaphragm

with a diameter of 1.5 mm was used to decrease the optical aberrations after the laser head optics designed for the laser beam wavelength. After the diaphragm, an OD 6 notch filter was placed to remove the scattered and reflected laser radiation, which is significantly higher than the thermal radiation from the process zone, even after passing the dichroic mirror.

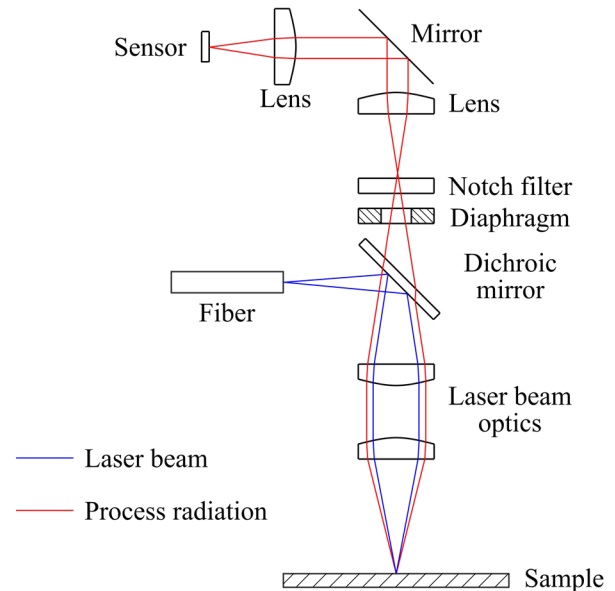


Fig. 1. Optical setup for monitoring system.

During cutting, the temperature of the process zone is higher than the melting point of steel, which is typically around 1800 K, resulting in maximum emission between 800 nm and 2000 nm according to Planck's law. Two types of photodiodes, the responsivity of which is shown in Fig. 2, were found suitable for this range: a Si photodiode, mainly sensitive in the visual spectral range from 350 to 1100 nm, and an InGaAs photodiode, responsive to the near-infrared radiation with wavelengths from 800 to 1700 nm. Since the radiation peak of the process temperatures is around 1500 nm, an InGaAs photodiode (FGA21) was selected.

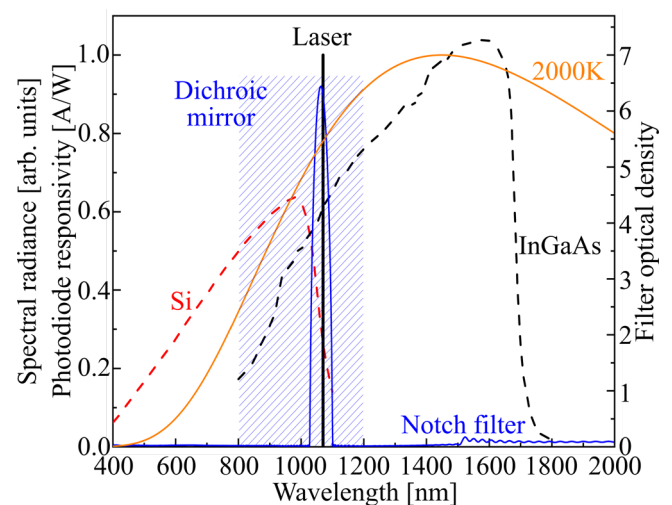


Fig. 2. Spectral characteristics of the setup: responsivity of photodiodes, optical density of the notch filter, spectral radiance of a black body with 2000 K. The laser wavelength and the non-transmitting zone of the dichroic mirror are shown approximately.

The photodiode signals were recorded by means of a data acquisition card with a sample rate of 50 kHz. Appropriate signal amplification and low pass filtering were applied. The obtained data were processed in MATLAB using a moving average to reduce the noise.

The cutting process was also analyzed by means of a Xenics Bobcat-3754 infrared camera that replaced the photodiode in the monitoring setup. An integration time of 50 μ s and a frame rate of 40 fps were used for the recordings.

2.3. Evaluation methods

A Keyence Digital Microscope VHX-6000 was used for high-resolution imaging of cut edge profiles. The surface roughness of cut edges (R_z) was measured by means of a Mitutoyo Formtracer CS-3200 using a Gaussian filter with a sample length of 2.5 mm and a cut-off of 0.008 mm. The measurements of each specimen were performed for five lines with an evaluation length of 12.5 mm. The measuring lines were spaced by 3.25 mm starting at 1 mm from the top surface. The average roughness value was calculated as a mean value of these five measurements.

3. Results and discussion

The photodiode signal during both piercing and cutting of a line is shown in Fig. 3. The full penetration has been achieved after three laser pulses and is accompanied by a significant drop of the signal. Although the laser was still on for a second after the full penetration, passing some energy to the plate, the signal dropped to a much lower value. The piercing end is characterized by reaching a negligible level of the signal. The cutting is described by a constant but noisy signal. In addition to the measurement noise, increased due to the signal amplification, there is the process noise caused by the melt flow dynamics of the cutting front [15]. In order to reduce the noise, the signal was smoothed by means of a Savitzky-Golay filter resulting in the processed signal which was used for further evaluation and comparison of all experiments.

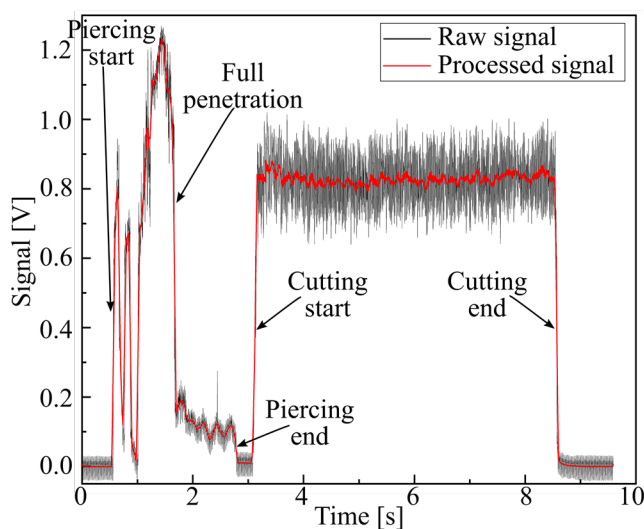


Fig. 3. Photodiode signal during piercing and cutting of a 15 mm S355MC plate.

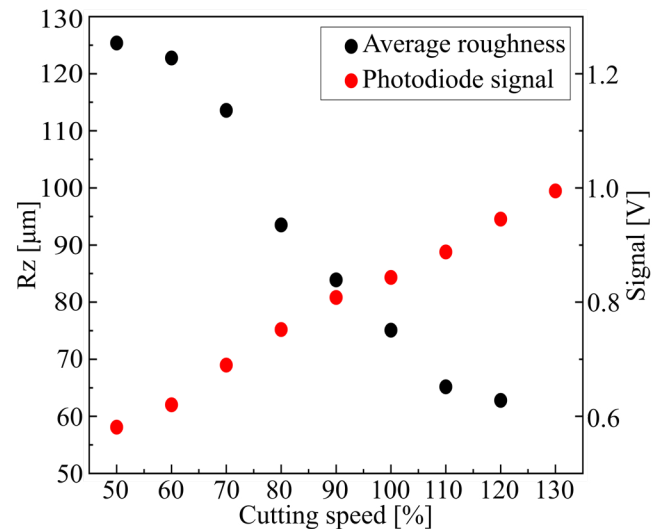


Fig. 4. Average roughness and photodiode signal during cutting of a 15 mm S355MC plate with different cutting speeds.

The average photodiode signals during straight line cutting at the nominal speed (100 %) as well as at higher and lower speeds are shown in Fig. 4. Moreover, roughness values were measured for every sample except 130 % where the edge quality drastically deteriorated causing dross occurrence that made measurement difficult and inappropriate. The change in cutting speed is clearly reflected in the cutting quality, in particular roughness, whereas the signal level is significantly higher when the cutting speed is increased.

Next to the signal level, the signal standard deviation depicted in Fig. 5 also provides useful information concerning the cutting process status. Since different behaviour of the standard deviation can be observed, the data are provided for a 1 s interval in the middle of the cutting line. When the process is seriously destabilized by the occurrence of burning defects since the energy input is too high or the cutting speed is too slow, a significant increase and variability of standard deviation can be noticed that corresponds to high roughness. Since the cutting front stability is the main factor affecting standard deviation, cutting too fast cannot be distinguished by this sensing parameter.

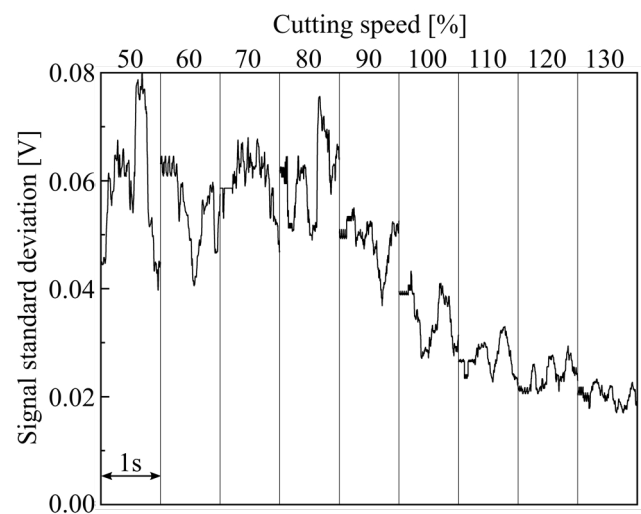


Fig. 5. Signal standard deviation during cutting of a 15 mm S355MC plate with different cutting speeds.

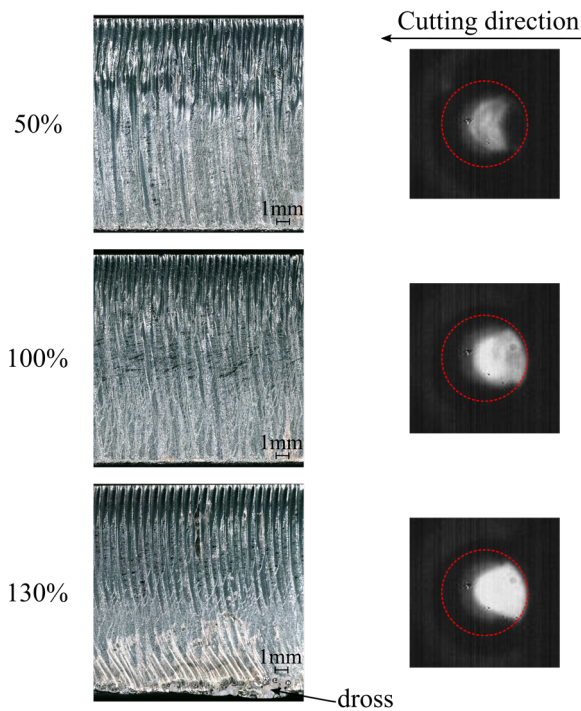


Fig. 6. Cut edges obtained during cutting of a 15 mm S355MC plate with different cutting speeds and the corresponding near-infrared camera images. The red circle indicates the nozzle border.

The cut edge profiles obtained during cutting with nominal and two extreme speeds, as well as corresponding images from the infrared camera, are shown in Fig. 6. The cut edge with a cutting speed of 100 % is characterized by a typical striation pattern in the top region and by a relatively smooth bottom part. The camera image represents the top view of the process zone. However, the nozzle does not allow to observe the whole melt pool, in particular the melt pool tail, with such an angle of the cutting front.

When the cutting is performed with a lower cutting speed (50 %), the length of the process zone becomes shorter and the melt pool intensity decreases significantly, which corresponds to the obtained lower photodiode signal. This is the result of the surplus of process energy leading to a straighter cutting front and easier melt removal. When the cutting speed is reduced significantly, the heat input becomes too large and burning defects start to occur, drastically increasing roughness. At the same time, due to the disturbance of the combustion wave generation, the process becomes less stable, leading to the increase of the photodiode signal standard deviation.

In line with the speed decrease effect, cutting faster changes the cutting front such that the proportion of the melt pool along the cutting direction increases. This can mainly be explained by a decrease of the cutting front angle due to the lack of energy. Therefore, an increase of the photodiode signal has been observed. Nevertheless, the cutting front is still stable, thus explaining only slight changes in the photodiode signal standard deviation if compared with the nominal speed. The dross appearance might significantly increase the signal due to additional radiation from the resolidified material. However, since it mainly occurs in the region clipped by the nozzle, a drastic increase of the photodiode signal has not been observed, while it has been more pronounced for flame cutting with CO₂ lasers [16].

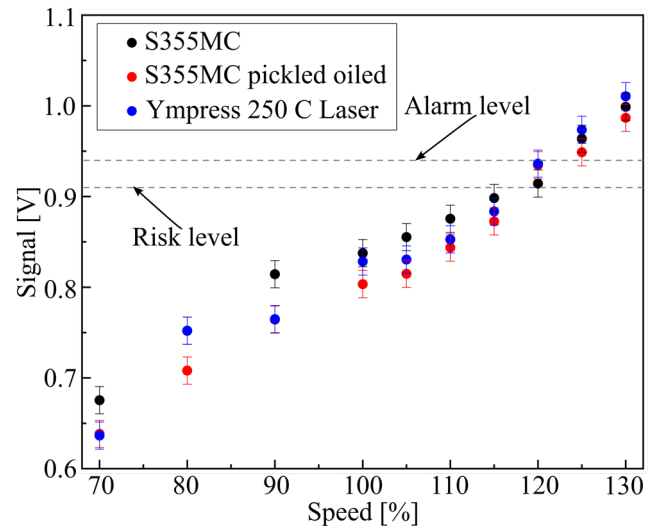


Fig. 7. Average photodiode signal during cutting of 15 mm plates with different cutting speeds.

The robustness of the photodiode signal was examined during cutting of various grades since the chemical composition of the material [17] and the surface condition [18] have a great impact on the cut quality. Therefore, in addition to the different chemical compositions of S355MC and Ympress 250C laser quality grades, S355MC plates without surface finishing, as well as pickled and oiled variants, were cut. The average photodiode signals during cutting of the above-mentioned material grades with speeds 30 % faster and slower than the nominal feed rate (100 %) are shown in Fig. 7.

Despite the difference in material grade, the same trend of the dependence of the photodiode signal from the cutting speed can be noticed. A speed increase leads to a higher signal level caused by the change of the cutting front angle. It should be noted that, even though the cut quality of samples with nominal speed is rather similar (no dross, roughness within 10 % deviation), the dross appearance is slightly different. For S355MC plates without surface finishing, as well as pickled and oiled, limited dross occurs already for cutting with a speed of 125 %, while Ympress 250C laser quality plates could be cut without dross at this speed. Nevertheless, heavy dross or a failed cut situation occurred during cutting with a speed of 130 % for all grades.

One of the main targets of an adaptive control system is to be able to cut at the maximum speed at which the cut quality does not deteriorate. In case of 15 mm mild steel plates, cutting at a speed 20 % faster than the nominal feed rate is possible with even slightly better quality. In this instance, gradual speed increasing before the photodiode signal reaches the risk level can be recommended as a guideline for the control system. When the risk level is reached, it indicates that the risk of unacceptable quality is high and that some precautionary measures should be taken, e.g. a slight speed decrease. The alarm level indicates that the cut quality deterioration is unacceptable and that the process control parameters need to be adapted drastically. In the most severe case, the cut can be completely lost and complete standstill of the cutting is required to correct the process status. These two threshold levels have to be determined for every set of cutting

parameters. In order to detect too slow cutting accompanied by the burning defects occurrence, the signal standard deviation can be used as well.

In order to validate the monitoring setup, flame cutting of mild steel of other thicknesses as well as fusion cutting of stainless steel were performed. Fig. 8 shows average photodiode signals for these experiments. It should be noted that relatively large nozzles are typically used for fusion cutting of thick stainless steel plates (in this case 3.5 mm) which makes the process zone easier to observe in a coaxial monitoring setup and allows transmitting all the radiation from the process towards the sensor.

The same trend as was noticed for 15 mm mild steel can be observed for both 10 mm stainless steel and 8 mm and 10 mm mild steel. Increasing speed results in a photodiode signal level increase induced by the change of the cutting front inclination. However, cutting too fast for stainless steel (e.g. 130 %) leads to signal saturation. This can be explained by the fact that lack of energy significantly changes the cutting front angle causing loss of the full penetration and resulting in an increase of the absorption of the laser beam by the melt layer which enhances the heat transfer to the assist gas. Consequently, instead of dross occurrence as for the flame cutting process, laser-induced plasma might be formed emitting much more light [19].

Another cut quality issue that can occur during flame cutting of thick plates is heat accumulation. Due to conductive heat losses during cutting, the temperature of the base material can rise significantly, enlarging the risk of quality deterioration due to preheating effects [20]. In the most severe cases, the overheating can even result in the occurrence of dross leading to loss of cut. This effect is particularly pronounced for cutting with oxygen, where the level of heat conduction loss is higher, which might lead to strong process limitations especially for nesting and tool path solutions.

In order to test the monitoring setup for the preheating effect, a test part geometry was chosen in such a way as to gradually accumulate heat on each subsequent cutting interval. The cutting was performed according to the sequence of the line numbers provided in Fig. 9. The length of each linear cut is 100 mm with a distance of 5 mm between the lines.

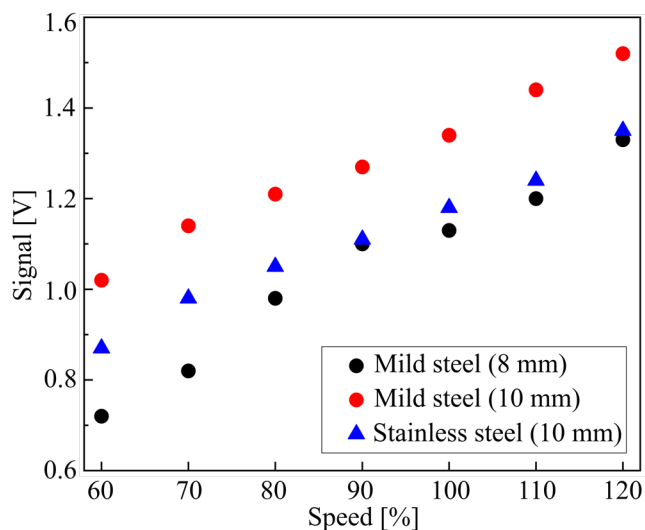


Fig. 8. Average photodiode signal during cutting of mild steel and stainless steel plates with different cutting speeds.

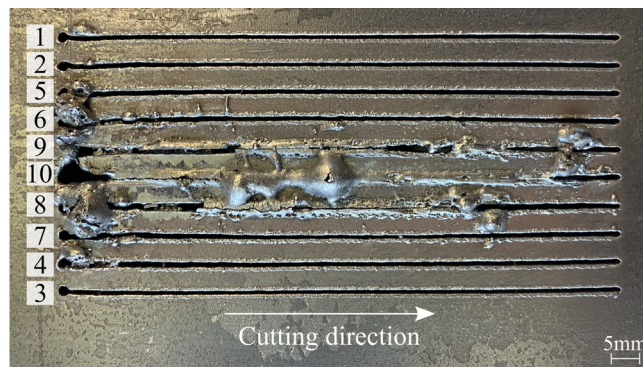


Fig. 9. Bottom view of a sample obtained by cutting a 15 mm S355MC plate with nominal speed showing no cut through in the most preheated regions.

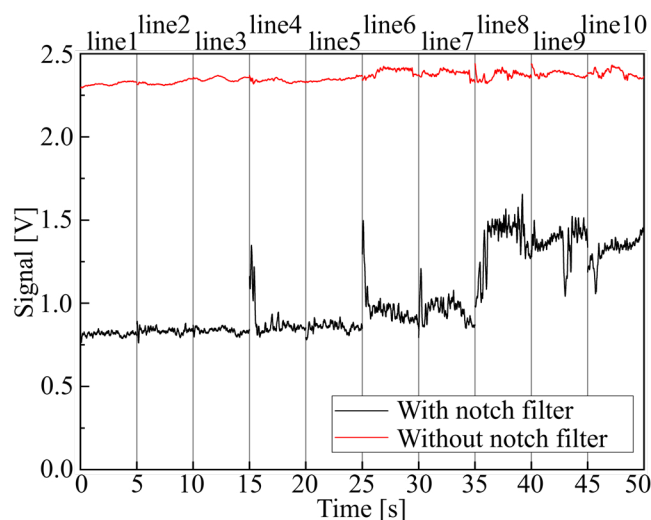


Fig. 10. Photodiode signals during cutting of a 15 mm S355MC plate with consecutive levels of heat accumulation.

The corresponding photodiode signals with and without using the notch filter are depicted in Fig. 10. The signals during the piercings for each line were removed for better visualization. Despite the fact that the temperature of the solid material around the melt pool should considerably increase due to the preheating effect, the sensor only captures radiation from the liquid metal or the resolidified material at a high temperature.

The signal level while using the notch filter starts to slightly rise for lines 6 and 7 which are characterized by considerable quality deterioration. Since piercing is a source of additional heat accumulation as well, the first significant quality degradation could be observed at the zones close to piercings corresponding to the signal peaks at the beginning of line 4 and line 6 related to unstable cutting at these regions. Furthermore, the signal is significantly higher from line 8 onward if compared with the previous lines. Despite the fact that occurrence of dross is unstable, leading to signal variation, the average signal during the cutting of each line undergoes an increase of 10 % for line 6 and line 7 and more than 50 % for lines 8, 9 and 10 compared to line 1. Moreover, the signal deviation is more pronounced at the lines where dross appears.

The experiment without using the notch filter was conducted in order to estimate the influence of laser back reflection on the obtained signal. Due to the high radiation intensity even after passing the dichroic mirror, an amplification eight times less than for other experiments was used for the test in order to

avoid signal saturation. Nevertheless, no significant changes in the photodiode signal level were observed especially when comparing with the results obtained with the notch filter. However, the signal deviation becomes higher starting from line 6 where quality deterioration appears. It might be concluded that the inclination angle of the cutting front does not significantly change while cutting in preheated regions since the signal with laser back reflection does not show any distinction between different lines. That can be used by the adaptive control system to detect the difference between cutting too fast and cutting in preheated areas.

A possible explanation of this result could be that due to the preheating effect the melt pool area expands and the material amount that has to be removed increases. At the same time, the melt pool and heat affected zone temperatures change which has a strong effect on the radiation intensity according to Planck's and Wien's laws. This difference in the measured signals becomes more evident when dross appears because the additional resolidified material has a lower temperature emitting even more radiation in the near-infrared spectral range.

4. Conclusion

The InGaAs photodiode signal rises with increasing speed since the inclination angle of the cutting front changes. Such a trend has been observed for different material grades as well as for flame cutting of mild steel with 8 mm and 10 mm thicknesses and fusion cutting of 10 mm stainless steel. Furthermore, the photodiode signal can be used to detect full penetration during piercing in order to reduce the overall piercing time.

The nozzle borders do not allow to observe the melt pool tail during flame cutting of thick plates which obstructs the opportunity to directly observe the appearance of dross. Therefore, the monitoring system is based on sensing parameters such as signal level and standard deviation that correlate with the cut quality but do not directly measure it.

The developed monitoring setup allows verifying the maximum cutting speed at which the cut quality does not degrade as well as detecting cutting in preheated regions. However, the threshold levels have to be adjusted for every material-thickness combination in order to couple the system with adaptive control.

References

- [1] Kek T, Grum J. AE signals as laser cutting quality indicators. *Insight Non-Destructive Test Cond Monit* 2009; 51:3:124-128.
- [2] Chen L-S. In-process monitoring of the cutting front of CO₂ laser cutting with off-axis optical fibre. *Int J Adv Manuf Tech* 1997; 13:10:685–691.
- [3] Wen P, Zhang Y, Chen W. Quality detection and control during laser cutting progress with coaxial visual monitoring. *J Laser Appl* 2012; 24:3:032006.
- [4] Purtonen T, Kalliosaari A, Salminen A. Monitoring and adaptive control of laser processes. *Phys Procedia* 2014; 56:1218-1231.
- [5] You DY, Gao XD, Katayama S. Review of laser welding monitoring. *Science and Technology of Welding and Joining* 2014; 19:3:181-201.
- [6] Everton SK, Hirsch M, Stravroulakis P, Leach RK, Clare AT. Review of in-situ process monitoring and in-situ metrology for metal additive manufacturing. *Mater Des* 2016; 95:431-445.
- [7] Liu S, Farahmand P, Kovacevic R. Optical monitoring of high power direct diode laser cladding. *Opt Laser Technol* 2014; 64:363-376.
- [8] Adelmann B, Schleier M, Neumeier B, Hellmann R. Photodiode-based cutting interruption sensor for near-infrared lasers. *Appl Opt* 2016; 55:7:1772-1778.
- [9] Schleier M, Adelmann B, Neumeier B, Hellmann R. Burr formation detector for fiber laser cutting based on a photodiode sensor system. *Opt Laser Technol* 2017; 96:13-17.
- [10] Schleier M, Adelmann B, Esen C, Hellmann R. Cross-correlation-based algorithm for monitoring laser cutting with high-power fiber lasers. *IEEE Sens J* 2018; 18:4:1585-1590.
- [11] Garcia SM, Ramos J, Lamikiz A, Figueras J. Influence of process parameters in laser piercing. *Appl Opt* 2019; 9:3231.
- [12] Dubrov AV, Dubrov VD, Zavalov YN, Panchenko VY. Application of optical pyrometry for on-line monitoring in laser-cutting technologies. *Appl Phys B Lasers Opt* 2011; 105:537-543.
- [13] Garmendia I, Ocaña R, Soriano C, Lambarri J. Optical monitoring of fiber laser based cutting processes for in-situ quality assurance. In: *Proceedings of Lasers in Manufacturing Conference* 2017.
- [14] Dufloy JR, Fallahi Sichani E, De Keuster J, Kruth J-P. Development of a real time monitoring and adaptive control system for laser flame cutting. In: *Proceedings of ICALEO* 2009; 527-536.
- [15] Levichev N, Costa Rodrigues G, Tomás García A, Dufloy JR. Trim-cut technique for analysis of melt flow dynamics in industrial laser cutting machine. *Procedia CIRP* (accepted).
- [16] De Keuster J, Dufloy JR, Kruth J-P. Monitoring of high-power CO₂ laser cutting by means of an acoustic microphone and photodiodes. *Int J Adv Manuf Technol* 2007; 35:115-126.
- [17] Nagels E, Dufloy JR, Van Humbeeck J. The influence of sulphur content on the quality of laser cutting of steel. *J Mater Process Technol* 2007; 194:159-162.
- [18] Manohar M. CO₂ laser beam cutting of steels: Material issues. *J Laser Appl* 2006; 18:2:101-112.
- [19] Fallahi Sichani E, Kohl S, Dufloy JR. Plasma detection and control requirements for CO₂ laser cutting. *CIRP Ann – Manuf Technol* 2013; 62:215-218.
- [20] Levichev N, Costa Rodrigues G, Dewil R, Dufloy JR. Anticipating heat accumulation in laser oxygen cutting of thick metal plates. *J Laser Appl* 2020; 32:022018.

11th CIRP Conference on Photonic Technologies [LANE 2020] on September 7-10, 2020

Multi objective optimization of water jet guided laser micro drilling on Inconel 718 using Taguchi Method

Levent Subasi^{a,b*}, Mustafa I. Gokler^b, Ulas Yaman^b

^aTUSAS Engine Industries Inc., 26210, Eskisehir, Turkey

^bMiddle East Technical University, 06800, Ankara, Turkey

* Corresponding author. Tel.: +90-222-211-2100. E-mail address: levent.subasi@tei.com.tr

Abstract

Water jet guided laser overcomes the adverse effects of conventional laser cutting and drilling processes, such as heat-affected-zone, spatter, burr formation, etc. Pressurized water in this novel process provides focusing, cooling and cleaning on the cut region, eliminating undesired side effects of the laser. The process is nowadays used in energy and aerospace industries for drilling micro cooling holes on turbine blades made of super alloys. However, more research on the process is required to understand the effects of the variables on cutting time and quality. Optimum conditions differ for various materials and geometries. In this study, a multi objective optimization is performed in terms of process time and taper of the micro holes drilled on Inconel 718, a commonly used material in gas turbines. Taguchi design of experiment and statistical analysis is used to perform the experiments and evaluate the results.

© 2020 The Authors. Published by Elsevier B.V.

This is an open access article under the CC BY-NC-ND license (<http://creativecommons.org/licenses/by-nc-nd/4.0/>)

Peer-review under responsibility of the Bayerisches Laserzentrum GmbH

Keywords: Laser drilling; Inconel718; Optimization; Taguchi

1. Introduction

Laser drilling is a widely used manufacturing technology in aerospace industry [1]. The process is especially useful for drilling micro cooling holes on turbine blades, which is of critical importance in order for the parts to withstand high temperatures in the gas turbine. However, although considered as a fast process, lasers have some quality issues associated with high heat input to the material [2].

Various optimization and modeling studies have been done to overcome these issues on different materials and with different kinds of laser systems. Chatterjee et al. [3] investigated the quality characteristics in Nd:YAG laser drilling of stainless steel using Taguchi method. They have found a relation between laser parameters, heat affected zone (HAZ), and spatter area formation. Wang et al. [4] focused on hole roundness, taper and recast layer in drilling cooling holes on a super alloy. They have found out that spiral tool path

should be used for better results. Su et al. [5] performed fiber laser drilling optimization on a ceramic material. They have found out the optimal peak power and ablation time for the best hole characteristics, such as diameter, circularity, taper and recast layer. Parthiban et al. [6] optimized the parameters for Nd:YAG laser micro-drilling process of a Nickel based super alloy with thermal barrier coating (TBC) using a galvo scanner. Taguchi orthogonal array was used for conducting the experiments. Surface roughness and surface crack density were the measured outputs. Optimum inclination angle, scan speed and number of passes were determined in return.

Water jet guided laser technology, which was developed by the Swiss company Synova S.A. in late 1990s as an innovative approach, has become an alternative to the dry lasers. The laser beams are guided within a water-jet, so that focusing, cooling and cleaning effects of the water are benefited from (see Fig. 1). The technology is used for various applications in different industries. Although its success is demonstrated

many times compared to the dry lasers in terms of quality (heat affected zone, recast layer, spatter, burr formation, etc.), the technology is still not widely elaborated. It is very difficult to model the process due to constantly flowing pressurized water splashing back from the surface. There are many variables in the process, which affects the material removal rates and quality of the cuts.

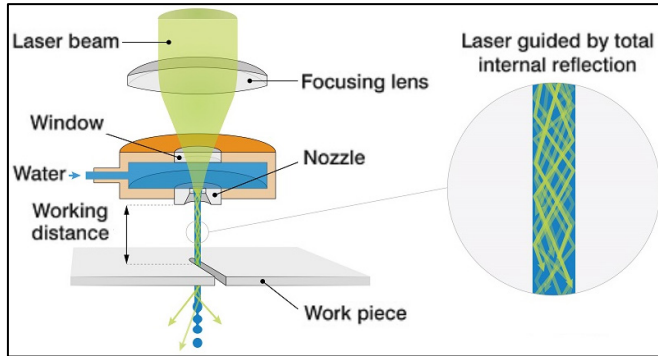


Fig. 1. Working principle of the water jet guided laser [7].

In this paper, the main aim is to perform a multi objective optimization in terms of process time and taper angle of the micro holes drilled on Inconel 718 super alloy using water jet guided laser. Taguchi method and Overall Evaluation Criteria (OEC) are used for this purpose. In the following sections, the related independent variables effecting the outputs and the experimental methods are presented and the results are discussed.

2. Materials and Methods

2.1. Material

Solution and Precipitation Heat Treated Wrought Inconel 718 material was used in the experiments. Nominal composition of the material is given in Table 1 per the specification SAE AMS 5663N and some of the material properties at room temperature are provided in Table 2.

2.2. Sample

A specimen with dimensions of $20 \times 20 \times 5.6$ mm was cut from a bulk material using Electrical Discharge Machining (EDM) method. The thickness was intentionally chosen as 5.6 mm, so that when cooling holes of diameter 0.4 mm were drilled, it would yield to an aspect ratio of 14:1, which is a design criterion. The surface area is large enough to perform repetitive tests.

2.3. Machine

The machine utilizes a diode pumped and pulsed Nd:YAG laser with 532 nm wavelength. The laser beam is carried to the nozzle with a 150 μ m fiber. The water used in the machine for the water jet is purified by reverse osmosis method to achieve a resistivity level of 17 M Ω cm. In order to stabilize the water jet, Helium is used as an assisting gas.

Table 1. Nominal composition of Inconel 718.

Al	C	Co	Cr	Cu	Fe	Mn	Mo	Nb	Ni	Si	Ti
0.5	0.08	1	19	0.3	16.7	0.35	3.1	5.2	52.5	0.35	0.9

Table 2. Material Properties of Inconel 718 [8].

Property	Unit	Value
Hardness	HB	331
Yield Strength at 0.2% Offset	MPa	1034
Ultimate Tensile Strength	MPa	1241
Density	kg m ⁻³	8190
Melting Temperature	°C	1260
Heat Capacity	J K ⁻¹ g ⁻¹	0.435

2.4. Cutting method

Since the laser beam can focus on a small spot, which is as wide as the water jet diameter, it is possible to apply different tool path strategies for drilling micro holes. This is different than the conventional methods used, such as percussion or trepanning drilling. The hole drilling process was completed in two steps. First, the hole was pierced with spiral drilling technique, and then another finishing tool path was used as shown in Fig. 2. The reason for employing the finishing step is to obtain the required diameter at the exit side of the hole. These tool paths can be parametrically adjusted by defining the spiral diameter and the size of the spiral step. The laser beam moves in X-axis, whereas the sample moves in Y-axis for this setup.

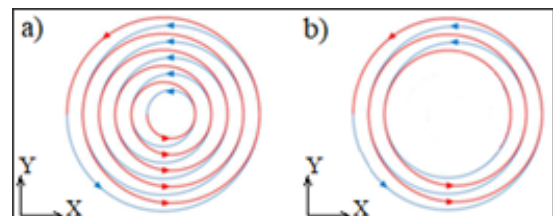


Fig. 2. (a) first step; (b) second step.

2.5. Hole geometry

Diameter of the holes to be drilled were 0.4 mm. The total depth was 5.6 mm, corresponding to an aspect ratio of 14:1. The holes were drilled perpendicular to the workpiece surface.

2.6. Process window

For the experiments, five different factors were considered, namely laser power, pulse width, frequency, feed and spiral step. The minimum and maximum levels of these factors chosen for the experiments depend on the machine constraints and previous experiences.

Among variety of nozzles, 50 μ m sapphire nozzle was selected for the experiments since it performed well during the screening tests. Water jet pressure and gas flow were set to 200 bar and 1 l/min, respectively. They were kept constant during the trials. Similarly, the standoff distance from the nozzle to the sample surface was kept constant at 10 mm.

2.7. Experiments

The factors and levels are shown in Table 3. Since there are 5 factors and two kinds of mixed levels, a modified Taguchi L-16 orthogonal table is used for the experiments [9]. The factors and levels for each trial are shown in Table 4.

Table 3. Factors and levels.

Factors	Level 1	Level 2	Level 3	Level 4
A. Laser Power (W)	25	30	35	–
B. Pulse Width (ns)	200	250	300	–
C. Frequency (kHz)	10	15	20	–
D. Feed (mm/min)	60	120	180	240
E. Spiral Step (mm)	0.010	0.015	0.020	0.025

Table 4. Modified Taguchi L-16 orthogonal table.

Trial	A.	B.	C.	D.	E.
1	25	200	10	60	0.010
2	25	250	15	120	0.015
3	25	300	20	180	0.020
4	25	250	15	240	0.025
5	30	200	15	180	0.025
6	30	250	10	240	0.020
7	30	300	15	60	0.015
8	30	250	20	120	0.010
9	35	200	20	240	0.015
10	35	250	15	180	0.010
11	35	300	10	120	0.025
12	35	250	15	60	0.020
13	30	200	15	120	0.020
14	30	250	20	60	0.025
15	30	300	15	240	0.010
16	30	250	10	180	0.015

In order to increase the reliability of the analysis, every trial was repeated three times. Therefore, 48 holes were drilled in total. The objective of the experiments was to decrease the process time and the taper of the holes.

2.8. Measurement

The process time was measured with a chronometer. Diameters of the holes were measured with a steel pin gage set, which has 0.01 mm increments. Then, the taper angle (T_a) was calculated as follows

$$T_a = \tan^{-1} \left(\frac{D_t - D_b}{2t} \right) \quad (1)$$

where, D_t is the diameter at the entrance (top), D_b is the diameter at the exit (bottom), and t is the hole depth (workpiece thickness), which is always 5.6 mm in these experiments.

3. Results and Discussion

Analysis is performed using Signal-to-Noise ratio (S/N) proposed by Taguchi [9]. S/N ratio is a variance index dependent on mean square deviation (MSD). The advantage of using S/N value is that it both contains the mean value and the variance of the data considered. The equation of S/N is

$$S/N = -10 \log_{10}(MSD) \quad (2)$$

The value of MSD in this equation, depends on the quality characteristic, whether it is “smaller is better”, “nominal is better” or “larger is better”. Considering process time and taper angle, they both fit with the “smaller is better” case, for which the equation is given as

$$MSD = (y_1^2 + y_2^2 + y_3^2 + \dots)/n \quad (3)$$

where, y_i 's are the obtained results for each repeated test and n is the number of repetitions, which is always 3 in this study.

The drilled specimen is shown in Fig. 3. The mean value and S/N values of the process time and taper angle of the holes obtained after the trials are given in Table 5.

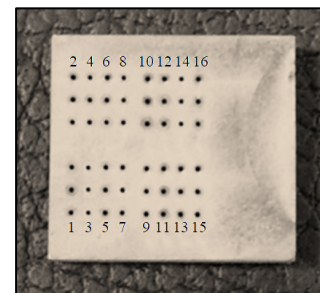


Fig. 3. Drilled specimen.

Table 5. Results of the experiments.

Trial	Process Time		Taper Angle	
	Mean (s)	S/N	Mean ($^\circ$)	S/N
1	361	-51.162	0.46	6.702
2	914	-59.217	0.49	6.106
3	2917	-69.300	0.53	5.569
4	1249	-61.936	0.53	5.528
5	668	-56.497	0.60	4.476
6	305	-49.773	0.46	6.702
7	880	-58.896	0.65	3.763
8	2390	-67.576	0.56	4.970
9	776	-57.814	0.55	5.203
10	312	-49.940	0.43	7.310
11	163	-44.262	0.34	9.322
12	285	-49.101	0.43	7.392
13	539	-54.640	0.38	8.498
14	2008	-66.058	0.41	7.760
15	821	-58.339	0.55	5.253
16	192	-45.666	0.36	8.861
Average	924	-56.261	0.48	6.463

The response plots with the mean values are given in Fig. 4 and Fig 5.

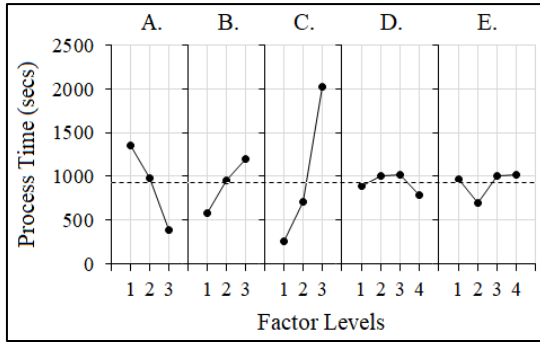


Fig. 4. Response plots for process time.

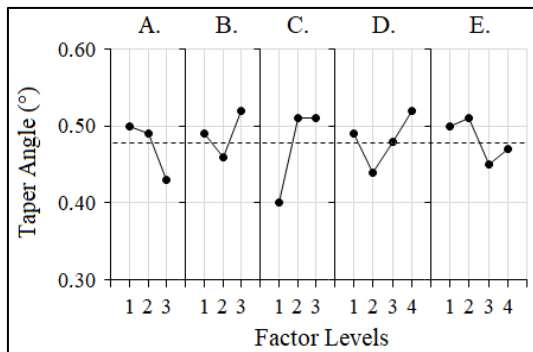


Fig. 5. Response plots for taper angle.

Tables of the main effects for process time and taper angle are provided in Table 6 and Table 7. When considering *S/N* values, larger value always indicates a better result. Thus, considering the values in the tables, laser power should be chosen as 35 W and frequency as 10 kHz for the optimal condition. However, there are conflicts with the optimum pulse width, feed and spiral step values.

Table 6. Main (average) effects of factors for process time in terms of *S/N*.

Factors	Average Effects			
	Level 1	Level 2	Level 3	Level 4
A. Laser Power (W)	-60.404	-57.181	-50.279	-
B. Pulse Width (ns)	-55.028	-56.159	-57.699	-
C. Frequency (kHz)	-47.716	-56.071	-65.187	-
D. Feed (mm/min)	-56.304	-56.424	-55.351	-56.966
E. Spiral Step (mm)	-56.754	-55.398	-55.703	-57.188

Table 7. Main (average) effects of factors for taper angle in terms of *S/N*.

Factors	Average Effects			
	Level 1	Level 2	Level 3	Level 4
A. Laser Power (W)	5.976	6.286	7.307	-
B. Pulse Width (ns)	6.220	6.829	5.977	-
C. Frequency (kHz)	7.897	6.041	5.876	-
D. Feed (mm/min)	6.404	7.224	6.554	5.671
E. Spiral Step (mm)	6.059	5.983	7.040	6.772

3.1. OEC analysis

It is not always possible to find the same optimum factor levels for every characteristic at the same time. In these circumstances, the relative weight of each characteristic can be combined into one *OEC* index. It is then possible to perform optimization based on these new values [9].

In order to calculate the *OEC*, which is a dimensionless index between 0 and 1, one needs to determine the weight of each characteristic, the best and worst readings of the experiments. Then, the *OEC* can be defined as

$$OEC = \frac{y_{1max} - y_1}{y_{1max} - y_{1min}} \times w_1 + \frac{y_{2max} - y_2}{y_{2max} - y_{2min}} \times w_2 + \dots \quad (4)$$

where, y_i is the measured reading, y_{imax} and y_{imin} is the worst and best readings of each characteristic for “smaller is better” case and w_i is the weight of each characteristic. The weights are determined based on the importance of the characteristics for the practitioner. Assuming taper angle (quality) is more important than process time, the related values for calculating *OEC* are given in Table 8.

Table 8. *OEC* description.

Criteria Description	Best Reading	Worst Reading	Relative Weight
1. Process Time (s)	161	2975	40%
2. Taper Angle (°)	0.31	0.67	60%

The mean and *S/N* values of the combined *OEC* index of process time and taper angle are given in Table 9. The main effects table of *OEC* is given in Table 10. The *MSD* value in order to find the *S/N* ratio is calculated according to “larger is better” case, for which the equation is given as

$$MSD = (1/y_1^2 + 1/y_2^2 + 1/y_3^2 + \dots)/n \quad (5)$$

Table 9. *OEC* scores.

Trial	Values of each repetition			Mean	<i>MSD</i>	<i>S/N</i>
	<i>OEC</i> #1	<i>OEC</i> #2	<i>OEC</i> #3			
1	0.80	0.63	0.71	0.71	2.013	-3.038
2	0.64	0.55	0.55	0.58	3.032	-4.817
3	0.23	0.26	0.23	0.24	17.598	-12.455
4	0.51	0.49	0.42	0.47	4.552	-6.582
5	0.41	0.42	0.50	0.44	5.230	-7.185
6	0.63	0.81	0.73	0.72	1.978	-2.961
7	0.29	0.30	0.39	0.33	9.869	-9.943
8	0.26	0.18	0.32	0.25	18.170	-12.594
9	0.39	0.66	0.49	0.51	4.341	-6.376
10	0.80	0.90	0.64	0.78	1.754	-2.440
11	0.91	1.00	0.91	0.94	1.132	-0.537
12	0.81	0.81	0.73	0.78	1.647	-2.166
13	0.77	0.86	0.86	0.83	1.457	-1.634
14	0.56	0.58	0.56	0.57	3.123	-4.946
15	0.55	0.48	0.49	0.51	3.939	-5.954
16	1.00	0.91	0.82	0.91	1.230	-0.898

Table 10. Main (average) effects of factors for *OEC* in terms of *S/N*.

Factors	Average Effects			
	Level 1	Level 2	Level 3	Level 4
A. Laser Power (W)	-6.723	-5.764	-2.880	-
B. Pulse Width (ns)	-4.558	-4.675	-7.222	-
C. Frequency (kHz)	-1.858	-5.090	-9.092	-
D. Feed (mm/min)	-5.023	-4.895	-5.744	-5.468
E. Spiral Step (mm)	-6.006	-5.508	-4.804	-4.813

When considering *OEC* values, larger value always indicates a better result. Thus, looking at the table, laser power should be chosen as 35 W, pulse width as 200 ns, frequency as 10 kHz, feed as 120 mm/min and spiral step as 0.020 mm for the optimal condition ($A_3B_1C_1D_2E_3$). These factor levels should allow a less tapered hole to be processed with minimal process time.

3.2. Analysis of variance (ANOVA)

ANOVA analysis is also performed to see the significance levels of all the factors. The *ANOVA* table for *OEC* mean values can be seen in Table 11. Looking at the percentage values in the table, frequency is the most dominant factor affecting the results. Feed and spiral step are less important, even statistically insignificant factors, so it is up to the practitioner to choose their levels arbitrarily.

Table 11. *ANOVA* analysis.

Factors	DOF (f)	S	V	F	S'	P (%)
A. Laser Power (W)	2	0.141	0.070	16.372	0.132	17.8
B. Pulse Width (ns)	2	0.048	0.024	5.637	0.040	5.4
C. Frequency (kHz)	2	0.369	0.185	42.996	0.361	48.6
D. Feed (mm/min)	3	0.015	0.005	1.134	0.002	0.2
E. Spiral Step (mm)	3	0.020	0.007	1.519	0.007	0.9
Other/Error	35	0.150	0.004	-	-	27.2
Total	47	0.743	-	-	-	100.0

3.3. Estimation of performance

It is also possible to calculate the expected outputs based on the selected factor levels at this point. Contribution of each factor level on the average value is taken into consideration one by one for each characteristic, as shown in Table 12.

Table 12. Estimation of performance for the optimal condition.

Factors	Process Time			Taper Angle		
	Average	<i>S/N</i> Opt	Contribution	Average	<i>S/N</i> Opt	Contribution
A.	-56.261	-50.279	5.981	6.463	7.307	0.847
B.	-56.261	-55.028	1.232	6.463	6.220	-0.240
C.	-56.261	-47.716	8.545	6.463	7.897	1.437
D.	-56.261	-56.424	-0.163	6.463	7.224	0.764
E.	-56.261	-55.703	0.558	6.463	7.040	0.580
Total		16.155			3.388	
Est.		-40.106			9.848	

The estimated *S/N* value is calculated by adding the total contribution to the average performance, which is -56.261 for process time and 6.463 for taper angle. Based on the estimated *S/N* values, the expected values for process time and taper angle can be found by the equation provided below.

$$MSD = \sigma^2 + (y_a - y_0)^2 \quad (6)$$

where, σ is the standard deviation, y_a is the sample average and y_0 is the target value. Considering the average value only and “smaller is better” case, $\sigma=0$ and $y_0=0$. Then, using Equation (2) and simplifying, Equation (6) becomes:

$$y_a = \sqrt{10^{-\frac{S/N}{10}}} \quad (7)$$

Therefore, using Equation (7) and the estimated *S/N* values in Table 12, the process time is calculated as 101 s and taper angle as 0.32° at the optimum condition.

3.4. Verification tests

In order to verify the estimated performance, verification tests with 5 repeats are performed. Using the optimal condition ($A_3B_1C_1D_2E_3$), the mean values of the obtained results are close to the expected values, as shown in Table 13.

Table 13. Confirming predicted results.

Criteria Description	Expected Reading	Verification Result
1. Process Time (s)	101	120
2. Taper Angle ($^\circ$)	0.32	0.24

The reason for errors or deviations between the expected and the verified results are related to the confidence interval of the estimated performance. Since there are other factors affecting the process, such as real-life disturbances, variations and/or interactions between factors, deviations are always expected. In this case, the results seem close. Average taper angle performance of 0.24° is even better than expected, which is a value that couldn't be obtained in the initial trials.

3.5. Peak Intensity

Since the power of the laser source is transmitted to the work piece through a fiber and water jet, a transmission loss should be taken into account. Experiments with the system show that the ratio is approximately 0.75. The pulse energy E_p (mJ) can be calculated as in [10] below.

$$E_p = 0.75P/f \quad (8)$$

where, P (W) is the average laser power and f (kHz) is the frequency. Then, the peak power P_p (kW) can be calculated as

$$P_p = E_p/\tau_p \quad (9)$$

where, τ_p (ns) is the pulse width. Finally, the power density or peak intensity I_p (GW/cm²) can be calculated by using the below equation.

$$I_p = P_p/A \quad (10)$$

where, A (cm^2) is the water jet cross-section area. The area is calculated by taking the diameter (μm) of the nozzle and multiplying it by a contraction factor, which shows the ratio of the water jet diameter compared to the nozzle diameter. Experiments with the system show that this factor is approximately 0.83.

Then, using Equations (8), (9), (10), taking the nozzle diameter as $50 \mu\text{m}$, using the related factors and the unit conversions, below equation is obtained.

$$I_p = \frac{55.475P}{f\tau_p} \quad (11)$$

Peak intensity is a compact value including all of the laser parameters used in the experiments. Calculating the peak intensity, and matching against the process time measured in the experiments, the plot shown in Fig. 6 can be obtained. It is clear that there is a strong dependence between the two variables.

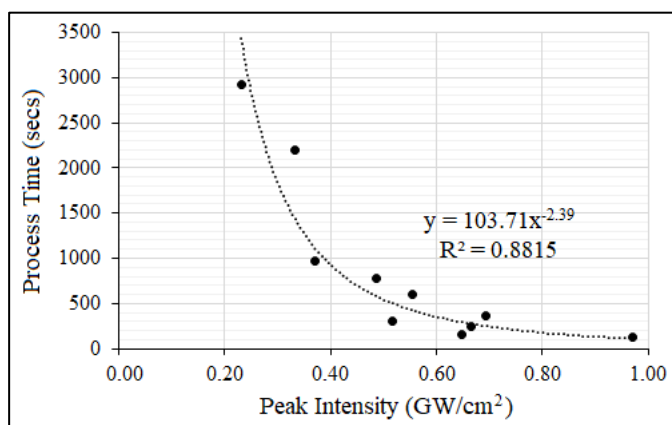


Fig. 6. Peak intensity vs. Process time plot.

Thus, it is justified that the optimum condition of 35 W, 200 ns and 10 kHz provides better processing time since their calculated peak intensity of 0.97 is higher compared to the values used at initial trials.

Considering Equation (11), it seems possible to increase the peak intensity even more, in order to decrease the process time. Laser power should be increased and/or frequency and pulse width should be decreased for this purpose. However, the power density is a constraint for the machine. The damage threshold of the water jet nozzle is approximately 1 GW/cm^2 . This limit should not be exceeded and the optimum condition is already very close to the limit. Thus, there is not much room for further improvement.

4. Conclusion

A multi objective optimization is performed in terms of process time and taper angle of the micro holes drilled on Inconel 718 material using water jet guided laser. Taguchi

design of experiment, *S/N* analysis, *OEC* analysis and *ANOVA* analysis were used for evaluation of results and optimization.

Taguchi approach is proved to be useful, as also verified by further tests. Both process time and taper angle objectives are optimized by adjusting the levels. Frequency is the key factor when both objectives are considered.

Other non-laser factors, such as feed and spiral step are insignificant. In fact, these two factors only control how much the laser beam is overlapping on the surface. More overlap means faster material removal in Z (hole depth) direction, whereas less overlap means faster material removal in XY plane. It turns out that the total process time is not highly affected by changing these values, so the total material removal rate is directly correlated with the laser parameters.

Faster process time is obtained by using the laser parameters that yields to higher peak intensity. Thus, for better performance laser power should be increased or pulse width and frequency should be decreased, taking into account the damage threshold of the nozzle.

The design of experiment did not include any possible interactions or noise factors. Looking at the *ANOVA* table, the error term percentage of 27.2% suggests that there might be some other effects, such as power and pulse width fluctuations, or water splash back blocking the laser beam. As a future work, further experiments shall be performed to understand the factor interactions and fine-tune the results even more. It is also possible to expand the process window to include different factor levels or experiment with different factors, such as nozzle diameter, water and gas pressure, etc.

Acknowledgements

The authors would like to thank to Ronan Martin (Synova SA) and Jérémie Diboine (Synova SA) for their support.

References

- [1] Darwish SMH, Ahmed N, Al-Ahmari AM. Laser Beam Micro-milling of Micro-channels in Aerospace Alloys. Singapore: Springer; 2017.
- [2] Gautam GD, Pandey AK. Pulsed Nd:YAG laser beam drilling: A review. Optics and Laser Technology; 2018; 100, p. 183-215.
- [3] Chatterjee S, Mahapatra SS, Sahu AK, Bhardwaj VK, Choubey A, Upadhyay BN, Bindra KS. Experimental Investigation Of Quality Characteristics In Nd:YAG Laser Drilling Of Stainless Steel (AISI 316). Materials Today; 2018; 5, p. 11526–11530.
- [4] Wang M, Yang L, Zhang S, Wang Y. Experimental investigation on the spiral trepanning of K24 superalloy with femtosecond laser. Optics and Laser Technology; 2018; 101, p. 284-290.
- [5] Su L, Chen R, Huang Z, Zhou M, Zeng Q, Shi Q, Liao Z, Lu T. Geometrical morphology optimisation of laser drilling in B4C ceramic: From plate to hollow microsphere. Ceramics International; 2018; 44, p. 1370-1375
- [6] Pathiban K, Duraiselvam M, Manivannan R. TOPSIS based parametric optimization of laser micro-drilling of TBC coated nickel based superalloy. Optics and Laser Technology; 2018; 102, p. 32-39.
- [7] www.synova.ch/technology/laser-microjet.html (last accessed 20.02.2020)
- [8] Mills KC. Recommended values of thermophysical properties for selected commercial alloys. Cambridge: Woodhead Publishing; 2002.
- [9] Roy RK. A Primer on the Taguchi Method. 2nd ed. Michigan: Society of Manufacturing Engineers; 2010.
- [10] Yeo CY, Tam SC, Jana S, Lau MWS. A technical review of the laser drilling of aerospace materials. Journal of Materials Processing Technology; 1994; 42, p. 15-49.

11th CIRP Conference on Photonic Technologies [LANE 2020] on September 7-10, 2020

Laser forming of holes in brittle materials assisted by stress reduction through heating

Anatoli A. Abramov^{a*}, Alejandro A. Becker^b

^aCorning Incorporated, Sullivan Park, SP-AR-02-02, Corning, NY 14831, USA

^bCorning Laser Technologies GmbH, Robert-Stirling-Ring2, Krailing 82152, Germany

* Corresponding author. Tel.: +1-607-974-9801; fax: +1-607-974-9271. E-mail address: abramova@corning.com

Abstract

A laser method for forming holes in brittle materials, such as glass and glass-ceramics, and the effect of heat treatment applied prior to and during hole formation on laser-induced transient and residual stresses, sample strength and hole quality are reported. We have shown, for the first time to our knowledge, that developed CO₂ laser-based hole forming technique utilizing pulse burst mode operation enables quick formation of the holes of various diameters in substrates of different thickness in the range from about 0.03mm up to 3mm without cracking or shattering of the material, mitigating a negative effect of an ablation process.

© 2020 The Authors. Published by Elsevier B.V.

This is an open access article under the CC BY-NC-ND license (<http://creativecommons.org/licenses/by-nc-nd/4.0/>)

Peer-review under responsibility of the Bayerisches Laserzentrum GmbH

Keywords: Laser; Glass; Glass-ceramics; Holes; Ablation

1. Introduction

Forming holes in brittle materials, such as glass and glass-ceramic substrates, is a necessity for various applications. For example, glass articles, such as cover glasses and glass backplanes, are employed in both consumer and commercial devices- LCD and LED displays or computer monitors, and may also be incorporated in portable electronic devices, such as mobile telephones, media players, watches, tablet computers and others. Depending on application, substrate thickness for drilling of through-holes (or blind holes) can vary in a wide range from about 10-30µm up to a few millimeters. Hole diameters might vary within the wide range from microns up to millimeters or centimeters. Some applications require uniform

hole diameter with small variation, while others need tapered holes.

Depending on requirements, different methods exist, which allow to produce holes in glass. Some of them are based on use of mechanical tools, especially for large diameter holes, but others use different types of laser processing in combination with additional process steps, such as the following acid etching, polishing, strengthening. Important process requirements include an ability to produce multiple holes in a short period of time without substrate breakage, to maintain substrate strength, to reduce processing and postprocessing time and overall cost of manufacturing of glass panels or devices. There are a few well-known laser-based

methods for forming of relatively small diameter holes in glass substrates. The most typical methods include the following:

- nanosecond pulse laser ablation by UV laser at wavelengths of 266nm or 355nm followed by acid etching [1];
- use of pulse laser with wavelengths of $\leq 1200\text{nm}$ [2];
- use of pulse or continuous wave CO₂ laser with wavelength of 9200-9800nm for drilling holes in substrates with thickness not exceeding 300 μm [3];
- use of focused short pulse laser beam (wavelength 390-700nm) to induce absorption within the material, and as a result create defect lines through the thickness followed by etching to enlarge the laser induced defects into holes of 10 to 100 μm diameter [4].

A number of other publications related to the topic could be found, which represent variations or modifications of the methods indicated above using fundamentally similar principles.

Methods [1] and [4] make relatively uniform diameter holes, where laser pulses create elongated defects through the substrate thickness, and the following etching forms actual holes of required diameter and removes cracks and defects originated during the initial laser exposure. These methods allow to create holes, but require significant process time for etching, since laser pulses create small filament type defects, which must be opened by etching process to achieve a certain diameter. During etching the overall thickness of the glass substrate is also reduced.

Method described in [2] is close to [1] since, it uses similar UV nanosecond pulse laser working at 355nm wavelength. It does not use etching, but it applies a multi-step drilling process, when, at first, a concave defect is created on the surface at a certain energy density of pulses, and then a pulse train with higher energy density is used to finish a through hole. This method also requires a significant amount of time to complete multiple holes and tends to generate cracks and defects.

Method [3] uses CO₂ laser in CW or pulse modes with wavelength of 9.2-9.8 μm to create holes in thin substrates. As all methods mentioned above, it tends to generate cracks during drilling. This publication indicates, that the used method significantly inhibits occurrence of cracks, but it does not prevent them. Better results with limited number of cracks can be obtained only in thin substrates with thickness not exceeding 100-300 μm . Thicker substrates require higher peak power of the pulses or longer laser exposure time, both leading to formation of cracks or, if not enough, to formation of partial holes, which do not penetrate through the substrate thickness, but still create cracks.

So, all known laser-based hole drilling methods in brittle materials, like glass, have a similar issue of formation of cracks around the hole and at its inner walls, which fundamentally linked to laser-induced heat-generated stress associated with an ablation process via formation of strong temperature gradients due to transient and residual stress. If not treated and removed by etching, the cracks reduce substrate strength and eventually cause its breakage.

The present paper is devoted to a new method allowing to avoid generation of cracks during hole drilling process in glass substrates. The new method is based on pulse laser drilling, but

unlike all other methods, it runs, while glass substrate is heated up to a temperature range above the glass annealing point, but below the glass softening point. Related to the presented process reference [5] describes benefits of cutting of strengthened glass at elevated temperatures assisted by stress reduction through additional heating.

In this paper we report on a CO₂ laser-based method utilizing pulse burst mode operation, which enables quick formation of the holes with diameters in the range from about 30 μm up to 300-500 μm in various types of glass substrates having thickness from 30 μm up to 3000 μm without cracking or shattering of the material, mitigating a negative effect of an ablation process. Furthermore, after optimization of the laser process nearly “crack-free” holes and multiple hole patterns might be achieved, which in some cases require no, or minimum post-treatment.

2. Hole drilling method and apparatus

It is known, that due to a wavelength (10.6 μm) of the CO₂ laser radiation in a far IR part of the spectrum, the absorption of oxide glasses at this wavelength can exceed 10⁵-10⁶1/m. This makes the effective penetration depth of CO₂ laser radiation of less than 10 μm , within which an absorbing material, when irradiated, experiences rapid raise of the temperature and associated generation of the sharp thermal gradients and of corresponding thermal stresses in substrate surface layer and through its thickness via relatively slow thermal conductivity. This process is accompanied by melting and by material removal due to an ablation process.

All these factors, even if a through or blind hole is made, cause substantial damage of the glass material around the hole in a form of macro and micro cracks, which make the substrate weak and can eventually lead to its breakage due to a high level of induced residual stress.

To mitigate negative effects described above, heating of a glass substrate up to and above annealing point was proposed and tested. This caused significant immediate transient stress relaxation during laser drilling process and thus inhibited crack formation around the hole.

Hole drilling was performed using the CO₂ laser in a burst mode, which allowed relatively high (but not excessive) controllable peak power with short exposure time and with limited number of pulses within the burst. Heating the glass substrate to annealing range was achieved by using specially designed infra-red heater and furnace. First, the glass substrate was placed into a heater, where the entire substrate was uniformly heated to the required temperature, and then the laser beam was focused and irradiated on glass surface through a window using long focal distance focusing optics.

Schematics of apparatus for laser hole drilling in glass or in glass ceramics using substrate heater are shown in Fig. 1. In one configuration laser scanner was used to create hole pattern (see Fig. 1a). In other configuration stationary focusing optics was used, and the substrate was moved by an X-Y motion system (see Fig. 1b).

Coherent Diamond J-2 series CO₂ laser was used as a laser source at the wavelength of 10.6 μm . The laser generated Gaussian beam with M² value of less than 1.2. The laser beam was focused to a variable spot diameter required to form the

targeted hole diameter. Typically, the spot diameter was set to be $\leq 0.5\text{mm}$. It could also be $\leq 0.25\text{mm}$ and even $\leq 0.05\text{mm}$, when different focusing optics was used. This enabled power density in the range of about $\sim 0.5\text{--}20\text{kW/cm}^2$. Peak power of the pulses could achieve 400W . Pulse burst mode was set to use limited number of pulses ($N \sim 1\text{--}100$) with pulse duration of $\sim 0.1\text{--}1\text{ms}$ within the burst and total irradiation time of $\sim 0.1\text{--}100\text{ms}$. Depending on glass thickness it was also possible to use a single-pulse operation mode, when several single pulses were generated with variable intervals between them.

Glass substrate thickness varied in the range from $30\mu\text{m}$ up to 3mm . Laser beam focusing/defocusing optics included combination of a few ZnSe spherical and aspherical lenses for beam expansion and collimation.

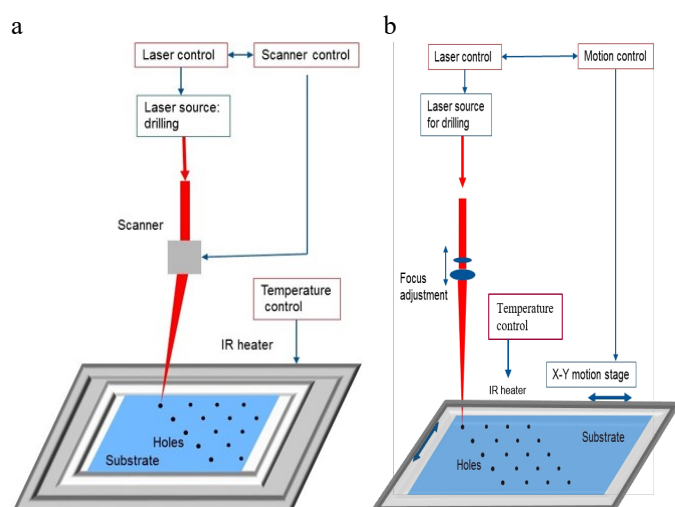


Fig. 1. Schematics of apparatus for laser hole drilling in glass or in glass ceramics substrates using:

(a) scanner; (b) stationary optics combined with X-Y motion of the substrate

3. Examples of hole drilling in different glasses

Use of the CO_2 laser ablation process for the fast drilling of holes of different diameters in glass or glass-ceramic substrates is an attractive approach, since CO_2 lasers are inexpensive and reliable tools for manufacturing. However, use of the CO_2 laser for hole drilling in glass has a major problem, as described above, which is related to a high laser-induced stress and stress/temperature gradients generated within a substrate during an ablation process.

This laser-induced stress typically creates an “arc-type” crack around the hole formed by hole drilling process, when the substrates are kept at room temperature. Fig. 2a and Fig. 3a show typical examples of the “arc” cracks generated during hole formation regardless of the glass composition and its coefficient of thermal expansion (CTE). In case of the glass substrate shown in Fig. 2 CTE was about $35.0 \times 10^{-7}/^\circ\text{C}$. In case of the glass substrate shown in Fig. 3 an average CTE was about $80.0 \times 10^{-7}/^\circ\text{C}$. The two glasses represent a broad family of commercially available oxide glasses of different composition and properties well-known in display industry and in consumer electronics. The “arc” cracks, as seen in Fig. 2a

and Fig. 3a, are deep and represent the weakest areas of the substrate, which lead to self-breakage of the substrate after hole formation, or to immediate breakage, when even small external force (bending) is applied to the substrate.

In principle, these cracks can be removed by the following substrate acid etching, but they cover a large area around the hole, so the volume of material to be removed is quite significant, and so is the etching time. The final hole diameter will be much larger, then the original one made by laser, and long etching process will significantly reduce thickness of the substrate.

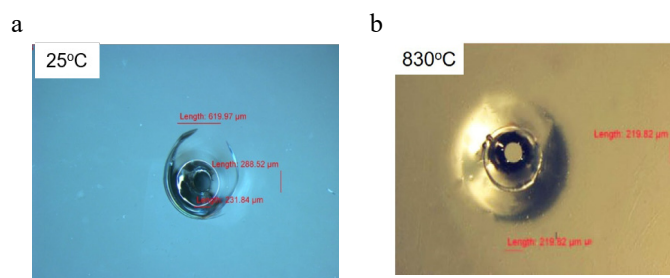


Fig. 2. Typical hole formation by a CO_2 laser in the glass with low expansion coefficient at: (a) the room temperature; (b) the temperature above annealing point, but below the glass softening point.

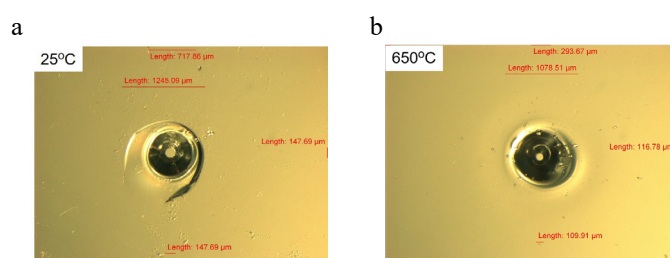


Fig. 3. Typical hole formation by a CO_2 laser in the glass with high expansion coefficient at: (a) the room temperature; (b) the temperature above annealing point, but below the glass softening point.

It was confirmed, that if the same drilling process was performed, when substrate was heated up to annealing range, then the “arc-type” cracks were not observed anymore, as shown in Fig. 2b, while the process ran at substrate temperature $\geq 820^\circ\text{C}$ for this glass composition. Similar effect was observed for a different glass composition, when substrate was heated up to $\sim 650^\circ\text{C}$ and no “arc” crack was formed because of this (see Fig. 3b).

Another example of good quality of tapered holes, formed in a laminate glass articles comprising a core and cladding layers [5], with entrance-to-exit hole diameter ratio of about 2.6, is shown in Fig. 4. In this example the entrance hole diameter was about $350\mu\text{m}$ (Fig. 4a) and exit diameter was about $135\mu\text{m}$ (Fig. 4b), while overall substrate thickness was 0.7mm . In this case optimization of the hole drilling process parameters and of internal glass substrate stress profile led to nearly “crack-free” hole formation.

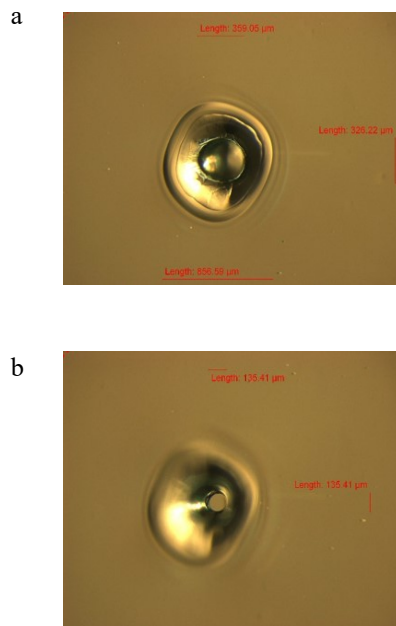


Fig.4. Example of laser formed tapered hole with ratio ~2.6:
(a) “entrance hole; (b) “exit” hole.

Figure 5 shows examples of hole patterns formed with different distances between the holes from ~1000 μm (Fig. 5a) down to $\leq 500\mu\text{m}$ (Fig. 5b), while individual hole diameter was close to about 200 μm . No crack-out of the samples was observed in all cases including the smallest interval of less than 500 μm .

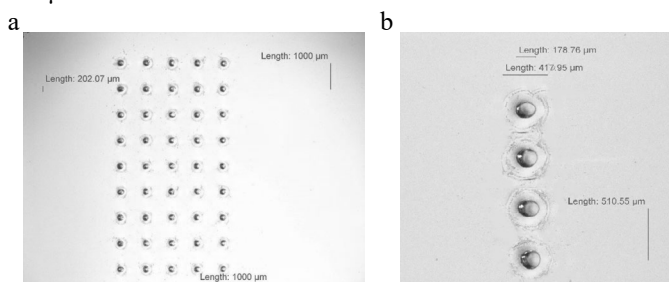


Fig.5. Examples of arrays of holes of about 180-200 μm in diameter each with different distance between holes of:
(a) 1000 μm ; (b) $\leq 500\mu\text{m}$.

Forming small diameter holes of $\leq 100\mu\text{m}$ requires tighter beam focus with spot diameter decreased down to at least 50 μm . This was achieved by using a dual-lens focusing system, which consists of a combination of spherical and aspherical lenses.

Figure 6a shows an example of a hole of about 100 μm in diameter formed in 0.7mm-thick glass substrate. Another example of a hole of about 35 μm in diameter is shown in Fig. 6b. This small size holes were made in 0.4mm-thick substrates.

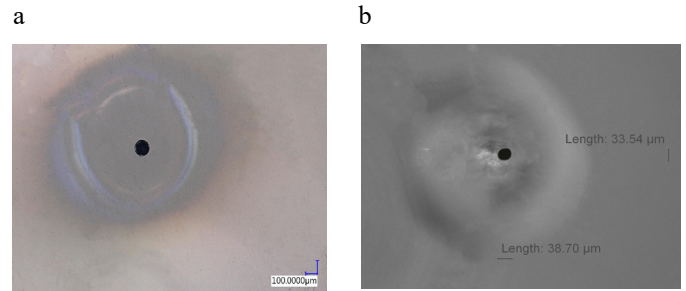


Fig.6. (a) example of a hole of $\leq 100\mu\text{m}$ in diameter (0.7mm thick substrate);
(b) example of a hole of about 35 μm in diameter (0.4mm thick substrate).

Experiments ran on forming holes in glass-ceramic substrates using the same laser drilling method showed, that stress generation and stress relaxation mechanisms in glass-ceramic differ from the ones in glass substrate. Good quality holes of different diameters can be formed in glass-ceramic substrates without pre-heating. Figure 7 shows an example of the hole of about 300 μm in diameter formed in a thin glass-ceramic substrate.

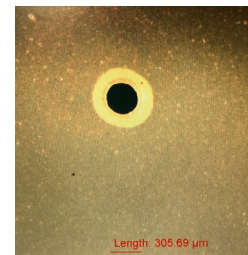


Fig.7. Example of a laser formed hole in a thin glass-ceramic substrate at room temperature.

Conclusion

A CO₂ laser-based hole forming technique utilizing pulse burst mode and assisted by a heating of the glass substrates up to annealing range, demonstrated an ability to form holes of various diameters down to 35 μm in substrates of different thicknesses without cracking or shattering of the brittle material. This technique allowed to improve quality of the drilling process, to decrease hole formation time and to minimize post-drilling treatment.

References

- [1] Liu A, Streltsov AM, Li X, Abramov AA. "Laser processing of glass for consumer electronics: opportunities and challenges", Proc. SPIE 9180, Laser Processing and Fabrication for Solar, Displays, and Optoelectronic Devices III, 918004 (Oct. 8, 2014).
- [2] Horiuchi K, Ono M. Method of forming hole in glass substrate by using pulsed laser, and method of producing glass substrate provided with hole. US20170096361A1; 2017.
- [3] Ono M. Manufacturing method for glass substrate, method for forming hole in glass substrate, and apparatus for forming hole in glass substrate. US20170282299A1; 2017.
- [4] Marjanovic S, Piech GA, Shanmugam S, Pons Siepermann CA, Tsuda S, Varga Z, Wagner RS. Method for rapid laser drilling of holes in glass and products made therefrom. US9517963; 2016.
- [5] Abramov AA, Bergman R, Golyatin VY, Lakhkar RS, Nikulin IA. Method of cutting a laminate glass article. Publication WO2016/073807A1; 2016.

11th CIRP Conference on Photonic Technologies [LANE 2020] on September 7-10, 2020

Macroscopic bending deformations and mechanical properties of Al2024-T351 thick plates with laser peen forming in a cantilever state

Junfeng Wu^{a,*}, Zhigang Che^a, Shikun Zou^a, Xia Huang^a, Ziwen Cao^a, Rujian Sun^a

^a Science and Technology on Power Beam Processes Laboratory, AVIC Manufacturing Technology Institute, Beijing, 100024, PR China

* Corresponding author. Tel.: +86-13522770620; fax: +86-010-85701428. E-mail address: wjf88813@163.com

Abstract

Laser peen forming (LPF) was used to study the macroscopic bending deformations and mechanical properties of Al2024-T351 thick plates in a cantilever state by surface morphologies, surface bending profiles, residual stresses, microstructure and micro-hardnesses. The results indicated that square micro-pits with about 49 μ m in depth were induced by the laser shock wave. Overlapping LPF induced curvature radii in the shocked area decreased with LPF impacts. Compressive residual stresses and refined grains were generated at both the top and bottom surfaces. Affected layer depth of micro-hardnesses was approximately 2.1 mm in the surface layer after LPF-2.

© 2020 The Authors. Published by Elsevier B.V.

This is an open access article under the CC BY-NC-ND license (<http://creativecommons.org/licenses/by-nc-nd/4.0/>)

Peer-review under responsibility of the Bayerisches Laserzentrum GmbH

Keywords: Laser peen forming (LPF); Al2024-T351 thick plates; Macroscopic bending deformations; Curvature radii; Mechanical properties.

1. Introduction

It has been increased in demand for precise and non-contact adjustments of shaped curves of wing components in the aviation industry [1]. On the basis of the principle of the laser shock wave, a new technology of laser peen forming (LPF) (which is also known as laser shock forming) has been developed [2]. LPF technology combines the advantages of surface modification and metal plastic forming, which makes it possible to improve the mechanical properties and form the complex curved surface [3]. Accordingly, LPF technology provides more space for the shaped design of aircraft wing skin panels.

Under the action of the high pressure laser shock wave, a plastically deformed layer with high strain rates (up to 10⁶ s⁻¹) is generated in the surface layer. In addition, the bending moment M' and the stretching force F of the target are induced by the accumulation of the plastically deformed layer after LPF. When the bending moment M' and the stretching force F are greater than the confined moment M_{con} and the confined force F_{con} of the target, the macro-bending deformation is

generated by LPF and plastic deformations are formed in both the surface and bottom layers. In contrast, plastic deformations are formed in the surface layer rather than in the bottom layer, which is also refined as LSP.

Many researchers have investigated the macroscopic bending deformation behaviors and mechanism, and mechanical properties of thin sheet metals with LPF. Hu et al. [3] examined the effects of process parameters on the bending deformation behaviors of thin aluminum alloy plates with different thicknesses, and then two-way bending deformation mechanism was put forward based on the analysis. Ocana et al. [4] investigated the effects of process parameters on the net bending angles of thin sheet metals. Sagisaka et al. [5] examined the effects of process parameters and elastic pre-bending on the bending properties of pure aluminum thin sheets. Hu et al. [6, 7] discussed the bending capability of titanium alloy thin sheet metals, as well as residual-stress distributions and microstructure variation in both the surface and bottom layers of thin sheet metals. Shen et al. [8] analyzed the surface modifications and bending deformations of aluminum-alloy thin sheets and medium-thick plates with LPF.

However, the above researches have never reported that the changing law of mechanical properties of the macro-bending Al2024-T351 thick plates with LPF.

In addition, it has been studied that bending deformations of medium-thick plates of wing skins with LPF. Hackel et al. [9–11] proposed that LPF was suitable to form the curves of metal plates with large thicknesses (≥ 19 mm). The company MIC [12] reported that LPF has been successfully used to form the curves of B747-8 wing panels. However, the above researches have also never reported that the macro-bending deformation rules and bending capacity of Al2024-T351 thick plates with LPF. Experimental studies would provide an important reference for LPF applications for aircraft wing skin panels.

Therefore, Al2024-T351 thick plates were investigated by LPF. It included surface morphology, macroscopic bending deformation, residual stress, microstructure and micro-hardness with and without LPF. The researched results can lay the foundation of shaped curves of wing integral stiffened wall panels.

2. Experiments and measurement methods

2.1. Material preparation and LPF experiments

Al2024-T351 thick plates with dimensions of 320 mm \times 102 mm \times 25 mm (length \times width \times thickness) were used as experimental material. They were cut from one piece of the plate, and the length direction was parallel to the rolling direction of the plate. Thus, the direction of length and width of thick plates was longitudinal (L) and transverse (T) directions. Three cylindrical tensile samples were machined in the L direction, and three were machined in the T direction, with a test diameter of 12.5 mm and a measuring length of 62.5 mm. Their mechanical properties are presented in Table 1.

Al2024-T351 thick plates in a cantilever state were subjected to multiple LPF impacts (denoted as LPF-X) using a Nd:YAG laser with a wavelength of 1064 nm, as shown in Fig. 1. Laser process parameters were as follows: a laser energy of 30 J/pulse, a repetition frequency of 2 Hz, a pulse width of 15 ns, square spots of 4 mm \times 4 mm, and LPF-2–LPF-8. Two samples were used for each LPF process parameters. The length L1 at the clamping end was approximately 40 mm. The shocked area L2 was approximately 120 mm, which was symmetrical to the centerline. LPF started from the clamping end and progressed to the free end (up to down). The scanning velocity V_x and the step interval Δ_y were both 3.8 mm. Square spots were focused on the surfaces of thick plates using a beam shaping device with a lens and a shaping lens[13]. During the LPF, a water curtain approximately 1–2 mm thickness was used as a confined layer to increase the peak pressure of the laser shock wave and extend its interaction time. An aluminum foil approximately 0.12 mm thickness was used as an absorbing layer to protect the target surface from thermal effects and to improve the energy-absorbing capacity.

Table 1. Mechanical properties of Al2024-T351 thick plates.

Tensile loading direction	Tensile strength R_m (MPa)	Yield stress $R_{p0.2}$ (MPa)	Elongation A (%)	Young's modulus E (GPa)
L	456.11	370.57	21.7	73.29
T	475.79	332.36	18.59	66.23

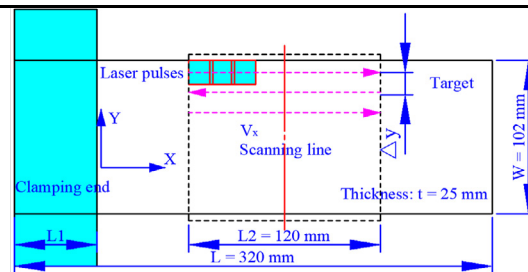


Fig. 1. A schematic diagram of Al2024-T351 thick plates subjected to LPF.

2.2. Measurement methods

The surface morphology was characterized by a WYKO NT 1100 optical profiler with four overlapped regions at each region of 120 μm \times 90 μm . The surface roughness was measured using a Talysurf PGI 1230 three-dimensional surface topography instrument with a line trace length of 20 mm. Surface bending profiles of Al2024-T351 thick plates were obtained by a testing platform with a dial indicator and its support frame. The measurement path of surface bending profiles was along the length direction and from the clamping end to the free end at the centerline. Curvature radii in the shocked area were calculated by the formula and are the average of two samples with same LPF process parameters. Surface residual stresses tests were performed via a laboratory X-ray diffraction using the $\sin^2\psi$ -method. The X-ray beam diameter was 2 mm, and the diffracted Cr-K α characteristic X-rays from a {311} plane were detected with a diffraction angle (2θ) of 139°. The spacing between three residual stress test points was 20 mm at both the top and bottom surfaces. Their test locations were at the centerline, and the second point was located at the intersection of two centerlines.

The samples were subjected to several successive steps of grinding and polishing and then etched using a professional reagent comprising of 95 % H₂O, 2.5 % HNO₃, 1.5 % HCL, and 1 % HF for 5 s at room temperature. Microstructures in both the surface and bottom layers were characterized via an optical microscope using a ZEISS instrument. Micro-hardnesses in both the surface and bottom layers were analyzed using an HXD-1000TMC LCD Vickers indenter with a spacing of 0.1 mm, a load of 100 gf, and a dwell time of 10 s.

3. Results and discussion

3.1. Surface morphology

Fig. 2 shows the surface morphology of a micro-pit of the Al2024-T351 thick plate with LPF. The micro-pit exhibits square profiles with maximum depths H of 53 μm in the X-direction and 49 μm in the Y-direction, which would induce the large plastic strain in the surface layer. It can improve the

amplitude and depth of compressive residual stresses, which increases the macroscopic bending deformations of Al2024-T351 thick plates. In addition, the positions of the 0.1H distance from the upper limits of square profiles are defined as the measuring datum lines. The intersection spacing between measuring datum lines and square profiles is defined as the laser-shocked size, as shown in Figs. 2(b) and 2(c). Therefore, laser-shocked sizes are 4.6 mm in both the X- and Y-directions. Then, the moving spacing of adjacent spots was set as 3.4 mm in both the X- and Y- directions to ensure the full coverage of laser spots in the shocked area.

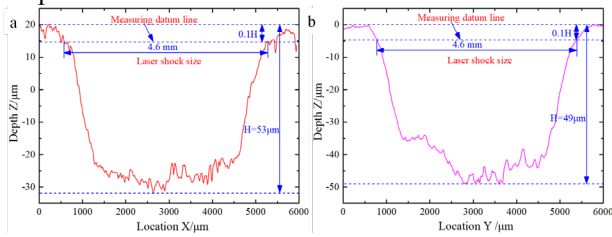


Fig. 2. Surface morphology of a micro-pit of the Al2024-T351 thick plate with LPF: (b) surface profile in the X- direction; (c) surface profile in the Y- direction.

Therefore, overlapping LPF was performed at the top surface of Al2024-T351 thick plates. Fig. 3 shows two-dimensional surface topographies of Al2024-T351 thick plates with and without LPF. Compared with as-received material, surface topography of the Al2024-T351 thick plate with LPF changed obviously, which is ascribed to the greater depth in the overlapped areas of micro-pits. Heights of peaks and valleys for as-received material rang from +0.75 to -1.25 µm, as shown in Fig. 3(a). Heights for LPF-treated samples fluctuate from +4 to -3.5 µm, as shown in Fig. 3(b). Surface-roughness of Al2024-T351 thick plates with and without LPF are measured to characterize the surface quality, as shown in Table 2. Compared with as-received material, the surface-roughness of the Al2024-T351 thick plate is increased by LPF. The surface-roughness value of as-received material is given by Ra = 0.187 µm and Rz = 1.21 µm. For LPF-treated sample, the surface-roughness value is given by Ra = 0.416 µm and Rz = 2.43 µm. It indicated that surface-roughness values of Al2024-T351 thick plates with and without LPF were less than Ra 1.6µm, which can satisfy the industrial requirement.

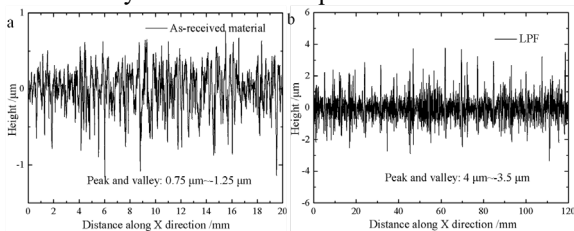


Fig. 3. Two-dimensional surface topographies of Al2024-T351 thick plates with and without LPF: (a) as-received material; (b) with LPF.

Table 2. Surface-roughness of Al2024-T351 thick plates with and without LPF.

State conditions	Ra (µm)	Rz (µm)
As-received material	0.187	1.21
LPF	0.416	2.43

Ra = arithmetic average roughness, Rz = ten-point height

3.2. Macroscopic bending deformation

Surface bending profiles of Al2024-T351 thick plates with multiple LPF impacts are presented in Fig. 4. As clearly shown in Fig. 4(a), bending deformations increase with LPF impacts because of great bending moments. Bending-deformation values at the free end are approximately -2.8 mm for LPF-2, approximately -5 mm for LPF-4, approximately -4.92 mm for LPF-6, approximately -5.36 mm for LPF-8, and approximately -5.72 mm for LPF-10. In addition, surface bending profile in the shocked area after LPF-8 is approximately equal to that after LPF-10, as shown in Fig. 4(b). It indicated that LPF-8 and LPF-10 were close to the saturation process parameter. Physical photographs of the Al2024-T351 thick plate subjected to LPF-8 are presented in Fig. 5. Severe microscopic plastic deformation in the shocked area is generated after LPF-8, as shown in Fig. 5(a). The accumulated severe microscopic plastic deformations lead to a convex macroscopic bending deformation of the Al2024-T351 thick plate with LPF-8, as shown in Fig. 5(b). An arc height of the convex deformation is approximately 2 mm after LPF-8. This is ascribed to great bending moments.

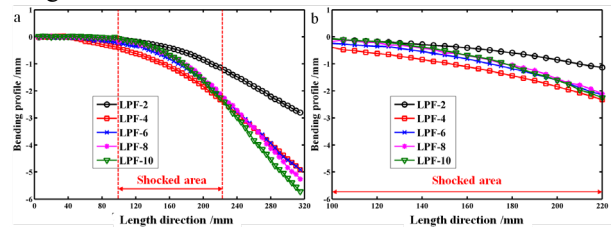


Fig. 4. Surface bending profiles along the length direction of Al2024-T351 thick plates with multiple LPF impacts: (a) overall outlines; (b) partial contours.

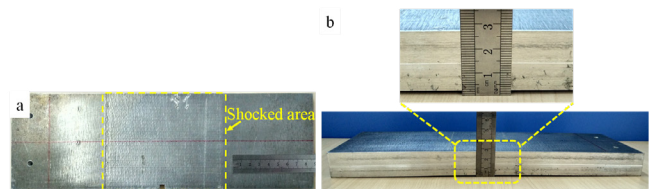


Fig. 5. Physical photographs of the Al2024-T351 thick plate subjected to LPF-8: (a) top view; (b) front view.

The formula of the curvature radius R in the shocked area is as follows [14]:

$$R = \frac{L_c^2}{8h_a} \tag{1}$$

Where $L_c = 120mm$ represents the span length and h_a represents the arc height.

Based on Eq. (1), curvature radii in the shocked area of Al2024-T351 thick plates with multiple LPF impacts are presented in Fig. 6. As shown, curvature radii in the shocked area decrease with LPF impacts. This was attributed to the large macroscopic plastic deformations induced by LPF impacts. Curvature radii in the shocked area are about 9000 mm for LPF-2, 6923 mm for LPF-4, 4865 mm for LPF-6, 4286 mm for

LPF-8, and 3529 mm for LPF-10. These results were similar to those of Dane [12], and indicated that LPF was an effective way of forming.

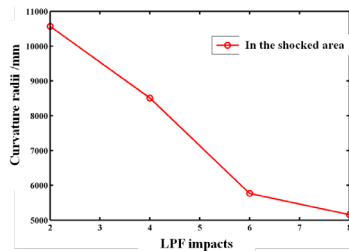


Fig. 6. Curvature radii in the shocked area of Al2024-T351 thick plates with multiple LPF impacts.

3.3. Residual stress

Surface residual-stress distributions of the Al2024-T351 thick plate subjected to LPF-2 are presented in Fig. 7. As shown, compressive residual stresses are generated at both the top and bottom surfaces in the two directions. Compressive residual stresses at the top surface were mainly ascribed to microscopic plastic deformations in the surface layer induced by laser shock wave [15]. In addition, compressive residual stresses at the center of the top surface are greater than those at two sides in the two directions, as shown in Fig. 7(a). This was owing to the larger tensile stress at the center induced by macroscopic bending deformations during the LPF. Compressive residual stresses at the top surface in the X-direction are -266.4 MPa on the left side, -335.3 MPa at the center, and -279.5 MPa on the right side. Compressive residual stresses at the top surface in the Y-direction are -238.2 MPa on the left side, -319.4 MPa at the center, and -308.2 MPa on the right side.

Furthermore, compressive residual stresses at the bottom surface come from extruded plastic deformations in the bottom layer induced by the negative bending moment M during the LPF. The theoretical calculation and experimental values of compressive residual stresses at the bottom surface are as follows:

The formula for the surface line strain ε is as follows [14]:

$$\varepsilon = \frac{t}{2R} \times 100\% \quad (2)$$

Where t represents the plate thickness, and R represents the curvature radius.

According to Eq. (2), the surface line strain at the bottom surface is 0.139% (plate thickness $t = 25\text{mm}$ and curvature radius $R = 9000\text{mm}$). Therefore, according to the elastic modulus of 66.23 GPa (Table 1), the theoretical value of compressive residual stress at the bottom surface is -92MPa. For experimental values, compressive residual stresses at the bottom surface in the X-direction are -46.9 MPa on the left side, -61.8 MPa at the center, and -82.4 MPa on the right side, as shown in Fig. 7(b). Compressive residual stresses at the bottom surface in the Y-direction are -96.8 MPa on the left side, -62.7 MPa at the center, and -79 MPa on the right side. In a word, experimental values are close to the theoretical value.

It was well known that fatigue cracks initiated at the surface of the material and compressive residual stresses effectively prevented the fatigue-crack opening and growth during the cycle fatigue loading [16]. Thus, compressive residual stresses at both the top and bottom surfaces induced by LPF could be beneficial to improve the anti-fatigue property of Al2024-T351 thick plates.

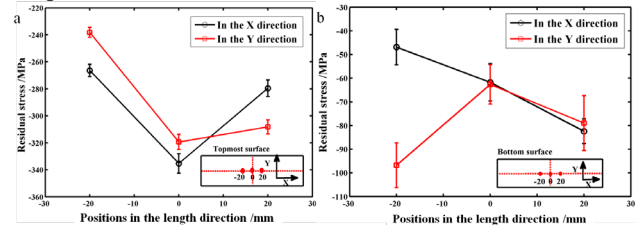


Fig. 7. Surface residual-stress distributions of the Al2024-T351 thick plate subjected to LPF-2: (a) at the top surface; (b) at the bottom surface.

3.4. Microstructure

Microstructures in the surface layer of Al2024-T351 thick plates with and without LPF are presented in Fig. 8. As shown, there are severe plastic deformation (SPD) and minor plastic deformation (MPD) layers with and without LPF. Compared with the as-received material, more deep affected layers are generated by LPF in both the SPD and MPD layers. This was ascribed to the high pressure and the great speeding depth of the laser shock wave. Similar results have been reported [17]. Thicknesses of the as-received material induced by the rolling loading are approximately 820 μm in the SPD layer and approximately 888 μm in the MPD layer, as shown in Fig. 8(a). LPF-induced thicknesses are approximately 946 μm in the SPD layer and approximately 959 μm in the MPD layer, as shown in Fig. 8(b). Additionally, compared with the as-received material, smaller average grain sizes are observed in both the SPD and MPD layers of Al2024-T351 thick plates subjected to LPF-2. Average grain sizes of the as-received material are 72.34 μm in the SPD layer and 131.23 μm in the MPD layer. LPF-induced average grain sizes are 71.88 μm in the SPD layer and 130.22 μm in the MPD layer.

Moreover, microstructures in the bottom layer of Al2024-T351 thick plates with and without are presented in Fig. 9. As shown, there are SPD and MPD layers with and without LPF. Compared with the as-received material, more deep affected layers are generated by macroscopic bending deformations induced by LPF in both the SPD and MPD layers. This was attributed to the severe plastic strain in the bottom layer induced by the negative bending moment M after LPF-2. The Rolling loading induces the following thicknesses in the as-received material: approximately 362 μm in the SPD layer and approximately 725 μm in the MPD layer, as shown in Fig. 9(a). LPF-induced thicknesses are approximately 720 μm in the SPD layer and approximately 750 μm in the MPD layer, as shown in Fig. 9(b). Additionally, compared with the as-received material, smaller average grain sizes are observed in both the SPD and MPD layers of Al2024-T351 thick plates subjected to LPF. Average grain sizes of the as-received material are 58.69 μm in the SPD layer and 111.12 μm in the MPD layer. LPF-

induced average grain sizes are 57.33 μm in the SPD layer and 110.68 μm in the MPD layer.

The results indicated that LPF could induce refined grains in both the surface and bottom layers of Al2024-T351 thick plates, which could be beneficial to improve the mechanical properties.

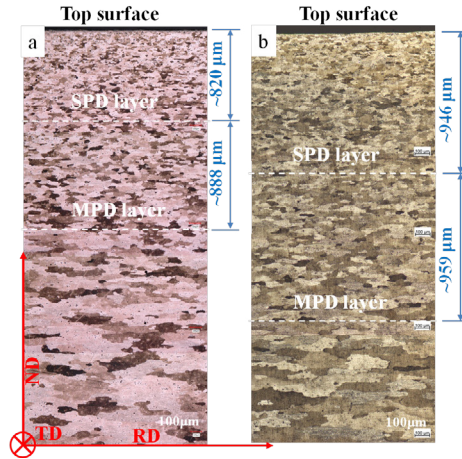


Fig. 8. Microstructures in the surface layer of Al2024-T351 thick plates with and without LPF: (a) as-received material; (b) LPF-2.

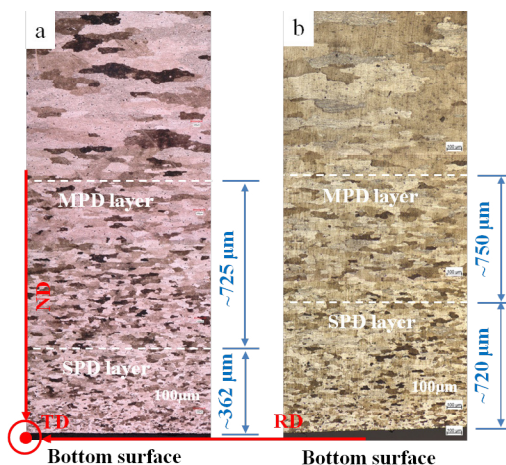


Fig. 9. Microstructures in the bottom layer of Al2024-T351 thick plates with and without LPF: (a) as-received material; (b) LPF-2.

3.5. Micro-hardness

Micro-hardnesses in depth of the Al2024-T351 thick plate subjected to LPF-2 are presented in Fig. 10. As shown in Fig. 10(a), the micro-hardness of the substrate material is approximately 140 HV, and the surface micro-hardness of the Al2024-T351 thick plate subjected to LPF-2 is approximately 166 HV, representing an improvement of 18.6%. According to the Hall-Petch formula, the improvement of the micro-hardness represented the grain refinement and high dislocation densities, which could be beneficial to improve the fatigue life of metals [18]. Additionally, micro-hardnesses in depth are approximately gradient-decreased in the surface layer and tend to be stable at a depth of approximately 2.1 mm, owing to the laser shock-wave attenuation and the reduction of the plastic strain. Moreover, as clearly shown in Fig. 10(b), micro-hardnesses in the bottom layer are slightly greater than that in

the substrate material. Thus, LPF can improve the micro-hardnesses in both the surface and bottom layers of the Al2024-T351 thick plate.

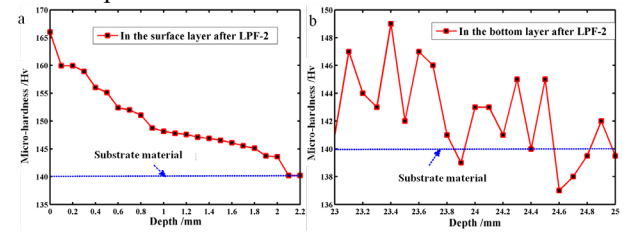


Fig. 10. Micro-hardnesses in depth of the Al2024-T351 thick plate subjected to LPF-2: in (a) the surface layer and (b) the bottom layer.

4. Conclusion

Macroscopic bending deformations and mechanical properties were investigated for Al2024-T351 thick plates subjected to multiple LPF impacts. The following conclusions were drawn:

LPF induced the square micro-pits with the depths of 53 μm in the X-direction and 49 μm in the Y-direction. Laser-shocked sizes were 4.6 mm in both the X- and Y- directions. Therefore, overlapping LPF induced the surface roughness of the Al2024-T351 thick plate from $R_a = 0.187 \mu\text{m}$ for the as-received material to $R_a = 0.416 \mu\text{m}$.

Overlapping LPF induced the macroscopic bending deformations of Al2024-T351 thick plates. Curvature radii in the shocked area decreased with LPF impacts and were about 3529 mm for LPF-10.

Compressive residual stresses were generated at both the top and bottom surfaces of Al2024-T351 thick plates with overlapping LPF. In addition, compressive residual stresses at the center of the top surface were greater than those at two sides in the two directions. Experimental values of compressive residual stresses at the bottom surface were close to the theoretical value.

Compared with the as-received material, more deep affected layers and smaller average grain sizes were observed in the SPD and MPD layers at both the top and bottom surfaces with LPF-2.

Surface micro-hardnesses were increased from approximately 140 HV for the as-received material to approximately 166 HV for LPF-2. Affected depth in the surface layer after LPF-2 was approximately 2.1 mm. Micro-hardnesses in the bottom layer were slightly greater than that in the substrate material.

Acknowledgements

This research is supported by the National Natural Science Foundation of China (No. 51875542, 51975084), Civil Aircraft Research Projects (No. MJ-2016-F-16), General assembly pre-research project (No. KZ011708), Aviation Fund (20185425009).

References

- [1] Edwards KR, Edwardson SP, Carey C, Dearden G, Watkins KG. Laser micro peen forming without a tamping layer. *Int J Adv Manuf Tech* 2010;47:191-200.
- [2] Hu YX, Zheng XW, Wang DY, Zhang ZY, Xie YF, Yao ZQ. Application of laser peen forming to bend fibre metal laminates by high dynamic loading. *J Mater Process Tech* 2015;226:32-39.
- [3] Hu YX, Xu XX, Yao ZQ, Hu J. Laser peen forming induced two way bending of thin sheet metals and its mechanisms. *J Appl Phys* 2010;108:073117-073117-7.
- [4] Ocana JL, Morales M, Garcia-Ballesteros JJ, Porro JA, Garcia O, Molpeceres C. Laser shock microforming of thin metal sheets. *Appl Surf Sci* 2009;255:5633-5636.
- [5] Yoshihiro S, Kiyomitsu Y, Wataru Y, Hiroyasu U. Microparts processing using laser cutting and ultra-short-pulse laser peen forming. *J Mater Process Tech* 2015;219:230-236.
- [6] Hu YX, Luo MS, Yao ZQ. Increasing the capability of laser peen forming to bend titanium alloy sheets with laser-assisted local heating. *Mater Design* 2016;90:364-372.
- [7] Hu YX, Li Z, Yu XC, Yao ZQ. Effect of elastic prestress on the laser peen forming of aluminum alloy 2024-T351: Experiments and eigenstrain-based modeling. *J Mater Process Tech* 2015;221:214-224.
- [8] Shen NG, Ding HT, Wang QH, Ding H. Effect of confinement on surface modification for laser peen forming without protective coating. *Surf Coat Tech* 2016;289:194-205.
- [9] Hackel LA, Harris F. Contour forming of metals by laser peening. EP, 2002.
- [10] Hackel LA, Halpin JM, Harris FB. Pre-loading of components during laser peen forming. EP, 2003.
- [11] Hammersley G, Hackel LA, Harris F. Surface prestressing to improve fatigue strength of components by laser shot peening. *Opt Laser Eng* 2000;34:327-337.
- [12] Dane CB, Hackel LA, Harris F, Francis D. Recent progress in laser technology for industrial laser peening. 4th International Conference on Laser Peening, Madrid, Spain 2013.
- [13] Cao ZW, Xu HY, Zou SK, Che ZG. Investigation of Surface Integrity on TC17 Titanium Alloy Treated by Square-spot Laser Shock Peening. *Chinese J Aeronaut* 2012;25:650-656.
- [14] Garipey A, Larose S, Perron C, Bocher P, Levesque M. On the effect of the orientation of sheet rolling direction in shot peen forming. *J Mater Process Tech* 2013;213:926-938.
- [15] Zhang H, Yu CY. Laser shock processing of 2024-T62 aluminum alloy. *Mat Sci Eng A-Struct* 1998;257:322-327.
- [16] Lu JZ, Zhang L, Feng AX, Jiang YF, Cheng GG. Effects of laser shock processing on mechanical properties of Fe-Ni alloy. *Mater Design* 2009;30:3673-3678.
- [17] Kopp R, Schulz J. Flexible sheet forming technology by double-sided simultaneous shot peen forming. *Cirp Ann-Manuf Techn* 2002;51:195-198.
- [18] Zhang YK, Lu JZ, Ren XD, Yao HB, Yao HX. Effect of laser shock processing on the mechanical properties and fatigue lives of the turbojet engine blades manufactured by LY2 aluminum alloy. *Mater Design* 2009;30:1697-1703.

11th CIRP Conference on Photonic Technologies [LANE 2020] on September 7-10, 2020

Experimental research on CFRTP-Al alloy laser butt joining

Junke Jiao^{a,b*}, Yiyun Ye^b, Shaohui Jia^b, Zifa Xu^b

^aSchool of Mechanical Engineering, Yangzhou University, Huayang west Road 196#, Yangzhou 225127, China

^bNingbo Institute of Materials Technology and Engineering, Chinese Academy of Sciences, Zhongguan Road 1219#, Ningbo 315201, China

* Corresponding author. Tel.: +86-574-86688270; fax: +86-574-86382329. E-mail address: jiaojunke@nimte.ac.cn

Abstract

Joining Al alloy with CFRTP has received significant attention because of its potential application in automobile, aviation industry. Lots of works have been carried out on CFRTP-metal lap welding. However, there is little work focused on CFRTP-Al alloy laser butt-welding. To improve the strength of the CFRTP-Al alloy butt joint, microtextures were prepared on the Al alloy surface by pulsed lasers and a PA resin layer with a proper thickness was added in the CFRTP-Al alloy interface. Six factors and five levels orthogonal experiments were designed and carried out. The joint strength with different welding parameters was examined and the joint fracture interface was detected. The result showed that with the proper welding parameters the melting PA resin flows into the microtextures of the Al alloy and a mechanical anchoring was produced, and a butt joint with the strength about 12MPa can be obtained.

© 2020 The Authors. Published by Elsevier B.V.

This is an open access article under the CC BY-NC-ND license (<http://creativecommons.org/licenses/by-nc-nd/4.0/>)

Peer-review under responsibility of the Bayerisches Laserzentrum GmbH

Keywords: Butt joining; Laser welding; Microtextures; CFRTP-Al alloy joint

1. Introduction

Carbon fiber reinforced thermoplastic (CFRTP) has a good prospect in automobile, aviation owing to its good characters such as light weight, high strength, fatigue resistance and corrosion resistance [1,2]. Aluminum alloy (Al alloy) have been widely used in the light manufacturing of new energy vehicles and aerospace [3] due to its low density and high strength. To this end, realizing a high-quality connection between CFRTP and Al alloy is one of the key problems in the lightweight manufacturing of advanced aircraft, new energy vehicles and rail transit. At present, the method to realizing the CFRTP-Al alloy connection includes the mechanical fastening, the bonding and the welding. Among them, the mechanical fastening is mature and reliable, but the weight of the workpiece is high and it is easy to form stress concentration. The bonding is practical and simple, but the environmental adaptability is poor, and the joint is easy to fail under the cold and hot alternating load [4]. Laser welding has the characteristics of non-contact, good welding quality and easy to realize automation, which has been widely used in the industrial field.

In recent years, lots of works have been carried out on the connection mechanism, process optimization, defects control and strength improvement on CFRTP-metal laser welding. Jung et al. [5, 6] realized the lap welding of CFRTP and the stainless steel, the Al alloy and the galvanized steel successively by using laser heat conduction welding method, and investigated the influence of process parameters on the connection strength. Roesner et al. [7, 8] machined grooves with width of 40 μ m and depth of 50 μ m on the surface of metal by pulse lasers, which makes the shear strength of CFRTP-metal lap joint increases to 24MPa. Tan et al. [9] [10] found that a chemical bond formed at the lap joint can effectively improve the strength of the joint by chromium plating on the stainless steel surface. Huang et al. [11] realized laser lap welding of PMMA and 304 stainless steel, and found that welding speed and the laser pulse duration are the two key parameters influencing the welding strength of the sample. Jiao et al. made a detailed and in-depth study on the lap welding of metal and CFRTP material [12-15], established a thermal contact finite element model of laser welding of CFRTP stainless steel, realized the effective prediction of the thermal effect in the welding process, and found that the micro texture

treatment on the metal surface and the addition of resin layer with appropriate thickness can greatly improve the strength of the CFRTP-metal joint, and the highest strength of the lap joint is about 37.5Mpa.

At present, researches of CFRTP-metal connection mainly focused on the lap welding, but there is almost no research on CFRTP-metal butt welding. The reason maybe is that the butt welding joint is relatively difficult to achieve and the joint strength needs to be further improved. However, the CFRTP metal butt welding joint is often encountered in the industry. In the lightweight manufacturing of some advanced aircraft parts, the butt joint cannot be replaced by the lap joint. Therefore, it is very important to carry out the exploration and research on the CFRTP-metal butt welding technology, and improve the joint strength. In this paper, the technology of laser butt welding of CFRTP-Al alloy is studied. The mechanism of the laser butt welding, the influence of welding process parameters on the joint strength, the failure form of the joint are analysed.

2. Experiment design

The principle of CFRTP-Al alloy butt welding is shown in Figure 1. The high-speed rotating laser beam heats the Al alloy surface, and the generated heat transmits to the interface. The added PA and the CFRTP matrix melts, and the molten resin flows into micro-textures on the Al alloy surface under the external clamp pressure. Then, the CFRTP-Al alloy butt joint formed in the cooling process. This experiment was carried out on a laser welding system, and this system mainly includes a 4000W continuous fiber laser set, a robot, a rotating laser welding head, the welding clumper, etc.

The rotating motor equipped with the welding laser head drives the optical lens to rotate the laser beam at high speed, and ABB Robot controls the direction of the laser head movement. Under the joint action of the two, a spiral scanning path is formed to realize laser high speed rotary welding. Compared with linear welding, this laser high speed rotary welding can effectively reduce the heat damage to Al alloy caused by laser local heating [13], reduce the porosity of the joint, and improve the fatigue life of the joint.

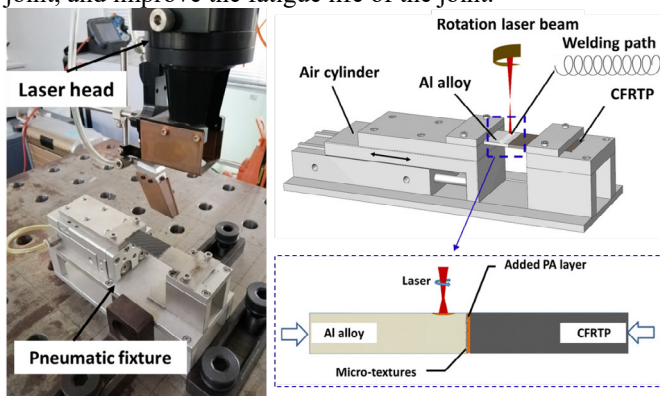


Fig.1. CFRTP-Al alloy butt joining setup

In addition, in order to further reduce the local thermal damage of the laser heat source to the Al alloy, the positive defocus laser was used in the welding process, and the argon concentration of 99.99% was used as the protective gas to

prevent the surface oxidation of the Al alloy. In addition, microtextures on the surface of Al alloy was prepared by nanosecond pulse laser before welding. The power of the laser is 100W, the wavelength is 1064nm, the pulse frequency is 20kHz, and the pulse width is 72ns. After welding, the tensile strength, microstructure and welding temperature of the sample were characterized by universal material testing machine, SEM and temperature recorder.

Table 1. Thermophysical parameters of materials

Material	Density/ (kg.m-3)	Capacity/ (J.Kg-1.°C-1)	Conduction/ (W.m-1.°C-1)	Melting point /°C
PA	1150	2500	0.25	215-225
T700	1760	712	6.5	3000
Al alloy	2800	860—1320	130	475-635

Both the dimension of CFRTP and the Al alloy used in the experiment are 50mm × 25mm × 2mm. The CFRTP material is consisted by the PA resin and the T700 continuous carbon fibers, the volume content of the PA is about 50%. The thermophysical parameters of CFRTP and the Al alloy is shown in Table 1. Before the experiment, the CFRTP surface was polished and cleaned and then dried in a drying oven at 35 °C for 8 hours. Microtextures were machined by using nanosecond pulse laser on the Al alloy surface. According to the previous experiments, the appropriate parameters were used for microtextures processing [14], and regular microtextures on the Al surface was shown in Figure 2.

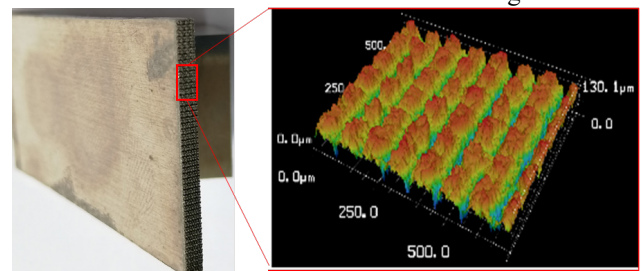


Fig.2. Microtextures on the Al alloy surface

Table 2. Configuration of experiment parameters

Factors Levels	p/W	v/(mm.s-1)	A/mm	f/Hz	Pr/MPa	Δf/mm
	1	250	2	0.6	10	0.1
2	300	4	0.8	20	0.2	30
3	350	6	1.0	30	0.3	35
4	400	8	1.2	40	0.4	40
5	450	10	1.4	50	0.5	45

In the process of laser butt welding of CFRTP and Al alloy, the main factors affecting the heat distribution at the joint include laser power (p), welding speed (v), amplitude (A) and frequency (f) of the rotational laser beam, clamp air pressure (Pr) and laser defocusing amount (Δf). In order to further fully characterize the influence of these various factors and simplify the experiment, the orthogonal experiment method was used to design the experiment. According to the previous experimental results, the range of each parameter was selected as in Table 2 and the six factors and five levels orthogonal experiment was

designed as in Table 3.

Table 3. The welding parameters

Number	p/W	v/(mm.s-1)	A/mm	f/Hz	Pr/MPa	Δf/mm
1	250	2	0.6	10	0.1	25
2	250	4	0.8	20	0.2	30
3	250	6	1.0	30	0.3	35
4	250	8	1.2	40	0.4	40
5	250	10	1.4	50	0.5	45
6(D)	300	2	0.8	30	0.4	45
7(A)	300	4	1.0	40	0.5	25
8	300	6	1.2	50	0.1	30
9(C)	300	8	1.4	10	0.2	35
10	300	10	0.6	20	0.3	40
11	350	2	1.0	50	0.2	40
12	350	4	1.2	10	0.3	45
13	350	6	1.4	20	0.4	25
14	350	8	0.6	30	0.5	30
15	350	10	0.8	40	0.1	35
16	400	2	1.2	20	0.5	35
17(B)	400	4	1.4	30	0.1	40
18	400	6	0.6	40	0.2	45
19	400	8	0.8	50	0.3	25
20	400	10	1.0	10	0.4	30
21	450	2	1.4	40	0.3	30
22	450	4	0.6	50	0.4	35
23	450	6	0.8	10	0.5	40
24	450	8	1.0	20	0.1	45
25	450	10	1.2	30	0.2	25

3. Results and discussions

3.1. Joint strength

After laser joining, the normal strength of the CFRTP-Al alloy joint was examined by using the electronic universal testing machine. The CFRTP-Al alloy butt joint test sample was shown in Figure 3. From this figure, it can be seen that the maximum normal strength of sample A is about 12MPa.

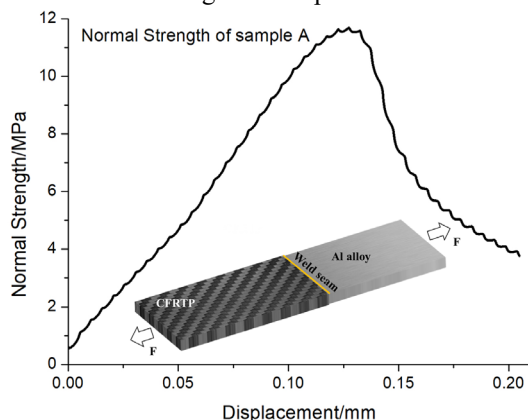


Fig.3. The joint normal strength of sample A

In order to study the influence of welding parameters on the CFRTP-Al alloy joint strength, joint strength test of sample as in Table 3 was carried out, and the maximum strength for each sample is shown in Figure 4. These samples can be divided into four different groups. For group I, the joint strength is larger than 10MPa. For group II, the joint strength is larger than 5MPa but smaller than 10MPa. For group III, the joint strength is smaller than 5MPa but larger than 0MPa. For group IV, the joint strength is about 0MPa. One sample is taken from each group for further analysis, which is 7, 17, 9 and 6, and is recorded as A, B, C, D respectively.

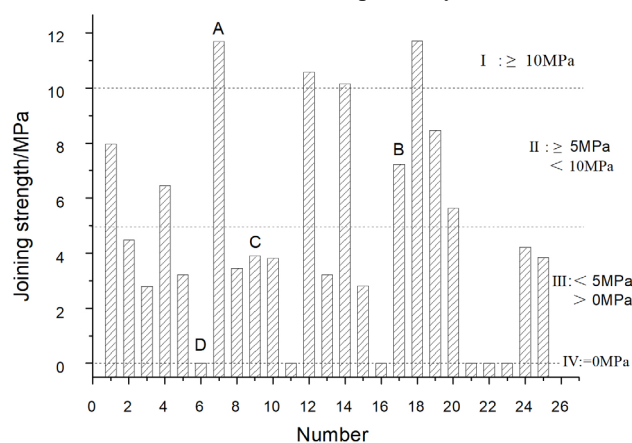


Fig.4. Joint strength for each sample in table 2

With the proper welding parameters such as those for number 7(A), a high quality CFRTP-Al butt joint can be obtained (Fig.5a). However, with the no proper welding parameters such as those in number 6(D), 11, 16, 21, 22 and 23, so much heat was generated that the CFRTP PA resin matrix was over melted or even burned, and the butt welded joint was not formed well (Fig.5b). The joining strength for those joints is about 0MPa.

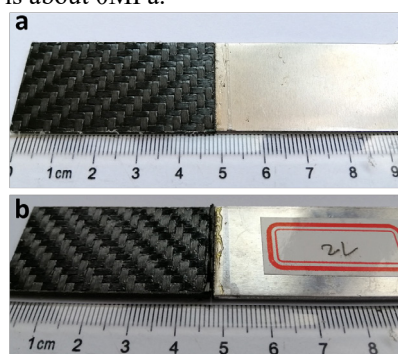


Fig.5. (a) Butt joining of sample A; (b) Butt joining of sample D

3.2. Joint failure mechanism

In order to further clarify the influence mechanism of the joining parameters on the CFRTP-Al alloy joint strength and the joint failure mechanism, the fracture morphology of sample A, B, C was tested by using SEM after strength test.

Figure 6 shows the joint surface morphology of sample A joint after strength test. From the figure, it can be seen that there are a large number of torn carbon fiber wires and resins on the

surface of Al alloy (Fig.6a). The melting resin filling into the microtextures, and a good combination of PA resin and metal surface was realized. On the other hand, a large area of broken fiber, and a large area of tear on the surface of CFRTP (Fig.6b). In this case, the PA resin melts fully and high connection strength joint between the CFRTP and the Al alloy was obtained, which is about 12MPa. Therefore, the fracture interface of the joint is the surface layer of CFRTP, and the failure mode of the joint is the tearing of CFRTP matrix.

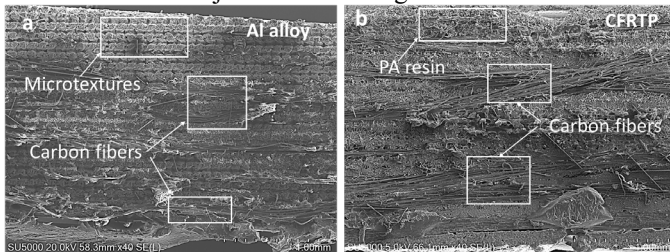


Fig.6. The fracture morphology of sample A

Figure 7 shows the surface morphology of sample C joint. From this figure, it can be seen that the melted resin coverage in the lower half of Al alloy surface (Fig.7a) is uniform. It is due to the complete melting of the resin during welding, and the melted PA resin flows into the microtextures. However, the thickness of the melted added resin on the upper half of the metal surface is lower than that in the lower half, which because of the lower conducted heat and lower melting degree. There is also a large amount of curly PA resin in the upper half of the metal surface, which is pulled-out from the microstructures in the normal strength test process. The surface of CFRTP (Fig. 7b) is covered by a large amount of resin. Some of the resin is torn from the surface of CFRTP, which means that the added PA layer has a high melting degree and bonding with metal and CFRTP surface well during the welding processing. However, the resin have some thermal damage such as some pores, which resulting in weak strength of the joint, the joint strength is about 7.2MPa. In this case, the tearing surface of the connecting joint is the added resin layer.

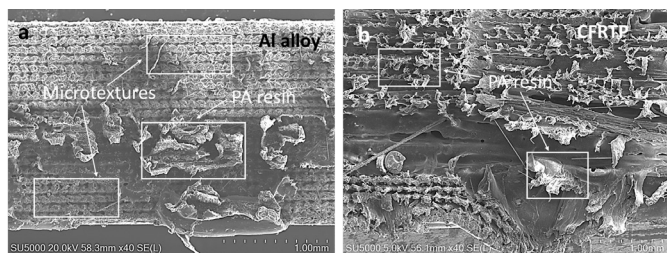


Fig.7. the fracture morphology of sample B

Figure 8 shows the surface morphology of sample D joint. From the figure, it can be seen that a large number of resins are adhered to the upper half of the Al alloy surface (Fig.8a), and the surface is smooth. This is because the added resin layer is not completely melted due to insufficient heat input during the welding process. There is a small amount of resin on the surface of the lower half of the Al alloy surface, and there is almost no residual resin in the microtextures. A small amount of resin remained in the upper half of CFRTP, but there was no obvious tear damage on the surface of CFRTP (Fig.8b). This is

because the melting degree of the added PA layer is very low during the welding process, the Al alloy and the CFRTP does not bond well with each other, and the joint strength is very low, which is about 3.9MPa. In this case, the joint tearing surface is the joint surface of resin and CFRTP.

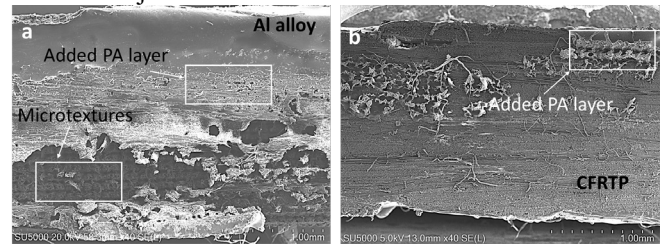


Fig.8. the fracture morphology of sample C

4. Conclusions

The CFRTP-Al alloy butt joining was realized by using laser welding technology. The influence of process parameters on joint normal strength was studied, and the failure form of joint were analysed. Some conclusions were obtained as bellow.

(1) The joint strength and the failure mode of CFRTP-Al joint was influenced greatly by the total energy input in the joining process. As the amount of energy input is too large, the CFRTP PA resin matrix will be over melted or even burned, and the joint strength is about 0MPa. As the heat input is too small, the resin will not melt enough, the joint strength is very low and the fracture interface of the joint is the joint surface of resin and CFRTP. As the heat input is appropriate, a good welding joint can be formed with the largest welding strength, the fracture interface of the joint is the surface layer of CFRTP, and the failure mode of the joint is the tearing of CFRTP matrix.

(2) Under the welding process parameters of laser power 400W, welding speed 4mm/s, mixing amplitude 0.6mm, mixing frequency 40Hz and clamp air pressure 0.5MPa, the maximum normal strength of the CFRTP-Al alloy joint can be obtained, which is about 12MPa.

(3) The failure modes of CFRTP-Al alloy butt joints are mainly the surface tear, resin added tear, resin Al alloy interface fracture. And the highest strength joint can be obtained as the failure modes is the CFRTP surface tear.

Acknowledgements

This work is supported by the Youth Innovation Promotion Association Chinese Academy of Sciences under grant No. 2017343.

References

- [1] Kenneth C C, Neil G. Reversibly assembled cellular composite materials. *Sciences* 2013; 341(6151):1219-1221.
- [2] Luo Yifeng, Luo Ximin. Recent advances in special fibers and composites used in modern aircraft. *China Textile Leader* 2018; 1:61-67.
- [3] Dursun T, Soutis C. Recent developments in advanced aircraft aluminium alloys. *Materials and Design* 2014; 56:862-871.
- [4] Zhou Li, Qin Zhiwei, Liu shan. Advances in thermoplastic resin matrix composite bonding technology. *Materials Reports* 2019;

- 33(19):3177-3183.
- [5] Jung K W , Kawahito Y, Takahashi M. Laser direct joining of carbon fiber reinforced plastic to zinc-coated steel. *Materials and Design* 2013; 47:179-188.
 - [6] Jung K W, Kawahito Y, Takahashi M. Laser direct joining of carbon fiber reinforced plastic to aluminum alloy. *Journal of Laser Application* 2013; 25(3):1-6.
 - [7] Roesner A, Scheikb S, Olowinskya A. Laser Assisted Joining of Plastic Metal Hybrids. *Physics Procedia* 2011; 12:370-377.
 - [8] Roesner A, Olowinsky A, Gillner A. Long term stability of laser joined plastic metal parts. *Physics Procedia* 2013; 41:169-171.
 - [9] Tan Xianghu, Shan Jiguo, Ren Jialie. Effect of Cr plating on shear strength and interfacial bonding characteristics of low carbon steel /CFRTP laser joint. *Acta Metallurgica Sinica* 2013; 49(6):751-756.
 - [10] Xianghu Tan , Jing Zhang , Jiguo Shan. Characteristics and formation mechanism of porosities in CFRTP during laser joining of CFRTP and steel. *Composites: Part B* 2015; 70: 35–43.
 - [11] Huang Yijie, Gao Xiangdong, Zheng Qiaoqiao. PMMA laser welding with 304 stainless steel. *Transactions of the China Welding Institution* 2018; 39(12):067–070, 076.
 - [12] Junke Jiao, Zifa Xu, Qiang Wang. CFRTP and stainless steel laser joining: Thermal defects analysis and joining parameters optimization. *Optics and Laser Technology* 2018; 103:170-176.
 - [13] Jia Shaohui, Jia Jianping, Jiao Junke. Experimental and simulation study on laser stirred welding of carbon fiber reinforced thermoplastic composites/aluminum alloy. *Chinese Journal of Lasers* 2019; 46(7):0702006.
 - [14] Junke Jiao, Shaohui Jia, Zifa Xu. Laser direct joining of CFRTP and aluminium alloy with a hybrid surface pre-treating method. *Composites: Part B* 2019; 173:106911.
 - [15] Junke Jiao, Yiyun Ye, Shaohui Jia, Zifa Xu. CFRTP-Al alloy laser assisted joining with a high speed rotational welding technology, *Optics and Laser Technology* 2020; 127:106187.

11th CIRP Conference on Photonic Technologies [LANE 2020] on September 7-10, 2020

Hybrid laser joining of RTM acrylic glass fiber composite with stainless steel

B. Cárcel^{a*}, S. López^a, A.C. Cárcel^b, P. Gerard^c

^a*Tecnoclad Laser Solutions, Av. Benjamin Franklin 12-15, Paterna 46980, Spain*

^b*Universitat Politècnica de Valencia, Cno. De Vera s/n, Valencia 46010, Spain*

^c*Arkema - Groupement de Recherche de Lacq, Lacq 64170, France*

* Corresponding author. Tel.: +34 634881061; E-mail address: info@tecnoclad.com

Abstract

Mechanical strength of metal-polymer hybrid joints (Steel AISI304 – Glass fiber reinforced acrylic composite) by laser joining has been analyzed, considering the effect of different input parameters: geometry of the metal textured surface, processing temperature or laser irradiation times. Likewise, temperature in the metal-composite interface was measured and related with mechanical properties. Fracture analysis has shown the predominance of cohesive failure in the fracture for this joining configuration. Lap shear strength was strongly dependent on surface texturing, temperature and irradiation time. Optimization of the process allowed to obtain fully cohesive failure with shear strength over 20MPa, comparable to structural adhesive joints.

© 2020 The Authors. Published by Elsevier B.V.

This is an open access article under the CC BY-NC-ND license (<http://creativecommons.org/licenses/by-nc-nd/4.0/>)

Peer-review under responsibility of the Bayerisches Laserzentrum GmbH

Keywords: Laser joining, hybrid polymer-metal, acrylic composite, LAMP, laser structuring

1. Introduction

There is an increasing demand for lightweight and multifunctional components made of hybrid composite materials for the transport industry.

One of the main challenges in this field is the need to join metallic to polymeric parts in hybrid structures. Joining of metals to plastics is not a new topic; conventional joining techniques such as adhesive bonding and mechanical fastening are mature procedures [1]. These conventional techniques, however, have some disadvantages. In the case of mechanical fastening, these disadvantages include, stress rising, long joining time owing to the requirement of hole-drilling and employment of external fasteners. Adhesive bonding frequently applies environmentally harmful or health-endangering chemicals and requires long curing periods, which increase energy consumption and manufacturing costs [2].

Laser hybrid metal-polymer joining could overcome some the above-mentioned limitations. Laser processing offers advantages over competitive joining processes: one step process, instantaneous bonding, highly localized heating, no vibration, low residual stresses [3] or lower pre-cleaning of the surfaces compared with adhesives [4]. Moreover, the laser heat is transferred directly in the contact zone, leading to very effective employment of energy. Physical or chemical bonding between the parts can be achieved with this technique [5].

Joining metal with polymer is a difficult task due to the different nature of metallic and polymeric materials. The Laser Assisted Metal and Plastic (LAMP) joining was initially developed at the Joining and Welding Institute (JWRI) of Osaka University, and demonstrated the potential for achieving several polymer-metal hybrids between metals and different thermoplastics.

The contribution of surface topography to adhesion cannot only be explained by the higher surface contact. Surface structuring is aimed at increasing contact between polymer and metal and creating geometrical interlocking. Different surface topography at the metallic surface is possible (holes, grooves, irregular patterns) normally in sub-mm-scale. This modification of surface can be by mechanical, chemical, electrochemical or physical processes. Recent research has shown that laser surface treatment allows a flexible manufacturing of the metal surface with bonding strength equal to electrochemical surface pre-treatments [6, 7, 8].

Regarding laser joining process topology, there are two procedural modes for hybrid joints, Transmission joining (TJ) and Heat-conduction joining (HCJ)

In transmission joining mode the laser beam is transmitted through the plastic material and heats the metal joining partner. This leads to an increasing temperature at the boundary layer between plastic and metal. As the temperature increases within the joining zone, the thermoplastic melts and moistens the metal surface. This process can only be applied for thermoplastics that show a high level of transparency for electromagnetic radiation of the laser wavelength.

In heat conduction joining mode the metal surface is irradiated directly by the laser beam. The heat is consequently conducted to the metal plastic interface, which leads to the melting of the plastic partner in the boundary layer. Lightweight Glass fibers (GF) and especially carbon fibers reduce the transparency of the material [9]. Consequently, for highly fiber reinforced thermoplastics, transmission joining is not applicable and the use of the heat conduction joining technique is preferable since it works independently of the fiber volume content of the reinforced polymer.

Laser metal-polymer hybrid joining is still on development, and more applied research is needed to completely understand the physics and nature of the joints and the effect that laser processing conditions and the composition and configuration of materials have on the behavior of these hybrid structures.

2. Experimental procedure.

2.1. Materials and samples

Materials used in this work were stainless steel (AISI 304) and RTM glass fiber reinforced acrylic resin (Arkema Elium® 190), a thermoplastic resin specifically designed for RTM fiber reinforced composites. The dimensions of specimens were 25x80x4 mm for the steel samples and 25x80x3 mm for GF composite samples.

2.2. Laser surface structuring

A ns pulsed laser (Rofin RS 90W) was used for the texturization of surfaces in metallic samples. Laser beam movement was generated by a 2D galvo-scanning system. The area of the structured surface was 25x10mm (Fig. 1.). Texturization of surface consisted of a grid with longitudinal and transversal grooves with a distance between tracks of 0.25mm, similar to other laser structures tested by other authors for different metal-polymer combinations [10,11]. The

morphology of the textured surfaces was analyzed by optical microscopy (Nikon Optiphot) and Scanning Electron Microscopy (SEM JEOL 6300 microscope).

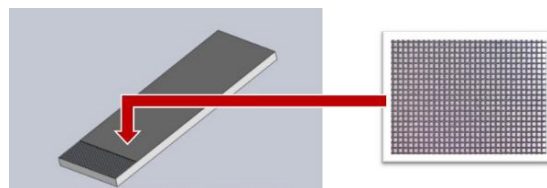


Fig. 1. Laser joining configuration of samples. a) Specimens position and overlap. b) Clamping system.

2.3. Laser joining

Laser joining was performed with a continuous wave (CW) High Power Diode Laser (Laserline LDF4000-60). A rectangular laser spot (dimensions 23x10mm) was used to heat the metal surface in order to achieve joining by heat conduction. Metal sample was placed on the composite sample (textured surface in contact with composite surface), using a 10mm overlap (Fig. 2.a).

A constant pressure was set by applying a tightening torque of 1Nm to the fastening screws of the clamping system (Fig. 2.b).

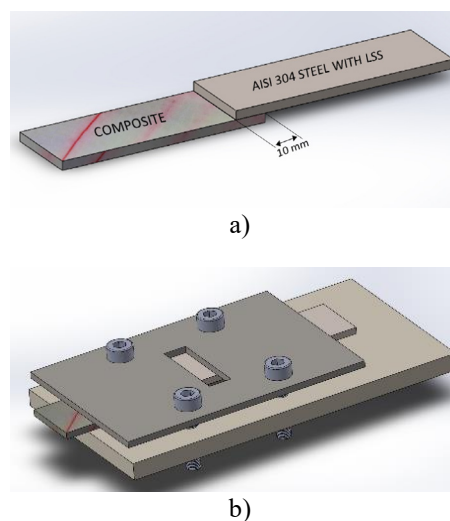


Fig. 2. Laser joining configuration of samples. a) Specimens position and overlap. b) Clamping system.

In this work a novel approach of laser irradiation based on surface temperature instead of laser power was used. Temperature on metal surface was set to a fixed temperature. The temperature signal was measured in real time by a two-color pyrometer, and the controller regulated the laser power by a closed control loop to ensure a constant temperature on the irradiated area (Lascon process controller – LPC03).

A fixed temperature of 400°C on metal surface was set for different irradiation times (3s, 6s, 9s,12s), tested in a single shot joining process (without movement).

The temperature on metal-composite interface was also measured for each joining condition using thermocouples

inserted between metal and composite samples just in the middle of laser irradiation area (Comark 2014 - thermocouples type K).

2.4. Lap shear mechanical testing.

Laser joined samples were tested (lap-shear) with a universal testing machine (Instron 4204). Traverse testing speed was set to 5mm/min.

2.5. Fracture analysis.

After lap-shear testing, fractured surfaces were analyzed by Stereo Magnifier and Scanning Electron Microscopy (SEM JEOL 6300 microscope).

3. Results.

3.1. Structure pattern.

The surface topography of the metal counterpart is a crucial factor to ensure a good mechanical interlocking between metal and composite. When the metal surface modification is performed by laser treatment, distance between tracks and geometry of grooves have been reported to be key factors to reach the best results in terms of joint strength [16].

In this study, a grid pattern (250 μ m distance) obtained after 2 consecutive laser tracks (laser power 120W, frequency 9000Hz, traverse speed 50 mm/s) was performed.

Depth and width of the grooves was 76 μ m and 89 μ m respectively, being this structure similar to optimized results reported by other authors for this kind of joints [10, 11, 16] (Fig. 3).

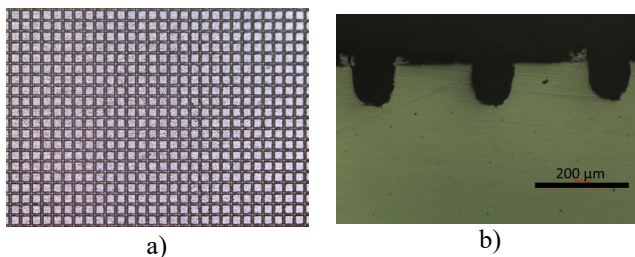


Fig 3. Laser surface structuring. a) Top view. b) Cross section

SEM analysis of structured surfaces revealed a high roughness in the grooves due to the high density of melted metal drops solidified during the structuring process (Fig. 4).

This morphology reveals that a combination of vaporization and melting occurred during the structuring process with ns laser, different from the surface morphology achievable with shorter pulsed laser (ps or fs) micromachining where the melting effect is negligible [12].

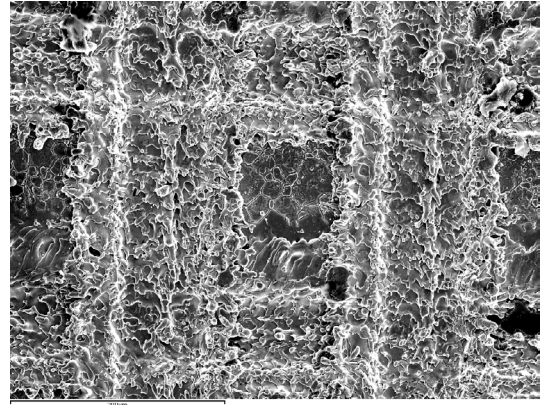


Fig. 4. SEM images of the structure with detailed morphology of grooves.

3.2. Temperature control on metal surface (pyrometry).

Fig. 6. shows a temperature acquisition graph from the pyrometry control system. Once laser shot starts, set temperature (400°C) is reached in 2-3 s, from this moment temperature remains constant ($\pm 2^\circ$ C) by controlling the laser power (closed control loop) until the laser stops irradiating. This behavior is reproduced for all the irradiation times tested.

Notes regarding Fig.5:

- Green line: Set temperature (400°C)
- Red line: Measured temperature (pyrometry)
- Black line: Laser power (%)
- Note that minimum temperature measurable by this pyrometer was 360°C (that is the reason why no lower temperatures are indicated).

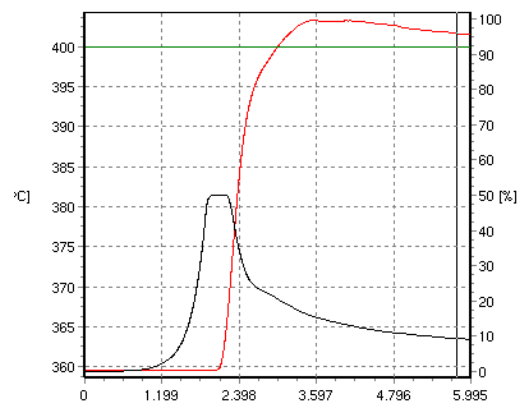


Fig. 5. Temperature acquisition graph (metal surface) from pyrometry control system.

3.3. Temperature on metal-composite interface (thermocouples).

Temperature evolution in the metal-polymer interface is critical to ensure a good adhesion [13]. An excess of temperature drives to a degradation of the polymer, formation of bubbles and lower expected mechanical results.

Alternatively, too low temperature does not allow the polymer to penetrate and wet completely the grooves of the

structured surface. Time is other important input affecting joining behavior. Depending on viscosity of the polymer a minimum dwell time is necessary to allow the polymer to wet and adhere to metal surface.

In Fig. 6. the evolution of temperature for different irradiation times is shown.

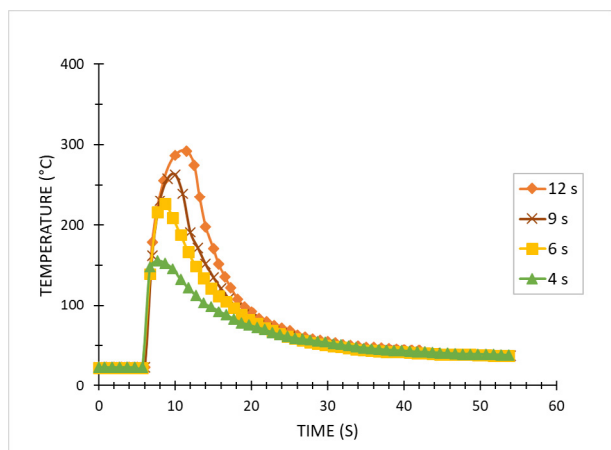


Fig. 6. Evolution of temperature in the metal-composite interface

As expected, the maximum temperature reached at the metal-composite interface increased with laser irradiation time. Table 1 shows the maximum temperature vs irradiation time for each condition.

Table 1. Maximum temperature metal-composite interface.

Laser irradiation time (sec)	Maximum Temperature (°C)
4	156
6	226
9	263
12	298

3.4. Mechanical behavior (Lap Shear Tests).

Lap shear strength results were in the range of 21 to 16 MPa depending on processing conditions. Results followed a gaussian distribution (Fig. 7.), with maximum resistance registered for an irradiation time of 6s (20,7 MPa).

For higher laser shot times (9s and 12s) the mechanical behaviour of the joints decreased progressively. The detrimental effect of an excess of temperature was previously reported in other publications, Bauernhuber [14] found a direct relationship between input parameters and temperature, bubble formation and polymer degradation when joining PMMA and steel.

Lower shear resistance found for shorter irradiation times (4s) is attributed to the low temperature (~150°C) in the interface during joining (see sub-section 3.2) to achieve a correct wetting of the texturized surface. The effect of laser input energy and temperature during laser joining was previously analysed by other authors [15].

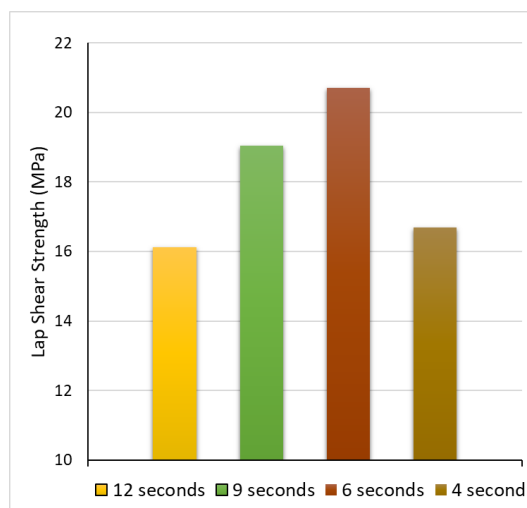


Fig 7. Average lap shear strength for single shot laser joining (Irradiation times: 4, 6 9, 12 s)

3.5. Fracture analysis.

SEM microscopy was used to analyze metal surface after fracture. Back scattered electron imaging allowed to identify the presence of resin and fibers (dark color) in the metal surface (light color).

Resin remained inside the voids of the metal structured surface after fracture (Fig. 8 and 9). This effect proved that resin in contact with metal surface broke by shear stress in a cohesive failure mechanism.



Fig 8. BSE image of fractured surfaces after lap shear tests. General view.

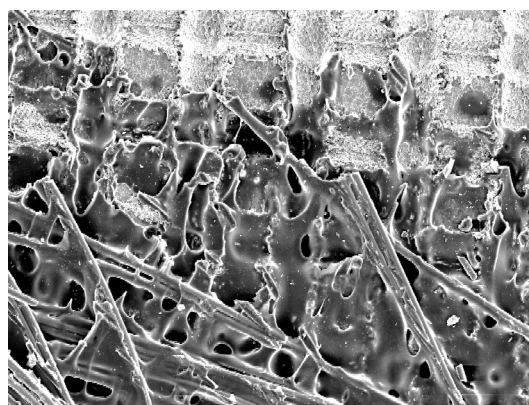


Fig 9. Detailed SEM image of resin and fibers attached to metal surface after fracture.

4. Conclusions.

The possibility of joining RTM fiber reinforced acrylic composites with stainless steel has been analyzed in this work. The optimum lap shear strength was found to be higher than 20 MPa (in the range of structural adhesives).

Laser heat conduction joining based on temperature control for single shot discrete joints has been tested. This approach allows to have a better control of the temperature on metal surface and also on metal-composite interface, being this a critical factor to achieve good bonding behavior. For the acrylic resin analyzed in this work an interface temperature in the range of 220°C was found to be the best in terms of mechanical properties for the acrylic resin analyzed. Higher or lower temperatures showed worse mechanical results due to resin degradation or lack of adhesion respectively.

Analysis of fracture after lap shear tests demonstrated the importance of laser structuring of metal surface previous to laser joining in order to achieve good mechanical results based on a cohesive failure mechanism.

Acknowledgements

This project has received funding from the European Union's Horizon 2020 Research and Innovation Programme under Grant Agreement n° 768737

References

- [1] Amancio-Filho S.T., Dos Santos J.F., Joining of polymers and polymers-metal hybrid structures: recent developments and trends, *Polym. Eng. Sci.* 49 (2009) 1461–1476
- [2] Rauschenberger J., Cenigaonaindia A., Keseberg J., Gubler U., Liébana F. *Lasers in Manufacturing Conference* (2015)
- [3] Yousefpour A., Hojjati M., Immarigeon J.-P., Fusion bonding/welding of thermoplastic composites, *J. Thermoplast. Compos. Mater.* 17 (4) (2004) 303–341
- [4] Tamrin K.F. , Y. Nukman, S.S. Zakariyah, Laser lap joining of dissimilar materials –a review of factors affecting joint strength, *Mater. Manuf. Process.* (2013)
- [5] Katayama, S., Kawahito, Y. Laser direct joining of metal and plastic. *Scripta Materialia* 59, 1247–1250, (2008)
- [6] Rechner, R., Jansen, I., Beyer, E. Influence on the strength and aging resistance of aluminium joints by laser pre-treatment and surface modification. In: *International Journal of Adhesion and Adhesives* 30 (7), 595–601 (2010)
- [7] Kurtovic, A., Brandl, E., Mertens, T., Maier, H. J. Laser induced surface nano-structuring of Ti–6Al–4V for adhesive bonding. In: *International Journal of Adhesion and Adhesives* 45, 112–117 (2013)
- [8] Amend, P., Pfindel, S., Schmidt, M. Thermal joining of thermoplastic metal hybrids by means of mono- and polychromatic radiation (2013)
- [9] Abed, S., Knapp, W., 2007. New Applications of Laser Welding in the Field of Thermoplastic Polymer Composites. *ICALEO Congress Proceedings*, 607–612 (2007)
- [10] E. Rodríguez-Vidal et al. Laser Joining of Different Polymer-metal Configurations: Analysis of Mechanical Performance and Failure Mechanisms. *Physics Procedia* 83 (2016) 1110 – 1117
- [11] Taki K., Nakamura S., Takayama T., Nemoto A., Ito H., 2016. Direct joining of a laser-ablated metal surface and polymers by precise injection molding. *Microsystem Technologies* 22 (1), 31–38
- [12] Sanjay Mishra, Vinod Yadava. *Laser Beam MicroMachining (LBMM) – A review.* *Optics and Lasers in Engineering.* Volume 73(2015), 89-122.
- [13] Schricker K., Stambke M., Bergmann J.P., and Bräutigam K. Laser-Based Joining of Thermoplastics to Metals: Influence of Varied Ambient Conditions on Joint Performance and Microstructure. *International Journal of Polymer Science Volume* (2016)
- [14] Bauernhuber A., Markovitis Investigating Thermal Interactions in the Case of Laser Assisted Joining of PMMA Plastic and Steel. *Physics Procedia* 56 (2014) 811 – 817
- [15] Lambiase F., Genna S. Laser-assisted direct joining of AISI304 stainless steel with polycarbonate sheets: Thermal analysis, mechanical characterization, and bonds morphology. *Optics & Laser Technology* 88 (2017) 205–214.
- [16] E. Rodríguez-Vidal, C. Sanz, C. Soriano, J. Leunda, G. Verhaeghe, Effect of metal micro-structuring on the mechanical behavior of polymer metal laser T-joints, *Journal of Materials Processing Technology*, Vol 229, p668-677 (2016).

11th CIRP Conference on Photonic Technologies [LANE 2020] on September 7-10, 2020

Laser-assisted joining of AISI 304 thin sheets with polymers

Klaus Schricker^{a,*}, Alexander Drebing^a, Marc Seibold^a, Jean Pierre Bergmann^a

^a Technische Universität Ilmenau, Department of Mechanical Engineering, Production Technology Group, 98693 Ilmenau, Germany

* Corresponding author. Tel.: +49-3677-69-3808; fax: +49-3677-69-1660. E-mail address: info.fertigungstechnik@tu-ilmenau.de

Abstract

Laser-assisted metal-polymer joining gains importance in several applications due to the possibility of a direct connection between both materials. Aside from lightweight construction, a direct metal-polymer connection shows a high economic potential especially in large series production, e.g. domestic appliances. Based on this motivation, laser-assisted simultaneous joining of AISI 304 thin sheets (0.3...1.0 mm, X5CrNi18-10) with unreinforced polypropylene (PP) as well as acrylonitrile butadiene styrene (ABS) is carried out. Starting from a generally valid process description based on the energy per sheet thickness, the distortion as well as the mechanical properties are examined, whereby up to 17.4 MPa are reached and the tensile shear strength drops by at least 15 % during alternating climate test (-20...75 °C, 40...75 % rel. humidity). Further investigations under cyclic load showed, that long life fatigue strength ($5 \cdot 10^6$ cycles) is achieved at about 47 % of the initial tensile shear strength.

© 2020 The Authors. Published by Elsevier B.V.

This is an open access article under the CC BY-NC-ND license (<http://creativecommons.org/licenses/by-nc-nd/4.0/>)

Peer-review under responsibility of the Bayerisches Laserzentrum GmbH

Keywords: laser welding; metal-plastic; metal-polymer; hybrid joint; hybrid joining; alternating climate test; fatigue; distortion; PP; ABS

1. Introduction and state of the art

The use of multi-material design is one of the leading issues in engineering constructions regarding functional integration and cost-efficiency. In this field, the combination of metals and polymers is a promising approach to meet the requirements combining materials with different properties. Especially in case of industrial applications for domestic appliances, steel sheets with thicknesses in the range from 0.3 mm up to 1 mm are widely used. On side of the plastic materials, unreinforced polymers are in the focus of interest and large-scale production relies mainly on thermoplastics manufactured by injection molding. Thereby, joining technology is a key parameter in creating multi-material components at a cost-efficient level. Especially in case of metal plastics joints, nowadays mostly adhesives or joining elements are used, with some restrictions, e.g. curing times or stress peaks. The named disadvantages of adhesive bonding and mechanical joining methods are avoided in laser-assisted joining [1] whereby cycle times below 15 s can be addressed.

For laser-assisted joining, the materials are arranged in overlap configuration. The metallic joining partner is heated, and the polymer melts due to heat conduction across the interface between both materials. This melted zone is now able to wet the metal surface and penetrate the surface structures [2]. Depending on the chemical structure of the polymer, the surface morphology and the structuring of the metal surface, a solid joint is formed after solidification [3].

The effect of surface preparation on tensile shear strength [4], distortion [5] and alternating climate test [6] is described for hybrid joints consisting of aluminum and steels with non-reinforced as well as fiber-reinforced polymers. Furthermore, investigations on fatigue are presented for ultrasonic welded [7] and friction welded [8] polymer-metal joints.

However, by addressing applications in the field of domestic appliance technology, thinner material thicknesses (≤ 1 mm) are coming to the fore, for which no comprehensive results are yet available.

In this contribution, laser-assisted joining of AISI 304 thin sheets with polypropylene (PP) as well as acrylonitrile butadiene styrene (ABS) is carried out under consideration of

the requirements of domestic appliance industry. Process-related investigations based on different laser beam powers, joining times and sheet thicknesses provide a general description of the joining process. The mechanical properties are then examined for different sheet thicknesses, whereby constant parameters are used for further investigations regarding alternating climate test and fatigue test. The investigations are concluded with a consideration of the distortion, which is of great interest for the addressed sheet thicknesses of the high-alloy steel below 1 mm and mainly induced due to the thermal joining process. Thus, a description of the relevant parameters and effects for the application of hybrid joints in domestic appliance technology is given.

2. Experimental setup

The experiments were carried out using a diode laser (Laserline LDM 1000) with a mean wavelength of 980 nm and a rectangular focus of 18.3 mm². The beam power P_L was varied from 50 to 150 W. The clamping device used is described in detail in [9]. In terms of fundamental research, spot joints were manufactured in heat conduction joining and based on an overlap configuration of 100 mm length and 40 mm width (see Fig. 1). Joining times τ_L were used from 1 up to 8 s without applying inert gas supply. The high-alloy steel AISI 304 (comparable to X5CrNi18-10, $t_m = 0.3 \dots 1.0$ mm) was chosen as metal joining partner. The metal surface was pre-treated by laser-structuring of grooves with a width of approx. 30 μm and a depth of approx. 40 μm by a pulsed fibre laser (Rofin PowerLine F20, see also [3]). On side of the thermoplastic, polypropylene (PP) and acrylonitrile butadiene styrene (ABS) were used with a thickness of 2 mm regarding the application in domestic appliances.

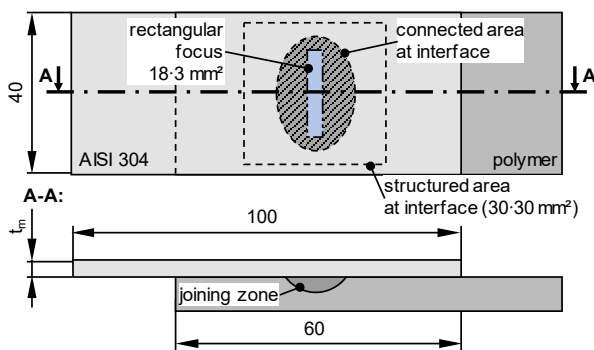


Fig. 1. Joint configuration of the metal-polymer hybrid

Based on the joining process, a melted zone is formed within the plastic material and evaluated regarding the area at the interface which is required to form the joint (see Fig. 1). This connected area was measured in fracture surfaces and depends on the laser beam power P_L , joining time τ_L and steel sheet thickness t_m , wherefore the energy per sheet thickness E^* is introduced as combined parameter in equation (1). Microsections were taken from position A-A.

$$E^* = \frac{P_L \tau_L}{t_m} \quad (1)$$

Mechanical short-term test of tensile shear strength was performed using a universal testing machine (Hegewald Peschke 1455). The fatigue test was carried out on a Sincotec PowerSwing Mot Evolution 50 (stress ratio $R = 0.1$) where the specimen is tested in natural frequency. The test was terminated when 5 million load cycles or a frequency drop of 3 Hz, which indicates the formation of cracks, was reached. Alternating climate tests were performed (-20...70 °C, 45...75 % rel. humidity, duty cycle: 26 h) up to 182 h (7 cycles). Distortion of the steel sheet was measured by photogrammetry using GOM Argus. A uniform size of the measuring field is implemented via number of points within the region of interest (approx. 3.5 million ± 10 %). The selected region prevents the inclusion of measuring errors at the sheet edges.

3. Results and discussion

3.1. Characterization of the joining process

A description of the joining zone is given by the connected area at the interface between steel and polymer. This area represents the load-bearing cross-section in which the polymer penetrates the surface structures. Fig. 2a shows the resulting connected area of PP depending the energy per sheet thickness E^* to provide the general dependency between several sheet thicknesses, joining times and laser beam powers.

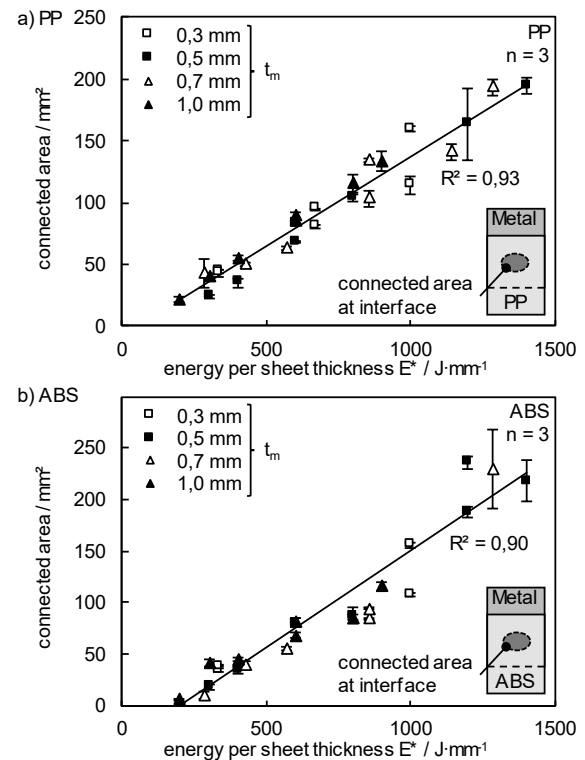


Fig. 2. Connected area at interface depending energy per sheet thickness E^* (for a) PP and b) ABS

The connected area increases linearly with rising E^* , whereby a coefficient of determination R^2 of 0.93 is reached by linear regression. ABS shows a comparable behavior achieving R^2 of 0.90 (see Fig. 2b). This characteristic response can be explained by the relatively low thermal conductivity of the

high-alloy steel, which is why the dissipated heat also increases linearly over the sheet thickness.

The relationship determined in the experiment between the connected area and the energy per sheet thickness E^* can be explained by a simplified physical model (see Fig. 3). The formation of the joint requires an increase in temperature ΔT to the processing temperature of the polymer, for example the end of the melting interval T_{em} for semi-crystalline materials [2]. This temperature also represents the maximum possible expansion of the connected area. The temperature increase can be calculated from the energy input Q , the mass m and the specific heat capacity c_p (2), whereby the energy input is given by the laser beam power P_L multiplied by the joining time τ_L (3). The heated mass can be expressed as volume V times density ρ (4). The results of [11] are utilized to describe the volume V in a simplified way. It was shown by numerical simulation that the isotherms of the process temperature propagate almost perpendicular to the interface for comparable sheet thicknesses and joining times [11]. Thus, the volume V of the heated material is considered simplified by the connected surface A multiplied by the sheet thickness t_m .

If these findings are plugged in (2) and rearranged according to the connected area A , equation (5) is obtained. Since the processing temperature ΔT , density ρ and specific heat capacity c_p can be assumed to be constant for experiments with the same materials, equation (6) follows: The connected area A is proportional to the ratio of P_L times τ_L to t_m , defined as E^* .

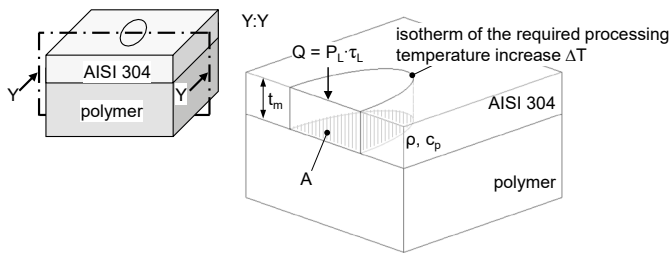


Fig. 3. Schematic representation of the simplified physical model to show the relationship between connected area A and energy per sheet thickness E^*

$$\Delta T = \frac{Q}{mc_p} = \frac{P_L \tau_L}{t_m A \rho c_p} \quad (2) \quad Q = P_L \tau_L \quad (3) \quad m = V \rho = t_m A \rho \quad (4)$$

$$A = \frac{1}{\Delta T \rho c_p} \frac{P_L \tau_L}{t_m} \quad (5) \quad A \sim \frac{P_L \tau_L}{t_m} \quad (6) \quad =: E^*$$

The suitability of the parameter E^* , which is derived directly from the model, has already been shown in Fig. 2 for PP and ABS for an estimation of the connected area. When it is applied simultaneously to both polymers considered, a coefficient of determination R^2 of 0.91 is achieved in the linear regression. From this, it can be concluded that comparable processing temperatures for ABS as for PP must be addressed in the joining process. The simplifications of the model are to be taken into account, e.g. that no enthalpy of fusion is considered, and the propagation of the isotherms is considered in a simplified way. Despite the strong simplifications of the model, it provides useful information regarding the size of the connected area in the joining process.

Further information of the joining zone is obtained by microsections. Fig. 4a depicts the melted area of PP for

different energies per sheet thickness. This area can be clearly determined due to the semi-crystalline character of PP. The melted area size increases with increasing E^* as previously shown for the connected interface.

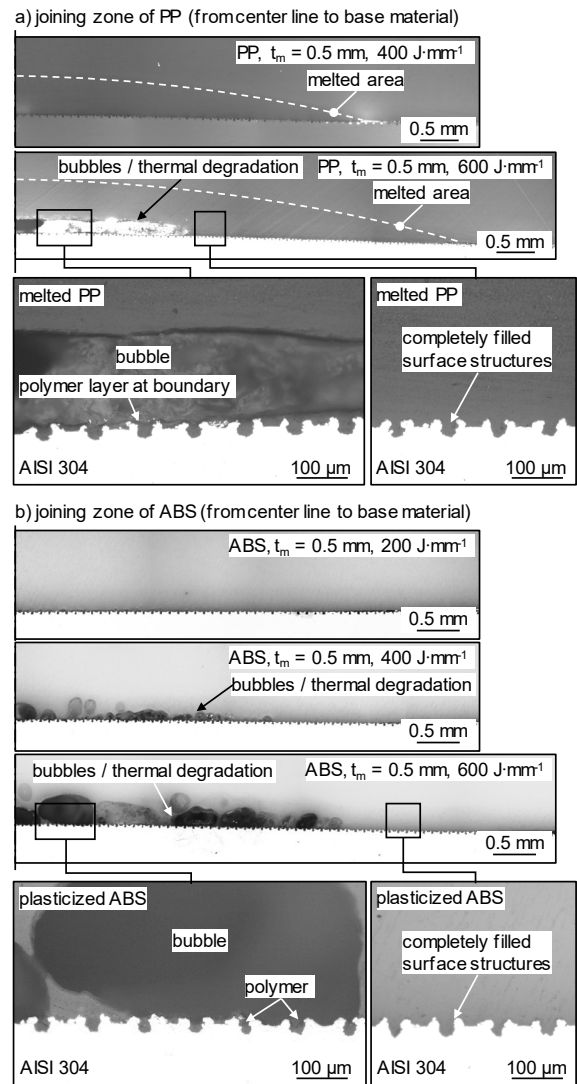


Fig. 4. Microsections from the joining zone for a) PP and b) ABS at different energies per sheet thickness E^*

At the same time, bubbles occur in the middle of the joining zone with increasing energies, caused by decomposition of the polymer in the area of the highest temperatures. For all investigated parameters, the structures in the middle of the joining zone are filled with polymer completely. In the area of bubble formation, a polymer layer appears below the bubbles. In case of ABS (see Fig. 4b), a plasticized area cannot be determined easily due to the amorphous structure of the polymer. However, completely filled surface structures were determined in all cases. In contrast to PP, a larger number of smaller bubbles occur close to the interface for increasing energies. This could be explained by water-based bubble formation by moisture dissolved in ABS. Again, the bubbles are separated from the steel surface by a polymeric layer in most cases. Further information of the mentioned effects are given in [10] for bubble formation with respect to moisture and

thermal degradation as well as in [2] for structure filling depending the temperature distribution in the joining zone.

3.2. Mechanical properties in short-term testing

Mechanical properties were investigated based on selected parameters chosen for achieving a large connected area with simultaneous minimization of defects in the joining zone. For PP and ABS, tensile shear strengths between 15.0 up to 17.4 MPa are achieved, whereby no large effect of sheet thickness and therefore stiffness could be determined with respect to the joint strength (Fig. 5a). Furthermore, the joint failure is generally characterized by a mixed fracture with adhesive and cohesive fracture components.

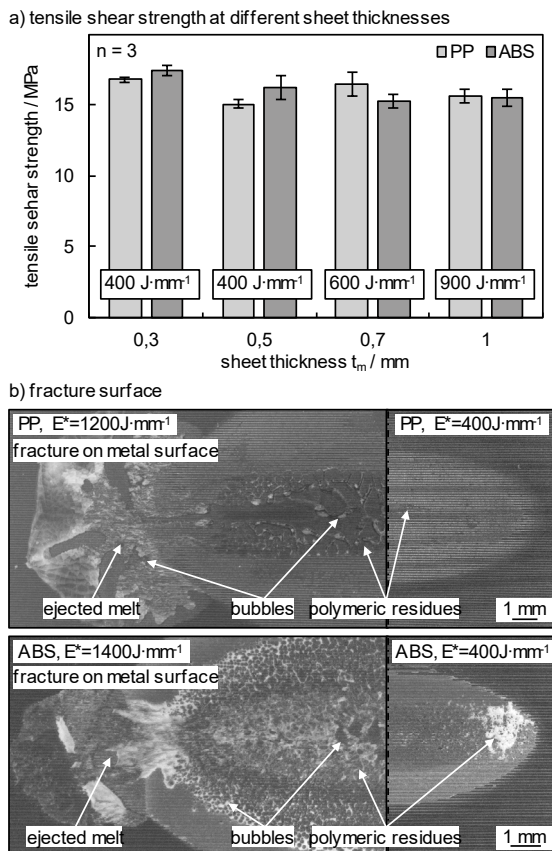


Fig. 5. a) Tensile shear strength at different sheet thicknesses and b) fracture surface at different energies per sheet thickness ($t_m = 0.5$ mm)

Fig. 5b shows typical fracture patterns on the metal surface for different energies per sheet thickness E^* and polymers (left: high E^* , right: low E^*). In case of low energies per sheet thickness, less polymer is remaining on the metal surface. By increasing the energy input, bubble formation is increased which affects the fracture behavior strongly by the failure of the polymer layer between bubbles and steel surface. Therefore, a larger amount of polymer residues at the metal surface can be determined. However, the tensile shear strength is not increased significantly because of the limitation of the load bearing cross section due to the thin polymer layer.

Furthermore, some molten polymer is ejected. The reason for melt ejection is the increase in volume with rising temperature as well as bubble formation, which displaces

plasticized material [2]. In addition, it is reasonable to assume that the clamping parallel to the laser beam prevents uniform melt ejection. Therefore, the ejection occurs in the longitudinal direction of the rectangular focus.

3.3. Durability of the joint

Based on the described parameters, further investigations are carried out on the behavior in alternating climate test and under cyclic load.

Fig. 6a provides the results of the alternating climate test for the AISI 304-PP joints depending on the test duration and sheet thickness. The reference value represents the shown tensile shear strengths between 15 up to 17 MPa depending on the sheet thickness (see chapter 3.2). The strength of the joint decreases by up to 14 % with increasing test duration. Fig. 6b shows half of the joining zone for the reference sample and after a test time of 182 h for the metal surface as well as the joining zone (left: reference, right: after the test). On the surface of the steel, a change in the annealing colors due to corrosion can be seen. The behavior of the joining zone was monitored by photography through the opaque PP. Within the joining zone, a white seam is formed which encircles the entire connected area and indicates a uniform, circumferential detachment of the joint starting from the outside. The detachment is caused by the different thermal expansion coefficient α of the two materials ($\alpha_{PP} \approx 150 \cdot 10^{-6} \text{ K}^{-1}$, $\alpha_{AISI 304} \approx 16 \cdot 10^{-6} \text{ K}^{-1}$). In addition, moisture can ingress into the structures adjacent to the joining zone, expand during the temperature change and thus support the progressive damaging of the joint. Furthermore, secondary crystallization of the polymer due to ageing well above the glass transition temperature ($T_{g,PP} \approx 0 \text{ }^\circ\text{C}$) could also have an effect, since further crystallization is accompanied by shrinkage.

Fig. 6c shows the results for ABS. In principle, a comparable joint behavior can be determined. For sheet thicknesses of 0.3 and 0.5 mm the bond strength decreases by approx. 12 %. At 0.7 and 1.0 mm the result is less distinct. Due to the overlapping standard deviation no significant change can be determined, but the maximum change in tensile shear strength is also in the range of approx. 11 %. The thermal expansion of ABS is reduced compared to PP ($\alpha_{ABS} \approx 100 \cdot 10^{-6} \text{ K}^{-1}$). However, the polymer can dissolve water, which leads to an increase in volume and thus expansion. On the other hand, secondary crystallization cannot occur due to the amorphous structure. Compared with PP, however, it cannot be stated that the different mechanisms lead to a significant change in resistance against alternating climate. Overall, the hybrid joint shows good performance compared to the climatic change test, as the loss of strength of at a maximum of approx. 14 %.

Furthermore, the fatigue behavior of the hybrid joints was investigated exemplarily for an AISI 304-PP joint with a metal sheet thickness of 0.5 mm. Fig. 7 depicts the corresponding Wöhler curve (a) as well as photographs of the joining zone at different numbers of load cycles (b). The samples were tested in natural frequency which was on average 29.80 ± 0.30 Hz on average over all samples.

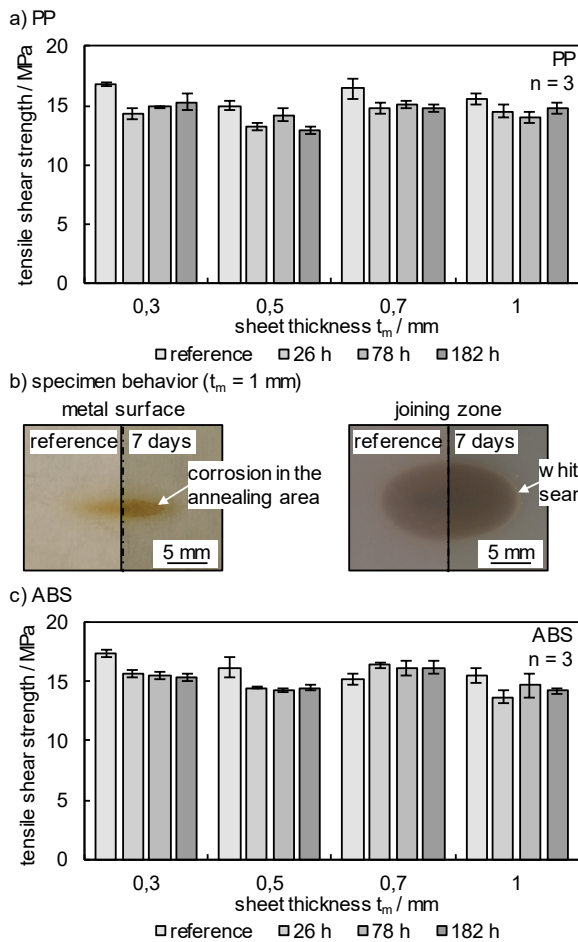


Fig. 6. Results of alternating climate test for a) AISI 304-PP joints with b) related pictures of specimens ($t_m = 1$ mm) and c) AISI 304-ABS joints

The Wöhler curve shows a linear drop of the tensile shear load for an increasing number of cycles n . Based on the reference in the shear tensile test ($n = 0.5$) and a strength of 15 MPa, 5 million load cycles are reliably achieved from 7 MPa onwards. This corresponds to a fatigue strength of approx. 47 % of the initial strength. Compared to other considerations in the state of the art, this value is relatively high, e.g. 35 % is achieved for ultrasonic welded AA5057-PA66CF48 joints [7]. This could be explained by the reduced stiffness of the joint due to the high-alloy steel and the non-reinforced plastic. On the other hand, a progressive damage of the joining zone can be seen starting circumferentially at the edge of the connected area, without the cracks being stopped by reinforcing materials, e.g. fibers (Fig. 7b). In the unloaded case ($n = 0$), the joining zone shows neither visible bubbles nor other damage. A white seam forms around the circumference as the number of load cycles increases, indicating that the composite detached in this area. Therefore, the fracture occurs in the interface between both joining partners for all investigated specimens. In the region of the ejected melt (see chapter 3.2), crack growth progresses faster towards the middle of the joining zone ($n = 2.2 \cdot 10^6$). This detachment of the joining zone progresses with an increasing number of load cycles ($n = 3.8 \cdot 10^6$). This behavior is minimized by a reduction of the load.

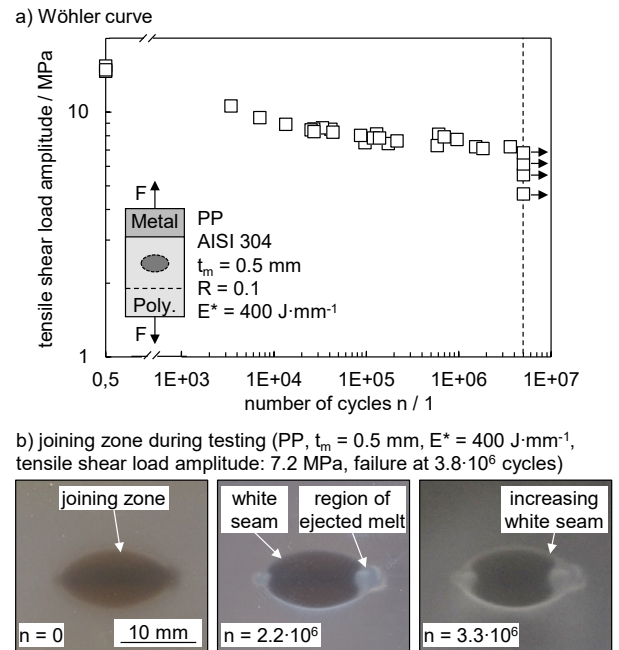


Fig. 7. a) Wöhler curve of AISI 304-PP joint and b) appearance of the joining zone during testing at different load cycles

3.4. Distortion of the joint

In case of the joints between AISI 304 thin sheets and thermoplastics for domestic appliances, thermal distortion is of particular importance due to possible applications in the visible range, e.g. for panels. The investigations were applied exemplarily for ABS as polymer joining partner.

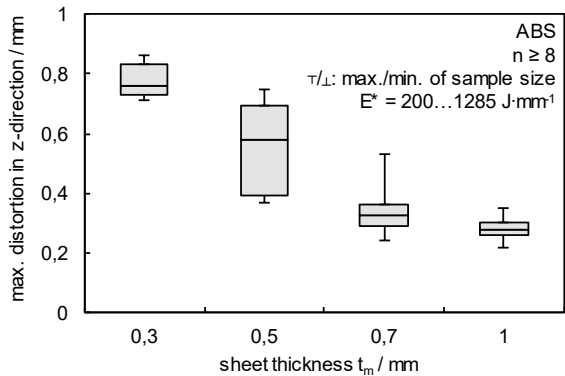
The considerations are carried out for different energies per sheet thickness E^* . Thereby, the material thickness t_m was identified as key criterion on distortion. Further correlations to parameters of the joining process could not be determined. Fig. 8a shows the maximum distortion in z-direction for sheet thicknesses from 0.3 up to 1.0 mm as box plot. In all cases, the maximum value of the height profile was considered for the evaluation. The median as well as the upper and lower quartiles are indicated. The whisker represents the minimum respectively maximum value of the sample size. Therefore, the graph allows a wide range of E^* to be considered and at the same time shows the statistical distribution of the distortion.

It can be determined that the distortion decreases with increasing sheet thickness and thus stiffness from 0.78 mm ($t_m = 0.3$ mm) to 0.28 mm ($t_m = 1.0$ mm). Particularly at 0.5 and 0.7 mm there is a wide spread of values. This effect occurs much more systematically at 0.5 mm, indicated by the larger area of upper and lower quartiles. At 0.7 mm, significantly more values are found in the area between the upper quartile and the maximum whisker, indicating more outliers to larger distortion. At 1.0 mm, the distortion shows less variance and reaches values between 0.22 and 0.35 mm.

Besides the maximum values, the local formation of distortion is not uniform. Fig. 8b shows a characteristic height profile for a sheet thickness of 0.3 mm and an energy per sheet thickness E^* of 200 J·mm⁻¹. On the one hand, this illustrates that the distortion is formed around the joining zone, whereby the connected area itself gains only slight deformation due to

the solid joint bond between polymer and metal. On the other hand, the maxima form in the edge areas of the overlap. The determination of the relationships will be the focus of further investigations.

a) maximum distortion in z-direction for different sheet thicknesses



b) height profile from top view on overlap area (ABS, $t_m = 0.3$ mm, 200 J·mm⁻¹)

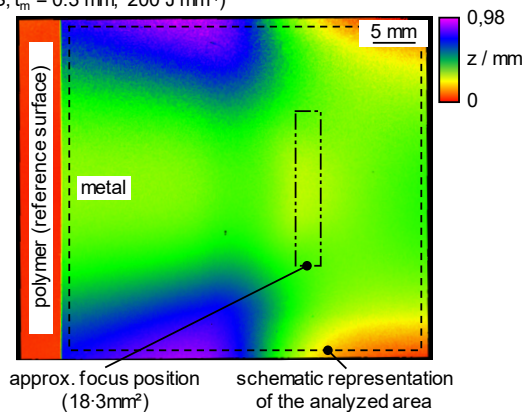


Fig. 8. a) Maximum distortion depending sheet thickness t_m and b) characteristic height profile

4. Summary and outlook

In this paper, the joining of AISI 304 thin sheets with PP and ABS was investigated regarding the requirements of domestic appliance industry.

The growth of the connected area between polymer and metal was described by a linear correlation to the energy per sheet thickness E^* , which was explained by means of a simplified physical model. The appearance of the joining zone as well as the formation of voids was investigated and correlated to the fracture in mechanical testing, whereby 15.0 up to 17.4 MPa were reached as tensile shear strength. Further investigations were applied regarding the durability of the joint. An alternating climate test (-20...70 °C, 45...75 % rel. humidity, duty cycle: 26 h) led to a decrease in tensile shear strength of maximum 14 % after 182 h. In addition, fatigue strength reached approx. 47 % of the initial tensile shear strength ($R = 0.1$). Subsequently, investigations on thermal

distortion were carried out, whereby a significant effect of the sheet thickness on the resulting distortion was shown which occurs strongly location dependent.

Further investigations will address distortion and its influencing variables in order to achieve a model-based description of relevant parameters. Additionally, the separation of effects regarding moisture, thermally induced expansion and secondary crystallization on the performance of the hybrid joints in alternating climate tests will be investigated.

Acknowledgements

The project on which these results are based was supported by the Free State of Thuringia under the number 2016 FE 9077 and co-financed by European Union funds under the European Regional Development Fund (ERDF). Furthermore, the authors would like to thank G. Notni, head of Quality Assurance and Industrial Image Processing Group at Technische Universität Ilmenau, for providing the GOM Argus system as well as M. Neugebauer and M. Lühtrath for carrying out the measurements on distortion.

References

- [1] Katayama S, Kawahito, Y., Niwa, Y, Kubota, S. Laser-Assisted Metal and Plastic Joining. Proceedings of the LANE 2007, Laser Assisted Net Shape Engineering 5, 2007, 41-51.
- [2] Schricker K, Bergmann JP. Temperature- and Time-Dependent Penetration of Surface Structures in Thermal Joining of Plastics to Metals. Key Engineering Materials 809, 2019, 378-385.
- [3] Schricker K, Samfaß L, Grätzel M, Ecke G, Bergmann JP. Bonding Mechanisms in Laser-Assisted Joining of Metal-Polymer Composites. Journal of Advanced Joining Processes 1, 2020, 100008.
- [4] Heckert A, Zaeh MF. Laser surface pre-treatment of aluminum for hybrid joints with glass fiber reinforced thermoplastics. Journal of Laser Applications 27, 2015, S20995-1-S20995-5.
- [5] Wunderling C, Scherm M, Meyer S, Zaeh MF. Thermal distortion in surface pretreatment of metal-polymer hybrids using continuous wave laser radiation. Proceeding of SPIE 10911, High-Power Laser Materials Processing: Applications, Diagnostics, and Systems VIII, 109110A, 2019.
- [6] Heckert A, Singer C, Zaeh MF, Daub R, Zeilinger T. Gas-tight thermally joined metal-thermoplastic connections by laser surface pre-treatment. Physics Procedia 83, 2016, 1083-1093.
- [7] Balle F, Eifler D. Monotonic and Cyclic Deformation Behavior of Ultrasonically Welded Hybrid Joints between Light Metals and Carbon Fiber Reinforced Polymers (CFRP), Fatigue Behaviour of Fiber Reinforced Polymers: Experiments and Simulations, DEStech Publications, 2012, 111-122.
- [8] Goushegir SM. Friction Spot Joining of Metal-Composite Hybrid Structures. Helmholtz-Zentrum Geesthacht, Zentrum für Material- und Küstenforschung, HZG REPORT 2015-5, 2015.
- [9] Schricker K. Charakterisierung der Fügezone von laserbasiert gefügten Hybridverbunden aus teilkristallinen thermoplastischen Kunststoffen und Metallen. Technische Universität Ilmenau, Fertigungstechnik – aus den Grundlagen für die Anwendung 8, 2018.
- [10] Schricker K, Diller S, Bergmann JP. Bubble formation in thermal joining of plastics with metals. Procedia CIRP 74, 2018, 518-523.
- [11] Schricker K., Bergmann JP. Determination of sensitivity and thermal efficiency in laser assisted metal-plastic joining by numerical simulation. Procedia CIRP 74, 2018, 511-517.